Michael Schlüter
Dieter Bothe
Sonja Herres-Pawlis
Ulrich Nieken *Editors*

Reactive Bubbly Flows

Final Report of the DFG Priority Program 1740

Springer

Fluid Mechanics and Its Applications

Founding Editor

René Moreau

Volume 128

Series Editor

André Thess, German Aerospace Center, Institute of Engineering
Thermodynamics, Stuttgart, Germany

The purpose of this series is to focus on subjects in which fluid mechanics plays a fundamental role. As well as the more traditional applications of aeronautics, hydraulics, heat and mass transfer etc., books will be published dealing with topics, which are currently in a state of rapid development, such as turbulence, suspensions and multiphase fluids, super and hypersonic flows and numerical modelling techniques. It is a widely held view that it is the interdisciplinary subjects that will receive intense scientific attention, bringing them to the forefront of technological advancement. Fluids have the ability to transport matter and its properties as well as transmit force, therefore fluid mechanics is a subject that is particulary open to cross fertilisation with other sciences and disciplines of engineering. The subject of fluid mechanics will be highly relevant in such domains as chemical, metallurgical, biological and ecological engineering. This series is particularly open to such new multidisciplinary domains. The median level of presentation is the first year graduate student. Some texts are monographs defining the current state of a field; others are accessible to final year undergraduates; but essentially the emphasis is on readability and clarity.

Springer and Professor Thess welcome book ideas from authors. Potential authors who wish to submit a book proposal should contact Dr. Mayra Castro, Senior Editor, Springer Heidelberg, e-mail: mayra.castro@springer.com

Indexed by SCOPUS, EBSCO Discovery Service, OCLC, ProQuest Summon, Google Scholar and SpringerLink

More information about this series at http://www.springer.com/series/5980

Michael Schlüter · Dieter Bothe ·
Sonja Herres-Pawlis · Ulrich Nieken
Editors

Reactive Bubbly Flows

Final Report of the DFG Priority Program
1740

✎ Springer

Editors
Michael Schlüter (ID)
Institute of Multiphase Flows
Hamburg University of Technology
Hamburg, Germany

Dieter Bothe (ID)
Mathematical Modeling and Analysis
Technical University of Darmstadt
Darmstadt, Germany

Sonja Herres-Pawlis (ID)
Institute for Inorganic Chemistry
RWTH Aachen University
Aachen, Germany

Ulrich Nieken
Institute of Chemical Process Engineering
University of Stuttgart
Stuttgart, Germany

Contents

Introduction

Michael Schlüter

Abstract Research groups throughout Germany have closely worked together in the DFG Priority Program 1740 "Reactive Bubbly Flows" in the fields of process engineering, chemistry, mathematics and fluid mechanics to develop new chemical reaction systems, measurement methods, mathematical models and numerical simulations. Individual results from the different projects as well as interdisciplinary research is presented that have enabled to shed light on the complex interplay between fluid dynamics and chemical reactions and demonstrated the opportunity of tailoring bubbly flows to achieve higher yields and selectivities.

Performing a chemical reaction with high yield and selectivity is one of the main tasks in chemical engineering. For the synthesis of many bulk chemicals such as polymers, coatings, flavours, cosmetics or pharmaceuticals, a gaseous reactant from a bubble must be transferred through a fluidic interface to be intensively mixed with a continuous liquid phase, e.g. in oxidation, hydrogenation or chlorination reactions. Many of these reactions are competitive and the yield and selectivity depend on the contact between reactive and catalytic molecules facilitated by mass transfer, diffusion and mixing. If the reaction is fast, as in many industrial applications, the transport processes in the immediate vicinity of a gas bubble are crucial. With a deep understanding of the interplay between such fluid dynamic time scales and the time scales of competitive reactions, the targeted tailoring of bubbly flows could become possible in order to significantly reduce the formation of undesired by-products and thus save resources, purification steps and waste production.

To gain such fundamental insights into gas–liquid reactions is the topic of this book. It summarises the research work carried out under the priority programme "Reactive Bubbly Flows" funded by the German Research Foundation (DFG) in the years 2014–2020. Twenty research groups throughout Germany have closely worked together in the fields of process engineering, chemistry, mathematics and

M. Schlüter (✉)
Institute of Multiphase Flows, Hamburg University of Technology, Eissendorfer Str. 38, 21073 Hamburg, Germany
e-mail: michael.schlueter@tuhh.de

1

fluid mechanics to develop new chemical reaction systems, measurement methods, mathematical models and numerical simulations to pave the way for tailor-made reactive bubbly flows.

Within this book, a survey of the individual results from the different projects are presented. The last four chapters are dedicated to survey the results from the interdisciplinary research that have enabled to shed light on the complex interplay between fluid dynamics and chemical reactions and demonstrated the opportunity of tailoring a bubbly flow to achieve higher yields and selectivities. A chapter to demonstrate the importance of the results for industrial applications completes the whole work.

Reactive Bubbly Flows—An Interdisciplinary Approach

Michael Schlüter

Abstract The research on reactive bubbly flows requires interdisciplinary collaboration among process engineers, chemists, physicists, and mathematicians. However, collaboration between these disciplines is often difficult due to differences in understanding of terminology and requirements in safety, accuracy, as well as spatial and temporal resolution. To overcome these difficulties and to support the scientists in their collaboration, four main research areas with guiding measures have been defined in the Priority Program "Reactive Bubble Flows" which are organized in a collaboration matrix. This collaboration matrix guides the reader through this book and is intended to provide some orientation.

To get deep insights into reactive bubbly flows, several disciplines have to work closely together. First, process engineers are involved to define the material properties and process conditions relevant for industrial bubbly flows. Secondly, experimentalists need to develop experimental methods and setups to investigate local transport processes and the interplay with chemical reactions. Crucial is the additional expertise of chemists to create and modify chemical reaction systems with appropriate kinetics of competitive reaction steps as well as systems whose reactants concentrations can be detected easily and that can be handled without expensive safety equipment in the laboratory. Finally, mathematicians are indispensable to accurately describe in detail all transport and reaction processes with analytical and numerical methods achieving reliable and transferable models.

All these complementary expertises have been bundled within the priority program 1740 "Reactive Bubbly Flows". To create a platform for intense collaboration, a matrix has been defined and used during the whole program (see Fig. 1).

This matrix should help the reader to navigate within this book and to understand the interdependencies and cross-references more easily.

M. Schlüter (✉)
Institute of Multiphase Flows, Hamburg University of Technology, Eißendorfer Straße 38, 21073 Hamburg, Germany
e-mail: michael.schlueter@tuhh.de

methods \ complexity	SuperFocus Mixer	Taylor bubble	Free rising bubble	Bubbly flows
A Experiments	Chapter 9 Chapter 12	Chapter 8 Chapter 9 Chapter 12	Chapter 9 Chapter 11 Chapter 12 Chapter 13	Chapter 6 Chapter 7
B Simulation and modeling	Chapter 17	Chapter 14 Chapter 15 Chapter 17	Chapter 14 Chapter 15	Chapter 16 Chapter 18
C Chemistry reaction networks	Chapter 3 Chapter 4 Chapter 5 Chapter 9	Chapter 3 Chapter 4 Chapter 5 Chapter9	Chapter 3 Chapter 4 Chapter 5	Chapter 4
D Transfer to industrial reactions in bubbly flows	**Chapter 20**	**Chapter 21**	**Chapter 22**	Chapter 10 Chapter 13 Chapter 19 **Chapter 23**

Fig. 1 Collaboration matrix of the different research groups with assignment of the different chapters in this book

This matrix helps to organize the research program from lower to higher complexity and forces the interdisciplinary collaboration between different research groups by means of guiding measures. The levels of complexity regarding fluid dynamics, mass transfer and chemical reactions reach from single phase mixing and reaction on the micro scale in **SuperFocus mixers** via confined gas–liquid **Taylor bubbles** and Taylor-flows to free rising single bubbles and **bubble swarms** up to **bubbly flows**. All complexity levels need to be investigated in an interdisciplinary effort and from different aspects like **experiments**, **simulation and modeling**, **chemistry reaction networks** and **transfer to industrial reactions in bubbly flows**. To motivate and strengthen the interdisciplinary research, two guiding measures—the **SuperFocus mixer setup** and the **Taylor bubble setup** have been developed and intensively used for the development of chemical reaction systems, the development and improvement of experimental methods and the validation of numerical simulations. In Chapters 3 to 19 of this book, the individual projects within the funding period from 2014 to 2020 of the DFG priority program 1740 "Reactive Bubbly Flows" are presented as a project report. The interdisciplinary research that has been done on the four levels of complexity—"SuperFocus mixer", "Taylor bubble", "free rising single bubbles" and "bubbly flows" are summarized in the last four chapters. These final chapters contain contributions from various research groups dealing with chemical reaction networks, experiments and numerical simulation and underline the great benefit of close interdisciplinary collaboration within this priority program. This

culminates in a joint chapter identifying opportunities for applying the fundamental results of this research to industrial applications and, finally, a chapter focusing on further research needed to push chemical industry towards more sustainable processes.

Control of the Formation and Reaction of Copper-Oxygen Adduct Complexes in Multiphase Streams

Larissa Laurini, Melanie Paul, Alexander Hoffmann, and Sonja Herres-Pawlis

Abstract Bioinorganic copper complexes can activate dioxygen and transfer it to substrates under very mild reaction conditions. By the choice of ligand, the rate of oxygen activation, stability of the Cu/O_2 species and rate of subsequent reaction can be tuned. Moreover, the spectroscopic response for spatially and temporarily resolved investigations can be tailored to the demands within the SPP1740. Based on the guanidine donor function, we developed several generations of guanidine systems for O_2 transfer in the SPP1740, starting with the classic btmgp bisguanidine over fluorescent bisguanidines (based on the toluene backbone) to highly efficient catalytically active aromatic hybrid guanidine systems. These systems allow the efficient transformation of a plethora of phenolic substrates to the corresponding quinones. To trap the highly reactive quinones, we used 1,2-phenylenediamine for the transformation into phenazines which can be isolated. In parallel, we investigated simple ammonia and bisamine systems for their utilization in Taylor bubbles and reaction apparatuses in the SPP. Selected systems have also been studied by stopped flow spectroscopy and in the SuperFocus mixer, as well as theoretical methods for the details of the oxygen activation process. This chapter lays the chemical foundation for the application of Cu/O_2 systems in Chapters "Determination of Kinetics for Reactive Bubbly Flows Using SuperFocus Mixers"–"Investigation of Reactive Bubbly Flows in Technical Apparatuses".

1 Introduction

Already in the planning phase of the SPP1740, we were fascinated by the natural versatility to use dioxygen for a plethora of tasks in biology and chemistry. Especially, copper enzymes are key for biological oxidation reactions. Very often, this goes along with color changes and prominent spectroscopic features detectable by fluorescence, UV/VIS or Raman spectroscopy useful for online monitoring (see Chapters

L. Laurini · M. Paul · A. Hoffmann · S. Herres-Pawlis (✉)
Institute of Inorganic Chemistry, RWTH Aachen University, Landoltweg 1a, 52074 Aachen, Germany
e-mail: sonja.herres-pawlis@ac.rwth-aachen.de

"Determination of Kinetics for Reactive Bubbly Flows Using SuperFocus Mixers"–
"Investigation of Reactive Bubbly Flows in Technical Apparatuses"). For efficient
use in the SPP1740, a chemical reaction system must fulfill several requirements:

- it should have tunable kinetics for oxygen activation and transfer,
- these steps should be traceable by characteristic spectroscopic features in order
  to obtain detailed mechanistic information,
- the mechanism should comprise consecutive and/or parallel reactions with
  competition for the gaseous component,
- the reaction system should be available in scale from 1 L to 1 m^3,
- the system should be not too expensive or toxic,
- the manipulation should be easy and not require a chemical hood.

Our Cu enzyme models fulfill several of these requirements (not all to the same
extent). The biologically used reaction by our Cu enzyme models is the catalytic
conversion of phenols to catechols and finally to quinones (Fig. 1) which are then
submitted to further oligomerization to melanin [1]. The reaction of phenols to cate-
chols is a C–H activation and oxygenation whereas the reaction to the quinone is
simply an oxidation (with water as by-product). Quinones are difficult to isolate
owing to their high reactivity [2]. Hence, we followed the strategy of condensation
of quinones with 1,2-phenylenediamine to obtain the corresponding phenazines (see
Sects. 2.3, 3.1, 3.2 and 3.3).

After pre-SPP studies on guanidine-stabilized Cu/O$_2$ complexes, it was known
that bisguanidines such as btmgp (see Sect. 1.2.1) do not exhibit bioinorganic hydrox-
ylation reactivity whereas guanidine-amine-stabilized species show stoichiometric
hydroxylation of phenols [3]. However, spatially and temporally resolved detection
of the oxygen uptake and substrate oxygenation in flow systems is not possible with
these systems. Hence, new developments within the SPP studies comprise fluores-
cence intensive bisguanidine complexes (see Sect. 2) which—at first sight—did not
convince with their hydroxylation activity [4]. More recent studies revealed their
catalytic activity which are summarized in Sect. 2.3. The combination of sterically
encumbering strong guanidine donors with rather slim amine donors was already
successful to yield a tyrosinase-analogue system in preceeding studies [3]. Hence, we
followed this strategy to combine guanidines with amines and a fluorescent backbone
(so-called hybrid guanidines) to obtain a superior catalytic hydroxylation system
(described in Sect. 3) with unprecedented substrate versatility [5].
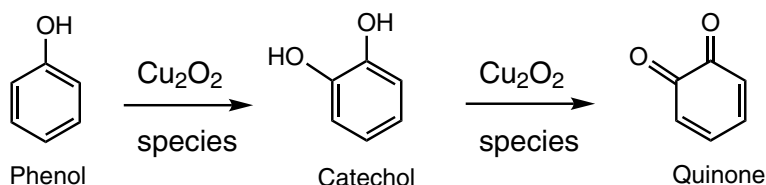
Fig. 1 Tyrosinase-like reaction of phenols to catechols to quinones mediated by Cu$_2$O$_2$ species

1.1 Basics of Cu/O$_2$ Chemistry

Copper dioxygen species are playing an important role for selective oxidation reactions in nature, for example for browning processes of fruits, hair and feathers [6–11]. In the active sites of copper enzymes Cu/O$_2$ species are formed during their reaction with dioxygen prior to the oxidation of organic substrates. Thus in the monooxygenase tyrosinase [12–16], a binuclear μ-η^2:η^2-peroxido copper(II)-adduct (**P**) is formed. During their work on tyrosinase model complexes Tolman and co-workers discovered the alternative formation of a related binuclear Cu(III)-bis-μ-oxido complex (**O**) and the possibility of a chemical equilibrium between these two species [6, 16, 17]. Historically, a trans-μ-peroxido (**^{T}P**) has been synthesized earlier by Karlin et al. but it has not been observed in biological systems [18, 19]. Recently, it was shown that this species is in an equilibrium with the **O** core [20]. Figure 2 shows these equilibria and generalizes some of the possible reactions that can occur when a mononuclear copper(I) complex reacts with dioxygen. Further details of Cu/O$_2$ chemistry have been summarized in several reviews [21, 22].

The reaction pathway starting with Cu(I) complexes and oxygen to the final bis(μ-oxido) species can be investigated by stopped-flow spectroscopic kinetic measurements [20] but a theoretical understanding is key to comprehension of the detailed kinetics. For a long time, real-life systems were too large for full density functional theory (DFT) simulation, but meanwhile, the general comparability of kinetic studies and DFT calculations was proven even for larger systems, e.g. consisting of hybrid guanidine and bisguanidine ligands [23]. The authors investigated the formation of the Cu$_2$O$_2$ species of both real-life systems with low-temperature stopped-flow UV/vis spectroscopy and determined the activation enthalpies and entropies. In the experiment, no superoxido species as intermediate was observed. Furthermore, they had a closer look at the mechanism of the formation of the Cu$_2$O$_2$ species with DFT. The formation of the Cu$_2$O$_2$ species can be divided into two individual reactions: in the first reaction, one Cu(I) complex reacts with dioxygen to a superoxido species. In the following reaction, a further Cu(I) complex reacts with this superoxido species to
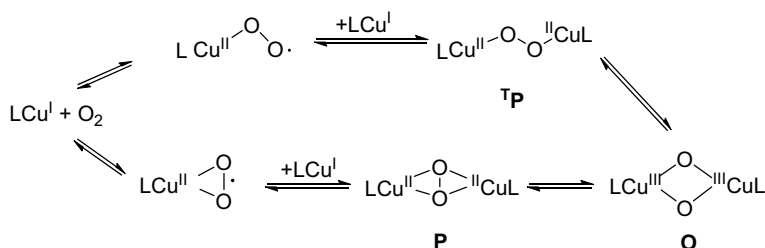
Fig. 2 Known reaction pathways for the formation of copper "dioxygen adduct" complexes (P = side-on peroxido, O = bis-μ-oxido and ^{T}P = trans-μ-peroxido complex) during the reaction of copper(I) compounds with dioxygen (charges are omitted for clarity)
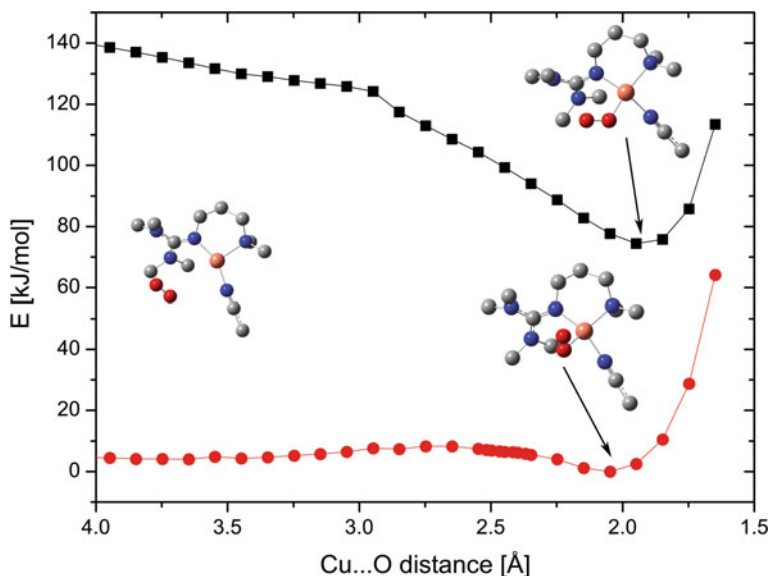
Fig. 3 Reaction pathway of superoxido formation (red: triplet; black: singlet) [23]

the Cu_2O_2 core. These reaction pathways were calculated with DFT (TPSSh/def2-TZVP, PCM, GD3BJ) and are depicted in Figs. 3 and 4. In the calculations of the first reaction, the Cu…O distance of the Cu(I)-acetonitrile precursor and dioxygen were shortened starting with 4 Å distance. The reaction pathway has two possible spin states: the singlet or the triplet state. The resulting energy profiles show a low-lying triplet state of the superoxido species and a low-lying transition state (Fig. 3). The theoretical values of the activation enthalpy and entropy agree with the experimental values. In the second reaction, the Cu…Cu distance was varied starting with 5.8 Å. The formation of the final **O** species (global minimum) goes downhill for both possible spin states without a further transition state (Fig. 4). The singlet **P** species is less stabilized than the **O** core and the triplet **O** core is clearly disfavored. A final stabilization of the singlet **O** species can be estimated by 100 kJ/mol which is in accordance with published data for the protein by Metz and Solomon [24]. The DFT calculated reaction pathways support the experimental kinetic data: the superoxido formation is rate-determining and the following reaction steps are extremely downhill without any relevant transition state, so the reaction is very fast: the superoxido species is not detectable due to the extreme rapid formation of the **O** species.
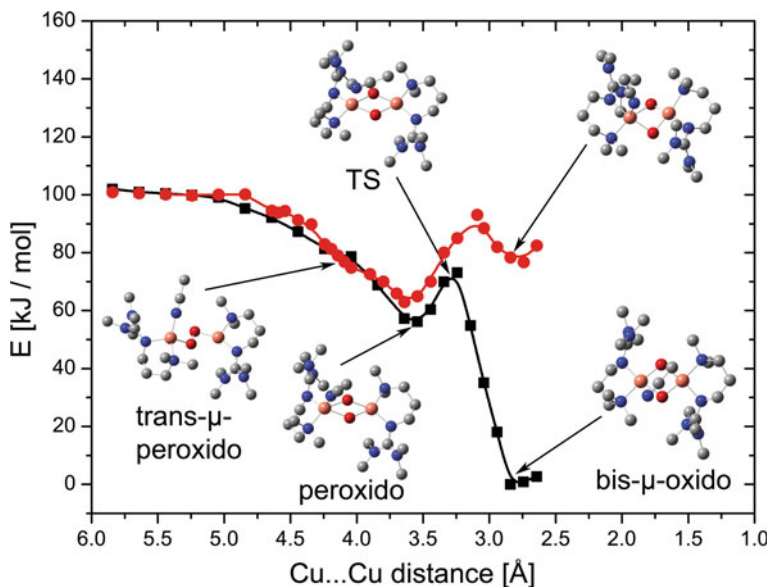
Fig. 4 Reaction pathway of the O core formation (red: triplet; black: singlet) [23]

1.2 Classical Systems

Historically, many N-donor ligand classes have been used in Cu/O_2 chemistry [21, 22]. In the following subchapters, we shed light on those ligand systems which have been found useful in the past for the desired SPP applications.

1.2.1 Btmgp—The First Bisguanidine for Many Applications

A classical ligand system for Cu_2O_2 species is the bisguanidine system btmgp [25]. It proved to be highly useful for luminescence reaction monitoring [26] and also for the application in the SuperFocus Mixer (see Chapter "Determination of Kinetics for Reactive Bubbly Flows Using SuperFocus Mixers") [27]. Two Cu(I) complexes and O_2 form in acetonitrile a bis(μ-oxido)dicopper(III) species (Fig. 5, top). This species possesses an intense orange-red color (depending on the concentration) which makes it useful to colorimetric monitoring. Afterwards the bis(μ-oxido)dicopper(III) species reacts concomitantly to the greenish bis(μ-hydroxido)dicopper(II) complex and the bis(μ-alkoxido)(μ-iodido)-bridged binuclear copper(II) complex in equal amounts [25]. The decay of the Cu(III) complex proceeds as first-order reaction with respect to the Cu(III) complex. In collaboration with the FERMAT consortium, we have examined its colorimetric response in a Hele Shaw cell (Fig. 5, bottom) [28].

In a collaboration with the Küppers group, we have studied the oxygenation of [Cu(btmgp)I] by NMR spectroscopy, namely relaxometry (Fig. 5c) [29]. Here,
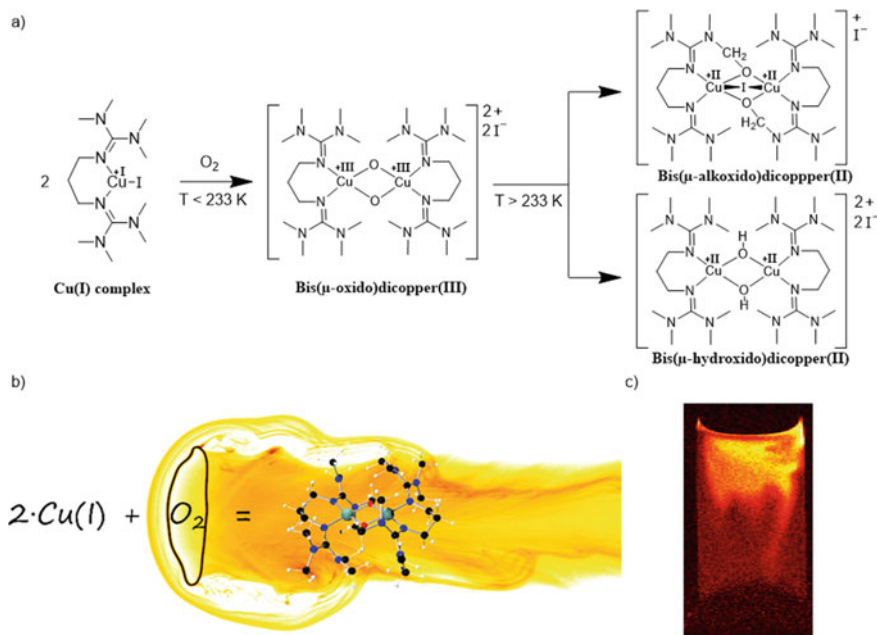
Fig. 5 (**a**) Reaction of a Cu(I) btmgp complex to the bis(μ-oxido) species and subsequent decay reaction; (**b**) colorimetric monitoring of the reaction in a Hele-Shaw cell [28] and (**c**) NMR relaxometry measurements of the formation of Cu(II) at oxygenation of [Cu(btmgp)I] [29]

[Cu(btmgp)I] is well suited since the Cu(I) species is diamagnetic and the final Cu(II) species paramagnetic. The unpaired spin of the Cu(II) ion speeds up the spin relaxation of the direct environment which enables a spatially resolved detection of the oxygenation reaction.

1.2.2 Bispyrazolylmethanes—Steps Towards Catalysis

In parallel, we investigated bis(pyrazolyl)methane copper complexes for oxygen activation and transfer. These tridentate N-donor ligands allow to selectively address peroxido species (in contrast to the guanidines which mostly stabilize **O** core complexes).

In 2013, we reported distinguished hydroxylation activity with the bis(pyrazolyl)methane ligand HC(3-*t*BuPz)$_2$(Py) (Fig. 6) [30]. After formation of the μ-η^2:η^2-peroxidodicopper(II) complex at $T = -78$ °C in dichloromethane (characterized by UV/vis and resonance Raman spectroscopy, cryo-ESI mass spectrometry and EXAFS), addition of different *para*-substituted sodium phenolates (substituted with OMe, Me, F, H, Cl, CO$_2$Me, and CN) resulted in the corresponding *ortho*-catecholates with > 95% yields. Substrates like estrone, *N*-acetyltyrosine ethyl ester and 8-hydroxyquinoline were also effectively converted (yields > 90%).
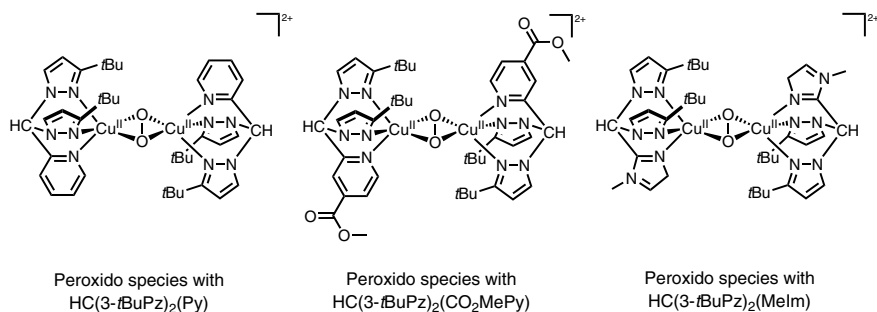
Fig. 6 Bis(pyrazolyl)methane-stabilized peroxido complexes with stoichiometric and catalytic tyrosinase activity

These reactions show a flexibility of this peroxido system toward electron-rich, electron-poor and sterically demanding substrates. The kinetic data for stoichiometric conversions displayed a pseudo-first-order process. The use of higher phenolate concentrations results in a phenolate-independent reaction rate. During hydroxylation, the oxidation is the rate-limiting step since C–H cleavage could be excluded as rate-limiting concerning the experiment with deuterated phenolate [intramolecular competitive kinetic isotope effect of 1.2(2)]. Further kinetic studies showed that electron-poor phenolates were hydroxylated slower (CO$_2$Me: k_{ox} = 0.36 s^{-1}) than electron-rich ones (OMe: k_{ox} = 1.33 s^{-1}), with a Hammett correlation parameter of $-$ 0.99, which indicates an electrophilic aromatic substitution mechanism. This complex system promotes efficient hydroxylation catalysis with biological and non-biological phenols. With *para*-methoxyphenol, we obtained 10 eq. of the corresponding *ortho*-quinone after 1 h, whereas after 24 h, the turnover number (TON) increased to 15 eq. quinone (Table 2). TONs of four after 6 h for estrone, eight after 16 h for 8-hydroxyquinoline (HOqu) and 15 after 16 h for *N*-acetyltyrosine ethyl ester show slightly less reactivity for these more complicated phenolic substrates.

By introducing an ester substituent at the pyridinyl moiety (HC(3-*t*BuPz)$_2$(4-CO$_2$MePy), Fig. 7), we succeeded in a more stable Cu$_2$O$_2$ species (t$_{1/2}$ = 50 min at 20 °C vs. 25 min of the parent peroxide complex without CO$_2$Me group). Moreover, this species showed faster substrate hydroxylation toward *para*-X-phenolates (X = OMe, Me, and CO$_2$Me) [31]. With sodium 4-methoxyphenolate, a k_{ox} value of 2.87 s^{-1} was obtained, which is twice as fast as the parent system without the ester substituent (k_{ox} = 1.33 s^{-1}). We related the faster hydroxylation reaction with the weaker donor strength of the pyridinyl moiety because of the electron-withdrawing ester substituent. The Hammett correlation parameter for this phenolate hydroxylation was calculated to -1.2 and confirmed the electrophilic aromatic substitution mechanism. The catalytic conversion of 8-HOqu with this peroxido complex resulted in the formation of the quinone product (λ = 413 nm), which was monitored via UV/vis spectroscopy. The maximal conversion was achieved within 7.5 min and the TON was calculated to 20. When forming the peroxido complex at room temperature,
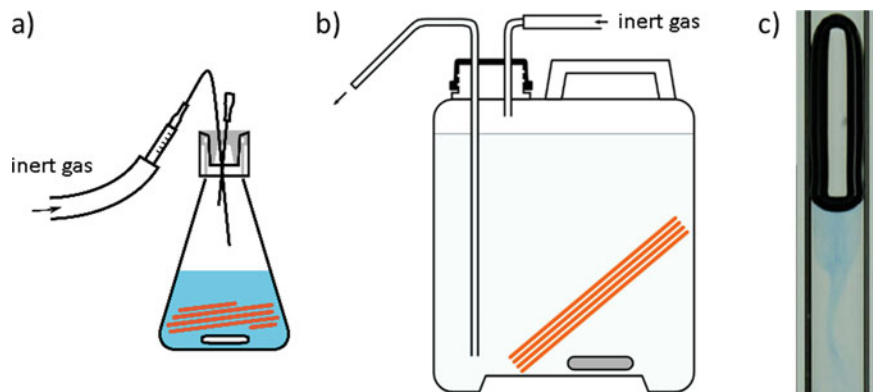
Fig. 7 **(a)** Copper tetraammine complex in an Erlenmeyer flask with septum; **(b)** scheme of the synthesis in a canister with elemental copper; **(c)** Taylor bubble with this system [33]

the substrate reaction is even faster, and maximal product formation was obtained in less than 10 s. Thus, this tyrosinase model was reported to be the fasted and most efficient system published until then. The peroxido complex of a related ligand HC(3-tBuPz)$_2$(1-MeIm) (Fig. 6) with an imidazole moiety instead of the pyridine promotes in stoichiometric reactions the rapid hydroxylation of phenolic substrates [32]. The stoichiometric hydroxylation is faster than with the CO_2Me-decorated system but the catalysis is slower. However, for SPP applications, these systems were too expensive for utilization in large scales and too fast in O_2 activation at room temperature.

1.2.3 Ammonia—The Simpliest Ligand for Large Scales

Since the bis(pyrazolyl)methane ligands are very expensive to produce and their peroxido complexes difficult to obtain in large scales, we targeted in the first SPP phase an inexpensive and simple reaction system which exhibits a fast color change upon oxygenation. Herefor, we utilize copper(I) chloride which forms in aqueous ammonia-containing solution a tetraamminecopper complex. This changes its color from colorless in oxidation state +I (when prepared under exclusion of O_2) to deep blue in oxidation state +II upon oxygenation (Eq. 1).

$$[Cu^{I}(NH_3)_4]^+ (colorless) \xrightarrow{O_2} [Cu^{II}(NH_3)_4]^{2+} (dark\ blue) \qquad (1)$$
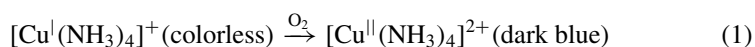
The starting chemicals are easily and low priced available. The CuCl is sensitive to moisture and can be produced from $CuCl_2$ or by purification of commercially available CuCl. Dry CuCl is relatively stable at dry air. This chemical system can be easily synthesized in large scales, e.g. in a 10 L canister (examples in Fig. 7a, b) and a detailed description for the production under simplistic laboratory conditions was developed (e.g. no Schlenk technique available). The rapid color change upon

O_2 contact serves as direct indicator for O_2 in the system as could be observed in a Taylor bubble (Fig. 7c) [33].

The utilization of the ammonia containing solution showed to be a disadvantage since this solution possesses a fluorescence background traced back to production impurities. This prevents the application for Laser Induced Fluorescence (LIF) measurements. Moreover, a well running hood is always needed owing to the corrosive properties of ammonia.

1.2.4 DBED—Simple Ligand Enabling Catalysis

There was a lively discussion about the catalytically active species in tyrosinase since different options are possible including the crystallographically characterized μ-η^2: η^2-peroxido-dicopper(II) core [13], the isomeric bis(μ-oxido)dicopper(III) species and the trans-μ-η^1:η^1-peroxidodicopper(II) complex (Fig. 2). Solomon and Stack et al. reported that they observed no bis(μ-oxido)dicopper(III) species when adding the substrate 2,4-di-*tert*-butylphenol (DTBP) to a solution of the peroxidodicopper(II) species supported by the ligand *N,N′*-di-*tert*-butylethylenediamine (DBED) at −80 °C. However, when going down to −120 °C, an intermediate phenolate-bound bis(μ-oxido)dicopper(III) species was proven by UV/vis, resonance Raman and X-ray absorption spectroscopy [34]. They investigated the oxidation of DTBP through Cu_2O_2 species with DBED (Fig. 8) [34]. Furthermore, they intensively analyzed the copper-oxygen species with bound phenolate, catecholate and semiquinone at −120 and −80 °C and upon addition of acid [35]. In the presence of protons, the colorless Cu(II)-μ-catecholato-μ-OH species turned into a mononuclear Cu(II)-semiquinone species [36]. The phenol hydroxylation with this system proceeded after an electrophilic aromatic substitution mechanism (Hammett constant $\rho = -2.2$) [34]. However, after these groundbreaking studies, they did not discover the catalytic abilities of the DBED system.
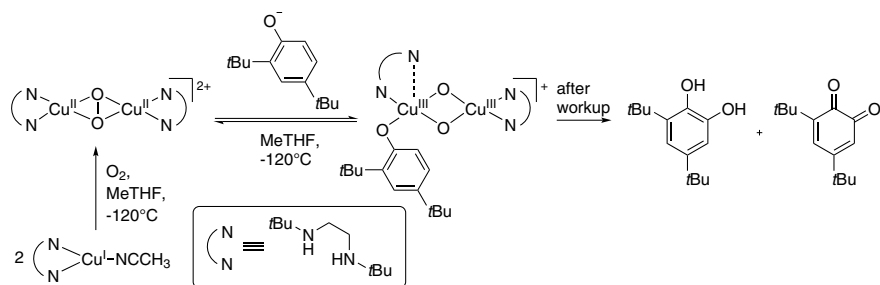
Fig. 8 Phenolate hydroxylation mechanism at −120 °C with a bis(μ-oxido)dicopper(III) species as intermediate [34]
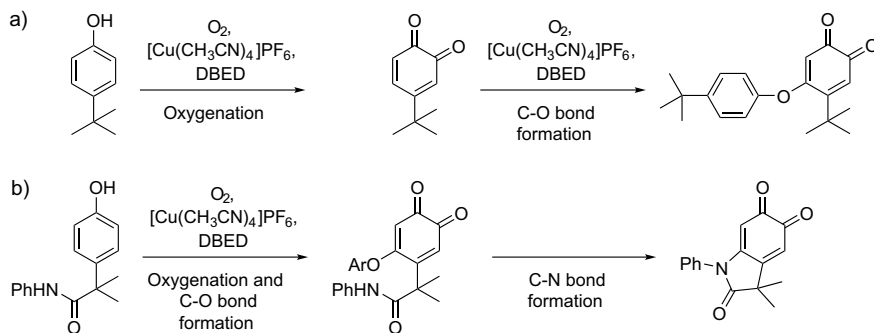
Fig. 9 (**a**) Oxygenation of p-*tert*-butylphenol by Cu/DBED systems with subsequent C−O coupling reaction; (**b**) heterocyclization mediated by Cu/DBED systems starting from acetanilide-substituted phenol as tyrosine analogon [38]

This task was solved by the Lumb group which examined the chemo- and regioselective oxygenation of phenols [37, 38]. In 2014, they found the influence of additional ligand as auxiliary base for the catalytic hydroxylation of *para-tert*-butylphenol to the corresponding quinone and the subsequent coupling with another molecule phenol to the coupled product (Fig. 9a) [39]. In 2016, Lumb et al. reported on the synthesis of oxindoles by performing C–N bond formations, bio-inspired by the melanogenesis [38]. The use of *para*-substituted phenols, where the substituent possesses an ethylene-bridged amine function (e. g. an acetanilide) led to the formation of indole derivatives as it is known from the cyclization of L-dopaquinone within the melanin biosynthesis. The reaction of the acetanilide-substituted phenol (Fig. 9b) resulted in the presence of [Cu(CH₃CN)₄]PF₆, DBED and O₂ in the C−O coupled quinone. Subsequently, a substitution reaction at the aromatic ring exchanged the phenoxy substituent to the N-atom of the acetanilide substituent. With this cyclization, the oxindoloquinone is formed as end product. Hence, DBED qualifies as exciting system for oxygenation reactions and following oxidation and coupling reactions.

2 Novel Bisguanidine Copper Systems for O₂ Activation and Transfer

2.1 *Bisguanidine Toluene Systems for O₂ Activation*

In search of a ligand system to achieve a wide range of applications from small-scale to industrial-scale, bisguanidine ligands offer a time-efficient and cost-effective synthesis, guaranteeing a facile access to large amounts of ligand, necessary for large scale applications like bubbly flows. Bisguanidine ligands consist of two strong basic

guanidine N-donor units linked by a spacer group. Variation of guanidine unit or spacer group affects donor properties, steric demands and functionality of the ligand [40]. Thereby simple, linear spacers as well as larger, electron-rich aromatic groups can be used. N-donor units can be divided into peralkylated guanidine groups such as tetramethyl guanidine and cyclic guanidine moieties such as dimethylethylene guanidine, in which the guanidine is bridged by an ethylene unit. The functional groups can be controlled by the choice of the reactants. The standard bisguanidine synthesis is a one-step reaction between a diamine, directing the design of the spacer group, and a Vilsmeier salt, defining the form of the guanidine units [41]. Until now, the fluorescence properties of bisguanidine systems have only been studied to a limited extent [26] but for the SPP, fluorescence serves as spatial-resolved monitoring method. Hence, the newly designed tol-system consists of two guanidine units bridged by a toluene spacer. Tol-systems can be synthesized using any kind of Vilsmeier salt in combination with 2-aminobenzylamine in the standard guanidine synthesis [4, 42]. 2-Aminobenzylamine is inexpensive (2.50 €/g) and purchasable by various suppliers [43–45]. The electron-rich π-system of the toluene bridge extends the spectrum of analytical methods from UV/VIS, Raman and IR by fluorescence spectroscopy [42]. Thus, the desired goal of an easy and cost-effective accessibility in combination with a variety of spectroscopically methods could be achieved as will be described in the following sections.

2.2 Synthesis of Bisguanidine Toluene Systems for O_2 Activation

The suitability of tol-systems for dioxygen activation was investigated by the use of two different types of tol-ligands with the TMG-Vilsmeier salt (IUPAC: *N*,*N*,*N'*,*N'*-tetramethylchloroformamidinium chloride) and DMEG-Vilsmeier salt (IUPAC: *N*,*N'*-ethylene-*N*,*N'*-dimethylchloroformamidinium chloride). The resulting ligands TMG$_2$tol (IUPAC: 2-(2-(((Bis(dimethylamino)methylene)amino)methyl)phenyl)-1,1,3,3-tetramethylguanidine) and DMEG$_2$tol (IUPAC: *N*-(2-((1,3-dimethylimidazolidin-2-ylidene)amino)benzyl)-1, 3-dimethylimidazolidine-2-imine) were diluted in acetonitrile under nitrogen atmosphere in a glovebox. Addition of the ligand solution to an equimolar solution of Cu(I) salt in acetonitrile at room temperature led to a colorless, moisture- and air-sensitive solution of the related Cu(I) complex (A, Fig. 10). Thereby three different copper(I) salts with coordinating anion (iodide) as well as non-coordinating ones (hexafluorophosphate and triflate) were used. When the colorless Cu(I) complex solution was added to an oxygen saturated tetrahydrofuran solution at −80 °C, the reaction mixture changes its color to orange-red within 5 min. The generated bis(μ-oxido) dicopper(III) complex C showed typical ligand-to-metal charge transfer (LMCT) absorption bands in the UV/VIS spectrum at 290 and 395 nm (ε_{395nm} = 12,000 M cm^{-1}) (C1–C3) [42]. An exchange of the guanidine units from TMG with four methylene
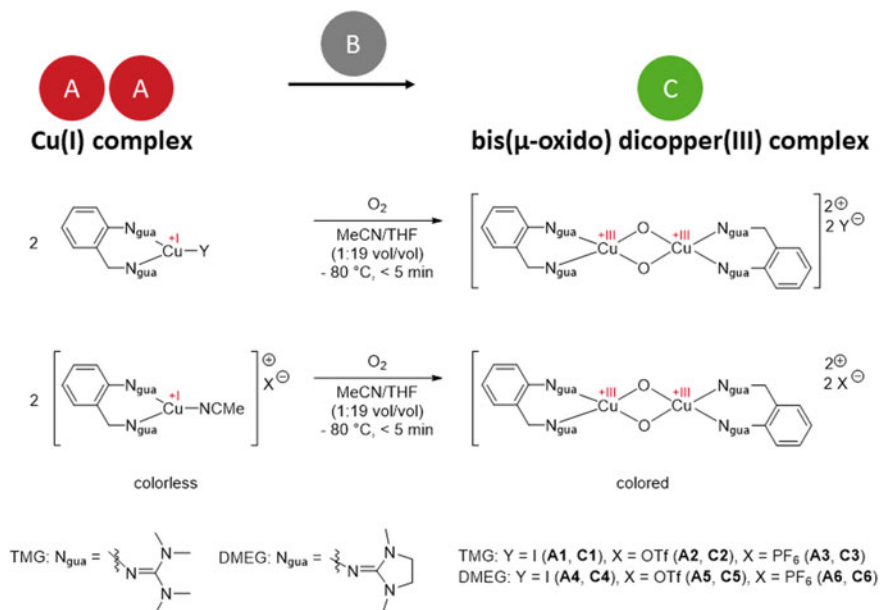
Fig. 10 Synthesis of various bis(μ-oxido) complexes C with coordinating and non-coordinating anions

groups to slightly more rigid DMEG units resulted in a shift of the characteristic absorption bands to 275 and 365 nm (C4) and 275 and 375 nm (C5, C6) [4]. Additionally, the bis(μ-oxido) species becomes less stable. The TMG-based oxido species C1–C3 were stable at −80 °C for more than 1.5 h while C4–C6, containing DMEG units, displayed an incomplete formation (58%) due to a faster decay rate compared to the formation rate.

2.3 Bisguanidine Toluene Systems for O$_2$ Transfer

As shown in the last chapter the copper(I) complexes A1–A6 can activate oxygen forming the bis(μ-oxido) species C1–C6 (Fig. 10). To examine the oxidation capability of the bis(μ-oxido) complexes, complex C1 was exemplarily used for hydroxylation experiments with *para*-methoxyphenol. The UV/VIS spectrum of the reaction mixture displayed the characteristic bands for the desired product 4-methoxycyclohexa-3,5-diene-1,2-dione at 418 nm. Via nuclear magnetic resonance (NMR) spectroscopy no resulting quinone could be detected [46]. A second study with bis(μ-oxido) complex C4 and the more complicated aromatic substrate 8-quinolinol showed the formation of the expected product 7,8-quinolinedione with UV/VIS spectroscopy. However, product formation could not be proven by NMR spectroscopy. Since no evidence for the synthesis of an oxygenation product could
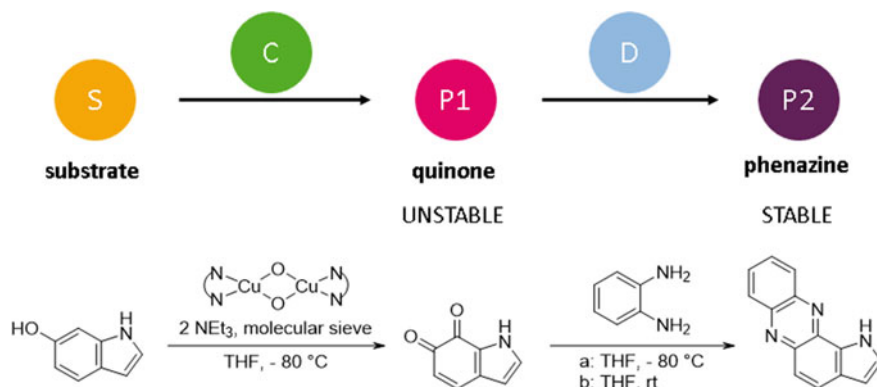
Fig. 11 Catalytic hydroxylation of a substrate S with bis(μ-oxido) complex C3 followed by an oxidation to the unstable quinone P1. Subsequent condensation with 1,2-phenylenediamine results in a stable phenazine product P2
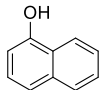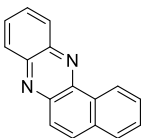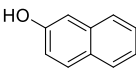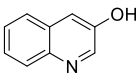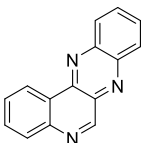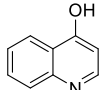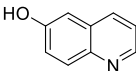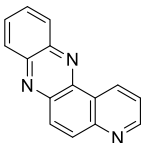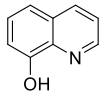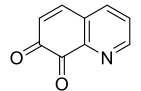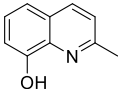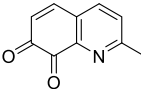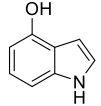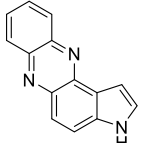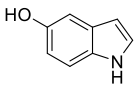
be provided beyond UV spectroscopy, no tests with other substrates or bis(μ-oxido) complexes were performed then [4].

A hydroxylation study with a hybrid guanidine stabilized bis(μ-oxido) complex under improved reaction conditions was able to prove the oxidation and hydroxylation capability of the bis(μ-oxido) species [5]. Most quinones are either highly reactive or unstable [47]. To stabilize the quinone product the hydroxylation reaction was coupled with a condensation reaction using 1,2-phenylenediamine (Fig. 11). The resulting phenazine product is stable and can be analyzed by UV/VIS and NMR spectroscopy or X-ray diffraction. With this 'phenazine' method, introduced by Tuczek et al. [1] and optimised by us (see Sect. 3) several aromatic alcohols like naphthols, quinolinols and indolols were tested using bis(μ-oxido) complex C3 [48]. This reaction can also be regarded as competitive consecutive reaction.

During the oxygenation study 1- and 2-naphthol were found to react to naphthalene-1,2-dione which was condensed to benzo[a]phenazine (Table 1, P2a, 1/31%), afterwards. Reaction of complex C3 with 3-quinolinol led to quinolino[3,4-b]quinoxaline (Table 1, P2b) in 5% yield whereas with 4-quinolinol no phenazine product could be obtained. Catalytic examination using 6-quinolinol generated 16% of pyrido[3,2-a]phenazine (Table 1, P2c). Although some quinolinol substrates described before could be transformed in the subsequent condensation of the quinone intermediate to a stable phenazine product, no phenazine formation could be found for 8-quinolinol and 2-methyl-8-quinolinol. However, oxygenation to the related quinones 7,8-quinolinedione (Table 1, P1a) and 2-methyl 7,8-quinolinedione (Table 1, P1b) was monitored with UV/VIS spectroscopy showing the characteristic absorption band at 416 nm.
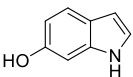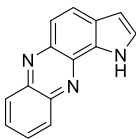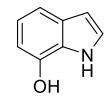
Another interesting contradiction was observed using indolols as substrates. While 5-indolol was successfully converted to pyrrolo[3,2-a]phenazine (Table 1, P2d, 4%), complex C3 was unable to generate a phenazine starting from 4-indolol.

Table 1 Catalytic oxidation and subsequent hydroxylation of a phenolic substrate S catalyzed by complex C3 with weakly coordinating anions PF_6^- in tetrahydrofuran at $-80\ °C^a$ and consecutive condensation of the quinone (P1) by using 1,2-phenylenediamine to generate phenazines (P2)[b]

Entry	Substrate	Conv. [%]	Product quinone (P1)/phenazine (P2)	Yield [%]	TON[d]
1	*(structure: 1-naphthol, OH)*	15[f]	*(structure)* (P2a)	1	0.5
2	*(structure: 2-naphthol, HO)*	57	(P2a)	31	8
3	*(structure: 3-hydroxyquinoline, OH, N)*	70	*(structure)* (P2b)	5	1
4	*(structure: 4-hydroxyquinoline, OH, N)*	54[f]		–	–
5	*(structure: 6-hydroxyquinoline, HO, N)*	100	*(structure)* (P2c)	16	4
6	*(structure: 8-hydroxyquinoline, N, OH)*	32	*(structure, O, O, N)* (P1a)	–	16[e]
7	*(structure: 2-methyl-8-hydroxyquinoline, N, OH)*	21	*(structure, O, O, N)* (P1b)	–	11[e]
8	*(structure: 4-hydroxyindole, OH, N-H)*	0[f]	*(structure, N, N, N-H)* –	–	–
9	*(structure: 5-hydroxyindole, HO, N-H)*	31	(P2d)	4	1

(continued)

Table 1 (continued)

Entry	Substrate	Conv. [%]	Product quinone (P1)/phenazine (P2)		Yield [%]	TON[d]
10	HO— indole	29	phenazine structure	(**P2e**)	3	1
11	indole OH	18[f]	-		-	-

[a]Conditions: THF, −80 °C, 8 h

[b]Conditions: THF, −80 °C, then rt, overnight

[c]Isolated yield after column chromatography

[d]Based on isolated yield in correlation with concentration of complex C

[e]Determined after reaction (a) via UV/Vis spectra and based on the concentration of complex C

[f]Incalculable due to inconclusive crude NMR spectra

A similiar inconsistency could be found using 6- and 7-indolol, whereby with 6-indolol pyrrolo[2,3-a]phenazine (Table 1 P2e, 4%) was formed while 7-indolol did not lead to a phenazine product.

2.4 Fluorescence Studies with Bisguanidine Toluene Systems for O_2 Transfer

Due to the electron-rich aromatic toluene spacer, the tol-system offers a high potential for fluorescence activity. To study its applicability for spatially and time-resolved fluorescence measurements, the hydroxylation and subsequent oxidation of several phenolic substrates was investigated as one-pot reaction with the TMG_2tol based bis(μ-oxido) complex C3 (Fig. 12).

The precursor complex [Cu(TMG_2tol)]PF_6 (A3) shows a high fluorescence activity with a broad emission signal around 440 nm, even at a low complex concentration (0.01 mM). The emission varied between 1000 a.u. (excitation at 250 nm) and > 10,000 a.u. (excitation at 375 nm) (Fig. 13).

The tested substrate solutions with 8-quinolinol, 2-methyl-8-quinolinol, 3-quinolinol, 6-quinolinol, 6-indolol and 7-indolol display broad signals around 400–500 nm (excitation: depending on the quinolinol: 360–380 nm; indolols: 230 nm). The reaction of the substrate with oxygen catalyzed by the bis(μ-oxido) species quenched the fluorescence (exemplary shown for 2-methyl-8-quinolinol (2-Me-8-OH-Qu) and 6-indolol (6-OH-Indol) in Fig. 14).

Test reactions with variation of the solvent indicated a dependency of the fluorescence intensity on the substrates and on the used solvents. Thus, the competitive consecutive reaction was performed using three different types of solvents (dichloromethane (DCM), tetrahydrofuran (THF) and acetonitrile (MeCN)) as

Table 2 Investigation of solvent dependent fluorescence in the competitive consecutive reaction from Fig. 12 with six different substrates und three varied solvents

Substrate	Solvent	Clear solution	Excitation [nm]	Emission substrate (S), O_2 free [nm]/[a.u.]	Reaction mixture, O_2 flushed [nm]/[a.u.]
8-quinolinol	THF	✔	370	420/700 500/500	500/700
8-quinolinol	MeCN	✘	370	420/800* 450/700*	470/6700*
8-quinolinol	DCM	✔	370	450/600	500/200
2-methyl-8-quinolinol	THF	✔	380	430/2600 520/3100	–
2-methyl-8-quinolinol	MeCN	✔	360	400/1400	–
2-methyl-8-quinolinol	DCM	✔	360	450/1400	–
3-quinolinol	**THF**	✔	**380**	**400/ >10,000**	**470/500**
3-quinolinol	MeCN	✘	380	470/ >10,000*	470/6500*
6-quinolinol	THF	✘	370	440/ >10,000*	–
6-quinolinol	MeCN	✘	370	510/6300*	520/700*
6-quinolinol	DCM	✘	370	460/ >10,000*	530/100*
6-indolol	THF	✘	230	330/2000* 420/2200*	330/300 460/200
6-indolol	MeCN	✘	230	330/100 460/300	330/200 460/400
6-indolol	DCM	✘	230	470/3500*	460/200*
7-indolol	**THF**	✔	**230**	**370/2200**	**–**
7-indolol	MeCN	✘	230	400/1300*	–
7-indolol	DCM	✘	230	380/900*	–

*Intensity approximated due to turbid solution

well as six different substrates (8-quinolinol, 2-methyl-8-quinolinol, 3-quinolinol, 6-quinolinol, 6-indolol and 7-indolol) (Table 2).

For fluorescence investigations at liquid gas interfaces with spectroscopic methods, a clear solution is necessary. Reactions with the substrates 6-indolol and 6-quinolinol are not useful under these circumstances, because the product precipitated and resulted in a turbid solution unsuitable for fluorescence analysis. Experiments with 8-quinolinol and 2-methyl-8-quinolinol generate clear solutions. With 3-quinolinol and 7-indolol only tetrahydrofuran-based experiments lead to clear solutions (Table 2).

Because the catalytic reaction should take place as a one-pot reaction, the whole reaction mixture consisting of the copper(I) complex, the substrate and triethylamine diluted in tetrahydrofuran needed to be fluorescence active. Thus, all substrates
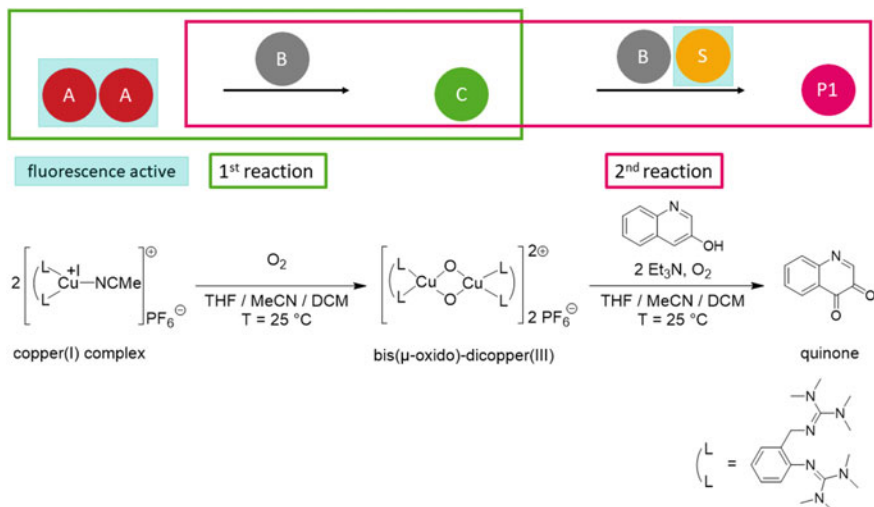
Fig. 12 Formation of bis(μ-oxido) complex C3 (catalyst) by the reaction of precursor A3 with dioxygen followed by a competitive consecutive reaction with a substrate S to give quinone P1
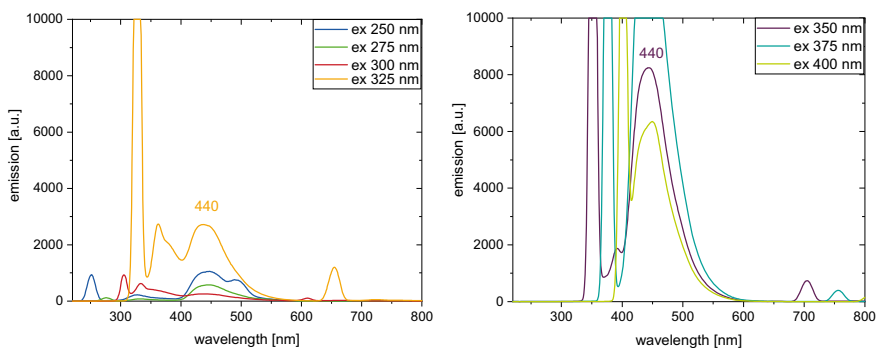
Fig. 13 Fluorescence spectra of precursor species [Cu(TMG$_2$tol)]PF$_6$ (A3, 0.01 mM) at 25 °C in THF with different excitation wavelength varying from λ = 250–325 nm and λ = 350–400 nm

displaying a clear solution were tested in a second study measuring the fluorescence of the one-pot reaction mixture before the conversion with oxygen. As many substrate solutions were highly fluorescence active most of the intensity maxima were outside the measurement area of the spectrometer. To generate fluorescence spectra with detectable fluorescence maxima, the concentrations of the reactants and the substrate to copper complex ratio were decreased from 0.5 mM and 50:1 to 0.25 mM and 10:1. Within the second study the one-pot solutions of 8-quinolinol and 2-methyl-8-quinolinol displayed a very low fluorescence intensity (<1000). The emission of the copper(I) complex and the substrate solution eliminated each other (due to unclear reasons). Therefore, the intensity difference to the oxygen-flushed
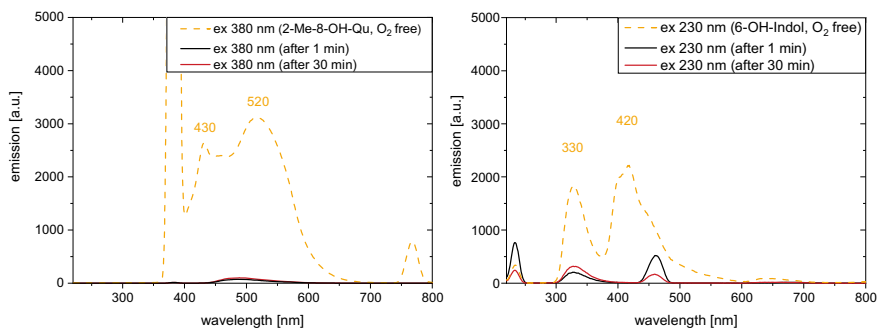
Fig. 14 Fluorescence spectra of the substrate solutions and of the reaction mixture after conversion of substrate S with catalyst C3 and dioxygen to give product P1 after 1 min and 30 min (c(C3) = 0.5 mM, C3: S = 1: 50, THF, 25 °C)

solution was too small to monitor changes via fluorescence spectroscopy. One-pot solutions with 3-quinolinol showed a high intensity (~10,000 a.u.) at excitation wavelengths between 350 and 375 nm before the conversion with dioxygen. Afterwards the intensity remained relatively high around 6,000 a.u. Variation of the excitation wavelength to 275–325 nm resulted in a very low fluorescence intensity (<2000) as observed with 8-quinolinol and 2-methyl-8-quinolinol before (Fig. 15). Hence, 3-quinolinol is not a suitable substrate for the online fluorescence monitoring as well. In contrast to the experiments with quinolinols as substrates, the oxygen-free one-pot mixture with 7-indolol showed an intensive fluorescence which was quenched by oxygenation to quinone P1 completely (Fig. 17).

To evaluate the suitability of a substrate for an application also price and availability of the reactants should be regarded. 7-Indolol is very expensive (56 €/g) and only purchasable in small amounts [49, 50], thus decreasing the demand of substrate is necessary for cost-effective experiment design.
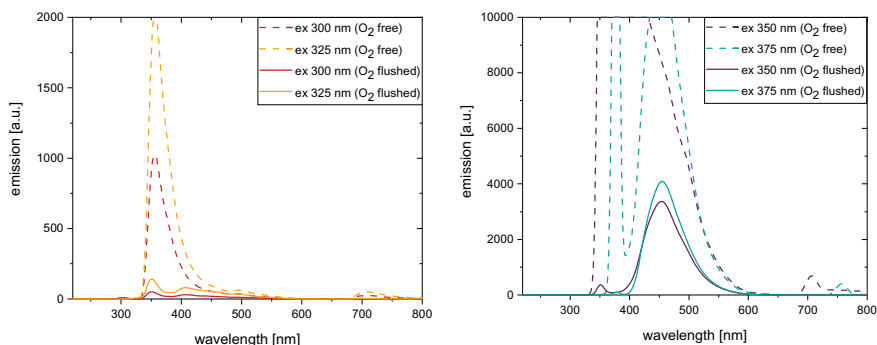
Fig. 15 Fluorescence spectra of the reaction mixture before and after the oxygenation using the substrate 3-quinolinol (S: C3 = 10:1) and catalyst C3 (c = 0.25 mM) in THF at T = 25 °C with varied excitation wavelength (λ = 300–375 nm)

Consequently, the third fluorescence study focused on the substrate 7-indolol varying the concentration of the one-pot solution and the complex to substrate ratio to minimize the amount of substrate needed. The concentration of catalyst C3 was halved from 0.5 to 0.25 mM, then lowered to 0.1 and 0.05 mM. The substrate ratio remained constant at 50:1. The fluorescence intensity decreased with diminishing catalyst concentration (Fig. 16, left). However, the intensity remained at a high level (4000 a.u.), even at a ten times lower concentration (0.05 mM). The same phenomenon occurred by the variation of the substrate to catalyst ratio. A lowering of the amount of substrate led to a decrease in the fluorescence intensity. As seen before, the fluorescence intensity remained on a high level (4000 a.u.) even at low concentrations and substrate to catalyst ratios (Fig. 16, right).
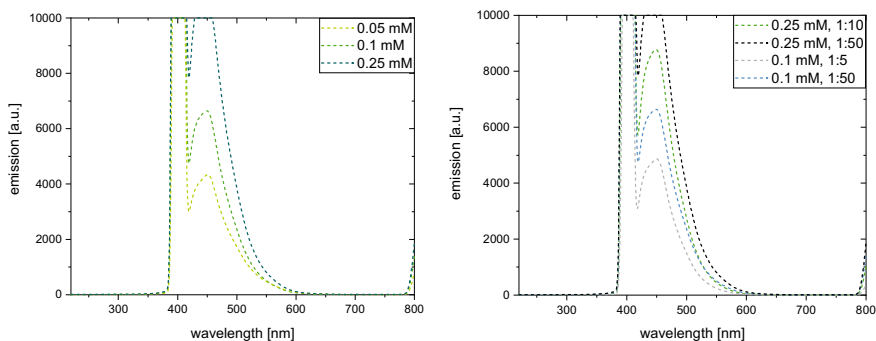
Fig. 16 Fluorescence spectra of the reaction mixture before and after the oxygenation using the substrate 7-indolol and catalyst C3 in THF at $T = 25\,°C$ using an excitation wavelength of $\lambda = 400$ nm with varied catalyst concentration (S: C3 = 50: 1; left) and varied substrate to catalyst ratio (right)
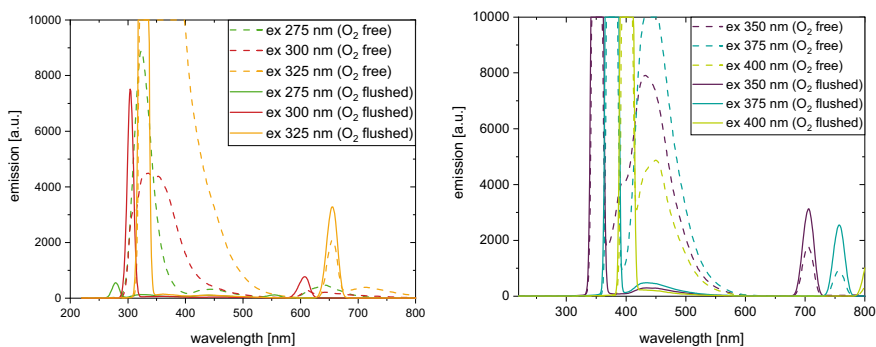
Fig. 17 Fluorescence spectra of the reaction mixture before and after the oxygenation using the substrate 7-indolol (S: C3, 5:1) and catalyst C3 ($c = 0.1$ mM) in THF at $T = 25\,°C$ with varied excitation wavelength ($\lambda = 275$–400 nm)

The high fluorescence intensity of 7-indolol even at low concentrations (0.1 mM) and substrate to catalyst ratios (5:1) could be maximized with a change in the excitation wavelength. An excitation at 325 nm as well as an excitation at 375 resulted in an intensity over 10,000 a.u. (Fig. 17). Additionally, the reaction mixture undergoes a strong color change starting with a slightly reddish solution which turned to dark black during the oxygenation. Thus, 7-indolol turned out to be the substrate most suitable for reaction monitoring by fluorescence spectroscopy, displaying a highly intensive fluorescence even at low concentration which is quenched by the reaction with oxygen and accompanied by a strong color change.

3 Novel Hybrid Guanidine Copper Systems for O_2 Activation and Transfer

3.1 Hybrid Guanidine Copper Systems for O_2 Activation with Non-coordinating Anions

Besides bis(guanidine) ligands, hybrid guanidine ligands were used to stabilize the reactive Cu_2O_2 core [3, 5, 51, 52]. Usually, a hybrid guanidine ligand consists of a guanidine unit and a second N-donor unit, such as an amine or a pyridine [3, 5, 51, 52]. By variation of the N-donor function of the ligand, donor strength and steric effects of the ligand system are controlled, enabling a beneficial interplay of electronic and steric factors regarding the accessibility of exogenous substrates to the Cu_2O_2 core.

The synthesis of the hybrid guanidine ligand system TMGbenza (IUPAC: 2-{2-((dimethylamino)methyl)phenyl]-1,1,3,3-tetramethylguanidine), which is structurally related to bis(guanidine) ligand TMG_2tol (see Sect. 2), followed a protocol consisting of three reaction steps [5]. Synthesis of the colorless, air- and moisture-sensitive Cu(I) complex A was achieved by dissolving equimolar amounts of TMGbenza and copper salt [Cu(MeCN)$_4$]PF$_6$ in acetonitrile at room temperature in a glovebox with nitrogen atmosphere. Oxygenation of Cu(I) complex A in a tetrahydrofuran/acetonitrile mixture at $-90\,°C$ resulted in the formation of the khaki-colored bis(μ-oxido) species C within 3 min, which was stable for at least one hour at that temperature (Fig. 18).

Complex C exhibited ligand-to-metal-charge transfer features at $\lambda = 392$ nm ($\varepsilon = 21,000$ M^{-1} cm^{-1}) and $\lambda = 280$ nm ($\varepsilon = 40,000$ M^{-1} cm^{-1}) in the UV/VIS spectrum. Those characteristic UV/VIS features were also observed in the presence of different weakly coordinating anions, such as BF$_4^-$, OTf$^-$ and ClO$_4^-$. Resonance Raman measurements with an excitation at $\lambda = 420$ nm revealed a specific vibration at 620 cm^{-1}, which is characteristic for the symmetrical expansion of the Cu_2O_2 core (breathing mode). A shift to 591 cm^{-1} was achieved by $^{16}O_2/^{18}O_2$ isotope exchange measurements in a tetrahydrofuran/acetonitrile mixture, which was also supported by theoretical studies. Calculations showed a favored bis(μ-oxido) species
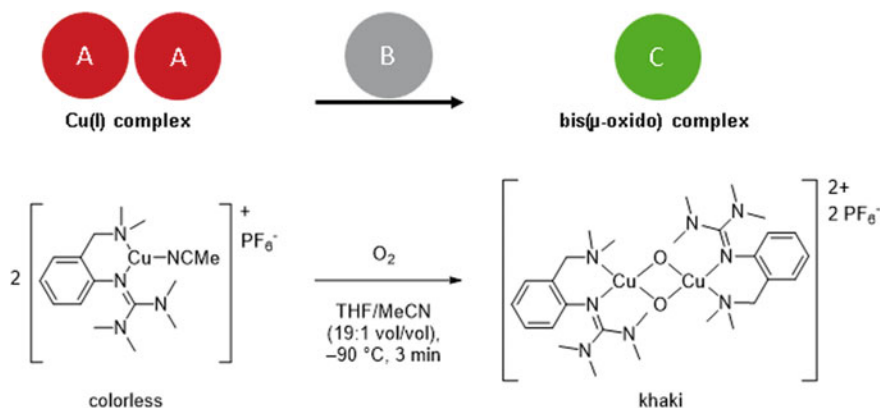
Fig. 18 Synthesis of bis(μ-oxido) complex C with weakly coordinating anions

by $c = 10$ kcal/mol over its related side-on peroxido species due to their small isomerization barrier. Cu K-edge EXAFS measurements confirmed an edge position with the assignment as Cu(III). The Cu–O_2 stoichiometry was determined by cryo-UHR-ESI mass spectrometry, revealing an isotopic pattern and m/z values of the monocationic species with a Cu–O_2 ratio of 2:1—{[$Cu_2(TMGbenza)_2O_2]PF_6$}$^+$. Thermal decomposition experiments of complex C exhibited a pseudo-first-order decay at low temperatures. At $T = -80$ °C, a half-life time of complex C of one hour was determined, whereas the half-life time at $T = -74$ °C only amounted to 5 min, underlining the temperature sensitivity of complex C. Thermal decay products of complex C were analyzed by single crystal X-ray diffraction and reported as a dicationic μ-alkoxido-μ-hydroxido Cu(II) complex.

Catalytic hydroxylation activity of complex C was tested initially towards an extended scope of challenging aromatic alcohols (including pyridinols, naphthols, quinolinols and indolols), in order to expand the commonly used substrate scope of simple (substituted) phenols and to achieve a competitive consecutive reaction (Fig. 19 and Table 3). Phenolic substrates S (for example 6-quinolinol), were oxygenated by complex C to generate a reactive quinone product P1 (quinoline-5,6-dione), which was captured by using 1,2-phenylenediamine to form stable phenazines as product P2.

3- and 4-pyridinol were found to react quickly to 3,4-pyridoquinone (Table 3, P1a), which is highly reactive, leading to C–O-coupled dimers instead of forming a phenazine. 1- and 2-naphthol were oxygenated to the corresponding quinone, which was selectively transformed into benzo[a]phenazine (Table 3, P2a) in 22–31% yield. 3- and 4-quinolinol were both converted in 87–95% via its quinone form into quinolino[3,4-b]quinoxaline (Table 3, P2b). 6-Quinolinol was oxidized quantitatively and captured as pyrido[3,2-a]phenazine (Table 3, P2c) in 30% yield. Surprisingly, even though 8-quinolinol and 2-methyl-8-quinolinol were converted into 7,8-quinolinedione (Table 3, P1b) and 2-methyl-7,8-quinolinedione (Table 3, P1c), which were characterized by its characteristic absorption band at 416 nm in the
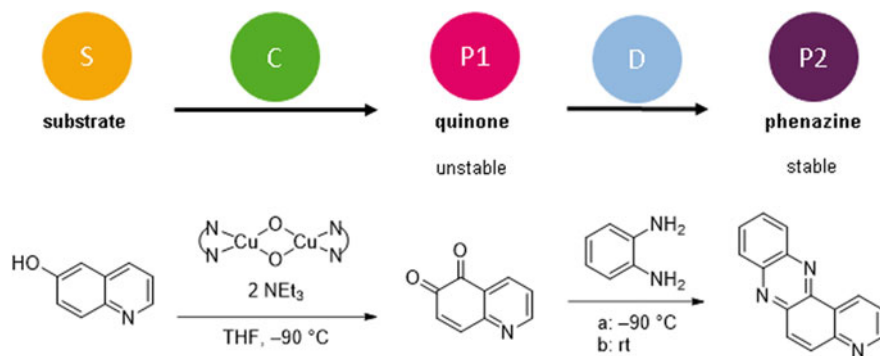
Fig. 19 Catalytic oxygenation of a phenolic substrate S mediated by bis(μ-oxido) complex C at low temperatures and subsequent condensation of the quinone product P1 by using 1,2-phenylenediamine D to generate the phenazine product P2

UV/VIS spectrum, phenazine formation was found in neither case. Related indolols were also found to form the bent phenazines. 4- and 5-indolol were transformed into pyrrolo[3,2-a]phenazine (Table 3, P2d), whereas 6- and 7-indolol were found to form pyrrolo[2,3-a]phenazine (Table 3, P2e).
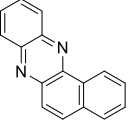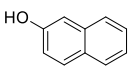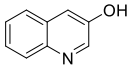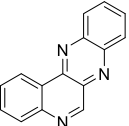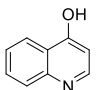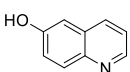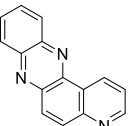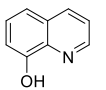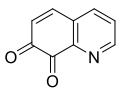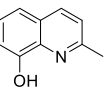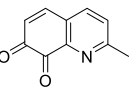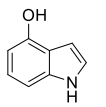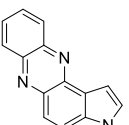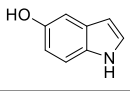
The observed reactivity is interesting due to the versatility of substrates but not very high. Since the bisguanidines are sterically crowded, we have already learned earlier that they can hinder the accessibility of substrates to the Cu_2O_2 core [3]. In the following section, we focus on hybrid guanidine systems which offer a better accessibility.

3.2 Hybrid Guanidine Copper Systems for O_2 Activation with Coordinating Anions

The hybrid guanidine ligand TMGbenza was also complexed with copper halides CuX (X = I, Br, Cl) to form colorless, air- and moisture-sensitive Cu(I) complexes of type A. In contrast to weakly coordinating anions such as PF_6^- (see Sect. 3.1), copper halides contain coordinating anions which directly bond to the copper center of the resulting complex. Complex A was generated by dissolving equimolar amounts of TMGbenza and copper salt in acetonitrile at room temperature in a glovebox with nitrogen atmosphere. Oxygenation of Cu(I) complex A in a tetrahydrofuran/acetonitrile mixture resulted in the formation of bis(μ-oxido) species C either at −100 °C or at room temperature (Fig. 20) [52].
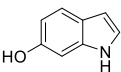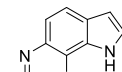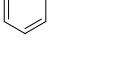
Complex C with bromide and chloride was formed within seconds at $T = -100$ °C and subsequently decayed very quickly due to its high reactivity. Both complexes featured a green color. While complex C with bromide exhibited absorption bands at λ = 399 nm (21,000 M^{-1} cm^{-1}) and λ = 270 nm (50,000 M^{-1}

Table 3 Catalytic oxygenation of a phenolic substrate S mediated by complex C with weakly coordinating anions PF_6^- in tetrahydrofuran at $-90\,°C^a$ and subsequent condensation of the quinone (P1) by using 1,2-phenylenediamine to generate phenazines (P2)[b]

Entry	Substrate	Conv. [%]	Product quinone (P1)/Phenazine (P2)	Yield [%]	TON[d]
1		>99	(P1a)	e	f
2		>99	(P1a)	e	f
3		80	(P2a)	22	11
4		89	(P2a)	31	16
5		95	(P2b)	32	16
6		87	(P2b)	22	11
7		>99	(P2c)	30	15
8		28	(P1b)	–	14[g]
9		24	(P1c)	–	12[g]
10		81	(P2d)	19	10
11		88	(P2d)	26	13

(continued)

Table 3 (continued)

Entry	Substrate	Conv. [%]	Product quinone (P1)/Phenazine (P2)		Yield [%]	TON[d]
12	 HO–⟨indole⟩	92	⟨phenazine-pyrrole structure⟩	(P2e)	27	14
13	⟨indole with OH⟩	84		(P2e)	31	16

[a]Conditions: THF, −90 °C, 1 h
[b]Conditions: THF, −90 °C, then rt, overnight
[c]Isolated yield after column chromatography
[d]Based on isolated yield in correlation with concentration of complex C
[e]Quinone too reactive to be isolated
[f]No extinction coefficient of the quinone reported
[g]Determined after reaction (a) via UV/Vis spectra and based on the concentration of complex C
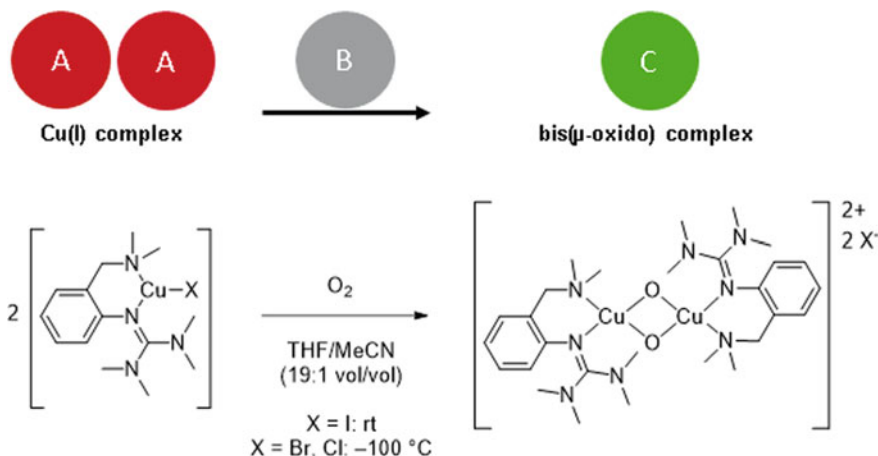
Fig. 20 Synthesis of bis(μ-oxido) complex C with coordinating anions

cm^{-1}), complex C with chloride showed bands at $\lambda = 386$ nm (21,000 M^{-1} cm^{-1}) and $\lambda = 270$ nm (50,000 M^{-1} cm^{-1}). Surprisingly, oxygenation of complex A with iodide was successfully achieved at both low temperatures and room temperature, underlining its tremendous stability. The resulting reddish-brown bis(μ-oxido) species C showed absorption features at $\lambda = 290$ nm (50,000 M^{-1} cm^{-1}) and $\lambda = 370$ nm (22,000 M^{-1} cm^{-1}) within two hours at room temperature. For quantitative formation two additional equivalents of copper iodide were necessary due to the formation of iodocuprate anions [52]. This complex C showed a remarkable stability of at least several days. Cryo-UHR-ESI measurements revealed the isotopic pattern of the

complex cation with one iodide as well as the isotopic pattern of the complex cation with one iodocuprate in the positive mode.
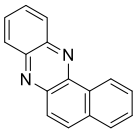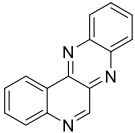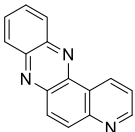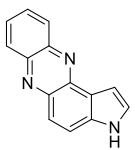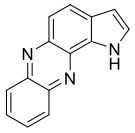
The bis(μ-oxido) complex [$Cu_2(TMGbenza)_2O_2I$](CuI_2) with iodocuprate anions exhibited a remarkable stability at room temperature, whereas the related bis(μ-oxido) complex [$Cu_2(TMGbenza)_2O_2$](PF_6)$_2$ with weakly coordinating anions was only stable at $T = -90$ °C (see Sect. 3.1). Since there is a huge difference in stability of these two complexes C with respect to the present anion, titration experiments were conducted to interconvert these two species C. Starting from the less stable bis(μ-oxido) species [$Cu_2(TMGbenza)_2O_2$](PF_6)$_2$ with weakly coordinating anions in tetrahydrofuran at $T = -90$ °C, addition of two equivalents of an iodide source resulted in a salt metathesis and therefore in the formation of the room temperature stable bis(μ-oxido) complex [$Cu_2(TMGbenza)_2O_2I$](CuI_2). The salt metathesis is accompanied by a color change from khaki to reddish-brown and a shift of the absorption band from $\lambda = 390$–370 nm.

When two copper(I) complexes A, [$Cu(TMGbenza)(MeCN)$]PF_6 with weakly coordinating anions PF_6^- and [$Cu(TMGbenza)I$] with coordinating anions, are oxygenated simultaneously at low temperatures, the competitive formation of the resulting bis(μ-oxido) complex C can be investigated because both complexes A compete for the present dioxygen. Initial formation of [$Cu_2(TMGbenza)_2O_2$](PF_6)$_2$ with weakly coordinating anions PF_6^- was observed within 3 min as expected. The absorption bands at $\lambda = 390$ nm shifted towards $\lambda = 370$ nm within $t = 40$ min due to the formation of the more stable complex [$Cu_2(TMGbenza)_2O_2I$](CuI_2) with bridging iodido anion in the bis(μ-oxido) species and iodocuprate anions. This competitive reaction highlights the significantly different time scale of the formation of complex C in dependence of the present anions and its corresponding stability.

The TMGbenza-stabilized system demonstrated its versatility regarding its spectroscopic properties, formation time and stability at different temperatures. The room temperature stable bis(μ-oxido) complex [$Cu_2(TMGbenza)_2O_2I$](CuI_2) with bridging iodido anion in the bis(μ-oxido) species and coordinating iodocuprate anions was also tested in catalytic oxygenation reactions of phenolic substrates S (Fig. 19 and Table 4).

2-Naphthol was converted in over 80% within two hours to give benzo[a]phenazine (Table 4, P2a) in 42% isolated yield. 3- and 6-quinolinol were fully transformed within three hours at room temperature, leading to quinolino[3,4-b]quinoxaline (Table 4, P2b) and pyrido[3,2-a]phenazine (Table 4, P2c) in 56–61% yield. A longer reaction time of 12 h was tested by using 5-indolol, showing no influence on the selectivity of the oxygenation reaction since pyrrolo[3,2-a]phenazine (Table 4, P2d) was observed as the only reaction product. Conversion of 7-indolol was achieved quantitatively after three hours and resulted in the formation of the pyrrolo[2,3-a]phenazine (Table 4, P2e). All evaluated substrates were successfully converted by complex C under ambient conditions, leading to bent phenazines and thus demonstrating a reaction system suitable for a competitive consecutive reaction at room temperature.

Table 4 Catalytic oxygenation of a phenolic substrate mediated by complex C with coordinating anions in tetrahydrofuran at room temperature and subsequent condensation of the quinone (P1) by using 1,2-phenylenediamine to generate phenazines (P2)

Entry	Cat.	Substrate	t* [h]	Conv.[a] [%]	Product P		Yield[b] [%]
1	C	2-naphthol	2	83		(**P2a**)	42
2	C	3-quinolinol	3	>99		(**P2b**)	56
3	C	6-quinolinol	3	>99		(**P2c**)	61
4	C	5-indolol	12	79		(**P2d**)	41
5	C	7-indolol	3	>99		(**P2e**)	58

[a]Determined by ^{1}H NMR spectroscopy
[b]Isoloated yield after column chromatography and/or sublimation

Compared to the preceeding section, the hybrid guanidine systems fulfill their promise of better substrate accessibility to the Cu_2O_2 core and enable considerably better yields.

3.3 Variations of the Amine Moiety in Hybrid Guanidine Ligands

In analogy to the hybrid guanidine ligand TMGbenza (see Sect. 3.1), a modified version of the ligand was created by variation of the amine donor function to investigate the influence on the donor strength and steric effects. Whereas TMGbenza

contains a permethylated amine donor function, the two new ligands possess a diethylamino donor function (R = ethyl) and a di-*iso*-propylamino donor function (R = *iso*-propyl), respectively [53].

Hybrid guanidine ligands TMGbenzNEt$_2$ (IUPAC: 2-{2-((diethylamino)methyl)phenyl]-1,1,3,3-tetramethylguanidine) and TMGbenzN*i*Pr$_2$ (IUPAC: 2-{2-((di-*iso*-propylamino)methyl)phenyl]-1,1,3,3-tetramethylguanidine) were synthesized according to a modified protocol established previously [5]. Synthesis of the colorless, air- and moisture-sensitive Cu(I) complex A was achieved by dissolving equimolar amounts of the hybrid guanidine ligand and a copper salt ([Cu(MeCN)$_4$]PF$_6$, [Cu(MeCN)$_4$]BF$_4$ or [Cu(MeCN)$_4$]OTf in acetonitrile at room temperature in a glovebox with nitrogen atmosphere. The oxygenation process of Cu(I) complex A in a tetrahydrofuran/acetonitrile mixture at −100 °C led to the formation of bis(μ-oxido) species C within 15–40 min depending on the ligand system and the present anion (Fig. 21).

TMGbenzNEt$_2$-stabilized bis(μ-oxido) complexes C1 with weakly coordinating anions PF$_6^-$, BF$_4^-$ and OTf$^-$ showed a green color and ligand-to-metal charge transfer absorption bands at $\lambda = 400$ nm ($\varepsilon = 20{,}000$ M^{-1} cm^{-1}) and $\lambda = 280$ nm ($\varepsilon = 40{,}000$ M^{-1} cm^{-1}) in the UV/VIS spectrum. All complexes C were stable for at least $t = 90$ min. at $T = -100$ °C and decayed quickly within minutes upon warming to higher temperatures, which was accompanied by discoloration of the reaction solution to yellow.

The orange bis(μ-oxido) species C2 supported by hybrid guanidine ligand TMGbenzN*i*Pr$_2$ were formed within $t = 25$ min at $T = -100$ °C and stable for at least $t = 60$ min. Characteristic absorption features at $\lambda = 420$ nm ($\varepsilon = 17{,}000$ M^{-1} cm^{-1}) and $\lambda = 280$ nm ($\varepsilon = 38{,}000$ M^{-1} cm^{-1}) were observed in the UV/VIS spectrum independent of the present weakly coordinating anion. Comparing the absorption
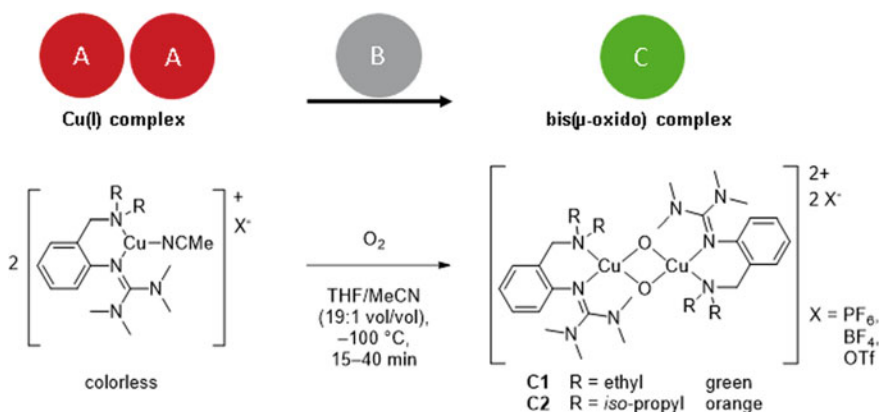
Fig. 21 Synthesis of bis(μ-oxido) complex C with varied amine donor units in the presence of weakly coordinating anions
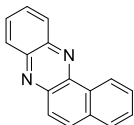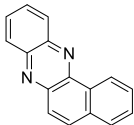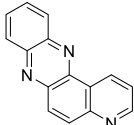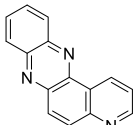
features of bis(μ-oxido) species C in dependence of the varied amine donor function, a wavelength shift of the characteristic absorption band at around $\lambda = 400$ nm for bis(μ-oxido) species was observed whereas the LMCT band at 280 nm remained constant. Weakening of the amine donor group NMe$_2$ > NEt$_2$ > NiPr$_2$ correlates to a red-shift of the LMCT band from $\lambda = 390$ nm to 400–420 nm and results in a decreasing stability of the bis(μ-oxido) complex C.

Cryo-UHR-ESI measurements revealed the isotopic pattern and m/z value of the monocationic species – {[Cu$_2$(TMGbenzNiPr$_2$)$_2$O$_2$]PF$_6$}$^+$, confirming a Cu-O$_2$ stoichiometry of 2:1. Same observations were made by using other weakly coordinating anions BF$_4^-$ and OTf$^-$ as well as hybrid guanidine ligand TMGbenzNEt$_2$.

Bis(μ-oxido) complexes C with TMGbenzNEt$_2$ and TMGbenz$i$Pr$_2$ ligation were evaluated in catalytic hydroxylation reactions of aromatic alcohols S to achieve a competitive consecutive reaction (Fig. 19 and Table 5) [53].

2-Naphthol was transformed by bis(μ-oxido) species C1 and C2 with coordinating anions PF$_6^-$ within two hours at 78–82% to afford benzo[a]phenazine (Table 5, P2a) in 23–28% isolated yield. 6-Quinolinol was converted in over 95% by both catalysts

Table 5 Catalytic oxygenation of a phenolic substrate S mediated by complex C1 and C2 with weakly coordinating anions PF$_6^-$ in tetrahydrofuran at $T = -100\,°C^a$ and subsequent condensation of the quinone (P1) by using 1,2-phenylenediamine to generate phenazines (P2)^b

Entry	Cat.	Substrate	t* [h]	Conv.^{a} [%]	Product P2		Yield^b [%]
1	C1	2-naphthol	2	82		(**P2a**)	28
2	C2	2-naphthol	2	78		(**P2a**)	23
3	C1	6-quinolinol	3	95		(**P2c**)	31
4	C2	6-quinolinol	3	>99		(**P2c**)	28

^{a}Conditions: THF, $-100\,°C$, t*
^{b}Conditions: THF, $-100\,°C$, then rt, overnight
^{c}Determined by ^{1}H NMR spectroscopy
^{d}isolated yield after column chromatography

within three hours. Pyrido[3,2-a]phenazine (Table 5, P2c) was isolated in 28–31% yield. Catalytic conversions of these substrate classes were successfully achieved by bis(μ-oxido) complexes C independent of the amine donor unit. Despite the higher steric demand of the NEt$_2$- and NiPr$_2$-donor group compared to the NMe$_2$-group of ligand TMGbenza, the Cu$_2$O$_2$ core of the bis(μ-oxido) species C was accessible to challenging substrate classes like naphthols and quinolinols. However, the increased temperature sensitivity makes these complexes less facile too handle.

4 Conclusion and Outlook

In summary, we have demonstrated that tyrosinase model complexes offer a large versatility to tune the stability, reactivity, substrate scope and spectroscopic patterns in UV/VIS and fluorescence spectroscopy. Within the SPP, the fastest catalytic model complexes known so far have been provided and robust systems for the collaboration partners have been provided (see Chapters "Determination of Kinetics for Reactive Bubbly Flows Using SuperFocus Mixers; Visualization and Quantitative Analysis of Consecutive Reactions in Taylor Bubble Flows; Chemical Reactions at Freely Ascending Single Bubbles; and Investigation of Reactive Bubbly Flows in Technical Apparatuses"). Moreover, fascinating insights into the interplay between donor strength, steric demand and backbone type and its influence on the stability and reactivity have been obtained.

We studied guanidine, bis(pyrazolyl)methane and amine systems in parallel and learned that bis(pyrazolyl)methane copper complexes provide with a fascinating tyrosinase model chemistry with fast catalytic processes of their peroxido complexes. However, the systems are too delicate and too sensitive to be up-scaled for the SPP partners. The rather simple ammonia system allowed real upscaling into canister amounts but the ammonia is corrosive which limits its broad utilization.

The guanidine ligand family convinced by application of the simple bisguanidine btmgp and its bis(μ-oxido) species in the SuperFocus mixer, Taylor bubbles and NMR relaxometry, but no oxygen transfer could be observed here. Moreover, the fluorescence behavior was not in a suited range for the SPP partners. In the next generation, aromatic bisguanidine copper complexes provide with strong fluorescence signals and catalytic hydroxylation abilities. The catalytic activity is interesting due to the substrate versatility (e.g. bicyclic substrates) but not very high. Owing to the exceptional fluorescence features, future application in Taylor bubbles is planned.

Aromatic hybrid guanidines were the next logical step giving better access to the Cu$_2$O$_2$ core: the catalytic abilities of their bis(μ-oxido) complexes convinced by a superior versatility enabling the fast catalytic oxidative transformation of a large array of phenols (including bicyclic derivatives). This is in accordance with earlier studies comparing aliphatic bisguanidines and hybrid guanidines where the substrate accessibility was key to reactivity of the bis(μ-oxido) cores [3]. Moreover, we found a challenging anion influence but also a distinct influence of the amine substituents

on the stability of the bis(μ-oxido) species. Large scale application, however, is here again limited.

To this end, we studied the bisamine DBED and developed a procedure to turn it useful for technical apparatuses and competitive consecutive reactions as is detailed in Chap. "Investigation of Reactive Bubbly Flows in Technical Apparatuses".

For future work, we envision the transfer of the most promising systems into large scale applications for sustainable oxidation reactions.

References

1. Hamann JN, Rolff M, Tuczek F (2015) Monooxygenation of an appended phenol in a model system of tyrosinase: implications on the enzymatic reaction mechanism. Dalton Trans 44:3251–3258
2. Xiao Y, Hu W, Sun S, Yu J-T, Cheng J (2019) Recent advances in the synthesis of acridines and phenazines. Synlett 30:2113–2122
3. Herres-Pawlis S, Verma P, Haase R, Kang P, Lyons CT, Wasinger EC, Flörke U, Henkel G, Stack TDP (2009) Phenolate hydroxylation in a bis(μ-oxo)dicopper(III) complex: lessons from the guanidine/amine series. J Am Chem Soc 131:1154–1169
4. Strassl F, Grimm-Lebsanft B, Rukser D, Biebl F, Biednov M, Brett C, Timmermann R, Metz F, Hoffmann A, Rübhausen M, Herres-Pawlis S (2017) Oxygen activation by copper complexes with an aromatic bis(guanidine) ligand. Eur J Inorg Chem:3350–3359
5. Paul M, Teubner M, Grimm-Lebsanft B, Golchert C, Meiners Y, Senft L, Keisers K, Liebhäuser P, Rösener T, Biebl F, Buchenau S, Naumova M, Murzin V, Krug R, Hoffmann A, Pietruszka J, Ivanović-Burmazović I, Rübhausen M, Herres-Pawlis S (2020) Exceptional substrate diversity in oxygenation reactions catalyzed by a Bis(μ-oxo) copper complex. Chem Eur J 26:7556–7562
6. Lewis AL, Tolman WB (2004) Reactivity of dioxygen−copper systems. Chem Rev:1047–1076
7. Mirica LM, Ottenwaelder X, Stack TDP (2004) Structure and spectroscopy of copper−dioxygen complexes. Chem Rev 104:1013–1045
8. Schindler S (2000) Reactivity of Copper(I) complexes towards dioxygen. Eur J Inorg Chem:2311–2326
9. Hatcher L, Karlin KD (2004) Oxidant types in copper-dioxygen chemistry: the ligand coordination defines the Cu(n)-O_2 structure and subsequent reactivity. J Biol Inorg Chem 9:669–683
10. Rolff M, Schottenheim J, Decker H, Tuczek F (2011) Copper–O_2 reactivity of tyrosinase models towards external monophenolic substrates: molecular mechanism and comparison with the enzyme. Chem Soc Rev 40:4077–4098
11. Citek C, Herres-Pawlis S, Stack TDP (2015) Low temperature syntheses and reactivity of Cu_2O_2 active-site models. Acc Chem Res 48:2424–2433
12. Decker H, Dillinger H, Tuczek F (2000) How Does tyrosinase work? Recent insights from model chemistry and structural biology. Chem Int Ed 39:1591–1595
13. Matoba Y, Kumagai T, Yamamoto A, Yoshitsu H, Sugiyama M (2006) Crystallographic evidence that the dinuclear copper center of tyrosinase is flexible during catalysis. J Biol Chem 281:8981–8990

14. Mauracher SG, Molitor C, Al-Oweini R, Kortz U, Rompel A (2014) Latent and active *ab*PPO4 mushroom tyrosinase cocrystallized with hexatungstotellurate(VI) in a single crystal. Acta Crystallogr D70:2301–2315

15. Bijelic A, Pretzler M, Molitor C, Zekiri F, Rompel A (2015) The structure of a plant tyrosinase from walnut leaves reveals the importance of "substrate-guiding residues" for enzymatic specificity. Angew Chem 127:14889–14893; Angew Chem Int End 54:14677–14680

16. Halfen JA, Mahapatra S, Wilkinson EC, Kaderli S, Young VG, Que LJ, Zuberbühler AD, Tolman WB (1996) Reversible cleavage and formation of the dioxygen O–O bond within a dicopper complex. Science 271:1397–1400

17. Tolman WB (1997) Making and breaking the dioxygen O–O bond: new insights from studies of synthetic copper complexes. Acc Chem Res 30:227–237

18. Karlin KD, Cruse RW, Gultneh Y, Hayes JC, Zubieta J (1984) Peroxide coordination to a dicopper(II) center. Dioxygen binding to a structurally characterized phenoxide-bridged binuclear copper(I) complex. J Am Chem Soc 106:3372–3374

19. Jacobson RR, Tyeklar Z, Farooq A, Karlin KD, Liu S, Zubieta J (1988) A copper-oxygen (Cu_2-O_2) complex. Crystal structure and characterization of a reversible dioxygen binding system. J Am Chem Soc 110:3690–3692

20. Kieber-Emmons MT, Ginsbach JW, Wick PK, Lucas HR, Helton ME, Lucchese B, Suzuki M, Zuberbühler AD, Karlin KD, Solomon EI (2014) Observation of a $Cu(II)_2(\mu\text{-}1,2\text{-}peroxo)/Cu(III)_2(\mu\text{-oxo})_2$ equilibrium and its implications for copper-dioxygen reactivity. Angew Chem Int Ed 53:4935–4939

21. Elwell CE, Gagnon NL, Neisen BD, Dhar D, Spaeth AD, Yee G, Tolman M, William B (2017) Copper-oxygen complexes revisited: structures, spectroscopy, and reactivity. Chem Rev 117:2059–2107

22. Liebhäuser P, Hoffmann A, Herres-Pawlis S (2016) Tyrosinase models: synthesis, spectroscopy, theory, and catalysis. Ref Modul Chem Mol Sci Chem Eng:1–22

23. Hoffmann A, Wern M, Hoppe T, Witte M, Haase R, Liebhäuser P, Glatthaar J, Herres-Pawlis S, Schindler S (2016) Hand in hand: experimental and theoretical investigations into the reactions of copper(I) mono- and bis(guanidine) complexes with dioxygen. Eur J Inorg Chem:4744–4751

24. Metz M, Solomon EI (2001) Dioxygen binding to deoxyhemocyanin: electronic structure and mechanism of the spin-forbidden two-electron reduction of O_2. J Am Chem Soc 123:4938–4950

25. Herres S, Heuwing AJ, Flörke U, Schneider J, Henkel G (2005) Hydroxylation of a methyl group: synthesis of $[Cu_2(btmmO)_2I]^+$ and of $[Cu_2(btmmO)_2]^{2+}$ containing the novel ligand {bis(trimethylmethoxy)guanidino}propane (btmmO) by copper-assisted oxygen activation. Inorg Chim Acta 358:1089–1095

26. Herres-Pawlis S, Berth G, Wiedemeier V, Schmidt L, Zrenner A, Warnecke H-J (2010) Oxygen sensing by fluorescence quenching of [Cu(btmgp)I]. J Lumin 130:1958–1962

27. Schurr D, Strassl F, Liebhäuser P, Rinke G, Dittmeyer R, Herres-Pawlis S (2016) Decay kinetics of sensitive bioinorganic species in a SuperFocus mixer at ambient conditions. React Chem Eng 1:485–493

28. Felis F, Strassl F, Laurini L, Dietrich N, Billet A-M, Roig V, Herres-Pawlis S, Loubière K (2019) Using a bio-inspired copper complex to investigate reactive mass transfer around an oxygen bubble rising freely in a thin-gap cell. Chem Eng Sci 207:1256–1269

29. Benders S, Strassl F, Fenger B, Blümich B, Herres-Pawlis S, Küppers M (2018) Imaging of copper oxygenation reactions in a bubble flow. Magn Reson Chem 56:826–830

30. Hoffmann A, Citek C, Binder S, Goos A, Rübhausen M, Troeppner O, Ivanovic-Burmazovic I, Wasinger EC, Stack TDP, Herres-Pawlis S (2013) Catalytic phenol hydroxylation with dioxygen: extension of the tyrosinase mechanism beyond the protein matrix, Angew Chem Int Ed 52:5398–5401; Katalytische Phenolhydroxylierung mit Sauerstoff: Substratvielfalt jenseits der Proteinmatrix von Tyrosinase, Angew Chem 125:5508–5512

31. Liebhäuser P, Keisers K, Hoffmann A, Schnappinger T, Sommer I, Thoma A, Wilfer C, Schoch R, Stührenberg K, Bauer M, Dürr M, Ivanović-Burmazović I, Herres-Pawlis S (2017) Record Broken: A copper peroxide complex with enhanced stability and faster hydroxylation catalysis. Chem Eur J 23:12171–12183

32. Wilfer C, Liebhäuser P, Hoffmann A, Erdmann H, Grossmann O, Runtsch L, Paffenholz E, Schepper R, Dick R, Bauer M, Dürr M, Ivanović-Burmazović I, Herres-Pawlis S (2015) Efficient biomimetic hydroxylation catalysis with a bis(pyrazolyl)imidazolylmethane copper peroxide complex. Chem Eur J 21:17639–17649

33. Strassl F, Timmermann J, Schlüter M, Herres-Pawlis S (2016) Kinetik der Sauerstoffaktivierung. GIT Labor-Fachzeitschrift:39–41

34. Mirica LM, Vance M, Rudd DJ, Hedman B, Hodgson KO, Solomon EI, Stack TDP (2005) Tyrosinase reactivity in a model complex: an alternative hydroxylation mechanism. Science 308:1890–1892

35. Holt BTO, Vance MA, Mirica LM, Heppner DE, Stack TDP, Solomon EI (2009) Reaction coordinate of a functional model of tyrosinase: spectroscopic and computational characterization. J Am Chem Soc 131:6421–6438

36. Verma P, Weir J, Mirica L, Stack TDP (2011) Tale of a twist: magnetic and optical switching in copper(ii) semiquinone complexes. Inorg Chem 50:9816–9825

37. Esguerra K, Lumb J-P (2015) Adapting Melanogenesis to a regioselective C–H functionalization of phenols. Synlett 26:2731–2738

38. Huang Z, Askari MS, Esguerra KVN, Dai T-Y, Kwon O, Ottenwaelder X, Lumb J-P (2016) A bio-inspired synthesis of oxindoles by catalytic aerobic dual C–H functionalization of phenols. Chem Sci 7:358–369

39. Esguerra KVN, Fall Y, Lumb J-P (2014) A biomimetic catalytic aerobic functionalization of phenols. Angew Chem Int Ed 53:5877–5881; Angew Chem 126:5987–5991

40. Pohl S, Harmjanz M, Schneider J, Saak W, Henkel G (2000) 1,3-Bis(N,N,N′,N′-tetramethylguanidino)propane: synthesis, characterization and bonding properties of the first bidentate, peralkylated guanidine ligand. J Chem Soc Dalton Trans:3473–3479

41. Herres-Pawlis S, Neuba A, Seewald O, Seshadri T, Egold H, Flörke U, Henkel G (2005) A library of peralkylated bis-guanidine ligands for use in biomimetic coordination chemistry. Eur J Org Chem:4879–4890

42. Strassl F, Hoffmann A, Grimm-Lebsanft B, Rukser D, Biebl F, Tran MA, Metz F, Rübhausen M, Herres-Pawlis S (2018) Fluorescent bis(guanidine) copper complexes as precursors for hydroxylation catalysis. Inorganics 6:114

43. https://www.sigmaaldrich.com/catalog/product/aldrich/348015?lang=de&region=DE

44. https://www.tcichemicals.com/DE/de/p/A1435

45. https://www.fishersci.at/shop/products/4-aminobenzylamine-98-acros-organics-1/10080173/en

46. Strassl F (2019) Copper dioxygen complexes for multiphase flows. Ph.D. thesis, RWTH Aachen 2019

47. Land EJ, Ramsden CA, Riley PA (2003) Tyrosinase autoactivation and the chemistry of ortho-quinone amines. Acc Chem Res 36:300–308

48. Laurini L, Hoffmann A, Herres-Pawlis S Manuscript in preparation

49. https://nl.vwr.com/store/product/23127406/7-hydroxyindool-95

50. https://www.abcr.de/shop/de/catalogsearch/advanced/result/?q=2380-84-9

51. Herres-Pawlis R, Haase P, Verma A, Hoffmann P, Kang TDP (2015) Stack: Formation of hybrid guanidine-stabilized bis(μ-oxo)dicopper cores in solution: electronic and steric perturbations. Eur J Inorg Chem 32:5426–5436

52. Paul M, Hoffmann A, Herres-Pawlis S (2021) Room temperature stable multitalent: highly reactive and versatile copper guanidine complexes in oxygenation reactions. J Biol Inorg Chem. https://doi.org/10.1007/s00775-021-01849-9

53. Paul M, Teubner M, Grimm-Lebsanft B, Buchenau S, Hoffmann A, Rübhausen M, Herres-Pawlis S (2021) Influence of the amine donor on hybrid guanidine-stabilized bis(μ-oxido) dicopper(III) complexes and their tyrosinase-like oxygenation activity towards polycyclic aromatic alcohols, manuscript in preparation

In Situ Characterizable High-Spin Nitrosyl–Iron Complexes with Controllable Reactivity in Multiphase Reaction Media

Martin Oßberger and Peter Klüfers

Abstract The chemistry of non-heme iron centres with the 'non-innocent' NO ligand has experienced a renaissance in the last decades because of findings of their biochemical significance. Our work concentrates on high-spin $\{FeNO\}^7$ complexes which show an $S = 3/2$ ground state, and their related $\{Fe(NO)_2\}^9$ species. Crystalline complexes were prepared from the reaction of NO with Fe^{II} and thoroughly characterized. Bonding, spin situation and oxidation states of the Fe–NO moiety are described. Using quantum-chemical calculations like DFT, CASSCF and EOS, frontier orbitals and spin populations of selected complexes are given. The results are leading to the interpretation of a largely covalent nature of the nitrosyl–iron bond. The investigation of the $[Fe(H_2O)_5(NO)]^{2+}$ ion, an enduring issue in Inorganic Chemistry since the nineteenth century, lead to the isolation of a gallate or ferrate salt of the general formula $[Fe(H_2O)_5(NO)][M^{III}(fpin)_2(H_2O)]_2 \cdot x H_2O$ (M = Fe, Ga; $x \approx 8.3$). Crystal structure analyses of halogenido-mononitrosyliron compounds (MNICs) and their dinitrosyl analogues (DNICs) are presented. The reaction process is analysed by in situ-UV–vis and in situ-IR measurements. Their application as a competitive-consecutive reaction pattern for engineer partners is introduced. Crystal-structure analyses and the calculation of the electronic properties for nitrosyl-iron compounds with different aminecarboxylato co-ligands like imino- and oxodiacetate as well as ethylenediaminetetraacetate (edta) enable a closer insight towards their structure-properties relationship.

1 Introduction

In the field of chemical engineering, the transformation of substances with high yield and high selectivity is one of the most important tasks. For the synthesis of many bulk chemicals, gaseous starting compounds have to be brought in close contact with

M. Oßberger · P. Klüfers (✉)

Department Chemie, Ludwig-Maximilians-Universität München, Butenandtstr. 5-13, Haus D, 81377 München, Germany
e-mail: kluef@cup.uni-muenchen.de

a continuous liquid phase. Since the hydrodynamic behaviour is not yet well under-
stood, engineers were seeking to apply chemical systems which can be investigated
in their experimental bubble columns to understand mass transfer from bubble to
liquid. For this purpose, one needs chemical reactive model systems, which meet a
variety of conditions: the chemicals must be readily available; the reaction should
be performed in manageable and harmless solvents, with reasonable stability of the
products. Kinetic properties should be tuneable by varying the components, and secu-
rity issues must be controlled to allow for upscaling of the reaction system. Further
constraints include the in situ traceability of the reaction progress, thus it should
exhibit colour and spectroscopic resonance. Detection is feasible with shadowgraphy
and measurements such as UV/VIS, IR or Raman spectroscopy.

All these specifications are met for a reaction system from the subdiscipline of
coordination chemistry, the two-phase systems of a dissolved ferrous complex and
gaseous nitric oxide. These systems offer bulk chemicals and easy disposal of product
solutions, water or alcohols as the reaction media, an intense colour of the products
with reasonable to high stabilities, and a fast intrinsic reaction of NO which offers
characterization within milliseconds. Furthermore, they exhibit a distinct and well-
resolved NO-valence-stretch frequency in IR spectra, and kinetics can be controlled
by the variation of ligands. NO, being a rather unpolar molecule, shows a retarded
gas-to-liquid mass transfer (Henry constant: 1.9×10^{-5} mol m^{-3} Pa^{-1} [1]) and, thus,
offers advantageous diffusion characteristics.

A period of particularly intense research on NO started when NO was recognized
a hormone three decades ago (*Science* rated NO as the "molecule of the year" [2]).
With iron(II) as the NO-binding centre in the physiological NO-receptors, the early
focus lay on low-spin heme–NO interactions, responsible for biochemical signal
transduction. It was demonstrated in recent years that high-spin non-heme Fe–NO
complexes are of biological relevance as well [3]. Since the triplett-NO$^-$ ligand
and O$_2$ in its ground state are isoelectronic, both species show similarities in their
interaction with the active site of an iron-enzyme–substrate complex. Due to the
higher stability of a Fe–NO linkage compared to its O$_2$ analogue, the investigation
of nitrosyl adducts is a frequent approach to obtain more insight into O$_2$ activation.

In nature, there are several examples of mononuclear non-heme iron proteins that
are able to bind nitric oxide, e.g., soy-bean lipoxygenase [4], protocatechuate-4,5-
dioxygenase [5] or a ferric uptake regulator protein (Fur) [6]. The reactivity of these
centres towards NO has been modelled by several mononuclear ferrous complexes
[7, 8].

The assignment of an oxidation state to the metal in a nitrosyliron compound is
impeded by the small energy difference between the metal-d orbitals and the two
NO-π* orbitals. Therefore, Enemark and Feltham introduced a notation for nitrosyl–
metal complexes by summarizing the metal-d and the NO-π* electrons [9]. Nitric
oxide binds reversibly to a ferrous active site stabilised by chelate ligands. According
to Enemark and Feltham, those nitrosyliron species are {FeNO}^{7} complexes which
may be interpreted as Fe^I(NO$^+$) [d^7 + (π*)^0], Fe^{II}(NO) [d^6 + (π*)^1] or Fe^{III}(NO$^-$)
[d^5 + (π*)^2]. These {FeNO}^{7} species show an $S = 3/2$ ground state by the anti-
ferromagnetic coupling of the single NO spin with the $S = 2$ state of a high-spin

Fig. 1 The so-called 'brown ring' which forms between the top layer containing ferrous sulfate and nitrate and the bottom layer of concentrated sulfuric acid. The colour stems from $\{FeNO\}^7$ species that form after the reduction of nitrate $(3Fe^{2+} + NO_{3-} + 4H^+ \rightarrow 3Fe^{3+} + NO + 2H_2O)$ from NO and excess Fe^{2+} Copyright Wiley–VCH Verlag GmbH & Co. KGaA. Reproduced with permission from [26]
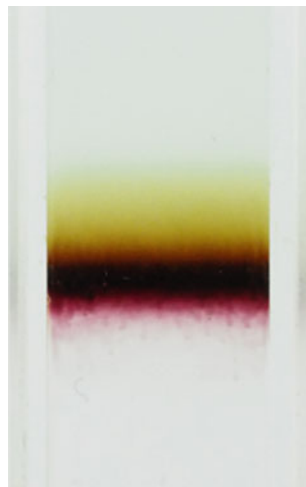
ferrous educt [8, 10]. A common interpretation of the total $S = 3/2$ spin assembles a high-spin iron(III) ($S = 5/2$) central atom and a triplet-NO^- ligand ($S = 1$) in antiferromagnetic coupling [8, 11–13] resulting in a quartet ground state.

Our work concentrates on these iron species, the $S = 3/2$ subclass of $\{FeNO\}^7$-complexes. Their biochemical issue can be studied in following references [14–19].

The underlying chemistry of this class of compounds has been known for more than a century, since the parent species forms in the course of the qualitative analytical nitrate detection—the so-called"brown ring test". It should be noted that the ultimate validation of this species by crystal-structure analysis succeeded in the project described here.

This parent species as well as other nitrosyl complexes of this class are formed in a simple reaction:

$$Fe^{II}(sln) + NO(g) \Leftrightarrow [Fe(NO)]^{2+}(sln)$$
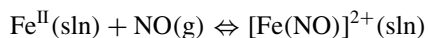
where $Fe^{II}(sln)$ stands for the solution of a high-spin ferrous species.

This article starts with the description of the brown-ring parent species, followed by halogenido and aminecarboxylato co-ligands, and ending up with perfluorpinacolato species. In particular the latter have been shown to clarify the ambiguous oxidation-state assignment.

2 $[Fe(H_2O)_5(NO)]^{2+}$, the 'Brown-Ring' Chromophore

The investigation of the $[Fe(H_2O)_5(NO)]^{2+}$ (**1**) ion, the coloured component of the 'brown ring' of the positive analytical nitrate test (Fig. 1), has been an enduring issue in Inorganic Chemistry since the nineteenth century.

The first period of intensive research dates back to the first decade of the twentieth century, where the competing groups of Manchot and Kohlschütter demonstrated the cationic nature of **1** as well as the equimolar amount of iron and nitric oxide in this species, which they obtained by the reaction of ferrous salts and nitric oxide gas in acidic aqueous solution [20, 21].

In the following years, actually up to now, synthetic and theoretical groups struggled with the correct formula, spin state and oxidation state of this Fe(NO) species [14, 22–25]. All these works were lacking a profound investigation of this cationic complex in the solid state. One reason is the low stability of this coordination entity. Prepared from a ferrous salt and NO gas in water, **1** rapidly releases NO on a purge of inert gas through the solution. The isolation of a salt of this brown chromophore succeeded with large gallate or ferrate anions, following the general formula $[Fe(H_2O)_5(NO)][M^{III}(fpin)_2(H_2O)]_2 \cdot xH_2O$ (M = Fe, Ga; $x \approx 8.3$) [26]. The dianionic ligand fpin is the bidentate perfluoropinacolato-κ^2O,O' chelator which we and others have used to prepare tetracoordinate high-spin ferrates(II) with the $[Fe(fpin)_2]^{2-}$ anion [27, 28]. Solutions containing this latter anion absorb NO to yield the five-coordinate $[Fe(fpin)_2(NO)]^{2-}$ ion, which is a topic of the final section. Since the ferrate route is challenged by the formation of N_2O due to oxidation of the ferrous precursor to a ferrate(III), we modified the preparation by using gallium as the anion's central atom in the overall acidic solution. The structure of **1** in the brown gallate crystals is shown in Fig. 2.

The structure analysis matches most of the predictions, e.g., the brown chromophore of the solids in fact *is* the pentaaquanitrosyliron(2+) ion. However, the

Fig. 2 The molecular structure of **1** in crystals of the gallate (50% ellipsoid probability). Monoclinic, $P2_1/n$. Distances in Å: Fe–O (a,b,c,d) 2.067, Fe–O(e) 2.121(3), Fe–N 1.786(4), N–O 1.143(5). Angle: Fe–N–O 160.6(4)°. N–O stretch in the solid: 1843 cm^{-1} Copyright Wiley–VCH Verlag GmbH & Co. KGaA. Reproduced with permission from [26]
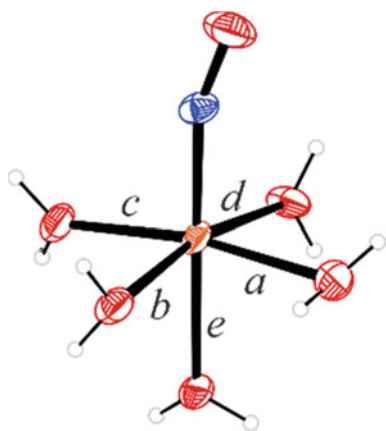
C_1-symmetry of **1** as well as distances and angles are at variance with the theoretical predictions. In particular, the claimed linearity of the Fe–N–O unit is not observed.

The result of a correlated analysis by means of a CASSCF approach using various active configurational spaces is depicted in Fig. 3 and explains the general instability of the compound in terms of markedly occupied antibonds (0.28) attributing to a destabilised Fe–NO bond.

MO42 and MO43 show the dominant π-bonding interaction of N–O-π^* orbitals with Fe-d(xz) and -d(yz) orbitals with their occupation clearly below two (1.72). Due to the higher share of the atomic orbitals of the Fe atom over the NO contribution,
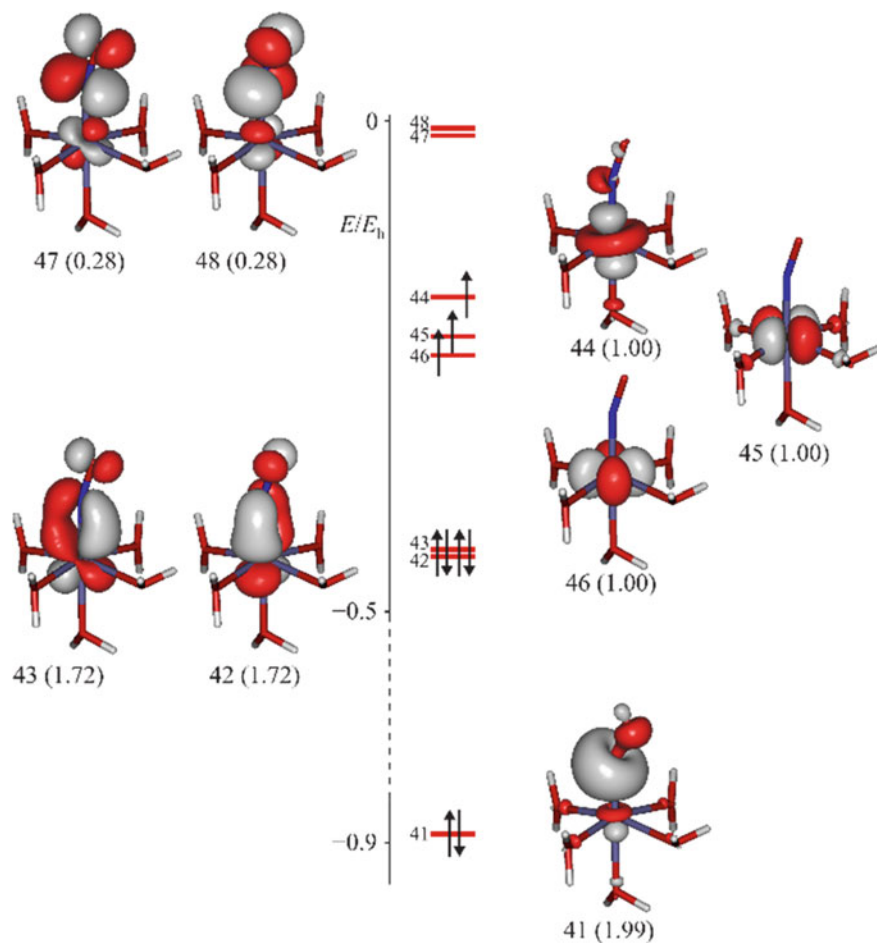
Fig. 3 Frontier orbitals of the $[Fe(H_2O)_5(NO)]^{2+}$ ion [CASSCF(9,13)/def2-TZVP; isovalue 0.06 a.u.]. Orbital numbering and occupation (in parentheses). The 22211100 occupation pattern indicated by the arrows refers to the ground state's leading configuration (62% contribution. Copyright Wiley–VCH Verlag GmbH & Co. KGaA. Reproduced with permission from [26]

Fig. 4 The spin population of **1** (BP86/def2-TZVP; positive spin values blue, negative values yellow; isovalue in a.u.: 0.1) Copyright Wiley–VCH Verlag GmbH & Co. KGaA. Reproduced with permission from [26]

$[Fe(H_2O)_5(NO)]^{2+}$
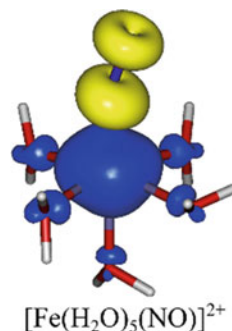
these interactions are π-backbonds from the central atom into the N–O-π* orbitals. It should be noted that the three excess spins are clearly metal-centred (MOs 44–46).

Due to the occupied Fe–NO antibonds, the leading configuration (arrows in Fig. 3) contributes only 62% to the species' ground state. This indicates a significant stretch of the Fe–NO-π-interactions and a weakend bond.

As one physical origin of this stretch, we see enhanced Pauli repulsion in the nitrosyl species in question, as a special aspect of quartet-$\{FeNO\}^7$ species. The obviously repulsive Fe-d(z^2)–NO-σ-contact (MO41 and MO44) appears provoking the typical Fe–N–O bending. Comparing these findings with the chromium analogue, where repulsive metal-d(z^2) electron is missing, one finds the M–NO bond length in $[Cr(H_2O)_5(NO)]^{2+}$ approx. 0.1 Å shorter than that in **1** (1.697 vs. 1.786 Å). Moreover, the Cr–N–O angle is close to 180° [29].

The spin-population analysis of **1** (Fig. 4) shows spin polarisation within the Fe–NO π-bonds due to their orthogonal interaction with the metal-centred major spin. Hence, both Fe–NO π-interactions accumulate α-spin density at the metal centre and thus leave β-spin density on the ligand.

The result, the Fe–NO-binding through two stretched, spin-polarized interactions, is a challenge of the concept of the oxidation state. This somewhat delicate issue is addressed in the last chapter of this publication.

3 Syntheses, Structure and Bonding of $\{FeNO\}^7$- and $\{Fe(NO)_2\}^9$-type Halogenido Nitrosyl Ferrates

Tetrahedral halogenido-mononitrosyliron compounds (halogenido-MNICs) are related to the $[Fe(H_2O)_5(NO)]^{2+}$ cation for some reasons. Both exhibit a $\{FeNO\}^7$(S = 3/2) ground state due to the weak field aqua and halogenido co-ligands. Since the brown ring cation was prepared originally from ferrous salts and NO in sulfuric acid, a chloride variant of the latter species, the green $[FeCl_3(NO)]^-$ ion, was first prepared analogously by using hydrochloric instead of sulfuric acid [30].

Halogenido-MNICs as well as halogenido-DNICs such as the $\{Fe(NO)_2\}^9$-type dinitrosyliron species $[FeCl_2(NO)_2]^-$, both are simple prototypes of sulfur-bonded iron compounds of biological significance with cysteinate or ferredoxin-bound sulfide [31–34]. Though being investigated for more than a century, including many biomimetic synthetic routes [35], neither clean preparative routes nor reliable structural parameters were available for both chlorido anions.

In fact, crystals of MNIC's can be obtained with a bulky counterion by carefully balancing educt and product solubilities [36]. Crystalline trichlorido- as well as tribromidonitrosylferrates of various, more or less bulky cations were prepared by a facile procedure at ambient conditions which uses inexpensive educts, like ferrous chloride tetrahydrate or ferrous triflate, the chloride or bromide of the desired counterion, degassed methanol as the solvent, and an excess of purified, i.e. NO_2-free, nitric oxide. The procedure follows the equation (for the chloride):

$$A^+Cl^- + FeCl_2 + NO \rightarrow A^+[FeCl_3(NO)]^-$$

The reaction's progress was easily monitored by the deepening of the characteristic green colour. The yield of isolated crystalline product reached 90% for the larger counterions PPh_4^+, $AsPh_4^+$, and PPN^+. All solids were stable to air for months, thus no special care had to be taken for investigating them. This property should be mentioned since purging the solutions with a stream of inert gas will destroy the nitrosyl complex rapidly by reversing its formation reaction. Seeding and growing crystals thus had to be performed under a NO atmosphere (Fig. 5).

Attempts to synthesise salts of an unknown $[FeF_3(NO)]^-$ or $[FeI_3(NO)]^-$ anion failed. Nitrosylation of iodide-containing solutions always yielded the respective DNIC $[FeI_2(NO)_2]^-$. Replacing the ferrous chloride component with ferric chloride in methanol, the $[FeCl_3(NO)]^-$ ion could be achieved as well.
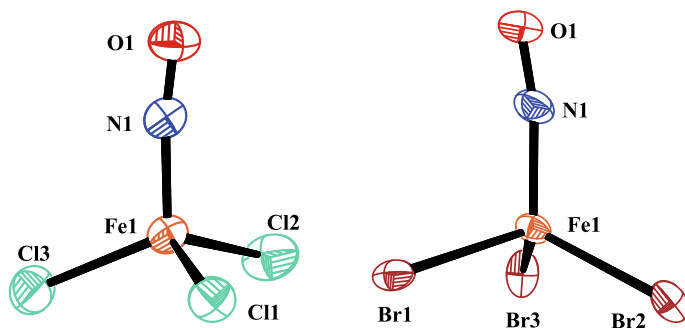
Fig. 5 Left: The molecular structure of the anion in crystals of $AsPh_4[FeCl_3(NO)]$ (50% ellipsoid probability). Monoclinic, $P2_1/n$. Distances (in Å): Fe1–Cl1 2.232(1), Fe1–N1 1.730(4); N1–O1 1.142(5). Angle: Fe1–N1–O1 171.6(4)°. Right: The structure of the anion in crystals of $PPN[FeBr_3(NO)]$ (50% ellipsoid probability). Monoclinic, $C2/c$. Distances (in Å): Fe1–Br1 2.3657(5), Fe1–N1 1.729(3), N1–O1 1.150(3). Copyright Wiley–VCH Verlag GmbH & Co. KGaA. Reproduced with permission from [36]

NO(g) works as the reductant according to the equation:

$$A^+Cl^- + FeCl_3 + 2NO + MeOH \rightarrow A^+[FeCl_3(NO)]^- + MeONO + HCl$$
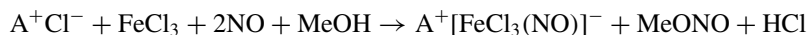
The formation of methyl nitrite is best monitored by UV–vis spectroscopy where a characteristic 'five-finger' motif indicated MeONO formation. However, this route becomes unattractive from a practical viewpoint. Yields were low, and a long crystallisation time resulted, and, as a more serious drawback, structure determination of $NEt_4[FeCl_3(NO)]$ revealed a contamination with about 15% $[FeCl_4]^-$ content. From this observation we conclude that the contaminant $NEt_4[FeCl_4]$ was not homogenously distributed in the NO-containing bulk but had served as a seed due to its lower solubility and thus gave rise to the epitaxial growth of the bulk. Crystallisation occurs within two weeks instead of the normal prolonged period of time (more than half a year). No Cl/NO disorder was detected although chloride and nitrosyl moieties on the point positions occupied by the ligands are exchangeable.

DFT investigation of the $[FeCl_3(NO)]^-$ ion produces a good agreement (Table 1) between experimental and calculated ν(N–O) values.

The frontier orbitals of a CASSCF approach are shown in Fig. 6. The most typical feature which shares the $[FeCl_3(NO)]^-$ ion with other nitrosyls, is the marked population of the Fe–NO π^* antibonds and the corresponding depopulation of the Fe–NO π bonds (compare the 0.27:1.73 antibond:bond population of this ion with a 0.28:1.71 ratio of the brown-ring aqua species). Accordingly, the leading 22,211,100 configuration (second shell omitted) depicted in Fig. 6 contributed only 65% to the ground

Table 1 Distances, (mean) angles, and energy of the N–O stretching vibration for six reliably analysed solids from the standard ferrous route, and the $[FeCl_3(NO)]^-$ ion in DFT calculations for the given method and the def2-TZVP basis set (Grimme's van-der-Waals correction; environment modelled by a COSMO [Orca3] or CPCM [Orca4] approach at practically infinite dielectric constant; uncorrected wave numbers tabulated)

	Fe–Cl/Å	Fe–N/Å	N–O/Å	Fe–N–O/°	Cl–Fe–Cl/°	$\tilde{\nu}$(N–O)/cm^{-1}
mean 6 × Xray	2.236 ± 0.006^a	1.726	1.149	173.5	110.1 ± 1.2^a	1797
BP86	2.249	1.705	1.167	177.5	108.7	1786
BP86[b]	2.248	1.702	1.165	179.9	108.7	1791
TPSS[c]	2.251	1.712	1.163	176.9	109.2	1792
B97-D	2.275	1.745	1.161	178.3	109.4	1799
B97-D + zora	2.268	1.733	1.163	178.4	109.0	1794

Copyright Wiley–VCH Verlag GmbH & Co. KGaA. Reproduced with permission from [36]
[a]The given standard deviation of the mean exceeds the tenfold of the mean standard deviation of the X-ray refinement, taken as indicating a 'soft' variable in a crystalline environment
[b]Orca4 with CPCM (water) instead of Orca3.03 with COSMO (water)
[c]The same values were obtained with the def2-aug-TZVPP basis set except 1790 cm^{-1} for the valence vibration
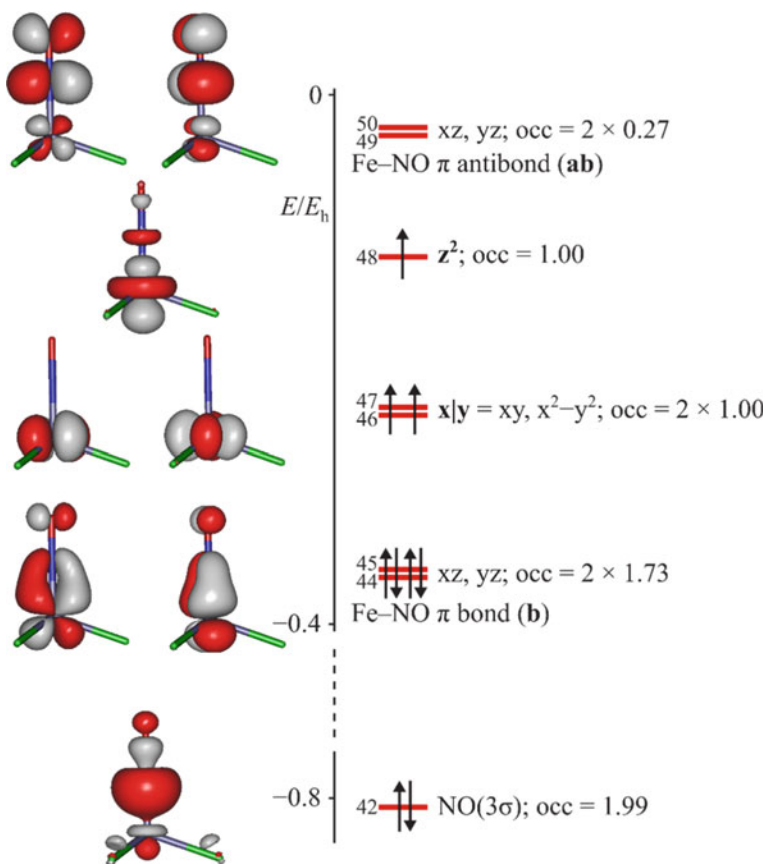
Fig. 6 Frontier orbitals of the $[FeCl_3(NO)]^-$ ion [CASSCF(9,13)/def2-TZVP; isovalue 0.06 a.u.]. Orbital labels refer to Cartesian axes: z up, y to the right, x to the viewer; orbital numbering starts with "1" (= Orca numbering + 1). The 22211100 occupation pattern indicated by the arrows refers to the ground state's leading configuration (65% contribution). Copyright Wiley–VCH Verlag GmbH & Co. KGaA. Reproduced with permission from [36]

state, leaving the rest to single and double excitations from the Fe–NO bonds to the antibonds. The reason for this hindered overlap of the metal–ligand orbitals in $[FeCl_3(NO)]^-$ is a twofold Pauli repulsion (see [36] for details).

The high-spin character of the $[FeCl_3(NO)]^-$ ion goes along with the singly occupied MOs 46–48. There is spin polarisation along the Fe–NO fragment, and spin populations of -0.50 for NO and 3.40 for the Fe atom are similar to the related $[Fe(H_2O)_5(NO)]^{2+}$ ion (see Radoń's study [37]).

A broken-symmetry approach offers an alternative perspective on the antiferromagnetic character of the Fe–NO interaction. As a result, the considerable overlap of

the α and β part of the Fe–NO π bonds in terms of a corresponding-orbital transformation resulted in $S = 0.84$ (TPSSh/def2-TZVP level). The value close to 1 indicates the largely covalent character of the Fe–NO interaction [38].

The bonding description of the Fe–NO moiety derived so far focuses on two Fe–NO π bonds formed by the interaction of Fe-d(xz) and Fe-d(yz) atom orbitals and the N–O-π*(x) and N–O-π*(y) molecular orbitals. Assuming a purely covalent interaction, the four electrons involved in these two bonds are shared equally between the metal and the ligand, leaving the nitrosyl ligand with the doubly occupied π* MOs as NO⁻, the iron centre as Fe^{III}. A mere inspection of the MOs in Fig. 6 tackles the perfect-covalence assumption. MOs 44/45 compared to MOs 49/50 show a higher contribution of the metal d orbital to the bond and a lower one to the antibond. Hence, we should end up with a smaller absolute value than −1 for the ligand. Thus we see a, more or less, covalent nitrosyl–iron interaction through two π bonds which are polarised towards the metal.

The computational analysis of the MNIC spectra reveals the origin of the major absorption bands in the visible region (see Fig. 8). β-Spin transitions should occur from the degenerate Fe–NO bonds (MOs 44 and 45) (1) to the degenerate metal-centred MOs of the xy-plane (MOs 46 and 47), (2) to the mainly metal-d(z^2)-centred MO 48. (1) can be assigned to the band at $\lambda = 595$ nm, (2) to the band at $\lambda = 472$ nm. In very diluted solutions a strong band at $\lambda = 354$ nm can be observed, which refers to an α-spin transition into the degenerate Fe–NO antibonds as the only acceptor orbitals starting from the degenerate xy-plane (MOs 46 and 47).

The coincidence of both spectra, the computationally analysed and the experimental one, in solution and as a $BaSO_4$-diluted powder sample were satisfactory.

In the presence of a base, a consecutive MNIC-to-DNIC transformation is possible. Publications from the second half of the last century reported the formation of DNICs if base was added [39, 40] according to:

$$FeCl_2 + 3NO + MeOH + B \rightarrow [FeCl_2(NO)_2]^-$$
$$+ MeONO + BH^+ \left(B = NEt_3, F^-\right)$$
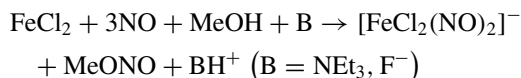
A two-stage procedure of this two-step reaction sequence thus accelerated the formation of the final product. An UV–vis (Fig. 8) and an in situ IR study (Fig. 9) were used to demonstrate this: first, ferrous chloride tetrahydrate was reacted rapidly in methanol with NO to the respective greenish MNIC and small amounts of DNIC only. In the second step, the addition of base resulted in the immediate increase of the reddish DNIC solutions and its signals with a decrease of the MNIC peak (Fig. 7).

To support the development of the MNIC intermediate, chloride or bromide salt was introduced. In the latter case aqueous solution of hydrobromic acid (ca. half a mole per mol iron) was added.

The isolation of pure material succeeded and crystallisation of chlorido- and bromido-DNIC yielded reliable X-ray data sets (Fig. 10). The bonding and spin situation in the $[FeCl_2(NO)_2]^-$ ion resembles the results for the MNIC.
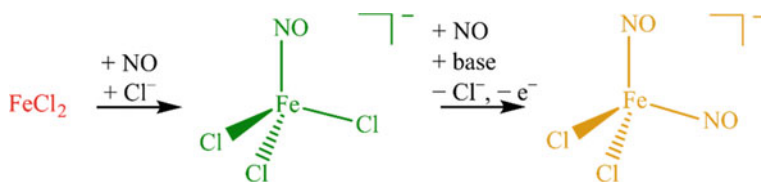
Fig. 7 Transformation from ferrous educt to MNIC and DNIC
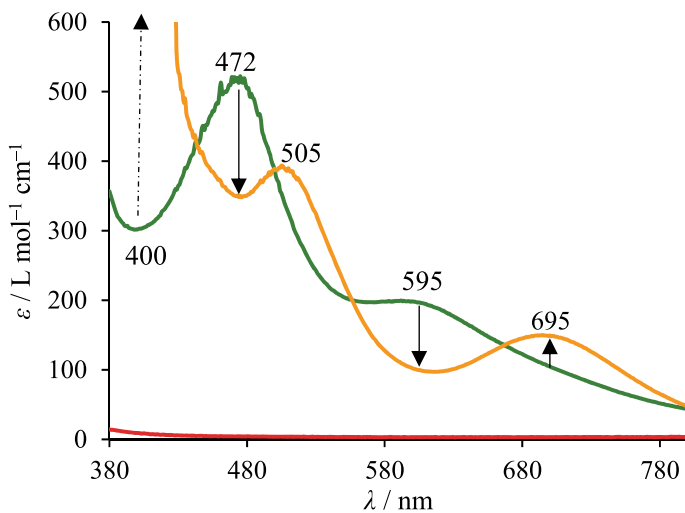
Fig. 8 UV–vis: $c(Fe^{2+}) = 5$ mM, $d = 1$ cm; transformation from MNIC to DNIC after addition of base
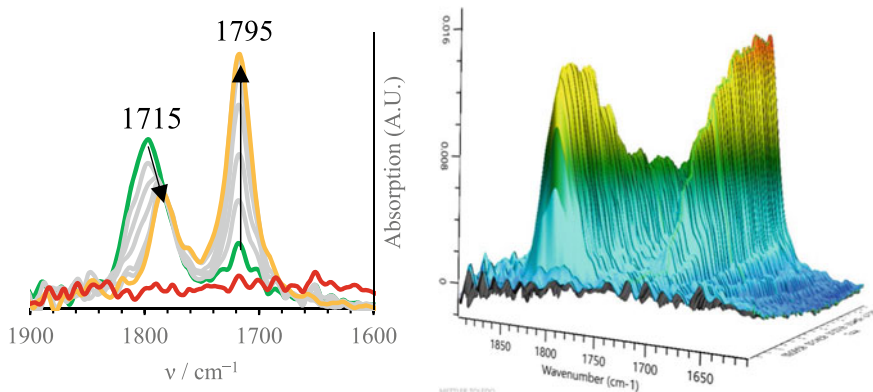
Fig. 9 In situ-IR: $c(Fe^{2+}) = 20$ mM; transformation from MNIC to DNIC after addition of base
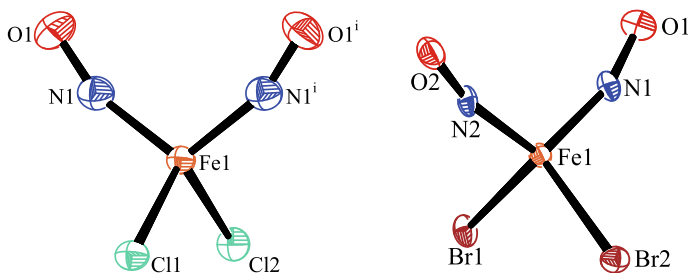
Fig. 10 Left: The molecular structure of the anion in crystals of $NMe_4[FeCl_2(NO)_2]$ (50% ellipsoid probability). Orthorhombic, *Pbcm*. Distances (in Å): Fe1–N1 1.709(2), N1–O1 1.146(2), Fe1–C1 2.2797(8), Fe1–Cl2 2.2751(7). Angles (in degrees): Fe1–N1–O1 160.8(2), N1–Fe–N1^i 108.30(8), C1–Fe1–Cl2 107.41(3). Right: The structure of the anion in red-brown crystals of $PPN[FeBr_2(NO)_2]$ (50% ellipsoid probability). Triclinic, P$\bar{1}$. Distances in Å: Fe1–Br1 2.4108(4), Fe1–Br2 2.4173(4), Fe1–N1 1.707(2), Fe1–N2 1.723(2), N1–O1 1.145(2), N2–2 1.099(3). Angles (in degrees): Fe1–N1–O1 162.73(18), Fe1–N2–O2 166.34(18), N1–Fe1–N2 112.26(9), Br1–Fe1–Br2 109.12(1). Copyright Wiley–VCH Verlag GmbH & Co. KGaA. Reproduced with permission from [36]

The MNIC/DNIC reaction system was selected by our engineer partners for a closer inspection since the competitive-consecutive reaction pattern allows the detection of two different complexes in the NO bubble wake. One important prerequisite is the formation velocity of the two products, MNIC and DNIC, which shouldn't differ too much. In a detailed kinetic study based on absorbance maxima of MNIC and DNIC (Fig. 8), in collaboration with the Schindler group, stopped-flow methods were applied and activation parameters could be obtained. It was observed that the rate constants for formation of MNIC, $k_{obs} = 5.0 \cdot 10^5$ s^{-1} and DNIC, $k_{obs} = 6.5 \cdot 10^{-4}$ s^{-1} at $T = 20\,°C$ differ by a factor of 10^9.[41]. Thus, the reaction rates differ by a factor of 10^9. This huge difference is most likely caused by the required electron transfer during the reaction of MNIC to DNIC (Fig. 7). The mononitrosyl iron complex of $\{FeNO\}^7$ type turns into a $\{Fe(NO)_2\}^9$ species, where the latter had received two electrons. Two NO, one as a ligand and one as a reducing agent, contribute one electron each. The resulting NO^+ binds to methanolate forming methylnitrite. However, the slow 'second' reaction to DNIC makes it impossible to detect this product within the wake of a NO bubble. Furthermore, the concentrations are limited to 5 mM, when adding the base at the start of an attempted DNIC formation.

An acceleration of the DNIC formation was achieved when the reducing agent NO was substituted by iodide salt. With ferrous chloride as a starting material and tetraethylammoniumiodide as an iodide source, first experiments showed that the reaction in methanol produces DNIC on a faster scale with $k_{obs} = 0.04$ s^{-1} ($T = -20\,°C$) [42] according to the proposed reaction mechanism:

MNIC Formation:

$$FeCl_2 + MeOH + NO \rightarrow [FeCl_2(MeOH)(NO)]$$

DNIC Formation:

$$[\text{FeCl}_2(\text{MeOH})(\text{NO})] + 3/2\,\text{NEt}_4\text{I} \rightarrow$$
$$\text{NEt}_4[\text{FeCl}_2(\text{MeOH})(\text{NO})] + 1/2\,\text{NEt}_4\text{I}_3$$
$$\text{NEt}_4[\text{FeCl}_2(\text{MeOH})(\text{NO})] + \text{NO} \rightarrow$$
$$\text{NEt}_4[\text{FeCl}_2(\text{NO})_2] + \text{MeOH}$$

Total:

$$\text{FeCl}_2 + 2\,\text{NO} + 3/2\,\text{NEt}_4\text{I} \rightarrow \text{NEt}_4[\text{FeCl}_2(\text{NO})_2] + 1/2\,\text{NEt}_4\text{I}_3$$
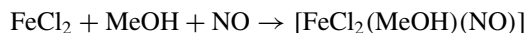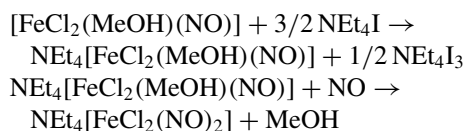
A fourfold amount of the iodide salt was found to be adequate in terms of velocity. The formation of the triiodide ion seems to support the reaction. Further analytical and kinetical measurements are currently underway.

No chloride salt was added to decrease the share of the stable $[\text{FeCl}_3(\text{NO})]^-$ ion. Instead, $[\text{FeCl}_2(\text{MeOH})(\text{NO})]$ might develop. We tested the addition of ascorbic acid, since it reduces triiodide to iodide and clears the UV–vis spectra in the near UV region. But as a potential ligand it might complicate the reaction process, thus we abstained from using it. The reaction process can be monitored by in situ IR (Fig. 11), since we could raise the starting concentrations to a maximum of 75 mM. The result shows the initial formation of MNIC which transforms rapidly into DNIC.
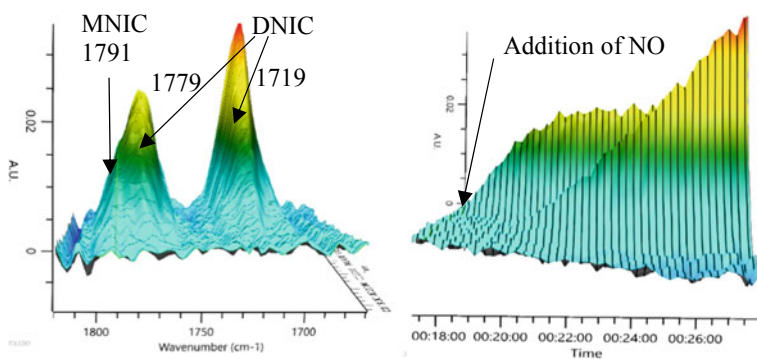
Fig. 11 In situ-IR 3D spectra of reaction: $c(\text{FeCl}_2) = 29$ mM, 4Äq NEt_4I in MeOH, T = -20 °C

4 Structure and Bonding of Nitrosyl–iron(II) Compounds with Aminecarboxylato Co-Ligands in Aqueous Solution

In the 1980s, aminecarboxylates were introduced into the field of $\{FeNO\}^7(S = 3/2)$ complexes, motivated by the idea of using the enhanced Fe^{II}–NO binding by aminecarboxylato co-ligands for the development of agents suitable for the removal of NO from power-plant flue-gas streams [43].

The data collected in this period indicated that the stability of the Fe^{II}–NO bond highly depends on the chelate used in the complex.

Later, the body of spectroscopic, kinetic and thermodynamic data on aqueous solutions of aminecarboxylate-supported ferrous nitrosyls was completed comprehensively in a series of publications by the van Eldik group [44–46]. The authors state that a higher stability of the Fe–NO linkage in the presence of multidentate aminecarboxylate co-ligands is correlated with a higher trivalent character of the central atom.

The lack of information in solid state may lead to many unproven suggestions. No species had been crystallised from an aqueous solution so far. Accordingly, no crystal structure was available that showed aqua co-ligands. We highlight the significance of both aspects—the isolation of hydrolytically stable quartet-$\{FeNO\}^7$ species, and the accompanying presence of aqua and nitrosyl ligands.

The importance may become clearer when confronting with published attempts to model the so-called facial triad (two histidine and one carboxylate ligand) of mononuclear non-heme iron oxygenases by aminecarboxylate ligands. Due to lack of structural data advanced EPR technology need to be used to elucidate the structure of the aminecarboxylate-aqua-$\{FeNO\}^7$ model compounds [17].

4.1 First Part: Less Stable Compounds

The aim of this section is to increase the knowledge of the structural chemistry of octahedrally coordinated quartet-$\{FeNO\}^7$ centres [47]. We use the stability criterion to organise the results. The first part is restricted to co-ligands which lead to aqueous solutions of limited NO-binding capability as detected by simply bubbling an inert gas such as argon through the respective solution. All solutions described in this first part lose nitric oxide during this procedure. Hence, the dark greenish $\{FeNO\}^7$ centres turn to almost colourless co-ligand–iron(II) complexes in the course of the experiment. With respect to this test, stable solutions are the focus of the second part.

Figure 12 illustrates the different co-ligands and where crystallization was successful. In their dianionic form they all serve as tridentate chelators.

Figure 13 displays the synthetic route employed for the preparation of the quartet-$\{FeNO\}^7$ compounds: $FeSO_4$ reacts in aqueous solution with nitric oxide and one equivalent of iminodiacetic acid (H_2ida) or its derivatives to yield dark green solutions of **2**. Under inert gas conditions these solutions are stable for several months at room
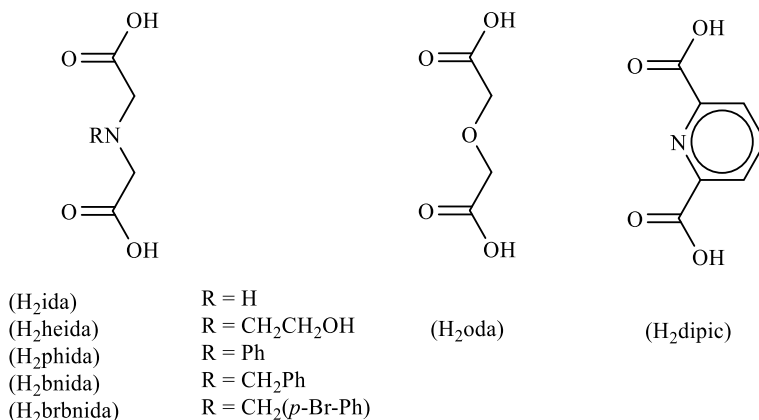
Fig. 12 The dibasic parent acids of chelating ligands used for the synthesis of the quartet-{FeNO}^{7} compounds of this work
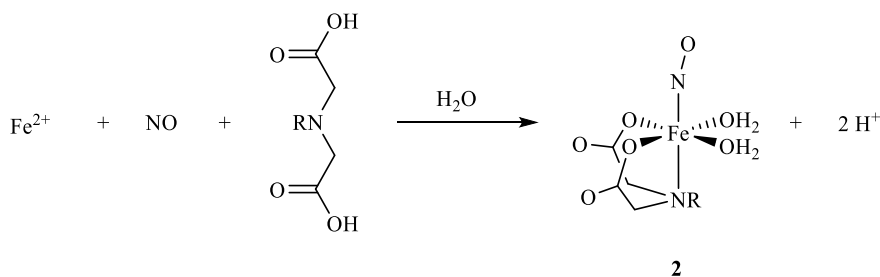
Fig. 13 Procedure for the synthesis of the quartet-{FeNO}^{7} compounds **2**

temperature. In contact with air they show their instability and decompose within several hours. By the diffusion of acetone into the solutions, we obtained black-green crystals of **2**, suitable for X-Ray diffraction analyses. The dried solid compounds are stable against oxygen and moisture.

Crystal-structure determination revealed the octahedral coordination of the iron central atom for all compounds **2** (Fig. 14). They are unique as they are the first crystalline {FeNO}^{7} compounds with aqua ligands. The chelating ligands coordinate either facially (**2a**) or meridionally (**2b**). Nitric oxide coordinates in a slightly bent fashion *trans* to the central hetero atom of the chelate ligand**.** The remaining positions are occupied by aqua ligands which support a three-dimensional hydrogen-bond network that connects the complex units. With Fe–N$_{NO}$ distances between 1.76 and 1.80 Å, N–O distances between 1.09 and 1.17 Å and Fe–N–O angles between 148° and 171°, the compounds **2** match the crystalline quartet-{FeNO}^{7} compounds with octahedral coordination, known to literature [48–51].

Compounds **2** feature slightly bent nitrosyliron moieties with Fe–N–O angles between 148° and 171°. IR and UV–vis spectroscopy show the vibration/absorption
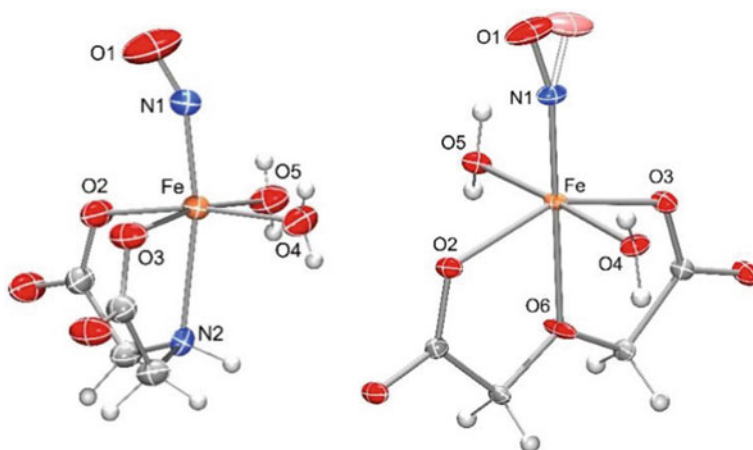
Fig. 14 Left: The molecular structure in crystals of [Fe(H$_2$O)$_2$(ida)(NO)] **(2a)** (50% ellipsoid probability). Orthorhombic, *Cmc*21. Right: The molecular structure in crystals of [Fe(H$_2$O)$_2$(NO)(oda)] **(2b)**. Orthorhombic, *Aba*2. O1 is disordered. Copyright Wiley–VCH Verlag GmbH & Co. KGaA. Reproduced with permission from [47]

Table 2 IR- and UV-vis data of compounds **2a** and **2b**

Compound	ν(NO)/cm^{-1}	λ/nm				
2a	1772	340	414	459	618	692
2b	1799	340	407	459	571	693

bands collected in Table 2 which also match the widely published results for octahedrally coordinated quartet-{FeNO}^{7} compounds [47].

The magnetism of **2a** was determined by SQUID magnetometry. Using Eq. (1), the magnetic moment μ_{eff} was calculated for $\mu_{\mathrm{eff}} = 3.95\ \mu_B$. This value lay in the expected range for quartet compounds with the spin-only value of $\mu_{\mathrm{s.o.}} = 3.88\mu_B$.

$$\mu_{\mathrm{eff}} = \sqrt{\frac{3k_B\chi_m T}{\mu_0 N_A \mu_B^2}} \tag{1}$$

$$\mu_{\mathrm{s.o.}} = 2\sqrt{S(S+1)} \tag{2}$$

We carried out quantum-chemical calculations, based on DFT and CASSCF methods to gain insight into the electronic properties of compounds **2**. In particular, we attempted to evaluate the oxidation state of the iron central atom and the nitrosyl ligand. Various theoretical and spectroscopic studies have been published on this issue. Most of them describe either a high-spin Fe$^{\mathrm{III}}$/^{3}NO$^-$ or a high-spin Fe$^{\mathrm{II}}$/^{2}NO [47] couple with antiferromagnetic Fe–NO coupling in both cases.

In terms of the X-ray-derived data for **2**, the best agreement between calculated and experimental data was achieved using the def2-TZVP basis set [52], the dispersion-corrected functional B97-D [53] and the D-COSMO-RS solvation model [54] to account for the hydrogen-bond network in the crystal structures. All calculations were performed using spin-unrestricted open-shell systems with three unpaired electrons.

The electronic description of the Fe(NO) moiety is the same for all compounds **2** and is influenced minimally by the different chelating ligands. Figure 15 illustrates the HOMO between Fe and NO of **2a**. The Fe–NO interaction is again dominated by the coupling of two spin-down NO-π^* orbitals with the symmetrically matching Fe-d_{xz} and Fe-d_{yz} spin-up orbitals. The orbitals possess a 30–40% Fe-d character, up to a 2% Fe–p character and a 50–60% NO-π^* character.

A broken-symmetry approach supports the view of a largely covalent Fe–NO bond. Using the Yamaguchi formula, coupling constants in the range of 2205–2318 cm^{-1} and overlap integrals $S_{\alpha\beta}$ between 0.82 and 0.84 were obtained for the compounds **2**. Both parameters indicating with a high probability normal bonds in terms of bond energies and α/β overlap. [55].

Focussing on charges on the iron atom and the nitrosyl ligand, we performed a Mulliken population analysis (MPA) and a natural population analysis (NPA) using the fragments NO and $Fe^{II}L$ (L = all ligands but NO) resulting in Fe-to-NO charge transfer of −0.04 and −0.03 for the α and the β regime, respectively. In agreement with these small numbers, the population analyses resulted in an approximately neutral nitrosyl ligand and a spin density close to unity (Table 3).

CASSCF calculations for **2a** with an active space of 9 electrons in 13 orbitals were performed also, corresponding to the DFT results. The bonding interactions of the NO-π^* orbitals with Fe-d orbitals are occupied each with two electrons and

Table 3 MPA and NPA analysis on **2**

	Charge		Spin	
	Fe	NO	Fe	NO
MPA	0.57	0.07	3.57	− 0.93
NPA	1.35	− 0.06	3.51	− 0.91

All values are elementary charges

Table 4 Mulliken population analysis on the CASSCF calculations of 2a. All values are elementary charges

	Fe	NO
Charge	1.12	−0.03
Spin	3.49	−0.55

the remaining Fe-d orbitals are occupied each with one unpaired electron. A strong contribution of excited states is also reflected in the occupation numbers: the Fe–NO π bonding orbitals are occupied by 1.71 electrons, their antibonding counterparts by 0.28 electrons.

As shown in Table 4, a Mullikan analysis on the CASSCF calculations assigns a more positive charge to the iron atom than the DFT calculations do (compare Table 3), but leaving the charge on the nitrosyl ligand as 0. The spin densities on the nitrosyl ligand (β spin) and the iron atom (α spin) are reduced.

In a different approach to analyse the results of the CASSCF calculations, the orbitals of the active space were localised to yield 10 iron orbitals and 3 NO orbitals. The oxidation state of each configuration-state function was taken as the sum of the occupied localised orbitals [37]. The interpretation shows, in terms of the Radon methodology: at 66% the dominant oxidation state of the iron atom is + II. The oxidation state + III accounts for 25%, the remaining 9% correspond to the oxidation state + I. However, note the more stringent oxidation-state treatment in the last section.

Comparing the experimental iron-ligand atomic distances of compounds of **2** with their nitrosyl-free Fe^{II} and Fe^{III} analogues shows the parameters of the nitrosyl complexes are close to those of Fe^{II}.

4.2 Second Part: Stable Compounds

Using ligands with a denticity four and higher produces stable {FeNO}^{7} species. By bubbling argon through complex solution, the dark brown colour stays dark indicating that the complex keeps nitric oxide; they even resist vacuum.

Dark green quartet-{FeNO}^{7} compounds with ligands (Fig. 16) were synthesised from ferrous sulfate heptahydrate and sodium or potassium hydroxide with the free acid of the aminecarboxylato co-ligand and nitric oxide gas in aqueous solution. [56].
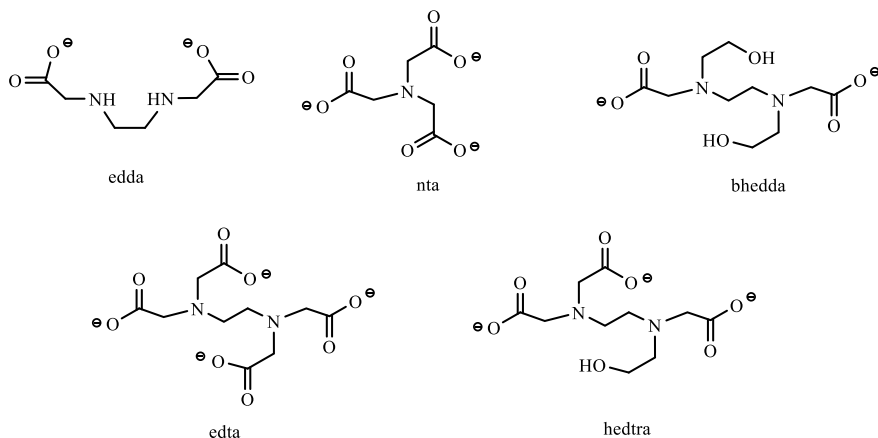
Fig. 16 Aminecarboxylato co-ligands: ethylenediamine-*N,N′*-diacetate (edda), nitrilotriacetate (nta), *N,N′*-bis-(2-hydroxyethyl)-ethylene-diamine-*N,N′*-diacetate (bhedda), ethylenediamine tetraacetate (edta) and *N*-hydroxyethyl-ethylenediamine-triacetate (hedtra)

Crystallisation succeeded by the diffusion of acetone or ethanol into the aqueous solutions.

In this ligand row edta seems to be the most important co-ligand. On a technologically applicable level, many most recently published investigations on the BioDeNOx process, a flue gas process, including the CABR method (chemical absorption—biological reduction) rely on edta [57–60]. In the field of basic research it should be noted that the molecular structure of the tentative $[Fe(edta)(NO)]^{2-}$ species was merely assumed when starting computational approaches, mostly on the basis of the heptacoordinate $[Fe(edta)(H_2O)]^{2-}$ parent species prior to NO bonding [61]. The potentially hexacoordinate edta ligand formed $\{FeNO\}^7$ solutions of pronounced stability towards NO loss on stripping with argon. Starting with an equimolar solution of ferrous salt and approximately half-neutralised ethylenediaminetetraacetic acid, a coordination polymer with higher Fe:edta molar ratio than supplied formed over a prolonged period of time.

Figure 17 shows the structure of the nitrosyl-containing monoanions (**3**) in crystals of $[Fe(H_2O)_2\{Fe(NO)(Hedta)\}_2]_{n/n}$. A carboxymethyl function is dangling and results in a pentadentate Hedta ligand, leaving a coordination site for nitric oxide, which is bonded *trans* to an edta-nitrogen atom.

It should be noted that, in the crystalline state, the NO-free precursor complex $[Fe^{II}(edta)(H_2O)]^{2-}$ is hepta-coordinate as is the Fe^{III} analogue [62]. This shows the sterical demand of NO. The distance of Fe–NO is 1.76 Å, forcing a carboxyl entity being uncoordinated, whereas the distance of Fe–OH$_2$ is 2.27 Å allowing heptacoordination.

The edta complex crystallises as a coordination polymer. Two-dimensional building blocks made up by diaquairon(II) cations instead of the attempted potassium counterions and anions **3** form layers along [001]. Within the 2D-blocks, a square

Fig. 17 The molecular
structure of
[Fe(edtaH)(NO)]$^-$ (**3**)
monoanions in crystals of
[Fe(H$_2$O)$_2$(**3**)$_2$]$_{n/n}$ (50%
ellipsoid probability).
Monoclinic, $P2_1/a$.
Distances (in Å): Fe1–N1
1.763(2), Fe1– O2 2.055(2),
Fe1– N3 2.241(2), Fe1– 2
2.196(2), Fe1– O3 2.069(2),
Fe1– O4 1.999(2), N1–O1
1.158(2). Angles (in
degrees): Fe1–N1–O1
148.8(2), N1–Fe1–N2
168.53(7) Copyright
Wiley–VCH Verlag GmbH
& Co. KGaA. Reproduced
with permission from [56]
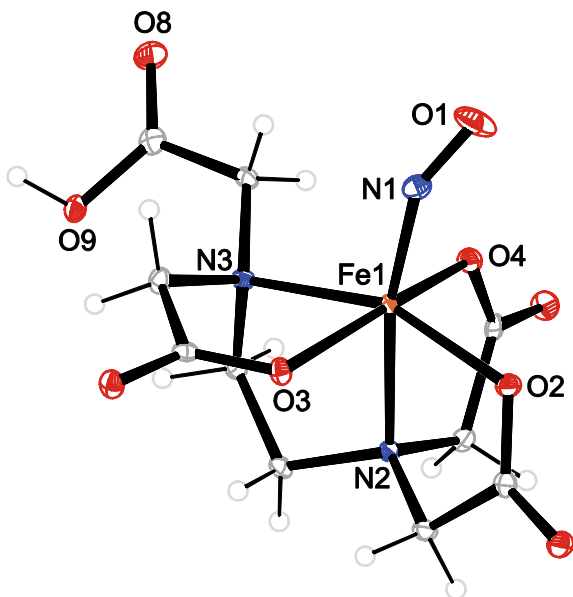
net of [Fe(H$_2$O)$_2$]$^{2+}$ building units was connected via iron–carboxylate contacts to
a square anion assembly above and a square anion assembly below, resulting in the
AB$_2$-type stoichiometry of the compound.

The mother liquor of the [Fe(H$_2$O)$_2$(**3**)$_2$]$_{n/n}$ species should exhibit fairly acidic
conditions to support the dangling non-deprotonated carboxymethyl function. As
the pH-range before NO absorption lay between 3 and 6, pH values of about 4–6
were measured after the reaction with NO. As a matter of fact, all solutions showed
slightly acidic conditions. The use of buffers is avoided in our experiments due to the
pronounced tendency of buffer components to crystallise and its potential tendency
to act as a ligand.

The formation of the {FeNO}^{7}($S = 3/2$) compounds in solution was traced by IR
and UV/vis spectroscopy. The obtained solution data agreed with those data collected
on the crystalline compounds. As in the case of the less stable aminecarboxylate
complexes, the IR and UV–vis data (Table 5) match published results for octahedral
{FeNO}^{7}($S = 3/2$) complexes. Similar results were achieved for the {FeNO}^{7}($S =$
3/2) complexes with the ligands edda, nta and bhedda.

Table 5 IR- and UV-vis-spectroscopic data of **3**; sol: the mother liquors; cry: solid-state
measurements on crystals

	ν(NO)/cm^{-1} (sol)	ν(NO)/cm^{-1} (cry)	λ/nm (sol)	λ/nm (cry)
3	1777	1781	342, 435, 634	432, 623

The absorption maxima given in the cry column were determined from Kubelka–Munk transformed
reflectance spectra [63]

4.3 Stability of the Fe–NO Linkage in Aqueous Solution

The molecular structures reveal a short Fe–NO σ/π interaction (compare the typical 1.78 Å Fe–N distance with the 2.27 Å Fe–O_{aq} distance in the heptacoordinate educt complex) leading to a considerable sterical demand of NO. Thus, the reaction of the $[Fe^{II}(edta)(H_2O)]^{2-}$ educt to the anion $[Fe(edtaH)(NO)]^-$ of the product goes along with a decrease of the coordination number from seven to six despite the fact that one of the chelating ligand's functional groups dangles. Obviously, an aqua ligand is sterically less demanding than a nitrosyl ligand. Accordingly, the molecular structures depicted in this section show the nitrosyl ligand in an environment of co-ligating atoms that are bent away from the NO group. In agreement with these rules, six-membered chelate rings which push the equatorial atoms towards the NO hemisphere result in unstable FeNO moieties [44].

What are the reasons for the different stabilities observed for the FeNO compounds with five-membered chelate rings? One aspect, that has to be considered, deals with the aqueous equilibria. With co-ligands of small denticity, the higher residual concentration of the less stable $[Fe(H_2O)_5(NO)]^{2+}$ species (see Sect. 2) in solutions of less stable co-ligand–iron(II) complexes seems responsible for the loss of NO from solutions exposed to an inert-gas stream, merely by the decomposition of the aquated species followed by equilibrium readjustment.

Figure 18 summarises the relevant equilibria for the edta co-ligand. The edta containing species are rather stable ($lg\beta_{ML} = 14.94$ at 0.1 mol L^{-1} ionic strength [64]), hence the dominant left-hand side of Fig. 18 allows for only minor quantities of both aqua species. Replacing the multidentate edta ligand by the tridentate ida as an example of a less supportive ligand results in a lower stability of the amincarboxylate complex by ten orders ($lg\beta_{ML} = 5.45$ at 1 mol L^{-1} ionic strength [65]). In this ligand's solutions, the less stable complex causes higher amounts of residual aqua complex and after NO absorption, and on continuous readjustment of the solution equilibria a higher amount of the markedly instable aqua ion $[Fe(H_2O)_5(NO)]^{2+}$ results.

The second aspect deals with structural parameters. They support the suggestion that the Fe–NO stability is correlated to the higher weight of the trivalent state of the central metal atom. It was found, that the mean metal–co-ligand distance with and without bonded nitric oxide mirrors the central atoms' valence state [47]. In

$$[Fe(edta)(H_2O)]^{2-} \rightleftharpoons [Fe(H_2O)_6]^{2+}$$

-NO, +H_2O ‖ +NO, -H_2O -NO, +H_2O ‖ +NO, -H_2O

$$[Fe(edta)(NO)]^{2-} \rightleftharpoons [Fe(H_2O)_5(NO)]^{2+}$$
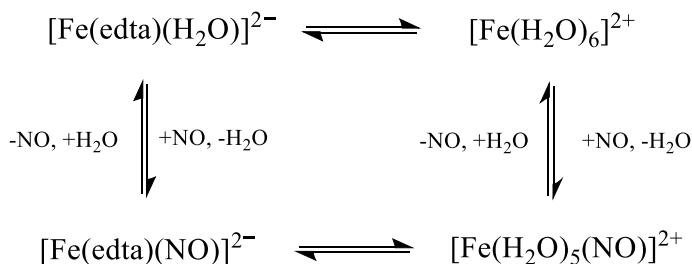
Fig. 18 Equilibria in aqueous Fe^{II}/edta/NO solutions

terms of Radon's methodology, the stable complex with anion $[Fe(edtaH)(NO)]^-$ show a one half contribution of the ferric state $Fe^{III}(NO^-)$, whereas the metal–co-ligand distances of $[Fe(H_2O)_5(NO)]^{2+}$ ion indicating a pure ferrous state $Fe^{II}(NO^0)$ for this least stable nitrosyl derivative [37, 56]. These results seemed to be typical for the class of aminecarboxylate-supported and, generally, anion-supported quartet-$\{FeNO\}^7$ centres.

For stable FeNO complexes both criteria have to be met at the same time, well-suited aqueous equilibria in the sense of Fig. 18 and a considerable weight of the ferric state.

In terms of stability it is interesting to compare the FeNO compounds with ligands edta and hedtra. As the crystal structure shows, NO-binding required one edta function to dangle. NO was thus the competitor to a reliably ligating function which, moreover, was part of a chelate. Obviously, a hemilabile function would perform better in terms of stable NO coordination. Hedtra proves this assumption, since this ligand was derived from edta by replacing one carboxymethyl by a hydroxyethyl function, supported NO binding best in van Eldik's survey.

5 The 'Non-Innocent' Nitrosyl Ligand and the Challenge of IUPAC's Oxidation-State Assignment

The nitrosyl ligand is *the* prototypic example of a so-called 'non-innocent' ligand—a subject that was dealt with by Jørgensen who attributed innocence to a ligand if it allowed the unambiguous assignment of the central metal's oxidation state (OS) [66]. According to IUPAC the OS is the charge of an atom or a molecular fragment after the ionic approximation (IA) of its heteronuclear bonds. The IA may be extracted from the mixing coefficients of molecular orbitals by assigning the electron pair in question to the atom with the major contribution to the bond and the minor to the antibond [67]. In the case of a nitrosyl–metal fragment, the focus lies on the two interactions of the M–(NO-π^*) bonds, the M $\rightarrow$ NO$^+$ backbond and the M $\leftarrow$ NO$^-$ donor-bond scenario.

In order to get more insight into the examination of the OS, we report three isostructural nitrosylmetallates yielding from the interaction of nitric oxide and a special class of low-coordinate bis(diolato)metallates, the tetracoordinate bis(perfluoropinacolato)metallates $[M(fpin)_2]^{2-}$ of chromium(II), cobalt(II) and iron(II), with the focus on the latter (Fig. 19).

The reaction proceeded through the coupling of the NO's unpaired spin to one of the spins of the high-spin metal centres (in the iron case: d^6-Fe^{II}). After crystallisation, the $S = 3/2$ compound $(NHEt_3)_2[Fe(fpin)_2(NO)]$, a quartet-$\{FeNO\}^7$ species, is obtained. For the other structures see reference [68].

The reddish brown iron compound **4** (Fig. 20) exhibits with its O-only coordination in the co-ligand part a relation to the $[Fe(H_2O)_5(NO)]^{2+}$ parent aqua species. Accordingly, **4** shares properties with the aqua ion such as the repulsion of the nitrosyl
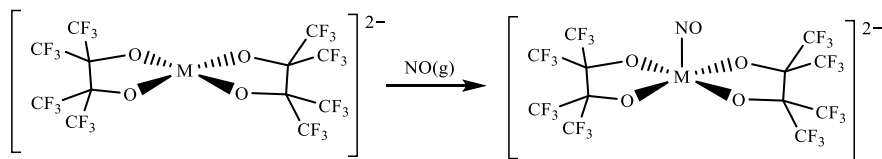
Fig. 19 The reaction of tetracoordinate perfluoropinacolatometallates with nitric oxide (M = Cr, Co, Fe)
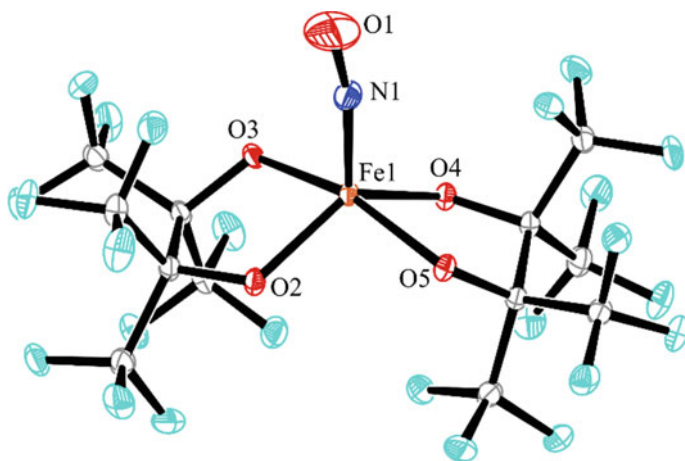
Fig. 20 Ortep plot of the [Fe(fpin)$_2$(NO)]$^{2-}$ anion (**4**), 50% ellipsoid probability. Monoclinic, $P2_1/c$. Distances in Å and angles in °: from Fe1 to: N1 1.757(2), O$_2$ 1.943(1), O3 2.042(1), O4 1.953(1), O5 2.058(1); N–O 1.149(2); Fe–N–O 168.5 (2)

ligand's N-centred lone pair and the singly populated Fe-d(z^2) orbital (Fig. 3) which makes the Fe–N bond about 0.1 Å longer than the Cr–N distance of the isostructural chromium product, and gives the nitrosyl ligand its typical tilt.

As in the FeNO-adducts presented in this article, the analysis of frontier orbitals of **3** show a largely covalent nature. In order to perform the IA reliably, a validated method instead of the mere inspection of MOs was required. For this task, the effective-oxidation-state (EOS) method was applied [69] showing the impact of spin polarisation onto the OS. The EOS method results that the α-part of each bond pair falls to the metal, and the β-part to the ligand. In total, the IA of the individual spins allocates both β spins of the two π-bonds to NO$^+$ which, thus, turns into NO$^-$.

Figure 21 gives the results of the IA procedures for **4** and **1**. The sketch shows the electron allocations in the winner-take-all scenario of an OS assignment. The quartet-{FeNO}^{7} compounds show a distinct α/β spread which is driven by three excess spins with the result that only the minority spin is found in covalent interaction—be it ligand- or metal-centred—with the majority spin at the metal ('β-covalence').

Fig. 21 A sketch of the various scenarios to find an electron right of the M–NO bond's 50%-NO-character threshold, thus falling to NO on IA. All electron pairs are part of M–NO-π-bonds
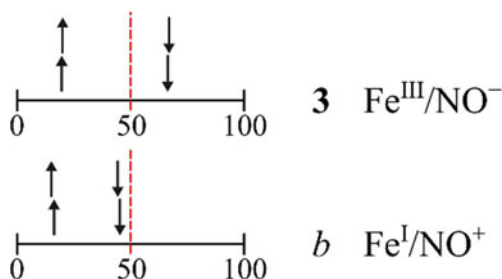
Despite the close similarity between **4** and the parent aqua species **1**, the EOS analysis end up with a $Fe^{III}(NO^-)$ case for **4** but for the aqua species with $Fe^I(NO^+)$.

In conclusion, the nitrosyl ligand's 'non-innocence' stems from a property of the two occupied Fe–NO bonds of the frontier-orbital region, which always imposes a problem in the OS framework: they are largely covalent. Thus, small shifts in the actual charge distribution within a bond close to the 50% threshold make the OSs jump up to four units (for more examples see [68]).

References

1. Sander R (2015) Compilation of Henry's law constants (version 4.0) for water as solvent. Atmos Chem Phys 15(8):4399–4981
2. Koshland DE Jr (1992) The molecule of the year. Science 258(5090):1861
3. Lehnert N, Fujisawa K, Camarena S, Dong HT, White CJ (2019) Activation of non-heme iron-nirosyl complexes: Turning up the heat. ACS Catal 9(11):10499–10518
4. Nelson MJ (1987) The nitric oxide complex of ferrous soybean lipoxygenase-1. J Biol Chem 262(25):12137–12142
5. Arciero DM, Lipscomb JD, Huynh BH, Kent TA, Münck E (1983) EPR and Mössbauer studies of protocatechuate 4,5-dioxygenase. Characterization of a new Fe2+ environment. J Biol Chem 258(24):14981–14991
6. D'Autréaux B, Horner O, Oddou JL, Jeandey C, Gambarelli S, Berthomieu C, Latour JM, Michaud-Soret I (2004) Spectroscopic description of the two nitrosyl-iron complexes responsible for fur inhibition by nitric oxide. J Am Chem Soc 126(19):6005–6016
7. Berto TC, Speelman AL, Zheng S, Lehnert N (2013) Mono- and dinuclear non-heme iron–nitrosyl complexes: models for key intermediates in bacterial nitric oxide reductases. Coord Chem Rev 257(1):244–259
8. Brown CA, Pavlosky MA, Westre TE, Zhang Y, Hedman B, Hodgson KO, Solomon EI (1995) Spectroscopic and theoretical description of the electronic structure of S = 3/2 Iron-Nitrosyl complexes and their relation to O2 activation by non-heme iron enzyme active sites. J Am Chem Soc 117(2):715–732
9. Enemark JH, Feltham RD (1974) Principles of structure, bonding, and reactivity for metal nitrosyl complexes. Coord Chem Rev 13(4):339–406

10. Rodriguez JH, Xia Y-M, Debrunner PG (1999) Mössbauer spectroscopy of the spin coupled Fe2+−{FeNO}7 centers of nitrosyl derivatives of deoxy hemerythrin and density functional theory of the {FeNO}7(S = 3/2) Motif. J Am Chem Soc 121(34):7846–7863

11. Shepherd RE, Sweetland MA, Junker DE (1997) Ligand field factors in promoting S = 3/2 {FeNO}7 nitrosyls. J Inorg Biochem 65(1):1–14

12. Ward MS, Shepherd RE (1999) A reversible NO complex of [FeII(edampda)] and the [NiII(edampda)] analogue (edampda2−-N, N′-bis(pyridylmethyl)ethylenediamine-N, N′-diacetate. Inorg Chim Acta 286:197–206

13. Hauser C, Glaser T, Bill E, Weyhermüller T, Wieghardt K (2000) The electronic structures of an isostructural series of octahedral nitrosyliron complexes {Fe−NO}6,7,8 elucidated by Mössbauer spectroscopy. J Am Chem Soc 122(18):4352–4365

14. Broclawik E, Stępniewski A, Radoń M (2014) Nitric oxide as a non-innocent ligand in (bio-)inorganic complexes: spin and electron transfer in FeII–NO bond. J Inorg Biochem 136:147–153

15. Van Stappen C, Lehnert N (2018) Mechanism of N-N bond formation by transition metal-nitrosyl complexes: modeling flavodiiron nitric oxide reductases. Inorg Chem 57(8):4252–4269

16. Kindermann N, Schober A, Demeshko S, Lehnert N, Meyer F (2016) Reductive transformations of a pyrazolate-based bioinspired diiron-dinitrosyl complex. Inorg Chem 55(21):11538–11550

17. McCracken J, Cappillino PJ, McNally JS, Krzyaniak MD, Howart M, Tarves PC, Caradonna JP (2015) Characterization of water coordination to ferrous nitrosyl complexes with fac-N2O, cis-N2O2, and N2O3 donor ligands. Inorg Chem 54(13):6486–6497

18. Chakraborty S, Reed J, Ross M, Nilges MJ, Petrik ID, Ghosh S, Hammes-Schiffer S, Sage JT, Zhang Y, Schulz CE, Lu Y (2014) Spectroscopic and computational study of a nonheme iron nitrosyl center in a biosynthetic model of nitric oxide reductase. Angew Chem Int Ed 53(9):2417–2421

19. Caranto JD, Weitz A, Giri N, Hendrich MP, Kurtz DM (2014) A diferrous-dinitrosyl intermediate in the N2O-generating pathway of a deflavinated flavo-diiron protein. Biochemistry 53(35):5631–5637

20. Kohlschütter V, Sazanoff P (1911) Zur Kenntnis der Metallnitrosoverbindungen. Ber Dtsch Chem Ges 44:1423–1432

21. Manchot W (1914) Über die Verbindungen des Stickoxyds mit Ferro- und Cuprisalzen. Ber Dtsch Chem Ges 47:1601–1614

22. Griffith WP, Lewis J, Wilkinson G (1958) Some nitric oxide complexes of iron and copper. J Chem Soc 3993–3998

23. Wanat A, Schneppensieper T, Stochel G, van Eldik R, Bill E, Wieghardt K (2002) Kinetics, mechanism, and spectroscopy of the reversible binding of nitric oxide to aquated Iron(II). An undergraduate text book reaction revisited. Inorg Chem 41:4–10

24. Conradie J, Hopmann KH, Ghosh A (2010) Understanding the unusually straight: a search for MO insights into linear {FeNO}7 units. J Phys Chem B 114:8517–8524

25. Harcourt RD (2017) Construction of valence bond structures for {FeNO}7 nitrosyl heme and non-heme complexes. Nitric Oxide 69:51–55

26. Monsch G, Klüfers P (2019) [Fe(H2O)5(NO)]2+, das Chromophor des „braunen Rings". Angew Chem 131:8654–8659

27. Wurzenberger X, Piotrowski H, Klüfers P (2011) A stable molecular entity derived from rare Iron(II) minerals: the square-planar high-spin-d6 FeIIO4 chromophore. Angew Chem Int Ed 50:4974–4978

28. Cantalupo SA, Fiedler SR, Shores MP, Rheingold AL, Doerrer LH (2012) High-spin square-planar Co(II) and Fe(II) complexes and reasons for their electronic structure. Angew Chem Int Ed 51:1000–1005

29. Døssing A, Mette FA (2006) A convenient preparation of pentaaquanitrosylchromium(2+) sulfate: The crystal structure revisited. Inorganica Chim Acta 359:1681–1684

30. Kohlschütter V, Kutscheroff M (1907) Notiz über Ferronitrosoverbindungen. Ber Dtsch Chem Ges 40:873–878

31. Schiewer CE, Müller CS, Dechert S, Bergner M, Wolny JA, Schünemann V, Meyer F (2019) Effect of oxidation and protonation states on [2Fe–2S] cluster nitrosylation giving {Fe(NO)2}9 dinitrosyl iron complexes (DNICs). Inorg Chem 58(1):769–784

32. Tsai M-L, Tsou C-C, Liaw W-F (2015) Dinitrosyl iron complexes (DNICs): from biomimetic synthesis and spectroscopic characterization toward unveiling the biological and catalytic roles of DNICs. Acc Chem Res 48(4):1184–1193

33. Fitzpatrick J, Kim E (2015) Synthetic modeling chemistry of iron-sulfur clusters in nitric oxide signaling. Acc Chem Res 48(8):2453–2461

34. Buet A, Simontacchi M (2015) Nitric oxide and plant iron homeostasis. Ann NY Acad Sci 1340(1):39–46

35. Cho SL, Liao CJ, Lu TT (2019) Synthetic methology for preparation of dinitrosyl iron complexes. J Biol Inorg Chem 24:495–515

36. In-Iam A, Wolf M, Wilfer C, Schaniel D, Woike T, Klüfers P (2019) {FeNO}7-type halogenido nitrosyl ferrates: syntheses, bonding, and photoinduced linkage isomerism. Chem Eur J 25:1304–1325

37. Radoń M, Broclawik E, Pierloot K (2010) Electronic structure of selected {FeNO}$_7$ complexes in heme and non-heme architectures: a density functional and multireference ab initio study. J Phys Chem B 114(3):1518–1528

38. Neese F (2004) Definition of corresponding orbitals and the diradical character in broken symmetry DFT calculations on spin coupled systems. J Phys Chem Solids 65(4):781–785

39. McDonald CC, Phillips WD, Mower HF (1965) An electron spin resonance study of some complexes of iron, nitric oxide, and anionic ligands. J Am Chem Soc 87(15):3319–3326

40. Gwost D, Caulton KG (1973) Reductive nitrosylation of Group VIIIb compounds. Inorg Chem 12(9):2095–2099

41. Specht P, Oßberger M, Klüfers P, Schindler S (2020) Kinetic studies on the reaction of NO with iron(II) complexes using low temperature stopped-flow techniques. Dalton Trans 49:9480–9486

42. Specht P., private communication: 16.11.19

43. Littlejohn D, Chang SG (1987) Stoichiometry of ferrous nitrosyl complexes. Ind Eng Chem Res 26(6):1232–1234

44. Schneppensieper T, Finkler S, Czap A, van Eldik R, Heus M, Nieuwenhuizen P, Wreesmann C, Abma W (2001) Tuning the reversible binding of NO to iron (II) aminocarboxylate and related complexes in aqueous solutions. Eur J Inorg Chem 491–501

45. Schneppensieper T, Wanat A, Stochel G, Goldstein S, Meyerstein D, van Eldik R (2001) Ligand effects on the kinetics of the reversible binding of NO to selected aminocarboxylato complexes of iron (II) in aqueous solutions. Eur J Inorg Chem 2317–2325

46. Schneppensieper T, Wanat A, Stochel G, van Eldik R (2002) Mechanistic information on the reversible binding of NO to selected iron (II) chelates from activation parameters. Inorg Chem 41(9):2565–2573

47. Wolf M, Klüfers P (2017) Structure and bonding of high-spin nitrosyl–iron(II) compounds with mixed N,O-chelators and aqua ligands. Eur J Inorg Chem 2303–2312

48. Chiou Y-M, Que JL (1995) Structure of a mononuclear iron(ii)-catecholate complex and its relevance to the extradiol-cleaving catechol dioxygenases. Inorg Chem 34(14):3270–3278

49. Majumdar A, Lippard SJ (2013) Mononitrosyl non-heme diiron complexes: importance of iron oxidation state in controlling the nature of the nitrosylated products. Inorg Chem 52(23):13292–13294

50. Li J, Banerjee A, Pawlak PL, Brennessel WW, Chavez FA (2014) Highest recorded N-O stretching frequency for 6-coordinate {Fe-NO}$_7$ complexes: an iron nitrosyl model for His3 active sites. Inorg Chem 53(11):5414–5416

51. Victor E, Minier MA, Lippard SJ (2014) Synthesis and characterization of a linear dinitrosyl-triiron complex. Eur J Inorg Chem 2014(33):5640–5645

52. Weigend F, Ahlrichs R (2005) Balanced basis sets of split valence, triple zeta valence and quadruple zeta valence quality for H to Rn: design and assessment of accuracy. Phys Chem Chem Phys 7(18):3297–3305

53. Grimme S (2006) Semiempirical GGA-type density functional constructed with a long-range dispersion correction. J Comput Chem 27(15):1787–1799
54. Klamt A, Diedenhofen M (2015) Calculation of solvation free energies with DCOSMO-RS. J Phys Chem A 119(21):5439–5445
55. Soda T, Kitagawa Y, Onishi T, Takano Y, Shigeta Y, Nagao H, Yoshioka Y, Yamaguchi K (2000) Ab initio computations of effective exchange integrals for H-H, H–He–H and Mn2O2 complex: comparison of broken-symmetry approaches. Chem Phys Lett 319(3–4):223–230
56. Aas BM, Klüfers P (2017) The structural chemistry of stable high-spin nitrosyl–iron(ii) compounds with aminecarboxylato co-ligands in aqueous solution. Eur J Inorg Chem 2313–2320 (2017)
57. Zhao J, Zhang C, Sun C, Li W, Zhang S, Li S, Zhang D (2018) Electron transfer mechanism of biocathode in a bioelectrochemical system coupled with chemical absorption for NO removal. Biores Technol 254:16–22
58. Zhao J, Xia Y, Li M, Li S, Li W, Zhang S (2016) A biophysical model for NO removal by the chemical absorption-biological reduction integrated process. Environ Sci Technol 50:8705–8712
59. Zhang S, Chen H, Xia Y, Liu N, Lu BH, Li W (2014) Current advances of integrated processes combining chemical absorption and biological reduction for NOx removal from flue gas. Appl Microboil Biotechnol 98:8497–8512
60. Gambardella F, Winkelmann JGM, Heeres HJ (2006) Experimental and modelling studies on the simultaneous absorption of NO and O_2 in aqueous iron chalet solutions. Chem Eng Sci 61:6880–6891
61. Westre TE, Di Cicco A, Filipponi A, Natoli CR, Hedman B, Solomon EI, Hodgson KO (1994) Determination of the Fe-NO angle in {FeNO}7 complexes using multiple-scattering EXAFS analysis by GNXAS. J Am Chem Soc 116(15):6757–6768
62. Huang H-M, Yang H-B, Li X-Y, Ren F-F (2009) Diammonium aqua(ethylenediaminetetraacetato)iron(II) trihydrate. Acta Crystallogr Sect E 65:m87–m88
63. Kubelka P (1948) New contributions to the optics of intensely light-scattering materials. J Opt Soc Am 38(5):448–457
64. Clark N, Martell A (1988) Ferrous chelates of EDTA, HEDTA and SHBED. Inorg Chem 27:1297–1298
65. Micskei K (1987) Equilibria in aqueous solutions of some iron(II) complexes. J Chem Soc Dalton Trans 255–257
66. Jørgensen CK (1963). Adv Chem Phys vol 5. Prigogine I (ed) Wiley-Interscience Publ., Hoboken, New York, pp 33–146
67. Karen P, McArdle P, Takats J (2016) Comprehensive definition of oxidation state (IUPAC Recommendations 2016). Pure Appl Chem 88(8):831–839
68. Ampßler T, Monsch G, Popp J, Riggenmann T, Salvador P, Schröder D, Klüfers P (2020) Not guilty on every count: the "non-innocent" nitrosyl ligand in the framework of IUPAC's Oxidation-State Formalism. Angew Chem Int Ed 59. https://doi.org/10.1002/ANIE.202003122
69. Postils V, Delgado-Alonso C, Luis JM, Salvador P (2018) An objective alternative to IUPAC's approach to assign oxidation states. Angew Chem Int Ed 57(33):10525–10529

Formation, Reactivity Tuning and Kinetic Investigations of Iron "Dioxygen" Intermediate Complexes and Derivatives in Multiphase Flow Reactions

Andreas Miska, Pascal Specht, Markus Lerch, and Siegfried Schindler

Abstract A dinuclear iron complex system had been developed that is capable to activate dioxygen in the protic solvent methanol forming a peroxido complex that is stable for a few seconds at room temperature. A full kinetic analysis of this reaction could be performed using stopped-flow techniques and furthermore by applying a SuperFocus mixer. Formation of the peroxido complex could be followed either by UV/VIS absorbance or by fluorescence. A reaction kit was developed that allowed to start with an air stable iron(III) complex that could be activated by reducing it with ascorbic acid prior to the reaction with dioxygen several times without decomposition of the complex. This reaction could be furthermore observed in bubbly flow columns. However, so far, the reaction rates were not in the necessary time window to perform accurate measurements. Ligand modification allowed to increase the solubility of the starting material to such an extent that it was possible to react it in water. Unfortunately, under these conditions the peroxido complex was not detected anymore. Still, from the results of this work, it seems likely that the iron system described herein can be further optimized to make it work as an oxygenation catalyst in aqueous solutions.

1 Introduction

Selective catalytic oxygenations of organic substrates are very important in chemical industry (e.g. oxidation of cyclohexane to so called KA oil, a mixture of cyclohexanol/cyclohexanone, for the synthesis of adipic acid, a precursor for the production of nylon) [1, 2]. Furthermore, these reactions are of high interest in the field of bioinorganic/coordination chemistry [3, 4]. Oxidants such as hydrogen peroxide usually are not selective and follow a radical pathway (e.g. Fenton type chemistry), often leading to a mixture of products [5]. Reactions with dioxygen on the other side can cause

A. Miska · P. Specht · M. Lerch · S. Schindler (✉)
Justus-Liebig University, Institute of Inorganic and Analytical Chemistry, Heinrich-Buff-Ring 17, 35392 Gießen, Germany
e-mail: siegfried.schindler@ac.jlug.de

Fig. 1 Reaction of dioxygen with methane

$$2 \; H_3C{-}H \xrightarrow{\;O_2\;} 2 \; H_3C{-}OH \xrightarrow[-2\,H_2O]{\;O_2\;} 2 \;\; \underset{H \quad H}{\overset{O}{\parallel}}$$

$$2 \; CO_2 \xleftarrow[-2\,H_2O]{\;O_2\;} 2 \;\; \underset{H \quad OH}{\overset{O}{\parallel}}$$
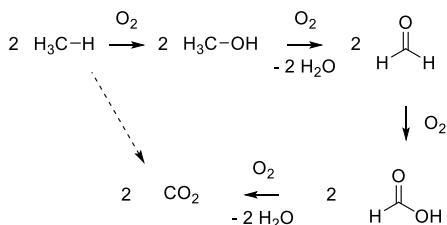
complete combustion once the oxidation process has been started. For example, it is easy to burn methane, ending up with carbon dioxide and water: $CH_4 + 2\,O_2 \rightarrow CO_2 + 2\,H_2O$. However, it seems to be sheer impossible to stop this reaction right at the stage of a formed intermediate, such as methanol (due to needing less activation energy for each oxidation step; a downhill reaction in the energy profile), according to Fig. 1. This is unfortunate in so far because methanol has a much higher value in comparison with methane and could be used in many ways (liquid fuel for direct combustion or in fuel cells etc.) [6].

In contrast the metalloenzyme methane monooxygenase (MMO) with either iron or copper ions in the active site is accomplishing this perfectly well under ambient conditions [7, 8]. In that regard it is promising to model the active site of metalloenzymes using low molecular weight (iron or copper) complexes to perform similar chemistry in the lab but especially in industry [9, 10]. Similar to the natural systems it would be preferable to perform oxygenation reactions in aqueous solutions using air as the sole oxidant. Working with air/dioxygen as an oxidant in organic solvents on an industrial scale always carries the danger of fire or explosions. Therefore, based on previous experience efforts were undertaken to develop a complex system that could be handled easily and be optimized for selective oxidations in protic solvents using air as the only oxidant.

2 O$_2$ Activation

Dioxygen needs to be activated to react with an organic substrate (due to different spin states: triplet dioxygen and singlet organic molecule) [11]. Different metal "dioxygen adduct" complexes can form as active species when low valent metal ions are reacted with dioxygen (see also Chapter "Control of the Formation and Reaction of Copper-Oxygen Adduct Complexes in Multiphase Streams" on dioxygen activation with copper complexes by Herres-Pawlis and co-workers). The first complex in this series is a so called, *end-on* superoxido complex that in consecutive reactions can form further active complexes such as e. g. an *end-on* or a *side-on peroxido* complex (Fig. 2, M here stands for either iron or copper).

An *end-on* superoxido complex usually is extremely labile and can only be "captured" briefly (detected spectroscopically) at low temperatures. However, providing

Fig. 2 Reaction of metal complexes with dioxygen (ligands and charges are omitted)
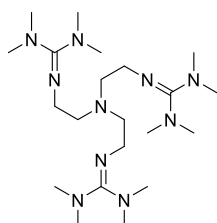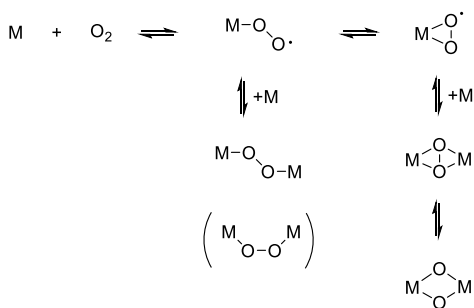
TMG$_3$tren
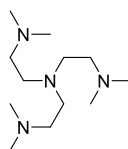
Me$_6$tren
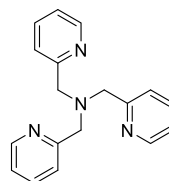
tmpa
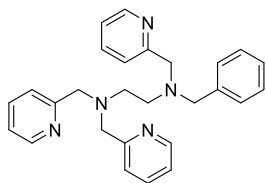
bztpen
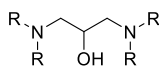
Et-HPTB

Fig. 3 Abbreviations of ligands (M = Cu or Fe)

an optimized ligand environment (sterically demanding ligand to avoid consecutive reactions and electronically stabilizing the whole system) it was possible previously to structurally characterize an *end-on* superoxido copper complex [12]. Furthermore, it was observed that this complex, [Cu(TMG$_3$tren)]$^+$ (TMG$_3$tren = tris(tetramethylguanidino)tren, Fig. 3), can react reversibly with dioxygen without decomposition.

Applying the sterically less demanding tripodal ligands Me$_6$tren (= tris (2-dimethylaminoethyl)amine) or tmpa (= tris (2-pyridylmethyl)amine), Fig. 3, the corresponding copper superoxido complexes could be observed only briefly spectroscopically (as discussed above) using low temperature stopped-flow methods. Investigations using low temperature stopped-flow methods are extremely useful for detecting such short-lived intermediates because they allow to follow their formation down to temperatures of $T = -90.0\,°C$ with UV/VIS spectroscopy and reaction times of milliseconds [3, 13, 14]. Usually iron or copper "dioxygen adduct" complexes are

intensively colored (characteristic charge transfer bands) and (often in combination with Raman and/or IR spectroscopy) can be easily assigned with a molecular structure description. Furthermore, with these measurements detailed kinetic data can be obtained that allow to propose a reaction mechanism for the interaction of low valent metal complexes and dioxygen [15]. With both ligands (L = Me$_6$tren or tmpa, Fig. 3) the dinuclear copper peroxido complexes [LCu-O–O-CuL]$^{2+}$ were prepared at low temperatures and could be structurally characterized [16, 17].

The tripodal ligand tmpa was applied in iron chemistry as well (here it is abbreviated as tpa) and an iron(III)-*bis*-μ-oxido complex had been investigated in detail in the past [18–20]. This diamond core system had been suggested to take part in methane oxidation in the active site in iron-based MMO [21, 22]. More recent work proposes a likely mechanism for the full reaction cycle [23]. In contrast to copper, so far no *end-on* iron superoxido complex (non-heme systems) could be stabilized enough to allow crystallographic characterization. On the other side iron(IV) oxido complexes by now can be obtained quite easily [3, 24–27] while it is still unclear if a mononuclear copper(III) oxido complex can exist at all.

Quite surprisingly, a few copper complexes with tripodal ligands, including the copper tmpa complex could be stabilized as solid copper peroxido complexes that proved to be capable to catalytically oxidize toluene to benzaldehyde [17]. However, so far efforts to take this system from the lab bench to a larger industrial setup did not work out. Currently work is in progress to immobilize these complexes (e.g. on silica) to use them as heterogeneous catalysts. Furthermore, investigations in the past on the reaction of some copper amine complexes with dioxygen in water did not allow the observation of any "oxygen" adduct complexes at all [28].

The iron complex [Fe(bztpen)Cl](ClO$_4$)$_2$ (bztpen = *N*-benzyl-*N*,*N'*,*N'*-tris(2-pyridylmethyl)-1,2-ethylenediamine, Fig. 3) can be reacted with hydrogen peroxide to form a hydroperoxido or *side-on* peroxido complex (addition of base is necessary) [29] and furthermore an iron(IV) oxido complex with iodosobenzene [30]. In contrast to our expectations we did not find a way to use dioxygen for the oxidation of the iron(II) bztpen system that excluded it from further study in that regard. In contrast it undergoes a clean reaction with nitrogen oxide, NO, and the product complex could be characterized structurally [31]. NO is related to dioxygen (one electron less with NO being a mono radical, dioxygen a diradical) and has been used previously as a "substitute" for dioxygen to learn more about the binding situation if reactions with dioxygen are not well suited for the investigation [32]. Recently we performed a kinetic study on the reaction of [Fe(bztpen)(CH$_3$CN)](OTf)$_2$ with NO in methanol [33]. The reaction turned out to be first order in complex as well as in NO concentration and from the activation parameters of $\Delta H^{\ddagger} = +17.8 \pm 0.8$ kJ mol^{-1} and $\Delta S^{\ddagger} = -181 \pm 3$ J K^{-1} mol^{-1} an associative mechanism has been postulated.

Stabilization and crystallographic characterization of iron "dioxygen adduct" complexes has been a challenge for a long time. So far, still only a few crystal structures have been reported. An interesting ligand system (Fig. 3) had been developed in the past to provide alkoxy bridged dinuclear iron complexes that are reactive towards dioxygen. These complexes can be regarded as model compounds for hemerythrin, an oxygen carrier protein that is found in some worms. As it turned out

these complexes proved to be quite useful in test reactions for bubbly flow columns and will be described in detail below.

3 The Iron HPTB System

3.1 General Aspects

It is definitely not easy to find/develop a chemical reaction system that can be applied for the investigation of the reaction with a gas, here dioxygen, in an industrial setup of bubbly flow columns. Some of the challenges are summarized here:

- Effective synthesis of the starting material in larger amounts, good yields and inexpensive chemicals
- Application of the compounds should be easy and should not require handling by an expert
- Recycling/regaining of the active species should be possible, decomposition should be minimal
- The reaction has to take place in a correct time window (kinetics needs to fit here) to allow observation of the progress of the reaction using different techniques for detection (UV/VIS spectroscopy, fluorescence measurements etc.)
- Mixing dioxygen with volatile solvents presents a high risk of fire and/or explosions. Therefore, it would be desirable to perform the oxygenation reactions in aqueous solutions.

In Sect. 2 some of efforts are described to deal with these challenges to find a suitable copper or iron complex system. While these were not successful (in regard to these requirements) we learned from our own research and in combination with results reported in the literature that the iron HPTB system (Fig. 3) seemed to be suitable to at least partially fulfill the requirements.

3.2 Previous Investigations on the Iron HPTB System

Dinuclear iron complexes with the general ligand type shown in Fig. 3 have been investigated in great detail with regard to modeling metalloproteins such as e. g. the oxygen carrier hemerythrin [34–36]. Especially the dinuclear iron(II) complex $[Fe_2(R\text{-}HPTB)(X)_2Y]^{n+}$ (Fig. 4) with the ligand Et-HPTB (R = Et; Et-HPTB = *N,N,N′,N′*-tetrakis(2-(1-ethylbenzimidazolyl)methyl)-2-hydroxy-1,3-diaminopropane) proved to be quite useful in this aspect. It reacts with dioxygen to form a dinuclear iron peroxido complex that could be structurally characterized [37].
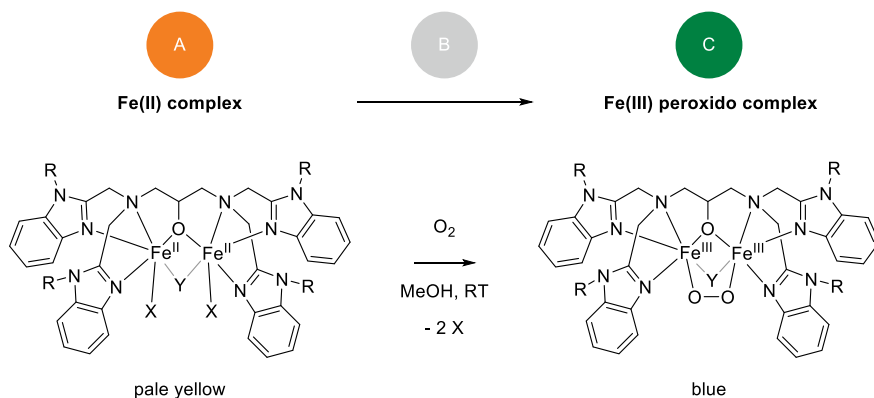
Fig. 4 The iron(II) R-HPTB complex (Fe$_2$(R-HPTB)(X)$_2$Y]) with R $=$ H or Et, X $=$ NO or Cl$^-$, Y $=$ benzoate or Cl$^-$

Kinetic studies were performed on this reaction in nitrile solvents by using low temperature and high pressure stopped-flow techniques [34]. Simple first order behavior was observed for both complex as well as for dioxygen concentration (rate law: d[Fe(II) complex]/dt $= k \times$ [Fe(II) complex] $\times$ [O$_2$]) and activation parameters were calculated to $\Delta H^{\#} \approx 16$ kJ mol^{-1} and $\Delta S^{\#} \approx -120$ J mol^{-1} K^{-1}. Together with the measured activation volume of $\Delta V^{\#} = -12 \pm 0.9$ cm^3 mol^{-1} (at $T = 20\,°$C) an associative mechanism could be proposed. No intermediates could be detected spectroscopically. The peroxido complex is labile and decomposes quite rapidly after its formation at room temperature (in less than a few seconds).

Alternatively, the same peroxido complex could be obtained by reacting corresponding iron(III) complexes with hydrogen peroxide in methanol [38]. Furthermore, it was possible using the iron(III) complex [Fe$_2$(H-HPTB)(NO$_3$)$_2$(μ–OH)](NO$_3$)$_2$ together with hydrogen peroxide to oxidize alkanes (in the presence of certain amino acids), however, in bad yields [39].

3.3 Investigations on the Iron HPTB System

3.3.1 Stopped-Flow and SuperFocus Mixer Measurements

As described above it is usually not possible to investigate dioxygen binding to copper or iron complexes in protic solvents (such as methanol) due to the formation of hydrogen peroxide (or decomposition reactions). This is a less interesting reaction because then it is unlikely to observe "dioxygen adduct" complexes as intermediates. Furthermore, it would suggest that hydrogen peroxide could be used from the beginning for any kind of oxidation/oxygenation reaction. However, it should be noted that

it might be possible to use such a reaction to synthesize hydrogen peroxide directly in solution from dioxygen/air for special applications.

The observation, as described above, that the iron peroxido complexes with the HPTB ligand system could form in methanol when iron(III) complexes were reacted with hydrogen peroxide suggested that it also should be possible to observe formation of these complexes starting from corresponding iron(II) complexes and dioxygen [38]. This was confirmed first in benchtop experiments followed by a detailed kinetic study using low temperature stopped-flow methods [40]. Due to solubility problems the ligand H-HPTB was applied instead of Et-HPTB. Reacting the complex [Fe$_2$(H-HPTB)Cl$_3$] (Fig. 4, X = Y = Cl$^-$) at $T = 22.0\,^\circ$C allowed to observe the formation of the peroxide complex with characteristic absorbance maxima at (color change from nearly colorless to a blueish color). Time resolved UV/VIS spectra of this reaction are presented in Fig. 5.

Our apprehension that the anion chloride might interfere in a negative way (due to strong binding as a ligand) were not confirmed and kinetic data ($\Delta H^\# = 15.0 \pm 0.4$ kJ mol^{-1} and $\Delta S^\# = -146 \pm 3$ J mol^{-1} K^{-1}) were identical (in the range of error) with the previous study on the iron Et-HPTB system described above [34, 40].

However, different to our stopped-flow measurements, oxygenation reactions in industry can be performed within large bubble columns. Contact with the oxidizing agent, here dioxygen/air in the solvent easily takes place and together with large liquid holdups and long liquid phase residence makes them quite suitable for these applications. So far, overall kinetics, hydrodynamic and mass transport mechanisms are still not well understood. Furthermore, many of the previous investigations only allowed some insight into the hydrodynamics because they were performed with gases in a non-reactive mode [41]. Hence, for studies on the reaction kinetics of
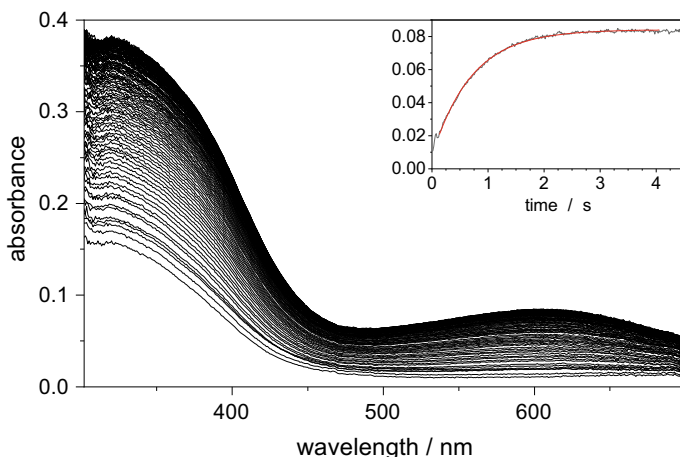
Fig. 5 Time resolved stopped-flow UV/VIS spectra of the reaction of (Fe$_2$(H-HPTB)Cl$_3$]) with dioxygen in methanol. c(complex) = 0.1 mmol/L, c(O$_2$) = 4.2 mmol/L, $T = 22.0\,^\circ$C, $d = 10$ mm. Inlay: absorbance versus time at 600 nm, experimental data and fit

the formation of the dinuclear peroxido complex a lab scale reactor with defined hydrodynamic conditions and without mass transport limitations is preferred. For this work, a homebuilt so called SuperFocus mixer was used (see Chapter "Determination of Kinetics for Reactive Bubbly Flows Using SuperFocus Mixers" for further details) for continuous flow measurements that are based on the principle of reducing the diffusional path length to speed up the mixing process [42]. Really helpful was the observation that kinetic data derived from these measurements (for the reaction of $[Fe_2(H\text{-}HPTB)Cl_3]$ with O_2) did fit perfectly well (in the range of error) the results of our stopped-flow measurements [40]. This furthermore confirmed that stopped-flow measurements can be used as well to obtain kinetic data for continuous flow setups.

That this went so well was not self-evident because kinetic parameters have to be in the correct range to allow the analysis using a SuperFocus mixer. We observed this problem previously during our efforts to find a suitable complex system for dioxygen activation that would meet at least some of the requirements described under 5.3.1 General Aspects. Similar to the iron HPTB system we had been investigating a mononuclear copper(I) complex, $[Cu(Pim^{iPr2})(CH_3CN)]CF_3SO_3$ (Pim^{iPr2} = tris[2-(1,4-diisopropylimidazolyl)]phosphine) that formed a quite stable dinuclear *side-on* peroxido complex in methanol. However, while here it was possible to gain a full understanding of the reaction mechanism from kinetic measurements using our stopped-flow equipment, all efforts to apply the SuperFocus mixer as well failed [43] (see Chapter "Determination of Kinetics for Reactive Bubbly Flows Using SuperFocus Mixers" for further details).

3.3.2 *NO in Comparison with O_2*

With regard to the mechanism of the reaction of $[Fe_2(H\text{-}HPTB)Cl_3]$ with O_2 only the reaction in Fig. 4 could be observed in our time resolved UV–vis spectra (Fig. 5). However, most likely (and at least known from related copper chemistry) a superoxido iron intermediate complex should form according to Fig. 6, prior to the peroxido product.

That the superoxido complex cannot be detected can be easily explained with a steady state approximation: the formation of the superoxido complex is rate determining and all consecutive reactions are much faster so no other compound besides the product complex can be observed. This approach has been described in the general literature on inorganic reaction mechanisms and most recently by us in great detail for the reaction of the copper complex $[Cu(Pim^{iPr2})(CH_3CN)]CF_3SO_3$
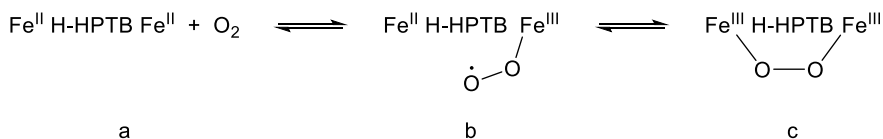
Fig. 6 Postulated formation of an iron superoxido complex (b) as intermediate

with O_2 mentioned above [43]. These findings furthermore were supported by DFT calculations [44].

As described above NO sometimes can be used instead of O_2 to gain a clearer picture about the reactivity of copper or iron complexes. When the iron(II) Et-HPTB complex (Fig. 4, R = Et, X = acetonitrile, Y = benzoate and BF_4^--anions) was reacted with NO each iron ion was coordinated by one NO molecule. More recently an iron HTPB complex with only one NO ligand coordinated to one iron in the dinuclear center has been reported. So far, no kinetic studies were reported on this system and therefore, we thought that the reaction of $[Fe_2(H-HPTB)Cl_3]$ with NO might help to give further insight into the fast formation of the superoxido complex. However, while we were able to successfully investigate this reaction, again using low temperature stopped-flow methods, the overall reaction was quite different compared with the reaction with dioxygen and in that regard it did not provide further insight [33].

It would have been interesting to have NO and O_2 react with $[Fe_2(H-HPTB)Cl_3]$ at the same time to distinguish their different reaction behavior. However, mixing NO with O_2 would immediately lead to the formation of NO_2 and therefore was not possible.

3.3.3 Reaction Behavior in Aqueous Solutions

Due to the fact that the reaction of $[Fe_2(H-HPTB)Cl_3]$ proceeded smoothly in methanol it was also attempted to transfer the system in an aqueous solution [45]. In contrast to water, methanol has the big advantage that kinetic measurements are possible at lower temperatures to decrease the reaction rates and furthermore, to get a better chance to detect labile intermediates. In aqueous solutions pH plays an important role and the complex system was tested in that regard. It turned out that while still an oxidation of the complex was observed, it was much slower and the decomposition reaction was too fast to allow observation of the formation of the peroxido complex. The rate could be increased slightly by adding benzoate as a bridging co-ligand, known to stabilize the peroxide unit. Due to solubility problems of the starting complex in water the ligand was synthetically modified and sulfonate groups were introduced, substituting R = H (Fig. 7).
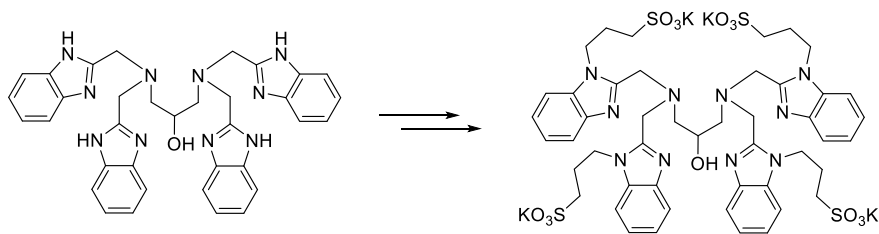
Fig. 7 Derivative of HPTB, the water soluble ligand N-$C_3H_6SO_3$K-HPTB

The new ligand derivative as well as the complex turned out to be very soluble in water, however, quite unfortunately it did not help to tune the reaction (rates) in a way to allow detection and stabilization of the peroxido complex. Important other factors for kinetic investigations in aqueous solutions such as influence of anions and ionic strength were not studied because so far, the complex system could not be applied in water at the current state. Still, mixtures of methanol/water can be used, however the main goal would be a complete transfer into water without an organic solvent.

3.3.4 Fluorescence Measurements

Detection of fluorescence is an excellent method to follow the consumption of dioxygen bubbles and has been used in Taylor flow systems [46]. Iron complexes are not known for excellent fluorescence properties but it also should be possible to use them together with a fluorescence indicator such as a ruthenium bipyridine or phenantroline complex, compounds that have their emission quenched in the presence of dioxygen (thus allowing to use them as chemical sensors for dioxygen). Fluorescence measurements of this type have been tried with our reaction system but failed. However, probably more interesting, it had been reported previously that using a reaction mixture of the iron complex $[Fe_2(Et-HPTB)(X)_2Y](ClO_4)_4$ (X, Y = H_2O, CH_3OH, CH_3O^-) together with $[Ru(bipy)_3](PF_6)_2$ (in acetonitrile) the formation of the peroxido complex could be reestablished photochemically after decomposition to the corresponding iron(III) complex with light [47]. This allowed complete oxidation of triphenylphospine as a substrate.

With the knowledge of the influence of carboxylate ion on the iron HPTB system (benzoate, stabilizing peroxido complex and increase of rate, see above) it was assumed that other carboxylate groups might be used for fluorescence detection. Fluorescein as well as rhodamine B (Fig. 8), well known for their strong fluorescence contain a carboxyl group and were tested in that regard.

Fluorescein turned out to be a better reaction partner and as expected, it was observed by UV/VIS spectroscopy that binding to the $[Fe_2(H-HPTB)Cl_3]$ complex occurred. During the reaction with dioxygen (Fig. 4 with Y = anion of fluorescein), a large increase of the intensity of the emission at 550 nm occurred. This is quite
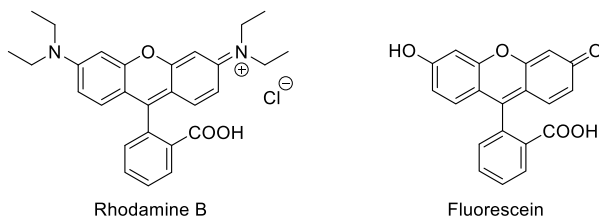
Fig. 8 Rhodamine B and Fluorescein

surprising in so far that usually, as described above, dioxygen is more likely an emission quencher.

A preliminary kinetic study using stopped-flow equipment, with fluorescence detection, showed that the kinetic data for the formation of the peroxido complex fit very well our previous results from absorbance versus time measurements. A detailed analysis of this reaction is in progress.

3.3.5 Reaction Kit

One of the big problems in regard to apply most of the complexes for dioxygen activation is that they need to be handled under inert conditions. This is a problem in regard to transportation, handling and inserting this material into larger setups. The same holds true for the iron complex $[Fe_2(H\text{-}HPTB)Cl_3]$ that will react/decompose once in contact with air. To overcome this huge problem it would be much better to start with a stable compound that will be activated prior to the oxidation reaction. In that regard a stable iron(III) complex should be used to turn it into the active iron(II) complex either photochemically (see above), electrochemically or chemically. After quite some time of "playing around" with the $[Fe_2(H\text{-}HPTB)Cl_3]$ complex it was found that ascorbic acid could do the trick [40, 45]. Other tested reductants such as e. g. sulfur dioxide or oxalic acid did not work out.

Synthesis of the iron(III) complex $[Fe_2(H\text{-}HPTB)Cl_4]Cl$ was easily accomplished and could be prepared in larger amounts without any problems. The complex is absolutely stable and can be stored, transported and handled under ambient normal conditions. After an inert gas, such as nitrogen or argon, is bubbled through a solution of this complex in methanol, ascorbic acid can be used to reduce it to the corresponding iron(II) complex that now is reactive towards dioxygen. The complete reaction cycle is shown in Fig. 9 [40].

Kinetic studies (stopped-flow as well as SuperFocus mixer measurements) showed that the activated complex derived from the iron(III) compound reacted in the same
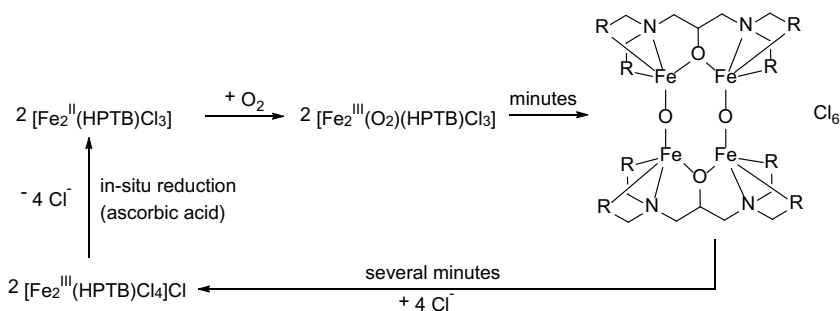
Fig. 9 "Recycling" of $[Fe_2(H\text{-}HPTB)Cl_4]Cl$

$$[Fe_2^{II}(HPTB)Cl_3] \xrightarrow{+ O_2} [Fe_2^{III}(O_2)(HPTB)Cl_3] \longrightarrow [Fe_2^{III}(HPTB)Cl_4]Cl$$
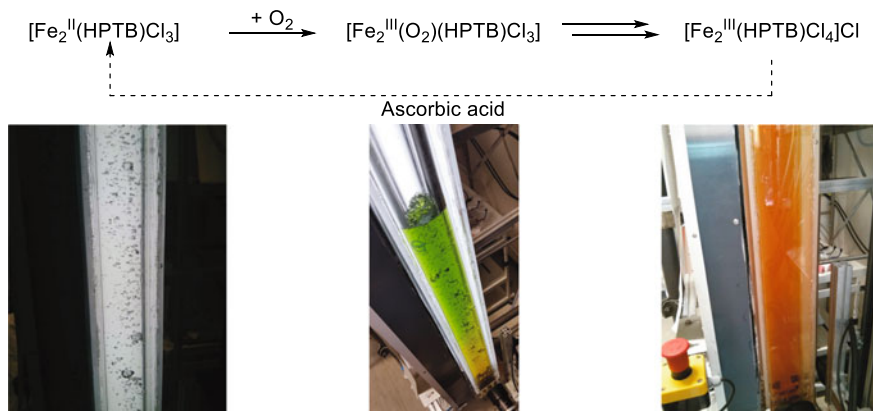
Ascorbic acid

Fig. 10 Activation of the iron complex by reducing the iron(III) complex [Fe$_2$(H-HPTB)Cl$_4$]Cl (picture on the right) to the iron(II) complex [Fe$_2$(H-HPTB)Cl$_3$] (picture on the left) in a bubbly flow column (ascorbic acid added, picture in the middle)

way as the iron(II) complex as starting material did [40]. Furthermore, it was possible to reactivate the complex again for many times without any sign of decomposition.

These positive results allowed to perform tests in bubbly flow columns on a large scale. In Fig. 10 the reduction from the orange brown colored solution of the iron(III) complex to the nearly colorless solution of the iron(II) complex is shown. The green color of the solution indicates formation of an intermediate during the reduction that could not be analyzed so far.

4 Conclusion and Outlook

An iron complex system has been developed that allows to study irreversible dioxygen binding of this complex in the protic solvent methanol. The goal to perform such a reaction in aqueous solutions/water so far was only partially achieved. Synthetic modification of the ligand R-HPTB (Fig. 1) by introducing water soluble groups (Fig. 7) allowed excellent solubility of the starting dinuclear iron(II) complex, however, stability of the formed peroxido complex was not sufficient to allow its observation at room temperature. Still, the development of a reaction kit that allowed "recycling" of the reactive species (Fig. 10) in a protic solvent indicated the potential of the complex system for future applications in catalytic oxidation setups. Reaction rates still need to be furthermore tuned to allow detailed studies in bubbly flow setups. The chemicals used in the facile (improved) synthesis for the iron complex are inexpensive and allow to prepare the complex on a large scale. Additionally, it is important to point out that chloride anions do not cause problems during these reactions. This could be a real advantage in an industrial setup because chloride ions are likely to be present in aqueous solutions as an impurity.

While the iron HPTB peroxido complex cannot be used for selective oxidation reactions it should be possible to either use it for (a) indirectly providing hydrogen peroxide or (b) to apply it (in an aprotic solvent) as a water free peroxide shuttle according to the following equations:

$$[Fe_2(H-HPTB)Cl_3] \xrightarrow[CH_3OH]{O_2} H_2O_2 + \left[Fe_2(H-HPTB)(OCH_3)_2Cl_3\right] \qquad (a)$$

$$[Fe_2(H-HPTB)Cl_3] \xrightarrow{O_2} [Fe_2(H-HPTB)(O_2)Cl_3] \qquad (b)$$
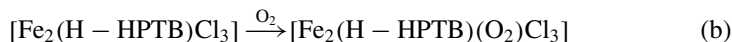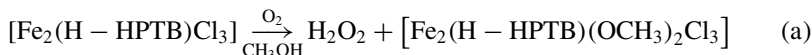
Either hydrogen peroxide or the water free peroxide then can activate another complex that actually performs the catalytic oxidation, a reaction that we call a tandem oxygenation. The goal would be to use regular air for these oxidations.

The reduction of the formed iron(III) complexes could be performed chemically as discussed above with ascorbic acid. Attempts should be made to find a cheaper reducing agent. However, depending on the oxygenation reaction the substrate might already do the job by itself. Options are furthermore to reduce the complex photochemically (as described above) or electrochemically.

Overall the iron HPTB system proved to be quite useful in these studies and will be further optimized in the future.

References

1. Gawlig C, Schindler S, Becker S (2020) One-pot conversion of cyclohexane to adipic acid using a μ_4-Oxido-copper cluster as catalyst together with hydrogen peroxide. Eur J Inorg Chem 2020(3):248–252. https://doi.org/10.1002/ejic.201901052
2. Ritz J, Fuchs H, Kiercka H, Moran WC (2000) Caprolactam. In: Ullmann's encyclopedia of industrial chemistry. Wiley-VCH Verlag GmbH
3. Jasniewski AJ, Que L Jr (2018) Dioxygen activation by nonheme diiron enzymes: diverse dioxygen adducts, high-valent intermediates, and related model complexes. Chem Rev 118(5):2554–2592. https://doi.org/10.1021/acs.chemrev.7b00457
4. Elwell CE, Gagnon NL, Neisen BD, Dhar D, Spaeth AD, Yee GM, Tolman WB (2017) Copper-oxygen complexes revisited: structures, spectroscopy, and reactivity. Chem Rev 117(3):2059–2107. https://doi.org/10.1021/acs.chemrev.6b00636
5. Strukul G (2013) Catalytic oxidations with hydrogen peroxide as oxidant. Springer, Netherlands
6. Olah GA, Goeppert A, Prakash GKS (2006) Beyond oil and gas: the methanol economy. Wiley
7. Ross MO, MacMillan F, Wang J, Nisthal A, Lawton TJ, Olafson BD, Mayo SL, Rosenzweig AC, Hoffman BM (2019) Particulate methane monooxygenase contains only mononuclear copper centers. Sci 364(6440):566–570. https://doi.org/10.1126/science.aav2572
8. Murrell JC, Smith TJ (2010) Biochemistry and molecular biology of methane monooxygenase. In: Timmis KN (ed) Handbook of hydrocarbon and lipid microbiology. Springer, Berlin, Heidelberg

9. Wang VCC, Maji S, Chen PPY, Lee HK, Yu SSF, Chan SI (2017) Alkane oxidation: methane monooxygenases, related enzymes, and their biomimetics. Chem Rev 117(13):8574–8621. https://doi.org/10.1021/acs.chemrev.6b00624

10. Que L, Dong Y (1996) Modeling the oxygen activation chemistry of methane monooxygenase and ribonucleotide reductase. Acc Chem Res 29(4):190–196. https://doi.org/10.1021/ar950146g

11. Que L (2017) 60 years of dioxygen activation. J Biol Inorg Chem 22(2):171–173. https://doi.org/10.1007/s00775-017-1443-6

12. Würtele C, Gaoutchenova E, Harms K, Holthausen MC, Sundermeyer J, Schindler S (2006) Crystallographic characterization of a synthetic 1: 1 end-on copper dioxygen adduct complex. Angew Chem Int Ed 45(23):3867–3869. https://doi.org/10.1002/anie.200600351

13. Weitzer M, Schatz M, Hampel F, Heinemann FW, Schindler S (2002) Low temperature stopped-flow studies in inorganic chemistry. J Chem Soc Dalton Trans 2002(5):686–694. https://doi.org/10.1039/b107927c

14. Zhang CX, Kaderli S, Costas M, Kim E-I, Neuhold Y-M, Karlin KD, Zuberbühler AD (2003) Copper(I)−dioxygen reactivity of [(L)Cu^I]$^+$ (L = Tris(2-pyridylmethyl)amine): kinetic/thermodynamic and spectroscopic studies concerning the formation of Cu−O$_2$ and Cu$_2$−O$_2$ adducts as a function of solvent medium and 4-pyridyl ligand substituent variations. Inorg Chem 42(6):1807–1824. https://doi.org/10.1021/ic0205684

15. Halfen JA, Mahapatra S, Wilkinson EC, Kaderli S, Young VG Jr, Que L Jr (1996) Reversible cleavage and formation of the dioxygen O–O bond within a dicopper complex. Sci 271(5254):1397–1400. https://doi.org/10.1126/science.271.5254.1397

16. Jacobsen RR, Tyeklár Z, Farooq A, Karlin KD, Liu S, Zubieta J (1988) A copper-oxygen (Cu2-O2) complex. Crystal structure and characterization of a reversible dioxygen binding system. J Am Chem Soc 110(11):3690–3692. https://doi.org/10.1021/ja00219a071

17. Würtele C, Sander O, Lutz V, Waitz T, Tuczek F, Schindler S (2009) Aliphatic C–H bond oxidation of toluene using copper peroxo complexes that are stable at room temperature. J Am Chem Soc 131(22):7544–7545. https://doi.org/10.1021/ja902327s

18. Ghosh A, Almlöf J, Que L Jr (1996) Electronic structure of non-heme high-valent oxoiron complexes with the unprecedented [Fe$_2$(μ-O)$_2$]$^{3+}$ Core. Angew Chem Int Ed 35(7):770–772. https://doi.org/10.1002/anie.199607701

19. Kryatov SV, Rybak-Akimova EV, MacMurdo VL, Que L (2001) A mechanistic study of the reaction between a diiron(II) complex [Fe^{II}$_2$(μ-OH)$_2$(6-Me$_3$-TPA)$_2$]$^{2+}$ and O$_2$ to form a diiron(III) peroxo complex. Inorg Chem 40(10):2220–2228. https://doi.org/10.1021/ic001300k

20. Que JL, Tolman WB (2002) Bis(μ-oxo)dimetal "diamond" cores in copper and iron complexes relevant to biocatalysis. Angew Chem Int Ed 41(7):1114–1137. https://doi.org/10.1002/1521-3773(20020402)41:7%3c1114::AID-ANIE1114%3e3.0.CO;2-6

21. Shu L, Nesheim JC, Kauffmann K, Münck E, Lipscomb JD, Que L Jr (1997) An Fe$_2$^{IV}O$_2$ diamond core structure for the key intermediate Q of methane monooxygenase. Sci 275(5299):515–518. https://doi.org/10.1126/science.275.5299.515

22. Hsu H-F, Dong Y, Shu L, Young VG, Que L (1999) Crystal structure of a synthetic high-valent complex with an Fe$_2$(μ-O)$_2$ diamond core. Implications for the core structures of methane monooxygenase intermediate q and ribonucleotide reductase intermediate X. J Am Chem Soc 121(22):5230–5237. https://doi.org/10.1021/ja983666q

23. Ross MO, Rosenzweig AC (2017) A tale of two methane monooxygenases. J Biol Inorg Chem 22(2):307–319. https://doi.org/10.1007/s00775-016-1419-y

24. Schaub S, Miska A, Becker J, Zahn S, Mollenhauer D, Sakshath S, Schünemann V, Schindler S (2018) Synthesis of an iron(IV) aqua-oxido complex using ozone as an oxidant. Angew Chem Int Ed 57(19):5355–5358. https://doi.org/10.1002/anie.201800475

25. de Visser SP, Rohde J-U, Lee Y-M, Cho J, Nam W (2013) Intrinsic properties and reactivities of mononuclear nonheme iron–oxygen complexes bearing the tetramethylcyclam ligand. Coord Chem Rev 257(2):381–393. https://doi.org/10.1016/j.ccr.2012.06.002

26. Hong S, Lee Y-M, Ray K, Nam W (2017) Dioxygen activation chemistry by synthetic mononuclear nonheme iron, copper and chromium complexes. Coord Chem Rev 334:25–42. https://doi.org/10.1016/j.ccr.2016.07.006

27. McDonald AR, Que L (2013) High-valent nonheme iron-oxo complexes: synthesis, structure, and spectroscopy. Coord Chem Rev 257(2):414–428. https://doi.org/10.1016/j.ccr.2012.08.002

28. Becker M, Heinemann FW, Knoch F, Donaubauer W, Liehr G, Schindler S, Golub G, Cohen H, Meyerstein D (2000) Syntheses, structures and properties of copper(I) and copper(II) complexes of the ligand N,N′-bis 2′-(dimethylamino)ethyl-N,N′-dimethylethane-1,2-diamine (Me_6trien). Eur J Inorg Chem 2000(4):719–726. https://doi.org/10.1002/(SICI)1099-0682(200004)2000:4%3C719::AID-EJIC719%3E3.0.CO;2-N

29. Hazell A, McKenzie CJ, Nielsen LP, Schindler S, Weitzer M (2002) Mononuclear non heme iron(III) peroxide complexes: syntheses, characterisation,mass spectrometric and kinetic studies. J Chem Soc Dalton Trans 2002(3):310–317. https://doi.org/10.1039/b103844n

30. Kaizer J, Klinker EJ, Oh NY, Rohde J-U, Song WJ, Stubna A, Kim J, Münck E, Nam W, Que L (2004) Nonheme $Fe^{IV}O$ complexes that can oxidize the C−H bonds of cyclohexane at room temperature. J Am Chem Soc 126(2):472–473. https://doi.org/10.1021/ja037288n

31. Nebe T, Beitat A, Wuertele C, Duecker-Benfer C, van Eldik R, McKenzie CJ, Schindler S (2010) Reinvestigation of the formation of a mononuclear Fe(III) hydroperoxido complex using high pressure kinetics. Dalton Trans. 39(33):7768–7773. https://doi.org/10.1039/c0dt00247j

32. Kryatov SV, Rybak-Akimova EV, MacMurdo VL, Que L Jr (2001) A mechanistic study of the reaction between a diiron(II) complex. Inorg Chem 40(10):2220–2228. https://doi.org/10.1021/ic001300k

33. Specht P, Oßberger M, Klüfers P, Schindler S (2020) Kinetic studies on the reaction of NO with iron(II) complexes using low temperature stopped-flow techniques. Dalton Trans 49(27):9480–9486. https://doi.org/10.1039/D0DT01764G

34. Feig AL, Becker M, Schindler S, van Eldik R, Lippard SJ (1996) Mechanistic studies of the formation and decay of diiron(III) peroxo complexes in the reaction of diiron(II) precursors with dioxygen. Inorg Chem 35(9):2590–2601. https://doi.org/10.1021/ic951242g

35. Feig AL, Lippard SJ (1994) Reactions of non-heme iron(II) centers with dioxygen. Chem Rev 94(3):759–805. https://doi.org/10.1021/cr00027a011

36. Dong Y, Menage S, Brennan BA, Elgren TE, Jang HG, Pearce LL, Que L (1993) Dioxygen binding to diferrous centers. Models for diiron-oxo proteins. J Am Chem Soc 115(5):1851–1859. https://doi.org/10.1021/ja00058a033

37. Dong Y, Yan S, Young VG Jr, Que L Jr (1996) Crystal structure analysis of a synthetic non-heme diiron-O_2Adduct: insight into the mechanism of oxygen activation. Angew Chem Int Ed 35(6):618–620. https://doi.org/10.1002/anie.199606181

38. Westerheide L, Müller FK, Than R, Krebs B, Dietrich J, Schindler S (2001) Syntheses and structural characterization of dinuclear and tetranuclear iron(III) complexes with dinucleating ligands and their reactions with hydrogen peroxide. Inorg Chem 40(8):1951–1961. https://doi.org/10.1021/ic0009371

39. Nizova GV, Krebs B, Süss-Fink G, Schindler S, Westerheide L, Cuervo LG, Shul'pin GB (2002) Hydroperoxidation of methane and other alkanes with H_2O_2 catalyzed by a dinuclear iron complex and an amino acid. Tetrahedron 58(45):9231–9237. https://doi.org/10.1016/s0040-4020(02)01182-1

40. Miska A, Schurr D, Rinke G, Dittmeyer R, Schindler S (2018) Frommodel compounds to applications: Kinetic studies on the activation of dioxygen using an iron complex in a SuperFocus mixer. Chem Eng Sci 190:459–465. https://doi.org/10.1016/j.ces.2018.05.064

41. Rollbusch P, Bothe M, Becker M, Ludwig M, Grünewald M, Schlüter M, Franke R (2015) Bubble columns operated under industrially relevant conditions—current understanding of design parameters. Chem Eng Sci 126:660–678. https://doi.org/10.1016/j.ces.2014.11.061

42. Schurr D, Strassl F, Liebhäuser P, Rinke G, Dittmeyer R, Herres-Pawlis S (2016) Decay kinetics of sensitive bioinorganic species in a SuperFocus mixer at ambient conditions. React Chem Eng 1(5):485–493. https://doi.org/10.1039/C6RE00119J

43. Lerch M, Weitzer M, Stumpf T-D, Laurini L, Hoffmann A, Becker J, Miska A, Göttlich R, Herres-Pawlis S, Schindler S (2020) Kinetic investigation of the reaction of dioxygen with the copper(I) complex $[Cu(Pim^{iPr2})(CH_3CN)]CF_3SO_3$ (Pim^{iPr2} = tris[2-(1,4-diisopropylimidazolyl)]phosphine). Eur J Inorg Chem 2020(33):3143–3150. https://doi.org/10.1002/ejic.202000462

44. Hoffmann A, Wern M, Hoppe T, Witte M, Haase R, Liebhäuser P, Glatthaar J, Herres-Pawlis S, Schindler S (2016) Hand in hand: experimental and theoretical investigations into the reactions of copper(I) mono- and bis(guanidine) complexes with dioxygen. Eur J Inorg Chem 2016(29):4744–4751. https://doi.org/10.1002/ejic.201600906
45. Miska A, Norbury J, Lerch M, Schindler S (2017) Dioxygen activation: potential future technical applications in reactive bubbly flows. Chem Eng Technol 40(8):1522–1526. https://doi.org/10.1002/ceat.201600684
46. Kück UD, Schlüter M, Räbiger N (2012) Local measurement of mass transfer rate of a single bubble with andwithout a chemical reaction. J Chem Eng 45(9):708–712. https://doi.org/10.1252/jcej.12we059
47. Avenier F, Herrero C, Leibl W, Desbois A, Guillot R, Mahy J-P, Aukauloo A (2013) Photoassisted generation of a dinuclear iron(III) peroxo species and oxygen-atom transfer. Angew Chem Int Ed 52(13):3634–3637. https://doi.org/10.1002/anie.201210020

Analysis of Turbulent Mixing Und Mass Transport Processes in Bubble Swarms Under the Influence of Bubble-Induced Turbulence

Katharina Haase and Christian J. Kähler

Abstract In a newly build counterflow water channel multiphase flows can be investigated with and without emulated background fluctuations. These fluctuations create a model swarm that allows to investigate single bubbles as if they are moving in a bubbleswarm without the visual obscuration of a real swarm. The fluctuations are created with specially designed particle grids that are mounted on-top of the channel and excited by the counterflow. These girds consist of small plastic beads in the size of the to be investigated bubble. Each bead is solely attached to the element in vertical direction, which allows the string of beads to move with the flow, creating a more truthful swarm agitation. Several grids, varying in design and volume fraction were characterized and the grid with a volume fraction of 10% and 5 mm beads showed the best accordance with real bubble swarms. With these grids it is possible to use optical methods like PIV (particle image velocimetry) to measure the flow statistics behind and around a single bubble. With a newly introduced 3D reconstruction the timeresolved shape of the bubble can be measured simultaneously with the flow around it. Investigation of the shape revealed that it is necessary even for small bubbles to apply a full 3D evaluation, for example with the surface-to-volume ratio. With this the shape oscillations can be described and shown the oscillations are hindered by the external fluctuations but not fully suppressed. In addition, it was shown that the movement of the bubble in an emulated swarm is mainly driven by the pressure gradients in the flow.

1 Introduction

Multiphase flows are the combination of two different phases, e.g. water and solid particles, air in liquid or even liquids with different density. One very prominent example is gas bubbles in liquid that can occur in various places in everyday life, for

K. Haase · C. J. Kähler (✉)

Institut Für Strömungsmechanik Und Aerodynamik (LRT 7), Fakultät Für Luft- Und Raumfahrttechnik, Universität Der Bundeswehr München, Werner-Heisenberg-Weg 39, 85577 Neubiberg, Germany

e-mail: christian.kaehler@unibw.de

example in soft drinks, water vapor in boiling water or in sea foam. But they also find use in various industrial, scientific and energy sectors. Examples are bioreactors, steel melts or nuclear power plants. Bubbles are often used as punctiform mass sources to supply a liquid with substances at the right time, but also for mixing purposes, since the bubble-induced turbulence leads to a gentler blending compared to mechanical stirring tools. Most often mixing processes are needed to improve chemical reactions or the heat transfer to enable certain processes or increase the selectivity of reactions. In most applications, bubbles up to $d_B = 10$ mm in size are used in swarms with around 18% volume fraction [1]. The experimental and numerical analysis of the flow statistics and the mass transport processes in such swarms of bubbles still represents an enormous methodical challenge.

In particular, the influence of swarm turbulence on the dynamics of the individual bubbles and the mass transfer across the phase boundary into the fluid are of fundamental importance for the designing of reactors. Until today, mechanical probes are usually used to characterize the physical processes in bubble swarms, e.g. for local measurement of the enriched substance. But intrusive probes always interfere with the flows within the plants and thus influence the measurement results. Therefore, the use of contactless optical methods is desirable in order to gain more detailed and precise knowledge about the processes. Unfortunately, optical methods do not provide reliable results in bubbly flows with large volume fraction due to the shadowing by the bubbles. However, by means of special techniques developed within this project is it possible to examine at least some processes using high resolution 2D and 3D optical techniques. In this chapter these approaches will be outlined, which allow to investigate specific aspects of the flow dynamics of bubbles and the surrounding flow. The essential idea is to use optical methods in combination with an apparatus that allows creating artificial swarm like turbulence. In this case the behavior of a single bubble in a swarm like turbulence can be investigated with none-intrusive optical method. Only bubble–bubble interactions do not take place, but at moderate bubble concentrations as typical in a swarm these interactions are not essential. The main scientific question is how to generate a bubble swarm like turbulence artificially so that a single bubble in a swarm like turbulence can be examined. To answer this question the following sub questions need to be answered:

- What are the characteristics of swarm turbulence? How can a swarm like turbulence be emulated? How does the emulated turbulence, compare to real bubble agitations?
- How can the trajectory and velocity of a single bubble moving in a 3D space be measured with optical techniques? How can the geometry of a single bubble be accurately described and the surface reconstructed with computer vision techniques? Can the flow around the bubble be measured simultaneously with the bubble geometry and what are the interference effects when both measurements are performed simultaneously?

- How do bubbles behave in emulated swarm turbulence compared to free rising bubbles? What is the difference compared to a free rising bubble? Which turbulence level is required to make a transition from a deterministic natural bubble motion to a stochastic turbulence driven motion of the bubble?

To answer these fundamental research questions a newly designed experimental facility was setup. In the following this channel is described and characterized.

2   Counterflow Water Channel

To emulate the flow structures and measure the bubbles in a swarm-like turbulence a new facility was constructed and built up. The general idea of this facility is to trap a bubble in the plane of a desired turbulence background level. This is achieved by creating a counter flow in which the velocity of the rising bubbles due to the lift force is compensated by a counterflow generated by the flow channel. By setting the velocity to the terminal rise velocity of the bubble it can either be slowed down, stopped or pushed downwards. In this way it is possible to move the bubble at a specific location in streamwise direction were the turbulence level is appropriate for the scientific analysis.

The channel is sketched Fig. 1. It has a height of four meter and is built out of stainless steel to avoid corrosion and to allow the usage of chemicals. The fluid moves from the basin (450 mm × 450 mm and 500 mm high) at the top of the channel trough the nozzle into the test section. The nozzle is designed to amplify the intensity and anisotropy of the generated turbulence as well as to increase the turbulent length scales. Due to the contraction of the nozzle the generated eddies are elongated while the strength and rotation is preserved.

The 80 mm × 80 mm and 1000 mm long measurement section is optical accessible through borosilicate glass (*SCHOTT Technical Glass Solutions GmbH*) from all four sides. On one side three 150 mm × 80 mm plastic windows are mounted that allow inserting for example a calibration target, chemicals or bubble generators. At the end an electrical valve (*Bürkert Fluid Control Systems Typ 2300*) is installed to regulate the flow in the channel. After passing through the channel the fluid is collected and pumped up by a rotary pump (*GRUNDFOS—CME25*) into the basin. To ensure a minimal error induced by the channel itself, it is important to generate the flow with little to no initial fluctuations or turbulence. Therefore a specially designed rain shower like distributor was manufactured as an inlet. It consists of over 7000 outlets, which distribute the fluid over the whole basin. The electronics are regulated by a in house *LabView* Program (*National Instruments*) and a *NI-USB6002/PCIe-6321* (*National Instruments*).

Since the material properties of water are highly dependent on the temperature a sensor is mounted on the bottom of the channel to monitor and note the temperature during a measurement. It is common that the temperature is rising by roughly 5–10 °C during one measurement session. The water initially when it's filled from the tap
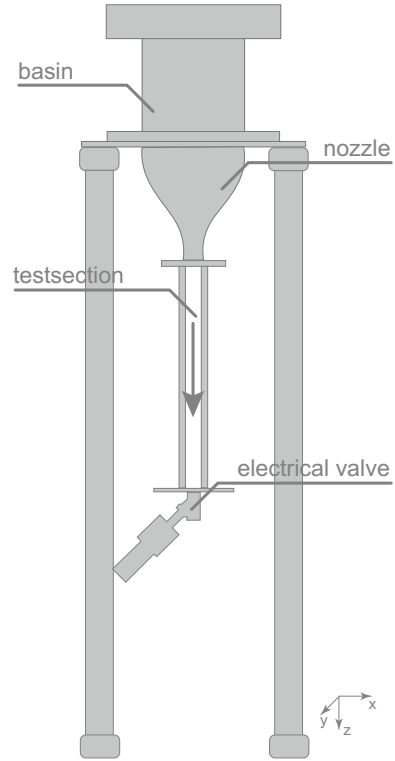
to the channel has a temperature of 16–18 degree Celsius, during the measurement
this rises up to 23–25 °C. To prevent the temperature to influence the measurement
the channel was running to heat up the water to a constant temperature of 25 °C.

3 Characterization of the Counter-Flow Channel

In order to generate a turbulent flow with similar properties as swarm turbulence,
the homogeneity of the inflow and the turbulence level of the channel itself needs
to be known. As described earlier the best inflow conditions were achieved with a
rain shower like distributor mounted a few centimeters above the water surface. The
following chart Fig. 2 shows the mean velocity and the turbulence distribution in the
free stream part of the measurement section.

The characterizations were performed with a planar PIV-System. Convergence
studies showed that 1000 images are sufficient for calculate the mean value. The PIV
measurements are performed with sCMOS cameras from *LaVision* in combination
with a Nd:YAG—Laser (*Innolas Spitlight* 4000, $\lambda = 532$ nm) and the measurements
are evaluated using the commercial *software DaVis* (*LaVision*). The light sheet is
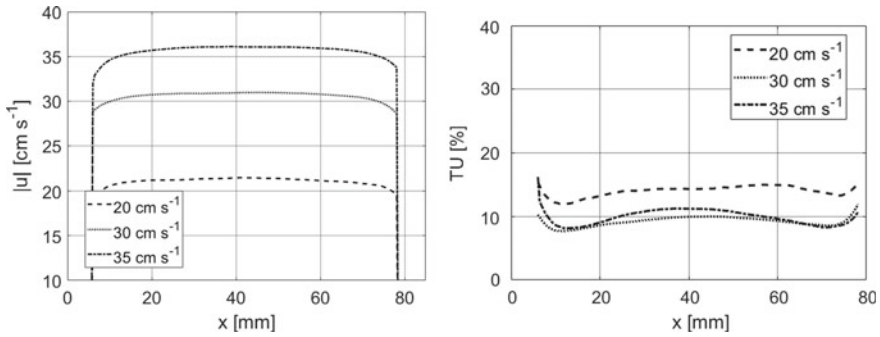
Fig. 2 Profile characterization across the channel. Left shows the mean velocity profile along the channel normal for three different velocities set in the program. On the right image is the corresponding turbulence level plotted

placed perpendicular to the channel walls in the middle of the channel with an estimated thickness of $d = 0.5$ mm. The measurement is performed with a double pulse ($\Delta t = 700\,\mu s$) and a repetition rate of $f = 10$ Hz. An interrogation window of 16 px × 16 px is achieved after an iterative multi-grid evaluation with interrogation window refinement. In the following, the coordinate system is defined as $\vec{z}$ in flow direction, $\vec{x}$ and $\vec{y}$ normal to that, where $\vec{x}$ is horizontal in the field of view. Systematic errors, resulting from the calibration or light sheet alignment are smaller than the uncertainty of the measurements, since special care is drawn to aligning both the target and light sheet with an error of less than 1°. Random uncertainties are affected by many parameters including particle image size, particle image density, turbulent fluctuations and interrogation window size [2]. With a mean pixel displacement between 10 and 12 pixels in the particle images and a particle images sizes of 3–4 pixels as well as a particle per image ratio of 0.1 the random uncertainties can be estimated to ~ 1%. From the PIV data the homogeneity, isotropy and statistical values, like the mean velocity field $\overline{u(x, z)}$, the corresponding fluctuations $u\prime(x, z, t) = u(x, z, t)\overline{u(x, z)}$ with a good local resolution are calculated. To determine the turbulent intensity Tu [%] the root-mean-square (rms) of the fluctuations is normalized by the mean velocity at that point resulting in $Tu(x, z, t) = u(x, z, t)\prime_{rms} \cdot \overline{u(x, z)}^{-1} \cdot 100$.

As depicted in Fig. 2 the velocity profile across the channel is homogeneous over a wide part in the middle and develops a boundary layer with a thickens of ~ 3–5 mm. The thickness of a boundary layer is defined for unaffected flows from the wall perpendicular to the point where U_{99} (99% of the free stream velocity) is reached.

Even up to a velocity greater than $v = 0.3$ m/s the inflow is constant with time and shows a flat profile with a slight increase in the middle section. The turbulent profile shows a similar behavior. For higher flow velocities the turbulence starts to show an increase in the middle of the channel due to the flow not being able to evolve in this short distance. For the interesting velocity ranges ($v = 0.2$–0.25 m/s) needed for these experiments however the turbulent profile is sufficiently homogeneous and boundary layer effects do not disturb the flow in the center. One thing to note here is

that the velocity close to the wall cannot be truthfully recorded or measured due to the steel beams holding the channel walls.

4 Emulation of Bubble Induced Turbulence

To better understand the mechanics of the mixing at high volume fraction, it is necessary to investigate the interaction between bubbles, their motion in a swarm, as well as their interaction with the induced wake turbulence. Attention must be placed on characteristic variables like the bubble size, gas volume fraction and liquid agitation to better understand their influence on aspects like the mass transport from the bubbles in the surrounding fluid. Since it is impossible due to the shadowing of the swarm, especially high-density swarms to study individual bubbles the one aim of the research project is to find a model swarm that creates agitations similar to real bubble swarms and study single bubbles in this flow. The bubble is supposed to experiences flow conditions as if it was moving a bubble swarm but can be recorded without the obstructions. Of course, bubble–bubble interactions cannot be considered using this approach but in a swarm this effect is of minor importance as the bubble density is moderate. In various publications, it is common to generate turbulence, similar to bubble dynamics by arranging spheres in a random 3D array [3, 4]. However, those neglect the motion of the bubbles.

This chapter introduces and characterizes this method to emulate these swarm statistics and compares them to real bubble swarms. The following results have been published in [5, 6].

4.1 Free Moving Particle Grids

In the literature [7, 8] small spheres in the size of the desired bubble, arranged in a random 3D space, are often used. Thus, a new extension of these grids was designed. The grids consist of free moving particles that also emulate the movement of the bubbles. While the first two layers of particle elements are fixed in *xyz*-direction, the lower elements (arranged in five layers) are only attached to the one above and can thus move freely in the *xy*-plane (Fig. 3).

Fig. 3 Foto of the free moving particle grid

The grids have been designed and manufactured with different sizes and volume fractions. Before making measurements with bubbles however, the flow turbulence that are created by those grids need to be characterized in regards to their flow statistics and compared to real bubble swarms. With this, a detailed investigation of single bubbles regarding their shape, movement and induced flow as well as the resulting mass transport, would contribute to the better understanding of physical phenomena in a bubble swarm of high-volume fraction. In the work presented herein, the characterization of the particle grid generated turbulence was performed with planar particle image velocimetry (PIV) as well as electro diffusion measurement technique (EDM) and compared to turbulent statistics of real two-phase flows. The EDM measurements were performed at the University of Bremen.

The same 2D planar PIV setup as before was used again for the grid characterization. The light sheet was placed close to the grids so that the last element of the grid was still visible in the recorded images. This resulted in a measurement window of at least 5 particle diameters and spanned over the whole channel cross section minus the framing. This was about 10 mm on the left and right side that was obscured, which is the boundary layer of the channel. Comparative measurements using EDM are performed at a comparable experimental setup with similar grids at the University of Bremen. The EDM measurement principle is described in [5] The EDM measurements only resolves data at a single point (no spatial resolution), but with high temporal resolution. The EDM provides localized velocity data which is used to calculate frequency-dependent spectral energy density. By combining the results of both measurement techniques, temporally and spatially resolved data can be obtained.

In Table 1 the specifications of the measured grids are listed. The grids have different particle shapes e.g. spheres or ellipses in two sizes $d_B = 5$ mm and 10 mm as well as particle volume fractions α ranging from 3.97 to 9.83 vol%. Each grid consists of at least five layers of beads with different spacing according to the desired volume fraction (ranging between 5 and 10 mm). While the first two layers are fixed, the following individual particles are only tethered to the one above to secure the vertical distance. All elements in the bottom layers can move randomly in, $\vec{x}$ and

Table 1 Overview of the grid shapes, diameters and volume fraction

	Grid particle shape	Particle size in mm	Particle volume fraction in vol%
1	Spheres	10	9.83
2	Spheres	10	3.97
3	Spheres	5	9.83
4	Spheres	5	3.97
5	Ellipsoids	3.91 × 5.65	3.97
6	Eellipsoids	8 × 12	9.83

$\vec{y}$ plane. The setup can be seen as a swarm of bubbles held in place above the measurement plane, so that the wake and induced liquid fluctuations behind this three-dimensional grid can be measured. In addition to the free moving particle grids a rigid grid with the threefold length (~15 layers) is characterized as well. This will give insight in the contribution of the particle motion to the turbulence, since the bubble-induced turbulence is a collective effect induced by the bubbles wake and the motion of the bubbles.

4.2 Characterization of the Particle Grids and Turbulence Analysis

As described in [8] a good model to generate swarm-like turbulence is achieved by using small spheres with the size of the desired bubble, arranged in a random pattern at fixed places in space. So it can be expected that the turbulence properties are even more realistic is moving particles are used. Since the turbulence created in bubbly flows results from a combination of the bubble motion, wake and the agitated liquid phase, it is important to take all these factors into account for emulating bubbly flow. With the proposed model of the free moving particle grids, these factors are included and can be modified freely. For this assessment, the mean velocity in the main and perpendicular flow direction are evaluated followed by the analysis of the fluctuations, turbulence levels, and energy spectra. To verify the validity of the particle-induced turbulence a comparison to the real bubbly flow of each characteristic will be given after each paragraph.

4.2.1 Velocity Profile

It is well known that in a bubbly flow with low gas volume fractions α a laminar velocity profile is present, but with increasing volume fraction α a transition from the laminar to the turbulent flow state takes place. In bubbly flows the velocity of the liquid phase is mainly determined by the void fraction of the swarm. At low to moderate volume fractions the bubbles are distributed statistically which results in
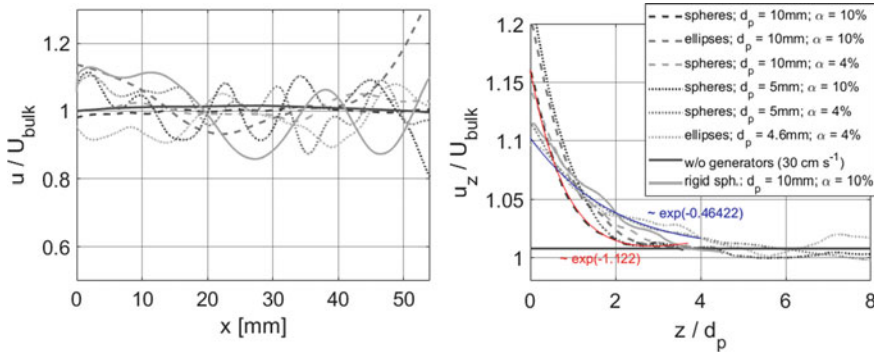
Fig. 4 A comparison of the flow velocities behind the free moving particle grids. Left image: comparison of the velocity profile in spanwise direction at ~3 d_p behind the last layer of grid elements. Right image: vertical velocity component u_z in flow direction under a grid element against the distance in particle diameters of the grid. The flow behind grids with big elements decays proportional to ~exp (-1.12), while the flow behind smaller elements decays slower, proportional to exp (-0.46)

the velocity profile of the liquid resembling a turbulent flow [7, 10]. With increasing α the shape deviates from the flat profile and the mean velocity lowers at the core and rises near the wall [11].

In Fig. 4 the velocity components in span wise direction $\vec{x}$ and flow direction $\vec{z}$ behind the grids, three particle diameters d_p behind the last layer of grid elements respectively, the velocity underneath a particle element is plotted against the distance normalized with the particle diameter d_p. For better evaluation velocities are normalized by the bulk velocity $\overline{u(x, z)}$. The field of view was placed to have the last row of particles in the top of the picture. As can be seen (Fig. 4) the mean velocity behind the grid takes roughly four particle diameters to become homogeneous since the wake of each individual particle is still present in the vicinity behind the particle grid but subsides within the range of ~ 4 particle diameters and a homogenous velocity distribution is present. The horizontal velocity $\overline{u_{x(x,z)}}$ is small in comparison to $\overline{u_{z(x,z)}}$. In Fig. 4 the decay of the flow behind the grids is compared between each other and to real bubbly flows. Further, the wake interactions are described as responsible for a faster dissipation [3]. Thus, three regions are defined in [12]:

- A strong decay near the bubble where the flow is similar to that behind a single bubble
- a region where only the wakes interaction is significant and decays much faster and
- a region where the velocity fluctuations reach an asymptotic state.

It is noted that the velocity agitation settles after roughly five bubble diameters and decays exponential behind a small bubble swarm. For all the particle grids a constant exponential decay is observed, which declines in a similar fashion as described in [22] with the best agreement behind the elliptical 5 mm and 4 vol% grids. While

the velocity gradient behind the grids with bigger elements is enhanced more than the smaller ones, the decay is also faster (~exp (−1.1) for the big elements and ~exp (−0.46) for small grid elements). In comparison, the rigid grid shows a much thinner wake region and it takes roughly 6–7 sphere diameters until the profile becomes homogeneous. With increasing velocity, the oscillation frequency around the initial position, hence the entrainment intensifies but the wake is a result of the amplitude of this oscillation, thus it takes roughly the same distance for all velocities to decay back to the same level. Due to the particles motion in a random pattern the free stream between two grid elements can flow freely until it gets entrained and thus enhanced. Because of the random movement of the grid elements the free stream gets continuously altered in its velocity, which creates different sheer stresses on the particles and thus generates different turbulent length scales. So, the movement of the particle enhances the development of the homogeneity of the flow profile.

4.2.2 Turbulence and Isotropy

In Fig. 5 the turbulence level Tu is plotted. The left image shows the profile normal to the channel direction $\vec{z}$ as a comparison for the different grids and the right the decay in flow direction $\vec{z}$. Again, the influence of the individual spheres is measurable but with increasing distance from the grid the profile becomes flatter and the influence of each individual row tails off until it becomes similar in shape to the undisturbed channel flow but with increased magnitude about 10%.

Due to the vortex shedding around the moving spheres the turbulence is enhanced underneath a row of obstacles, which is the same behavior for real two-phase flows. In the core regions, where the bubbles are concentrated, the induced turbulence becomes larger. The lateral motion/rotation of the spheres has an influence on the turbulence level, thus grids with a high-volume fraction induce a greater turbulence, as well
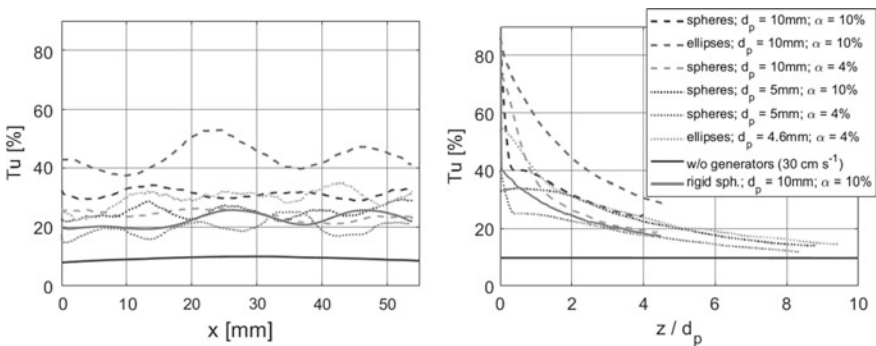
Fig. 5 Comparison of the introduced turbulence by the different grids. Left image: comparison of the turbulence profile in spanwise direction at ~ 3 d_p behind the last layer of grid elements. Right image: vertical decay of the turbulence TU under a grid element against the distance in particle diameters of the grid

as bigger spheres due to their greater blockage effect in downstream direction. Both fluctuations in flow direction and span wise direction are in the same order, considered for all sphere distances. Due to the random particle's movement, different turbulent length scales can be generated. The free stream between two grid element strings gets entrained and thus continuously altered which results in different sheer stress on the particles and thus generates different turbulent length scales. Again, do the grids with 10 mm particle diameter introduce a higher agitation after the last layer of spheres, which decays rapidly in comparison to the small spheres. Both again decay exponentially. After two sphere diameters for the small and big spheres, the turbulence decreases in the same way. The flow velocity influences the magnitude of the enhancement while the volume fraction and size determine the shape and decay. Taken from [13] the turbulence level for swarms with 2% is ~6%, which would, by extrapolating lead to a turbulence of 30% for swarms with 10% volume fraction. In [13, 14] is the turbulence described with the fluctuations $u'(x, z, t)_{rms}$ and $\sqrt{u'^2}/u$. The fluctuations in vertical and horizontal directions for real bubbly flows are comparable to each other due to the oscillating path of bubbles, even though the main flow direction is vertical [10]. Again, using the grids shows, that the bubble motion has a significant influence on the turbulence level as well. As shown in Fig. 5 the overall turbulent intensity is lower by 5–10% under a rigid grid element. In addition, it takes almost double the length downstream until the inhomogeneity decays and a homogeneous flow profile is present.

4.2.3 Liquid Fluctuations and PDF

Gas bubbles induce a characteristic kind of turbulence, that is also called pseudo-turbulence or bubble-induced turbulence. In contrast to shear-induced turbulence, the probability density function (p.d.f.s) show a non-Gaussian behavior [12]. When trying to emulate this specific bubble turbulence the design of the grids must be take these into account, since the shear-induced turbulence is increased and shifts the p.d.f. more and more to a Gaussian profile. In [12] a detailed description of the p.d.f.s behavior is given. Measurements with a homogeneous swarm at a wide variety of Reynolds numbers were evaluated and normalized by an empirical factor $u_b \cdot \alpha/\alpha_0^{0.4}$, with u_b being the bubble rise velocity, α the gas volume fraction and α_0 a reference volume fraction of 0.01.

The fluctuation profile $u'(x, z, t) = u(x, z, t) - \overline{u(x, z)}$ in the single-phase flow has a convex hull in the middle and peaks near the wall (Fig. 6). Due to the bubble induced turbulence, the plateau widens and the peaks disappear. In the core region, the shear induced turbulence is not dominant and the bubbles and wakes are responsible for the creation of fluctuations. The shear induced turbulence becomes more influential at the wall regions with increasing liquid velocity. While $|u'_x|$ and $|u'_y|$ (span wise directions) are in the same order and thus isotropic, $|u'_z|$ (flow direction) reaches larger values [11]. The turbulent profile is evenly distributed over the whole channel and shows no preferences in a peak development, neither at the center nor near
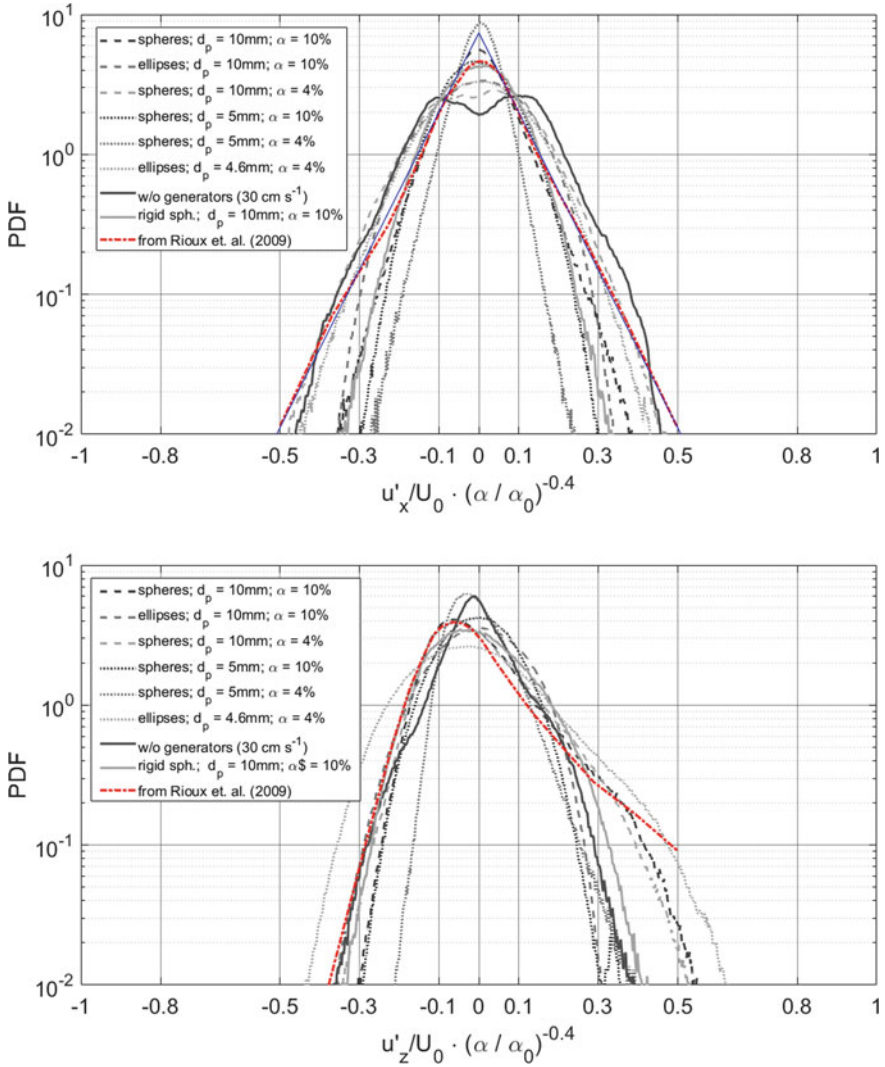
Fig. 6 Comparison of the normalized p.d.f. of horizontal (top image) and vertical fluctuations (bottom image) for all grids. Both are normalized and scaled with the volume fraction. ($\alpha_0 = 0.001$ and U_0 is the mean bulk velocity)

the wall [15, 16]. This can be also seen in the p.d.f. While the horizontal ones are axisymmetric, the vertical p.d.f. has a tail pointing to greater fluctuations [8, 17].

In real bubbly flows the velocity fluctuation u' is mainly determined by the gas hold up α [18]. At moderate gas volume fractions the liquid is entrained by a random bubble accumulation. In the core region the bubble wakes are more influential, while the bubbles in the near wall region reduce the fluctuations significantly.

In Fig. 8 the normalized p.d.f.s of the axial and radial velocity fluctuations for the various particle grids are shown. The horizontal fluctuations for all grids are symmetric, while the fluctuations in flow direction show a non-isotropic behavior with strong upward fluctuations. In both plots, a comparison with the results published in [8] is made. Also, a scaling factor $u = U_0 \cdot \alpha^{0.4}$ for the velocity fluctuations is provided so that the p.d.f.s become self-similar. This scaling was first proposed by [7]. For this experiment, the bulk velocity U_0 was chosen as the bubble rise velocity. For the different grids, the overall shape is similar to the one in real bubbly flows, but some of the grids compare better to the data taken from real bubbly flows. As stated, the vertical fluctuations decay exponentially. All the grids show this behavior. However, in comparison to the real bubbly flows show differences in the horizontal fluctuations. Due to the strong wake, the p.d.f. shows a trail to higher fluctuations that can only be seen in some of the grids. For example, as can be seen in Fig. 7, the spherical 10 mm–10 vol% and elliptical 5 mm–3 vol% shows a developed shifted p.d.f. For the other grids, the p.d.f. are almost symmetric in the vertical direction, like the 5 mm–10 vol% or the rigid grid. Therefore, a detailed comparison with the data published in [12] is shown in Figs. 6 and 7 for the horizontal fluctuations and for the vertical fluctuations. Risso describes the turbulence is comprised of three different effects, the wakes, the turbulence in the liquid and the potential flow generated by the bubble rising while assuming the bubbles move independently of each other. For the grids, these different agitations can be explained by the following. The wake effect is mainly introduced by the sphere/bubble size which for the grids is fixed and set by the grid element diameter. For the $d_B = 10$ mm spheres the wakes are brought and induce constantly strong fluctuations, which results in an overall shift of the p.d.f. shape to higher fluctuations. With the elliptical shape of the small elements mainly fluctuation in the size of the particle are induced, but due to the tumbling motion and thus changing of the effective radius, a broad range of fluctuation scales are generated. This phenomenon gives the p.d.f. also a shift to higher fluctuations but with a slower decline. The second portion is due to the particle movement. Thus, the volume fraction and space the particle strings can move in. While the grids with a high volume fraction do not allow the elements to move with large amplitude, the p.d.f. becomes thinner and the volume fraction is overall responsible for the width of the p.d.f. The potential flow in this setup is provided by the counter flow since this emulates the bubble rise velocity. This effect is responsible for the height of the p.d.f. However, since the data is normalized with both the volume fraction and the mean bulk velocity the shape is only dictated by the induced wake and freestream entrainment, and following from that the fluctuations. One can conclude that the grid induced turbulence, resulting from the spherical $d_B = 10$ mm – 10 vol% and elliptical 5 mm – 4 vol% shows the best accordance with the p.d.f. and generated by a real bubble swarm the best agreement with real bubble swarms [12].
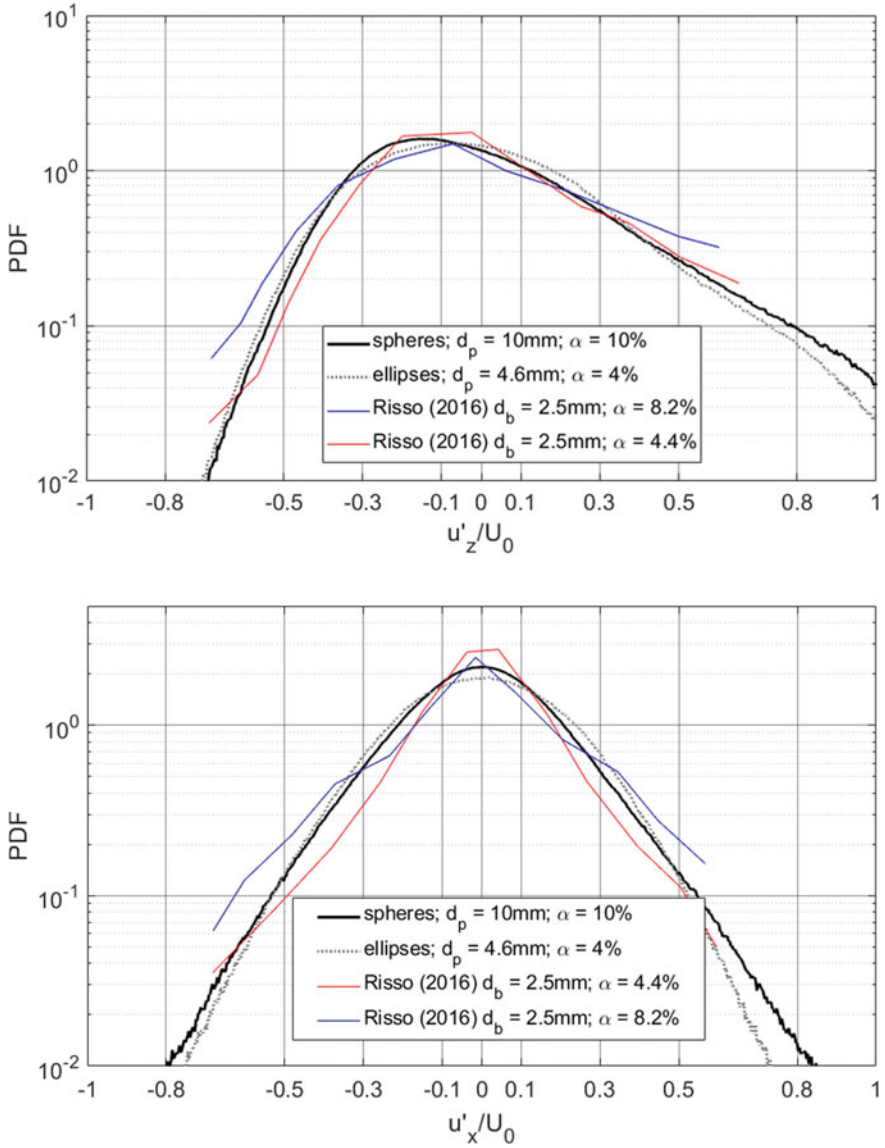
Fig. 7 First image Shows the normalized p.d.f. of liquid velocity fluctuations in span wise direction and the second in the flow direction in comparison with measurements published in [8] that were performed for different bubbles sizes and volume fractions
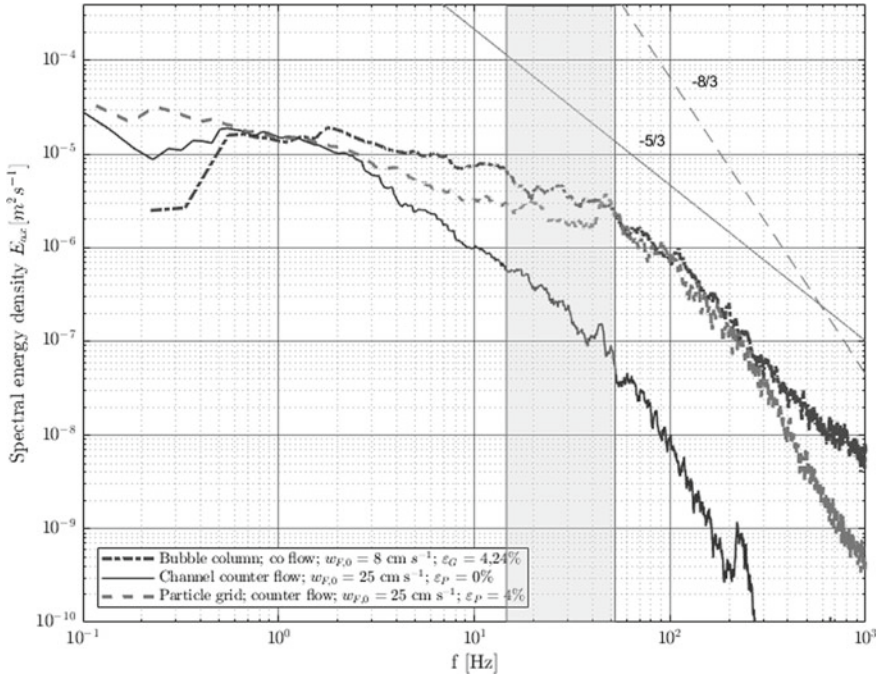
Fig. 8 Energy spectra measured with EDM at the facility at the University of Bremen. The $-5/3$ and $-8/3$ slopes are added. The range of frequencies that are responsible for the bubble deformation are marked

4.2.4 Liquid Energy Spectra

Various experimental and numerical publications report a specific behavior of the energy spectra in pseudo turbulences such as the bubble-induced one [3, 9]. The energy spectra of bubble induced turbulence are independent of d_B and α [3]. Here the energy spectra of a bubble swarm, after it passed the measurement section, are calculated from PIV with a spatial fast Fourier transformation (FFT) in flow direction. In addition, [19] measured the spectra with constant temperature anemometry. Divided into three sections the spectra can be described as follows: Below 10^2 Hz the spectra show a $\lambda^{-5/3}$ slope, which describes the classic Kolmogorov inertial subrange. Above 10^2 Hz till approximately 10^3 Hz the spectral energy density follows a λ^{-3} law. These regions are both independent of d_B, the bubble diameter and α, but scale with the integral length scale Λ. In [8] a value of $\Lambda = 15$ mm for the spectra in flow direction is given. The integral length scale Λ can be calculated as the first value in the spectra normalized by the mean velocity and indicate the biggest possible fluctuation. The $-5/3$ law describes in isotropic turbulence the eddy cascade resulting purely from shear flows. In [5], hot film anemometry is presented that revealed a $-8/3$ power law. This adjustment of the exponent can be used as an indication to distinguish between purely isotropic turbulence and turbulence induced by bubbles.

To characterize the time-resolved energy spectra of particle grids, EDM is used to measure the power spectral density. These measurements are performed utilizing the flow channel at the University of Bremen. Comparable grids are used and the results evaluated with the measurements in a real bubble column. [5] compare the energy spectra taken in real high dense bubble swarms with that under the elliptical particle grids (d_p = 4.6 mm, 4 and 10 vol%). Both, a real bubble column in co-flow (u = 80 mm/s) with a volume fraction α = 4.24 vol% and the free moving particle grids are characterized with the time-resolved EDM. The mean counter flow is set to v = 0.15 and v = 0.30 ms^{-1}. In Fig. 8 the –5/3 slope derived from Kolmogorov's law as well as the –8/3 to indicate the energy cascade slope of bubble-induced swarm turbulence is inserted. The transition is between the initial turbulent energy, and the onset of the energy cascade can serve as a reference length L since the wake structures of swarm turbulence arise in the bubble dimension (d_B ~5 mm). In [9, 20] a deduction of this scaling is provided. The largest eddies that need to be considered for the bubble motion and deformation are in the order of three times the diameter. Larger ones result in a lateral movement of the bubble. Thus, the appropriate frequencies to this range of bubble diameter are between 15 < f < 50 Hz, which are highlighted in Fig. 8. In the energy dissipation range, different zones with characteristics comparable to Kolmogorov's law can be recognized. The slope of the spectra for real bubbly flows, and the particle grid is in good agreement with each other as can be seen in the highlighted area in Fig. 8. Thus, a good comparison between the particle induced and real bubbly flow turbulence can be observed for the given conditions.

To further describe the flow, the integral time and length scales for the dominant largest structures can be derived from this time resolved signal and its auto-correlation function. The similar time scale describes the longest periodic flow structure that can in turn be used to describe the length scales by applying the Taylor's-hypothesis. In [5] a detailed analysis regarding the length scale and turbulence level is given. Mießner describes that the particles introduce turbulence with the initial length scale of swarm turbulence. As well as stated by Mießner the devices generate a variety of length scales. While on the lower half of the considered range the grids produce smaller values while in the higher frequency ranges larger scales.

4.3   Conclusion

In the present work, the flow statistics behind free moving particle grids with different characteristics were evaluated by using PIV. Also, EDM was used to measure the spectral density of selected particle grids with elliptical elements and a volume fraction of 4% as well as in comparison to a bubble swarm with properties like multiphase flows in industrial reactors. The aim of this chapter is to characterize the specially designed particle grids and evaluate the induced turbulence to clarify whether they mimic the flow and turbulence introduced by real bubble swarms or not.

From the PIV data, the spatial distribution of the velocity, turbulence, and the velocity fluctuations are calculated. It is shown that the turbulence characteristics can

be controlled over a broad parameter range by varying the size, shape and volume fraction of the particles and by selecting the suitable location measurement position. It can be stated that the larger the particles and the higher the volume fraction, the larger the turbulence level behind the particle grid becomes. While grids with 10 mm particles introduce greater velocity fluctuations than the small 5 mm spheres, for all grids it takes ~5 particle diameters for the disturbed flow to relax back to the bulk velocity and generate a flow with homogeneous turbulence. By comparing the particle form, the elliptical particles introduce a greater turbulence level than the spherical one. Regarding the velocity and turbulence decay with increasing distance, the grid with small elliptical elements shows an exponential decay that is in the same order as the real bubble induced turbulence [3]. By comparing the p.d.f.s for the velocity fluctuations behind the different grids, not only the small elliptical grid, but also the spherical grid with 10 mm and 10 vol% show good agreement. This in turn is also comparable to real bubble swarms with 2.5 mm and 4–8 vol%, as shown by comparing to the p.d.f.s taken from Risso's publication [12].

The EDM measurements further give insight into the integral length scales and scale distribution. For this, a real bubble swarm with a gas hold-up of 4.24 vol% was measured as a reference. By comparing the respective energy spectra in the relevant frequency range, a good agreement can be found for the grid with 5 mm elliptical elements and a volume fraction of 4 vol%. To find the right condition for designing an experiment, it has to be considered that the influence of the individual grid elements is still measurable in the vicinity of the grids. It can be solved by conducting experiments roughly 3–4 particle diameters further downstream from the grid this leads to a homogeneous flow profile several particle diameters downstream.

The rigid particle grids produce much lower turbulence levels due to the missing random motion of the particles. Due to the random movement of the particles in different particle layers, the turbulence varies strongly, as typical for real bubbly flows. Furthermore, different length scales are generated by the randomly moving particles and constantly changing entrainment of the free stream between the particle strings. These length scales were measured and characterized by EDM and discussed in detail in [9]. The devices induce a range of length scale, while on the lower half of the considered range the grids produce smaller values while in the higher frequency ranges larger scales. Taking all these factors into account, we can conclude that these flexible grids generate a good, but not perfect model swarm-turbulence. Hence, it allows conducting experiments with small bubble swarms or even single bubbles in a swarm like background turbulence with optical measurement techniques without introducing disturbances with probes.

5 Behavior of a Single Bubble in Swarm like Background Turbulence

It is obvious that the transfer of chemicals from the bubbles in the liquid depends strongly on the flow state of the surrounding media (laminar/turbulent). But also, the size of the bubble is an important parameter since larger bubbles deform which results in a variation of the surface area and thus changes the transfer of chemicals through the interface. In order to better understand the procedure and its effects and individual mechanics, it is necessary to investigate the interaction between bubbles as well as their interaction with the induced wake turbulence. Special value has to be placed on characteristic variables like the bubble size, gas volume fraction and liquid agitation and their influence on the mass transport from the bubbles in the surrounding fluid.

The introduced turbulence generating grids, were used to perform experiments to gain further insight in the movement and behavior of individual bubbles in a swarm. As a comparison and reference, free rising bubbles have been studied. This allows for a correlation between the bubble shape, the wake's shape and the overall flow structures to be made. In the following, the experimental setup is outlined with an explanation of the camera setup and a detailed description of the evaluation and reconstruction.

5.1 Experimental Setup

The oscillation and 3D shape were measured with a four-camera tomographic setup. With the algorithm, that is described in the following the volume and surface of bubbles can be accurately measured and are evaluated here. For the free rising case two bubble sizes, ranging from $d_B = 4$ and 4.5 mm with several individual bubbles are recorded and evaluated. For the bubbles in the turbulent background. Bubbles between $d_B = 2$ and 7 mm were recorded and reconstructed.

To understand the motion of the bubble and how it is influenced by the grid, both the path of the bubble and the grid needs to be reconstructed. To record the movement of the bubbles in the turbulence the 3D path was recorded with a stereoscopic two camera setup. Different bubble sizes, one smaller than the grid element one in the size of the grid element and one bigger were released in the counter-flow and recorded until the bubbles move either out of the camera view or get transported into the channel wall boundary layers. Thus between 1000 and 6000 images were recorded, which correlates to a recording times between $t = 1$ and 15 s that the bubble moves in the turbulence. To binarize the images a simple threshold could be used due to the homogeneous background lighting. For the grid elements an additional circle finder was used to determine the position, since at times the spheres overlap and thus a threshold is not sufficient anymore. From the binarized images of both cameras the position of the bubbles as well as the lowest grid elements are triangulated. From

which the 3D position of the bubble relative to the grid can be determined. In Fig. 9 an example of the evaluation result is shown.

To measure the time dependent wake structures and shape oscillations, a four-camera setup was used, in addition to the background LEDs a green laser with a wavelength of 532 nm excited fluorescent (~566 nm) rhodamine PIV tracer particles. These particles prevent a strong reflection of the laser light from the bubble shines on the camera. Due to the different refractive index of the water and the air in the bubble, the laser gets strongly diffused and the cameras would record a bright glare. With corresponding filters on the cameras, the green laser light is filtered so only the
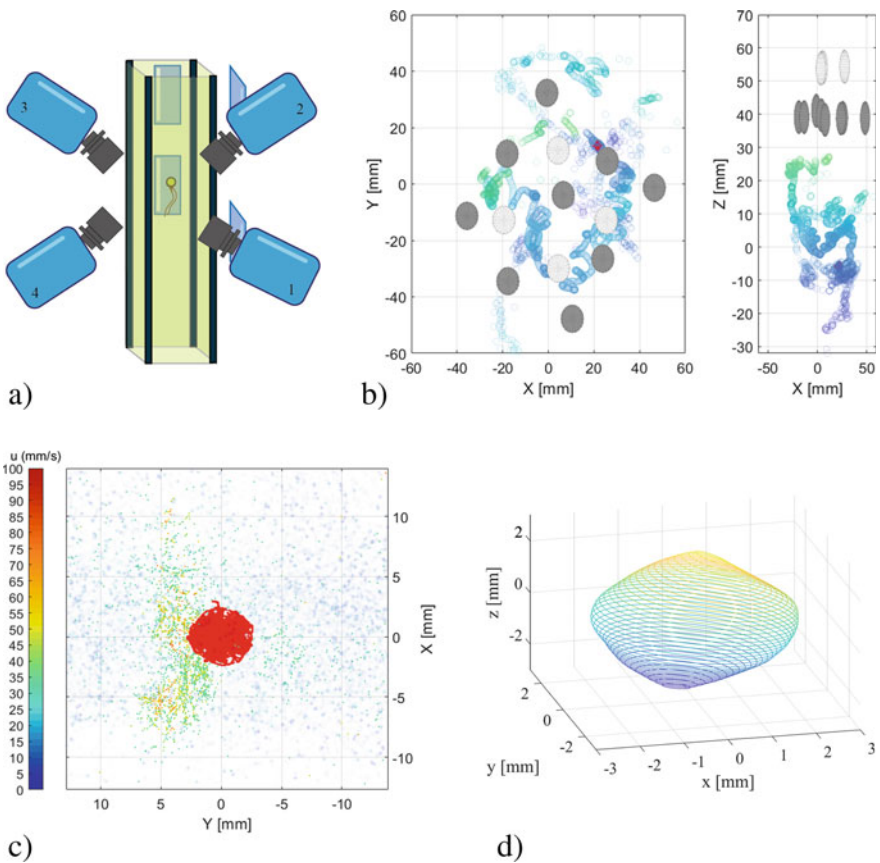
Fig. 9 **a** Schematic representation of the camera setup with controlled background lighting. White LEDs are used as backlight for better contrast in the shadows. **b** Example of a path and sphere position evaluation. Both the position of the 2 lowest grid layers as well as the bubble path is reconstructed. The path of the bubble over the whole measurement is printed in blue. The coloring denotes the distance to the grid. The red marker shows the current position in relation to the grid. **c** Timestep of a reconstructed Bubble (red) in the surrounding fluid, indicated by the particle tracks. The color of the particles indicates the velocity. **d** Example reconstruction. Each line represents one fit in the z plane. The color only visualizes the heights to make it easier to see the shape

fluorescent rhodamine B is visible to the cameras. To simultaneously record the shape and the wake structures the particle images and the shadow images were separated by a phase shift. The setup was triggered that alternatingly one image of the particles and one image of the shadow images were recorded. A rather big measurement volume ($3 \times 3 \times 3$ mm^3) was chosen, because the bubble position varies over the channel cross section.

For the bubble shapes, a novel 3D reconstruction method was introduced that allows describing bigger bubbles as long as they don't show concave surface elements. The 3D-surface of the bubble was reconstructed based on the shadow images of four high speed cameras with a MLOS algorithm [21], as it is implemented in the commercial software DaVis. The algorithm needs binarized images to calculate the 3D shape. The images were only processed by removing a background image followed by a binarization with a threshold. Those images are then unfolded by the MLOS algorithm parallel to the calibration plate in different distances for every camera. The images are then multiplied with each other and the remaining image represent the slice of the bubble in a certain distance to the calibration plate. In this case the calibration plate was placed horizontally in the middle of the measurement volume. So, the algorithm calculates the bubble shape in a certain xy-plane (parallel to the calibration plate) with a certain z value (distance to the to the calibration plate) and stacks them on top of each other. This can be imagined as the bubbles are built up stack wise from pole to pole. With a Matlab-Code, splines were fitted to the data of each slice to measure the shape and finally calculate the surface area. In Fig. 9d an example of a reconstructed bubble is shown. Each ring represents one reconstructed z-plane. For a better visualization only, a few rings are plotted. Due to the camera arrangement the pole areas of the bubble still show artifacts. These could be removed by adding additional cameras.

To estimate the error introduced by the 3D reconstruction first the error that are made with the 2D approach shall be discussed. To simplify the first case a perfect circle or sphere is assumed. In various publications e.g. [22] the volume or shape of the bubble was estimated from two 2D images. This can be visualized similar to the here described algorithm, just with 2 cameras, from the first image a cut through the bubble is made, that is then projected in the second image. From the length of both lines a bounding box can be made. With a circular fit in this bounding box, the bubble is then similarly stacked up. Is the bubble or the bubble slice a perfect circles the fit yields an errorless result. However, to make an accurate allocation between the two images, the bubble images in both cameras need to have the same resolution to have a nearly identical number of pixels rows, otherwise a unknown error is introduced. In addition, this approach has another disadvantage. The correct bubble form can only be reconstructed, when the bubble is rising perpendicular to the camera planes, if it is tilted or angled to the camera the 2D approach reconstructs a false image. This is easily avoided with the 3D reconstruction.

The error can be estimated with some assumptions, first, that the calibration is without error, the bubble is perfectly circular or spherical.

Is the approach taken by [22] an error of roughly 27% can be estimated. This was calculated by comparing the volume that the intersection of two Line-of-sight

cylinders are encasing and the real volume of a sphere. If the estimation is done in a three-dimensional space the calculation gets more complicated. The analysis was done for the four-camera reconstruction. The reconstruction was simulated with a perfect sphere. By comparing the two volumes an error of 11% was calculated.

Since real bubbles are not perfectly spherical but rather elliptical, the error is smaller, since the circle is the extreme form of the ellipses. But then again, the errors that are made by the mask, the calibration and the reconstruction add up to the final error. Like stated above the error made with the mask can be neglected or be estimated to be less than 1%. The error of the calibration or rms value of the calibration can be recursively improved to a value below 0.01, so also below 1%. Thus, the biggest error that is made is a systematical error by the nature of the reconstruction. However, with the 3D reconstruction bubble shapes can be reconstructed that would otherwise with the 2D approach not be possible or only if the bubble is oriented correctly.

6 Movement in Emulated Turbulence

At first the bubbles are slowly rising towards the grids. After reaching the right distance to the grids was the desired turbulence level exists the bubbles are slowed down by the counter flow. It is noticeable that the bubbles still follow their original path pattern, even though it is sometimes contracted in z-direction, so that the distance between the spirals gets shorter until they experience a certain turbulence level. With a certain threshold of background turbulence, the bubbles start either to contract their path even further in z-direction or the bubble starts to be moved by the surrounding turbulence, rather than its own motion. In some cases, the bubble even got moved downwards out of the measurement region again. It can be seen that there is a threshold around 15% that the bubbles are influenced and it is assumed that depending on the size a different threshold is necessary, but the range seems to be narrower than what can be resolved in this measurement.

If the bubble now moves in the emulated turbulence the bubbles have a higher probability to stay in regions with low turbulence/high velocity such as between the grid elements (Fig. 9). Between the particle's higher velocity fluctuations, both in flow direction and perpendicular to it, are present. This can be seen in the p.d.f.s in Fig. 6. Depending on their initial position the bubbles move to the nearest position between the spheres or regions with high turbulence. When they pass underneath a sphere, they get accelerated towards the grid elements due to the slow wake behind a sphere. The spheres however are also moving. The lowest element can describe a circular motion and depending on the density of the grid the amplitude of that circle's changes. For the low-density grids, the amplitude can be up to two particle diameters. It should be noted, that it takes some time for the wake to get transported from the grid element to the bubble. Usually the bubbles are about three sphere diameters downstream and with a velocity of 200–250 mm/s the fluctuations need 0.1–0.12 s to reach the bubble. With a recording rate of 600 frames per second the grid position 60–72 frames in the past needs to be used to compare the bubble and

the grid position. Thus, in the images shown in Fig. 9 the bubble position and the grid position 75 frames in the past is shown.

The bubbles tend to stay longer at position in between the grid elements and move depending on their size only small distances. This can be explained by the velocity gradient that is induced by the slower wakes behind the grid elements. This velocity gradient in return creates pressure gradient that can be understood by taking into account that the dynamic pressure is proportional to the square of the velocity. In the measurements it is shown that small bubbles (d_B < sphere element) tend to follow this well. On the contrary, big bubbles are more deformable and experience a wider pressure gradient over the whole bubble volume and cannot settle in the small low-pressure regions between the grid particles like the small ones. The bubbles get instead more deformed and tend to follow bigger or the stronger structure. In a real bubble swarm, a single bubble is specially restricted by the swarm, this stabilizes the path the bubble can take and is thus forced to rise in a confined space. When moving in a turbulent fluid by itself, the bubble seems to take the path of lowest turbulence and is not confined by the swarm, which results in a more random nature of the path movement.

From the Navier-Stoks-Equation, dimensionless numbers and forces can be derived, and used to estimate the effects that are dominant in this flow structure.

$$\rho \left(u \frac{\partial u}{\partial x} + v \frac{\partial u}{\partial y} + w \frac{\partial u}{\partial z} \right) = -\frac{\partial p}{\partial x} + \eta \left(\frac{\partial^2 u}{\partial x^2} + \frac{\partial^2 u}{\partial y^2} + \frac{\partial^2 u}{\partial z^2} \right) \qquad (1)$$

By introducing characteristic length scales, the Navier-Stokes-Equation can be used to calculate dimensionless numbers to estimate the forces that apply in the current system. For this case three characteristic length are introduced, the distance between the spheres a_K, the bubble diameter d_B and the bubble rising velocity u_b. With the three forces that results from pressure gradients F_D [N/m^3], the force that is introduced by the inertia of the bubble F_T and the one from friction effects F_R can be estimated.

$$\rho \cdot \rho_c \frac{u_C^2}{l_C} \left(u \frac{\partial u}{\partial x} + v \frac{\partial u}{\partial y} + w \frac{\partial u}{\partial z} \right) = -\frac{p_C}{l_C} \frac{\partial p}{\partial x} + \eta \frac{u_C}{l_C^2} \left(\frac{\partial^2 u}{\partial x^2} + \frac{\partial^2 u}{\partial y^2} + \frac{\partial^2 u}{\partial z^2} \right) \quad (2)$$

In this case for the individual terms the following data can be used for the critical values:l_C is the distance between the spheres, u_C the rising velocity of the bubble u_p. ρ is again the density, v the velocity of the liquid, a the mean distance between the grid elements, d the diameter of the bubble, μ the viscosity and finally u the effective rising velocity of the bubble $(u_{\text{bulk}} - u_{\text{rising}})$. Δ_V is the velocity difference between the free stream between the elements and the wake right under a sphere element. As written in the above equations, normally the pressure gradient is used to calculate F_D, but since the pressure can't be measured in this system, the mean pressure was roughly approximated with the Bernoulli equation and the velocity. The subscript L denotes that the property of the liquid is used, while B the properties from the bubble. This leads to the following approximations for the forces present in this system:

Table 2 Comparison of the different estimated forces resulting from the pressure F_D the inertia F_T and the friction F_R. Listed are different grid compositions. The data is calculated for a 5 mm bubble and 3 sphere diameters behind the grids

Gridelement	d_k [mm]	α_k [%]	F_D [N/m³]	F_T [N/m³]	F_R [N/m³]
Sphere	10	10	2.3	0.24	1.26
Sphere	10	05	2.5	0.24	1.26
Sphere	05	10	30.01	0.24	1.26
Ellipses	05	03	5	0.24	1.26
Ellipses	10	10	38.61	0.24	1.26

$$F_D = \frac{1}{2} \cdot \rho_L \cdot \frac{\Delta v^2}{a_K} \quad F_T = \rho_B \cdot \frac{u_B^2}{d_B} \quad F_R = \mu_L \cdot \frac{u_B}{a_k^2} \tag{3}$$

For five grids, three spheres and two elliptical grids, those forces were approximated. The specifications are listed in Table 2 with the corresponding results. The inertia force is dependent on the bubble diameter, thus Table 2 is calculated with a 5 mm diameter.

As can be seen in Table 2 the forces introduced by the pressure are a factor 10 higher in comparison to the inertia forces. To note is, that the friction force cannot be compared directly, since its calculated with both parameters from the liquid and the bubbles. Thus, only the pressure force and the inertia force are compared. Since the inertia force is dependent on the bubble diameter, a critical diameter can be calculated when the bubble is no longer affected by the pressure introduced from the grids. This critical diameter of bubbles would be around 50 mm bubble diameter. However, these bubbles will not be evaluated in this work, since they are five times bigger then then bubbles usually used in industrial applications and are redacted from this work. For comparison a graph for the here relevant bubble diameters is shown. Furthermore, bubbles with sizes bigger then 7–8 mm start to deform and the pressure gradient does not result in a path shift anymore, but in a deformation of the bubble. For the other grids even, higher diameters would be needed which is not feasible anymore. Thus, concluding, that the motion effects are mainly due to pressure and velocity gradients introduced, by the grid elements.

In the literature various different publications explain the oscillation of free rising bubbles and describe their behavior [15, 23, 24]. But to the authors knowledge the behavior in turbulent background was not reported before. Thanks to the 3D reconstruction, it is possible to investigate the surface-to-volume ratio in order to gain a better understanding of the complexity of the 3D deformation. Figure 10a shows the surface-to-volume ratio calculated from the 3D measurement. Two dominant frequencies can be clearly seen in the measured data, called f_R and f_S. f_R describes the frequency of the superimposed oscillation (mean value of the individual frequencies), and f_S the frequency of the envelope. With a spectral analysis the two frequencies or rather a range for those frequencies can be determined. By considering the specific frequencies of the bubble deformation modes that describe the lateral
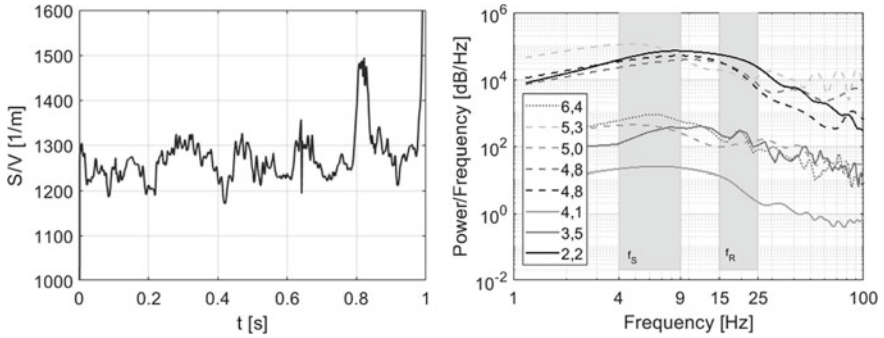
Fig. 10 Example of the surface-to-volume ratio with time. The two frequencies are calculated from this with the welch method. The evaluation for different bubble diameters is shown in the right image. The most common frequency range is marked with grey boxes

$f_{2.0}$ and axial deformation $f_{2.2}$ oscillations, we can write $f_R = (f_{2.0} + f_{2.2})/2$ and $f_S = |f_{2.0} - f_{2.2}|/2$. A summary of all frequencies for the measured bubble diameters is given in Table 4 and a comparison of the spectral analysis in Fig. 10b.

6.1 Deformation of the Surface

Before the bubbles in the turbulent background flow are studied, free rising bubbles are discussed. The shape of a free rising bubble can fluctuate in response to oscillations in the pressure field in the liquid surrounding the bubble. The intermittent vortex shedding associated with the lateral motion of bubbles, see, e.g., [23], will cause regular fluctuations in the velocity and therefore in the pressure field around the bubble. In their review on bubble wakes, [24] refer to several instances where the shape of (mainly large) bubbles was observed to oscillate at the frequency of the lateral motion. It is evident that the fluctuating shape of the bubble is a result of the turbulent shear and pressure forces of the surrounding liquid. In addition to that, the coupled vortex shedding behind rising bubbles leads to lateral motion of the bubbles, inducing drag and lift forces on the bubbles. The oscillations frequencies for small bubbles with a diameter up to 2–5 mm is well reported in the literature, but the deformation dynamics of larger bubbles is less well documented, see [15] or [23]. Bubbles with a larger diameter become unstable and start to deform in such a manner that it is more difficult to measure or simulate their dynamics and surface motion. To describe the oscillations in general, two different modes are discussed in the literature: the oscillations in the equivalent major axis e, named mode 2.0 and of that in the axes ratio R, as mode 2.2. In [15], a simple model is described linking the shape oscillations to capillary waves traveling on the bubble surface. The 2.0 waves are moving from the front to the rear stagnation points (from pole the pole), and mode 2.2 waves are traveling around the equator of the bubbles. It is further described in

[15] that the modes correlate with the bubble volume and deformation. It is also noted that the 2.0 mode has a strong correlation with the motion of the bubble itself. The 2.2 mode however does not show any relation to the bubble motion. The frequencies of the oscillations can be formulated in terms of the spherical equivalent diameter and the ellipticity ϵ. In this formula σ the surface tension, and ρ the density of the liquid. The mode 2.0 and 2.2 frequencies can be calculated according to [15] as follows:

$$f_{2.0} = 1/2\pi \sqrt{\frac{16\sqrt{2}\epsilon^2\sigma}{\rho_L(\epsilon^2+1)^{3/2}r_\epsilon^3}} \quad f_{2.2} = 1/2\pi \sqrt{\frac{8\sigma}{\rho_L\epsilon r_\epsilon^3}} \tag{4}$$

With the introduced 3D reconstruction technique, the oscillation behavior was studied in more detail. With both approaches (2D and 3D) different sizes are evaluated and presented in Table 1. The 2D measurement shows values in the range that are also reported by [15]. Unlike Perkins, that used the Fourier descriptors in this evaluation an ellipse was fitted around the bubble to measure the two frequencies $f_{2.0}$ and $f_{2.2}$. With a spectral analysis the modes where then extracted from the signal. In this data as well the two dominating frequencies of the deformation dynamics a low one with f_S, and a high one with f_R were calculated in good agreement with the literature data. These are written in Table 2. It is easy to see that the 2D evaluation yields the same results as the literature values. The small discrepancies arise from the different qualities of the water that were used. As stated before, surfactants show a significant influence on the behavior. Even small amounts of surfactants influence the behavior of the bubble greatly [14]. But nevertheless, all values are in good agreement.

On the contrast however from the 3D data the frequencies f_R and f_S are measured. From the spectral analysis of the surface-to-volume ratio the frequencies can be identified. With the following correlation the two sets can be calculated into each other: $f_R = (f_{2.0} + f_{2.2})/2$ and $f_S = |f_{2.0} - f_{2.2}|/2$. Since the bubble was only a short time in the measurement volume the recorded signal is not long enough for a reliable Fourier transformation. Thus, three bubbles with a similar radius were evaluated and a mean range for the frequencies calculated. Again, the data is written in Table 3. Here the oscillation frequencies are increased by almost a factor of three, from the expected ones and the one yielded by the 2D data. This can especially be seen in the measurement with 4 mm bubbles that are moving freely. This clearly shows that even for smaller bubbles a 2D evaluation is not sufficient to fully describe the shape oscillations with the simple approach of 2D elliptical fitting. The 3D method clearly indicates that the two modes $f_{2.0}$ and $f_{2.2}$ superimpose on each other and create a complex oscillating motion and thus the resulting frequencies vary in the 3D and 2D approach.

Similar to the evaluation for the free rising bubble the bubbles in the emulated turbulence are evaluated with both the 2D and 3D approach. As can be seen in Table 4 all four frequencies are in a similar range if the data is valuated in a 2D manner. The data shows that all bubbles no matter the size are oscillating in the same frequency range. This would suggest that the native bubble oscillation is overwritten by the turbulence. If the bubbles are however evaluated with the 3D approach a different

Table 3 Comparison of the different frequencies from the reconstruction (exp.), and theoretical calculation taken from literature [23]

D_{eq} (mm)	$f_{2.0}$ (Hz)	$f_{2.2}$ (Hz)	f_R (Hz)	f_S (Hz)
Literature/theoretical				
4.0	14	28		
5.0	28	20		
Experimental 2D				
4.0	37–47	24–34	30–40	~6
4.5	20–30	18–28	19–29	~1
Experimental 3D				
4.0	108–128	~72	90–100	18–28
4.5	98–118	~68	83–93	15–25

Table 4 Comparison of the different frequencies from the reconstruction (exp.), and theoretical calculation taken from literature. For the first literature/theoretical values f_R and f_S are calculated from $f_{2.0}$, $f_{2.2}$. From the experimental data f_R and f_S are measured and from those values $f_{2.0}$ and $f_{2.2}$ are derived

D_{eq} (mm)	$f_{2.0}$ (Hz)	$f_{2.2}$ (Hz)	f_R (Hz)	f_S (Hz)
Literature/theoretical	4.0	41	28	34.5
	5.0	29	20	24.5
Experimental 2D				
2.2 with	15–25	16–26	15.5–25.5	~ 0.5
3.5 with	17–27	19.27–29.75	18.37–28.37	~ 1.37
4.1 with	14–24	14–24	14–24	–
5.0 with	17–27	15–25	16–26	~0.5
5.3 with	17.5–27.5	17–27	17–25–27.25	~0.25
6.5 with	17–28	19.5–29.5	18.75–28.75	~0.875
Experimental 3D				
2.2 with	44–58	28–34	36–46	8–12
3.5 with	46.5–64	34.5–36	40–50	6.5–14
3.5 with	46.5–75	33.5–45	40–60	6.5–15
4.1 with	33–38	23–29	28–38	5–9
5.0 with	23–37	17–23	20–30	3–7
5.3 with	13–23	10–16	13–23	3–7
6.5 with	–	–	–	–

picture can be seen. The superimposed turbulence seems to hinder the eigenfrequency of the bubble oscillation and forces a slower shape oscillation on the bubble. But as know from the literature a decrease in the oscillation frequency is visible again.

Even for smaller bubbles the influence is significant. The oscillation frequencies are almost reduced by a factor 3, even greater for bubbles with a higher diameter. For smaller bubbles the turbulence length scales are in the range of the bubble size and the turbulent fluctuations lead more to a change in the path then in the deformation. This is further suggested by the fact, that, as was shown in the previous section, smaller bubbles are more prone to be displaced by the fluctuations then bigger bubbles, that get more deformed and hence the oscillation changes. Here the fluctuations are not big enough to cause a displacement of the bubble but rather deform the surface which in return causes the bubble to change their oscillation frequencies. For the biggest bubble this frequency also seems to merge at 3–7 Hz, suggesting that for even bigger bubbles this behavior becomes quite chaotic and cannot be truthfully reconstructed since it shows concave parts or the bubble oscillation is fully random or that no oscillation takes place anymore. As can be seen for the 6 mm bubble. This is also be shown in the 2D evaluation for the free rising bubble that the two frequencies merge for higher bubbles and the oscillation is not describable any longer.

6.2 Influence of the Turbulence on the Bubbles Wake Structures

The bubble wakes can be visualized with the aid of a chemical tracer. The oxygen in the bubbles is bound to the iron complex in the fluid and thus darkens the water. Further information about the system can be found in [25]. The wake can then be easily be recorded on the shadow images. From the time resolved data it could be shown, that while a bubble is rising, the wakes develop depending on the position of the bubble in the path. Is the bubble rising the wakes start to grow, while in the turning points however the feet of the wake close, the bubble turns and the closed structures stay stationary while the bubble is rising again and the wake starts to form again. In some of the images, especially in the first few spiraling turns, Crow instability can be seen. These instabilities dissolve the wake tails of the bubbles in the signature sinus wave structures. They occur when small disturbances happen in the system, just like the closing of the vortex pairs. In addition, the separated and close structures stay stationary for roughly 20 bubble diameters before they diffuse. This shows that the chemical tracer is only trapped in the inner most regions and does not span over the whole vortex. The MLOS reconstruction was again used to create 3D images of the rising bubble and its wake structures. From a spatial temporal reconstruction, the overall shape and size of the bubble wakes can be estimated. In addition, the seeding density is rather low and thus also the density of the measurement points. However, the shape and size of the wakes can be estimated to be roughly in the size of 2 bubble diameters, one wake vortices span the size of one bubble diameter.

In comparison to the description of free rising bubbles, the wake structures in turbulent flows are not well understood. The interaction of the surrounding turbulence with the wake is highly dependent on the local flow field. In addition, the bubble itself gets moved and deformed in the flow thus making an explicit description complicated. Some aspects can however be described with the data form the tomographic 3D reconstruction. First the wake is noticeably shorter and gets diffused only a few bubble diameters behind the bubble. While in a free rising case, it is recorded that the bubble wake takes up to 20 bubble diameters, it can be seen in the 3D flow that wake is noticeably shorten. For comparison a spatial temporal reconstruction of both a free rising and a wake behind a bubble in the emulated turbulent flow is shown. For the spatial temporal reconstruction, the displacement was chosen to create a bubble fixed origin point. In the free rising case, the flow particles were displaced with the rising velocity of the bubble. In the turbulent case the velocity difference between the bubble and the flow was chosen as the displacement factor. This allows the comparison between the two cases for a bubble fixed coordinate system.

The wake in noticeably shortened in comparison to a bubble the same size rising freely in stagnant water. The structures behind free rising bubbles are persistent for more than 20 bubble diameters (depending on the size and the path). The wakes in the emulated truculence dissipates after roughly 8 bubble diameters. Then the wake gets diffused and some parts are transported downstream. To identify the particles that belong to the wakes a velocity threshold is applied. For the free rising bubble, the threshold of 30 mm/s and for the turbulent case the threshold was chosen to 13 cm/s. The wake of the free rising bubble starts to decay roughly 23 bubble diameters downstream, however the full wake was not recorded, suggesting it be even longer, in addition, the width of the wake on the order of the bubble size. To note here is that the wake also follows a spiraling or zigzagging motion like the bubble. To reconstruct this pattern a position of the bubble for the whole measurement would need to be known, however the bubble was in the measurement volume only for a short time. If the bubble path would be known for the whole time it could be fully reconstructed. Thus, for this evaluation the main focus was placed on the decay behavior. Even though the bubbles are rising with a mean velocity of about 25 cm/s the flow behind the bubble is in the mean of $v = 5$ cm/s. While directly under the bubble the flow could not be measured due to the shadowing of the bubble but close to the bubble the flow accelerates the same velocity as the bubble. But the velocity reduces quickly.

In the turbulent case, the bubble and flow position are adjusted to the effective flow that the bubble experiences. The bubbles are heavily influenced by the turbulent flow and the wake cannot develop nor can the bubble follow its path, thus making it impossible for defined structures to develop. Thus, the main structures are accumulated up to 7–8 bubble diameters behind the bubble. In addition to it some smaller structures do still persist downstream that got picked up by the flow and transported away from the bubble. The width of the wake is also wider than the free rising case. In this instance the wake structure is roughly double the size of the bubble. However, it can be seen that the flow's velocity, behind the bubbles is reduced by roughly 50% in comparison the surrounding flow. The mean flow of the liquid is set to $v = 0.225$ m/s the measured flow velocity behind the bubble's wakes measured to $v =$

0.13 m/s. With this it can be seen that the turbulence for the most part is dominating the behavior of the bubble and the wake.

6.3 Conclusion

In order to study the flow behavior of individual bubbles in a bubble swarm, this work presented not only a method to simultaneously record the flow field around a bubble, but also correlate it with the shape of the bubble. The shape is reconstructed from the shadow images thus not influencing the surface with tracer particles or other markers. With the tomographic camera setup, it was possible to record a three-dimensional flow around the bubble shape as well as influence on the shape by the turbulence.

In conclusion it can be said that the behavior of the bubble is largely dictated by the turbulence and the fluctuations in the liquid. The first aspect that was looked at was the path. It was shown that the bubble path is mainly driven by the pressure gradients induced by the velocity gradients that are created by the moving particle grids. The bubbles are pushed by the Bernoulli-Effect to regions with lower turbulence levels and higher velocity. In comparison to real bubble swarms the bubble is here not hindered by other bubbles and can freely rise over the whole channel width. In real bubble swarm this behavior is restricted by the swam itself. While the small bubbles tend to stay in the low-pressure regions the bigger bubbles experience a gradient over the whole volume and can't settle in the turbulent field created by this particular type of grid.

Secondly the shape oscillations are measured in the also for bubbles moving in the turbulent field. Here it's clearly shown that a 2D evaluation is not suitable anymore for any kind of bubble size. The 2D evaluation shows that the turbulence is influencing the bubble oscillation but it rather suggests that the oscillation gets overwritten by the turbulence fluctuations. In contrast the 3D evaluation gets more insight with the surface to volume ration that reveals that the bubbles still have some degree of dependence on the size even though the eigenfrequencies are hindered by the turbulent fluctuations up to a factor of 3. It also again gets clearly shown that there is similar to the free rising ones that a critical diameter exists after that the bubble oscillation is becoming chaotic and the two frequencies are not sufficient anymore to describe that behavior.

Is the bubble freely raising the wake or rather the pressure gradients induced by it determine the movement of the bubble. In a turbulent flow the wake gets diffused shortly behind the bubble and the structures induced by the bubble are accumulated behind it. Thus, making it impossible for the wake to form and the movement and the wakes are fully determined by the emulated fluctuations.

7 Conclusions and Outlook

To improve on industrial multiphase applications, it is important to understand, the complex interaction between bubbles in a swarm and in order to do that many questions still need to be answered that are important to evaluate industrial application. Especially experimental models and measurement techniques are important to better understand how the mechanism in a bubble swarm in intertwine and interact with each other. Thus, this work focuses on experimental methods that allow studying swarms and the behavior of individual bubbles in it. In order to that in the beginning three questions were asked.

- What is a good experimental model to describe swarm like turbulence?
- How can a swarm be emulated and induced in a flow?
- How does it need to be characterized, to compare to real bubble agitations?

To answer these questions a new counter flow channel was designed to emulate bubble swarms. With the optical access from all four sides it is possible to utilize a variety of measurement techniques. The turbulence is induced by letting the water flow through specially designed grids. These free moving particle grids consist of small plastic spheres or ellipsoids are connected with a loose string. This allows the sphere strings to almost move freely in the counter flow. From 2D flow field measurements, done with planar PIV different size and volume fraction combinations were characterized in regards to turbulence level, homogeneity, probability density functions and energy spectra. Last was done by at the University of Bremen. From these the best agreement with real statistics was found to be from grids with 10 mm spheres and a volume fraction of 10% and a grid with elliptical elements and a volume fraction of ~ 4%. With these grids it was a goal to evaluate the behavior of single bubbles in swarm like turbulence. This allows to measure bubbles as if they were moving in a real bubble swarm. Within this chapter a comparison of the behavior and different aspects of the bubble motion with and without an external fluctuation was shown and discussed. With the channel and model swarm in place the bubbles need to be evaluated. For this further question arose:

- How can a single bubble be measured without intrusive techniques?
- How can a single bubble be accurately described and the surface be reconstructed?
- Can the flow around the bubble be measured simultaneously and how are they affecting each other?

One aspect, that is especially important for the mass transport is the bubble's surface and the three-dimensional shape changes. To measure the shape and its oscillations a new technique was developed that allows to reconstruct the bubble surface from shadow images. This has the advantages that no tracer or other marker needs to be placed on the bubble and thus influencing the physical aspects like the surface tension. It does however not allow for a reconstruction of convex surfaces. Thus this method can only reconstruct bubbles reliably up to a size of 6 mm. With this method

it is now possible to studied not only free rising bubbles but also bubbles moving in this emulated turbulence, which proposes new questions:

- How do bubbles behave in this emulated swarm turbulence compared to free rising bubbles?
- What is the difference compared to a free rising bubble?

With this technique free rising bubbles and bubbles moving in emulated turbulence are compared to each other. Different behaviors are investigated, like the bubble path, the bubble shape and its deformation with time and the wake structures. To create a basis for comparison and validation of the measurement technique free rising bubbles of different sizes were recorded. Those showed the well-known different path oscillation and deformations. In current publications the deformation was mainly evaluated from 2D data, which is correct for small bubbles. For bigger bubbles however it is important to evaluate the 3D shapes, since different modes start to deform the bubbles in a complex manor. Thus, this work used the surface-to-volume ratio was studied the deformation behavior and showed that the two frequencies, in literature named as the $f_{2.0}$ and $f_{2.2}$ start to overlap. These can then be described as a beat of the two frequencies and they can be measured from the surface to volume ratio. The two new frequencies are named in this work as f_R and f_S. Thus this work suggests that for small bubbles up to a range of 4 mm the 2D evaluation with $f_{2.0}$ and $f_{2.2}$ is sufficient, but for bigger bubbles the 3D effects need to be taken into account and instead the deformation is described with f_R and f_S.

If the bubbles are now moving in the emulated turbulence, the first thing that is notable that the bubbles move in between the grid elements. The bubbles get pushed by the pressure gradients induced by the strong velocity gradients due to the grid elements. The main forces that drive this process can be estimated with the Bernoulli and Navier–Stokes-Equation. This shows that the main driving force is the pressure difference. By adding seeding particles into the flow, the wake structures behind the bubble can be visualized and reconstructed. In comparison to freely rising bubbles the wakes are shortly after diffused by induced turbulence. While the wakes of free rising bubbles persist up to 10 bubble diameter the wake structures are diffused in roughly 2–3 bubble diameters. While the wake structures behind free rising bubbles are dependent on the path motion, like zigzagging or spiraling, the wake structures in the flow structures are similar in strength but accumulate behind the bubble which stretches the width and the wakes are quickly diffused.

References

1. Deckwer WD (1985) Reaktionstechnik in Blasensäulen. Salle

2. Kähler CJ, Scharnowski S, Cierpka C (2012) On the resolution limit of digital particle image velocimetry. Exp Fluids 52:1629–1639
3. Risso F (2011) Theoretical model for k-3 spectra in dispersed multiphase flows. Phys Fluids 23:011701
4. Riboux G, Legendre D, Risso F (2013) A model of bubble-induced turbulence based on large-scale wake interactions. J Fluid Mech 719:362–387
5. Mießner U, Kück UD, Haase K, Kähler CJ, Fritsching U, Thoming J (2017) Experimental assessment of an innovative device to mimic bubble swarm turbulence. Chem Eng Technol 40:1466–1474
6. Haase K, Kück UD, Thoming J, Kähler CJ (2017) Emulation of bubble-induced turbulence using randomly moving particles in a grid structure. Chem Eng Technol 40:1502–1511
7. Risso F, Ellingsen K (2002) Velocity fluctuations in a homogeneous dilute dispersion of high-Reynoldsnumber rising bubbles. J Fluid Mech 453:395–410
8. Riboux G, Risso F, Legendre D (2009) Experimental characterization of the agitation generated by bubbles rising at high Reynolds number. J Fluid Mech 643:509
9. Martinez J, Chehata D, van Gils DPM, Sun C, Lohse D (2009) On bubble clustering and energy spectra in pseudo-turbulence. J Fluid Mech:1–35
10. Liu TJ, Bankoff SG (1993) Structure of air-water bubbly flow in a vertical pipe-I. Liquid mean velocity and turbulence measurements. Int J Heat Mass Transf 36:1049–1060
11. Kim M, Lee JH, Park H (2016) Study of bubble-induced turbulence in upward laminar bubbly pipe flows measured with a two-phase particle image velocimetry. Exp Fluids 57:55
12. Risso F (2016) Physical interpretation of probability density functions of bubble-induced agitation. J Fluid Mech 809:240–263
13. Lance M, Bataille J (2006) Turbulence in the liquid phase of a uniform bubbly air–water flow. J Fluid Mech 222:95
14. Takagi S, Matsumoto Y (2011) Surfactant Effects on bubble motion and bubbly flows. Annual Rev Fluid Mech 43:615–636
15. Lunde K, Perkins RJ (1998) Shape oscillations of rising bubbles. Appl Sci Res 58:387–408
16. Hosokawa S, Tomiyama A (2013) Bubble-induced pseudo turbulence in laminar pipe flows. Int J Heat Fluid Flow 40:97–105
17. Abbas M, Climent E, Simonin O, Maxey MR (2006) Dynamics of bidisperse suspensions under Stokes flows: linear shear flow and sedimentation. Phys Fluids:121504
18. Serizawa A, Kataoka I, Michiyoshi I (1975) Turbulence structure of air-water bubbly flow-II. Local properties. Int J Multiph Flow 2:235–246
19. Pannek S, Pauli J, Onken U (1994) Determination of local hydrodynamic parameters in bubble columns by the electrodiffusion method with oxygen as depolarizer. J Appl Electrochem 24:666–669
20. Michiyoshi I, Serizawa A (1986) Turbulence in two-phase bubbly flow. Nucl Eng Des 95:253–267
21. Elsinga GE, Scarano F, Wieneke B, Van Oudheusden BW (2006) Tomographic particle image velocimetry. Exp Fluids 41:933–947
22. Brücker C (1999) Structure and dynamics of the wake of bubbles and its relevance for bubble interaction. Phys Fluids 11:1781–1796
23. De Vries AWG (2001) Path and wake of a rising bubble. Eng Fluid Dyn:106
24. Fan LS, Tsuchiya K (1990) Bubble wake dynamics in liguids and liquid-solid. Butterworth-Heinemann, Stoneham
25. Aas BM, Klüfers P (2017) The structural chemistry of stable high-spin nitrosyl–iron(II) compounds with aminecarboxylato co-ligands in aqueous solution. Eur J Inorg Chem 2017:2313–2320

Experimental Studies on the Hydrodynamics, Mass Transfer and Reaction in Bubble Swarms with Ultrafast X-ray Tomography and Local Probes

Ragna Kipping, Holger Kryk, and Uwe Hampel

Abstract The main focus of this project was the experimental investigation of hydro-dynamics and mass transfer characteristics together with a chemical reaction in a bubble column at higher gas holdup. Experiments were performed for chemical absorption of CO_2 in alkaline solution of different pH, at homogenous bubbly flow conditions and up to 17% gas holdup. Ultrafast electron beam X-ray tomography (UFXCT) has been used to obtain local gas holdup data and bubble characteristics and a wire-mesh sensor was used to measure species concentration fields in the liquid bulk. In addition, experiments with the reaction of NO and $Fe^{II}(edta)$ were carried out and a new fiber optical probe was employed for local measurement of product concentration in the bubble wake.

Experimental data is available at the RODARE Open Data Link (reference "DFG SPP1740") [1]

1 Introduction

Bubble columns are a widely used reactor type for gas–liquid reactions, such as e. g. oxidation and hydrogenation, in the chemical industries. To optimize industrial reaction processes with respect to yield and selectivity in such devices, adequate and accurate modeling of hydrodynamics, mass transfer and the reaction progress is needed. Numerical analysis tools developed for this purpose need experimental data for validation and with that dedicated measurement techniques for transient flow analysis. Fast and high-resolution camera-based methods, such as Shadowgraphy and Particle

R. Kipping · U. Hampel (✉)
Institut für Energietechnik, Technische Universität Dresden, 01062 Dresden, Germany
e-mail: uwe.hampel@tu-dresden.de

H. Kryk · U. Hampel
Institut für Fluiddynamik, Helmholtz-Zentrum Dresden - Rossendorf, Bautzner Landstraße 400, 01328 Dresden, Germany

Tracking Velocimetry, which are well-established in general experimental flow analysis, do fail for higher gas fractions as the two-phase system becomes more and more opaque for light. Cross-sectional imaging techniques provide a way out of this dilemma. For that, different kinds of tomographic systems exist, which provide high resolution either in space or time. Recently, ultrafast electron beam X-ray computed tomography (UFXCT) was developed at Helmholtz–Zentrum Dresden–Rossendorf, which achieves both [2–4]. It has been employed in this project. Moreover, the minimally intrusive wire-mesh sensor, a fast electrical imaging instrument for gas–liquid flow, was qualified and used for the study of chemical species conversion.

Scientific studies of chemical reactions in bubbly flows require easy to handle and well-understood reaction systems, whose educts and products are preferably nontoxic, easily disposable and affordable in larger quantities. Moreover, they should offer easy ways for quantitative in situ concentration measurement. One of such potential systems, which has been used before many times in scientific studies, is the chemical absorption of CO_2. Here, CO_2 bubbles are contacted with alkaline solution. The absorption causes bubble shrinkage, which is quantifiable with imaging tools, and reduction of the pH value of the liquid phase as an effect of chemical reaction. From the latter, reactive mass transfer rates can be determined using electrochemical measurement techniques. Experimental studies reported in the literature have so far mostly employed camera techniques and local probes [5–7]. Hence, they were limited to lower gas holdup and point-wise measurement of species concentrations. In this study, we employed novel tomographic imaging techniques to extend the existing experimental data bases towards high gas holdup and concentration field measurements. For that UFXCT was used to obtain time-averaged and transient gas phase parameters, such as gas holdup and bubble sizes. Simultaneously, transient cross-sectional concentration fields of OH^- were obtained from the wire-mesh sensor data. Furthermore, a fiber optical photometric probe was qualified to measure species concentration in the liquid bulk for the reactive system Fe^{II}(ligand)/NO, which has been developed within Priority Programme SPP 1740 (see chapter "In situ Characterizable High-Spin Nitrosyl–Iron Complexes with Controllable Reactivity in Multiphase Reaction Media)".

2 Reaction Systems Used for Experimental Investigation of Bubbly Flows

2.1 Chemical Absorption of CO_2

When carbon dioxide gas is injected into an aqueous sodium hydroxide solution it physically dissolves:

$$CO_{2(g)} \rightarrow CO_{2(aq)}. \tag{1}$$

Thereafter, sodium hydroxide dissociates into sodium and hydroxide ions:

$$NaOH \Leftrightarrow Na^+_{(aq)} + OH^-_{(aq)}. \tag{2}$$
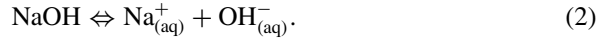
The presence of hydroxide ions increases the pH value of the solution. The physical absorption of CO_2 is followed by chemical reactions in the liquid phase. For $pH <$ 10 only a portion of CO_2 is converted into ions, whereas for $pH > 10$ carbon dioxide reacts almost immediately with the dissociated hydroxide ions to carbonate and bicarbonate ions according to:

$$CO_{2(aq)} + OH^- \Leftrightarrow HCO_3^-. \tag{3}$$

$$HCO_3^- + OH^- \Leftrightarrow CO_3^{2-} + H_2O. \tag{4}$$
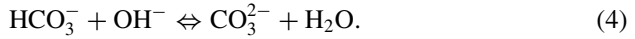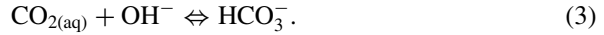
At high pH values, reaction (4) is dominant according to the pH-dependent dissociation equilibrium [8]. Due to consumption of OH^- ions the pH value of the solution changes during chemical reaction.

2.2 Reaction of FeII(ligand)/NO

One of the reaction systems, developed during SPP 1740 is the reaction of Fe^{II}(ligand)/NO. It is used, e.g. in BioDeNOx technology where NO binds to an aqueous Fe^{II}(edta) compound and is subsequently reduced in a bioreactor by bacteria [9, 10]. More details on that reaction system can be found in chapter "In Situ Characterizable High-Spin Nitrosyl–Iron Complexes with Controllable Reactivity in Multiphase Reaction Media".

The fundamental reaction of the absorption of NO in ferrous solutions follows the scheme:

$$Fe^{2+}_{(aq)} + NO_{(g)} \Leftrightarrow [Fe(NO)]^{2+}_{(aq)}. \tag{5}$$
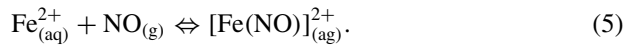
Working in an aqueous solution, water acts as a ligand and NO substitutes one aqua ligand:

$$\left[Fe(H_2O)_6\right]^{2+} + NO \Leftrightarrow \left[Fe(H_2O)_5(NO)\right]^{2+} + H_2O. \tag{6}$$
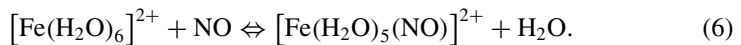
The selection of chelate ligands of the aminecarboxylato group has a strong influence on the reaction rate and the equilibrium constant as shown by Schneppensieper et al. [11]. The substitution of water by chelate ligands like edta (ethylenediaminetetraacetic acid) changes the stability constant K_{NO} significantly. Its value raises from $(1.15 \pm 0.05) \times 10^3$ L mol^{-1} to $(2.05 \pm 0.15) \times 10^6$ L mol^{-1} for the water and the edta complex, respectively.

Adding edta with its potential six metal binding sites to the aqueous ferrous solution and adding subsequently NO to the solution results in the very stable complex of $[Fe(edta)(NO)]^{2-}$:

$$\left[Fe(H_2O)_6\right]^{2+} + edta^{4-} \Leftrightarrow [Fe(edta)(H_2O)]^{2-} + 5H_2O \tag{7}$$

$$[Fe(edta)(H_2O)]^{2-} + NO \Leftrightarrow [Fe(edta)(NO)]^{2-} + H_2O \tag{8}$$
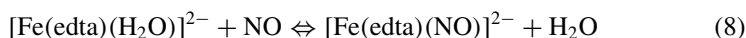
Since the resulting complex shows an intense color in aqueous solution (ε_{435nm} = 820 L mol^{-1} cm^{-1}), the reaction system allows for the visible detection of the bubble wake structure.

3   Experimental Setup and Methods

3.1   Bubble Column Setup for CO$_2$ Absorption Measurements

All experiments were run in a cylindrical bubble column with D = 100 mm inner diameter (Fig. 1). The column itself is made of acrylic glass, while all remaining parts that are in contact with the reaction medium are made of stainless steel. A
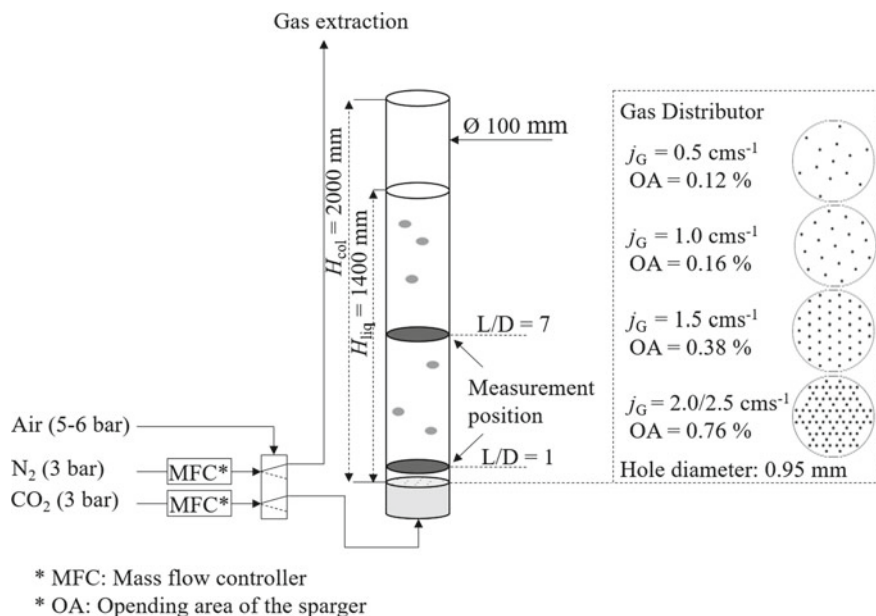
Fig. 1   Scheme of bubble column setup with specification of capillary gas distributor (right)

capillary gas distributor produces a uniform bubbly flow with a narrow bubble size distribution. A modular design of this sparger allows the use of different numbers of needles, depending on the gas flow rate. Its configurations and ranges of application are schematically depicted in Fig. 1 (right). Experiments were performed within the homogenous bubbly flow regime at gas flow rates of $j_G = 0.5 - 2.5$ cm s^{-1}, with steps of 0.5 cm s^{-1}. Chemically inert N_2 and deionized water is used for non-reactive experiments. Furthermore, mass transfer measurements were carried out for CO_2 in deionized water and sodium hydroxide solution of different concentrations. The initial pH value of the solution varied between $pH = 11.0$–12.5. The maximum pH value was limited to 12.5 in order to avoid temperature effects of the exothermic chemical absorption reaction. For each experiment, the column was prepared with fresh deionized water or sodium hydroxide solution of the desired concentration, respectively. At the beginning of each experiment, the column was flushed with nitrogen at the targeted flow rate to generate a stationary flow profile within the reactor. Experiments were performed at ambient temperature and pressure conditions. Once stable operating conditions were reached, the tomographic scans were performed in two planes located at 0.1 and 0.7 m above the sparger. Measurements close to the sparger were performed to provide data of initial bubble size and phase distribution. The second measurement height is located in the fully developed bubbly flow region, which is known to be the case at $L/D \geq 5$ for these experimental conditions [12]. Mass transfer measurements were carried out at continuous gas flow. Therefore, the gas flow was switched to CO_2 shortly after starting the data acquisition, initiating the chemical reaction. The gas supply was controlled via a pneumatically driven 5/2-way valve, which ensures gas switching without any pressure surges.

3.2 Ultrafast X-ray CT for Investigation of Bubble Column Hydrodynamics

Ultrafast X-ray computed tomography (UFXCT) is used to investigate the gas phase hydrodynamics, such as local gas holdup distribution, bubble sizes and interfacial area, in the DN100 bubble column. This section provides information about the measurement principle and a brief description of the post-processing steps.

The principle is based on the measurement of the attenuation of X-rays penetrating the bubble column. The attenuation depends on the material mixture in the imaging region and thus gives information about the gas phase distribution in the column. In contrast to medical X-ray CT systems, the measurement system used here contains no moving parts. Instead, an electron beam is focused on a tungsten target and creates a moving X-ray source that allows for fast imaging (Fig. 2). The attenuation data is recorded by a dual-plane circular detector with 2×432 detector elements. The dual plane approach allows simultaneous scans in two planes with an axial pitch of 11 mm, which enables the extraction of bubble rise velocities. The in-plane spatial resolution is about 1 mm. For more details on UFXCT see [13] and [14]. For this study, an
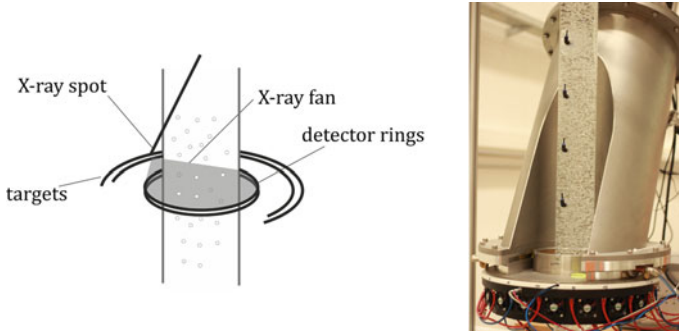
Fig. 2 Schematic of UFXCT facility (left) and photograph of the bubble column setup installed in the UFXCT scanner (right)
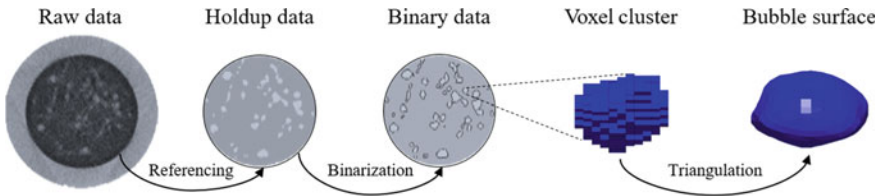
Fig. 3 Schematic of the post-processing of X-ray measurement data

image frequency of 1000 frames per second and plane is used and measurements were carried out for up to $t = 20$ s scanning time.

The basic steps of post-processing of UFXCT data are schematically depicted in Fig. 3. The measured attenuation data are reconstructed using the method of filtered back-projection. The reconstructed data sets are stacks of cross-sectional images of size 180×180 pixels with the X-ray attenuation coefficients $\mu_{i,j,k}$ as values (see Fig. 3 left). Each voxel is described by its spatial in-plane coordinates i and j, and k indicates the sampling time.

Together with attenuation coefficients of the completely filled column μ^{full} and the empty column μ^{empty}, the gas holdup ε is calculated according to Eq. (9) (referencing step in Fig. 3).

$$\varepsilon_{i,j,k} = \frac{\mu_{i,j}^{full} - \mu_{i,j,k}}{\mu_{i,j}^{full} - \mu_{i,j}^{empty}} \tag{9}$$

Based on this, a binarization and segmentation algorithm is applied, which extracts voxel clusters of single bubbles from the data stack [15]. Following, the bubble equivalent diameter $d_{B,eq}$ is computed based on the three-dimensional volume V_B of each bubble:

$$d_{B,eq} = \sqrt[3]{\frac{6}{\pi} V_B} \tag{10}$$

and bubble size distributions are computed. From the three-dimensional image stacks, also bubble surfaces are extracted and subsequently the Sauter mean diameter is computed according to

$$d_S = 6 \frac{V_B}{A_B}.$$

(11)

In that way, the computation of the Sauter diameter is independent of the shape of the bubbles and thus less uncertain. Further details on the post processing of UFXCT measurement data can be found in [16].

3.3 Wire-Mesh Sensor for Mass Transfer Measurements

The wire-mesh sensor is a minimally invasive imaging instrument based on an electrical measuring principle. Two orthogonal sets of non-contacting wire electrodes, acting as receivers and transmitters, are stretched in a matrix-like arrangement in the flow cross-section (see Fig. 4). An electronics samples electrical currents in the crossing points of this grid, which are representative for the local electrical conductivity. For e.g. gas–liquid systems one can obtain local gas holdup or the mixing of a conductivity tracer [17]. In this project, the wire-mesh sensor was employed to measure the change of concentration of CO_2 in deionized water and the local species conversion during chemical absorption of CO_2 [18].

The design of the wire-mesh sensor was optimized for this study. As the primary objective is measurement of high conductivity from the NaOH solution and not bubble parameters, we devised a design with low intrusiveness, which is depicted in Fig. 4. Based on the expected bubble size of $d = 5$ mm generated by the capillary gas sparger, the lateral wire distance was chosen as 12.5 mm, which corresponds to 2×8 wires in total. As the high conductivity of the NaOH solution may cause crosstalk between neighboring wires a large ratio of lateral and axial wire distance with 1 mm axial wire spacing was chosen. This sensor design gives 52 equally distributed crossing points in the circular cross-section and thus an in-plane spatial resolution of 6.25 mm. Measurements were carried out with a frame rate of $f =$
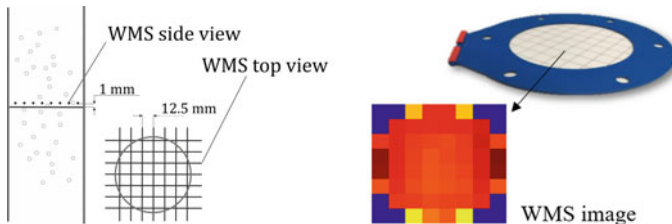
Fig. 4 Left: Geometric dimensions of the wire-mesh sensor and right: Photo of wire-mesh sensor used in this study

5000 Hz. The total scanning time was adjusted so that saturation of the liquid phase was reached.

As a wire-mesh sensor was used for the first time for such an application, new post processing steps for evaluation of measurement data had to be developed. This includes the extraction of the liquid phase signal from the data, which is done by a step-wise histogram calibration, and the extraction of mass transfer related parameters [18], which are briefly described in the following.

Based on the normalized conductivity signals of the wire-mesh sensor, the volumetric mass transfer coefficients are determined. The dissolution of CO_2 in deionized water is followed by the formation of carbonate and bicarbonate ions, which increases the conductivity of the solution. Assuming a linear dependency between the concentration of dissolved CO_2 and conductivity, the step responses of the change of CO_2 concentration in deionized water is analyzed via the following model:

$$\frac{\partial c_l}{\partial t} = \frac{k_L a}{\varepsilon_l} \left(c_l^* - c_g \right) \tag{12}$$

By fitting our experimental data to this model, the volumetric mass transfer coefficient $k_L a$ is determined in each single crossing-point. The gas holdup used for calculation of the $k_L a$ value is determined from the simultaneously measured UFXCT data. Following, with the interfacial area determined from UFXCT data, also the liquid side mass transfer coefficient k_L is evaluated.

For chemical absorption measurements of CO_2 consumption rates of OH^- are determined from WMS data in the following way. Conversion of ionic species during chemical absorption of CO_2 changes the conductivity of the liquid phase. Thereby, hydroxide ions have a significantly higher equivalent conductivity ($\Lambda_{eq,OH-}$ = 198.6 S cm^2 mol^{-1}) in comparison to carbonate ($\Lambda_{eq,CO32-}$ = 55 S cm^2 mol^{-1}) and bicarbonate ions ($\Lambda_{eq,HCO3-}$ = 44.5 S cm^2 mol^{-1}). As hydroxide ions are dominant their consumption can be readily measured during the reaction. For validation of this method, an analytical study has been performed. A reactor model has been set up to predict theoretical concentration profiles of the chemical species during the reaction (see Fig. 5, left) [18]. Based on this, the conductivity of the solution is computed, normalized and compared to wire-mesh sensor data of validation measurements. An exemplary time signal of normalized conductivity measured with WMS and predicted from the reactor model is depicted on the right of Fig. 5. It shows a characteristic course including two kinks. In the first sector, a sharp decrease of the conductivity is obtained. This results mainly from the consumption of the OH^- with its high equivalent conductivity. After the first kink, the decrease of conductivity becomes less. In accordance with the concentration profiles on the left of Fig. 5 the turning point in the conductivity course characterizes the consumption of the OH^- ions. In the third section, the conductivity tends towards a stationary value, which indicates the end of the chemical absorption reaction.

The subdivision of the signal into three temporal sectors, which are indicated by the interval boundaries, has been carried out for each crossing point in the cross-section using spline approximation function [19]. For analysis of the impact of
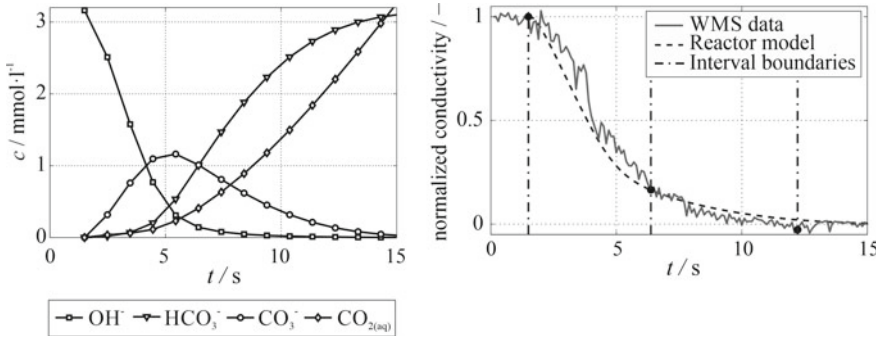
Fig. 5 Left: Concentration courses of the different ionic species during chemical absorption of CO_2 in NaOH solution of $c_{0,NaOH} = 3.2$ mmol l^{-1} determined from reactor model and right: comparison of normalized conductivity course computed from reactor model and wire-mesh sensor measurement signal

different experimental conditions, e.g. initial concentration of NaOH and superficial gas velocity, on the OH^- consumption, the first time interval is evaluated to determine the consumption rate of OH^- according to:

$$\upsilon_{OH^-} = \frac{\Delta c_{OH^-}}{\Delta t_{OH^-}}. \qquad (13)$$

This is done for each single crossing point in the cross-section, allowing the evaluation of radial consumption rates. According to Darmana et al., the consumption rate of OH^- is proportional to the rate of CO_2 mass transfer, since dissolved CO_2 immediately reacts with OH^- at these pH values [20].

3.4 Experimental Setup for Experiments with the Fe^{II}(edta)/NO System

For experiments on the Fe^{II}(ligand)/NO system, changes of the experimental setup were necessary. A schematic of the setup is depicted in Fig. 6. Due to use of toxic NO gas, special attention was paid on the safety implementation and experiments are initially carried out with single bubbles and in a fume hood. For measurements with this reaction system, the reaction solution Fe^{II}(edta) must be prepared directly in the bubble column. First, the column is filled with deionized water. Since oxygen interferes with the desired reaction, the whole setup and the deionized water needs to be flushed with nitrogen as inert gas to get the setup oxygen free. Then the reaction solution is prepared by adding iron(II)sulfate heptahydrate and 1.1 equimolar edta salt hydrate. In these experiments the gas supply is stopped before starting the measurements. The feed lines are then filled with NO gas up to the capillary to feed

Fig. 6 Schematic of the bubble column setup for measurements using the reactive system FeII(ligand)/NO
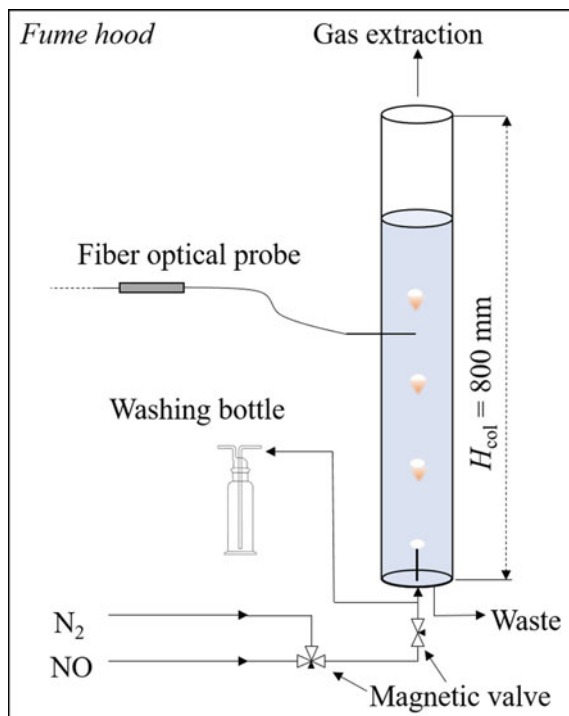
only pure NO into the bubble column. For the injection of NO gas in the column a single capillary in the center of the column is used. The gas throughput is controlled by a magnetic valve, which ensures shedding of single bubbles.

After injection of NO gas the product $[Fe^{II}(edta)(NO)]^{2-}$ is formed in the liquid phase. The formation is indicated by a local color change of the solution from colorless/slight yellow to orange/brown. For the measurement of the color change, which reveals the local concentration of the complex, a fiber optical probe was developed which can be installed in different heights of the reactor. The probe allows for minimally invasive in situ measurement of local concentration of the product complex in the liquid phase and, simultaneously, the phase discrimination of gas bubbles and the liquid.

A photograph and a schematic of the design of the probe is depicted in Fig. 7. The fiber optical probe is designed for absorption measurements at individual wavelengths. Thus, monochromatic light traverses a small control volume at the probe tip and its attenuation is measured. Light is generated via LEDs in a remote unit and transferred to and from the probe via optical fibers. For this study, two wavelengths of $\lambda = 435$ and 780 nm were used. The selection of the wavelengths is based on the characteristic absorption band of $[Fe^{II}(edta)(NO)]^{2-}$ at $\lambda = 435$ nm and a reference at 780 nm, where the change of absorption at different concentrations of $[Fe^{II}(edta)(NO)]^{2-}$ is negligible (see Fig. 7 top left). To meet requirements on the
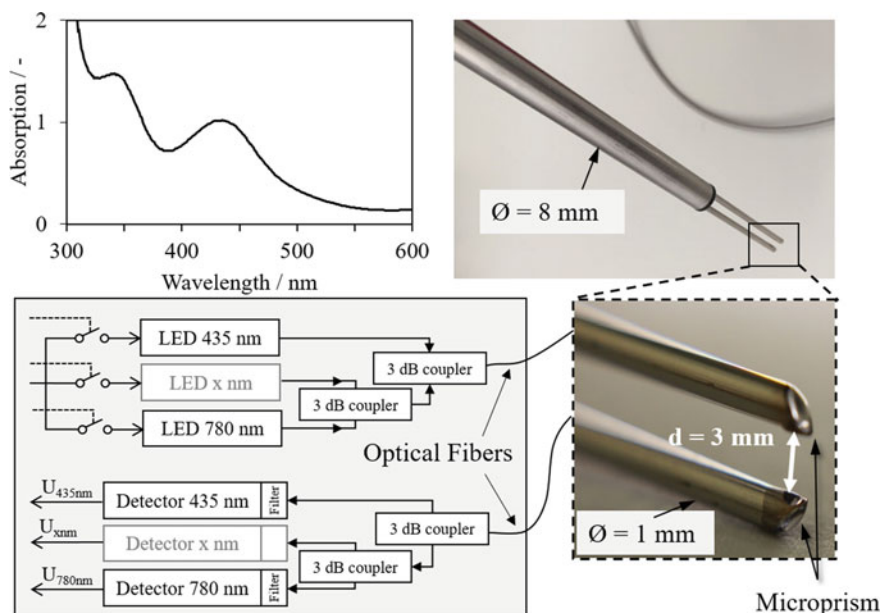
Fig. 7 Top left: Absorption spectrum of $[Fe^{II}(edta)]^{2-}$. Right: Photograph of the sensor tip of the photometer probe and bottom left: Schematic of the illumination circuit

chemical material stability and minimal intrusiveness, special attention has been paid to the design of the probe. The probe has a fork-like structure, each arm containing the fiber in a 1 mm stainless steel tube. Micro prisms are installed at the tip of the fibers for a tip-crossing light beam. The distance of the optical fibers at the tip of the probe is $d = 3$ mm, which results in a measurement volume of about $V = 2$ mm^3. To eliminate effects of ambient light, the emitter light is modulated with a sine wave of $f = 100$ kHz and the detector signal demodulated using a Lock-In Amplifier (*SR840 DSP*). The output voltage signal ($U = 0$–1 V) is sampled with a frequency of $f = 5$ kHz.

The calculation of the extinction values E for each wavelength λ is based on the Lambert–Beer law, that is

$$E(\lambda) = -\log_{10} \frac{I(\lambda) - I_{\text{Dark}}(\lambda)}{I_0(\lambda) - I_{\text{Dark}}(\lambda)'} \tag{14}$$

where I_0 is the intensity of the pure solution before reaction, I is the intensity of the solution during and after reaction and I_{Dark} is the intensity without light source (dark current of detectors). Eventually, the difference of the extinction values ΔE is calculated according to:

$$\Delta E = E(\lambda = 780 \text{ nm}) - E(\lambda = 435 \text{ nm}). \tag{15}$$
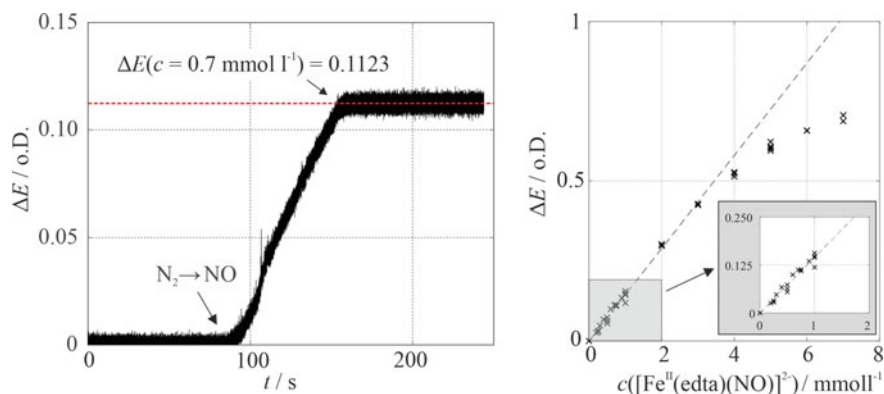
Fig. 8 Example of calibration measurement for $c([Fe^{II}(edta)(NO)]^{2-}) = 0.7$ mmol l^{-1} (left) and calibration function for fiber optical probe (right)

To convert the extinction values into concentrations, a calibration was carried out with a reduced reaction volume of 250 ml. NO was added to aqueous solutions of various concentrations of $[Fe^{II}(edta)(H_2O)]^{2-}$ to form $[Fe^{II}(edta)(NO)]^{2-}$ until $[Fe^{II}(edta)(H_2O)]^{2-}$ was completely consumed. Voltage signals of the fiber optical probe were continuously recorded. The computed extinction values are depicted in Fig. 8 left. The complete consumption of $[Fe^{II}(edta)(H2O)]^{2-}$ results in a constant value of the absorption.

Thus, an extinction value can be assigned to each concentration and consequently a calibration function

$$c([Fe^{II}(edta)(NO)]^{2-}) = \Delta E / k \tag{16}$$

with k being the calibration constant, is determined. For the probe used in the present study, the calibration constant was found to be $k = 0.145$. The extinction values determined for different concentrations of $[Fe^{II}(edta)(NO)]^{2-}$ are depicted in Fig. 8 right. A linear dependency according to the Lambert–Beer law is observed up to a concentration of $c = 3$ mmol l^{-1}.

For application in the bubble column reactor additional post-processing is necessary to discriminate gas and liquid phase from the measured signals. The contact of a bubble with the probe tip produces a clear peak in the time signal of the intensities. By applying a threshold to the time derivative of the extinction signal of the reference wavelength, these bubble-probe contacts can be identified and subsequently applied to the species-specific wavelength, allowing the distinction between bubble contact and concentration information in the bubble wake.

4 Experimental Results

4.1 Gas Dynamics and Bubble Properties of Uniform Bubbly Flow

This section provides selected results of the hydrodynamic measurements in the DN100 bubble column. For clarity, results are exemplarily presented for the superficial gas velocities $j_G = 0.5, 1.0, 2.5$ cm s^{-1}, deionized water and two concentrations of NaOH solution, corresponding to pH 11.5 and pH 12.5. Further results can be found in [16].

Initially, a characterization of the hydrodynamics produced by the capillary gas sparger was performed using deionized water and nitrogen. Measurement data at $h = 0.1$ m above the gas distributor were recorded to obtain information about the distribution of the gas through the gas distributor and the initial bubble size distribution, which are crucial parameters for CFD simulations. Figure 9 left presents the time-averaged cross-sectional images of the phase distributions together with the radial profiles at the measurement position 0.1 m above the gas distributor. The result indicate a radial symmetry of the distribution of the gas within the cross-section and confirms a radially uniform injection of the gas bubbles. The bubble size distributions presented in Fig. 9 right shows a narrow distribution of bubble sizes and a most probable bubble diameter of $d_{B,eq} \approx 5$ mm for all superficial gas velocities.

All following results are referred to the measurement height $L/D = 7$, where the flow structure is assumed to be fully developed [12]. In Fig. 10a the global gas holdup data are presented in dependence of the gas superficial velocity. The global gas holdup of N_2 in NaOH solution is higher compared to the one in deionized water. This results from expected smaller bubble sizes in electrolyte solutions [21], which is also confirmed by the bubble size distributions (see Fig. 10c). In Fig. 10b exemplary X-ray tomography image stacks are depicted, showing the structure of the gas phase in the column and the temporal averaged distribution in the cross-section of
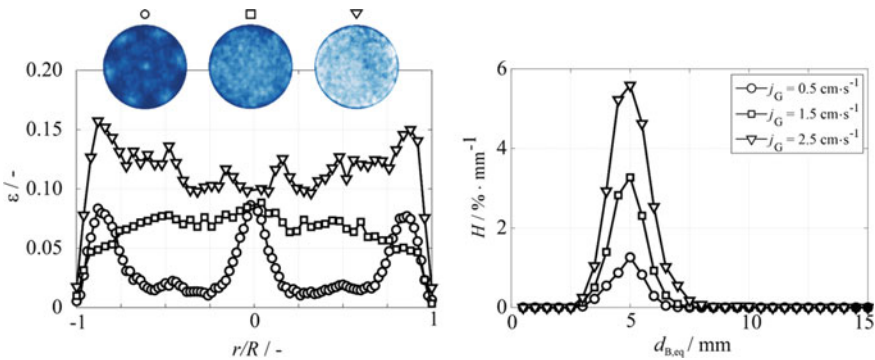
Fig. 9 Left: Radial gas holdup profiles, right: Bubble size distributions at L/D = 1
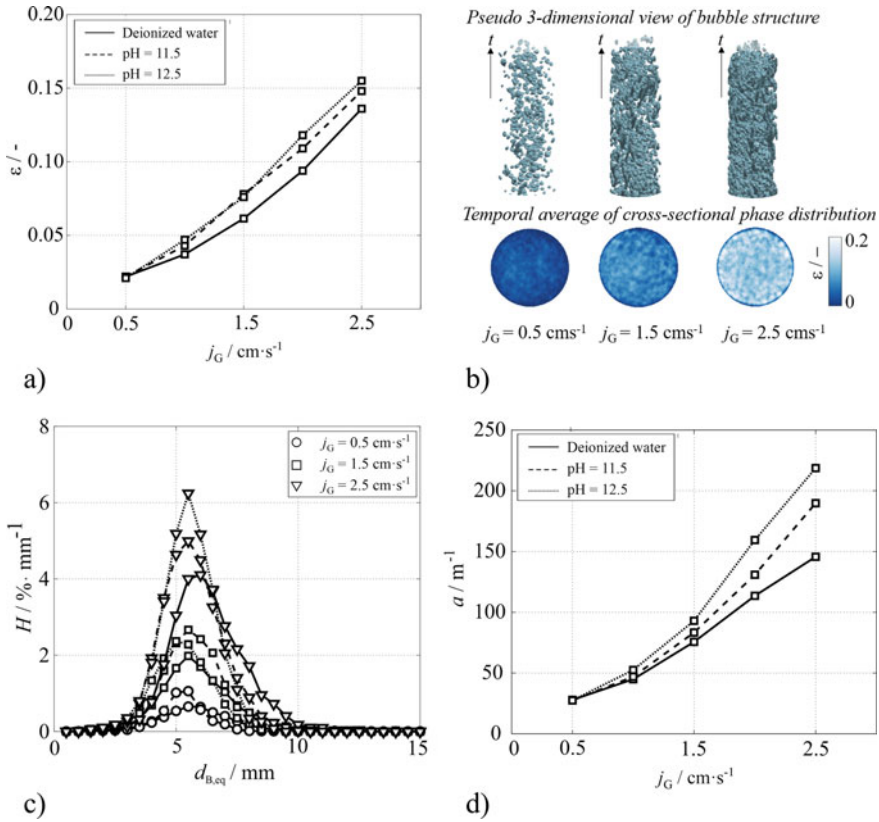
Fig. 10 Global gas holdup data for deionized water (full line) and NaOH solution of two different concentrations (dashed lines) in dependence of superficial gas velocity (**a**), X-ray tomography image stacks of flow structure in the bubble column together with temporal averaged cross-sectional images for deionized water (**b**), corresponding bubble size distributions (**c**) and interfacial area (**d**)

the column, from which a radially uniform distribution of the gas can be concluded. Figure 10d shows the values obtained for interfacial area in dependence of the gas superficial velocity for different pH values of the solution. In accordance with the results from gas holdup and bubble size distribution, the interfacial area is increasing with concentration of NaOH solution.

Cross-sectional analysis of the gas–liquid distribution allows evaluating radial gas holdup profiles, which are presented in Fig. 11, left. Here, data of three superficial gas velocities are compared for deionized water and sodium hydroxide solution with $pH = 11.5$ and $pH = 12.5$. In general, the profiles are flat in the center and show a minimum gas holdup at the column wall. For $j_G = 2.5$ cm s^{-1} a gas holdup peak is observed 5 mm away from the wall, which can be related to the effect of the lift force or column dimensions [16]. Comparing experiments in deionized water and NaOH solution, the shape of the radial profiles is changing. For $j_G = 0.5$ and 1.5 cm s^{-1}
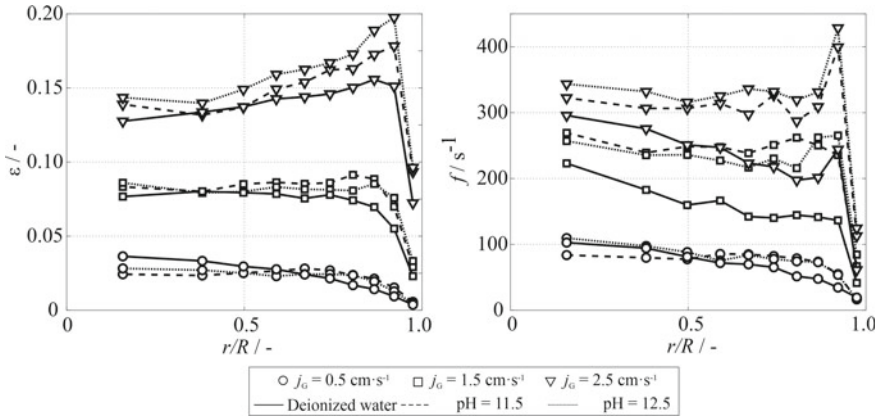
Fig. 11 Left: Radial gas holdup profile and right: radial bubble frequency

the profiles measured for NaOH solution are flatter compared to measurements in deionized water. This results from a narrower bubble size distribution for NaOH and therefore more homogenous flow conditions. Indication on this is also given by the profile of the radial bubble frequency, which changes from center-peaking to a flat profile with addition of NaOH (see Fig. 11, right).

The results obtained from hydrodynamic studies, which also comprise e. g. axially averaged gas phase velocities and radially resolved bubble sizes [16], provide a comprehensive description of the hydrodynamic conditions in the setup presented here and will be used together with the results of the mass transfer studies for improved understanding of their interrelation.

4.1.1 Absorption of CO_2 in Deionized Water

The absorption of CO_2 in deionized water was studied and volumetric mass transfer coefficients were determined from simultaneously measured wire-mesh sensor and UFXCT data. Therefore, the normalized conductivity signal of WMS data is evaluated and the $k_L a$ value in each single crossing point is determined according to Eq. (12). In Fig. 12 left the spatially averaged volumetric mass transfer coefficients for absorption of CO_2 in deionized water are depicted together with data from empirical correlations and in dependence of the superficial gas velocity. From the present experiments, the following correlation for $k_L a$ has been derived:

$$k_L a = 1.24 \, j_G^{0.89}. \tag{17}$$

Since, WMS measurements allow the cross-sectional measurement also radial distributions of the volumetric mass transfer coefficients are evaluated. In turn, the
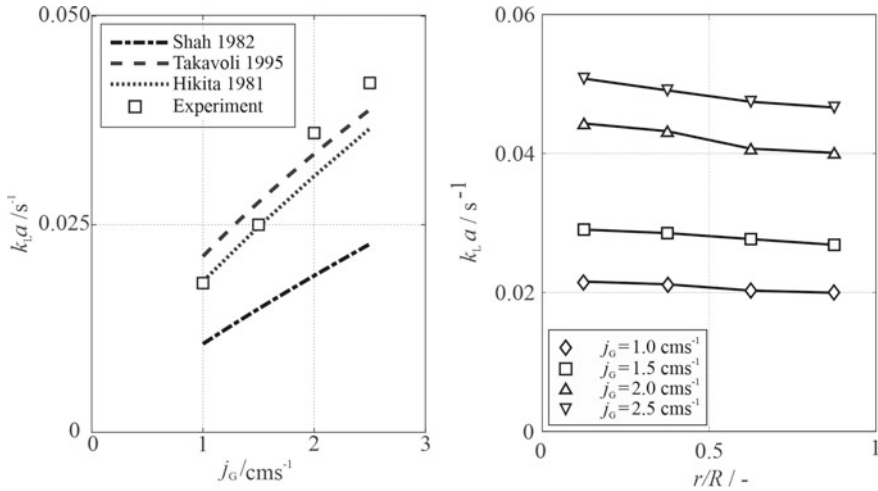
Fig. 12 Volumetric mass transfer coefficients as function of superficial gas velocity (left) and radial profile of volumetric mass transfer coefficients from experimental data

radial distribution is shown on the right of Fig. 12 and exhibits uniform values over the cross-section with slightly higher $k_L a$ values in the center of the column.

Together with the values of interfacial area determined from *UFXCT* measurements, the liquid side transfer coefficient is evaluated and eventually the Sherwood number is calculated according to

$$Sh = \frac{k_L d}{D_c} \tag{18}$$

with D_c being the gas molecular diffusion coefficient of CO_2 in water according to Versteeg and Swaaji [22]. In Fig. 13, the experimentally determined Sherwood numbers are depicted in comparison with values of empirical correlations for non-spherical bubbles [23, 24]. Assuming a constant mass transfer coefficient for this

Fig. 13 Comparison of calculated Sherwood numbers from experimental data and empirical correlations in dependence of the Reynolds number for absorption of CO_2 in deionized water
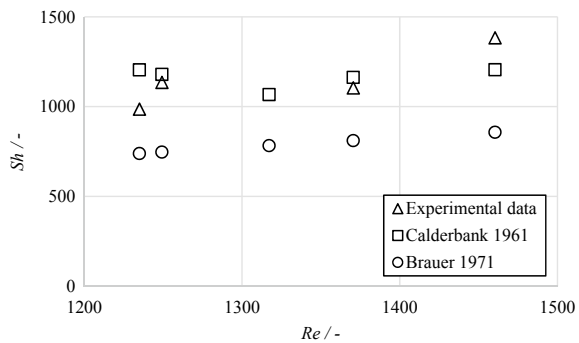
bubble size class the values obtained from the empirical correlation of Calderbank [24] are in good agreement with experimental data. The correlation of Brauer predicts significantly lower values. Deviations are mainly due to different values of the interfacial area, which are dependent on the method or measurement technique used for determination and the fluid dynamic conditions which are heavily influenced by the type of sparger.

4.1.2 *Chemical Absorption of CO$_2$*

In this section, exemplary experimental results of hydrodynamics and chemical species conversion during chemical absorption of CO$_2$ are presented. Simultaneous measurements with UFXCT and wire-mesh sensor provide complementary results on the bubble column hydrodynamics and conversion of chemical species.

On the left of Fig. 14 the cross-sectional averaged consumption rates for two different initial pH-values of NaOH solution are depicted in dependence of the gas superficial velocity. According to Darmana, the consumption rates are assumed to
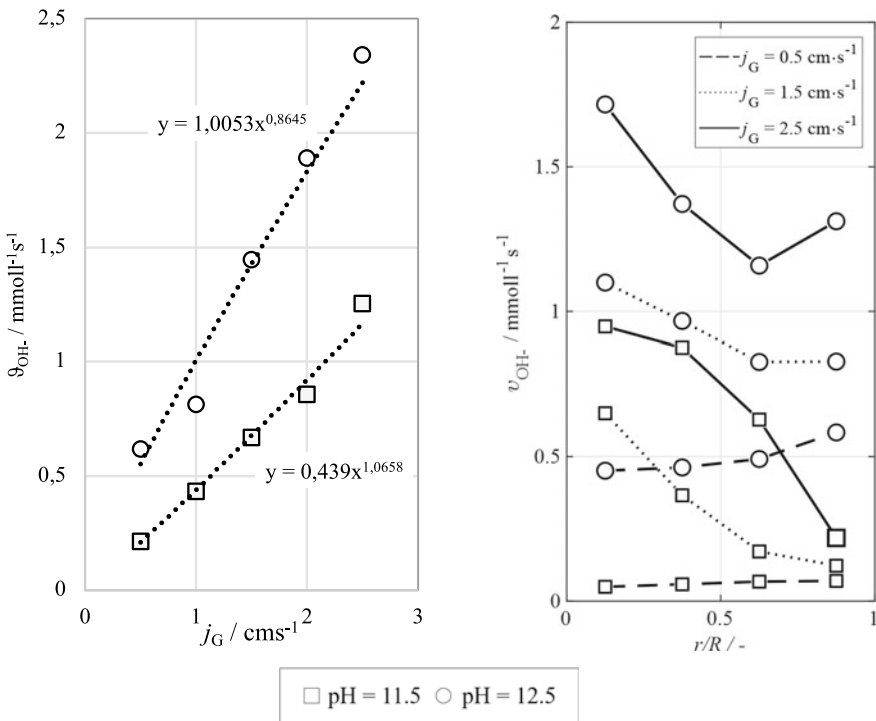
Fig. 14 Left: Global consumption rates in dependence of gas superficial velocity and right: radial consumption rates for three different superficial gas velocities and two pH values of NaOH solution

be proportional to the mass of CO_2 being transferred [20] and thus give direct indications on the reactive mass transfer. The global consumption rate of OH^- is seen to increase almost linearly with increasing superficial gas velocity for both pH values, respectively. However, the slope of increase is higher for $pH = 12.5$, which is in accordance with higher concentration gradients and higher interfacial area (see Fig. 10d) in this case. On the right of Fig. 14 the consumption rates of OH^- are depicted as radial profiles. For $j_G = 0.5$ cm s^{-1} the consumption rates show similar values for both initial pH values of the solution. With increasing flow rate, the values of the consumption rate increase towards the center of the column. One reason could be the more pronounced velocity profile with higher gas throughputs, leading to increased bubble induced turbulence.

In Fig. 15 the temporal evolution of the gas holdup during chemical absorption is exemplarily shown for $j_G = 1.5$ cm s^{-1} and two different initial pH values of the solution. The reaction is initiated by gas switching from nitrogen to CO_2, which causes a drastically reduce of the gas holdup and reaches a stationary value after $t \sim 10$ s measurement time for this experimental conditions. For two time steps, namely at the beginning of the reaction and after 18s measurement time, the bubble size distributions are depicted in Fig. 15, right. From this, we can conclude a gross reduction of the bubble size but no complete dissolution of the bubbles after $t = 20$ s measurement time. However, the rate of reduction is higher for $pH = 12.5$ which results from higher concentration gradients. From the bubble size distributions the variance of the bubble size can be determined. Together with the gas holdup, it is summarized in Table 1.
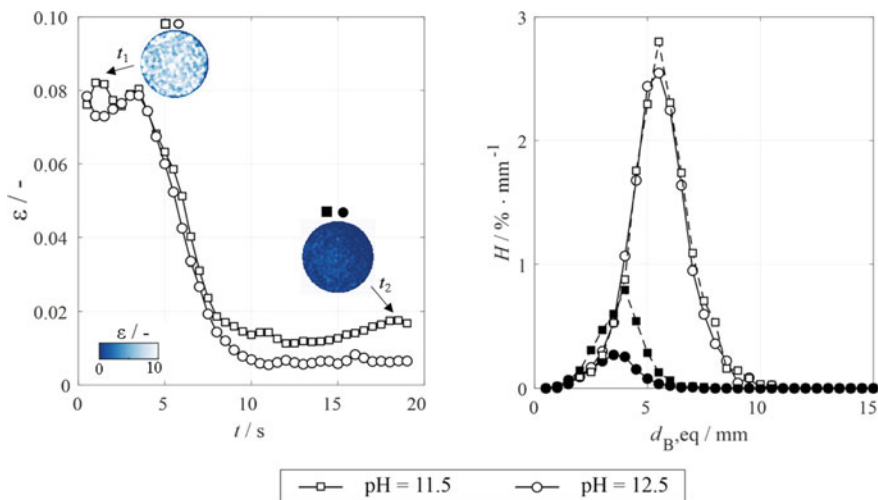
Fig. 15 Transient gas phase hydrodynamics during chemical absorption of CO_2 for $j_G = 1.5$ cm s^{-1}. Left: Temporal evolution of global gas holdup and corresponding cross-sectional images of the phase distribution and right: Bubble size distribution for $t_1 = 0$–2 s and $t_2 = 18$–20 s measurement time

Table 1 Values of gas holdup and variance of bubble size distribution before chemical absorption reaction and after 18 s measurement time

	j_G/cm s^{-1}	$t = 0$–2 s		$t = 18$–20 s	
		$\varepsilon \cdot 10^{-2}$/-	$\sigma^2_{d,eq}$/mm^2	$\varepsilon \cdot 10^{-2}$/-	$\sigma^2_{d,eq}$/mm^2
pH = 11.5	0.50	2.20	2.34	0.59	0.73
	1.50	7.86	2.93	1.65	1.08
	2.50	14.6	2.12	2.53	0.91
pH = 12.5	0.50	2.09	2.39	0.33	0.54
	1.50	7.52	2.75	0.66	0.91
	2.50	15.56	2.21	0.88	0.67

4.1.3 *Local Species Concentration Measurement of [Fe^{II}(Edta)(NO)]$^{2-}$ Using Fiber Optical Probe*

This section provides results of the first measurements of local species concentration using the fiber optical local probe. Single bubbles were injected into the column and bubble-probe contacts were evaluated. A typical time signal provided from fiber optical probe data is depicted in Fig. 16, left. The contact of a bubble with the probe leads to a strong signal peak at both wavelengths as the optical transmission path is interrupted. In the liquid phase the extinction values of the reference wavelength $\lambda = 780$ nm are close to zero. Contrary, for the product specific wavelength $\lambda =$
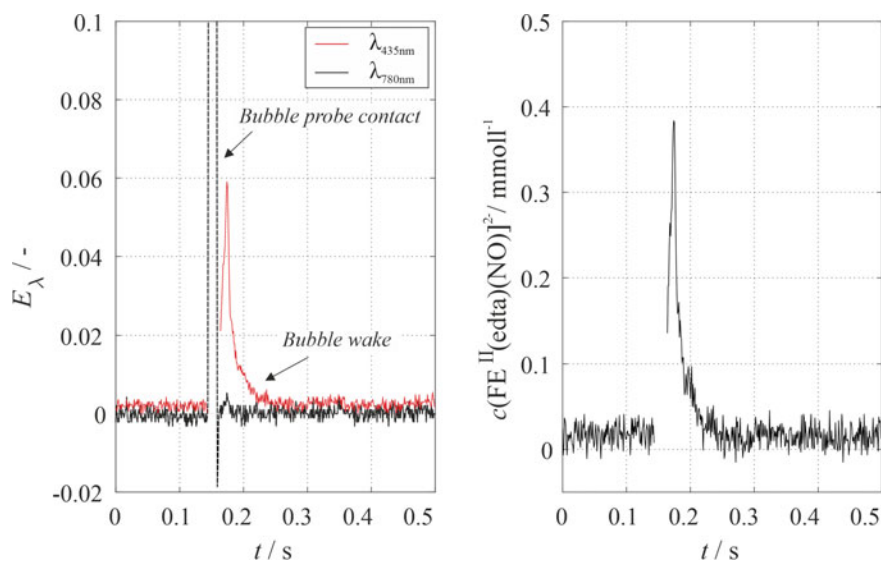
Fig. 16 Typical time signal of extinction values measured by fiber optical probe (left) and converted time signal of concentration (right)
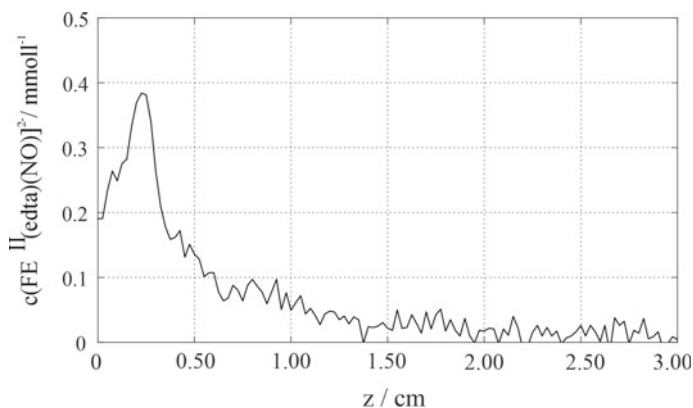
Fig. 17 Local product concentration depending on the bubble-probe distance based on a converted time scale. Assuming a bubble diameter of 4.5 mm, the decrease of concentration with distance from the probe is evaluated

435 nm, a clear increase of the extinction values is obtained, e. g. behind the bubble, which diminishes with further distance of bubble and probe. Based on the signal of the reference wavelength, the bubble probe contact is removed for further data processing. Following, according to Eq. 16, the concentration signal is computed. On the right of Fig. 16 a typical signal of the concentration course is depicted. Directly behind the bubble a maximum concentration of $[Fe^{II}(edta)(NO)]^{2-}$ is measured, which then drops rapidly. Even if this is a characteristic signal, which can be found often in a measurement sequence, other signal courses also occur, namely when there is no complete passage of the bubble through the probe or no bubble contact is recorded. However, these sequences are neglected for further analysis.

If the bubble size is known, the velocity of the bubble can be computed by the contact time of the bubble and the probe assuming a complete bubble passage. Following, the time signal can be converted into length scale. In Fig. 17 the concentration of $[Fe^{II}(edta)(NO)]^{2-}$ is depicted in dependence of the distance from the bubble. By analyzing the concentration gradients in the bubble wake, the structure of the wake can be derived and valuable information about the mixing of reactive species in the wake can be obtained. The main advantage of this technique lies in the possibility of its application to dense bubble swarms. With the help of the reference wavelength information about the gas phase, such as phase fraction, can be obtained simultaneously.

5   Conclusion and Outlook

Within this project a comprehensive experimental data base for hydrodynamic and mass transfer data were obtained by the use of tomographic measurement techniques, ultrafast X-ray tomography and wire-mesh sensor. A bubble column with a capillary gas sparger producing a uniform bubbly flow was set up. The wire-mesh sensor was provided for the application of chemical species conversion during chemical absorption of CO_2, allowing a profound analysis of local consumption rates through the cross-sectional resolved measurement. Together with simultaneous measured transient hydrodynamic parameters, these data provide a valuable basis for CFD simulations of homogenous bubbly flows with gas holdup up to 17%. To date, these data were used for validation of Euler–Lagrange simulations by the group of Sommerfeld (see Chap. 6 "Chemical Reactions in Bubbly Flows"). Besides studies on hydrodynamic and mass transfer during the absorption of CO_2 in bubbly flows, also investigations on the reaction system $Fe^{II}(edta)$/NO system were carried out. A fiber optical probe was designed and validated for the measurement of local concentrations of the product complex of the reaction in the vicinity of the bubbles. First results are promising to analyze the concentration gradients behind bubbles and in that way better understand the mixing of reactive species in bubble wakes at different hydrodynamic conditions. This is of main importance, since there are indications of significant influence of the mixing in the wake on the selectivity of chemical reactions. In the future, this probe will be used for further experimental studies on the influence of bubble size distribution and holdup on local product concentrations in the bubble wakes.

References

1. Kipping R, Hampel U (2020) Experimental gas phase hydrodynamic data of lab scale bubble column. https://doi.org/10.14278/rodare.283
2. Zalucky J, Wagner M, Schubert M, Lange R, Hampel U (2017) Hydrodynamics of descending gas-liquid flows in solid foams: liquid holdup, multiphase pressure drop and radial dispersion. Chem Eng Sci 168:480–494. https://doi.org/10.1016/j.ces.2017.05.011
3. Sohr J, Schubert M, Flechsig S, Kenig EY, Hampel U (2019) Experimental investigation of the froth height in columns with sandwich packings. Chem-Ing-Tech 91:139–144. https://doi.org/10.1002/cite.201800069
4. Möller F, Kipping R, Schleicher E, Löschau M, Hampel U, Schubert M (2019) Comparative hydrodynamic analysis of narrow and pilot-scale bubble columns with internals. Chem-Ing-Tech. https://doi.org/10.1002/cite.201800110
5. Fleischer C, Becker S, Eigenberger G (1996) Detailed modeling of the chemisorption of CO_2 into NaOH in a bubble column. Chem Eng Sci 51:1715–1724. https://doi.org/10.1016/0009-2509(96)00030-9

6. Darmana D, Henket RLB, Deen NG, Kuipers JAM (2007) Detailed modelling of hydrodynamics, mass transfer and chemical reactions in a bubble column using a discrete bubble model: Chemisorption of CO_2 into NaOH solution, numerical and experimental study. Chem Eng Sci 62:2556–2575. https://doi.org/10.1016/j.ces.2007.01.065

7. Yoo M, Han SJ, Wee JH (2013) Carbon dioxide capture capacity of sodium hydroxide aqueous solution. J Environ Manage 114:512–519. https://doi.org/10.1016/j.jenvman.2012.10.061

8. Pohorecki R, Moniuk W (1988) Kinetics of reaction between carbon dioxide and hydroxyl ions in aqueous electrolyte solutions. Chem Eng Sci 43:1677–1684. https://doi.org/10.1016/0009-2509(88)85159-5

9. Zhang S, Chen H, Xia Y, Liu N, Lu BH, Li W (2014) Current advances of integrated processes combining chemical absorption and biological reduction for NOx removal from flue gas. Appl Microbiol Biotechnol 98:8497–8512. https://doi.org/10.1007/s00253-014-6016-9

10. Gambardella F, Winkelman JGM, Heeres HJ (2006) Experimental and modelling studies on the simultaneous absorption of NO and O_2 in aqueous iron chelate solutions. Chem Eng Sci 61:6880–6891. https://doi.org/10.1016/j.ces.2006.07.003

11. Schneppensieper T, Finkler S, Czap A, van Eldik R, Heus M, Nieuwenhuizen P, Wreesmann C, Abma W (2001) Tuning the Reversible Binding of NO to Iron(II) Aminocarboxylate and Related Complexes in Aqueous Solution. Eur J Inorg Chem 2001:491–501. https://doi.org/10.1002/1099-0682(200102)2001:2<491::AID-EJIC491>3.0.CO;2-2

12. Kantarci N, Borak F, Ulgen K O (2005) Bubble column reactors. Process Biochem 40:2263–2283. https://doi.org/10.1016/j.procbio.2004.10.004

13. Fischer F, Hampel U (2010) Ultra fast electron beam X-ray computed tomography for two-phase flow measurement. Nucl Eng Des 240:2254–2259. https://doi.org/10.1016/j.nucengdes.2009.11.016

14. Barthel F, Bieberle M, Hoppe D, Banowski M, Hampel U (2015) Velocity measurement for two-phase flows based on ultrafast X-ray tomography. Flow Meas Instrum 46:196–203. https://doi.org/10.1016/j.flowmeasinst.2015.06.006

15. Banowski M, Lucas D, Szalinski L (2015) A new algorithm for segmentation of ultrafast X-ray tomographed gas-liquid flows. Int J Therm Sci 90:311–322. https://doi.org/10.1016/j.ijthermalsci.2014.12.015

16. Kipping R, Kryk H, Hampel U (2020) Experimental analysis of gas phase dynamics in a lab scale bubble column operated with deionized water and NaOH solution under uniform bubbly flow conditions. Chem Eng Sci 229: 116056. https://doi.org/10.1016/j.ces.2020.116056

17. Möller F, Maclsaac A, Lau YM, Schleicher E, Hampel U, Schubert M (2018) Advanced analysis of liquid dispersion and gas–liquid mass transfer in a bubble column with dense vertical internals. Chem Eng Res Des 134:575–588. https://doi.org/10.1016/j.cherd.2018.04.018

18. Kipping R, Kryk H, Schleicher E, Gustke M, Hampel U (2017) Application of a wire-mesh sensor for the study of chemical species conversion in a bubble column. Chem Eng Technol 40:1425–1433. https://doi.org/10.1002/ceat.201700005

19. Schwetlick H, Schütze T (1995) Least square approximation by splines with free knots. BIT Numer Math. 35:361–384. https://doi.org/10.1007/BF01732610

20. Darmana D (2006) On the multiscale modelling of hydrodynamics, mass transfer and chemical reactions in bubble columns, PhD Thesis, University of Twente

21. Ribeiro JRCP, Lage PLC (2004) Experimental study on bubble size distributions in a direct-contact evaporator. Brazilian J Chem Eng 21:69–81. https://doi.org/10.1590/s0104-66322004000100008

22. Versteeg GF, Van Swaaij WPM (1988) Solubility and diffusivity of acid gases (carbon dioxide, nitrous oxide) in aqueous alkanolamine solutions. J Chem Eng Data 33:29–34. https://doi.org/10.1021/je00051a011

23. Brauer H (1971) Grundlagen der Einphasen- und Mehrphasenströmungen. Sauerländer

24. Calderbank PH, Moo-Young MB (1961) The continuous phase heat and mass-transfer properties of dispersions. Chem Eng Sci 16:39–54. https://doi.org/10.1016/0009-2509(61)87005-X

Experimental Investigation of Local Hydrodynamics and Chemical Reactions in Taylor Flows Using Magnetic Resonance Imaging

Philip Kemper, Ekkehard Küstermann, Wolfgang Dreher, and Jorg Thöming

Abstract In today's industrial processes reactions in dispersed gas–liquid systems are of major importance. Many products originate from gas–liquid reactions inside the bubble wake, acting as a mixing zone. High reaction yields are mainly influenced by the hydrodynamics within these zones. However, undisturbed hydrodynamic measurements of low viscous systems inside the bubble wakes are lacking. In this work we report on non-invasive MRI of gas–liquid Taylor flows. A detailed explanation of the developed MRI setup and sequence is given.

1 Introduction

In modern day industry gas–liquid reactions are of great importance for production processes as they serve different purposes such as oxidation, chlorination and hydrogenation. For this reason, an improvement of the selectivity and yield of these processes is aimed. Commonly, gas liquid reactions are carried out in large scale bubble columns and gas sparged tanks, which only allow efficiency measurements by globally quantifying the product stream in terms of selectivity and yield. However, these chemical reactions can only be selectively improved and optimized by investigating concentration fields and mass transfer on a local scale. Furthermore, an in-depth knowledge of the underlying flow field is required, as flow and chemical reactions are superimposed and significantly influence residence times and local concentrations. Rather than conducting experiments inside bubble swarms [1], the complexity of the investigated systems is often reduced by looking at freely rising single bubbles in large columns [2], emulating bubble swarm effects [3] or most frequently by using gas–liquid Taylor flows. They enable the investigation of single bubbles, rising inside a confined space under well-defined and reproducible measurement conditions at laboratory scale. Taylor flows are often utilized for systematic studies inside multiphase flows when looking at flow dynamics [4–8], mass transfer [9–11] and chemical reactions [12].

© The Author(s), under exclusive license to Springer Nature Switzerland AG 2021
M. Schlüter et al. (eds.), *Reactive Bubbly Flows*, Fluid Mechanics
and Its Applications 128, https://doi.org/10.1007/978-3-030-72361-3_8

In confined tubes the gas phase forms the so-called Taylor bubbles, characterized by an elongated bullet shape, with a region of flow behind the bubble, referred to as the wake. Typically, Taylor bubbles fill the cross-section of the capillary, only being separated from the capillary's wall by a thin liquid film, which allows the bubble to move inside the confined space. In vertically aligned capillaries, the ratio between gravitational and surface tension forces defines whether a buoyancy driven bubble movement occurs. This ratio is also known as the dimensionless Eötvös number:

$$Eo = \frac{\left(\rho_{\text{liquid}} - \rho_{\text{gas}}\right) g d_{\text{i}}^2}{\sigma} \tag{1}$$

It consists of the density difference between the liquid and the gas phase $\left(\rho_{\text{liquid}} - \rho_{\text{gas}}\right)$, the gravitational acceleration g, the capillary diameter squared d_{i}^2 and the surface tension σ of the gas–liquid system [13]. Inside an air–water system, the critical number of $Eo = 4$ has to be exceeded for buoyancy driven bubble rise to occur [14]. This results in a critical capillary diameter of about $d_{\text{i}} = 5.5$ mm. Long-term hydrodynamic investigations are made possible by holding a buoyancy driven bubble ($Eo > 4$) in place with a countercurrent flow. The flowrate is adjusted to the terminal rise velocity of the bubble until it is spatially fixed. The terminal rise velocity of the Taylor bubble increases with larger capillary diameters, which also alters the flow inside the bubble's wake region [12, 15]. This alteration occurs due to the increasing inertia of the system at larger capillary diameters. The ratio between inertial and viscous forces is described by the dimensionless Reynolds number:

$$Re = \frac{\rho_{\text{liquid}} v d_{\text{i}}}{\eta_{\text{liquid}}} \tag{2}$$

The inertia depends on the fluid density ρ_{liquid}, the flow velocity v and the capillary diameter d_{i}, whereas the viscous term is only described by the dynamic viscosity of the liquid phase η_{liquid} [13]. Another dimensionless number often found in literature regarding hydrodynamics is the Capillary number:

$$Ca = \frac{\eta_{\text{liquid}} v_0}{\sigma} \tag{3}$$

It describes the interaction between interfacial forces and viscous forces. The interfacial term consists of the dynamic viscosity of the liquid phase η_{liquid} and the superficial flow velocity v_0, whereas the viscous term is only described by the surface tension σ of the gas–liquid system. Further information of transport processes is given in the book *Transport Processes at Fluidic Interfaces* [16], which resulted from the same named DFG priority program 1506. The results helped to develop the setup of this study.

A common approach to visualize and study hydrodynamics inside Taylor flows is particle image velocimetry (PIV). Therefore, the liquid phase is seeded with fluorescent tracer particles. The particles follow the streamlines of the flow under stationary conditions. A precisely timed series of images is acquired in which local velocity

vectors are determined by evaluating ensembles of tracer particles [12, 17]. The visualization of local mass transfer requires tailored reaction systems [18–20]. Some of them were recently developed within DFG priority program 1740 to assist the experimental research. They are based on color changing reactions after contact with the gas phase. The utilized metal complexes are dissolved in water or organic solvents, acting as the liquid phase. The change in color is determined by optical measurement techniques, meaning that they are limited to optically accessible and transparent systems.

Nuclear magnetic resonance (NMR) based imaging (MRI) is one method to face these challenges. MRI makes slice-by-slice multidimensional imaging inside opaque systems possible. It allows to directly measure positions and distances and also enables to encode different parameters, such as chemical information about the sample, diffusion coefficients and flow parameters into the complex NMR signal. The field strength dependent resonance frequency of protons builds the basis of MR imaging. The specimen is placed inside a static magnetic field with superimposed field gradients. The field gradients are essential to spatially resolve the data. An external magnetic field is applied for a short period of time in form of a radio frequency (RF) signal via a transmitter coil. A receiver coil detects the time dependent signal emitted from the system, containing spatial information of the molecules inside the sample [21, 22].

The signal intensity of an image depends on the spin density of nuclei within each examined voxel. Contrast is created by varying spin density inside the sample. Additionally, relaxation processes are used for creating image contrast: T1 (spin–lattice relaxation time), which characterizes the time needed for spin populations to return to their equilibrium state, T2 (spin–spin relaxation time), which describes the decay constant needed for the transverse magnetization to exponentially decay to zero, and T2*, (effective transverse relaxation time), which may be shorter than T2 as also the effect of spatial inhomogeneities of the static magnetic field of the signal decay are considered. As the relaxation times can change with the composition of the sample, these relaxation processes can be used to indirectly measure chemical reactions. This effect can be enhanced by utilizing paramagnetic contrast agents, leading to a strong decrease of relaxation times, particularly T1. Furthermore, chemical shift imaging can be performed to gain specific and spatially resolved information on the chemical composition of the sample, which, however, requires longer measurement times [23].

As MRI offers many possibilities, its application in the field of multiphase flows is constantly increasing [24, 25]. A review of MRI focusing on hydrodynamics is given by [26]. Experiments on 2D single phase flow velocities in simple geometries [27], as well as the quantification of bubble size distributions and bubble shapes inside gas–liquid flows [28] were successfully conducted. A first step towards the investigation of chemical reactions inside gas–liquid flows was taken by using a contrast agent inside a highly viscous gas–liquid system. It was reported on the chemical reaction around a freely and slowly rising single bubble [29]. However, all these innovative works still rely on sufficiently low flow rates, steady state conditions of the investigated flow or special chemical systems to reduce motion blurring or artifacts due to long acquisition times. This frequently leads to experimental conditions far from real application

requirements. By overcoming these hurdles, real-time studies of flow dynamics inside Taylor flows can be successfully conducted under relevant conditions.

Here we report on the development of an MRI compatible Taylor flow setup for low viscous solutions. This includes the analyses of flow dynamics inside the counter-current flow setup by PIV, the design of a custom-made radio frequency coil for signal excitation and detection, as well as the development of a MRI sequence for hydro-dynamic studies inside the wake of Taylor bubbles. In a further step we demonstrate possibilities and limitations to simultaneously observe a chemical reaction taking place in the wake of a Taylor bubble.

2 Experimental Flow Setup for the Investigation of Taylor Flows Inside a Horizontal Bore MRI Scanner

The experimental Taylor flow setup for precise bubble generation and observation was designed in order to fulfil the spatial and material requirements of the MRI scanner. The experimental flow setup evolved during the project. This evolution is described in the following section, beginning with the first working setup for Taylor flow generation inside a horizontal bore MRI scanner.

2.1 Initial Version of the Flow Setup

The initial version of the flow setup is shown in Fig. 1. It was designed with the aim of creating a Taylor flow inside a setup of limited height, with the ability of using capillaries with different inner diameters to alter the flow dynamics inside the bubble's wake. In this approach, the fluidic connectors were horizontally aligned with the test section to minimize disturbances of the flow. A glass membrane was used at the inlet, acting as a flow straightener. Gas was injected into the setup by a thin HPLC capillary, running inside a larger HPLC capillary. The larger capillary carried the liquid phase into the test section. This particular setup allowed the use of a single HPLC connector. A gear pump with manual speed control for flow rate regulation was used to feed the liquid phase into the system. The gas phase was manually injected with a single use syringe. Outflowing liquid was collected inside a waste vessel.

Taylor bubbles were created inside round capillaries of $d_i = 5\,mm$, $d_i = 6\,mm$ and $d_i = 7\,mm$. Additionally, rectangular capillaries with hydraulic diameters of $d_h = 3\,mm$, $d_h = 4\,mm$ and $d_h = 5\,mm$ were investigated. Taylor bubbles were created inside the rectangular capillaries, however, the liquid film between bubble and capillary ruptured in all cases within a matter of seconds, making long term measurements impossible. A treatment with piranha solution for better wettability showed no significant improvement. The de-wetting was presumably caused by the
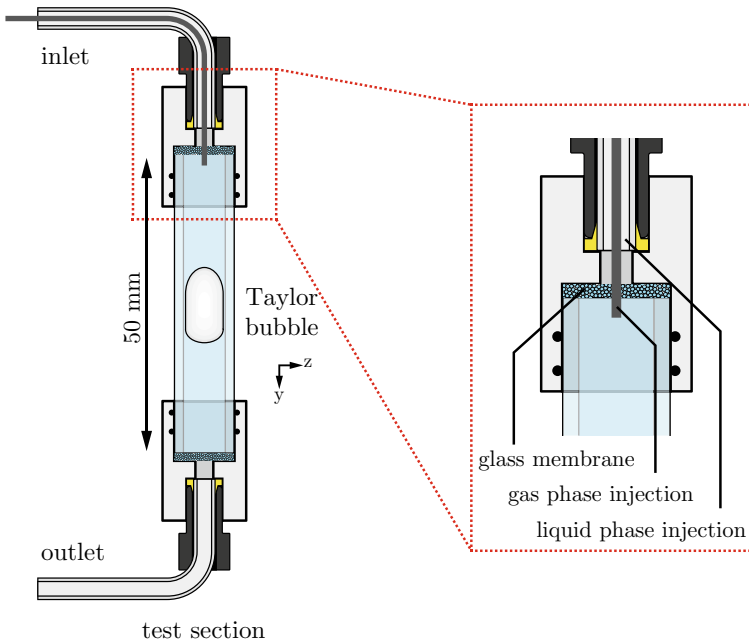
Fig. 1 Initial version of the flow setup, showing a glass capillary embedded into two holders. Gas is injected into the setup by a thin HPLC capillary, running inside a larger HPLC capillary used for liquid supply

surface finish of the glass capillaries. For this reason, square capillaries were not further investigated.

The setup was successfully used for first MRI test measurements and performed well, however, two main problems were encountered. Firstly, the gear pump induced noticeable flow fluctuations which made a spatial fixation of the bubble difficult. Secondly, the used double-capillary setup for gas and liquid supply strongly reduced the cross-sectional area passed by the fluid, resulting in high flow velocities at the inlet of the glass capillary. This led to an uncontrollable swirling motion of the fluid which further complicated the spatial fixation of the bubble. The encountered problems were addressed with an improved version of the setup.

2.2 Improved Version of the Flow Setup

A schematic representation of the improved flow setup is shown in Fig. 2. The experiments were performed in a vertically aligned test section consisting of a circular borosilicate glass tube mounted into two holders. The liquid phase was fed from a pressurized vessel to prevent pump-induced fluctuations. The liquid downflow rate
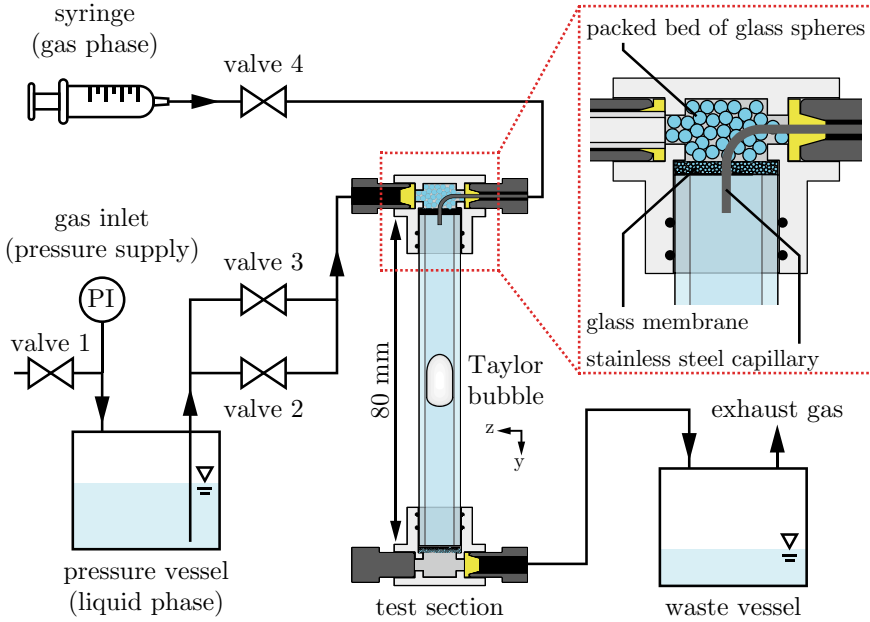
Fig. 2 Schematic representation of the flow setup for Taylor bubble generation. The bubble is generated and spatially fixed inside the test section by a countercurrent flow. A close-up of the test section's inlet reveals the internal components for flow straightening and bubble generation

inside the capillary was manually adjusted by a coarse and a fine control valve. A gas-tight syringe was used to manually inject the gas phase for Taylor bubble creation. Fluid was collected in a waste vessel and the exhaust gas was released into the fume hood. Long-term measurements were realized by keeping the buoyancy driven bubble suspended in a countercurrent flow. This presupposes a capillary diameter large enough to allow buoyancy driven bubble rise ($Eo > 4$). Rather than choosing an arbitrarily large capillary diameter, the smallest possible diameter, fulfilling the $Eo > 4$ criterion, was selected to reduce inertia (Re) inside the system. This allowed for more homogeneous flow conditions by viscous dissipation of disturbances, as the total height of the system was limited by the bore diameter of the MRI scanner and sufficiently long entrance lengths were not realizable. For this reason, a circular capillary with a diameter of $d_i = 6$ mm was chosen. Additional measures were taken to further reduce disturbances of the flow. A closeup of the top holder is given in Fig. 2. A packed bed of glass spheres helped to deflect the lateral fluid inflow downwards into the capillary, with a fine pored glass membrane placed before the capillary, acting as an additional flow straightener. A stainless-steel tube injected the gas phase directly into the capillary.

Dimensionless numbers of this particular setup were calculated using literature data [30] for an air–water system at $T = 293$K to enable classification and comparability with other studies. The flow velocity was estimated by measuring the bubble's

Table 1 Dimensionless numbers for an air–water system and a $d_i = 6$ mm capillary	Eötvös number	Eo	4.77
	Reynolds number	Re	31.69
	Capillary number	Ca	7.19×10^{-5}

terminal rise velocity $v_{\text{rise}} = 5.3\,\text{mms}^{-1}$. The resulting dimensionless numbers are given in Table 1.

2.3 Hydrodynamic Investigation by PIV

To get an overall understanding of the prevailing flow dynamics inside the setup, the local hydrodynamics inside the test section and around the Taylor bubble were investigated with particle image velocimetry (PIV). For this purpose, fluorescent particles were excited using a laser and particle movement was recorded with a highspeed camera. Fluorescence excitation was performed with a $P = 12$ W ($\lambda = 447$ nm) continuous wave laser (*CNI laser, China*) combined with a laser sheet optic to achieve an almost 2D illumination plane inside the test section. The light sheet was aligned along the capillary's center plane. Highspeed image acquisition was performed with a pco.dimax HS4 (*PCO AG, Germany*) CMOS camera at a frame rate of $f = 300$ Hz and an exposure time of $t = 900$ μs. A 105 mm 1:2:8 DG macro lens (*Sigma, Japan*) allowed a high magnification and a shallow depth of field (DOF). A spatial resolution of 0.012 mm × 0.012 mm was achieved. The DOF was estimated [31] to be 0.725 mm with the given optical setup. A high-pass filter ($\lambda = 475$ nm, Carl Zeiss, Germany), mounted in front of the lens, shielded the camera's CMOS chip from scattered laser light. The camera was focused on the center plane of the capillary. Refractive index matching (RIM) minimized optical disturbances at the curved capillary interface. For this purpose, a borosilicate box was built around the test section. The box contained a glycerol/water mixture [32], matching the refractive index of the borosilicate glass ($\eta = 1.473$). A fluorescent polystyrene particle solution (Polyscience Fluoresbrite Carboxy YG Microspheres 4.5 μm, packed as 2.5% aqueous solution, $\lambda_{\text{ex}} = 441$ nm, $\lambda_{\text{em}} = 486$ nm) was suspended $(1\,\text{ml}\,\text{l}^{-1})$ in ultrapure water and used as the liquid phase. Bubbles were manually created using air. Mass transfer and bubble shrinkage was avoided by saturating the ultrapure water with air. The investigated Taylor bubbles had a length to diameter (l/d) ratio between 2 and 3.

PIV images were captured at the capillary's center plane. The camera was focused to the phase boundary of the rear cap with a high precision linear stage. A bubble was introduced, manually placed and held within the experimental reference frame. A series of 3000 – 4000 images was captured at a frame rate of $f = 300$ Hz and saved. The images were postprocessed in MATLAB before applying the actual PIV algorithm. They were cut to size and background noise was removed by using a threshold. The particle intensity was at least two times higher than the background

signal. A 2D cross-correlation approach (*xcorr2*) with a manually chosen ROI was used to align the phase boundary layer at the bubble's rear cap on all images. The bubble position of the first image acted as reference. A movement of ± 100 pixel around the reference position was tolerated. 1200 valid and consecutive images were manually checked for outliners and saved for the PIV analysis.

The flow field was analyzed by an ensemble correlation algorithm in MATLAB using the PIVlab 2.31 toolbox [33]. Interrogation window sizes were successively decreased from 64×64, over 32×32 to 16×16 pixel. The overlap was set to 50%.

The hydrodynamic results of the ensemble PIV analyses inside two cross sections ($Y–X$, $Y–Z$) are shown in Fig. 3. The full 2D flow field inside the measurement plane is represented by streamlines. The velocity magnitude is indicated by color coding. Each view shows the liquid downflow inside an empty test section, followed by the flow field inside the wake region of two independent bubbles, held in a countercurrent flow. The streamlines of the fluid inside the empty test section show a rather homogeneous flow along the capillary. Only minor disturbances in radial direction are noticeable. However, looking at the wake region of a spatially fixed bubble, the flow patterns inside both cross sections differ significantly. Inside the $Y–X$ plane very pronounced and unequal flow velocities on the left and right side of the bubble's cap are present, with streamlines pointing towards the capillary's center line. In contrast, the $Y–Z$ plane shows velocities up to one order of magnitude lower and the streamlines are pointing away from the capillary's center line. Furthermore, an additional flow arises in the vicinity of the bubble. This is explained by out of plane motion of the 3D flow field. The investigation of a series of independent bubbles has shown a reproducible asymmetrical behavior of the flow field without vortices or back mixing. This enables the use of PIV as a reference method for the MRI results inside the given setup.

3 Development of an MRI Setup for Taylor Flow Investigations Inside a Horizontal Bore MRI Scanner

MRI experiments were performed inside a BioSpec 70/20 USR (*Bruker Biospin MRI GmbH, Germany*) 7 T MRI scanner with a magnetic field gradient insert BGA 12S2 ($d_i = 116$ mm, maximum gradient strength $= 441$ mT m^{-1}). A custom-made radio frequency coil was built around the test section for excitation and reception of the magnetic resonance signal. The design of the RF coil is based on the principle of a loop-gap resonator, which was connected to a preamplifier of the MRI hardware by an inductively coupled single turn pickup coil [34]. Similar to the flow setup, the design of the RF coil and the MRI setup is described in the following section.

A first prototype of a loop-gap resonator was constructed around a single-use syringe as a proof-of-principle, investigating how it performs at the required size. Results of the first MRI measurements are shown in Fig. 4. A 5 ml single-use syringe filled with deionized water acted as a specimen and was placed inside the coil. The
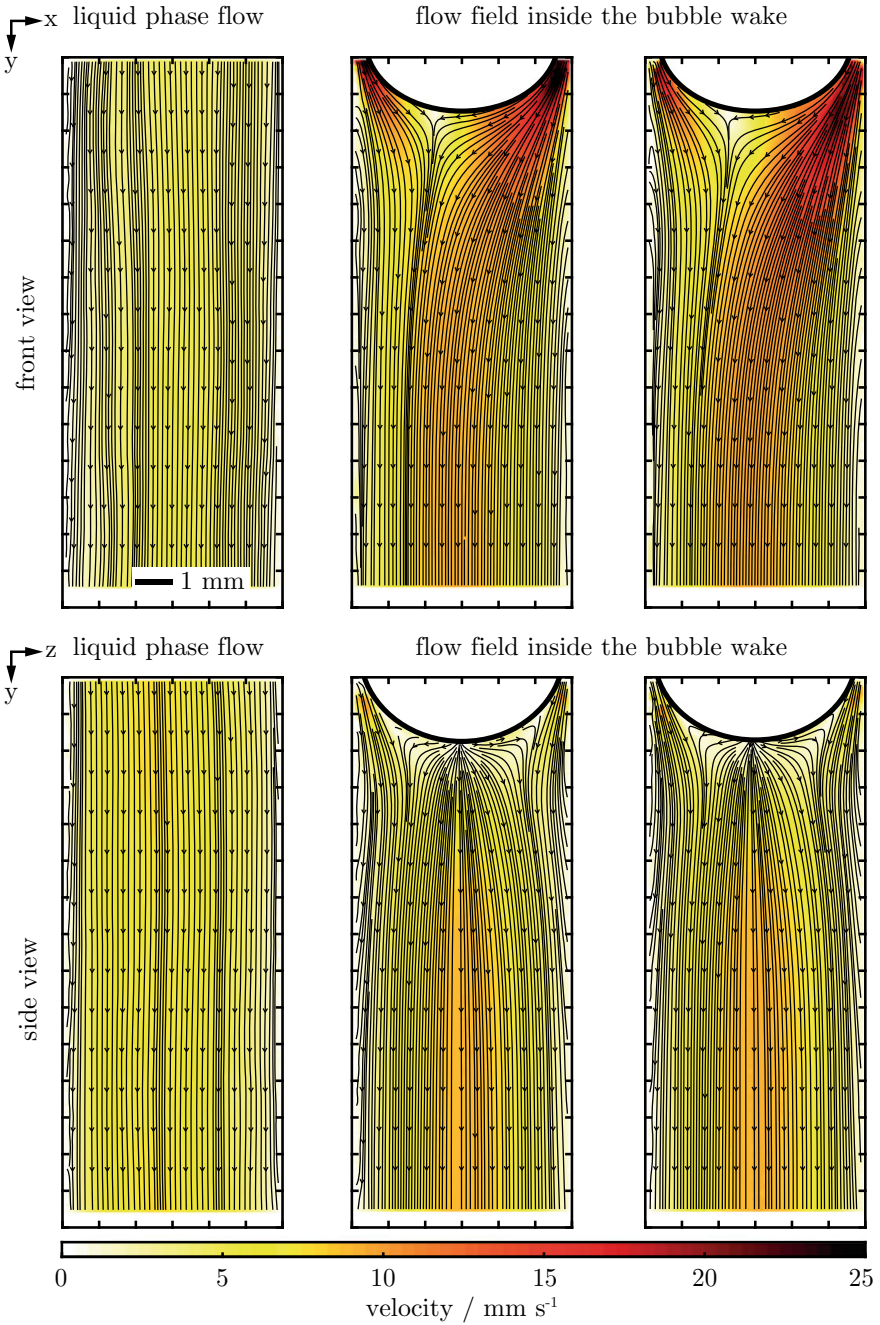
Fig. 3 Results of the hydrodynamic PIV analyses inside two cross sections (Y–X, Y–Z). The downflow inside the empty test section, as well as the flows inside the wake region of independent bubbles are shown. The 2D in-plane flow direction of the 3D flow field is represented by streamlines. The velocity magnitude is color coded and the gas liquid interface of the bubble is indicated
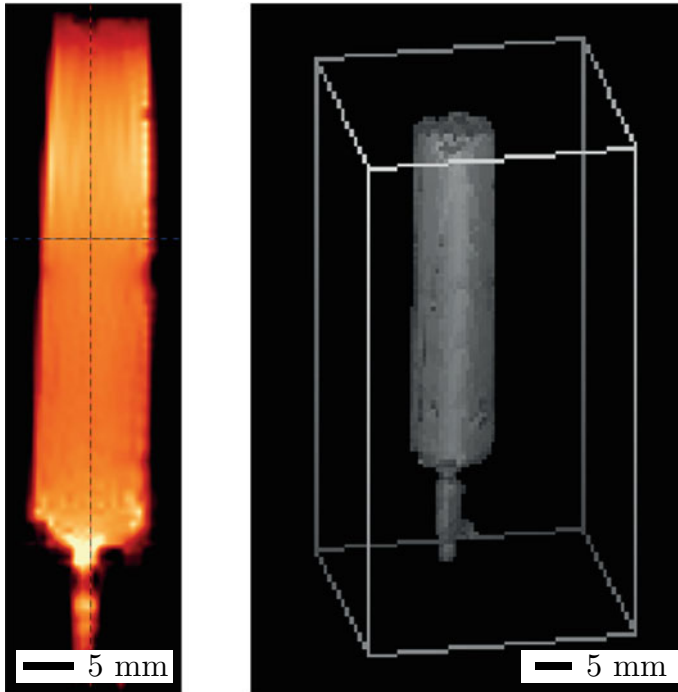
Fig. 4 Result of the first MRI measurement using a prototype of the loop-gap resonator. A 5 ml single-use syringe filled with deionized water acted as a specimen. The signal of the liquid phase was mapped in 2D and 3D using a FLASH sequence. The 2D image represents a single slice from the 3D volumetric data

signal of the liquid phase was mapped in 2D and 3D using a FLASH sequence, resulting in a strong and rather homogeneous signal. The first provisionally built version of the loop-gap resonator performed well, with promising results in mapping the water phase and was therefore further developed.

The improved loop-gap resonator was built around an acrylic tube as shown in Fig. 5a. A resonant circuit is formed by the inductance of the copper foil, glued onto the acrylic tube, and the capacitance of the chip capacitors, soldered onto the copper foil. A variable tuning capacitor allowed manual frequency matching to the ^{1}H NMR frequency at 7 T of approximately $f = 300.3$ MHz. The correct distance between the coupled coils is of crucial importance as it alters the impedance of the system. Matching it to 50 Ω avoids reflection losses and allows even small signals to be detected [35]. The vertical position of the pickup coil could be precisely adjusted by a 3D printed scissor-lift mechanism as depicted in Fig. 5b. A special holder was designed, enabling exact positioning of the test section inside the center of the MRI scanner. The holder was machined from PTFE (Polytetrafluoroethylene) which is proton-free and does not interfere with the ^{1}H NMR signal. A modular design allowed for safe and rigid mounting of the used components. An early CAD design
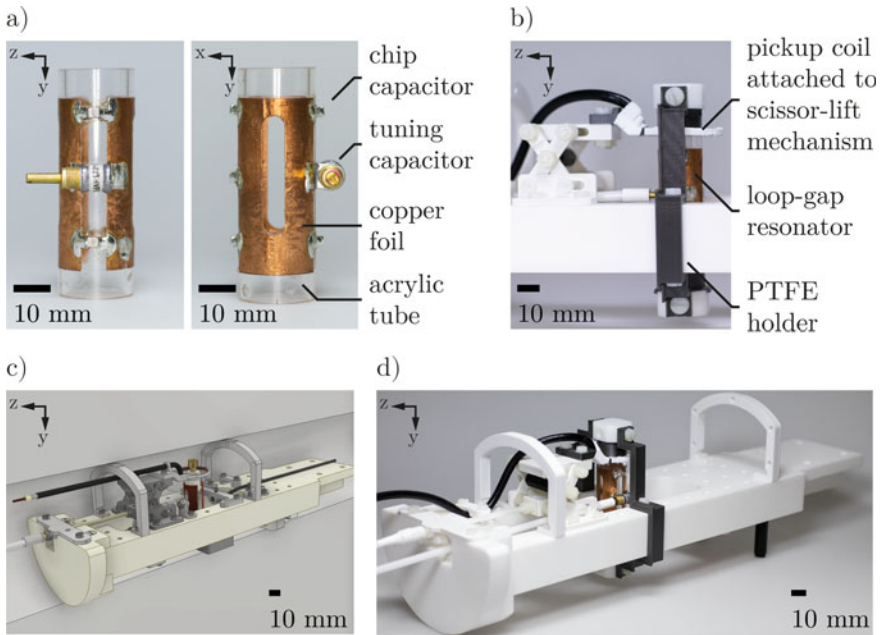
Fig. 5 Parts of the experimental MRI setup. **a** The loop-gap resonator consists of a copper foil, glued onto an acrylic tube. Chip capacitors and a tuning capacitor are soldered to the copper foil, forming the resonant circuit. **b** The pickup coil is attached to the height adjustable scissor-lift mechanism for impedance matching. **c** All parts are designed and fitted using CAD. **d** The components are mounted to the PTFE holder, which is inserted into the MRI scanner

of the holder with added parts is shown in Fig. 5c. The CAD construction of the setup helped to make full use of the limited size inside the MRI scanner. Figure 5d shows a photograph the latest MRI setup using the improved flow setup.

In-process monitoring of the test section was enabled with a camera (*Grasshopper FLIR Systems Inc, United States*) connected to an optical fiber endoscope (*Hinze Optoengineering GmbH, Germany*). This allowed a precise bubble adjustment during flow experiments inside the test section while being inserted inside the MRI scanner.

Further tests were performed with the improved loop-gap resonator. The signal intensity of a capillary filled with deionized water was measured using an MRI FLASH sequence. An overlay of the acquired MRI data and a CAD model of the specimen is shown in Fig. 6. The measured signal intensity of the water is color coded. The overlay clearly shows a good dimensional accuracy of the data, as no scaling was applied. The signal intensity fluctuates slightly within the center region of the capillary and clearly decreases at the bottom holder. This is mainly caused by a strong signal loss towards the ends of the loop-gap resonator and may also depend on the material of the capillary holder, meaning that further flow experiments should be conducted around the center of the resonator.
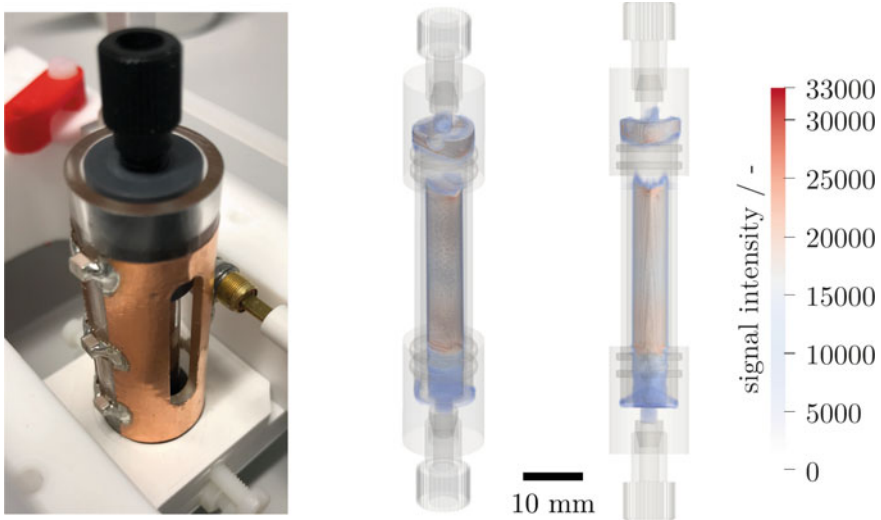
Fig. 6 A capillary filled with deionized water is placed inside the loop-gap resonator. The acquired MRI data and the CAD model of the specimen are overlaid to check for dimensional accuracy of the data. The signal intensity is color coded

An attempt has been made to extend the measurement range by using a longer loop-gap resonator, covering the complete test section of the improved flow setup. To this end, a second resonator was calculated and built. A capillary filled with deionized water was used for signal intensity measurements. A comparison of both, the short and the long resonator, is given in Fig. 7. The signal intensity of two cross-sections (Y–X, Y–Z) along the capillary's center line is shown. The short resonator shows a rather constant signal intensity with only minor fluctuations inside both views. The signal loss towards the ends of the loop-gap resonator is clearly visible, as previously seen in Fig. 6.

The long resonator was constructed to extend the field of view by 30 mm in axial direction. Unfortunately, this extension comes at a cost: The Y–Z plane shows an unevenly distributed signal intensity which is strongly pronounced at the center and towards the ends of the resonator. In between, a significant loss of signal is observed. The Y–X plane reveals a region of high intensity at the right side of the resonator. The position of greater intensity corresponds to the placement of the variable tuning capacitor. Several rearrangements of the capacitors have not improved the inhomogeneous intensity inside the longer resonator. The exact cause was not further examined, but the effect can be caused by eddy currents. Due to the inhomogeneous intensity distribution, the longer loop-gap resonator was not considered further.
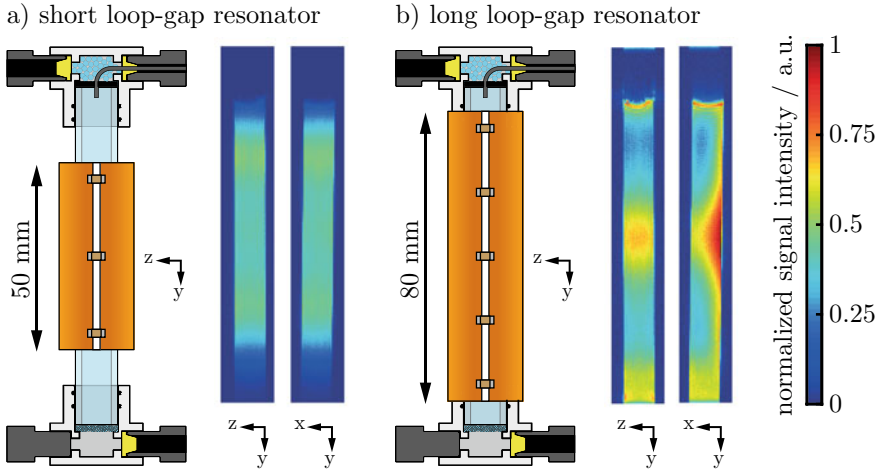
Fig. 7 Signal intensities of a deionized water sample inside two cross sections (Y–X, Y–Z). Two loop-gap resonators of different length were tested. The short 50 mm resonator **a** shows a rather constant signal across the whole field of view, whereas the long 80 mm resonator **b** has some strongly pronounced intensity maxima and minima

4 Development of an MRI Method for Taylor Flow Investigations

When performing an MR experiment, the specific method can be chosen from a large variety of different pulse sequences to obtain the data of interest. The measured data result as a response to an applied RF excitation pulse. The data are obtained in the time-domain, describing the system's response to the equilibrium state. Subsequently, a Fourier transformation is used to transform the data into the frequency-domain, providing the MRI image.

4.1 Influence of Different MRI Parameters on the Acquired Data

In order to study the influence of different MRI parameters on the resulting images, a series of measurements of an acetonitrile/N_2 system was performed inside the first version of the flow setup with a $d_i = 5$ mm capillary. Acetonitrile was chosen as the liquid phase, as the usage of a contrast agent for MRI investigations of chemical gas–liquid reactions was intended in further steps which relies on acetonitrile as a solvent. A first examination of different flip angles revealed a relationship between greater flip angles and higher signal intensities. Measurements of the fluid at rest showed a partial saturation, resulting in a signal decrease in subsequently acquired

images until a steady state was reached after around five to seven images. This effect occurs due to short repetition times of 1000 ms as the system needs sufficiently long to restore its initial magnetization. As soon as liquid flows through the capillary, the effect gets less visible due to the freshly entering fluid which has not been excited by the MRI sequence before. The saturation effect can only be seen between the first two images.

Further measurements of N_2 bubbles held in a countercurrent flow indicated an increased signal in the vicinity of the bubble. The effect can be seen in Fig. 8a. Preparation pulses were used to systematically saturate and suppress the signal arising from the liquid phase, showing only the flow related changes. The effect of pulse preparation is clearly visible in Fig. 8b.

In order to understand the investigated flow effect, the thickness of the measurement slice was varied. Figure 9a shows a series of images acquired within a slice of 2 mm thickness. Again, a defined and constant region of increased intensity is located behind the bubble, followed by altering patterns downstream the capillary. The patterns in front of the bubble are mainly caused by swirling motions of the fluid due to high flow velocities at the inlet of the glass capillary.

The observed effect is explained by protons which entered the measurement plane. Initially, the signal of all protons inside the measurement plane was nulled by preparation pulses. Protons which were carried into the measurement plane by the local flow dominated the signal. This particularly happened directly behind the bubble.

a) number of preparation pulses = 0

b) number of preparation pulses = 20

x10⁵

signal intensity / -

flip angle = 16°
repetition time = 1000 ms
slice thickness = 2000 µm

flip angle = 16°
repetition time = 1000 ms
slice thickness = 2000 µm
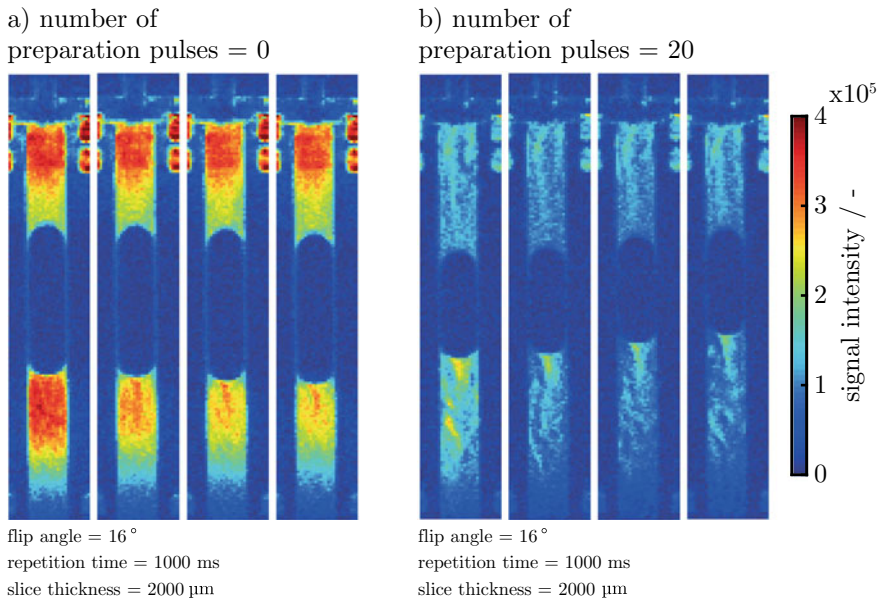
Fig. 8 MRI series showing the influence of preparation pulses on the observed wake structure. The flow pattern inside the bubble's wake is visible in both cases (**a**, **b**). The flow related effect of the liquid phase can be separated by presaturation of the observed slice (**b**)

a) slice thickness = 2000 μm   b) slice thickness = 9000 μm

flip angle = 32 °
repetition time = 1000 ms
preparation pulses = 20

flip angle = 32 °
repetition time = 1000 ms
preparation pulses = 20
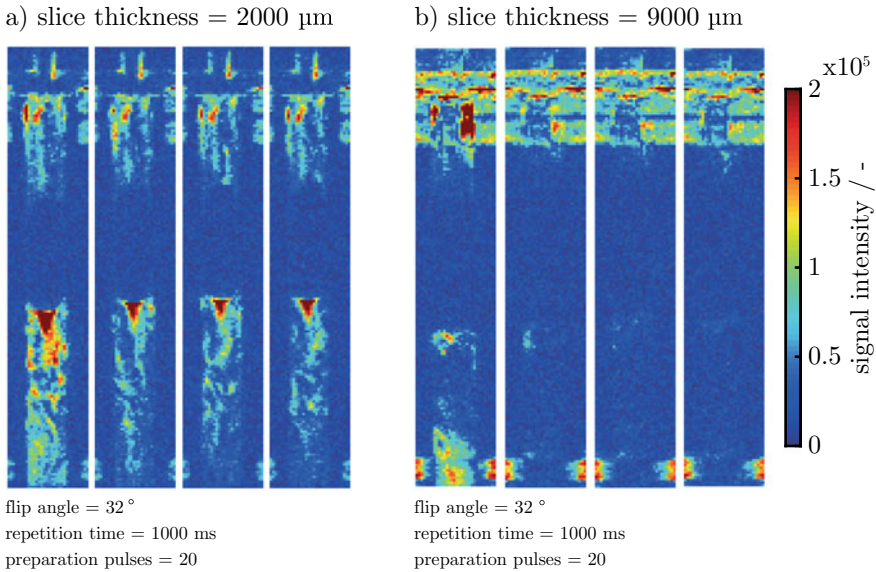
Fig. 9 MRI series showing the influence of the measurement slice thickness on the observed wake structure. A slice thickness smaller than the capillary diameter d_i (**a**) clearly shows structures within the bubble's wake, whereas no structures are visible if a slice thickness greater than d_i (**b**) is chosen

The effect of an increased measurement slice thickness of 9 mm can be observed in Fig. 9b. As the slice thickness is increased, the signal inside the wake region vanishes. By choosing a slice thickness greater than the capillary's diameter, the flow effect can no longer be mapped.

4.2 Influence of Gas–Liquid Mass Transfer on the Acquired Data

It was additionally checked if mass transfer from the gas phase to the liquid phase has any influence on the measured MRI data. Therefore, the acetonitrile was saturated with N_2. By using pure N_2 as the gas phase, no mass transfer takes place, as shown in Fig. 10a. In contrast, mass transfer is enabled by changing the gas phase to O_2. The corresponding results are shown in Fig. 10b. Both cases show similar results. Thus, no significant effect of gas–liquid mass transfer on the acquired MRI data was found.

Further measurements were carried out using a deionized water/N_2 system inside the improved version of the flow setup with a $d_i = 6$ mm and $d_i = 7$ mm capillary. An exemplary result is given in Fig. 11. Even without preparation pulses, no significant flow distortions are visible in front of the bubble.

a) N$_2$ saturated acetonitrile with N$_2$ bubble

b) N$_2$ saturated acetonitrile with O$_2$ bubble

flip angle = 16 °
repetition time = 1000 ms
preparation pulses = 20
slice thickness = 2000 µm

flip angle = 16 °
repetition time = 1000 ms
preparation pulses = 20
slice thickness = 2000 µm
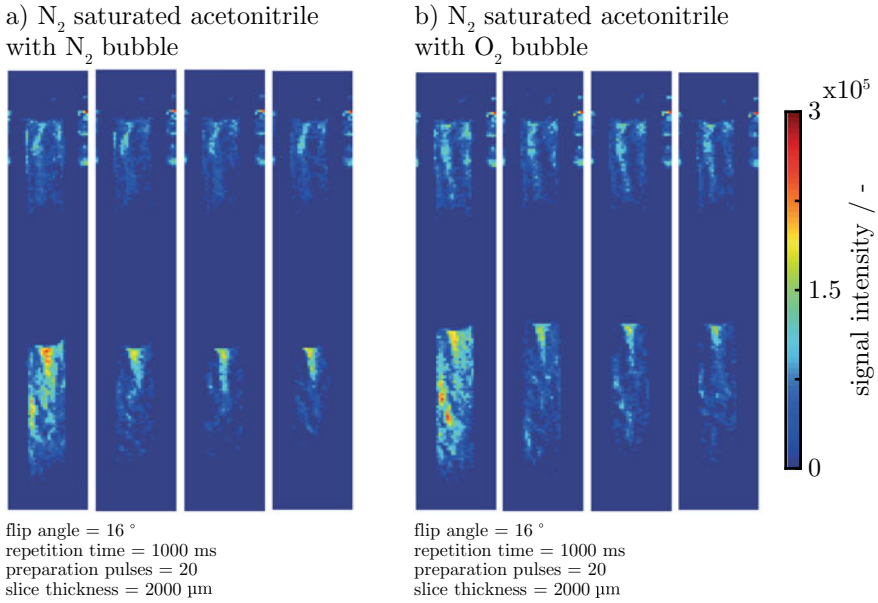
Fig. 10 MRI series showing the influence of mass transfer on the observed wake structure. In both cases, without (**a**) and with (**b**) mass transfer, the same structure inside the bubble's wake is visible

flip angle = 8 °   repetition time = 1000 ms   preparation pulses = 0   slice th. = 3000 µm
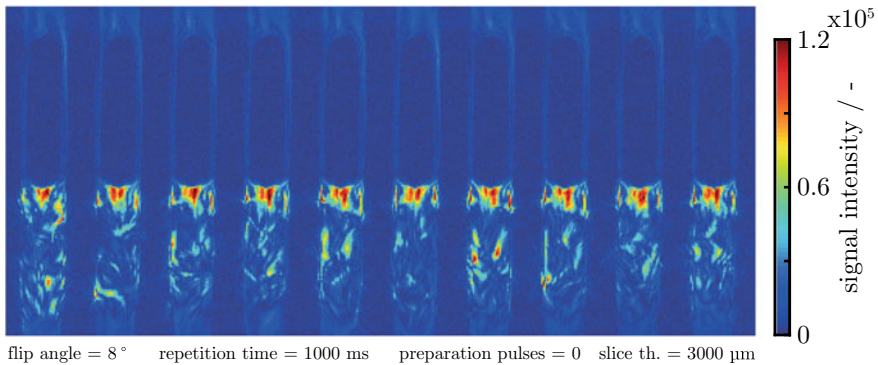
Fig. 11 MRI series showing the wake region behind a N$_2$ bubble inside a deionized water countercurrent flow. A capillary of $d_i = 7$ mm was used. The signal inside the wake is significantly increased

The results from the water/N$_2$ experiments were used to develop an MRI sequence for time resolved flow mapping inside the test section. Furthermore, the MRI and PIV data from the $d_i = 6$ mm capillary were acquired under identical hydrodynamic conditions and can be compared with each other to validate the results measured by MRI.

The final flow experiments with the specially developed MRI sequence were conducted with N_2 as the gas phase. N_2 does not contribute to the ^{1}H NMR signal and is therefore completely invisible within the MRI data. Deionized water acted as the liquid phase. To avoid any mass transfer between both phases, the water was saturated with N_2. Preventing mass transfer helps to maintain a constant bubble size which results in a better flow control. The flowrate was manually adjusted to hold the bubble in place. The investigated Taylor bubbles had a length to diameter (l/d) ratio between 2 and 3. The sequence for MRI flow mapping as well as the data acquisition and processing procedures are described in the following sections.

4.3   MRI Sequence for Taylor Flow Investigation

A snapshot-FLASH sequence [36] was used for time-resolved flow mapping. Therefore, data were acquired within a vertical single plane through the capillary's center line. Initially, the signal of all water protons inside the measurement plane was nulled by a presaturation module. After a specified delay time t_d, the signal was read out. Water protons which entered the measurement plane during the specified delay time dominated the signal. Increasing the delay time lead to stronger MRI signals, dominated by inflow of unsaturated water protons. The T1 relaxation of stationary spins contributed only partially to the signal. The MR experiments were performed using ParaVision 5.1. A snapshot-FLASH sequence was used and extended by an additional presaturation module. The slice thickness of the acquired MR images was set to 2 mm. A field of view of 42 mm × 16 mm with an isotropic in-plane resolution of 0.5 mm was chosen. A frame rate of 1 Hz was achieved by acquiring an image in four segments with a partial Fourier acceleration rate of 1.5 and an interval of 250 ms. The data read out was performed in parallel direction to the flow (Y-axis) with an echo time of 0.811 ms, excitation pulses of 3°, an echo position of 30% and an image bandwidth of 200 kHz. The presaturation module consisted of three slice-selective 90° hyperbolic secant pulses, followed by crusher gradients with a total length of 13.46 ms. The delay times t_d were set to 4.88, 24.88, 54.88 and 104.88 ms and mark the time span between the last saturation and the first excitation pulse. MR images were acquired in two orthogonal planes. The orientation of the planes is referenced to the convention of MRI magnets, where the front view describes the Y–X and the side view the Y–Z plane. Detailed information on the used MRI sequence and setup is given in [40].

4.4   MRI Data Acquisition and Processing

MRI images were acquired along the capillary's center line. A bubble was manually introduced and placed within the experimental reference frame. The bubble position was monitored by an optical fiber endoscope. 64 images were captured at a frame
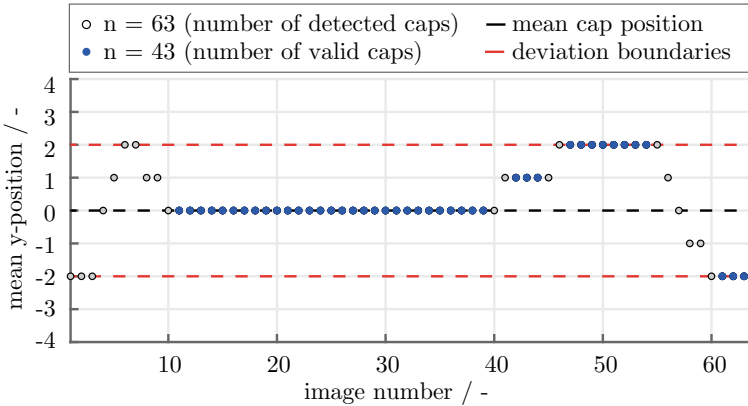
Fig. 12 Temporal bubble movement of one exemplarily chosen MRI dataset. The shift around the mean y-position is determined. Valid images (blue dots) are used for further processing

rate of 1 Hz. Postprocessing of the MRI data was performed in MATLAB to correct possible bubble movement during the experiment. As multiple images were used to calculate the mean data, a precise alignment of the images, with respect to the bubble's rear cap position, was crucial. The data were imported into MATLAB using ParaVision's specific format. Required information were extracted from the method, 2dseq and reco files. A 2D cross-correlation approach (*xcorr2*) was used for bubble tracking. The bubble position of the first image acted as reference with a region of interest (ROI) of 23 by 23 voxel around the rear cap position. The vertical movement for the whole dataset was calculated with respect to the reference image, resulting in a mean cap position. Valid images were then selected according to two criteria as shown in Fig. 12. Firstly, the tolerated movement around the mean position was constrained by manually set boundaries of ± 2 voxel to eliminate outliners. Secondly, an image was only recognized as valid, if the previous and next cap positions equaled the one under investigation. This helped to prevent artefacts and blurred images from quickly moving bubbles. The valid images were shifted and used to calculate the averaged MRI image and standard deviation. At least 30 valid images were used for the Taylor flow investigations. Additionally, the signal to noise ratio (SNR) was estimated [37] as a measure of quality. A 12 by 12 voxel region inside the wake (signal) was compared to an equally spaced region inside the bubble (noise).

5 MRI of Hydrodynamics Inside Taylor Flows

The hydrodynamics around a N_2 Taylor bubble were investigated by using the improved countercurrent flow setup shown in Fig. 2 and the developed MRI specific methods described in 8.4.3. Images were acquired from two cross sections (Y–X, Y–Z) at four different delay times t_d. Water molecules are exchanged between the

surrounding volume and the measurement plane during the delay time. Higher flow velocities, as well as longer delay times increase the number of interchanged water molecules, resulting in higher signal intensities. The resulting averaged MRI signal intensities for four different delay times are exemplarily shown for the $Y–X$ plane in Fig. 13. Clear distinct flow maxima inside the wake are visible, especially at longer delay times, due to the increased number of exchanged water molecules.

In the $Y–X$ plane, high flow velocities are present on the left and right side of the bubble, whereas the $Y–Z$ plane shows a maximum signal centered below the bubble. The flow pattern shown by the MRI data cannot be characterized as symmetric or homogeneous as the results show neither rotational nor axial symmetry. Previous hydrodynamic investigations of gas–liquid Taylor flows [9, 12] have shown rotational symmetry. Prerequisite for this is a sufficiently long entrance length, allowing the
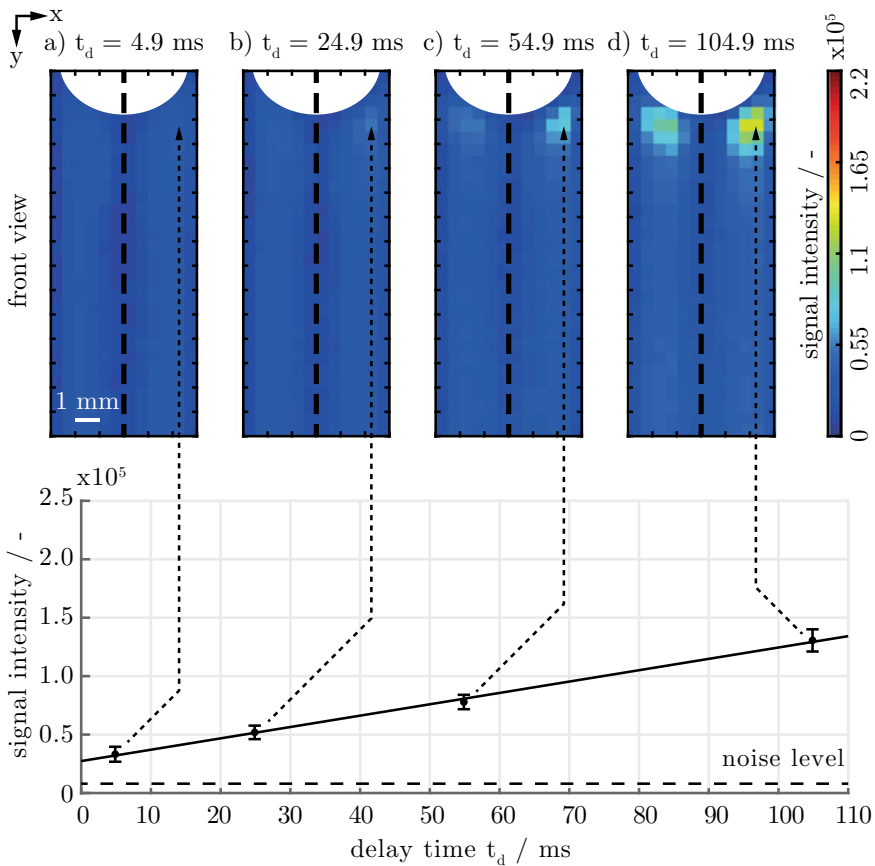
Fig. 13 Averaged MRI images of the bubble's wake region inside the $Y–X$ plane. The time-dependent intensity increase of the signal is plotted at the voxel position of the overall highest intensity. The voxel position is additionally indicated by the dashed arrows

Table 2 Number of processed images and SNRs for different delay times of both views

Y–X plane/front view				
Delay time t_d	4.9 ms	24.9 ms	54.9 ms	104.9 ms
Images (n)	44	32	31	33
SNR	3.7	4.4	5.2	6.9
Y–Z plane/side view				
Delay time t_d	4.9 ms	24.9 ms	54.9 ms	104.9 ms
Images (n)	58	33	30	43
SNR	3.4	4.4	5.7	8.2

flow to develop. As the experimental MRI setup is limited in height, this requirement cannot be fulfilled. Measures were taken to minimize flow alterations, even at small heights. After the flow enters sideways into the test section, it is deflected downwards by a bed of packed glass beads and passes a small pore glass membrane before entering the capillary. Both, the beads and the membrane, acting as flow straighteners. Additionally, the inertia of the system was kept as low as possible by choosing the smallest possible capillary diameter. With this, alterations of the flow were further reduced but not fully suppressed. However, an advantage can be taken from the present asymmetric and stationary flow field: Systematic errors are eliminated by clearly distinguishing between both cross-sectional views.

In addition to the averaged MRI signals, the time-dependent signal increase is plotted at the voxel position of the overall highest signal intensity and is also exemplarily given in Fig. 13. The corresponding voxel positions are indicated by the dashed arrows. Even at short delay times, signal intensities are large enough to differentiate them from background noise, as marked by the dashed horizontal line. This means that fast measurements are possible. However, short delay times will significantly reduce the signal to noise ratio as listed in Table 2.

Even delay times of 104.9 ms were sufficiently short to resolve the present flow field with a high SNR of around 8.2. A signal readout time of around 58 ms would be necessary for a snapshot-FLASH sequence with 32 phase encoding steps. This readout time was significantly reduced by using a partial Fourier acceleration rate of 1.5 to asymmetrically truncate the k-space. The image acquisition was segmented into four parts with a readout time of 8.9 ms for each segment. This means that all MRI images are marginally biased by flow related artifacts, which are particularly noticeable at short delay times up to several ms with a vanishing impact at long delay times.

Local MRI intensity plots inside the Y–X plane are shown in Fig. 14. The distance from the bubble is increased voxel-vise from I to VII, starting directly behind the maximum value. A linear regression line has been fitted, representing the time dependent signal intensity of a given voxel at different delay times. The intensity will presumably reach an overall maximum if sufficiently long delay times are chosen, as all water molecules inside the measurement plane are replaced and longitudinal magnetization is restored by T1 relaxation. At increasing distances from the bubble,
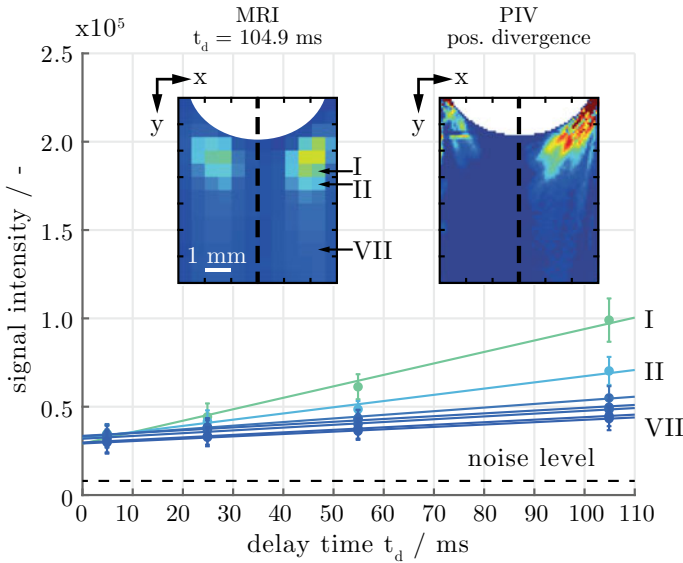
Fig. 14 Local MRI intensity plot inside the Y–X plane. The distance from the bubble is increased voxel-vise from I to VII and plotted for all delay times. Additionally, MRI data at $t_d = 104.9$ ms is compared with the divergence calculated from the PIV results. Only the positive part of the divergence is mapped, resembling the same data as obtained from MRI measurements

a flattening of the slope is observed. This is explained by the stronger radial flow in the vicinity of the bubble, as more water molecules are carried into the measurement plane. This makes the slope an indicator for the amount of flow entering over a given time period, which relates to a measure of velocity. The linearity of the intensity demonstrates the presence of a simple flow inside the wake region without vortices or back mixing.

To directly compare MRI and PIV results, the divergence of the PIV flow field was calculated. It resembles the flux into (positive part) and out of (negative part) the measurement plane. As the MRI data solely represents the flux into the measurement plane, only the positive part of the divergence was examined. Due to the high spatial resolution and accuracy of the results, PIV is particularly suitable as a reference method for hydrodynamic investigations. Figure 14 exemplarily shows a side-by-side comparison of the measured MRI data and the divergence, calculated from the PIV flow data inside the Y–X plane. The data is normalized for each method between zero and the maximum value inside the wake of the Y–Z plane (not shown here). The stationary, and asymmetrical behavior of the flow field is equally observed in both methods. The Y–X plane reveals two regions of increased flux, located in the vicinity of the bubble with a stronger pronounced signal on the right hand. In contrast, a region of strong flux appears directly centered behind the bubble within the Y–Z plane.

It is important to note that the measurement plane thickness differs between both methods. For the MRI measurements, it is defined by the gradient strength of the experiment and amounts to 2.0 mm. The thickness of 0.725 mm for the PIV measurements is defined by the optical setup's depth of field. Furthermore, it is to mention that MRI measurements were conducted using N_2 whereas PIV measurements used air as the gas phase. The liquid phase was saturated with the used gas phase in all experiments to avoid bubble shrinkage and mass transfer. An influence of the used gas phase on the results can be ruled out, as only hydrodynamic studies without any mass transfer were conducted and N_2 and air have similar physical properties. The MRI experiments benefit from the use of N_2, as it gives no ^{1}H NMR signal. The results show good qualitative agreements between MRI and PIV.

6 MRI of Chemical Reactions Inside Taylor Flows

As a first approach to investigate chemical reactions by MRI under real Taylor flow conditions, T1 relaxation time measurements were performed inside the MRI setup. The test section inside the loop-gap resonator was replaced by 2 ml crimp top vials, containing the chemical samples. A Cu(btmgp)I complex was dissolved inside pure acetonitrile and filled into the vials under exclusion of air. At room temperature Cu(btmgp)I experiences a transition of Cu(I) over Cu(III) to Cu(II) which takes place in around 4 s when exposed to dioxygen. The formation of Cu(III) takes place very fast and is assumed to be limited by mass transfer, which means that the decay of the Cu(III) complex is the rate-indicating step of the chemical reaction [38]. The same copper complex was already used for MRI investigations of chemical gas–liquid reactions inside a high-viscous acetonitrile/polyethylene glycol solution ($\eta = 800$ mPa s) with O_2 bubble rise velocities ranging from 0.14 to 0.5 mm s^{-1} [29].

T1 relaxation times of two different Cu(btmgp)I concentrations (1 and 10 mmol l^{-1}) were determined by inversion recovery measurements after the reaction with O_2 (Fig. 15).

Compared to pure acetonitrile, a noticeable decrease of the T1 relaxation times with increasing Cu(btmgp)I concentrations after reaction with dioxygen is observed. After contact with dioxygen, T1 and T2 relaxation times are shortened due to the paramagnetic behavior of the formed Cu(II) species [29].

Two fundamental problems are encountered for the investigation of chemical reactions by MRI under real Taylor flow conditions: Firstly, the necessary transition time from Cu(I) to the paramagnetic Cu(II) species lies within the same order of magnitude as the residence time of the fluid inside the test section. One possible workaround would be to preheat the solution to increase the rate constant of the Cu(III) decay and therefore the formation of Cu(II). A temperature increase of 10 K has shown to cut the decay period by one half [38]. In this case a temperature increase of $\Delta T = 60$ K is required to perform measurements in below $t = 100$ ms. This would result in a total temperature just below the boiling point of the solvent. A
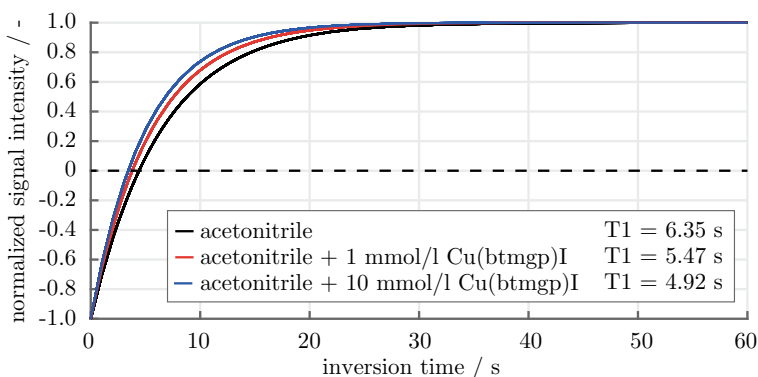
Fig. 15 Inversion recovery measurements for T1 relaxation time calculations of pure acetonitrile and two different Cu(btmgp)I concentrations dissolved in acetonitrile

drawback is the adverse effect of increased temperatures on the SNR of the MRI data. Furthermore, a precise temperature measurement inside the test section is necessary to precisely determine the rate constant of the reaction.

Secondly, the results of Fig. 15 show that at short measurement times, as required for fast flow mapping, the signal intensity between the pure solvent and the paramagnetic Cu(II) species is indistinguishable. Choosing higher Cu(btmgp)I concentrations is not an option, as the concentration of $10 \, \text{mmol} \, \text{l}^{-1}$ already showed a precipitation inside the sample, which will most likely influence the MRI measurements.

A second chemical reaction system used during this priority program is the FeII(edta)/NO system [39]. Its color changing reaction has already been used for optical mass transfer studies [2, 20]. The system is currently prepared for MRI Taylor flow investigation at the time of writing. No statement can be made at this point whether the system is suitable for chemical reaction measurements under real Taylor flow conditions or not.

There are many fundamental requirements to successfully perform MRI studies, especially when dealing with fast spatially resolved measurements of chemical reactions inside two-phase flows. Special demands are placed on the experimental setup. It has to fulfill the requirements of MRI compatibility in terms of size, materials, periphery, etc. Ferromagnetic materials cannot be used inside or near the MRI system. The same applies to electrical peripheries such as pumps, cameras, sensors etc. If possible, the usage of any kind of metal should be avoided inside the MRI scanner to prevent eddy currents, resulting in erroneous measurements. Furthermore, a suitable and MRI active reaction system is needed. The kinetics of the reaction need to go well with the residence times inside the investigated setup. Fast kinetics are needed for time-critical investigations of e.g. complex flows. Also, an appropriate MRI sequence for the phenomena or parameters of interest is required. If possible, an existing sequence should be used and potentially modified for the investigated problem. Depending on the investigated flow, a tradeoff between acquisition speed and image quality has to be accepted. If steady state measurements are possible, the

image quality can be increased at the cost of losing temporal information by averaging a large number of single images. If complex flows are analyzed, the image resolution has to be adjusted to the required temporal resolution.

7 Conclusion and Outlook

Non-invasive flow measurements of pure low-viscous gas–liquid Taylor flows inside a horizontal bore MRI scanner were successfully conducted. For that, a MRI compatible Taylor flow setup and a suitable loop-gap resonator were built. A countercurrent flow configuration was used to conduct measurements over an extended period of several minutes. Preliminary experiments were conducted to develop a suitable MRI sequence for the visualization of Taylor flows.

MRI flow visualization was performed with a modified snapshot-FLASH pulse sequence with presaturation. The sequence was improved in terms of reduced motion blurring and shorter acquisition times. PIV experiments were conducted inside the same flow setup and compared to the MRI results. Taylor flows could successfully be generated inside the setup of limited height, showing an asymmetrical but stationary flow. These asymmetrical flow conditions were beneficial, as they contributed to a better understanding of the developed method. A time dependent flow analysis is enabled by the introduced variable delay time t_d, allowing to spatially resolve the flow progression over time. A qualitative comparison of both methods reveals certain similarities of local changes in flow, which are in good qualitative agreement.

First tests were performed using a chemical reaction system. The utilized Cu(btmgp)I complex dissolved in the aqueous solution acts as a contrast agent by reducing T1 relaxation times after contact with O_2 entering the solution from the bubble. It could be shown that the reaction kinetics are to slow for the investigated problem. A significant reduction of T1 relaxation times was measured between pure solvent and two concentrations of the copper complex. However, the signal intensities were only marginally different and undistinguishable at low measurement times. Future investigations will be performed for the FeII(edta)/NO reaction system [39].

An initial step in paving the way towards a spatially resolved 3D flow analysis of gas–liquid Taylor flows under relevant flow conditions is presented. The described method for flow analysis provides an important contribution to separately quantify the effect of superimposed chemical reactions. However, the investigation of chemical reactions by MRI under relevant Taylor flow conditions is still at the beginning an especially challenging for low viscous liquids. Future investigations require reaction systems with suitable reaction kinetics as well as fast and distinguishable MRI detectability of reactants and products.

References

1. Shen G, Finch JA (1996) Bubble swarm velocity in a column. Chem Eng Sci 51(14):3665–3674
2. Merker D, Böhm L, Oßberger M, Klüfers P, Kraume M (2017) Mass transfer in reactive bubbly flows–a single-bubble study. Chem Eng Technol 40(8):1391–1399
3. Kück UD, Mießner U, Aydin M, Thöming J (2018) Mixing time and mass transfer of rising bubbles in swarm turbulence. Chem Eng Sci 187:367–376
4. Direito FJN, Campos JBLM, Miranda JM (2017) A Taylor drop rising in a liquid co-current flow. Int J Multiph Flow 96:134–143
5. Hayashi K, Kurimoto R, Tomiyama A (2011) Terminal velocity of a Taylor drop in a vertical pipe. Int J Multiph Flow 37(3):241–251
6. Helmers T, Kemper P, Thöming J, Mießner U (2019) Modeling the excess velocity of low-viscous Taylor droplets in square microchannels. Fluids 4(3):162
7. Meyer C, Hoffmann M, Schlüter M (2014) Micro-PIV analysis of gas–liquid Taylor flow in a vertical oriented square shaped fluidic channel. Int J Multiph Flow 67:140–148
8. Nogueira S, Riethmuller ML, Campos JBLM, Pinto AMFR (2006) Flow patterns in the wake of a Taylor bubble rising through vertical columns of stagnant and flowing Newtonian liquids: an experimental study. Chem Eng Sci 61(22):7199–7212
9. Boden S, Haghnegahdar M, Hampel U (2017) Measurement of Taylor bubble shape in square channel by microfocus X-ray computed tomography for investigation of mass transfer. Flow Meas Instrum 53:49–55
10. Butler C, Cid E, Billet AM (2016) Modelling of mass transfer in Taylor flow: investigation with the PLIF-I technique. Chem Eng Res Des 115:292–302
11. Kastens S, Hosoda S, Schlüter M, Tomiyama A (2015) Mass transfer from single Taylor bubbles in minichannels. Chem Eng Technol 38(11):1925–1932
12. Kastens S, Timmermann J, Strassl F, Rampmaier RF, Hoffmann A, Herres-Pawlis S, Schlüter M (2017) Test system for the investigation of reactive Taylor bubbles. Chem Eng Technol 40(8):1494–1501
13. Bergman TL, Lavine AS, Incropera FP, DeWitt DP (2018) Fundamentals of heat and mass transfer, 8th edn. Wiley
14. White ET, Beardmore RH (1962) The velocity of rise of single cylindrical air bubbles through liquids contained in vertical tubes. Chem Eng Sci 17(5):351–361
15. Liao Q, Zhao TS (2003) Modeling of Taylor bubble rising in a vertical mini noncircular channel filled with a stagnant liquid. Int J Multiph Flow 29(3):411–434
16. Bothe D, Reusken A (2017) Transport processes at fluidic interfaces. Springer Publishing
17. Raffel M, Willert CE, Scarano F, Kähler CJ, Wereley ST, Kompenhans J (2018) Particle image velocimetry: a practical guide (experimental fluid mechanics), 3rd edn. Springer
18. Felis F, Strassl F, Laurini L, Dietrich N, Billet AM, Roig V, Herres-Pawlis S, Loubière K (2019) Using a bio-inspired copper complex to investigate reactive mass transfer around an oxygen bubble rising freely in a thin-gap cell. Chem Eng Sci 207:1256–1269
19. Herres S, Heuwing AJ, Flörke U, Schneider J, Henkel G (2005) Hydroxylation of a methyl group: synthesis of [Cu$_2$ (btmmO) 2I]+ and of [Cu$_2$ (btmmO) 2] 2+ containing the novel ligand bis (trimethylmethoxy) guanidino propane (btmmO) by copper-assisted oxygen activation. Inorg Chim Acta 358(4):1089–1095

20. Hlawitschka MW, Oßberger M, Backes C, Klüfers P, Bart HJ (2017) Reactive mass transfer of single NO bubbles and bubble bouncing in aqueous ferric solutions–a feasibility study. Oil Gas Sci Technol-Revue D'IFP Energies Nouvelles 72(2):11
21. Reiser MF, Semmler W, Hricak H (2007) Magnetic resonance tomography. Springer Publishing
22. Stapf S, Han S (2006) NMR imaging in chemical engineering, 1st edn. Wiley-VCH
23. Britton MM (2017) MRI of chemical reactions and processes. Prog Nucl Magn Reson Spectrosc 101:51–70
24. Sadeghi M, Mirdrikvand M, Pesch GR, Dreher W, Thöming J (2020) Full-field analysis of gas flow within open-cell foams: comparison of micro-computed tomography-based CFD simulations with experimental magnetic resonance flow mapping data. Exp Fluids 61:1–16
25. Ulpts J, Kiewidt L, Dreher W, Thöming J (2018) 3D characterization of gas phase reactors with regularly and irregularly structured monolithic catalysts by NMR imaging and modeling. Catal Today 310:176–186
26. Gladden LF, Sederman AJ (2017) Magnetic resonance imaging and velocity mapping in chemical engineering applications. Annu Rev Chem Biomole Eng 8:227–247
27. Hosotani K, Ono A, Takeuchi K, Hashiguchi Y, Nagahata T (2017) Flow visualization of simple pipe and channel flows obtained by MRI time-slip method. J Visualization 20(2):321–335
28. Tayler AB, Holland DJ, Sederman AJ, Gladden LF (2012) Applications of ultra-fast MRI to high voidage bubbly flow: measurement of bubble size distributions, interfacial area and hydrodynamics. Chem Eng Sci 71:468–483
29. Benders S, Strassl F, Fenger B, Blümich B, Herres-Pawlis S, Küppers M (2018) Imaging of copper oxygenation reactions in a bubble flow. Magn Reson Chem 56(9):826–830
30. Stephan P, Kabelac S, Kind M, Mewes D, Schaber K, Wetzel T (2019) VDI-Wärmeatlas: Fachlicher Träger VDI-Gesellschaft Verfahrenstechnik und Chemieingenieurwesen (Springer Reference Technik) (German Edition) (12. Aufl. 2019 edn). Springer Berlin Heidelberg
31. Rowlands A (2017) Physics of digital photography. IOP Publishing
32. Helmers T, Kemper P, Mießner U, Thöming J (2020) Refractive index matching (RIM) using double-binary liquid–liquid mixtures. Exp Fluids 61(2):64
33. Thielicke W, Stamhuis E (2014) PIVlab–towards user-friendly, affordable and accurate digital particle image velocimetry in MATLAB. J Open Res Softw 2(1)
34. Mispelter J, Lupu M, Briguet A (2015) NMR probeheads for biophysical and biomedical experiments: theoretical principles and practical guidelines, 2nd edn. Imperial College Press
35. Mispelter J, Lupu M (2008) Homogeneous resonators for magnetic resonance: a review. C R Chim 11(4–5):340–355
36. Haase A (1990) Snapshot FLASH MRI. Applications to T1, T2, and chemical-shift imaging. Magn Resonan Med 13(1):77–89
37. Dietrich O, Raya JG, Reeder SB, Reiser MF, Schoenberg SO (2007) Measurement of signal-to-noise ratios in MR images: influence of multichannel coils, parallel imaging, and reconstruction filters. J Magn Resonan Imaging Official J Int Soc Magn Resonan Med 26(2):375–385
38. Schurr D, Strassl F, Liebhäuser P, Rinke G, Dittmeyer R, Herres-Pawlis S (2016) Decay kinetics of sensitive bioinorganic species in a SuperFocus mixer at ambient conditions. React Chem Eng 1(5):485–493
39. Schneppensieper T, Wanat A, Stochel G, Goldstein S, Meyerstein D, van Eldik R (2001) Ligand effects on the kinetics of the reversible binding of NO to selected aminocarboxylato complexes of iron (II) in aqueous solution. Eur J Inorg Chem 2001(9):2317–2325
40. Kemper P, Küstermann E, Dreher W, Helmers T, Miessner U, Besser B, Thöming J (2021) Magnetic Resonance Imaging for Non-invasive Study of Hydrodynamics Inside Gas-Liquid Taylor Flows. Chem Eng Technol 44(3):465–476

Investigation of the Influence of Transport Processes on Chemical Reactions in Bubbly Flows Using Space-Resolved In Situ Analytics and Simultaneous Characterization of Bubble Dynamics in Real-Time

Jajnabalkya Guhathakurta, Daniela Schurr, Günter Rinke, Daniel Grottke, Manfred Kraut, Roland Dittmeyer, and Sven Simon

Abstract For investigations of concentration profiles around bubbles in millichannels as Taylor flow and in bubble columns two in situ real-time process analysis systems were developed. The first system uses laser Raman spectroscopy combined with real-time digital holography. The Raman part of the system is based on a custom pulsed high-energy laser. With this process analysis system, it is possible to measure concentrations of many chemical compounds selectively, with a spatial resolution in the micrometer range during a $10\,\mu s$ laser pulse. Due to the two combined principles, the determination of the position of a measured local concentration relative to the gas bubble is possible and has been demonstrated. The second real-time process analysis system is especially suited for colored chemical reactions. The system is based on real-time UV/VIS 2D tomography such that with time the third dimension of a 3D concentration profile in the bubble wake can be determined. It consists of fast line sensors illuminated by a laser light sheet. This light sheet originates from a laser spot moving around one third of the bubble column repeatedly. This system is applicable to freely ascending single bubbles as well as bubbly flows in bubble columns.

1 Introduction and Aims

The task of chemical process engineering is to optimize productions in terms of high yield, good selectivity and low waste streams. For this purpose, chemical industry often carries out reactions such as oxidations, hydrogenations or chlorinations in

J. Guhathakurta (✉) · D. Grottke · S. Simon
Institute for Parallel and Distributed Systems, University of Stuttgart, Universitätsstraße 38,
70569 Stuttgart, Germany
e-mail: jajnabalkya.guhathakurta@ipvs.uni-stuttgart.de

D. Schurr · G. Rinke · M. Kraut · R. Dittmeyer
Karlsruhe Institute of Technology, Institute for Micro Process Engineering,
Hermann-von-Helmholtz-Platz 1, 76344 Eggenstein-Leopoldshafen, Germany

163

bubble columns in which gases are injected into liquids [1]. Here, the transport resistances of phase boundaries and boundary layers as well as flows play an important role [2, 3]. More recent approaches aim at the use of more defined flow states, such as Taylor flows [4, 5] in structured reactors. In the past, integrally measured data were used to model mass transport in bubbly flows. Here, an average bubble size and the ascending velocity as well as the mass system (viscosity and diffusion coefficient) are considered. The transport resistance is seen as a fluid-side influence. Local hydrodynamic effects in the swarm of bubbles (e.g. mixing by wake vortices) are so far only considered empirically in the form of constants. The hydrodynamic conditions within a bubble column are characterized by bubble-induced uplift flows and swarm turbulence, which are unsteady and anisotropic. Therefore, for description of the hydrodynamic conditions in the bubble swarm, the characterizations of the gas phase flow (bubble size distribution, dynamic bubble shape, bubble velocity, gas content) as well as the liquid flow (flow fields, turbulence) are necessary. In order to understand the chemical interaction of gas phase flow and liquid flow, it is essential to measure the concentration of the educt and product with a high spatial and temporal resolution in order to deduce the selectivity which is the focus of this Priority Program SPP 1740 of the German Research Foundation.

In this project, new in situ concentration measurement methods will be developed and applied to Taylor flows and bubble columns in collaboration with SPP 1740 partners from the fields of simulation, process engineering and chemistry. In addition, a continuous-flow setup with UV/VIS spectroscopy for a SuperFocus Mixer has been applied to gain fundamentally new knowledge in process engineering for Taylor flows and bubble columns using UV/VIS spectroscopy according to the focus of the Priority Program SPP 1740.

The following list of proposed methods and their realizations reflect the structure of the following subsections:

1. **Real-time Raman Process Analysis System**
2. **Real-time Tomographic Process Analysis System**
3. **Continuous-flow UV/VIS Spectroscopy for a SuperFocus Mixer**

The respective bubbles may be free rising single bubbles in a bubble column or a small swarm in a 'pulsed' bubble column with low or medium gas content. In this case, the observed gas bubble or the small bubble swarm follows the bubbles with medium gas content, which produce an instationary flow profile. The hydrodynamic properties of this profile are very similar to usual continuously rising bubbles in bubble columns with medium gas content which is the relevant test object of investigation.

An established method to perform in situ concentration measurements in liquids is Laser-induced fluorescence (LIF) [6]. It has the advantage that it is sensitive and fast such that low concentrations can be measured quickly. However, it must be taken into account that the fluorescence can be quenched by other ingredients and is temperature-dependent. LIF is used in particular for the observation of mixing processes if fluorescent dissolved substances or tracer particles are used. The investigation of chemical reactions by LIF requires fluorescent educts or products, which greatly limits the application.

Raman spectroscopy [7, 8] is more universally applicable, since almost all molecules show a Raman spectrum. Like IR spectroscopy it is very selective. However, IR is a pure transmission method and does not allow the measurement of a small volume, since it is integrated along the absorption path. Raman spectroscopy allows a quantitative analysis that can be used in situ and allows a local resolution of about 10 μm within liquids [9, 10]. While water in the IR absorbs all light after only a few micrometers, it hardly interferes with the Raman spectra of other substances. Limitations of Raman spectroscopy are low sensitivity, interference from fluorescent substances and disturbing absorption of laser radiation and Raman light in case of colored solutions.

Since colored reaction systems are also developed within the framework of the SPP 1740, UV/VIS spectroscopy can also be applied. However, just like IR spectroscopy, this is one-dimensional and only allows the determination of the average concentration along the light beam. Therefore, the classical UV/VIS spectroscopy shall be extended for a real-time 2D tomographic system providing 3D information over time.

2 Experimental Setups

In this work two real-time process analysis systems for concentration measurements in bubbly flows are presented namely: the real-time Raman process analysis system and the real-time tomographic process analysis system based on UV/VIS tomography. As fluidic setup, gas-liquid flows in capillaries as Taylor flow and freely rising gas bubbles and swarms of gas bubbles shall be investigated.

2.1 Taylor Flow Setup

For the Taylor flow experiments a rectangular borosilicate capillary with an inner cross section of 2.0 mm × 2.0 mm and a wall thickness of 0.3 mm was used. The capillary is mounted vertically on a vibration-isolated table movable in x-, y-, and z-direction. The gas and the liquid are contacted via a co-flow injector made of a PEEK capillary with an inner diameter of $d_i = 0.2$ mm. The gas flow is adjusted by mass flow controllers, the liquid by a syringe pump. Aqueous sodium hydroxide solutions were produced by weight of the appropriate amounts of sodium hydroxide and deionized water. For the experiments, pure CO_2 was used as gas phase.

2.2 Real-Time Raman Process Analysis System

In order to measure concentrations in liquids spatially and time-resolved at a defined distance in the liquid medium (slug) behind a fast-moving gas bubble, an in situ real-time Raman process analysis system was developed combining Raman spectroscopy with a pulsed laser and Mach-Zehnder holography as depicted in Fig. 1. The blue section in Fig. 1 (right) is the Taylor flow setup as described in Sect. 2.1. The cross-section of the capillary O is marked as O′ in Fig. 1 (left). The green section in Fig. 1 (left) corresponds to the Raman setup while the red section corresponds to the holographic setup.

Raman spectroscopy uses the vibrational properties of molecules and is very selective. To achieve a good spatial resolution, the exiting laser light must be focused to a small spot in the microchannel. Furthermore, the measurement time has to be much shorter than the time in which a slug in a Taylor flow passes the focus. To achieve good limits of detection for several different components involved in the reaction, it is important to acquire a complete Raman spectrum in a short period of time by coupling a large amount of laser energy into the microchannel. However, the maximum laser power must be balanced with restrictions originating from the small dimensions of the microstructured devices. The Raman subsystem is depicted in the green subsection of Fig. 1. (left). For these purposes a customized Nd:YAG laser is used and based on an oscillator-amplifier concept: The laser radiation of a continuous-wave laser of high beam quality at $\lambda = 1064$ nm is used as a seed laser. Afterwards, the seed laser beam is shaped by an acousto-optic modulator, which results in laser pulses with rectangular shape, a width of 10 µs, and a repetition rate of $f = 5$ Hz [11]. Four Nd:YAG rods, pumped by xenon flash lamps, amplify the laser signal. The strong IR laser radiation is converted to 532 nm wavelength by
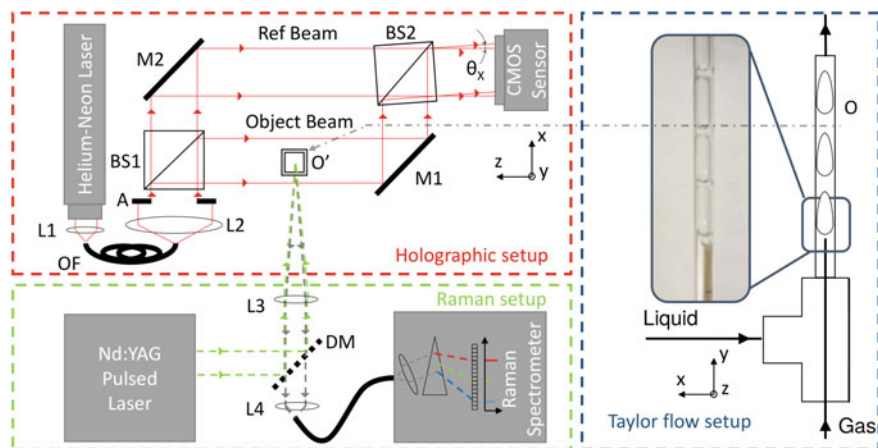
Fig. 1 In situ analysis system (left) optical setup with 2 axes concept of the Raman analysis system with holographic setup, right: experimental Taylor flow setup

using nonlinear crystals. The pulse length may be chosen between 1 and 10 μs. It was set to $t = 10\,\mu$s, in order to achieve the smallest maximum peak power at a given laser energy.

To get a good spatial resolution in the microchannel, a special confocal arrangement was used. The pulses of the Nd:YAG laser have a pulse energy of about 40 mJ and are coupled into a microscope by mirrors with a free optical light path and focused into the microchannel by a microscope objective with a short focal length of $l = 4$ mm, a numerical aperture of 0.6, a magnification of 40, and a variable cover glass correction of up to 2 mm. The wavelength-shifted Stokes Raman light emitted from the molecules within the laser focus is collected by the microscope objective, again, and separated from the exciting laser light by a dichroic mirror. The confocal optics for depth resolution is achieved by coupling the Raman light into an optical fiber. Its small core diameter of $d = 50\,\mu$m acts as a pinhole. The light guide is connected to a spectrometer (Acton). A thermoelectrically cooled EM-CCD camera with *1600 pixels* in the direction of spectral dispersion and 200 pixels parallel to the entrance slit of the spectrometer used for binning is coupled to the spectrometer. It uses internal electron multiplication (EM) technology to reduce the readout noise, which is the predominant type of noise for short integration times and small characteristic Raman signals. The EM-CCD camera is triggered externally by the laser. The exposure time is set to $t = 50\,\mu$s. Each Raman spectrum is obtained by a single 10 μm laser pulse. Additionally, a conventional CCD camera is mounted on the microscope, which is illuminated with a halogen lamp by inserting a beam splitter and removing the dielectric mirror.

To determine the bubble position relative to the laser spot, digital Mach-Zehnder holography was integrated in the process analysis system, as shown in the red section in Fig. 1 (left). The benefit of holography is that a 3D position of the bubble can be determined with a single optical axis instead of using 2 orthogonal optical axes with 2 cameras. The advantage of using only one optical axis to determine the 3D position with holography is that the second optical axis can be used for localized concentration measurement using the high-energy laser for Raman spectroscopy.

In Mach-Zehnder holography a laser beam is split into two equal parts. Out of these only one part is made to pass through the object while the other part functions as a reference beam. Subsequently, both parts are redirected and recombined to generate the interference pattern which is captured with a sensor. This captured interference pattern is called a hologram and it encodes the intensity as well as the phase information of the object. A Helium-Neon (He-Ne) laser ($\lambda = 633$ nm) is used as the coherent source which is coupled into a monomode glass fiber, OF, with 4 μm core diameter using the coupler L1. From the fiber the laser beam is collimated into a parallel beam with a diameter of 10.8 mm (1/e^2 level of Gaussian intensity distribution) using L2. The collimated beam is split by a 50:50 beam splitter BS1. The beam passing through the object O in its optical path is referred to as the object beam and the other one as the reference beam. The object beam and reference beam are then directed by mirrors M1 and M2 respectively to the second beam splitter BS2. The angles, at which they meet (θx and θy) at the camera sensor, determine the fringe pattern of the hologram and also the position of the twin image. The hologram

is recorded using a customised real-time process analysis system developed at *IPVS, University of Stuttgart*. This camera sensor features a high speed 1696×1710 pixels CMOS sensor with a pixel size of $8\,\mu m$. It allows real-time imaging with an exposure time as low as $80\,ns$ and with frame rates up to $485\,fps$ at full resolution. The short exposure time makes the holographic setup resistant to vibrations of the experimental setup. Due to the huge volume of data generated by the sensor it is connected to a powerful field-programmable gate array (FPGA) to process the data and also to apply image processing algorithms like holographic reconstruction directly in the real-time process analysis system.

The information contained in the hologram about the intensity and phase of the object can be reconstructed using a Fresnel transformation according to Eq. (1) [12],

$$U(x, y, z) = \frac{e^{ikz}}{i\lambda z} e^{\frac{ik}{2z}(x^2+y^2)} \cdot F\left\{h(x_0, y_0)e^{-\frac{ik}{2z}(x_0^2+y_0^2)}\right\} \tag{1}$$

where the Fourier transform and the wavelength of the He-Ne laser ($\lambda = 632$ nm) are reconstructed. Equation (1) shows that the reconstruction takes place on different planes in the z-direction. The plane in which the object is located in the z-direction is determined by an auto-focus algorithm based on the variance. On this plane, the position in x- and y-direction of the object and thus the exact position in space can now be determined. The reconstructed hologram also contains an unwanted twin image and the first order components. The latter are eliminated by a filter in the pre-processing stage. The twin image is separated from the virtual image by adjusting the angles and between the reference and the object beam appropriately. This holographic approach to determine the bubble position can be realized by capturing the hologram with a camera without a lens and thus without limitation by the depth of field. This is advantageous compared to shadowgraphy approaches in large bubble columns with two required optical axes. To determine the bubble position, a 2D FFT is calculated several times and is therefore acceptable in terms of the effort required. The overall structure is shown in Fig. 2, where (1) denotes the lens, (2) the CMOS sensor and (3) the FPGA unit. The complete assembly is mounted on a vibration isolated table (5) The capillary, microchannel (O), is fixed to a movable holder (4) so that the capillary can be moved relative to the laser focus and the CMOS sensor.

The two optical systems, Raman spectroscopy and holography, have been synchronized by means of a real-time trigger module on the FPGA, so that the hologram is recorded $t = 3\,\mu s$ before the corresponding laser pulse, in order to prevent interference from the high intensity of the laser. The local calibration of the laser focus in the hologram was performed with a high-precision injection needle. All in all, this setup of the real-time Raman process analysis system made it possible to measure Raman spectra well even in millimeter-sized capillaries and to determine the position of the bubbles using holography.
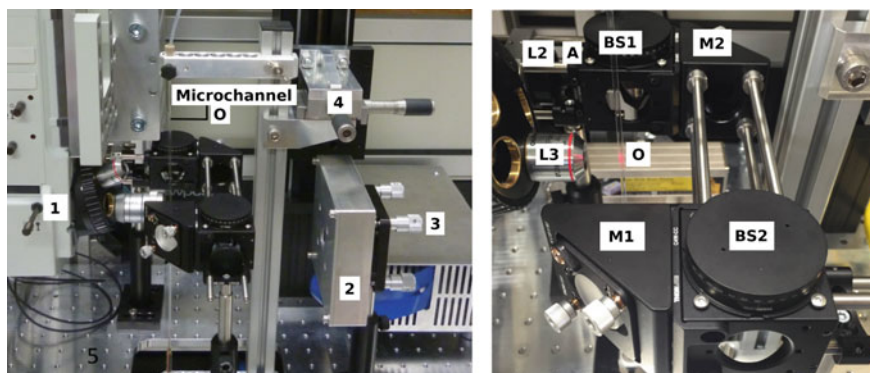
Fig. 2 Experimental setup of in situ analysis system (left) overall setup: (1) microscope, (2) CMOS sensor, (3) FPGA, (4) position adjustment for millichannel and (5) vibration free optic table. Right: zoomed in version of the setup

2.3 Continuous-Flow Setup with UV/VIS Spectroscopy

In contrast to Raman- and IR-spectroscopy, UV/VIS spectroscopy uses electron transitions in atoms and molecules. This will be used for UV/VIS tomography here. It is especially suitable for the coloured chemical reactions developed by several groups of the SPP 1740. To apply these chemical reactions in bubble columns, their intrinsic kinetics must be known.

In this section we first describe the development of a continuous-flow setup with a fluidic mixer and a CCD spectrometer.

2.3.1 SuperFocus Mixer

Part of the SPP 1740 is the development of chemical reaction systems for the transfer of gas in a bubble to the surrounding liquid. On the one hand the reaction should not be too fast. Otherwise, the reaction would take place directly in the liquid film surrounding the bubble. On the other hand, there is little influence of the characteristics of the bubbly flow on the reaction if the latter one is too slow. Best would be a reaction whose rate can be adjusted relative to the rate of absorption of the gaseous phase in the liquid phase in order to consider both cases: mass transport limited reactions and kinetics limited reactions. We performed experimental studies on the intrinsic kinetics of such chemical reactions systems within a continuous flow setup and of a SuperFocus Mixer, which is described in detail in Chapter "Determination of Kinetics for Reactive Bubbly Flows Using SuperFocus Mixers".

We used a mixer design according to the SuperFocus Mixer (SFM), initially developed by Hessel et al. [11, 13, 14]. The contacting of the fluids to be mixed is realized by multiple microchannels which provide an alternating arrangement of the two fluids. Consequently, a high surface area in-between the two fluids is achieved. It

is followed by a focusing zone where the diffusional length is reduced gradually by reducing the width of the lamellae of the fluids. The structure of the mixer is etched anisotropically into a silicon wafer using the deep reactive ion etching process. Glass plates of $s = 0.5$ mm thickness are anodically bonded to the bottom and the top of the silicon wafer. Two fluids enter continuously via two curved fluidic inlets. Each of them is split into 64 feed channels. The focusing zone has a length of $l = 22$ mm. For the experiment, we used two different designs of the mixing channel. Both of them have a cross section of 0.5 mm $\times$ 0.5 mm. However, one has a total length of $l = 200$ mm, the other one a total length of $l = 60$ mm. After the mixing, the progress of the reaction can be monitored along the channel in order to determine the kinetics as described in Chapter "Determination of Kinetics for Reactive Bubbly Flows Using SuperFocus Mixers". By calculating the velocity of the liquid flow the spatial coordinate is converted into a time scale. Viz., the residence time is calculated by dividing the traversed volume, focusing zone and mixing channel up to the measurement point, by the total flow.

2.3.2 Experimental Setup with a Diode-Array Spectrometer

The experimental setup for continuous-flow measurements was designed for mobile applications in order to measure the kinetics of the chemical reactions at several chemical groups within the SPP 1740. The SFM was attached to a stainless-steel holder. The two inlets are coupled via Luer connectors and 1/8″ FEP capillaries to 100 ml syringes of glass and PTFE. The total flow rates were set between $\dot{V} = 0.4$ mL/min and 52 mL/min (corresponding to a residence time between $t = 130$ ms and 17 s at a distance of $x = 22.5$ mm from the outlet of the focusing zone) for the shorter mixing channel, respectively $\dot{V} = 0.4$ mL/min and 34 mL/min (corresponding to a residence time between $t = 260$ ms and 22 s at a distance of $x = 157$ mm from the outlet of the focusing zone) for the longer one. The maximum flow rate is limited by the pressure resistance of the cover glass of the focusing zone. The pressure in the mixing channel results from the pressure drop, which is mainly caused by the mixing channel [15].

For the concentration measurements, an in situ analysis technique based on UV/VIS spectroscopy with multimode fiber optics was used. The light of a combined halogen and deuterium lamp was coupled into a first fiber and focused into the mixing channel on a spot of 0.6 mm diameter using lenses with short focal lengths of 5 mm. They are included in a holder that can be manually positioned relative to the SFM. This results in a transmission of 97% through the channel. The optical path length is determined by the channel depth of 0.5 mm. The transmitted light was collected by a second identical lens, focused into a second fiber and guided to a miniature diode array spectrometer (*ocean optics USB2000*). During the measurements at different partners within the SPP 1740 (Herres-Pawlis, Klüfers, Schindler) the fibers were fixed on a table to avoid spectral baseline fluctuations (angle dependence of the evanescent waves). With this setup we can monitor a spectral range between $\lambda = 270$ nm and 800 nm.

2.4 Real-Time Tomographic Process Analysis System

The colored reaction systems developed within the framework of the SPP 1740, can be measured using UV/VIS spectroscopy. However, just like IR spectroscopy, this is an integral measurement along a light beam and only allows the determination of the average concentration along the light beam. Therefore, the classical UV/VIS spectroscopy shall be extended to a real-time tomographic process analysis system to get localised concentration measurement. It will be applied to monitoring of wakes behind bubbles in a bubble column.

2.4.1 Bubble Column Setup

The construction is based on the design of SPP 1740 partner, Technical University of Berlin. It consists of a glass tube with $d = 75$ mm inner diameter and a wall thickness of 6 mm, see Fig. 3. This tube is surrounded by an octagonal tube made of PMMA with a wall thickness of 8 mm. It has 8 plane regions with a width of 48 mm. The whole bubble column has a height of $h = 876$ mm. The bottom plate has two inlets, one in the center and one between the center and the inner wall. The central inlet is used for an injector for gas bubbles and the other one for purging or draining. The volume between the two tubes can be filled by side connectors to match the refractive indices of the walls of the two tubes.
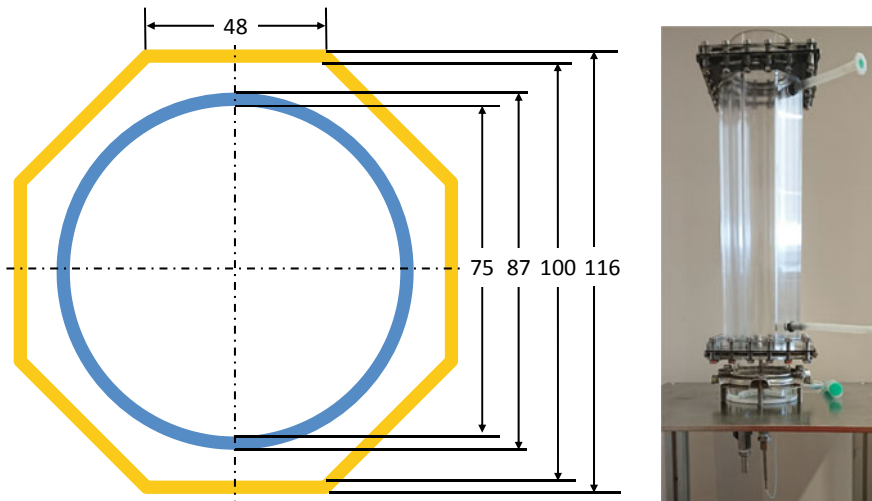
Fig. 3 Cylindrical bubble column with refractive index matching octagonal mantle

2.4.2 Setup with Two Orthogonal Laser Beams

Based on kinetic measurements done with the continuous-flow setup and spectro-scopic measurements of different colored chemical reaction systems, some of them were chosen for UV/VIS tomography with free rising bubbles. As a first experiment two laser beams were directed under 90° to the bubble column. Figure 4 shows the optical setup with two lasers. In this example laser 1 is a He-Ne gas laser with $\lambda = 633$ nm wavelength and $P = 15$ mW continuous wave (cw) power. Laser 2 is a diode laser with $\lambda = 516$ nm wavelength and variable cw power up to $P = 50$ mW. Both laser beams are coupled into fibers and collimated as parallel beams of 10 mm diam-eter at the entrance of a beam combiner which incorporates a dichroic mirror. At the outlet of this beam combiner these two laser beams are aligned exact collinear. An optical filter with rotatable broadband filters allows the attenuation of the combined laser beam. The intensity ratio of the two beams can be adjusted by the intensity of the diode laser ($\lambda = 516$ nm). The combined laser beam is splitted into two beams and directed by two mirrors to the bubble column at 90°. At the opposite sides two CMOS cameras are mounted.

This setup can be used with different lasers, only changing the dichroic mirror, or can be used with one laser only. Furthermore, depending on the laser, they can be pulsed, e. g. our diode laser up to $f = 100$ kHz. Additionally, a third laser may be coupled into the beam combiner with a second dichroic mirror. The wavelengths of the lasers can be adapted to the chemical reaction system in order to detect one or more products. Furthermore, short laser pulses allow the use of slow cameras and also leads to low blurring.
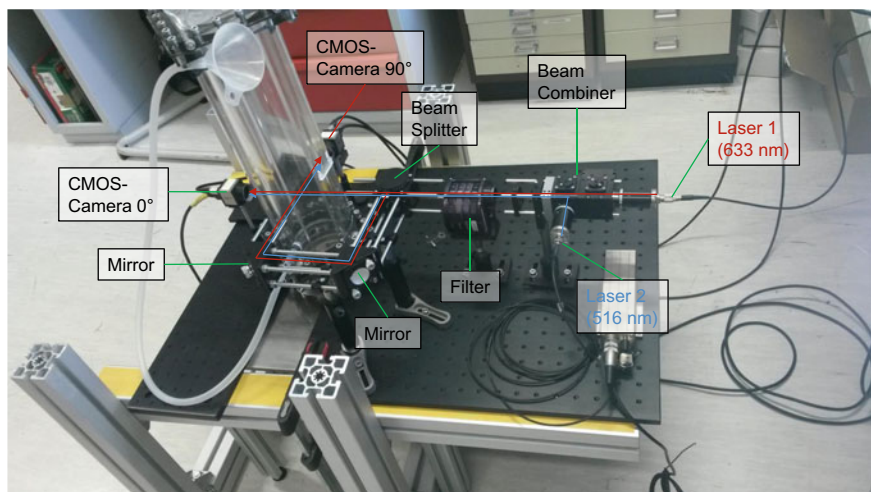
Fig. 4 Optical setup with bubble column and two orthogonal laser beams

2.4.3 UV/VIS Tomography Setup

The core concept of UV/VIS tomography system to obtain 3D concentration data, is to capture the UV/VIS absorption image of the component being measured from various angles at a very high speed. The principle of such a system is shown in Figs. 5 and 6. A laser beam of 1 mm diameter consisting of several collinear time multiplexed laser beams of different wavelengths is reflected by a fast rotating polygon mirror. The custom polygon mirror has 12 facets and the distance between two opposite facets is 150 mm. Each facet is 80.38 mm wide and 10 mm in height.

The laser beams are reflected to three cylindrical micro lens arrays via mirrors or directly. A rotation of the Polygon mirror of 30° results in an angle sweep of the reflected beam of 60° which covers all three cylindrical lens arrays. So, at the maximum speed of the polygon mirror of $n = 15,000$ rpm (rotations per minute) one mirror facet covers 3 cylindrical lens arrays and a complete 2D picture of the
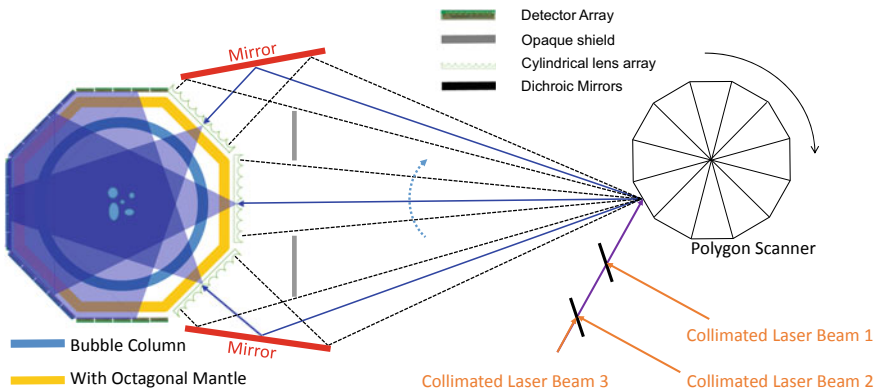
Fig. 5 Optical layout of UV/VIS tomography setup
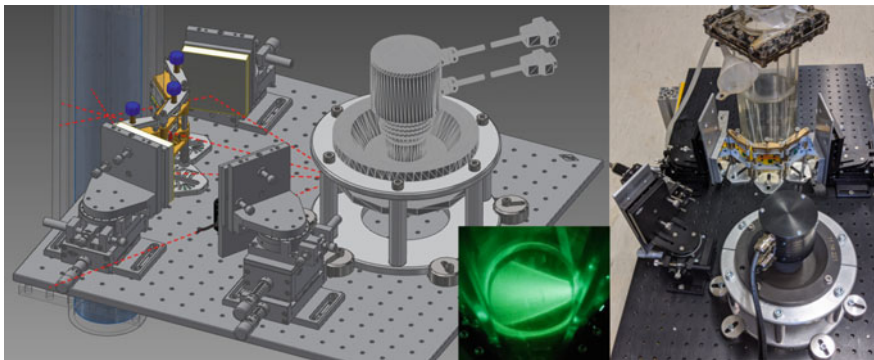
Fig. 6 UV/VIS tomography setup with fan beam laser profile within bubble column

bubble column in $t = 0.3$ ms. The laser beam may be composed of three pulsed lasers of different wavelength. These three lasers can be combined to one collinear time multiplexed beam. A beam combiner with two dichroic mirrors at 45° can be used to produce such collinear beams at the outlet.

There are two possibilities to choose the repetition rates and pulse durations of each laser. One possibility is that each of the three lasers, pulsed one after the other with a pulse duration of $t = 0.1$ ms and a repetition rate of $f = 1$ kHz. The other possibility is that switching between these three lasers is much faster with a pulse duration $t = 10$ μs, repetition rate $f = 33$ kHz. The two versions have different requirements for pulsed laser properties or opto-electronical modulation of cw lasers including costs and the CMOS array readout. The different optical integration times of the detector array output signals and noise will be different. At this stage of development, only one cw laser was used for all experiments.

The cylindrical lens array is a custom-design and consists each of 20 concave cylindrical lenses, each with a radius of curvature of 1 mm. This array is 40 mm long, 10 mm wide and 4 mm thick and is made of *Schott glass B270* (RI = 1.523). Each cylindrical lens produces a laser cone with an opening angle of 60°, which runs through the bubble column onto a detector array on the opposite side, as indicated in Fig. 5.

In order to achieve a high temporal resolution, projections from all 60 lenses must be captured within a timeframe where the motion of a gas bubble within the bubble column is negligible. Hence for every projection a very short exposure time of $t = 10$ μs must be used. At such low exposure time the amount of photons reaching the sensor must be high enough to detect the absorption of the corresponding component. To ensure this, a large pixel size of the detector is needed as typical camera sensors with a pixel size of a few micrometer will not be able to collect sufficient photons for an exposure time of $t = 10$ μs. Also, to get a high sensitivity the sensor must have a high dynamic range with high bit depth. These criteria of short exposure time, large pixels and high bit depth per pixel demanded a need for a custom sensor system design. A CMOS line sensor from *Hamamatsu (S11107-10)* fulfilled all these conditions. It was capable of a minimum exposure time of 1.7 μs at line rate of $f = 100$ kHz. Each sensor has *64 pixels* and the pixels are 60 μm wide and 127 μm high. The sensor has a spectral response from $\lambda = 400$ nm to 900 nm (40% values) with maximum sensitivity at $\lambda = 700$ nm which facilitates choosing a wide variety of laser sources suitable for numerous chemical reactions. The sensor provides an analog video signal which, for the high sensitivity, is sampled by an 18-bit ADC (analog-digital-converter) at $f = 10$ MHz. Since the sensor has a width of 9.1 mm, to capture data from one octagonal side of the setup of size 48 mm (Fig. 3) 5 sensors are concatenated in a custom PCB (printed circuit board). In total, to cover all 5 detector sides of the bubble column 25 such sensors are required to be generating data of 18-bits for every pixel at $f = 10$ MHz amounting to a serious design challenge of data acquisition at 5 Gb/s.

To handle such a high amount of data in real-time an FPGA (field-programmable gate array) based data acquisition system was developed. The architecture for this system is depicted in Fig. 7 (top). The sensors are triggered by an external
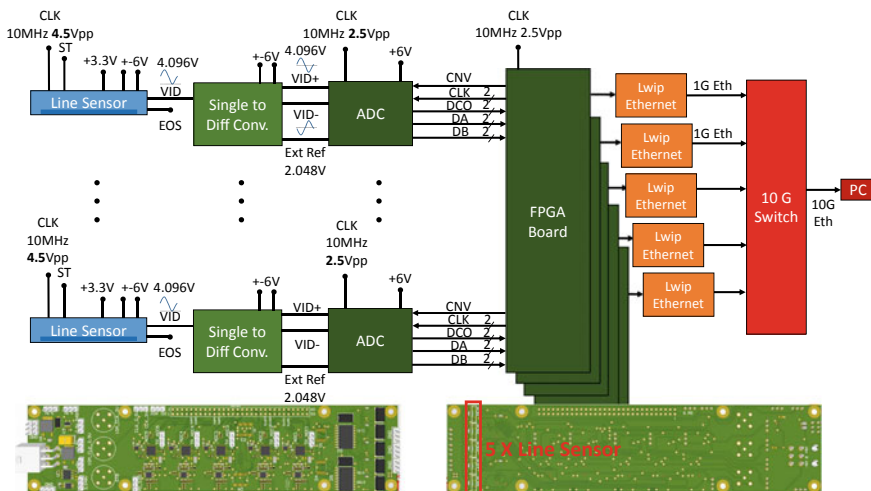
Fig. 7 Top: Hardware architecture for high speed data acquisition system and bottom: custom sensor PCB

synchronous clock controlled by the rotating polygon mirror. The video signal from each of the 25 sensors are converted into differential signals for better noise immunity and then sampled by an 18-bit ADC at 10 MHz. The digital data from 5 ADCs are collected by a FPGA at 240 MHz and is then passed onto the computer through a 10 Gb Ethernet network.

The custom PCB with the sensors, single to differential convertor and ADC is shown in Fig. 7 (bottom). The challenge was to match the width of the PCB to the width of the octagonal side of the bubble column (48 mm). This PCB connects to a MicroZed FPGA board over a high speed 60 pin connector. The FPGA in turn has a 1 Gb Ethernet connection which connects to a 10 Gb Ethernet switch to collect data from 5 FPGAs in parallel.

2.4.4 Reconstruction of the 2D Concentration Field

The data captured by the custom detector array must be reconstructed from the measured laser intensities from many angles, to extract the 2D concentration field of a specific reaction product within the bubble column. This step is inherently the inverse of the data capturing step where the values captured by the detector (projections) are back projected into a virtual volume to reconstruct the absorbance at particular laser wavelengths. The absorbance values are then converted into concentration fields using the correlation of the UV/VIS spectrum on the educts and products being measured.

Tomographic reconstruction algorithms are extensively available for X-ray based systems and there is a wide variety of literature and implementation found like the

most commonly used FDK algorithm [16]. However, they are not suitable for the developed UV/VIS tomography system due to two major reasons. First, they are designed for X-rays which are assumed to have no refraction effect and pass through objects in a straight line and second, the number of projections required is in the range of 1000–5000 projections. In the developed system the lasers beams undergo various refraction and reflection which bends the light through the various interfaces of the bubble column. These must be taken into consideration during the reconstruction process using ray-tracing techniques. Furthermore, the number of projections in our case is limited to 60 which are two orders of magnitude lower than the ones required by standard reconstruction algorithms. To alleviate this problem a neural network based reconstruction algorithm was developed to extract information even with the low number of projections.

In order to get accurate results the ray-tracing must be modelled to reality as closely as possible. Each projection is from a fan beam generated by one of the 60 micro-cylindrical lenses distributed over 3 sides of the octagonal mantle. The fan beam has an opening angle of 61°. For each projection, the entire sensor data from the rest of the 5 sides of the octagonal mantle are captured. In total, for every projection *1600 pixel* data is captured. The ray-tracing model also takes into account the exact positions and number of the sensor pixels as well as the gaps in between the line sensor chips. The source of ray-tracing is a virtual point within the lenses, so that the corresponding opening angle is realized. 65,000 rays with a Gaussian profile of $\sigma = 1$ were used to simulate each fan beam. The paths of these rays were modelled with the physical and optical properties of the bubble column setup. The dimensions of the bubble column as well as the octagonal mantle were accurately determined by X-ray based CT scans and depending on the material the optical properties like refractive indices were also added to the respective of the entire setup. Within the bubble column absorption of the fan beam was modelled using the CFD simulation data of bubble columns from TU Darmstadt. Refractive indices change within the fluid of the bubble column due to the reaction was measured to be 0.001. This is extremely low and is ignored by the ray-tracing model. Each of the 65,000 rays from a single projection were propagated through the model to reach the detector plane. A final check is made to see which detector element was hit by the ray and its corresponding intensity is accumulated.

The intensity profile captured by the sensor array for such a fan beam through the ray-tracing model is depicted in Fig. 8. The left image is the ray-tracing from a central micro cylindrical lens while the middle image is the ray-tracing from a micro cylindrical lens at the edge of the array. In both cases, one can observe the optical effects due to the corners of the octagonal mantle. Also, for the fan beams from the edge of the lens array, there are additional refraction, reflection and total internal reflection effects which are observed by the detectors. For a single reconstruction, the data from all 60 projections are captured which is depicted in Fig. 8 (right). Here every column of data corresponds to the data captured by the detector array from one projection.

To speed up the calculations, an intensity threshold of 10^{-4} of the maximum light intensity was set. If the intensity falls below this value, the beam is excluded
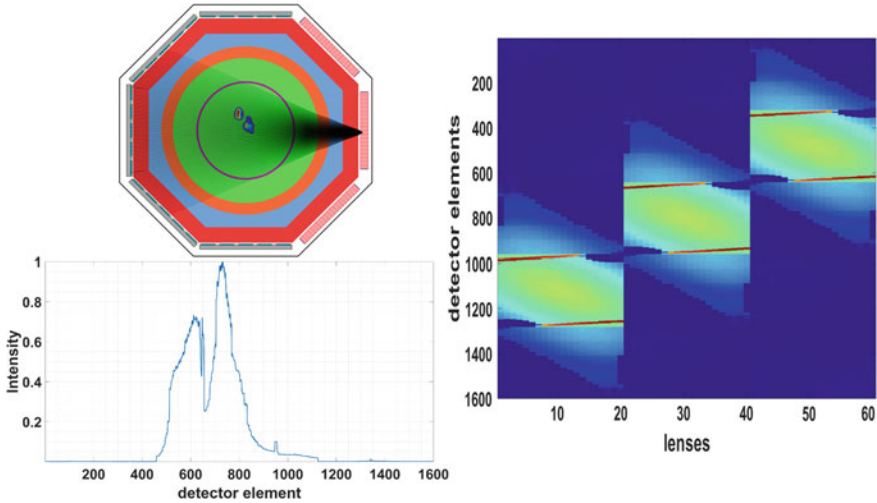
Fig. 8 Left: Ray-tracing of the fan beams emerging from the cylindrical lens arrays. Right: Sensor data from all 60 projections. Each column represents the sensor data from one projection

from further considerations. Beam parts, which are outside the octagon (for example between the lens arrays and octagon) due to the refraction of light, are also not considered further. Moreover, to accelerate the computation, a circular region-of-interest (ROI) with $d = 50$ mm is defined in the center of the bubble column where the CFD simulation data were mapped for the absorbance characteristics of the components being measured. Reference data were captured by setting the absorbance of the ROI to $d = 0$, and this intensity must be subtracted from each captured projection data.

Using the ray-tracing model a backprojection of the captured projection data is performed to a virtual ROI. This is similar to unfiltered backprojection in the X-ray CT domain but with the rays back projected using the ray-tracing model instead of a straight line. Evidently, the results of the backprojection step include a lot of artifacts due to the limited angle of the available rays and only 60 projections. However, the usage of neural networks improve the reconstructed data significantly and sufficiently. The neural network is trained using a large number of CFD simulation data from the SPP 1740 project 'Direct numerical simulation of multi-physics reactive mass transfer at single and multiple bubbles' directed by Professor Bothe. These data are fed to the ray-tracing model to calculate the projections which are then backprojected to get the reconstructed 2D concentration field. From the SPP 1740 totally 2,184,000 reference cases obtained by CFD simulations are used to train the neural network improving the reconstruction quality as shown in Fig. 9. It should be mentioned that the CFD simulation data provided so far are 2D velocity data instead of 2D concentration data. However, this is not really a fundamental problem for the following reasons.

An arbitrarily chosen
2D concentration field

Correct reference concentration
for the CNN learning phase

The reconstructed
2D concentration field

Ray tracing based
backprojected
reconstruction

Artefact Removal NN
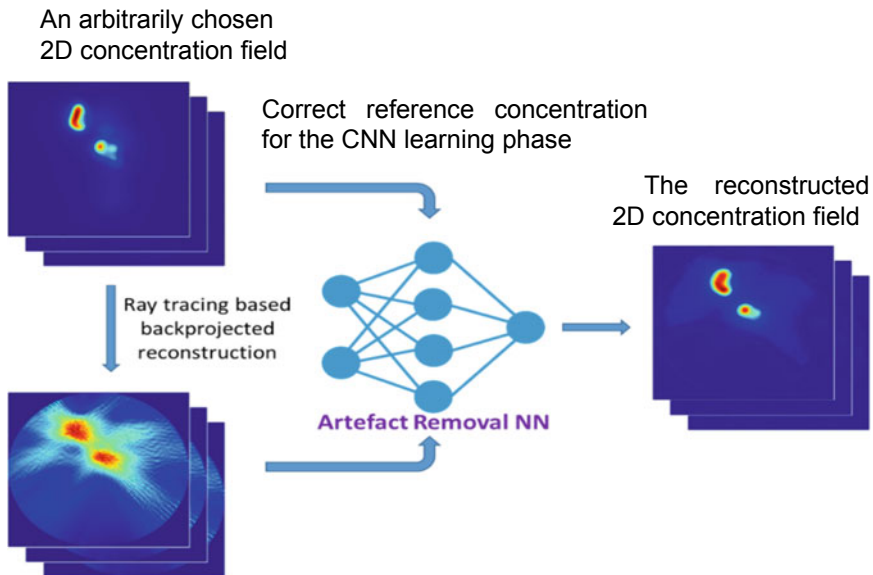
Fig. 9 Overview of the reconstruction algorithm developed for the UV/VIS tomography system

Firstly, the neural network works only with dimensionless quantities so that only the characteristics of the data are relevant but not the actual physical meaning of the data. Therefore, data of different physical quantities with similar characteristics regarding spatial distribution can be used for learning and for the application of the neural network. To what extent the spatial velocity field has a sufficiently similar characteristic for the spatial concentration still has to be investigated in principle. Intuitively, however, spatial structures like vortex structures should exist in a similar way in both physical field sizes.

Secondly, independent of these arguments based on the structure of the data, it can be easily verified that the neural network trained in the above mentioned way calculates physically meaningful concentration fields. In order to carry out this verification, the tomographic projection data of an arbitrarily assumed concentration fields can be calculated with the physically highly accurate ray-tracing simulation model. In the next step, the reconstructed tomographic concentration field, which would be applied in the same way to measured data, can be compared with the original, i.e. the exactly known concentration field of the first step. In this respect, the quality of the reconstruction of the concentration fields based on the neural network trained with the velocity data can be verified with high accuracy. The results so far are very satisfactory and shall be extended with concentration fields measured on the basis of light absorption. The details of the neural network implementation are discussed later in Sect. 3.

3 Experimental Results

In the following the experimental results of the above-mentioned setups of the real-time Raman process analysis system, the real-time tomographic process analysis system and the SuperFocus Mixer are described.

3.1 Evaluation of Chemical Reaction Systems Based on Spectroscopy

Within the SPP 1740 a lot of chemical reaction systems were developed, which are described in detail in Chapters "Control of the Formation and Reaction of Copper-Oxygen Adduct Complexes in Multiphase Streams", "In Situ Characterizable High-Spin Nitrosyl–Iron Complexes with Controllable Reactivity in Multiphase Reaction Media" and "Formation, Reactivity Tuning and Kinetic Investigations of Iron "Dioxygen" Intermediate Complexes and Derivatives in Multiphase Flow Reactions" of this book.

3.1.1 Raman Spectroscopy

In order to evaluate the chemical reaction systems for measurements with the real-time Raman process analysis system, they were first examined with a pure Raman system.

Based on the work of our SPP 1740 partner Ludwig-Maximilians-Universität München (Prof. Klüfers, see Chapter "In Situ Characterizable High-Spin Nitrosyl–Iron Complexes with Controllable Reactivity in Multiphase Reaction Media") a Fe-NO complex without the coordinated gas, the complex with the coordinated gas and the solvent water for the respective reaction system were filled into a standard cuvette ($s = 10$ mm) and spectra were recorded. For these Raman measurements, a continuous-wave argon ion laser (488 nm) was used, which makes it possible to detect even very small signals with longer measurement times. Furthermore, it has a low laser power and the focus can therefore be placed closer to the wall of the cuvette compared with a high-energy pulsed laser. This proves to be particularly helpful if the solutions to be examined are colored. Within the low penetration depth the absorption of the laser and Raman radiation is reduced, resulting in a better signal-to-noise ratio. Comparing the coupled in laser energy of this continuous-wave laser during a measurement with the later used high-energy of the pulsed laser, the determined detection limit for the systems can be calculated on the Raman measurements with the pulsed laser. As an example, the Raman spectra of the Fe-NO system are shown on the left in Fig. 10. A comparison of the three spectra of the solvent (water, blue), the aqueous precursor solution without NO (green) and the complex with NO (red) shows a characteristic signal of NO coupled to the complex at about 500 cm^{-1}. With
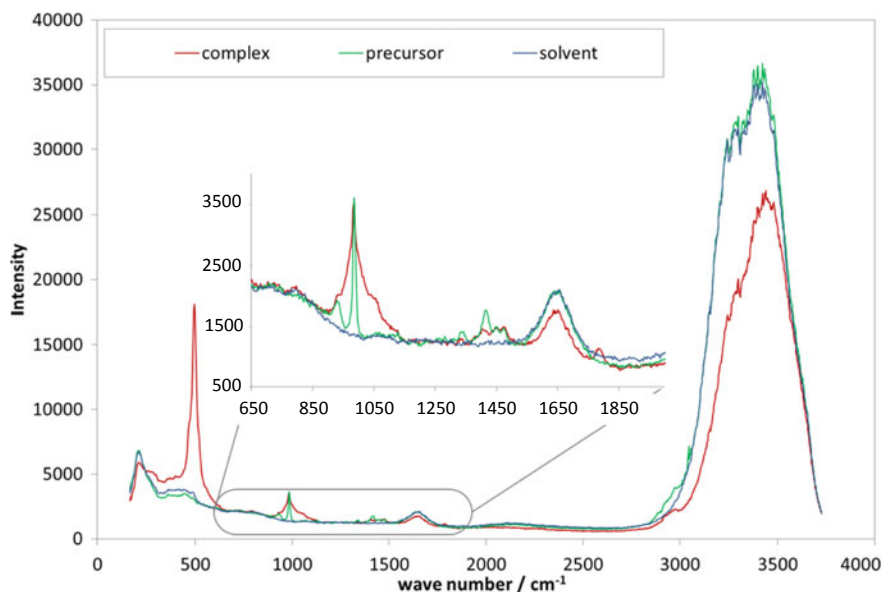
Fig. 10 Raman measurements to study the Fe-NO chemical reaction system

the ligand hedta, a limit of detection (LOD) of 5 mmol L^{-1} was calculated for the pulsed laser. However, it was found that the high signal intensity at 500 cm^{-1} is due to the resonance Raman effect. It occurs for this Fe-NO bond only when excited at wavelengths around or slightly below $\lambda = 500$ nm. Thus, if the pulsed laser intended for two-phase measurements is used at $\lambda = 532$ nm, these signals are much smaller. They can hardly be distinguished from the background noise.

For other systems of our SPP partners RWTH Aachen (Prof. Herres-Pawlis, see Chapter "Control of the Formation and Reaction of Copper-Oxygen Adduct Complexes in Multiphase Streams") and Justus-Liebig-Universität Gießen (Prof. Schindler, see Chapter "Formation, Reactivity Tuning and Kinetic Investigations of Iron "Dioxygen" Intermediate Complexes and Derivatives in Multiphase Flow Reactions"), Fe-O system (ligand: HPTB (N,N,N′,N′-tetrakis[2-benzimidazolylmethyl]-1,3-diamino-2-propanol)) and Cu-O system (ligand: bis (3-tert-butylpyrazolyl) (2-pyridinyl) methane), no Raman signals were determined for the Fe-O system and only a very high LOD for the Cu-O system due to the low concentrations in the case of Fe-O. An increase in the concentration is limited by the solubility or leads to very strongly colored solutions. Therefore, the Raman light is absorbed and the signal-to-noise ratio deteriorates significantly. For this reason, these two systems, i.e. the reaction of the gas with the complex, are not suitable for measurements with the existing real-time Raman process analysis system. However, if these systems are used in more complex reaction systems as catalysts for the oxidation of various substrates, Raman spectroscopy can be used to observe product formation.

3.1.2 UV/VIS Spectroscopy

A large part of the SPP 1740 was the development of colored chemical reaction systems, which can be used for our UV/VIS tomographic system. As a first example the Fe-NO reaction of our SPP 1740 partner Ludwig-Maximilians-Universität München (Prof. Klüfers, see Chapter "In Situ Characterizable High-Spin Nitrosyl–Iron Com-plexes with Controllable Reactivity in Multiphase Reac-tion Media") was used. It is based on competitive consecutive chemical reactions and shown in Fig. 11. The corresponding spectra are shown in Fig. 12.

MNIC : $FeCl_2$ + $(NHEt_3)Cl$ + NO   ⟶ $NHEt_3[FeCl_3(NO)]$
$[FeCl_3(NO)]$

DNIC : $FeCl_2$ + 3NO + MeOH + NEt_3 ⟶ $NHEt_3[FeCl_3(NO)]$ + MeONO (*)
$[FeCl_3(NO)_2]$
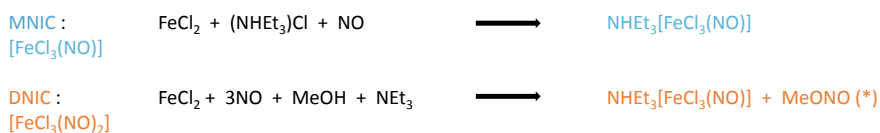
Fig. 11 Fe-NO chemical system (LMU Munich, Prof. Klüfers)
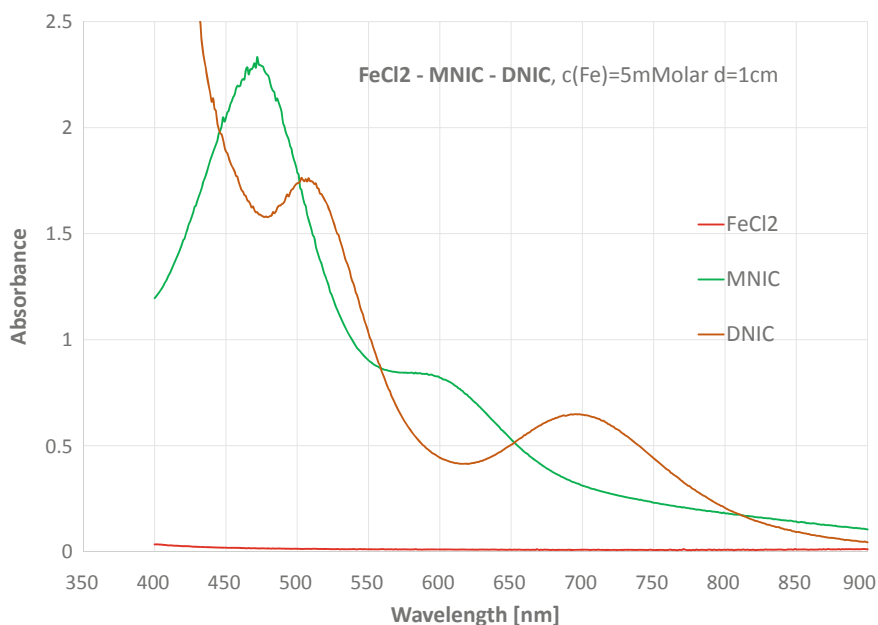
Fig. 12 Absorption spectra of the Fe-NO chemical system

3.2 Evaluation of the Confocal Laser Raman Spectroscopy Setup

The properties of the confocal laser Raman system are important for the precise measurement of concentrations behind fast moving gas bubbles and are described in this section.

The spatial laser intensity profile was measured with a CCD camera from Data Ray Inc. with 1360×1024 pixels and an active area of 14.4 mm $\times$ 10.8 mm. It showed a symmetrical Gaussian form. The temporal profile was measured with a silicon photodiode. It has an almost rectangular pulse with 10 µs duration. The pulse energy at $\lambda = 532$ nm was measured with a broadband pyroelectric detector and amounted to $P = 20$–40 mJ.

The spatial resolution, lateral and in depth, is a further important parameter of the laser Raman system and is dependent on different parameters. It is difficult to determine it theoretically [17, 18] therefore it was measured experimentally at an interface between two transparent fluids. This is important for high-power pulsed lasers. Since the laser beam in our setup (Fig. 1) is horizontally arranged and bubbles move vertically, this interface has to be oriented vertically. We used a laminar jet of two liquids, of which one is laying in the center of an annular gap and one in the gap. To determine the lateral resolution, the focus is approached to the inner ring by varying its position from the gap to the ring until the maximum signal intensity is reached. For the depth resolution, the ring is penetrated frontally. For these measurements we used two fluids with similar indices of refraction. In the jet the Raman active Na_2SO_4 aqueous solution was used (0.77 mol L^{-1}, $RI = 1.346$) and outside the non-Raman active NaCl aqueous solution (1.54 mol L^{-1}, $RI = 1.347$). As a result, we got a spatial resolution of 15 µm vertically (flow direction) and 70 µm horizontally (laser beam direction).

The validation of the system was performed on a non-reactive Taylor flow at ambient pressure and temperature. The liquid phase consisted of cyclohexane dissolved in methanol with a concentration of $c = 0.73$ mol L^{-1}, the gas phase consisted of air. At volume flows of 0.5 ml/min of liquid and 5 ml/min of air, the characteristic Raman signal of cyclohexane could be detected by the choosen wavenumber at about 800 cm^{-1} (yellow region) The Raman spectra were recorded with a single laser pulse and are shown in Fig. 13, the pure spectra in blue and grey for cyclohexane and methanol and the spectrum recorded in Taylor flow in red. Despite the apparently low intensity of the characteristic cyclohexane Raman line at 800 cm^{-1} an evaluation is possible.

The sensitivity of the Raman system is defined for very small signals above the detection limit (LOD) according to Eq. (2).

$$LOD = \frac{N_{3\sigma}}{I(i)} c(i) \tag{2}$$

Fig. 13 Raman spectra of a mixture of cyclohexane in methanol (0.73 mol L^{-1}) in non-reactive Taylor flow (red) and the corresponding pure spectra of cyclohexane (blue) and methanol (grey), staggered for better representation
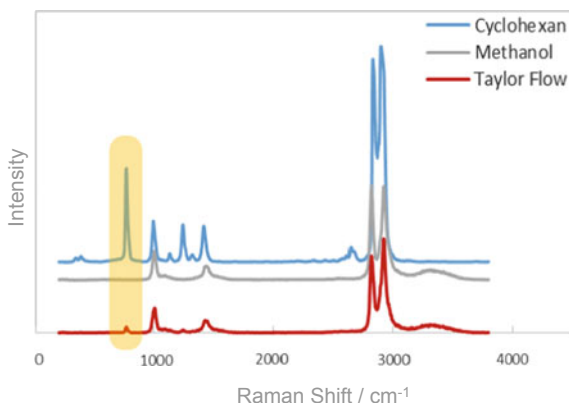
It depends on the signal-to-noise ratio of the characteristic Raman signal I of component i and the concentration $c(i)$ used for calibration. The $N_{3\sigma}$ noise is calculated by multiplying the standard deviation caused by the noise by a factor of three. In the spectrum shown in Fig. 10, the standard deviation is 27 counts and the signal intensity 1934 counts, which results in a detection limit of $c = 0.03$ mol L^{-1} [19].

The result of the work is that confocal laser Raman spectroscopy is very well applicable for concentration determination with high spatial and time resolution as long as the concentrations exceed the detection limits.

3.3 Measurements of Reaction Kinetics with a SuperFocus Mixer

The SuperFocus Mixer (SFM) was used to investigate the Fe-NO system of our SPP partner Ludwig-Maximilians-Universität München (Prof: Klüfers) [20, 21] with the ligands hedta and edta. However, the reaction proved to be so fast that even at maximum possible flow, the reaction took place completely in the focusing chamber immediately after contacting and reducing the concentration. For this reason, no change in the characteristic absorbance (435 nm) and thus no change in concentration could be detected in the reaction channel. Similar investigations were carried out with the reaction system from our SPP partner (Prof. Schindler) [22, 23]. The formation of the complex with the ligand HPTB (N,N,N′,N′-Tetrakis[2-benzimidazolylmethyl]-1,3-diamino-2-propanol) in the mixing channel of the Super-Focus Mixer was observed. It shows an absorption band between 550 and 600 nm and was very well measurable. Thus, a reaction constant of 1.14 s^{-1} was determined for the formation of the Fe-O_2 complex at room temperature and ambient pressure, which could be confirmed with the stopped-flow system available in the Schindler working group. After the reaction the complex was reactivated with ascorbic acid [24].

Furthermore, the Cu-O$_2$ complex with btmgp(bis(tetramethylguanidino) propylene) ligand was investigated in collaboration with our SPP partner RWTH Aachen (Prof. Herres-Pawlis) [6, 25–30]. This is a subsequent reaction in which the Cu(I) complex first reacts with oxygen to form bis (μ-oxo) dicopper(III) complex, but then decays quite rapidly to form a bis (μ-alkoxo) (μ-iodo)-bridged, dinuclear copper(II) complex. In the SFM the decay of the copper(III) complex, which has a characteristic band at 395 nm, could be observed very well. The reaction constant for this decay was determined with the SFM for a pseudo-first order kinetics of 0.90 s^{-1} at room temperature and ambient pressure. The formation of the copper(III) complex could only be observed at very high flow rates in the mixing channel of the SFM and could therefore not be investigated in detail [15, 31].

The joint work with the SFM allows a time-resolved measurement of the partly transient absorption spectra, a quantitative determination of the reaction constants of the planned reaction systems and thus an evaluation for the later use in bubble columns. These results are described in more detail in Chapter "Determination of Kinetics for Reactive Bubbly Flows Using SuperFocus Mixers" of this book.

3.4 Concentration Measurements with the Real-Time Raman Process Analysis System Applied to a Taylor Flow of Gaseous CO$_2$ in Aqueous Sodium Hydroxide Solutions

First investigations with the real-time Raman process analysis system were carried out with air and water in the Taylor flow. Holograms were recorded and reconstructed to obtain the 3D position of the bubble using a single optical axis only. An example is shown in Fig. 14 (left).

Furthermore, the CO$_2$ absorption in caustic soda solution was investigated. This system was chosen because it can be used in large bubble columns on an industrial scale. This chemical reaction and their kinetic parameters are well known [32–36]. At a pH value greater than 12, the CO$_2$ dissolved in the caustic soda solution is very
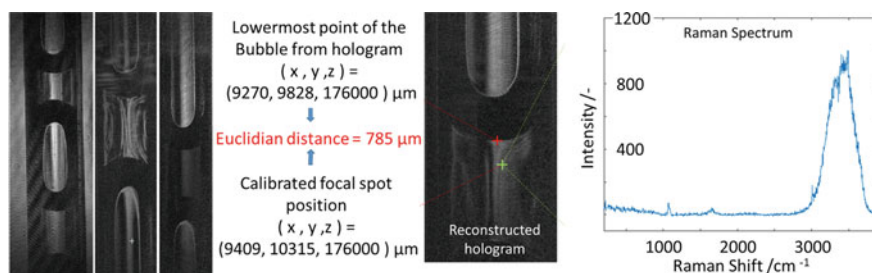
Fig. 14 Left to right: holograms in different chemical systems: water-air; CO$_2$ caustic soda; Fe-NO; Position of the concentration measurement (green cross) and lowermost point of the bubble (red cross); Raman spectrum at green cross

quickly converted to the carbonate CO_3^{2-} according to the carbonic acid equilibrium, which can be detected by Raman spectroscopy. For the experiments, a volume flow of 17 ml/min for the CO_2 and 0.5 ml/min for the caustic soda solution was set. The capillary was positioned so that the focus of the laser was in the middle of the capillary. Measurements were made at several points along the capillary, always recording a spectrum and a corresponding hologram. Figure 14, left, shows such a pair of measurements taken at a distance of 207 mm from the gas/liquid contact. The position in z-direction of the bubble, and thus the plane in which the bubble is sharply represented in the reconstructed hologram, was determined with an auto-focus algorithm. The x and y coordinates of the lowest point of the bubble are marked by the red cross. This point was determined using image processing algorithms. A two-stage edge detection algorithm was used. In the first step, the image was filtered with a median filter with a 3×3 pixel mask to minimize image noise. Subsequently, vertical intensity profiles from the microchannel were analysed using the canny edge detector to determine the lowest edge of a bubble. The intensity profile with the lowest edge showed the x-position of the bubble. The determination of the y-position of the bubble was determined from the unfiltered image data, for which purpose the canny edge detector was applied to the intensity profile of the pixel column with the same x-position. The green cross in the hologram represents the position of the laser spot in the reconstructed hologram determined by the injection needle (calibration process). Knowing the pixel resolution and the coordinates, the distance between bubble and measuring point can now be calculated. The Raman spectrum recorded at this measurement point is shown in Fig. 14, right. The broad water band at 3000–3500 cm^{-1} and the characteristic carbonate signal at 1050 cm^{-1} can be recognized. The determined concentration of the carbonate ion at this point is 0.20 mol L^{-1} and the LOD 0.05 mol L^{-1}. Further results can be found in [12].

Dissolved CO_2 is accumulated in the liquid reducing the concentration gradient in the liquid film around the bubble and thus reducing the absorption of the gaseous CO_2. This was verified by evaluating the Raman spectra concerning the concentration of carbonate and bicarbonate. All measurements were located in close to the center of the cross section of the channel, see Fig. 14. We used integral concentration profiles, and locally dissolved measurement points at the same distance from the injection. They show a mean value for the carbonate and bicarbonate concentration for all measurements that were done at the same distance from the injection point regardless of their distance to a bubble cap and tail. On the other hand, each measurement point may be plotted for itself with the corresponding distance to the bubble cap and/or tail. The latter method enables the detection of concentration profiles in the slug at a certain distance from the injection.

The integral results are depicted in Fig. 15. Along the channel, several distances from the injection point (Δy) between 10 and 200 mm were chosen. As a fast increase of the concentration was expected directly at the entrance, the density of the chosen distances is closer than further up in the channel. This is confirmed experimentally: Directly in the first few millimeters from the injection, viz. during the bubble formation, a steep concentration increase for the carbonate is observed. At the end, a maximum concentration of about $c = 500$ mol m^{-3} is achieved. According to the

Fig. 15 Integral
concentration profiles of
filled circle: HCO_3^- and
filled triangle: CO_3^{2-} along
the channel
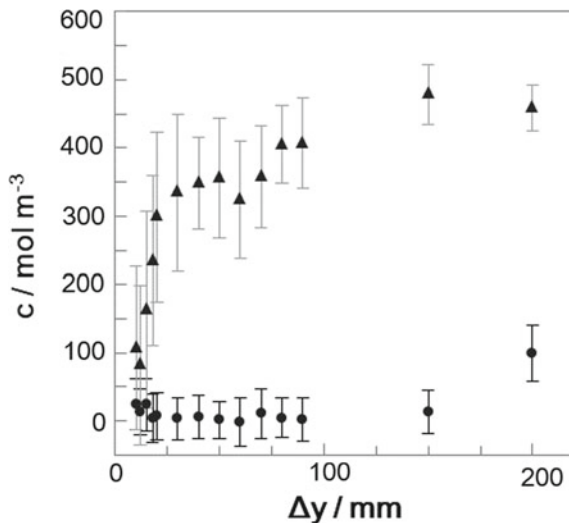
stoichiometry, two hydroxide ions are consumed for the formation of one carbonate
ion. Thus, at about 150 mm, almost all of the hydroxide ions are consumed and the
pH value is reduced drastically. This corresponds to the fact that the formation of the
bicarbonate is monitored far up in the channel.

A locally resolved treatment of each measurement point will provide a better
insight. Its position in the slug is described with a dimensionless distance $l*$ defined
in Eq. (3).

$$l^* = \frac{j_t - j_f}{j_t - j_c} = \frac{\Delta l_c}{l_s} \tag{3}$$

It describes the distance Δl_c of the laser focus to the preceding bubble tail during
the measurement. Divided by the slug length l_s determined in the image, it results in
a non-dimensional identifier. j_t, j_c and j_f are the pixel positions of bubble tail and cab
and the laser focus. According to this definition, $l^* = 0$ describes a position directly
attached to the end of the preceding bubble tail, $l^* = 1$ a position at the cap of the
bubble following.

Measurements at heights of $h = 10$ mm, 15 mm, 20 mm and 70 mm along the
channel were made with Raman spectroscopy and holography, simultaneously. As
an example, Fig. 16 shows the results at a height of 15 mm.

These profiles show that the carbonate concentration increases at the bubble tail
of the preceding bubble further up in the channel. This effect is attributed to mass
transfer from the preceding bubble into the slug and the film. Furthermore, the Taylor
circulation in the slug enhances the equalization of the concentration in the slug. The
carbonate enriched in the stagnant film is passed to the cap of the following bubble,
where it is directed into the center of the cross section and forwarded to the tail. The
observed scatter is higher than the uncertainty of the concentration of the carbonate
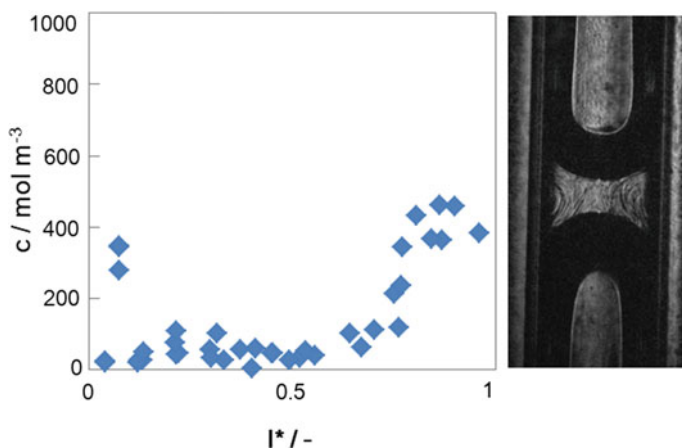
Fig. 16 Spatially resolved concentration of the carbonate in the center of the capillary at a distance of 15 mm from the injector

derived from the Raman spectra in two-phase flows and based on the fluidic flow within the slug. The holographic picture (Fig. 16), shows fluctuations of the refractive index and correlated concentrations.

With this work it could be shown that the real-time Raman process analysis system is in principle operational, even in small capillaries, and can be used for CO_2 absorption in caustic soda as an industrially relevant process.

3.5 Measurement of a Wake Below a Gas Bubble Using Laser Beams

The combined Raman and holography real-time process analysis system and the results, described in Sects. 2.2, 3.1 and 3.2, is advantageous when colorless liquids are used. However, the focus of nearly all chemical reactions developed within the SPP 1740 are colored liquid systems. For these reactions UV/VIS spectroscopy is suitable. As a step between absorption in a cuvette and UV/VIS tomography, a bubble column together with a two laser-beam arrangement was used, see Sect. 2.4.2 and Fig. 4.

We applied different chemical reactions in the bubble column with a focus on a chemical reaction system producing MNIC and DNIC with NO bubbles which was developed by the SPP partner Ludwig-Maximilians-Universität München (Prof. Klüfers). However, this chemical reaction system requires that the liquids in the bubble column contains no oxygen, even impurities are disturbing. Furthermore, the NO gas may not contain NO_2 which builds up in a pressure bottle within a few months.
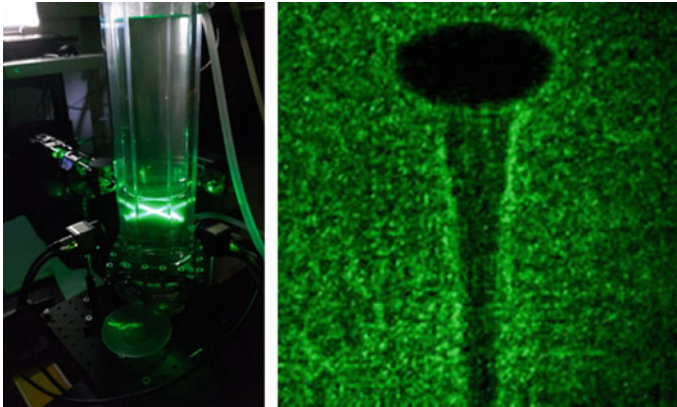
Fig. 17 Rising NH_3 gas bubble in a bubble column using two laser beams

In order to observe a wake below a gas bubble and check optics, detectors and electronics we used the solution of NH_3 gas in a Phenolphthalein solution. Figure 17 (left) shows the two laser beams entering the bubble column at 90° and Fig. 17 (right) as an example the wake below the rising NH_3 bubble. It was recorded with 40 µs, only.

3.6 Characterization of the Real-Time Tomographic Process Analysis System

In this section the real-time tomographic process analysis system described in Sect. 2.4.3 is evaluated.

3.6.1 Characterization of the Optical Raytracing Paths

Before characterizing the optical ray-tracing paths within the bubble column a medium between the inner cylindrical bubble column (borosilicate glass 3.3 tube, *RI* $= 1.472$) and the outer octagon (PMMA, *RI* $= 1.492$) should be evaluated concerning the optimum index of refraction (RI).

Methanol is the main component of the bubble column. For the medium in the interstitial space one could also choose methanol, water or a liquid for the adjustment of glass and PMMA. Methanol would have the advantage that it is also used in the inner bubble column, but the disadvantage that it could attack PMMA or the adhesive used. An 'inert' medium with a similar refractive index to methanol would also be conceivable. If one wants to adapt to the higher RI of glass and PMMA, one could, for example, use mixtures of organic liquids with water or aqueous solutions of

inorganic salts. Possible media and their RI are methanol ($RI = 1.329$), glycerol ($RI = 1.474$) or water (1.333).

Since the RI of water and methanol are almost the same and there are also some salts dissolved in methanol, which increases the RI, you can use water for the interstitial space with a good conscience. If one rather wants to adjust the glass and PMMA, an average refractive index of 1.482 would be favorable. For this purpose, pure glycerol (preferred) or a 76% sugar solution ($RI = 1.480$) could be used. But both have a viscosity about 2000 times higher than water. First of all, it was investigated how the radiation pattern with water (adaptation to methanol in bubble column) in the interstitial space and glycerol (adaptation to glass and PMMA) are. Not only the beam deflection plays a role here, but also a possible total reflection and (angle-dependent) reflection losses.

Since it is possible to work with lasers and polarized light, the more favorable case is assumed that the linear polarization of the light is parallel to the interface. Then the reflection losses decrease with increasing angles of incidence to zero until the Brewster angle and then increase again, but always remain below the reflection losses for vertically polarized light:

First calculations are done with the following pairs of media within the inner bubble column and the outer octagon: methanol—methanol, methanol—glycerol, methanol—water, water—water, air—air. Important results:

- It does not make a big difference whether water, methanol or glycerol is used as RI matching liquid. The straightest way is even with water, which should be used.
- The greatest angular change is due to the strong RI difference between air and the 1st PMMA interface.
- To illuminate three adjacent segments of the octagon, the laser must cover an angle range of $\pm 45°$ at the entrance. So far we have assumed $\pm 30°$, without RI jumps.
- The total reflection losses at all interfaces are surprisingly low. One reason is that we have planned laser light that is polarized parallel to the glass surfaces. Then, even the reflection losses decrease with increasing angle up to the Brewster angle.

The influence of dispersion (RI) was calculated for the case that the main component methanol is contained in the inner bubble column and water in the interspace bubble column—octagon: For all components, PMMA, borosilicate glass 3.3, methanol and water, the RI depends on the wavelength and temperature. The wavelength dependence of the RI has a stronger effect than temperature. In particular, methanol has the greatest dispersion and the effective length is also the longest.

The wavelength range $\lambda = 590$–700 nm, which is relevant for the proposed reaction systems, was analyzed. The wavelength dependent RI for all relevant substances was taken from literature.

As an example, the position shift with wavelength change from 590 to 700 nm on the detector array for an angle of $-10°$, $-15°$ (reaching the opposite segment) and $45°$ (reaching an oblique opposite segment at $45°$) is $140\,\mu m$ displacement at an angle of incidence of $-10°$, $210\,\mu m$ displacement at an irradiation angle of $-15°$ and $1050\,\mu m$ displacement at irradiation angle of $-45°$.

With a pixel center distance of $x = 127$ µm, the point of impact of the laser beam on the CMOS array shifts by 1 pixel when changing the wavelength from $\lambda = 590$–700 nm under $-10°$ irradiation, by 1 pixel at $-15°$ and by *8 pixels* at $-45°$.

The influence of the temperature was calculated for the case that the main component methanol is contained in the inner bubble column and water in the interspace bubble column—octagon. Temperature variations around 5 °C were analyzed. The temperature-dependent RI for all relevant substances were taken from literature. Due to different temperatures, the laser beams are directed slightly differently through the bubble column to the CMOS sensors.

As an example, the position shift on the array with temperature fluctuations from $T = 20$ to 25 °C for angles of $-10°$, $-15°$ (reaching the opposite octagon segment) and 45° (reaching an obliquely opposite octagon segment below 45°) is given are 50 µm displacement at an angle of incidence of $-10°$, 80 µm displacement at an irradiation angle of -15 and 470 µm displacement at an irradiation angle of $-45°$.

With a pixel center distance of $x = 127$ µm, the point of impact of the laser beam on the CMOS array shifts by *0.4 pixels* at a temperature fluctuation of $T = 5$ °C under $-10°$ irradiation, by 0.6 pixels at $-15°$ and by 4 pixels at $-45°$.

The influence of the temperature is therefore significantly less than the wavelength dependence of the RI. The assumed temperature fluctuation of $T = 5$ °C could certainly be reduced. We would have to perform a calibration before every measurement.

3.6.2 Characterization of the Tomographic Concentration Measurement Process

The concentration profile is extracted from the imaging process based on the optical tomographic 2D reconstruction of the detector images as shown in Fig. 18. After raw data reconstruction the reconstructed image data are normalized to the maximum ray-tracing sensor pixel intensities for each angular position of the laser beam. The subsequent backprojection reconstruction creates strong artifacts because of the combination of limited angle and sparse-view reconstruction problem of our setup. For artifact compensation a neural network has been implemented. A big challenge when using neural networks is the usually very limited amount of training data. This was partly solved by choosing the neural network architecture of the U-Net which originates from biomedical image segmentation [37]. With the U-Net shown in Fig. 18, it was possible to train with a smaller number of images sufficiently well accelerating the learning process. The neural network was trained with 2,184,000 CFD simulation data from the SPP 1740 partner from TU Darmstadt, see Sect. 2.4.4.

The special feature of the U-Net is the pixel by pixel classification, so that the input and output image have the same size [$512^2 Pixel$]. The architecture is symmetrical and represents a U-shape. It starts with the contraction path and the folding process (downsampling). On the opposite side is the expansion path and the transposed 2D convolution layers (upsampling). There is a multiple loop function, where each "step" has two times a convolution layer, a group normalization and Mish-Activation
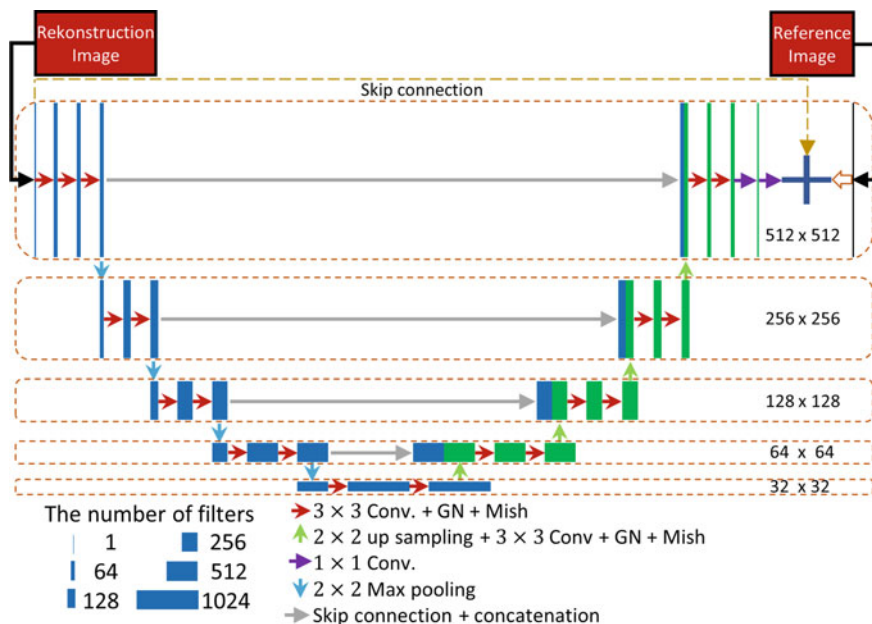
Fig. 18 Neural network based on the U-net architecture for artifact reduction in concentration measurement with the real-time tomographic process analysis system

function [38]. Using a Pooling layer, the image size is halved in each step. Finally, the image size is only 32^2 and the expansion path begins, returning the image to its original size. The described network is terminated with its regression layer.

The normalization is performed using group normalization instead of batch normalization, due to the significantly better performance with a small number of batches [39]. The typical division of the image data was used (70% training, 20% testing and 10% validation). By using the reconstruction algorithm in combination with this neural network a significant part of the artifacts can be removed. After applying the full imaging process of Fig. 19, the concentration field of the reaction products has been reconstructed with remarkable accuracy.

4 Summary and Conclusion

For the investigation of concentration profiles around bubbles in millichannels as Taylor flow and in bubble columns, two in situ real-time process analysis systems were developed and applied to different chemical reaction systems. One system uses a combined measurement system based on laser Raman spectroscopy and digital holography, suitable for transparent media. The second real-time process analysis
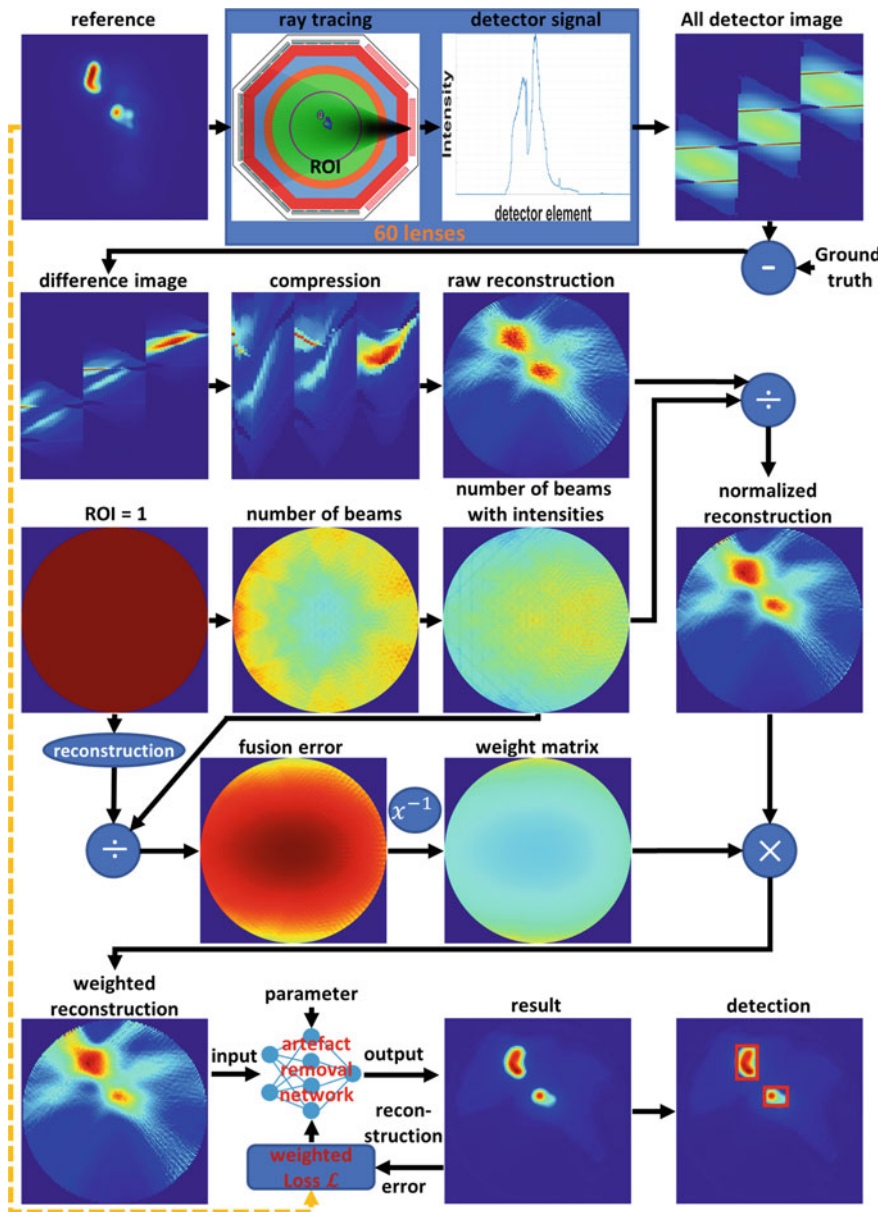
Fig. 19 Concentration measurement as the result of the imaging process based on the tomographic 2D reconstruction

system is based on UV/VIS tomography which is suited for colored chemical reaction systems.

The real-time Raman process analysis system allows a concentration measurement within 10 μs with a spatial resolution of 15 μm laterally and 70 μm in depth. The laser spot, where concentrations are measured, may be positioned up to 150 μm to a glass interface. Furthermore, the laser spot can be located relative to a fast moving bubble precisely by combined digital holography. This in situ measuring system was adapted to a Taylor flow in a minichannel. In contrast to laser induced fluorescence (LIF) the laser Raman system can be applied to a lot of chemical systems and needs no fluorescent marker. The combination of laser Raman spectroscopy and digital holography was applied to a Taylor flow of CO_2 bubbles in an aqueous solution of sodium hydroxide in a minichannel with 2 mm × 2 mm inner cross section. The concentrations of the carbonate ions CO_3^{2-} and bicarbonate ions HCO_3^- were measured locally and with known distance to the gas bubbles within the minichannel. Along the length of the channel, the concentration profiles of the carbonate are changing and the carbonate concentration increases at the bubble tail of the preceding bubble further up in the channel. The Taylor flow circulation in the slug can be seen in the concentration profiles.

In contrast to usual absorption spectroscopy with only integral measurements the real-time tomographic process analysis system based on UV/VIS tomography allows spatial concentration measurements. For this purpose one or more pulsed laser beams with different wavelengths can be combined using dichroic beam combiners and hit as collimated beam on a fast rotating polygon mirror. This mirror deflects the beam on three cylindrical lens arrays with 20 elements, each. Every lens produces a divergent beam (60°) in the horizontal plane (perpendicular to the flow direction in the bubble column), which traverses the bubble column and hits 5 CMOS sensors arrays on the opposite side. This system can take a complete 2D concentration field in a bubble column within 1 ms. To achieve these goals, a fast sensor electronics has been developed including fast amplifiers, high-resolution analogue-digital-converters and FPGAs. Furthermore, fast and accurate reconstructions algorithms have been developed.

This UV/VIS tomographic system will be applied to a NO-Fe reaction system: NO gas bubbles freely rise and produce MNIC and DNIC in the wake of these bubbles. Because MNIC and DNIC show different absorption spectra, their concentrations can be determined.

As a result of this part of the SPP 1740 two in situ real-time process analysis systems were developed. They can be used to measure concentrations of various chemical compounds in a spatially resolved and fast manner. Depending on optical variants it is possible to apply these real-time process analysis systems e. g. for Taylor flows in microchannels, single bubbles in a bubble column or even small bubble swarms.

References

1. Haase S, Murzin DY, Salmi T (2016) Review on hydrodynamics and mass transfer in minichannel wall reactors with gas-liquid Taylor flow. Chem Eng Res Des 113:304–329. https://doi.org/10.1016/j.cherd.2016.06.017

2. Tanaka S, Karstens S, Fujioka S, Schlüter M, Terasaka K (2019) Mass transfer from freely rising microbubbles in aqueous solutions of surfactant or salt. Chem Eng J 378. https://doi.org/10.1016/j.cej.2019.03.122

3. Timmermann J, Hoffmann M, Schlüter M (2016) Influence of bubble bouncing on mass transfer and chemical reaction. Chem Eng Technol 39(10):1955–1962. https://doi.org/10.1002/ceat.201600299

4. Gupta R, Fletcher DF, Haynes BS (2010) Taylor flow in microchannels: a review of experimental and computational work. J Comput Multiph Flows 2(1):1–32. https://doi.org/10.1002/ceat.201100643

5. Angeli P, Gavriilidis A (2008) Hydrodynamics of Taylor flow in small channels: a review. Mech Eng J 222(5):737–751. https://doi.org/10.1243/09544062JMES776

6. Kastens S, Timmermann J, Strassl F, Rampmaier RF, Hoffmann A, Herres-Pawlis S, Schlüter M (2017) Test system for the investigation of reactive Taylor bubbles. Chem Eng Technol 40(8):1494–1501. https://doi.org/10.1002/ceat.201700047

7. Larkin PJ (ed) (2011) Infrared and Raman spectroscopy: principles and spectral interpretation. Elsevier, Amsterdam. ISBN 978-1-28-311412-7

8. Lewis IR, Edwards HGM (eds) (2001) Handbook of Raman spectroscopy: from the research laboratory to the process line. In: Practical spectroscopy series, vol 28. Marcel Dekker, New York. ISBN 0-8247-0557-2

9. Chrimes AF, Khoshmanesh K, Stoddart PR, Mitchella A, Kalantar-zadeh K (2013) Microfluidics and Raman microscopy: current applications and future challenges. Chem Soc Rev 42:5880–5906. https://doi.org/10.1039/C3CS35515B

10. Fräulin C, Rinke G, Dittmeyer R (2014) Characterization of a new system for space-resolved simultaneous in situ measurements of hydrocarbons and dissolved oxygen in microchannels. Microfluid Nanofluid 16(1–2):149–157. https://doi.org/10.1007/s10404-013-1223-8

11. Schurr D, Guhathakurta J, Simon S, Rinke G, Dittmeyer R (2017) Characterization of a raman spectroscopic and holographic system for gas-liquid flows in microchannels. Chem Eng Technol 40:1400–1407. https://doi.org/10.1002/ceat.201600622

12. Guhathakurta J, Schurr D, Rinke G, Dittmeyer R, Simon S (2017) Simultaneous in situ characterisation of bubble dynamics and a spatially resolved concentration profile: a combined Mach-Zehnder holography and confocal Raman-spectroscopy sensor system. J Sens Sens Syst 6(1):223–236. https://doi.org/10.5194/jsss-6-223-2017

13. Hessel V, Hardt S, Lowe H, Schonfeld F (2003) Laminar mixing in different interdigital micromixers: I. Experimental characterization. AIChE J 49:566–577. https://doi.org/10.1002/aic.690490304

14. Hessel V, Löwe H, Müller A, Kolb G (2005) Mixing of miscible fluids. In: Chemical micro process engineering. Wiley-VCH, Weinheim. https://doi.org/10.1002/3527603581.ch1b

15. Schurr D, Strassl F, Liebhäuser P, Rinke G, Dittmeyer R, Herres-Pawlis S (2016) Decay kinetics of sensitive bioinorganic species in a SuperFocus mixer at ambient conditions. React Chem Eng 1:485–493. https://doi.org/10.1039/C6RE00119J

16. Feldkamp LA, Davis LC, Kress JW (1984) Practical cone-beam algorithm. J Opt Soc Am A 1(6):612–619. https://doi.org/10.1364/JOSAA.1.000612

17. Everall NJ (2000) Modeling and measuring the effect of refraction on the depth resolution of confocal Raman microscopy. Appl Spectrosc 54:773–782. https://doi.org/10.1366/0003702001950382

18. Everall NJ (2000) Confocal Raman microscopy: why the depth resolution and spatial accuracy can be much worse than you think. Appl Spectrosc 54(10):1515–1520. https://doi.org/10.1366/0003702001948439

19. Schurr D, Guhathakurta J, Simon S, Rinke G, Dittmeyer R (2017) Characterization of a Raman spectroscopic and holographic system for gas-liquid flows in microchannels. Chem Eng Technol 40(8):1400–1407. https://doi.org/10.1002/ceat.201600622

20. Merker D, Böhm L, Oßberger M, Klüfers P, Kraume M (2017) Mass transfer in reactive bubbly flows—a single-bubble study. Chem Eng Technol 40(8):1391–1399. https://doi.org/10.1002/ceat.201600715

21. Hlawitschka MW, Oßberger M, Backes C, Klüfers P, Bart HJ (2017) Reactive mass transfer of single NO bubbles and bubble bouncing in aqueous ferrous solutions—a feasibility study. Oil Gas Sci Technol – Rev. IFP Energies nouvelles 72(2):1–11. https://doi.org/10.2516/ogst/2017006

22. Miska A, Norbury J, Lerch M, Schindler S (2017) Dioxygen activation: potential future technical applications in reactive bubbly flows. Chem Eng Technol 40(8):1522–1526. https://doi.org/10.1002/ceat.201600684

23. Hoffmann A, Wern M, Hoppe T, Witte M, Haase R, Liebhäuser P, Glatthaar J, Herres-Pawlis S, Schindler S (2016) Hand in hand: experimental and theoretical investigations into the reactions of copper(i) mono- and bis(guanidine) complexes with dioxygen. Eur J Inorg Chem 29:4744–4751. https://doi.org/10.1002/ejic.201600906

24. Miska A, Schurr D, Rinke G, Schindler S (2018) From model compounds to applications: kinetic studies on the activation of dioxygen using an iron complex in a SuperFocus mixer. Chem Eng Sci 190:459–465. https://doi.org/10.1016/j.ces.2018.05.064

25. Paul M, Teubner M, Grimm-Lebsanft B, Golchert C, Meiners Y, Senft L, Keisers K, Liebhäuser P, Rösener T, Biebl F, Buchenau S, Naumova M, Murzin V, Krug R, Hoffmann A, Pietruszka J, Ivanović-Burmazović I, Rübhausen M, Herres-Pawlis S (2020) Exceptional substrate diversity in oxygenation reactions catalyzed by a bis(μ-oxo) copper complex. Chem Eur J 26(34):7556–7562. https://doi.org/10.1002/chem.202000664

26. Felis F, Strassl F, Laurini L, Dietrich N, Billet A-M, Roig V, Herres-Pawlis S, Loubière K (2019) Using a bio-inspired copper complex to investigate reactive mass transfer around an oxygen bubble rising freely in a thin-gap cell. Chem Eng Sci 207:1256–1269. https://doi.org/10.1016/j.ces.2019.07.045

27. Paul M, Strassl F, Hoffmann A, Hoffmann M, Schlüter M, Herres-Pawlis S (2018) Reaction systems for bubbly flows. Eur J Inorg Chem 20–21:2101–2124. https://doi.org/10.1002/ejic.201800146

28. Benders S, Strassl F, Fenger B, Blümich B, Herres-Pawlis S, Küppers M (2018) Imaging of copper oxygenation reactions in a bubble flow. Magn Reson Chem 56(9):826–830. https://doi.org/10.1002/mrc.4742

29. Schlüter M, Billet A-M, Herres-Pawlis S (2017) Special issue: reactive bubbly flows. Chem Eng Technol 40(8):1379–1528

30. Strassl F, Grimm-Lebsanft B, Rukser D, Biebl F, Biednov M, Brett C, Timmermann R, Metz F, Hoffmann A, Rübhausen M, Herres-Pawlis S (2017) Oxygen activation by copper complexes with an aromatic bis(guanidine) ligand. Eur J Inorg Chem 2017(27):3350–3359. https://doi.org/10.1002/ejic.201700528

31. Oppermann A, Laurini L, Etscheidt F, Hollmann K, Strassl F, Hoffmann A, Schurr D, Dittmeyer R, Rinke G, Herres-Pawlis S (2017) Detection of copper bisguanidine NO adducts by UV-vis spectroscopy and a SuperFocus mixer. Chem Eng Technol 40(8):1475–1483. https://doi.org/10.1002/ceat.201600691

32. Pinsent BRW, Pearson L, Roughton FJW (1956) The kinetics of combination of carbon dioxide with hydroxide ions. Trans Faraday Soc 52:1512–1520. https://doi.org/10.1039/TF9565201512

33. Knuutila H, Svendsen HF, Juliussen O (2009) Kinetics of carbonate based CO_2 capture systems. Energy Procedia 1(1):1011–1018. https://doi.org/10.1016/j.egypro.2009.01.134

34. Darmana D, Henket RLB, Deen NG, Kuipers JAM (2007) Detailed modelling of hydrodynamics, mass transfer and chemical reactions in a bubble column using a discrete bubble model: chemisorption of CO_2 into NaOH solution, numerical and experimental study. Chem Eng Sci 62(9):2556–2575. https://doi.org/10.1016/j.ces.2007.01.065

35. Wang X, Conway W, Burns R, McCann N, Maeder M (2010) Comprehensive study of the hydration and dehydration reactions of carbon dioxide in aqueous solution. J Phys Chem 114(4):1734–1740. https://doi.org/10.1021/jp909019u

36. Knuutila H, Juliussen O, Svendsen HF (2010) Kinetics of the reaction of carbon dioxide with aqueous sodium and potassium carbonate solutions. Chem Eng Sci 65(23):6077–6088. https://doi.org/10.1016/j.ces.2010.07.018

37. Ronneberger O, Fischer P, Brox T (2015) U-net: convolutional networks for biomedical image segmentation. In: Proceedings of international conference on medical image computing computer-assisted intervention, vol 9351. Springer, Cham, pp 234–241. https://doi.org/10.1007/978-3-319-24574-4_28

38. Misra D (2019) Mish: a self regularized non-monotonic neural activation function. arXiv preprint arXiv:1908.08681

39. Wu Y, He K (2018) Group normalization. In: Proceedings of ECCV, pp 3–19

Determination of Intrinsic Gas-Liquid Reaction Kinetics in Homogeneous Liquid Phase and the Impact of the Bubble Wake on Effective Reaction Rates

Sebastian Gast, Ute Tuttlies, and Ulrich Nieken

Abstract The interplay between fluid dynamics, mass transfer and chemical reaction in bubbly flows is not yet sufficiently understood. In order to determine the reaction kinetics without mass transfer limitations a new reactor concept has been developed. As an example for industrial relevant reactions, the non-catalyzed oxidation of toluene with oxygen was investigated. For a simplified reaction network rate expressions and corresponding kinetic coefficients have been identified. The reaction kinetics was used to numerically study the impact of the bubble wake on conversion and selectivity. The oxidation of toluene was found to be too slow for being affected by the bubbly flow. This has been confirmed by experiments in a technical size bubble column at industrial conditions. Numerical studies show that only reactions with a rate constant in the range of $0.1 < Da_1 < 1000$, the so-called mixture-masked range, are influenced by the flow pattern behind a rising bubble. Slow reactions can be treated as bulk phase reactions, while fast reactions take place exclusively in the vicinity of the bubble surface, thus are not biased by the non-ideal mixing in the bubble wake. In the mixture-masked range, transport barriers from the stationary bubble vortex have a significant influence on the course of the reaction.

1 Introduction/Motivation

Gas-liquid multi-phase reactors are widely used in industrial processes. Yet, many of them run at very low conversion rates to achieve high selectivities, leading to high cost in the after treatment to extract the products of wealth. Scale up and optimal design of industrial reactors is challenging, since model predictions are still not sufficiently reliable.

Challenges are the range of length scales on which different processes are taking place, such as the macro mixing due to turbulences on the reactor (meter) scale versus the micro mixing behind the rising bubbles, missing transport correlations for

S. Gast · U. Tuttlies · U. Nieken (✉)

Institute of Chemical Process Engineering, University of Stuttgart, Böblinger Straße 78, 70199 Stuttgart, Germany

e-mail: ulrich.nieken@icvt.uni-stuttgart.de

Fig. 1 Dependencies within
a reactive bubbly flow

Mass transfer

Species concentrations
enhancement

Mixing

chemical

reaction

Mixing

fluid properties
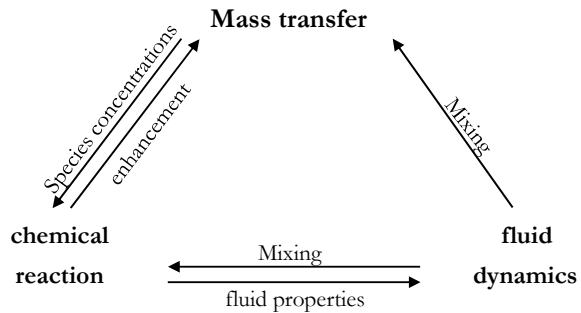
fluid

dynamics

industrially interesting conditions, and finally the strong interplay between reaction
kinetics, transport effects and fluid dynamics. This project is focusing on the interplay
of reaction kinetics and mixing at the bubble scale.

These dependencies are known for a long time. The enhancement of the mass
transfer by the chemical reaction is often taken into account by empirical enhance-
ment factors. The chemical reaction, itself limited by the educt concentration supplied
by the mass transfer, influences the fluid dynamics by changing the fluid properties
(see Fig. 1). The fluid dynamics in turn impacts the mass transfer and the reaction
by changing the local mixing. Bubbles tend to build up vortexes in their wake which
influence the mixing on the macro- and microscale. The fluid recirculation behind a
rising bubble may lead to areas of accumulation of reaction species where the selec-
tivity of a reaction is likely to be influenced. Although the dependencies are known
qualitatively, model-based predictions are still insufficient.

In order to investigate the dependencies of mass transfer, fluid dynamics and
chemical reaction around a rising bubble, each effect needs to be evaluated
independently.

Thereby, especially the chemical reaction of a gas-liquid system is hard to be
studied independently from mass transfer. Kinetic models of industrially relevant
gas-liquid reaction systems are typically measured in two-phase apparatuses, either
by bubbling the gas with high gas contents through the liquid phase, or in an idealized
system with known interfacial area. In the first case, the total interfacial area is
unknown but sufficiently large to assume saturation of the liquid by the gaseous
component.

In the second approach, the interfacial area is known, which allows to determine
the mass transfer from known partial pressure and temperature of the gas. Thereby
the gas- as well as liquid phase must be stirred continuously to achieve ideal mixing.
This leads to a conflict of objectives between ideal mixing and a known and stable
surface between the phases.

The overall aim of this work is to investigate the influence of micro mixing in
the bubble wake on the yield and selectivity of the ongoing reactions. Therefore,
in a first step a new reactor concept has been developed to measure the reaction
rates independently from mass transfer (see Sect. 2). As a model system of industrial
relevance, the oxidation of toluene has been chosen. The oxidation precedes via free

radicals and a high number of elementary steps as described by Hermans et al. [1]. Quantification of all rate constants is practically impossible and unnecessary for engineering purposes.

Thus, an effective reaction kinetics model has been developed, which includes only experimentally accessible and measurable species in the reaction network.

In a second step, the reaction kinetics has been implemented in a direct numerical simulation model of a simplified flow around a single bubble. This allows to study the interplay of the fluid dynamics, mass transfer and chemical reaction at the bubble scale (see Sects. 3 and 5). The results are validated in a pilot plan bubble column at industrial operating condition (see Sect. 4).

2 Determination of Gas-Liquid Reaction Kinetics in Homogeneous Liquid Phase

For the determination of the reaction kinetics of gas-liquid syntheses, usually two-phase reactors are used. This bears an increased risk of explosion at high oxygen concentrations when using organic educts or solvents. To avoid a flammable gas phase the oxygen partial pressure is therefore limited. This in turn leads to low conversions, which does not correspond to industrially required operating conditions. In addition, an undesired discharge of volatile components from the liquid phase may distort the experiments and the determination of the interface and therefore the mass transfer is a great challenge.

In order to avoid these difficulties, our approach intends to measure the reaction kinetics in homogeneous liquid phase. Therefore, the gas phase is completely dissolved in a chilled circulating liquid stream before the mixture reenters the stirred-tank reactor and the reaction takes place. This local decoupling of mass transfer and reaction avoids the problem of explosion hazard, since a potentially dangerous gas phase exists only for a short time in the cold circulating stream. However, no gas phase is present in the hot reactor itself. Therefore, the setup is inherently safe and there is no limitation for the oxygen concentration. We assume that no reaction takes place at the low temperature level of the circulation loop and that there is no decay of unstable intermediate products.

Due to the complete dissolution of the supplied gaseous educts, the amount of gas dissolved in the liquid phase is known. As the circulating stream is liquid when reentering the stirred-tank reactor, sufficient mixing rates can be achieved easily.

In the following the realization of the proposed reactor concept is described in detail.

2.1 Experimental Setup

In order to ensure a homogeneous liquid phase in the reactor, the following requirements are crucial:

- For a fast dissolution of the desired amount of oxygen, the setup must be operated at an increased system pressure. Using the PC-SAFT-EOS the phase diagram of the oxygen-toluene solution has been calculated (see Fig. 2). As working pressure *70 bars* has been chosen, allowing a dissolved oxygen concentration of 7 mol% (see scale-up in the corner of the figure), while the experimental setup is designed to withstand $p = 100$ bar. In case of an unexpected formation of gaseous components the pressure can be increased up to $p = 100$ bars to ensure a homogeneous liquid phase.
- To avoid inert gases entering the reactor, pure oxygen is used. In addition, all liquid feeds into the system must be degassed.
- All dead spaces where gas may accumulate must be avoided. An accumulating gas phase would have a potentially explosive composition.
- In multiphase reactors, the concentration of dissolved gas is usually assumed to be the saturation limit. The amount of gas consumed by the reaction can then be determined from the incoming and outgoing gas concentrations. This is not possible in our setup, since there is no exiting gas stream and the reactor is not operated in thermodynamic phase equilibrium. Therefore, a measurement of the dissolved oxygen in the organic liquid phase under elevated pressure has to be developed.

Fig. 2 Phase diagram of the oxygen-toluene mixture calculated with the PC-SAFT-method [2]
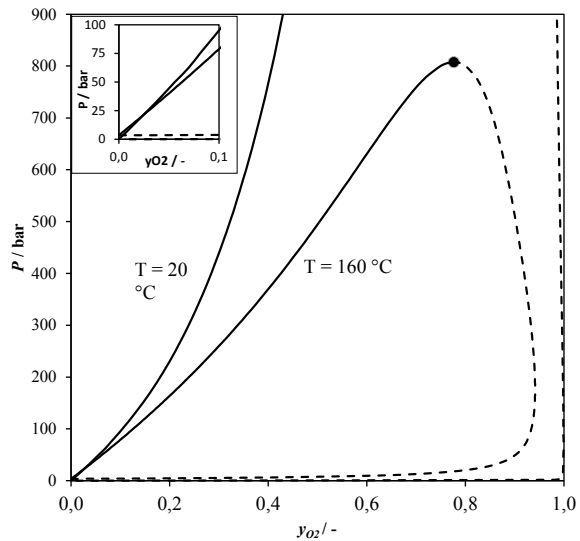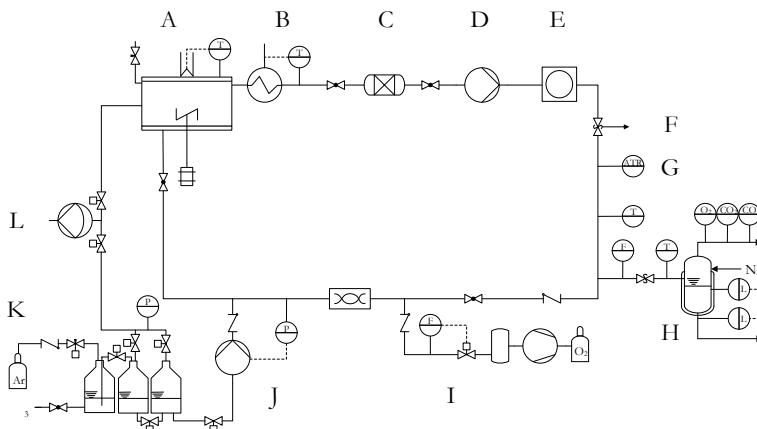
Fig. 3 Flow chart of the experimental setup. A: optically accessible high-pressure reactor, B: flow cooler, C: water absorber, D: annular gear pump, E: viewing window, F: pressure relief valve, G: ATR-FITR spectrometer, H: on-line oxygen analysis, I: oxygen dosing unit, J: toluene dosing and pressure maintenance unit, K: Toluene preparation unit, L: vacuum pump

The experimental setup for the investigation of gas-liquid reaction kinetics consists of a heated reactor (A) and a chilled external circulation (see Fig. 3).

The reactor is designed as an optically accessible cell (see Fig. 4) and is manufactured by *SITEC high-pressure Technology*. It has an integrated heater and is designed for operation at temperatures up to $T = 200$ °C and pressures up to $p = 200$ bar. A safety factor of 4.5 was considered. This means that the reactor can withstand the pressure increase by a factor of 7.7 [3, 4] in the event of a deflagration at operating pressures of up to $p = 115$ bar.

The stirrer is mounted on the reactor from below. This has multiple advantages: First, the stirrer shaft is flooded with liquid, so there is no possibility of a hidden gas phase in the reactor. Second, the head of the reactor, which is in addition the highest point of the whole setup, can be monitored through two opposite display windows with a diameter of $d = 18$ mm. If a gas phase develops during the reaction it can be detected optically. Thus, it can either be drained via a fine dosing valve at the head of the reactor or it can be dissolved again by increasing the pressure. At the bottom as well as at the head of the reactor lateral connections are attached at an angle of 45° (see Fig. 4). Furthermore, a total of three connections are attached to the head of the reactor, through which the highest point of the reactor is accessible.

Analytical and process equipment is mounted at the chilled, external circulation. A constant circulation of $\dot{V} = 50$ mL min^{-1} is applied by means of an annular gear pump. The temperature of the hot reaction mixture is reduced to room temperature at the reactor outlet using a continuous cooler. After passing through the circulation, the circulated liquid stream, enriched with oxygen, is returned to the reactor.

The circulation itself is equipped with the following assemblies in the direction of flow:
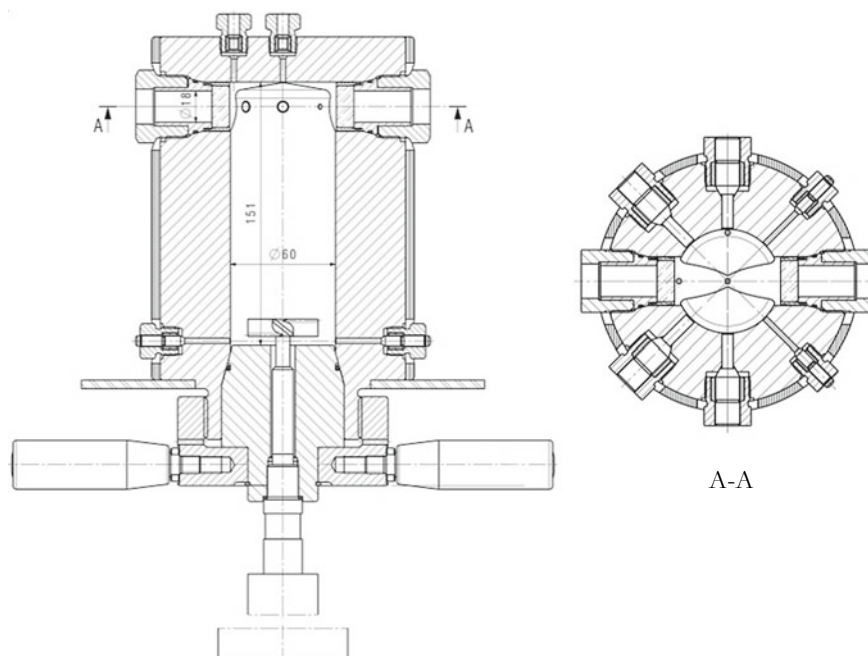
Fig. 4 Technical drawing of the high-pressure reactor

- a continuous cooler (B) with,
- a water absorber (C),
- an annular gear pump (D),
- a viewing window (E) for early detection of a developing gas phase,
- a pressure relief valve to ensure process safety (F),
- an Attenuated Total Reflection Fourier Transformation Infrared Spectrometer (short: ATR-FTIR) Spectrometer (G),
- an analytical unit (H) for measuring the dissolved oxygen concentration and for taking liquid samples for offline concentration determination,
- an oxygen dosing system with an associated static mixer (I), and
- a high-performance liquid chromatography (short: HPLC) pump for pressure control and dosing of toluene (J).

The supplied gas is dosed with a Mass Flow Controller (MFC) from Bronkhorst. A four-liter buffer tank is connected upstream of this, which serves to buffer pressure fluctuations caused by the pressure reducer of the gas cylinder. To ensure that the oxygen is dissolved as quickly as possible, the gas is introduced into the circulation through a nozzle with a diameter of 0.01 mm. Furthermore, the nozzle increases the flow resistance for the liquid and thus also serves as a check valve to prevent flooding of the MFC. Between oxygen analysis (H) and gas dosing (I) a check valve is installed to prevent gas backflow into the oxygen analysis. Before toluene is added, it is dried

and degassed in a preparation unit (K). To ensure a gas and water free system during filling, the reactor and the toluene preparation unit are connected to a vacuum pump (L).

To the best of our knowledge, only two commercial sensors could be found which, according to the manufacturer, can detect the oxygen content in the organic phase under the operating conditions used. The following methods for measuring the dissolved oxygen concentration were developed or tested:

- Photochemical determination of the oxygen content with the FireSting Solvent-Resistant Oxygen Probe by PyroScience.
- Electrochemical determination with the solvent-resistant Clark electrode Orbisphere by Hach company.
- Volumetric determination of the gas phase.
- Determination of the dissolved gas concentration by analyzing the gas phase of a small side stream.

The first three methods did not lead to a continuous and reliable recording of the dissolved oxygen concentration for the used operating conditions.

However, the determination of the concentration of the gas phase of a small side stream using continuous degassing, phase separation and gas analysis allowed reliable measurements of oxygen concentration. This method was developed within this project. In Fig. 5 the method is shown schematically as a flow chart.

The oxygen concentration was determined inside the external loop by continuously draining a small side stream of the reaction mixture. A pressure drop is applied to the stream by passing an overflow valve, which leads to degassing due to the low solubility of gases in toluene at ambient conditions. In a small separator the gas phase is separated from the liquid and diluted by a known inert gas stream of nitrogen. A gas analyzer, containing a paramagnetic and FTIR unit, measures the concentrations of oxygen, CO and CO_2 in the resulting gas stream.

Fig. 5 Flow chart of online oxygen analysis [5]
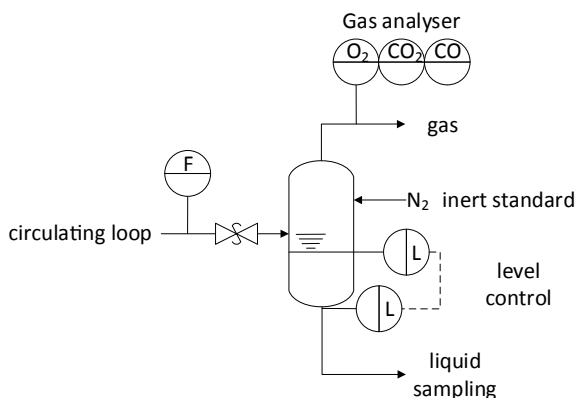
Knowing the flow rate of the discharged reaction mixture, the flow rate of the inert gas stream and the concentrations of the resulting gas stream, the concentrations of dissolved gases within the reaction mixture can be calculated. The amount of dissolved gases remaining in the liquid was found to be negligible and can be omitted [2]. A level control unit collects the resulting liquid phase up to a volume of 1 mL before discharge, which can then be used as a liquid sample for an offline concentration analysis.

In the literature no comparable measuring system for the concentration of a gas dissolved in organic liquid at elevated pressure could be found. Therefore, the functionality of the developed oxygen analysis is tested and validated in [5].

Product concentrations were analyzed via double injection by an *Agilent 7890A* gas chromatograph using a flame ionization detector (for a detailed description of the analyzing method see [2, 5]).

Unless otherwise stated, all experiments were carried out at a temperature of $T = 190\,°C$ and a system pressure of $p = 70$ bar. First the reactor is heated up to the desired temperature, then pressure control is activated. With the addition of oxygen, the actual measurement of the reaction kinetics starts. The volume flow of the oxygen to be dosed is kept constant. Experiments with oxygen input flow rates from $\dot{V} = 25$ mLn min^{-1} to a maximum of 90 mLn min^{-1} were performed. Normalized to the reactor volume this correlates to 52.5–189 Ln m^{-3} min^{-1}. Every $t = 20$ min liquid samples were taken.

2.2 Experimental Results

Figure 6 displays the experimental data of a regular experimental run at temperatures of $T = 190\,°C$. The pressure is maintained at $p = 70$ bar by a PI controller. Both parameters were kept constant after heating up (see Fig. 6a).

The grey areas display the start-up and shut-down of the setup. At time $t = 0$ min the dosing of oxygen starts with a constant volume flow (in this example $\dot{V} = 94.5$ Ln m^{-3} min^{-1}). The period during which oxygen was dosed is highlighted in white. The start and end of the oxygen supply are each marked by a red bar marking the time frame relevant for the investigation of the reaction kinetics. In subsequent applications, the grey colored areas are not considered.

Figure 6c shows the transient concentration profiles of the main reaction products, benzaldehyde, benzyl alcohol, benzoic acid and benzyl hydroperoxide, when the setup is operated at a constant oxygen feed rate. After starting the addition of oxygen at time $t = 0$ min, the concentrations of the intermediate products benzaldehyde, benzyl alcohol and benzyl hydroperoxide increase rapidly. The aldehyde concentration is always slightly higher than the alcohol concentration. After an induction time (in this example 50 min) the concentration of benzoic acid starts to rise linearly. After $t = 100$ min the peroxide concentration drops to a level close to zero and the increase in aldehyde and alcohol concentration stops. While the concentrations of all
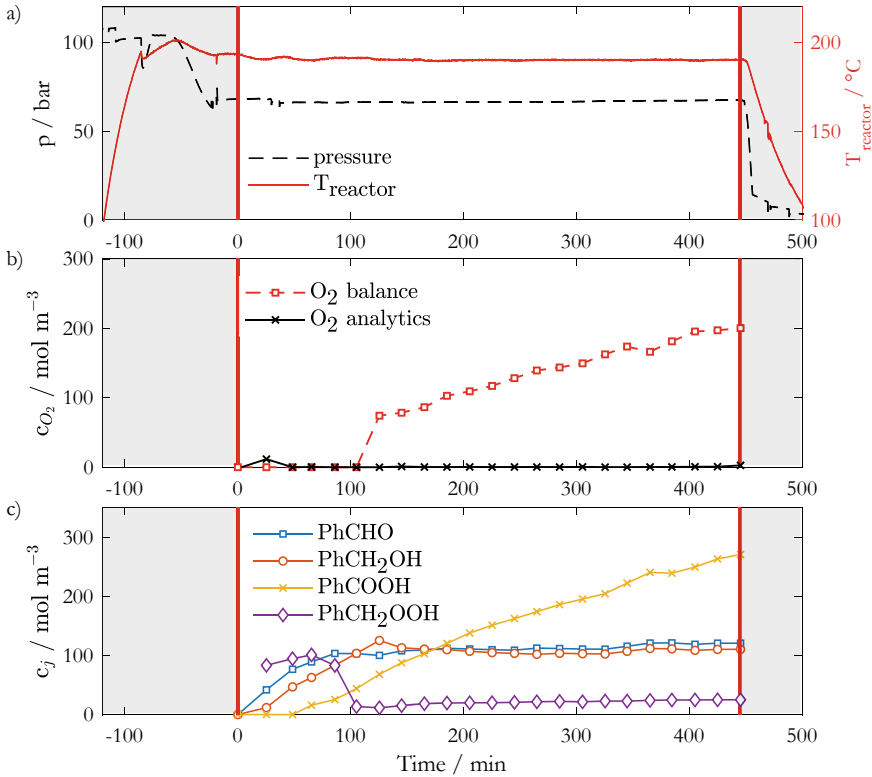
Fig. 6 Course of an experiment with an oxygen dosage of $\dot{V}_{O_2}^{zu} = 94.5 \frac{Ln}{m^3\,min}$, T = 190 °C and p = 70 bar. **a** Operating pressure and reactor temperature, **b** atomic oxygen balance and measured oxygen concentration dissolved in toluene, **c** concentration course of benzaldehyde, benzyl alcohol, benzoic acid and peroxide as function of time

intermediates settle at a stationary value, the concentration of benzoic acid continues to rise linearly.

Figure 6b shows the comparison of the atomic oxygen balance and the measured oxygen concentration as described above. The atomic oxygen balance considers all incoming and outgoing oxygen flows (including small amounts of CO and CO_2 in the derived analytical gas stream) and the stoichiometric amount of oxygen consumed by the reaction. The course of the atomic oxygen balance starts to increase linearly after $t = 100$ min, while the measured concentration remains at a level close to zero after a small maximum at 30 min (before acid production starts). This increasing deviation, starting with the decrease of the peroxide concentration, indicates a change in the reaction mechanism and a related oxygen consumption by a previously unknown species. This consumption could be due to the production of hydrogen peroxide (H_2O_2) and the associated hydroperoxide radical (HO_2*) as described by Hermans et al. [1]. The addition of the oxygen balance would result in

an accumulated concentration of the hydrogen peroxide and hydroperoxide radical of $c_{H_2O_2} + c_{HO_2^*} = 200\,mol\,m^{-3}$. However, neither hydrogen peroxide nor hydroperoxide radical are included in the atomic oxygen balance or in the kinetic model. There are two reasons for this. Firstly, it is not possible to measure the two species online within the experimental setup developed and the analytical methods available. Secondly, in order to correctly include the species and the change in the reaction mechanism, a number of other, mostly radical and therefore not measurable species would also have to be considered in the kinetic model. This in turn leads to a very detailed and complicated reaction network. Such a complex reaction network contradicts the aim of this work to determine an effective kinetic model.

2.3 Kinetic Model of the Toluene Oxidation

Starting from a model suggested by Sandhiya and Zipse [6] without peroxide species, the extended kinetic model R1 to R6 (see Fig. 7 and Table 1) has been developed to numerically describe the experimental results. The center of the model is the benzyl hydroperoxide and its bimolecular reaction as described by Hermans et al. and Sandhiya and Zipse [1, 6-8]. The expansion of the kinetic model with the benzyl

Fig. 7 Reaction network of the kinetic model [5]
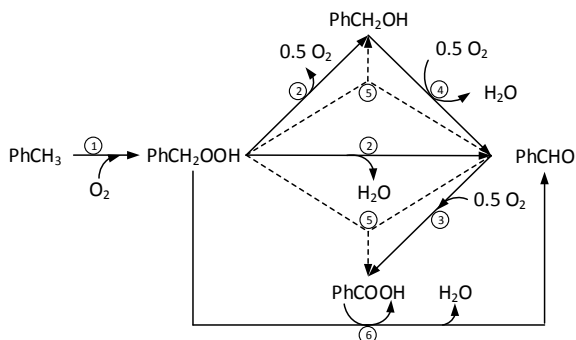
Table 1 Kinetic model of the toluene oxidation [5]

R1	$PhCH_3 + O_2 \rightarrow PhCH_2OOH$	$r_1 = k_1[PhCH_3][O_2]$
R2	$2\,PhCH_2OOH \rightarrow PhCH_2OH + PhCHO + H2O + 0.5\,O_2$	$r_2 = k_2[PhCH_2OOH]^2$
R3	$PhCHO + 0.5\,O_2 \rightarrow PhCOOH$	$r_3 = k_3[PhCHO][O_2]$
R4	$PhCH_2OH + 0.5\,O_2 \rightarrow PhCHO + H_2O$	$r_4 = k_4[PhCH_2OH][O_2]$
R5	$PhCH_2OOH + PhCHO \rightarrow PhCH_2OH + PhCOOH$	$r_5 = k_5[PhCH_2OOH][PhCHO]$
R6	$PhCH_2OOH + PhCOOH \rightarrow PhCOOH + PhCHO + H2O$	$r_6 = k_6[PhCH_2OOH][PhCOOH]$

Fig. 8 Oxygen concentration of simulation with the basic kinetic model without PhCH$_2$OOH (solid line) and the extended kinetic model including PhCH$_2$OOH (dotted line) and measured data (filled square) as function of reaction time [5]
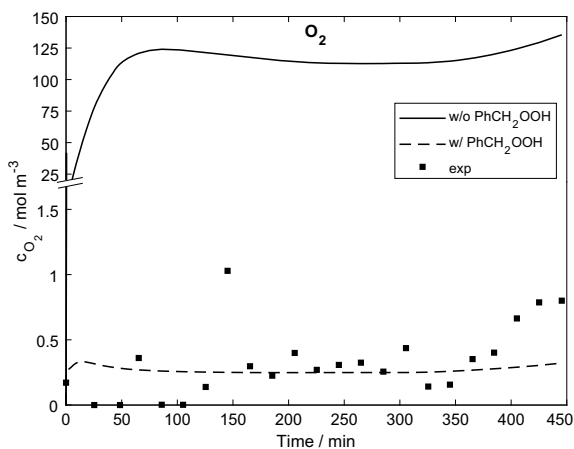
Table 2 Kinetic parameter of model of the toluene oxidation

Parameter	Values	Unit
k_1	3.7928e−5	m^3 mol^{-1} s^{-1}
k_2	4.1630e−6	m^3 mol^{-1} s^{-1}
k_3	4.2042e−4	m^3 mol^{-1} s^{-1}
k_4	3.8642e−6	m^3 mol^{-1} s^{-1}
k_5	1.7609e−6	m^3 mol^{-1} s^{-1}
k_6	8.3924e−6	m^3 mol^{-1} s^{-1}

hydroperoxide leads to an improvement in the description of the oxygen concentration compared to basic models without peroxides, as suggested by Sandhiya and Zipse [6] (see Fig. 8). This finding is unique to this project since the online monitoring of the oxygen was never done before and is described in more detail in [5].

Table 2 summarizes the results of the parameter adjustment. Both the values of the reaction parameters and the reaction conversion are one to two orders of magnitude lower than the values determined by Hoorn et al. [9, 10]. This can be explained by the absence of a catalyst in this work. Hoorn et al., however, catalyzed his reaction with bromide.

Hermans et al. also investigated toluene oxidation without the use of a catalyst. While the reaction conversions are of the same order of magnitude, no comparative values for kinetic parameters are given in the publications [1, 11–13].
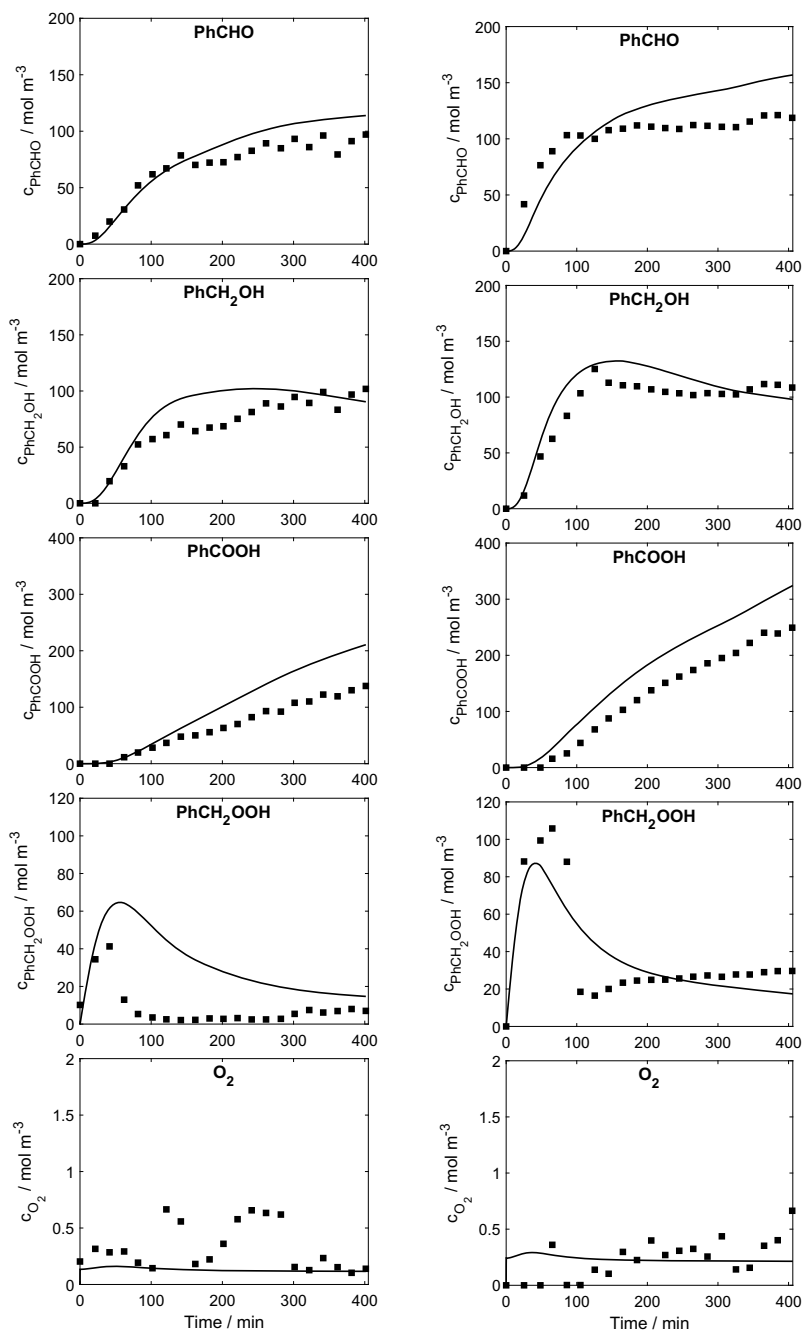
Fig. 9 Comparison of model prediction (solid line) and experimental values (filled square) of the concentration of PhCHO, $PhCH_2OH$, $PhCH_2OOH$, PhCOOH, O_2 as function of reaction time for an O_2 input flow rate of 52.5 Ln m^{-3} min^{-1}(left) and 94.5 Ln m^{-3} min^{-1} (right)

2.4 Validation of the Kinetic Model

The kinetic model has been validated against experiments for oxygen input flow rates from $\dot{V}$ = 52.5 to 115.5 Ln m^{-3} min^{-1}. Figure 9 shows the comparison of oxygen flow rates of 52.5 and 94.5 Ln m^{-3} min^{-1}. Further results are given in [5].

The kinetic model is able to map the steep increase in the concentrations of the intermediate products benzaldehyde, benzyl alcohol and benzyl hydroperoxide at the beginning of the reaction as well as the delayed production of benzoic acid. Furthermore, the maximum in the peroxide concentration and the resulting reduced production rates of benzaldehyde and benzyl alcohol are also described.

In addition, the model represents the oxygen concentration, which is about two orders of magnitude lower than the concentrations of all other intermediate products.

The previously mentioned neglect of hydrogen peroxide and hydroperoxide radicals within the reaction network and the focus on the oxygen concentration during parameter adjustment leads in all comparisons to a systematic overestimation of the concentrations of benzaldehyde and benzoic acid with increasing reaction time.

While the kinetic model can describe low oxygen dosage rates of $\dot{V}$ = 52.5–94.5 Ln m^{-3} min^{-1} well, volume flows of more than 115.5 Ln m^{-3} min^{-1} are not adequately represented. For large oxygen flow rates, the concentrations of all species are overestimated, with the exception of oxygen, which is underestimated. The systematic overestimation indicates a change in the reaction mechanism. Already 1967 Morimoto and Ogata described a change in the reaction mechanism at high oxygen concentrations in the inflowing gas.

Therefor the presented kinetic model is valid for oxygen input flow rates smaller than $\dot{V}$ =115.5 Ln m^{-3} min^{-1}, which corresponds to a dissolution of 4.73 mol m^{-3} min^{-1}. Under industrial conditions, the oxidation of toluene runs at p = 10–30 bars and T = 150–250 °C [14, 15], not allowing such fast dissolution of oxygen. Therefore, the model covers the range of oxygen concentrations which can occur under industrial operation conditions.

Furthermore, since the model has been determined in homogeneous liquid phase, it is not limited by mass transfer. Therefore, the model is independent of any operating conditions influencing the mass transfer and can be used for example in numerical studies without any restrictions regarding those properties.

3 Numerical Study of the Toluene Oxidation in a Reactive Bubbly Flow

In order to obtain a better understanding of the dependencies and interactions between the fluid dynamics, mass transfer and chemical reaction, a simplified flow field around a single bubble is studied. For this purpose, direct numerical simulations (short: DNS) were performed using OpenFOAM to investigate the ongoing reaction in the vicinity of a bubble. Fluid dynamics, mass transfer and reaction are modeled and

Fig. 10 Principle of the representative elementary volume (REV) of a bubble column
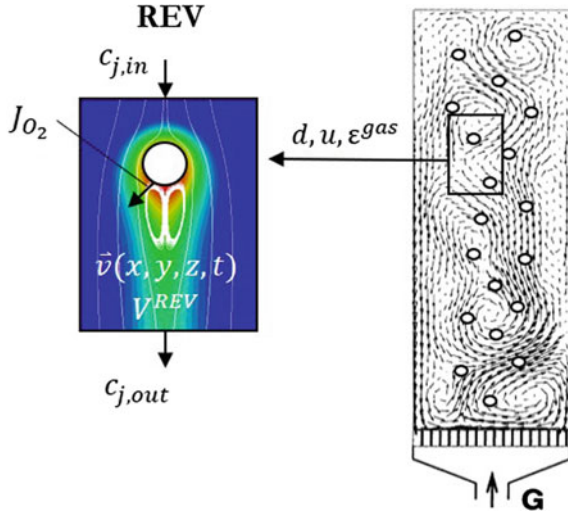
implemented separately. The reaction is based on the reaction kinetics of toluene oxidation developed in the previous chapter.

Since the high numerical effort of a DNS does not allow to calculate a reactor in detail, a single rising bubble is studied. Based on the idea that the reactor is uniformly filled with identical bubbles and neglecting swarm effects a single rising bubble describes the processes within a multi-phase reactor as a representative elementary volume (REV).

In the REV (see Fig. 10) the diameter of the bubble d_b, the ascent velocity u and the gas content ε^{gas} are mean values and are equal to that of the multiphase reactor. The bubble is modeled as a rigid, 2D sphere with a constant oxygen concentration. The concentration of oxygen at the bubble surface is calculated by Henry's law. The mass transfer of the oxygen J_{O_2} from the gas phase to the liquid phase results from the concentration gradient between the oxygen concentration in the bulk phase and the bubble surface. The transport equations of the individual species represent the mass transport in the liquid phase. The chemical reaction is considered as the source term.

The description of the bubble as rigid and in 2D is a very strong reduction of the complexity of the fluid dynamics. Nevertheless, qualitative statements can be made, since the interplay between the physio-chemical processes in 2D and 3D is expected to be comparable.

3.1 Numerical Model

The bubble has a fixed diameter of $d_B = 2$ mm. The length of the model geometry is divided into 2 areas. In front of the bubble there is an inlet zone of 20 mm. The

Table 3 Simulation parameters

Parameter	value
p	30 bar
T	463.15 K
$c_{O_2,cyl}$	101.4 $\frac{Mol}{m^3}$
$H_{O_2 Tol}$	0.06905 $\frac{bar\, m^3}{Mol}$
v_{Tol}	2.3232e^{-7} $\frac{m^2}{s}$
η_{Tol}	1.429e^{-4} Pa s
ρ_{Tol}	695.85 $\frac{kg}{m^3}$

area from the front of the bubble to the outlet of the domain is called the tailing zone and is also $l = 20$ mm long. For the investigations shown in the following, only the tailing zone is relevant, since only here the reaction takes place. The inlet zone is required for numerical reasons for the correct representation of the fluid dynamics. The gas content of the tailing zone corresponds to a gas hold-up of $\varepsilon^{gas} = 1\%$.

The concentrations at the inlet are set to $c_{PhCH_3} = 7552.1$ Mol m^{-3} for toluene and zero for all other species. The oxygen concentration on the bubble surface is set to $c_{O_2} = 101.4$ Mol m^{-3}. Further conditions are summarized in Table 3. Binary diffusion coefficients were calculated according to the correlation by Wilke and Chang [16], the molar volume at the boiling point according to the additive method of Poling et al. [17] (Fig. 11).

The fluid dynamics and the reactive mass transport are sequentially solved in each timestep. Therefor the PISO (pressure-implicit split-operator) algorithm it used. For the mesh spacing a grid convergence index of $GCI = 1.5\%$ has been found using
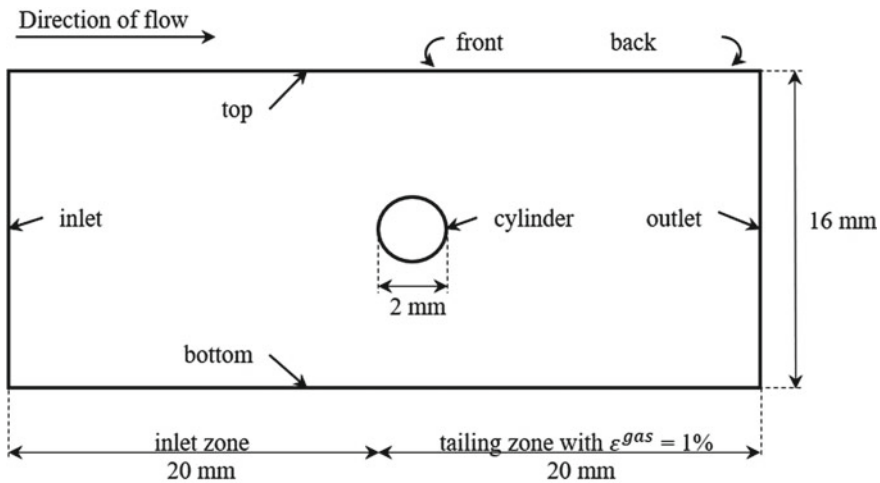
Fig. 11 Geometry of the mesh used for the direct numerical simulation

Fig. 12 Validation of
calculated fluid dynamics by
the drag coefficient
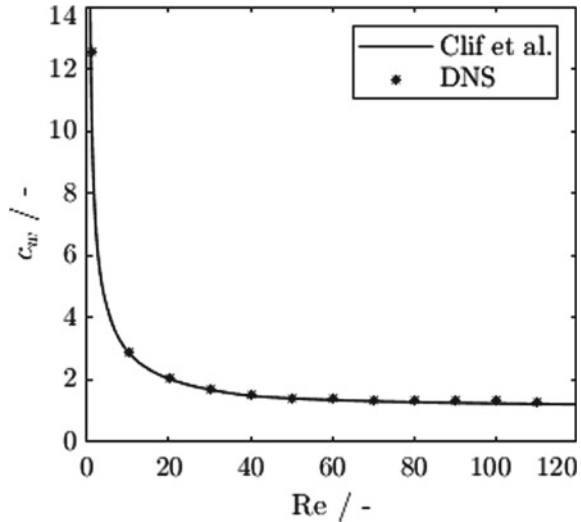
120×48 cells. This corresponds to a cell size at the bubble surface of 0.0103 mm
including five refinement steps towards the bubble. The comparison of the calculated
drag coefficient with correlation by Clif et al. [18] validates the calculation of the
fluid dynamics (see Fig. 12).

3.2 Results

Figure 13 illustrates the reaction rate of the first reaction R1 in the vicinity of the
bubble for three simulations with different reaction kinetics and a rising velocity of
$Re = 100$, where Re is referring to the bubble diameter. For the plot, the reaction
rate of the first reaction was chosen, since it is of essential importance for the whole
reaction network. In this reaction toluene is converted to benzyl hydroperoxide,
which further reacts to various subsequent products. If the benzyl hydroperoxide is
not produced in the first reaction, the subsequent reactions cannot take place.

The reaction kinetics as determined in Sect. 2 exhibits a very slow reaction rate
close to zero (see Fig. 13a). This leads to the conclusion that the reaction network of
the toluene oxidation is not limited to the vicinity of the bubble but takes place in the
bulk phase. In that way, the reaction is not influenced by the flow around the bubble.
Speeding up the reaction kinetics by a factor of 100 the reaction R1 is taking place at
the bubble surface and its vicinity (see Fig. 13b), leading to the conclusion that this
reaction might be influenced by the fluid dynamics of the bubbly flow. The reaction
network which has been sped up by a factor 10,000 is running in a very limited
volume only at the bubble surface, again, not being influenced by fluid dynamics.
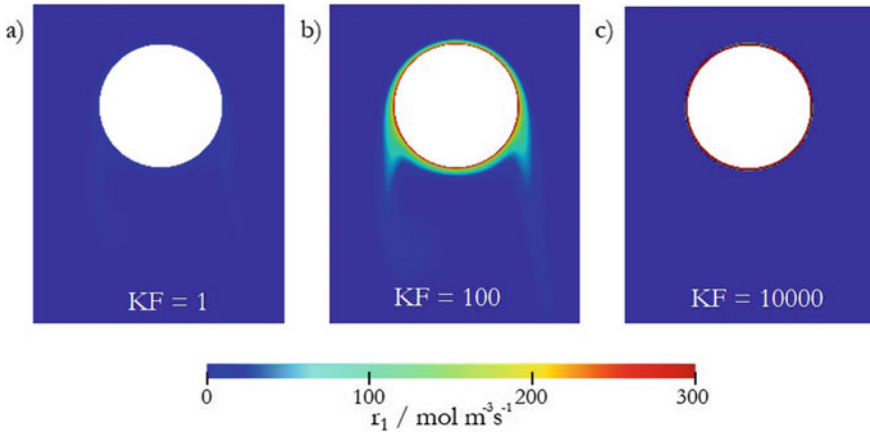
Fig. 13 Field of the reaction rate r_1 of the toluene oxidation with an accelerated kinetics by the factor **a** 1, **b** 100, **c** 10,000 at Re $= 100$

These qualitative statements should be further examined and experimentally confirmed. Therefore, in the following chapter the toluene oxidation is studied in a bubble column at the same conditions as in the DNS calculations of $p = 30$ bars and $T = 190\,°\mathrm{C}$. In Sect. 5 further numerical studies with changed reaction velocities are presented.

4 Study of the Toluene Oxidation in a Technical Bubble Column

The previous chapter showed that the toluene oxidation seems to be too slow to exhibit a dependency of reaction yield/selectivity from the bubble size. To prove this, the toluene oxidation was measured on freely rising bubbles under industrial conditions. For this purpose, experiments were carried out in an optically accessible high-pressure bubble column reactor at $T = 190\,°\mathrm{C}$ and $p = 30$ bar. The setup is explained below.

4.1 Experimental Setup

The experimental setup used is similar to the one presented in Chapter "Investigation of Reactive Bubbly Flows in Technical Apparatuses". As shown in the flow chart in Fig. 14 the setup around the optically accessible high-pressure bubble column (developed within the dissertation by Schäfer [19] at the ICVT in Stuttgart) is modified and extended for the use of toluene at high temperatures. To heat up the column
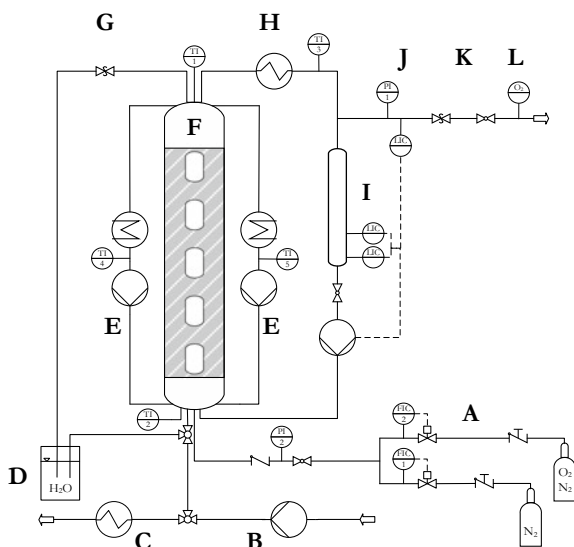
Fig. 14 Flow chart of the experimental setup of the high-pressure bubble column for the investigation of gas-liquid reactions under industrially relevant conditions. A: gas supply via two mass flow controllers, B: gear pump for fluid supply, C: heat exchanger, D: water barrel for emergency shutdown, E: heating circuit with thermostat and oil pump, F: visible high-pressure bubble column reactor, G: safety relief valve, H: cooler, I: phase separator, J: pressure sensor, K: pressure controller, L: explosion-proof paramagnetic oxygen analyzer

two heating circuits (E in Fig. 14) have been added. Further, to recover vaporized toluene from the exhaust gas a condenser unit consisting of a cooler (H in Fig. 14) and a phase separator (I in Fig. 14) has been installed. The collected condensate is automatically returned to the bottom of the bubble column at regular intervals by means of a level control in the phase separator.

Further safety equipment is similar to the one in Chapter "Investigation of Reactive Bubbly Flows in Technical Apparatuses". In case of an emergency shutdown the reactor can be emptied at any time into a barrel (D in Fig. 14) filled with water by a three-way valve at the bottom of the column or by a safety valve (G in Fig. 14) at its top. An optical liquid sensor is installed at the exhaust tract to prevent the accumulation of liquid in the exhaust gas. After an experimental run, the outflowing reaction mixture is passed through a heat exchanger (C in Fig. 14), preventing the evaporation of the highly volatile toluene.

The reaction gas is fed into the column by a gas distributor at its bottom. The gas distributor can be mounted with differently sized nozzles. For the presented experiments single injectors with outlet openings of the nozzles of $d_n = 0.1$–0.4 mm were chosen. The produced bubble size distributions are determined optically on several rising heights by image processing as again explained in more detail in Chapter "Investigation of Reactive Bubbly Flows in Technical Apparatuses".

4.2 Experimental Conditions

The experiments presented in the following were carried out at a reactor temperature of $T = 190$ °C and a pressure of $p = 30$ bar. The column was filled with 1.5 L of toluene, which corresponds to a filling height of $h = 655$ mm. To ensure a homogeneous temperature distribution, the reactor temperature was monitored at the bottom and at the top of the column. The experiment started at a temperature gradient of less than three Kelvin.

To create an oxygen-free atmosphere, the column was flushed with nitrogen for $t = 20$ min before filling. Continuous aeration of the column with nitrogen prevented the toluene from flowing back into the gas line during the heating up process. After reaching operating temperature and pressure, the experiment started by adding oxygen.

Diluted air with 8 vol% oxygen and 92 vol% nitrogen with a purity of 99.9999% (purity grade 5.0) was used as reaction gas. Due to explosion prevention, the oxygen concentration in the gas phase must not exceed 10 vol%. The volume flow of the reaction gas of $\dot{V} = 50$ mLn min^{-1} remained constant throughout the entire experiment. In relation to the reactor volume, this corresponds to an aeration rate of $\dot{V} = 33.3$ Ln m^{-3} min^{-1}. If the aeration rate is increased well above $\dot{V} = 50$ mLn min^{-1}, the overlapping of individual bubbles increases, leading to an increasing error in the optical analysis of the bubble size distribution.

Liquid samples were taken every $t = 30$ min at a reactor height of $h = 112$ mm, 282 mm and 452 mm. For this purpose, capillaries were led through the viewing windows into the interior of the reactor. The concentrations within the samples have been determined by a gas chromatographic analysis as described in [5].

4.3 Results

Figures 15 and 16 show the concentrations of benzaldehyde and benzyl alcohol for different bubble sizes produced by the gas distributer with outlet openings from 0.1 to 0.4 mm at different rising heights. The obtained bubble diameters d_B can be found in the legend of Fig. 15. The measured concentrations are at a very low level of less than $c = 20$ mol m^{-3} and thus more than one order of magnitude smaller than the concentrations observed in the kinetic reactor (see Sect. 2). Benzyl alcohol just exceeds the lower detection limits of the GC used. Benzyl hydroperoxide and benzoic acid could not be detected. The low concentrations are due to the low oxygen input.

In relation to the reactor volume, $\dot{V} = 2.66$ Ln m^{-3} min^{-1} oxygen were added in the bubble column reactor compared to $\dot{V} = 52.5$–135.5 Ln m^{-3} min^{-1} in the kinetic reactor in Sect. 2. This is due to the optical analysis requiring a low aeration rate and the prevention of the risk of explosion leading to a low oxygen concentration in the reaction gas. Therefore, compared to the experiments in the kinetic reactor, the oxygen addition in relation to the reactor volume is smaller by a factor of 20 to 50.
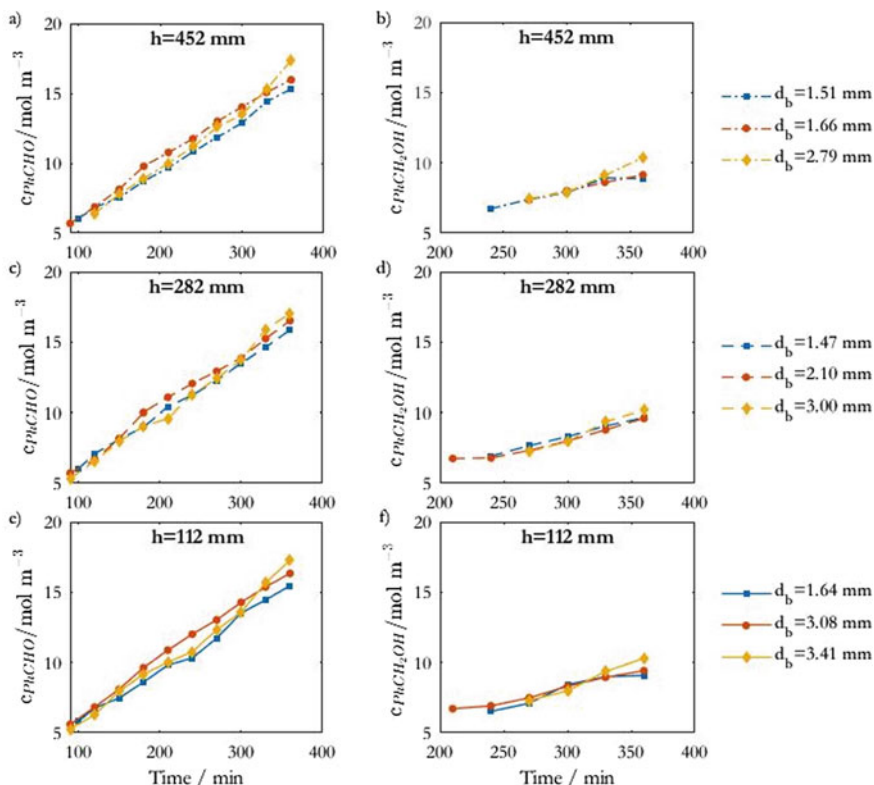
Fig. 15 Concentrations for benzaldehyde (left) and benzyl alcohol (right) for a bubble generation with gas distributors with outlet openings of 0.1 mm (filled square), 0.2 mm (filled circle) and 0.4 mm (filled diamond) at a reactor height of 112 mm (bottom), 282 mm (middle), 452 mm (top)

The shown concentration curves in Fig. 15 are nearly superimposed. The comparison shows that reaction yield and selectivity do not depend on bubble sizes. This confirms the results of the simulation for $KF = 1$ in the previous chapter.

Further, the superimposed concentration curves in Fig. 16 show that there are no concentration gradients over the reactor height which means that the reactor can be regarded as ideally mixed. Thus, the bubble column reactor can be regarded simply as an ideally mixed semi-batch reactor for reactions that are sufficiently slow.

A semi-batch model, using the reaction kinetics determined in Sect. 2 meets the order of magnitude of the experimental determined concentrations quite well (see Fig. 17). Since no oxygen could be detected in the exhaust gas, the semi batch model assumes that all added oxygen dissolves in the liquid phase. Yet the semi-batch model overestimates concentrations by predicting an exponential rise, while in the experiment the concentrations rise in a linear manner. This may be explained by the cooled recirculation of the condensed toluene, leading to a short, but strong
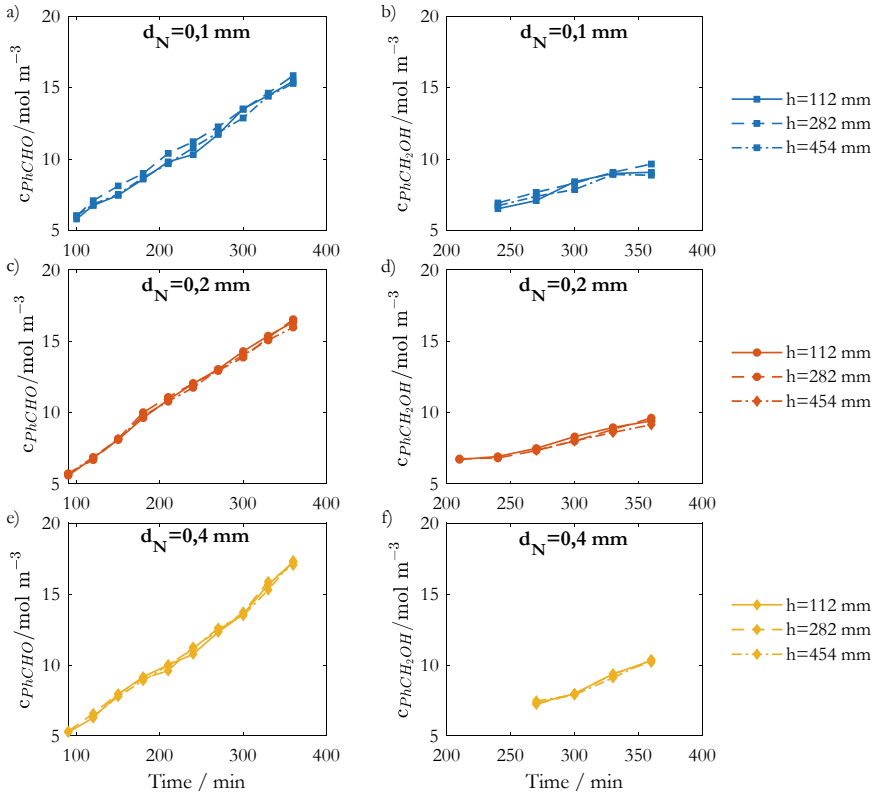
Fig. 16 Concentrations for benzaldehyde (left) and benzyl alcohol (right) at a reactor height of h = 112 mm, 282 mm, 452 mm for bubble generation of with gas distributors with outlet openings of d_n = 0.1 mm, 0.2 mm and 0.4 mm

and regularly occurring temperature reduction in the bottom of the column. Theses fluctuations in temperature may reduce the reaction rate.

Yet one can conclude that the reaction course of the toluene oxidation is not influenced by the bubble size of the rising oxygen containing bubble. Further, the rising bubbles lead to an ideally mixing within the reactor. Therefore the bubble column reactor can be described with a semi-batch reactor model, which, although the course of the concentration curves are not met, can describe the yield of the reaction.

The investigation of a faster reaction system, being influenced by the bubble sizes is presented in Chapter "Investigation of Reactive Bubbly Flows in Technical Apparatuses".

Fig. 17 Comparison of concentrations of benzaldehyde and benzyl alcohol determined by a semi-batch model (solid) and experimental values
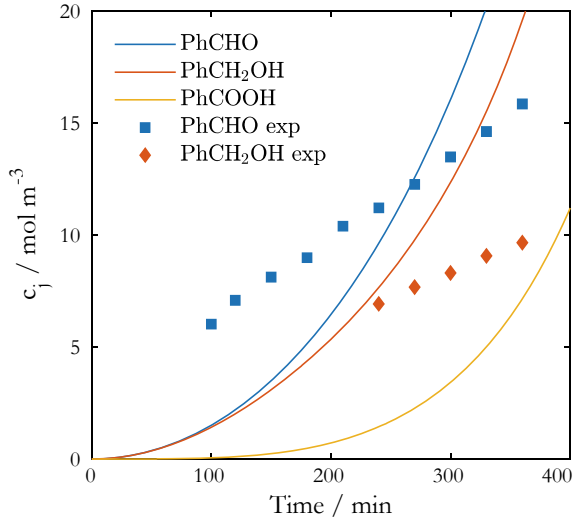
5 Numerical Study of the Mixing Dependencies in a Reactive Bubbly Flow

As discussed in Sect. 3 the toluene oxidation that has been sped up by a factor 100, runs at the bubble surface and in its vicinity. This leads to the conclusion, that reactions running on a certain time scale, which is not too fast and not too slow, can be influenced by the flow pattern in the bubble wake. In the following this statement is studied in more detail by looking at the questions:

- Does the mixture masking in the wake of the bubble have an influence on the reaction that takes place?
- Which reactions are influenced by mixture masking?
- What causes the mixture masking?

5.1 Preliminary Considerations

No matter which parameter is varied, always all physical processes are changed, due to their strong coupling. A change in the velocity with the purpose of varying the fluid dynamics leads, for example, to a change of the thickness of the boundary layer at the bubble surface and therefore to a faster removal of the oxygen that has passed over. This changed concentration gradient in turn leads to an enhanced mass transfer rate. This example shows how distinct and close the linkage of these processes actually is.

To illustrate the dependencies, in the following, non-dimensional numbers are used. The flow around the bubble is characterized by the Reynolds number (Re).

$$\text{Re} = \frac{\rho_{\text{PhCH}_3} u_\infty d_b}{\eta_{\text{PhCH}_3}} \tag{1}$$

Thereby, u_∞ is the rising velocity and d_b the diameter of the bubble, ρ_{PhCH_3} and η_{PhCH_3} are the density and viscosity of toluene. For the results presented, the inflow velocity was varied. To characterize the chemical reaction the selectivity ($S_j^{O_2}$) in relation to the converted oxygen is used.

$$S_j^{O_2} = \frac{|\nu_{O_2}|}{\nu_j} \frac{N_{j,out} - N_{j,in}}{N_{O_2,in} - N_{O_2,out}} \tag{2}$$

Thereby ν_j is the stoichiometric coefficient and N_j the in or out flowing molar flow of the component j. In all simulated cases the dissolved oxygen is completely consumed. Thus, the amount of converted oxygen is also a measure for the amount of oxygen transferred into the liquid phase. In this case the selectivity can be regarded as a conversion normalized by the mass transfer. Thus, it allows the mass transfer to be excluded from the analysis. Furthermore, the selectivity is a direct measure for the efficiency of a reactor. If it is possible to increase the selectivity of a reaction by changing the operating mode of the reactor, a reactor can be operated more efficiently, for example by generating large or small bubbles.

Another important dimensionless number for the characterization of a reactive bubbly flow is the Damköhler number of first order (Da_1).

$$\text{Da}_1 = \frac{k_1 \, d_b \, c_{\text{PhCH}_3,in}}{u_\infty} \tag{3}$$

Thereby k_1 is the kinetic coefficient of the first reaction and $c_{\text{PhCH}_3,in}$ the inflowing concentration of toluene. Da_1 describes the relationship between the time scales of fluid dynamics (given by the inflow velocity) and the chemical reaction (given by the reaction kinetics). Thus, the first order Damköhler number can also be interpreted as the dimensionless residence time of a volume element until its complete consumption through the reaction and is thus an indication of the location of the reaction. For small Da_1 numbers the reaction takes place in the bulk of the surrounding liquid phase. With an increasing Da_1 number the reaction site approaches the bubble surface.

5.2 Is the Overall Reaction Influenced by Mixing?

To emphasize the influence of non-ideal mixing in the bubble wake, the total reaction in a representative volume around a bubble (REV), as introduced in Sect. 3, is compared with that of an ideal tubular reactor (see Fig. 18). Inflowing concentrations, the reactive volume and the mean residence time of the dissolved gaseous species are chosen identical for both models. The models differ in their mixing characteristics and the way oxygen is supplied to the liquid. The REV represents a non-ideal mixed

Fig. 18 Idea of the comparison of the REV-Model with an ideal plug flow tubular reactor (PFTR)
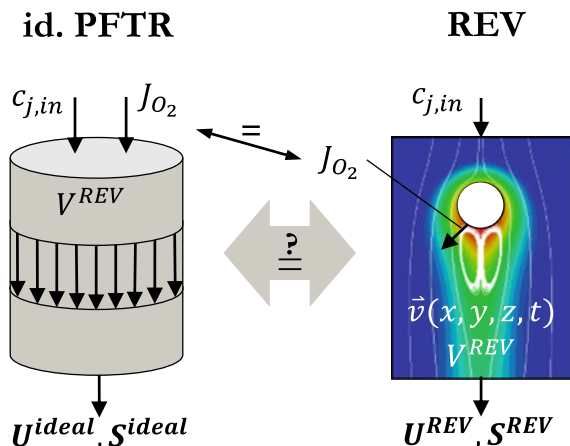
case, where mixing is dependent on the Reynolds number and oxygen is fed into the system via the mass transfer at the surface of the rigid bubble. The ideal reactor, on the other hand, represents an ideal mixed case, where the mixing is independent of any velocity, and the oxygen is added ideally mixed at the reactor inlet. Hence, differences in the produced product spectrum, given in terms of selectivity, are due to the differences in the ideal and non-ideal mixing as well as mass transfer. In other words, the comparison of the two settings permits to estimate whether the flow around a bubble has an influence on the overall reaction.

Figure 19 displays the selectivity of the oxidation of toluene as function of the Reynolds number for an accelerated reaction kinetics by the factors $KF = 1$, 100 and 10,000. For the reaction kinetics as determined in Sect. 2 ($KF = 1$), the time scale of fluid dynamics is significantly faster than the one of the reaction. Therefore, only the first reaction step, the formation of benzylhydroperoxide, takes place and peroxide is the only product. The reaction time constant is so large, that the REV can be regarded as ideally mixed and thus the flow does not have any influence on the selectivity of the reaction network (see Fig. 19 left column). An exception is the potential flow at $Re = 1$, where the diffusive transport is the dominant radial transport mechanism.

An increasing acceleration of the reaction kinetics causes the reaction zone to migrate towards the bubble. At an acceleration factor of $KF = 100$, the first reaction takes place at the bubble surface and in its vicinity, as shown in Fig. 13. Consequently, the selectivity shows a strong dependence on the flow around the bubble (see Fig. 19 center column).

In the ideal reactor, the acceleration of the flow leads to a decrease in residence time, thus leading to an incomplete reaction pathway, which again leads to a shift of the selectivity towards benzyl hydroperoxide. For longer residence times at $Re < 10$, also the consecutive reactions take place, resulting in the formation of benzaldehyde, benzyl alcohol and benzoic acid.

Although the bubbly flow of the REV shows the same trends of the selectivity with respect to the residence time, the formation of a stationary vortex leads to a
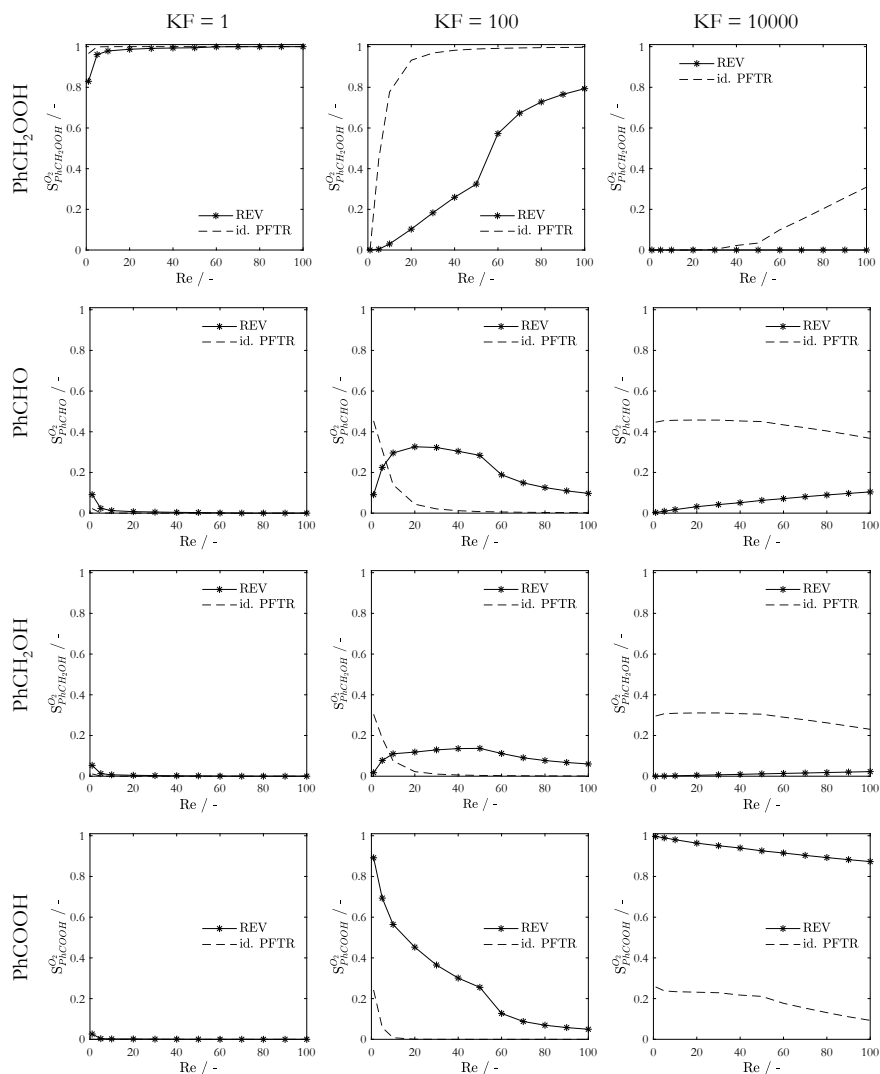
Fig. 19 Comparison of the reaction in the bubbly flow of the REV and in the ideal tubular reactor by the selectivity of the components of benzyl hydroperoxide, benzyl alcohol, benzaldehyde and benzoic acid with respect to the consumed oxygen as a function of the Reynolds number for toluene oxidation with accelerated kinetics by the factor KF = 1 (left), 100 (center) and 10,000 (right)

delay of this influence. The vortex forms a transport barrier between its interior and exterior [20, 21], so the residence time distribution significantly widens and a pronounced tailing is formed. This tailing of the residence time distribution, caused by the stationary vortex, slows down changes of the selectivities compared to the ideal tubular reactor.
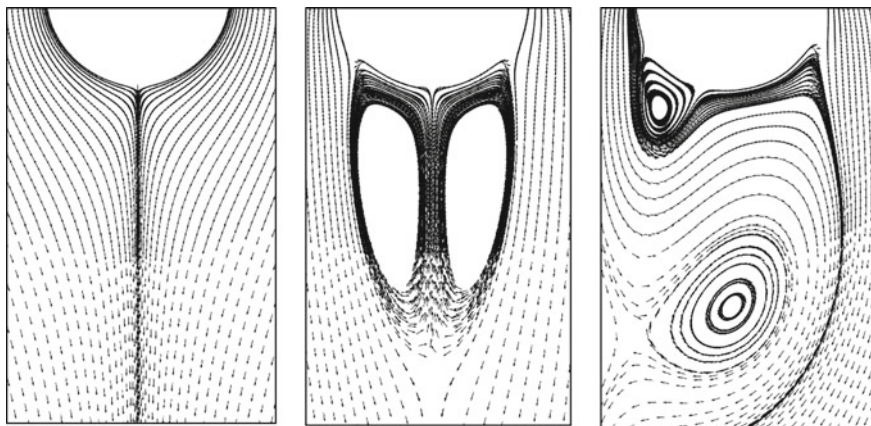
Fig. 20 Locally resolved velocity field around a bubble at Re = 1, Re = 30, Re = 100

Figure 20 shows the velocity fields for the typical flow patterns around a bubble with a potential flow at $Re = 1$ (left), a stationary bubble wake at $Re = 30$ (middle) and a snapshot of a dynamically shedding vortex at $Re = 100$ (right). At $Re = 30$, the transport barrier by the stationary vortex is clearly visible.

The kink in the selectivities at $Re = 50$ is due to the change in the flow regime. For the flow around a 2D bubble with Reynolds numbers greater than 54 [20, 21], the wake starts to shed from the bubble, leading to the formation of the Kármán vortex street, (see Fig. 20 right). The vortex shedding breaks up the transport barrier and thus improves the mixing, whereby the reaction process is increasingly converging to that of the ideally mixed reactor.

With a further acceleration of the reaction kinetics of $KF = 10,000$ the reaction takes place exclusively at the bubble surface. Consequently, the selectivity is only a weak function of the Reynolds number. The differences between the REV and the ideal reactor model result from the mass transport limitation in the REV due to the introduction of the oxygen at the bubble surface, while in the ideal reactor case oxygen is added ideally mixed at its entrance.

To conclude, Fig. 19 shows that the ongoing toluene oxidation would be significantly influenced by the fluid dynamics of a bubbly flow if the reaction occurs by reaction rates that are around 100 times higher ($KF = 100$).

5.3 When Does Micro Mixing Affect the Overall Reaction Rate?

As shown above, the selectivity is influenced by the fluid dynamics for a reaction on the certain reaction time scale, which in this example corresponds to an acceleration factor of $KF = 100$. In order to define this reaction time scale more precisely and to

be able to make a generally valid statement, it is compared to the time scale of the flow around a bubble. For this purpose, in the following, the first-order Damköhler number (Da_1) is used. It describes the relationship between time scale of reaction and flow. For better readability the first-order Damköhler number is referred to as Damköhler number subsequently.

Figure 21 shows the course of the selectivity with respect to the consumed oxygen from the DNS simulations for the components benzyl hydroperoxide, benzaldehyde, benzyl alcohol and benzoic acid as a function of the Damköhler number at constant Reynolds numbers of $Re = 1$, 30 and 100. The graphs have two characteristics. Firstly, the course of the selectivity differs for the three Reynolds numbers only in the range of $0.1 < Da_1 < 1000$. Secondly, all selectivity curves can be divided into a kinetics-limited, a mixture-masked and a mass transport limited range.

Kinetics Limited Range ($Da_1 < 0.1$): In the kinetics limited range the reaction is significantly slower than the fluid dynamics. The ratio of the time scales is much smaller than unity. This means that the reaction does take place far away from the bubble in the bulk of the liquid. Consequently, the selectivities of the components do not depend on the flow pattern. Accordingly, the selectivities of the three characteristic Reynolds numbers are superimposed. The diagrams shown in Fig. 19 with a kinetics factor $KF = 1$ are assigned to this area. To increase the yield in a process with this Damköhler number range, it is sufficient to intensify the mass transfer of oxygen into the liquid phase.

Mass Transport Limited Range ($Da_1 > 1000$): In the mass transport limited range, the time scale of the reaction is significantly faster than that of fluid dynamics. Accordingly, the reaction takes place exclusively on the bubble surface. This results in the mass transport limitation, which favors reactions to the end product benzoic acid. To improve the reaction yield, the mass transfer of oxygen needs to be intensified. The diagrams shown in Fig. 19 with a kinetics factor $KF = 10,000$ are to be assigned to this range.

Mixture-Masked Region ($0.1 < Da_1 < 1000$): The mixture-masked region represents a transition between the kinetics-limited and mass transfer-limited regions. The time scales of the reaction and the fluid dynamics are similar, so that the reaction takes place both at the bubble surface and in the wake of the bubble.

In contrast to the aforementioned regions, selectivity is a function of the Reynolds numbers. If the reaction takes place in the mixture-masked region, a variation of the flow pattern leads to significant changes in selectivity.

While the curves for Reynolds numbers $Re = 1$ and 100 are similar, the curve for $Re = 30$ differs significantly. This confirms the previously mentioned conclusion that the shedding vortex at $Re = 100$ improves the mixing, while the stationary vortex at $Re = 30$ represents a transport barrier (see Fig. 20). For $Re = 1$, the reaction as well as the convective mass transport are significantly slower than the diffusive mass transport, thus the fluid is well mixed. This is similar to the situation of the detached vortex at $Re = 100$.
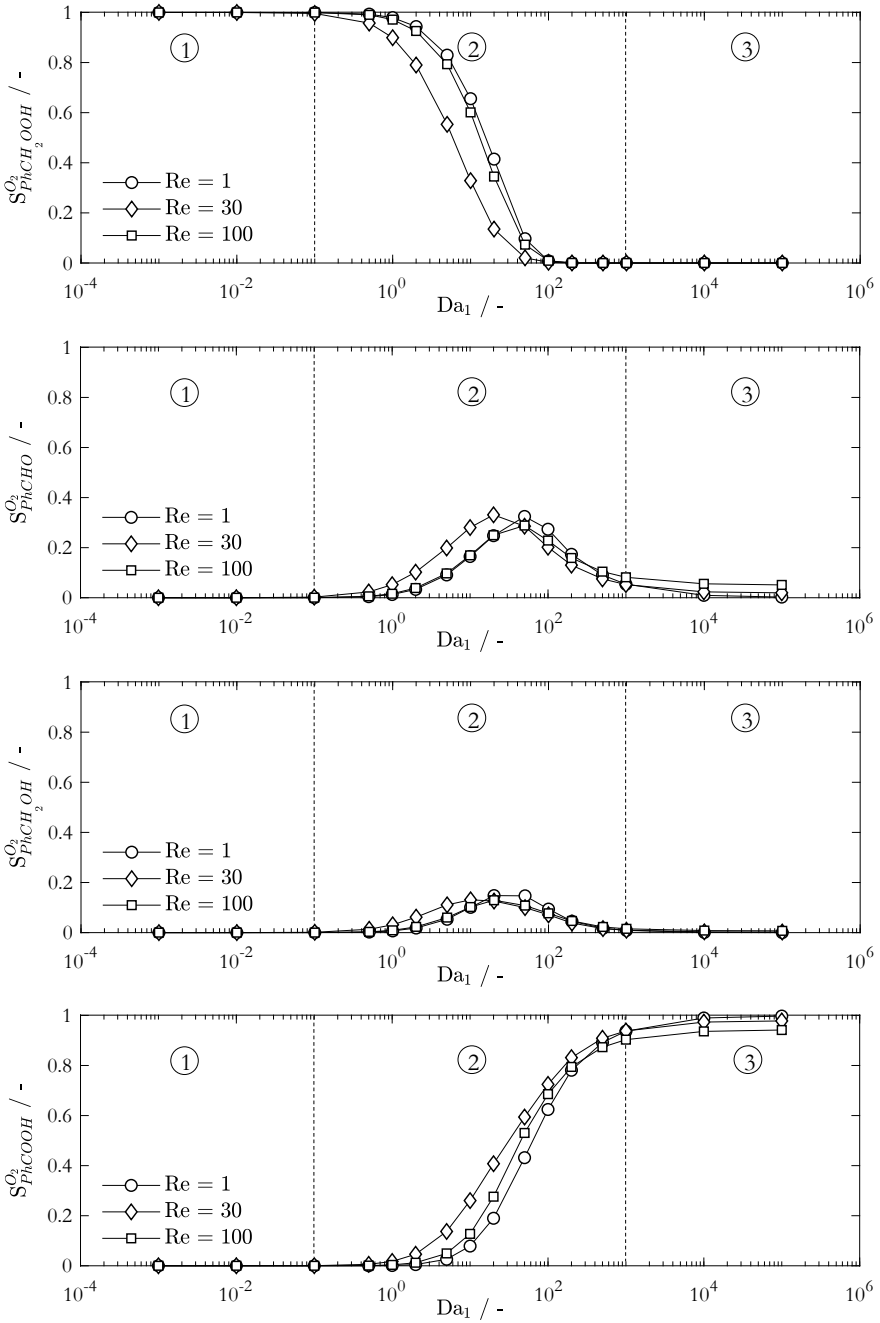
Fig. 21 Selectivity of benzyl hydroperoxide, benzaldehyde, benzyl alcohol, benzoic acid (from top to bottom) with respect to the consumed oxygen as a function of the first order Damköhler number. ①: kinetics limited area, ②: mixture masked area, ③: mass transport limited area

For the intermediate components, benzaldehyde and benzyl alcohol, there is a maximum in selectivity at $10 < Da_1 < 100$, with the maximum shifting to low Damköhler numbers for flows forming a stationary vortex. With increasing reaction speed and constant residence time, the subsequent reactions to the intermediate and end products are more intense. In the case of very fast reactions (Damköhler numbers $Da_1 > 100$) the reactions shift more and more towards the end product, here to benzoic acid. The diagrams shown in Fig. 19 with a kinetic acceleration factor *KF* = 100 can be assigned to this area.

In summary, the range in which mixing in the bubble wake affects the selectivity can be limited to $0.1 < Da_1 < 1000$. Outside this range, for these kind of reaction systems, the reaction cannot be influenced by a change in the fluid dynamics of a bubbly flow.

5.4 What Causes Mixture Masking?

In the previous chapter it has been shown, that reactions running on a relative time scale of $0.1 < Da_1 < 1000$ take place in the vicinity of a bubble and on its surface leading to a significant impact of the fluid dynamics of the bubbly flow on the chemical reaction.

In order to generate a better understanding this dependency of the selectivities with respect to the consumed oxygen at constant Damköhler numbers is discussed below (see Fig. 22). As explained above, the Damköhler number describes a dimensionless "place" of the reaction along the stream line of a flow around a bubble. Therefore, a consideration of the product spectrum at a constant Damköhler number but varying Reynolds numbers is a suitable way to show the influence of the bubbly flow on the reaction.

Figure 22 represents a vertical cut through Fig. 21. Thereby, each Damköhler number represent one of the previously discussed reaction ranges. As mentioned before, $Da_1 = 0.01$ describes slow reactions taking place in the bulk phase which therefore are not influenced by the fluid dynamics of a bubbly flow. This is confirmed by the graphs in Fig. 22. As well as the independence of the fluid dynamics of very fast reactions at $Da_1 = 10,000$.

$Da_1 = 10$ characterizes a reactive bubbly flow in the mixture-masked area. As described above, in that case, the fluid dynamics and the reaction take place on similar time scales, leading to a reaction zone at the surface and in the wake of the bubble. To describe this case in more detail, the concentration fields in the vicinity of the bubble at $Da_1 = 10$ are displayed in Fig. 23. Thereby the color code is the same for each species.

The course of the selectivity over the Reynolds number, displayed Fig. 22 shows a weakening descend for the selectivity of benzyl hydroperoxide up to $Re = 50$, followed by a sudden increase between $Re = 50$ and $Re = 60$, which then flattens out. For all other components this course is inverted and can be explained by the different flow regimes of the bubbly flow. Starting from the potential flow around
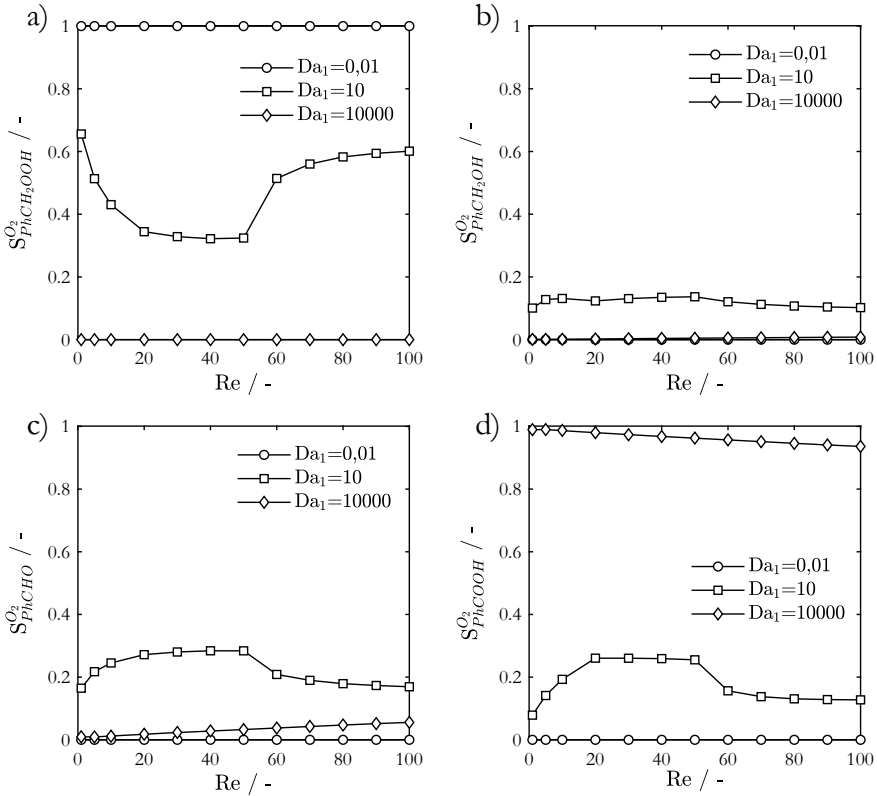
Fig. 22 Selectivity of **a** benzyl hydroperoxide, **b** benzyl alcohol, **c** benzaldehyde, **d** benzoic acid with respect to the consumed oxygen as a function of the Reynolds number at constant first order Damköhler number

the bubble at $Re = 1$ (see Fig. 23 first line) with the increase of the rising velocity a standing vortex slowly forms. This leads to a transport barrier, so that the center of the vortex is separated from the outside (see Fig. 23 second line). Leading to the complete consumption of benzyl hydroperoxide inside the vortex, which further results in an increased production of intermediate and final products. This is reflected in an increase in selectivity of benzaldehyde, benzyl alcohol and benzoic acid.

At $Re = 54$ there is a sudden change of the flow regime from a stationary vortex to a shedding vortex. By the detachment and subsequent dissolution of the vortex, the transport barrier is eliminated and the content of the vortex is mixed with the bulk phase. As the Reynolds number increases, the frequency of the vortex shedding and consequently the mixing quality increases. The increased mixing quality is confirmed by the locally low concentrations (see Fig. 23 lower line). The improvement of the mixing leads to the reduction of the mass transfer limitation, so that the behavior increasingly approaches that of an ideally mixed reactor.
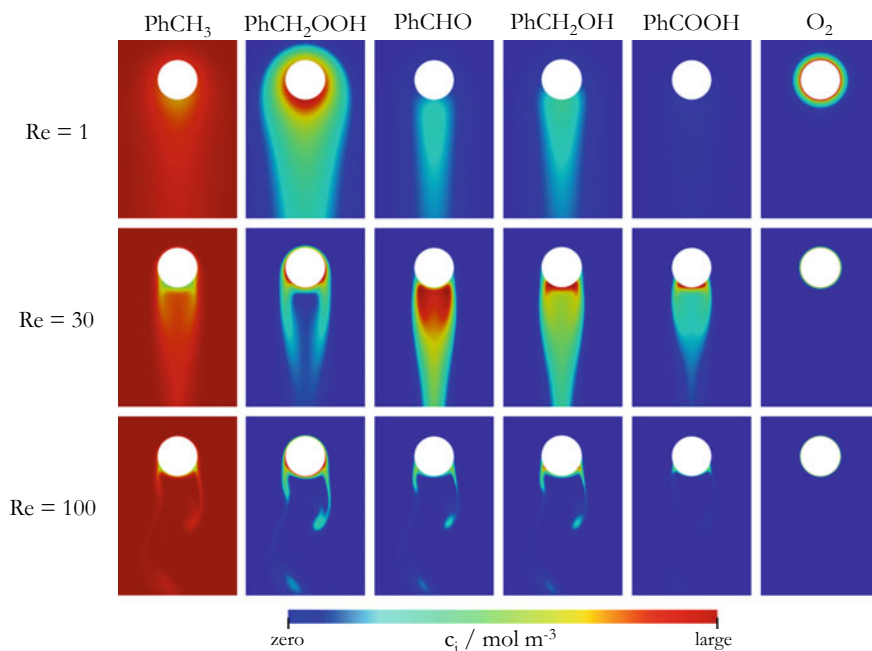
Fig. 23 Spatially resolved concentration fields for the components toluene, benzyl hydroperoxide, benzaldehyde, benzyl alcohol, benzoic acid and oxygen with a bubbly flow at $Da_1 = 10$ and $Re = 1, 30, 100$ The color scale is the same for each component

To the best of our knowledge, in literature, Khinast et al. are the only ones who have done similar studies. By investigating a competitive consecutive reaction, they found quantitatively the same reasons for the changes in the selectivity [21, 22]. In Chapter "Development and Application of Direct Numerical Simulations for Reactive Transport Processes at Single Bubbles", a similar study has been performed using a 3D and unsteady dynamics of the bubble interfaces. The authors found that the product selectivity for a competitive consecutive reaction is monotonously decreasing with increasing bubble Reynolds numbers, while Khinast et al. have observed a non-monotone behaviour. The differences in the results are explained by effects introduced by the 3D representation.

6 Conclusions

In this project a new reactor concept to determine the reaction kinetics of a gas liquid synthesis was developed and successfully implemented. Within this new setup, experiments in the homogeneous liquid phase have been performed and a kinetic model was developed. As model system the oxidation of toluene has been used. For

the experiments the oxygen input flow rate was varied from $\dot{V} = 52.5$ to $136.5\,\mathrm{Ln\,m^{-3}}$ $\mathrm{min^{-1}}$. Since the experiments were performed in homogeneous liquid phase, the kinetic model is not affected by mass transport. The new setup requires to analyze the oxygen concentration in an organic liquid at elevated pressure. To do so, the withdrawal of a small side streams was found to be the most robust online analysis. Using a cooled outer loop to dissolve oxygen also requires that at this temperature level reactions are slow and intermediate liquid components do not degenerate.

The kinetic model meets the experimental data well for industrially relevant oxygen concentrations. For high oxygen concentrations, a further investigation of the reaction mechanism and its change due to these high concentrations is recommended. Thermochemical calculations could make a considerable contribution to the clarification of the underlying mechanisms.

Further, the determined reaction kinetics has been applied in a numerical model of a single rising bubble. The single rising bubble is introduced as a representative elementary volume (REV) to describe the physio-chemical processes and their interactions within a multiphase reactor.

Thus, it could be shown that the determined reaction kinetics is too slow to be influenced by the fluid dynamics of a bubbly flow. This has further been verified with an experimental study conducted in an optically accessible high-pressure bubble column. Besides the verification of the aforementioned statement, it was shown that the bubble column is, due to the rising bubbles, ideally mixed and can be modeled as an ideal semi-batch reactor.

In further numerical studies the mixture masking has been investigated in more detail by using the REV-Model and accelerated reaction kinetics.

It could be shown that reactive bubbly flows can be classified in three zones:

- Kinetic limited zone ($\mathrm{Da_1} < 0.1$): describes slow reactions compared to fluid dynamics which take place in the bulk phase.
- Mixture masked zone: ($0.1 < \mathrm{Da_1} < 1000$): describes intermediate reaction on a similar time scale as the fluid dynamics. Reactions take place at the bubble surface and in its vicinity.
- Mass transfer limited zone ($\mathrm{Da_1} > 1000$): describes very fast reactions compared to fluid dynamics which take place exclusively at the bubble interface.

It could be shown that reactions in the mixing masked range are strongly influenced by the mass transport properties and the fluid dynamics of the bubbly flow. This impact is generated by the non-ideal mixing due to the bubble wake. For intermediate Reynolds numbers $5 < Re < 54$ a stationary vortex is building up, leading to a transport barrier between its interior and exterior. When vortex shedding starts (at $Re = 54$) the transport barrier beaks up and the behavior slowly converges to that of an ideally mixed reactor again.

In order to estimate the yield and selectivity of an industrial reactor the REV-Modell can be studied as differential loop reactor. To do so, in further works, the REV-Model needs to be extended by cyclic boundary condition including a dilution factor for all reaction species. By a scaling factor all relevant processes are scaled to the reactor size. The dilution and scaling factors are given by the reactor geometry

and the fluid properties. Further, a reduced model, which is explained in Chapter "Chemical Reactions at Freely Ascending Single Bubbles" has been implemented to predict the reaction products with respect to the mixture masking in the vicinity of the bubble.

References

1. Hermans I, Peeters J, Vereecken L, Jacobs PA (2007) Mechanism of thermal toluene autoxidation. ChemPhysChem 8(18):2678–2688
2. Gast S, Matthies JH, Tuttlies U, Nieken U (2017) A novel experimental setup for kinetic studies of toluene oxidation in the homogeneous liquid phase. Chem Eng Technol 40(8):1445–1452
3. Chemsafe Database (2014) Sicherheitstechnische Kenngroessen 6
4. Goethals M, Vanderstraeten B, Berghmans J, De Smedt G, Vliegen S, Van't Oost E (1999) Experimental study of the flammability limits of toluene–air mixtures at elevated pressure and temperature. J Hazard Mater 70(3):93–104
5. Gast S, Tuttlies U, Nieken U (2020) Kinetic study of the toluene oxidation in homogeneous liquid phase. Chem Eng Sci 217
6. Sandhiya L, Zipse H (2015) Initiation chemistries in hydrocarbon (aut)oxidation. Chem Eur J 21(40):14060–14067
7. Sandhiya L, Zipse H (2017) O-O bond homolysis in hydrogen peroxide. J Comput Chem 38(25):2186–2192
8. Sandhiya L, Zipse H (2019) Radical-pair formation in hydrocarbon (aut)oxidation. Chem Eur J 25(36):8604–8611
9. Hoorn JAA, Alsters PL, Versteeg GF (2005) A kinetic model for toluene oxidation comprising benzylperoxy benzoate ester as reactive intermediate in the formation of benzaldehyde. Int J Chem React Eng 3(1)
10. Hoorn JAA, Van Soolingen J, Versteeg GF (2005) Modelling toluene oxidation: incorporation of mass transfer phenomena. Chem Eng Res Des 83(2):187–195
11. Hermans I, Nguyen TL, Jacobs PA, Peeters J (2005) Autoxidation of cyclohexane: conventional views challenged by theory and experiment. ChemPhysChem 6(4):637–645
12. Hermans I, Jacobs PA, Peeters J (2006) Understanding the autoxidation of hydrocarbons at the molecular level and consequences for catalysis. J Mol Catal A Chem 251(1–2):221–228
13. Teles JH, Hermans I, Franz G, Sheldon RA (2015) Oxidation. In: Ullmann's encyclopedia of industrial chemistry. Wiley-VCH Verlag GmbH & Co. KGaA, Weinheim, Germany, pp 1–103
14. Brühne F, Wright E (2011) Benzaldehyde. In: Ullmann's encyclopedia of industrial chemistry. Wiley-VCH Verlag, Weinheim, Germany
15. Brühne F, Wright E (2000) Benzyl alcohol. In: Ullmann's encyclopedia of industrial chemistry. Wiley-VCH Verlag, Weinheim, Germany
16. Wilke CR, Chang P (1955) Correlation of diffusion coefficients in dilute solutions. AIChE J 1(2):264–270
17. Poling BE, Prausnitz JM, O'Connel JP (1987) The properties of gases and liquids. McGraw-Hill, New York
18. Clift R, Grace JR, Weber ME (1978) Bubbles, drops, and particle. Academic Press Inc., New York
19. Schäfer R (2004) Bubble interactions, bubble size distributions and reaction kinetics for the autocatalytic oxidation of cyclohexane. PhD thesis, Universität Stuttgart

20. Bhaga D, Weber ME (1981) Bubbles in viscous liquids: shapes, wakes and velocities. J Fluid Mech 105:61
21. Khinast JG (2001) Impact of 2-D bubble dynamics on the selectivity of fast gas-liquid reactions. AIChE J 47(10):2304–2319
22. Khinast JG, Koynov A, Leib TM (2003) Reactive mass transfer at gas-liquid interfaces: impact of micro-scale fluid dynamics on yield and selectivity of liquid-phase cyclohexane oxidation. Chem Eng Sci 85:3961–3971

Mass Transfer Around Gas Bubbles in Reacting Liquids

David Merker, Lutz Böhm, and Matthias Kraume

Abstract Within this project, the mass transfer of single bubbles in an unconfined environment was investigated. Most published works with longer rising paths lack the three-dimensional resolution of the bubble interface while smaller systems lack the long-term effects appearing during the ascent. Here, two cameras were moved in real-time with the bubble allowing a three-dimensional resolution of the bubble for a long rising path. For validation purposes of the bubble dynamics, the ascent of inert bubbles was investigated in clean systems and, due to the chemical systems of interest within this project, in systems with surface active components (metal-based complexes and different ligands). Furthermore, for comparison with widely used Sherwood correlations, purely physical mass transfer of different gas types was investigated in the same systems confirming a significant time-depending influence of the surfactants not only on the bubble dynamics but on the mass transfer, as well. For chemical reaction enhanced mass transfer, CO_2 in $NaOH_{aq}$ and NO in a nitrosyl-iron complex system with different ligands were investigated. The dependency of the Sherwood number on the Péclet number was confirmed and concentration dependent enhancement factors were determined. The results show a complex interaction of ligand-depending contamination kinetics. Bubble dynamics and reaction rates and the mass transfer can increase or decrease.

1 Introduction

To describe mass transfer in reactive gas/liquid systems with high accuracy, a fundamental understanding of all occurring effects is required. Especially the correct consideration of the interactions between fluid dynamics, mass transfer and chemical reaction is still a big challenge. To evaluate certain influencing parameters accurately, measurements with known boundary conditions and with a high degree of detail must be available. The overall aim of predicting processes in a complex swarm of bubbles

D. Merker · L. Böhm · M. Kraume (✉)
Department of Process Engineering, Technische Universität Berlin, Ackerstraße 76, 13355 Berlin, Germany
e-mail: matthias.kraume@tu-berlin.de

and optimizing processes to certain target parameters can only be achieved with valid descriptions of fluid dynamics, mass transfer and the chemical reaction. In the literature, mass transfer is often determined by integral quantities in the liquid phase or described by a volume specific mass transfer coefficient. To reduce the system's complexity in comparison to a bubble swarm, single bubble experiments are performed with a high temporal and spatial resolution over an ascending height of almost 2 m. Thus, effects occurring at a single bubble can be precisely observed. Since such a high resolution is not possible with swarm measurements, the knowledge gained from single bubble measurements can be used to optimize the assessment of swarms of bubbles.

1.1   Fluid Dynamics of Single Bubbles

An important parameter in the design and evaluation of mass transfer is the velocity of a bubble since this not only determines the residence time, but also the occurring mass transfer and mixing behavior in the wake and thus, if relevant, the yield and selectivity of a chemical reaction. Therefore, it is of high significance to describe the fluid dynamics correctly. In the literature there are mostly correlations for final velocities, which neglect a potential transient behavior. Numerous publications can be found discussing the fluid dynamics of drops and bubbles. Clift et al. [1] summarized a lot of relevant effects and measurements. To compare single free rising bubbles in stagnant liquids, different dimensionless numbers are used. The Reynolds number

$$Re = \frac{vd}{v} \tag{1}$$

characterizes the flow behavior. It contains v as the rise velocity, d the equivalent bubble diameter of a sphere and v the kinematic viscosity.

From the force balance for spherical particles the terminal rise velocity v_t results in:

$$v_t = \sqrt{\frac{4\Delta\rho g d}{3\rho_L C_D}}, \tag{2}$$

with the drag coefficient C_D. Tomiyama et al. [2] published empirical correlations that distinguish between how strongly a system is contaminated. For pure systems the drag coefficient can be calculated with

$$C_D = max\left(min\left(\frac{16}{Re}\left(1 + 0.15Re^{0.687}\right), \frac{48}{Re}\right), \frac{8}{3}\frac{Eo}{Eo + 4}\right), \tag{3}$$

for slightly contaminated systems with

$$C_D = max\left(min\left(\frac{24}{Re}(1 + 0.15Re^{0.687}), \frac{72}{Re}\right), \frac{8}{3}\frac{Eo}{Eo + 4}\right) \quad (4)$$

and contaminated systems with

$$C_D = max\left(\frac{24}{Re}(1 + 0.15Re^{0.687}), \frac{8}{3}\frac{Eo}{Eo + 4}\right). \quad (5)$$

To evaluate the deformation of bubbles, the Eötvös number

$$Eo = \frac{\Delta\rho g d^2}{\gamma}, \quad (6)$$

is of interest where $\Delta\rho$ represents the density difference and γ the surface tension.

An alternative approach was pursued by Park et al. [3]. They developed a correlation which gives results over a broad bubble spectrum from spherical bubbles to large deformed bubbles with one correlation for the terminal rise velocity:

$$v_t = 1/\left(\sqrt{f_{sc}^2\left(\frac{144\mu_L^2}{g^2\rho_L^2 d^4} + \frac{\mu_L^{4/3}}{0.14425^2 g^{5/3}\rho_L^{4/3} d^3}\right) + \frac{1}{\frac{2.14\sigma}{\rho_L d} + 0.505gd}}\right). \quad (7)$$

The factor f_{sc} varies between 1 and 1.5 and depends on the specific contaminants present and their concentrations. A simple suggestion is

$$f_{sc} = 1 + \frac{0.5}{1 + exp\left(\frac{\log Eo + 1}{0.38}\right)}. \quad (8)$$

In addition to the rise velocity, the horizontal movement is also a characteristic parameter for the ascent of bubbles. To perform a dimensionless characterization of the frequency of the oscillations, the Strouhal number is used which is defined by:

$$Sr = \frac{f_{os}d}{v}, \quad (9)$$

where f_{os} is the oscillation frequency. To consider the fluid dynamics of the bubble, the Tadaki number is used, which is calculated by

$$Ta = ReMo^{0.23}. \quad (10)$$

The Morton number is defined as

$$Mo = \frac{\eta^4\Delta\rho g}{\rho_L^2\gamma^3}, \quad (11)$$

where η represents the dynamic viscosity and ρ_L the density of the liquid. Fan and Tsuchiya [4] collected different measurements and gave two empirical correlations for the oscillation frequency in a pure system

$$Sr = 0.40\left(1 - \frac{1.80}{Ta}\right)^2 \quad at \; all \; Ta \tag{12}$$

and in a contaminated system:

$$Sr = 0.16\left(1 - \frac{0.57}{Ta}\right)^2 \quad at \; Ta < 8. \tag{13}$$

The oscillation onset for pure systems is estimated with $Ta_{os,pure} \approx 0.57$ and for contaminated systems $Ta_{os,conta} \approx 1.8$.

In addition to the oscillation frequencies, the shape of the bubbles must be taken into consideration. The shape of an ellipsoid bubble can be described by the eccentricity. It is the aspect ratio of the maximum vertical axis d_v to maximum horizontal axis d_h:

$$Ec = \frac{d_v}{d_h} = \frac{1}{\chi}. \tag{14}$$

The lengths are perpendicular to each other, but can be angled with the bubble orientation. Spherical bubbles have a value of Ec = 1. Some authors also use the reciprocal value here χ. The influence of surfactants on the shape of bubbles was analyzed in many studies [1, 5–8]. Aoyama et al. published correlations for clean liquids [9]:

$$Ec_{clean} = \left(1 + 0.016 Eo^{1.12} Re\right)^{-0.388}, \tag{15}$$

as well as for contaminated systems [10]

$$Ec_{conta} = \left(1 + 0.024 Eo^{1.17} Re^{0.44}\right)^{-0.57}. \tag{16}$$

1.2 Mass Transfer of Single Bubbles

To describe mass transfer phenomena in a gas–liquid-system, a common parameter is the volumetric mass transfer coefficient $k_L a$. Since, here, the interfacial area between gas and liquid can be measured precisely for a single bubble, the mass transfer coefficient k_L is measured. In dimensionless form, the Sherwood number

$$Sh = \frac{k_L d}{D_L} \tag{17}$$

is usually used to describe the mass transfer, where D_L represents the diffusion coefficient in the liquid phase. The Schmidt number characterizes the fluid in which the mass transfer takes place and is defined as:

$$Sc = \frac{\nu}{D_L}. \tag{18}$$

It can be seen as the ratio of the boundary layer thicknesses of velocity and concentration. Often, the Péclet number instead of the Reynolds number is used in correlations:

$$Pe = \frac{\nu d}{D_L} = ReSc. \tag{19}$$

A set of Sherwood correlations is given in Deising et al. [11]. Figure 1 shows various correlations of the Sherwood number as a function of Reynolds and Schmidt number (or Péclet number) using the material properties of the system CO_2 in water and the velocity is calculated with the drag coefficient of Tomiyama (Eq. 3) for clean systems.

Lochiel and Calderbank [16] found

$$Sh = \frac{2}{\sqrt{\pi}} (ReSc)^{0.5} f(\chi) \tag{20}$$

as a suitable correlation which additionally considers the inverse eccentricity χ with
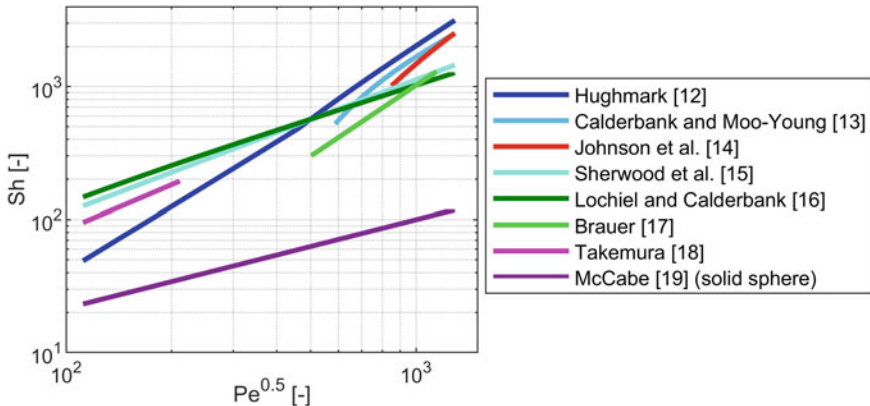
Fig. 1 Compilation of Sherwood correlations from literature [12–19]

$$f(\chi) = \left[\frac{2}{3}(1+k)\right]^{1/2} \frac{2\chi^{1/3}(\chi^2-1)^{1/2}}{\chi(\chi^2-1)^{1/2} + \ln\left(\chi + (\chi^2-1)^{\frac{1}{2}}\right)}, \tag{21}$$

$$k = \frac{e\chi^2 - \chi \sin^{-1} e}{e - \chi \sin^{-1} e}, \quad e = \left(1 - \chi^{-1}\right)^{1/2}. \tag{22}$$

The correlation of Hughmark [12] has one of the steepest slopes and gives the largest Sherwood numbers for large bubbles (and Péclet numbers):

$$Sh = 2 + 0.061 \, Sc^{0.546} \, Re^{0.779} \left(\frac{dg^{1/3}}{D_L^{2/3}}\right)^{0.116}. \tag{23}$$

In processes involving a chemical reaction, significantly larger mass transfer rates are observed. An enhancement factor is defined to consider the increase in mass transfer due to the occurrence of a chemical reaction:

$$E = \frac{k_{Reac,L}}{k_{0,L}} \tag{24}$$

where $k_{Reac,L}$ is the reactive mass transfer coefficient and $k_{0,L}$ is the physical mass transfer coefficient. It is the ratio between a reaction enhanced transport to a purely physical mass transfer.

2   Experimental Setup and Methods

For the precise determination of the mass transfer from rising bubbles in a stagnant liquid a setup was designed, which allows reproducible measurements of mass transfer and bubble dynamics both spatially and temporally at a high resolution.

The experimental setup for the measurement of rising bubbles is shown in Fig. 2. A previous version of this setup is described in Merker et al. [40]. The setup consists of a vertical glass pipe of $l = 2$ m length with a diameter of $d = 80$ mm (1). It is filled with the liquid phase. In all cases was ultrapure water with a conductivity of $\kappa = 0.055$ mS cm^{-1} was used. At the bottom of the column, a glass capillary is centrally located (2). Here, single bubbles are produced (3), which rise through the stagnant continuous phase. To measure a wide spectrum of bubble diameters, capillaries with different inner diameters are used, ranging from $d_i = 0.05$ mm up to 0.8 mm. In addition to the cylindrically shaped capillaries produced by *Hilgenberg GmbH*, glass capillaries with a divergent inner diameter are used which feature a trumpet-shaped opening as shown in Fig. 3. A pressurized gas tank contains the desired gas to generate single bubbles. It is connected to the glass capillary at the bottom of the glass column via PTFE tubing. The required volume is varied with a pressure reducer and a car injection valve via the pre-pressure and the opening
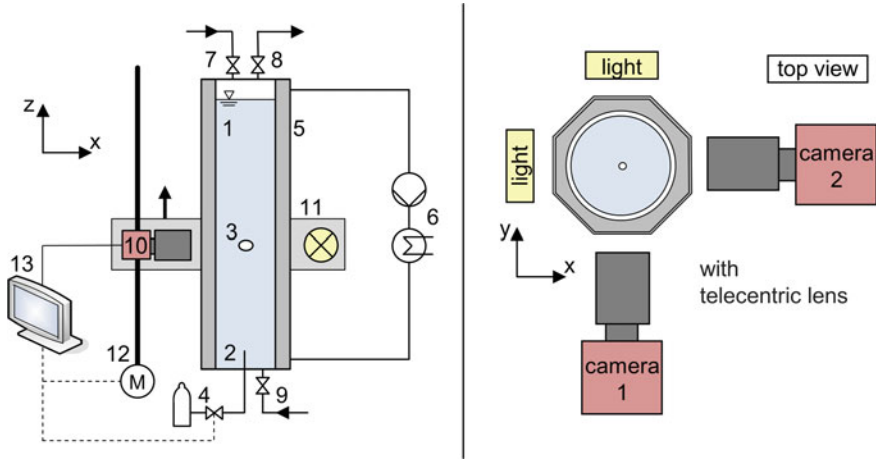
Fig. 2 Experimental setup of the rising test cell (left): (1) column, (2) glass, capillary, (3) bubble, (4) gas source, pressure reducer and injection valve, (5) acrylic glass jacket, (6) thermostat, (7) inlet inert gas, (8) pressure-control valve/extractor, (9) stripping gas, (10) two cameras, (11) LED-panels, (12) traverse system, (13) computer; cross section at bubble height (right)
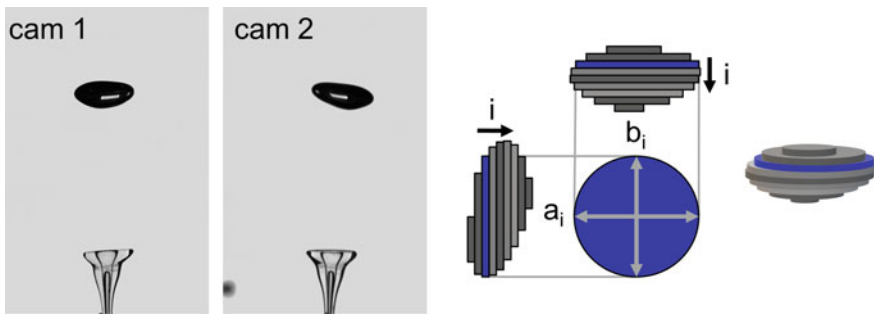
Fig. 3 Reconstruction of the bubble volume with two views for every pixel row

time (4). This procedure is similar to the one described by Ohl [20]. The PTFE tube leading to the inlet tip of the glass capillary is always filled with gas and no additional T-piece was applied to flush the gas out. To avoid any interaction between bubbles, a waiting period of $t = 8$ s was used between individual bubbles.

The round glass tube is encased in an octagonal acrylic glass jacket (5). The space in between is filled with water. With the help of a thermostat (6) the temperature of the glass tube can be controlled in a range of $T = 10\text{--}55$ °C. The deviation is below ± 1 °C. The tube is closed at the top to allow working under an atmosphere of an inert gas like N_2 and under pressures above the atmospheric one. There is an inlet for an inert gas (7) and an outlet with a pressure-control valve (8), with which an overpressure of up to $p = 3$ bar can be realized at the top of the glass tube. The

exhaust gas is led into an extractor. At the bottom of the tube there is an inlet next to the capillary to fill and empty the system and to inject a stripping gas into the liquid (9). The solutions were gassed for $t = 2$ h with a stripping gas and a gas holdup of approx. 10% to saturate the liquid, remove other dissolved gases and create defined, oxygen-free conditions. The liquid is solely in contact with glass, stainless steel and PTFE.

When a bubble is generated, two high-speed cameras (*Vieworks VC-4MC-M180E0-CM* with a max. resolution of 2048×2048 pixels^2) with telecentric lenses (*Sill TZM 2298*) are used to observe the rising bubble with an angle of 90° between each other. The two cameras (10) and LED panels (11) are mounted on a traversing system with a motor (12). The cameras capture the bubble with a shadowgraph technique, see Fig. 2 right. The start of the motor and the generation of the bubble are synchronized by a computer (13). The position of the bubble in the image is used to control the speed of the carriage with a real-time image analysis. Thus, the bubble can be tracked with a high temporal (100–250 fps) and spatial resolution (43.4 pixel/mm) over a maximum rising height of in $h = 1.8$ m, depending on liquid level. The control of the injection valve, the motor and image evaluation are realized in LabVIEW from *National Instruments (NI)*.

A large number of the measurements was recorded at 125 fps and a resolution of 1400×1696 pixels^2. This corresponds to approximately (width × height) 32×39 mm^2, whereby a volume of (width × depth × height) $32 \times 32 \times 1800$ mm^3 can be observed by moving the cameras.

The two images, recorded synchronously by the cameras which are arranged at right angles, are used to determine the bubble volume. Figure 3 shows an example of a bubble. The 8-bit grayscale images are converted into binary images. Both views show the same bubble height. For each pixel line k_i, the widths of the two views a_i and b_i are determined. With the approximation that the bubble can be represented by ellipse-shaped slices with the height of one pixel (Δz_{Pixel}), the volume is calculated according to

$$V_{Pixel} = \sum_{i=1}^{k} \left(\frac{\pi}{4} a_i b_i \Delta z_{Pixel} \right). \tag{25}$$

With the knowledge of the image scale, the determined pixel volume can be converted into a real volume.

The shape of the bubble can be evaluated with the eccentricity according to Eq. (14). Due to the potential three-dimensional trajectory, the two cameras do not have an optimal viewing angle of the bubble at all times. The width d_h of the bubble is determined more accurately from both camera 1 and camera 2. The height d_v is more error-prone if the direction of trajectory is not orthogonal to the viewing axis. To reduce the possible error, the minimum heights d_h captured by the two cameras is used, because one of the two cameras with a non-orthogonal viewing angle overestimates the height and thus the volume of an oblate bubble more.

Fig. 4 Parity plot of bubble diameters measured with picture analysis compared to thus measured with a suction probe ($d_i = 0.5$ mm)
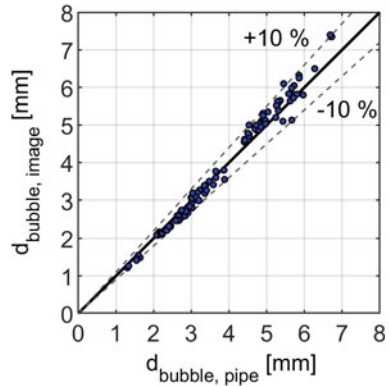
For validation of the bubble diameter, for selected cases, individual bubbles are collected with a funnel and sucked into a thin PTFE tube with a syringe. This tube has an inner diameter of $d_i = 0.50$ mm. The real volume can be determined by the length of the bubbles in the tube and compared with the volume measured by the image evaluation of the cameras. Figure 4 shows a parity plot in which the equivalent bubble diameters measured in the tubing are plotted over the equivalent bubble diameters measured in the tubing. The deviations are below $\pm 10\%$. If the value determined via the tube is assumed to be correct, then for small bubbles with a diameter smaller than approx. $d_B = 3$ mm, the volume is slightly underestimated by the image analysis and for larger bubbles the determined volume is slightly overestimated. This is due to the image processing and the reconstruction via the two shadow projections. With small bubbles it has a greater influence if pixels on the edge of the bubble are included or excluded in the analysis due to threshold settings. For larger bubbles, which are no longer rotationally symmetric and the trajectory is not orthogonal to the camera views, the volume reconstruction overestimates the real volume. In the considered bubble spectrum, the optical measuring method shows satisfying results. Especially for medium sizes, the optical reconstruction with two projection views results in very accurate valid measurements and the measuring method can follow fast volume changes well, because a high frame rate allows a good temporal resolution.

2.1 Measurement of Velocities

The detailed optical measurements allow an experimental determination of vertical and 3D bubble velocities with high temporal resolution. The analysis is done by evaluating the vertical and horizontal position of the centroid of the projected greyscale area seen in both viewing angles. While the horizontal component of the 3D particle velocity can be extracted solely from the images, the vertical position of the traverse system has to be considered for determination of the vertical rising velocity. By

combination of both viewing angles, the 3D position and movement of the bubble is experimentally accessible.

For validation of the measurement technique, different inert gases (regarding mass transfer and chemical reactions), namely nitrogen (N_2), helium (He) and argon (Ar) were measured in water. For each series of measurements, the continuous phase was stripped with the respective inert gas for two hours before the start of the measurements. Therefore, no mass transfer occurred during the rise of the bubble. The bubble diameter stayed almost constant. The measured change in size can be explained by the change in hydrostatic pressure: The decrease in hydrostatic pressure of approximately $p = 0.2$ bar for two meters of water column results in a decrease of approximately 20% in volume or roughly 6% in diameter. In case of mass transfer measurements, the correction of the volume change caused by the change in hydrostatic pressure has to be considered, see Sect. 2.2 for a detailed analysis.

Figure 5 shows the experimental results for the inert gas experiments compared with results from the literature. For the calculation of the drag coefficients Eqs. (3)–(5) of Tomiyama et al. [2] for pure systems, slightly contaminated and contaminated systems were chosen. The experimental results fit well with experimental data from the literature. The velocities for the pure systems can be measured with high accuracy and reproducibility. For bubble diameters in the range of $d_B = 1.5$–4 mm, larger terminal velocities were measured than calculated from the correlations. Tomiyama's correlations are valid for a wide range of Morton numbers. Comparing Tomiyama's experimental results with our own, the maximum values are in good agreement. Nevertheless, the correlation predicts lower values for deformed bubbles as the experiments would suggest, see in Fig. 5. Therefore accurate and reproducible
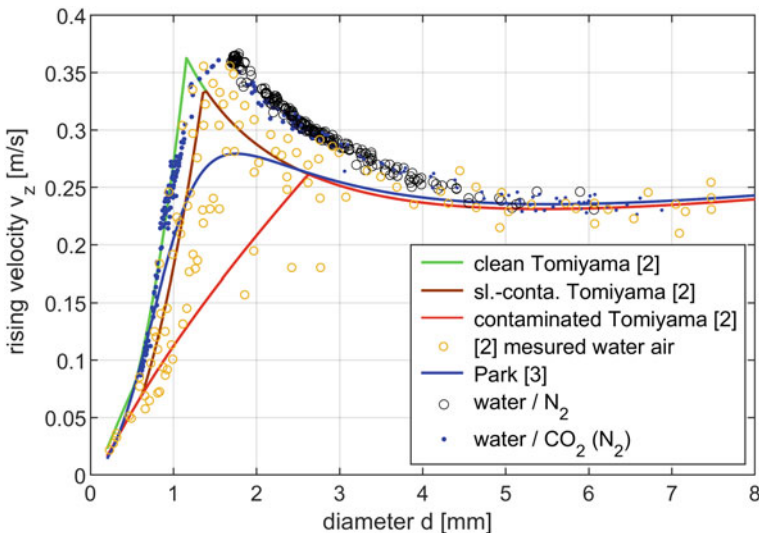
Fig. 5 Terminal rise velocities of bubbles in water

measurements of fluid dynamics can be performed. It is possible to measure in clean systems with a negligible surfactant influence and thus to detect differences by adding single components.

Besides the inert gas measurements, the diagram includes results from constant final bubble diameters reached in mass transfer measurements of CO_2 in water. These bubbles reached constant bubble diameters with a terminal rise velocity comparable to those expected from spheres with a mobile interface. The reason for the appearance of a constant bubble diameter as a result of the occurring mass transfer is discussed in Sect. 3, where the mass transfer of a single bubble is evaluated in detail.

In addition to the determination of the vertical terminal rise velocity, the 3D rising path, oscillation frequencies and bubble shape can be measured with high accuracy. All these parameters can have a significant influence on mass transfer. Figure 6 shows exemplarily the 2D and 3D rise velocity and 3D trajectory of a nitrogen bubble of $d_B = 2$ mm in diameter in water. The trajectory shows the characteristic zig zag movement.

The change in volume due to reduced hydrostatic pressure (max $p = 0.2$ bar) and its influence on fluid dynamic, illustrated in Fig. 6, could almost be neglected, because the bubble diameter can change by a maximum of 6.2%.

Focusing on the vertical and 3D rise velocities of the bubbles, a distinct oscillation of the velocity is obvious, which is not random but connected to the bubble movement and the oscillation noticeable by detailed consideration of the bubble trajectory. In case of zig zag movement, the vertical velocity decreases before each turning point and the bubble reaccelerates after changing its direction. This behavior is more prominent for the vertical component shown in red in Fig. 6 and almost vanishes when considering the 3D velocity. Analyses of the main frequency show good agreement
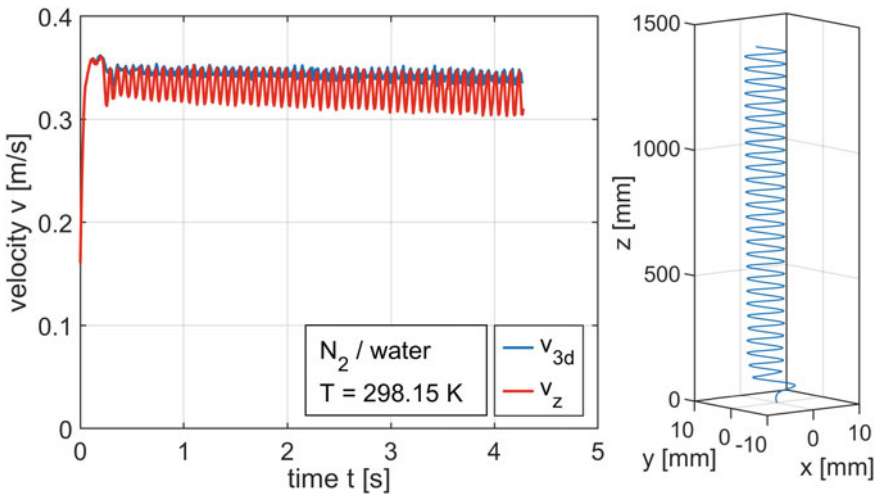
Fig. 6 Rise velocities and 3D velocity of bubbles $d_B = 2$ mm—N_2 bubble in water (left); 3D trajectory (right)
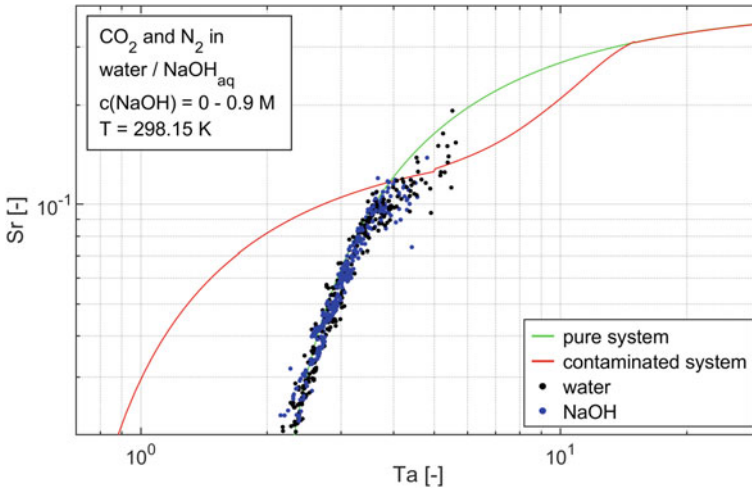
Fig. 7 Strouhal–Tadaki plot of N_2 and CO_2 bubbles in water and $NaOH_{aq}$

between the path and velocity oscillations. Therefore, the oscillation is connected to the trajectory during the ascent and not to statistical measuring errors. Figure 7 compares the resulting characteristic oscillation frequencies with values from the literature by application of the Strouhal number (Sr) and the Tadaki number (Ta). The experimental data show good agreement with the correlations for pure systems (Eq. 12), thus, validating the precise measurement of the experimental setup. As expected, for helical trajectories the rise velocity is not affected by a superimposed oscillation but stays nearly constant over the whole ascent.

For the frequency determination a Fast Fourier Transformation (FFT) is done for the last fifth of the measurement. Its challenging for large bubbles because the bubbles start to wobble and the frequencies that occur are not uniform, causing results to be somewhat scattered for large Tadaki numbers and to be below the values calculated by the correlation.

2.2 Evaluation of Mass Transfer Coefficients

The mass transfer measurement is based on the change of volume over time during the ascent of the bubble. The line-wise evaluation of the current bubble volume, as shown in Fig. 8, is applied to each pair of the two perpendicular recorded images taken during the measurement. As a result, the bubble volume for each time step is accessible. In combination with temperature and pressure information, the ideal gas law yields the amount of substance
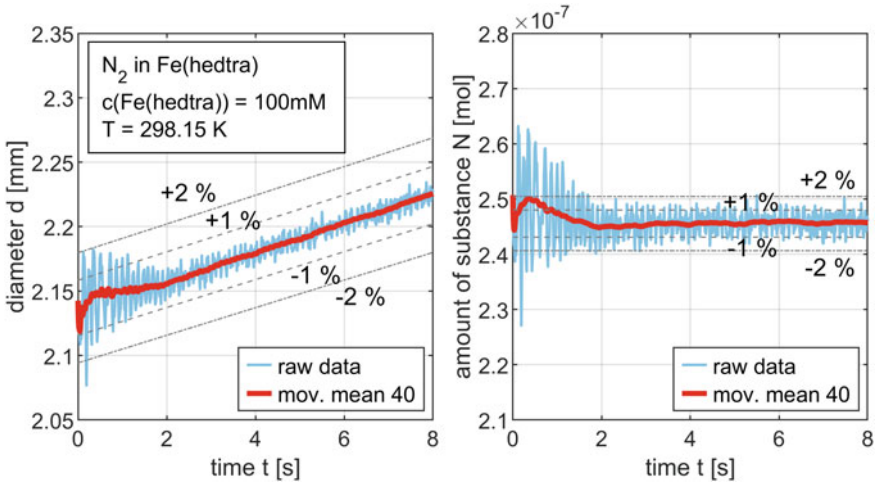
Fig. 8 Bubble diameter and amount of substance of a N_2 bubble (approximately $d_B = 2.2$ mm) in water with 100 mM Fe^{II}(hedtra)

$$N = \frac{pV}{RT} \tag{26}$$

constituting the bubble with R representing the ideal gas constant. For validation purposes, a case without mass transfer is analyzed first. Figure 8 shows a measurement of a N_2 bubble in water with 100 mM Fe^{II}(hedtra). This system is described in detail in Sect. 2.3. On the left side, the measured bubble diameter is plotted over time. On the right, the amount of substance calculated using the ideal gas equation can be found. The measured value is shown in blue and the moving average with ± 20 data points is shown in red. The measuring noise is due to the oscillation of the bubble. It can be seen that the bubble diameter slightly increases with decreasing hydrostatic pressure. As expected, the amount of substance in the bubble remains constant and shows the precision of the measuring method.

Different time-dependent values are determined for the evaluation of the mass transfer. Measured are, e.g.,

$$Pe = Re(t)Sc = \frac{v(t)d(t)}{D_L} \tag{27}$$

and with the knowledge of the driving concentration difference Δc the mass transfer coefficient

$$k_L = \frac{dN/dt}{A(t)\Delta c(t)} \tag{28}$$

can be calculated. The assumptions made are discussed in more detail in Sect. 3 on the basis of experimental results.

2.3 Material Properties and Fluid Dynamics of Fe^{II}(Ligand) Systems

A reactive system that has been investigated by several groups in the priority program is the Fe^{II}(ligand) system, also called nitrosyl-iron complex system (Chapters "In Situ Characterizable High-Spin Nitrosyl–Iron Complexes with Controllable Reactivity in Multiphase Reaction Media", "Experimental Studies on the Hydrodynamics, Mass Transfer and Reaction in Bubble Swarms with Ultrafast X-Ray Tomography and Local Probes", "Multi-scale Investigations of Reactive Bubbly Flows", "Chemical Reactions at Freely Ascending Single Bubbles" and "Chemical Reactions in Bubbly Flows"). Iron sulfate heptahydrate was dissolved in water with a ligand. By the choice of the ligand the reaction rate can be influenced. Especially Schneppensieper has published a detailed overview [21–23]. In addition to pure iron sulfate hepathydrate ($FeSO_4 \times 7\,H_2O$), five ligands were used. The chemicals used are listed in Table 1. To ensure that each dissolved Fe^{II} molecule forms a desired complex, the ligands were dissolved with an excess of 10% of the corresponding iron concentration. Only sodium citrate dihydrate was used with a metal/ligand ratio of 1/2.3. The ratio of iron to ligand is determined by the coordination number of the components.

Table 2 and Fig. 9 show the measured densities (*Anton Paar DSA 5000M*) and viscosities in relation to the concentrations tested. A rotational viscometer from *Anton Paar* with a cone plate system was used (*MCR302* with *CP60-1, P-PTD200, H-PTD200*). The results were averaged from shear rates $\dot{\gamma} = 100$, 179 and 316 1/s with a measuring point duration of $t = 60$ s and triple determination. In the concentration range used, the quantities can be linearly approximated using the following equations:

$$\rho(c) = 0.997\,\text{g/cm}^3 + s_{dens}c, \tag{29}$$

Table 1 Chemicals in the Fe^{II}(ligand) system

Abbreviation	Name	CAS No
$FeSO_4 \times 7\,H_2O$	Iron(II) sulphate heptahydrate	7782-63-0
edta	Ethylenediaminetetraacetic acid tetrasodium salt dihydrate	10378-23-1
hedtra	N-(2-hydroxyethyl)ethylenediaminetriacetic acid trisodium salt hydrate	207386-87-6
nta	Nitrilotriacetic acid trisodium salt monohydrate	18662-53-8
citrate	Sodium citrate dihydrate	6132-04-3
ida	Iminodiacetic acid	142-73-4

Table 2 Density, viscosity and interfacial tension of Fe^{II}(ligand) systems

Ligand	c (mM)	H_2O	ida	nta	citrate	edta	hedtra
Density ρ (g/cm^3)	25				1.0098	1.0059	1.0052
	50	1.0048	1.0077	1.0125	1.0223	1.0145	1.0131
	100	1.0122	1.0183	1.0273	1.0474	1.0322	1.0283
s_{dens} 10^{-4} (g/(cm^3 mM))		1.519	2.127	3.037	5.047	3.511	3.145
Viscosity η (mPa s)	25				0.945	0.924	
	50	0.934	0.930	0.938	1.048	0.950	0.944
	75						0.968
	100	0.964	0.963	0.997	1.117	1.018	0.988
Lin-fit s_{visc} 10^{-3} (mPa s/(mM))		0.742	0.722	1.028	2.742	1.239	0.986
Interfacial tension γ (mN/m)	100	72.8	73.1	<67	73.6	<55	<46
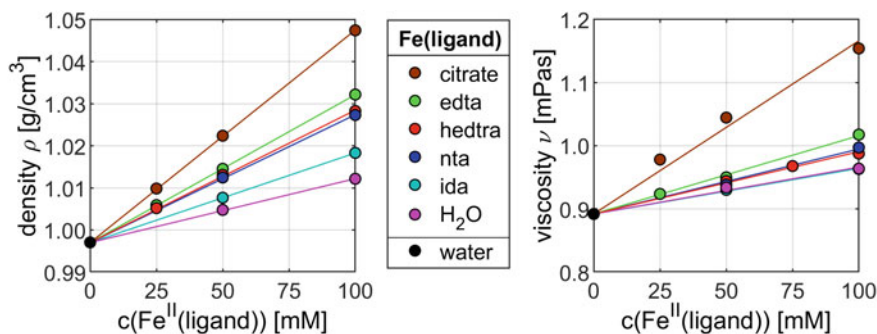
Fig. 9 Density and viscosity of Fe^{II}(ligand) systems

$$\eta = 0.892 \, \text{mPa s} + s_{visc}c. \tag{30}$$

The slope s_i considers the concentration-dependent deviations of the systems to water.

The choice of ligands influences the reaction rate of the system. Studies with chemical reaction are shown in Sect. 4.2.

In addition to the reaction rate, the ligands can also influence other thermophysical properties. The interfacial tension may change significantly. The interfacial tensions of solutions with a concentration of $c = 100$ mM were measured with a pendant drop tensiometer of the company *Dataphysics* (*OCA 15*), where a pure gas (N_2) forms the disperse phase and the complex solution the stagnant continuous phase. The bubble is located on the needle. A clear influence of the active component's adsorption kinetics on the measured value of the interfacial tension is evident. This leads to the temporal behavior shown in Fig. 10 and summarized in Table 2.
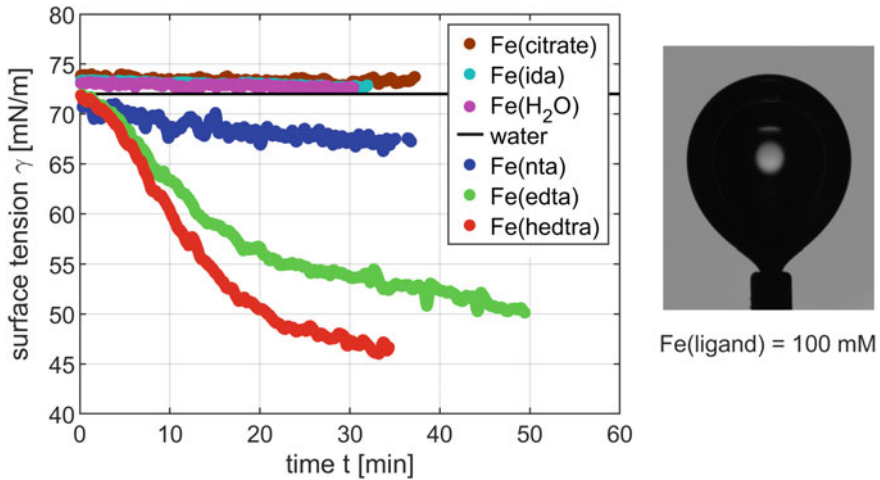
Fig. 10 Time-dependent surface tension of Fe^{II}(ligand) systems

The pure iron sulfate with water and the ligands ida and citrate show a negligible temporal influence on the interfacial tension. During the measuring time of at least 30 min, only a very slight decrease of the interfacial tension is observed. The trend is clearly different for the ligands nta, edta and hedtra. At the beginning of the measurement, a similar value as in pure water was measured. The diffusive mass transfer of the surfactant to the interfacial area requires longer measurements. In a measuring time of more than $t = 30$ min the interfacial tension dropped significantly. The measurement did not result in a full interfacial coverage since no stationary value could be measured. However, clear trends can be seen. The ligand hedtra has the strongest influence followed by edta and nta. The measuring method determines an integral interfacial tension over the entire surface of the bubbles at a given time, because the shape of the bubble is analyzed using the Young–Laplace equation.

In contrast to the $t = 30$ min measurement time shown here, the longest time measured for a single bubble ascent was 8 s. In real bubble columns, however, this can be considerably longer due to larger scales and in countercurrent flow it can be basically any desired time. The measurement of rise velocities shows that the choice of ligand can have a strong influence on the fluid dynamics of the bubble. To disconnect fluid dynamic and mass transfer effects, inert nitrogen bubbles were measured in the potentially reactive system along with the actual mass transfer measurements in which the bubbles reach a stationary bubble size in the observation period. Figure 11 shows that iron sulfate heptahydrate does not have a major influence on the fluid dynamics of the freely rising gas bubbles. The ligands citrate, ida and nta measurably reduce the rise velocity. Nevertheless, the results are close to the values of pure water and to the values resulting from the correlations of Tomiyama and Park for bubbles in pure water. In contrast, the ligands edta and hedtra clearly reduce the rise velocities.
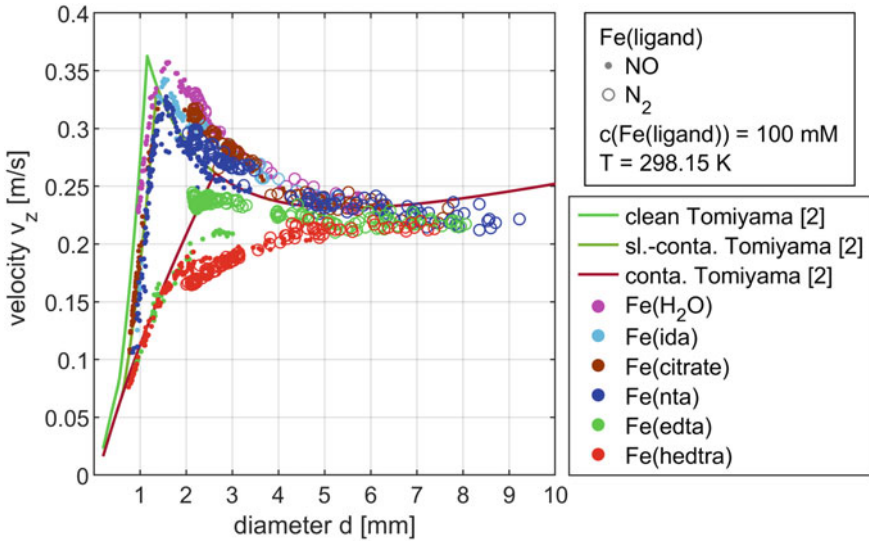
Fig. 11 Terminal rise velocities of bubbles in Fe^{II}(ligand) systems

The values of hedtra are significantly below the correlation for fully contaminated systems of Tomiyama. For bubbles smaller than $d_B = 1.5$ mm, there is a good agreement with the correlation.

A change in fluid dynamics can have different reasons. The addition of the iron complex could significantly change the density, viscosity or interfacial tension. The density of the fluid is increased by a maximum of 6% by adding the educts. The viscosity is also increased by the complexes from $\eta = 0.89$ mPa s maximum to 1.15 mPa s. The system Fe^{II}(citrate) has the largest change by adding $c = 100$ mM. However, the rise velocities are only slightly reduced compared to measurements in pure water and the system with only ferrous sulfate heptahydrate. The changes in density and viscosity do not have a significant influence on the rise velocity in the concentration range investigated. In addition, the effects can weaken each other, since the ascent rate increases with a higher density difference, but decreases with increasing viscosity.

The measurements of the interfacial tensions show that in the three systems with the ligands H_2O, ida and citrate the interfacial tension is constant or changes only slightly. For the ligands nta, edta and hedtra a time-depending adsorption can clearly be measured. In contrast to the pendant drop measurement, where the bubble is fixed in a stagnant system, fresh fluid flows around the freely rising bubble and surface-active ligand can adsorb in other time scales.

In pure water, the bubbles have a mobile interface and a high rise velocity. Contamination of the interface restricts mobility and, therefore, reduces the rise velocity. The shape of the bubble is different and the eccentricity is closer to 1. To evaluate the temporal influence of the adsorption of a surfactant, bubbles with a diameter
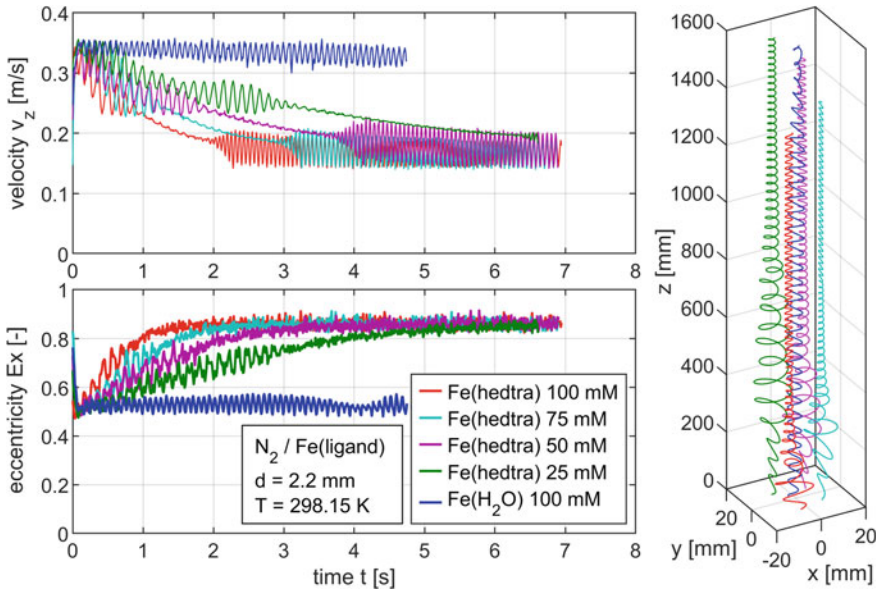
Fig. 12 Time-dependent rise velocities and eccentricities of $d_B = 2.2$ mm (N$_2$) bubbles in water and Fe^{II}(hedtra)

of about $d_B = 2.2$ mm are considered. Figure 12 shows the time dependence of rise velocity and eccentricity. In water with only iron sulfate dissolved (Fe^{II}(H$_2$O)) with a concentration of $c = 100$ mM, a constant rise velocity and eccentricity is measured, comparable with pure water. With increasing Fe^{II}(hedtra) concentration the rise velocity decreases faster and the eccentricity increases. At the beginning of the measurements the values are comparable with the pure system. The measurement signal shows fluctuations that correspond to the frequency of the oscillation of the bubble.

Since the measuring time is limited by the height of the measuring cell, no stationary value can be measured for the lowest concentration ($c = 25$ mM). With increasing concentration, these constant values are reached earlier. As the interfacial mobility of the bubbles is reduced by the surface coverage, the rise velocity decreases. In the stationary case, the bubble has almost a spherical shape. Besides the change in velocity, a different oscillation frequency can be measured.

To analyze the change of the frequency more precisely, Fig. 13 shows the dimensionless analysis with the application of the Strouhal over the Tadaki number for different bubble sizes. For the system Fe^{II}(hedtra), a clear shift towards larger Strouhal and lower Tadaki numbers is visible. The frequency increases as soon as the interface is exposed to surfactants.

Fluid dynamic measurements in dichloromethane/Cu(DBED) and methanol and the influence of the MNIC/DNIC system are discussed in Sect. 3.1 of Chapter "Chemical Reactions at Freely Ascending Single Bubbles".
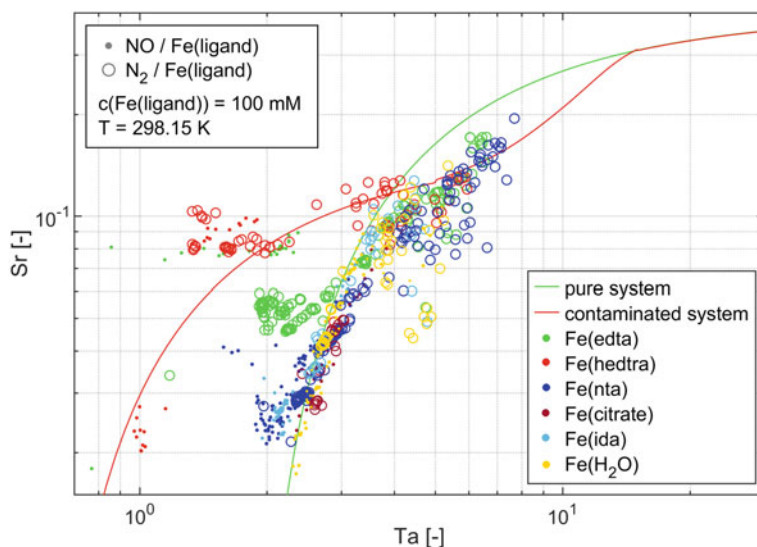
Fig. 13 Sr(Ta) plot for Fe^{II}(ligand) of N$_2$ and NO determined at the end of a measurement (last 1/5)

3 Physical Mass Transfer

For validation, the physical mass transfer of single bubbles was observed and compared with values from literature. Here, the mass transfer takes place due to an existing concentration difference but is not enhanced by a chemical reaction. An example is the dissolution of gases in unsaturated liquids.

The simplest description of mass transfer considers only one component in the gas phase. In the case of a pure gas, it could be assumed that the gas component is completely dissolved in the liquid phase as long as the liquid is not saturated with the component. In the experiments, the liquid phase was gassed with a stripping gas (in most cases nitrogen) for two hours to avoid traces of CO_2 in the liquid phase.

The measurement of a CO_2 bubble with an initial diameter of 3.8 mm is shown in Fig. 14. The measured molar amount is plotted over time on the left side. The decrease of the measured total amount of gas can be seen. At the end of the measurement the bubble size approaches a stationary diameter. The mass transfer decreased at the end of each measurement significantly. To evaluate the mass transfer and to compare it with correlations from the literature, the Sherwood number is shown on the right in Fig. 14.

The one component approach (1C), plotted in blue, assumes that the bubble consists only of CO_2 and the mass transfer is initially well described by a correlation from literature [12]. Although the velocity may increase with decreasing diameter, the influence of the diameter change is more dominant, which causes the Péclet number to decrease during the measurement. With decreasing Péclet number, the
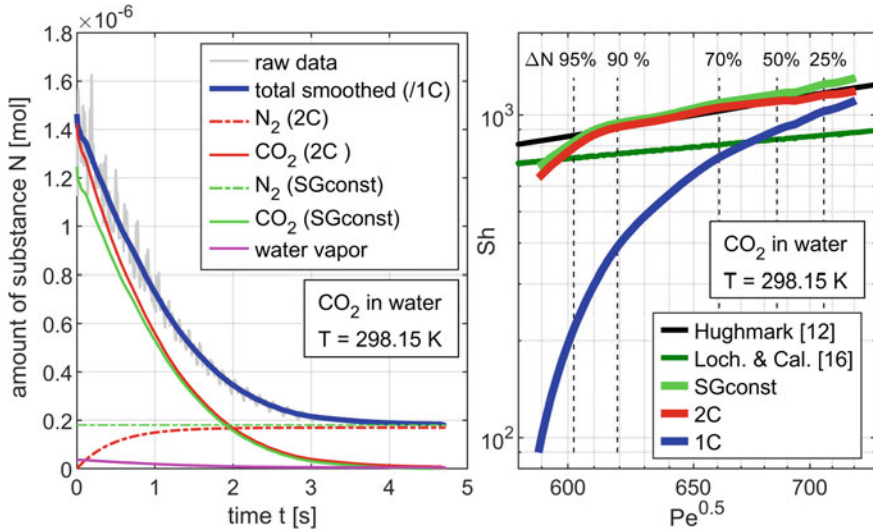
Fig. 14 CO_2 bubble in water $d_{B,0} = 3.8$ mm—$d_{B,end} = 2$ mm with different assumption for the time-dependent concentration change in the bubble $N(t)$ (left); Sh(Pe) (right) ΔN is the transferred amount of substance

Sherwood number decreases much more than predicted by the correlation. In this one-component-case, the pressure in the bubble corresponds to the partial pressure of CO_2, the driving concentration difference is assumed to be constant. This results in a strongly decreasing mass transfer coefficient k_L and thus Sherwood number at the end of the measurement.

Investigations of the gas phase showed that the CO_2 concentration changes significantly. Therefore, the rising bubbles were collected with a funnel at different heights and, thus, contact times. The collected gas sample was analyzed with a GC (*SRI 8610C* with *TCD* and *HID—6′ Mol Sieve 13X* and *6′ Silica Gel*). For one measurement, a gas volume of approx. $V = 3$ mL gas is necessary. Therefore, it is a cumulative sample of many single bubbles. The gas phase could not be separated from the liquid phase until the required sample volume was reached. An unwanted mass transfer could not be prevented completely. The interface between gas and liquid was minimized by gradually sucking off the gas phase. The determined gas compositions are shown in Fig. 15. With increasing height, thus, contact time, the CO_2 mole fraction decreases. At the beginning, the bubble consists of more than 95% CO_2. Actually, gas with a higher purity was used. Obviously, mass transfer takes place during bubble formation and between the bubble production at the interface at the capillary, as well as at the gas/liquid interface in the funnel until the sample volume is reached. To insert the funnel into the system, the lid was opened, allowing oxygen to enter the system via the water surface and, therefore, contaminate the water. The measured amounts of CO_2 can be seen as the lower limit, as it is less than the actual amount in
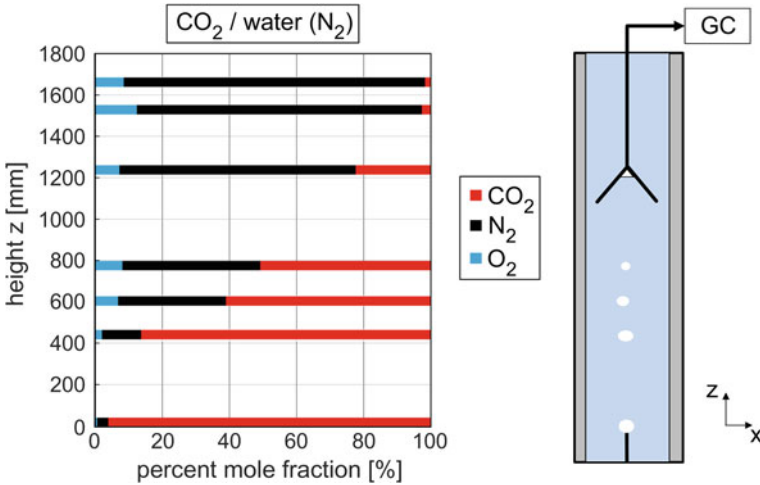
Fig. 15 Gas composition of CO_2 bubbles over height

the single bubble. At the end of the measurement after an ascent height of $h = 1.6$ m less than 2% CO_2 is detectable.

When a second gas component is considered, the partial pressure of the CO_2 changes not only because of the decreasing hydrostatic pressure, but also because the partial pressure of the second component increases during the measurement. Taking this aspect into account, the driving concentration difference decreases and changes the measured mass transfer coefficient. It is difficult to estimate how much stripping gas dissolves in the pure gas before and during the formation of a bubble. The capillary is not closed at the top, which means that mass transfer can take place only at a small interface. To be able to compare the measurements, it is assumed that the bubble consists of one component at the beginning of the measurement.

The calculation of the mass flow of the stripping gas into the bubble could be done with the same Sherwood correlation as for the CO_2 transport into the liquid with the corresponding Henry and diffusion coefficients. However, the amount of the stripping gas determined in this way inside the bubble is significantly lower than the measured amount of material in the stationary bubble at the end of a measurement. To be able to evaluate measurements with a stationary amount of substance more precisely, it is assumed that the bubble consists of a pure gas component at the beginning of the measurement. At the beginning the change of the stripping gas amount is stronger until it asymptotically increases to 98% of the measured constant final value. This case is named in the following (**2C**). As a result the Sherwood number does not decrease as much and the progression remains closer to the values predicted by the correlation, as can be seen in Fig. 14 because a corresponding correction calculation was made.

A worst case consideration results in the following two cases:

- Only one component is considered and the driving concentration difference remains constant (**1C**).
- The amount of substance that is in the bubble at the end of the measurement would be stripping gas and would be present in the bubble from the beginning (stripping gas constant—**SGconst**). This reduces the amount of CO_2 in the bubble and due to the lower concentration difference the measured Sherwood numbers for large Péclet numbers, shown in green, increase.

Figure 14 shows the two extreme cases and the results with a concentration profile in the bubble. For all the time-dependent partial pressures, the vapor pressure of the continuous phase was also taken into account. Table 3 lists the Antoine parameters used for the consideration of the vapor pressure. For the calculation of the mass transfer further parameters like Henry's law constants and the diffusion coefficient of the gases in the liquid are necessary, see Table 4.

Table 3 Antoine parameter—vapor pressure

$\log_{10}(P) = A - (B/(T + C))$		H_2O	H_2O	Methanol
Antoine parameter	A	5.40221	5.20389	5.20409
	B	1838.675	1733.926	1581.341
	C	−31.737	−39.485	−33.50
Temp. (K)		273–303	304–333	288.1–356.83
Ref.		[25]	[25]	[26]

Table 4 Henry and diffusions coefficients ($T_{ref} = 298.15$ K)

	H^{cp} (at T_{ref}) (mol/(m^3 Pa))	$d\ln H^{cp}/dT^{-1}$ (K)	Ref.	Diff. coef. D (10^{-5} m^2/s)	Ref.
Water					
CO_2	3.3×10^{-4}	2400	[27]	1.92	[28]
NO	1.9×10^{-5}	1600	[29]	2.6	
N_2	6.4×10^{-6}	1600		1.88	
O_2	1.2×10^{-5}	1700		2.1	
Ar	1.4×10^{-5}	1700		2.00	
He	3.9×10^{-6}	15	[30]		
Methanol					
NO	1.43×10^{-4}		[31]	2.14	[32][a]
N_2	1.52×10^{-4}		[33][a]	3.29	[34]
At 293.15 K	1.51×10^{-4}				
O_2	2.60×10^{-4}			1.88	
At 293.15 K	2.63×10^{-4}				

[a]Calculated or derived values

The diffusion coefficients are given for the reference temperature $T = 298.15$ K. A rough adjustment to other temperatures can be made with the Stokes–Einstein equation [24]:

$$D(T) = \frac{T(T)}{T_{ref}} \frac{\eta(T)}{\eta_{ref}} D_{ref}. \tag{31}$$

Since in the single bubble measurements both the Sherwood and Péclet number change transiently, an average is applied to compare numerous measurements.

Shortly after detachment, in many cases the bubble is strongly deformed and the volume determination is slightly incorrect. To obtain a single measurement value, averaging is performed in a time interval starting $t = 100$ ms after bubble detachment until 70% of the transferred amount of substance has been transferred. Thus a curve becomes a single data point. By varying the initial size, different Péclet numbers can be generated. Figure 16 shows CO_2 bubbles with an initial diameter of $d_B = 2$–10 mm.

The first 70% were chosen because averaging the temporal behavior of the Sherwood and Péclet numbers is less prone to error and the influence of surfactants/ligands is not strong for the systems studied. This enables a better comparison of all systems. As shown in Fig. 16, the temporal concentration change in the bubble must be considered. The bars show the possible ranges in which a determined Sherwood number can be located, depending on the assumptions used. The lower limit (**1C**) would take into account only one gas component (CO_2) in the bubble. For the upper limit it
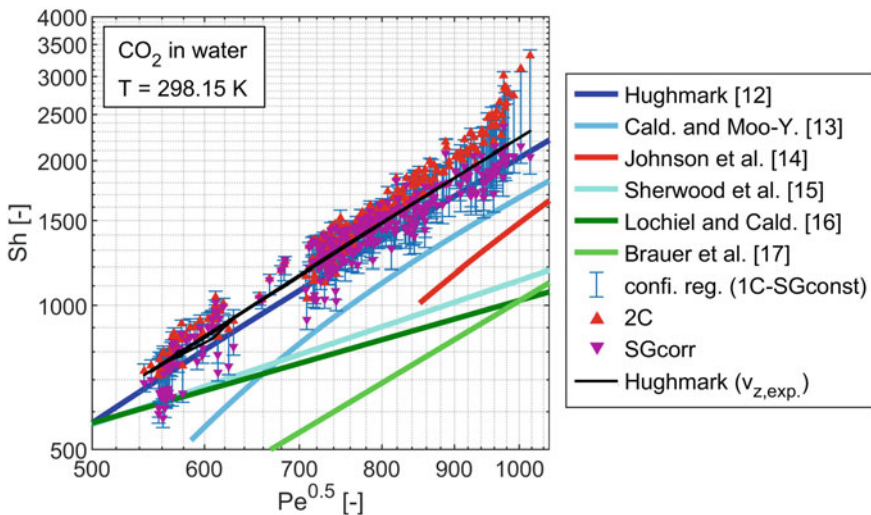
Fig. 16 Sh(Pe) of CO_2 in water—averaged Sh and Pe for single bubble experiments with different initial diameters and assumptions compared to correlations from the literature with v_z (Eq. 3)

was assumed that the amount of substance in the bubble at the end of the measurement was stripping gas and was already present in the bubble from the beginning (**SGconst**). The two cases described are the extreme cases that could be imagined, so the real value must lie between them. It can, therefore, be considered a confidence interval.

To determine the real Sherwood number more accurately, a partial pressure curve is assumed, whereby the bubble would consist of pure gas at the beginning and the remaining amount of substance of the bubble would consist of 98% stripping gas (**2C**). The lower border takes the mass transfer from stripping gas into the bubble with the correlation of Hughmark into account (**SGkorr**). Thus, the amount of the stripping gas is underestimated. In all cases (except SGconst) it is assumed that the bubble consists of pure CO_2 after formation. The contamination of the gas phase by mass transfer of stipping gas during bubble formation and between capillary measurements is not considered.

A good agreement with the correlation of Hughmark is observed. If, for the calculation of the Reynolds number, the measured rise velocity is taken from the experiment, the correlation describes the measurement results even more accurately, because the 2C approach probably gives more realistic results than the SGcorr. For large bubbles the mass transfer with the 2C approach is overestimated. These bubbles do not reach a stationary size during the observation period and the molar amount of CO_2 during the measurement is more than 2%. Therefore, the Sherwood number should be in the lower part of the confidence region and thus a good correlation with Hughmark should be available for large bubbles.

Other correlations show too low mass transfer coefficients and also postulate a lower dependence on fluid dynamics (Pe). In the literature an exponent of 0.5 is often given for the Péclet number. This cannot be confirmed by the measurements obtained. Both the quantitative results and the slope results were in good agreement with Hughmark according to Eq. (23) with a dependence of $d^{0.895} \, v^{0.779}$.

The characterization of the physical mass transfer is of great importance to realistically evaluate the results of measurements with chemical reactions.

4 Chemical Reaction

The physical mass transfer can be significantly enhanced by a chemical reaction. A common description is the enhancement factor E according to Eq. (24), which relates the reactive to the physical mass transfer.

4.1 Enhancement Factors Due to Chemical Reaction of CO_2 in $NaOH_{aq}$

The system CO_2/water can be modified by adding sodium hydroxide (NaOH). This leads to a neutralization reaction in the liquid phase, which intensifies the mass transfer from the bubble to the surrounding liquid. Different NaOH concentrations (or pH values) were investigated. The fluid dynamics of the bubbles are almost not influenced by the addition of NaOH. It can still be considered a pure system, as indicated by the rise velocities and oscillation frequencies (see Fig. 7).

Figure 17 shows the Sherwood number as a function of the Péclet number. A concentration range from $c = 1$ to 900 mM of NaOH in water was investigated. The diameter of the bubbles after generation was varied in a spectrum between approximately $d_B = 4$ and 9 mm. The measured mass transfer coefficients increase with increasing NaOH concentration. The Sherwood and Péclet numbers which decrease during a single bubble measurement are plotted as lines. The mean values of the Sherwood and Péclet numbers for a single measurement are plotted as points. For lower concentrations a higher noise is visible, which is due to the slower mass transfer and generally larger oscillating bubbles. Initially, as expected, the enhancement increases with increasing concentration. For comparison with the purely physical transport case, Fig. 17 also shows the enhancement factor over the Péclet number. Here, the purely physical transport used for comparison was calculated with the Hughmark correlation. A dependency of the enhancement factor on the Péclet number is shown. The measured mass transfer is relatively higher for larger bubbles than for small CO_2 bubbles. The dependency gets stronger with increasing concentration. A clear
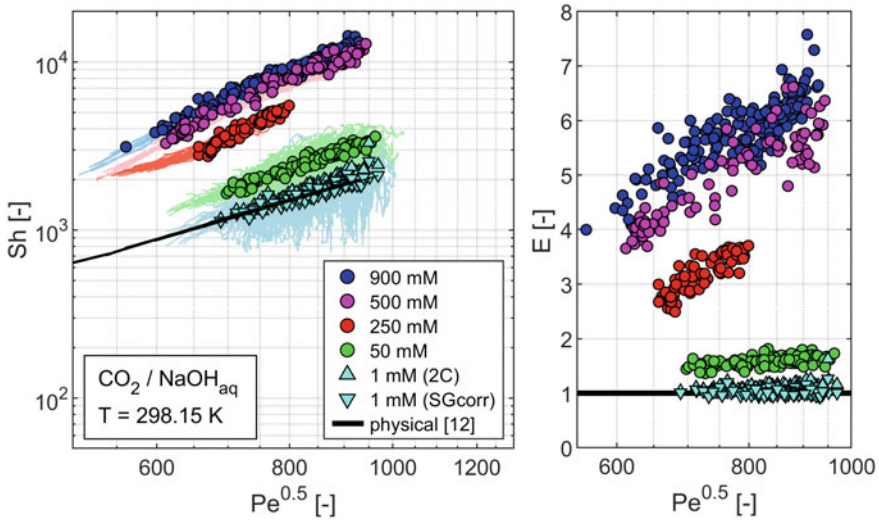
Fig. 17 Sh(Pe) and E(Pe) of CO_2 in $NaOH_{aq}$—averaged Sh and Pe for single bubble experiments
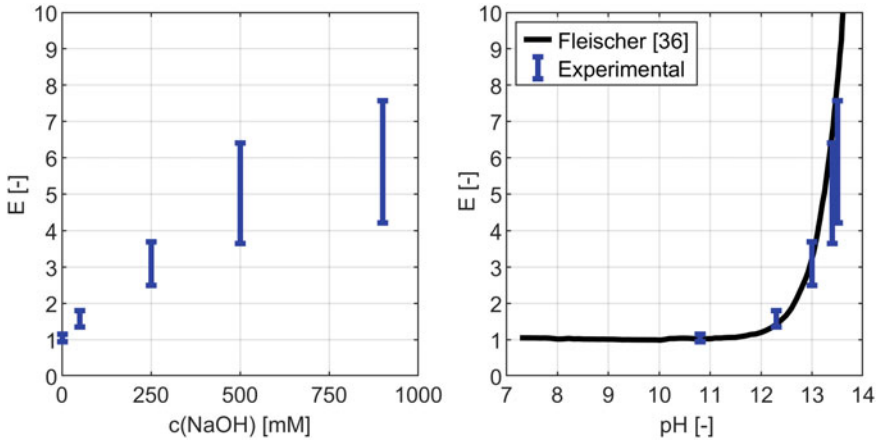
Fig. 18 Enhancement factor CO_2 in $NaOH_{aq}$ $d_0 \approx 4$–10 mm—$E(c)$ (left); $E(pH)$ (right) compared with calculations of Fleischer et al. [35]

explanation has not yet been found. Potential explanations could be that in earlier measurements, the strongly enhanced bubble dynamics for larger bubbles was not considered. The shape of large bubbles changes very dynamically. This wobbling could lead to a better mixing in the liquid, which in turn would result in a larger mass flow. Or for larger bubbles, especially at high NaOH concentrations, interfacial phenomena such as the Marangoni effect could appear, which are not detectable with the applied material property measurement techniques.

Figure 18 shows the dependency of the enhancement factor on the NaOH concentration. The given range is valid for the measured bubble spectrum. In the diagram on the right, the obtained measurement results are compared with a simulation by Fleischer et al. [35]. It is the pH-dependency of the enhancement factor, determined by detailed simulations with the two-film model for a system with a well-mixed liquid phase.

The measured enhancement factors agree with the values calculated by the two film models. For high NaOH concentrations ($c = 500$ mM/pH > 13), the value of Fleischer is only achieved with very large bubbles. For smaller bubbles a lower mass transfer coefficient was determined experimentally.

4.2   System NO in Fe^{II}(Ligand)

For the nitrosyl-iron complex system, six ligands were investigated within this project. Nitrogen monoxide (NO) was chosen as the gas phase. Table 5 lists the ligands used, their reaction rate and stability constant according to Schneppensieper et al. [21]. To keep the influence of the pH on the reaction low, a *pH* value of 7 ± 0.5 was adjusted by adding diluted sulfuric acid. Only ida, citrate and pure $FeSO_4$

Table 5 Reaction rate constants and stability constants in $Fe^{II}(ligand)_{aq}$/NO system [21]

Ligand	H_2O	ida	citrate	nta	hedtra	edta
Reaction rate constant k_f $(M^{-1} s^{-1})$	1.6×10^6	N/A	N/A	1.4×10^7	3.1×10^7	1.7×10^8
Stability constant K_{NO} (M^{-1})	1.2×10^3	1.2×10^4	2.1×10^4	1.8×10^6	1.5×10^7	2.1×10^6

(ligand: H_2O) were not adjusted, since the *pH* value of the dissolved educts/complex solution was below 7. No buffer was used to keep the number of components and their potential influence low.

Measurements were carried out in a concentration range from $c = 25$ to 100 mM. Figure 19 (left) shows an example of the results for the nitrosyl-iron complex system with edta as ligand for different concentrations. Again, the first 70% of the transferred amount of substance was evaluated. In the measured bubble spectrum with an initial bubble diameter of about $d_B = 2$–8 mm, the Sherwood number decreases with decreasing Péclet number. As expected, the mass transfer increases with higher reactive component concentration. To examine the influence more closely, the enhancement factors are shown in Fig. 19 on the right. In contrast to the CO_2/NaOH system, as one would rather expect, the enhancement factors are almost independent of the Péclet number, for high concentrations and Péclet numbers a slight decrease is measurable. The cause has not yet been clearly identified. The enhancement is approximately linear with respect to the iron complex concentration.
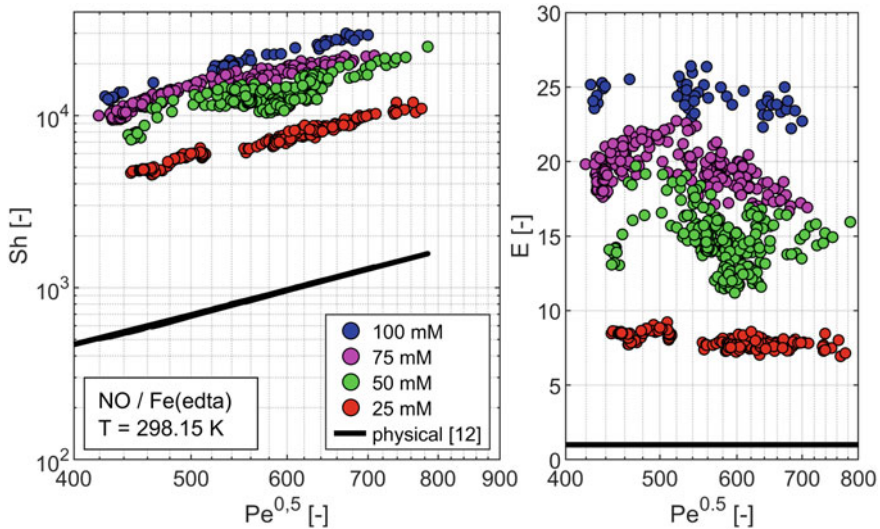
Fig. 19 Averaged Sh and Pe for single bubble experiments—Sh(Pe) NO in Fe^{II}(edta) in a concentration range of 25–100 mM (left), enhancement factor (Pe) (right)
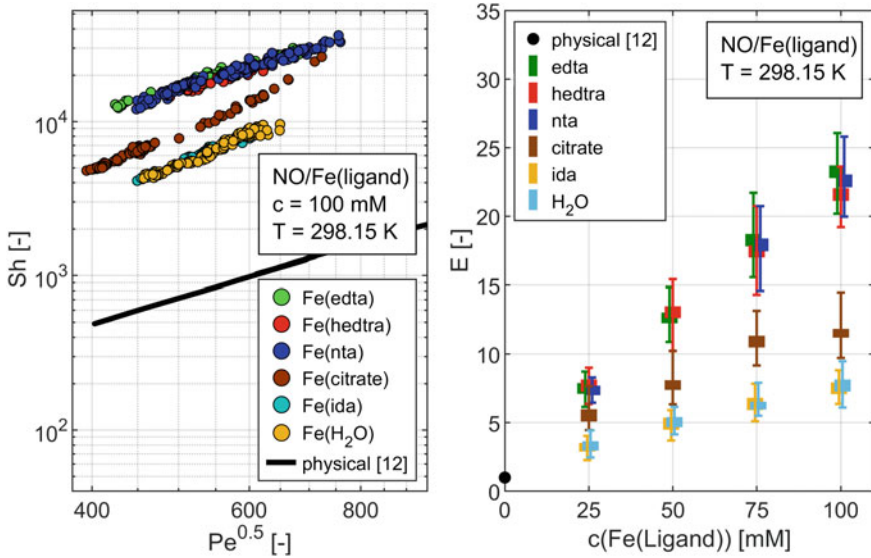
Fig. 20 Averaged Sh(Pe) in NO/Fe^{II}(ligand) systems $c = 100$ mM (left); averaged concentration-dependent enhancement factors with the range of measured enhancement factors over the bubble spectrum (right)

A comparison of the different ligands with the highest concentration of $c(Fe^{II}(ligand)) = 100$ mM is shown in Fig. 20 (left). Qualitatively, all systems show an increase in mass transfer with increasing Péclet number. The measured enhancement factors differ significantly. Three groups can be identified. The ligands ida and H$_2$O show the lowest mass transfer coefficients. In the middle range is citrate and the highest Sherwood numbers were measured with edta, nta and hedtra as ligand systems. This is only roughly in agreement with the expectation, since reaction rates and stability constants can vary by orders of magnitude between the different complexes. The expected order is shown in Table 5. Mass transport is improved by fast reaction kinetics. The differences between edta, nta and hedtra should be more distinct. Such a consideration do not take into account the effects of changing fluid dynamic behavior or interface properties that may occur. The grouping of the ligands edta, nta and hedtra could have different causes.

To give a complete overview of the measured enhancement factors, they are shown for all investigated iron complex systems as concentration-dependent values in Fig. 20 on the right side. For all systems, an almost linear dependency of the enhancement factor on the iron complex concentration has been measured. For high concentrations, the slope decreases slightly. The displayed error bars show the range of the measured enhancement factors in the considered bubble spectrum.

The slope of citrate, ida and H$_2$O is slightly larger than that of the correlation of Hughmark and the other ligand systems. This results in a dependency of the enhancement factor on the Péclet number. These systems show a fluid dynamic

behavior close to that of pure systems like shown in Fig. 11. Deviations can be explained by deviating material parameters such as viscosity and interfacial tension. The enhancement factor seems to increase in media without or with a small amount of interface-active substances with increasing Péclet number, i.e., bubble size. The same trend of the Péclet number dependency was already observed in the system CO_2/NaOH. A possible explanation is the stronger surface deformation (wobbling) and intensified mixing of the liquid. Since the measured mass transfer is related to the purely physical mass transfer for the determination of the enhancement factors, deviations from the Sherwood correlation of Hughmark could lead to an erroneous dependency of the enhancement factor on the Péclet number. Figure 16 illustrates that for the CO_2/water system the Hughmark correlation provides satisfactory agreement with the measurements. Other correlations from the literature predict lower mass transfer coefficients and also a weaker relation on the Péclet number. The use of such correlations would lead to higher enhancement factors in the measured systems, where a dependency on fluid dynamics would be even more pronounced.

The three systems with the highest reaction rate constants show an influence over time in the measurement of interfacial tension (Fig. 10), which can be explained by a coverage of the interface with surfactant. The experiments with N_2 as an inert bubble (Fig. 12) show that the fluid dynamics also depends on the contact time and thus on the degree of surface coverage. At the beginning of the measurements, even at the highest concentration, the bubbles show rise velocities comparable to those of pure systems.

For the previous evaluations, the first 70% of the transferred amount of substance was considered, so the influence of the surfactant was neglectable. In Fig. 21, the time-dependent Sherwood numbers are shown as a function of the Péclet number for the ligands edta and hedtra at $c(Fe^{II}(ligand)) = 100$ mM. The first 70% are plotted in blue. The circles show the corresponding determined averaged values. The last 30% of the observed mass transfer are shown in red.

On the right side, the averaged rise velocities with a moving mean value are plotted over the bubble diameter. Therefore, fluctuations in velocity due to oscillations are not visible. The color of the curves differentiates again between the first 70% (blue) and the remaining mass transfer (red).

For short contact times, during which most mass transfer takes place due to initially very high concentration gradients and to the highest difference in concentration, the fluid dynamics of the bubble is not yet strongly influenced. With decreasing bubble size and increasing surface contamination, the rise velocity of the bubble decreases. The values given by Tomiyama's correlation for fully contaminated systems (Eq. 5) are in a good agreement with the measured velocities at the end of the measurement for the system Fe^{II}(edta).

In the blue area, the measured mass transfer can be described with the approach of one enhancement factor and the correlation of Hughmark multiplied with one specific enhancement factor. As soon as the contamination by the surfactant influences the fluid dynamics, the Sherwood numbers increase for the system Fe^{II}(edta). The mobility of the interface decreases and the shape of the bubble changes, which, on the one hand side, is manifested by the low velocity, and on the other hand, by
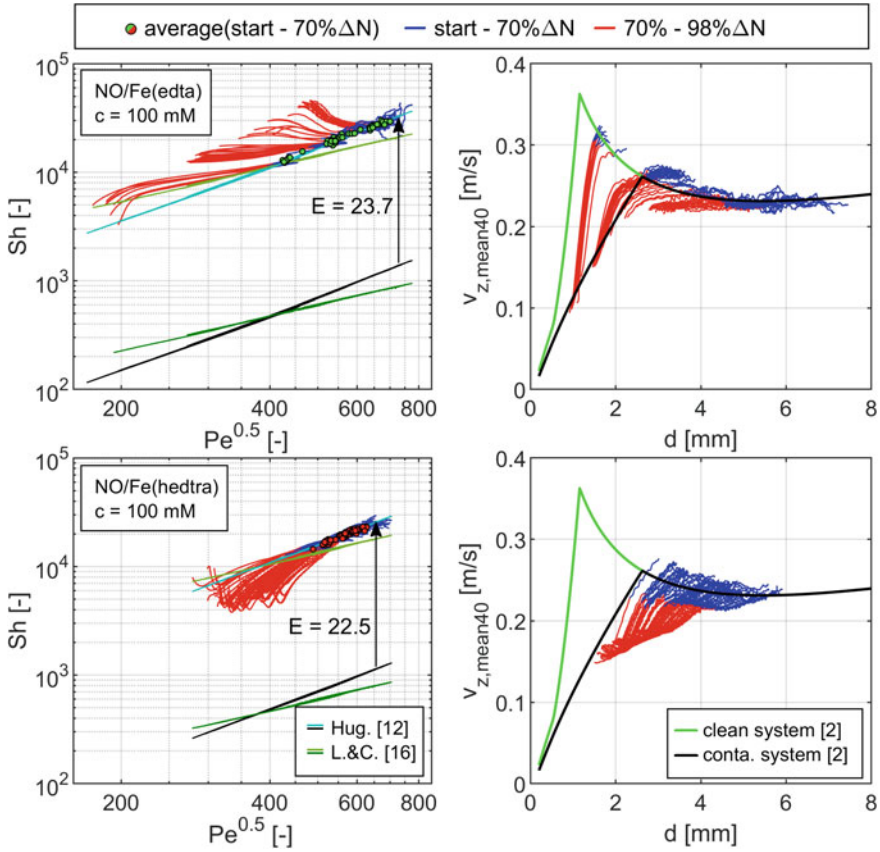
Fig. 21 Measured Sh(Pe) (left) compared to correlations of Hughmark and Lochiel and Calderbank with an enhancement factor; moved mean $v_z(d)$ (right) compared to velocities of clean and contaminated system [2] for NO in Fe^{II}(edta) (top) and Fe^{II}(hedtra) (bottom) at $c(Fe^{II}(ligand)) = 100$ mM

a higher oscillation frequency. Even small bubbles, which would rise straight up in pure systems, oscillate in the considered bubble spectrum. Local differences in interfacial tension can also lead to the occurrence of Marangoni convection. It cannot be concluded from the measurements so far which effect is responsible for an increased mass transfer coefficient.

In the lower part of the figure the results for the system Fe^{II}(hedtra) are shown. In this case, the fluid dynamics are influenced more strongly and the measured velocities are significantly below the correlation of Tomiyama. At the end of the measurement, a slight increase of the velocity is visible. The change in the oscillation frequency is more emphasized than with edta, which was shown in Fig. 13 with the Strouhal and Tadaki number. Also in this system, the mass transfer can be described at the beginning by one enhancement factor, when the fluid dynamics are taken into account.

In the further process, the influence of the coverage of the interface has a reducing effect on the mass transfer. The mobility of the surface seems to be even more restricted and an additional mass transport resistance is probably formed. At the end of the measurement, when an approximately stationary bubble size is reached, the rise velocity increases and the mass transfer coefficient also increases.

Although both ligands are surface active and reduce the rise velocity in comparison to same-sized clean bubbles, edta intensifies the mass transfer, whereas hedtra reduces it, more than just a change in the Péclet number would cause.

Figure 22 shows the investigations in the systems $Fe^{II}(nta)$ and $Fe^{II}(citrate)$. In the case of $Fe^{II}(nta)$ an influence on the fluid dynamics with longer contact time can also be measured. This is consistent with the slight decrease of interfacial tensions during the pendant drop measurement. However, the influence is less pronounced
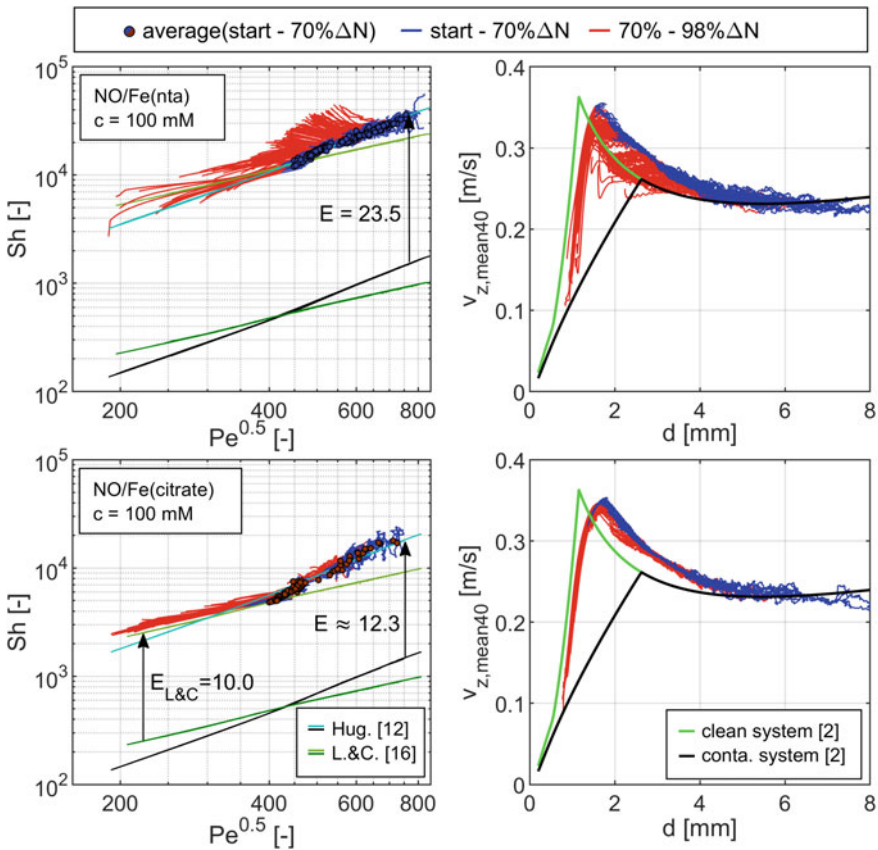
Fig. 22 Measured Sh(Pe) (left) compared to correlations of Hughmark and Lochiel and Calderbank with an enhancement factor; moved mean $v_z(d)$ (right) compared to velocities of clean and contaminated system [2] for NO in $Fe^{II}(nta)$ (top) and $Fe^{II}(citrate)$ (bottom) at $c(Fe^{II}(ligand)) = 100$ mM

than in the systems shown before. The mass transfer behavior is analog to that of the Fe^{II}(edta) system. For bubbles with an initial diameter larger than $d_B = 2$ mm, the mass transfer is intensified with decreasing bubble size. Only for some small straight rising bubbles a slight decrease in mass transfer could be measured.

Only citrate as ligand shows a fluid dynamic behavior as measured for the clean system. The initial bubble size has hardly any influence on the mass transfer as a function of the Péclet number. For oscillating bubbles with a Péclet number larger than 400, the enhancement factor increases with increasing Péclet number. Bubbles with a straight rise path show a lower dependence on fluid dynamics. Correlations with an exponent of 0.5 for the Péclet number, such as Lochiel and Calderbank (Eq. 20) and Sherwood et al. [15, 16] describe the slope of the course properly.

To evaluate the enhancement factor in the nitrosyl-iron complex system, many information must be available. The measurement of the interfacial tension can be an indicator for the fluid dynamic behavior. If the ligand has an interfacial effect it reduces the rise velocity and mass transfer can be enhanced or reduced. For systems where the fluid dynamics do not change due to contamination kinetics, the enhancement factor depends solely on the bubble size.

In the literature [36–39], measurements with surfactant systems have shown that the mass transfer in pure systems is higher than in contaminated systems. Cases investigated are pure water and tap water as well as surfactants like *Triton X-100* and *SDS*. For the ligand hedtra, a decrease of mass transfer can be confirmed by contaminating the interface. For the ligands nta and edta, however, an improvement in mass transfer was clearly shown for oscillating bubble at the end of the measurements. Figure 13 shows that the oscillation behavior of bubbles with the lower reaction rates and frequencies differs from the clean system. Thus, Marangoni convection could be responsible for the increased mass transfer. The Fe^{II}(hedtra) system shows these largest differences to clean systems, both in oscillation frequencies and rise velocities. In this case this leads to a decrease in mass transfer.

5   Conclusion

The mass transfer of single bubbles in an unconfined environment was investigated. Here, two cameras were moved in real-time with the rising bubble allowing a three-dimensional resolution of the bubble for a long rising path. During the ascent of up to $h = 1.8$ m, the change of bubble size and, therefore, amount of substance was tracked. Together with a detailed reconstruction of the current interfacial area, this approach allowed a detailed investigation of the influence of numerous parameters on the mass transfer coefficient, i.e., the Sherwood number. Varied parameters were the initial bubble size, pressure, temperature, gas and liquid systems.

For validation purposes of the bubble dynamics, the ascent of inert bubbles was investigated in clean systems and, due to the chemical systems of interest within this project, in systems with surface active components (metal-based complexes and different ligands). The shape, oscillation frequency and rise velocity can be used to

determine the mobility and contamination of the interface. The measurement of the interfacial tension shows the presence of a contamination kinetics for the nitrosyl-iron complex systems Fe^{II}(nta), Fe^{II}(edta) and Fe^{II}(hedtra). This behavior could also be confirmed in the measurement of bubble dynamics, since the rise velocity is reduced with increasing contact time and the shape of the bubble changes.

Furthermore, for comparison with widely used Sherwood correlations, purely physical mass transfer of different gas types was investigated in the same systems confirming a significant time-depending influence of the surfactants not only on the bubble dynamics but on the mass transfer, as well. To evaluate the occurring mass transfer, the desorption effects on the driving concentration difference must be considered as well, otherwise, the mass transfer coefficients will be too low.

For chemical reaction enhanced mass transfer, CO_2 in $NaOH_{aq}$ and NO in a nitrosyl-iron complex system with different ligands were investigated. In these systems, it was shown that CO_2 in $NaOH_{aq}$ and NO in nitrosyl-iron complex solutions with the ligands H_2O, ida and citrate show bubble dynamics independent of the contact time of the bubble with the liquid. The velocities of the bubbles are comparable to those of clean systems. The dependence of the Sherwood number on the Péclet number was confirmed and concentration-dependent enhancement factors were determined. Surprisingly, for CO_2 in $NaOH_{aq}$, the measured enhancement factors were found to dependent on the Péclet number in the measured bubble spectrum from approx. $d_B = 2$ to 8 mm initial diameter and increase with growing diameter. In case of the nitrosyl-iron complex system, for the evaluation of mass transfer, the changing bubble dynamics with surfactants must be considered. For the three systems with the highest reaction rates, no consistent influence was measured. The ligand hedtra with the strongest impact on bubble dynamics reduces the mass transfer coefficient. The ligands nta and edta show an enhancement compared to the expected mass transfer with decreasing Péclet number and increasing contact time. Applying local concentration measurement methods might give a deeper insight into such phenomena. The results show a complex interaction of ligand-depending contamination kinetics, bubble dynamics and reaction rates.

Still, the presented integral mass transfer coefficient determination approach proved to be widely applicable and gave consistent results in a level of detail not reached before. These findings confirm known Sherwood correlations but still point out certain limits and crucial details that have to be considered in the mass transfer analysis.

References

1. Clift R, Grace JR, Weber ME (1992) Bubbles, drops, and particles, 3, print edn. Acad. Press, New York
2. Tomiyama A, Katakoa I, Zun I, Sakaguchi T (1998) Drag coefficients of single bubbles under normal and micro gravity conditions. JSME Int J Ser B Fluids Therm Eng 41(2):472–479. https://doi.org/10.1299/jsmeb.41.245
3. Park SH, Park C, Lee JY, Lee B (2017) A simple parameterization for the rising velocity of bubbles in a liquid pool. Nucl Eng Technol 49(4):692–699. https://doi.org/10.1016/j.net.2016.12.006
4. Fan L-S, Tsuchiya K (1990) Bubble wake dynamics in liquids and liquid–solid suspensions. Butterworth-Heinemann. https://doi.org/10.1016/C2009-0-24002-5
5. Legendre D, Zenit R, Velez-Cordero JR (2012) On the deformation of gas bubbles in liquids. Phys Fluids 24:043303. https://doi.org/10.1063/1.4705527
6. Myint W, Hosokawa S, Tomiyama A (2007) Shapes of single drops rising through stagnant liquids. J Fluid Sci Technol 2(1):184–195. https://doi.org/10.1299/jfst.2.184
7. Okawa T, Tanaka T, Kataoka I, Mori M (2003) Temperature effect on single bubble rise characteristics in stagnant distilled water. Int J Heat Mass Transfer 46:903–913. https://doi.org/10.1016/S0017-9310(02)00345-9
8. Sanada T, Sugihara K, Shirota M, Watanabe M (2008) Motion and drag of a single bubble in super-purified water. Fluid Dyn Res 40:534–545
9. Aoyama S, Hayashi K, Hosokawa S, Tomiyama A (2016) Shapes of ellipsoidal bubbles in infinite stagnant liquids. Int J Multiph Flow 79:23–30. https://doi.org/10.1016/j.ijmultiphaseflow.2015.10.003
10. Aoyama S, Hayashi K, Hosokawa S, Tomiyama A (2018) Shapes of single bubbles in infinite stagnant liquids contaminated with surfactant. Exp Therm Fluid Sci 96:460–469. https://doi.org/10.1016/j.expthermflusci.2018.03.015
11. Deising D, Bothe D, Marschall H (2018) Direct numerical simulation of mass transfer in bubbly flows. Comput Fluids 172(30):524–537. https://doi.org/10.1016/j.compfluid.2018.03.041
12. Hughmark GA (1967) Holdup and mass transfer in bubble columns. Ind Eng Chem Process Des Dev 6(2):218–220
13. Calderbank PH, Moo-Young MB (1961) The continuous phase heat and mass transfer properties of dispersions. Chem Eng Sci 16:39–54. https://doi.org/10.1016/0009-2509(61)87005-X
14. Johnson AI, Besik F, Hamielec AE (1969) Mass transfer from a single rising bubble. Can J Chem Eng 47:559–564. https://doi.org/10.1002/cjce.5450470615
15. Sherwood TK, Pigford RL, Wilke CR (1975) Mass transfer. McGraw-Hill
16. Lochiel AC, Calderbank PH (1964) Mass transfer in the continuous phase around axisymmetric bodies of revolution. Chem Eng Sci 19(7):471–484. https://doi.org/10.1016/0009-2509(64)85074-0
17. Brauer H (1979) Particle/fluid transport processes. Fortschr Verfahrenstech 17. VDI-Verlag, Düsseldorf
18. Takemura F, Yabe A (1998) Gas dissolution process of spherical rising gas bubbles. Chem Eng Sci 53(15):2691–2699. https://doi.org/10.1016/S0009-2509(98)00094-3
19. McCabe WL, Smith JC, Harriott P (2005) Unit operations of chemical engineering, 7th edn. McGraw-Hill
20. Ohl CD (2001) Generator for single bubbles of controllable size. Rev Sci Instrum 72(1):252–254. https://doi.org/10.1063/1.1329900
21. Schneppensieper T, Wanat A, Stochel G, Goldstein S, Meyerstein D, van Eldik R (2001) Ligand effects on the kinetics of the reversible binding of NO to selected aminocarboxylato complexes of Iron(II) in aqueous solution. Eur J Inorg Chem 2001:2317–2325. https://doi.org/10.1002/1099-0682(200109)2001:9%3c2317::AID-EJIC2317%3e3.0.CO;2-F
22. Schneppensieper T, Finkler S, Czap A, van Eldik R, Heus M, Nieuwenhuizen P, Wreesmann C, Abma W (2001) Tuning the reversible binding of NO to Iron(II) aminocarboxylate and

related complexes in aqueous solution. Eur J Inorg Chem 2001:491–501. https://doi.org/10.1002/1099-0682(200102)2001:2%3c491::AID-EJIC491%3e3.0.CO;2-2

23. Schneppensieper T, Wanat A, Stochel G, van Eldik R (2002) Mechanistic information on the reversible binding of NO to selected Iron(II) chelates from activation parameters. Inorg Chem 41(9):2565–2573. https://doi.org/10.1021/ic011220w

24. Einstein A (1905) Über die von der molekularkinetischen Theorie der Wärme geforderte Bewegung von in ruhenden Flüssigkeiten suspendierten Teilchen. Ann Phys 17:549–560

25. Bridgeman OC, Aldrich EW (1964) Vapor pressure tables for water. J Heat Transfer 86(2):279–286. https://doi.org/10.1115/1.3687121

26. Ambrose D, Sprake CHS (1970) Thermodynamic properties of organic oxygen compounds XXV. Vapour pressures and normal boiling temperatures of aliphatic alcohols. J Chem Thermodyn 2(5):631–645. https://doi.org/10.1016/0021-9614(70)90038-8

27. Sander R (2015) Compilation of Henry's law constants (version 4.0) for water as solvent. Atmos Chem Phys 15:4399–4981. https://doi.org/10.5194/acp-15-4399-2015

28. Cussler EL (1997) Diffusion: mass transfer in fluid systems, 2nd edn. Cambridge University Press, New York

29. Warneck P, Williams J (2012) The atmospheric chemist's companion: numerical data for use in the atmospheric sciences. Springer

30. Fernández-Prini R, Alvarez JL, Harvey AH (2003) Henry's constants and vapor-liquid distribution constants for gaseous solutes in H_2O and D_2O at high temperatures. J Phys Chem Ref Data 32:903–916. https://doi.org/10.1063/1.1564818

31. Young CL, Battino R, Clever HL, Young CL (eds) (1981) Solubility data series, vol 8. Pergamon Press, New York. https://doi.org/10.1002/bbpc.19820861029

32. Wilke CR, Chang P (1955) Correlation of diffusion coefficients in dilute solutions. AIChE J 1:264–270

33. Malviya A, Vrabec J (2020) Henry's law constant of nitrogen, oxygen and argon in ternary aqueous alcoholic solvent mixtures. J Chem Eng Data 65:1189–1196. https://doi.org/10.1021/acs.jced.9b00571

34. Sada E, Kito S, Oda T, Ito Y (1975) Diffusivities of gases in binary mixtures of alcohols and water. Chem Eng J 10:155–159. https://doi.org/10.1016/0300-9467(75)88030-0

35. Fleischer C, Becker S, Eigenberger G (1996) Detailed modeling of the chemisorption of CO_2 into NaOH in a bubble column. Chem Eng Sci 51(10):1715–1724. https://doi.org/10.1016/0009-2509(96)00030-9

36. Sardeing R, Painmanakul P, Hébrard G (2006) Effect of surfactants on liquid-side mass transfer coefficients in gas–liquid systems: a first step to modeling. Chem Eng Sci 61(19):6249–6260. https://doi.org/10.1016/j.ces.2006.05.051

37. Hori Y, Bothe D, Hayashi K, Hosokawa S, Tomiyama A (2020) Mass transfer from single carbon-dioxide bubbles in surfactant-electrolyte mixed aqueous solutions in vertical pipes. Int J Multiph Flow 124. https://doi.org/10.1016/j.ijmultiphaseflow.2020.103207

38. Painmanakul P, Loubière K, Hébrard G, Mietton-Peuchot M, Roustan M (2005) Effect of surfactants on liquid-side mass transfer coefficients. Chem Eng Sci 60:6480–6491. https://doi.org/10.1016/j.ces.2005.04.053

39. Vasconcelos JMT, Orvalho SP, Alves SS (2002) Gas-liquid mass transfer to single bubbles: effect of surface contamination. AIChE J 48(6):1145–1154. https://doi.org/10.1002/aic.690480603

40. Merker D, Böhm L, Oßberger M, Klüfers P, Kraume M (2017) Mass transfer in reactive bubbly flows—a single bubble study. Chem Eng Technol 40:1391–1399. https://doi.org/10.1002/ceat.201600715

Experimental Investigation of Reactive Bubbly Flows—Influence of Boundary Layer Dynamics on Mass Transfer and Chemical Reactions

Felix Kexel, Sven Kastens, Jens Timmermann, Alexandra von Kameke, and Michael Schlüter

Abstract Bubbly flows are extensively used processes in the chemical industry. Since the complex interaction of fluid dynamics, mass transfer and chemical reaction is not yet fully understood, a reliable prediction of yield and selectivity is not possible. Within this work different benchmark experiments are developed, allowing the investigation of the interplay of mixing and chemical reactions. For precise predictions of the chemical process, a detailed knowledge about the intrinsic kinetics is essential. Therefore, the guiding measure "SuperFocus Mixer" (SFM) has been developed and successfully tested by determining the kinetics of a model system and of the oxidation of a temperature sensitive copper complex. In a second step, the identified reaction is transferred into the Taylor bubble setup, marking the second benchmark system. Here the effect of mixing on the production of the products in consecutive and competitive-consecutive reaction is investigated. The conducted experiments show significant influence of the mixing intensity on the production of the first reaction product MNIC and the side product DNIC, favoring the first product at intensified mixing. Finally, the local mass transfer at freely ascending bubbles superimposed by a chemical reaction is determined by applying planar-LIF, and the influence of bubble–bubble bouncing is quantified. In addition, a novel method, the Time Resolved Scanning-LaserInduced Fluorescence (TRS-LIF) for the visualization of 3D concentration fields, is introduced and tested at single rising oxygen bubbles.

1 Introduction

Bubbly flows, dispersing a gaseous phase into a continuous liquid phase, are widely used within the chemical industry to perform fast gas–liquid reactions as oxidations, hydrogenations or chlorinations. As all processes aim for a possibly high yield and selectivity, a deep knowledge about the complex interplay of fluid dynamics, mixing, mass transfer and chemical reactions is of imminent importance. While the fluid

F. Kexel · S. Kastens · J. Timmermann · A. von Kameke · M. Schlüter (✉)
Institut für Mehrphasenströmungen, Technische Universität Hamburg, Eißendorfer Straße 38, 21073 Hamburg, Germany
e-mail: michael.schlueter@tuhh.de

dynamic behavior of bubbles has been the topic of several comprehensive studies in the past, e.g. by Clift et al. [1], Fan and Tsuchiya [2], Peebles and Garber [3] and many others, the interplay of mixing in the bubble wake, mass transfer and the ongoing chemical reaction is not fully understood. Although it is known that mass transfer, mixing and the proceeding chemical reaction are depending on each other, the impact of those dependencies cannot be quantified yet.

In order to obtain a better understanding of these complex processes, this project aims to experimentally determine and model transport processes and the time scales of mixing near the boundary layer of gas bubbles with superimposed chemical reactions.

Evaluating the effects of mixing and transport processes in a gas–liquid chemical reaction precisely is a challenging task, as both effects ideally need to be evaluated separately but strongly depend on each other. To overcome those dependencies three experimental setups have been developed within this project:

- The SuperFocus Mixer setup to determine the intrinsic kinetics of fast gas–liquid reactions
- The Taylor bubble setup to identify suitable chemical reaction systems for further studies
- A setup to investigate single bubbles, freely ascending or colliding with each other in 2-D and 3-D.

The SuperFocus Mixer (Sect. 2) is one of the guiding measures within the SPP1740 as it allows to determine suitable chemical systems, which are ideally consecutive and competitive. In addition the intrinsic kinetics can be determined under ambient conditions and in combination with numeric approaches, with only small amounts of reactants being necessary. The Taylor bubble setup (Sect. 3) marks the second step in order to further understand mixing, mass transfer and chemical reactions. The Taylor bubble setup allows to determine reactive systems suitable for further investigations in a larger scale and at freely ascending bubbles. Especially the well-defined and reproducible conditions at Taylor bubbles are ideal to gain a first insight into the production of the reaction products in dependency of the wake structures and the mixing behavior. The last setup allows to study single freely ascending bubbles or the bubble–bubble interaction and their effect on local mass transfer and the proceeding chemical reaction by means of Laser Induced Fluorescence (Sect. 4).

1.1 Mass Transfer in Reactive Bubbly Flows

The mass transfer of species from the gaseous to the liquid phase is a complex interlinked process between both phases and occurring interfacial effects. Therefore, the mass transfer phenomena are usually investigated at single bubbles and simplified models as the two-film theory by Lewis and Whitman [4] or the penetration theory by Higbie [5] are applied. Both theories are widely accepted and have been extended only slightly [6–8].

If the mass transfer is superimposed by a chemical reaction, the exemplary description becomes more complex, as the chemical reaction equals a sink with respect to the transferred species. Therefore, the concentration of the transferred species decreases stronger than with purely physical mass transfer. This mass transfer enhancement caused by the chemical reaction is defined by the enhancement factor

$$E = \frac{k_L^R}{k_L^0} = \frac{\delta_L}{\delta_{L,reaction}} \tag{1}$$

where k_L^R is the reactive mass transfer coefficient and k_L^0 is the physical mass transfer coefficient. In dependency on the reaction kinetics, different concentration profiles within the boundary layer can occur, which have been classified by Levenspiel [9, 10], Baerns et al. [11] and others. According to Levenspiel, a classification of the mass transfer with chemical reactions is possible by applying the Hatta number

$$Ha = \sqrt{\frac{t_D}{t_R}}, \tag{2}$$

postulated by Hatta [12]. It is the ratio of the relaxation time of the diffusion t_D and the relaxation time t_R of a chemical reaction, which is depending on the reaction order [13]. In addition Hatta derived the enhancement factor E based on the condition of a fast first order reaction that takes place only in the liquid film

$$E = \frac{Ha}{\tanh Ha}. \tag{3}$$

2 Determination of Mass Transfer Relevant Kinetics in a SuperFocus Mixer

For the understanding, prediction and numerical simulation of chemical reactions in bubbly flows, the knowledge of the intrinsic kinetics is vital, but a challenging and complex task and choosing a suitable reaction system for further experimental studies is of essential significance.

For detailed investigations of the intrinsic kinetics and the decision on promising model chemical reactions the guiding measure "SuperFocus Mixer" is used. It aims for the elimination of mass transfer limitations by measuring in a single phase system with small mixing times and high spatiotemporal resolution. The combination of the Super FocusMixer (SFM) and a Confocal Laser Scanning Microscope (CLSM) allows concentration field measurements with a high resolution while enabling time independent investigations with the desired small mixing time.

The SuperFocus Mixer developed by Hessel et al. in 2003 [14], shown in Fig. 1, is a laminar interdigital micromixer ideal for mixing two fluid streams. Interdigital
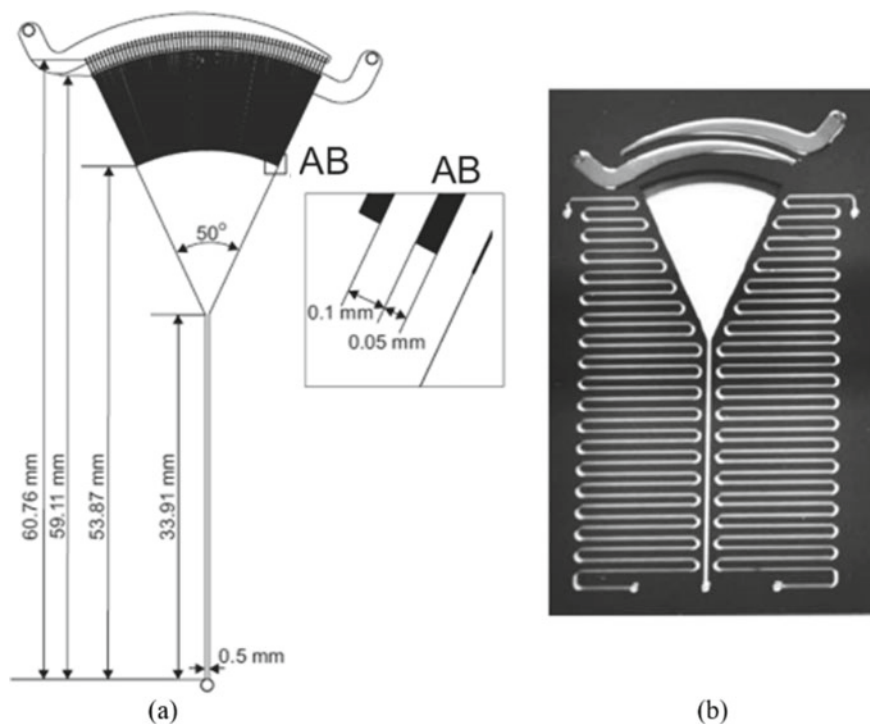
Fig. 1 a Layout scheme of the SuperFocus Mixer according to Hessel et al. [14]; **b** Si-glass-Si SuperFocus Mixer manufactured at the TUHH by the Institute of Microsystems Technology

mixing is achieved by the use of alternating feed channels that lead to a periodically alternating liquid lamella. Within the SFM 124 micro channels with a width of 100 µm are merged in a triangular shaped focus chamber with a curved inlet arrangement to obtain a more equal distribution. The mixing chamber rejuvenates from 20 to 0.5 mm to achieve rapid mixing.

Early publications state mixing times of a few ms [14, 15] and a mixing time of 5 ms for a 95% completion of mixing is stated by Drese [16]. However, these mixing times seems to exclude the focusing chamber, as Kashid et al. [17] proposed in 2014 a mixing time of 4 ms for a 95% completion, while neglecting the residence time of the focusing chamber. Depending on the flow rate, the residence time is in a range of a few 100 ms up to seconds. Therefore, mixing through diffusion cannot be neglected.

Nevertheless, a laminar operating SFM in combination with numerical approaches provides an excellent tool to determine intrinsic kinetics of chemical reactions.

2.1 Sodium Sulfite Oxidation as a Model Reaction

For the precise investigation of mass transfer enhanced by chemical reactions and boundary layer dynamics, a reaction system is chosen, widely discussed in the literature and frequently used. The oxidation of sodium sulfite to sulfate is generally used in process engineering as a simple model reaction to determine the mass transfer performance and interfacial area. The formal reaction equation found in literature is

$$SO_3^{2-} + \frac{1}{2}O_2 \rightarrow SO_4^{2-}.\tag{4}$$
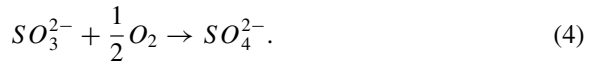
Though this reaction progression is only the overall reaction equation assembling from several partial reactions, yielding a very complex reaction network. As the reaction is not fully understood yet, the reaction kinetics cannot be determined without any assumptions. Within this work a simplified reaction mechanism according to Kück et al. [18] is used. This simplification is very close to the mechanism of Bäckström [19], who published a reaction network in 1934 that marks the basis of most mechanisms until today.

It is presumed that the reaction is catalyzed by metal ions within the solution, in case of the experimental procedure cobalt(II)sulfate.

$$Me^{2+} + HSO_3^- \rightleftharpoons Me^+ + HSO_3^{\cdot}$$

$$HSO_3^{\cdot} + O_2 \rightleftharpoons HSO_5^{\cdot}$$

$$HSO_5^{\cdot} + HSO_3^- \rightleftharpoons HSO_4^- + HSO_4^- + HSO_4^{\cdot}$$

$$HSO_4^{\cdot} + HSO_3^- \rightleftharpoons HSO_4^- + HSO_4^- + HSO_3^{\cdot}$$
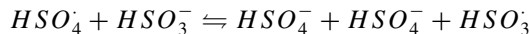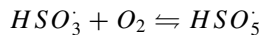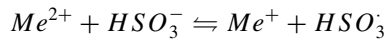
The advantage of this simplified mechanism is the possibility to formulate a second order kinetics easily, yielding

$$\frac{d[O_2]}{dt} = -k_1 \cdot [O_2] \cdot \left[HS_3^-\right].\tag{5}$$

This reaction system is used to proof the applicability of the SuperFocus Mixer for the visualization of chemical reactions by means of Laser Induced Fluorescence (LIF) and determining diffusion coefficients as well as kinetic constants.

2.2 Concentration Measurements Using Laser Induced Fluorescence (LIF)

As the phenomena in the rather thin concentration boundary layer around gas bubbles are crucial for the understanding of mass transfer and fluid dynamics in bubbly flows, a measurement with a very high spatial and temporal resolution is necessary [20].

Laser induced fluorescence enables the visualization and investigation of concentration fields in the vicinity of interfaces, with the desired high resolution. A big advantage of LIF is that it allows local investigations due to a thin illuminated plane and moreover, enables the detection of instantaneous concentration fields. Thus, with the recently developed temporal and spatial highly resolved equipment like pulsed laser systems and cameras, LIF enables the investigation of time depended processes such as vortexes, mixing layers and convective transport phenomena [20].

While the implementation is elaborate, the measurement principle is rather simple, by adding a fluorescent dye to the bulk phase acting as a tracer. The dye ideally acts as a passive scalar not changing the fluid properties [20]. Therefore, there are several aspects and requirements which need to be fulfilled by the dye: It must be soluble in the bulk phase, it has to be stable under the influence of the laser radiation and the absorption and emission spectra of the dye need to be clearly distinguishable [21].

To correlate the grey scale images with concentration values, a calibration becomes indispensable. For this purpose, the fluorescent dye is mixed with defined concentrations of the desired reactant and calibration images are recorded. The relation between concentration and grey value is then detected by fitting a curve. In case an indirect measurement is performed and the fluorescence is quenched, the Stern–Volmer equation is applied for fitting the signal to the concentrations [20, 22].

2.3 Experimental Setup and Methods

The experimental setup used for the determination of the intrinsic kinetics at the TUHH is given in Fig. 2. The core elements of the setup are the SuperFocus Mixer as described in the previous chapter and the *Olympus Fluoview 1000 CLSM*, allowing measurements of the local concentration fields on a micro-scale in high resolution. The CLSM works very similar to a conventional microscope. In addition to the lenses, it contains two pinholes, through which solely focused light is reaching the detector. The remaining light is cut off, allowing a very small focus depth. Therefore, only light from a chosen, narrow plane is detected and the obtained data is not influenced by planes above or below the measurement plane. Using a laser beam as a light source, several points in front of the microscope objective are scanned to obtain a two-dimensional measurement plane. Each measured point equals a pixel in the resulting image. The data acquisition enables a high spatial resolution below $0.35\,\mu m$ per pixel. The detailed working principle of the CLSM is described in [23].
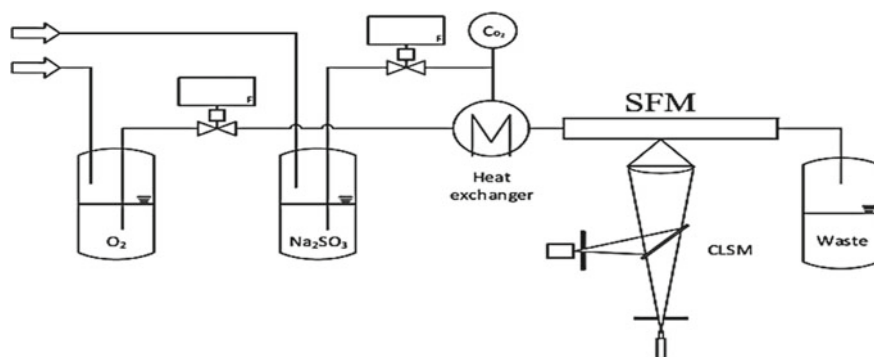
Fig. 2 Scheme of the function principle of a confocal laser scanning microscope [23]

To obtain reproducible two-dimensional recordings, the SuperFocus Mixer is placed on an X–Y table, allowing the exact positioning in front of the objective of the CLSM. When changing the objective position relative to the scanned mixer, slices in different depth are recorded, enabling a three-dimensional reconstruction of the concentration fields [24].

The concentration fields within the SuperFocus Mixer are recorded using the LIF technique (compare Sect. 2.2). Therefore, a fluorophore providing a reliable calibration is necessary. The fluorophore allows the assignment of the recorded fluorescence intensity to the concentration of an analyte. The experiments are carried out using the dye Dichlorotris(1,10-phenanthroline)ruthenium(II)hydrate (*Sigma Aldrich*), which shows a dependency of the fluorescence intensity in relation to the oxygen concentration. The fluorescence signal of the chosen dye decreases with increasing oxygen concentration. This effect is described by the Stern–Volmer correlation and allows the calibration of the fluorescence signal to the oxygen concentrations, which are monitored using a *PreSens* oxygen sensor. Preliminary investigations [25] have shown a high temperature dependency of the florescence signal. Therefore, the CLSM is enclosed by an air-conditioned box, an additional heat exchanger is positioned in front of the SFM and a cooling zone is implemented within to maintain a temperature of $T = 20\,°C \pm 0.5\,°C$ at any time [26]. Each measurement is performed with an aqueous solution containing a concentration of $\rho = 30$ mg L^{-1} of Dichlorotris(1,10-phenanthroline)ruthenium(II)hydrate and, in the case of the catalyzed reactions, additionally $\rho = 16$ mg L^{-1} of cobalt sulfate hydrate as a catalyst. The catalyst is added since high sodium sulfite concentrations influence the liquid properties, leading to a density difference of up to 8% in the two reactant streams [27].

One half of the prepared solution is saturated with atmospheric oxygen while the other half is oxygen desorbed by applying nitrogen to the solution. To enable the measurement of the reactive mass transfer, sodium sulfite is added to the oxygen desorbed solution. The oxygen saturated and the sodium sulfite solution are supplied to the SuperFocus Mixer by pressurized vessels with a relative pressure of $p = 0.5$ bar.

The mass flow rates are controlled by two *Bronkhorst* mini Cori-Flow M13 Coriolis mass flow meters.

2.4 Experimental Results

2.4.1 Comparison of Physical and Reactive Mixing

In a first experimental setup to evaluate the intrinsic reaction constants, the catalyzed oxidation of sodium sulfite is used. For the determination of the intrinsic kinetics, the reaction parameters are adjusted. The oxygen concentration is set to $\rho = 12$ mg L^{-1} equivalent to $c = 3.75 \times 10^{-4}$ mol L^{-1} and the sodium sulfite concentration is adjusted to $\rho = 10.4$ g L^{-1} equivalent to $c = 3.17 \times 10^{-3}$ mol L^{-1}, resulting in a sulfite excess of approximately 10 with respect to the oxygen consumption.

Figure 3 shows the concentration fields obtained with the CLSM for a flow rate of $\dot{V} = 300$ g h^{-1} (top) and $\dot{V} = 30$ g h^{-1} (bottom) for physical (a) and reactive mixing (b). In the case of physical mixing (left), a narrow diffusion-dominated layer forms at the edge of the oxygen enriched stream. This diffusion-dominated layer
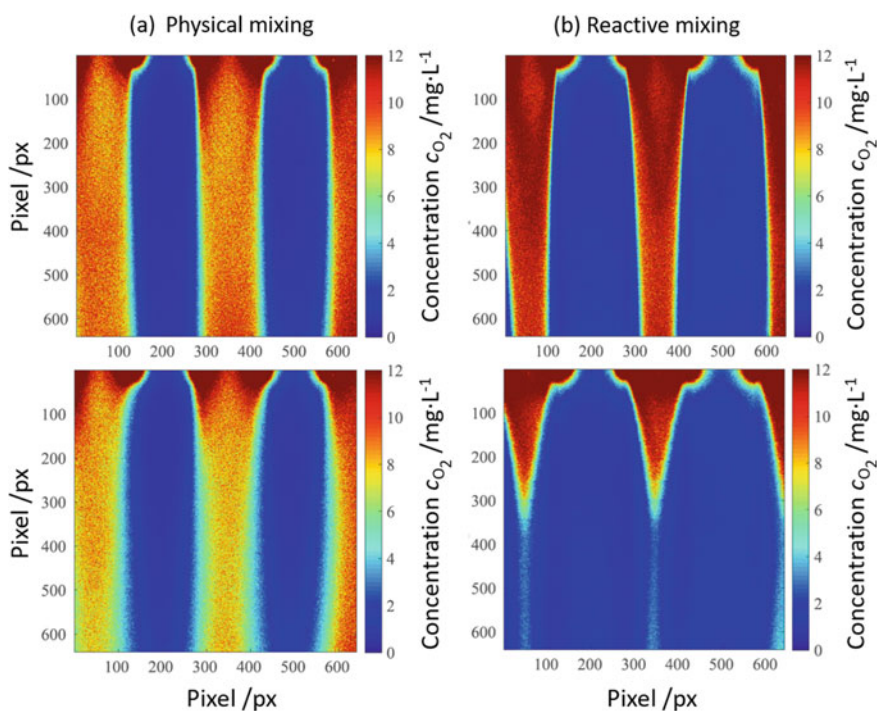
Fig. 3 Concentration fields of physical (**a**) and reactive (**b**) mixing at the inlet of the SuperFocus Mixer for $\dot{V} = 300$ g h^{-1} (top) and $\dot{V} = 30$ g h^{-1} (bottom). Data from [27]

Table 1 Listing of the diffusion coefficient and reaction rate determined for the reaction of sodium sulfite with O_2 in a SFM [26]

	Result	Value	Unit
Diffusion coefficient	D_{eff}	1.0×10^{-9}	$m^2 \, s^{-1}$
Reaction rate	k_{CR2}	5.5×10^4	$L \, mol^{-1} \, s^{-1}$

becomes clearly more pronounced with decreasing flow rate. This circumstance is caused by the 10 times higher residence time at the flow rate of $\dot{V} = 30 \, g \, h^{-1}$ and is in accordance with theory.

When looking at the reactive mixing, the oxygen enriched stream is getting constricted over the course of time, due to the superimposed sodium sulfate reaction, causing an increased demand of oxygen. The reaction starts to consume the oxygen within the diffusion zones at the edges of the stream. At the high flow rate this effect can be observed by the narrowing of the oxygen enriched stream. Furthermore, the influence of the reaction becomes more explicit while looking at the lower mass flow. The oxygen enriched areas (red) are more distinct, while the oxygen depleted areas (blue) are much broader and the oxygen is almost totally consumed by the chemical reaction after approximately $x = 300 \, \mu m$.

The experimentally obtained data are the basis for the determination of the intrinsic kinetics. The experimental values can be validated and improved by numerical simulations with a parameter optimization. The numerical simulations are conducted by the group of Prof. Turek, TU Dortmund, yielding precise information on the diffusion coefficients D_{eff} and kinetic parameters like the reaction rate k_{CR2}, given in Table 1. The performed numerical simulations are presented and discussed in more detail in Chapter "Determination of Kinetics for Reactive Bubbly Flows Using SuperFocus Mixers". The determined reaction rate k_{CR2} for sodium sulfite is in good agreement to those of Kück et al. [23], who proposes reaction rates in the observed concentration range of $k_{CR2} = 10^4 – 10^6 \, L \, mol^{-1} \, s^{-1}$.

Another approach for determining the intrinsic kinetics by experiments in a SFM only is performed by Schurr et al. [28]. The study is conducted at the oxidation of a copper(I) complex traceable by means of UV/VIS-spectroscopy in a continuous flow setup using an SFM with a fast mixing behavior. By means of the setup, Schurr was able to detect the formation and decay of a thermally very sensitive bis(μ-oxo)dicopper species, provided by the working group of Prof. Herres-Pawlis, RWTH Aachen. The SuperFocus Mixer is used as the experiments can be conducted under ambient conditions, without the need of cooling down the entire system significantly, as it is done e.g. with a stopped-flow method. In addition the SuperFocus Mixer is applicable for very fast reacting systems in which the application of the Stopped Flow Method reaches its limits. In order to validate the data obtained by the use of the SuperFocus Mixer, it is compared to data measured with the stopped-flow method. Since the values obtained are in the range of those obtained by stopped-flow methods, they pave the way for further experimental studies on kinetics using an SFM setup [28].

Both studies, the one performed by Schurr et al. and the one conducted by Timmermann and Mierka, show that the SuperFocus Mixer is a useful tool for the determination of intrinsic kinetics, as it can be easily adapted to any reactive system if one species is clearly traceable. Through the conversion of the reaction time scale on a length scale in steady state operated microfluidic devices, a time independent investigation is possible with low reactant consumption. Nevertheless, the mixing through diffusion is not neglectable in a lamination device as the SFM, so that diffusion has to be taken into account for the determination of the time constants (see Chapter "Determination of Kinetics for Reactive Bubbly Flows Using SuperFocus Mixers").

3   Investigation of Chemical Reactions by Means of Taylor Bubbles

The guiding measure "Taylor bubble" has been established to bridge the gap between chemistry and process engineering. The experimental setup is designed for the characterization of different chemical systems on a small scale with well-defined gas/liquid phase boundaries and within a safe environment since the complete setup fits easily under a fume hood.

Taylor bubbles are elongated, bullet shaped gas bubbles in narrow channels or capillaries surrounded by a thin liquid film. The maximum bubble diameter d_B reached by those bubbles is only slightly smaller than the hydraulic channel diameter D_h, as can be seen in Fig. 4. Taylor bubble flows appear in multiphase applications as monolith-reactors, pipe reactors and many more.

Due to the well-defined fluid dynamic conditions, volume independent bubble rising velocity and a high degree of reproducibility, Taylor bubbles are very well suited for detailed studies of fast gas–liquid reactions. The fluid dynamic behavior of Taylor bubbles is described by the Reynolds number using the hydraulic diameter D_h as the characteristic length. However, the rising behavior of Taylor bubbles is dependent on the ratio of buoyancy and surface tension yielding the Eötvös number

$$Eo_D = \frac{(\rho_L - \rho_G)g D_h^2}{\sigma} \tag{6}$$

where ρ_L and ρ_G are the liquid and gas phase densities, g is the magnitude of the gravitational acceleration and σ is the surface tension [29].

In vertical channels, two flow conditions can be distinguished, a pressure driven bubble, set in motion by a liquid flow, and the free rising Taylor bubble, which induces a flow field driven by the buoyancy force. Buoyancy is the dominating force as long as the channel diameter is larger than a critical inner diameter D_{crit} calculated by the critical Eötvös number $Eo_{crit} \approx 4$ [29]. Hence, the critical diameter is strongly dependent on the system properties and especially on the surface tension. For aqueous systems, this results in a critical inner diameter of $D_{crit} = 5.4$ mm, while
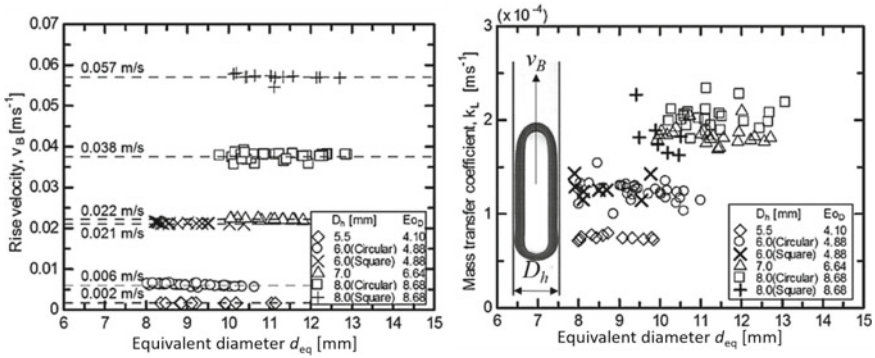
Fig. 4 Rise velocity (left) and mass transfer coefficient (right) of Taylor bubbles in dependency of the equivalent diameter d_{eq} and the channel diameter D_h for different channel geometries [33]

organic solvents as Tetrahydrofuran or Methanol allow critical diameters of down to $D_{crit} = 4$ mm. At low Eötvös numbers, no shape oscillation of the bubble occurs and the bubble is self-centering within the channel, as long as it stays elongated. During the dissolution process, the bubble is only decreasing in length and remains in the centered position [30–32].

By varying the inner diameter of the channel, a change in rise velocity v_B and therefore the contact time of the species can be achieved, influencing the fluid dynamic time scales in a well-defined way, as shown in Fig. 4.

Within the DFG project SPP1506 "*Transport Processes at Fluidic Interfaces*" [33] it has been found, that the mass transfer coefficient strongly depends on the pipe inner diameter D_h. Therefore the Sherwood number Sh_d correlates with the Eötvös number [33]

$$Sh_D = 290 Eo_D^{0.524} - \left[\frac{1.23}{(Eo_D + 1)^{0.0517}} \right]^{50.1}. \tag{7}$$

Additionally, it was found that due to a constant rise velocity the mass transfer is constant for a wide range of bubble diameters in case of small circular channels.

The well-defined adjustment of the fluid dynamic conditions is used in this work to create characteristic and reproducible flow patterns behind Taylor bubbles with certain defined residence time distributions. As the characteristic flow patterns affect the mixing process of the diluted gas, they are also able to influence the ongoing chemical reaction. For instance, the local availability of the gas species might influence the yield and selectivity of a competitive chemical reaction.

3.1 Experimental Setup and Methods

3.1.1 Test Systems for the Investigation of Reactive Bubbly Flows

To gain detailed information about the interplay of local fluid dynamics, mass transfer and chemical reactions suitable test systems are necessary. Besides the already introduced and commonly known oxidation of sodium sulfite another test system known from literature is used. The oxidation of an aqueous copper(I)ammonia solution $[Cu(NH_3)_4]^+$ results in the immediate formation of a deep blue complex, so that the wake structures behind rising bubbles become visible [34].

Supplementary to the already known reactive systems from literature, new reactive test systems meeting the desired criteria of being consecutive or even consecutive and competitive have been developed within the SPP1740. To overcome the influence of surfactants at the stagnant cap of the bubbles rear end in aqueous systems, and to acquire industrial relevant results, organic systems are required [35–37]. Within the priority program, basically three different chemical systems have been developed, which are shown in Fig. 5. In case of these reaction systems, only small amounts of reactants are available and therefore, a small substance usage within the experiments is essential. Here, the small volume of the Taylor bubble experiments is a strong benefit. All three systems show a color change with progression of the reaction
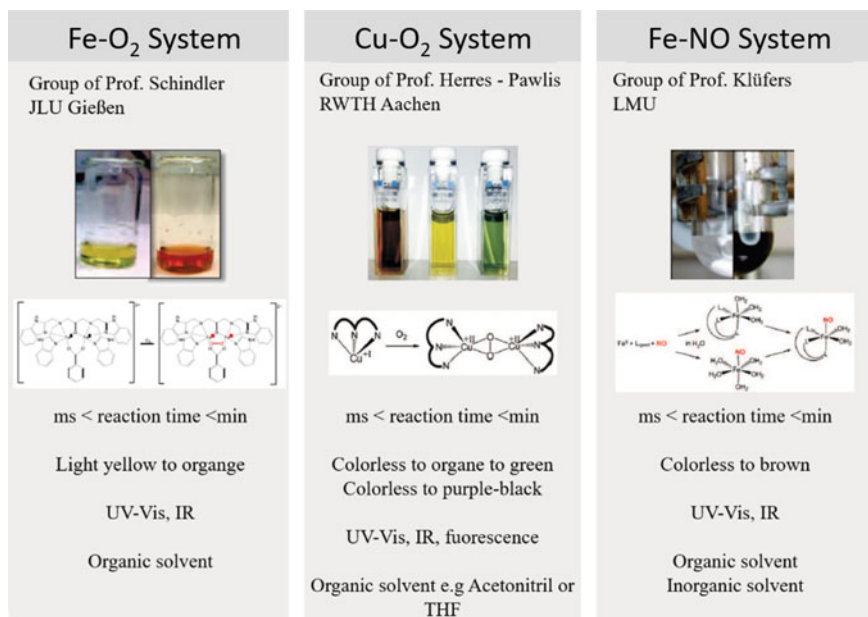
Fig. 5 Overview of the different reaction systems available for the experimental studies

allowing an easy qualitative visual evaluation of product and side product generation and are observable by means of UV/VIS spectroscopy for the quantification of yield and selectivity. While the Fe–NO system is applicable in both organic and inorganic solvents, the Fe–O_2 and the Cu–O_2 reaction system require an organic solvent as methanol, acetonitrile or tetrahydrofuran. However, the Fe–NO system is only observable by means of UV/VIS showing a strong coloration but no fluorescent answer is detectable. In comparison, the Cu–O_2 and the Fe–O_2 system are showing fluorescence signals and are therefore rather applicable for local investigations by means of planar Laser Induced Fluorescence (p-LIF). A more detailed description of the underlying chemistry can be found in the chapters of the corresponding working groups listed in Fig. 5.

3.1.2 Experimental Setup

The Taylor bubble set up implemented for the experimental work of the SPP1740 is developed based on the experiences made in the SPP1506 "Transport Processes at Fluidic Interfaces". The setup is used to identify suitable chemical systems and adjust the timescales of mixing and mass transfer in order to fine tune them to meet the timescales of the chemical reaction. Especially the strongly reproducible fluid dynamic conditions and the controllable mass transfer performance is of great benefit. In addition, the experiments in the Taylor bubble setup need only a small volume of reactants and can be placed in the fume hood, allowing to work with hazardous chemicals if necessary.

For the experimental work, two Taylor bubble setups have been developed, which enable an oxygen free environment necessary when dealing with oxygen sensitive reaction systems. Both setups are shown in Fig. 6. The main part of the setup is the exchangeable 300 mm borosilicate capillary, ranging in diameter from around $D_h = 4$ mm to $D_h = 10$ mm depending on the desired Eötvös number and the fluid dynamic conditions. The flow rate in the capillary is variable which enables a fixation of the Taylor bubble and allowing long experimentation times. The flowrate is adjusted by valve 1. The gas is injected using a *Hamilton 1001* gas-tight syringe via a three port valve located below the capillary. To match the refractive index, the capillary is surrounded by a borosilicate cuvette, containing a solution of 97 wt% dimethyl sulfoxide DMSO (*Sigma Aldrich*) and deionized water. To ensure the oxygen free environment the entire setup is flushed with either argon or nitrogen, depending on the observed reaction [30].

Various light sources can be coupled into the setup. In the first case a laser system is applied as light source, enabling local investigations within the wake of the bubble via Laser Induced Fluorescence (p-LIF) and Particle Image Velocimetry (PIV). Depending on the chemical system and the resulting excitation wavelengths of the fluorophore a high-speed laser ($\lambda = 527$ nm, repetition rate of $f = 20$ kHz) or a *Pulsar* UV laser ($\lambda = 355$ nm, repetition rate of $f = 10$ Hz) can be applied. In addition, the UV laser provides the opportunity to act as light source for a dye laser (*PulsarePro*), which can be adjusted to nearly any wavelength desired. The second
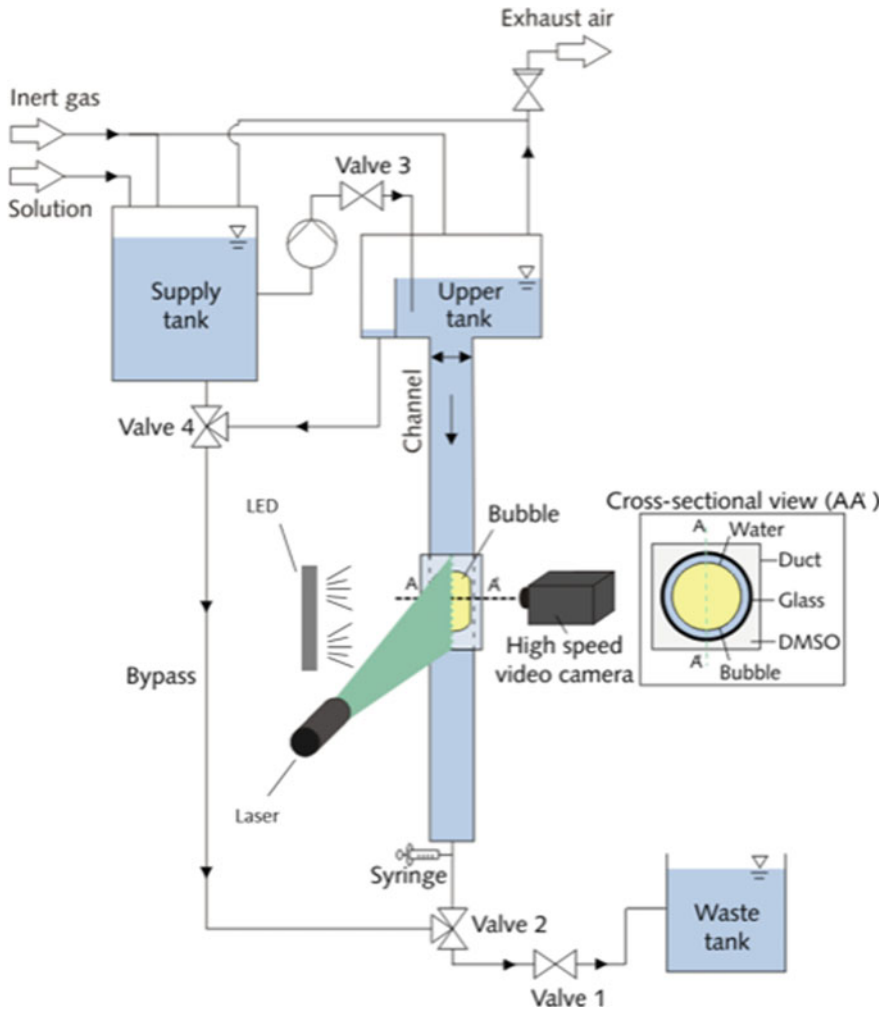
Fig. 6 Experimental setup for Taylor bubble experiments with laser and backlight imaging according to [30]

configuration of the setup uses customized LED backlights as a light source. The wavelengths of the LEDs are chosen to match the absorption peaks of the different products and side products allowing for a broad variability and an easy adjustable system, with low time and cost effort.

3.2 Experimental Results

3.2.1 Fluid Dynamics of Taylor Bubbles in Aqueous Solvents

To compare wake structures occurring in reactive systems with wake structures influenced only by physical mass transfer, a chemical reaction is needed, which allows an easy observation of the wake structures e.g. by color change. Therefore, the oxidation of an aqueous copper(I)ammonia solution is investigated, changing nearly immediately from colorless to deep blue, when reacting with oxygen [34].

In Fig. 7, it is observed, that the wake structures are very similar for the physical dissolution of CO_2 in deionized water measured with p-LIF/PIV and the reactive consumption of oxygen by the oxidation of the copper complex. For an Eötvös number of Eo = 4.9, a laminar flow field becomes visible. With increasing capillary diameters and therefore increasing Eötvös as well as Reynolds numbers, the flow structure becomes more complex. At the intermediate Eötvös number, a toroidal vortex is forming with an increased product concentration in the bubble wake. In the largest capillary the flow structure becomes very turbulent, leading to a broad product distribution in the wake. Furthermore, for all capillary diameters a high correspondence between the p-LIF/PIV flow fields and the flow structures due to the chemical reaction can be detected [30].

The results show that the wake structures and in conclusion the degree of mixing can be adjusted by changing the capillary diameter, described by changing Eötvös and Reynolds numbers. Hence, the setup allows to adjust the mixing timescales, and is, therefore, particularly suitable for further investigations concerning the impact of
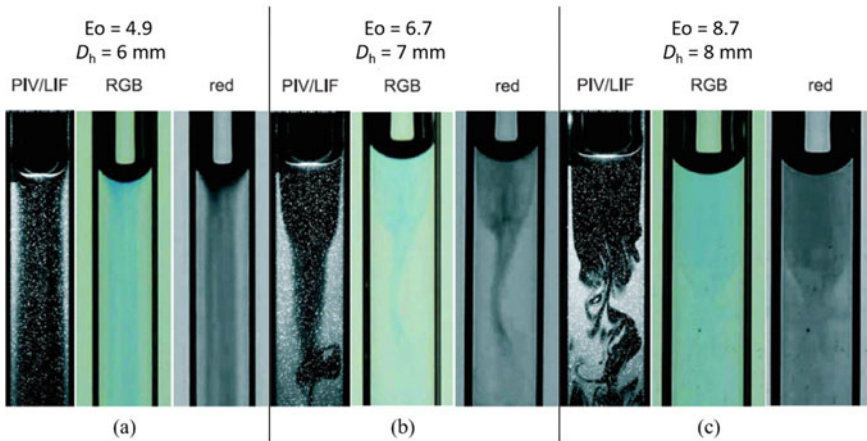
Fig. 7 Comparison of wake structures of rising Taylor bubbles in channels in stagnant water. **a** D_h = 6 mm: laminar wake; **b** D_h = 7 mm: toroidal vortex; **c** D_h = 8 mm: turbulent wake with combined p-LIF/PIV data of Kastens et al. [30]

mixing timescales on yield and selectivity of competitive reactions. A tool for identifying and defining the timescales of mixing is the analysis using Lagrangian Coherent Structures (LCS), explained and discussed in detail in Sect. 3.3. Concluding, the exact conduction of the oxidation of an aqueous copper(I)ammonia solution shows the feasibility of experiments under the exclusion of atmospheric oxygen [30].

3.2.2 Fluid Dynamics of Taylor Bubbles in Organic Solvents

To rule out the influence of surfactants on the mass transfer performance observed in water based systems [35–37], and to be more relevant for industrial applications, organic systems are also considered. In a first step a consecutive Cu–O$_2$ reaction is observed, which has been studied by Schurr et al. in a SFM already [28]. In the first step, the reaction forms an orange bis(μ-oxo) complex when brought into contact with oxygen and is subsequently decomposing to a greenish bis(μ-hydroxo) complex, with the reaction rate of the first step being $k = 10$ s^{-1} and for the second time step $k = 1.5$ s^{-1}. Figure 8 shows the results for three different capillary sizes and the corresponding Eötvös numbers.

At the lowest Eötvös number, a laminar wake is observed and due to the low rising velocity and, therefore, long residence time, the green colorization indicating the second reaction step is clearly visible. With increasing Eötvös numbers, a turbulent wake structure results and the second step is not taking place within the field of view

Fig. 8 Backlight image of the wake structures for the Cu(btmgp)I-oxygen system at a concentration of $c = 10$ mmol L^{-1} in argon saturated acetonitrile at $Eo = 4.4$, 6.8 and 9.8 [23]
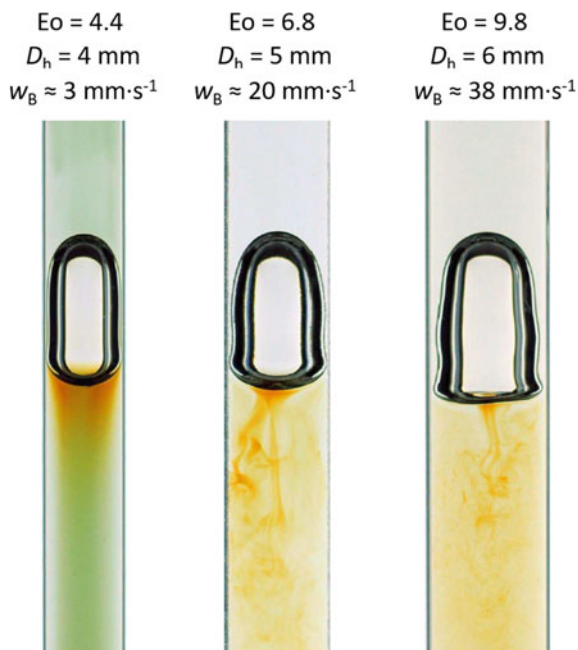
Table 2 Listing of the mass transfer coefficients, Hatta numbers and enhancement factors for the reaction of O_2 with Cu(btmgp)I in a Taylor flow capillary for Eo = 4.4 and Eo = 5.5

	Result	Value	Unit
Eo = 4.4			
Mass transfer coefficient	k_L^0	$1.91 \times 10^{-4} \pm 4.8 \times 10^{-5}$	m s^{-1}
Reactive mass transfer coefficient	k_L^R	$2.67 \times 10^{-4} \pm 7.8 \times 10^{-4}$	m s^{-1}
Hatta number	Ha	$0.86 \pm 2.8 \times 10^{-2}$	–
Theoretical enhancement factor	E	$1.23 \pm 3.49 \times 10^{-2}$	–
Experimental enhancement factor	E*	$1.38 \pm 2.8 \times 10^{-1}$	–
Eo = 5.5			
Mass transfer coefficient	k_L^0	$3.10 \times 10^{-4} \pm 5.4 \times 10^{-5}$	m s^{-1}
Reactive mass transfer coefficient	k_L^R	$5.34 \times 10^{-4} \pm 5.1 \times 10^{-5}$	m s^{-1}
Hatta number	Ha	$0.53 \pm 6.7 \times 10^{-2}$	–
Theoretical enhancement factor	E	$1.09 \pm 3.49 \times 10^{-2}$	–
Experimental enhancement factor	E*	$1.74 \pm 5.1 \times 10^{-1}$	–

Data from [23]

due to an increasing liquid velocity and a decreasing residence time. Though the boundary layer becomes more unstable, resulting in a stronger mixing within the bubble wake, which can influence the yield and selectivity in the case of a parallel-consecutive reaction. Therefore, the mass transfer coefficient and enhancement factor for two Eötvös numbers Eo = 4.4 and 5.5 are investigated, by conducting mass transfer measurements with oxygen bubbles in argon saturated acetonitrile and in a solution containing $c = 10$ mmol L^{-1} of the Cu(btmgp)I complex. The resulting values for both cases are listed in Table 2.

As expected, the reactive mass transfer coefficient is higher than the physical mass transfer coefficient for both cases and the flow regime behind the Taylor bubble seems to influence the mass transfer performance. On the one hand, the differing enhancement of mass transfer by the reaction can be ascribed to inaccuracies in the measurement technique, e.g., through the injection of oxygen. On the other hand, the assumption of reaction kinetics of first order through the excess of oxygen, as needed for the reaction, is most likely incorrect [23].

3.2.3 Visualization of Competitive Consecutive Reactions

To determine the influence of the fluid dynamic conditions on yield and selectivity, a competitive consecutive reaction is used, where the reaction progress is ideally traceable via UV–VIS or fluorescence. For the first successful studies, a Fe–NO system dissolved in methanol is applied, providing characteristic UV–VIS peaks for the desired products MNIC (mononitrosyliron-compounds) and DNIC (dinitrosyliron-compounds). The reactive system developed by the group of Prof.

Table 3 Experimentally determined extinction coefficients for the products MNIC and DNIC

ε	MNIC	DNIC
$\lambda_1 = 470$ nm	0.4048	0.895
$\lambda_2 = 700$ nm	0.051	0.195

Klüfers is explained in more detail in Chapter "In Situ Characterizable High-Spin Nitrosyl–Iron Complexes with Controllable Reactivity in Multi-phase Reaction Media".

As mentioned in the experimental setup Sect. 3.1, LEDs covering the characteristic peaks are used for backlight imaging. In the observed case, those characteristic wavelengths are $\lambda_1 = 470$ nm and $\lambda_2 = 700$ nm. To convert the obtained grayscale images into concentration fields, the working principle of an UV–VIS spectrometer is used, which is utilizing Beer-Lamberts law

$$E_\lambda = log\left(\frac{I_0}{I}\right) = \varepsilon_\lambda dc. \tag{8}$$

E_λ represents the extinction, I_0 corresponds to the incident light intensity, I to the light intensity behind the sample, ε is the extinction coefficient, d is the layer thickness of the liquid and c is the concentration. Since the products MNIC and DNIC have a certain absorption at both wavelengths, it is assumed that the total measured absorbance is a composition of the signals of both products. Therefore, two equations

$$E_{470} = log\left(\frac{I_{0,470}}{I_{470}}\right) = d\left(c_{MNIC}\varepsilon_{MNIC,470} + c_{DNIC}\varepsilon_{DNIC,470}\right) \tag{9}$$

$$E_{700} = log\left(\frac{I_{0,700}}{I_{700}}\right) = d\left(c_{MNIC}\varepsilon_{MNIC,700} + c_{DNIC}\varepsilon_{DNIC,700}\right) \tag{10}$$

describing the light absorption at the two wavelength are resulting [38]. The extinction coefficients of the two products required for evaluation are given in Table 3. The values are determined experimentally directly within the setup for the used wavelengths of $\lambda_1 = 470$ nm and $\lambda_2 = 700$ nm by measuring a concentration series of both products.

The layer thickness is assumed to be constant and is set equal to the respective capillary diameter of $D_h = 4$ and 5 mm. The initial light intensity I_0 is determined for both wavelengths. For this purpose, the capillary filled with the reaction solution is recorded without a bubble and an average value is determined from 10 grayscale images. With all the necessary information and values, Eqs. (9) and (10) are solved yielding the concentrations of the two products. The equations are then solved individually for each pixel within the region of interest. The resulting concentration fields are shown in Fig. 9, displaying the formation of the two products MNIC and DNIC in the wake of the bubble. Though the applied methodology is capable to yield conclusions about the local yield and selectivity of the investigated model reaction.

Fig. 9 Concentration gradients of the product MNIC and DNIC in the wake of a nitrogen monoxide bubble within the $D_h = 4$ mm capillary (**a**) and $D_h = 5$ mm capillary (**b**) [38]
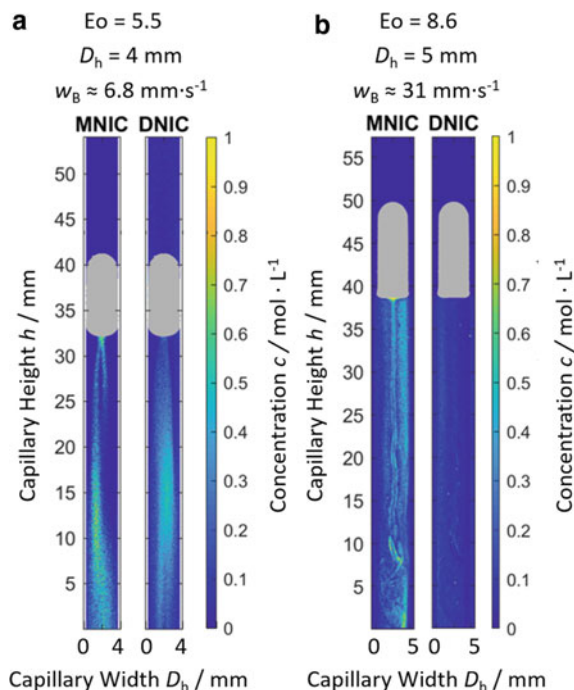
The concentration fields shown in Fig. 9 indicate similar flow structures than the previous data in Fig. 8. With increasing capillary diameter, the flow structure behind the bubble becomes more complex and turbulent as within the Cu(btmgp)I-oxygen system. As both systems are dissolved within an organic solvent, the similarity is, therefore, not unexpected. Likewise, Fig. 9 shows clearly that the first product MNIC, following a rather fast kinetic of $k_{obs(MNIC)} = 5.0 \times 10^5$ s^{-1} ($T = 20$ °C), is formed directly in the bubble vicinity in both capillaries. In the further course of the flow, the second product DNIC is formed in the $D_h = 4$ mm capillary (a). This means that there is still unreacted, dissolved nitrogen monoxide available in the flow, enabling the formation of the second reaction product DNIC, following a slower kinetic of $k_{obs(DNIC)} = 6.5 \times 10^{-4}$ s^{-1} ($T = 20$ °C). However, this second reaction step is not taking place within the $D_h = 5$ mm capillary. The nitrogen monoxide dissolved by the convective flow is strongly mixed immediately behind the bubble and reacts with the subsequent iron chloride almost completely. Though, only the first product MNIC is formed and within the further course of the flow there is thus no free nitrogen monoxide available, meaning that the second reaction step is almost absent. From this it can be concluded that the selectivity of this model reaction depends strongly on the mixing and its time scale in the bubble wake. If the mixing is faster than the time that is necessary for the second reaction step, as is the case with the $D_h = 5$ mm capillary, no further reaction can take place. Though, the nitrogen monoxide is mixed so quickly that it reacts almost exclusively with the fresh reaction solution. However,

if the mixing time is longer than the reaction time necessary for the second reaction, the second reaction step may occur as it happens within the smaller capillary [38].

3.3 Analyzing Wake Structures at Taylor Bubbles Using Lagrangian Coherent Structures

The progress of chemical reactions is determined by the interplay of the timescales of mixing t_{mix} and the timescales of the chemical reaction t_{reac}. This has long been known and can be decribed by the Damköhler number for reactions formed by the ratio of both

$$Da = \frac{t_{mix}}{t_{reac}}. \tag{11}$$

If mixing is slow and this number is very large, the reactant can be treated as a passive tracer that is already reacted when advected. If the number is very small, then a perfect mixture of the liquid can be assumed and the whole liquid reacts at once. A more complex picture is drawn whenever the mixing timescales are of the same order as those for the reaction and $Da = 1$. Then the interaction of both dynamical systems is less predictable and a detailed understanding of the local mixing and its timescales is relevant. In this section, the transport within the wake of Taylor bubbles is analysed for three different channel sizes as presented in Fig. 10. To this end, PIV data of fluorescent particles are analyzed to obtain spatiotemporally resolved velocity fields in which the pathlines of passive tracers are integrated. From this pathlines the detailed mixing structures of the bubble wake can be obtained. For the illumination of the PIV particles (Polystyrol $d_P = 3.16$ μm, *Microparticles GmbH*), a green laser light sheet (Nd-YLF laser, $\lambda = 527$ nm, *Darwin Duo 527–100 M, Quantronix/Continuum*) is introduced perpendicular to the field of view of a high speed camera (*pco.dimax HS2, PCO AG*). The images are recorded with a frame rate of $f = 600$ fps, while the field of view was $A = 11.49 \times 30$ mm^2 resulting in a resolution of 35 μm pix^{-1}. The velocity fields are evaluated using the software PIVview 2C 3.63 (*PIVTec GmbH, multipass*). The exact details of the PIV settings are reported in [31, 32].

To analyze the local mixing, we rely on recent developments in Lagrangian transport analysis stemming from dynamical systems theory. The so-called Lagrangian coherent structures (LCS) methods extend the concept of fixed points and stable/unstable manifolds in time independent velocity fields to unsteady flows. Here the finite time Lyapunov exponent (FTLE) and the hyperbolic LCS are determined. The FTLE fields provide information about the Lagrangian stretching/contraction rates at every point of the flow Λ for a finite time interval $t \pm \tau$ and are defined as

$$\Lambda_{\pm}(x_0, t, \tau) = \frac{1}{\tau} ln \left(\sqrt{\lambda_{max}(x_0, t, t \pm \tau)} \right) \tag{12}$$
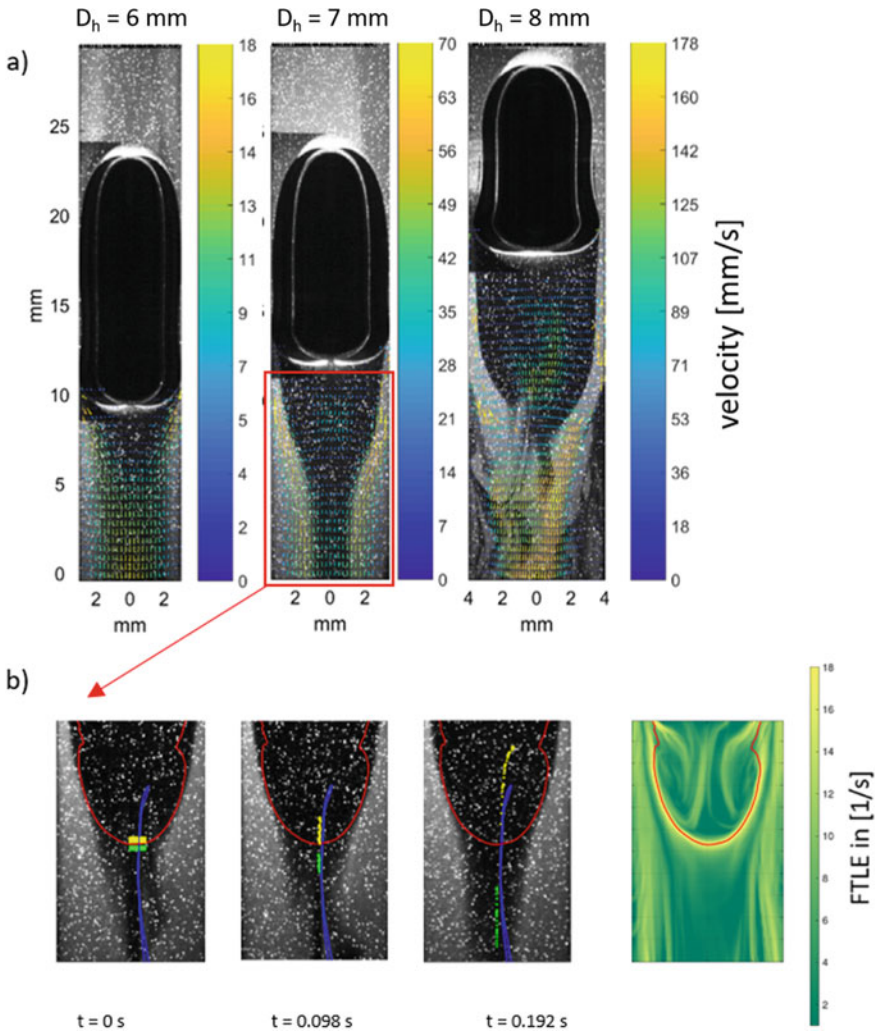
Fig. 10 a Instantaneous velocity fields from PIV/LIF experiments behind a Taylor bubble for different capillary sizes. **b** Lagrangian coherent structure (LCS, red line) in the wake of a Taylor bubble ($D_h = 7$ mm) separates the tracers that become entrapped behind the bubble (yellow) from those that are flushed away (green) [31]

where λ_{max} is the largest Eigenvalue from the Cauchy-Green strain tensor $C_t^{t+\tau}(x_0)$ that maps the square of an initial small perturbation to a trajectory at time t to its final value at a time $t + \tau$ as introduced in [39]. The stretching rate and the forward FTLE values are high where particles separate strongly in the future, while the contraction rate and the backward FTLE values are high, where particles previously far apart have come together. The most repelling and attracting material lines in the flow can be more rigorously determined using the hyperbolic LCS theory, where additionally to the

stretching and contraction rates also the stretching/contraction directions are taken into account to determine the most repelling/attracting lines in the tracer fields [40, 41]. The hyperbolic LCS are determined using the freely available *matlab* toolbox *LCS-tool* [41]. Figure 10a shows the instantaneous velocity fields from which the pathline integration for the LCS detection was performed.

For the intermediate capillary size $D_h = 7$ mm and, thus, intermediate rise velocity, a coherent LCS structure is found for an integration time of $\tau = 0.2$ s (out of ~2 s of experiment until the bubble changed its behavior). The red LCS depicted in Fig. 10b separates the vortical structure in the direct bubble wake from the fluid that passes the vortices by with a velocity faster than the mean superficial velocity ahead of the bubble. The red repelling LCS coincides with the horseshoe like structure in the FTLE fields where FTLE values are high. The colored points in Fig. 10 depict the numerically advected tracers in the flow field at different time instants to show
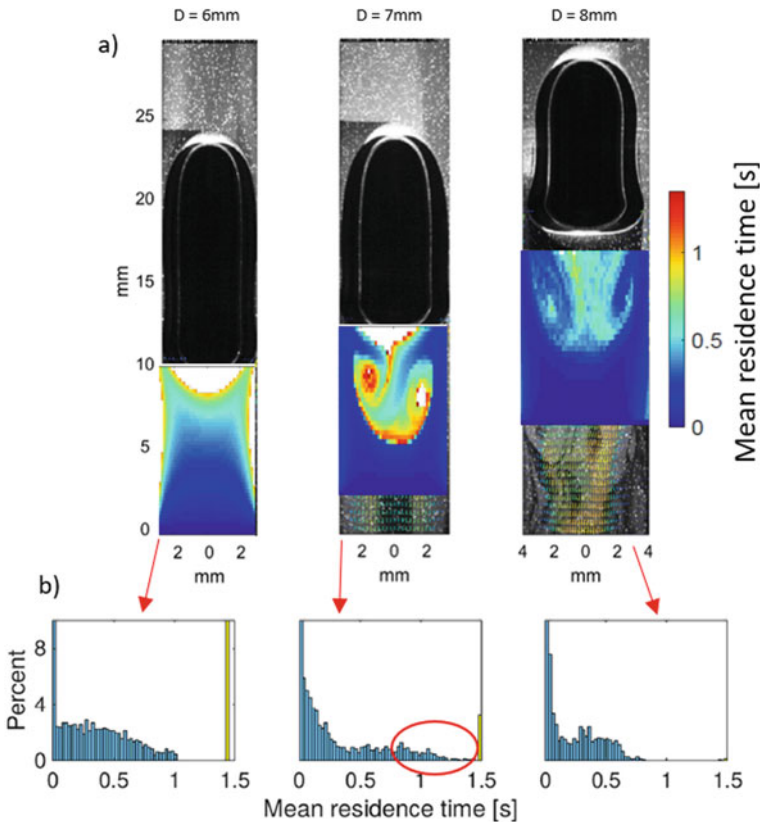
Fig. 11 a Mean local residence time distribution in the wake of Taylor bubbles. White areas indicate regions where no tracer has left the field of view and no residence time can be determined. **b** Histogram over all tracers. A tail is observed for the $D_h = 6$ mm capillary (red ellipse) indicating regions with long residence times [34]

that the LCS is truly repelling. The yellow tracers get entrapped into the vortices while the green tracers are rapidly flushed away. In this way tracers on the bubble side of the red line are trapped behind the bubble. To further study the indication of this coherent structure, the residence times of the tracers in the field of view are calculated for all three bubbles (Fig. 11). A clear peak of long residing tracers is found for the intermediate capillary size ($D_h = 7$ mm). The region coincides with the detected LCS and, thus, confirms its importance as a transport barrier. The gradients of the residence time distributions are much sharper for the intermediate case then for the other two cases, where more smooth distributions are observed. A histogram of the same data in time (Fig. 11b) reveals an unexpected phenomenon occurring due to the red LCS: The residence time distribution has a tail towards longer times in the intermediate capillary experiment. This seems counterintuitive at first, since the mean liquid velocity increases by a factor of $f \sim 3.6$ from the $D_h = 6$ mm to the $D_h = 7$ mm capillary and therefore the residence time should decrease. This finding shows the importance of obeying and controlling possible coherent structures in chemical reactors because they can drastically change expected residence times due to backmixing.

A possible competitive-consecutive reaction in this flow might exhibit increased side product formation and a break down in selectivity because the first (desired) product recirculates close to the bubble where gas is largely available to form the second (undesired) product. For the largest capillary diameter ($D_h = 8$ mm) the rapid flow around the bubble increases mixing and disturbs the vortices coherency. Therefore, less backmixing result that brings liquid into contact with the gaseous phase again and a higher selectivity of a competitive consecutive reaction might occured, if the timescales of the reactions are in the right order of magnitude.

3.4 Mass Balance for Wake Structures in Taylor Flows

The Taylor bubble experiment facilitates the simultaneous observation of the bubble and its wake due to the confined bubble motion in the focal plane of the camera. This effect and the high rotational symmetry enables to compare the volume of gas transferred from the bubble to the liquid by two complementary measurement techniques, namely measurements of the dissolved gas concentration by LIF and the measurements of bubble volume reduction by bubble boundary detection. For this study carbon dioxide gas in deionized water is used. To visualize the dissolved CO_2 by means of LIF a pH sensitive dye (*Acid Yellow 73, F6377 Sigma Aldrich/Merck*) in preparation of a $c = 10$ mmol L^{-1} solution is applied and the liquid temperature is kept constant at $T_L = 298 \pm 1.0$ K. The reduced brightness of the dye due to dissolved carbon dioxide was calibrated after intense purging with carbon dioxide and subsequent degassing. The carbon dioxide concentration within the solution is monitored using a pCO$_2$ mini device with sensor spots (*PreSens GmbH*). A double exponential function

$$c_{CO_2}(int) = a \exp(b \, int) + c \exp(d \, int) \tag{13}$$

is fitted to about 20 calibration pair points (CO_2 vs. grey scale) for every pixel in order to take the different local light settings and sensitivities of the pixels on the camera chip into account. The resulting two-dimensional calibration matrices A, B, C and D where stored and recalled for determination of the actual CO_2 values during measurements in the wake of the Taylor bubble. Especially for fast rising bubbles in a $D_h = 7$ mm capillary, as shown in Fig. 12, where counter diffusion can be neglected, the mass balance in between the two methods coincides well and is exact within 5%. The reduction of the bubble volume is measured by manually detecting the bubble boundary at two different timestamps (t_1, t_2) and calculating the absolute difference in mol assuming rotational symmetry [30] which turned out to be, $\Delta M_{1,2} = 2.73 \times 10^{-6}$ mol. This reduction is compared to the total wake concentration from LIF assuming again rotational symmetry and using angular integration of the concentration of half of the wake as described in [42] where the final absolute mol value was determined to be $M_C = 2.84 \times 10^{-6}$ mol. Therefore, the ratio of both
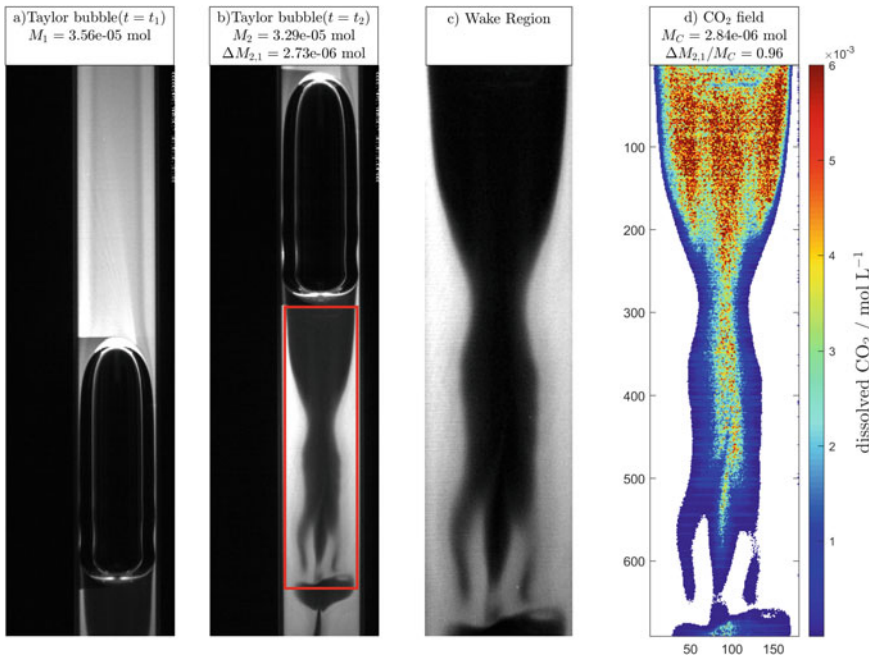
Fig. 12 LIF images of a Taylor bubble wake structure for $D_h = 7$ mm. Dark areas below the bubble indicate high concentrations of dissolved CO_2 due to a pH sensitive dye. **a** Initial bubble position at t_1, **b** final bubble position at t_2, **c** wake carrying liquid passed during the time interval $t_2 - t_1$, **d** mass balances from bubble volume reduction and from the integration of the concentration wake matching up to 5% deviation [42]

measurements is $\frac{\Delta M_{1,2}}{M_C} = 0.96$. This extraordinary agreement shows the potential of Taylor bubble wake concentration measurements of dissolved gas using planar LIF.

4 Local Mass Transfer Measurements at Ascending Bubbles

For free ascending bubbles the situation gets even more complicate compared to the confined steady flow around a Taylor bubble that enables reproducible experiments and detailed investigations. Small spherical bubbles are following a straight vertical rising path and the mass transfer at their interface is following more or less the film theory [1, 6, 43, 44]. Because of its rotational symmetry, only a single plane of the flow and concentration field can be investigated to get an entire view of the mass transfer situation. Such kind of experiments on local mass transfer phenomena at rising bubbles have already often been performed by using p-LIF [43, 45–47]. If the bubbles get larger and non-spherical, a more complex three dimensional rising path as well as flow and concentration field have to be expected. In this case, a reproducible rising pass can be achieved by the use of a hypodermic needle as sparger [23] and a time series of planar LIF images can be reconstructed to a pseudo-threedimensional image of the flow and concentration field. In case of larger wobbling bubbles with dynamic shape oscillations and therefore complex boundary layer geometries and unsteady three dimensional concentration fluctuations, the more sophisticated Time Resolved Scanning Laser Induced Fluorescence (TRS-LIF) is necessary [29, 48–53] to image all information's about the flow and concentration field instantaneously.

4.1 Experimental Setup and Methods

The basic flow scheme used for the p-LIF and TRS-LIF measurements is shown in Fig. 13. The main part is the measurement cell with a cross section of $A = 15 \times 15\,\text{cm}^2$, made of stainless steel and glass, allowing an optical access from all directions. For the accurate investigation of the local mass transfer at rising or interacting bubbles, the generation of bubbles with reproducible shapes and trajectories is necessary. This can be achieved by using a hypodermic needle as an orifice for the bubble formation. The certain shape of the needle forces a deformation of the bubble interface at the exact same position. This yields a highly reproducible bubble shape and rising trajectory [54]. The bubble size mainly depends on the orifice and the adjusted flow rate, which needs to be adjusted very accurately. Within all experiments the flow rate is controlled by an injection valve and a function generator [55]. The pre-pressure is controlled by a precision pressure regulator. The hypodermic needle is placed rotatable within the center axis at the bottom allowing the adjustment of the trajectory e.g. for a well-defined trajectory and point of impact with a second bubble. The lid contains a
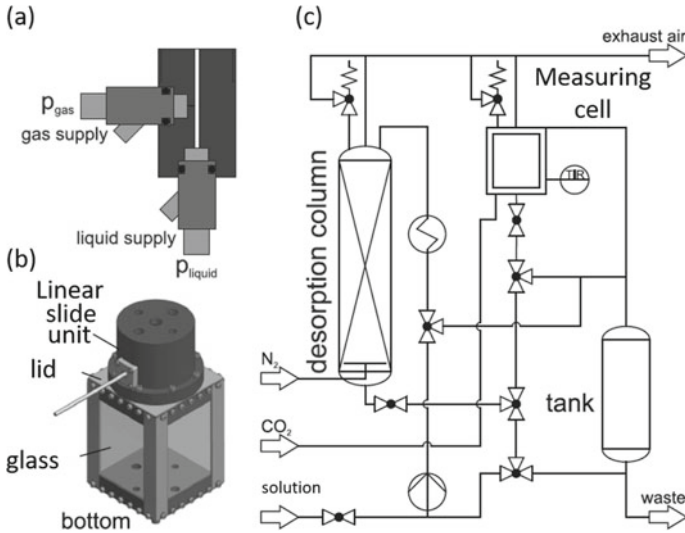
Fig. 13 Basic setup for mass transfer investigations with **a** injection valves, **b** flow scheme and **c** measuring cell [23, 56]

linear slide unit, enabling the positioning of a second bubble, if needed by attaching a capillary. The measurement cell is connected to a desorption column supplying the cell with oxygen free solution, if desired. The oxygen concentration and temperature within the measurement cell and desorption column is constantly monitored with a sensor probe (*PreSens*) to ensure an oxygen free solution and a constant temperature.

4.1.1 Experiments on Rectilinear Rising Bubbles by Means of p-LIF

For the investigation of the interplay between mass transfer and chemical reaction at rectilinear rising bubbles and the determination of the influence of interface deformation by bubble bouncing, the p-LIF measuring technique is used (Fig. 14). For the p-LIF measurements, oxygen bubbles with a diameter range of $d_B = 0.5 - 0.9$ mm are generated according to Kück et al. [57]. To visualize the local mass transfer, $\rho = 30$ mg L^{-1} of the oxygen sensitive dye Dichlorotris(1,10-phenanthroline)ruthenium(II)hydrate is added to the deionized water. The fluorescence of the dye is quenched in dependency to the oxygen concentration. This allows the correlation of the grey values to the oxygen concentration using the Stern–Volmer correlation. For the investigation of reactive mass transfer, additionally sodium sulfite and $\rho = 16$ mg L^{-1} of the catalyst cobalt sulfate is dissolved in deionized water.

The fluorophore is excited by a pulsed Nd:YLF laser with a wavelength of 527 nm (*Continuum*®), pulse width $t < 210$ ns and at a repetition rate of $f = 1$ kHz. The laser beam is widened by a light sheet optic. The emitted light is recorded with a *PCO Dimax HS2* camera at a frame rate of $f = 1000$ fps, positioned perpendicular to the
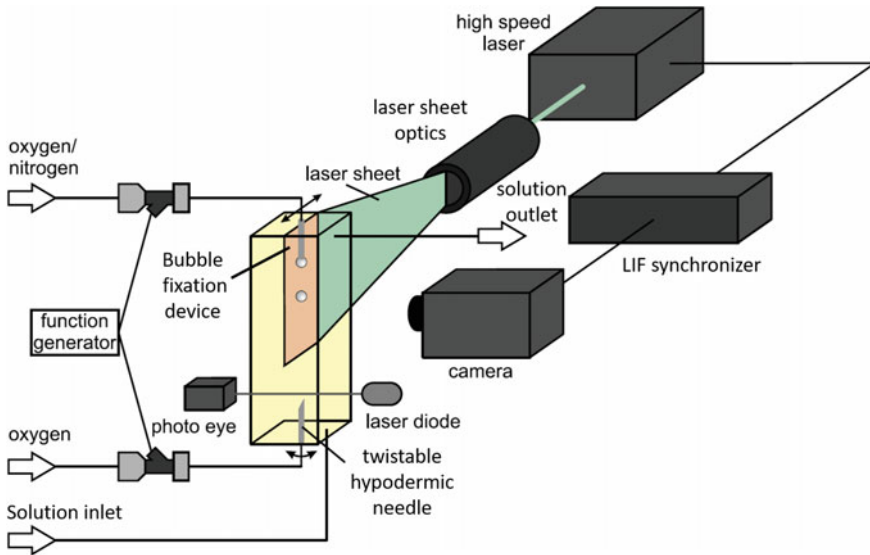
Fig. 14 Scheme of the experimental setup for the rectilinear bubble rise and the bubble bouncing using p-LIF [56]

light sheet. The camera chip is protected by a bandpass filter with a center wave length of $\lambda = 590 \pm 2$ nm. To visualize the physical and reactive mass transfer it is necessary to provide an oxygen free environment and solution. Therefore, the entire setup and reaction solution is purged with nitrogen for $t = 30$ min and the oxygen concentration is monitored [23, 56, 58].

For the quantitative analysis of the recordings, a post processing of the images is required, due to the non-uniform illumination. To obtain reliable concentration information, a background correction based on the work of Dani is performed [59]. By recording a short sequence of images from the oxygen desorbed solution an averaged background image is computed. The recorded raw image of a bubble is shown in Fig. 15a. The raw image divided by the background image results in the corrected images (Fig. 15b). Since high speed recordings are performed, the background noise is reduced by averaging of the recorded sequences as shown in Fig. 15c. Therefore, the already corrected images were processed using MATLAB® with an automatic edge detection and the bubble center was specified. The bubble center is then used to adjust the region of interest (ROI), so that the bubble center is always placed at the same position. The resulting ROI images are again averaged to obtain one image with a low noise information. Nevertheless, sub-pixel shifts of the bubble center are not compensated, yielding a light blur [23, 58].

To gain a more profound understanding of the influence of bubble–bubble inter-actions like bubble bouncing on the local mass transfer the setup displayed in Fig. 14 is used. The camera and laser settings are the same than for the investigations of the rectilinear bubble rise. Therefore, a N_2 bubble is fixed at the upper capillary and
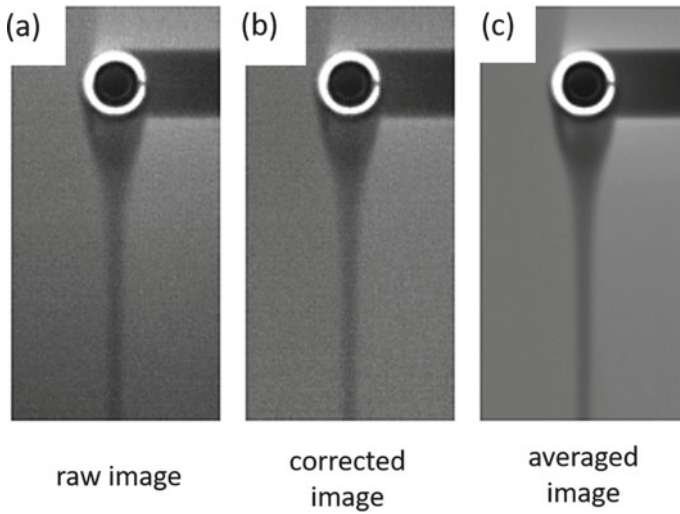
Fig. 15 Processing sequence of the raw images (**a**) resulting in the corrected image (**b**) and the averaged image (**c**) according to Timmermann [23, 58]

the oxygen concentration profile of the rising and impacting O_2 bubble is visualized using LIF. Like the hypodermic needle at the bottom, the capillary is connected with an injection valve to ensure reproducible bubbles. The upper N_2 bubble is generated $t = 100$ ms ahead of the rising O_2 bubble to allow an unimpeded generation. The camera recordings are controlled by a light barrier to allow an ideal use of the camera data storage. To enable the investigation of reactive mass transfer while bubble bouncing, the same oxygen free environment as already described is established. As the timescales of the oxidation of sodium sulfite can be adjusted fairly easy over a broad range, this reaction is again used as a model system [23, 56].

4.1.2 Experiments on Wobbling Bubbles by Means of TRS-LIF

To overcome the limitations of the planar LIF that restricts the investigations to linearly rising and fixed bubbles, a new setup was developed using a very fast scanning approach inspired by scanning particle image velocimetry firstly introduced by Brücker [48] and custom designed by the *ILA5150 GmbH*. The Time Resolved Scanning Laser Induced Fluorescence (TRS-LIF) is shown in Fig. 16.

The planar LIF setup with a cylindrical focus lens right behind the light sheet optics (2) that widens the beam from the laser (1) was modified adding a rotating mirror (3). The synchronization of the polygon rotation and the laser pulse emission can be adjusted to vary the number of light sheets, the volume scan rate and the light sheet distances. The rotational speed of the polygon is limited to 10,000 rpm $\approx$ 166.667 Hz while the maximum pulse rate of the laser is $f = 20,000$ Hz. Here, the polygon
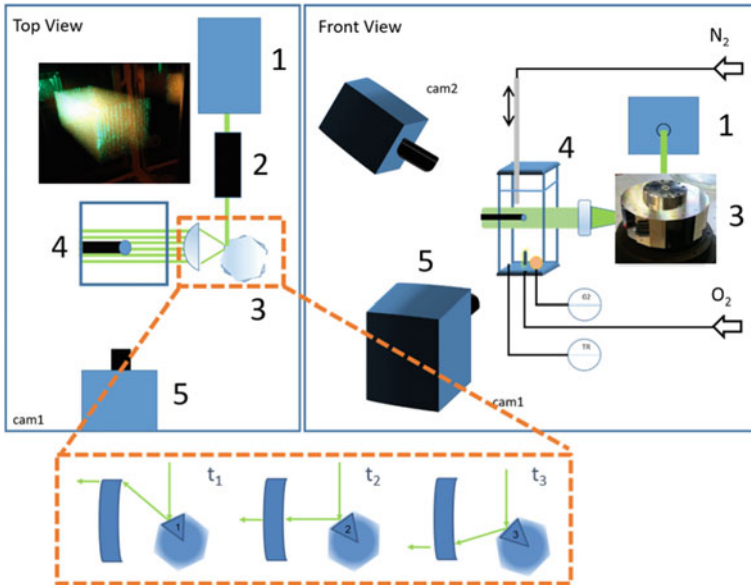
Fig. 16 Sketch of the experimental setup of TRS-LIF. A rotating mirror is introduced which spins with a tuned frequency such that successive laser pulses hit neighboring facets of the mirror under slightly different angles to produce a series of close-by light sheets (as shown exemplarily for a large inter-light-sheet distance at the top left corner)

rotation was set to its maximum. An additional laser and a photodiode which detect the actual rotation speed of the polygon mirror act as the master trigger for the high-speed laser and the cameras, assuring, that after each volume scan all signals are synchronized. The single light sheets were adjusted to an approximate minimal thickness of 0.5 mm. Using a number of $N = 40$ light sheets and a laser pulse rate of $f = 6400$ Hz the light sheets lay arbitrarily close together as was monitored by a second high-speed camera of the same type (*pco.dimax HS2 using a 50 mm Zeiss Makro-Planar objective*). Both cameras were triggered with the same signal as the laser and image recording was, thus, synchronized to maximal laser light intensity. Again, the same ruthenium solution as an oxygen sensitive dye was used as in the planar LIF case and the emitted fluorescent light was recorded using the same bandwidth filter. However, the calibration procedure deviates largely from the one used in planar fluorescence and is, therefore, explained in some detail here. The procedure is as follows: after the recording of a rising bubble the setup is flushed alternately with oxygen and nitrogen to obtain a well-controlled state with a stable oxygen level. Seven different oxygen levels were recorded in between $c = 0$ and 23 ppm. As described above, the oxygen level is constantly monitored using an oxygen sensor spot (*PreSens GmbH*). Only after reaching a constant level of oxygen and by assuring visually that no concentration gradients are left in the solution the calibration measurements are recorded. By performing six volume scans at each

concentration level, six distinct calibration images for every single light sheet are obtained at each concentration. These six images for each light sheet are averaged and stored in a multidimensional matrix $M(l, k, m, n)$ with indices (m, n) being the image pixels spanning the recorded field of view while k denotes the number of concentration levels and l the number of light sheets. From this matrix an exponential fit according to Eq. (14) is performed for each pixel in the light sheet.

$$c = a \exp(b \, int) \tag{14}$$

This accounts for different sensitivities of the camera pixels and locally varying light sheet intensities. Here, c is the measured concentration from the sensor spot reading and int is the greyscale intensity from the pixel recording of the camera. This yielded two different calibration matrices $A(l, m, n)$ and $B(l, m, n)$ from which the oxygen concentrations in mg L^{-1} in the wake of the rising bubbles were calculated.

Furthermore, due to defects in the rotating mirror and thickness variations in the container glass the TRS-LIF images are additionally altered by a horizontally
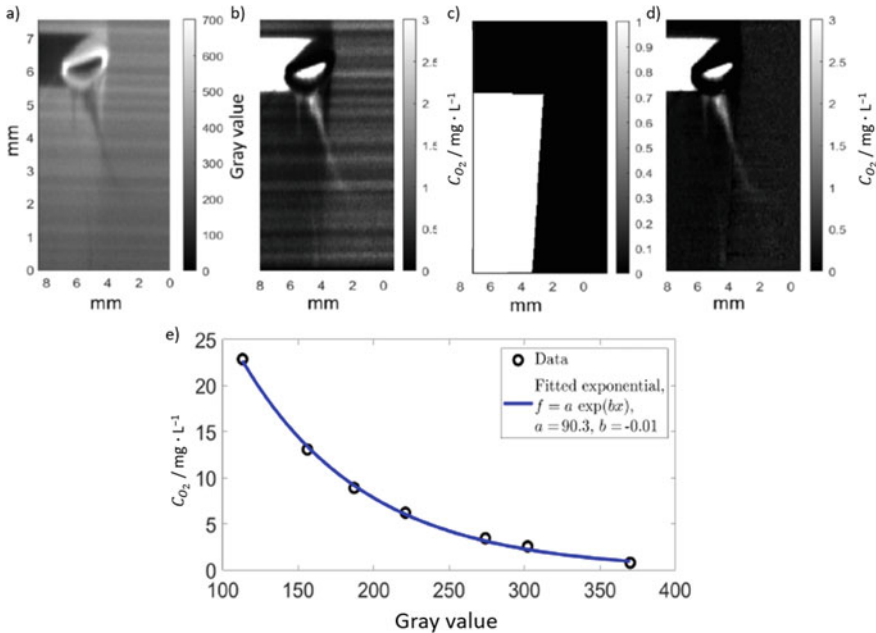
Fig. 17 **a** The raw image of a laser light sheet hitting the rising oxygen bubble just shortly behind the second inflection point [53]. **b** Using a pixel- and sheetwise calibration procedure the oxygen concentration of the bubble wake can be calculated. **c** A manually chosen mask indicates where the bubble reflection alters the recorded concentrations. The left profile of the stripy pattern is subtracted from the images where the mask equals one while, where the mask is zero, the profile is subtracted from the other border (here right side). **d** The finally recovered wake concentration of one single TRS-slice. **e** Exemplary experimental fit for one pixel to derive the calibration parameters a and b

orientated stripy pattern. Most likely, this pattern occurs because of attenuated laser intensity due to defects in the rotating mirror. Since the mirror speed is fluctuating slightly the laser does not visit the very same spot periodically and the resulting stripy pattern does never repeat exactly. These stripes bias the concentration values and are hindering to the reconstruction of the bubble wake. Therefore, to reduce the effects of the stripes the knowledge about the boundary conditions of the experiments are considered. Right after stripping, there is still zero oxygen level on both sides of the bubble trajectory therefore a vertical reference profile is taken from the left or right edge of the recorded image and subtracted everywhere in the picture. However, the stripes are not entirely perpendicular to the image boundaries as the camera is slightly tilted. To subtract the reference profile from the obtained image, the image needs to be slightly rotated, ensuring the occurring stripes are perpendicular to the boundaries at any time. This procedure works well as long as the light sheet does not hit the bubble. In this case, the bubble reflects the laser light randomly. In these cases (around 5–7 images in one volume scan) a customized algorithm allows for a manual definition of the brighter region in the raw images from which then the reference profile from the image edge within this region is subtracted (the whole procedure is depicted in Fig. 17).

4.2 Experimental Results

4.2.1 Reactive Mass Transfer at Rectilinear Rising Bubbles

A typical result for an oxygen bubble rising rectilinear in water with mass transfer and rising in a sodium sulfite solution with reactive mass transfer is shown in Fig. 18. The three left images of Fig. 18 show the physical mass transfer and the three right images the reactive mass transfer. In Fig. 18a it can be observed, that the wake of the oxygen concentration directly behind the bubble is broader and starts to elongate shortly after, leaving a linear concentration wake behind the bubble. This behavior has been already described in literature [60] and is confirmed for Reynolds numbers between Re = 39 and 82.

The oxygen concentration field is visualized for different sodium sulfite concentrations at bubbles of a similar size and rising velocity. However, it needs to be noted, that in accordance to literature [1, 61] the rise velocity is influenced by the dye, contaminating the system. Thus, the rising velocity is higher than in a fully contaminated system, but lower than in a slightly contaminated one. Therefore the mass transport is realistically similar to that of a rigid sphere and the contamination caused by the dye needs to be considered in numerical approaches [23].

To determine the mass transfer coefficient, the qualitative data needs to be evaluated and converted into a molar flow rate $\dot{M}$. The analysis is based on the work of Kück et al. [18, 45, 57] and Jimenez et al. [46].

The evaluation of the transferred mass is performed only for the physical mass transfer, since the amount of oxygen consumed by the reaction cannot be determined. The mass flow rate of oxygen
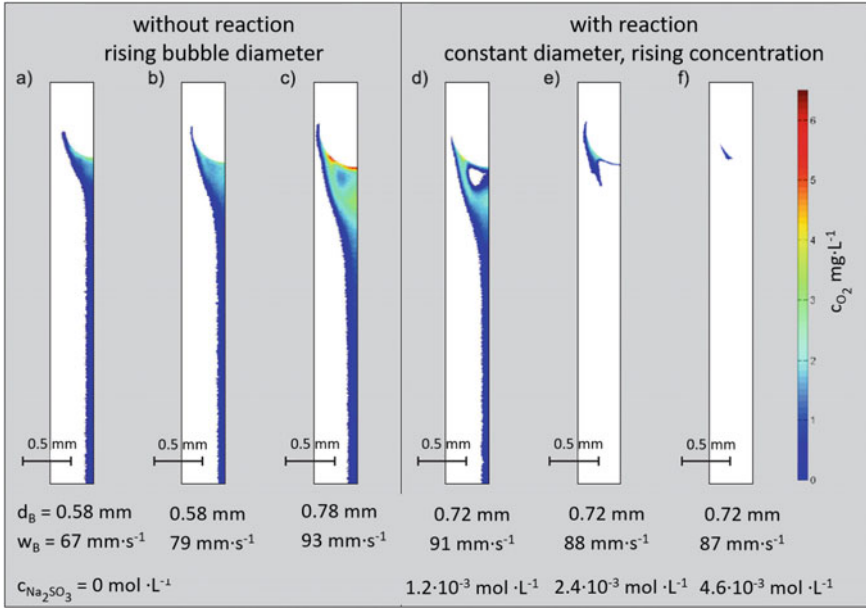
Fig. 18 Influence of bubble size and sulfite concentration on the oxygen concentration as pseudo color image [23, 58]

$$\dot{M} = \dot{V} \cdot c_{O_2} \tag{15}$$

is defined as the product of the volume flow rate $\dot{V}$ and the concentration of oxygen c_{O_2}. While the oxygen concentrations result from the LIF measurements [18], the volume flow rate is approximated by assuming that the liquid velocity w_L within the wake equals the rise velocity of the bubble v_B [45]. By solving the surface integral in cylindrical coordinates and balancing the concentration with the considered plane, the transferred mass is determined. Additionally, due to the rectilinear bubble rise it can be assumed that $c_{O_2}(\varphi)$ is constant [18]. Considering all simplifications and assumptions, the mass flow rate is calculated by

$$\dot{M} = 2\pi v_B \int_r^R c_{O_2}(r)r\,dr \tag{16}$$

enabling the calculation of the mass transfer coefficient k_L by

$$k_L = \frac{\dot{M}}{\pi d_B^2 \cdot \left(c_{O_2}^* - c_{O_2,bulk}\right)} \tag{17}$$
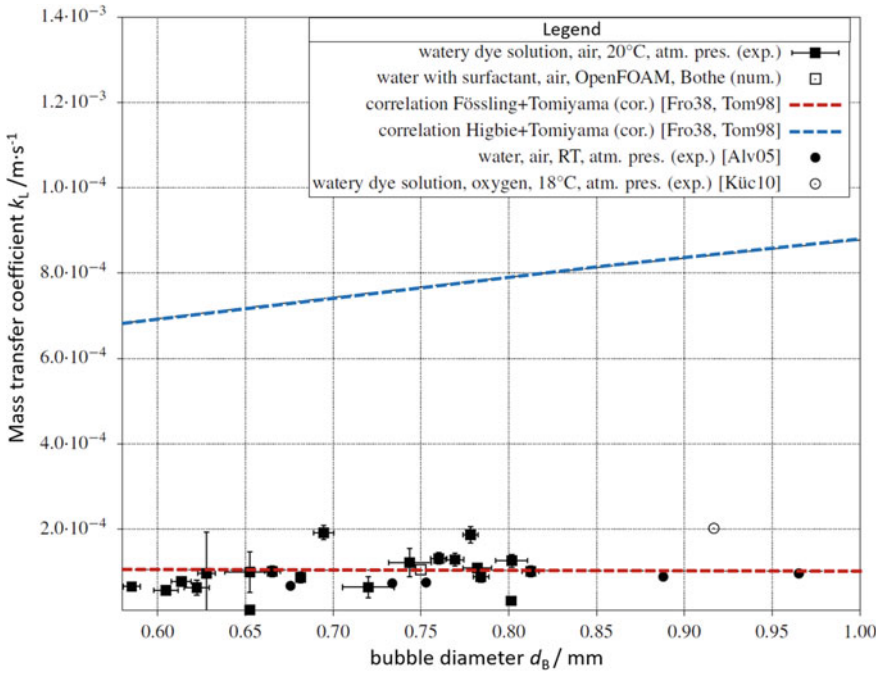
Fig. 19 Comparison of the experimental and numerical determined mass transfer coefficients with correlations from literature [23]

with the saturation concentration $c_{O_2}^*$ at the interface and the bulk concentration $c_{0_2,bulk}$. The mass transfer coefficients calculated through integration of the oxygen concentrations in the lateral planes in dependency of the distance to the bubble is displayed in Fig. 19. The calculated mass transfer coefficients agree well with the correlation of Frössling [62] for rigid particles in combination with the rise velocity according to Tomiyama [61] for contaminated systems, proving the surfactant behavior of the dye. In addition, there is an excellent agreement of the experimental results, the numerical approaches of the group of Prof. Bothe, TU Darmstadt and the correlation of Frössling [57, 62].

The determination of mass transfer coefficients by means of high-speed p-LIF yields excellent results in case of rectilinear rising bubbles. Based on the averaging procedure of several ROI images, the signal-to-noise ratio is significantly improved, allowing a more accurate determination of mass transfer compared to [18, 46, 57]. Additionally the p-LIF technique allows a precise determination of bubble diameters and velocity [23].

4.2.2   Reactive Mass Transfer at Bouncing Bubbles

To understand the mass transfer enhancement caused by bouncing and chemical reactions in bubbly flows, the local mass transfer and oxygen concentration distribution is visualized by means of p-LIF as described in Sect. 4.1.1. Figure 20 shows the oxygen concentration field in the wake of a helical rising ellipsoidal bubble, with an equivalent diameter of $d_{eq,V} \approx 2.0$ mm and a rising velocity of $v_B \approx 320$ mm s^{-1} for physical and reactive mass transfer. As the fluorescence signal becomes weaker with increasing oxygen concentrations, the darker regions are indicating directly the presence of oxygen. The first image (a) shows a saturated concentration wake behind the bubble. In the second and third image a medium reaction rate is superimposed by adding sodium sulfite and the oxygen concentration is getting consumed by the reaction. Therefore, only within the regions of a rapid mass transfer oxygen remains detectable in the bulk. However, the concentration field looks very similar in both cases, indicating a similar reaction rate as well. If the sodium sulfite concentration is
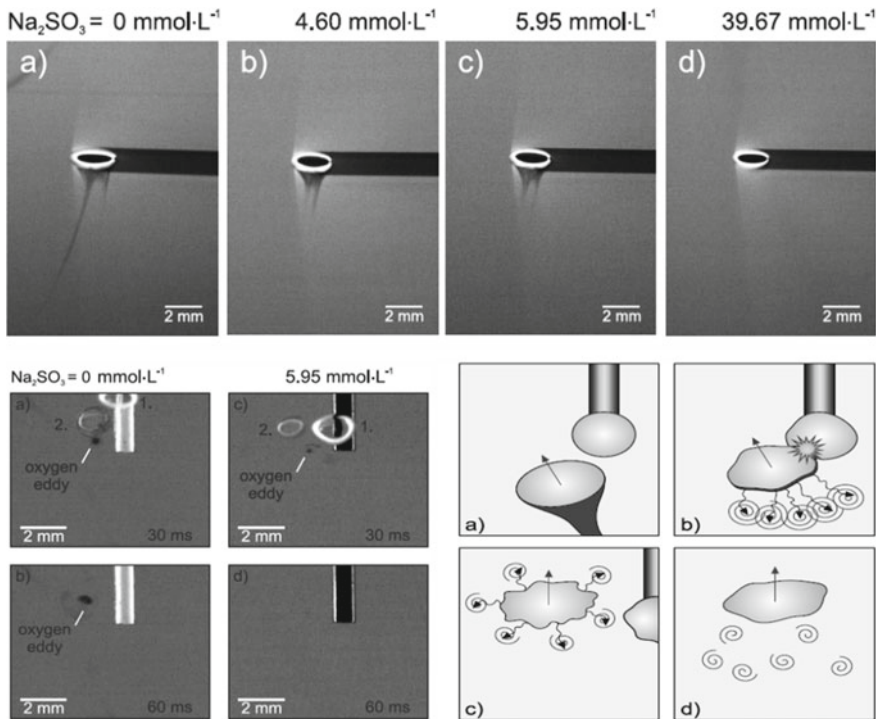
Fig. 20 *Top* qualitative oxygen concentration field around free rising bubble with superimposed Na$_2$SO$_4$ reaction; *bottom left* oxygen concentration field 30 and 60 ms after bouncing of a mechanically fixed bubble (1) and rising bubble (2) with physical (**a, b**) and reactive mass transfer (**c, d**); *bottom right* model concept for the influence of bouncing on mass transfer [23, 56]

further increased, the reaction rate is faster than the mass transfer rate and the oxygen is consumed immediately at the boundary layer, so that no oxygen remains visible.

For studying the impact of bubble bouncing on local mass transfer, a nitrogen bubble is fixed in the field of view and within the rising trajectory of an oxygen bubble. The mean equivalent diameter of the fixed bubbles is $d_{eq,V} = 2.42 \pm 0.06$ mm and $d_{eq,V} = 2.03 \pm 0.05$ mm for the rising bubbles, which have a mean rising velocity of $v_B = 31.8$ cm s^{-1}. A set[1] of the resulting images is displayed in Fig. 20 on the bottom left. Again physical (a, b) and reactive (c, d) mass transfer are compared at $t = 30$ ms and $t = 60$ ms after bouncing. In case of physical mass transfer, an oxygen eddy is formed after the impact by the detached wake and is dissipating over time. At reactive mixing, the detaching wake is forming an eddy with high oxygen concentration that is getting consumed by the chemical reaction [56].

The detachment of the wake structure and the formation of the eddy indicate that bouncing causes a higher mixing intensity in the close proximity to the bubbles. In addition, the deformation of both boundary layers becomes visible. The deformation causes further detachments of smaller eddies at the rising bubble after the collision, likewise contributing to the mass transfer enhancement as already described by Glaeser [44]. This is especially important for parallel-consecutive reactions, where the product formation and distribution and, therefore, yield and selectivity are determined by the degree of mixing [53, 56].

On the basis of the experimental data, some phenomena are identified, allowing the development of a model concept for rising and colliding bubbles, presented in Fig. 20 on the bottom right. While there is no reaction superimposed and the bubble is rising, the concentration wake is maximally saturated and the oxygen is mixed within the bulk phase primarily by diffusion. As soon as the bubble is bouncing into another bubble, the concentration wake detaches and eddies are formed inducing an area of increased mixing into the bulk phase. As a result from the collision, the interfaces of the bubbles and with it the boundary layers are deformed, contributing to the mixing of the bulk phase. Since the stable appearance of the rising bubble is an ellipsoid, the shape oscillation is damped and the boundary layer deformation is reduced, meaning no additional eddies are detaching from the bubble. A qualitative evaluation about the influence of bubble bouncing and the dependency of the collision frequency can be found in [56].

Nevertheless, due to the three-dimensional rising behavior and resulting complex boundary layer effects, a mass balance for oxygen cannot be obtained by the two-dimensional measurements. Therefore, further experiments aiming for the three-dimensional concentration fields need to be obtained, to provide the necessary information for numerical approaches and the development of a mathematical model.

---

[1] The video sequences are available in the supporting information of [55].

4.2.3 Three Dimensional Mass Transfer at Free Rising Wobbling Bubbles

The experiments shown in this section concern the concentration wake of a freely rising oxygen bubble of an equivalent diameter of $d_B = 2.63$ mm ± 0.05 mm resulting in a typical helical rising path. For the analysis the focus lies on the bubble trajectory right after the first inflection point, at which the direction of movement of the bubble is changing from the linear into the helical path. The position is indicated in the sketch on the right of Fig. 21 similar as reported in [47] as, here, the maximal deceleration and therefore interesting wake structures are expected. Due to the formation of the bubbles using a hypodermic needle of $d_N = 0.5$ mm diameter as described above, the rising paths of the bubbles are largely reproducible. However, measurements with Time Resolved Scanning Particle Image Velocimetry (TRS-PIV) in the same setup show, that the bubble repetition rate of $f = 1$ Hz is still too fast and that the liquid has not fully settled to zero velocity in between two consecutive bubbles (not shown). The repetition rate should, thus, be chosen smaller in follow-up studies but it must be considered that one cannot get arbitrarily slow because other unwanted effects such as diffusion of nitrogen gas from the oversaturated solution into the needle might occur resulting in bubbles of gas mixtures. An effect on oxygen concentration was
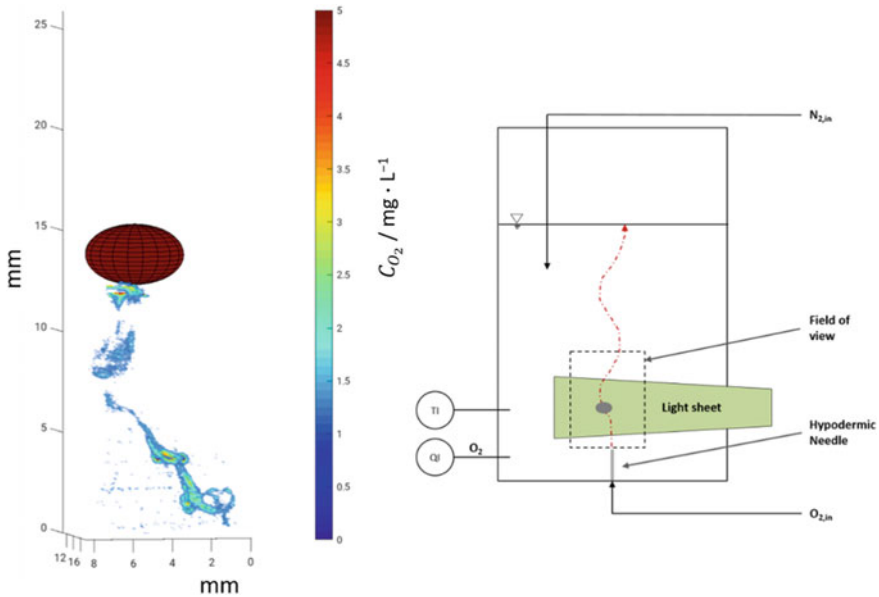
Fig. 21 The three-dimensional concentration wake CO_2 of a freely rising ellipsoidal oxygen bubble reconstructed from the TRS-LIF measurements and elaborated calibration (left). Two shedding vortices are recorded in the bubble wake before the second inflection point of the bubble rise. High oxygen concentration is confined to the regions of high vortical motion. The measurement section is depicted in the sketch on the right [53]

observed qualitatively, since, after nitrogen purging the first two bubbles sometimes showed only a very faint wake. After the elaborate image processing described in the experimental procedure above, the wake structure can be reconstructed three-dimensionally as shown in Fig. 21.

Here the voxels have a size of $V = 0.042 \times 0.042 \times 0.5$ mm^3. Two typical horseshoe like structures are distinguishable, similar to those described by Huang and Saito [47] for a mean wake of several CO_2 bubbles rising in clean and contaminated water. However, in the current study no binarization of the concentration fields was performed to obtain the wakes but a direct calibration and some image correction as elaborated above. Further, for the first time, these structures and their concentration distributions are quantitatively analyzed from single bubbles. The spatial resolution is thereby around five times coarser then claimed in [47] and is limited by the light sheet thickness. It is, thus, very likely that fine structures of less than a voxel size are missed, which are reported to exist in the vicinity of the second inflection section. The two typical horse-shoe like structures that are detected further rise upwards, since they are entrained by the bubbles rise. It can be clearly seen that the oxygen concentration is highest inside the vortex cores and that the concentration almost does not decrease during the successive time steps. This finding suggests that the vortices have a stabilizing effect and might locally prevent the dissolved oxygen from mixing with the surrounding fluid. Further analysis, e.g. of the amount of total transferred oxygen concentration in the wake in time remains to be calculated. Also, more bubbles need to be analyzed to be able to compare the fluctuations in between different experiments. The results further suggest that spots of high oxygen concentration form that stay "coherent" during a considerable amount of time (seconds) and prevent the dissolved oxygen from mixing. This could potentially affect chemical reactions that depend on the concentration of the dissolved gas.

5   Conclusion and Outlook

In this project, three experimental setups have been developed and successfully implemented which all three provided new insights into the complex interplay of fluid dynamics, mass transfer and chemical reactions. By applying the guiding measure "SuperFocus Mixer", it is possible to determine the intrinsic kinetics of the oxidation of sodium sulfite acting as a model reaction and the oxidation of a copper complex yielding a thermally sensitive bis(μ-oxo)dicopper intermediate. Especially the determination of the intrinsic kinetics at the second reaction shows that the SuperFocus Mixer is a helpful tool working under ambient conditions, supporting already established methods as the stopped flow method, allowing the evaluation of fast gas–liquid reactions with a low demand of chemicals and effort. Moreover, the results obtained are a valuable basis for numerical approaches, which have been conducted by the working group at the TU Dortmund, proving the experimental findings [26].

The Taylor bubble experiments, already known from the SPP1506, were successfully extended to reactive flows and proved to be able to visualise and quantify the

influence of mixing on yield and selectivity. The investigation of the already known copper complex, studied by Schurr et al. [28] in the SuperFocus Mixer, show the influence of the mixing behavior in the wake of a bubble. Those results are supported by the measurements of an aqueous ammonia test system, showing the similarities of the wake structures and the formation of the reaction product, by means of backlight imaging and PIV-LIF measurements [30]. Furthermore, it is possible to describe the wake structures occurring behind the Taylor bubble by means of Lagrangian Coherent Structures. The Taylor bubble experiments are concluded by the visualization of the main product MNIC and the side product DNIC of a competitive-consecutive reaction by applying imaging UV/VIS spectroscopy [31]. The results of those measurements are showing that the influences of the mixing time scales are of great importance, if they are much faster than the time scale of the second reaction step, shifting the selectivity towards the first reaction product MNIC [38].

Within the last experimental stage, the local mass transfer at freely ascending bubbles superimposed by a chemical reaction is studied, the influence of bubble–bubble bouncing is quantified and a suitable model for the bubble bouncing is conducted [56]. In order to visualize the unsteady concentration field around dynamically wobbling bubbles the Time Resolved Scanning Laser Induced Fluorescence (TRS-LIF) has been developed, allowing the investigation of threedimensional bubble wakes [53].

In summary, it can be concluded, that the results of this project provide new and deep insights into the complex interplay of mixing, mass transfer and chemical reactions. The project established new tools for the detailed investigation of reactive bubbly flows. In the future, the influence of the mixing on yield and selectivity, which has been proved within the well-defined Taylor bubble setup need to be further quantified and transferred into a setup with freely ascending bubbles. Furthermore, the TRS-LIF setup opens up new opportunities to investigate structures in the wake of rising bubbles in a quantitative manner.

References

1. Clift R, Grace JR, Weber ME (1978) Bubbles, drops, and particles. Academic Press, New York
2. Fan L-S, Tsuchiya K (1990) Bubble wake dynamics in liquids and liquid-solid suspensions. Butterworth-Heinemann, Boston
3. Peebles F, Garber HJ (1953) Studies on the motion of gas bubbles in liquids. Chem Eng Progr 88–97
4. Lewis WK, Whitman WG (1924) Principles of gas absorption. Ind Eng Chem 16:1215–1220. https://doi.org/10.1021/ie50180a002
5. Higbie R (1935) The rate of absorption of a pure gas into a still liquid during short periods of exposure. New York

6. Tsuchiya K, Saito T, Kajishima T, Kosugi S (2001) Coupling between mass transfer from dissolving bubbles and formation of bubble-surface wave. Chem Eng Sci 56:6411–6417. https://doi.org/10.1016/S0009-2509(01)00278-0

7. Redfield JA, Houghton G (1965) Mass transfer and drag coefficients for single bubbles at Reynolds numbers of 0·02–5000. Chem Eng Sci 20:131–139. https://doi.org/10.1016/0009-2509(65)85006-0

8. Toor HL, Marchello JM (1958) Film-penetration model for mass and heat transfer. AIChE J 4:97–101. https://doi.org/10.1002/aic.690040118

9. Levenspiel O (1972) Chemical reaction engineering. Wiley, New York

10. Levenspiel O (1999) Chemical reaction engineering. Wiley, New York

11. Baerns M, Hofmann H, Renken A (1992) Chemische Reaktionstechnik—Lehrbuch der Technischen Chemie, Bd. 1. Georg-Thieme-Verlag, Stuttgart. ISBN 3-1368-7502-8

12. Hatta S (1932) On the absorption velocity of gases by liquids. Tohoku Imperial University

13. Hikita H (1964) Gas absorption with (m, n)-th order irreversible chemical reaction. Ind Eng Chem 332–340

14. Hessel V, Hardt S, Löwe H, Schönfeld F (2003) Laminar mixing in different interdigital micromixers: I. Experimental characterization. AIChE J 49:566–577. https://doi.org/10.1002/aic.690490304

15. Hardt S, Schönfeld F (2003) Laminar mixing in different interdigital micromixers: II. Numerical simulations. AIChE J 49:578–584. https://doi.org/10.1002/aic.690490305

16. Drese KS (2004) Optimization of interdigital micromixers via analytical modeling—exemplified with the SuperFocus mixer. Chem Eng J 101:403–407. https://doi.org/10.1016/j.cej.2003.10.023

17. Kashid MN, Renken A, Kiwi-Minsker L (2015) Microstructured devices for chemical processing. Wiley-VCH, Weinheim

18. Kück UD, Kröger M, Bothe D, Räbiger N, Schlüter M, Warnecke H-J (2011) Skalenübergreifende Beschreibung der Transportprozesse bei Gas/Flüssig-Reaktionen. Chem Ing Tech 83:1084–1095. https://doi.org/10.1002/cite.201100036

19. Bäckström HLJ (1934) Der Kettenmechanismus bei der Autoxydation von Aldehyden. Z Phys Chem 25B. https://doi.org/10.1515/zpch-1934-2509

20. Rüttinger S, Spille C, Hoffmann M, Schlüter M (2018) Laser-induced fluorescence in multiphase systems. ChemBioEng Rev 5:253–269. https://doi.org/10.1002/cben.201800005

21. Karasso PS, Mungal MG (1997) PLIF measurements in aqueous flows using the Nd:YAG laser. Exp Fluids 23:382–387. https://doi.org/10.1007/s003480050125

22. Francois J, Dietrich N, Guiraud P, Cockx A (2011) Direct measurement of mass transfer around a single bubble by micro-PLIFI. Chem Eng Sci 66:3328–3338. https://doi.org/10.1016/j.ces.2011.01.049

23. Timmermann J (2018) Experimental analysis of fast reactions in gas-liquid flows

24. Hoffmann M, Schlüter M, Räbiger N (2006) Experimental investigation of liquid–liquid mixing in T-shaped micro-mixers using μ-LIF and μ-PIV. Chem Eng Sci 61:2968–2976. https://doi.org/10.1016/j.ces.2005.11.029

25. Spille VC (2015) Experimentelle Analyse lokaler Konzentrationsfelder in einem Superfokusmischer zur Bestimmung von Mikrokinetiken. Masterthesis, Hamburg University of Techchnology

26. Mierka O, Munir M, Spille C, Timmermann J, Schlüter M, Turek S (2017) Reactive liquid-flow simulation of micromixers based on grid deformation techniques. Chem Eng Technol 40:1408–1417. https://doi.org/10.1002/ceat.201600686

27. Spille C (2016) Characterization of reactive systems by means of a SuperFocus mixer

28. Schurr D, Strassl F, Liebhäuser P, Rinke G, Dittmeyer R, Herres-Pawlis S (2016) Decay kinetics of sensitive bioinorganic species in a SuperFocus mixer at ambient conditions. React Chem Eng 1:485–493. https://doi.org/10.1039/C6RE00119J

29. Hayashi K, Kurimoto R, Tomiyama A (2011) Terminal velocity of a Taylor drop in a vertical pipe. Int J Multiph Flow 37:241–251. https://doi.org/10.1016/j.ijmultiphaseflow.2010.10.008

30. Kastens S, Timmermann J, Strassl F, Rampmaier RF, Hoffmann A, Herres-Pawlis S, Schlüter M (2017) Test system for the investigation of reactive Taylor bubbles. Chem Eng Technol 40:1494–1501. https://doi.org/10.1002/ceat.201700047

31. Kameke AV, Kastens S, Rüttinger S, Herres-Pawlis S, Schlüter M (2019) How coherent structures dominate the residence time in a bubble wake: an experimental example. Chem Eng Sci 207:317–326. https://doi.org/10.1016/j.ces.2019.06.033

32. Llamas CG, Spille C, Kastens S, Paz DG, Schlüter M, Kameke A (2020) Potential of Lagrangian analysis methods in the study of chemical reactors. Chem Ing Tech 92:540–553. https://doi.org/10.1002/cite.201900147

33. Bothe D, Reusken A (eds) (2017) Transport processes at fluidic interfaces. Springer International Publishing, Cham. https://doi.org/10.1007/978-3-319-56602-3

34. Rolff M, Schottenheim J, Decker H, Tuczek F (2011) Copper–O_2 reactivity of tyrosinase models towards external monophenolic substrates: molecular mechanism and comparison with the enzyme. Chem Soc Rev 40:4077. https://doi.org/10.1039/c0cs00202j

35. Orhan R, Dursun G (2016) Effects of surfactants on hydrodynamics and mass transfer in a co-current downflow contacting column. Chem Eng Res Des 109:477–485. https://doi.org/10.1016/j.cherd.2016.02.030

36. Painmanakul P, Loubière K, Hébrard G, Mietton-Peuchot M, Roustan M (2005) Effect of surfactants on liquid-side mass transfer coefficients. Chem Eng Sci 60:6480–6491. https://doi.org/10.1016/j.ces.2005.04.053

37. Álvarez E, Sanjurjo B, Cancela A, Navaza JM (2000) Mass transfer and influence of physical properties of solutions in a bubble column. Chem Eng Res Des 78:889–893. https://doi.org/10.1205/026387600527950

38. Kexel F, von Kameke A, Oßberger M, Hoffmann M, Klüfers P, Schlüter M (2020) Bildgebende UV-VIS Spektroskopie zur Untersuchung des Einflusses der Fluiddynamik auf die Selektivität und Ausbeute von schnellen konkurrierenden konsekutiven gas-flüssig Reaktionen. Chem Ing Tech

39. Haller G (2015) Lagrangian coherent structures. Annu Rev Fluid Mech 47:137–162. https://doi.org/10.1146/annurev-fluid-010313-141322

40. Farazmand M, Haller G (2012) Computing Lagrangian coherent structures from their variational theory. Chaos 22:013128. https://doi.org/10.1063/1.3690153

41. Onu K, Huhn F, Haller G (2015) LCS tool: a computational platform for Lagrangian coherent structures. J Comput Sci 7:26–36. https://doi.org/10.1016/j.jocs.2014.12.002

42. Kastens S (2020) Transport processes at Taylor bubbles in vertical channels

43. Bork O, Schlueter M, Raebiger N (2005) The impact of local phenomena on mass transfer in gas-liquid systems. Can J Chem Eng 83:658–666. https://doi.org/10.1002/cjce.5450830406

44. Glaeser H (1977) Berechnung des Impuls- und STofftransports durch die Grenzfläche einer formveränderlichen Blase. Berlin

45. Kück UD, Schlüter M, Raebiger N (2012) Local measurement of mass transfer rate of a single bubble with and without a chemical reaction. J Chem Eng Japan/JCEJ 45:708–712. https://doi.org/10.1252/jcej.12we059

46. Jimenez M, Dietrich N, Hébrard G (2013) Mass transfer in the wake of non-spherical air bubbles quantified by quenching of fluorescence. Chem Eng Sci 100:160–171. https://doi.org/10.1016/j.ces.2013.01.036

47. Huang J, Saito T (2017) Discussion about the differences in mass transfer, bubble motion and surrounding liquid motion between a contaminated system and a clean system based on consideration of three-dimensional wake structure obtained from LIF visualization. Chem Eng Sci 170:105–115. https://doi.org/10.1016/j.ces.2017.03.030

48. Brücker C (1999) Structure and dynamics of the wake of bubbles and its relevance for bubble interaction. Phys Fluids 11:1781–1796. https://doi.org/10.1063/1.870043

49. Deusch S, Dracos T (2001) Time resolved 3D passive scalar concentration-field imaging by laser induced fluorescence (LIF) in moving liquids. Meas Sci Technol 12:188–200. https://doi.org/10.1088/0957-0233/12/2/310

50. Crimaldi JP (2008) Planar laser induced fluorescence in aqueous flows. Exp Fluids 44:851–863. https://doi.org/10.1007/s00348-008-0496-2

51. Stöhr M, Schanze J, Khalili A (2009) Visualization of gas–liquid mass transfer and wake structure of rising bubbles using pH-sensitive PLIF. Exp Fluids 47:135–143. https://doi.org/10.1007/s00348-009-0633-6

52. Soodt T, Schröder F, Klaas M, van Overbrüggen T, Schröder W (2012) Experimental investigation of the transitional bronchial velocity distribution using stereo scanning PIV. Exp Fluids 52:709–718. https://doi.org/10.1007/s00348-011-1103-5

53. von Kameke A, Kexel F, Rüttinger S, Colombi R, Kastens S, Schlüter M (2019) 3D-reconstruction of O_2 bubble wake concentration. In: Proceedings of the 13th international symposium on particle image velocimetry, Munich

54. Sone D, Sakakibara K, Yamada M, Sanada T, Saito T (2008) Bubble motion and its surrounding liquid motion through the collision of a pair of bubbles. JPES 2:306–317. https://doi.org/10.1299/jpes.2.306

55. Ohl CD (2001) Generator for single bubbles of controllable size. Rev Sci Instrum 72:252–254. https://doi.org/10.1063/1.1329900

56. Timmermann J, Hoffmann M, Schlüter M (2016) Influence of bubble bouncing on mass transfer and chemical reaction. Chem Eng Technol 39:1955–1962. https://doi.org/10.1002/ceat.201600299

57. Kück UD, Schlüter M, Räbiger N (2009) Analyse des grenzschichtnahen Stofftransports an frei aufsteigenden Gasblasen. Chem Ing Tech 81:1599–1606. https://doi.org/10.1002/cite.200900034

58. Weiner A, Timmermann J, Pesci C, Grewe J, Hoffmann M, Schlüter M, Bothe D (2019) Experimental and numerical investigation of reactive species transport around a small rising bubble. Chem Eng Sci X 1:100007. https://doi.org/10.1016/j.cesx.2019.100007

59. Dani A, Guiraud P, Cockx A (2007) Local measurement of oxygen transfer around a single bubble by planar laser-induced fluorescence. Chem Eng Sci 62:7245–7252. https://doi.org/10.1016/j.ces.2007.08.047

60. Wasowski T, Blaß E (1987) Wake-Phänomene hinter festen und fluiden Partikeln: Wake-Phänomene hinter festen und fluiden Partikeln. Chem Ing Tech 59:544–555. https://doi.org/10.1002/cite.330590704

61. Tomiyama A, Kataoka I, Zun I, Sakaguchi T (1998) Drag coefficients of single bubbles under normal and micro gravity conditions. JSME Int J Ser B, 41(2):472–479

62. Frössling N (1938) The evaporation of falling drops (in German). Gerlands Beitr Geophys 52:170–216

Experimental Characterization of Gas–Liquid Mass Transfer in a Reaction Bubble Column Using a Neutralization Reaction

Katharina Zähringer and Péter Kováts

Abstract The bubble column developed at Otto-von-Guericke-Universität Magdeburg (OVGU, AG Zähringer) was intended to facilitate the detailed characterization of a bubble column with a quick neutralization reaction as an interesting limiting case. The model column used for this purpose had a volume of about $V = 12$ L and a modular injection system for the production of bubble chains and a bubble curtain, consisting four bubble nozzles. Exclusively optical measurement techniques have been used to measure bubble sizes, velocities and aspect parameters, as well as liquid velocity and concentration of the transferred component. The reaction examined in this column was the absorption of CO_2 from the bubbles to the slightly basic liquid phase. The pH-change in the liquid phase could then be monitored by a laser induced fluorescence technique, called Two-Tracer LIF, involving two different tracer dyes. One of these dyes traces the pH-change, the other stays passive and images the lightening situation in the column, including bubble shadows and reflections. This "live-background" allows then for the correction of the pH images. The knowledge of bubble parameters, liquid velocity and pH-fields enables the calculation of further quantities like mass transfer coefficient and volumetric mass transfer coefficient. These kinds of measurements have been executed for a variety of parameters like gas flow rate, filling height, increasing liquid viscosity or decreasing liquid surface tension. The results, used also for validation purposes of numerical calculations in partner groups (see Chapters "Euler-Euler Modeling of Reactive Flows in Bubble Columns", "Multi-scale Investigations of Reactive Bubbly Flows" and "Chemical Reactions in Bubbly Flows"), are made available for interested research groups in a data-base accessible under https://www.lss.ovgu.de/Info/Downloads.html.

K. Zähringer (✉) · P. Kováts
Otto-von-Guericke-Universität Magdeburg, Lehrstuhl für Strömungsmechanik und Strömungstechnik, 39106 Magdeburg, Germany
e-mail: katharina.zaehringer@ovgu.de

1 Experimental Setup of the Bubble Column

Since optical measurement techniques should be employed, a completely transparent three-dimensional bubble column was constructed. It consists of an acrylic glass cylinder with a thickness of 4 mm and was surrounded by a rectangular acrylic box for refractive index matching (Fig. 1 left). It has a diameter of $D = 0.14$ m and a filling height of $H = 0.73$ m, that gives a volume of $V = 11.5$ L and an aspect ratio of $H/D = 5$. The outer rectangular box was filled with the working fluid, generally deionized water, but also in some experiments with solutions of water-glycerol-surfactant mixtures. This allows for the correction of refraction, occurring on curved walls, when optical measurement techniques are used. The interchangeable bottom of the bubble column (Fig. 1 right) can be equipped with a single nozzle gas outlet or a bottom with 4 in-line nozzles, which are spaced by $x = 2.2$ cm. The nozzles are made from stainless steel capillaries with an inner diameter of $d = 0.25$ mm. Through these nozzles, bubbles with a diameter of about $d_B = 2$–4 mm are produced.

In this column the absorption of CO_2 in a deionized water–NaOH solution has been examined, where NaOH is only used to increase the initial pH value in the column to $pH \approx 9$, that is necessary for the fluorescent tracer reaction used here to start (see 2.2). CO_2-gas with a purity of 99.5% was supplied from a pressurized bottle into the initially stagnant liquid phase. The flow rate of the CO_2 gas was set through a rotameter to values between $\dot{V}_G = 3.5$ and 10 l/h. This corresponds to superficial
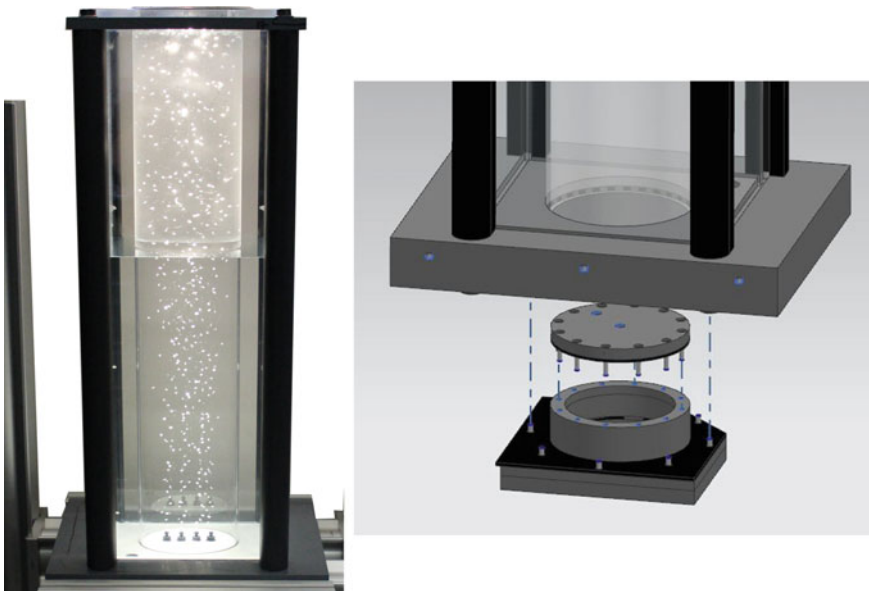
Fig. 1 Bubble column with rectangular box for refractive index matching (left). Modular column bottom for different bubble generation configurations (right)

gas velocities of $j_G = 6.14 \times 10^{-5}$ to 1.75×10^{-4} m/s. With the present sparger and flow settings homogenous bubbly flows were achieved. The four nozzle setup had a maximum gas holdup around 0.1%. This low gas holdup is crucial for planar laser measurement techniques, because the higher the gas holdup, the bigger is the area covered by shadows of the bubbles, where no information can be recorded. Another important advantage of this homogeneous bubbly flow is, that bubble coalescence or break-up were not observed. Therefore, all bubbles in the column are generated originally within the gas sparger capillaries.

Other typical values of the bubbly flow in the column, calculated for an air equivalent CO_2 flow rate of $\dot{V}_G = 8$ l/h, that has been mostly used, are given in Table 1. All measurements have been done at atmospheric pressure and room temperature. Further details of the experimental setup can be found in [1–4].

The influence of viscosity and surface tension of the liquid was also studied in this column [1]. For this, mixtures of 0, 25, 50, and 60 mass percent glycerol in deionized water were used and combined with the surfactant sodium dodecyl sulphate (SDS) in three different concentrations: $c = 0.0$, 1.9 and 5.69 g L^{-1}. The physical properties of these different mixtures are shown in Table 2. The values were obtained with a

Table 1 Main flow parameters in the investigated bubble column at $\dot{V}_G = 8$ l/h air equivalent CO_2 flow rate

d_e (mm)	d_B (mm)	C_B (–)	U_B (m s^{-1})	$U_{B,mean}$ (m s^{-1})	f (s^{-1})	V_B (mm^3)	A_B (mm^2)	v_l (m s^{-1})
1.44–6.3	2.8	0.453	0.044–0.56	0.30	130–150	12.8	29.98	0.045

Dimensionless numbers

Re_b	Re_c	We_b	We_c	Fr_b	Fr_c	Eo	Mo	Sc
724	6368	3.53	3.94	3.28	0.0015	1.08	2.56E−11	558.38

Table 2 Physical properties of water/glycerol/SDS mixtures

Glycerol conc (m%)	Surfactant (g/l)	ρ (kg/m^3)	μ (mPa s)	σ (mN/m)	$\log_{10}(Mo)$ (–)
0	0	996.89	0.9	72.24	−10.7673
0	1.9	996.89	0.86	58.19	−10.5645
0	5.69	996.89	0.89	51.34	−10.3417
25	0	1057.7	1.78	69.45	−9.5569
25	1.9	1057.7	1.79	52.7	−9.1876
25	5.69	1057.7	1.82	50.79	−9.1106
50	0	1123.6	4.76	67.81	−7.8433
50	1.9	1123.6	4.78	49.29	−7.4204
50	5.69	1123.6	4.538	47.52	−7.4630
60	0	1150.7	8.752	66.51	−6.7704
60	1.9	1150.7	8.875	48.86	−6.3443
60	5.69	1150.7	9.286	44.8	−6.1527

Malvern Kinexus pro+ rotational rheometer, and the pendant drop method, realized with an in-house Matlab script.

2 Applied Measurement Techniques

The purpose of the measurements at OVGU AG Zähringer, was the acquisition of a complete as possible data set of bubble parameters (velocity, size, aspect ratio), liquid velocity and mass transfer (concentration of transferred component in the liquid) in the three-dimensional bubble column. For this, optical measurement techniques have been used.

2.1 Bubble Characterization with Shadowgraphy and Particle-Tracking-Velocimetry

The aim of the shadowgraphy experiments was to gain information about the influence of different parameters, as liquid composition, filling height, surface tension and viscosity on bubble size, form, motion, and rising velocity at different gas flow rates. A typical experimental setup is shown in Fig. 2 (see also [1, 2, 4]). It consists of two 4 Mpixel high-speed cameras (*LaVision Imager pro HS 4M*) with 2016 × 2016 pixels and $f = 1279$ Hz maximal frame rate at maximal resolution (1 in Fig. 2) fixed one above the other, in order to simultaneously record all bubbles over the

Fig. 2 Experimental setup for shadowgraphy
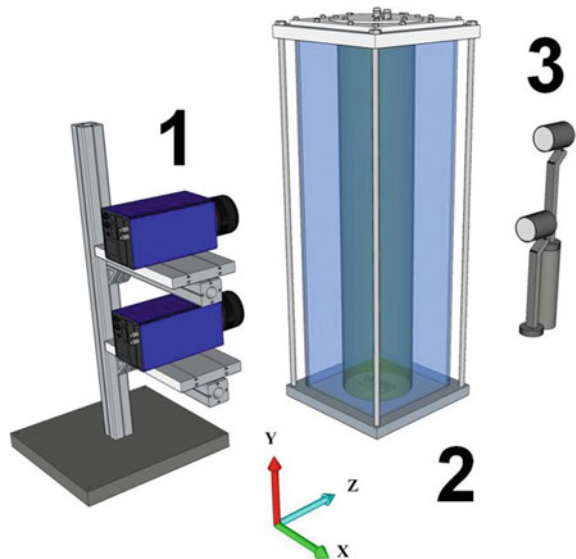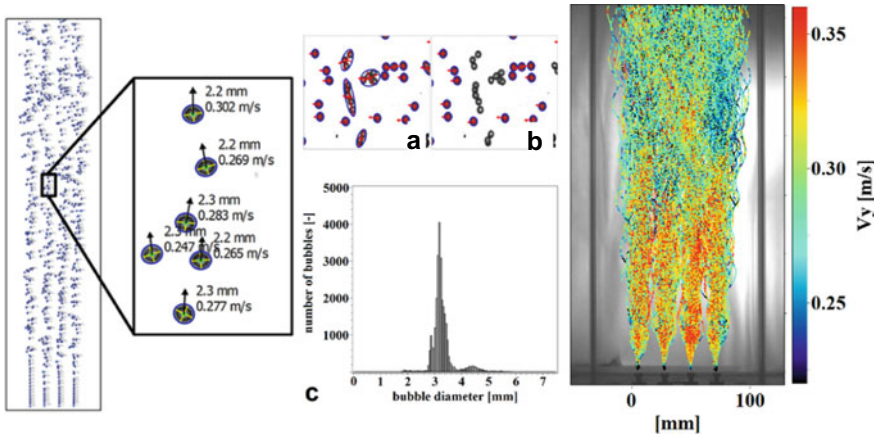
Combination of two images and detection of bubble diameters and velocities	*Bubble detection (a) and filtering (b), bubble size distribution (c)*	*Bubble velocities and trajectories*

Fig. 3 Shadowgraphy processing steps

entire height of the column (2 in Fig. 2), by keeping a sufficient spatial resolution for bubble size determination. On each camera, a Micro 50 mm lens was mounted and allowed for a final pixel-resolution of 0.15 mm/pixel. Two *Dedocool* halogen lights (3 in Fig. 2) assure contrast-full background illumination. The light was diffused on a white background, which was located on the back wall of the column and produced a very homogeneous light distribution. For each parameter variation, several experimental runs with up to 1000 pictures each were acquired at $f = 100$ Hz imaging rate with *DaVis software* (*LaVision*).

Post-processing of the shadowgraphy images (*DaVis 8.4 software from LaVision*) comprises first of all a geometrical calibration via calibration plates, background correction and bubble detection (Fig. 3 left). After filtering (Fig. 3 centre a and b), position coordinates and equivalent diameters (Fig. 3 centre c) are calculated, as well as centricity parameters and orientation angles. After combining always two successive images and using an additional PTV algorithm [5], the velocity and bubble trajectories could be determined (Fig. 3 right).

2.2 Mass Transfer Measurements through 2-Tracer-Laser-Induced-Fluorescence

The reaction to be investigated in this reactor is the chemisorption of CO_2 in a stagnant basic water–NaOH solution ($pH \approx 9$) (see Sect. 3). During this reaction, the *pH* value is decreasing. In order to quantify and track this change optically,

without being troubled by the shadows, that are produced by the rising bubbles in a light sheet, the Two-Tracer Laser Induced Fluorescence technique (2T-LIF) is used [6, 7]. The reactor is filled for this purpose initially with the liquid (de-ionised water and NaOH, $pH = 9$) that contains also two fluorescent dyes. One of these dyes (uranine) is changing its fluorescence intensity with the pH, the other (pyridine 2) stays passive. Both are imaged simultaneously, but separately, by two cameras and appropriate optical filters. With the help of the passive dye, as a kind of live background, reflections on the bubble surface, bubble shadows and the laser light sheet inhomogeneities can be reduced drastically by dividing both images (see Fig. 4 from left to right). Both tracers can be separated by their fluorescence wavelength: uranine fluoresces at $\lambda = 550$ nm, pyridine 2 at $\lambda = 700$ nm.

The experimental setup for such 2T-LIF measurements is shown in Fig. 5, here in combination with simultaneous liquid velocity measurements via Particle Image Velocimetry (PIV). On the front side of the column, two Imager-Intense CCD cameras (LaVision) (1 in Fig. 5) with a resolution of 1376×1040 pixels were installed for 2T-LIF. The cameras were equipped with appropriate lenses and, additionally, one with a $\lambda = 550$ nm band-pass filter ($\Delta\lambda = 10$ nm @ FWHM) for the detection of uranine fluorescence, and the other with a $\lambda = 705$ nm band-pass filter ($\Delta\lambda = 30$ nm @ FWHM) for pyridine 2 fluorescence. The tracer concentrations used here were c= 10–20 mg L^{-1} for uranine (*CAS: 518-47-8; Acros*) and c = 2 mg L^{-1} for pyridine-2 (*CAS: 89846-21-9; Exciton*), respectively. Both LIF-cameras were situated side-by-side in front of a 50–50% beam splitter (3 in Fig. 5), that allows for the observation of the same region of interest with very low perspective distortion and used for a better overlapping of the fields of view during latter post-processing. With this setup, pixel-resolutions of 0.15 mm/pixel were achieved.
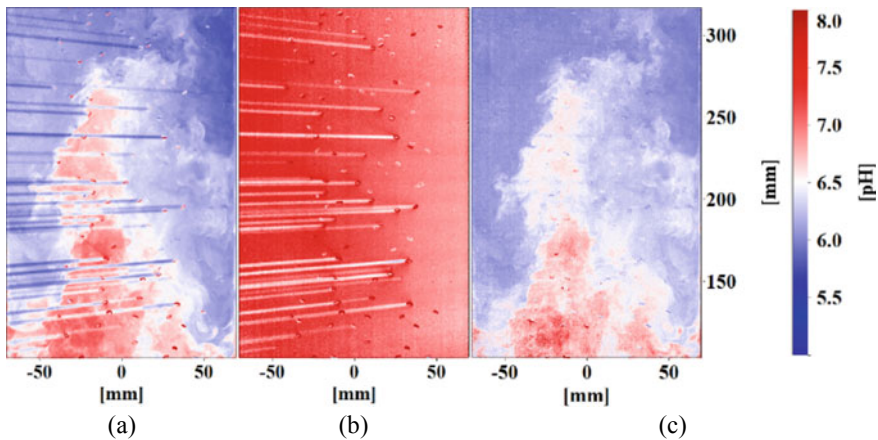
Fig. 4 **a** Raw image from 1st camera imaging the pH-tracer uranine; **b** raw image from 2nd camera imaging the inert tracer pyridine 2; **c** treated image after calibration showing the pH. Bottom part of the column (100–320 mm)

Fig. 5 Experimental setup
for simultaneous
2-tracer-LIF and PIV
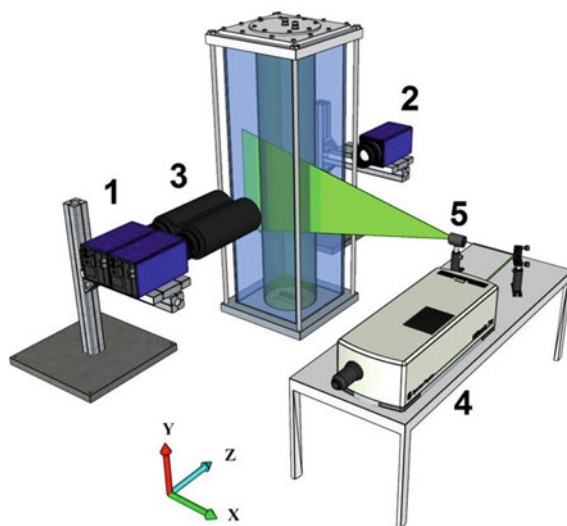
For excitation of the two fluorescent tracers and simultaneously the PIV particles, a two-cavity, frequency-doubled Nd:YAG laser from Spectra Physics (4 in Fig. 5) was used with a wavelength of $\lambda = 532$ nm and an energy of $E = 95$ mJ/pulse. The light sheet optics (5 in Fig. 5) expanded the laser beam to a field of view of maximum 350×140 mm, with a sheet thickness of less than 0.5 mm. It crosses the bubble column in the centre, along the line of bubble capillaries perpendicular to the camera axes. The cameras and the laser were controlled and synchronized by a timing unit and *DaVis Software from LaVision*. The image frequency was $f = 5$ Hz for 2T-LIF and $f = 3.33$ Hz for simultaneous 2T-LIF and PIV. For each parameter, several measurement series with up to 1000 images were taken, which corresponds to a physical time of $t = 500$ and 333 s respectively. In order to obtain a sufficient geometrical resolution, the full column height was divided into several sections, which were monitored one after the other by moving the cameras and laser light sheet to the corresponding height.

Post-processing of the images comprises first of all classical steps, like noise, background and laser-sheet correction, geometrical calibration and dewarping of the two simultaneously acquired images. This allows then to divide the uranine fluorescence image, containing the pH information, by the live background pyridine 2 image. The result is converted into pH values by the help of a calibration curve, which is established for each experimental run by recording the fluorescence of fillings with different pH, controlled by a *WTW Profiline 3320 Multi pH-meter*. With that, every pixel intensity on the 2T-LIF images can be associated to a specific *pH* value (e.g. Fig. 6). A detailed description of the processing steps can be found in [1, 2, 4].
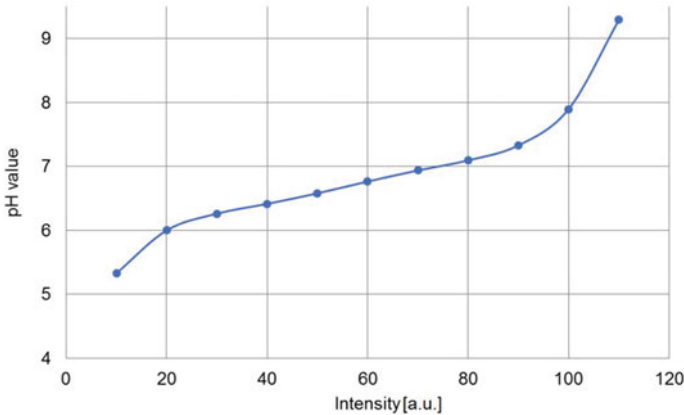
Fig. 6 Example of a calibration curve for a 25 m% glycerol/water solution in the upper part of the column. Intensity is given in arbitrary units (a.u.)

2.3   Measurement of the Liquid Flow Field by Means of Particle Image Velocimetry

The liquid velocities in the column have been measured by Particle Image Velocimetry (PIV). Depending on the parameters to be examined, different PIV setups have been used, starting with classical PIV using frame rates of $f = 10$ Hz, over simultaneous 2T-LIF and PIV at 3.33 Hz, to high-speed PIV (HS-PIV) at 1000 Hz. For this, different camera, lens and arrangement combinations have been used. Details can be found in [1–4, 8].

For simultaneous concentration and velocity measurements, the PIV camera was located on the backside of the column (2 in Fig. 5) and equipped with a polarization filter to minimize the reflections on the LIF cameras situated in front of it. Fluorescent rhodamine-B doped PMMA particles (*Microparticles GmbH, Berlin*) with a mean diameter of $d_P = 10$ μm were used in all cases. These fluoresce at $\lambda = 580$ nm and can thus be separated by appropriate optical filters from the fluorescence of the tracer dye, used for concentration measurements. The geometrical positions were calibrated with a 3D calibration target.

The PIV images were processed with *Davis 8.4 software* from *LaVision*. This includes pre-processing steps like masking walls, bubbles and their shadows, elimination of high light levels due to reflections on the bubble surface and the vector calculation itself. For this, cross-correlations (multi-pass with decreasing size from 64×64 pixels to 16×16 pixels with and without overlap) have been used (details can be found in [1, 2, 4]). Due to the presence of the bubbles, postprocessing of the PIV results is very important. A detailed description of the postprocessing steps can be found in [1, 2, 4]. Finally, vector resolutions of about 1 vector/mm were achieved.

3 Reaction System

The reaction system used in AG Zähringer at Magdeburg is the chemisorption of CO_2 in basic water. Due to the method used (see Sect. 2.2) the pH range for the chemisorption is limited to $4.5 < pH < 8…9$. Only in this range the pH-tracer used for Laser Induced Fluorescence is stable and shows a monotonic calibration curve between concentration and fluorescence.

The chemisorption starts with the mass transfer of gaseous CO_2 into the liquid:

$$CO_{2,(g)} \rightarrow CO_{2,(l)}$$
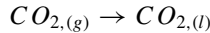
There, as first major reaction step, the dissolved $CO_{2,(l)}$ reacts with hydroxide ions (OH^-) and forms hydrogen carbonate ions (HCO_3^-).

$$CO_{2,(l)} + OH^- \rightleftharpoons HCO_3^-$$

An alternative reaction pathway is the reaction of dissolved $CO_{2,(l)}$ with water as

$$CO_{2,(l)} + H_2O \rightleftharpoons HCO_3^- + H^+$$

$$CO_{2,(l)} + H_2O \rightleftharpoons H_2CO_3$$
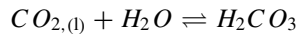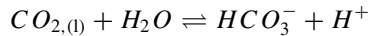
The relative importance of both reactions depends on the *pH* value. According to [9] the hydroxylation dominates for $pH > 10$ and the hydration for $pH < 8$ while in between those values both reactions are important.

As a second reaction step, the HCO_3^- ions react with OH^- ions to carbonate ions (CO_3^{2-}).

$$HCO_3^- + OH^- \rightleftharpoons CO_3^{2-} + 2H^+$$
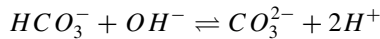
The pH-tracer uranine then reacts with the H^+ ions and its fluorescence intensity is dependent on the *pH* (Fig. 6). For $pH > 9$ the calibration curve saturates, thus it is no longer possible to determine the exact *pH*. At $pH < 5$, uranine starts to dissociate and fluorescence disappears.

4 Results

Some exemplary results obtained by optical measurement techniques in AG Zähringer at Magdeburg University are presented in the following. The detailed data for different column arrangements, and viscosity and surface tension variation

of the liquid can be found in [1–4, 8]. This data is also made available to the interested research community via an online database, accessible with a password under (https://www.lss.ovgu.de/Info/Downloads.html).

4.1 Bubble Parameters

In Fig. 7 size distributions of the equivalent sphere diameter (ESD) of bubbles in different viscous liquids are shown without surfactant (top) and with surfactant SDS (bottom). Important differences can be recognized depending on the viscosity and surface tension: the size distribution of CO_2-bubbles in pure water (squares on Fig. 7, top) shows a large standard deviation, whereas an increase of viscosity (Fig. 7, top) or decrease of surface tension (on Fig. 7, bottom) leads to much narrower bubble size distributions. Also with decreasing surface tension, the mean bubble diameter is reduced considerably, while the average bubble size increases with growing viscosity.

These bubble size changes are related to changes of their rising velocity (Fig. 8). With increasing viscosity, the velocities decrease, while their distributions show similar aspects (Fig. 8, top). The addition of surfactant (c = 1.9 g L^{-1} SDS, Fig. 8, bottom) also leads to smaller velocities. The monodisperse velocity distribution turns to a polydisperse distribution with two peaks at 50 and 60% glycerol concentration. This reflects the fact, that in these cases straight upward rising, nearly spherical bubbles with higher velocity exist near the bottom of the bubble column, and in the centre and top section wobbling spheroid bubbles with lower velocity are dominant.

These results are compared to known bubble velocity and diameter correlations and results from the literature in Fig. 9. The results obtained for pure water (red squares) fit very well to Clift's correlation [10] for pure water. The results for the lowest surface tension (yellow symbols in Fig. 9, left) are between the correlations of Ishii-Zuber [11] and Tomiyama et al. [12], and that of Clift for contaminated water. Compared to the data reported by Bryn [13], Haberman et al. [14], and Maxworthy et al. [15] for clear water (Fig. 9, right), the velocities measured in this study for the solutions without and with 25% glycerol, but without surfactants, correspond very well. The high viscosity results, as well as all mixtures with surfactant, show good agreement with data for a 60% water-glycerol solution from Maxworthy.

The aforementioned bubble variables can be used to calculate Eötvös, Reynolds and Morton numbers, that are plotted in Fig. 10 in a diagram originally proposed by Grace [16]. The experimental results of this study in the 0% Glycerol-water mixtures lay, as expected, on the $log(Mo) = -11$ isoline. The Morton number increases with the addition of surfactant or increasing viscosity, while the Reynolds number decreases, thus these conditions are situated lower in the diagram. The influence of the surface tension is, in contrary, rather weak (some symbols are overlapping). All investigated cases are situated in the "Spheroid" region of the diagram, even for the high viscosity and low surface tension cases, where bubbles seem to be spheres. But, a detailed analysis of the aspect ratios revels a smaller vertical, than horizontal axis in these cases.
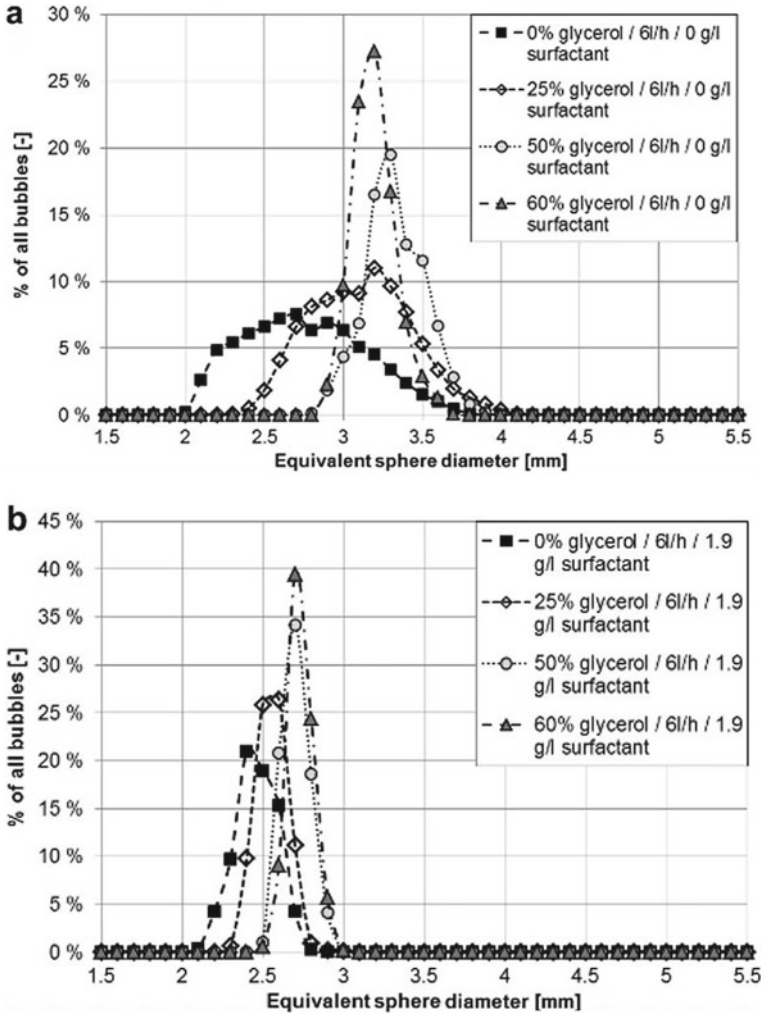
Fig. 7 Distributions of equivalent sphere diameter of bubbles at different viscosity (top) and surface tension (bottom) at 6 l/h CO_2 gas volume flow rate
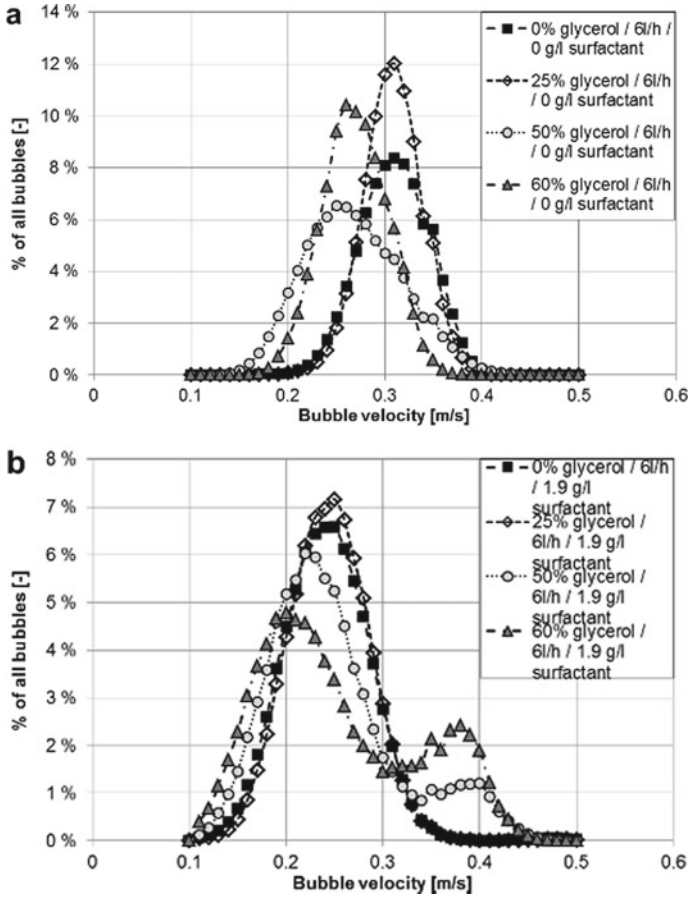
Fig. 8 Distributions of bubble rising velocity distributions for different viscosity (top), and surface tension (bottom) at $\dot{V} = 6$ l/h CO_2 gas volume flow rate
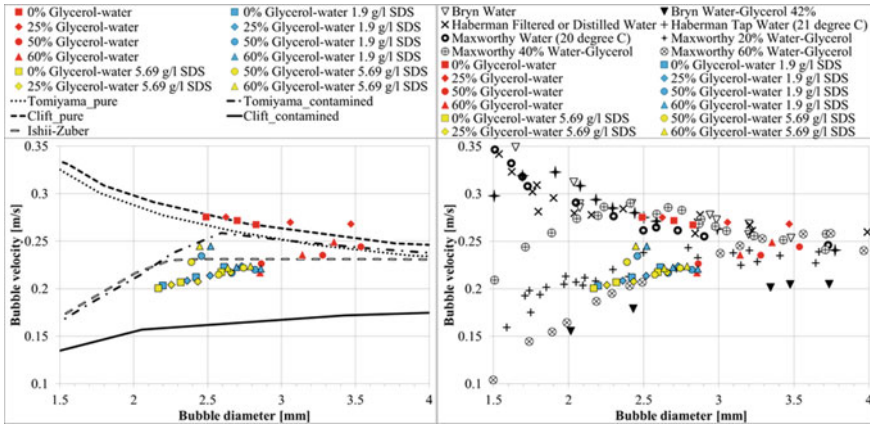
Fig. 9 Experimental results of bubble velocity versus bubble diameter compared to the correlations of Clift et al. [10], Tomiyama et al. [12], and Ishii [11] (left) and to experimental data from Bryn [13], Haberman et al. [14], and Maxworthy et al. [15] (right)
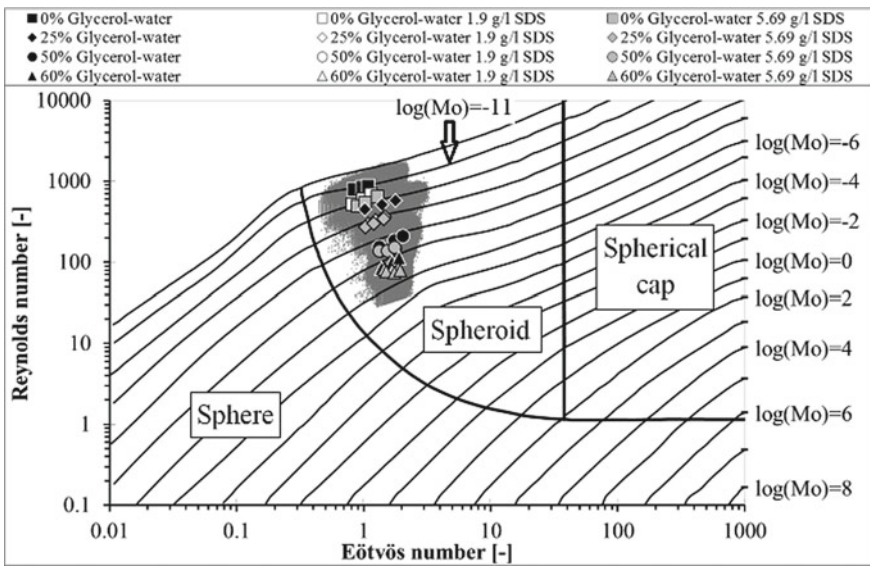
Fig. 10 Bubble shape regime map according to Grace: mean results (symbols) and complete investigated region (grey cloud)

4.2 Mass Transfer from CO₂-Bubbles

The development of mass transfer from the bubbles to the liquid in the complete column is represented in Fig. 11. There, snap-shot images of the *pH* in the centre
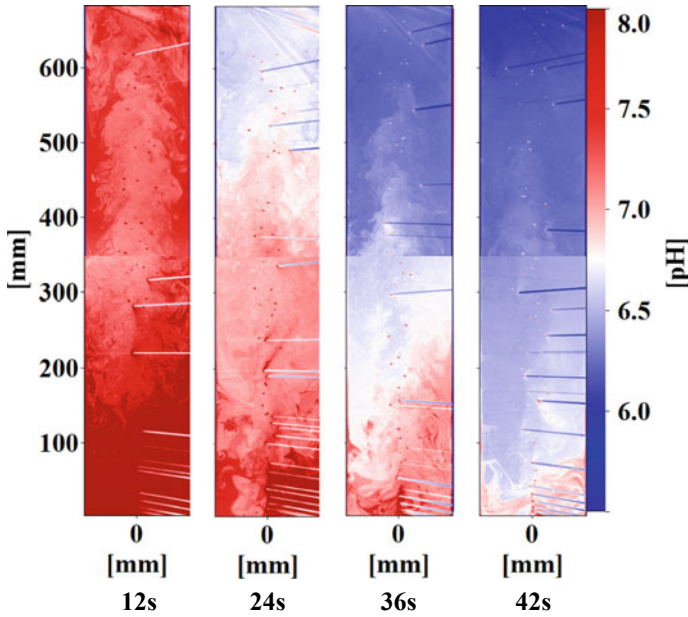
Fig. 11 Example of pH measurements represented for the complete column at different time steps for the one nozzle configuration

plane of the column are shown for different times after release of the first bubble from the nozzles for the bubble chain configuration with one nozzle. It becomes obvious, that CO_2 is first transferred in the centre of the column on the ascending path of the bubbles. Then, the liquid movement in the column establishes and liquid with higher CO_2 concentration (lower pH, blue) is transported from the surface downwards, along the column walls, to the bottom after approximately $t = 42$ s.

This *pH* change versus time is represented in Fig. 12 for six horizontal sections of $s = 20$ mm thickness in the four nozzle configuration during the first $t = 100$ s for different liquid compositions. The slowest *pH* change can be observed in the lowest section close to the inlet nozzles, where *pH* change is mainly due to the convective transport of the liquid from the upper regions of the column. Until a *pH* of about *pH* $= 6.5$ (that means during about the first $t = 40$ s) the *pH* drops much quicker than during the following about $t = 60$ s. First the *pH* in the upper sections decreases, then in the lower ones. The *pH* value stagnates at the bottom of the column, for up to $t = 40$ s in the high viscosity case (Fig. 12, c) around the starting *pH*, while in the upper investigated sections the CO_2-absorption is already in progress. For increasing viscosity, the pH change becomes slower, showing the decreased mass transfer rate.
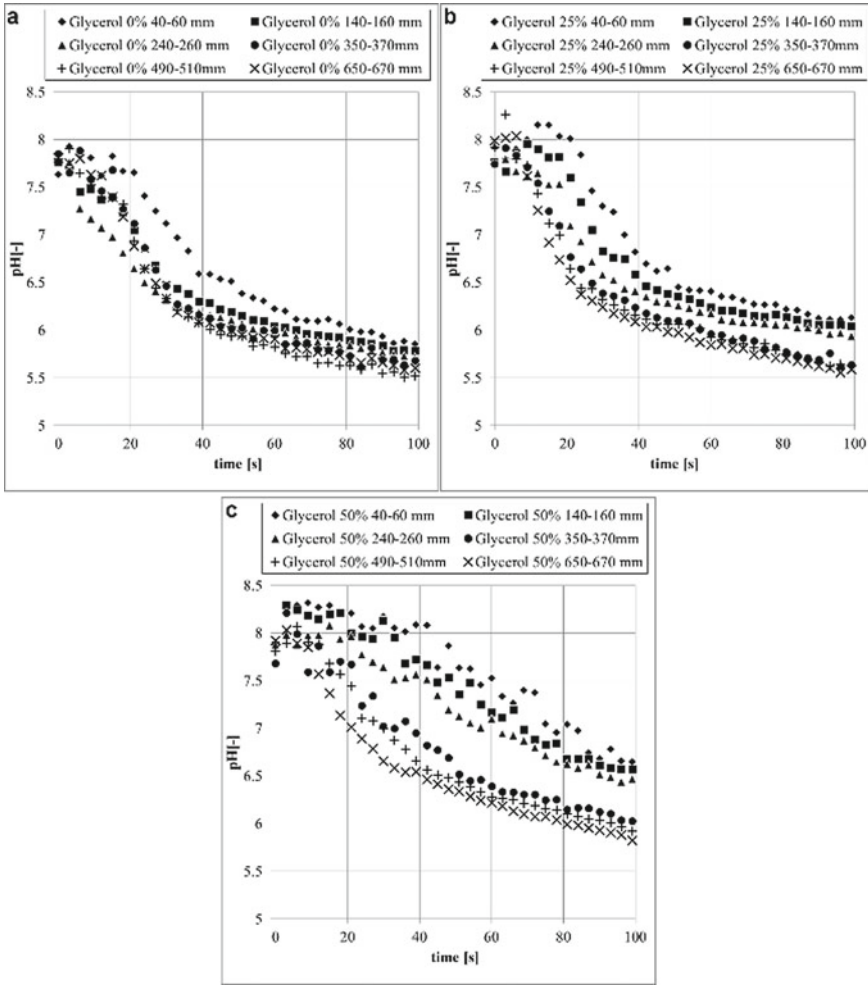
Fig. 12 Change of pH at different vertical positions in the column during the first 100 s: **a** pure water, **b** 25% glycerol, and **c** 50% glycerol

4.3 Mass Transfer Coefficients

From the known bubble parameters and pH-measurements the mass transfer coefficients in the bubble column can be calculated. For this, first of all, the total bubbly liquid volume in the bubble column can be determined from the bubble formation frequency f, the column height h, the mean absolute bubble velocity u_b, the liquid volume in the column V_c and the bubble volume V_b:

$$V_{tot} = V_c + V_b f \frac{h}{u_b} \tag{1}$$

The gas holdup can then be expressed as:

$$\varepsilon = \frac{V_{tot} - V_c}{V_{tot}} \tag{2}$$

The specific interfacial area of the bubbles is then calculated by an equation from Akita and Yoshida [17]:

$$a = 6\frac{\varepsilon}{d_b} \tag{3}$$

The diffusion coefficient of CO_2 is calculated by a correlation of Song et al. [18], since it is in good agreement with experimental results for water-glycerol mixtures, measured at different temperatures.

$$D^{CO_2, water-glycerol} = 0.3169\, T\,(°C)^{0.5206} \mu(cP)^{-0.7407} \tag{4}$$

The mass transfer coefficient k_l can then be calculated from the Sherwood number Sh, the mean bubble diameter d_b and the diffusion coefficient D^{CO_2} as:

$$k_l = \frac{Sh \cdot D^{CO_2}}{d_b} \tag{5}$$

A correlation for oscillating bubbles [19] has been applied to compute the Sherwood number:

$$Sh = 2 + 0.015\, Re_b^{0.89} Sc^{0.7} \tag{6}$$

with:

$$Re_b = \frac{u_s \cdot d_b \cdot \rho_l}{\mu_l} \text{ and } Sc = \frac{\mu_l}{D^{CO_2} \cdot \rho_l}$$

The volumetric mass transfer coefficient can now be calculated as

$$k_l a = k_l \cdot a \tag{7}$$

As an example, in Fig. 13, the change of the mass transfer coefficients k_l and $k_l a$, calculated like this from the Sherwood number, is represented for different liquid viscosities and surface tensions. The value of k_l (Fig. 13, left) continuously decreases with increasing viscosity and decreasing surface tension (higher SDS surfactant concentration). On the other hand, with the addition of surfactant, the bubble size decreases and the gas holdup increases, which results in higher $k_l a$ values (Fig. 13, right) for the mixtures with surfactant. But, with increasing viscosity, also $k_l a$ shows a decreasing trend.
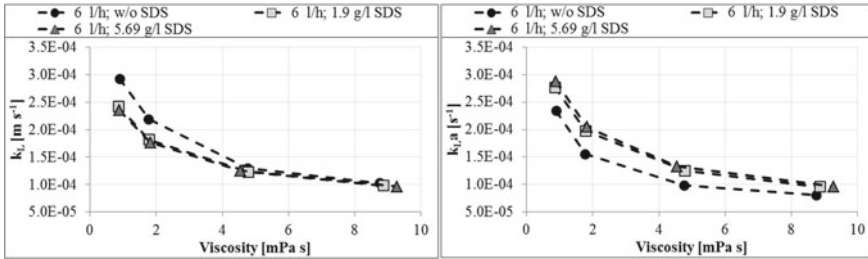
Fig. 13 Mass transfer coefficient k_l (left) and volumetric mass transfer coefficient $k_l a$ (right), calculated from the Sherwood number, at different surface tension and viscosity

4.4 Liquid Velocity

An example of results obtained by PIV for the liquid velocity in the column is shown on Fig. 14. The complete mean vertical liquid velocity field in the centre of the column, assembled from the different measurement sections can be seen on the left, with the strong upward flow in the centre, induced by the rising bubbles, and the descending flow along the column walls. A zoom on the liquid surface region, where the flow is reversed, is shown on the top right image on Fig. 14. A zoom on the bottom, where the four injection nozzles of the bubbles induce four liquid jets, can be found on the right bottom image.

This general aspect changes in details, depending on viscosity and surface tension (profiles on Fig. 15 show, due to symmetry, only one half of the column diameter). The biggest difference can be recognized for the lowest velocity profiles close to the nozzles (Fig. 15, bottom). Higher velocity peaks due to the injection nozzles are observable for the 50% glycerol-water-surfactant solution in the centre part of the column ($0.35 < x < 0.7$). The vertical velocity profiles become more even above $h = 0.2$ m, since the bubbles occupy the whole column width (Fig. 15, centre). After $h = 0.35$ m, the highest vertical liquid velocity can always be measured in the highest viscosity solution. The profile of the section close to the liquid surface (Fig. 15, top) shows the reversing vortex near the column wall ($x = 0$).

5 Conclusions

In a model bubble column bubble size and velocity, CO_2-mass transfer from gas to liquid, and the liquid velocity were examined experimentally by optical measurement techniques for different parameter variations, viscosities and surface tensions. For this, the optical techniques had to be further developed, to take into account bubble shadows and reflections, occurring in the laser light sheet when using such techniques (Shadowgraphy, 2T-LIF and PIV). Instantaneous and mean, temporarily and spatially highly resolved results of 2D flow and concentration fields in the column could thus
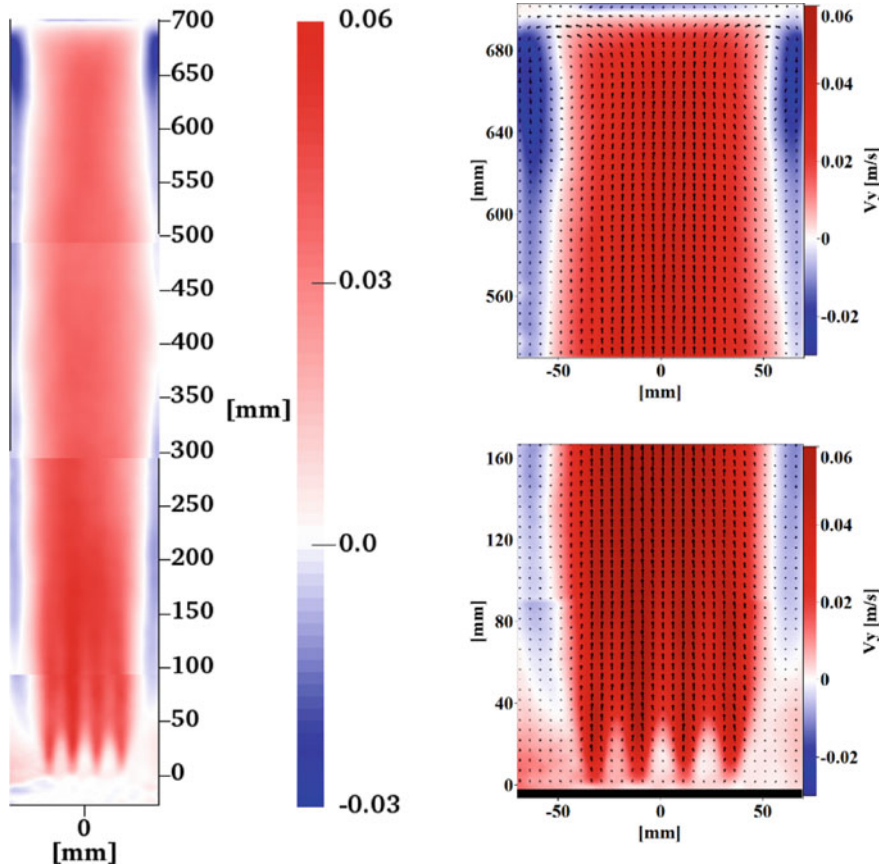
Fig. 14 Example of mean vertical liquid velocity measurements in the four-nozzle configuration of the column. Four measurement sections are assembled in the left image to show the overall aspect of the flow. The top right image shows a detail of the head of the column with the free liquid surface, inducing the downward flow at the column walls. The bottom right image represents the corresponding bottom velocity field, showing the four liquid jets induced by the bubble outlets

be obtained. Significant bubble shrinkage, as well as bubble velocity change from bottom to the top of the column, were observed in the cases without surfactant. With increasing viscosity and surface tension bubble size is increasing. Bubble velocity decreases with increasing viscosity and decreasing surface tension. The effect of surface tension and viscosity change was also investigated on mass transfer through simultaneous 2T-LIF and PIV experiments. The highest mass transfer from gas to liquid can be achieved with pure distilled water. The addition of surfactant and glycerol has no advantageous effect on mass transfer, as could be shown by the calculation of k_L and $k_L a$ values. The liquid flow field is evidently also not the same for different viscosities and surface tensions, due to the change in bubble size and velocity. The highest liquid velocities could be found in the high viscosity solutions.

Fig. 15 Mean vertical velocity profiles at $h = 90$–110 mm (left), $h = 340$–360 mm (centre), and $h = 650$–670 mm (right) for the mixtures with $c = 1.9$ g L^{-1} surfactant
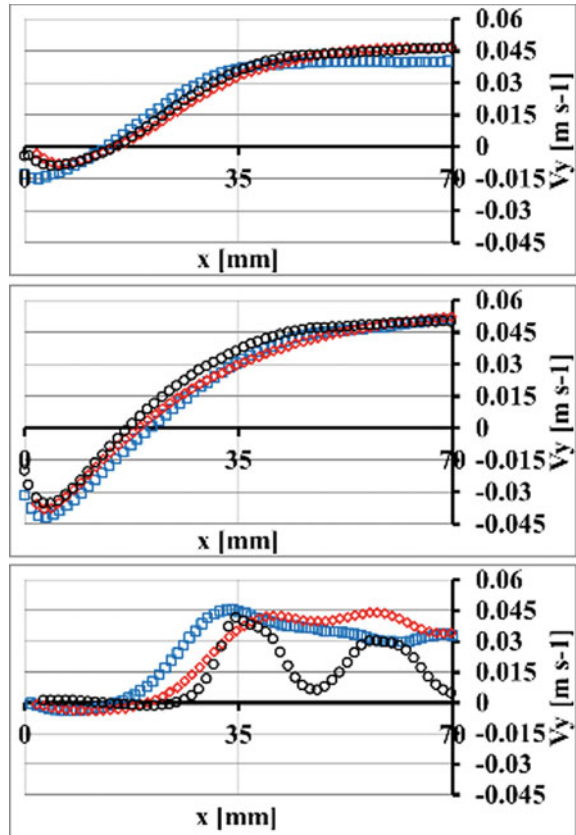
These experimental results are made available to the interested research community via an online database, accessible under https://www.lss.ovgu.de/Info/Downloads.html and have been used for comparison and validation purposes by several numerical groups of this SPP. The comparisons and further details of the measurement results are presented in Chapter "Chemical Reactions in Bubbly Flows".

References

1. Kováts P, Thévenin D, Zähringer K (2020) Influence of viscosity and surface tension on bubble dynamics and mass transfer in a model bubble column. Int J Multiph Flow 123:103174. https://doi.org/10.1016/j.ijmultiphaseflow.2019.103174

2. Kováts P, Thévenin D, Zähringer K (2018) Characterizing fluid dynamics in a bubble column aimed for the determination of reactive mass transfer. Heat and Mass Transfer/Waerme und Stoffübertragung 54(2):453–461. https://doi.org/10.1007/s00231-017-2142-0

3. Rzehak R, Krauß M, Kováts P, Zähringer K (2017) Fluid dynamics in a bubble column: new experiments and simulations. Int J Multiph Flow 89:299–312. https://doi.org/10.1016/j.ijmultiphaseflow.2016.09.024

4. Kováts P, Thévenin D, Zähringer K (2017) Investigation of mass transfer and hydrodynamics in a model bubble column. Chem Eng Technol 40(8):1434–1444. https://doi.org/10.1002/ceat.201600679

5. Bordas R, Roloff C, Thevenin D, Shaw RA (2013) Experimental determination of droplet collision rates in turbulence. New J Phys 15. Artn 045010. https://doi.org/10.1088/1367-2630/15/4/045010

6. Lehwald A, Thévenin D, Zähringer K (2010) Quantifying macro-mixing and micro-mixing in a static mixer using two-tracer laser-induced fluorescence. Exp Fluids 48(5):823–836. https://doi.org/10.1007/s00348-009-0769-4

7. Lehwald A, Janiga G, Thévenin D, Zähringer K (2012) Simultaneous investigation of macro- and micro-mixing in a static mixer. Chem Eng Sci 79:8–18. https://doi.org/10.1016/j.ces.2012.05.026

8. Hlawitschka MW, Kováts P, Zähringer K, Bart HJ (2017) Simulation and experimental validation of reactive bubble column reactors. Chem Eng Sci 170:306–319. https://doi.org/10.1016/j.ces.2016.12.053

9. Kern DM (1960) The hydration of carbon dioxide. J Chem Educ 37:14–23

10. Clift R, Grace JR, Weber ME (1978) Bubbles, drops, and particles. Academic Press, New York, xiii, 380 p 012176950X

11. Ishii MZ (1979) Drag coefficient and relative velocity in bubbly, droplet or particulate flows. AIChE J 25:843–855. https://doi.org/10.1002/aic.690250513

12. Tomiyama A, Kataoka I, Zun I, Sakaguchi T (1998) Drag coefficients of single bubbles under normal and micro gravity conditions. JSME Int J Ser B 41:472–479. https://doi.org/10.1299/jsmeb.41.472

13. Bryn T (1933) Steiggeschwindigkeit von Luftblasen in Flüssigkeiten. Forschung auf dem Gebiet des Ingenieurwesens, A 4:27–30. https://doi.org/10.1007/bf02716943

14. Haberman WL, Morton RK, David WTMB (1953) An experimental investigation of the drag and shape of air bubbles rising in various liquids. David W. Taylor Model Basin, Washington. https://www.biodiversitylibrary.org/item/102131

15. Maxworthy T, Gnann C, Kurten M, Durst F (1996) Experiments on the rise of air bubbles in clean viscous liquids. J Fluid Mech 321:421–441

16. Grace JR (1973) Shapes and velocities of bubbles rising in infinite liquids. Trans Inst Chem Eng 51:116–120

17. Akita K, Yoshida F (1974) Bubble size, interfacial area, and liquid-phase mass transfer coefficient in bubble columns. Ind Eng Chem Process Des Dev 13(1):84–91. https://doi.org/10.1021/i260049a016

18. Song D, Seibert AF, Rochelle GT (2014) Effect of liquid viscosity on the liquid phase mass transfer coefficient of packing. In: 12th international conference on greenhouse gas control technologies, GHGT-12. Energy Procedia 63:1268–1286. https://doi.org/10.1016/j.egypro.2014.11.136

19. Brauer H (1981) Particle/fluid transport processes. Chem Eng 19:81–111

Modeling and Simulation of Convection-Dominated Species Transport in the Vicinity of Rising Bubbles

Andre Weiner and Dieter Bothe

Abstract For multiphase contactors, like bubble column reactors, it is of highest interest to predict how the gas dissolves and reacts in the liquid phase. This mass transfer process strongly depends on convection-dominated, extremely thin species boundary layers forming at the liquid-side of the bubble's surface. Numerical simulations can play a significant role in understanding and predicting the complex interactions between flow dynamics and species transport, but the direct solution of both phenomena at the same time is currently not possible. This chapter summarizes two approximation approaches for the efficient and accurate simulation of convection-dominated concentration boundary layers. The first approach is a subgrid-scale model which allows to handle boundary layer widths that can be far smaller than the first cell layer at the interface in the computational mesh. Convective fluxes, diffusive fluxes and reaction source terms in the finite volume method are corrected based on non-linear reconstructions of the species boundary layer profiles normal to the interface. The second method is a hybrid simulation approach that solves the two-phase flow problem based on the Volume-of-Fluid method and uses a single-phase solver for species transport simulations. The concentration boundary layer is computed using a highly resolved surface-aligned single phase mesh.

1 Introduction

Bubbly flows in bubble column reactors exhibit a large range of bubble sizes undergoing topological due to break-up or coalescence. However, state-of-the-art numerical methods for interface-resolved simulations struggle already with much simpler settings due to enormous computational costs. A millimeter-sized bubble rising in water at room temperature reaches a terminal velocity of approximately $v = 0.25$ m/s. Assuming a kinematic liquid viscosity of $\nu = 10^{-6}$ m^2/s yields a Reynolds number of

A. Weiner · D. Bothe (✉)

Technical University of Darmstadt, Mathematical Modeling and Analysis, Alarich-Weiss-Str. 10, 64287 Darmstadt, Germany

e-mail: bothe@mma.tu-darmstadt.de

$$Re = \frac{d_b U_b}{\nu_l} = \frac{0.001 \times 0.25}{10^{-6}} = 250. \tag{1}$$

In the absence of surface active agents or contaminants, the gas-liquid interface may be considered as fully mobile. The shear forces at the bubble surface are small compared to, for example, the ones acting at the solid-liquid interface of a rising particle. As a consequence, only a small layer of liquid is significantly set in motion around a rising bubble. The wake region may be considered an exception to this observation in some cases. The thickness of the flow boundary layer δ_h around a nearly spherical rising bubble can be estimated using the relation

$$\delta_h = \frac{d_b}{\sqrt{2\,Re}}. \tag{2}$$

We refer to page 263 in Ref. [1] for more details. Also for non-spherical bubble shapes, the scaling often follows the relation $\delta_h \propto d_b/\sqrt{Re}$. Coming back to the example of a millimeter-sized bubble, the average flow boundary layer width is roughly fifteen times smaller than the bubble diameter.

The transport of chemical species within the liquid bulk occurs on smaller length scales compared to the transport of momentum. The ratio of the length scales is often characterized by means of the Schmidt number $Sc = \nu_l/D$, where D stands for the molecular diffusivity of a chemical species dissolved in the liquid phase. As an example, the Schmidt number for oxygen dissolved in water at room temperature is about 400. The ratio between species and flow boundary layer at a clean gas-liquid interface follows the trend $\delta_c \propto \delta_h/\sqrt{Sc}$. Considering a millimeter-sized oxygen bubble and the previous specimen calculation for the flow boundary layer, it can be stated that the average species boundary layer width is roughly twenty times smaller than its flow counterpart, and that it is even 300 times smaller than the bubble size. The latter fact may be also expressed more directly using the Péclet number $Pe = Re\,Sc$ and the scaling $\delta_c \propto d_b/\sqrt{Pe}$.

The consequence of this large gap between bubble size and boundary layer thickness can be experienced firsthand by looking at Fig. 1. An oxygen bubble moves in a confined channel and forms a Taylor bubble. The gaseous oxygen dissolves and reacts with a copper complex present in the liquid phase. The reaction product

Fig. 1 Oxygen bubble moving (from left to right) in a channel filled with water. The oxygen dissolves and reacts with a copper complex present in the water phase yielding a brownish color. Picture from www.dfg-spp1740.com

displays a yellow-brown color. Looking at the picture, it appears that most of the oxygen is dissolved at the bottom of the bubble (the left end in Fig. 1). What actually happens is that the oxygen dissolves over the entire surface of the bubble while being transported in an extremely thin layer to the rear part of the bubble. Only when the flow detaches from the interface, the reaction product becomes visually accessible in the bubble wake.

The problem of thin boundary layers or, in terms of dimensionless numbers, high Schmidt and Péclet numbers poses an enormous challenge for both experimental and numerical means of investigation. The mass transfer rate, but also yield and conversion in the presence of a chemical reaction are to a large extend determined by the species boundary layers. It goes without saying that investigations are even more challenging if chemical reactions take place and multiple species have to be considered.

The only class of numerical approaches that is currently able to approximate species transfer at rising bubbles for realistic Péclet numbers relies on subgrid-scale (SGS) modeling. There are currently two branches of such subgrid-scale models available in the literature. The first model type was designed for Front-Tracking based two-phase flow solvers [2–4] and completely omits the numerical solution of the species transport equation on the Eulerian grid in a defined narrow region around the interface. Instead, each front marker point carries an additional scalar value representing the amount of species in the boundary layer in its vicinity. The boundary layer mass is updated each time step by reconstructing and evaluating the species distribution in interface normal direction. Once the boundary layer mass of a marker point exceeds a certain threshold, the species is released into the liquid bulk. The approach is relatively simple but very effective in terms of accuracy. A drawback is that it is currently not clear how to incorporate two-sided interactions between boundary layer and liquid bulk. Recent approaches only release species into the liquid bulk but ignore the ambient bulk concentration.

The second class of subgrid-scale models was developed for finite volume solvers and reconstructs the concentration profile in interface normal direction based on the liquid-side concentration in an interfacial cell [5–11]. The reconstructed profile is then used to correct the face-fluxes in the typical finite volume discretization of convection and diffusion terms. In the context of two-phase approaches this correction mechanism has been implemented in Volume-of-Fluid [5, 6, 9] and Interface-Tracking [7, 11] approaches. Since the profile reconstruction is based on concentration values close to the interface, changes in the liquid bulk concentration are naturally included. However, this advantage comes at the cost of increased algorithmic complexity or restricted mesh topology support close to the gas-liquid interface.

This chapter summarizes recent developments in the flux-based subgrid-scale modeling approach [8–10]. These developments concern the profile reconstruction, the flux correction, the extension to multiple species and reactions, and the validation of new models.

2 Numerical Methods

2.1 Geometrical Volume-of-Fluid Approach

The results presented in the following sections have been obtained with two Volume-of-Fluid based solvers, namely Free Surface 3D[1] (FS3D) [5, 6, 9] and Basilisk[2]; we refer to the literature cited in Chap. 3.1 of [8] for more information on Basilisk. Both solvers transport the volume fraction field using geometrically calculated fluxes. Also the curvature computation, needed for the application of surface tension forces, relies on height functions in both approaches. The main differences between the solvers relates to two important features: adaptive mesh refinement and the two-scalar approach for species transport.

The concentration jump of chemical species at the gas-liquid interface poses a severe difficulty for numerical modeling. The two-scalar approach implemented in FS3D [5] overcomes this challenge by introducing two distinct scalar fields for each chemical species: one for the liquid and one for the gas phase. Both fields are connected via mass-exchange terms in interface cells. Moreover, convective species fluxes in interface cells rely in the geometrically computed fluxes for the volume-fraction transport. Therefore, no artificial mass transfer due to erroneous convective fluxes takes place. The two-scalar approach requires more memory than, for example, the single-field approach, but the numerical solution of the species transport is characterized by a comparatively high accuracy, especially in the interface vicinity.

The computational mesh in FS3D consist always of one or more structured Cartesian blocks. Structured meshes allow efficient computations and enable simplified implementation and testing of new algorithms. Such meshes are also favorable when a uniformly high resolution is required and the spatial scales vary over less than three to four orders of magnitude. In the field of bubbly flows, the uniform resolutions practically limits simulations to Reynolds numbers below roughly 500 and moderate shape deformations. Currently, it is not feasible to simulate the flow dynamics of characteristic bubble shapes like spherical cap or dimpled ellipsoidal.

The range of investigated scales can be increased by means of numerical techniques like adaptive mesh refinement, as employed in the Basilisk-based flow solver; see Fig. 2. The mesh resolution is adapted locally according to the flow features in the simulation. The results presented in the following sections were obtained using a so-called wavelet refinement. The mesh adaptation algorithm works as follows: first, the solution on the current grid is mapped to the next coarsest refinement level by an averaging process. Then, the fine grid solution is reconstructed from the mapped field. The discrepancy between the up-sampled and the actual field is used as an error estimator and can be compared against a fixed user-defined criterion. If the accuracy loss due to down-sampling is higher than the given threshold, the grid is

---

[1] www.mma.tu-darmstadt.de.

[2] www.basilisk.fr.
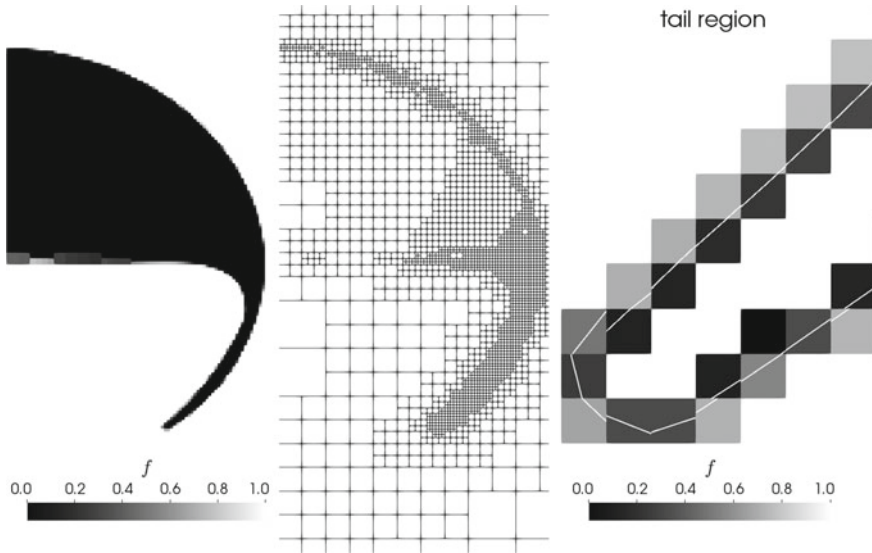
Fig. 2 Typical elements of a Volume-of-Fluid simulation in Basilisk (www.basilisk.fr). Volume fraction field (left), adaptively refined background mesh (center), and reconstructed interface elements (right)

refined. If the information loss is marginal, the grid is coarsened. The refinement and un-refinement operations are limited by a prescribed lower and upper bound of the allowed refinement level.

A drawback of two-phase flow solver implemented in Basilisk is that the two-scalar approach for species transport is currently not implemented. Therefore, the following chapters present results obtained with FS3D as well as with Basilisk.

2.2 Single-Phase Approximation

The single-phase approximation or hybrid approach was developed due to a lack of available reference data for subgrid-scale model validation. The idea is to combine the robustness and efficiency of Volume-of-Fluid simulations with the accuracy of surface aligned unstructured meshes. The combination of these favorable attributes happens in three steps:

1. A two-phase Volume-of-Fluid simulation, as described in the previous section, is executed to obtain the bubble rise velocity, the interface deformation, and the velocity vector at the gas liquid interface.
2. An explicit representation of the bubble shape is created based on the volume fraction field and saved as a geometry file; see Fig. 3.
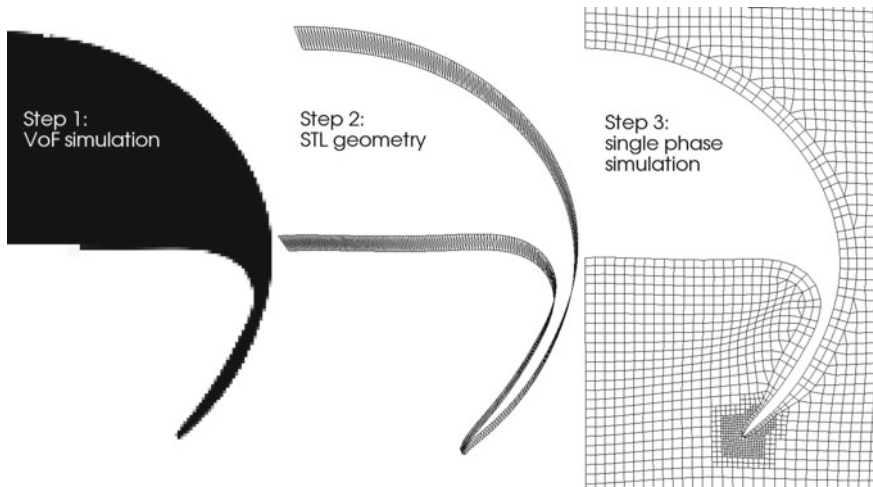
Fig. 3 Three essential steps in the single phase approximation

3. A standard single-phase simulation for flow dynamics and species transport is executed with the bubble being a prescribed and fixed domain boundary. The unstructured mesh employs surface-aligned cell-layers at the surface of the bubble.

The single-phase approach requires to recompute the steady flow field in the liquid phase. Based on the bubble rise velocity, an inflow velocity is applied at the outer domain boundary. Due to the absence of the gas phase, the interface velocity at the bubble-boundary must be modeled. A standard free-slip boundary condition may lead to qualitatively different flow fields compared to the two-phase flow simulation. Therefore, the interfacial velocity is mapped from the two-phase simulation to the single-phase simulation by means of machine learning. For more details on the implementation and the setup, the reader is referred to Sect. 3.3 in [8].

Once the flow field in the liquid phase is recomputed, transport equations for chemical species can be solved with excellent accuracy at low computational costs. At the bubble surface, a Dirichlet boundary condition for the transfer species is employed. For bulk or product species, a Neumann condition is applied. The current implementation does not account for the varying species concentration in the gas phase, which is a drawback compared to the two-scalar approach in FS3D. However, the main aim of the single-phase approach is the creation of high-fidelity reference data for the local and global mass transfer under complex conditions. Here, complex relates to the shape deformation, the flow field close to the bubble, or the mass transfer enhancement in the presence of chemical reactions.

3 Modeling of Convection-Dominated Concentration Boundary Layers

3.1 Overview

As outlined in the introduction, in a two-phase flow simulation it is hardly possible to place sufficient cells in the species concentration boundary layer. In the best case scenario, there is only a quantitative impact on the computed mass transfer performance. In scenarios where the species transport is tightly coupled with the flow dynamics [7, 11], more drastic side-effects occur. Results may be qualitatively wrong or the entire flow simulation may become unstable due to numerical problems in the solution of the species transport equations. Therefore, it is an essential step to understand the influence of low mesh resolution on the species transport. Once the main effects are isolated, subgrid-scale models can be designed to mitigate these effects. Here, two attempts to improve the species transport solution in the boundary layer are presented: the first one is based on analytical solutions of a simplified substitute problem, and the second one leverages highly resolved boundary layer data by means of machine learning. Both approaches are relatively easy to implement if the cells of the computational mesh are aligned with the interface. If the discrete interface is given by the PLIC elements in a Volume-of-Fluid simulation, the analytical profile functions are favorable, as detailed in Sect. 3.4.

3.2 Effect of Insufficient Mesh Resolution

Figure 4 depicts the first cell-layers of a mesh suitable for a finite-volume discretization of the liquid phase. The interface Σ separates the gas domain Ω^- from the liquid domain Ω^+. In gas-liquid systems, the high-Schmidt number problem is specific to the liquid phase because the Schmidt number in the gas phase is at least one order of magnitude smaller than in the liquid phase. Therefore, we focus only on the liquid phase in the explanations following hereafter. Important for further considerations are the cell-faces aligned with the interface, denoted by f_i^Σ, and the first layer of cell-faces normal to f_i^Σ, denoted by f_i^o ("opposite"). Moreover, it is assumed that the scalar fields for the species concentration are available in the cell-center of each control volume as values c_i.

In the numerical solution of a convection-diffusion equation using a finite volume discretization, the values and normal derivatives of a field have to be interpolated to the cell faces f_i to compute convective and diffusive fluxes. The species concentration field in a convection-dominated boundary layer is characterized by strong changes in direction normal to the interface. Therefore, the flux computation in interface normal direction is, in most cases, the one introducing the largest errors to the solution. The
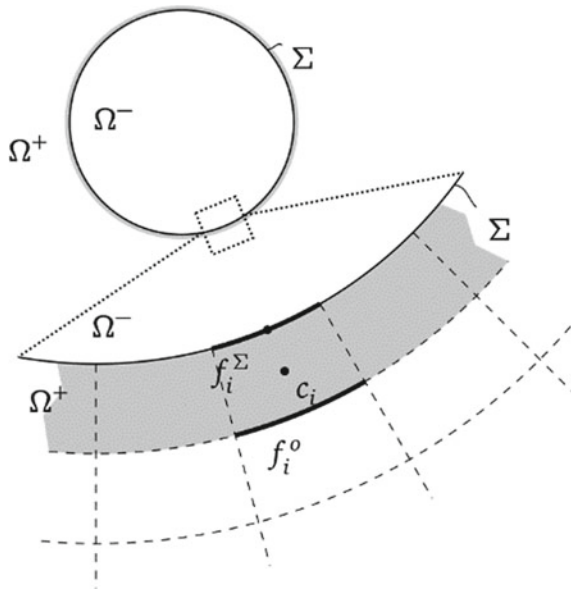
Fig. 4 Simplified 1D scenario to analyze the effect of low mesh resolution on convective and diffusive fluxes in the boundary layer

following explanations focus on the 1D scenario described before with x/δ_c being the normalized distance to Σ. A single reaction of type $2A + B \rightarrow P$ is considered, where A is the species being transferred from the gas to the liquid, B is a species present in the liquid bulk, and P is the formed product. This reaction is complex enough to explain also the main error sources in reactive species boundary layers with several parallel reactions involving additional species. It should also be noted that the reference concentration profiles, the cell averages and the interpolation lines in the following figures are computed from the numerical solution of boundary-value problems; see the footnotes in Chap. 5 of [8] for more details. The profiles are not artificially exaggerated but rather mitigated to allow a visual assessment.

Figure 5 focuses on the flux interpolation for the transfer species A. The typical normalized concentration profile $\tilde{c}_A$ corresponds to the solid blue line. In the scenario depicted in Fig. 5, the transfer species decays to zero within the first two cells. The numerical solution provides cell-centered values $\tilde{c}_{A,i}$ that correspond to profiles which are assumed to be constant within each control volume. In Fig. 5, the shaded blue areas correspond to the exact cell-averages in each cell computed from the solid-blue reference profile. Based on these values, the derivatives $d_x\tilde{c}_A(x/\delta_c = 0)$ and $d_x\tilde{c}_A(x/\delta_c = 0.5)$ as well as the concentration value $\tilde{c}_A(x/\delta_c = 0.5)$ have to be reconstructed (interpolated) in the first cell. A standard linear interpolation between the cell-centered values corresponds to the solid orange lines depicted in Fig. 5. Comparing the slope of the blue reference profile and the orange line segments clearly shows that the magnitude of the diffusive fluxes is underestimated at $x/\delta_c = 0$
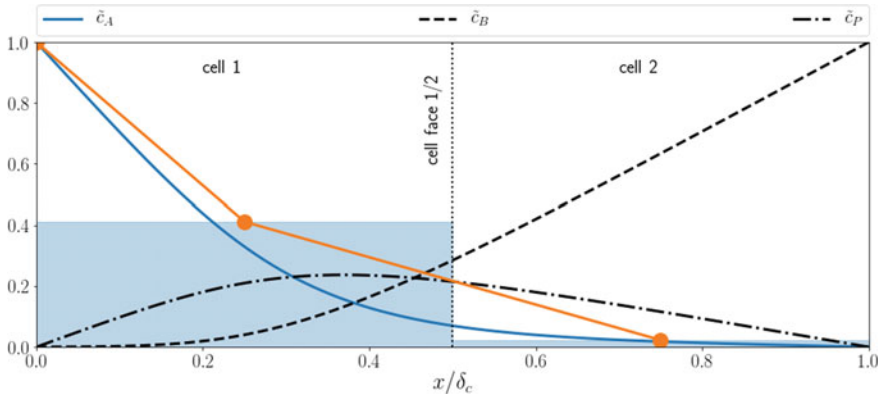
Fig. 5 Effect of low mesh resolution on convective and diffusive fluxes for the transfer species A

and over-predicted at $x/\delta_c = 0.5$. Considering the interpolated face value at $x/\delta_c = 0.5$, convective fluxes are strongly over-predicted. As the mesh gets refined, and more cells are located within the boundary layer, the interpolation error changes quantitatively and qualitatively. For this 1D scenario with exact cell-centered values, the interpolation error in the diffusive flux at $x/\delta_c = 0$ decreases monotonically with increasing resolution. The error in the diffusive flux at $x/\delta_c = 0.5$ is non-monotonous and changes sign. The interpolation error in the convective flux at $x/\delta_c = 0.5$ is also non-monotonous but does not change sign.[3]

All the aforementioned interpolation errors have a different weight in the resulting error of the species concentration field depending on the local Péclet number. Due to the complex changes of the individual error sources, the fact that even more error sources are present in the numerical solution of the full boundary layer problem, and the propagation of errors make it extremely difficult to provide a general estimate on how the resulting mass transfer is affected. However, the concentration boundary layer in 3D simulations of rising bubbles is typically so far below the necessary one that the global mass transfer is almost always underestimated. The same statement does not necessarily hold true for the local mass transfer.

The over- and underestimation of diffusive and convective fluxes also occurs for the bulk species B and the product species P. In many scenarios it is sensible to assume that the diffusive fluxes of both species is zero at the interface, meaning that neither B nor P is transferred to the gas phase or adsorbed onto the interface. Then the remaining error sources result from the interpolation at the first cell face normal to the interface. In contrast to the transfer species, even for the 1D example, errors in both diffusive and convective fluxes change non-monotonously, and the errors also change sign. For more information and visualizations, the reader is referred to Sect. 5.1 in [8].

---

[3] https://andreweiner.github.io/reveal.js/phd_defence.html#/3/2.
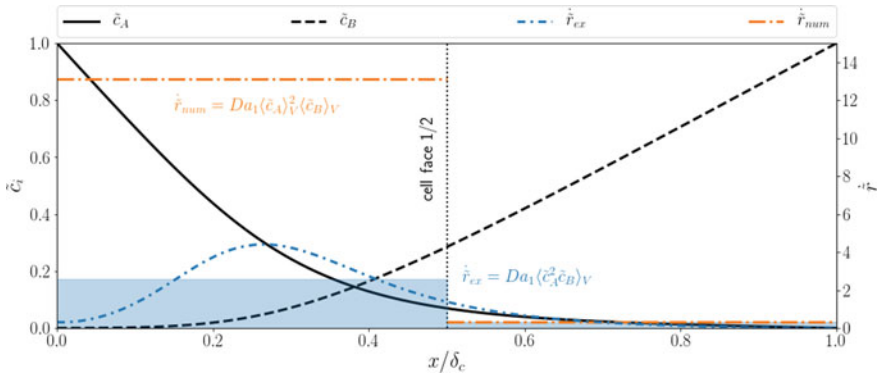
Fig. 6 Effect of low mesh resolution on the approximation of the reaction source term

Besides the fluxes, also reaction source terms introduce an error in case of insufficient mesh resolution. This effect has not been considered in the first data-driven implementation of the SGS model [10] because only a decay reaction was investigated. The effect depicted in Fig. 6 occurs if multiple educts are involved in a reaction. The effect is best described by the statement that the product of two averages is not necessarily equal to the average of the product. Computing the reaction source term in a single reaction from the cell-centered values $\tilde{c}_{A,i}$ and $\tilde{c}_{B,i}$ yields a much larger source term in the first cell compared to the one computed from the exact profiles. The effect is enhanced if the reaction order is higher, e.g., if two molecules of A are consumed in the reaction, and the overall reaction becomes third order.

Finally, it should be emphasized that all the error sources introduced in this section will influence one another, and it is difficult to predict the integrally observed effect on the concentration field. Moreover, for coupled reactions, the errors in one species concentration field influence the solution of all other species via the reaction source terms. Fortunately, the reference profiles depicted and analyzed in Figs. 5 and 6 can be approximated with high accuracy even if the boundary layer is completely embedded in a single cell layer. Non-linear profile reconstructions allow to compute improved flux estimates. The following section describes how physical profiles can be reconstructed based on analytical solutions and machine learning.

3.3 Analytical and Data-Driven Profile Reconstruction

Figure 7 shows the analytical solutions of a simplified substitute problem in case of physisorption and a first-order chemical reaction of the transfer species. These two-dimensional profiles have been used previously in subgrid-scale models for species transport in two-phase flows, and mathematical details on the substitute problem may be found in [5] for physisorption and in [6] for the reactive scenario. The mathematical expressions for both cases are depicted above each sub-figure. Useful approximate
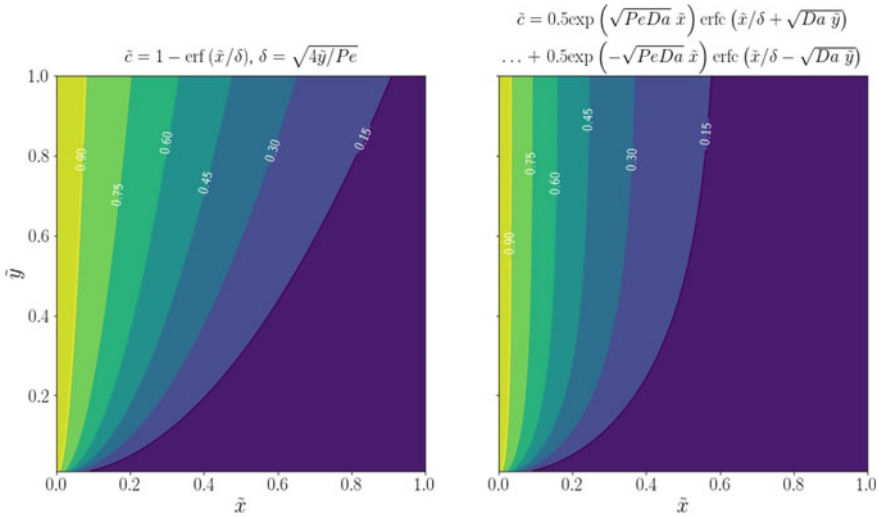
Fig. 7 Analytical solution of a simple substitute problem for physisorption (left) and a first order decay reaction (right)

profiles for the correction of numerical fluxes can be generated by evaluating the analytical solutions at a constant value of $\tilde{y}$. The resulting profile may be imagined as a slice through the concentration field in $\tilde{x}$-direction. The next logical step is to determine a sensible value for the unknown $\tilde{y}$.

Sensible approximations for $\tilde{y}$ may be found in two different ways outlined hereafter for physisorption. The known variables for each interfacial cell are the concentration at the liquid-side of the interface, the concentration in the cell center, and the cell geometry. To avoid round-off errors, the concentration profile of the transfer species is typically normalized with its interfacial value. In the simplified 1D scenario, the cell geometry may be reduced to the extension of the cell in interface normal direction and the position of the cell center. The cell-centered concentration can be interpreted in several ways, namely as the value of some concentration profile at the center or as the average concentration value in the cell. The latter interpretation is consistent with the formal definition of field values in a standard second-order finite volume discretization.

Figure 8 depicts the estimation of $\tilde{y}$ based on the interpretation that the cell-centered concentration value in the flow solver must be equal to the concentration value of the approximate profile function at the given distance from the interface. Note that for the special case of pure physisorption, it is more practical to adjust directly the parameter δ instead of $\tilde{y}$. In the example depicted in Fig. 8, the iteratively found fitting parameter is labelled as δ_{num}. If the model parameter is known, the reconstructed profile is suitable to compute improved numerical fluxes. In [5, 6], the concentration profile was used only to correct the diffusive flux at the interface. This fitting and correction scheme also appears in wall function modeling for turbulent flows or heat
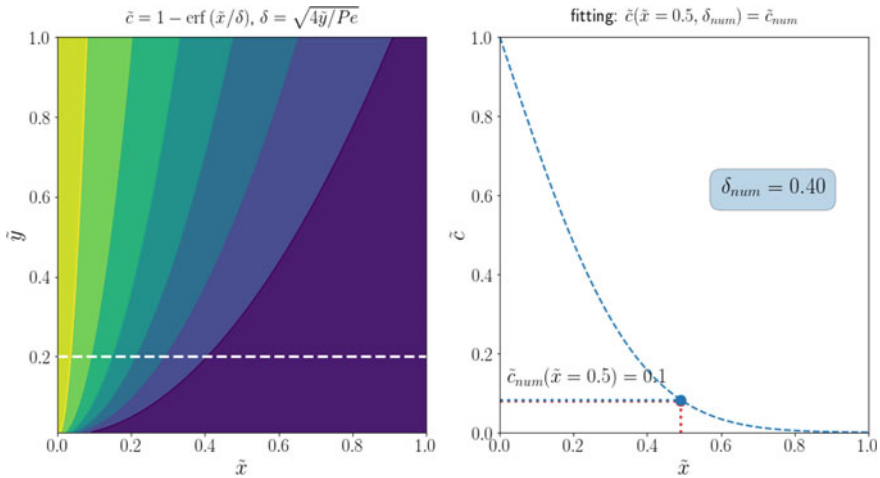
Fig. 8 Distance-based fitting of the model parameter for physisorption

transfer. Bothe and Fleckenstein [5] state that approximately one refinement level can be saved employing the non-linear flux correction at the interface, which results in a significant reduction of the mesh size, especially in 3D simulations. However, mass transfer simulations with physical Schmidt numbers require a saving factor of roughly 10–20.

Fortunately, the effectiveness of the profile reconstruction and flux correction can be significantly improved with a few small changes. The first modification, introduced in [9], is related to the profile reconstruction. Figure 9 visualizes how the model parameter δ_{num} is estimated based on the interpretation of the cell-centered concentration as the average cell value. The model parameter is iteratively adjusted until the integral of the approximate profile function over the cell volume is equal to the cell-centered value provided by the flow solver. Especially if the species transport equation is discretized explicitly in time, the integral fitting approach yields better flux approximations compared to the distance-based fitting because small errors in the numerical fluxes quickly lead to unphysical concentration over- and undershoots. The integral fitting condition significantly improves the connection between the amount of the species present in an interface cell and the amount of species leaving or entering the cell due to convective or diffusive fluxes. A second improvement introduced in [9] is a logical consequence of the error analysis in the previous section, namely that the reconstructed profile is also used to correct the convective and diffusive fluxes at all cell faces of each interfacial cell. The modified profile reconstruction and flux correction allows to approximate fully embedded boundary layers with astonishingly high accuracy. In [11], this approach was extended to account for a first-order reaction of the transfer species.
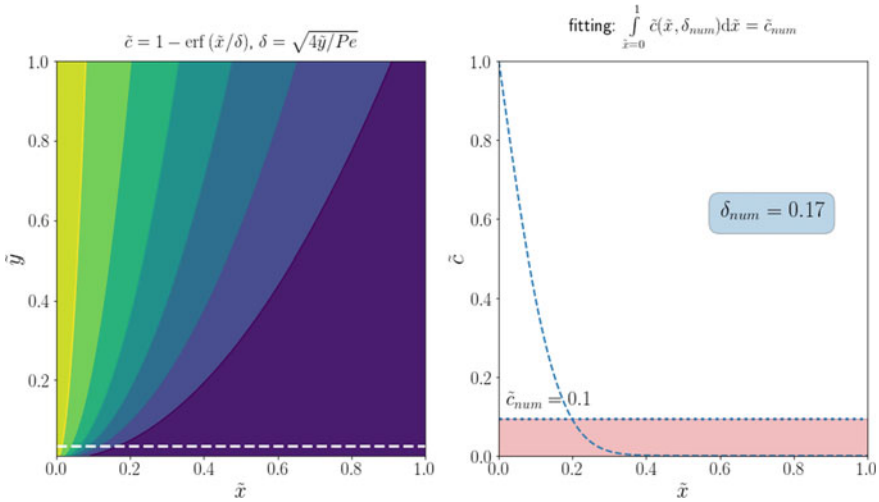
Fig. 9 Integral fitting of the model parameter for physisorption

Going beyond a single species and more complex or multiple reactions, the aforementioned approaches are limited by the availability of analytical profile functions. However, the numerical solution of moderately complex substitute problems, complex in terms of geometry and flow field, requires little effort and is practically not limited by the reaction type. A purely data-driven version of the subgrid-scale modeling approach described before would require the following steps:

1. Define a substitute problem that encompasses the main transport and reaction mechanisms and that can be solved with little computational effort.
2. Define model parameters characterizing the transport and reaction mechanisms, e.g., the Péclet and Damköhler numbers of all species.
3. Run a parameter variation of the substitute problem such that the target regime in the full simulation is included in the parameter space.
4. Extract the model parameters and the corresponding fluxes from the numerical data and employ them in the full simulation as replacement of the analytical solution.

The data extraction in the fourth step presumably requires some more detailed information and is therefore outlined in Fig. 10. A 1D species concentration profile in interface normal direction is considered. The mesh resolution in the numerical solution of the substitute problem should be high enough to place at least 10–20 cells within the boundary layer. Note that this value range is simply a rule of thumb. Fewer cells are possible if some loss in accuracy can be tolerated. More cells might be required if the concentration profiles are, for example, non-monotonous and have several extrema within the considered distance from the interface. The discretization scheme used to solve the substitute problem must be able to capture convective and diffusive fluxes, as well as the reaction sources terms with high accuracy. If this

l/l_{max}	$\langle \tilde{c}_A \rangle_l$	$\tilde{c}_A|_l$	
0.25	0.65	0.32	...
0.50	0.41	0.07	...
0.75	0.29	0.02	...
...	...	...	...
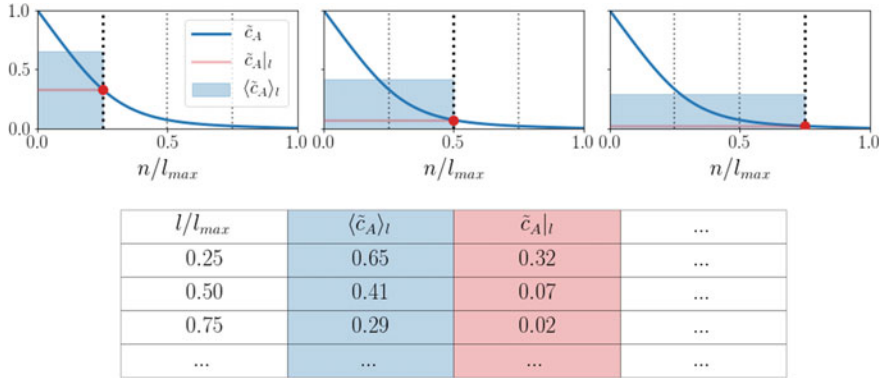
Fig. 10 Feature extraction from the numerical solution of the substitute problem

criterion is fulfilled, one can now start to merge the cells in interface normal direction, one cell at a time, and compute how a well-resolved solution would look like on a coarser mesh. For example, considering the rightmost subfigure in the upper row of Fig. 10, the exact average concentration $\langle \tilde{c}_A \rangle_l$ of a single cell of length $l/l_{max} = 0.75$ can be computed by the volume-weighted average of the cell-centered concentration values in the first three cells. Moreover, the concentration at the first cell face of the extended cell $\tilde{c}_A(l/l_{max} = 0.75)$ can be approximated with high accuracy from the two neighboring cell-centered values. In the same way, the concentration normal derivative at the first cell face and at the interface can be computed. Following this procedure up to a sensible maximum distance l_{max} from the interface, one assembles input-target-value-pairs depicted in the table in Fig. 10.

An important step in the creation of data-driven SGS models is to decide which information should be extracted from the numerical solution of the substitute problem. An important criterion is that the model input data must be available in the target simulation. This requirement is more challenging to fulfill than it may seem on first sight. For example, the numerical solution of the substitute problem might be time-dependent and so is the full simulation. However, time is not a suitable candidate as model input. The transient behavior of both numerical solutions is most likely very different such that the concentration fields at the same time-instance are not comparable. This difference is by design since the substitute problem must be significantly simpler than the full problem. However, it is not necessarily true that there are no comparable states. The main challenge and maybe the art of SGS modeling is to find a small set of model inputs to map between similar states in both solutions.

A quite efficient feature to map results from the substitute to the full problem is the average concentration in interface normal direction. In the data-driven SGS modeling approach presented in [8, 10], it is identified as the feature explaining most of the variance in the numerical fluxes in convection-dominated concentration boundary layers. Due to the design of the substitute problem, the average concentration also

encompasses, to a large extend, effects like developing boundary layers, acceleration and deceleration as well as curvature effects. Note that it is still possible that additional model features may lead to an improved model performance.

The final question discussed in this section details how the discrete input-target-value-pairs might be employed in the full simulation. If the gathered data are relatively small, the simplest approach is to interpolate fluxes between the K nearest neighbors in the input space. However, as the data size increases, such non-parametrical approaches become less and less practical since many search operations have to be performed. Instead, in [8, 10] we used multilayer-perceptrons (MLP) to create approximate functions based on the extracted data. MLPs are characterized by high parameter efficiency. For example, in [10] a model with only 230 parameters was sufficient to approximate about two million training data points.

3.4 Implementation in Simulation Approaches

The SGS modeling approaches outlined in the previous section have been implemented and tested in several different two-phase and single-phase flow solvers. The implementation in a geometrical Volume-of-Fluid approach is the most effortful one and was only performed based on the analytical profile functions. In contrast to the explanations in the previous section, the reconstructed interface is typically not aligned with the surrounding cell faces. The concentration profile in each interface cell is still considered to be 1D in interface normal direction, but the integral fitting as well as the flux computation require the solution of complex volume and surface integrals. In Fig. 11, the reconstructed plane segment splits the cubic volume cell

Fig. 11 Cartesian background mesh cell with reconstructed interface and embedded concentration profile normal to the interface
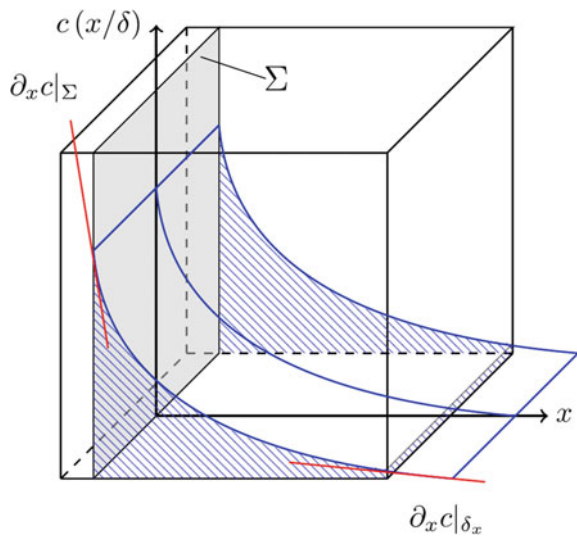
into two sub-cells representing the two phases. The profile function has to be integrated over the remaining volume, representing the liquid phase, to find the model parameter via the integral fitting approach. Once the model parameter is determined, the face average of each flux-term over each face of the liquid phase volume has to be computed. In [9], both volume and surface integrals were evaluated analytically for pure physisorption. Even for a simply decay reaction, the analytical evaluation is no longer practical, and numerical integration would be necessary. If numerical integration is available, it is also possible to employ the data-driven modeling approach in the Volume-of-Fluid context.

The SGS model has been also implemented in an Interface-Tracking approach [7, 11] and in a single-phase solver [8], with the latter case serving mainly for validation. Both implementations are very similar in nature and are therefore outlined jointly hereafter. The implementation requires that the mesh has at least one interface-aligned cell-layer. In contrast to the Volume-of-Fluid approach, the time-discretization is implicit. Therefore, the flux-terms cannot be overwritten directly with SGS information coming from the analytical profile or approximate functions. Instead, the molecular diffusivity coefficient and the face-velocity are adjusted based on the ratio of SGS-prediction to standard discretization. For example, if the standard discretization underestimates the diffusive flux at the interface, then the diffusivity coefficient is artificially increased at these faces. This correction approach is also applied in wall function models in the field of turbulence modeling. For more detailed information, the reader is referred to the literature [7, 8].

3.5 Validation

This section presents only a small excerpt of the extensive validation in [9] for the Volume-of-Fluid implementation, in [7, 11] for the implementation in Interface-Tracking based on analytical profile functions, and in [8, 10] for the data-driven approach. The difficulty in validating the various SGS-model flavors lies in the absence of high-fidelity reference data. Experimental data are only available in the form of integral mass transfer coefficients. Moreover, even for simple cases, the 95% confidence interval can easily be about 50% of the computed mean value [11] and, hence, such data is not suitable to validate a numerical method, where the relative improvement due to the modeling is in the same range. It has been also shown that the local Sherwood number might be sometimes over- and sometimes underestimated as a consequence of insufficient mesh resolution [8]. Consequently, global mass transfer quantities may appear more accurate due to a favorable compensation of different error sources. Therefore, local and global quantities should be compared against reference data. Such reference data can be obtained using semi-analytical approaches. In [5, 6, 9], the analytical flow field solution for a spherical particle rising in Stokes-flow was used to obtain a highly resolved numerical solution of the concentration field in the species boundary layer. This approach provides local and global reference data of high quality. A drawback is that shape and flow field

are not very representative for the highly chaotic regimes encountered in bubble swarms at high Reynolds numbers. Hence, it is difficult to assess how well a model will perform in such complex circumstances. As a step towards more realistic reference data, the hybrid approach outlined in Sect. 2.2 was developed. Currently, the hybrid approach allows to create reference data for the steady rise of highly deformed bubbles with complex flow fields. The extension to dynamic scenarios is planned for future developments.

Based on the hybrid simulation approach, the data-driven SGS models have been assessed for several reaction mechanisms, with the most complex reaction being a parallel-consecutive reaction involving four different species. Important criteria for data-driven SGS models are the ability to generalize to various flow scenarios and an independence of the model performance from the underlying mesh resolution. In both categories, the data-driven SGS model performs approximately as well as the versions based on analytical profile functions for physisorption. Even for complex reactions with multiple species, the deviation in terms of global Sherwood number typically ranges between one and four percent [8, 10]. An analysis of the local Sherwood numbers shows that there is some space for further improvements in regions of high species concentrations close to the interface, for example, in the presence of recirculation zones and flow detachment. Additional model features could help to improve the model's accuracy in these regions.

4 Reactive Species Transport Around Single Rising Bubbles

4.1 Overview

The single-phase approach introduced in Sect. 1.2 was originally developed to create highly realistic reference data to validate SGS modeling approaches. A positive side-effect is that the generated concentration fields allow detailed insights into the species transport around highly deformed bubbles. Such data are typically not accessible by experimental means, and numerical results obtained with two-phase flow solvers are little insightful due to insufficient mesh resolution or unphysical simulation parameters. This section presents an excerpt of the results obtained with the hybrid approach in terms of concentration fields, local and global mass transfer parameters, and local selectivity fields for a parallel-consecutive reaction.

4.2 Velocity and Concentration Fields

Based on the hybrid approach, the steady species transport around bubbles of various shapes has been investigated in [8]. Three of the more exotic rise behaviors are depicted in Fig. 12. The figure visualizes the full two-phase flow field computed
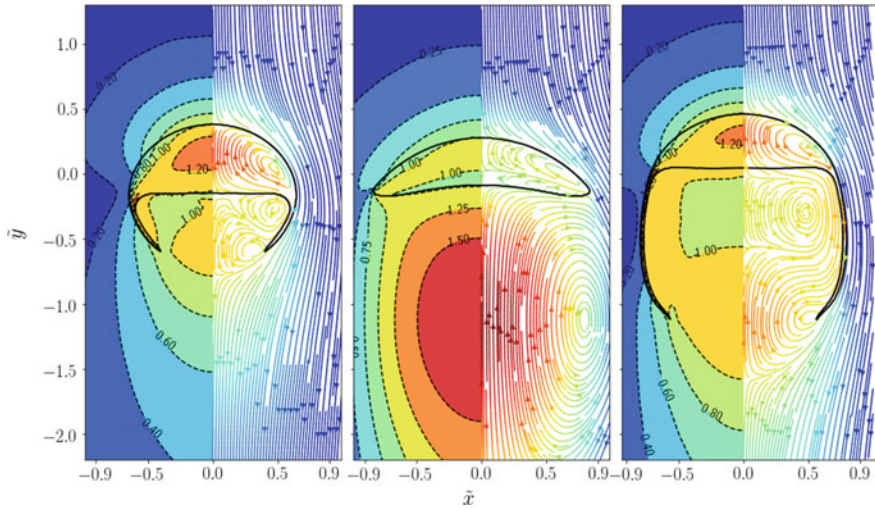
Fig. 12 Velocity field around dimpled ellipsoidal, spherical cap, and skirted bubbles (from left to right) visualized as contour plot of the velocity's magnitude and as streamline plot colored by the magnitude. For the exact simulation settings in terms of Morton, Eötvös, and Galilei number, refer to Table 6 in [8]

using the Basilisk flow solver introduced in Sect. 2.1. The two-phase flow field is a required input for the single-phase solver because the gas phase is omitted and sensible boundary conditions for velocity and pressure at the bubble-boundary of the single-phase domain must be derived. The examples in Fig. 12 have been selected because several recirculation zones appear despite the steadiness of the rise. When employing a free-slip boundary condition at the bubble surface instead of a data-driven boundary condition based on the two-phase flow solution, these flow patterns will not appear in the same form; see Sect. 6.4.2 in [8] for a visualization. Especially the dimpled-ellipsoidal and skirted bubbles contain recirculation zones in the rear part of the bubble that keep a portion of the liquid bulk trapped. From the point of view of reaction engineering, these zones are of interest because reaction products and transfer species accumulate, while bulk-species become slowly depleted. Therefore, such shape regimes might be favorable or unfavorable towards the formation of products or side-products. Consequently, it is essential to have a single-phase flow field that resembles its two-phase counterpart as closely as possible.

Also for relatively simple cases in which the flow field around the rising bubble is closed, a standard free-slip boundary condition for the velocity introduces a significant quantitative error even though the flow field is qualitatively correct. Figure 13 compares the velocity fields obtained with the data-driven and the free-slip boundary condition against the two-phase flow field. There is an obvious discrepancy in the wake velocity obtained with the free-slip boundary condition. This difference results
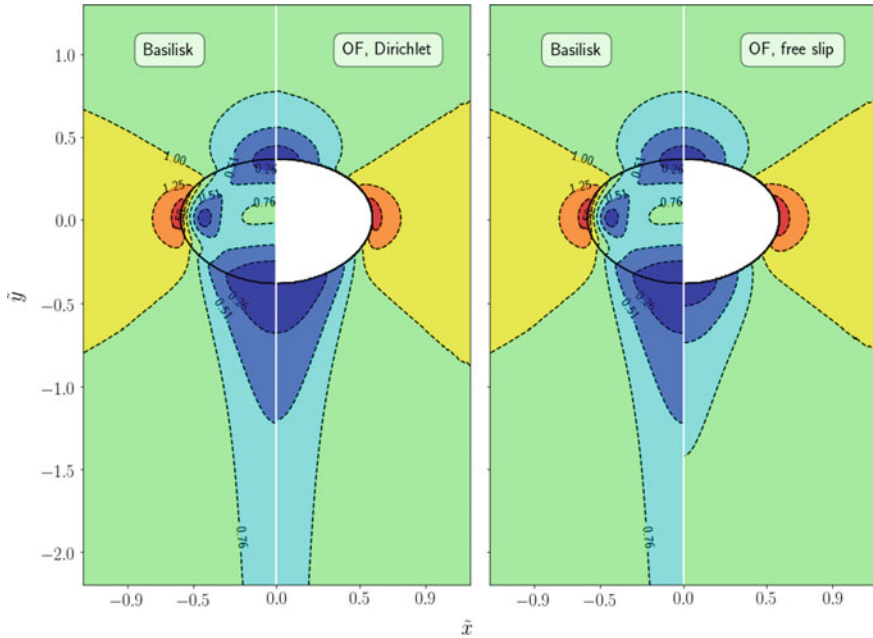
Fig. 13 Comparison of the velocity fields obtained with two-phase and single-phase simulation approaches

from the shear stresses introduced by the gas phase that is by definition zero when employing a free-slip boundary condition. There is also a subtle difference in the velocity field close to the bubble surface. As will be shown in Sect. 4.3, such a small deviation in the velocity boundary layer is enough to cause a difference larger than 5% in the computed mass transfer. On the other hand, the data-driven boundary condition results in a velocity field that is almost indistinguishable from the two-phase flow solution. Since the species transport is modeled as a passive process in the results presented hereafter, it is assumed that concentration field and mass transfer properties computed with the hybrid approach reflect the true two-phase species transport solution more closely than single-phase simulations employing a free-slip boundary condition.

Figure 14 depicts exemplary species concentration fields for a parallel-consecutive reaction occurring around a dimpled ellipsoidal bubble. An advantage of the single-phase simulation is that extremely dense meshes can be created such that it is possible to use realistic values for the molecular species diffusivities. Unfortunately, the resulting concentration boundary layers are so thin that they are hardly observable in images. This observation emphasizes the need for complementary numerical simulations since a visual inspection of the boundary layer by experimental means is currently not feasible.
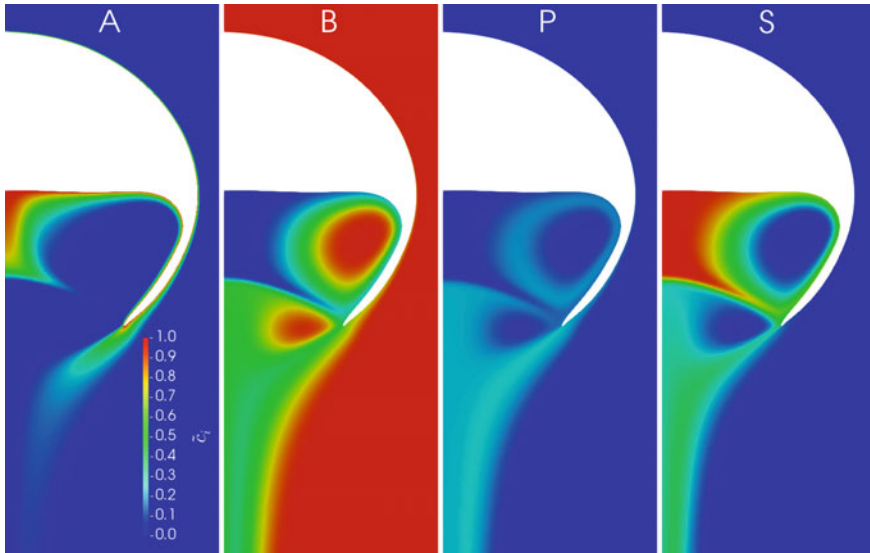
Fig. 14 Concentration fields around a dimpled ellipsoidal bubble in case of a competitive-consecutive reaction (A + B → P and A + P → S)

The liquid portion in Fig. 14 enclosed by the bubble's tail presents an interesting example for the interplay of different transport and reaction mechanisms. The transfer species A reacts with the bulk species B and forms the product P. Since the diffusive transport from the surrounding liquid bulk into the entrapped liquid portion is slower than its consumption by the chemical reaction, a significant depletion of B occurs close to the center line. At the same time, the consumption of A in this region drops due to the absence of B, and A accumulates. The presence of both species A and P in the entrapped liquid portion increases the formation of the side product S. The side product accumulates in the wake region. Note that the naming convention of product and side product is rather arbitrary. If S was the desired product, then the dimpled ellipsoidal bubble itself would be a favorable "micro-reactor". An additional analysis of the product formation, also for other bubble shapes, follows in Sect. 4.4.

4.3 Species Transfer and Enhancement

The global Sherwood number and the enhancement factor are the two most important quantities for scale-reduced modeling of reactive mass transfer processes. The Sherwood number Sh is a dimensionless version of the mass transfer coefficient k_L defined as:

$$Sh_{\text{eff}} = \frac{k_L d_{eq}}{D} \text{ with } k_L = \frac{\dot{n}}{A_{\text{eff}} \Delta c}. \tag{3}$$
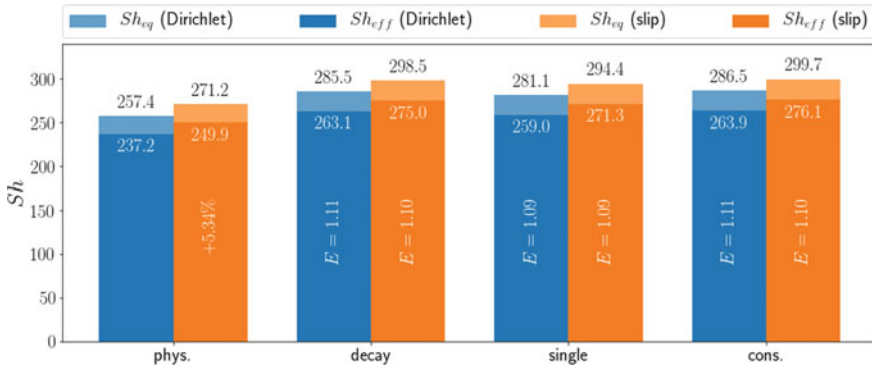
Fig. 15 Global Sherwood number and enhancement factor for a $d_b = 1.8$ mm air bubble rising in water

The effective surface area A_{eff} is often not known and not explicitly computed in experimental investigations. Instead, the bubble volume is measured, and volume-equivalent diameter d_{eq} and surface area A_{eq} are used to compute Sh. These different definitions are important to keep in mind when comparing the mass transfer at non-spherical bubbles between simulations and experiments or literature correlations. Both Sh-relations are connected to one another by the ratio of equivalent to effective surface area:

$$\frac{Sh_{\text{eff}}}{Sh_{eq}} = \frac{A_{eq}}{A_{\text{eff}}}. \tag{4}$$

Figure 15 depicts the global Sherwood numbers at a small air bubble rising in water. The investigated reaction mechanisms are as follows:

Label	Reaction
Decay	$A \rightarrow P$
Single	$A + B \rightarrow P$
Consecutive (cons.)	$A + B \rightarrow P \,\&\, A + P \rightarrow S$

Figure 15 depicts both effective and equivalent Sherwood number. From their ratio, the increase of the surface area due to the interface deformation can be inferred. Noticeably, even for the simplest investigated case with a closed flow around the bubble, employing a free-slip boundary condition for the velocity at the bubble surface leads to a five percent higher prediction of the mass transfer. In contrast, the computed enhancement factors remain mostly unaffected.

Visualization 16 depicts equivalent information as Fig. 15 but for the dimpled ellipsoidal bubble analyzed in previous sections. A striking difference is the more than two times enlarged effective surface area. Due to the complex flow field, which is not reproduced well employing a free-slip boundary condition, also the discrepancy

between the two different velocity boundary conditions increases. A difference of roughly 30 percent manifests for the Sherwood number and the deviation of the enhancement factor ranges between 9% and 13% (Fig. 16).

A strong side of numerical simulations is the availability of local information close to the gas-liquid interface. For example, one may analyze the local Sherwood number Sh_{loc} to understand the behavior of the global Sherwood number in different flow regimes or reaction systems. Figure 17 depicts the local Sherwood number at a dimpled ellipsoidal bubble for different reaction types. Plots depicting the local Sherwood number over the polar angle φ for axis-symmetric bubble shapes are common in literature. However, the curves depicted in Fig. 17 require some more explanation. In contrast to spherical or ellipsoidal bubbles, the surface of a dimpled ellipsoidal bubble does not form a convex hull. However, it is still possible to analyze
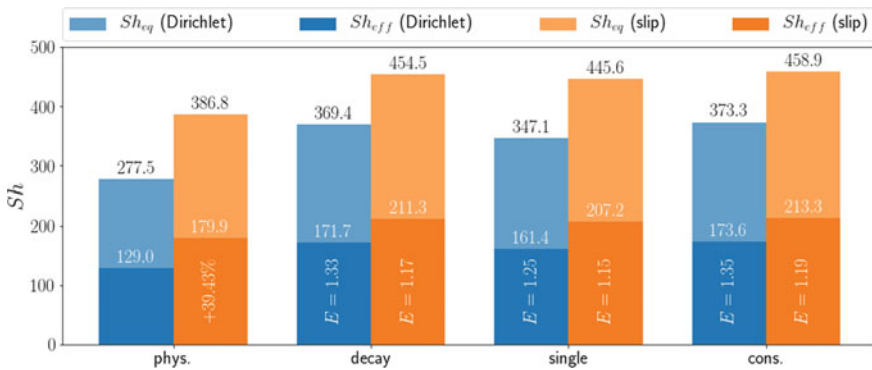
Fig. 16 Global Sherwood number and enhancement factor for a dimpled ellipsoidal bubble
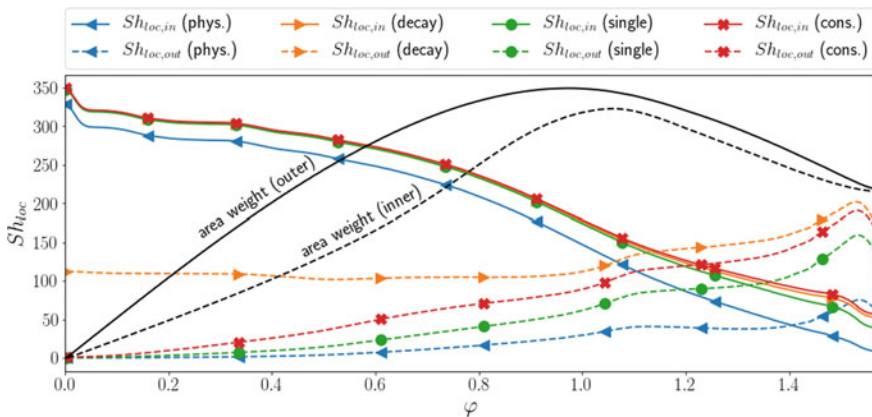
Fig. 17 Local Sherwood number for a dimpled ellipsoidal bubble. The area weight indicates to which extend the local Sherwood number at a given polar angle contributes to the global Sherwood number

the mass transfer with respect to the polar angle, but for each polar angle two local Sherwood numbers are available, one for the inner and one for the outer contour. Moreover, it helps for the interpretation of the influence on the global Sherwood number to know the contribution (weight) of the local Sherwood number to its global counterpart. The weight is nothing but a normalized version of the circumference at a given point on the interface. As for the local Sherwood number, there are two weighting factors for each polar angle.

On the outer contour of the dimpled ellipsoidal bubble, the mass transfer is qualitatively similar for all reaction types. On the inner contour, the picture changes drastically. In case of physisorption, the mass transfer drops to almost zero due to the accumulation of the transfer species in the entrapped liquid volume. Consequently, the presence of a chemical reaction leads to a relatively strong enhancement at the inner contour of the bubble. For a simple decay reaction, the enhancement is mostly uniform with respect to the polar angle. In contrast, the enhancement for single and parallel consecutive reactions decreases to zero close to the center line because of the strong depletion of bulk species in that region.

4.4 Local Selectivity

A quantity of high interest for chemical engineers is selectivity. While it is ultimately important to know how much product and side product are formed integrally, the local selectivity depicted in Figs. 18 and 19 reveals regions where product or side product are mainly formed. We define the local selectivity for a parallel-consecutive reaction as
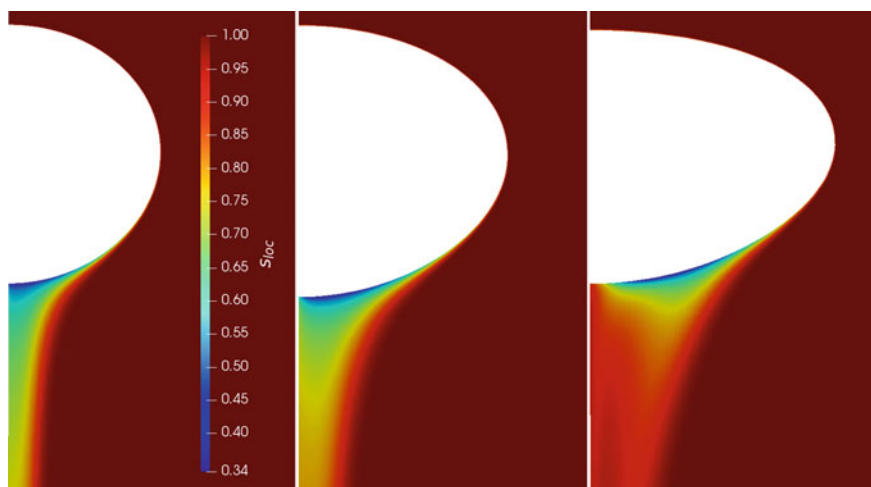
Fig. 18 Local selectivity around small ellipsoidal bubbles with increasing aspect ratio from left to right
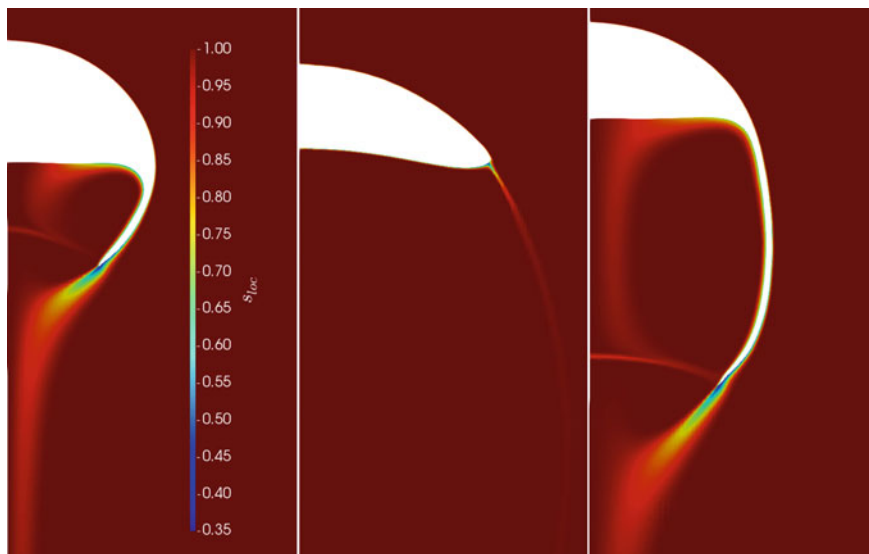
Fig. 19 Local selectivity around dimpled ellipsoidal, spherical cap, and skirted bubbles (from left to right)

$$s_{loc} = \frac{r_1 - r_2}{r_1 + r_2}, \qquad (5)$$

where r_1 and r_2 are the reaction source terms for the first and second reaction, respectively. Following the naming scheme from before, the source terms are computed as $r_1 = k_1 c_A c_B$ and $r_2 = k_2 c_A c_P$ with the reaction rate constants k_i. Note that there are several sensible definitions for the local selectivity. A disadvantage of the definition above is that integrating s_{loc} over the fluid domain does not yield the global selectivity. However, an advantage is that the fields in Figs. 18 and 19 are not masked by other transport mechanisms.

Figure 18 shows the local selectivity in the wake of ellipsoidal bubbles for three different aspect ratios. Such ellipsoidal bubbles occur, for example, if small air bubbles rise in uncontaminated water at room temperature. The increasing aspect ratio and Reynolds number reflects an increase in the bubble volume. Regions of low selectivity towards the primary product occur in the rear part of the bubbles. As the aspect ratio increases, the point of lowest selectivity shifts from the pole towards the equator. Moreover, there is a tube-like region of low selectivity in the wake of the almost spherical bubble. As the aspect ratio increases, this region becomes shorter. Note that it is not straightforward to judge from these observations which bubble size might be favorable to maximize the global selectivity. However, Fig. 18 may help to identify the various effects that lead to a change in the global selectivity.

The local selectivity fields in Fig. 19 are much more diverse compared to the ones in Fig. 18. Comparing Figs. 14 and 19, one observes that regions of low selectivity in the entrapped liquid volume coincide with regions of high product accumulation for

the dimpled ellipsoidal bubble. Another region of low selectivity forms around the tail of the bubble's skirt. The skirted bubble shows a similar behavior. Interestingly, only a very small region of low selectivity forms around the spherical cap bubble. This region coincides with the point (or ring), where the flow detaches from the interface. Due to the enormous size of the recirculation zone behind the spherical cap bubble, no significant depletion of the bulk species occurs, which is in contrast to the other bubble shapes analyzed here.

5 Conclusion and Outlook

In this chapter we presented new modeling techniques to investigate the reactive mass transfer at rising bubbles. Regarding the high-Schmidt number problem, a subgrid-scale modeling approach was described that allows to approximate species concentration boundary layers with high accuracy even if they are fully embedded in a single cell layer around the gas-liquid interface. This modeling approach may be used in the future to investigate the reactive mass transfer in bubble swarms. Numerical simulations of bubble swarms allow to investigate their chaotic behavior, and the subgrid-scale model may aid to compensate the decreased mesh resolution per bubble diameter, which would be insufficient to resolve the species boundary layers for realistic Schmidt numbers. To validate the SGS model performance, a hybrid simulation approach was developed that maps the two-phase interfacial velocity onto a single-phase simulation domain based on machine learning. The hybrid approach also allows to take a close look at the local species transport around various typical bubble shapes.

For future investigations it is desirable to investigate the data-driven version of the SGS model in greater detail than presented here and in [8, 10]. Regarding the hybrid approach, a version of the tool *snappyHexMesh* optimized for two-dimensional meshes would greatly simplify the creation of meshes that are dense enough to resolve the extremely thin species concentration boundary layers. Moreover, the potential of the hybrid approach should be exploited to create high-fidelity reference data for the reactive mass transfer at realistic bubble shapes. Such data can be used in consecutive steps to create more accurate Sherwood number and enhancement factor correlations and to validate the SGS model performance under more realistic and challenging conditions.

References

1. Levich VG (1962) Physicochemical hydrodynamics. Prentice Hall, Upper Saddle River
2. Aboulhasanzadeh B, Hosoda S, Tomiyama A, Tryggvason G (2013) A validation of an embedded analytical description approach for the computations of high Schmidt number mass transfer from bubbles in liquids. Chem Eng Sci 101:165–174
3. Aboulhasanzadeh B, Thomas S, Taeibi-Rahni M, Tryggvason G (2012) Multiscale computations of mass transfer from buoyant bubbles. Chem Eng Sci 75:456–467
4. Claassen CMY, Islam S, Peters EAJF, Deen NG, Kuipers JAM, Baltussen MW (2020) An improved subgrid scale model for front-tracking based simulations of mass transfer from bubbles. AIChE J 66(4):e16889
5. Bothe D, Fleckenstein S (2013) A volume-of-fluid based method for mass transfer processes at fluid particles. Chem Eng Sci 101:283–302
6. Gründing D, Fleckenstein S, Bothe D (2016) A subgrid-scale model for reactive concentration boundary layers for 3D mass transfer simulations with deformable fluid interfaces. Int J Heat Mass Transf 101:476–487
7. Pesci C, Weiner A, Marschall H, Bothe D (2018) Computational analysis of a single rising bubble influenced by soluble surfactant. J Fluid Mech 856:709–763
8. Weiner A (2020) Modelling and simulation of convection-dominated species transport at rising bubbles. PhD thesis, Technical University of Darmstadt, Darmstadt, Germany
9. Weiner A, Bothe D (2017) Advanced subgrid-scale modeling for convection-dominated species transport at fluid interfaces with application to mass transfer from rising bubbles. J Comput Phys 347(1):261–289
10. Weiner A, Hillenbrand D, Marschall H, Bothe D (2019) Data-driven subgrid-scale modeling for convection-dominated concentration boundary layers. Chem Eng Technol 42(7):1349–1356
11. Weiner A, Timmermann J, Pesci C, Crewe J, Hoffmann M, Schlüter M, Bothe D (2019) Experimental and numerical investigations of reactive species transport around a small rising bubble. Chem Eng Sci X 1:100007

Development and Application of Direct Numerical Simulations for Reactive Transport Processes at Single Bubbles

Holger Marschall and Dennis Hillenbrand

Abstract In reaction engineering one major concern is with reactor performance for competitive reaction networks in which the formation of desired product and by-product takes place depending on process conditions. Particularly for gas-liquid reaction systems, process design and analysis require detailed knowledge on the local interplay of two-phase fluid dynamics, interfacial species transport and chemical reactions to assess product yield and selectivity reliably. Direct Numerical Simulations play a significant role in understanding these coupled processes. This chapter focuses on numerical simulations of reactive mass transfer at bubbles using the Arbitrary Lagrangian-Eulerian interface tracking methodology. For a prototypical competitive consecutive reaction at freely rising and Taylor bubbles in a circular milli-channel, we study local mass transfer coefficients, reaction enhancement and local product selectivity for different reaction intensities, i.e. Damköhler numbers. Local data gained from comprehensive simulation campaigns provide insights into regions of enhanced mass transfer and high product selectivity in the bubble wake. For realistic Schmidt numbers the influence of the bubble Reynolds number is found to decrease.

1 Introduction

Many industrial applications in chemical process engineering include the reaction of gaseous and liquid components. They range from large scale applications, such as bubble column reactors to small monolith reactors processing Taylor flow [1, 2].

An important goal in intensifying chemical processes is to gain a high product yield and selectivity, i.e. to maximize reactor performance. Local insights into the underlying physico-chemical processes at the fluid interface are of high relevance for reactor design and process intensification. Therefore, both local mass transfer coefficients and local selectivity fields in reactive bubbly flows are analyzed in this chapter

H. Marschall (✉) · D. Hillenbrand
Technical University of Darmstadt, Mathematical Modeling and Analysis, Alarich-Weiss-Str. 10, 64287 Darmstadt, Germany
e-mail: marschall@mma.tu-darmstadt.de

so as to disclose the regions with the highest potential to improve the overall reactor performance. The main objective of this work has been to reveal the local interplay between fluid-dynamics, mass transfer and chemical reaction, and its influence on selectivity. To gain detailed insights, we perform Direct Numerical Simulation (DNS) of single bubble systems, either freely rising in a quiescent liquid bulk phase or confined in channels under counter flow of the liquid bulk phase (Taylor bubbles).

However, simulations of mass transfer at bubbles under realistic conditions are numerical very demanding and computationally costly. One reason is the high spatial resolution requirement of the typically thin species concentration boundary layer around the bubble [3]. This is becoming more severe when considering reactive mass transfer and further complicated by the presence of impurities such as surface active agents in most industrial applications. Therefore, the vast majority of simulation-based research work in this field is based on simplified setups, such as single-phase flow around bubbles of fixed shapes [4, 5] or unduly small Schmidt numbers [6].

In this study, however, we attempt to investigate reactive mass transfer at bubbles which are dynamic in shape. We focus on DNS of reactive mass transfer with realistic transport parameters considering two different bubbly flow types:

Single Bubbles This includes the rise of initially spherical, deformable bubbles of different sizes. These are ubiquitous in industrial reactors and their hydrodynamic behavior significantly affects the overall mass transfer. Although interactions between bubbles are always present in applications such as bubble column reactors, it is important to investigate the main aspects of the mass transfer at single rising bubbles. An overview of the most important results, both numerically and experimentally, for single rising bubbles can be found in Chapter "Chemical Reactions at Freely Ascending Single Bubbles". One of the few fully three-dimensional numerical analyses of two phase flow around rising bubbles was performed within this project [7]. The mass transfer highly depends on the hydrodynamic behavior and shape of the bubble, which is known to depend on the bubble size and fluid properties. The bubble rising paths vary from straight to zig-zagging or helical ones. Numerical simulations are able to give insights into local processes, which influence the performance of the overall reaction process.

Taylor Bubbles Taylor bubbles are elongated bubbles, which almost completely fill the cross-sectional area of a surrounding channel, separated from the walls only by a small liquid film, see Chapter "Visualization and Quantitative Analysis of Consecutive Reactions in Taylor Bubble Flows" for more details. The liquid flow pattern in Taylor flows, sometimes called slug flow, has several advantages for chemical process engineering. The large ratio of interfacial area to volume leads to efficient heat and mass transfer across the bubble interface, and recirculation in the liquid slug behind the Taylor bubble leads to intense mixing of the involved species. For experimental investigations, Taylor bubbles are advantageous because the flow parameters can be well-defined and flow structures are reproducible, see Chapter "Experimental Investigation of Reactive Bubbly Flows—Influence of Boundary Layer Dynamics on Mass Transfer and Chemical Reactions". The terminal rise velocity of long Taylor bubbles is independent of their volume, which ensures that the rise velocity does not

change during the process. The stationary rise velocity can be measured in experiments or an appropriate downstream counter flow can be applied such that the centre of the bubble remains at its initial position [8]. As it is still challenging to obtain local data from experiments, especially near the bubble interface and in the small liquid film, we have conducted a numerical study to investigate these regions more thoroughly regarding local mass transfer and product selectivity for the specific bubble rising in water introduced in [9]. Additional comparisons of numerical and experimental investigations for different fluids can be found in Chapter "Visualization and Quantitative Analysis of Consecutive Reactions in Taylor Bubble Flows".

Reaction Engineering Quantities For the following investigations we define a prototypical competitive consecutive reaction system, which is representative of many chemical engineering applications in bubbly systems:

$$A + B \xrightarrow{k_1} P, \tag{1a}$$

$$P + B \xrightarrow{k_2} S, \tag{1b}$$

where B is the transfer species initially present in the gas bubble, A is the educt in the liquid bulk, P is the desired product, while S is an undesired side product. Rate constants of the chemical reactions are denoted by k_1 and k_2 for the individual reaction steps, respectively. A summary of several bio-inspired complexes which react according to the reaction scheme presented above is given in [10] and used in both experimental and numerical investigations of bubbly flows [11]. Details on the chemical substances and their properties following such reaction schemes can be found in Chapters "Control of the Formation and Reaction of Copper-Oxygen Adduct Complexes in Multiphase Streams", "In Situ Characterizable High-Spin Nitrosyl–Iron Complexes with Controllable Reactivity in Multiphase Reaction Media" and "Formation, Reactivity Tuning and Kinetic Investigations of Iron "Dioxygen" Intermediate Complexes and Derivatives in Multiphase Flow Reactions".

The overall selectivity for the above reaction scheme can be defined as [7]

$$S(t) = \frac{n_P(t) - n_{P,0}}{n_{B,0} - n_B(t)}, \tag{2}$$

where n_i is the total number of moles and $n_{i,0}$ represents the initial amount of moles. To investigate the contribution from different regions to the overall selectivity, a local selectivity can be defined as

$$S_{\text{loc}}(\mathbf{x}, t) = \frac{r_1 - r_2}{r_1 + r_2} = \frac{k_1 c_A c_B - k_2 c_A c_P}{k_1 c_A c_B + k_2 c_A c_P}, \tag{3}$$

where r_i is the local reaction rate of the single reaction steps.

The mass transfer of the gaseous species from the bubble into the liquid can be measured as the liquid sided concentration gradient at the bubble interface. The local non-dimensionalized concentration gradient is expressed by the local Sherwood number

$$\text{Sh}_{\text{loc}} = \frac{\partial_n c_B d_{\text{eq}}}{c_{B,\Sigma}},\tag{4}$$

where ∂_n is the normal derivative at the interface, d_{eq} is the diameter of a volume-equivalent sphere and $c_{B,\Sigma}$ is the interfacial concentration of the transfer species B. The overall mass transfer can be quantified by the global Sherwood number, for which several correlations exist in the literature, e.g. [12]. The global Sherwood number will be used to compare the numerical results to the experimentally gained correlations and to assess the influence of fluid dynamics on the mass transfer. Another possibility is to evaluate the efficiency of mass transfer per interfacial area by means of the specific mass transfer coefficient:

$$k_l A = \int\limits_{S_\Sigma} D_B \frac{n_\Sigma \cdot \nabla c_B}{c_{B,\Sigma}} ds,\tag{5}$$

where D_B is the diffusivity of the transfer species in the liquid and the interfacial area is denoted by $A = |S_\Sigma|$.

In the forthcoming section, the governing equations for fluid dynamics and species transport are introduced. Moreover, the used numerical discretization technique is described briefly. Section 3 is devoted to the validation of the utilized flow solver, while Sect. 4 puts forth the results for freely rising single bubbles. Section 5 relates to the Taylor bubble flow and discusses local insights into the physico-chemical processes at the interface with relevance to possible local mass transfer enhancement and product selectivity improvement.

2 Model and Method

2.1 Mathematical Model

We employ a so-called sharp interface model, which means we presume a sharp jump of material properties at the interface. The interface $\Sigma(t)$ itself is assumed as a surface of discontinuity of zero thickness, which separates two immiscible, Newtonian, and incompressible fluid phases $\Omega^\pm = \Omega^+(t) \cup \Omega^-(t)$. We shall further restrict ourselves to isothermal conditions (i.e., disregard phase change due to evaporation or condensation) and to dilute multi-component systems. This yields the transport equations for mass and linear momentum,

$$\nabla \cdot \boldsymbol{v} = 0, \tag{6a}$$

$$\partial_t(\rho \boldsymbol{v}) + \nabla \cdot (\rho \boldsymbol{v}\boldsymbol{v}) = -\nabla p + \nabla \cdot \boldsymbol{\tau} + \rho \boldsymbol{g}, \tag{6b}$$

being valid in the bulk regions, $\Omega^{\pm} \backslash \Sigma(t)$. Herein, the gravitational acceleration is denoted as $\boldsymbol{g}$ and the viscous stress tensor for a Newtonian fluid reads $\boldsymbol{\tau} = \mu(\nabla \boldsymbol{v} + (\nabla \boldsymbol{v})^{\mathsf{T}})$, where ρ denotes the fluid density and μ its dynamic viscosity, both being constant within a respective phase.

We assume zero velocity jump at the interface, in particular volume effects due to dissolution and phase change are disregarded. The presence of surfactants in the bulk phases and on the interface is taken into account. Then, the interfacial jump and transmission conditions are

$$[\![\boldsymbol{v}]\!] = 0, \tag{7a}$$

$$[\![p\,\boldsymbol{I} - \boldsymbol{\tau}]\!] \cdot \boldsymbol{n}_{\Sigma} = \sigma \kappa \, \boldsymbol{n}_{\Sigma} + \nabla_{\Sigma}\sigma, \tag{7b}$$

on the fluid interface $\Sigma(t)$, where $[\![\cdot]\!]$ denotes the jump bracket, n_{Σ} the outer unit normal at the interface and $\kappa = \nabla_{\Sigma} \cdot (-\boldsymbol{n}_{\Sigma})$ is twice the mean interface curvature.

In order to account for transport of chemical species, the governing equations for fluid dynamics are accompanied by bulk and interface species transport equations as well as by species transmission and jump conditions. For a species k, being subject to interfacial mass transfer and chemical reactions within the bulk, these read

$$\partial_t c_k + \nabla \cdot (c_k \boldsymbol{v} + \boldsymbol{j}_k) = r_k, \tag{8}$$

and

$$[\![\boldsymbol{j}_k]\!] \cdot \boldsymbol{n}_{\Sigma} = 0, \tag{9a}$$

$$c_k^+ = H_k c_k^-. \tag{9b}$$

Herein, c_k denotes the molar concentration of the species k and $\boldsymbol{j}_k$ the diffusive flux. For species transport in the bulk we assume a dilute system (negligible inertia of chemical constituents), thus the Fickian law of diffusion is applied $\boldsymbol{j}_k = -D_k \nabla c_k$. Diffusivities D_k are assumed as constant (but different, $D_k^+ \neq D_k^-$) in each fluid phase. The Henry coefficient H_k in the interfacial jump condition is assumed as constant along the interface, for more details refer to [13]. The term r_k denotes the chemical reaction rate depending on the system under investigation. For example, for the reaction network introduced in (1a, 1b) the transfer species B is consumed by two reactions making it a competitive consecutive reaction where the second reaction gives rise to the undesired by-product by consumption of product. A more detailed discussion can be found in [7]. In the case of surfactants, the interfacial transport of a species k reads

$$\partial_t^\Sigma c_k^\Sigma + \nabla_\Sigma \cdot \left(c_k^\Sigma \boldsymbol{v}_{||} + \boldsymbol{j}_k^\Sigma \right) - c_k^\Sigma V_\Sigma \kappa = \dot{s}_k^\Sigma. \tag{10}$$

Here, $\partial_t^\Sigma c_k^\Sigma$ denotes the partial time derivative along a path which follows the normal interface motion (Thomas derivative), where V_Σ is the normal speed of displacement of the interface. The surfactant system on the fluid interface should be treated as non-dilute employing surface Maxwell-Stefan constitutive modelling [14].

The remaining constitutive equations for the unclosed terms, i.e., the surface tension $\sigma = \sigma\left(c_i^\Sigma \right)$, the diffusive fluxes $\boldsymbol{j}_k$ and $\boldsymbol{j}_k^\Sigma$ and the sorption source term $\dot{s}_k^\Sigma$ as well as the reaction source r_k can be found by closure modeling. Different modeling options and corresponding constitutive equations are set out elsewhere but would go beyond the scope of this contribution. The interested reader is thus referred to [7, 15] and references therein.

2.2   Numerical Methods

The two-phase Navier Stokes equations and species transport equations are discretized using a second-order Finite Volume Method (FVM) in *OpenFOAM* (*FOAM-extend version 3.1*) with support for moving polyhedral meshes. This allows to employ the Arbitrary Lagrangian Eulerian interface tracking methodology (ALE-ITM). Within the framework of a previous DFG-funded project, namely within the DFG priority program SPP 1506, we have advanced the ALE-ITM with respect to interfacial mass transfer and multicomponent surfactant transport at fluid interfaces. In this project, we have significantly improved the overall robustness (i.e. stability and convergence) properties of the ALE algorithm allowing for dynamic interface deformation while accurately solving for species transport including reactions. This has enabled us for a detailed numerical study on the mutual influence of bubble dynamics, mass transfer and chemical processes.

Within the ALE-ITM, the flow within each fluid phase is governed by a separate set of (integral) conservation equations in Arbitrary Lagrangian Eulerian (ALE) formulation. The fluid interface itself is represented by a computational mesh boundary, or a part of it. Notably, this results in an explicit rather than an implicit interface representation. The boundary mesh is of particular relevance as it enables to solve for surfactant transport equations along the interface. Coupling between the bulk regions is achieved through enforcement of interfacial transmission and jump conditions by means of boundary condition updates to each fluid domain at the respective locations in the PIMPLEC algorithm (combination of SIMPLEC and PISO) used for pressure velocity coupling [16]. The motion of the interfacial boundary is obtained as a part of the numerical two-phase flow solution, during which corresponding mesh boundary faces and control points are moved so as to satisfy discretized forms of the interfacial conditions. For their discretization we make significant use of the Finite-Area Method (FAM) provided within *OpenFOAM*. The interface is then advected in a semi-Lagrangian fashion in order to fulfill the Space Conservation Law (SCL), which

is crucial for phase volume conservation. More details on the numerical method can be found in [17, 18]. A detailed explanation of the overall solution methodology, including surfactant transport and their sorption processes, can be found in [15]. The extension for treating species transport within the ALE framework is set out in detail in [7, 19].

Different strategies have been developed, implemented and tested within this project to approach a great challenge for numerical simulations, which lies in unduly high demand for spatial resolution of the species boundary layer near the bubble interface for high Schmidt numbers. The first approach introduces a second mesh for the discretization of the species transport in the liquid phase only. This mesh is statically refined in normal direction to the interface [7] to resolve the species boundary layer, which is much thinner than the hydrodynamic boundary layer. The additional computational cost for flow solution on the finer mesh is significantly alleviated. Nevertheless, this approach is limited by the number of refinement steps, as each refinement reduces the mesh quality.

To remedy the refinement requirements, sub-grid-scale models may be used to augment the interpolation schemes by information based on analytical solution of a simplified substitute problem [20], being valid close to the bubble interface. Numerical results using such sub-grid-scales models are presented in Chapter "Modeling and Simulation of Convection-Dominated Species Transport in the Vicinity of Rising Bubbles" and show convincing agreement with experimental results. Such a sub-grid scale model augmented discretization has already been successfully applied for cases with high Peclet numbers, but is only applicable for physisorption or simple decay reactions for which an analytical model expression can be devised, see Chapter "Modeling and Simulation of Convection-Dominated Species Transport in the Vicinity of Rising Bubbles". To extend the applicability of sub-grid-scale models such that chemical reactions can be included, this procedure can be replaced by machine learning techniques [21]. Despite these promising results, each subgrid-scale model can only be used for one specific reaction system at present. Therefore, the usage of sub-grid-scale models for reactive mass transfer will be included in future work, expecting improved computational performance.

The numerical code used for the simulations in this work has been considerably extended and enhanced to enable accurate and robust simulations of bubbly flow with reasonable computational effort. To ensure physical fidelity, the revised code has been subject to validation as set out in the next section.

3 Numerical Validation

3.1 Computational Case Setup

Within the ALE interface tracking framework, the mesh motion is accomplished by means of an appropriate mesh velocity. The interface is represented as a part of the

mesh boundary. For all simulations, meshes with prismatic layers on both sides of the interface are used so as to improve the mesh quality and to ensure accuracy, particularly regarding mesh skewness during interface deformation.

For all simulations of single rising bubbles, the bubble interface has been initialized as a sphere. The outer domain boundary is at a distance of at least eight times the bubble radius in order to avoid numerical bias of the solution close to the interface from the domain boundary condition. The outer mesh consists of prismatic layers which extend from the initially spherical bubble to the domain boundary. A part of the outer layered mesh for a single bubble with $d_b = 4$ mm is depicted in the right part of Fig. 1. The inset shows the high spatial mesh resolution close to the interface. To reduce the overall number of cells, while maintaining sufficiently high mesh resolution at the interface, aggressive mesh grading in radial direction is employed.

Figure 1 (left) shows the simulation setup regarding boundary conditions. A mixed Dirichlet/Neumann boundary condition is set for the velocity at the domain boundary. If the current velocity points inward on a specific boundary face, an inlet velocity equal to $v_{\partial\Omega,\text{in}}$ is imposed. Otherwise, a zero normal gradient is applied. For the pressure field, the normal gradient is set to zero on the entire domain boundary $\partial\Omega$. For all species of the multi-component system, the same mixed Dirichlet/Neumann boundary condition as for the velocity is used. The concentrations of product P and by-product S are initialized to 0 mol/m^3 in the entire domain. The transfer species B has an initial uniform and non-zero concentration value inside the bubble and $c = 0$ mol/m^3 in the liquid phase. The opposite situation holds for the educt A. The inlet value is set to $c = 1$ mol/m^3 for the species A and $c = 0$ mol/m^3 for the remaining components.

a) Sketch of case setup   **b)** Computational mesh
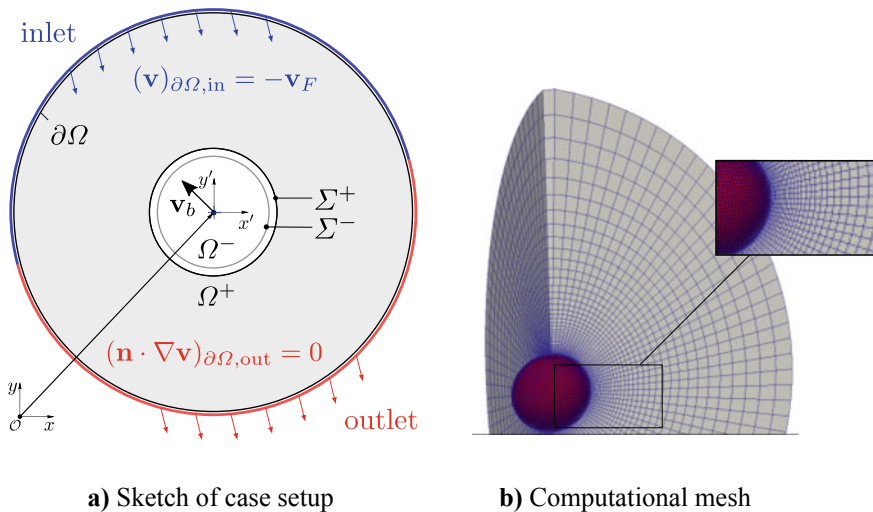
Fig. 1 Case setup and mesh for a single rising bubble with $d_b = 4$ mm

The jump and transmission conditions for the pressure and the velocity fields as well as the transfer species B are enforced by means of a partitioned Dirichlet-Neumann Algorithm (DNA) according to Eqs. (7) and (9), respectively. For non-transfer species zero normal-gradient boundary conditions are applied.

3.2 Validation Study

The employed ALE interface tracking solver has been subject to in-depth validations studies elsewhere, see [7, 15, 19]. However, as the solver has been substantially revised and improved with respect to robustness (stability and convergence), we set out an excerpt of validation results in the remainder. Here, we employ the analytical solution of Satapathy and Smith [22] with corrections from [23], on the basis of which the revised ALE interface tracking two-phase flow solver is validated considering a highly viscous flow around a spherical bubble. Due to the low Reynolds number the bubble remains spherical and the solution is axisymmetric. As the solution is independent from the azimuthal angle, this validation case is also of high relevance to verify the correct treatment for axisymmetric setups in the ALE interface tracking framework.

The results from both the 3D and axisymmetric simulations are compared to the analytical solution. For the 3D case, three different mesh resolutions are used, which are referred to in the following as mesh1, mesh2 and mesh3, respectively. The total number of cells for each mesh is 6000, 24,000 and 192,000 respectively. To demonstrate agreement with the axisymmetric simulation results, a wedge-type mesh with 2000 cells is employed. It is important to note that the spatial resolution of the axisymmetric mesh is finer in radial and tangential direction, while the overall cell size is of course significantly smaller.

The parameter set used for the present validation study is given in Table 1. For these parameters, the terminal flow velocity is $U = 0.0288$ m/s, which results in a Reynolds number $Re = 0.3104$. The numerically calculated Reynolds numbers along with their relative errors are reported in Table 2.

The analytical solution provides local velocity profiles which makes it possible to spot errors better than with global data only, such as the bubble rise velocity for

Table 1 Material parameters for Satapathy-Smith validation

Parameter	Value
ρ_l	1235 kg/m^3
ρ_g	1.173 kg/m^3
μ_l	0.46 kg/ms
μ_g	1.856×10^{-5} kg/ms
σ	0.07232 kg/s^2
d_b	4 mm

Table 2 Mesh study of velocity and pressure errors compared to the solution of Satapathy and Smith

Mesh	Re	$Re_{rel,err}$ in %	$\varepsilon_u \times 10^{-4}$	$\varepsilon_p \times 10^{-4}$
mesh1	0.3010	3.032	8.55	3.32
mesh2	0.3059	1.444	7.15	3.48
mesh3	0.3104	0.004	6.49	3.27
Wedge	0.3168	2.065	11.13	3.84

a) 3D setup

b) wedge setup
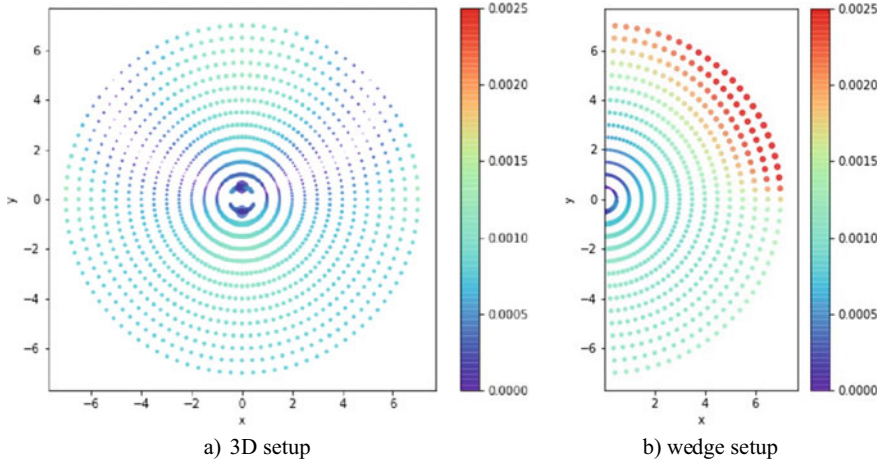
Fig. 2 Local velocity errors

instance. For local insights, the local errors are shown as a scatter plot in Fig. 2. The color indicates the absolute error ε_u of the velocity magnitude, while the scatter size scales with the corresponding relative error. The local velocity error is defined as

$$\varepsilon_u(\mathbf{x}_i) = \frac{1}{N}\sqrt{\sum_i^N \|\mathbf{u}(\mathbf{x}_i) - \mathbf{u}_{num}(\mathbf{x}_i)\|^2}, \qquad (11)$$

where i denotes the current cell index and N is the total number of cells. The local pressure error can be defined in an analog manner. Figure 2 depicts local velocity errors for the finest resolutions for the 3D as well as for the axisymmetric simulation results. The scatter sizes show that the maximum relative errors occur near the interface at the stagnation points of the bubble. The absolute errors are very small and the numerical solution agrees well with the analytical one. The good agreement between the results of the two numerical setups underpins the suitability of axisymmetric simulations if applicable. Here, the highest errors occur at the domain boundary, where the aspect ratio of the cells is much larger than for the 3D case.

Table 3 Global Sherwood numbers

Source	Sh_{gl}
Clift (1978)	221.0
Oellrich (1973)	223.3
Takemura (1998)	229.6
mesh1	237.3
mesh2	225.1
mesh3	230.8
Wedge mesh	222.8

However, these errors have been found neither to bias the rise velocity nor to alter the numerical solution inside the boundary layer, which is important for accurate numerical predictions of interfacial mass transfer. We employ axisymmetric simulation whenever applicable in order to reduce the overall computational mesh size and thus to save computational time, which enables either higher spatial resolution or faster computation for the parameter studies investigating the physico-chemical processes in bubbly flow.

In Table 2 the global error for both the velocity and pressure, defined as the average of the local error over the whole computational domain, is shown for the different meshes. The global error decreases for increasing mesh resolution, which implies numerical consistency. In addition to validation of two-phase fluid dynamics, the steady-state velocity field has been used for the calculation of the transport of a gaseous species into the liquid phase. Here, a realistic diffusion coefficient $D = 1 \times 10^{-9}$ m^2/s is employed, which results in a Peclet number of Pe $= 1.16 \times 10^5$. We further compare the global Sherwood number Sh_{gl} from the numerical reference solution to correlations presented in literature in Table 3. A good agreement of numerical Sherwood numbers has been found, especially with the most recent correlation presented in [12]. The axisymmetric ALE interface tracking simulations are also reproducing the Sherwood numbers accurately and thus can be used for interfacial mass transfer computations if applicable.

4 Reactive Species Transfer from Single Rising Bubbles

4.1 Computational Case Setup

The computational setup for DNS cases of reactive interfacial mass transfer from single rising bubbles is the same as described in the previous section, cf. Fig. 1. However, while the initial bubble shape remains approximately spherical in the validation study, the bubbles considered in the present section are significantly deforming during the transient simulations. Moreover, the concentration boundary layers are

Table 4 Values of physical quantities

Parameter	Value
ρ_l	1000 kg/m^3
ρ_g	1.205 kg/m^3
μ_l	4.46×10^{-3} kg/ms
μ_g	1.81×10^{-5} kg/ms
σ	0.072 kg/s^2
d_b	{1.49, 2.11, 2.73, 3.34, 3.86} mm

significantly thinner than the hydrodynamic boundary layers at the bubble interfaces. This numerical challenge of sufficiently resolving the concentration boundary layer becomes pronounced with increasing Schmidt numbers and is known as the High Schmidt Number Problem (HSNP). In the case of reactive mass transfer, this multi-scale problem becomes even more severe. In order to alleviate the HSNP but keeping the computational costs reasonable, the standard approach of solving both for the bubble dynamics and for chemical species transport on the same mesh has been revised. Instead, for the solution of the physico-chemical processes involved in interfacial mass transfer, we use a second mesh to be able to provide higher spatial resolution where needed, i.e. at the interface, while for two-phase fluid dynamics, a coarser mesh can be used which has to provide only sufficient resolution for accurate pressure-velocity coupling particularly at the interface, i.e. resolving the interfacial viscous boundary layer.

The simulation campaign carried out has been based on a system of fluid properties corresponding to a Morton number $\left(\text{Mo} := g \Delta \rho \mu_l^4 / \rho_l^2 \sigma^3\right)$ equal to 10^{-8}. The values of fluid properties are given in Table 4.

The parameter space considered includes five different bubble diameters d_b, resulting in Eötvös numbers $\left(\text{Eo} := g \Delta \rho d_b^2 / \sigma\right)$ ranging from 0.3 to 2 and bubble Reynolds numbers (Re $= \rho_l U_b d_b / \mu_l$) ranging from 58 to 232, which covers the full range from nearly spherical, straight rising bubbles to strongly deformed bubbles rising on helical paths.

For each bubble diameter, eight distinct simulations have been carried out with computational analysis focus on reaction engineering aspects (see below). Additional numerical results for smaller bubbles rising on a straight path are compared to experiments in Chapter "Chemical Reactions at Freely Ascending Single Bubbles".

The underlying reaction system is a competitive consecutive reaction network as introduced in Eq. (1a, 1b). The rate coefficients of both chemical reactions have been varied by adopting different values for the Damköhler number of the first reaction $\left(\text{Da}_1 = d_b k_1 c_{A,\text{in}} / U_b\right)$ and for the ratio $\kappa := \text{Da}_2 / \text{Da}_2$ of Damköhler numbers of both reactions involved. Rate coefficients have been chosen such that the Damköhler number of the first reaction is $\text{Da}_1 \in \{0.01, 0.1, 1, 10\}$ and $\kappa = \{10, 100\}$. Such a parameter space allows to cover the technically relevant range of reaction intensities from very slow to fast chemical reactions in bubble column reactors.

All simulations within the simulation campaign have been accomplished with a single 3D mesh being scaled to the desired bubble diameter. The computational

mesh in the inner (bubble) part consists of polyhedral cells, while for meshing of the outer part, prismatic cell layers and mesh grading have been used. Here, a second mesh is introduced so as to resolve the concentration boundary layer region by using additional cell layers. The number of refinements necessary for an adequate resolution has been obtained by means of a mesh independence study, which identified three refinement levels to be sufficient. More precisely, upon further refinement, the global Sherwood number has been found to change only insignificantly (below 0.1% relative deviation).

In case of a competitive consecutive reaction scheme, which has been central to the present 3D study, scientific questions which have been approached and answered are

1. What is the effect of changing the bubble equivalent diameter on mass transfer and selectivity for different Schmidt number regimes?
2. What are the reaction time scales, for which local product selectivity changes significantly and where does this occur?
3. Where is the local enhancement most effective and how much does it increase the overall mass transfer?

An overview of results is set out and discussed in the next two sections. The interested reader is referred to [7] for more details.

4.2 Reactive Mass Transfer

Significant dependence of the local mass transfer coefficient k_l on the bubble equivalent diameter has been identified and quantified [7] for both nonreactive and reactive cases, i.e. for physisorption and chemisorption (competitive-consecutive reaction according to (1a, 1b)). Figure 3 depicts profiles of the local mass transfer coefficient along the bubble polar angle θ for different bubble diameters. Note that the displayed values are computed by averaging along the bubbles' azimuthal angles. It can be easily seen for both cases of physisorption (Fig. 3a) and chemisorption (Fig. 3b) that decreasing values of the local mass transfer coefficients in region I correspond to increasing bubble sizes. This can be ascribed to longer residence times, the flatter the bubble shapes become. In the vicinity of the equatorial planes (region II), a significant increase of the mass transfer coefficient can be observed. The higher the deformation of the bubbles, the higher the tangential velocities in this region and the thinner the concentration boundary layers. In region III, the local mass transfer coefficients are found to rapidly decrease due to the appearance of closed wake zones in the rear of the bubbles which effectively hinders exchange with fresh fluid by advection, leaving diffusion the only transport mechanism for species to leave this region. In region III, there are also noticeable differences between non-reactive and reactive cases in the profiles for the local mass transfer coefficients corresponding to the same bubble sizes. Here, the liquid slows down and thus higher local concentration values of the transfer species cause the chemical reaction to intensify. This renewal

a) physisorption

b) chemisorption (competitive consecutive reaction)
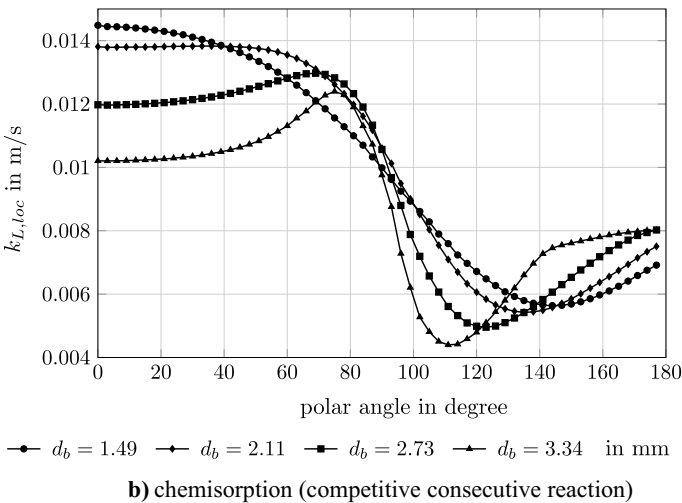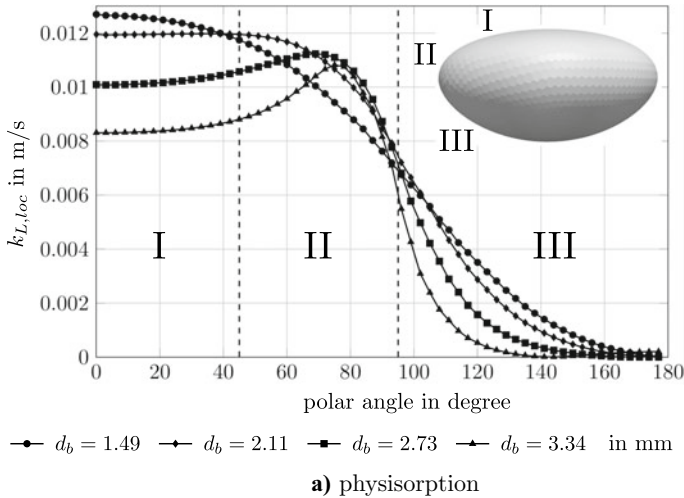
Fig. 3 Local mass transfer coefficients as a function of polar angle

of the boundary layers becomes even more evident in the presence of the recircu-
lating vortices. This enhancement due the chemical reaction significantly increases
the mass transfer locally. Obviously, this effect becomes more pronounced for higher
reaction rates, i.e. larger Damköhler numbers. However, the interfacial area affected
by mass transfer enhancement is only a small part of the total bubble surface (cf.
Fig. 5, upper row) with a limited contribution to the overall enhancement.

Regarding global reaction engineering parameters, the global Sherwood numbers
have been found to increase monotonically with increasing bubble Reynolds
numbers, while for the global mass transfer coefficient a maximum is observed

at $Re_b = 118 (d_b = 2.11 \text{ mm})$, which is explained above analyzing the local mass transfer coefficient profiles. A particular good agreement has been found with the Sherwood number correlation of Takemura and Yabe [12] for Reynolds numbers less than 150, and with the one by Winnikow [24] for higher Reynolds numbers. The global enhancement factor has been found to be nearly independent of both the bubble Reynolds number and the Schmidt number, particularly for realistic parameters, i.e. high Schmidt numbers. This almost independence is in agreement with the film theory for species transfer, where the enhancement factor is solely dependent on the Hatta number ($Ha := \sqrt{k_1 c_{A,\text{in}} D_{A,l}}/k_l^{\text{phys}}$). For more details, the interested reader is referred to [7].

4.3 Product Selectivity

Regarding the impact of different fluid dynamic conditions and chemical reaction intensities on the product selectivity of the competitive consecutive system (1a, 1b), the present simulation campaign [7] revealed important differences to results from a detailed computational analysis by Khinast et al. [4, 5]. The key point here has been that, while Khinast et al. used a 2D fixed-bubble model, in this simulation campaign a 3D ALE interface tracking method has been deployed, which enables to gain detailed insights into the local interplay of the 3D and unsteady dynamics of the bubble interfaces, transient mass transfer and chemical reactions. In particular, it has been found for moderate to fast reaction intensities and for a given ratio of reaction intensities of $\kappa = 10$ that the product selectivity is monotonously decreasing with increasing bubble Reynolds numbers Re_b, while Khinast et al. have observed a non-monotone behaviour. This discrepancy of simulation outcomes of [4] versus [7] is due to a combination of 3D and unsteady effects, which have been captured solely in the latter work (see Fig. 5). More precisely, it can be observed that, if breakup of the azimuthal symmetry occurs (cp. Fig. 5c for the largest bubble in this simulation campaign, i.e. ($d_b = 3.86$ mm)), this leads to a flow configuration such that fluid elements going around the bubble experience significantly different contact times depending on the bubble side, along which the elements flow around the bubble. Moreover, the presence of vortical structures developing perpendicular to the streamwise main direction, further increases residence time close to the bubble surface. As a consequence, due to locally high concentrations of transfer species B, significant amount of side product S is formed, leading to the formation of a region characterized by low local product selectivity at the rear, see Fig. 5c for $Eo = 2$ (bottom row). Increasing the ratio of reaction intensities (here to $\kappa = 100$), the global product selectivity is observed to become almost independent from the bubble Reynolds numbers for fast reactions [7]. Under such conditions, the reaction zone becomes even smaller. Thus, there is no noticeable influence of the fluid dynamic conditions of rising single bubbles on the local product selectivity in their wake. Increasing the

Fig. 4 Global selectivity
versus bubble Reynolds
number for the competitive
consecutive reaction network
for Schmidt numbers Sc ∈
{10, 100}, $Da_1 = 1$, $\kappa = 10$,
reproduced from [7] with
permission
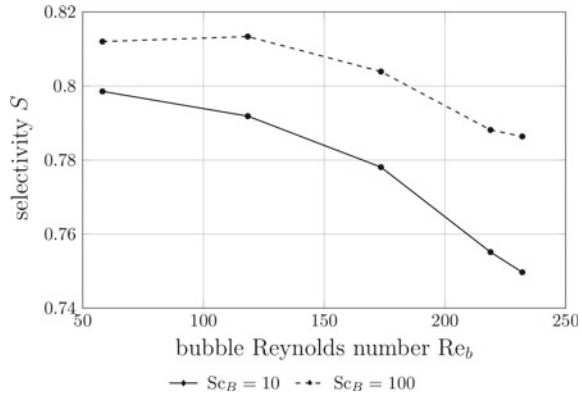
Schmidt number, the dependence of product selectivity from the bubble Reynolds
numbers is likewise diminishing—cf. Fig. 4.

5 Reactive Species Transfer for Taylor Bubbles

Taylor bubbles are elongated bubbles which almost completely fill the cross-sectional
area of typically straight milli- or micro-channels. The advantages of Taylor flow
in reaction engineering are [25]: high values of specific exchange area, low axial
dispersion due to separation of the liquid by bubbles into distinct slugs, high mixing
rates within the liquid slugs due to recirculation. Clearly, due to the high characteristic
interfacial area density per unit volume and short diffusion lengths for mass transfer
from the gaseous phase through the thin liquid film to the channel wall, high heat
and mass transfer rates can be realised. Thus, Taylor bubbles have been a guiding
measure of the present priority program DFG-SPP 1740 and have been subject to
in-depth investigation in the second period.

In the present work we have numerically investigated a specific Taylor bubble
setup, which has been originally studied experimentally in [9] and since then has
been subject to further theoretical work in [26, 27]. Experimental details can be found
in the original article and also in Chapter "Visualization and Quantitative Analysis
of Consecutive Reactions in Taylor Bubble Flows" of this book. This work aims
to validate the most important geometrical parameters of the Taylor bubble, using
experimental data as a sensitive measure for correctly capturing the fluid dynamics.
Then, chemisorption with a chemical reaction scheme according to (1a, 1b) is inves-
tigated with focus on the product selectivity. In particular, we aim to reveal local
selectivities in the vicinity of the Taylor bubble surface and its wake region using
highly resolved computational data gained here.

a) Eo = 1

b) Eo = 1.5

c) Eo = 2

Fig. 5 Local distributions of Sherwood number on bubble surfaces and product selectivity in cutting plane (images in top row). Local concentrations and reaction rates of transfer and product species and resulting selectivity (images in mid and bottom rows)

5.1 Computational Case Setup

From a computational point of view, it is utmost demanding to accurately resolve the thin film region between the bubble and the wall. Previous studies, e.g. [28], have revealed that at least five mesh cells are required along the radial direction in the film region for accurate results. Effectively, this decreases cell sizes in this region to a

few micrometers. It is emphasized that capturing the velocity profile in the thinnest film region is crucial for correctly predicting both the Taylor bubble's shape and its rise velocity. Since such challenging resolution requirements increase the overall number of computational mesh cells significantly, particularly 3D simulations suffer from high computational costs. For this reason, most numerical studies either have used modified physical fluid parameters [29] (resulting in thicker liquid films) or simplified geometries [4] (e.g. 2D setups). In this study, axisymmetry is exploited and a wedge setup is employed for the present Taylor bubble case. This is justified due to the low Reynolds number of the flow and the symmetric velocity field including symmetric vortex structures in the bubble wake, which have been observed in the experimental studies.

To efficiently arrive at a stationary bubble shape and velocity field at affordable computational time, the bubble shape from the experimental results has been used for initialization. The in- and outlet boundaries of the channel are placed in such a way that they do not bias the flow around the bubble. In Fig. 6 (left), the numerical setup for a Taylor bubble using a moving reference frame is shown. On the right hand side of Fig. 6, the mesh is depicted with focus on the liquid film region around the investigated Taylor bubble, the inset reveals details of the fine mesh resolution applied in this region. As shown, the mesh is hexahedra-dominated, with static mesh refinement

a) Sketch of case setup   **b)** Computational mesh
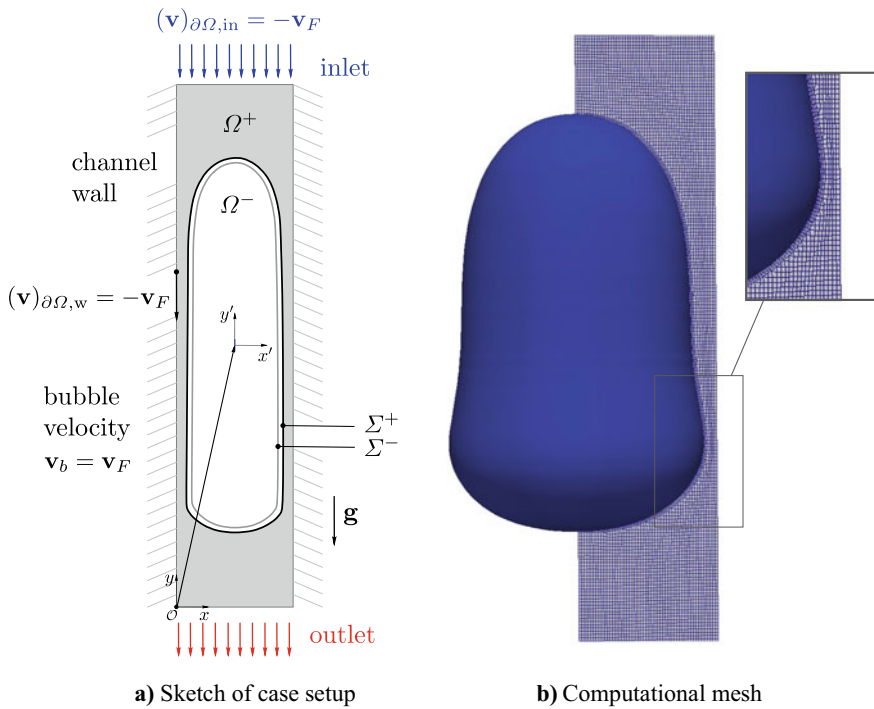
Fig. 6 Case setup and initial mesh for the Taylor bubble investigated experimentally in [9]

Table 5 Values of physical quantities for Taylor bubble

Parameter	Value
ρ_l	1000 kg/m^3
ρ_g	1.205 kg/m^3
μ_l	4.46×10^{-3} kg/ms
μ_g	1.81×10^{-5} kg/ms
σ	0.072 kg/s^2
D_l	1.62×10^{-8} m^2/s
d_{eq}	7.58 mm

at the bubble interface. Additionally, this practice allows to refine the mesh, where required. For instance, for species transport simulations with realistic diffusivities, the mentioned high-Schmidt-number problem, i.e. species boundary layers of only a few micrometers thickness, require significantly higher mesh resolutions around the bubble. The axisymmetric setup used in the present study is shown to allow for accurate simulation results at affordable computational times and high spatial resolution of regions of interest for reaction engineering.

The physical parameters for the hydrodynamics and the physisorption of the considered O_2 Taylor bubble in water are reported in Table 5. The volume-equivalent sphere diameter of the bubble is $d_b = 7.58$ mm, cf. [9].

5.2 Taylor Bubble Hydrodynamics

In analog to previous studies [25] and to Chapter "Visualization and Quantitative Analysis of Consecutive Reactions in Taylor Bubble Flows", we compare the shape of the Taylor bubble with experimental results for validation. The comparison is performed for a set of geometrical target parameters which has been shown to be suitable for validation of the bubble fluid dynamics, cf. [25]. As depicted in Table 6, the bubble volume, length and minimum film thickness are in good agreement with the experimental results. The deviation of the minimum film thickness corresponds to the maximum camera resolution from the experiments (approximately 1 pixel).

Table 6 Geometrical target quantities assessing the Taylor bubble shape

	Bubble volume	Bubble length	Min. film thickness
Experiment [9]	2.28×10^{-7} m^3	9.67 mm	174 µm
Simulation	2.285×10^{-7} m^3	9.55 mm	184 µm
Deviation	0.002%	1.24%	5.75%

The bubble volume remains constant over the whole simulation time, although the bubble is subject to large shape oscillations until the steady state is reached.

Comparing the velocity field and rise velocity of the simulated Taylor bubble with the experimental results, discrepancies are still observed and are subject to ongoing research. Most obviously, where the experimental results suggest a closed vortex behind the bubble, the numerical results show a closed wake region. Moreover, the velocity values are significantly higher in the simulation than in the experiments.

The good agreement in geometric target quantities but differences in fluid dynamics might be an indication for the presence of contamination, e.g. low concentrations of surface active agents (surfactants). With the influence of surfactant being accounted for, it is expected that the resulting local Marangoni forces induced by surfactants along the interface would lead to reduced velocities in the film region and a smaller overall rise velocity of the Taylor bubble. Some examples for experimental investigations on the influence of surfactants in Taylor bubble flow can be found in [30–32]. Nevertheless, a high-fidelity computational analysis of surfactant influence on the behavior of Taylor bubbles is not straightforward and indeed literature results even contradict each other [33]. Therefore, this influence on hydrodynamics and reactive mass transfer as well as product selectivity has to be investigated in-depth within the remaining time of the present project. For these simulations, the above mentioned subgrid scale models introduced in [13, 15, 21] will be utilized for the sorption of surfactants onto the interface.

5.3 Reactive Mass Transfer

The competitive-consecutive reaction system (1a, 1b) is studied. To investigate the local interplay of fluid dynamics, reactive mass transfer and chemical reaction, a simulation campaign varying the reaction rates of both equations has been performed.

The same chemical parameters as for the case of single bubbles rising in quiescent liquid have been used such that the Damköhler number of the first reaction is $Da_1 \in \{0.01, 0.1, 1, 10\}$ and $\kappa = \{10, 100\}$. For the Taylor bubble, only faster reactions with $Da_1 \geq 1$ are investigated for comparison reasons to the reaction systems provided in Chapter "Control of the Formation and Reaction of Copper-Oxygen Adduct Complexes in Multiphase Streams". Figure 7 shows the local simulation results regarding the concentration fields of the involved chemical species and the local product selectivity for two different physico-chemical cases. The upper row shows the local Sherwood number distribution on the interface as well as the local product selectivity in the cutting plane. Additionally, streamlines of the resulting steady state are shown. Note, that all fields are axisymmetric—only displayed in different cutting planes for clarity.

The depletion of selectivity, which corresponds to a higher production of the undesired side product, is mainly present in the wake of the bubble as it has been observed as well for the single rising bubbles, see Fig. 5. In the previous section, Fig. 5a shows the local product selectivity for $Da_1 = 1$ and $\kappa = 10$ for a rising
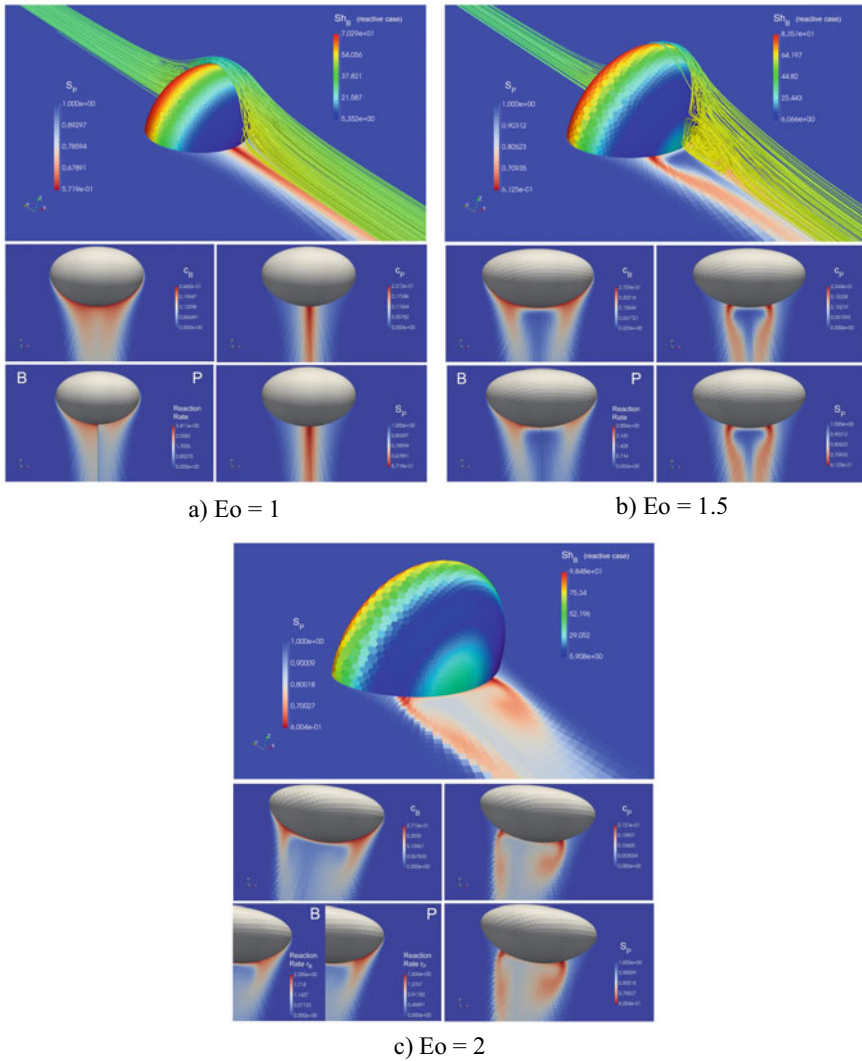
a) Da = 1 and = 10   b) Da = 10 and = 100
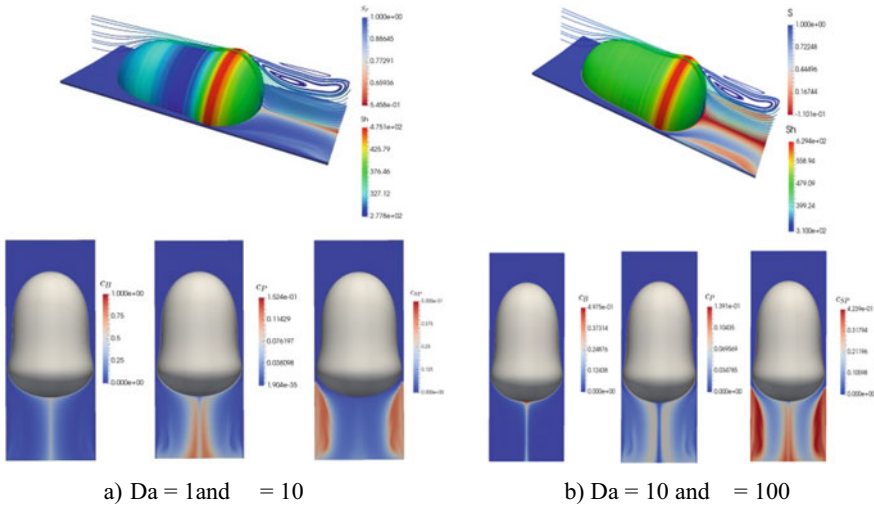
Fig. 7 Local distributions of Sherwood number on bubble surfaces and product selectivity in cutting plane (images in top row). Local concentrations of transfer species, product and by-product (images in bottom row)

bubble with a closed wake. Note that the minimum value of product selectivity in Fig. 7a is still much higher than the one found for the freely rising single bubble, and is ascribed to more intense mixing behind Taylor bubbles leading to the formation of the desired product P rather than the side-product. Figure 7 also depicts the local Sherwood number. In the bottom part of Fig. 7a the local concentration fields of the transfer species B, the product P and the side-product SP are provided. The product concentration is observed to be highest directly at the rear part of the bubble close to the symmetry axis, where the species is quickly advected downwards and can thus not react further with the transfer species. The side-product concentration is highest in the vicinity of the channel wall, where the velocity is low. For comparison, the same fields are shown for a reaction scheme with higher reaction rates in Fig. 7b. For both conditions, the influence of fluid dynamics is qualitatively the same. However, due to the higher reaction rates, the local concentrations of the transfer species are significantly lower. Consequently, the local Sherwood number and mass transfer rate are found to be higher. The selectivity is lower for higher reaction rates in the bubble wake, particularly in regions of small fluid velocities, i.e. close to the channel axis. Here, the product selectivity even becomes negative, which means that more of the product P is consumed by the second reaction than locally formed by the first reaction. In future work, the ALE interface tracking code, enhanced within this project, will be deployed to systematically investigate the reactive mass transfer at Taylor bubbles.

6 Conclusion

Direct numerical simulations of reactive mass transfer at rising bubbles have been performed deploying an ALE interface tracking flow solver which has been enhanced to account for mass transfer and chemical reactions (chemisorption). A prototypical competitive-consecutive reaction mechanism was employed to investigate the influence of bubble dynamics on local Sherwood numbers, enhancement factors and product selectivities.

Two different method enhancements have been implemented, tested and employed in order to cope with the high bubble dynamics and multiscale issue of reactive mass transfer at rising bubbles. The first approach, devised for freely rising bubbles, used a second computational mesh for the liquid domain, which has been refined to capture the thin concentration boundary layer in the vicinity of the bubble interface and used for the species transport only. This has enabled the accurate computation of mass transport across the interface of deformable bubbles at higher Schmidt numbers for 3D simulations. In the second step, a different two-mesh approach has been developed and utilized. Herein, each fluid phase is represented by a separate mesh. The two-phase fluid dynamics is realised in a coupled (partitioned) fashion by means of a Dirichlet-Neumann algorithm, leading to significantly improved robustness (stability and convergence) properties even for high interfacial dynamics. After validation, both approaches have been used for simulation campaigns with focus on chemisorption from single rising bubbles and Taylor bubbles, respectively. A detailed computational analysis revealed the influence on bubble dynamics on local reaction engineering quantities such as Sherwood numbers, enhancement factors and product selectivities.

Local selectivity fields, which are not available from experiments, have been accessible from local simulation data gained within the present project. On this basis, regions at the rear of the bubbles have been identified, which are characterized by enhanced formation and high local selectivity of the desired product. The results show that for realistic model parameters, i.e. high Schmidt and Damköhler numbers, the influence of fluid dynamics vanishes, i.e. become virtually independent from the bubble Reynolds number. Then, most of the relevant chemical conversion takes place within the boundary layer.

References

1. Krishna R, Sie ST (2000) Design and scale-up of the Fischer-Tropsch bubble column slurry reactor. Fuel Process Technol 64(1):73–105
2. Tsaoulidis D, Angeli P (2015) Effect of channel size on mass transfer during liquid-liquid plug flow in small scale extractors. Chem Eng J 262:785 –793. issn: 1385-8947

3. Kück U, Schlüter M, Räbiger N (2009) Analyse des grenzschichtnahen Stofftransports an frei aufsteigenden Gasblasen. Chem Ing Tec 81(10):1599–1606
4. Khinast JG (2001) Impact of 2-D bubble dynamics on the selectivity of fast gas-liquid reactions. AIChE J 47(10):2304–2319
5. Khinast JG, Koynov AA, Leib TM (2003) Reactive mass transfer at gas-liquid interfaces: impact of micro-scale fluid dynamics on yield and selectivity of liquid-phase cyclohexane oxidation. Chem Eng Sci 58(17):3961–3971
6. Darmana D, Deen NG, Kuipers JAM (2006) Detailed 3D modeling of mass transfer processes in two-phase flows with dynamic interfaces. Chem Eng Technol 29(9):1027–1033
7. Falcone M, Bothe D, Marschall H (2018) 3D direct numerical simulations of reactive mass transfer from deformable single bubbles: an analysis of mass transfer coefficients and reaction selectivities. Chem Eng Sci 177:523–536
8. Kastens S et al (2015) Mass transfer from single Taylor bubbles in minichannels. Chem Eng Technol 38(11):1925–1932
9. Kastens S et al (2017) Test system for the investigation of reactive Taylor bubbles. Chem Eng Technol 40(8):1494–1501
10. Paul M et al (2018) Reaction systems for bubbly flows. Eur J Inorg Chem 2101–2124
11. Felis F et al (2019) Using a bio-inspired copper complex to investigate reactive mass transfer around an oxygen bubble rising freely in a thin-gap cell. Chem Eng Sci 207:1256–1269
12. Takemura F, Yabe A (1998) Gas dissolution process of spherical rising gas bubbles. Chem Eng Sci 53(15):2691–2699. issn: 0009-2509.
13. Bothe D, Fleckenstein S (2013) A Volume-of-fluid-based method for mass transfer processes at fluid particles. Chem Eng Sci 101:283–302
14. Dieter-Kissling K, Marschall H, Bothe D (2015) Numerical method for coupled interfacial surfactant transport on dynamic surface meshes of general topology. Comput Fluids 109
15. Pesci C et al (2018) Computational analysis of single rising bubbles influ-enced by soluble surfactant. J Fluid Mech 856:709–763
16. Sørensen LS (1999) An introduction to computational fluid dynamics: the finite volume method. English
17. Peric M, Kessler R, Scheuerer G (1988) Comparison of finite-volume numerical methods with staggered and colocated grids. Comput Fluids 16(4):389–403
18. Tukovi´c Z, Jasak H (2008) Simulation of free-rising bubble with soluble surfactant using moving mesh finite volume/area method. In: 6th international conference on CFD in Oil & Gas, Metallurgicaland Process Industries SINTEF/NTNU. Trondheim, Norway, Oct 2008
19. Weber P, Marschall H, Bothe D (2017) Highly accurate two-phase speciestransfer based on ALE Interface-Tracking. Int J Heat Mass Transfer 104:759–773
20. Weiner A, Bothe D (2017) Advanced subgrid-scale modeling forconvection-dominated species transport at fluid interfaces with applica-tion to mass transfer from rising bubbles. J Comput Phys 347:261–289. issn: 0021-9991
21. Weiner A et al (2019) Data-driven subgrid-scale modeling for convection-dominated concentration boundary layers. Chem Eng Technol 42(7):1349–1356
22. Satapathy R, Smith W (1961) The motion of single immiscible dropsthrough a liquid. J Fluid Mech 10(4):561–570
23. Hasslberger J, Marten S, Klein M (2019) A theoretical investigation of flow topologies in bubble- and droplet-affected flows. Fluids 4(3)
24. Winnikow S (1967) Letter to the editors. Chem Eng Sci 22(3):477, Mar 1967
25. Marschall H et al (2014) Validation of interface capturing and tracking techniques with different surface tension treatments against a Taylor bubble benchmark problem. Comput Fluids 102:336–352
26. von Kameke A et al (2019) How coherent structures dominate the residence time in a bubble wake: an experimental example. Chem Eng Sci 207:317–326
27. Llamas CG et al (2020) Potential of Lagrangian analysis methods in the study of chemical reactors. Chem Ing Tec 92(5):540–553

28. Langewisch DR, Buongiorno J (2015) Prediction of film thickness, bubble velocity, and pressure drop for capillary slug flow using a CFD-generated database. Int J Heat Fluid Flow 54:250–257
29. Dang M, Yue J, Chen G (2015) Numerical simulation of Taylor bubble formation in a microchannel with a converging shape mixing junction. Chem Eng J 262:616–627
30. Haghnegahdar M, Boden S, Hampel U (2016) Investigation of surfactant effect on the bubble shape and mass transfer in a milli-channel using high-resolution microfocus X-ray imaging. Int J Multiph Flow 87:184–196
31. Hayashi K, Tomiyama A (2012) Effects of surfactant on terminal velocity of a Taylor bubble in a vertical pipe. Int J Multiph Flow 39:78–87
32. Hori Y et al (2020) Mass transfer from single carbon-dioxide bubbles in surfactant-electrolyte mixed aqueous solutions in vertical pipes. Int J Multiph Flow 124
33. Nekoeian S et al (2019) Effect of surfactants on mass transfer coefficients in bubble column contactors: an interpretative critical review study. Rev Chem Eng

Modelling the Influence of Bubble Dynamics on Motion, Mass Transfer and Chemical Reaction in LES-Euler/Lagrange Computations

Manuel A. Taborda and Martin Sommerfeld

Abstract The Euler/Lagrange approach is an attractive and descriptive method for numerically computing large-scale dispersed multi-phase flows, such as reactive bubbly flows, where however the dispersed phase elements are treated as point-masses. This approach was extended in the present study in order to account for finite size effects, specifically shape and trajectory oscillations as well as the resulting dynamic mass transfer, which are essential in bubble column flows. The flow field was computed by the Large Eddy Simulation (LES) concept with full two-way coupling in momentum and the modelled sub-grid-scale (SGS) turbulence, respecting also bubble-induced turbulence (BIT). Bubble motion was calculated including all relevant forces (i.e. drag, lift, wall force, added mass, fluid inertia, gravity/buoyancy and Basset force), which were extended considering the modelled instantaneous bubble eccentricity and also incorporating bubble transport by the SGS turbulence. Mass transfer was modelled also accounting for bubble dynamic behaviour (i.e. shape oscillations). For validating the model extensions thorough numerical computations were conducted for a number of experimental test cases with only CO_2 absorption as well as chemical reactions considering single bubble rise and also bubble swarms in laboratory bubble columns. It is demonstrated that for point-particle approaches the modelling of bubble dynamics in motion and mass transfer is essential for accurate predictions. Only with this extension it is possible to obtain correct bubble lateral dispersion (i.e. bubble fluctuating velocities) and a remarkably higher mass transfer provoked by larger surface area of deformed bubbles. Thereby, the bubble size distribution variation along the bubble column in a reactive system can be predicted with a very good agreement compared to measurements. The transient evolution of species concentration in the column occurred much faster considering the bubble dynamics model resulting in a much better agreement with the measured *pH* variation.

M. A. Taborda · M. Sommerfeld (✉)

Institute for Process Engineering, Multiphase Flow Systems, Otto-von-Guericke Magdeburg University, Hoher Weg 7b, 06120 Halle (Saale), Germany
e-mail: martin.sommerfeld@ovgu.de

1 Introduction

Numerical modelling of bubble column reactors has been an intensive research area during the last decades (see e.g. [1]), but due to the involved numerous transport phenomena occurring at the bubble-level, the numerical computation of such two-phase flows and their accurate modelling is still a challenge. Based on the assumption of point-bubbles, numerous different models and closures have been proposed and used for describing the transport of the bubbles during their rising path. However, the dynamics of bubbles, i.e. tumbling motion and oscillations, is so far mostly neglected when mass transfer and chemical reactions are involved. Therefore, it is essential to propose and evaluate models that can adequately capture the bubble rising dynamics, their effect on the liquid phase characteristics and likewise be able to use them in computational modelling.

Euler/Lagrange method is a computational approach for disperse two-phase flows, in which the continuous phase is treated as a continuum. However, the disperse phase is simulated with a discrete approach where a large number of point-wise bubbles are tracked through the previously calculated liquid flow field, taking into account relevant forces on the basis of Newton's law of motion. The local properties of the disperse phase are then obtained from temporal and spatial statistical averaging. The benefit of such a Lagrangian computation is the high degree of detail with which elementary processes can be modelled at the bubble scale (e.g., bubble-wall interaction, coalescence, shrinking) despite the use of the point-particle approximation [2], however, accurate models have to be devised. This method has also been applied very frequently for flows in bubble columns [3–6]. A further advantage of this approach, especially in the case of bubbly flows with mass transfer, coalescence and break-up, is that the transient evolution of the bubble size distribution can be easily computed with no additional numerical complexity [7, 8], and also allowing for modelling of a possible back-diffusion [9].

2 Summary of Numerical Modelling

Numerical simulations were based on a custom CFD model using the open-source platform *OpenFOAM*®, including an in-house developed advanced Euler/Lagrange approach. In addition, this model for bubbly flows takes into account the effects of bubble dynamics on motion, mass transfer and chemical reaction, grounded on experimental observations, treating the bubbles with the "point-mass" approximation method. In order to give an overview of the developments, a summary of the numerical modelling used for the description of the treatment of both phases is presented below.

2.1 Continuous Phase

The hydrodynamics of the flow field is computed based on the volume-averaged Navier-Stokes equations and turbulence of the continuous phase is modelled by the Large Eddy Simulation (LES) approach, requiring a fully transient solution of the continuity and momentum transport equations, as follows:

$$\frac{\partial(\alpha_c \rho_c)}{\partial t} + \nabla \cdot (\alpha_c \rho_c \boldsymbol{u}_c) = 0 \tag{1}$$

$$\frac{\partial(\alpha_c \rho_c \boldsymbol{u}_c)}{\partial t} + \nabla \cdot (\alpha_c \rho_c \boldsymbol{u}_c \boldsymbol{u}_c) = -\nabla p - \nabla \cdot (\alpha_c \rho_c \boldsymbol{\tau}_c) + \alpha_c \rho_c \boldsymbol{g} + \overline{\boldsymbol{S}_{u,p}} \tag{2}$$

$$\boldsymbol{\tau}_c = -\mu_{eff} \left\{ \left(\nabla \boldsymbol{u}_c + (\nabla \boldsymbol{u}_c)^{\mathrm{T}} \right) - \frac{2}{3} I (\nabla \cdot \boldsymbol{u}_c) \right\} \tag{3}$$

In which, $\boldsymbol{u}_c$ represent the velocity vector of the carrier phase, p indicates the pressure and α_c is the volume fraction of the carrier phase due to the presence of bubbles. The effective viscosity $\mu_{eff} = \mu_c + \mu_{t,c}$ for the continuous phase is composed of two contributions: the molecular viscosity μ_c and the so-called turbulent viscosity $\mu_{t,c}$. The interaction between the two phases is described by the cell-based momentum source-term $\overline{\boldsymbol{S}_{u,p}}$, in Eq. (4) and it is calculated by summing over all the parcels k crossing the computational cell with n Lagrangian time steps:

$$\overline{\boldsymbol{S}_{u,p}} = -\frac{1}{V_{cv} \Delta t_{\mathrm{E}}} \sum_{k} m_k N_k \sum_{n} \left[\left(\boldsymbol{u}_k^{n+1} - \boldsymbol{u}_k^{n} \right) - \boldsymbol{g} \left(1 - \frac{\rho_c}{\rho_{\mathrm{B}}} \right) \Delta t_{\mathrm{L}} \right] \tag{4}$$

Herein, V_{cv}, Δt_{E}, Δt_{L} and m_k, indicates the volume of a cell, the Eulerian and Lagrangian time-steps and the mass of the bubble, respectively. N_k is the number of real bubbles in the parcel k and in this study one parcel represents one real bubble only. $\boldsymbol{u}_k^{n}$ and $\boldsymbol{u}_k^{n+1}$ are the bubble velocities at the beginning and the end of a Lagrangian time step, ρ_c and ρ_{G} are the density of the continuous and gas phase, respectively. Typically, the Lagrangian bubble tracking time steps Δt_{L} (see below) are much lower than the Eulerian time step Δt_{E} so that during one Eulerian time step multiple Lagrangian time steps may be performed. Thus, in this quasi-unsteady approach, the bubbles see a frozen flow field [10] and the source terms are obtained by ensemble and temporal averaging during one Eulerian time step.

The turbulent viscosity accounts for the contribution of the sub-grid scales to turbulence (Eq. 5) and it was described by the work of Yoshizawa [11], which uses a one-equation eddy viscosity model to describe the SGS turbulent kinetic energy k_{SGS}, transport equation (Eq. 6). It was derived to account for the production, diffusion and dissipation transient effects. Furthermore, the bubble contribution to the turbulent modification, generally called as bubble-induced turbulence (BIT), was also considered including its effect as a source term in the k_{SGS} transport equation, as follows:

$$\mu_{t,c} = \rho_c \Delta C_k \sqrt{k_{SGS}} \tag{5}$$

$$\frac{D}{Dt}(\rho_c k_{SGS}) = \nabla \cdot \left(\rho_c \nu_{eff} \nabla k_{SGS}\right) + \rho_c G - \frac{2}{3}\rho_c k_{SGS} \nabla \cdot \boldsymbol{u}_c$$
$$- \frac{C_e \rho_c k_{SGS}^{3/2}}{\Delta} + S_{k,BIT}$$

$$G = \nu_{eff} \nabla \boldsymbol{u}_c \left(2\overline{S_{i,j}} - \frac{1}{3} tr\left(2\overline{S_{i,j}}\right)\delta_{ij}\right) \tag{6}$$

$$\overline{S_{i,j}} = \frac{1}{2}\left(\nabla \boldsymbol{u}_c + (\nabla \boldsymbol{u}_c)^{\mathrm{T}}\right) \tag{7}$$

$$S_{k,BIT} = \sum_{i=1}^{3} \overline{u_{B,i} S_{u,p,i}} - \overline{u_c S_{u,p,i}} \tag{8}$$

Here, the SGS length scale is giving by Δ, based on the volume of the computational cell and $C_k = 0.094$ as well as $C_e = 1.048$ are model constants. Furthermore, $\overline{S_{i,j}}$ is the symmetric deviatory part of strain tensor of the resolved scales. $S_{k,BIT}$ term accounts for the dissipation and enhancement of turbulence by the bubbles through their lagged response behaviour and a possible wake separation [3].

The presence of chemical species in the modelling is accounted for through a transport equation for each species as follows:

$$\frac{\partial \left(\alpha_c \rho_c Y_{i,c}\right)}{\partial t} + \nabla \cdot \left(\alpha_c \rho_c u_c Y_{i,c}\right) = \nabla \cdot \left[\alpha_c D_{i,eff} \nabla \left(\rho_c Y_{i,c}\right)\right] + \alpha_c S_{i,c} + S'_{Y,i,p} \tag{9}$$

$$S'_{Y,i,p} = -\frac{1}{V_{cv}\Delta t_E} \sum_{k}\sum_{n}\left[\left(m_k^{n+1} - m_k^{n}\right)N_k\right] \tag{10}$$

where $Y_{i,c}$ is the mass fraction of the species i in the continuous phase, the last term in the Eq. (9) is the source term that accounts for production or consumption of the species i due to chemical reactions. The cell-based species source term $S'_{Y,i,p}$ correspond to the phase interaction of the species transfer from the bubbles to the continuous phase. In the same approach as for the momentum source term, the species source term is summed over all parcels k traversing the control volume within a number of n Lagrangian time steps. The effective diffusion coefficient is also taken into account based on SGS turbulence, as follows:

$$D_{i,eff} = D_{i,c} + D_{t,i,c} \tag{11}$$

$$D_{t,i,c} = \frac{\mu_{eff}}{\rho_c Sc_{SGS}} \tag{12}$$

where Sc_{SGS} is the subgrid-scale Schmidt number of the small unresolved structures of turbulence, considered to be equal to 0.7. In this work, the SGS term is much larger than the molecular diffusion coefficient $D_{i,c}$, wherefore it could be practically neglected.

2.2 Dispersed Phase and Bubble Dynamics

Transient and three-dimensional dispersed phase model describes the dynamics of individual bubbles in a Lagrangian way. The motion of each individual bubble is calculated by considering all the relevant forces such as drag, transverse lift, added mass, wall-lubrication, Basset (history-term), gravity/buoyancy and pressure gradient. The bubble tracking is described by the Eqs. (13) and (14), presented with a complete explanation in Taborda et al. [9], and therefore only briefly summarized here:

$$\frac{d\boldsymbol{x}_B}{dt} = \boldsymbol{u}_B \tag{13}$$

$$
\begin{aligned}
m_B \frac{d\boldsymbol{u}_B}{dt} = {} & \frac{3}{4} \frac{\rho_c}{\rho_B d_B} m_B C_D (\boldsymbol{u}_c - \boldsymbol{u}_B) |\boldsymbol{u}_c - \boldsymbol{u}_B| \\
& + C_L m_B \frac{\rho_c}{\rho_B} [(\boldsymbol{u}_c - \boldsymbol{u}_B) \times (\nabla \times \boldsymbol{u}_c)] \\
& + C_{AM} m_B \frac{\rho_c}{\rho_B} \left(\frac{D\boldsymbol{u}_c}{Dt} - \frac{d\boldsymbol{u}_B}{dt} \right) \\
& + m_B \frac{2}{d_B} C_{BW} \left(\frac{d_B}{2h} \right)^2 \rho_c |(\boldsymbol{u}_c - \boldsymbol{u}_B) \cdot \boldsymbol{k}|^2 \boldsymbol{n} \\
& + C_B \int_{-\infty}^{t} K_B(t - \tau) \boldsymbol{f}(\tau) d\tau + m_B \boldsymbol{g} \left(1 - \frac{\rho_c}{\rho_B} \right) + m_B \frac{\rho_c}{\rho_B} \frac{D\boldsymbol{u}_c}{Dt}
\end{aligned} \tag{14}
$$

$$d_B = \sqrt[3]{\frac{6}{\pi} V_B} \quad ; \quad V_B = \frac{m_B}{\rho_B} = m_B \frac{RT}{p} \frac{1}{\sum_i Y_{B,i} W_i} \tag{15}$$

where C_D, C_L, C_{AM}, C_{BW}, C_B correspond to the coefficients for drag, transverse lift, added mass, wall-force, Basset-force coefficients respectively. K_B is the Basset integration kernel, $\boldsymbol{f}(\tau)$ the derivative of the relative velocity between the bubble and the liquid phase, and $\boldsymbol{n}$ and $\boldsymbol{k}$ are unit vectors normal and parallel to the column wall, respectively. With Eq. (15) the volumetric change of the bubbles due to pressure variation along the column height is calculated, based on the ideal gas law. Table 1 summarizes the closures for each force coefficient used in the Eq. (14).

Table 1 Description of coefficients of the considered forces

Force	Coefficient closure description
Drag force	Composite model with instantaneous eccentricity for Re_B- and Eo-regimes [12]
Transversal lift	Composite model with instantaneous eccentricity for Re_B- and Eo-regimes [12]
Added mass	Eccentricity and wall effect—[13, 14]
Wall-lubrication	Normal force with wall distance—Hosokawa et al. [15]
Basset force	Coefficient: Michaelides and Roig [16], solution algorithm: van Hinsberg et al. [17]

In Table 1, instantaneous values of the resistant coefficients were calculated based on the instantaneous properties of the bubbles, i.e. eccentricity and motion angle determined with the mentioned bubble dynamics model, explained below.

The stochastic turbulent dispersion model from Lipowsky and Sommerfeld [18] was considered in order to capture the bubble transport by the SGS turbulence fluctuations. Hence, it is necessary to generate the fluctuation of the fluid velocity seen by the bubbles (i.e. unresolved turbulence), which is required for the calculation of the forces. The model uses a generated single-step Langevin equation, dependent on correlation functions and adapted for LES applications, as follows:

$$\acute{u}_i^{n+1} = R_{P,i}(\Delta t_L, \Delta r)\, \acute{u}_i^n + \sigma_c \sqrt{1 - R_{P,i}^2(\Delta t_L, \Delta r)} \xi_i \tag{16}$$

in which the superscripts n and $n + 1$ denote the time step and the subscripts i corresponds to the spatial component. Δr is the spatial separation between the fluid element and the bubble during the Lagrangian time step Δt_L. The SGS turbulence may be considered to be isotropic so that σ_c represents the rms (root mean square)-value of the fluid velocity fluctuation and ξ_i denote independent Wiener processes with zero mean and unit variance. The correlation functions $R_{P,i}(\Delta t_L, \Delta r)$ have Lagrangian and Eulerian components:

$$R_{P,i}(\Delta t_L, \Delta r) = R_L(\Delta t_L) R_{E,ij}(\Delta r) \tag{17}$$

$$R_L(\Delta t_L) = exp\left(-\frac{\Delta t_L}{T_L}\right) \tag{18}$$

$$R_{E,ij}(\Delta r) = \{f(\Delta r) - g(\Delta r)\} \frac{\Delta r_i \Delta r_j}{|\Delta r|^2} + g(\Delta r)\delta_{ij} \tag{19}$$

where $f(\Delta r)$ and $g(\Delta r)$ are the longitudinal and transverse two-point correlation functions [19]. The required integral time T_L and the turbulent length scale L_E of the SGS turbulence were estimated with the turbulent kinetic energy and the dissipation rate, making use of approximation introduced by Lilly [20] for the dissipation rate:

$$T_L = 0.16 \frac{k_{SGS}}{\epsilon_{SGS}} \quad ; L_E = 3.0 \sigma_c T_L \tag{20}$$

$$\epsilon_{SGS} = \frac{C_\epsilon k_{SGS}^{3/2}}{\Delta} \tag{21}$$

$$\sigma_c = \sqrt{\frac{2}{3} k_{SGS}} \tag{22}$$

the dissipation constant was selected as $C_\epsilon = 0.7$ [21] and the SGS length scale is $\Delta = (V_{CV})^{1/3}$ based on the volume of the local computational cell.

The Lagrangian time-step for bubble tracking was dynamically calculated based on the different relevant times scales. The drag response time τ_B, the SGS turbulence time-scale T_L, and the bubble oscillation period τ_{osc} according to Lunde and Perkins [22] in order to provide an efficient use of the computational resources without losing temporal resolution. The minimum value was selected and making it one order of magnitude lower. A first-order Euler integration of the equations for bubbles position and velocities was used with a time step independently for each bubble.

$$\Delta t_L = 0.1 \min(\tau_B, T_L, \tau_{osc}) \tag{23}$$

$$\tau_B = \frac{4(\rho_B + 0.5\rho_c)d_B^2}{3\mu_c C_D Re_B} \tag{24}$$

$$\tau_{osc} = 2\pi \left(\frac{16\sqrt{2}\sigma \overline{\chi}^2}{\rho_c \left(\frac{d_B}{2}\right)^3 \left(1 + \overline{\chi}^2\right)^{3/2}} \right)^{-1/2} \tag{25}$$

Even with the consideration of SGS turbulent dispersion and bubble-induced turbulence it is of course not possible to represent the oscillatory motion of bubbles with point-particle Euler/Lagrange approaches [23]. This interaction is a consequence of the coupling of the flow around the bubbles and the wake separation. Typically, this bubble dynamics cannot be resolved when tracking point-masses and therefore an additional model which mimics bubbles oscillations is required. This oscillatory effect on bubble motion within the point-particle Euler/Lagrange approach was described based on experimental observations [24], mimicking bubble shape and trajectory oscillations as illustrated in Fig. 1 [12, 23]. This model extends the classical Lagrangian tracking approach for bubbles in a liquid, considering additional properties for the bubbles, such as eccentricity and motion angle, and predicting them stochastically over time. On the one hand, the model was designed in a simple way, ensuring low computational requirements and on the other hand, the model should mimic bubble dynamics as close as possible, without the necessity to solve the asymmetric deformation of the bubbles or the surrounded liquid flow.

In this framework, a Langevin model is used to describe the temporal evolution of the instantaneous bubble eccentricity calculated thought a combination of a correlated

Fig. 1 Illustration of parameters and angles used for the bubble dynamics model (the trajectory angle is γ and the orientation angle is defined as β; *Source* [23])
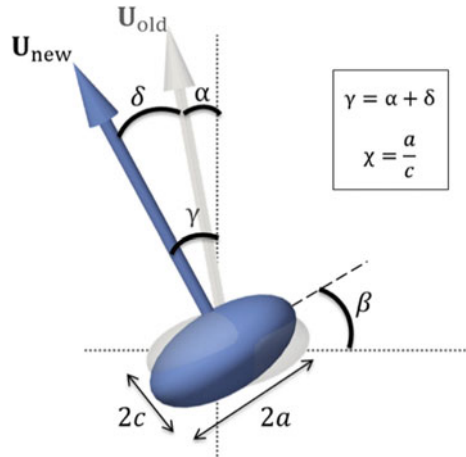
and a random part as follows:

$$\chi^{n+1} = \overline{\chi} + \left(\chi^n - \overline{\chi}\right)R_\chi + \sigma_\chi \xi \sqrt{1 - R_\chi^2} \tag{26}$$

$$R_\chi = exp\left(-\frac{\Delta t_L}{\tau_{osc}}\right) \tag{27}$$

where $\overline{\chi}$ and σ_χ are the mean bubble eccentricity and its correspondent rms value, respectively. These values will of course depend on the system properties (e.g. flow conditions or kind of liquid) and have to be available through experimental observation. In the present study these parameters were taken from detailed experiments performed in a bubble column using air bubbles in purified water from a reverse osmosis and considering gas volume fractions below 5% [24, 25].

The movement of the bubbles and the characteristic oscillation time scale are related in a fully three-dimensional way; therefore, it is necessary to evaluate two motion angles by the following equation:

$$\gamma_i^{n+1} = \alpha_i^n \left[1 + K_c\left(R_\gamma - 1\right)\right] + \sigma_\gamma \xi_i \sqrt{1 - R_\gamma^2} \tag{28}$$

$$R_\chi = R_\gamma = exp\left(-\frac{\Delta t}{\tau_{osc}}\right) \tag{29}$$

where in the present study the correlation coefficient $K_c = 0.5$ is used in order to obtain a good balance between entirely random in time when $K_c \to 0$, or completely correlated when $K_c \to 1$ as suggested by Muniz and Sommerfeld [12] based on a detailed experimental validation.

2.3 Mass Transfer

In order to simplify the modelling of mass transfer from bubbles to the liquid, it is common and practical to consider that the resistance for species transport remains only on the liquid side [5, 8, 26, 27]. Consequently, the mass transfer rate $\dot{m}_i$ is dependent on the concentration gradient between the liquid side interface and the liquid bulk defined as follows:

$$\frac{dm_i}{dt} = \dot{m}_i = E\rho_c k_c A_e \left(Y_{s,i,k} - Y_{\infty,i,k}\right) \tag{30}$$

$$A_e = 2\pi \left[a^2 + c^2 \frac{a \tanh(e)}{e}\right]$$

$$e = \sqrt{1 - \chi^{-2}} \quad ; a = \frac{d_{\mathrm{B}}}{2} \sqrt[3]{\chi} \quad ; c = \frac{a}{\chi} \tag{31}$$

where k_c represents the mass transfer coefficient defined in function of the Sherwood number, $k_c = \frac{Sh_i D_i}{d_B}$, $Y_{\infty,i,k}$ represents the bulk mass fraction of species i and $Y_{s,i,k}$ at the bubble surface (Fig. 2), both on the liquid side. A_e is the ellipsoidal bubble interfacial area, which is determined with the modelled instantaneous eccentricity.

A relation between the mass fractions at both sides of bubble interface can be obtained using Henry's constant $Y_{s,i,k} = H_{i,k} Y_{B,i} \frac{\rho_B}{\rho_c}$. In a similar way to the determination of the liquid velocity seen by the bubble, fluctuations of the species concentration around the bubble may be taken into account by assuming that $Y_{\infty,i,k}$ consists of two contributions, the mean mass fraction of the species interpolated to the bubble position $\overline{Y_{\infty,i,k}}$ and a standard deviation $\acute{Y}_{\infty,i,k}$ resulting from the variations of the mean values in the region around the bubble location as follows:

$$Y_{\infty,i,k} = \overline{Y_{\infty,i,k}} + \acute{Y}_{\infty,i,k} \tag{32}$$

Fig. 2 Illustration of species mass fraction profile for a bubble in a given computational cell n; constant value inside the bubble, bubble interface, species boundary layer and outside bulk value
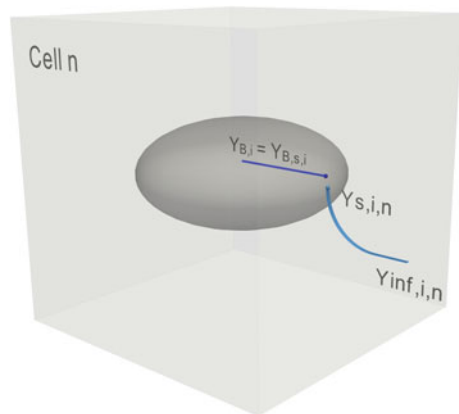
$$\acute{Y}_{\infty,i,k}{}^{n+1} = \acute{Y}_{\infty,i,k}{}^{n} R_L + \sigma_{Y,i} \xi_i \sqrt{1 - R_L^2} \tag{33}$$

$$\sigma_{Y,i} = \sqrt{\frac{1}{nb} \sum_{nb} \left(\frac{\overline{Y_{\infty,i,k}}_{nb} - \overline{Y_{\infty,i,k}}}{2} \right)^2} \tag{34}$$

where $\sigma_{Y,i}$ is the local rms (root mean square) cell value for the mass fraction of species i in the vicinity of the bubble position obtained from the nb (*neighbouring*) control volumes surrounding the bubble, which are typically the six control volumes connected to the faces of the control volume the bubble is residing in.

Numerous Sherwood number correlations for bubbles are commonly found in the literature in dependence of the Reynolds and Schmidt dimensionless numbers [28–31]. The bubble behaviour depends on its size, the bubbles are deformable and can oscillate leading an extra contribution to the mass transfer rate. The bubble oscillation is characterized by the fluid properties, bubble volume, and the available energy in the system. Montes et al. [32] proposed a correlation for the Sherwood number, taking into account effects of modification of the concentration profiles surrounding the bubbles as function of bubble oscillations:

$$Sh_i = \frac{2}{\sqrt{\pi}} Pe_i^{1/2} \left[I_{n1} + I_{n2} \frac{A}{\omega_n^2} We^{1/2} \right] \tag{35}$$

$$Pe_i = Re_B Sc_i \quad ; Sc_i = \frac{\mu_c}{\rho_c D_i} \quad ; We = \frac{\rho_c |u_B - u_c|^2 d_B}{\sigma} \tag{36}$$

$$A = \frac{1}{2} \left(\frac{\chi - 1}{\chi^{2/3}} \right) \tag{37}$$

In which A correspond to the oscillation amplitude and *We* is the Weber number. I_{n1} and I_{n2} are integral constants depending on the oscillation amplitude [32]. Pe, Sc and ω_n are Peclet number, Schmidt number and oscillation frequency of the bubble, respectively. These integrals can be solved for the range of amplitudes in use $(0 \leq A < 0.6)$ and fitted by a polynomial function of third order. Table 2 shows the results for the parameters with respect to the second mode of oscillation, having the form $I_{n(A)} = p_0 + p_1 A + p_2 A^2 + p_3 A^3$.

Table 2 Parameters determined for the integral constants I_{n1} and I_{n2} in Eq. (35)

	I_{n1}	I_{n2}
p_0	1	0.70538
p_1	0.05189	0.04875
p_2	0.34382	0.22029
p_3	0.29444	0.22087

Note that the terms inside the brackets of Eq. (35) become unity when the amplitude reaches a null value ($A \to 0$), at this point the correlation recovers the form introduced by Boussinesq [28] for an oscillating sphere, which is a reasonable assumption for the considered bubble size spectrum:

$$Sh_i = \frac{2}{\sqrt{\pi}} Pe_i^{1/2} \tag{38}$$

In some reactive systems, chemical reactions can influence the mass transfer. This influence is usually modelled through the multiplication with a so-called enhancement factor E, that relates the reactive mass transfer flux and the non-reactive mass transfer flux. In which a proper correlation is required for each reaction system [33–35] as described below.

2.4 Reaction Modelling

Reactions describe the transformation of one set of chemical elements into another. The solver can model the chemical reaction for a general stoichiometric equation for I species that are included in the reactions by:

$$\sum_{i=1}^{I} v_j^{i'} X^i \rightleftharpoons \sum_{i=1}^{I} v_j^{i''} X^i \tag{39}$$

where $v_j^{i'}$ and $v_j^{i''}$ are the stoichiometric coefficients of the reaction j for the reactant side and the product side and X^j represents the species j summation formula. For a chemical system with J reactions the production rate of a species i is specified by:

$$S_{i,c} = W^i \sum_{j=1}^{J} r_j \left(v_j^{i''} - v_j^{i'} \right) \tag{40}$$

The reactions velocity r_j of the j-th reaction depends on the forward and backward chemical reaction rates k_j' and k_j'', respectively. In addition, it depends on the concentrations of the participating species:

$$r_j = k_j' \prod_{i=1}^{I} \left(C_{i,c} \right)^{v_j^{i'}} - k_j'' \prod_{i=1}^{I} \left(C_{i,c} \right)^{v_j^{i''}} \tag{41}$$

The concentrations of the species are derived from the mass fractions, density and molecular weight:

$$C_{i,c} = Y_{i,c} \frac{\rho_{i,c}}{W^i} \tag{42}$$

Naturally, the reactions rates depend on the particular reaction case simulated, a detailed description of the reaction rates can be found for the specific studied case.

3 Cases Description, Setup and Results

In the present work a comparison with experimental data was realized in two stages using data which were obtained in the frame of the DFG priority research program in Germany, namely the SPP-1740 "Reactive Bubbly Flows". In the first case, the size reduction of single rising bubbles composed of CO_2 in pure water was evaluated in time, according to experimental setup of [36]. In the second test case, a swarm of bubbles (also CO_2) dissolving in a highly concentrated NaOH solution decreases its pH value due to reactions occurring with OH^- ions in the liquid phase [37]. These two cases were computed as a batch-process; therefore, they need to be simulated and evaluated also in a transient way, very well suitable for validation of mass transfer rates. Although in the second situation a consecutive-competitive reaction takes place, its mechanism has been extensively evaluated [38–43] and integral models were evaluated and validated [5, 44].

3.1 Single Bubbles

The results described in the following part have been obtained in collaboration with Prof. Matthias Kraume and his Ph.D. student David Merker, in which the experiments were conducted considering single CO_2 bubbles rising in a cylindrical column filled with water at the Technical University of Berlin. With the purpose to improve the evaluation of mass transfer in the experiments, distilled water was stripped with N_2 before each experiment. The column had a diameter of 75 mm and a height of 2 m. A single bubble case with, $d_{B0} = 4.5$ mm was considered here and evaluated in time with respect to their volume during 6 s, making use of a high speed camera which follows the rising bubble with a traversing system. In order to compute this case, a numerical structured O-grid with 51,939 volumes in total (261 per cross-section and 199 in the height) was used. The resulting ratio between the bubble size d_{B0} and the mean grid length scale Δx was $d_{B0}/\Delta x \approx 0.54$, which respects the limit proposed by Milleli et al. [45] given as $d_{B\text{-}mean}/\Delta x \leq 0.67$ for LES computations considering point-particles. All wall boundaries were set as no-slip condition for the liquid and the bubbles were rebound inelastically. Naturally, for this single bubble case only one bubble was injected and then tracked through the quiescent liquid without any flow and turbulence, similar to the experiment. Therefore, also two-way coupling is not relevant for this case. The applied Henry's dimensionless constant

Table 3 Description of the modelling assumptions related to describing bubble behaviour for different computational setups

Case	Model case description
Case 0	Pure CO_2 bubbles full dynamic model (dynamic Sherwood number Eq. (32))
Case 1: NO	Spherical bubbles—**no trajectory oscillations**, Sherwood number for non-deformable spherical bubble, Eq. (38)
Case 2: TO	Spherical bubbles—**only trajectory fluctuations**, Sherwood number for non-deformable spherical bubble, Eq. (38)
Case 3: FDM	Bubble trajectory and eccentricity oscillations (**full dynamics model**) and dynamic Sherwood number for deformed bubbles, Eq. (35)

for $T = 25$ °C was $H_{CO_2-H_2O} \cong 0.833$ [46], the diffusivity coefficient was set to $D_{CO_2-H_2O} = 1.92 \times 10^{-9} m^2/s$ and the Eulerian time-step was set to 5 ms in this case.

The simulations using the present model were conducted for the initial bubble size $d_{B0} = 4.5$ mm, considering at the beginning to consist of pure CO_2 (Case 0 specified in Table 3). The computed transient bubble diameter is compared with the experimental data (see also [36]) as shown in Fig. 3. In the experiments, after 6 s, bubble was still present in the system. In the simulations for Case 0 (Table 3) on the other hand the bubble has disappeared completely after 4 s already due to mass transfer. This situation is explained by a possible presence of a second component dissolved in the system and diffusing into the bubbles. This issue was already discussed by Merker et al. [36]. Considering pure CO_2 bubbles rising in such a system, they should be completely dissolved in the liquid which however was not observed experimentally. Therefore, only a back-diffusion of another species from the liquid into the bubble or the initial purity of the CO_2 bubbles was not 100% may yield such a finite size of the bubbles at the end. For comparison, the saturation concentration of oxygen and nitrogen in the liquid were calculated. Therefrom, a possible maximum concentration of both gases inside the bubbles could be estimated, giving values of 1.0% for oxygen and 2.02% for nitrogen. Hence, it seems that both

Fig. 3 Decay of bubble diameter in time; Case 0: pure CO_2, full dynamic model; Case 1 (NO): CO_2 + back diffusion, no oscillations; Case 2 (TO): CO_2 + back diffusion, trajectory oscillations; Case 3 (FDM): CO_2 + back diffusion, trajectory and shape oscillations, dynamic Sh (Eq. 35), compared with experimental results
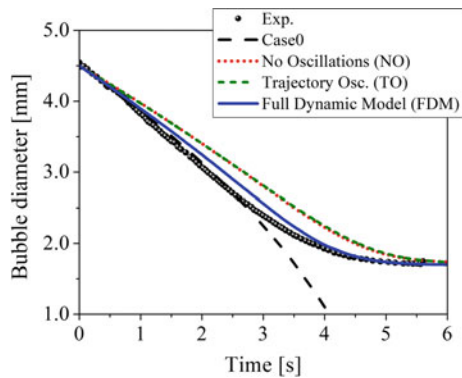
effects were present in the experiments, back-diffusion and an additional species inside the bubble.

Therefore, and with the idea of imitating the experiments in a more realistic way, two simulations were conducted; the first, as an initial condition of the second, was injecting N_2 bubbles for a time of 60 min and transfer during this time a certain amount of the N_2 into the liquid. With this absorbed N_2 condition in the liquid phase, the second simulation was started by injecting CO_2 bubbles with an initial purity of 98%, while the remaining fraction of 2% was assumed to be N_2. The results regarding the temporal evolution of the bubble diameter can be seen in Fig. 3.

The subsequent simulations were then performed by allowing for back-diffusion of N_2 into the bubble for the cases listed in Table 3, in which the effect of bubble oscillation on the mass transfer is evaluated. Case 1 assumes that the bubbles remain spherical and have therefore no shape and trajectory oscillations. Case 2 considers also spherical bubbles, but trajectory oscillations were taken into account whereby naturally lateral dispersion and the residence time of the bubbles in the system will be increased. Case 3 considers the complete dynamic model, i.e. effects of bubble dynamics are taken into account not only on their motion, but also on shape and mass transfer, in which the bubble eccentricity increases contact area and the dynamic Sherwood number accounts for the oscillation amplitude. In this case, the resulting mass transfer rates are enhanced, since here larger bubbles are considered which exhibit a pronounced dynamic behaviour. The comparison with the measurement clearly shows when bubbly dynamics is not modelled properly (i.e. Case 1 and Case 2) the bubble size is remarkably over-predicted. With the complete FDM the predicted bubble size almost falls on the measured values in the initial period, but in the middle time period the bubble size is slightly over-predicted. After 4 s however the numerical result again overlaps with the measured size approaching the correct final value at the end of the test section.

The consideration of an additional species initially inside the bubble and also allowing for back-diffusion of N_2, improved the results significantly with respect to bubble size. This behaviour can be better understood comparing the mass fraction of CO_2 at the bubble surface, estimated by Henry's law, as shown in Fig. 4. When a pure CO_2 bubble is considered (Case 0), the mass fraction inside the bubble is obviously

Fig. 4 CO_2 mass fraction at bubble surface on the liquid side comparing all four cases (see Table 3)
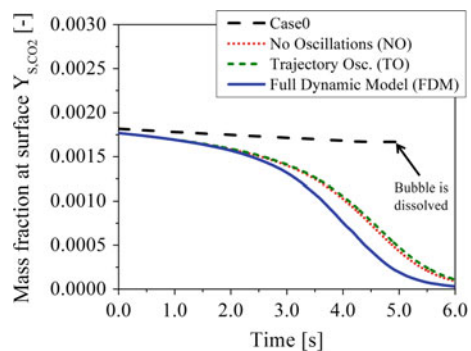
constant and equal to unity. In this manner, a nearly constant mass concentration at the surface is the result, with a very slight decrease caused by hydrostatic pressure effects on the bubble density during its ascendance in the column. Here, the driving gradient is totally over-estimated resulting in high mass transfer rates and rapidly shrinking bubbles (see Fig. 3). On the other hand, the presence of a second species inside the bubble and its possible diffusion from the liquid into the bubbles for Case 3 produces a transient decay of CO_2 mass fraction according to their instantaneous composition. Although a "point-mass" approximation is being used, such level of modelling can be handled practically without additional computational costs, and this information is calculated and stored individually for each bubble, at each Lagrangian time-step.

The bubbles considering the Full Dynamic Model (FDM) exhibit oscillations in shape and motion, based on experimental information regarding the bubble eccentricity and trajectory angle [47]. Such a behaviour produces a direct effect on mass transfer, since the ellipsoidal bubble surface area is greater than that of the volume equivalent sphere; beside the additional increase of Sherwood number considering dynamic effects (i.e. integration over oscillation periods, see Eq. (35)) as described by Montes et al. [32].

The influence of the degree of modelling on the mass transfer of CO_2 given by Eq. (30) can be best visualized by looking at the temporal development of the mass transfer coefficient k_c being closely connected to the bubble size and rise velocity (Fig. 5). Again, for Case 1 without modelling any bubble dynamics, a smooth increase of k_c in time is observed, mainly driven by the reduction of bubble size and hence surface area. Now if bubble tumbling motion is modelled (Case 2), the mass transfer coefficient in the entire period is below that of Case 1 and shows some low intensity fluctuations which slightly increase towards the end (Fig. 5). For Case 3 with the full dynamics model (FDM) the mass transfer coefficient shows stronger fluctuation over time (i.e. due to random variation of surface area and relative velocity) and the values of k_c are mostly above those obtained with the model simulations Case 1 and Case 2 since ellipsoidal bubble have larger surface area. At larger times, towards the end, the fluctuations in k_c become even larger since the bubble size has reached about

Fig. 5 Comparison of temporal evolution of the mass transfer coefficient k_C, considering the three different modelling approaches, NO, TO and FDM cases (see Table 4)
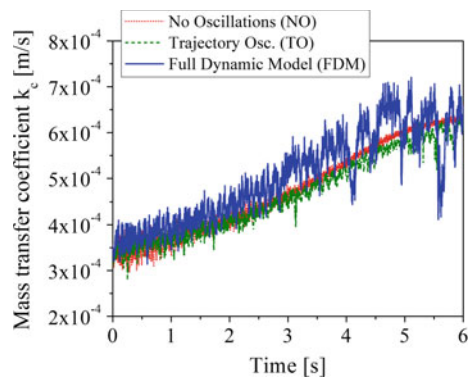
Table 4 Cases description of the modelling assumptions for the computational setups

Case	Model case description
Case 1: NO	Spherical bubbles—**no trajectory oscillations**, Sherwood number for non-deformable spherical bubble, Eq. (38)
Case 2: TO	Spherical bubbles—**only trajectory fluctuations**, Sherwood number for non-deformable spherical bubble, Eq. (38)
Case 3: FDM	Bubble trajectory and eccentricity oscillations (**full dynamics model**) and dynamic Sherwood number, Eq. (35)

Fig. 6 Comparison of the computed correlation between Sherwood and Peclet number with experiments (Exp. one component: only mass transfer of CO_2; Exp. two components: allowing for Nitrogen back-diffusion) considering Case 1 and Case 3 in the modelling
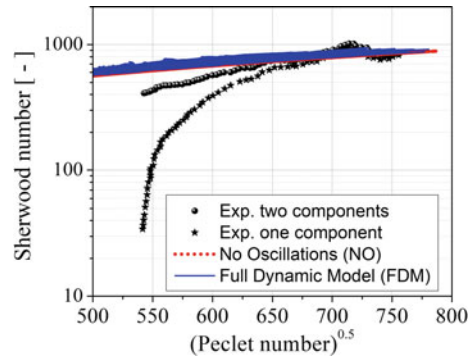
2 mm where the randomness in eccentricity fluctuations is larger (see Sommerfeld et al. [23]).

A comparison of the numerically obtained correlation between Sherwood number and the square root of the Peclet number (see Eq. (35)) with experimental data is shown in Fig. 6. The standard point mass approach (NO: Case 1) shows practically a straight line (in red) following the Boussinesq [28] correlation (Eq. 38). However, with the full dynamic model (FDM: Case 3) the Sherwood number is always above this line showing strong fluctuations over the entire span of Pe-numbers. Please note that the Sh-axis is plotted with a log-scale. The experimental results are shown for the same experiment but with two evaluations approaches; one without species back-diffusion (one component) and the other one accounting for back-diffusion (two components). It is clear that the first case yields too small bubbles (see Fig. 3), especially at a later stage, whereby a strong decay of the Sherwood number is observed. The correct case with back-diffusion provides the expected decay of the Sherwood number along the bubble rise path coupled with a decrease of the Peclet number (i.e. running from right to left). The decay slope however is slightly higher as obtained in the numerical simulations. For the initial bubble rise period the trend is not very clear (i.e. $Pe^{0.5} > 700$) since there is also a region with increasing Sherwood number. This might be caused by the development of a bubble rise just after release from the injection nozzle and associated variations in bubble velocity. Unfortunately for this case the measured bubble rise velocity is not available for comparison.

3.2 Bubble Swarms

The experiment conducted by Darmana et al. [48] used a rectangular laboratory scale bubble column reactor. The column with a cross-section of $A = 0.2$ m $\times$ 0.03 m was filled up to $H = 1$ m with $V = 6.0$ L of NaOH solution. Bubbles consisting of pure CO_2 were generated by a 21-needle gas distribution system located in the middle region of the bottom plate of the column (see Fig. 8) which then move through the NaOH solution. The gas flow rate through all nozzles was 2.832 L/min and the initial bubble size was specified with 5.5 mm, yielding a low gas hold-up of around 1.2%. The bubble size was obtained applying imaging technique while the bubble velocity was evaluated using PIV (particle image velocimetry) technique. An electrode probe was placed 20 mm submerged from the surface in the centre of the column, in order to follow the process of chemical absorption of CO_2. The experiment was initiated using first N_2 gas for aeration for 20 s until the flow pattern was almost fully developed. Afterwards, the gas supply was switched to CO_2, which started the beginning of the measurements. This period lasted for 260 s and time-averaged properties were determined.

The reaction mechanism of the chemisorption of CO_2 into aqueous NaOH solution has been widely studied [5, 8, 44, 49–51], since it considers important phenomena encountered also in practice. Initially, during the physisorption process, the carbon dioxide must be transported from the gaseous phase into the liquid phase (Eq. 43):

$$CO_{2(g)} \rightleftharpoons CO_{2(aq)} \tag{43}$$

$$NaOH \rightleftharpoons Na^+_{(aq)} + OH^-_{(aq)} \tag{44}$$

$$CO_{2(aq)} + OH^- \rightleftharpoons HCO_3^- \tag{45}$$

$$CO_{2(aq)} + H_2O \rightleftharpoons HCO_3^- + H^+ \tag{46}$$

$$HCO_3^- + OH^- \rightleftharpoons CO_3^{2-} + H_2O \tag{47}$$
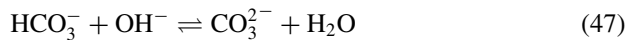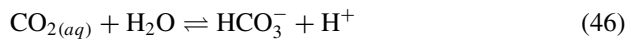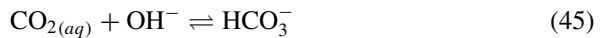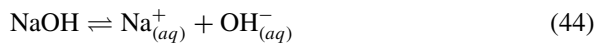
The sodium hydroxide dissociates in aqueous solutions into sodium and hydroxide ions as shown in Eq. (44). After the CO_2 dissolution, two consecutive and competitive reversible reaction mechanisms take place, the first mechanism considers the reaction between the dissolved CO_2 in contact with the hydroxide ions in the water (Eq. 45), which is dominant for pH > 10 [39]. The second mechanism, the reaction between the dissolved CO_2 and H_2O (Eq. 46), is dominant at pH < 8 [39]. In principle both mechanisms result in a formation of bicarbonate ions HCO_3^- which further react to form carbonate ions CO_3^{2-} (Eq. 47). In the pH range 8–10, both mechanisms are crucial [39]. The reaction constants corresponding to each reaction mechanism are presented as follow.

The forward rate constant of the first reaction k_1' (Eq. 45) is calculated with the relation presented by Pohorecki and Moniuk [43]:

$$\log k_1' = 11.895 - \frac{2382}{T} \tag{48}$$

This equation is valid in the temperature range of 291–314 K. The backward reaction rate of the first reaction k_1'' is calculated via the equilibrium constant K_3 and K_w. K_3 is calculated according to [41]:

$$K_3 = \exp(-12092.1/T - 36.786 \ln T + 235.482) \tag{49}$$

and the solubility product K_w was taken from [40]:

$$K_W = 10^{-(5839.5/T + 22.4773 \log T - 61.2062)} \tag{50}$$

The backward reaction k_1'' is then obtained using the following relation:

$$K_1 = \frac{k_1'}{k_1''} = \frac{K_3}{K_W} \tag{51}$$

The forward constant rate of the second reaction k_2' (Eq. 46) is calculated with the relation presented by Johnson [42]:

$$\log k_2' = exp\left(-\frac{61900}{T}[K] - 183.0 \, ln(T[K]) + 1246.98\right) \tag{52}$$

and the backward reaction rate k_2'' is obtained using the relation:

$$k_2'' = \frac{k_2'}{K_3} \tag{53}$$

For the third reaction rate (Eq. 47) Eigen [38] concluded that the reaction involves a proton transfer and the rate have a rage of 10^{10}–10^{11}. A value of 10^6 m^3/kmol s was used according to Darmana et al. [52] due to computational savings. The backward reaction rate is calculated using the equilibrium constant proposed by Hikita and Asai [34]:

$$\log\left(\frac{K_3}{K_3^\infty}\right) = \frac{1.01[Na^+]^{1/2}}{1 + 1.27[Na^+]} + 0.125[Na^+] \tag{54}$$

With: $\log\left(K_3^\infty\right) = 1568.94/T + 0.4134 - 0.00673T$.
The backward reaction constant k_3'' is obtained using the following relation:

Fig. 7 Enhancement factor
E as a function of pH-value,
accounted for chemisorption
of CO_2 according to Eq. (57)

Enhancement Factor relation [-]

Two-film model Fleischer et al. (1996)
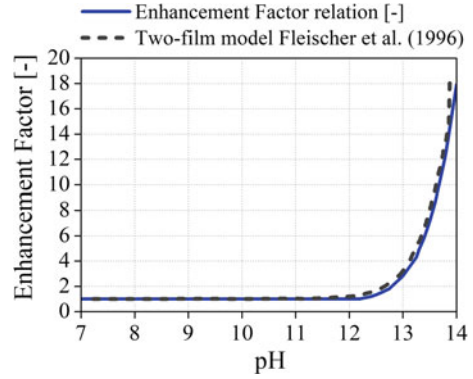
$$K_3 = \frac{k_3'}{k_3''} \tag{55}$$

For the present study case, namely the consideration of the chemical absorption of CO_2 in basic (alkaline) solutions there exists an influence of the chemical reaction on mass transfer, this is accounted for through the enhancement factor E. This property is the ratio between mass fluxes through the phase interface with and without reaction, based on the same driving force of concentration [35]. The enhancement factor E is calculated according to an algebraic equation (Eq. 57), as a function of the Hatta number and it is strongly increased for growing pH-values beyond about 12 (Fig. 7).

$$E = \frac{k_{creac}}{k_c} \tag{56}$$

$$E = \begin{cases} -\frac{Ha^2}{2(E_\infty - 1)} + \sqrt{\frac{Ha^4}{4(E_\infty - 1)^2} + E_\infty \frac{Ha^2}{E_\infty - 1} + 1}; & E_\infty > 1 \\ 1; & E_\infty \leq 1 \end{cases} \tag{57}$$

$$E_\infty = \left(1 + \frac{D_{OH^-}\left[OH^-\right]}{2D_{CO_2}C_{l,s}}\right)\sqrt{\frac{D_{CO_2}}{D_{OH^-}}} \tag{58}$$

$$Ha = \frac{\sqrt{k_1' D_{CO_2}\left[OH^-\right]}}{k_c} \tag{59}$$

4 Simulations Case Setup

The numerical mesh consists of 50,400 volumes in total (400 per cross-section and 126 in the height) as shown in Fig. 8. In this case bubbles with a constant diameter
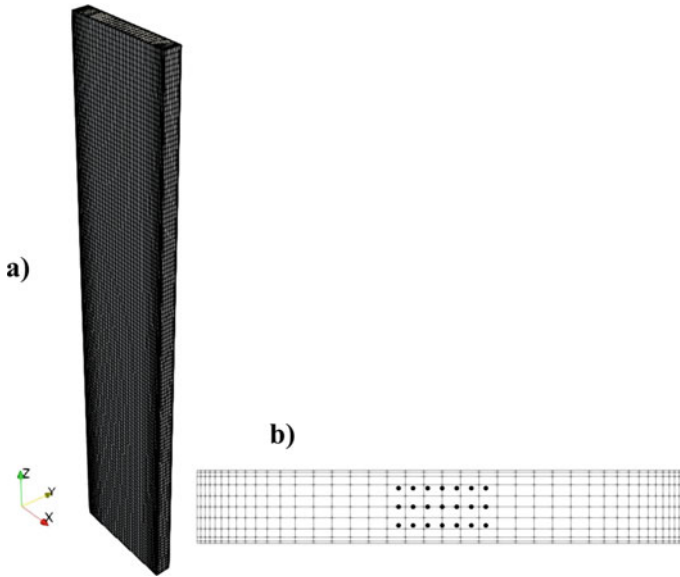
Fig. 8 Numerical mesh for the considered rectangular bubble column with a cross-section of A = 0.2 m × 0.03 m and a height of 1 m, **a** total view of the grid including coordinate system, **b** cross-sectional grid with location of the 21 gas injection needles in the bottom of the column

of 5.5 mm were injected according to the experimental flow rate. The resulting ratio between the bubble size d_{B0} and the mean grid length scale Δx was $d_{B0}/\Delta x \approx 0.626$, which is within the limit suggested by Milleli et al. [45] for LES simulations using a point-particles approach. All wall boundaries were set as non-slip condition for the liquid phase and bubbles were reflected in-elastically. The free surface of the bubble column was considered as planar with slip velocity boundary for the liquid at atmospheric pressure. For the species no transfer across the surface was allowed. The bubbles were injected through the equally spaced 21 injection nozzles in a rectangular array of 35 mm × 15 mm (Fig. 8b). In this case each computational parcel corresponds to one real bubble. With the predefined flow rate about 530 bubbles were injected per second, which resulted in roughly 1300 bubbles residing inside the column. Bubbles reaching the free surface are removed from the computation.

For resolving the temporal variation, the LES time-step was selected as $\Delta t_E = 5$ms, which guaranteed a CFL number below 1. All bubbles after injection move simultaneously through the column using a dynamic tracking time step independent for each bubble according to the criterion given by Eq. (23). The computations were run with an initial aeration with N_2 bubbles for 20 s in column, although without mass transfer, and then for a sequence of 260 s CO_2 bubbles are injected and average procedure is done throughout this period.

The diffusivity coefficient was set to $D_{CO_2-H_2O} = 1.91818 \times 10^{-9}$ m^2/s and the applied Henry's dimensionless constant for $T = 25°C$ was $H_{CO_2-H_2O} = 0.8472$ [53]. Five species transport equation are used to compute the mass fractions, $CO_{2\,(aq)}$,

OH^-, CO_3^{2-}, HCO_3^-, H^+ and H_2O. The initial mass fraction of each species was set to zero, except for OH^- which is computed from the initial pH of 12.5, and H_2O, which is considered the background species and calculated as $\sum_{i=1}^{N} Y_{i,c} = 1$.

5 Results and Discussion

The system behaviour in the reactive bubble column and its modelling is a very challenging procedure due to the fully transient process which involves different linked phenomena. The dynamics of the bubbles and the appropriate modelling of the accumulation and transfer of the carbon dioxide inside the column, have to be considered in detail. In order to demonstrate the effect of bubble dynamics modelling in the frame of the point-mass Lagrangian approach (see also [9]), three different computations with increasing model refinement were conducted and compared (Table 4). The classical point-mass approach which neglects completely bubble dynamics for motion and mass transfer is studied in Case 1. One step further in modelling, which include trajectory fluctuations in order to mimic an enhancement of bubble lateral dispersion is studied in Case 2 where mass transfer is not yet directly affected. Case 3 is the most representative modelling approach, where bubble shape oscillations (i.e. eccentricity fluctuations) and trajectory fluctuations are modelled just like in reality. The mass transfer is enhanced through the considered effective ellipsoidal surface area of deformed bubbles as well as a dynamic Sherwood number. Surely, chemical reactions are influenced by the enhanced mass transfer, therefore in this case a strong coupling between hydrodynamics, mass transfer and chemical reaction is observed.

First the integral gas hold-up numerically obtained with the advanced fully dynamics bubble model (FDM: Case 3) is compared with the results of Darmana et al. [48] in Table 5. Muniz and Sommerfeld [47] experimental result gives a value of 1.2%, while their simulations give a much larger value of 1.6%. The present simulations with the FDM give clearly a better agreement, namely a gas hold-up value of 1.3%. This better agreement is the result of considering oscillating bubbles combined with a dynamic Sherwood number yielding higher mass transfer rates, thus the bubble volume becomes smaller and consequently the gas hold-up reduces. Darmana et al. [48] attribute the larger numerical hold-up prediction to an over-estimation in the bubble size distribution.

Table 5 Integral gas hold-up obtained in the present computations using the full dynamic model, comparison with experimental and simulation data [48]

Experiment Darmana et al. [%]	Simulation Darmana et al. (%)	Present simulation with FDM (%)
1.2	1.6	1.3

5.1 Bubble Size

Hydrodynamics and mass transfer are considerably affected by the local bubble size distribution and only an appropriate prediction of both is a good basis for reliable bubble column computations. The temporal evolution and spatial distribution of bubble sizes is a good point of comparison and validation. In order to compare the results including the effect of bubble dynamics in mass transfer, the three different simulation cases were computed (see Table 4).

First, a comparison of numerical and experimental results may be conducted for the bubble size distribution evolving along the column. For that purpose, the local computed number mean diameter is selected and normalised with the initial diameter of $d_0 = 5.5$ mm. In order to be comparable with the measurements, this mean diameter was taken for the core region of the column and averaged over a time period of $t = 20$–95 s. As expected, the trend is a continuous decreasing of the bubble size from the gas distributor to the column surface (Fig. 9). In the experimental results there exist an unreliable region for $z/H < 0.4$, since here bubbles are closely spaced and therefore may be identified as clusters and hence were rejected from further processing. Thereby, the detected bubbles do not represent the correct size and hence in this region bubbles are much too small [48]. All the computations considering the different model assumptions with and without bubble dynamics have a similar trend following the experimental observation, except for the region z/H < 0.4. Shortly above the injection needles, the three models give very similar values. However, further away from the injection, the two reduced models (NO Model (Case1) and TO (Case2)) yield remarkably larger bubble mean diameters due to the achieved lower mass transfer rates. Even the result neglecting the oscillating model (i.e. NO:
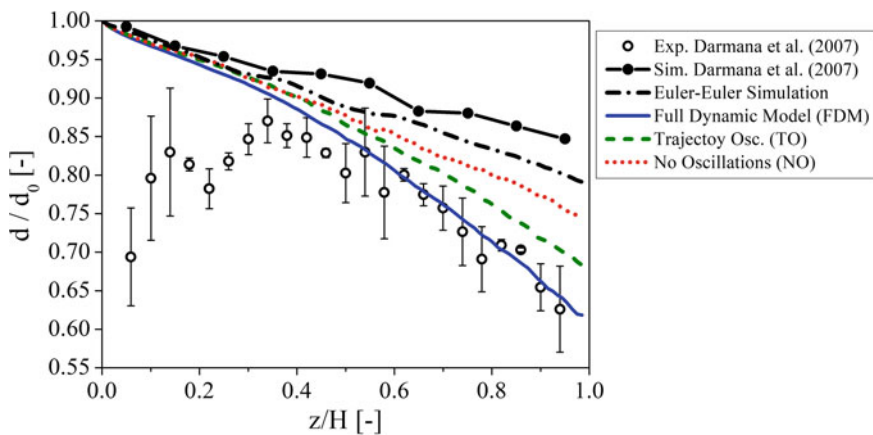
Fig. 9 Volume equivalent number-based bubble diameter ratio (normalized by the injection diameter of $d_n = 5.5$ mm) along the bubble column core region averaged over a time interval t = 20–95 s, comparison of numerical simulations using different model assumptions (see Table 4) with experimental and simulation results of Darmana et al. [48] as well as Krauß and Rzehak [51]

the standard point-mass approach) shows much lower values compared with the Euler/Lagrange results of Darmana et al. [48]. This is of course associated with a number of different modelling assumptions. In this study different formulations of the force resistance coefficients were used and it was accounted for SGS bubble transport as well as BIT. Likewise, a comparison using an Euler-Euler method (see Krauß and Rzehak [51]) is presented which is just between the Darmana et al. [48] result and the present NO (Case 1) model case (Fig. 9). This results was obtained with the MUSIG (Homogeneous multiple size group) model for describing bubble shrinkage. The full dynamic model (FDM, Case 3) which includes shape oscillations and a dynamic Sherwood number yields the best agreement with the measurements, although the bubble mean diameter is still slightly over-predicted in the upper part of the column. This difference may be caused by an unclear specification of the injection bubble size. It is probably not true that the injected bubbles are really mono-sized, so that it would be worth to analyse the influence of injecting bubbles with a size distribution.

In order to analyse the performance of the bubble phase modelling, instantaneous distributions of bubble sizes are compared in Fig. 10. Here results for two different modelling depths are compared, namely, the standard point-mass approach neglecting completely bubble dynamics (NO case, see also Table 4) and the full dynamic model in bubble motion and mass transfer (FDM case). Moreover, the size distributions are averaged over three different cross-sections along the column and shown for two different time levels, i.e. $t = 70$ s and 180 s. As to be expected, in the initial reaction period ($t = 70$ s) the CO_2 concentration in the liquid is relatively low, so that the driving gradients of species are high and hence mass transfer causes a remarkable reduction of bubble size, the effect of which becomes evident especially in the upper region of the column, after a certain residence time. Comparing the two model versions reveals that the full modelling of bubble dynamics (FDM) yields smaller bubbles in the upper part of the column. Certainly, above the aeration system, the two models give almost identical size distributions due to the available short time for mass transfer. When time proceeds (i.e. $t = 180$ s) of course the CO_2 concentration in the column has grown and the driving gradient has reduced, therefore the bubbles loose less CO_2. Nevertheless, the FDM case results in smaller bubbles compared to the NO case, which neglect the bubble dynamics (see also Fig. 9).

As mentioned above, the entire reaction process in the bubble column is fully dynamic with regards to hydrodynamics and mass transfer. Naturally, the flow is induced by the buoyancy driven bubble rise, characterized mostly by a zig-zag shape. This movement leads to the generation of vortex structures in the liquid phase. Figure 11 shows the instantaneous bubble distribution within the column and the resulting flow velocity structure of the liquid at two different time levels ($t = 70$ s and $t = 180$ s) for both modelling approaches, i.e. NO and FDM. At the first glance, the dynamics of the bubble plume seems not to be very different for both cases; nevertheless, when looking more closely, it is clear that the bubbles are more homogeneously distributed with the refined FDM, especially in the upper part of the column. The bubble symbols are also coloured coded based on bubble size (bright
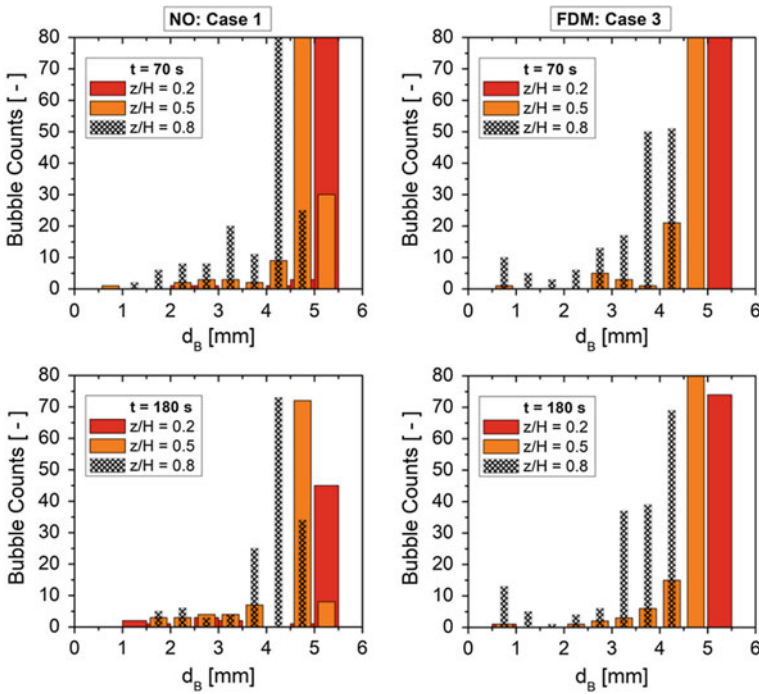
Fig. 10 Instantaneous bubble size counts for two representative times (upper row t = 70 s, lower row t = 180 s) collected within three cross sections (i.e. ±5 mm) along the column (z/H = 0.2, 0.5 and 0.8); comparison of numerical computations using two model variants (left column) NO: standard point-mass approximation and (right column) FDM: full bubble dynamics model (see Table 4)

colour is large and dark colour is small), which gives some impression about the prevailing small bubbles in the FDM case.

In Fig. 11b the developing liquid hydrodynamics is presented for the two model simulations and two time levels. Here the liquid velocity distributions in the centre plane of the flat bubble column are clearly more homogeneous when considering the more realistic FDM case, which mainly concerns the upper part of the column. This is of course the result of the better lateral bubble dispersion. For the standard Lagrangian point-mass model, both the up- and down-flow regions are stronger and more concentrated for both time levels. Therefore, there exists a qualitative difference comparing the full dynamics model (FDM) and the point-mass model (NO).

Fig. 11 Comparison of numerical results obtained with the fully dynamic model FDM and the standard point-mass model r the temporal evolution of **a** the instantaneous bubble distribution (all simulated bubbles are shown) where the size is scaled in grey levels (m) as well as by symbol size and **b** the vertical liquid velocity (m/s) in the centre plane of the column at two different time levels, i.e. t = 70 and 180 s
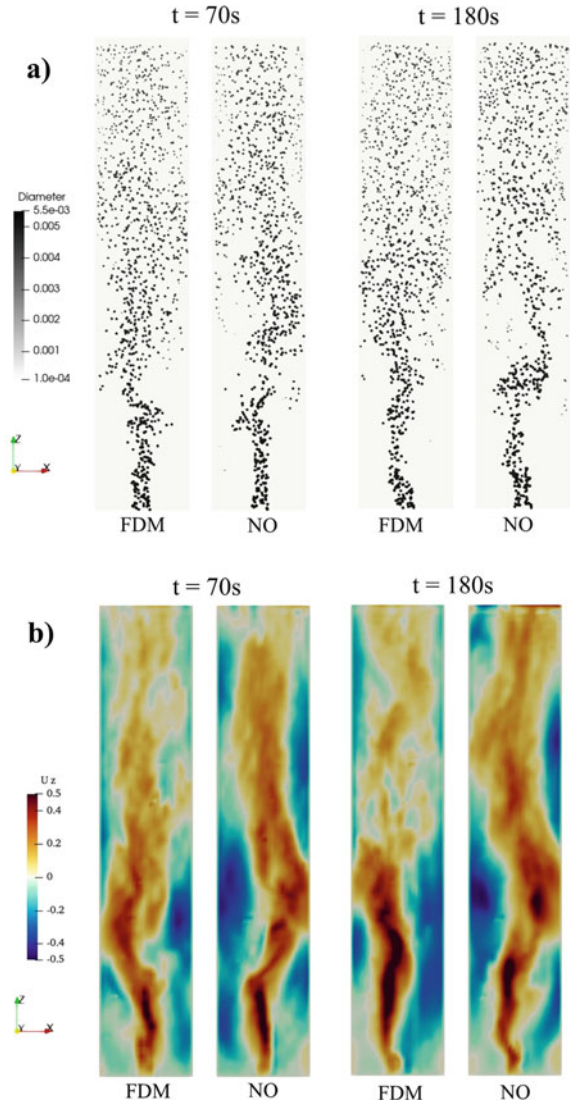
5.2   Mean Velocity Profiles

From the experimental studies of Darmana et al. [48] the vertical bubble mean velocity at *z/H* = 0.75 was also available as an average over the time period of *t* = 260 s. Therefore, the simulations using the three modelling assumptions (see Table 4) were compared with these data for the same averaging time (Fig. 12). Additionally, Euler-Euler simulation performed by Krauß and Rzehak [51] were considered. Expectedly the best agreement is found with the full bubble dynamics model (FDM
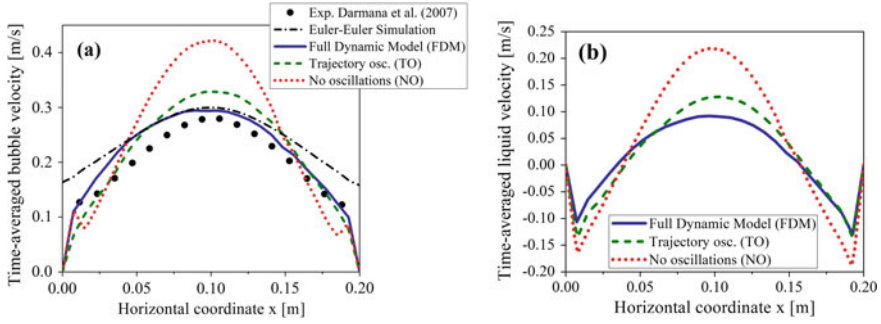
Fig. 12 Computed velocity profiles for the time-averaged (i.e. t = 260 s) vertical components for **a** the bubbles and **b** the liquid phase; comparison of present simulations with the three different model assumptions and for the bubbles comparison with experimental results [48]; cross-section z/H = 0.75 above the bottom of the column

Case 3), which yields the best lateral dispersion and due to the modelled bubble tumbling motion and the bubble eccentricity giving higher values for the drag force. Surprisingly, the Euler-Euler simulations [51] not considering any bubble dynamics show similar values for the bubble velocity in the core of the bubble column, however, a remarkable over-prediction is found in the outer region between core and wall. This was explained by the trend of the bubbles to move towards the wall caused by the lateral lift force. Moreover, a free slip boundary condition was applied for the dispersed phase which also yields a finite bubble velocity at the walls. Especially, the model neglecting completely bubble dynamics (i.e. NO: Case 1, Fig. 12a) produces too high bubble velocities in the column core due to the lower drag force when considering spherical bubbles, but also due to the larger bubble size (see Fig. 9) when not considering bubble dynamics in the mass transfer. On the other hand, the case with Trajectory Oscillation (i.e. TO: Case 2) gives a reasonable prediction of lateral bubble dispersion, but the velocity is still slightly overestimated in the core of the column.

A comparison of the three different model results (Table 4) with regard to the resulting vertical liquid velocity profile is shown in the Fig. 12b, however, without experimental validation since these data is not available. The trends are very similar to the bubble velocities with the different models, since of course the bubbles drive the fluid flow. Because in the FDM case the bubble dynamics model for motion and mass transfer gives smaller bubble sizes and rise velocities also the liquid velocity is lower in the core of the column. Analogously, neglecting this important effect (i.e. NO: Case 1) gives very high liquid velocities in the core of the column and consequently because of mass flow conservation stronger downward flow near the wall.

Fig. 13 Temporal species concentration evolution in the liquid phase obtained from simulations with the three different modelling cases (see Table 4); recorded at the location x/W = 0.5, y/D = 0.5, and z/H = 0.95
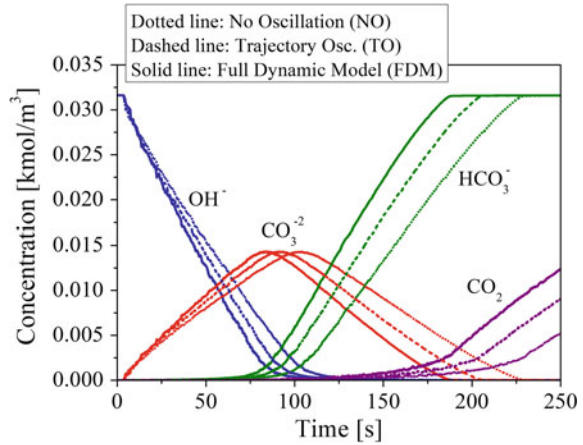
5.3 Reaction Progress and pH Values

As mentioned above, hydrodynamics, mass transfer and chemical reaction are highly coupled and completely transient in the considered bubble column, consequently all the physical details should be taken into account in the simulations. The entire chemical reaction process is related not only to the mass transfer but also to the dynamics of the bubbles which is very often not considered. During the rise of the bubbles from the injectors to the liquid surface, the bubbles will transfer CO_2 gas to the liquid through the interface, and subsequently initiate the chemical reactions within the liquid phase. The evolution of the chemical species inside the bubble column was measured in a centre-point at $z/H = 0.95$ (i.e. just underneath the surface) and is shown in the Fig. 13. It is observed that there is a small delay at the beginning of the evolution since the bubbles have no yet reached the measuring point. After that, the dissolved CO_2 reacts with the hydroxide ions, while at the same time it is converted into carbonate. The reaction products are transported by the convective flow to the top of the column in the centre of the column (Fig. 12b), but due to recirculation zones close to the wall, some products are also transported downwards. While the reactions are carried out, the decrease of OH^- is proportional to the increase of the carbonate, and a shift of equilibrium of the first reaction mechanism occurs at approximately 85 s. At this time the hydroxide is consumed and the maximum concentration value for the carbonate is reached, leading the increase of the bicarbonate. As the bicarbonate concentration increases, a time is reached where no more reaction takes place, and therefore the carbon dioxide begins to accumulate because all the hydroxide has been completely consumed.

This evolution behaviour occurs for all the three different modelling cases simulated (see Table 4), but there is a clear shift in time between them (Fig. 13), showing the faster variation when the bubble dynamics (i.e. FDM) is considered. This is explained by the higher mass transfer rate when including the dynamic model, also

Fig. 14 pH-value variation
in time measured centrally at
z/H = 0.95, comparison of
the different models with
experimental and numerical
results of Darmana et al. [48]
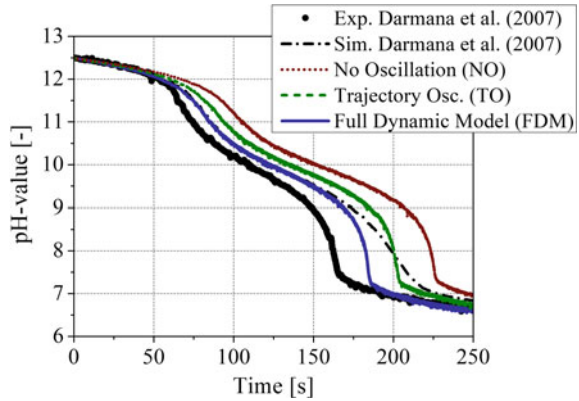
seen in the bubble size change, where the CO_2 is transferred faster to the liquid activating the reaction system earlier. Naturally, when the dynamics of the bubbles is omitted, the mass transfer rate is lower; causing a slow activation of the chemical reaction (dashed and dotted lines in Fig. 13).

Since it is not possible to measure in-vitro the concentration of species in the experiments, the change of the local pH value, which reflects the consumption of hydroxide ions, was measured to follow the reaction process. Hence, a satisfactory mass transfer rate prediction leads to a good prediction of the pH value evolution. The resulting variation of pH-values is shown in the Fig. 14, considering the different models (see Table 4) and compared with the experimental data.

It is clear that the model neglecting bubble oscillations (NO Case1) overestimates the pH-value during the reaction period (Fig. 14), demonstrating low mass transfer and thus a slow reaction (see also Fig. 13). This happens because the predicted residence time of the bubbles is too low and the mass transfer is remarkably underestimated. When trajectory oscillations are modelled (TO Case 2) the bubble residence time increase, leading to a higher mass transfer and therefore, to a faster variation of the consumption of the hydroxide. Including additionally shape oscillations (eccentricity) and a dynamic Sherwood number for mass transfer (FDM Case 3), the simulations can capture the experimental variation of the pH in a much better way, but still slightly shifted in time. This is mainly caused by the higher driving gradient that leads to a substantial mass transfer of CO_2 (see also Fig. 9) when the dynamic eccentricity is included in mass transfer model. Surprisingly, the initial part of the predicted pH-variation (i.e. up to t = 150 s) runs almost parallel to the numerical result of Darmana et al. [48]. Here this may be coming from the different models considered in his work, such as, drag and lift coefficients and more important the Sherwood number. The improvement for the present numerical results with the FDM at a later stage of the reaction progress (i.e. from about $t = 175$ s) with respect to the experiments, is a consequence of the use of the second mechanism reaction (see Eq. 46), neglected by Darmana et al. [48] in the simulations and it is noticeable for *pH*-value <9.
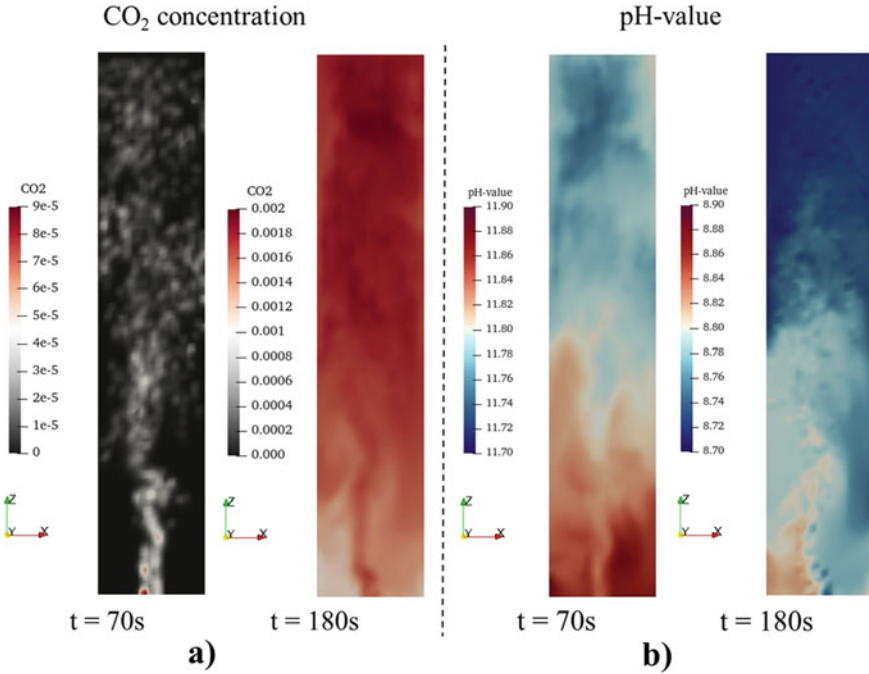
Fig. 15 Images of instantaneous CO_2 concentration (**a**) and pH-values (**b**) in the vertical midplane of the column for different simulations times, using the full bubble oscillation model and the dynamic Sherwood-number (FDM), please note the different ranges of the colour coding for both CO_2 and pH-value for the different time levels

With the purpose of illustrate the temporal and spatial evolution of the reaction process, colour fields of CO_2 concentration and pH-value in the middle cut of the column, are shown for the full dynamic model (bubble dynamics and dynamic Sherwood number, FDM Case 3) in Fig. 15 for two different time levels during the reaction process. At the beginning of the process is clear that small traces of dissolved CO_2 are found in the whole domain, naturally, at this time the pH-value in the liquid is high, but as the mass transfer of CO_2 and the chemical reaction proceed, pH-value decrease (see Fig. 14). Large vortical structures are mainly present in the lower part of the column, driving the transport of CO_2 from the bottom to the top in the core region, thereby mass transfer and reactions occurs faster from the middle part to the upper part of the column. It is also observed, that the recirculation of liquid close to the walls (see also Fig. 12b) supports a convective transport of the reacting species in this region from the top region towards the bottom, which is most pronounced at $t = 180$ s, when the recirculation is developed. Consequently, the fresh carbonate and consumed hydroxide ions will be transported to the top of the column in the core region by the flow and are transported downwards close to the column walls. At the final stage (i.e. $t = 180$ s) a drastic increase of dissolved CO_2 has occurred showing however still strong inhomogeneity due to the involved transport

processes. On the other hand, pH has reached a lower value which however appears very homogeneously throughout the column.

6 Conclusions and Outlook

Bubbly flows with mass transfer and chemical reactions have been numerically computed and the results were validated based on different experiments conducted with the DFG-SPP "Reactive Bubbly Flows". In such reactors both bubble motion and mass transfer are strongly influenced by bubble shape and trajectory (zig-zag or spiral rising) oscillations. These effects are not captured by standard numerical methods for dispersed multi-phase flows applicable to large-scale industrial systems, such as the Euler/Euler (also called multi-fluid) or the Euler/Lagrange approaches, since herein the bubbles have to be smaller than the size of the numerical mesh and are assumed to be point-masses for numerical efficiency.

In the present research project an LES-based Euler/Lagrange approach was developed which accounts for transport processes going beyond a point-mass representation, but still being numerically very efficient. A bubble dynamics model was elaborated considering shape and trajectory oscillations as well as employing dynamic bubble deformation in mass transfer and the Sherwood number. The features of the LES-Euler/Lagrange method implemented in the *OpenFOAM®* library are additionally the following:

- Large eddy simulations using an one-equation eddy-viscosity model by solving an additional transport equation for the SGS turbulent kinetic energy,
- Two-way coupling accounts for momentum transfer and direct SGS turbulence modification; dissipation and bubble induced turbulence (BIT),
- Bubble motion was calculated considering all forces; i.e. drag, lift, wall force, added mass, fluid inertia, gravity/buoyancy and Basset force; all extended to account for bubble eccentricity if possible,
- Bubble transport by SGS turbulence is modelled through a single step Langevin model,
- The Sherwood number for an oscillating spheroid is extended by a term accounting for the bubble oscillation amplitude.

The validation of the developed models was conducted for several experimental test cases, where only two cases are presented here; CO_2 absorption for a single bubble rising in a vertical column (Case with only mass transfer) and a CO_2 bubble swarm rising in a rectangular column filled with a NaOH-solution yielding a quite low gas hold-up of only 1.2% (Case with mass transfer and chemical reaction). The major findings from these studies are:

- A possible back-diffusion of species from the liquid into the bubbles has to be considered for correctly predicting the bubble size evolution,

- The full bubble dynamics model (FDM) yields higher mass transfer compared to the classical point-bubble approximation due to the larger surface area of deformed bubbles,
- Applying the FDM provides stronger lateral dispersion of the bubbles and therefore strongly modifies the hydrodynamics in a bubble column,
- Consequently, only the FDM produces in comparison to measurements the correct bubble velocity fields (i.e. mean velocities and their rms-values),
- Due to the higher mass transfer obtained with the FDM, chemical reaction occurs remarkably faster compared to the point-bubble method,
- As a result, the temporal evolution of pH in the bubble column agrees much better with the measurements and also other numerical computations,
- For the bubble column case with an initial bubble size of $d_B = 5.5$ mm and a height of 1 m, the bubbly full dynamic model (FDM) predicts about 15% smaller bubbles at the end, compared to the standard point-bubble assumption.

References

1. Sommerfeld M (ed) (2004) Bubbly flows: analysis, modelling and calculation. Series: Heat and mass transfer. Springer, Berlin/Heidelberg
2. Sommerfeld M, van Wachem B, Oliemans R (2008) Best practice guidelines for computational fluid dynamics of dispersed multi-phase flows, Brussels
3. Lain S, Bröder D, Sommerfeld M, Göz MF (2002) Modelling hydrodynamics and turbulence in a bubble column using the Euler–Lagrange procedure. Int J Multiph Flows 28:1381–1407
4. Lapin A, Lübbert A (1994) Numerical simulation of the dynamics of two-phase gas-liquid flows in bubble columns. Chem Eng Sci 49:3661–3674. https://doi.org/10.1016/0009-2509(94)E0121-6
5. Darmana D, Deen NG, Kuipers JAM (2005) Detailed modeling of hydrodynamics, mass transfer and chemical reactions in a bubble column using a discrete bubble model. Chem Eng Sci 60:3383–3404. https://doi.org/10.1016/j.ces.2005.01.025
6. Radl S, Khinast JG (2010) Multiphase flow and mixing in dilute bubble swarms. Am Inst Chem Eng 56:2421–2445
7. Sommerfeld M, Bourloutski E, Bröder D (2008) Euler/Lagrange calculations of bubbly flows with consideration of bubble coalescence. Can J Chem Eng 81:508–518. https://doi.org/10.1002/cjce.5450810324
8. Gruber MC, Radl S, Khinast JG (2015) Rigorous modeling of CO_2 absorption and chemisorption: the influence of bubble coalescence and breakage. Chem Eng Sci 137:188–204. https://doi.org/10.1016/j.ces.2015.06.008
9. Taborda MA, Sommerfeld M, Muniz M (2020) LES-Euler/Lagrange modelling of bubble columns considering mass transfer, chemical reactions and effects of bubble dynamics. Chem Eng Sci 116121. https://doi.org/10.1016/j.ces.2020.116121

10. Sommerfeld M (2017) Numerical methods for dispersed multiphase flows. In: Bodnár Š, Galdi T, Nečasová GP (eds) Part. Flows, series adv. Springer International Publishing, pp 327–396
11. Yoshizawa A (1986) Statistical theory for compressible turbulent shear flows, with the application to subgrid modeling. Phys Fluids 29:2152. https://doi.org/10.1063/1.865552
12. Muniz M, Sommerfeld M (2020) On the force competition in bubble columns: a numerical study. Int J Multiph Flow 128:103256. https://doi.org/10.1016/j.ijmultiphaseflow.2020.103256
13. Lamb H (1932) Hydrodynamics, New York
14. Simcik M, Ruzicka MC, Drahoš J (2008) Computing the added mass of dispersed particles. Chem Eng Sci 63:4580–4595. https://doi.org/10.1016/j.ces.2008.06.011
15. Hosokawa S, Tomiyama A, Misaki S, Hamada T (2002) Lateral migration of single bubbles due to the presence of wall. In: Proceedings of ASME joint US-European fluids engineering division conference FEDSM2002, Montreal, Canada, p 855
16. Michaelides E, Roig V (2011) Reinterpretation of the Odar and Hamilton data on the unsteady equation of motion of particles. Am Inst Chem Eng 57:2997–3002
17. van Hinsberg MAT, ten Thije Boonkkamp JHM, Clercx HJH (2011) An efficient, second order method for the approximation of the Basset history force. J Comput Phys 230:1465–1478. https://doi.org/10.1016/j.jcp.2010.11.014
18. Lipowsky J, Sommerfeld M (2007) LES-simulation of the formation of particles strands in swirling flows using an unsteady Euler-Lagrange approach. In: Proceedings of 6th international conference on multiphase flow ICMF, Leipzig, Germany, Paper No. S3_Thu_C_54
19. von Karman T, Horwarth L (1938) On the statistical theory of isotropic turbulence. Proc R Soc Lond A 164:192–215
20. Lilly DK (1967) The representation of small scale turbulence in numerical simulation experiments. In: Proceedings of IBM scientific computing symposium on environmental sciences
21. Deardorff JW (1980) Stratocumulus-capped mixed layers derived from a three-dimensional model. Bound-Layer Meteorol 18:495–527. https://doi.org/10.1007/BF00119502
22. Lunde K, Perkins RJ (1998) Shape oscillations of rising bubbles. Appl Sci Res 58:387–408. https://doi.org/10.1023/A:1000864525753
23. Sommerfeld M, Muniz M, Reichardt T (2018) On the importance of modelling bubble dynamics for point-mass numerical calculations of bubble columns. J Chem Eng Jpn 51:301–317. https://doi.org/10.1252/jcej.17we277
24. Sommerfeld M, Bröder D (2009) Analysis of hydrodynamics and microstructure in a bubble column by planar shadow image velocimetry. Ind Eng Chem Res 48:330–340. https://doi.org/10.1021/ie800838u
25. Bröder D, Sommerfeld M (2007) Planar shadow image velocimetry for the analysis of the hydrodynamics in bubbly flows. Meas Sci Technol 18:2513–2528
26. Hosoda S, Abe S, Hosokawa S, Tomiyama A (2014) Mass transfer from a bubble in a vertical pipe. Int J Heat Mass Transf 69:215–222. https://doi.org/10.1016/j.ijheatmasstransfer.2013.10.031
27. Hlawitschka MW, Kováts P, Zähringer K, Bart H-J (2017) Simulation and experimental validation of reactive bubble column reactors. Chem Eng Sci 170:306–319. https://doi.org/10.1016/j.ces.2016.12.053
28. Boussinesq J (1905) Calcul du pouvoir refroidissant des fluides. J Math 1:285–332
29. Lochiel AC, Calderbank PH (1964) Mass transfer in the continuous phase around axisymmetric bodies of revolution. Chem Eng Sci 19:471–484. https://doi.org/10.1016/0009-2509(64)85074-0
30. Brauer H (1981) Particle/fluid transport processes. Prog Chem Eng 19:81–111
31. Bird E, Stewart RB, Lightfoot WE (2007) Transport phenomena, 2nd edn, New York
32. Montes FJ, Galan MA, Cerro RL (1999) Mass transfer from oscillating bubbles in bioreactors. Chem Eng Sci 54:3127–3136. https://doi.org/10.1016/S0009-2509(98)00314-5
33. van Krevelen DW, Hoftijzer PJ (1948) Kinetics of gas-liquid reactions. Part I. General theory. Recl Trav Chim Pays-Bas 67:563–586

34. Hikita H, Asai S (1963) Gas absorption with (m, n)-th order irreversible chemical reaction. Int Chem Eng 27:823–830
35. Westerterp A, Swaaij KR, Beenackers WPM (1998) Chemical reactor design and operation, New York
36. Merker D, Böhm L, Oßberger M, Klüfers P, Kraume M (2017) Mass transfer in reactive bubbly flows—a single-bubble study. Chem Eng Technol 40:1391–1399. https://doi.org/10.1002/ceat.201600715
37. Kováts P, Thévenin D, Zähringer K (2017) Investigation of mass transfer and hydrodynamics in a model bubble column. Chem Eng Technol 40:1434–1444. https://doi.org/10.1002/ceat.201600679
38. Eigen M (1954) Methods for investigation of ionic reactions in aqueous solutions with half-times as short as 10^{-9} sec. Discuss Faraday Soc 17:194–203. https://doi.org/10.1039/df9541700194
39. Kern DM (1960) The hydration of carbon dioxide. J Chem Educ 37:14. https://doi.org/10.1021/ed037p14
40. Tsonopoulos CM, Coulson DM, Inman LB (1976) Ionization constants of water pollutants. J Chem Eng Data 21:190–193
41. Edwards TJ, Maurer G, Newman J, Prausnitz JM (1978) Vapor-liquid equilibria in multicomponent aqueous solutions of volatile weak electrolytes. AIChE J 24:966–976. https://doi.org/10.1002/aic.690240605
42. Johnson KS (1982) Carbon dioxide hydration and dehydration kinetics in seawater: CO_2 reaction kinetics. Limnol Oceanogr 27:849–855. https://doi.org/10.4319/lo.1982.27.5.0849
43. Pohorecki R, Moniuk W (1988) Kinetics of reaction between carbon dioxide and hydroxyl ions in aqueous electrolyte solutions. Chem Eng Sci 43:1677–1684. https://doi.org/10.1016/0009-2509(88)85159-5
44. Kipping R, Kryk H, Schleicher E, Gustke M, Hampel U (2017) Application of a wire-mesh sensor for the study of chemical species conversion in a bubble column. Chem Eng Technol 40:1425–1433. https://doi.org/10.1002/ceat.201700005
45. Milleli M, Smith B, Lakehal D (2001) Large eddy simulation of turbulent shear flows laden with bubbles. In: Direct large-eddy simulation. IV ERCOFTAC series, pp 461–470
46. Sander R (2015) Compilation of Henry's law constants (version 4.0) for water as solvent. Atmos Chem Phys 15:4399–4981. https://doi.org/10.5194/acp-15-4399-2015
47. Muniz M, Sommerfeld M (2019) On the force competition in bubble columns: a numerical study. Int J Multiph Flow
48. Darmana D, Henket RLB, Deen NG, Kuipers JAM (2007) Detailed modelling of hydrodynamics, mass transfer and chemical reactions in a bubble column using a discrete bubble model: chemisorption of CO_2 into NaOH solution, numerical and experimental study. Chem Eng Sci 62:2556–2575. https://doi.org/10.1016/j.ces.2007.01.065
49. Hlawitschka M, Drefenstedt S (2016) Local analysis of CO_2 chemisorption in a rectangular bubble column using a multiphase Euler-Euler CFD code. J Chem Eng Process Technol 7. https://doi.org/10.4172/2157-7048.1000300
50. Krauß M, Rzehak R (2017) Reactive absorption of CO_2 in NaOH: detailed study of enhancement factor models. Chem Eng Sci 166:193–209. https://doi.org/10.1016/j.ces.2017.03.029
51. Krauß M, Rzehak R (2018) Reactive absorption of CO_2 in NaOH: an Euler-Euler simulation study. Chem Eng Sci 181:199–214. https://doi.org/10.1016/j.ces.2018.01.009
52. Darmana D, Deen NG, Kuipers JAM (2006) Parallelization of an Euler-Lagrange model using mixed domain decomposition and a mirror domain technique: application to dispersed gas-liquid two-phase flow. J Comput Phys 220:216–248
53. Versteeg GF, Van Swaaij WPM (1988) Solubility and diffusivity of acid gases (carbon dioxide, nitrous oxide) in aqueous alkanolamine solutions. J Chem Eng Data 33:29–34. https://doi.org/10.1021/je00051a011

Numerical Simulation Techniques for the Efficient and Accurate Treatment of Local Fluidic Transport Processes Together with Chemical Reactions

Otto Mierka and Stefan Turek

Abstract This work describes a numerical framework developed for the efficient and accurate simulation of microfluidic applications related to two leading experiments of the DFG SPP 1740 research initiative, namely the 'Superfocus Micromixer' and the 'Taylor bubble flow'. Both of these basic experiments are considered in a reactive framework using the SPP 1740 specific chemical reaction systems. A description of the utilized numerical components related to special meshing techniques, discretization methods and decoupling solver strategies is provided and its particular implementation is performed in the open-source CFD package FeatFlow (FeatFlow Homepage, www.featflow.de, version from July 2020 [5]). A demonstration of the developed simulation tool is based on already defined validation cases and on suitable examples being responsible for the determination of the related convergence properties (in the range of targeted process parameter values) of the developed numerical framework. The subsequent studies give an insight into a parameter estimation method with the aim of determination of unknown reaction-kinetic parameter values by the help of experimentally measured data.

1 Introduction

Micromixers and microreactors provide a novel technology from which their suitable application even in industrial processes is expected. The mechanisms related to the flow dynamics are in general considered to be more deterministic than of those associated to their larger counterparts. This advantageous property is even more dominant in the field of numerical simulations, which therefore might possess an important role in the stage of design of the underlying equipment in order to achieve their theoretically best performance. Since numerical simulations are suitable tools to describe the flow dynamics and/or reaction kinetics in the underlying equipment for the accurately prescribed (physical, geometric or process) parameters, they also

O. Mierka · S. Turek (✉)
Chair of Applied Mathematics and Numerics (LS3), TU Dortmund, Vogelpothsweg 87, 44227 Dortmund, Germany
e-mail: stefan.turek@math.tu-dortmund.de

offer the advantage of determination of parameters—which due to different sorts of reasons cannot be determined with other techniques. Such an interplay between experimentally obtained measurement results and numerical simulations is the main idea described in the present work. However, it also has to be emphasized that the particular numerical techniques employed by the individual simulation software are extremely influential on the range of parameters in which the given simulation software can be applied for reliable predictions. Even in cases of just simple single-phase flow problems accompanied by mixing of species and chemical reactions there are high requirements put on the accuracy and efficiency of the given simulation tool, since the resolution of the steep concentration gradients is unavoidably inevitable for obtaining the mesh independent solution of the underlying problems. Suppressing the numerical diffusion and exploiting the highest non-oscillatory resolution of the results by the number of available grid points is the prerequisite of the employed efficient and robust solvers. In case of simulation problems extended by the presence of multiple phases with dynamically moving interfaces are even larger restrictions on the employed solution software introduced.

In this work we present a suitable numerical framework which is fulfilling the challenges requested by the targeted applications, which are the two basic leading experiments (Superfocus Micromixer and the round capillary Taylor bubble) of the SPP 1740 research initiative, both applied in the framework of SPP 1740-specific reaction systems. In Sect. 2 we describe the mathematical model with special emphasis on the series of employed numerical components in the framework of the used Projection Method. In the subsequent Sects. 3 and 4 we provide numerical results in terms of (1) validation cases, (2) model problems estimating convergence of the developed numerical framework and (3) reverse engineering applications with the aim of estimation of kinetic parameters with respect to experimentally measured reference results. Finally, the presented work is closed by conclusions in Sect. 5 which provides the summary of the numerical simulations and the possibilities of the presented reverse engineering method.

2 Mathematical Model

The developed numerical simulation method is based on the open-source FEM software package FeatFlow [5] which provides the backbone of the flow solver supported by geometrical multigrid methods, domain decomposition based MPI parallelization and higher order FEM discretization of the Navier–Stokes equations. These are essentially the main features, which define the accuracy and efficiency of the basic FeatFlow flow solver, which has already proven to provide benchmark solutions for numerous numerical benchmark problems [2, 8]. The main numerical feature of the basic single phase FeatFlow flow solver is related to the Discrete Projection (DP) method which provides a solution strategy for the nonlinear algebraic system of equations of the arising fully (spatially and temporally) discretized system of Navier–Stokes equations.

Since the targeted numerical framework involves additional concentration transport problems of species undergoing chemical reactions, which are partially related to gas/liquid flows, the basic flow solver has been extended with the corresponding multiphase and reaction modules. The general solution strategy is related to a direct numerical simulation (DNS) of the corresponding multiphase flow problem in a framework of an interface tracking approach, which requires an instationary direct resolution of the g/l interface by the computational mesh. The arising set of governing equations written in the generalized ingle- or multiphase) framework is as follows:

$$\rho(\mathbf{x})\left[\frac{\partial \mathbf{u}}{\partial t} + \mathbf{u} \cdot \nabla \mathbf{u}\right] - \nabla \cdot \left(\mu(\mathbf{x})\left[\nabla \mathbf{u} + \nabla \mathbf{u}^T\right]\right) + \nabla p = \rho(\mathbf{x})\mathbf{a}_g + \mathbf{f}_\Gamma(\mathbf{x}, t) \quad (1)$$

$$\nabla \cdot \boldsymbol{u} = 0 \tag{2}$$

$$\frac{\partial c_i}{\partial t} + \nabla \cdot (\mathbf{u}c_i) - D_{i,l} \cdot \Delta c_i = s_i\left(c_{j=1,2,\ldots,N}\right) \quad \text{for} \ \ i = 1, 2, \ldots, N_p. \tag{3}$$

where $\rho(\mathbf{x})$ and $\mu(\mathbf{x})$ represent the density and viscosity of the given phase which, however, depend on (in case of application for a multiphase problem) the particular interface location Γ separating the liquid and the gas phase from each other. Furthermore, at the arising dynamically evolving interface the surface tension force $\mathbf{f}_\Gamma(\mathbf{x}, t)$ is activated, which is defined as:

$$\mathbf{f}_\Gamma = \sigma_{l/g}\kappa\mathbf{n}_\Gamma \tag{4}$$

where $\sigma_{l/g}$, κ and $\mathbf{n}_\Gamma$ stand for particular (material dependent) interfacial tension coefficient, curvature and outward normal to the interface Γ, respectively. The last parameters in the above equations are $\mathbf{a}_g$—gravitational acceleration, $D_{i,l}$—diffusion coefficient of the ith species in the liquid phase, and s_i represents the source/sink terms of the ith species due to the occurring chemical reactions. The system of the resulting nonlinear equations is therefore defined for the quantities $\mathbf{u}$, p and c_i, corresponding to velocity, pressure and concentration of the individual species from all present N_P species taking part in N_R chemical reactions defined by the underlying chemical reaction mechanisms. Now, depending on if the particular numerical problem involves the presence of multiple phases or only a single phase, determines the activation of the next transport equation controlling the deformation of the computational mesh with respect to the dynamic interface, Γ. Therefore, in case of gas–liquid simulations with resolved interfaces according to the used Interface Tracking (IT) approach the above defined system of equations is to be appended by the Mesh Deformation (MD) equation for the displacement vector $\mathbf{d}$, as follows:

$$\nabla \cdot \left(\nabla \mathbf{d} + (\nabla \mathbf{d})^T\right) = 0 \tag{5}$$

The equation above is solved with respect to the updated deformation vector on the interface and for the side condition allowing a free slip of the mesh nodes on the

already updated and constructed interface Γ. It has to be noted that due to the adopted IT approach the underlying computational mesh is of constant topology during the whole simulation, only the coordinates of the individual element vertices are being modified giving therefore rise to a mesh velocity $\boldsymbol{\omega}$. More details to the developed IT method is provided in Sect. 2.1.

Since all the listed equations defining the addressed problem are mutually coupled with each other in a strong nonlinear fashion, their solution requires a robust mechanism, unless their simultaneous monolithic solution is to be performed. However, due to the targeted full 3D applications and thus the related high number of degrees of freedom, only a decoupling solution mechanism in a framework of the already mentioned DP method is feasible. According to the applied DP method, the solution of the system is decomposed into individual solution steps as explained below. Due to the fact, that the particular target applications are characterized by strictly laminar flow conditions and are expected to develop towards steady flows, the main decomposition of the system consists of decoupling the flow solution from the transport and reaction of the chemical species. According to such an (at the first look) *invasive* decoupling mechanism it is assumed that (1) the characteristic time-scale of hydrodynamics (i.e. reaching steady state flow conditions) is much smaller than the characteristic time-scale of the transport of species and the related chemical reactions and that (2) the chemical species are present in the respective phases only in such low concentrations that their back-coupling on the flow can be neglected (such as buoyancy or Marangoni effects). Therefore, the solution algorithm is directly decomposed into 2 simulation sub-steps, which in particular means the solution of the Navier–Stokes system in the first step and with the obtained velocity solution to solve the corresponding mutually coupled species transport problem in the next step. In this respect, we provide more details for the underlying numerical methods used for the particular IT approach in Sect. 2.1 and for the solution of the scalar transport problems in an Operator Splitting (OS) framework in Sect. 2.2. Therefore, it is inevitable to introduce our generalized DP method of the fully discretized Navier–Stokes system already now, so to present the overall computational scheme before describing its special features in details. The fully discretized Navier–Stokes equations can be written in the following representation:

$$\begin{bmatrix} A & \Delta t\, B \\ B^T & 0 \end{bmatrix} \begin{bmatrix} \mathbf{u} \\ p \end{bmatrix} = \begin{bmatrix} \mathbf{g}_u \\ 0 \end{bmatrix} \tag{6}$$

where A is the complete transport operator $A = M + \theta \Delta t (K + D)$, consisting of the contribution of mass, convection and diffusion operators. B and B^T are the discrete gradient and divergence operators, Δt is the time step between t^n and t^{n+1}, and $\mathbf{g}_u$ represents the right hand side encompassing the explicit contributions of the particular time stepping method and the explicit force terms. Now, if A is nonsingular the velocity can be formally expressed as $\mathbf{u} = A^{-1}(\mathbf{g}_u - \Delta t\, Bp)$ and plugged into the discrete continuity equation $B^T \mathbf{u} = 0$, which gives the Schur complement equation for the pressure:

$$\left(B^T A^{-1} B\right) p = \frac{1}{\Delta t} B^T A^{-1} \mathbf{g}_u \tag{7}$$

However, due to the fact that the $B^T A^{-1} B$ operator is impossible to build for realistic 3D problems (as it is a full, not a sparse matrix) the solution is realized by a preconditioned Richardson iteration where $S := B^T A^{-1} B$ (the so-called Schur complement) operator is approximated by a suitable counterpart. Now, assuming a framework of flows characterized by moderate Re numbers and the use of small time step sizes [18], the Schur complement can be suitably approximated by $S \cong P = B^T M_L^{-1} B$, ($M_L$ being the lumped mass matrix) which allows us to define the iteration step $l \to l+1$ for computing the pressure at the new time level t^{n+1}.

$$p^{l+1} = p^l + \left[B^T M_L^{-1} B\right]^{-1} \frac{1}{\Delta t} B^T A^{-1} \left[\mathbf{g}_u - \Delta t B p^l\right], \tag{8}$$

Finally, the overall solution strategy can be described by the following steps:

1. Solve the nonlinear momentum equations for $\tilde{u}$ with the pressure from previous time level p^n

$$\tilde{u} = A\left(\tilde{u}, \Gamma^n, \omega^n\right)^{-1} \left(g_u\left(u^n, \Gamma^n, \omega^n\right) - \Delta t B p^n\right)$$

2. Solve the Pressure-Poisson problem for the pressure update q

$$P\left(p^{n+1} - p^n\right) := Pq = \frac{1}{\Delta t} B^T \tilde{u}$$

3. Correct the pressure and the velocity

$$p^{n+1} = p^n + q, \quad u^{n+1} = \tilde{u} - \Delta t M_L^{-1} B q$$

4. Update the interface position (only in the interface normal direction)

$$\Gamma^{n+1} = \Gamma^n + \left(n_\Gamma \cdot u_\Gamma^{n+1}\right) n_\Gamma \Delta t$$

5. Solve the mesh deformation equation for the displacement d^{n+1}

$$A_d d^{n+1} = 0$$

for the boundary conditions given by Γ^{n+1}, where A_d represents the discrete deformation operator being reconstructed at every time step.

2.1 Realization of the Interface Tracking (IT) Approach

According to the general framework of the IT method the computational mesh is perfectly aligned with the free interface Γ which consequently means that the mesh has to be deformed at every single timestep and that not only at the interface but also in the volume of the present phases. This deformation may be realized on an algebraic basis, however a more robust realization is performed by means of the PDE based MD equation [6] which is to be solved to "steady state" at every timestep for the updated coordinates of the vertices at the interface. Due to the stability of the numerical scheme, the Q_2/P_1 FEM discretization of the Navier–Stokes system is extended with an additional Q_1 FEM PDE for the displacement MD equation. The accompanying effect of the used IT approach is related to the mesh movement treated by the ALE (Arbitrary Lagrangian–Eulerian) method, which gives rise to the mesh velocity $\boldsymbol{\omega}(\mathbf{x}, t)$. The applied ALE method leads to the transformation of the underlying Navier–Stokes equations, which depending on the applied temporal discretization results in the problem of evaluating the old velocity distribution on the new mesh. Therefore, the currently implemented realization is performed only by use of an implicit Euler scheme, which completely overcomes these interpolation difficulties, however, for the price of using smaller timestep sizes, which on the other hand, due to the presence of the relatively large surface tension forces, is constrained anyways. The next special feature of the used IT approach is the resulting semi-implicit treatment of the surface tension force by taking advantage of the Laplace–Beltrami transformation following the work of Hysing [7]. The surface tension force in the context of FEM discretization for the IT approach is introduced as a surface integral into the momentum equation in the following form:

$$f_{st} = \int_{\Gamma} \sigma \kappa n_{\Gamma} \cdot v \, d\Gamma \tag{9}$$

which by taking advantage of the surface tangential derivatives $\underline{\nabla}$ and $\underline{\Delta}$ can be formulated as:

$$f_{st} = \int_{\Gamma} \sigma \left(\underline{\Delta} x |_{\Gamma} \right) \cdot v \, d\Gamma \tag{10}$$

Since the new interface position $(x|_{\Gamma})^{n+1}$ can be expressed as the function of the old interface position and the new velocity at the interface:

$$(\mathbf{x}|_{\Gamma})^{n+1} = (\mathbf{x}|_{\Gamma})^n + \mathbf{u}_{\Gamma}^{n+1} \Delta t \tag{11}$$

by substituting it into (10) it allows us to represent the surface tension term in a semi-implicit manner by building its contribution into the transport operator A and into the right hand side of the Navier–Stokes equation.

Last, but not least, it is important to mention that the Q_2/P_1 FEM discretization for the Navier–Stokes system is performed by the use of isoparametric interpolation functions, which offer the advantage of exploiting the higher order discretization also for the geometric representation of the computational domain. Accordingly, the corresponding face- or edge-vertices located on the interface are not defined implicitly as simple coordinate averages of the corresponding corner points but are assigned to uniquely computed coordinates defining the curved interface. This is especially beneficial for the related element faces located on the interface, because it allows a higher order approximation of the interface. Moreover, it provides the necessary framework for the surface integration of the surface tension force term by means of the above-described Laplace–Beltrami transformation.

2.2 Realization of Scalar Transport Problems in Operator Splitting (OS) Framework

As described in Sect. 2, the scalar transport problem is solved subsequently, after obtaining the corresponding steady state flow distribution for the considered problem. Under the condition of fulfilling the related assumptions this approach offers the possibility of performing the scalar transport problem on an essentially differently constructed computational mesh than it was used for the flow simulation. This advantage is related to the fact that the transport of species is governed by a strongly convection dominated mechanism (compared to diffusion fluxes) according to which steep gradients of the species concentrations are expected to be resolved what might be possible only by the use of specially constructed high resolution computational meshes. For this reason, it is absolutely inevitable to enrich the arising discretization schemes with additional mechanisms (1) providing the necessary resolution there where needed and (2) to protect the discretization scheme from numerical diffusion as much as possible, so to gain maximum profit from the provided mesh resolution. The first component is provided in the current work by the Algebraic Mesh Deformation (AMD) method, which is essentially the extension of the classical *umbrella mesh smoothening* method [6] which is commonly used for mesh regularization purposes, however its application with a variable weight function enables its use for mesh adaptation purposes. Thus, the application of this AMD method requires a construction of a weight (or *monitor*) function, $w(\mathbf{x}, c_{i=1,\dots,N_p})$, which might be related to different sort of measures, but it has to be designed in such a way that it has large values there where the mesh nodes are required to be dragged to and small elsewhere. In this work, the construction is directly related to the distribution of maximum concentration gradient of all species, so to guarantee the maximum resolution possible (which is limited by the total number of elements) for all species. The second component being responsible for suppressing numerical diffusion but sustaining an oscillation-free high-resolution discretization is the Algebraic Flux Correction (AFC) method developed by Kuzmin and Turek [11]. This component transforms the originally

linear spatial transport equation to a nonlinear one. However, it provides the local extremum diminishing property (maximum due to convection does not increase, minimum does not decrease) which controls and enforces the conservation of convective fluxes on the algebraic level. This last property is especially of high interest for the reason that the velocity field is interpolated onto the deformed computational mesh used by the scalar transport module from the computational mesh used by the flow solver. The interpolation of the velocity field is performed in the framework of an L_2 projection, which is supported by an octree based search engine to provide an efficient mapping between the two computational meshes.

An additionally used mesh deformation mechanism is related to the PDE based MD method already described in the previous chapter. In particular, it is used for the multiphase simulation problems where the computational meshes have to be inflated with additional boundary layers along the mesh layer surrounding the gas phase.

The discretization of the scalar transport equations is performed by Q_1 FEM discretization supplemented by the above mentioned AFC method. Due to the possibility of numerical simulations of problems where the corresponding time-scales of reaction might be orders of magnitude faster than the corresponding timescales of spatial transport (convection or diffusion) the arising transport equations of the individual species were decomposed from each other in an Operator Splitting framework. Accordingly, the spatial transport step is performed for all species independently from each other for the given time step size Δt, which is followed by the next step—decomposed to arbitrary number of sub-time-steps covering the same time step size Δt used for the spatial transportation—taking the chemical reaction into consideration. This transport of species (happening in the dimension of the species) is then performed independently in space—i.e. in each Q_1 nodal value of the computational mesh—by means of an ODE step for which we used the numerical realization described and implemented in the open-source library of Shampine and Gordon [16].

3 Numerical Results of Single-Phase Problems

3.1 T-Mixer

The results of the simulation analysis provided in this chapter has been used for validation purposes with respect to the originally described studies of Bothe et al. [4] and has already been described in a detailed way in our paper [13]. Therefore, here we present only a brief summary of proofs demonstrating the capabilities of the developed framework for the simulation of reacting single-phase flows. The underlying problem is related to a T-shape micromixer (for the geometrical representation the reader is referred to [4]) into which the two inlet streams are provided in a 1:1 volumetric ratio for a range of characteristic Reynolds numbers from which the most interesting case is the one with the upmost value $Re = \frac{\overline{U}d_h}{\nu} = 186$. As a result, the interaction of the two inflow streams transforms into an engulfment flow, which

is characterized by complex flow structures thus drastically affecting the mixing of the reacting species. The inflow streams provide the reactants for the chemical reaction in an equimolar ratio so to enable a classical neutralization reaction of sodium-hydroxide (A) and hydrochloric acid (B), which is considered to be a nearly instantaneous chemical reaction:

$$A + B \xrightarrow{k} P \quad \text{with } k \approx 10^{11} \text{L}/(\text{mol s}). \tag{12}$$
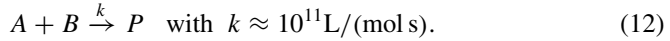
This property is exploited for the numerical simulations in a framework of a transformation (see Toor and Chiang [17]), which allows us to simulate the evolution of the distribution of only one scalar quantity, namely $\phi = c_A - c_B$. According to this transformation the reaction sink and source terms for the transported quantity ϕ cancel out each other and the corresponding reactant concentrations can be simply recovered by $c_A = \max\{\phi, 0\}$ and $c_B = \max\{-\phi, 0\}$. Considering that the values of the diffusion coefficients of the relevant species are on the order of $D_{A,B} \approx 3 \times 10^{-9} \text{m}^2/\text{s}$ (and thus resulting in a Schmidt number of $Sc = \frac{\nu}{D_{A,B}} = 300$) the occurrence of steep concentration gradients is expected which imposes high resolution requirements on the simulation software. Since the occurrence of such regions is a priori not known, but obtained only after the simulation, the approach of simulations by means of pre-refined static meshes is not realizable, instead simulation approaches using adaptively moving meshes offer the possibilities to deliver most accurate and most effective (compute power per simulation accuracy) results. Therefore, the realization of the simulations here was decomposed into the following two steps:

1. Since the velocity field exhibits a much more regular and smooth distribution as ϕ, recovering the *steady* flow field was performed on a moderately fine static mesh of $\approx 2 \times 10^4$ structured mesh consisting of uniform hexahedral elements.
2. Simulation of the transport of the scalar quantity ϕ was performed on an initially equidistant mesh of $\approx 1 \times 10^7$ hexahedral elements, the distribution of which was then adaptively changing based on the evaluated monitor function distribution until reaching steady state of ϕ distribution and therefore also of the mesh movement. The convective term has been updated by means of an L_2 interpolation from the previously computed flow field onto the deformed computational mesh.

The mechanism and the performance of the computational framework is demonstrated by means of Fig. 1, which provides the distribution of the transported scalar quantity ϕ at the same axial (reference) position as it is published in the original study from Bothe et al. [4] using roughly the same number of elements. As it can be seen from the corresponding figure, the regions characterized by the presence of steep gradients are resolved with the necessary quality so to guarantee a high accuracy of the computational framework. The additional subfigures of Fig. 1 display the distribution of the computational mesh along the reference slice, such as the distribution of the monitor function, which has been related to the gradient of the scalar quantity ϕ. As it can be seen from the individual figures, the adaptation of the computational mesh with respect to the overall number of available elements is capturing the critical
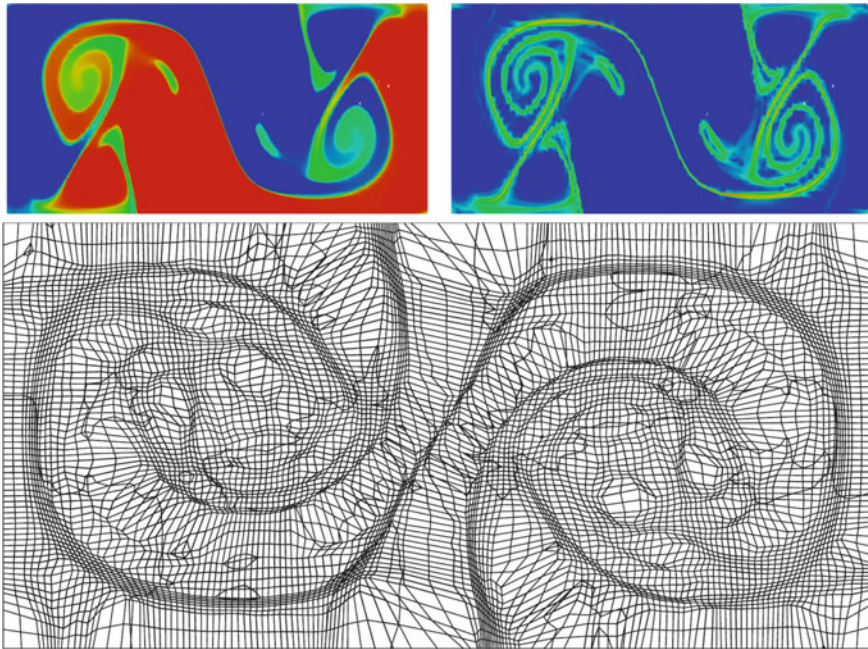
Fig. 1 Computational results computed for the T-mixer. Visualization of the results are displayed at a cutplane normal to flow direction at the position $z = 250\ \mu$m. Top-left: representation of the quantity ϕ. Top-right: distribution of the monitor function. Bottom: distribution of the computational mesh

regions in a very accurate way. However, due to the relatively large overall differences of the results for the analyzed resolutions it cannot be estimated if a next resolution level would already provide a satisfactory quantitative match with the here computed highest resolution results. Nevertheless, the results presented here—considering the achieved resolution—provide the most accurate numerical approximations to the considered problem.

3.2 Validation of the Numerical Framework for SFM

Due to the geometrical realization of the Superfocus Micromixer the mixing efficiency of this engineering equipment is much higher than of the T-mixer described in the previous subchapter. Since the inflow streams contact each other in an interdigital manner, the chemical species from the individual inlet streams need to tackle a much shorter distance by molecular diffusion so to provide a high mixing efficiency of the mixing unit. Since the concentration gradients in the liquid mixture are expected to be very high the numerical simulation of such flows, especially in combination with chemical reactions is not only a challenging problem, but if once such a simulation

Fig. 2 Geometrical representation of the computationally simulated SFM with a mesh detail showing the distribution of the generated hexahedral elements
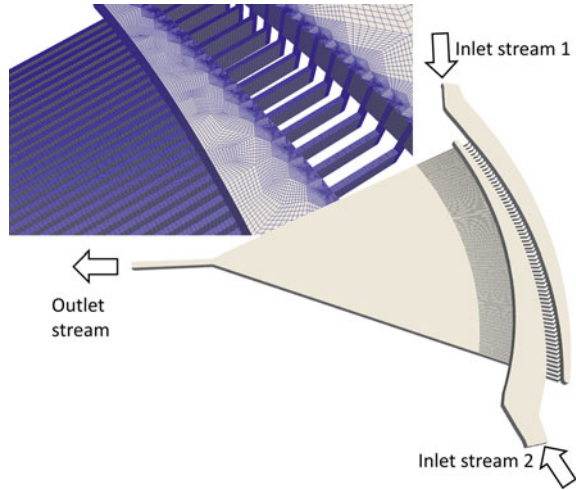
tool is successfully designed, it offers the possibility of a reverse engineering framework being suitable for determination of missing parameters of the system. According to such a reverse engineering framework, by the help of performing simulations for parameter variations (in certain parameter ranges) with respect to experimentally measured data, parameters like diffusion coefficients or reaction constants might be determined. The prerequisite of such a computational engineering tool is to guarantee its spatial convergence for the corresponding parameter space. For this reason, we have adopted the geometry of a standard SFM displayed in Fig. 2.

It has to be noted that the flow distributor located upstream of the SFM plays an extremely important role since it is responsible to provide the inflow streams into the mixer as equally homogenized as possible. Subsequently, its geometrical representation had to be included into the numerical simulations, however only in those stages, which concern the hydrodynamics. Details of the half-automatically created hexahedral coarse mesh (Level 1) used for the flow simulations are displayed as shown in subfigures in Fig. 2. The fluid parameters for the simulations correspond to water and the concentration of the chemical species were considered at such low levels that their respective back-coupling effects on the flow could be neglected. For the underlying convergence study the same reaction mechanism has been assumed as described for the T-mixer above (see Sect. 3.1). Accordingly, the transformation of Toor and Chiang [17] was utilized resulting in a simulation of only one single scalar transport equation for ϕ. In order to guarantee larger range of parameter spaces for subsequent simulation problems the diffusion coefficient of the respective species (and thus also ϕ) has been chosen 10 times lower as in the previous T-mixer case, namely $D_{A,B} = 3.0 \times 10^{-10} \text{m}^2/\text{s}$. The considered total flowrates were $\dot{V} = [100, 250, 500]$ cm^3/h resulting in characteristic Reynolds numbers on the order of Re $= [50, 125, 250]$ with respect to the average outflow velocity and channel depth. Since the underlying Q_2/P_1 FEM flow simulations provided

smooth velocity distributions of the computed flow fields, already the Level 2 spatial refinement solutions were considered as mesh independent solutions for all considered liquid throughput cases. The correspondingly obtained velocity solutions were utilized in the subsequent scalar transport simulations which have been interpolated onto the dynamically deformed computational meshes. The originally structured mesh spanning the tapering geometry of the SFM has been simulated on two successively refined mesh resolutions corresponding to number of hexahedral elements of $N_{El} = 1.25 \times 10^6$ and $N_{El} = 1.0 \times 10^7$. Only these two mesh resolution levels have been considered because a coarser representation of the computational mesh was a priori excluded from the analysis and an even finer representation was due to the resulting computational requirements unrealizable. Some typical deformations of the computational meshes are visible as additional subpicture of Fig. 3. As it can be seen from the corresponding figures, an alignment of the final steady state
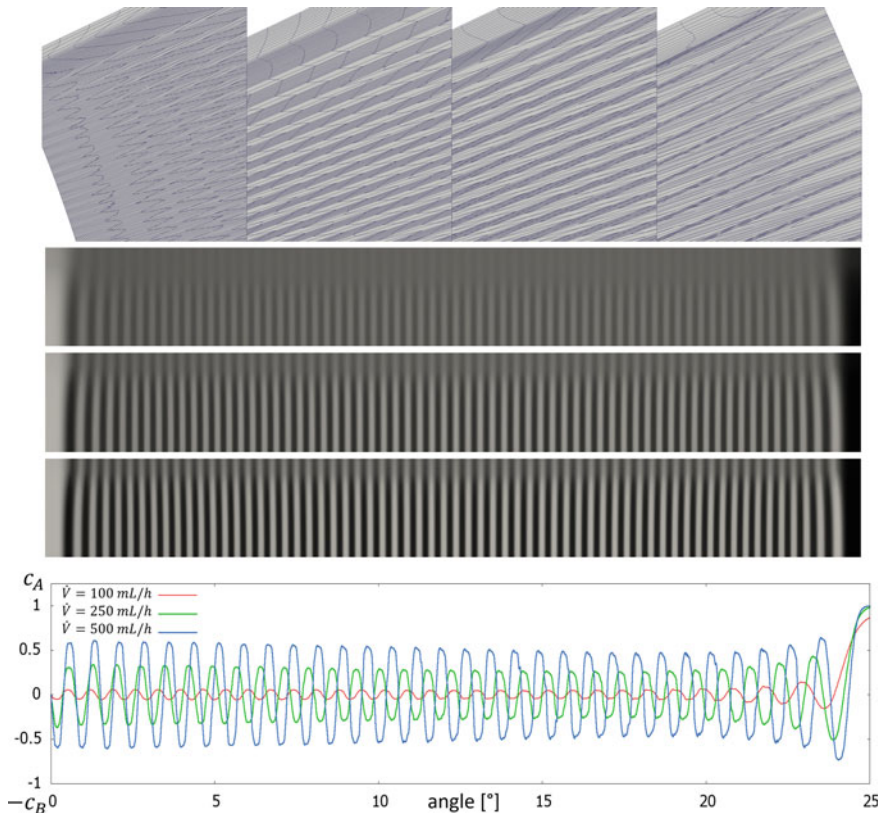
Fig. 3 Top: details of the computational mesh used for the scalar transport problem at different positions. Middle: distribution of the scalar quantity ϕ at the 80% axial length position (circular slice) for 100, 250 and 500 cm^3/h. Bottom: Concentration distribution along the symmetry line at the outflow plane from the SFM

Table 1 Mesh convergence of the chemical reaction conversion χ_r for the analyzed flowrates

Mesh Resolution N_{El}	$\chi_r[\%]$		
	Re = 50	Re = 125	Re = 250
1.25×10^6	97.3	88.5	75.4
1.00×10^7	95.8	81.9	68.3

mesh is observable along the inlet streams; moreover, also the circumferential adaptation of the mesh density is also clearly visible which gradually homogenizes in the flow-direction by the flattening of the scalar gradient used as monitor function. The corresponding steady state solutions have been used for post-processing and for mutual comparisons with respect to the determined overall conversion of the chemical reaction χ_r, defined as a ratio of generated product amount to the initial amount of reactant (A or B, since they are present in an equimolar ratio). Accordingly, the concentrations of the individual reactants have been integrated and averaged with respect to the outflow area, as follows:

$$\overline{c}_{A(B)} = \frac{\int_A (v \cdot n) c_{A(B)} dA}{\int_A (v \cdot n) dA} \tag{13}$$

where v and n stand for velocity and outflow normal, respectively. The integration surface A corresponds to the outflow surface, and since $c_{A_0} = c_{B_0}$ and the chemical reaction is equimolar $\overline{c}_A = \overline{c}_B$ at the outflow, as well. The corresponding simulation results are summarized in Fig. 3, showing the fine level representation concentration profiles along the circumferential direction at the outflow for the considered flowrates as a (1) graphical representation along the symmetry line and as a (2) spatial distribution at a respective axial positions. According to the related figures, the effect of the increasing flowrate is clearly observable by means of the sharper segregation of the black/white signal representing the individual species. Besides of such a qualitative representation of the results a more comprehensive evaluation is provided in Table 1, which shows the dependency of the determined conversion χ_r with respect to the applied mesh resolution. As it can be seen from the table, the differences between the mesh resolutions are increasing for the increasing flowrate, what is due to the occurrence of the increasing concentration gradients. Therefore, the differences between the resolution levels are increasing because the resolution of the arising concentration gradients is more restricted with the amount of available elements. However, the effective differences are in the range of only 10% for the largest flowrate (and only 2% for the smallest one) which due to the employed finite element framework gives a well-founded expectation for an already negligibly small deviation for an even higher resolution simulation. Finally, yet importantly, it also has to be noted that the diffusion coefficient has also been chosen to be a magnitude lower than diffusion coefficients of typical chemical species (used in our subsequent studies). The correspondingly estimated mesh resolutions were determined as reference for our subsequent studies, which have been supported by experimentally measured data.

3.3 Reaction Parameter Estimation by the Help of SFM

In this subchapter we provide an insight into the developed reverse engineering framework applied in the framework of the SFM which is one of the basic leading experiment units of the SPP 1740. The description of the numerical realization of the developed tool is essentially identical to the above described two applications (see Sects. 3.1 and 3.2) with the difference that instead of a numerical reconstruction of the experimentally measured behavior with known parameter settings here the determination of unknown parameters is performed. Realization of a suitable prototype exploiting the designed numerical components has already been reported by Mierka et al. [13] that tackled the problem of estimation of the diffusion coefficient of oxygen in the carrying liquid by means of utilizing optimization methods with respect to the experimentally measured spatially resolved concentration distributions at different locations of the mixer. Furthermore, a kinetic parameter of a Sulfite/Sulfate chemical reaction was also estimated by the utilization of similar optimization techniques supported by experimental data corresponding to a large range of operating conditions. The only drawback experienced in the mentioned studies is related to the computational efficiency, since the necessary computational resources might explode by covering a large range of parameter values in case of a multi-parameter optimization framework. As a remedy a geometrical acceleration of the optimization procedure has been developed which exploits the similarity of the core-region of the SFM with the performance of the overall mixing unit. Accordingly, a predictor/corrector realization of the optimization procedure has been proposed which allows a quick estimation of the narrow parameter ranges (predictor) which in the next step can be further improved to an optimal combination of parameters by means of performing the corresponding simulations on the full geometrical representation (corrector).

The particular chemical reaction system used for the demonstration of reaction parameter estimation of a consecutive reaction system (for details see [15]) is an oxidation reaction of a btmgp copper(I) complex (A). The first reaction gives rise to formation of a thermally unstable intermediate bis(μ-oxo)dicopper species (C) which is then subsequently transforming to bis(μ-hydroxo)dicopper(II) species (D) being the final product of the reaction scheme (for details of the reaction system we refer to [15]):

$$2A + B \xrightarrow{k_1} C \xrightarrow{k_2} D \tag{14}$$

In the above equation (B) referring to the dissolved O_2 species in acetonitrile, k_1 and k_2 are the reaction constants specifying the speed of the reaction rates r_1 and r_2, which are defined as follows:

$$r_1 = k_1 c_A^1 c_B^0 = -\frac{dc_A}{2dt} = -\frac{dc_B}{dt} = \frac{dc_C}{dt} \tag{15}$$

$$r_2 = k_2 c_C^1 = -\frac{dc_C}{dt} = \frac{dc_D}{dt} \tag{16}$$

The experimentally measured reference data has been provided by our collaboration partners from RWTH Aachen and therefore for details of the utilized experimental techniques, the reader is referred to Schurr et al. [15]. The such provided reference data—evaluated in terms of averaged concentration values of the intermediate species (C)—corresponds to a large range of flowrates of the inlet streams $\dot{V}_{min} = 0.44$ mL/min up to $\dot{V}_{max} = 56.0$ mL/min and was measured for two inflow concentrations of the reactants $c_{Cu^I}^{in} = 2.0$ mM and $c_{Cu^I}^{in} = 5.0$ mM. The diffusivity values of the underlying Cu complexes in acetonitrile have been experimentally determined as $D_A = D_C = D_D = 1.40 \times 10^{-9}$ m²/s and the diffusivity of oxygen has been estimated by means of the proposed correlation of Schumpe and Lühring [14] as:

$$D_B = \left(2.6 \times 10^{-11}\right)\mu_L^{-2/3} \cong 5.0 \times 10^{-9}\ \text{m}^2/\text{s} \tag{17}$$

but because of the undetermined accuracy of the proposed correlation this parameter has been also included into the reverse engineering framework. Thus, the complete initial parameter space has been estimated as:

$$k_1 = \langle 3, 30 \rangle\ \text{s}^{-1};\quad k_2 = \langle 0.6, 2.0 \rangle\ \text{s}^{-1};\quad D_B = \langle 4.0, 6.0 \rangle \times 10^{-9}\ \text{m}^2/\text{s} \tag{18}$$

The two geometrical representations used for the reverse engineering framework correspond only to the tapering part of the SFM (without the inflow distributor and without the residence channel at the outflow), which considering their geometrically defined volume ratios correspond to a small ($N_{El} = 2.8 \times 10^4$) and to a large ($N_{El} = 1.0 \times 10^6$) computational mesh covering the core (2 + 2 streams) and the full (64 + 64 streams) geometrical representation of the SFM. The provided resolutions are in agreement with the estimated resolution requirements found in the previous Sect. 3.3, especially with respect to the roughly 10 times higher diffusion coefficients values of the considered species. Concerning the boundary conditions and the numerical realization the large geometrical variant has been treated in the same way as in the previous validation chapter. However, it is worth to mention, that for the smaller geometrical variant the simulations were restricted only to the scalar transport equations of the individual species, because the flow field has been sampled according to the analytical parabolic solution. Therefore, the velocity **v** for an arbitrary point $[x_0, y_0, z_0]$ in the smaller geometrical variant is prescribed as follows:

$$v = \frac{v_{\max}\left(h^2 - z_0^2\right)}{16\left(x_0^2 + y_0^2\right)}[x_0, -y_0, 0] \tag{19}$$

where $v_{\max}$ is a parameter used for calibrating the corresponding flowrate and h represents the half of the thickness of the SFM, i.e. $h = 250$ μm. The correspondingly designed flow field fulfills periodicity at the tapering sides and therefore it is also suitable for numerical simulation of the respective transport equations in the framework of periodic boundary conditions at the corresponding boundaries. The
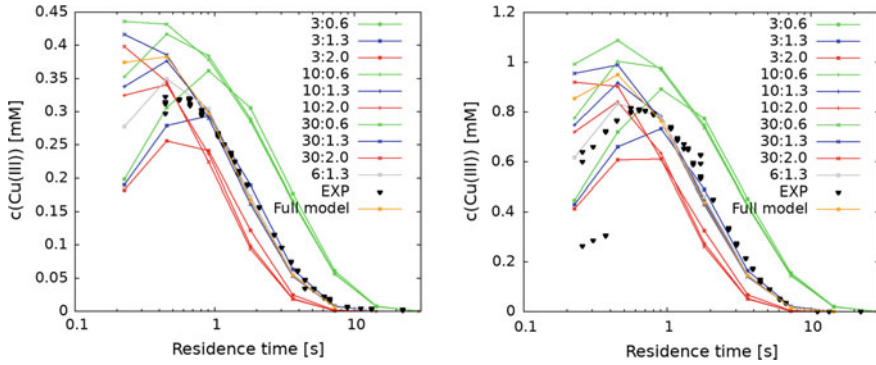
Fig. 4 Comparison of computational results against the experimental references obtained for a sequence of simple and a full geometric representation for two inflow concentration values of the reactant species Cu(I). Left: $c_{Cu^I}^{in} = 2.0$ mM and right $c_{Cu^I}^{in} = 5.0$ mM. Computational values of the full representation (with orange) correspond to the ratios of reaction constants $k_1 : k_2 = 10 : 1.3$ in s^{-1} and $D_B = 400 \times 10^{-7}$ cm^2/s. The parameters of the individual curves are the corresponding ratios of kinetic constants, $k_1:k_2$

mesh deformation with the aim of mesh adaptation at the regions of steep gradients is then performed analogously as for the full geometrical variant.

The results of the performed optimization process are displayed at Fig. 4, which shows the variation of simulation results for the small geometrical representation with respect to the experimental reference data. Based on the initial simulations in the searched parameter space the optimal combination of reaction constants has been estimated as $[k_1, k_2] = [6 \text{ s}^{-1}, 1.3 \text{ s}^{-1}]$. The value of the diffusion coefficient was found to be only slightly influential in the considered range of values and was determined to be best fitting the experimental reference data for $D_B = 4.0 \times 10^{-9}$ m^2/s. Concerning the prediction quality of this predictor step we have performed a corresponding simulation for the full geometric representation for the parameter values $[k_1, k_2, D_B] = [10 \text{ s}^{-1}, 1.3 \text{ s}^{-1}, 4.0 \times 10^{-9} \text{ m}^2/\text{s}]$. The average concentration values for the intermediate species (C) obtained by this way are matching the corresponding smaller geometrical representation results in an almost perfect way (see Fig. 4). Considerable differences are observed only for the high flowrate cases what is attributed to the arising differences in the underlying flow fields occurring especially at the entrance regions. Aside of these extreme flowrate cases it can be concluded that the accuracy but especially the efficiency of the developed reverse engineering toolbox has been considerably improved compared to its basic realization described in Mierka et al. [13].

4 Numerical Results of Chemically Reacting Multi-phase Problems

The presented numerical framework used for the multiphase flow simulations is essentially based on the method already presented in [13], which at the same time provided results for the benchmark problem of a single 3D rising bubble originally introduced by Adelsberger et al. [1]. The presented work has provided—up to the best knowledge of the authors—the so far most accurately determined (benchmark) evolution of quantities involving the bubble circularity, bubble rise velocity and characteristic bubble sizes. All these carefully chosen quantities are extremely sensitive with respect to the accuracy of the underlying numerical method, and therefore in light of the generated results the used numerical framework has proved its applicability and efficiency for a segment of multiphase flow problems, which neither undergo topological changes, nor experience strong deformations of the interface. Therefore, this numerical framework has been extended with an additional simulation module enabling the simulation of chemical reactions. Since the flows standing in the focus of our presented studies are characterized by a rather low Re numbers and rather low concentrations of chemical species taking part at chemical reactions, it allowed us to decompose the two transport problems of momentum and species concentration into two (from each other) decoupled computational modules. The first computational module is responsible for the determination of the steady state shape of the interface and the related flow field for an initially prescribed bubble volume enclosed by an initially defined regular interface separating the two present phases. The next computational module consists of a mesh construction method which is related only to the liquid phase since the gas phase is from the scalar transport simulations excluded (under the assumption of a very low effective mass transfer of the reactant from the gas to the liquid phase). The coarse mesh (in the context of geometrical multigrid) is extended with additional recursively refined boundary layers along the layer surrounding the bubble from the liquid side and is used for further successive refinements in the framework of the same PDE based mesh deformation method as used in the previous hydrodynamics simulation step. The previously determined velocity distribution is then in the last step projected in an L_2 projection sense on the such obtained high-resolution computational (static) mesh, which is subsequently used for the numerical simulation of the species transport accompanied by chemical reactions. The highlighted computational method is demonstrated and used in the next two numerical subchapters with the aim to present its convergence properties (Sect. 4.1) and, moreover, to undergo a reverse engineering framework in order to estimate kinetic parameters of the underlying chemical reactions (Sect. 4.2).

4.1　Numerical Simulation of a Large Taylor Bubble

Before providing computational details for a chemically reacting Taylor bubble flow let us demonstrate the accuracy and suitability of the developed framework for Taylor bubble flows. An excellent example for this purpose has been reported from Marschall et al. [12] that provides all prerequisites of a numerical multiphase flow benchmark, since aside of the precise description of the problem with all necessary parameters it provides numerical predictions for several computational methods supported by an experimentally measured high-quality segmentation of the bubble surface [3]. The geometrical realization of the problem corresponds to a bubble of a prescribed volume V_b located in a straight and vertically aligned square-cross-sectional capillary. The free rise of the bubble is modified by providing a flowrate of the liquid phase represented by an average plug velocity of v_L resulting in a final transportation velocity of the bubble U_b. The liquid phase used in the experiments corresponds to an aqueous solution of glycerol (resulting in a $\approx$ 30 times larger viscosity than water), while the gas phase corresponds to air. The combination of material properties together with the related operation conditions can be characterized by means of the corresponding Capillary $Ca = \mu_l U_b / \sigma$ and the Reynolds $Re = \rho_l d_h U_b / \mu_l$ numbers, which for the here considered flow result in $Ca = 0.088$ and the $Re = 17.0$. The particular values of the above introduced parameters and physical properties are provided below:

$$\rho_l = 1195.6 \ \text{kg/m}^3, \quad \mu_l = 28.54 \ \text{mPa s}$$
$$\rho_g = 1.3 \ \text{kg/m}^3, \quad \mu_g = 2.0 \times 10^{-5} \ \text{Pa s} \quad \sigma = 66.69 \times 10^{-5} \ \text{N/m}$$
$$d_c = 1.98 \ \text{mm}, \quad V_b = 17.49 \ \text{mm}^3 \quad L_c = 13.5 \ \text{mm}$$
$$U_b = 205.57 \pm 0.82 \ \text{mm/s}, \quad v_L = 138.2 \ \text{mm/s}.$$

The numerical simulations were performed in a transient fashion starting from rest, so that an initial bubble volume V_b was prescribed which then due to the interaction of the individual forces started to move and deform its surface. Due to the adopted *Reference Frame Transformation* with respect to the center of mass of the bubble, it is possible to minimize the deformation of the bubble, which is this way relatively—to the computational domain—always at the same axial position. According to the corresponding translational transformation, the boundary conditions become nonstationary and therefore are updated at every timestep together with the acceleration related force term, which vanishes by reaching steady state. The simulations have been initially performed on the coarsest resolution Level 2, which after reaching steady state (relative changes become smaller than the threshold defined for this purpose) have been interpolated to the higher resolution Level 3 and subsequently to the highest resolution Level 4. However, because the bubble volumes after interpolations have changed ($\approx 0.2\%$) all coarser level simulations (Level 2 and 3) have been restarted for the bubble volume determined from the finest Level 4 solution. This enabled us to organize the results into a suitable format for a mesh-convergence study

Table 2 Mesh convergence of the large Taylor bubble problem with respect to the experimental references [3]

	Sim L_2	Sim L_3	Sim L_4	Exp
L_b[mm]	7.185	7.204	7.214	7.200
Φ_d[μm]	431.6	434.4	435.4	433.1
Φ_l[μm]	46.8	49.7	49.7	50.5
U_b[mm/s]	19.17	19.78	20.07	20.56
$\dot{\chi}_b$[%/s]	0.025	0.0003	<0.00001	–

L_b stands for length of the bubble, Φ_d and Φ_l stand for the diagonal and lateral film thickness between the bubble and wall of the capillary, U_b is the terminal bubble velocity and $\dot{\chi}_b$ stands for the rate of change of bubble volume

with respect to a list of several sensitive quantities, such as the bubble length L_b and rising speed of the bubble U_b, and the related film thicknesses in the lateral Φ_l and diagonal direction Φ_d. The such extracted data is displayed in Table 2 which shows that already the coarse level resolution results are very close to the experimentally measured references and by the increased resolution the changes remain very small with respect to the higher resolution levels.

However, due to the still remaining differences in the corresponding bubble volumes (< 0.01%) it is not possible to clearly identify a convergence order of the computational method. It also has to be noted that the simulations are performed in a transient fashion, which are unfortunately influenced by a marginal volume loss, which on the different resolution levels exhibits a different mass-loss-rate violating the assumption of reaching an asymptotical steady state. Nevertheless, the volume loss of the coarse level is on the order of 0.02% for the simulation time of 1 s—what is already nearly identical to a characteristic time interval needed to achieve a steady state solution of the corresponding problem—which is already a challengingly low mass loss rate compared to the capabilities of classical front capturing methods even on very fine mesh resolutions. Moreover, the decrease of the corresponding mass-loss-rate with respect to the higher resolution levels shows the expected high convergence order (see Table 2). Last but not least, the convergence of the computations are also well demonstrated by means of the bubble shapes for the individual resolution levels as displayed in Fig. 5, which are practically overlapping with each other and are in a fairly good agreement with the experimentally provided measurement data.

Due to the above-considered square-cross-sectional capillary the liquid film squeezed between the bubble and the capillary wall has a varying thickness which has still a relatively large minimum thickness being only on the order of $\cong 2.5\%$ of the hydraulic diameter. However, in case of a subsequent simulation of transport of species the boundary layer around the bubble might have orders of magnitude smaller thickness the numerical resolution of which without using special meshing techniques is nearly impossible and therefore can be approached only by the use of suitable sub-grid scale models [19]. This is the reason why the underlying setup
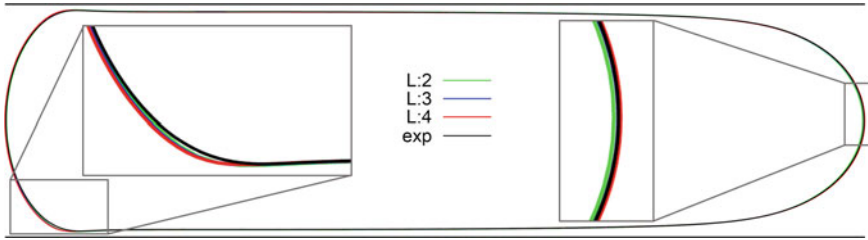
Fig. 5 Mesh convergence of the bubble shape for the large Taylor bubble problem with close-ups at regions characterized by the largest deviation. Experimental reference is plotted with black line and the mesh resolution levels 2, 3 and 4 are colored by green, blue and red, respectively

has been used in combination of the SPP1740-specific copper based chemical reaction system [15] for a convergence study, however considering the targeted round capillaries of the SPP1740 the realization of the problem was changed to a circular capillary. Accordingly, the hydraulic diameter and length of the capillary, volume of the bubble and the respective material properties of the two phases were kept identical as in the previous flow validation example and only a different imposition of boundary conditions has been realized, namely, via periodic boundary conditions at the inflow and outflow of the capillary. This realization is utilized in order to mimic an infinite sequence of bubbles and liquid slugs, which will be the central mechanism in our subsequent reverse engineering analysis. Therefore, a pressure drop value of $\Delta p = 385$Pa has been used in order to obtain a comparable transportation velocity $U_b = 206.9$mm/s of the bubble in the capillary as for the above described validation example. According to the developed computational strategy the coarse mesh of the obtained steady state solution has been extended with additional recursively inflated boundary layers (Fig. 6) and refined to the required mesh resolutions up to Level 6 with the use of the corresponding PDE based mesh deformation. For demonstration purposes, the Level 3 resolution of the correspondingly prepared computational mesh for the scalar transport problem is displayed in Fig. 6.

The numerical simulations of the subsequent reacting flow problems were performed by using the already determined diffusion coefficients and reaction kinetics from Sect. 3.3 for the corresponding consecutive Cu complex chemical reactions. The initial boundary conditions of the chemical species were defined as $c_{A_0} = 0.001$ M/L and as zero for all other species and the boundary conditions were defined as $c_{B_\Gamma} = 0.008$ M/L on the bubble surface and as zero flux of all other species at all other outer walls of the computational domain. Finally, the previously mentioned periodicity (without concentration jump) at the inflow/outflow faces of the capillary was imposed. The numerical simulations were performed for a time window of 2 s, which for the considered highest mesh resolution (Level 6) took roughly a day on 4 nodes of a 16 core intel Xeon cluster on LiDo3. A visual comparison of the obtained results with the results of a one level coarser simulation (Level 5) is displayed in Fig. 7, which provides the spatial distribution of the individual species at time $t = 2$ s and provides close-ups of the critical regions with respect to
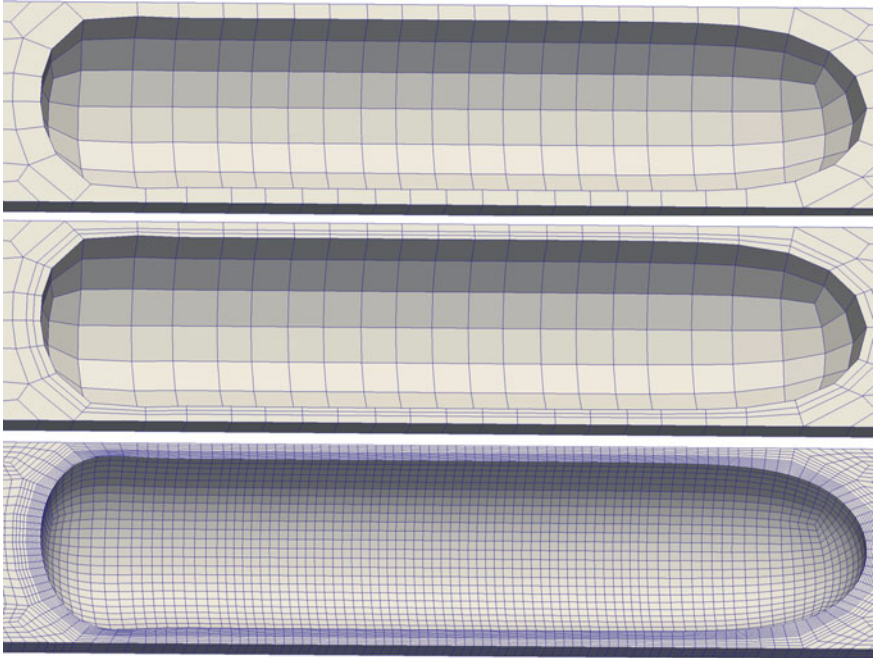
Fig. 6 Visualization of the computational meshes constructed for the scalar transport problem. Top: original coarse mesh (without the bubble phase) used for the flow simulation. Middle: boundary layer extension of the above mesh. Bottom: final computational mesh (visualized on Level 3) after adaptation to the bubble surface and deformation of the inner nodes

the corresponding mesh resolution. As it is clearly seen from the provided graphical proofs, the qualitative agreement of the respective species concentrations is excellent between the two mesh resolutions and therefore the obtained results might be considered as spatially converged numerical solutions. The concentration boundary layer of oxygen (B) shown in the subpictures exhibits nearly identical representations on both mesh resolutions thus the corresponding resolution requirements are considered to be fulfilled and therefore were applied in this sense for the subsequent studies. Furthermore, it also has to be noted that the considered numerical problem is characterized by a rather high value of the Schmidt number $Sc = \mu_l/(\rho_l D_A) \cong 5000$, for which by the use of the here applied resolution techniques a nearly mesh independent solution has been obtained. Considering, that for the forthcoming numerical example the corresponding Schmidt number is of an order of magnitude smaller offers the potential of obtaining even more accurate results.
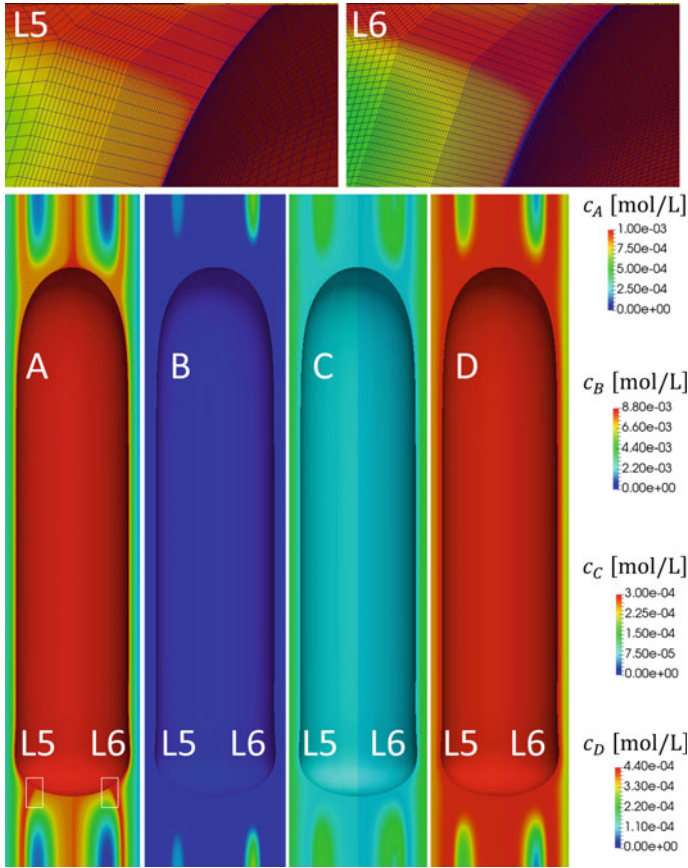
Fig. 7 Mesh convergence of the scalar transport problem extended with chemical reactions after 2 s of real-time simulations. Top: two subpictures showing the distribution of the computationally most critical species A (oxygen) at the bubble surface and its wake on mesh resolutions of Level 5 (left) and 6 (right). Bottom: concentration distribution of all A, B, C and D species with respect to the two considered mesh resolutions: L5 and L6

4.2 Kinetic Parameter Estimation for Reacting Taylor Bubble Flow

In this subchapter we will provide computational details for the application of reverse engineering technique in the framework of the reaction parameter estimation of a consecutive-competitive reaction system. The experimentally measured results—supporting the presented studies—were obtained by the chair of Laboratory of Equipment Design, Department of Biochemical and Chemical Engineering at the TU Dortmund. A detailed description of the corresponding innovative experimental setup is provided by Krieger et al. [10] which has utilized Arduino based regulation

techniques for the camera movement during the experiments. The analyzed chemical reaction system corresponds to the oxidation of leuco-indigo carmine (B) to an intermediate (C) which then further oxidizes in the second step to keto-indigo carmine (D) according to the following reaction scheme:

$$A + B \xrightarrow{k_1} C \quad \text{and} \quad A + C \xrightarrow{k_2} D \tag{20}$$
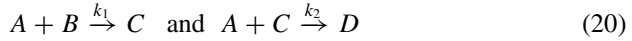
where the species (A) stand for oxygen. The chosen reaction system is not related to any industrially relevant production, however, due to the two distinct color changes of underlying oxidation steps it offers the advantage of spatial concentration measurements of the individual indigo species (B, C and D) at the same time. Additionally, due to the developed experimental technique of a sliding camera travelling with the liquid slug along the capillary the corresponding measurements could have been done not only spatially but also temporally in a highly resolved fashion. The reaction constants k_1 and k_2—in the meantime also estimated by experimental techniques by Krieger et al. [9]—have been targeted to be determined by means of numerical simulations in a framework of reverse engineering techniques. As reference data the spatial distributions of the optically active species have been used at distinct time levels referring to $t = 3.3$ s, 6.6 s and at 11.0 s, with respect to the time elapsed from contacting the two phases, i.e. the bubble formation at the needle downstream in the capillary. The such generated bubbles were produced periodically leading to a periodic sequence of gas bubbles and liquid slugs. The liquid stream entering the capillary contained only species B of a concentration $c_{B:t=0} = 3 \times 10^{-4}$ mol/L, and no species of A, C and D, thus $c_{A,C,D:t=0} = 0 \times 10^{-4}$ mol/L. Oxygen has entered the system by blowing it periodically into the capillary through the coaxial needle as a controlled volume air bubble, which due to the overall volumetric flow rate ($\dot{V}_t = \dot{V}_g + \dot{V}_l = 4.0$ cm^3/min) were travelling through the capillary. The generated air bubbles began gradually releasing oxygen by means of mass transfer into the liquid slugs, which subsequently gave rise to the above described chemical reactions. The complete list of physical properties used for the numerical simulations is provided for the here considered system in Table 3.

The numerical realization of the underlying problem has been done on the same basis as in the previously described example of Sect. 4.1 according to which only

Table 3 List of parameters used for the numerical simulations of the reacting small Taylor bubble problem

Phase	$\rho[\text{kg/m}^3]$	μ $[10^{-3} \times \text{Pa.s}]$	σ [N/m]	Species	D $[10^{-9} \times \text{m}^2/\text{s}]$
Liquid	1000	1.12	0.075	A	2.0
Gas	1.2	0.018		B, C, D	0.6

Diffusion coefficients have been determined by Krieger et al. [9]

one single pair of a slug and bubble has been considered with the use of periodic boundary conditions at the inflow/outflow planes. Thus, the geometrical representation was restricted to a capillary of a diameter of $D = 1.6$ mm and of length $L = 3.32$ mm. The experimentally provided bubble volume—assuming to be constant due to neglecting its volume change due to mass transfer—has been $V_b = 1.98$ mm^3 which has been initialized in the flow computations as a perfect sphere and in the course of the simulation sequences on low and high mesh resolutions it has reached its final steady shape. The underlying flow simulations were iterated with respect to the prescribed pressure drop as long as the requested flow rates have been achieved. The correspondingly obtained pressure drop was estimated as $\Delta p = 3.3$ Pa and the obtained flow field and interface distributions were used for the subsequent concentration transport equations with the corresponding chemical reactions.

As already described before, the gas bubble was represented in the numerical simulations of the concentration scalar equations only in terms of a Dirichlet boundary condition with respect to the oxygen species in the framework of a Henrys Law approximation. The corresponding value of this boundary concentration was represented by the value of $c_{A,\Gamma} = 2.5 \times 10^{-4}$ mol/L. The value of the characteristic Schmidt number for the here considered numerical simulations was Sc $= 330$, thus the use of the previously introduced meshing strategy in terms of the boundary layer resolution such as overall resolution was expected to provide nearly mesh independent solutions, as for the numerical example analyzed in Sect. 4.1. Accordingly, a graphical comparison of the two finest resolution level solutions for the found combination of kinetic parameters in terms of the oxygen concentration distribution is displayed in Fig. 8 at the time level of $t = 6.6$ s. According to the inserted graphics, it can be seen that the concentration distribution of this most critical species A is nearly identical along the interfacial boundary surface and in the core of the liquid slug, as well. The values of the computationally found kinetic constants is $k_{1,comp} = 8.0 \times 10^5$ L/(mol s) and $k_{2,comp} = 8.0 \times 10^5$ L/(mol s) which compared to the experimentally found kinetic constants by Krieger et al. [9]—$k_{1,exp} = 6.3 \times 10^5$ L/(mol s) and $k_{2,exp} = 22.4 \times 10^5$ L/(mol s)—are matching reasonably well. According to the numerical simulations, the ratio of these two kinetic parameters is the most influential on the intermediate product C, which in case that $k_1 : k_2 < 1.0$ clearly underpredicts the concentration of these intermediate species. Therefore, the experimentally determined combination of parameters was computationally not confirmed and the experimentally provided reference data could be reproduced in the most accurate way only with a ratio of $k_1:k_2 = 1.0$.

It has to be noted that the comparison of the computational results with the experimental references had to be performed in a framework of a data transformation, which in particular means a projection of the full 3D data into a 2D representation, with the aim to provide a compatible analogy between the two (experimental and computational) methods. The corresponding representation of the results is presented in Fig. 9, which shows the computational and the respective experimental concentration distributions at the three reference time levels. From the displayed sequence of
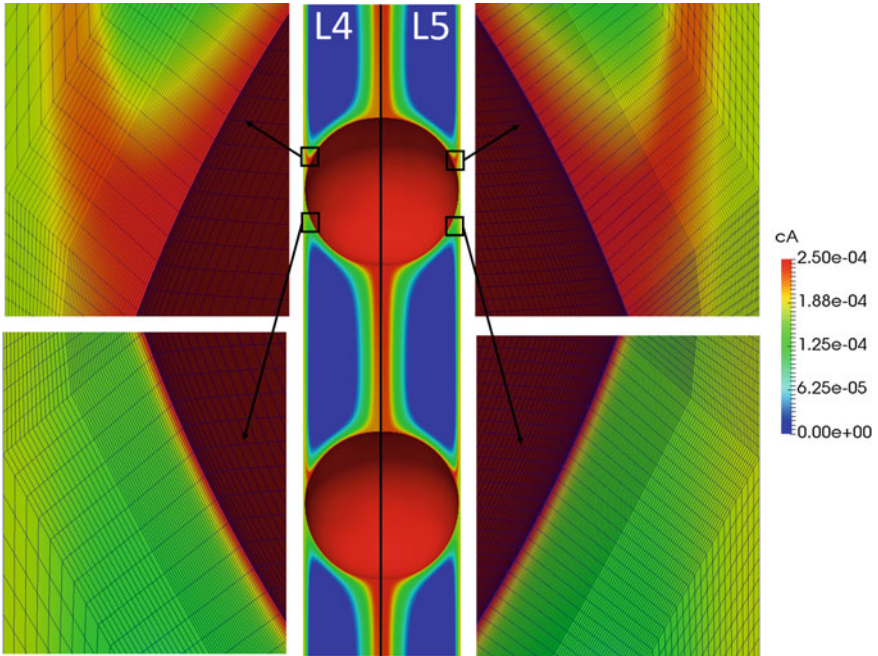
Fig. 8 Visualization of the spatial convergence analysis of the reacting small Taylor bubble problem with mesh details. The full simulation domain with the corresponding concentration distribution is displayed in the middle for the two finest resolutions (L4 and L5) and at the sides close-ups of two representative regions at the bubble interface
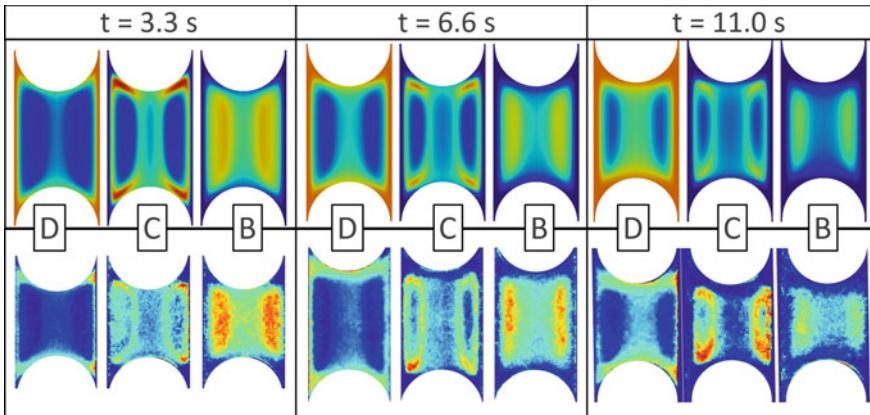
Fig. 9 Comparison of the computationally obtained (top sequence) and experimentally measured (lower sequence) concentration distribution of the optically measurable species (B, C and D) at three reference time levels of $t = 3.3$ s, 6.6 s and 11.0 s. The color scales refer to $0 : 4 \times 10^{-4}$ mol/L for species B and D and $0 : 4 \times 10^{-5}$ mol/L for species C

pictures, it can be seen that the dynamics of the reaction is reasonably well captured—namely the consumption rate of B and the production rate of D—by the computations for the found kinetic parameters. Moreover, also the shape and the thickness of the characteristic ring of the intermediate product C is computationally resembled in a very good agreement with the experimentally recorded pictures.

5 Conclusion

In this study we have developed and demonstrated a reverse engineering framework applied in the field of single- and multiphase flows accompanied by chemical reactions. The computational strategy consisting of the individual numerical components has been applied for typical validation problems—mixing of species in a T-mixer [4] and the non-reacting Taylor bubble benchmark [12]—yielding fairly good agreement with the available reference results. Next, the basic flow modules (single- and multiphase) have been combined with the corresponding module of transport of species with chemical reaction and convergence estimation of the developed numerical simulation software has been performed. Based on the estimated necessary resolutions, the determination of reaction parameters has been performed for experimentally measured systems. The correspondingly estimated parameters have been proven to be in a very good accordance with assessments through independently performed experiments, which justifies that the use of the developed technique also in the framework of other possible reaction systems operating under the here considered assumptions. Moreover, the here developed numerical toolbox makes possible its application for detailed performance analysis of the chemical reactions in the framework of simple multiphase flows with respect to engineering quantities expressing the efficiency of the overall process like the yield of the wanted product or selectivity of a system of chemical reactions with respect to the desired product.

References

1. Adelsberger J, Esser P, Griebel M, Groß S, Klitz M, Rüttgers A (2014) 3D incompressible two-phase flow benchmark computations for rising droplets. In: Proceedings of the 11th World Congress on Computational Mechanics (WCCM XI), Barcelona, Spain
2. Bayraktar E, Mierka O, Turek S (2012) Benchmark computations of 3D laminar flow around a cylinder with CFX, OpenFOAM and FeatFlow. Int J Comput Sci Eng 7(3):253–266

3. Boden S, Haghnegahdar M, Hampel U (2017) Measurement of Taylor bubble shape in square channel by microfocus X-ray computed tomography for investigation of mass transfer. Flow Meas Instrum 53:49–55
4. Bothe D, Lojewski A, Warnecke H-J (2009) Computational analysis of an instantaneous chemical reaction in a T-microreactor. AIChE J 56:1406–1415
5. FeatFlow Homepage, www.featflow.de, version from July 2020
6. Grajewski M, Köster M, Turek S (2008) Mathematical and numerical analysis of a robust and efficient grid deformation method in the finite element context. SIAM J Sci Comput 31(2):1539–1557
7. Hysing S (2007) Numerical simulation of immiscible fluids with FEM level set techniques. PhD Thesis, University of Dortmund, Dortmund
8. Hysing S, Turek S, Kuzmin D, Parolini N, Burman E, Ganesan S, Tobiska L (2009) Quantitative benchmark computations of two-dimensional bubble dynamics. Int J Numer Methods Fluids 60(11)
9. Krieger W, Bayraktar E, Mierka O, Kaiser L, Dinter R, Hennekes J, Turek S, Kockmann N (2020) Arduino-based slider setup for gas-liquid mass transfer investigation: experiments and CFD simulations. AIChE J 66(6):e16953
10. Krieger W, Hörbelt M, Schuster S, Hennekes J, Kockmann N (2019) Kinetic study of Leuco-Indigo carmine oxidation and investigation of Taylor and dean flow superposition in a coiled flow inverter. Chem Eng Technol 42(10):1–10
11. Kuzmin D, Turek S (2004) High-resolution FEM-TVD schemes based on a fully multidimensional flux limiter. J Comput Phys 198(1):131–158
12. Marschall H, Boden S, Lehrenfeld Ch, Falconi CJ, Hampel U, Reusken A, Wörner M, Bothe D (2014) Validation of interface capturing and tracking techniques with different surface tension treatments against a Taylor bubble benchmark problem. Comput Fluids 102:336–352
13. Mierka O, Munir M, Spille C, Timmermann J, Schlüter M, Turek S (2017) Reactive liquid flow simulation of micromixers based on grid deformation techniques. Chem Eng Technol 40(8)
14. Schumpe A, Lühring P (1990) Oxygen diffusivities in organic liquids at 293,2 K. J Chem Eng 35:24–25
15. Schurr D, Strassl F, Liebhäuser P, Rinke G, Dittmeyer R, Herres-Pawlis S (2016) Decay kinetics of sensitive bioinorganic species in a SuperFocus mixer at ambient conditions. React Chem Eng 5
16. Shampine L, Gordon M (1975) Computer solution of ordinary differential equations: the initial value problem. Freeman. ISBN: 0716704617
17. Toor HL, Chiang SH (1959) Diffusion-controlled chemical reactions. AIChE J 5:339–344
18. Turek S (1997) On discrete projection methods for the incompressible Navier-Stokes equations: an algorithmical approach. Comput Methods Appl Mech Eng 143(3–4):271–288
19. Weiner A, Hillenbrand D, Marschall H, Bothe D (2019) Data-driven subgrid-scale modeling for convection-dominated concentration boundary layers. Chem Eng Technol 42(7):1349–1356

Euler-Euler Modeling of Reactive Flows in Bubble Columns

Roland Rzehak

Abstract In the present project, closure models for chemical reactions as well as the associated mass transport are included in the Euler-Euler description of bubbly flows. This approach allows to capture inhomogeneous distributions of gas fraction as well as local differences in concentration and flow fields on the scale of the bubble column. In this way, calculations up to the size of industrial equipment or components thereof become feasible. To achieve this goal, suitable closure models for processes occurring on the scale of individual bubbles have to be devised. The simulation results are then compared with experimental data to validate the employed models. The challenge in this endeavor based on the state-of-the-art at the beginning of the project, is threefold: First, the available understanding of mass transfer from or to single bubbles both without and with the simultaneous occurrence of a chemical reaction is limited. Second, experimental data of a quality which is suitable for the purpose of model validation are scarce. Third, for reactive systems the intrinsic reaction kinetics and material parameters depending on the concentrations of all involved species and temperature are often not known.

1 Introduction

In Euler-Euler simulations, both phases are treated as interpenetrating continua, each described by a set of conservation equations for mass and momentum (aka continuity and Navier–Stokes equations). Momentum exchange between the phases is accounted for by coupling terms between both sets of conservation equations [1]. These describe the average volumetric force exerted by the liquid on the bubbles and the corresponding volumetric reaction force, which is equal and opposite. In addition to drag, the typically considered bubble forces comprise (shear-) lift, wall (-lift), and virtual mass, while the (Basset-) history force is most often neglected. Contributions to the drag force arising from the mean flow and the turbulent fluctuations are frequently separated, the latter describing the effect of turbulent dispersion. Only

R. Rzehak (✉)

Helmholtz-Zentrum Dresden—Rossendorf, Bautzner Landstrasse 400, 01328 Dresden, Germany
e-mail: r.rzehak@hzdr.de

the mean flow contribution is typically considered for the other forces. In deriving these force models, a point-bubble approximation is tacitly made, which imposes a restriction on the possible grid-refinement.

Concerning turbulence, the Euler-Euler approach is most frequently combined with a RANS turbulence model ranging from simple k-ε to sophisticated Reynolds stress models. These models, which have originally been developed for shear-induced turbulence in singlephase flows, are extended to multiphase flows by adding source terms in the model equations describing the bubble-induced contribution to turbulence [2]. The use of LES models has been attempted as well, but common subgrid-scale models have requirements on the grid-resolution that often conflict with those due to the point-bubble approximation [3].

In all of the mentioned submodels, the bubble size appears as a parameter. Setting this to a constant value gives the monodisperse approximation, which has been adopted in the majority of studies. In addition, swarm-effects have not been considered in most previous works, which is appropriate for dilute flows. Within these approximations, a model that has been validated over an extended period of time for a rather large database of experimental test cases, comprising bubbly flows in pipes as well as bubble- and airlift-columns, is described in Ref. [4].

A distribution of bubble sizes which changes in time may be accommodated by coupling the approach described so far to a population balance equation. In doing so, it is important to allow bubbles of different size to move in different directions when necessary. An example where this is important, is furnished by the finding of e.g. Tomiyama et al. [5] that the lift force changes its direction at a certain bubble size. While different frameworks have been proposed to numerically solve the population balance equation, one that meets this requirement in a rather straight forward way is the so-called inhomogeneous MUSIG model [6]. Among physical phenomena that change the bubble size distribution, bubble coalescence and breakup have received most attention so far, but a consensus on the most appropriate models has not yet been reached [7].

As obvious from the foregoing discussion, the Euler-Euler approach has been widely used for purely fluid dynamical processes in bubbly flows. In contrast, Euler-Euler modeling and simulation studies involving mass transfer both with and without chemical reaction to date are rather scarce. In order to account for mass transfer processes as well, the conservation equations for mass and momentum have to be complemented by additional ones for the species concentration in each phase. If highly endo- or exothermic chemical reactions occur, the energy equation has to be considered as well, but this topic is excluded from the present work.

Phenomena for which closure models are needed, are summarized in Fig. 1, most obvious being the mass transfer between the gas bubble and the liquid surrounding it, which is quantified by the mass transfer coefficient. Turbulent diffusion of the transferred species within the liquid can be modeled in the same way as in singlephase flows, assuming that the bubble-induced contribution to the turbulence is properly accounted for. In the reactive case, one needs to distinguish between fast reactions, which occur predominantly in the boundary layer around the bubble, and slow reactions, which take place mostly in the bulk of the liquid. Fast reactions increase the
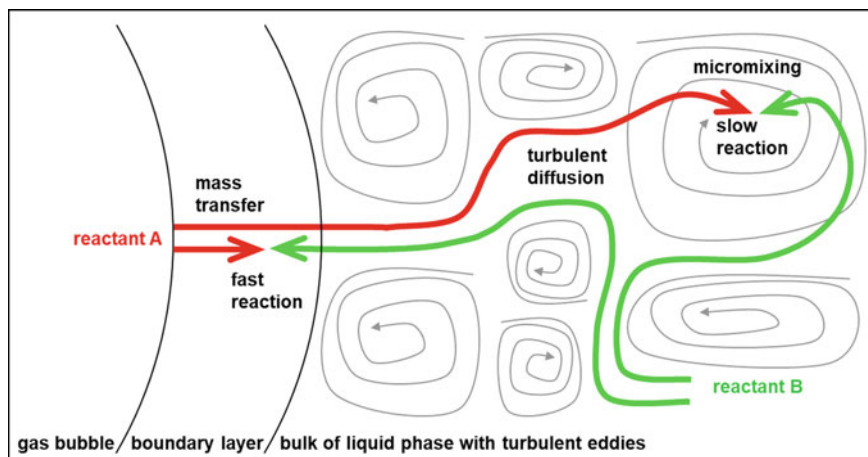
Fig. 1 Illustration of small-scale phenomena requiring closure models for Euler-Euler simulations. A second order reaction between two reactants A and B is assumed, one of which is supplied in the gas bubbles, the other one in the liquid. Two cases corresponding to the limits of fast and slow reactions are shown

mass transfer, which is described by a so-called enhancement factor. For slow reactions, micro-mixing has to be accounted for, which can be done again in the same way as in singlephase flows. Preferably, a single model for each of these quantities would be desirable that gives reasonably accurate results over a wide range of conditions. The validity of all models should be established by comparison to comprehensive measurements that resolve the local variations in the species concentrations on the large scale of the bubble column or other apparatus.

In the case of high mass transfer rates, where the bubbles shrink during absorption or grow during desorption, suitable source terms for the MUSIG model are needed to capture this change in bubbles size and the resulting interaction between fluid dynamic and mass transfer phenomena. Since mass transfer rates are particularly high in the reactive case, yield and selectivity may be affected significantly by the fluid dynamic conditions.

Last but not least, CFD simulations must be fed by reasonably accurate values of the material properties. For purely fluid dynamical questions this rarely poses a problem since constant values for density and dynamic viscosity of each phase together with the surface tension between them suffice. For questions involving non-reactive mass transfer the Henry constant describing the solubility of the transferred species and its molecular diffusion coefficient must be added to this list and all quantities become concentration-dependent unless the solution remains dilute. In the presence of chemical reactions, furthermore the intrinsic reaction rates are needed, which are often not available.

This chapter describes progress made during the 3-year funding period towards the overall goal of developing Euler-Euler simulations including mass transfer to

a state similar to that already achieved for purely fluid dynamical problems. All simulations are performed using the software *ANSYS CFX 15*.

The first section provides a validation example of the already established fluid dynamical modeling that is used as a basis of the development. Comparison is made with experimental data obtained by one of the project partners within the SPP1740 (see Chapter "Experimental Characterization of Gas-Liquid Mass Transfer in a Reaction Bubble Column Using a Neutralization Reaction").

The second section is concerned with non-reactive mass transfer. Simple conceptual models for the mass transfer coefficient for different flow conditions around the bubble are discussed and unified and an initial attempt to validate an Euler-Euler simulation model using data found in the literature prior to the project is presented.

The third section focuses on the effect of chemical reactions on the mass transfer. Again, simple models for the enhancement factor are evaluated first. These depend strongly on the reaction network and the absorption of CO_2 into an aqueous solution of NaOH is considered. This choice is determined by the literature data available for model validation prior to the project. Results of the comparison between these data and the simulation results are shown.

Finally, a summary of the achievements is given and prospects for further investigations are discussed.

2 Fluid Dynamics

The fluid dynamical part of the models has been amply described in previous works (e.g. [1] and references therein). Therefore, only a brief summary is given here for the sake of completeness. The conservation equations for mass and momentum of the disperse gas and continuous liquid phases are summarized as follows:

$$\frac{\partial}{\partial t}(\alpha_G \rho_G) + \nabla \cdot (\alpha_G \rho_G \boldsymbol{u}_G) = 0 \tag{1}$$

$$\frac{\partial}{\partial t}(\alpha_L \rho_L) + \nabla \cdot (\alpha_L \rho_L \boldsymbol{u}_L) = 0 \tag{2}$$

$$\frac{\partial}{\partial t}(\alpha_G \rho_G \boldsymbol{u}_G) + \nabla \cdot (\alpha_G \rho_G \boldsymbol{u}_G \otimes \boldsymbol{u}_G) = \\ - \alpha_G \nabla p + \nabla \cdot \left(\alpha_G \left(\mathbf{T}_G + \mathbf{T}_G^{Re} \right) \right) + \alpha_G \rho_G \boldsymbol{g} + \boldsymbol{F}_G^{inter} \tag{3}$$

$$\frac{\partial}{\partial t}(\alpha_L \rho_L \boldsymbol{u}_L) + \nabla \cdot (\alpha_L \rho_L \boldsymbol{u}_L \otimes \boldsymbol{u}_L) = \\ - \alpha_L \nabla p + \nabla \cdot \left(\alpha_L \left(\mathbf{T}_L + \mathbf{T}_L^{Re} \right) \right) + \alpha_G \rho_G \boldsymbol{g} + \boldsymbol{F}_L^{inter} \tag{4}$$

Here, the indices $\phi = $ G, L denote gas and liquid phases, α_ϕ, ρ_ϕ, and $\boldsymbol{u}_\phi$ the phase fraction, density, and phasic velocity. The pressure p is shared between both phases

Table 1 Summary of fluid dynamical closure models

Sub-model	Reference
Drag force	Ishii and Zuber [9]
(Shear-) lift force	Tomiyama et al. [5]
Wall (-lift) force	Hosokawa et al. [10]
Turbulent dispersion force	Burns et al. [11]
Virtual mass force	$C_{VM} = 0.5$
Base turbulence model	k-ω SST (Menter [12])
Bubble-induced turbulence	Rzehak and Krepper [2]
Liquid-phase wall model	Single-phase wall function
Gas-phase wall model	Free-slip

and $\boldsymbol{g}$ is the gravitational acceleration. Two terms require closure models. First, the interfacial forces $\boldsymbol{F}_\phi^{inter}$, which due to momentum conservation are related as $\boldsymbol{F}_G^{inter} = -\boldsymbol{F}_L^{inter}$. As already mentioned, these comprise of a number of contributions, here specifically drag, (shear-) lift, wall (-lift) turbulent dispersion and virtual mass. Second, the Reynolds stresses, which are expressed in terms of an eddy viscosity as $\mathbf{T}_\phi^{Re} = \mu_\phi^{turb}\left(\nabla\boldsymbol{u}_\phi + \left(\nabla\boldsymbol{u}_\phi\right)^T\right)$. The eddy viscosity is computed from a turbulence model, here specifically the k-ω SST model with added source terms to describe the bubble-induced turbulence. A variant using a Reynolds stress turbulence model with anisotropic bubble-induced source terms has been developed within the present project [8], but is not applied in the simulations presented herein. Due to the small density of the gas phase in comparison with the liquid one, the gas phase Reynolds stresses can be neglected. A compound single phase turbulent wall function assuming a smooth wall is employed to avoid the need to resolve the viscous sub-layer. A free-slip condition is applied for the gas phase. The main ingredients of the model are summarized in Table 1.

Within the present project, comparison of the fluid dynamical part of the model has been made with experimental results from a partner, the research group of Dr. Zähringer, Magdeburg (see Chapter "Experimental Characterization of Gas-Liquid Mass Transfer in a Reaction Bubble Column Using a Neutralization Reaction") [13]. There, the two-phase flow of CO_2 bubbles in water at a superficial velocity of $J_G = 12$ mm/s was investigated in a cylindrical bubble column. Diameter and ungassed fill height of the column were $D = 0.142$ m and $H = 0.73$ m. The gas was supplied through four nozzles arranged in a line at the column bottom, which created bubbles of a size of $d_B = 2.7$ mm. Optical measurement techniques were employed to determine gas fraction and liquid mean velocity as well as turbulent fluctuations. An example of the comparison is shown in Fig. 2. Both panels display the mean liquid velocity field in the plane of observation, which is in the center of the column at the position of the nozzles superimposed on the color-coded value of the vertical liquid velocity component. As can be seen, the overall structure of the flow field from the experiment (left) is well reproduced by the simulations (right). Quantitatively, the calculated velocities are somewhat too low compared with the measured ones in
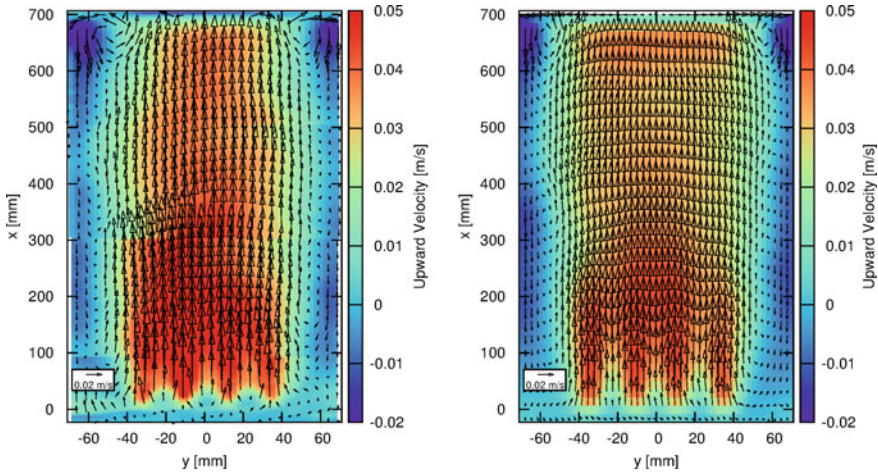
Fig. 2 Comparison of mean liquid velocity in a vertical central plane through the column containing the gas-supplying nozzles obtained from the experiments (left) and from the simulations (right) for CO_2 bubbles in water at $J_G = 12$ mm/s. Flow field (arrows) with superimposed color-coded vertical velocity component [13]

the middle of the measurement plane, but the agreement is still reasonable. For more detailed results we refer to Chapter "Chemical Reactions in Bubbly Flows" of this volume.

3 Mass Transfer Without Reaction

An overview of the scarce literature on Euler-Euler simulations with mass transfer [14] shows that despite the small number of works, the applied models for the mass transfer coefficient varied widely. There was not even agreement about the parameters on which this quantity depends. Some works considered the size and relative velocity of the bubbles in a laminar flow, others the turbulence of the liquid. In the latter case, contradicting assumptions about the size of the relevant turbulent eddies were made, with some works taking the smallest ones, i.e. those of a size corresponding to the Kolmogorov scale, and others the largest ones, having a size of the order of the integral length scale.

Specifically, the penetration model yields an expression

$$k_L = \frac{2}{\pi^{1/2}} \left(D_A \tau_c^{-1} \right)^{1/2} \tag{5}$$

for the liquid side mass transfer coefficient k_L by considering one-dimensional time-dependent diffusion of the transferred component A from the interface with a bulk concentration imposed at infinity, D_A denoting the diffusion coefficient. The mass

flux at the interface is evaluated from Fick's law and averaged over a time-interval up to the so-called contact time τ_c. After this time the surface is supposed to be renewed, i.e. to be brought into contact with liquid at the bulk concentration. Depending on the mechanism by which this renewal occurs, different expressions are used for the contact time. For the laminar mechanism [15]

$$\tau_c^{-1} = \frac{u_{rel}}{d_B} \tag{6}$$

where d_B is the size of the bubble and u_{rel} its velocity relative to the liquid. For the turbulent mechanism based on the largest eddies [16]

$$\tau_c^{-1} \propto \frac{\epsilon}{\kappa} \propto \frac{\kappa^{1/2}}{\Lambda} \propto \frac{\epsilon^{1/3}}{\Lambda^{2/3}} \tag{7}$$

where κ, ϵ, and Λ denote the turbulent kinetic energy, dissipation rate and integral length scale. For the turbulent mechanism based on the smallest eddies [17]

$$\tau_c^{-1} \propto \left(\frac{\epsilon}{\nu}\right)^{1/2} \tag{8}$$

where ϵ is again the turbulent dissipation rate and ν the viscosity of the liquid. For both of the turbulent mechanisms, an unknown prefactor C_c has to be determined by comparison to experimental data.

To facilitate comparison with literature data on the mass transfer from single bubbles in different duct flow configurations, the dependence on the pipe Reynolds number $Re_H = J_L D_H / \nu$, where J_L denotes the liquid superficial velocity and D_H the hydraulic pipe diameter, has to be made explicit for the turbulent models. This is achieved by assuming that the turbulent dissipation rate equals the total power input, the latter being obtained using the Blasius correlation for the friction factor. For the model based on the large eddies, furthermore a correlation for the integral length scale is applied. For details of the derivations we refer to the original work [18] and state here only the final results. For the large eddy model

$$k_L \propto 1.7 \frac{(\nu D_A)^{1/2}}{D_H} Re_H^{0.46} \tag{9}$$

while for the small eddy model

$$k_L \propto 0.71 \frac{(\nu D_A)^{1/2}}{D_H} Re_H^{0.69} \tag{10}$$

For the laminar model the bubble Reynolds number $Re_B = u_{rel} d_B / \nu$ is readily introduced to obtain

$$k_L \propto 1.13 \frac{(\nu D_A)^{1/2}}{d_B} Re_B^{1/2} \tag{11}$$

Suitable data for the comparison are found in the works of Lamont and Scott [17] for horizontal and upward vertical flow in round pipes of two different diameters and Alves et al. [19] for downward flow in a slightly diverging square duct. For the former, the flow rate was varied and the bubble size changed only moderately during the absorption process. For the latter, the flow rate was constant, but the bubble size varied strongly due to the long residence time in the downward flow. A comparison between these two data sets and predictions obtained from the above three models is made in [18], the main results of which are summarized in Fig. 3.

For the data of Lamont and Scott [17] (left) in horizontal pipes the mass transfer coefficient data (symbols) follow a power law with an exponent close to the value obtained for the large eddy model (solid lines) over the entire range of Reynolds numbers. The prefactor in Eq. (7) needed to match the data is determined as $C_c = 0.56$. The exponent predicted by the small eddy model (dashed lines) in contrast is in clear disagreement with the data. Best match with the data is achieved by a prefactor of $C_c = 0.063$ in Eq. (8). For the vertical pipes, a power law behavior is found only at large values of Re_H. At smaller values, crossover to a constant value of k_L is found, which agrees well the prediction of the laminar model without an additional prefactor. This clearly shows the existence of the two mechanisms: In the horizontal pipe, there is no relative velocity due to bubble rise and the laminar mechanism is absent. For the data of Alves et al. [19] (right) the overall trend in the data is well captured by the laminar model, although deviation from a pure power law behavior is obvious. This could be caused by changes in the bubble shape, path, or wake, which are not captured by the simple penetration model. At large values of Re_B, values of
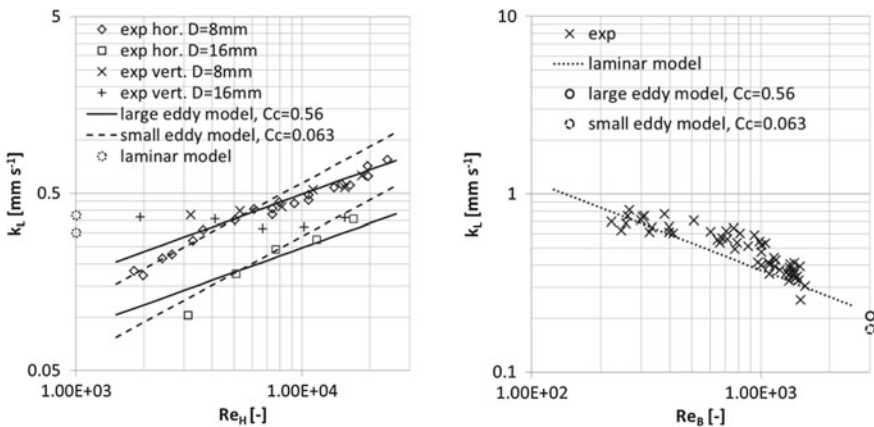

Fig. 3 Comparison of experimental data with predictions of the penetration model using different expressions for the contact time [18]. Left: data of Lamont and Scott [17]. Right: data of Alves et al. [19]

k_L in line with the turbulent models are approached. The deviation between large and small eddy models, each calibrated by its respective parameter C_c, is rather small in this case, which is possibly due to a lower value of the duct Reynolds number for this setup. The transition between both mechanisms appears rather sharp and a unified model comprising both limiting cases is proposed as

$$k_L = \frac{2}{\pi^{1/2}} \left(D_A \cdot \max\left(\frac{u_{rel}}{d_B}, 0.56\frac{\epsilon}{\kappa} \right) \right)^{1/2} \qquad (12)$$

Further work should focus on improving the accuracy of the modeling by including effects of bubble shape, path, and wake, which have been neglected in the laminar type of models and by accounting for the full spectrum of eddy sizes in the turbulent type of models. DNS techniques developed within the SPP1740 will be of great value to this end.

Concerning validation of the applied models for the mass transfer coefficient, previous simulation studies only considered global quantities like the integral $k_L a$-value, because measurements of spatially resolved concentration profiles hardly exist in the literature [14]. The work of Deckwer et al. [20] is identified as one that provides such measurements and other information necessary to set up a simulation. It was concerned with the absorption of CO_2 from air bubbles into water in a bubble column at $T = 14$ °C. Diameter and height of the column were 150 mm and 4400 mm, respectively. Gas was supplied through a circular porous plate of 140 mm diameter, the remaining gap was used to feed liquid for co-current flow. A peculiarity found in that work is that despite a significant mass loss of the bubbles, the measured average bubble size did not appear to change over the column height. This was interpreted as a result of simultaneously occurring coalescence processes.

For the simulations, additional balance equations for the species concentrations, here only CO_2, are needed. In fluid dynamics, mass fractions $Y_\phi^{CO_2}$ are customarily used as variables. Transformation to mole fractions $X_\phi^{CO_2}$ is easily achieved by means of the molar mass, so both may be used interchangeably. The balance equations read

$$\frac{\partial}{\partial t}\left(\alpha_G \rho_G Y_G^{CO_2} \right) + \nabla \cdot \left(\alpha_G \rho_G \boldsymbol{u}_G Y_G^{CO_2} \right) =$$
$$\nabla \cdot \left(\alpha_G \rho_G D_G^{turb} \nabla Y_G^{CO_2} \right) + \Gamma_G^{CO_2} \qquad (13)$$

$$\frac{\partial}{\partial t}\left(\alpha_L \rho_L Y_L^{CO_2} \right) + \nabla \cdot \left(\alpha_L \rho_L \boldsymbol{u}_L Y_L^{CO_2} \right) =$$
$$\nabla \cdot \left(\alpha_L \rho_L D_L^{turb} \nabla Y_L^{CO_2} \right) + \Gamma_L^{CO_2} \qquad (14)$$

Again, two terms require closure models. These are the mass sources due to transport across the phase interface $\Gamma_\phi^{CO_2}$, which due to mass conservation are related as $\Gamma_G^{CO_2} = -\Gamma_L^{CO_2}$, and for absorption $\Gamma_L^{CO_2} > 0$. Considering the resistance to mass transfer only on the liquid side and using Henry's law to relate CO_2 concentrations

in gas and liquid at the interface one gets

$$\Gamma_L^{CO_2} = k_L \rho_L a_I \left(He Y_G^{CO_2} \frac{\rho_G}{\rho_L} - Y_L^{CO_2} \right) \tag{15}$$

where the interfacial area concentration a_I can be obtained assuming spherical bubbles as

$$a_I = \frac{6\alpha_G}{d_B} \tag{16}$$

The Henry constant He is a material property, which leaves the liquid side mass transfer coefficient to be modeled.

The further terms to be modeled are the diffusion coefficients D_ϕ^{turb}. Assuming turbulent transport to dominate, these do not depend on the chemical species. For the continuous liquid phase, the somewhat crude but frequently used approximation of a constant turbulent Schmidt number is made [21], i.e.

$$Sc_L^{turb} = \frac{\mu_L^{turb}}{\rho_L D_L^{turb}} \tag{17}$$

For the dispersed gas phase no diffusive transport occurs between bubbles so $D_G^{turb} = 0$.

On impermeable walls, the boundary conditions $Y_G^{CO_2} = Y_L^{CO_2} = 0$ are imposed.

Due to the mentioned peculiarity found in the experiments, two further simplifications are made in the simulations, namely constant values of the bubble size were imposed according to the measured values and the experimentally determined values of the mass transfer coefficient were applied. Due to these restrictions, only a preliminary validation could be obtained. An example of the results obtained is shown in Fig. 4. For this case, gas and liquid volume fluxes are $J_G = 27.5$ mm/s, $J_L = 47.2$ mm/s, the initial mole fraction of CO_2 in the air bubbles is $X_G^{CO_2} = 0.835$, the bubble size is $d_B = 2.9$ mm, and the mass transfer coefficient has a value of $k_L = 0.21$ mm/s. To obtain the material properties at the unusual temperature of the experiment, correlations were assembled from the literature as described in detail in Ref. [14].

The comparison for the axial profiles of gas fraction (left) and CO_2 mole fraction (right) in Fig. 4 shows quite good agreement between simulation and experiment.

Data which are more suitable for a full model validation have now become available from other projects in the SPP1740 that will enable more definite conclusions about the suitability of correlations for the mass transfer coefficient in the future.
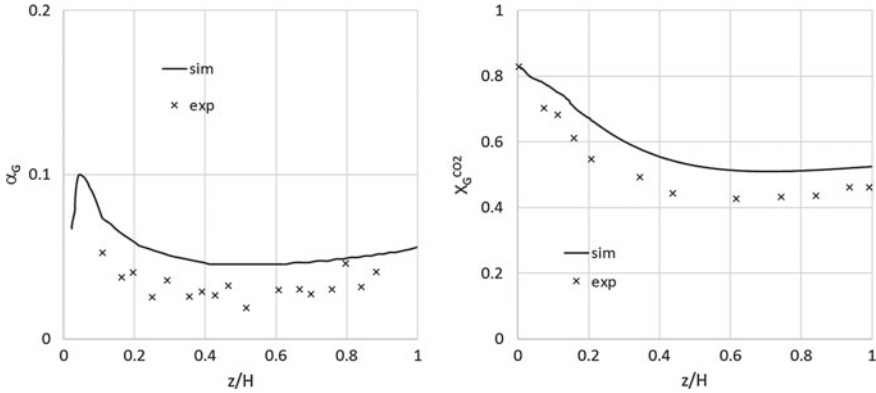
Fig. 4 Axial profiles of gas fraction (left) and CO_2 mole fraction (right) in the setup of Deckwer et al. [20] compared with Euler-Euler simulations [14]

4 Reactive Mass Transfer

A reaction system that has received significant attention in the literature so that the required material properties and reaction rates are known is the absorption of CO_2 into aqueous NaOH solution. The complete reaction network for this system is shown in Fig. 5.

Two reaction pathways exist, a hydroxylation (upper branch) and a hydration (lower branch) reaction [22]. Both lead to the formation of bicarbonate, which then reacts further to carbonate. This latter reaction can be considered as instantaneous and only the equilibrium is relevant. The hydroxylation is fast and practically irreversible, while the hydration occurs at a slower rate and is reversible. The hydroxylation is frequently combined with the bicarbonate-carbonate equilibrium into a single effective reaction. This reaction dominates at pH values larger than 10, while the hydration is dominant for pH < 8. In between, both reactions play a role. All investigations described in this section apply to this reaction system. Expressions used for material properties and reaction rates are detailed in Refs. [23, 24].

Fig. 5 Reaction network for the system of CO_2 in aqueous NaOH solution
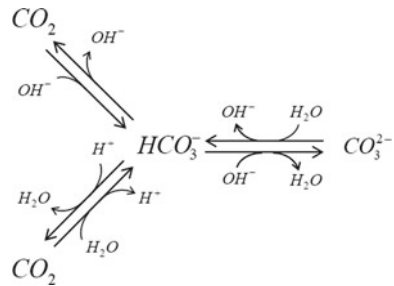
If the mass transfer is accompanied by a fast chemical reaction, the enhancement factor E appears as an additional factor on the right hand side of Eq. (15), which requires a closure model. In general it depends on the entire network of occurring reactions. In view of the intended application, the CO_2/NaOH reaction system, we restrict ourselves to a single irreversible second order reaction corresponding to the hydroxylation branch in Fig. 5. For this case a number of results are available in the literature. An extensive comparison between these is made in Ref. [23]. First it is found that expressions based on the renewal, penetration, and film models show only insignificant numerical deviations, although the obtained formulas look very different. Thus the simplest and most frequently applied expression may be used, which is the one based on the renewal model [25]

$$E = \left(\frac{Ha^4}{4(E_a - 1)^2} + E_a \frac{Ha^2}{(E_a - 1)} + 1 \right)^{1/2} - \frac{Ha^2}{2(E_a - 1)} \qquad (18)$$

Here, Ha is the Hatta number and E_a the enhancement factor for the asymptotic limiting case of an instantaneous reaction. For this latter quantity, an implicit relation that applies to both the penetration and renewal models has been given by Danckwerts [26]. Since this implicit relation is impractical to use in simulations, an approximate explicit expression valid for $E_a \gg 1$ is often substituted, namely

$$E_a = \left(\frac{D_A}{D_B} \right)^{1/2} + \frac{C_{B,\infty}}{\nu_B C_{A,I}} \left(\frac{D_B}{D_A} \right)^{1/2} \qquad (19)$$

where D_A and D_B are the diffusion coefficents, $C_{A,I}$ and $C_{B,\infty}$ the concentrations at the interface and in the bulk liquid, and ν_B the stoichiometric coefficient of the reactants A and B.

A comparison of this approximate explicit expression with the numerical solution of the implicit relation is shown on the left panel of Fig. 6. It is clearly seen that depending on the ratio of the diffusion coefficients the explicit expression Eq. (19) produces large errors at lower values of E_a. A fit formula is developed in Ref. [23], which matches the numerical solution of the implicit relation over a large range of parameters as shown on the right panel of Fig. 6.

Experimental data suitable for an assessment of models for the enhancement factor appeared in the work of Darmana et al. [27] on the absorption of CO_2 into aqueous NaOH solution in a rectangular bubble column of D = 200 mm width and T = 30 mm depth. The column was initially filled up to a level of $H = 1000$ mm with aqueous NaOH at a pH of 12.5. Pure CO_2 gas was supplied at a superficial velocity of $V_G = 0.007$ m/s through 21 needles arranged with a square pitch of 5 mm in the center of the column bottom. The size of the bubbles generated in this way was $d_B = 5.5$ mm and an integral gas fraction of $\alpha_G = 1.2\%$ was obtained. Measurements related to the absorption process were the time-dependent pH-value at a single point located 2 cm below the liquid surface and a time-averaged vertical profile of bubble size,
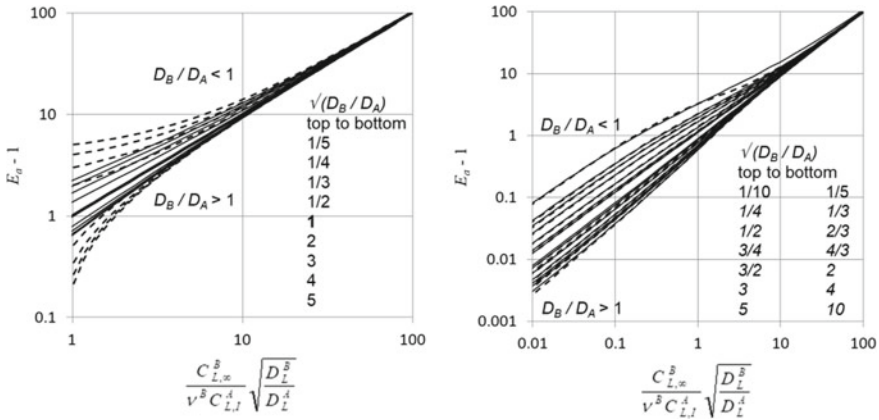
Fig. 6 Expressions for the enhancement factor of an instantaneous irreversible second order reaction. Left: approximate explicit expression Eq. (19) (dashed) versus numerical solution of the implicit relation from Danckwerts [26] (solid). Right: fit formula from Ref. [23] (dashed) versus numerical solution of the implicit relation from Danckwerts [26] (solid)

both in the centre of the column. The average bubble size at the pH measurement point was $d_B = 3.5$ mm.

In addition to the experiment, Darmana et al. [27] also presented simulation results using an Euler–Lagrange method. In these simulations two simplifications were tacitly made: (i) the hydration reaction between dissolved CO_2 and water was neglected and (ii) the approximate expression for the enhancement factor E Eq. (19) was applied.

As a first step of the present investigation, these assumptions are challenged by means of a simple zero-dimensional model valid at the pH measurement point [23]. In this model, the time-dependent equations for the species concentrations in the liquid accounting for all occurring reactions are solved, i.e. Eq. (14) augmented by source terms describing the chemical reactions but without any terms involving spatial gradients. In the source term describing mass transfer from the gas phase the mass transfer coefficient correlation from Brauer [28] is used, which had also been applied by Darmana et al. [27] and the interfacial area is determined using the local values of bubble size and gas fraction. The main results from this investigation are summarized in Fig. 7.

The thick dotted and dashed lines in Fig. 7 show the experimental and simulation results from the work of Darmana et al. [27]. While both are qualitatively similar, quantitative deviations are readily visible. The thin dotted line shows the outcome of a calculation based on the zero-dimensional model making the same two approximations as the simulations from Darmana et al. [27] described above. The good agreement with the Euler–Lagrange simulations shows that the simplified model provides reasonable predictions for the pH value at the measurement point. For the thin dashed line, the approximate expression for the enhancement factor is replaced by the correlation evaluated on the right panel of Fig. 6, which is very accurate over a

Fig. 7 Evolution of pH value in the setup of Darmana et al. [27] based on a simplified zero-dimensional model [23]
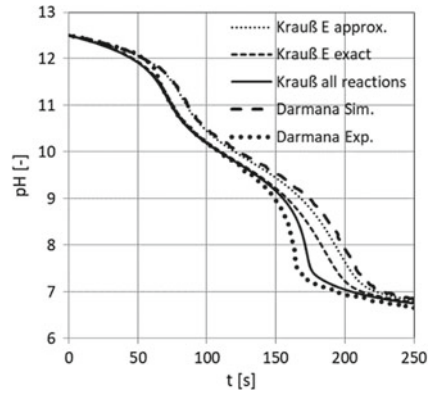
large range of parameters. This is seen to improve the agreement with the measured data up to ~ 150 s, which is consistent with the observation that the maximum value of the enhancement factor is only $E(t = 0s) \approx 1.5$. For the solid line, in addition the hydration reaction between CO_2 and water is taken into account. This results in quite good agreement with the measured data also beyond $t = 150$ s. Since by then the pH is already down to a value of 9, this has to be expected due to the increased importance of the water reaction pathway. Investigation of additional model variants using the zero-dimensional model showed that an effective one-step reaction is valid for the hydroxylation pathway under the present conditions and no enhancement effect results from the hydration reaction. For full details of these investigations we refer to the original work [23].

By combining the thus qualified mass transfer model, which accounts for all occurring reactions and employs an expression for the enhancement factor valid over the entire range of conditions, with the fluid dynamic model validated in the beginning of this chapter, a fully three-dimensional Euler-Euler simulation of the test from Darmana et al. [27] was undertaken in Ref. [24]. The main findings are shown in Fig. 8 with the experimental and simulation results from Darmana et al. [27] again shown as the thick dotted and dashed lines and the previous result using the simplified model as the thin solid line. As may be seen, the Euler-Euler simulation results (thick solid line) quantitatively differ as much from the measurements as the earlier Euler–Lagrange simulations of Darmana et al. [27]. However, the origin of the deviations must obviously be different. Since shortcomings of the mass transfer modelling have been remedied, the most likely source of errors for the present Euler-Euler simulations is the treatment of bubble shrinkage within the MUSIG model. Starting from a sharply peaked shape at the inlet, the distribution broadens rather than simply shifts to smaller values while maintaining its shape. This latter behaviour is quite easy to achieve in Euler–Lagrange simulations, but devising numerical methods to ensure it within the MUSIG method to discretize the population-balance equation remains subject for future work.
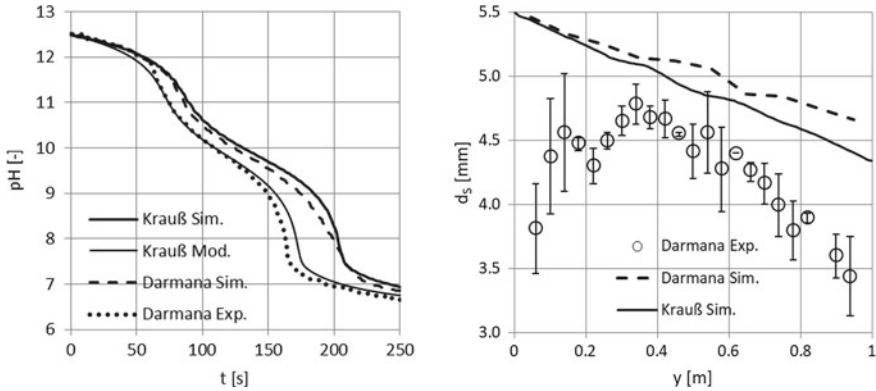
Fig. 8 Evolution of pH value (left) and axial profile of mean bubble size (right) in the setup of Darmana et al. [27] based on a fully three-dimensional Euler-Euler simulation [24]

5 Summary and Further Directions

A first step has been made towards the goal of including mass transfer and reaction phenomena in the Euler-Euler description of bubbly flows. The additionally needed balance equations for chemical species have been set up and source terms for the MUSIG model describing shrinkage or growth of bubbles due to absorption or desorption have been derived. Terms requiring closure models have been identified and initial tests for model candidates have been performed. In particular the absorption of CO_2 in water and aqueous NaOH solutions has been studied.

Major achievements comprise (i) a model for the mass transfer coefficient unifying laminar and turbulent mechanisms; (ii) a broadly applicable model for the enhancement factor of an irreversible second order reaction, (iii) a complete model for material properties and reaction rates in the CO_2/water + NaOH system.

Clearly, further improvements are desirable concerning a more detailed and accurate model for the mass transfer coefficient, enhancement factor models for more complex reaction networks, and a more comprehensive validation of the overall model. By building on results obtained in other projects of the SPP1740 progress in these directions has now come within reach.

References

1. Rzehak R (2017) Euler-Euler modeling of poly-dispersed bubbly flows. In: Yeoh GH (ed) Handbook of multiphase flow science and technology. Springer
2. Rzehak R, Krepper E (2013) CFD modeling of bubble-induced turbulence. Int J Multiph Flow 55:138–155
3. Ma T, Ziegenhein T, Lucas D, Krepper E, Froehlich J (2015) Euler-Euler Large Eddy simulations for dispersed bubbly flows International. J Heat Fluid Flow 56:51–59
4. Rzehak R, Ziegenhein T, Kriebitzsch S, Krepper E, Lucas D (2017) Unified modeling of bubbly flows in pipes, bubble columns, and airlift columns. Chem Eng Sci 157:147–158
5. Tomiyama A, Tamai H, Zun I, Hosokawa S (2002) Transverse migration of single bubbles in simple shear flows. Chem Eng Sci 57:1849–1858
6. Krepper E, Lucas D, Frank T, Prasser H-M, Zwart P (2008) The inhomogeneous MUSIG model for the simulation of polydispersed flows. Nucl Eng Des 238:1690–1702
7. Liao Y, Rzehak R, Lucas D, Krepper E (2015) Baseline closure model for dispersed bubbly flow: bubble-coalescence and breakup. Chem Eng Sci 122:336–349
8. Parekh J, Rzehak R (2018) Euler-Euler multiphase CFD-simulation with full Reynolds stress model and anisotropic bubble-induced turbulence. Int J Multiph Flow 99:231–245
9. Ishii M, Zuber N (1979) Drag coefficient and relative velocity in bubbly, droplet or particulate flows. AIChE J 25:843–855
10. Hosokawa S, Tomiyama A, Misaki S, Hamada T (2002) Lateral migration of single bubbles due to the presence of wall. In: Proceedings of ASME Joint U.S.-European Fluids Engineering Division Conference, FEDSM 2002, Montreal, Canada
11. Burns AD, Frank T, Hamill I, Shi J-M (2004) The Favre averaged drag model for turbulence dispersion in Eulerian multi-phase flows. In: Proc. 5th Int. Conf. on Multiphase Flow, ICMF2004, Yokohama, Japan (2004).
12. Menter FR (2009) Review of the shear-stress transport turbulence model experience from an industrial perspective. Int J Comput Fluid Dyn 23:305–316
13. Rzehak R, Krauß M, Kováts P, Zähringer K (2017) Fluid dynamics in a bubble column: New experiments and simulations. Int J Multiph Flow 89:299–312
14. Rzehak R, Krepper E (2016) Euler-Euler simulation of mass-transfer in bubbly flows. Chem Eng Sci 155:459–568
15. Higbie R (1935) The rate of absorption of a pure gas into a still liquid during short periods of exposure. Trans AIChE 31:36–38
16. Fortescue G, Pearson J (1967) On gas absorption into a turbulent liquid. Chem Eng Sci 22:1163–1176
17. Lamont JC, Scott DS (1970) An Eddy cell model of mass transfer into the surface of a turbulent liquid. AIChE J 16:513–519
18. Rzehak R (2016) Modeling of mass-transfer in bubbly flows encompassing different mechanisms. Chem Eng Sci 151:139–143
19. Alves SS, Vasconcelos JM, Orvalho SP (2006) Mass transfer to clean bubbles at low turbulent energy dissipation. Chem Eng Sci 61:1334–1337
20. Deckwer W-D, Adler I, Zaidi A (1978) A comprehensive study on CO_2-interphase mass transfer in vertical cocurrent and countercurrent gas-liquid flow. Can J Chem Eng 56:43–55
21. Cockx A, Do-Quang Z, Audic J, Line A, Roustan M (2001) Global and local mass transfer coefficients in waste water treatment process by computational fluid dynamics. Chem Eng Process 40:187–194
22. Kern DM (1960) The hydration of carbon dioxide. J Chem Educ 37:14–23
23. Krauß M, Rzehak R (2017) Reactive absorption of CO_2 in NaOH: Detailed study of enhancement-factor models. Chem Eng Sci 166:193–209
24. Krauß M, Rzehak R (2018) Reactive absorption of CO_2 in NaOH: an Euler-Euler simulation study. Chem Eng Sci 181:199–214
25. DeCoursey WJ (1974) Absorption with chemical reaction: development of a new relation for the Danckwerts model. Chem Eng Sci 29:1867–1872

26. Danckwerts PV (1970) Gas-liquid reactions. McGraw-Hill
27. Darmana D, Henket R, Deen N, Kuipers J (2007) Detailed modelling of hydrodynamics, mass transfer and chemical reactions in a bubble column using a discrete bubble model: Chemisorption of CO_2 into NaOH solution, numerical and experimental study. Chem Eng Sci 62:2556–2575
28. Brauer H (1979) Particle/fluid transport processes. Prog Chem Eng 17:61–99

Multi-scale Investigations of Reactive Bubbly Flows

Mark Hlawitschka

Abstract Reactive bubble columns are widely used in chemical, petrochemical, biochemical and metal industries. Besides many other apparatuses applied in the process industry, bubble columns are governed by a complex, non stage-wise flow structure and concentration distribution, that limits the application of simplified models. Recent research indicated a good agreement when coupling computational fluid dynamics (CFD) simulations with mass transfer models. However, there still exists a gap between detailed modelling, including interface tracking algorithms, and model based approaches such as Euler-Euler based population balance models (PBM) and Euler–Lagrange simulations. On the one hand, this gap can be closed by enhanced multi-scale analysis. On the other hand, the numerical models were until now not able to describe the existing uncertainties such as the bubble shape variations, rise, interactions and mass transfer without experimental investigations. Therefore, an experimental and computational multi-scale closure of the layout process is presented to reduce these uncertainties based on the system $Fe^{II}(edta)/NO$.

1 Introduction to the Design of Reactive Bubbly Flows

Reactive bubble columns are widely used in the chemical, petrochemical, biochemical and metallurgical industries [1–3]. The bubble columns are used for the oxidation, chlorination, alkylation, polymerization and hydrogenation [4, 5] and the column involves a liquid and a gaseous phase, often also applied with a catalyst phase that are brought into contact. For high interface areas and efficient contact between gas, liquid and solid phases, the gas is dispersed as bubbles. Despite their widespread technical application, the interaction between product quality, yield, hydrodynamics and mass transfer mechanism and chemical reactions is unsatisfactory described so far. For example, an overview of high-pressure bubble columns [6] showed that the gas phase hold-up is highly dependent on the operating conditions such as pressure,

M. Hlawitschka (✉)

Institute of Process Engineering, Johannes-Kepler Universität Linz, Altenbergerstraße 69, 4040 Linz, Austria

e-mail: mark.hlawitschka@jku.at

temperature, superficial gas velocity, dispersion as well as the used system properties. The influence of the column geometry is reduced from diameters of $D = 0.7\,m$ as well as height-to diameter ratios of 5.

Despite an evaluation from Leonard et al. [6] of 122 literatures, no independent (empirical) correlation could be found to describe the hydrodynamics. One of the reasons behind the huge deviations is the relatively simple construction and the wide variety of applications from slow to instantaneous reaction, resulting in a multitude of different designs. The advantages of bubble columns are the absence of moving parts, minimal maintenance, small footprint, good heat transfer and mixing characteristics, handling of solids (e.g. catalysts), high pressures and temperatures, low costs and high throughputs. Besides the advantages, the high number of influencing factors, such as backmixing, coalescence and breakage, affecting efficiency, yield and selectivity are tough to grasp.

However, the layout of these columns is commonly based on simplified integral models that are not able to track the complex interactions between the local hydrodynamics and the mass transfer/reactions and the system properties, implicating that a layout based on zero- or one-dimensional models is restricted to a limiting number of well-defined applications. Factors affecting gas–liquid mass transfer rates and making a universal correlation impossible are reported by Sideman et al. [7]:

- physical properties of gas and liquid
- type of distributor, orifice diameter, spacing and position
- dimensions of column or tank, baffles (number, position, size)
- type of mechanical agitator, size and relative dimensions
- velocity of rotating impeller and energy input
- gas flow rate
- continuous phase flow rate in counter current flow system
- presence of chemical reaction, concentration of electrolytes
- position of downcomers in multiplate counter current systems
- presence of solid catalyst
- bubble size
- gas hold-up
- bubble velocity or relative slip velocity
- actual power input

However, these phenomena can be studied by experimental and numerical investigations on the respective scale and the gain in knowledge can be transferred to a successful layout of an industrial scale bubble column.

2   The Multi-scale Appraoch

An optimum layout of bubble columns requires a reasonable description of the phenomena on different scales (Fig. 1).

At the beginning of SPP 1740, new reactive systems gave new challenges to the process design and analytics. The focus was set in this work on the Fe^{II}(ligand)/NO system. In addition, barely no data was available in literature and this brought up new questions that had to be answered:

- How can we handle the system in the lab and the pilot plant scale?
- How can we measure the concentration profiles without intrusive measurement techniques?
- How can we estimate adequate data e.g. for diffusion coefficients, enhancement factor, etc. in the respective liquids?
- What are the parameters required for a predictive CFD bubble column simulation?

For the smallest scale, a mini bubble column was constructed with a volume of approximately $V = 500$ mL which allowed principal investigations using a small amount of chemicals. The cell cross section was constructed rectangular for optical analyses with its dimensions of $90 \times 55 \times 115$ mm, similar to the one used for liquid–liquid systems [8]. The cell was sealed additionally by a top plate, which enabled to work under inert conditions.

At the bottom of the cell, a single needle is positioned that is connected via a magnetic valve to the NO gas bottle. At the top, an additional needle could be positioned to investigate the bubble/bubble repulsion influence to reactive mass transfer. In addition, an inlet for inert gas is given. Together with the TU Munich, first results could be obtained about the safe handling of the system. It could be shown that the system shows a light absorption peak at $\lambda = 450$ nm due to the reaction that can

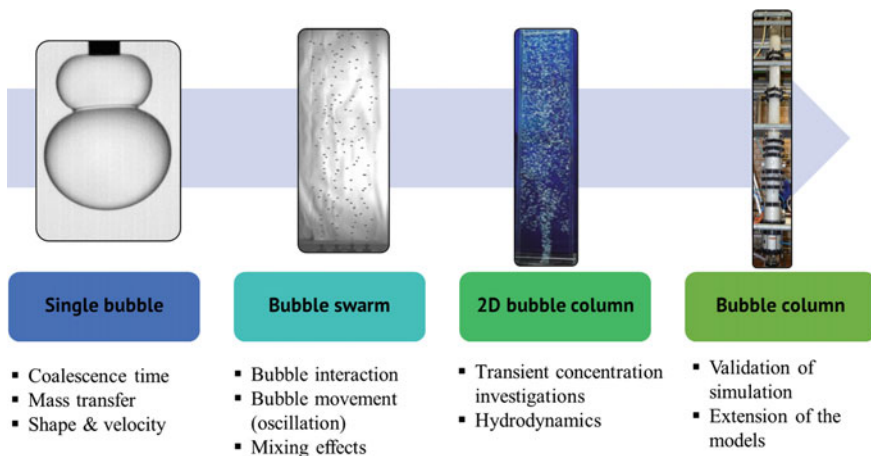| Single bubble	Bubble swarm	2D bubble column	Bubble column
▪ Coalescence time ▪ Mass transfer ▪ Shape & velocity	▪ Bubble interaction ▪ Bubble movement (oscillation) ▪ Mixing effects	▪ Transient concentration investigations ▪ Hydrodynamics	▪ Validation of simulation ▪ Extension of the models

Fig. 1 Experimental and numerical multi-scale approach
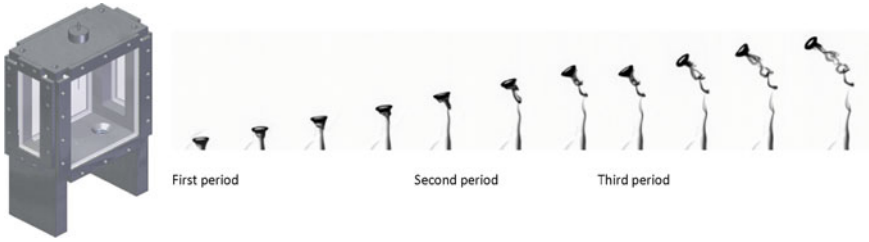
Fig. 2 Bubble interaction cell (left) and bubble rise with reaction (right)

be used for concentration analyses e.g. by high speed cameras (Fig. 2). The wake structure and integral concentrations could be determined by the application of two high speed cameras. The quantity of the concentrations in the wake as well as the wake structure can be significantly enhanced by more cameras. The interaction of two colliding bubbles revealed that the mass transfer is enhanced after the contact of the bubbles.

Furthermore, the smallest scale of the here presented multi-scale approach enabled investigations of the single bubbles, such as coalescence times, for the NO system and the influence of different ions to the coalescence time. The coalescence time itself was also identified as a reasonable parameter for the detection of impurities in the system, affecting the hydrodynamics of the bubbles. It could be shown that some ions influence the repulsion behaviour and others show a small effect on the repulsion. The coalescence time in reversed osmosis water was found to be $t = 75$ ms (Fig. 3). The addition of e.g. NaCl leads to an increased coalescence time. At

Fig. 3 Cumulative distribution of the coalescence time at different NaCl concentrations

Fig. 4 Schematic of the two-dimensional bubble column setup

a concentration of $c = 0.2$ M NaCl, the coalescence time of the bubble is above one second. In technical applications, where 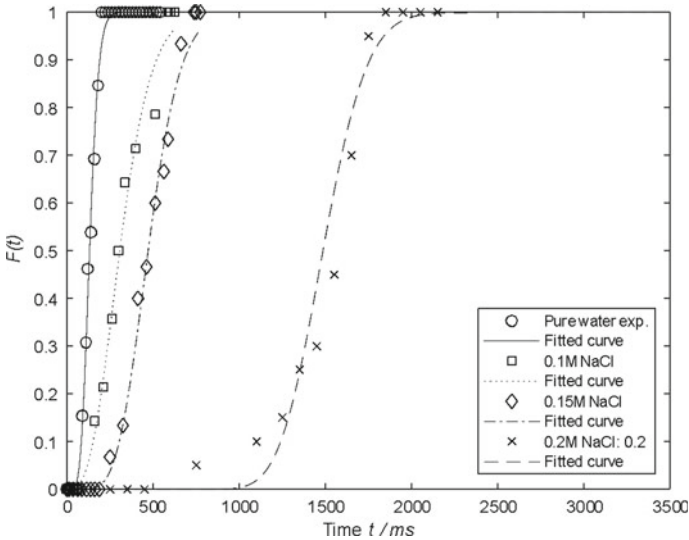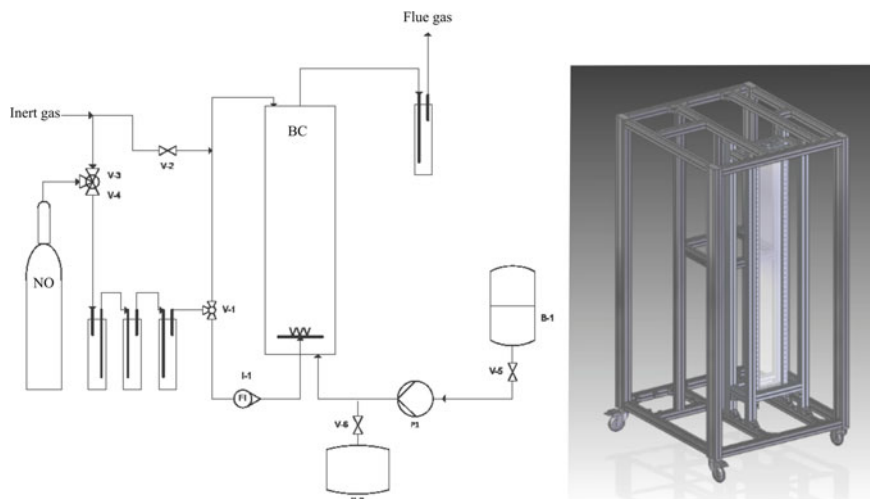bubbles rise side by side with short contact times, the system is described as a coalescence inhibited system. A first database was developed for alcohols and electrolytes and will be extended in the next few years. This will enable the engineer to identify the coalescence behaviour of the applied system and therefore gives a direct identification about the flow regime.

On the next scale, bubble swarm investigations, e.g. in pseudo two dimensional columns, were frequently applied to study the hydrodynamic behaviour of reactive systems. We developed a pseudo two-dimensional column made of stainless steel that enabled further investigations with liquids other than water (Fig. 4). The column was used to investigate the transient reaction of Fe^{II}(edta)/NO at different flow rates and initial concentrations. The height of the bubble column is $H = 1500$ mm, the width $b = 200$ mm and the depth is $s = 40$ mm. The bubble column inlet is a 21 needle disperser which can be easily replaced by another inlet structure. The needles have a spacing of $t = 9$ mm to each other. The needle tip ends are $x = 5$ mm above the inlet plate. The diameter of the needle is $d_n = 1$ mm with a wall thickness of $s = 0.25$ mm. The gas flow rate is measured by a Rotameter (*Rota L63/2400–13430*).

For the experiments, only six needles were used: three to the left and three to the right from the middle position. The needles were connected to the NO gas bottle. In between, three washing bottles with sodium hydroxide were installed to remove impurities. At the outlet, a bottle filled with amidosulfuric acid is applied to remove possible NO in the outlet stream. In addition, nitrogen is used as purge gas as well as to degas the column for at least 2 h. Behind the column, an LED panel (Lead LED Panel *Dynamic PDW120W*) is used to illuminate the bubble column. In front of the column, a high speed camera (*Imaging Solutions, OS8*) enables a tracking of the bubble movement as well as a detection of the concentration change by light

absorption. For the investigation of concentration change, the column was operated at five different concentrations of $Fe^{II}(edta)$ solutions. The column was operated at a superficial gas velocity of $v_G = 6.2$ mm/s. The sequence of concentration change is shown in (Fig. 5) and the corresponding bubble size distribution is depicted in (Fig. 6).

Further data was exchanged with AG Zähringer from University of Magdeburg regarding reaction and bubble hydrodynamics [9, 10]. These could be used to extend the applied CFD models.

The investigations of the flow behavior in cylindrical bubble columns represent the pilot scale. The circular structure corresponds to the industrial bubble column scale. Bubble sizes and hold-up can be determined and compared to analytical solutions. Furthermore, accumulation and non-ideal and long term effects such as foaming at the column top can be studied. Modern techniques, such as pressure sensors combined with data analytical approaches enable a description of the different flow regimes inside the mostly non-transparent columns and build the basis for the digitization of bubble columns together with optical bubble size detection.

The pilot plant scale enables in addition a validation or extension of the numerical tools, e.g. Euler-Euler and Euler–Lagrange approaches, but also to identify transition regimes e.g. by pressure sensors. The experimental approach was accompanied and further replaced by Computational Fluid Dynamics (CFD). The CFD helped to identify single phenomena, such as mass transfer and enhancement, but also enabled studies at different operational conditions. The extension and investigations using CFD will be explained in the following section.
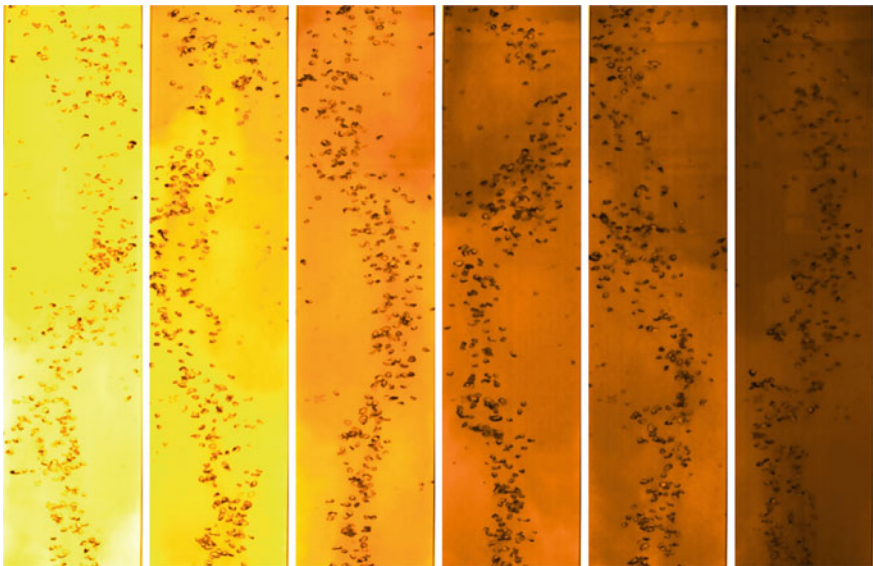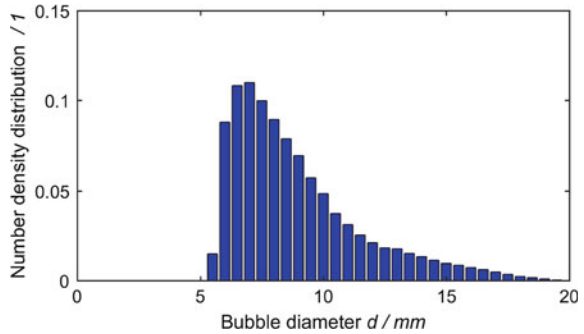

Fig. 5 Sequence of the reaction at a gas superficial velocity of $v_G = 6.2$ mm/s

Fig. 6 Measured bubble size distribution at a gas superficial velocity of $v_G = 6.2$ mm/s

3   Simulation Methods

A recent review of the methods for bubbly flow simulations is presented in Mühlbauer et al. [11]. The introduction of meshless methods, such as the finite pointset methods are beneficial compared to other methods, when it comes to the description of complex deformations. The shape of the bubble is directly given by a defined set of moving particles carrying the information for velocity, density, viscosity, surface tension, etc. The finite pointset method was applied to study the bubble rise and deformation as well as the breakage of bubbles [12] (Fig. 7). Compared to VoF simulations, FPM enables a direct investigation of bubble repulsion there the interphase is directly tracked (Fig. 8).

However, the computational time required for simulation exceeds a reasonable time for further mass transfer investigation focusing on an industrial layout procedure. Therefore, a two-dimensional reactive mass transfer model was developed accounting for variations in fluid flow velocity and reactive mass transfer studies, such as variations in reaction rate and diffusion coefficient. The single bubble investigations by simplified models, such as the developed two-dimensional simulations, help to reveal unidentified parameters for an engineering purpose. The code is developed in Matlab and allows to study concentration profiles, mass transfer coefficients and enhancement factors within minutes (Fig. 9).

The results of the simulations can be used in addition to literature data as an input for bubble column simulations, such as Euler–Lagrange and Euler-Euler simulations. In the first period of SPP 1740, a Euler-Euler multiphase solver was extended to enable investigations of reactive mass transfer in bubble columns by enabling a coupling of the complex hydrodynamics, bubble size and shape and reactive mass transfer.

Experiment : $t = 0.19s$ Simulation : $t = 0.19s$

Experiment : $t = 0.21s$ Simulation : $t = 0.21s$

Experiment : $t = 0.23s$ Simulation : $t = 0.23s$
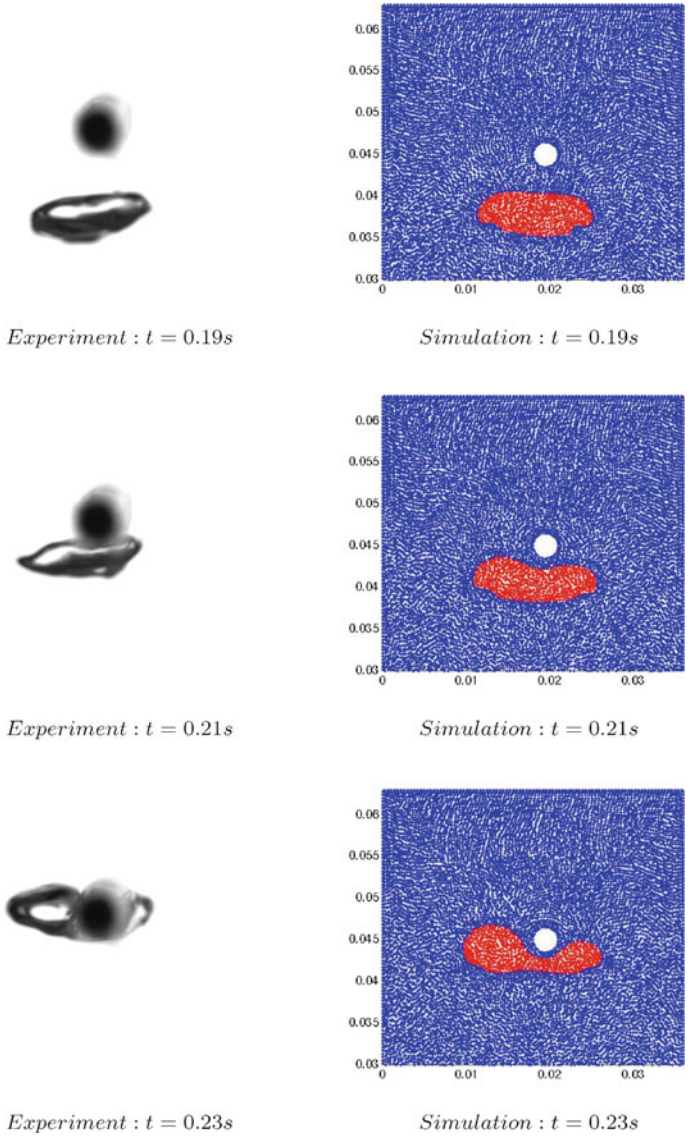
Fig. 7 Bubble breakage at a tube [12]

The solver is based on the multi-fluid model "multiphaseEulerFoam" which is part of the *OpenFOAM®* toolbox (www.openfoam.org, version 2.3.1). The Euler-Euler based approach treats the phases as interpenetrating continua. The hydrodynamics of the continuous and the dispersed phases are represented by the volume-averaged Navier–Stokes momentum equations. The continuity equation, representing the conservation of volume of the liquid phase *l* is given by:
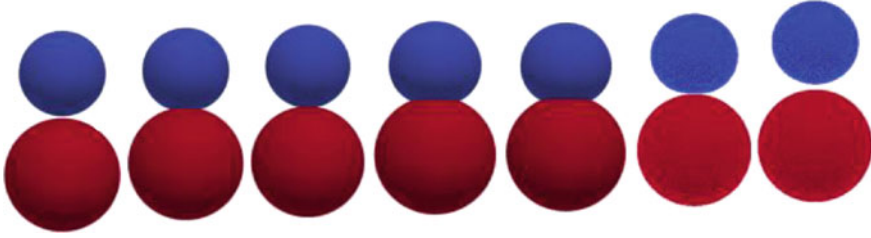
Fig. 8 Bubble repulsion simulation
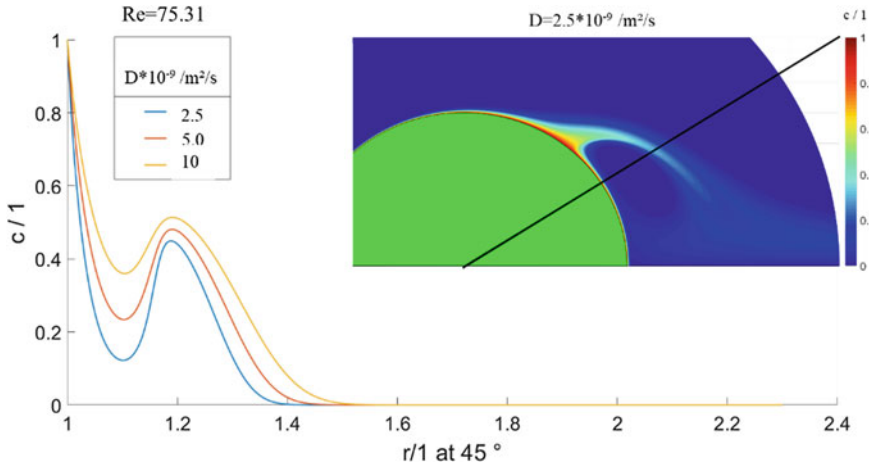
Fig. 9 Concentration profile around a bubble and the influence of different diffusion coefficients to the local concentration profile

$$\frac{\partial \alpha_l}{\partial t} + \vec{u}_l \cdot \nabla \alpha_l + \nabla \cdot \left(\alpha_l \vec{u}_{comp}(1 - \alpha_l)\right) = \frac{1}{\rho_l} \sum_{p=1}^{n} \left(\dot{m}_{gl} - \dot{m}_{lg}\right) + \alpha_l S_l \qquad (1)$$

S_l defines the source term applied to the liquid phase and α_l is the liquid holdup. The first term on the left hand side handles the accumulation, the second term the convection and the third term a possible interface sharpening. The interface compression velocity is given by Wardle and Weller [13]:

$$\vec{u}_{comp} = C_\alpha |\vec{u}| \frac{\nabla \alpha}{|\nabla \alpha|} \qquad (2)$$

where

$$C_\alpha = \begin{cases} 0, & no\ interface\ sharpening \\ 1, & interface\ sharpening\ active \end{cases} \qquad (3)$$

In addition, the momentum equation has to be solved for each phase and is described here for the liquid phase:

$$\frac{\partial}{\partial t}(\alpha_l \rho_l \vec{u}_l) + \nabla \cdot (\alpha_l \rho_l \vec{u}_l \vec{u}_l) = -\alpha_l \nabla p + \nabla \cdot (\mu_l \alpha_l \nabla \vec{u}_l)$$

$$+ \alpha_l \rho_l \vec{g} + \vec{F}_{D,l} + \vec{F}_{Lift,l} + \vec{F}_{VM,l} + \sum_{p=1}^{n} (\dot{m}_{gl} \vec{u}_{gl} - \dot{m}_{lg} \vec{u}_{lg}) \tag{4}$$

The velocity $\vec{u}_l$ represents the velocity of the continuous (liquid) phase and $\dot{m}_{gl}$ describes the mass transfer from the liquid phase l to the dispersed (gaseous) phase g and $\dot{m}_{lg}$ is the mass transfer vice versa. The viscosity of the liquid phase is given by μ_l, the gravitational vector is named $\vec{g}$. The interaction between the continuous and dispersed phases are given by a set of forces ($\vec{F}_{D,l}$, $\vec{F}_{Lift,l}$ and $\vec{F}_{VM,l}$) as is the drag force, lift force and virtual mass force.

The drag force $\vec{F}_{D,l}$ is given by

$$\vec{F}_{D,l} = \frac{3}{4} \rho_l \alpha_l \alpha_g C_D \frac{|\vec{u}_g - \vec{u}_l|(\vec{u}_g - \vec{u}_l)}{d} = \alpha_l \alpha_g K (\vec{u}_g - \vec{u}_l), \tag{5}$$

where

$$K = \frac{3}{4} \rho_l C_D \frac{|\vec{u}_g - \vec{u}_l|}{d}. \tag{6}$$

The dispersed phase fraction is given by α_g and the corresponding velocity is described by $\vec{u}_g$. The drag coefficient may depend on the purity of the used liquid and gas. For the validation of these, a simple bubble rise experiment, such as the bubble rise in a mini plant bubble column helps to reduce possible uncertainties.

In general, the drag coefficient C_D can be described by a various number of correlations. Among them are are models from Ishii and Zuber [14]

$$C_D = \frac{2}{3} \sqrt{Eo}, \tag{7}$$

and Tomiyama et al. [15]

$$C_D = max \left(min \left(\frac{16}{Re}(1 + 0.15 Re^{0.687}), \frac{48}{Re} \right), \frac{8}{3} \frac{Eo}{Eo + 4} \right) \tag{8}$$

where the Eötvös number Eo is defined by the bubble characteristic length as follows:

$$Eo = \frac{g(\rho_l - \rho_g)d_h^2}{\sigma} \tag{9}$$

The model of Tomiyama et al. [16] is applicable at conditions of low phase fraction and deformable bubble shape.

$$
\begin{aligned}
C_D = 8/3 \cdot & \left(\frac{Eo}{E_{sh}^{2/3} \cdot \left(1 - E_{sh}^2\right) + 16.0 \cdot E_{sh}^{4/3}} \right) \\
& \cdot \left(\frac{1 - E_{sh}^2}{(1 - E_{sh}^2)^{1/2} - E_{sh} \cdot \left(1 - E_{sh}^2\right)^{1/2}} \right)^2
\end{aligned}
\tag{10}
$$

The shape factor, or aspect ratio, E_{sh} as the relation between shortest to longest ellipsoidal bubble diameter can be derived by as correlations by Moore [17], Wellek et al. [18] for contaminated systems, Clift el al. [19], Okawa et al. [20], Sanada et al. [21], Legendre et al. [22]. Due to the uncertainties arising from surfactants and their determination, the aspect ratio has to be determined by experiments (Fig. 10).

The virtual mass force $\vec{F}_{VM,l}$ includes the virtual mass effect occurring when a phase accelerates relative to another phase:

$$
\vec{F}_{VM,l} = C_{VM} \rho_l \alpha_g \alpha_l \left(\frac{d_l \vec{u}_l}{dt} - \frac{d_g \vec{u}_g}{dt} \right)
\tag{11}
$$

The lift force $\vec{F}_{Lift,l}$ is a shear-induced force on the fluid particle. It is the most important force besides the drag force, since it acts lateral to it. Hence, it may have an impact on the shape of the radial profiles:

$$
\vec{F}_{Lift,l} = C_L \rho_l \alpha_g \left(\vec{u}_l - \vec{u}_g \right) \times rot \ \vec{u}_l
\tag{12}
$$

The coefficient C_L is taken from analytical, numerical or experimental approaches. Since 1980, a huge variety of models have been developed. Here, the model of Tomiyama et al. [23] is presented:
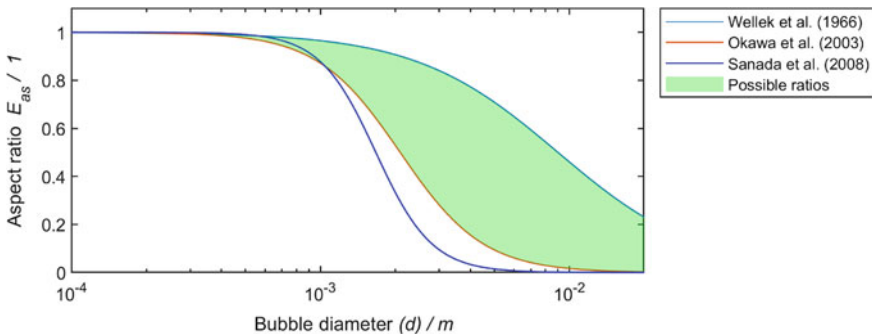

Fig. 10 Comparison of different aspect ratio models

$$C_L = \begin{cases} \{\min[(0.288 \tanh{(0.121\,\mathrm{Re})},\ f(Eo)] & for\ Eo < 4 \\ f(Eo) & for\ 4 \leq Eo \leq 10.7 \end{cases} \tag{13}$$

with

$$f(Eo) = 0.00105 Eo^3 - 0.0159 Eo^2 - 0.0204 Eo^3 + 0.474 \tag{14}$$

The preferred turbulence modelling is based on the large eddy approach with a simulation of large-scale turbulence structures and a fine-tuned modelling of the smaller scales there it gives a good prediction of e.g. bubble plume oscillation time and hold-up for a wide variety of conditions. In this work the latter is by the Smagorinsky model [24], where the turbulent viscosity is given by:

$$\mu_{sgs} = C_s^2 \Delta^2 \left(2 \hat{S}_{mn} \hat{S}_{mn}\right)^{0.5} \tag{15}$$

where Δ represents the grid size and $\hat{S}_{mn}$ is the rate-of-strain tensor. In the used OpenFOAM version, Smagorinsky constant C_s is defined as follows:

$$C_s^2 = C_k \sqrt{\frac{2C_k}{C_e}} \tag{16}$$

The turbulence model constants are given by $C_k = 0.03742$ and $C_e = 1.048$. In addition, bubble induced turbulence is accounted for the turbulent viscosity by Sato and Sekoguchi [25]:

$$\mu_{sgs,BIT} = C_{BIT} \alpha_g d |u_l - u_g| \tag{17}$$

The parameter C_{BIT} is set to 0.6 [26, 27]. The effect of the turbulent fluctuations of liquid velocity on the bubbles is described by the turbulent dispersion force [28]:

$$\vec{F}_{disp} = -\frac{3}{4} \frac{\alpha_g}{d} \rho_l C_D \frac{|\vec{u}_g - \vec{u}_l|}{d} \frac{\mu_l^{turb}}{\sigma_{TD}} \left(\frac{1}{\alpha_g} + \frac{1}{\alpha_l}\right) grad\alpha_g \tag{18}$$

where σ_{TD} is referred to as turbulent Schmidt number, given as a value of 0.9 [27].

Further details on the selection of adequate models are presented in [29].

4   Absorption Modelling

Gas absorption involves mass transfer from the gas phase to the liquid phase (water). Gas molecules must diffuse from the inner part of the bubble to the gas–liquid interface, cross the interface into the liquid side and finally diffuse from the interface

to the main (homogeneous) part of the liquid. The mass transfer across the interface is accounted for by the film theory

$$\dot{m}^j = k^j a \rho_l \left(Y_l^* - Y_l^j \right) \tag{19}$$

The specific interfacial area is given by a. The concentrations in the liquid (bulk) and at the interface are given by Y_l^j and Y_l^* respectively. The mass transfer coefficient k^j for each chemical species j is calculated based on the Sherwood Sh^j number and the diffusion coefficient D^j.

$$k^j = \frac{Sh^j D^j}{d} \tag{20}$$

Therefore, we use a Sherwood correlation for gas bubbles [30]:

$$Sh^j = 2 + 0.6415 \sqrt{Re^j Sc^j}, \tag{21}$$

which is in good agreement to the measurements of Nock et al. [31]. The concentration at the interface is derived by the Henry constant H for species j.

$$H^j = \frac{c_l^{j*}}{c_g^j} = \frac{Y_l^{j*}}{Y_g^j} \frac{\rho_l}{\rho_g} \tag{22}$$

This finally results in the following mass transfer across the interface:

$$\dot{m}^j = \frac{A_{bubble}}{V_{bubble} d} E \alpha_g D^j Sh^j \rho_l \left(H^j \frac{\rho_g}{\rho_l} - Y_l^j \right) \tag{23}$$

5 Reaction

The measurements for validation are based on the pH-value. Therefore, we have to solve additionally the reactions in the liquid phase. The solver allows solving any number of reactions in the liquid phase. The general stoichiometry equation for a reversible reaction for J species taking part in a reaction is given by:

$$\sum_{j=1}^{J} \beta_m^{j'} X^j \rightleftharpoons \sum_{j=1}^{J} \beta_m^{j''} X^j \tag{24}$$
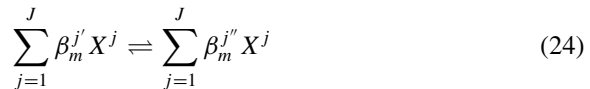
$\beta_m^{j'}$ and $\beta_m^{j''}$ are the stoichiometric coefficients of the reaction m for the educt side (left) and product side (right). X^j represents the summation formula of species j.

For a chemical system with M reactions the production rate $\dot{S}^j$ of a species j is described by:

$$\dot{S}^j = \sum_{m=1}^{M}\left(\beta_m^{j''} - \beta_m^{j'}\right)\omega_m \tag{25}$$

We use the production rates $\dot{S}^j$ as source terms in the species transport equation. The reaction velocity ω_m of the m-th reaction depends on the rate coefficients k_m' and k_m'' for the forward chemical reaction and the backward chemical reaction. Furthermore it depends on the concentrations c^j of the participating species j.

$$\omega_m = k_m' \prod_{j=1}^{J}\left(c^j\right)^{\beta_m j'} - k_m'' \prod_{j=1}^{J}\left(c^j\right)^{\beta_m^{j''}} \tag{26}$$

The concentration c^j of the species j is derived from the mass fractions Y^j, the density ρ_l and the molar mass W^j.

$$c^j = Y^j \frac{\rho_l}{W^j} \tag{27}$$

The temperature dependence of the rate coefficient k_m' is described by the Arrhenius equation for the forward reaction:

$$k_m' = A_m e^{-\frac{T_A}{T}}, \tag{28}$$

where A_m is the pre-exponential factor. The activation temperature T_A can be interpreted as thermal energy required to start the reaction. The rate constant k_m'' of the backward reaction is derived from the equilibrium constant $K_{Eq,m}$:

$$K_{Eq,m} = \frac{k_m'}{k_m''} \tag{29}$$

Besides the existing models in OpenFOAM 2.3.1, an additional model for the rate constant k_m' was implemented to account for the literature data:

$$k_m' = A_m e^{\left(B_m \ln \ln T + \frac{C_m}{T} + D_m + E_m T\right)} \tag{30}$$

where A_m, B_m, C_m, D_m and E_m are reaction specific constants.

For a first validation of the mass transfer, a case study of Cachaza et al. [32] was used. This study considers only a global mass transfer coefficient, which does not allow a universal use. Nevertheless, our own results were in good agreement to literature data and own experimental measurements (Fig. 11). A comparison to a reactive

Fig. 11 Numerical investigation of the O_2 absorption in degassed water
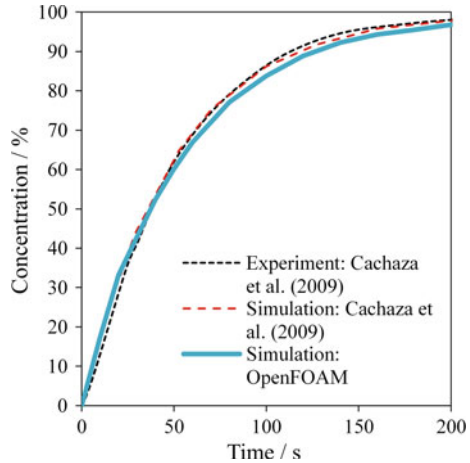
bubble column was successfully achieved in collaboration with AG Zähringer from University of Magdeburg [10].

Concerning the heterogenous bubble regime, optimized results were found using the Euler-Euler multiphase approach by a continuous improvement of the numerical techniques, e.g. by considering the bubble size distribution by the sectional quadrature method of moments [33]. The application of the multi-scale approach for the Fe^{II}(edta)/NO system [29] required further investigation of the system. Based on the single bubble experiments, repulsion was dominant. The mass transfer coefficient and enhancement factor were obtained by the work of Merker et al. [34]. Similar results could also be obtained by the described two-dimensional bubble modelling framework [29]. The diffusion coefficients were taken from Fuller et al. [35] for the gas phase and Wilke and Chang [36] for the liquid phase. For the NO/water system, a gas diffusion of $D = 2.0E^{-5}$ m^2/s could be determined and for the liquid phase, a diffusion coefficient of $D = 2.23E^{-9}$ m^2/s was found. For the NO/methanol system, the liquid phase diffusion coefficient is $D = 2.14E^{-9}$ m^2/s. Based on the multi-scale investigation (detection of bubble size at the inlet, determination of mass transfer from single bubble experiments and modelling), a successful simulation (Fig. 12) of the pseudo two dimensional bubble column was possible and indicates, that CFD in combination with the developed models may be a promising tool for reactive bubble column layout in the near future.

While Euler-Euler simulations are beneficial at higher gas fractions, Euler–Lagrange simulations track the particle position and diameter of each bubble. The bubble diameter is directly influenced by pressure differences as well as mass transfer. The mass transfer into the liquid as well as mass transfer from the liquid to the bubble is accounted for. The bubble behaviour at higher gas fraction is governed by the turbulence in the liquid. However, a single bubble or at low gas hold up, bubbles start to tumble at a certain size and velocity. A recent extension of the Euler–Lagrange framework enabled a study of different viscosities and surfactant concentrations to

Fig. 12 Product concentration over time for the Fe^{II}(edta)/NO system in the rectangular bubble column
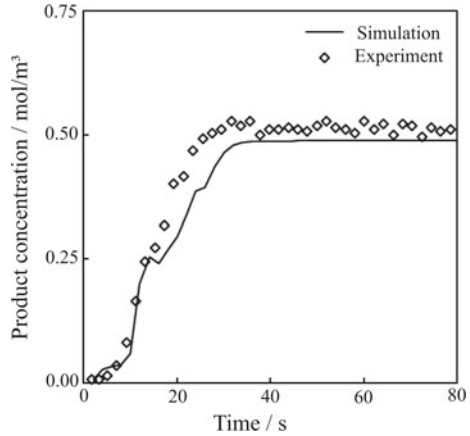
the bubble motion and reaction development. The extensions and a comparison to experimental results are presented in Hlawitschka et al. [36]. From this study, the following conclusions could be drawn:

- Bubble oscillation modelling is required at low hold-up
- Bubble motion transition point inside the column changes with viscosity and surfactant concentration
- An increased viscosity leads to a longer straight path of the bubbles and to a delayed concentration change

A current study on bubble coalescence and breakage using the bubble oscillation revealed a distinct influence and the need to account for bubble oscillatory motion in combination with the Euler–Lagrange approach, especially at lower bubble concentrations.

6 Visualization Techniques

In Euler-Euler data sets, the bubbles are represented by the total gaseous phase fraction in a numerical cell and the diameter in each cell. A direct comparison to experimental data is hardly given. To overcome this disadvantage, Tomiyama et al. in [37] showed a principle visualization of bubbles and compared them to experimental data. The approach assumes spherical, equivalent sized bubbles and combines the phase fraction and the bubble diameter in a single figure. The limitation of spherical, equi-sized bubbles can be overcome by a stochastic sampling visualization (Fig. 13). A more detailed description of this approach is given in Hlawitschka et al. [38]. The total bubble volume is conserved and the bubble shape is reconstructed. Further techniques, such as the Lambda2 vortex criterion enables an objective identification and localization of vortex structures from a three-dimensional velocity field [39]. In
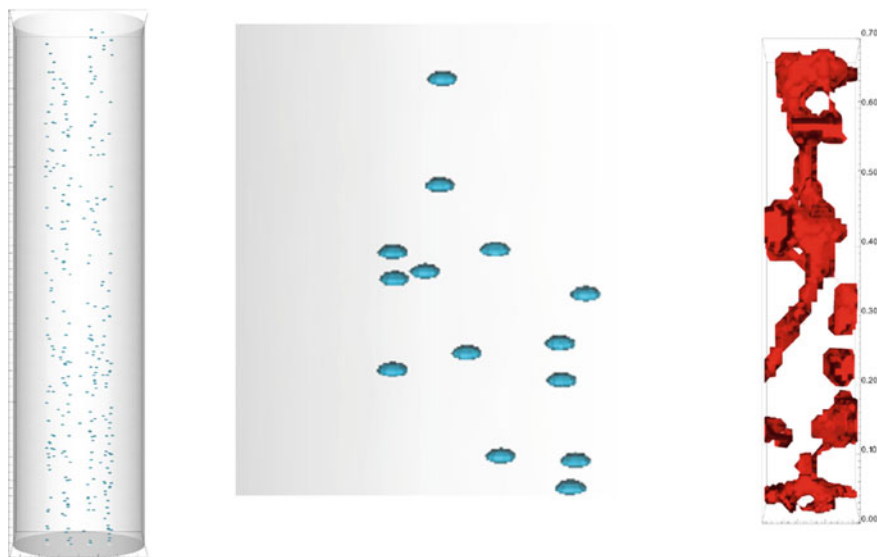
Fig. 13 Stochastic visualization of bubble position, size and shape (left), middle detailed view (middle), visualization of the Lambda2 vortex criterion (right)

bubble columns, it enables a description of mixing efficiency of the continuous phase and together with comparing visualization, an evaluation of different fluid properties to the column layout.

7 Conclusion

The developed multi-scale approach allows an interlinking step-by-step investigation of reactive bubble columns starting from single bubble investigations, over swarm investigations up to a pilot-scale bubble column. In each scale, relevant characteristics such as bubble rise, coalescence, repulsion, swarm behavior and mass transfer coefficients can be identified and used for a better prediction of a numerical layout procedure based on one, two and three dimensional CFD methods. The aim of the project, by obtaining a deeper insight into the complex coupling between hydrodynamics and mass transfer could be achieved by model extensions, e.g. reaction scheme, bubble motion, as well as by the development of advanced visualization techniques.

From an experimental point of view, many publications focused on the CO_2/NaOH(aq) system, where the reaction kinetics as well as the basic models are given in literature. A first investigation of the Fe^{II}(edta)/NO system in the presented single bubble cell enabled further investigation of the system in other projects. In

addition, the cell enabled an investigation of coalescence at the interface and therefore provides an adequate indication of e.g. the effect of alcohols (as surface active agent) and this indication about the coalescence time can be used for bubble column layout accounting for the correct bubble size distribution and (reactive) mass transfer. For industrial applications, high pressure tanks equipped with inspection glasses are commercially available and could build a reference setup for the future application. A further reduction of the liquid e.g. to $V = 250$ mL is possible.

The newly developed pseudo two-dimensional bubble column allows easily accessible investigations of the flow structure, bubble size and reaction and was the basis for the validation of Eulerian based CFD simulations. The extension of population balance and reactive mass transfer, as well as oscillation in the Euler–Lagrange framework enabled a description of the hydrodynamics (e.g. hold-up) and chemisorption for a wide range of applications based on a view experimental studies to validate the applied correlations. The principle multi-scale approach, ranging from the determination of diffusion coefficient and enhancement factor to the simulation of a bubble column, was finally successfully validated by comparing the results to the pseudo two-dimensional bubble column experiment.

To conclude, experiments on the smaller scale were developed that enable an identification of system properties and a selection of adequate models. Validated models based on the multi-scale approach are a key changer to account for the complex hydrodynamics and to replace the experimental effort by computational modelling on the larger scale.

References

1. Shah YT, Kelkar BG, Godbole SP, Deckwer W-D (1982) Design parameters estimations for bubble column reactors. AIChE J 28:353–379
2. Deckwer W-D, Schumpe A (1985) Blasensäulen - Erkenntnisstand und Entwicklungstendenzen. Chem Ing Tech 57:754–767
3. Fan L-S (1989) Gas-liquid-solid fluidization engineering. Elsevier Science, Burlington
4. Degaleesan S, Dudukovic M, Pan Y (2001) Experimental study of gas-induced liquid-flow structures in bubble columns. AIChE J 47:1913–1931
5. Kantarci N, Borak F, Ulgen KO (2005) Bubble column reactors. Process Biochem 40:2263–2283
6. Leonard C, Ferrasse J-H, Boutin O, Lefevre S, Viand A (2015) Bubble column reactors for high pressures and high temperatures operation. Chem Eng Res Des 100:391–421
7. Sideman S, Hortaçsu Ö, Fulton JW (1966) Mass transfer in gas liquid contacting systems. Ind Eng Chem 58:32–47
8. Gebauer F, Villwock J, Kraume M, Bart H-J (2016) Detailed analysis of single drop coalescence—influence of ions on film drainage and coalescence time. Chem Eng Res Des 115:282–291

9. Hlawitschka MW, Kováts P, Dönmez B, Zähringer K, Bart H-J (2020) Bubble motion and reaction in different viscous liquids, Exp. Comput. Multiph. Flow: 1-13.

10. Hlawitschka MW, Kováts P, Zähringer K, Bart H-J (2017) Simulation and experimental validation of reactive bubble column reactors. Chem Eng Sci 170:306–319

11. Mühlbauer A, Hlawitschka MW, Bart H-J (2019) Models for the numerical simulation of bubble columns: a review. Chem Ing Techn 91:1747–1765

12. Hlawitschka MW, Tiwari S, Kwizera J, Klar A, Bart H-J (2017) Simulation of fluid particle cutting—validation and case study. Arxiv: 1709.01729v1

13. Wardle KE, Weller HG (2013) Hybrid multiphase CFD solver for coupled dispersed/segregated flows in liquid-liquid extraction. Int J Chem Eng 128936:1–13

14. Ishii M, Zuber N (1979) Drag coefficient and relative velocity in bubbly, droplet or particulate flows. AIChE J 25:843–855

15. Tomiyama A, Kataoka I, Zun I, Sakaguchi T (1998) Drag coefficients of single bubbles under normal and micro gravity conditions. JSME Int J Ser B 41:472–479

16. Tomiyama A, Celata GP, Hosokawa S, Yoshida S (2002) Terminal velocity of single bubbles in surface tension force dominant regime. Int J Multiphase Flow 28:1497–1519

17. Moore DW (1965) The velocity of rise of distorted gas bubbles in a liquid of small viscosity. J Fluid Mech 23:749–766

18. Wellek RM, Agrawal AK, Skelland AHP (1966) Shape of liquid drops moving in liquid media. AIChE J 12:854–862

19. Clift R, Grace JR, Weber ME (1992) Bubbles, drops, and particles, 3 print. Acadmic Press, New York

20. Okawa T, Tanaka T, Kataoka I, Mori M (2003) Temperature effect on single bubble rise characteristics in stagnant distilled water. Int J Heat Mass Transfer 46:903–913

21. Sanada T, Sugihara K, Shirota M, Watanabe M (2008) Motion and drag of a single bubble in super-purified water. Fluid Dyn Res 40:534–545

22. Legendre D, Zenit R, Velez-Cordero JR (2012) On the deformation of gas bubbles in liquids. Phys Fluids 24:43303

23. Tomiyama A, Tamai H, Zun I, Hosokawa S (2002) Transverse migration of single bubbles in simple shear flows. Chem Eng Sci 57:1849–1858

24. Smagorinsky J (1963) General circulation experiments with the primitive equations. Mon Weather Rev 91:99–164

25. Sato Y, Sekoguchi K (1975) Liquid velocity distribution in two-phase bubble flow. Int J Multiphase Flow 2:79–95

26. Sato Y, Sadatomi M, Sekoguchi K (1981) Momentum and heat transfer in two-phase bubble flow—II. A comparison between experimental data and theoretical calculations. Int J Multiphase Flow 7:179–190

27. Rzehak R, Krepper E (2013) Bubble-induced turbulence: Comparison of CFD models. Nucl Eng Des 258:57–65

28. Burns AD, Frank T, Hamill I, Shi J-M (2004) The Favre averaged drag model for turbulence dispersion in Eulerian multi-phase flows. In: Proceedings of 7th international conference on multiphase flow, ICMF2004, Yokohama, Japan

29. Hlawitschka MW (2019) Multiscale investigations of reactive bubble columns, Habilitation. TU Kaiserslautern, Kaiserslautern

30. Bird RB, Stewart WE, Lightfoot EN (2007) Transport phenomena, Rev, 2nd edn. Wiley, New York

31. Nock WJ, Heaven S, Banks CJ (2016) Mass transfer and gas–liquid interface properties of single CO_2 bubbles rising in tap water. Chem Eng Sci 140:171–178

32. Cachaza EM, Díaz ME, Montes FJ, Galán MA (2009) Simultaneous computational fluid dynamics (CFD) simulation of the hydrodynamics and mass transfer in a partially aerated bubble column. Ind Eng Chem Res 48:8685–8696

33. Schäfer J, Hlawitschka MW, Attarakih M, Bart H-J (2019) Modelling of bubble column hydrodynamics using CFD and SQMOM as a population balance solver. In: 29th European symposium on computer aided process engineering. Elsevier, Amsterdam, pp 715–720

34. Merker D, Böhm L, Oßberger M, Klüfers P, Kraume M (2017) Mass transfer in reactive bubbly flows—a single bubble study. Chem Eng Technol 40:1391–1399
35. Fuller EN, Schettler PD, Giddings JC (1966) New method for prediction of binary gas-phase diffusion coefficients. Ind Eng Chem 58:18–27
36. Wilke CR, Chang P (1955) Correlation of diffusion coefficients in dilute solutions. AIChE J 1:264–270
37. Serizawa A, Bataille J, Fukano T (eds) Multiphase flow 1995: Proceedings of the second international conference on multiphase flow, Kyoto, Japan, 3–7 Apr 1995. Elsevier Science, Amsterdam
38. Hlawitschka MW, Schäfer J, Hummel M, Garth C, Bart H-J (2016) Populationsbilanzmodellierung mit einem Mehrphasen-CFD-Code und vergleichende Visualisierung. Chem Ing Techn 88:1480–1491
39. Jeong J, Hussain F (1995) On the identification of a vortex. J Fluid Mech 285:69

Determination of Kinetics for Reactive Bubbly Flows Using SuperFocus Mixers

Otto Mierka, Stefan Turek, Günter Rinke, Sven Simon, Siegfried Schindler, Alexander Hoffmann, Marko Hoffmann, Michael Schlüter, and Sonja Herres-Pawlis

Abstract For the well-defined investigation of reactive bubbly flows it is crucial to know the kinetics of the chemical reaction steps as detailed as possible which means that the hindrance due to mixing should be minimized (intrinsic kinetics). This is especially difficult for fast chemical reactions that are addressed in this book. Therefore, to distinguish between convective mixing and diffusion a tool should be used that enables an optical access to visualize and detect the instant mixing on a microscale and the comparison with numerical simulations. Furthermore, this tool should be easy to handle for chemical engineers and inexpensive. A SuperFocus mixer in a continuous-flow setup is used for this purpose, in which two mixable liquid streams are mixed, with the gas phase dissolved in one of the streams. The results are compared with a classical stopped-flow apparatus. Because chemical reactions are generally following a complex reaction network with many reaction steps and intermediates that are mostly difficult to detect, the measurement of the formation of the relevant products and by-products is a difficult task by its own. Spectroscopic

O. Mierka · S. Turek
Faculty of Mathematics, Chair III of Applied Mathematics, TU Dortmund, Vogelpothsweg 87, 44227 Dortmund, Germany

G. Rinke
Institute for Micro Process Engineering, Karlsruhe Institute of Technology, Hermann-von-Helmholtz-Platz 1, 76344 Eggenstein-Leopoldshafen, Germany

S. Simon
Institute for Parallel and Distributed Systems, University of Stuttgart, Universitätsstr. 38, 70569 Stuttgart, Germany

S. Schindler
Institut für Anorganische und Analytische Chemie, Justus-Liebig-Universität Gießen, Heinrich-Buff-Ring 17, 35392 Gießen, Germany

M. Hoffmann · M. Schlüter
Institute of Multiphase Flows, Hamburg University of Technology, Eissendorfer Str. 38, 21073 Hamburg, Germany

A. Hoffmann · S. Herres-Pawlis (✉)
Institute of Inorganic Chemistry, RWTH Aachen University, Landoltweg 1a, 52074 Aachen, Germany
e-mail: sonja.herres-pawlis@ac.rwth-aachen.de

methods including absorption or fluorescence measurements are used here to detect the formation of the relevant products and to determine the gross kinetics for the relevant reaction steps. Finally, the experimental results are used to adapt direct numerical simulations for an estimation of the corresponding diffusion coefficients and reaction constants.

1 Introduction into SuperFocus Mixers

For the evaluation of the influence of hydrodynamics and mass transfer in bubbly flows on the performance of a chemical reaction concerning yield and selectivity, a deep knowledge of the reaction kinetics is necessary. If the reaction is faster than the timescales of hydrodynamics, it will take place directly in the liquid film surrounding the bubble. If the reaction is slower than the timescales of hydrodynamics (respectively mixing times), there is little influence of the characteristics of the bubbly flow on the reaction. For chemical reactions that are sensitive to the mass transfer and flow structure in the vicinity of a bubble, the reaction products should be formed within the range of one hundredth of a second to one second (compare Sect. 4.1 in Chapter "Chemical Reactions at Freely Ascending Single Bubbles"). This influence can be shown clearly with a reaction whose rate can be adjusted relative to the rate of absorption of the gaseous phase in the liquid phase in order to consider both cases: mass transport limited reactions and kinetics limited reactions. The first step to estimate whether a chemical reaction is influenced by the local hydrodynamics in bubbly flows is the determination of the overall reaction kinetics. At this point, not the detailed kinetics of the reaction network is of interest but the most sensitive reaction step that influences the selectivity toward the valuable reaction product. For research groups that are not equipped with high sophisticated devices for kinetic measurements (like stopped-flow apparatuses), a SuperFocus Mixer (SFM) can be used for the determination of the relevant reaction kinetics. In the continuous-flow SuperFocus mixer two mixable liquid streams are mixed, with the gas phase dissolved in one of the streams. This method has been developed as a guiding measure in the DFG priority program 1740. Several chemical reaction systems have been tested and studies on the kinetics have been performed in a continuous-flow setup by means of a SuperFocus Mixer and for comparison in a stopped-flow setup. The design of the SuperFocus Mixer is based on the development by Hessel et al. [1, 2]. The principal concept is shown in Fig. 1.

The contacting of the two miscible fluids to be mixed is realized by multiple microchannels which provide an alternating arrangement of the two fluids. Consequently, a high contact area in-between the two fluids is achieved. It is followed by a focusing zone where the diffusional length is reduced gradually by reducing the width of the lamellae of the fluids. In comparison to other micromixers, the SuperFocus Mixer is characterized by a large focusing ratio of a to b, respectively the ratio of the widths of the arc at the feed channels to the width at the beginning of the
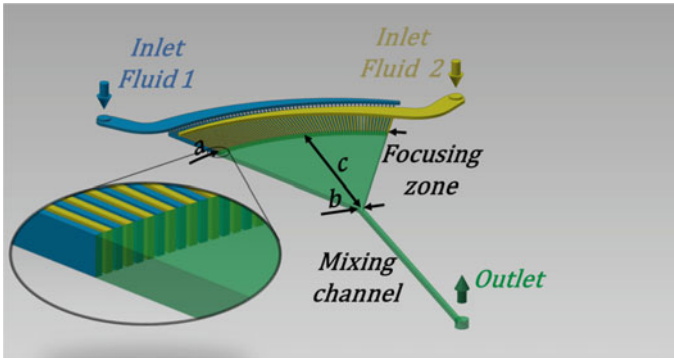
Fig. 1 Schematic drawing of the SFM according to Hessel et al. with its characteristic dimensions *a*, *b* and *c* [3]

rectangular mixing channel. *c* is the distance between the arc of the feed channels and the beginning of the rectangular mixing chamber.

A special SFM based on the design of Hessel et al. [2] has been developed at the Institute of Microsystems Technology at Hamburg University of Technology and was used for the determination of kinetics by Schurr et al. [3] and Mierka et al. [4]. The structure of the mixer is etched anisotropic into a silicon wafer using the deep reactive ion etching process. Glass plates of 0.5 mm thickness are anodic bonded to the bottom and the top of the silicon wafer. The design of the mixer is shown in Fig. 2a. The two fluids enter continuously via two curved fluidic inlets. Each of them is split into 64 feed channels. The focusing zone has a length *c* of $l = 22$ mm and a ratio *a/b* of 38; see notations in Fig. 1. For the experiment two different designs

Fig. 2 (**a**) Design of the SFM with a total length of the mixing channel of (i) $l = 200$ mm, respectively (ii) $l = 60$ mm and (**b**) photo of a SFM with cooling or heating channels [3]

of the mixing channel have been used, shown in Fig. 2a. Both of them have a cross section of $A = 0.5$ mm $\times$ 0.5 mm. However, one has a total length of $l = 200$ mm (i), the other one a total length of $l = 60$ mm (ii). Figure 2b shows the photo of a version with additional heating or cooling channels.
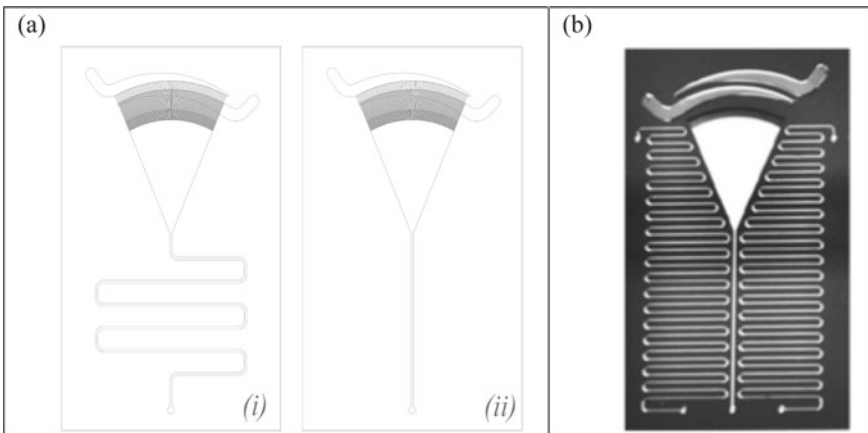
During the mixing in continuous-flow mode, the progress of the reaction can be monitored along the channel in order to determine the kinetics. By calculating the velocity of the liquid flow the spatial coordinate can be converted into a time scale. The residence time can be roughly calculated by dividing the traversed volume, beginning with the focusing zone and mixing channel up to the measurement point, by the total flow rate.

2 Experimental Setup: Benchmark Experiment

Depending on the chemical reaction that has to be studied, two different experimental setups of the SFM can be used to determine the kinetics. If the reaction product can be detected by UV/VIS spectroscopy, the so-called "clamp-on" system can be used. If the reaction product shows fluorescence, the diffusion coefficients and kinetics can be measured by means of Laser Induced Fluorescence (LIF). Both systems need an optical access.

For the clamp-on system, the SuperFocus Mixer is attached to a stainless-steel holder. The two inlets are coupled via Luer connectors and $1/8''$ fluorinated ethylene-propylene (FEP) capillaries to 100 ml syringes of glass and PTFE. For the exemplary experiment shown below, the total flow rates have been set between $\dot{V} = 0.4$ and 52 mL/min (corresponding to a residence time between $t = 130$ ms and 17 s at a distance of $x = 22.5$ mm from the outlet of the focusing zone) for the shorter mixing channel (ii), respectively $\dot{V} = 0.4$ mL/min and 34 mL/min (corresponding to a residence time between $t = 260$ ms and 22 s at a distance of $x = 157$ mm from the outlet of the focusing zone) for the longer one (i). The maximum flow rate is limited by the pressure resistance of the cover glass of the focusing zone. The pressure in the mixing channel results from the pressure drop, which is mainly caused by the mixing channel [3].

For the concentration measurements an in situ analysis technique based on UV/VIS spectroscopy with multimode fiber optics is used, see Fig. 3 [3].

The light of a combined halogen and deuterium lamp is coupled into a first fiber including a beam attenuator and focused into the mixing channel on a spot of 0.6 mm diameter using a lens with a short focal length of 5 mm. This results in a transmission of 97% through the channel. The optical path length is determined by the channel depth of 0.5 mm. The transmitted light is collected by a second identical lens, focused into a second fiber and guided to a miniature diode array spectrometer (*ocean optics USB2000*). With this setup a spectral range between $\lambda = 270$ nm and 800 nm can be monitored.

For a fluorescing system, the Confocal Laser Scanning Microscopy (CLSM) can be used (see Fig. 4). The core elements of the setup are the SuperFocus Mixer as

Fig. 3 Optical setup using UV/VIS spectroscopy [3]

Fig. 4 Scheme of the experimental setup for measuring intrinsic kinetics and function principle of a Confocal Laser Scanning Microscope [4, 6]

described in the previous section and the CLSM, allowing measurements of the local concentration fields on a micro-scale in high resolution. The CLSM works very similar to a conventional microscope [5]. In addition to the lenses, it contains two pinholes, through which solely focused light is reaching the detector. The remaining light is cut off, allowing a very small focus depth. Therefore, only light from a

chosen, narrow plane is detected and the obtained data is not influenced by planes above or below the measurement plane. Using a laser beam as a light source, several points in front of the microscope objective are scanned to obtain a two-dimensional measurement plane. Each measured point equals a pixel in the resulting image. The data acquisition enables a high spatial resolution below 0.35 μm per pixel, though it is not instantaneous [6]. The working principle of the CLSM is displayed in Fig. 4.

In order to obtain reproducible two-dimensional recordings, the SuperFocus Mixer is placed on an X–Y table, allowing the exact positioning in front of the objective of the CLSM. When changing the objective position relative to the scanned mixer, slices in different depths are recorded, enabling a three-dimensional reconstruction of the concentration fields [5].

The concentration fields in the SuperFocus Mixer are recorded using Laser Induced Fluorescence. The fluorophore allows the assignment of the recorded fluorescence intensity to the concentration of an analyte. For example, the dye dichlorotris(1,10-phenanthroline)ruthenium(II)hydrate shows a dependency of the fluorescence intensity in relation to the oxygen concentration. After a calibration of the fluorescence signal, a measurement of the oxygen concentration is possible e.g. for an oxygen consuming reaction, like the oxidation of sulfite (see Sect. 3.4).

3 Chemical Reaction Systems and Experimental Investigation of Reactions in SuperFocus Mixers

In this section, an overview is given on the chemical reaction systems which have been investigated by SuperFocus Mixers. All selected reaction systems are detectable by UV/VIS or fluorescence spectroscopy and their kinetics can be adapted to the time scales of a bubbly flow. Table 1 summarizes the chemical reaction systems used and their reaction types. All systems use consecutive reaction types where a chemical

Table 1 Overview of the investigated systems

Reaction system	Particular features	Measured with	Section
Bis(μ-oxido)dicopper complex	Kinetics in a fine range, proof of principle, comparison between clamp-on SFM and stopped-flow setup	SFM UV/VIS	3.1.1
Peroxido dicopper complex	Too fast for detection	SFM UV/VIS	3.1.2
Copper NO complex	Too fast for detection	SFM UV/VIS	3.2
Diiron peroxido complex	In methanol, validation of clamp-on setup	SFM UV/VIS	3.3
Sulfite/Sulfate	Aqueous, simple to use, local measurements possible by means of LIF and CLSM	SFM CLSM	3.4

precursor reacts with a dissolved gaseous component which decays afterwards. The challenge lies in the detection of the mostly short-lived species. By using different systems, we were able to clarify the detection limits of the SFM setups.

3.1 The Cu–O₂ Chemical Reaction Systems

3.1.1 The Bis(μ-oxido)dicopper Complex Starting with Cu(btmgp)I

As described in Chapter "Control of the Formation and Reaction of Copper-Oxygen Adduct Complexes in Multiphase Streams", [Cu(btmgp)I] offers a consecutive reaction with O_2 and the subsequent decay of the intermediate bis(μ-oxido) dicopper(III) species (Fig. 5). Because Cu(III) is UV/VIS sensitive, the clamp-on measuring method has been used and the formation and decay of this species has been monitored successfully in the SuperFocus Mixer. For the experiments a continuous flow setup has been used and compared with the results to those obtained with a stopped-flow setup. Thus, in terms of ideal reactor concepts the first one is comparable to a continuous process with steady state flow and the latter one to a batch process.

The formation of the Cu(III) complex is very fast at ambient temperature. Due to the optical access to the mixing zone it can be shown that the Cu(III) complex is formed directly after contacting, respectively at the outlet of the feed channels. In Fig. 6a the characteristic orange color of the Cu(III) complex formed in the focusing zone is shown.

By varying the flow rates, it was possible to change the residence time. The measured spectra are shown in Fig. 7.

With increasing flow rate the maximum absorbance at $\lambda = 395$ nm is increasing. The absorbance for the Cu(III) complex decreases with time. Thus, we observe the
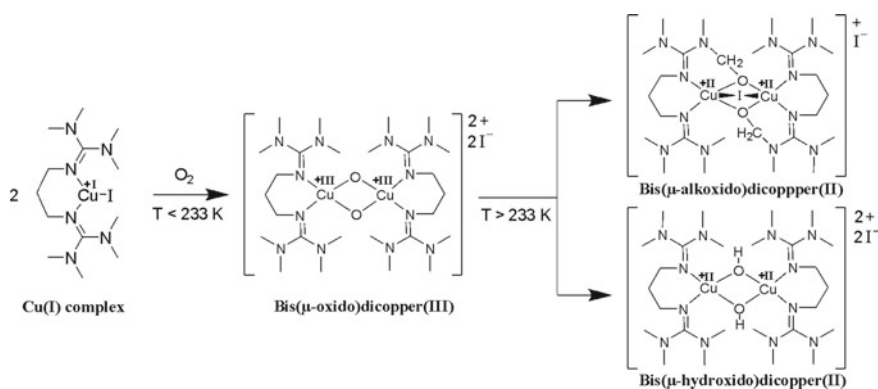

Fig. 5 Scheme of the consecutive reaction of [Cu(btmgp)I] to a bis(μ-oxido) species and subsequent decay [3]
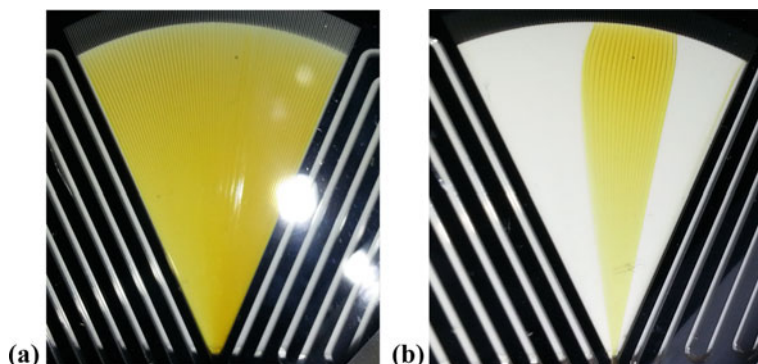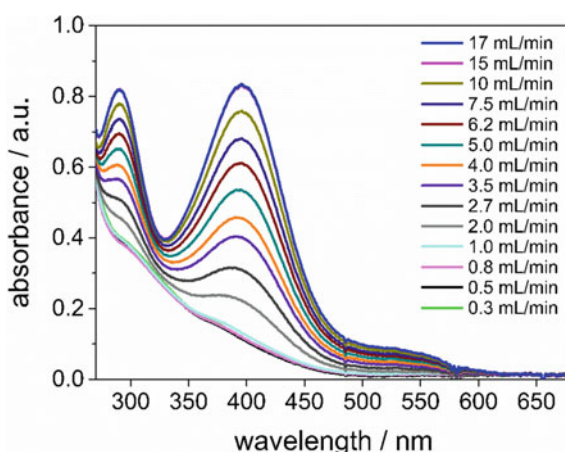
Fig. 6 Formation of the Cu(III) **(a)** good mixing and **(b)** several channels blocked by air bubbles [3]

Fig. 7 UV/VIS spectra obtained in the SFM when varying the flow rate with an average initial concentration of $c = 2.5 \times 10^{-3}$ mol L^{-1} at 295 K [3]

decay to the Cu(II) complex for $t > t_{max}$. Regarding the straight logarithmic plot of the absorbance against the residence time in Fig. 8, an exponential decay can be confirmed and the decay constant is determined to be $k = 0.87$ s^{-1} for an initial averaged concentration of $c = 2.5 \times 10^{-3}$ mol L^{-1} of the Cu(I) in the focusing zone.

The Cu(I) concentration has varied from $c = 2 \times 10^{-3}$ mol L^{-1} to 5×10^{-3} mol L^{-1} (Fig. 9).

The initial concentration of the Cu(I) complex does not affect the rate constant of the decay rate of the Cu(III) complex. The average rate constant of the decay was determined to be $k = 0.90$ s^{-1}. To review the results on the kinetics obtained with the SFM and to investigate the reaction further, stopped-flow measurements were carried out with the same chemical system. Hereby, the rate constant of the decay was elicited to $k = 1.57$ s^{-1} at $T = 295$ K and to $k = 1.27$ s^{-1} at $T = 293$ K. Thus, the value for the rate constant deviates by the maximum factor of 1.7. However, the studies
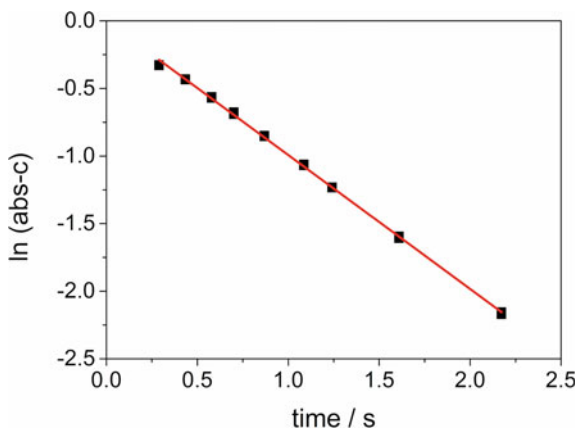
Fig. 8 Logarithmic plot of the decay in the SFM with an average initial concentration of $c = 2.5 \times 10^{-3}$ mol L^{-1} at $T = 295$ K, slope = -0.87 s^{-1}, $R^2 = 0.9989$ [3]
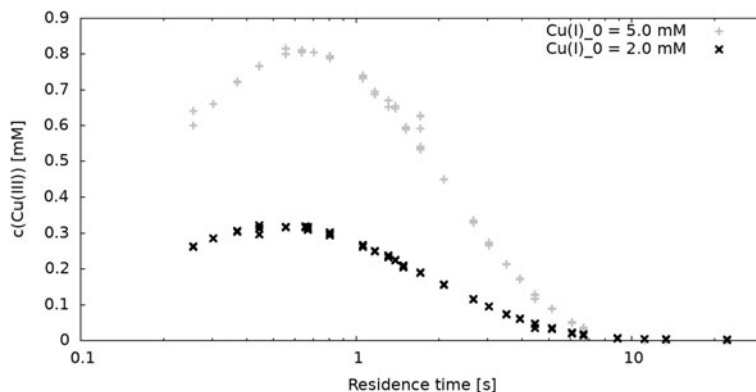
Fig. 9 Experimental results obtained for two inflow concentration values of the reactant species Cu(I)

with the stopped-flow device showed a very strong dependency of the decay constant on temperature. $\Delta T = 2$ K temperature difference does change the rate constant by 20%. In the stopped-flow setup, the temperature was well adjusted by the cryostat and kept isothermal within the flow cell as well as throughout the measuring time. The simple SFM setup was not thermostatically controlled, but chemicals as well as setup were maintained at the same lab with defined room temperature of $T = 295$ K.

Taking into account the experimental effort of a SFM vs. a stopped-flow setup, the advantages of the SFM become clear: The SFM is a mobile and robust apparatus which can be transported in a backpack and needs only 50 cm of bench space whereas the stopped-flow setup needs 4 m of bench space and can hardly be moved. Moreover,

Fig. 10 Reaction of [Cu(Pim^{iPr2})CH$_3$CN]CF$_3$SO$_3$ with O$_2$ to form the copper peroxido complex [7, 8]

the SFM needs an investment of approx. 15,000 € which is only one sixth of the investment costs of the stopped-flow setup.

3.1.2 The Peroxido Dicopper Complex Using a Tris(Imidazolyl)phosphine as Ligand

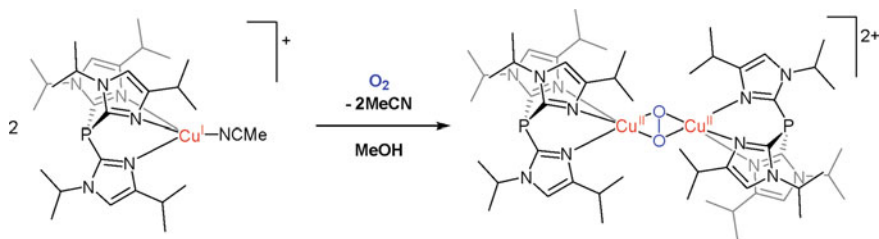The copper(I) complex [Cu(Pim^{iPr2})CH$_3$CN]$^+$ (Pim = tris[2-(1,4-diisopropylimidazolyl)]phosphine) reacts reversibly with dioxygen to the dinuclear side-on peroxido complex [{Cu(Pim^{iPr2})}$_2$O$_2$]$^{2+}$ according to Fig. 10 [7]. The obtained UV/VIS spectra show maxima at $\lambda = 343$ nm and 549 nm typical for a side-on peroxido copper complex but the peroxido species decays within seconds at room temperature. In contrast to [Cu(btmgp)I], the reaction of [Cu(Pim^{iPr2})CH$_3$CN]CF$_3$SO$_3$ with O$_2$ at room temperature is slower with a faster decay (for decay: $k_{obs} = 0.06$ s^{-1} at $T = 25$ °C). Hence, the detection of the peroxido species with the SuperFocus Mixer was difficult. Variation of complex concentration and flow rates revealed that formation and decay of this species already occur during mixing and thus prevent kinetic data collection. This is supported by stopped-flow measurements under the same conditions indicating that reliable kinetic data for the formation only can be obtained using this instrumentation [8].

3.2 The Cu–NO Complex Starting with [Cu(btmgp)I]

Cu(I) guanidine complexes do not only react with O$_2$ but also with NO with color change. In a large series of experiments, we evaluated the reaction of 20 Cu(I) guanidine systems and found a reaction with NO, but only at low temperatures ($T < 60$ °C). NO chemistry is not trivial and for a deep insight, we recommend to read Chapter "In situ Characterizable High-Spin Nitrosyl–Iron Complexes with Controllable Reactivity in Multiphase Reaction Media". At higher temperatures, NO is again released from the adduct complexes. Only in the case of [Cu(btmgp)Br], a NO adduct could be detected at low temperature which lives some minutes and then
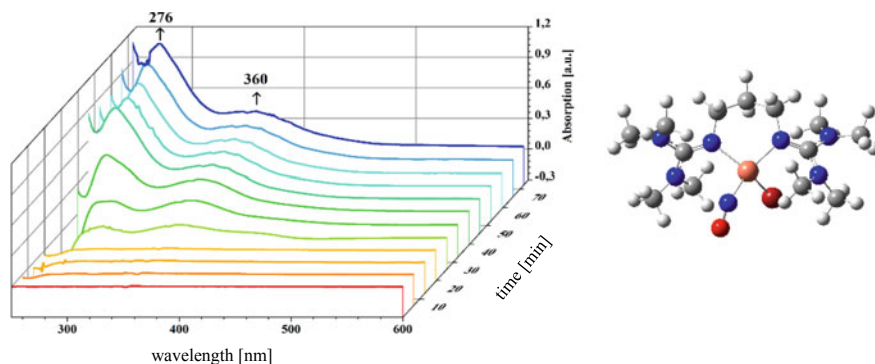
Fig. 11 Left: time-dependent UV/VIS spectra of the reaction of [Cu(btmgp)Br] with NO, right: DFT-optimized structure (TPSSh, def2-TZVP) [9]

decays (Fig. 11) [9]. The reaction could also be monitored in the SuperFocus Mixer but the intermediate decays within seconds which is too slow for the investigation of reactive bubbly flows and shows only a weak absorption at $\lambda = 360$ nm that is difficult to detect.

3.3 Diiron Peroxido Complex and Iron NO Systems

The dinuclear iron(II) complex [Fe$_2$(H-HPTB)Cl$_3$] (Fig. 12, R = H, X = Y = Cl$^-$) reacts with dioxygen to form the corresponding iron(III) peroxido complex that is persistent for a few seconds in the protic solvent methanol prior to decomposition (Fig. 12).

The reaction therefore can be easily followed using low temperature stopped-flow techniques thus obtaining time resolved UV/VIS spectra. Analysis of the kinetic data allowed to obtain activation parameters for this reaction with $\Delta H^{\#} = 15.0 \pm 0.4$ kJ mol^{-1} and $\Delta S^{\#} = -146 \pm 3$ J mol^{-1} K^{-1} and supported an associative
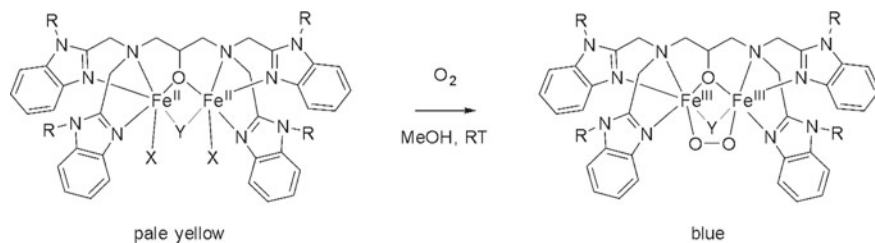
Fig. 12 The reaction of the iron(II) HPTB complex with dioxygen to form the corresponding peroxido complex [10]
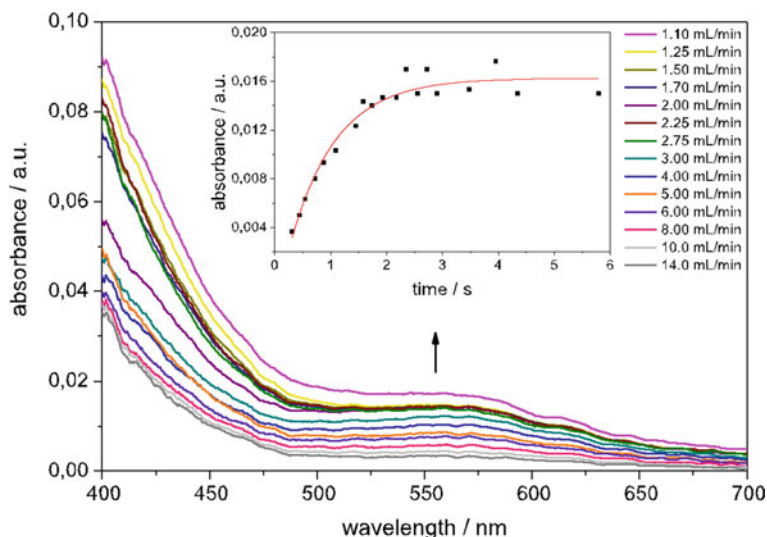
Fig. 13 The reaction of [Fe$_2$(H-HPTB)Cl$_3$] complex with O$_2$ in methanol. c(complex) = 1.0 mmol/L, c(O$_2$) = 4.2 mmol/L, T = 21 ± 1 °C, d = 0.5 mm. Inlay: absorbance versus time at λ = 560 nm together with fit (reprinted with permission from Ref. [10])

mechanism [10]. This reaction was investigated in the SuperFocus Mixer with clamp-on UV/VIS system based on a continuous-flow technique described previously to above [3]. It was possible to perform a full kinetic analysis using the SuperFocus Mixer. Spectral changes are shown in Fig. 13. The same rate law, $v = k \times [complex][O_2]$ was observed with identical (in the range of error) pseudo first order constants of k_{obs} = 1.14 s^{-1} (SuperFocus Mixer) and k_{obs} = 1.45 s^{-1} (stopped-flow) at T = 21 ± 1 °C. The confirmation that the results of the kinetic data of the stopped-flow measurements and the SuperFocus Mixer are identical in the range of error clearly demonstrates that kinetic data obtained from the clamp-on UV/VIS spectroscopic measurements can be used for calculations in industrial setups [10].

As seen in the proceeding sections, the clamp-on UV/VIS SuperFocus Mixer is limited by the pressure in the glass system. Chapter "In situ Characterizable High--Spin Nitrosyl–Iron Complexes with Controllable Reactivity in Multiphase Reaction Media" has summarized the rich chemistry of iron complexes with NO but those systems are too fast to allow detection with this setup.

3.4 Sulfite-Sulphate System

As a model reaction system that can be easily used in aqueous systems, the oxidation of sodium sulfite to sulfate is well known. The typical reaction equation (Eq. 1) found in literature is

$$SO_3^{2-} + \frac{1}{2}O_2 \rightarrow SO_4^{2-} \tag{1}$$

although this formal course of reaction is only the overall reaction equation, which is composed of several partial reactions, yielding a very complex reaction network which is not fully understood yet and is controversially discussed in literature. As the reaction is not totally determined yet, the reaction kinetics cannot be determined without assumptions. Within this work a simplified reaction mechanism according to Kück [11] (Eqs. 2–5) is used. This simplification is very close to the mechanism of Bäckström [12], who published a reaction network in 1934 that marks the basis of most mechanisms until today.

It is presumed that the reaction is catalyzed by metal ions within the solution, in case of the experimental procedure cobalt(II)sulfate.

$$Me^{2+} + HSO_3^- \rightleftharpoons Me^+ + HSO_3^{\cdot} \tag{2}$$

$$HSO_3^{\cdot} + O_2 \rightleftharpoons HSO_5^{\cdot} \tag{3}$$

$$HSO_5^{\cdot} + HSO_3^- \rightleftharpoons HSO_4^- + HSO_4^- + HSO_4^{\cdot} \tag{4}$$

$$HSO_4^{\cdot} + HSO_3^- \rightleftharpoons HSO_4^- + HSO_4^- + HSO_3^{\cdot} \tag{5}$$

The advantage of this simplified mechanism is the possibility to formulate a second order kinetics easily, yielding Eq. 6:

$$\frac{d[O_2]}{dt} = k_1 \cdot [O_2] \cdot \left[HSO_3^-\right]. \tag{6}$$

For the detailed visualization of the reaction, Laser Induced Fluorescence is used. Because the reaction products are not fluorescing by themself, the reaction is measured indirectly by detecting the consumption of oxygen. This can be visualized in the SuperFocus Mixer with an aqueous solution containing a concentration of $c = 30 \, \text{mg L}^{-1}$ of dichlorotris(1,10-phenanthroline)ruthenium(II)-hydrate as fluorescent dye. The fluorescence of the dye is quenched in dependency of the oxygen concentration, which allows to recover the local oxygen concentration from camera recorded grey values by prior calibration. To avoid influencing the liquid properties by high sodium sulfite concentrations, additionally $c = 16 \, \text{mg L}^{-1}$ of cobalt sulfate hydrate is added to catalyze the reaction [13].

One half of the prepared solution is saturated with atmospheric oxygen while the other half is oxygen desorbed by applying nitrogen to the solution. To enable the measurement of the reactive mass transfer, sodium sulfite is added to the oxygen desorbed solution. The oxygen saturated and the sodium sulfite solution are supplied into the SuperFocus Mixer by pressurized vessels with a relative pressure of $p = 0.5$ bar. The mass flow rates are controlled by two *Bronkhorst mini Cori-Flow M13*
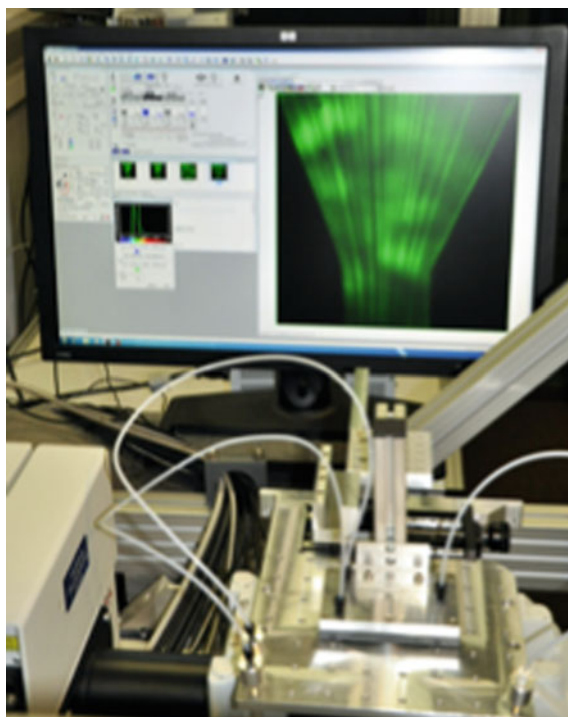
Fig. 14 Photo of the confocal laser scanning microscope Olympus Fluoview 1000 with attached SFM

Coriolis mass flow meters (compare Sect. 2). For the visualization and quantitative analysis of the oxygen concentration distribution within the SFM a Confocal Laser Scanning Microscope (*CLSM Olympus Fluoview 1000*) is used (see Fig. 14).

The numerical simulations are shown in Fig. 15.

4 Numerical Simulation of Reactions Within the SuperFocus Mixer

The relatively simple geometrical setup of the SFM (especially the focusing region downstream from the interdigitally organized inflow streams) offers the possibility of numerical simulations for the transport of all relevant species being involved in the underlying chemical reactions. However, all the transport equations and their respectively discretized counterparts are coupled and therefore dependent on the corresponding flowfield, which is to be determined by the solution of the incompressible Navier–Stokes equations. In the special case that the chemical species taking

Fig. 15 Geometrical representation used for numerical simulation of the flow for the SuperFocus Mixer with the flow distributor supplying nearly uniformly distributed flowrates into the focusing mixing chamber. On the right are provided subpictures of simulation results demonstrating the corresponding flow distribution at the sides and middle of the SFM

part in the chemical reactions are present only in diluted amounts opens the possibility of decoupling the system of these two transport phenomena. Subsequently, this allows the computation of (a) the velocity distribution in the mixer and us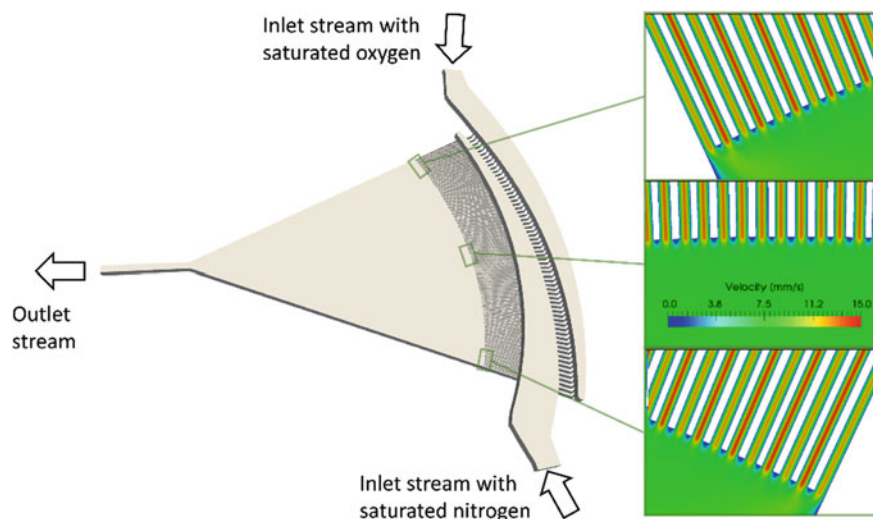e it in a subsequent step for (b) computation of the transport of species in space, time and in the dimension of the species due to the presence of chemical reactions. The realization of the above described framework has been performed on the basis of the open-source Finite Element (FEM) software package FeatFlow [14] which has been extended by additional numerical mechanisms offering the performance of robust and accurate simulations for challenging problems involving a large range of flowrates and different reaction networks. In particular, the extension modules introduced into the standard software package are related to the increase of overall efficiency of the simulation tool, such as:

- Mesh deformation algorithm (MD), which adapts the computational mesh by means of an anisotropic (*umbrella*) mesh smoothening method on the basis of a concentration-gradient related monitor function [15]
- Algebraic Flux Correction (AFC), which is a non-linear stabilization method being responsible to limit the amount of numerical diffusion while preventing the system from numerical oscillations and over- and undershoots of the predicted concentration values [16]
- Operator Splitting (OS) technique, which makes it possible to efficiently decompose the two transport equations (momentum and concentration of species) from each other and to allow interpolation of the velocity solution from the

computational fluid dynamics (CFD) solution onto the dynamically changing computational grid used for the simulation of transport of species.

The such designed simulation software has been integrated into a reverse engineering toolbox making possible the determination of such parameters of the system (diffusion coefficient, reaction rate constant) the value of which was either not possible to be estimated by experimental methods or their respective prediction accuracy was not satisfactory. The used reverse engineering framework was supported by numerous experimentally measured reference results providing either integral or even spatially resolved concentration values of at least one of the species (mostly optically detectable) taking part in the related chemical reactions.

4.1 Physical Mixing of Oxygen in Aqueous Solutions

The necessary step before approaching chemically reactive systems of multiple chemical species is the validation of the numerical components and a calibration of the required computational resolution. In this regard a system related only to physical mixing offers itself as an optimal framework, which allows for validation of the two main transportation mechanisms of species, namely, convection and diffusion. The necessary resolution is determined in a framework of a spatial convergence study, which is supported by the use of an adaptive mesh deformation algorithm. The validation of the simulation results has been based on the experimentally measured reference data corresponding to an indirect measurement described in [6] of solved oxygen in a SuperFocus Mixer. The particular realization of the experiment was related to mixing of two liquid streams of an aqueous solution of $c = 0.03$ g L^{-1} ruthenium complex dichlorotris(1,10-phenanthroline)ruthenium(II) hydrate. Both material streams were provided in a 150 mL h^{-1} flowrate but one contained oxygen and the other one nitrogen. In order to provide an extended dataset for the validation the concentration of the oxygen has been recorded at 8 different locations along the 22.0 mm symmetry axis of the mixer. At each location a 0.64 mm × 0.64 mm large snapshot has been recorded representing the luminescence of the quencher, which based on the calibration measurements has been converted to concentration distributions allowing a one-to-one comparison with the computational results.

In order to investigate the influence of the efficiency of the distributor unit (being responsible for equal distribution of the volumetric flowrate into the interdigital mixer) it was necessary to involve its geometrical representation (see Fig. 15) into the computational framework, however, only concerning the hydrodynamics but not the subsequent transport of the oxygen species, since upstream of the inflow positions the liquid streams exhibit a known composition. As it is visible from Fig. 15 at the sides of the mixer the liquid streams experience a slight deviation of flowrates which in the core of the mixer completely vanishes. The obtained velocity solution was used for the subsequent simulation of species transport on two respective resolutions of computational meshes ($N_{EL} = 0.8 \times 10^6$ and $N_{EL} = 6.4 \times 10^6$ hexahedral elements)
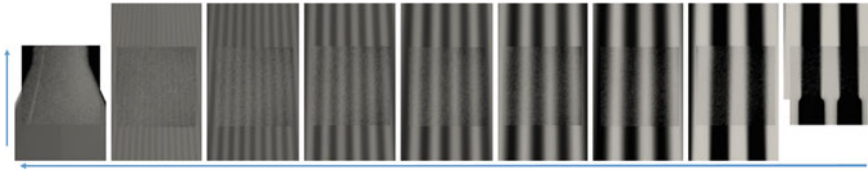
Fig. 16 Graphical representation of the computational results for physical mixing of oxygen in an aqueous solution. Experimentally measured reference distributions are rendered into the computational figures at respective positions (from right to left, flow direction in the subpictures is upwards): 1.0, 4.0, 7.0, 10.0, 13.0, 16.0, 19.0 and 22.0 mm downstream from the 64×2 inlet into the mixing chamber

which proved spatial convergence of the results by the low relative changes between the obtained results. Let us note that only due to the use of the dynamic mesh deformation method it was possible to achieve spatial convergence since for the underlying low value of diffusion coefficient of $D_{O_2/H_2O} = 200 \times 10^{-7}$ cm^2 s^{-1} [17] simulations on static meshes would have required orders of magnitude larger number of elements in order to resolve the relevant scales. In order to enable a relatively simple but efficient verification of the computational predictions against the experimental references, the experimental pictures have been rendered into the computationally obtained ones at the respective positions, as displayed in Fig. 16. As it can be seen from the figure, for the determined diffusion coefficient value D_{O_2/H_2O} an excellent match between the results has been found, which enables the extension of the framework towards chemically reacting systems. In addition, an estimate of the required resolution has been achieved which for the subsequent simulations characterized by similar flowrates and similar diffusion coefficients guarantee us to obtain spatially converged computational results.

4.2 Reactive Mixing in the Framework of a Simple Reaction System

In this section a typical use of a reverse engineering framework is described for the estimation of intrinsic reaction parameters. For this approach, the system described in Sect. 4.1 is applied to the previously mentioned Sulfite-Sulfate reaction system which has been experimentally measured as described in [6]. The modification of the physical mixing system is related mainly to the fact that sodium sulfite (as one of the reactants) is added to the nitrogen saturated solution which is able to react with the solved oxygen being present in the other material stream, as described in detail in Sect. 3.4.

$$2A + B \xrightarrow{k_1} 2C \tag{7}$$
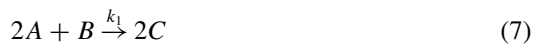
The underlying rather slow chemical reaction has been catalyzed by additional cobalt sulfate hydrate which due to the facts that (a) it was introduced in a same amount into both material streams (b) in such a large excess ($c = 0.016$ g L^{-1}) that its transport had not been needed to take into consideration in the numerical simulations. However, the presence of the catalyst is reflected by the modified reaction constant $\tilde{k}_1 > k_1$, which is used for the definition of the rate of the chemical reaction, as follows Eq. 8:

$$r_1 = \tilde{k}_1 c_A^{\chi_{1,A}} c_B^{\chi_{1,B}} \tag{8}$$

The above defined reaction rate r_1 is identical to the consumption rate of oxygen $\left(-\frac{dc_B}{dt}\right)$ and is chosen to follow a bimolecular reaction mechanism with the orders of $\chi_{1,A} = \chi_{1,B} = 1.0$. Furthermore, the value of $\tilde{k}_1$ was unknown and therefore this parameter was subjected to estimation by the reverse engineering framework. The presence of the catalyst, especially due to its excess has also been taken into consideration via the modified value of the diffusion coefficient of solved oxygen D_B in the solution. Since this value could not be experimentally determined, the searched parameter set of the underlying optimization framework has been extended by this parameter. On the other hand, the diffusion coefficients of the two anions were available, experimentally determined by Leaist [18] and set to the values of $D_A = D_C = 100 \times 10^{-7}$ cm^2 s^{-1}.

In order to complete the list of simulation parameters, the initial concentration of oxygen and sodium sulfite used for the simulations (just as in the experiments) were $c = 0.012$ g/L for oxygen and $c = 0.4$ g/L for sodium sulfite, respectively, resulting in its nearly 10 times excess based on the stoichiometry of the underlying chemical reaction. Just as in case of the previously described physical mixing case also in this case experimentally obtained concentration distributions were used as reference data [6] for the simulations, which have been recorded for three different flowrates, namely $\left(\dot{V}_1 = 150, \ \dot{V}_2 = 150\right)$, $\left(\dot{V}_1 = 75, \ \dot{V}_2 = 75\right)$ and $\left(\dot{V}_1 = 15, \ \dot{V}_2 = 15\right)$ cm^3 h^{-1} resulting in different residence times of the species in the mixer. The parameter space used for the parameter estimation was related to $D_B = \langle 50, 400 \rangle \times 10^{-7}$ cm^2 s^{-1} and $\tilde{k}_1 = \langle 1.0, 20.0 \rangle \times 10^4$ L mol^{-1} s^{-1}. The simulation results were converted to images displaying the concentration distribution of oxygen in the mixer along the symmetry axis of the mixer and the corresponding experimentally obtained oxygen concentration distributions were rendered to their respective locations into the computational distributions. The corresponding representations for the optimal combination of parameters – $D_B = 100 \times 10^{-7}$ cm^2 s^{-1} and $\tilde{k}_1 = 5.5 \times 10^4$ L mol^{-1} s^{-1} are displayed in Fig. 17 which shows that for the short residence time case the agreement with the experimental reference is almost perfect, however the reduction of the flowrate gives rise to discrepancies, which are appearing in the numerically predicted low oxygen concentration regions (red bordered sampling locations). Larger or smaller values of the D_B diffusion coefficient leads to higher and lower smearing of the oxygen signal, and respectively, larger or smaller $\tilde{k}_1$ value implies a faster or slower consumption of oxygen along the
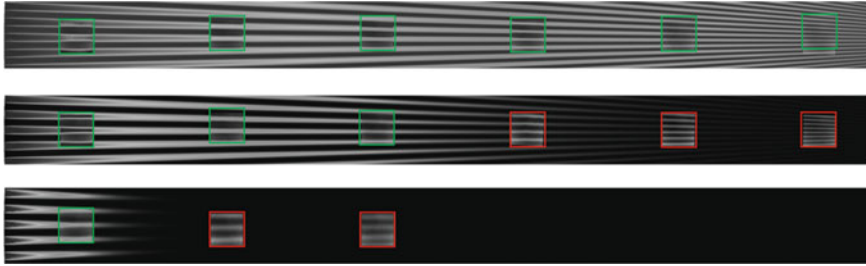
Fig. 17 Graphical representation of the computational results for reactive mixing of solved oxygen with sodium sulfite. The subpictures (from top to bottom) refer to flowrates of $(\dot{V}_1 = 150,\ \dot{V}_2 = 150)$, $(\dot{V}_1 = 75,\ \dot{V}_2 = 75)$ and $(\dot{V}_1 = 15,\ \dot{V}_2 = 15)$ cm³ h⁻¹. Experimental references are rendered into the computational ones with a surrounding green (large numerically predicted concentration of oxygen) and red (small numerically predicted concentration of oxygen) border around the experimentally recorded images

flow direction allowing an "orthogonal" parameter estimation, since the responses of these two parameters are visible in the oxygen concentration signal orthogonally to each other. The explanation of the discrepancies between the numerical and experimental (reference) results for the found parameter values are due to the change of the reaction mechanism reported by Linek [19], which comes into play exactly in situations of lower concentration presence of oxygen. Since this change of the reaction mechanism was not in scope of our study the corresponding locations –affected by the change of reaction mechanism – were removed from the parameter estimation thus enabling the determination of the reaction constant $\tilde{k}_1$ referring to the original reaction mechanism representing the system for large oxygen concentrations. Since the introduced concentration of sodium sulfit is in such a large excess with respect to the solved oxygen the reaction constant $\tilde{k}_1$ allows us to condense it into a pseudo reaction constant including the inflow concentration of sodium sulfite $\tilde{k}^* = \tilde{k} \times c_{A,0}$, what allows its interpretation as an integral reaction rate constant of $\tilde{k}^* = 176$ s⁻¹. Concluding the here presented parameter estimation study, it was shown that its application leads to determination of those missing parameters which are experimentally either not or only by relatively large errors to be determined. Of course, experimentally measured datasets in a large parameter space are inevitable for the utilization of such frameworks. It is also necessary to note that the here described reverse engineering framework is most efficiently applicable for diluted solutions, where the presence of the reactive species does not affect the hydrodynamics, otherwise the resulting effects would need to be reflected in a non-linearly coupled system between the transport of species and momentum equation. In the current study, for each flowrate combination only one solution of the momentum equation was necessary to be performed due to the considered low concentration of all reactive species. Another advantageous aspect of the parameter estimation framework is that in case of having reference (experimental) datasets covering a large parameter range, the parameter estimation has to be performed against all such available datasets which unfortunately might lead to an overkill of computational resources. However, this

unwanted effect might be reduced by introducing a simpler but physically consistent representation of the mixer. Such a framework will be presented in the subsequent Sect. 4.3.

4.3 Reactive Mixing in the Framework of a Consecutive Reaction System

Based on the experiences collected in the previous reverse engineering frameworks a new, more efficient mechanism has been developed allowing us to approach more challenging reverse engineering problems related to simultaneous estimation of multiple parameters at the same time. The most substantial argument behind the developed framework is the very low variance of the flow features in the SFM in the circumferential direction. Except for the 2 to maximally 3 streams at the side of the SFM the flow features are nearly periodic in a large extent of operating conditions, especially for the ones analyzed in the current studies (see Fig. 15). This special flow feature is guaranteed by the optimal construction of the underlying SFM (for the geometrical description see Fig. 15), namely the distributor located upstream of the interdigitally introduced inflow streams into the focusing part of the geometry. Taking advantage of this property makes it possible to decompose the complexity of the system into two representations, first to the original *full* system and second to a representative core region resembling only a periodical geometrical section corresponding to a $2 + 2$ stream representation of the micromixer. The *simplified* representation is then not subjected to any CFD simulation since the velocity distribution can be analytically computed (within the laminar flow regime) as a parabolic function which is accelerated due to the tapering geometry along the radial flow-direction until reaching the position of the outflow capillary (right before reaching singularity). Accordingly, the effect of the residence capillaries is not reflected in the simplified geometrical representation. The benefit of the periodic geometrical representations is that a considerably faster loop of simulations can be performed for a relatively wider range of parameter space which can serve as an efficient and relatively fast predictor for reverse engineering purposes. The subsequent fine tuning of the parameter values within the full system is subjected only to an already narrow parameter-space estimation or in best case the full system only confirms the previously determined parameter values. The here described reverse engineering strategy has been performed for a system of two consecutive reactions involving the oxidation of a btmgp copper(I) complex (A), which is giving rise to formation of a thermally unstable intermediate bis(μ-oxido)dicopper species (C) which is then subsequently transforming to bis(μ-hydroxido)dicopper(II) species (D) as the final product of the reactions (for details of the reaction system we refer to Sect. 3.1):

$$2A + B \xrightarrow{k_1} C \xrightarrow{k_2} D \tag{9}$$

B in Eq. 9 refers to the dissolved O_2 species in acetonitrile, k_1 and k_2 are the reaction constants determining the speed of the reaction rates r_1 and r_2 defined as follows:

$$r_1 = k_1 c_A^{\chi_{1,A}} c_B^{\chi_{1,B}} = -\frac{dc_A}{2dt} = -\frac{dc_B}{dt} = \frac{dc_C}{dt} \tag{10}$$

$$r_2 = k_2 c_C^{\chi_{2,C}} = -\frac{dc_C}{dt} = \frac{dc_D}{dt} \tag{11}$$

It is important to mention that the above defined reaction rates are dependent on the reaction mechanisms and therefore on the related reaction orders of the individual reaction species. Accordingly, to the experimentally determined reaction mechanisms (see Sect. 3.1), the resulting orders were used as $\chi_{1,A} = 1.0$, $\chi_{1,B} = 0.0$ as the solved oxygen is present in excess, and $\chi_{2,C} = 1.0$. However, in a more general reverse engineering framework these quantities might also belong to the parameter set whose value has to be estimated. In this study the unknown parameters subjected to reverse engineering are only the reaction constants k_1 and k_2. The necessary input into the applied reverse engineering should be a possibly large set of experimentally measured data, which in the here reported case has been provided by the experimental collaboration partners covering a large space of operation conditions. In particular, response functions of the system in the form $c_c = f\left(c_{A_0}, \dot{V}\right)$ have been measured (see Fig. 17) by taking advantage of the optical activity of the intermediate species (C), the concentration of which was measured as an averaged absorbance value at specific locations downstream in the residence channel, namely at a distance of $x = 22.5$ mm. It is important to note that due to the extreme focusing of the SFM the acceleration of the flow is so large in the residence channel that the distant location of the sampling region (at $x = 22.5$ mm) does not experience a considerable influence on the concentration values with respect to the location at end of the focusing zone, which has been considered as the outermost location of the simplified geometry for the simulations. It will be shown that the simulations of the large system involving the $x = 22.5$ mm section of the residence channel will also prove this fact. The experimentally measured response functions in Fig. 18 are related to a challenging situation because it perfectly renders the progress between the 1st and 2nd chemical reaction and captures the point from which on the decay of (C) dominates above its production. The prerequisite for a successful numerical reconstruction of this phenomenon is the exact modeling of the interplay of the three transport mechanisms in the numerical simulations, namely convection, diffusion and reaction. Especially the first reaction step is from this point of view of key importance since the species have to diffuse to each other orthogonally to the flow direction and react together forming the intermediate product (C). Uncertainties from here on are related only to diffusion, since its extent is related to the diffusion coefficient of each species. The diffusivity values of the underlying Copper complexes in acetonitrile have been experimentally determined as $D_A = D_C = D_D = 140 \times 10^{-7}$ cm^2/s (see Sect. 3.1) and the diffusivity of oxygen has been estimated by means of the proposed correlation of Schumpe and
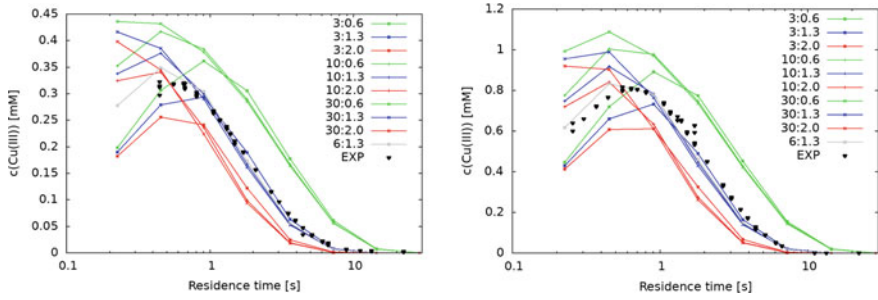
Fig. 18 Experimental (reference) and computational results obtained for two inflow concentration values of the reactant species Cu(I). Left: $c_{Cu^I}^{in} = 2.0$ mM and right $c_{Cu^I}^{in} = 5.0$ mM. Computational values correspond to the ratios of reaction constants $k_1 : k_2$ in s^{-1} and $D_B = 400 \times 10^{-7}$ cm^2/s

Lühring [20] as:

$$D_B = (2.6 \times 10^{-11})\mu_L^{-2/3} \cong 500 \times 10^{-7} \text{ cm}^2/\text{s} \tag{12}$$

but because of the undetermined accuracy of the correlation this parameter has been also included into the reverse engineering framework.

The complete parameter space of the resulting reverse engineering framework has therefore been chosen, as follows:

$$k_1 = \langle 3, 30 \rangle \text{ s}^{-1}; \ k_2 = \langle 0.6, 2.0 \rangle \text{ s}^{-1}; \ D_B = \langle 400, 600 \rangle \times 10^{-7} \text{ cm}^2/\text{s} \tag{13}$$

It is important to note that for any of the triplet of optimized parameters a full spectrum of flowrates had to be simulated for two inflow concentration values, $c_{Cu^I}^{in} = 2.0$ mM and $c_{Cu^I}^{in} = 5.0$ mM of the Cu(I) complex in order to be able to quantify the correlation of the simulated results versus the experimental reference data. In particular, the range of the analyzed flowrates (following the experimental reference) were from $\dot{V}_{\min} = 0.44$ mL/min up to $\dot{V}_{max} = 56.0$ mL/min for altogether 8 flowrate values which are of course inversely related to the residence time values in Fig. 19. The benefit of the here used geometrically simplified prediction tool makes it possible to explore a triplet of optimized parameters for the considered 8 flowrate values in
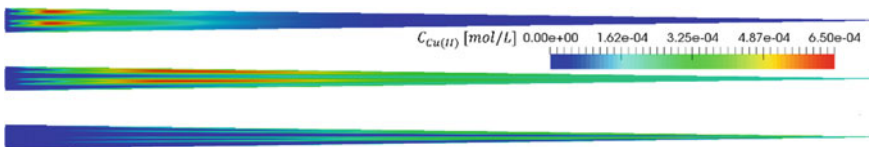

Fig. 19 Computational results of the species (C) obtained for the simplified geometrical representation corresponding to flowrates (from top to bottom) [1.75, 7.0, 56.0] mL/min for the combination of parameter values $[k_1, k_2, D_B] = [10 \text{ s}^{-1}, 1.3 \text{ s}^{-1}, 400 \times 10^{-7} \text{ cm}^2/\text{s}]$ and $c_{Cu^I}^{in} = 2.0$ mM

an incomparably faster (32 times, due to the ratio of geometrical reduction, resulting in simulations of only 4 instead of 128 streams) manner as if the full geometry had to be used. In particular, the computational mesh for these simulations has been guaranteed by a mesh resolution provided by 27,648 hexahedral elements. The spatial distribution of the elements has been adapted during the simulation by the underlying mesh deformation algorithm, which was coupled to the gradients of the concentration fields of the underlying species. The incorporation of the mesh deformation algorithm was absolutely inevitable in order to provide the required resolution of the steep concentration gradients, which in case of a static mesh simulation framework might have required incomparably smaller mesh sizes overall in the computational domain (no a priori knowledge of where the steep gradients will occur). Such mesh resolutions would have practically prohibited us to scan through wider ranges of parameter spaces.

Solution of the individual cases was performed in a framework of a non-stationary simulation (with varying timesteps, depending on the given flowrate case) until steady state has been reached. This way roughly the same number of timesteps were necessary for all flowrate cases totaling in ca. $t = 8$ min per single flowrate simulation on a 16 core *Intel® Core (TM) i5-6500* CPU architecture. Typical representations of the simulation results are visible in Fig. 18 which displays the distribution of the intermediate species (C) for the two extreme and medium flowrate cases for the operation point $[k_1, k_2, D_B] = [10 \text{ s}^{-1}, 1.3 \text{ s}^{-1}, 400 \times 10^{-7} \text{ cm}^2/\text{s}]$ and $c_{Cu^I}^{in} = 2.0$ mM. As it is seen from the figure, for the large residence time the first reaction runs quantitatively through directly at the inflow region, moreover even the second reaction has enough time for conversion of the produced (C) to the final product (D). On the other hand, in case of the analyzed maximum flowrate the maximum of the production of species (C) was not observed due to the resulting short residence time. By taking advantage of averaging of the concentration values at the outflow the comparison of the simulation results might be performed on the basis of the reference experimental results. Such a representation is visible in Fig. 18, which displays the simulational response functions for the two extreme and medium parameter values of $[k_1, k_2]$ and a fixed value of $D_B = 400 \times 10^{-7} \text{ cm}^2/\text{s}$.

As it can be seen from Fig. 18 an optimal set of parameters matching in the whole range of residence times for both inflow concentrations of the reactant is attributed to the reaction rate ratio $[k_1, k_2] = [6 \text{ s}^{-1}, 1.3 \text{ s}^{-1}]$. It is important to note that the maximum concentration of the intermediate species (B) has been detected for both inflow Cu(I) concentration cases in an excellent accordance with the experimental references. The location of this maximum concentration value of species (C) is for the varying diffusion coefficient parameter D_B being shifted to the right or left depending on its value, since its increase accelerates and its decrease decelerates the performance of the 1$^{\text{st}}$ reaction, respectively. Therefore, the best match of the computationally predicted response functions has been achieved for the diffusion parameter value of $D_B = 400 \times 10^{-7} \text{ cm}^2/\text{s}$.

For the demonstration of the prediction quality of the here used reverse engineering framework in the following the simulation results obtained for the very same parameter set $[k_1, k_2, D_B] = [10 \text{ s}^{-1}, 1.3 \text{ s}^{-1}, 400 \times 10^{-7} \text{ cm}^2/\text{s}]$ and $c_{Cu^I}^{in} = 2.0$ mM are

presented for the full, as well as for the simplified geometrical representation. First, as for a qualitative comparison the spatial distribution of the species (C) is displayed for the same flowrate ranges as for its simplified counterpart in Fig. 20.

As it can be seen from the figure and according to the expectations, the core region (referring to > 90% of the mixer volume) of the full geometrical representation resembles the simplified representation in a nearly identical way. Moreover, the differences—caused by boundary effects—are also not experiencing large deviations from the core region, which is thanks to:

1. the proper construction of the flow distributor unit providing nearly equal flowrates for each inflow stream into the mixer,
2. the low influence of the tapering side walls, which is achieved by the small overall depth of the mixer (0.5 mm).

Quantitative comparisons of the predictions of the two representations are provided in Fig. 21 where the averaged outflow concentrations of the intermediate species (C) are plotted for the full range of considered flowrates for both inflow $c_{Cu^I}^{in}$ concentration cases. As it can be seen in Fig. 21, the prediction of the geometrically simpler representations is nearly identical to the ones obtained for their geometrically complete counterparts, however for the low residence time values (large flowrates) the differences between the predictions are marginally increasing. Additionally, the residence time attributed to the maximum concentration is also predicted in a satisfactory precision, only the simulation results below these residence times are somewhat underpredicting the concentration of the intermediate species (C). This arising difference can only be attributed to the increasing difference between the flowstructures (wake formations behind the inlet streams) predicted by the geometrically full representation with respect to the analytically 'prescribed' velocity distribution of the geometrically simpler system. Accordingly, the mixing of the reactants is predicted to be slower in the full system, which therefore results in a seemingly decreased performance of the first chemical reaction.

5 Conclusion

In this chapter it was shown that the benchmark experiment "SuperFocus Mixer" is an excellent tool to create a solid basis for the collaboration between chemists, mathematicians and engineers. The reaction within the SFM enables a detailed analysis of the chemical network as well as diffusion coefficients and kinetic constants and provides insights into the interplay between convection, diffusion and reaction—relevant for the timescales of hydrodynamics and chemical reaction in reactive bubbly flows. A simple and inexpensive clamp-on UV/VIS system for the SFM has been developed that enables the measurement of reaction constants with an acceptable accuracy compared to a stopped-flow apparatus. However, for very fast chemical reactions the SFM-clamp-on system is not suitable and the stopped-flow system should be used. As it was shown on the numerical examples presented in this work,
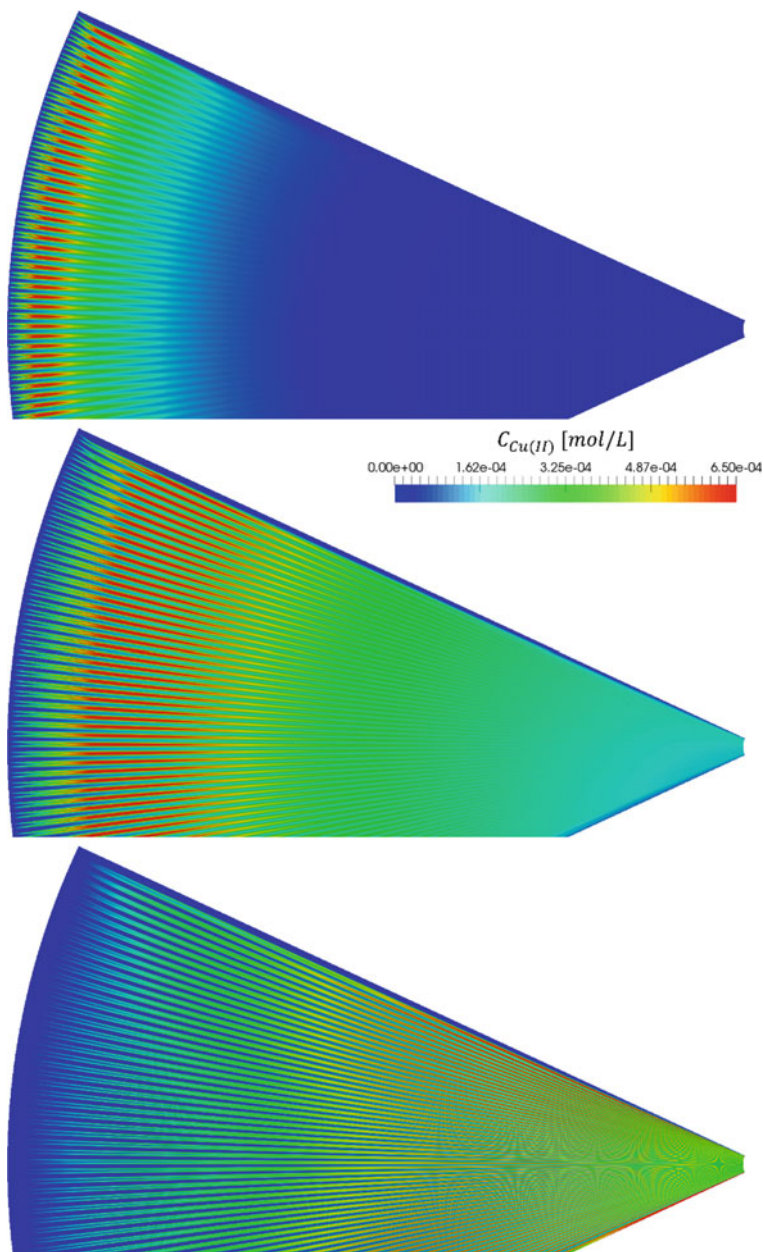
Fig. 20 Computational results of the species (C) obtained for the full geometrical representation corresponding to flowrates (from top to bottom) [1.75, 7.0, 56.0] mL/min for the combination of parameter values $[k_1, k_2, D_B] = [10 \text{ s}^{-1}, 1.3 \text{ s}^{-1}, 400 \times 10^{-7} \text{ cm}^2/\text{s}]$ and $c_{Cu^I}^{in} = 2.0$ mM
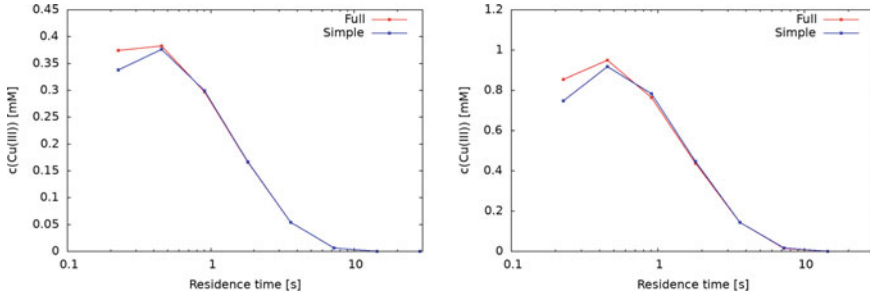
Fig. 21 Comparison of computational results obtained for the two (simple and full) geometric representations for two inflow concentration values of the reactant species Cu(I). Left: $c_{Cu^I}^{in} = 2.0$ mM and right $c_{Cu^I}^{in} = 5.0$ mM. Computational values correspond to the ratios of reaction constants $k_1 : k_2$ in s^{-1} and $D_B = 400 \times 10^{-7}$ cm^2/s

the SFM offers paramount advantages for the estimation of missing parameters by taking advantage of numerical simulations supported by experimentally obtained measurement results. The such designed reverse engineering framework has been proved to be an efficient tool in determination of reaction parameters of the individual reactions taking part in the investigated system or the diffusion coefficients of species, the value of which is experimentally rather difficult to be accurately determined. The successful interplay between the numerical and experimental methods is strongly supported by the deterministic flow structures arising in the SFM which on the other hand can be only guaranteed by an optimized inflow distributor and by highly accurate fabrication standards promoting the most even distribution through the interdigital inflow channels. It was shown that an enhanced parameter estimation mainly profits from the experimental advantages of the geometric realization of this mixer, which is mainly related to the possibilities of recording local mixing phenomena at arbitrary locations (even at varying depth positions) in the micromixer under stationary conditions. However, at the same time a successful parameter estimation can also be performed on simply averaged concentration values of some selected species, if a large range of operation conditions is provided. This method allows the analysis and characterization of chemical reaction systems in order to estimate how strongly the time scales of hydrodynamics are influencing yield and selectivity in reactive bubbly flows.

References

1. Hessel V, Hardt S, Löwe H, Schönfeld F (2003) Laminar mixing in different interdigital micromixers: I. Experimental Characterization. . AIChE J 49:566–577. https://doi.org/10.1002/aic.690490304

2. Hessel V, Löwe H, Müller A, Kolb G (2005) Mixing of miscible fluids: sections 1.3.17–1.3.33. In: Chemical micro process engineering. Wiley-VCH Verlag GmbH & Co. KGaA, Weinheim, FRG. https://doi.org/10.1002/3527603581.ch1c, pp 182–280

3. Schurr D, Strassl F, Liebhäuser P, Rinke G, Dittmeyer R, Herres-Pawlis S (2016) Decay kinetics of sensitive bioinorganic species in a SuperFocus mixer at ambient conditions. React Chem Eng 1:485–493. https://doi.org/10.1039/C6RE00119J

4. Mierka O, Munir M, Spille C, Timmermann J, Schlüter M, Turek S (2017) Reactive liquid-flow simulation of micromixers based on grid deformation techniques. Chem Eng Technol 40:1408–1417. https://doi.org/10.1002/ceat.201600686

5. Hoffmann M, Schlüter M, Räbiger N (2006) Experimental investigation of liquid–liquid mixing in T-shaped micro-mixers using μ-LIF and μ-PIV. Chem Eng Sci 61:2968–2976. https://doi.org/10.1016/j.ces.2005.11.029

6. Timmermann J (2018) Experimental analysis of fast reactions in gas-liquid flows. Cuvillier Verlag Göttingen, Dissertation Hamburg University of Technology. ISBN 978-3-7369-9875-9.

7. Sorrell TN, Allen WE, White PS (1995) Sterically hindered [Tris(imidazolyl)phosphine]copper complexes: formation and reactivity of a Peroxo-Dicopper(II) adduct and structure of a dinuclear carbonate-bridged complex. Inorg Chem 34:952–960. https://doi.org/10.1021/ic00108a030

8. Lerch M, Weitzer M, Stumpf T-DJ, Laurini L, Hoffmann A, Becker J, Miska A, Göttlich R, Herres-Pawlis S, Schindler S (2020) Kinetic investigation of the reaction of dioxygen with the Copper(I) complex $[Cu(Pim^{iPr2})(CH_3CN)]CF_3SO_3$ {Pim i^{Pr2} = Tris[2-(1,4-diisopropylimidazolyl)]phosphine}. Eur J Inorg Chem 3143–3150. https://doi.org/10.1002/ejic.202000462

9. Oppermann A, Laurini L, Etscheidt F, Hollmann K, Strassl F, Hoffmann A, Schurr D, Dittmeyer R, Rinke G, Herres-Pawlis S (2017) Detection of copper bisguanidine NO adducts by UV-vis spectroscopy and a SuperFocus mixer. Chem Eng Technol 40:1475–1483. https://doi.org/10.1002/ceat.201600691

10. Miska A, Schurr D, Rinke G, Dittmeyer R, Schindler S (2018) From model compounds to applications: kinetic studies on the activation of dioxygen using an iron complex in a SuperFocus mixer. Chem Eng Sci 190:459–465. https://doi.org/10.1016/j.ces.2018.05.064

11. Kück UD, Kröger M, Bothe D, Räbiger N, Schlüter M, Warnecke H-J (2011) Skalenübergreifende Beschreibung der Transportprozesse bei Gas/Flüssig-Reaktionen. Chem Ing Tec 83:1084–1095. https://doi.org/10.1002/cite.201100036

12. Bäckström HLJ (1934) Der Kettenmechanismus bei der Autoxydation von Aldehyden. Zeitschrift für Physikalische Chemie 25B. https://doi.org/10.1515/zpch-1934-2509

13. Spille C (2016) Characterization of reactive systems by means of a SuperFocus-mixer. Master thesis, Hamburg University of Technology (TU Hamburg), Institute of Multiphase Flows

14. FeatFlow, www.featflow.de

15. Grajewski M, Köster M, Turek S (2009) Mathematical and numerical analysis of a robust and efficient grid deformation method in the finite element context. SIAM J Sci Comput 31:1539–1557. https://doi.org/10.1137/050639387

16. Kuzmin D, Turek S (2004) High-resolution FEM-TVD schemes based on a fully multidimensional flux limiter. J Comput Phys 198:131–158. https://doi.org/10.1016/j.jcp.2004.01.015

17. Davidson J, Cullen E (1957) The determination of diffusion coefficients for sparingly soluble gases in liquids. Trans Inst Chem Eng 51–60

18. Leaist DG (1985) Moments analysis of restricted ternary diffusion: sodium sulfite + sodium hydroxide + water. Can J Chem 63:2933–2939. https://doi.org/10.1139/v85-486

19. Linek V, Vacek V (1981) Chemical engineering use of catalyzed sulfite oxidation kinetics for the determination of mass transfer characteristics of gas—liquid contactors. Chem Eng Sci 36:1747–1768. https://doi.org/10.1016/0009-2509(81)80124-8
20. Schumpe A, Luehring P (1990) Oxygen diffusivities in organic liquids at 293.2 K. J Chem Eng Data 35(1):24–25. https://doi.org/10.1021/je00059a007

Visualization and Quantitative Analysis of Consecutive Reactions in Taylor Bubble Flows

Michael Schlüter, Felix Kexel, Alexandra von Kameke, Marko Hoffmann, Sonja Herres-Pawlis, Peter Klüfers, Martin Oßberger, Stefan Turek, Otto Mierka, Norbert Kockmann, and Waldemar Krieger

Abstract Taylor bubbles are bubbles that are filling a capillary fixed or rising in a liquid flow. Due to their well-defined size, shape and velocity the flow field around Taylor bubbles is well controllable. Furthermore, only a small amount of gas and liquid is required for experiments, making the study of Taylor bubbles simple and safe. In this chapter, Taylor bubbles are used to study mass transfer with chemical reaction in dependency of various fluid dynamic conditions. Experimental setups are presented to study chemical reactions at Taylor bubbles and in Taylor flows. Furthermore, a Taylor bubble benchmark experiment is presented and used for the validation of numerical simulations that are performed with a front tracking technique in a FEM framework to enable a high resolution of interfaces and boundary layers. It is shown that the interplay of mass transfer, hydrodynamics and chemical reactions can be successfully determined using experimental and numerical methods presented. It is shown further how the selectivity of competitive-consecutive reactions can be influenced by the local fluid dynamics, especially in the wake of a Taylor bubble or within the liquid slug in a Taylor flow.

M. Schlüter (✉) · F. Kexel · A. von Kameke · M. Hoffmann
Institute of Multiphase Flows, Hamburg University of Technology, Eißendorfer Straße 38, 21073 Hamburg, Germany
e-mail: michael.schlueter@tuhh.de

S. Herres-Pawlis
Institute of Inorganic Chemistry, RWTH Aachen University, Landoltweg 1, 52056 Aachen, Germany

P. Klüfers · M. Oßberger
Department Chemie, Ludwigs-Maximilian-Universität München, Butenandtstraße 5-13, 81377 Munich, Germany

S. Turek · O. Mierka
Faculty of Mathematics—Chair III of Applied Mathematics, TU Dortmund University, Vogelpothsweg 87, 44227 Dortmund, Germany

N. Kockmann · W. Krieger
Laboratory of Equipment Design, TU Dortmund University, Emil-Figge-Str. 68, 44227 Dortmund, Germany

1 Introduction into Taylor Bubble Flows

Taylor bubbles are elongated, bullet shaped gas bubbles in narrow channels or capillaries surrounded by a thin liquid film, with a bubble diameter d_B only slightly smaller than the hydraulic channel diameter D_h. Taylor bubble flows appear in multiphase applications as monolith-reactors, pipe reactors and many more.

Due to their well-defined fluid dynamic conditions, volume independent bubble rising velocity and a high degree of reproducibility, Taylor bubbles are very well suited for detailed studies of fast gas-liquid reactions. The fluid dynamic behavior of Taylor bubbles is depending on the ratio of buoyancy and surface tension and can be characterized by the Eötvös number

$$Eo_D = \frac{(\rho_L - \rho_G)g D_h^2}{\sigma} \tag{1}$$

where ρ_L and ρ_G are the liquid and gas phase densities, g is the gravitational constant, D_h is the hydraulic diameter of the channel and σ is the surface tension.

In vertical channels, two flow conditions can be distinguished, a pressure driven bubble, set in motion by a liquid flow, and a rising Taylor bubble, driven by the buoyancy force. Buoyancy is the dominating force as long as the channel diameter is larger than a critical inner diameter D_{crit} calculated by the critical Eötvös number $Eo_{crit} \approx 4$. Hence, the critical diameter is strongly dependent on the system properties and especially on the surface tension. For aqueous systems this results in a critical inner diameter of $D_{crit} = 5.4$ mm, while organic solvents such as Tetrahydrofuran or Methanol allow critical diameters of up to $D_{crit} = 4$ mm. At low Eötvös numbers no shape oscillation of the bubble occurs and the bubble is self-centering within the channel, as long as it stays elongated. During the dissolution process the bubble is only decreasing in length and remains in the centered position [1]. By varying the inner diameter of the channel, the rise velocity v_B, the wake structure behind the bubble and therefore the backmixing can be varied, influencing the fluid dynamic time scales and contact times of reactive species in a well-defined way, as shown in Fig. 1.

For industrial applications, usually many Taylor bubbles are used in a row, called Taylor flows, to enable a sufficient interfacial area for mass transfer.

2 Experimental Methods

Taylor bubbles are well suitable for the detailed experimental observation of flow and concentration fields because they can be fixed at a certain position and therefore an observation under well defined conditions and a long time integration of measurement signals becomes possible. Therefore a Taylor bubble benchmark experiment has been developed in the DFG priority program SPP1740 to enable different groups
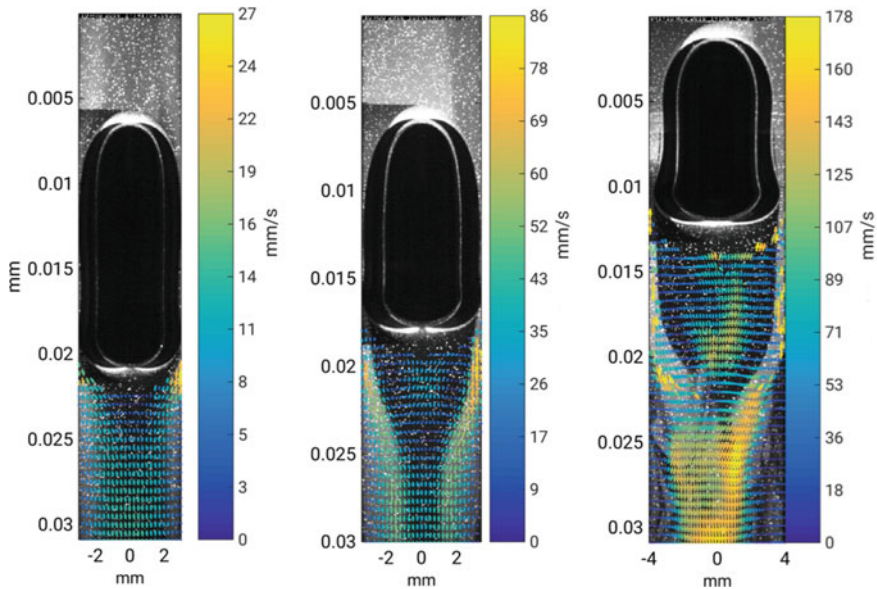
Fig. 1 The instantaneous velocity fields from PIV measurements and simultaneous LIF measurements for three different flow regimes. Left to right: $D_h = 6$ mm, $D_h = 7$ mm, $D_h = 8$ mm capillaries with circular cross section [2]

from academia and industry worldwide to study the influence of fluid dynamics on the yield and selectivity of a chemical reaction and to compare the results among each other and with numerical simulations. In the following two setups used in the DFG priority program 1740 for Taylor bubbles as well as Taylor flows will be described in detail.

2.1 Taylor Bubble Benchmark Experiment

The Taylor bubble benchmark setup consists of vertical glass capillaries with different diameters, which are sealed against oxygen contamination. The setup is described in detail in [3] (Figs. 2 and 3).

The setup is filled with the liquid, after being flushed with demineralized water or ethanol to exclude contamination. It has to be assured that no reactive gas is present inside the apparatus or the liquid phase prior to the experiment. For this purpose the apparatus is flushed carefully with inert gas (e.g. argon) and the gas free liquid phase is injected via a first gas tight syringe into the capillary, forcing any gas inside the apparatus into the upper storage tank. After making sure that no gas is left in the setup, the reactive gas is injected into the capillary using a second gas tight syringe. To make sure that the bubble reaches the test section within 5 s, the first syringe is
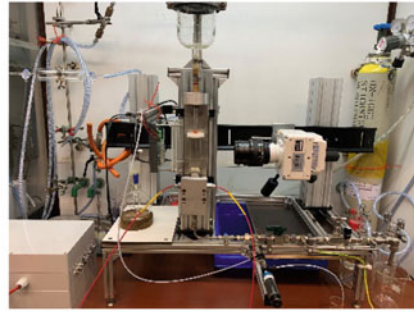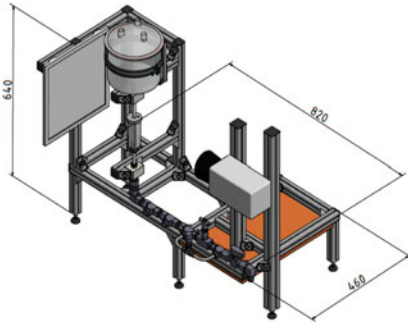
Fig. 2 3D model of the experimental setup for the Taylor bubble benchmark experiment (left) and picture of the setup (right) [3]
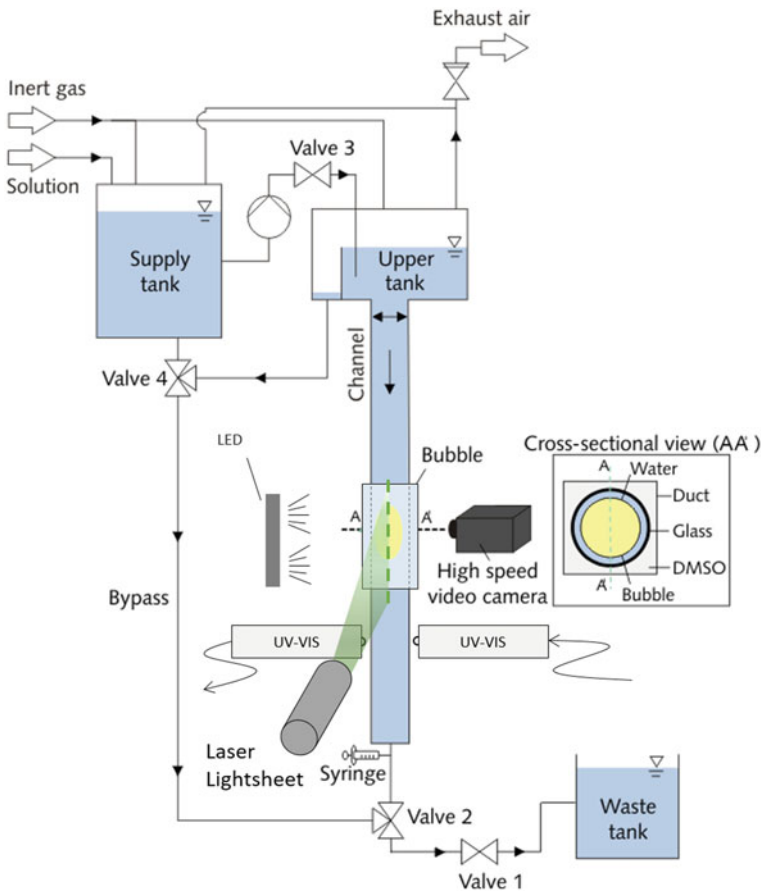

Fig. 3 Flow chart of the experimental setup for the Taylor bubble benchmark experiment [4]

Original image   Binary (grey) &   Reconstruction
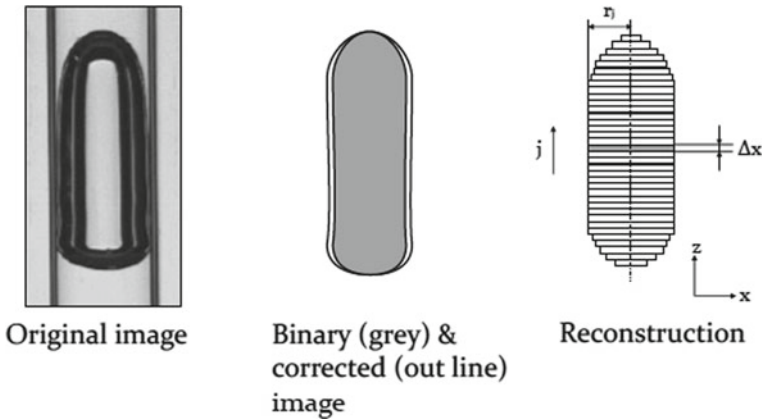   corrected (out line)
                      image

Fig. 4 Image processing method [5]

used again to push the bubble rise by injecting liquid. Once the bubble has reached the measurement position for image capturing, its position is fixed by opening the valves and forcing a counter-current flow of liquid. All experiments are captured with a high speed camera positioned in a right angle to the glass capillary with a frame rate of at least $f = 250$ fps, an exposure time of $t = 1$ ms, a field of view of $A = 128$ pixel $\times$ 512 pixel and a spatial resolution of $x = 0.08$ mm per pixel. After the image of a bubble is taken, the bubble is drained out by opening the valves. For a high reproducibility, the temperature T, the conductivity κ of the solution and the atmospheric pressure p should be checked before each experiment. The position of the liquid level before and after each experiment is crucial as well due to its influence on the static pressure and bubble volume.

For the calculation of the physical mass transfer coefficient k_l, the change of the bubble volume over time is evaluated by image analyses and the equivalent bubble diameter d_{eq} is calculated. Therefore first an original bubble image is transformed into a binary image (Fig. 4, left, middle). Since the refractive indices of water ($n_i = 1.333$) and glass ($n_i = 1.473$) are different, the binary image is corrected using Snell's law, where the grey area and the outline correspond to the binary image and the corrected image, respectively. The method assumes that all the horizontal cross sections of a bubble are circular. The height Δx of each circular disk has a physical length of one pixel. The resultant circular disks are piled up in the vertical direction to reconstruct a 3D bubble shape (Fig. 4, right).

The sphere-volume equivalent bubble diameter d_{eq} is evaluated by

$$d_{eq} = \sum_{j=1}^{N} \left(6 \cdot r_j^2 \cdot \Delta x\right)^{\frac{1}{3}} \tag{2}$$
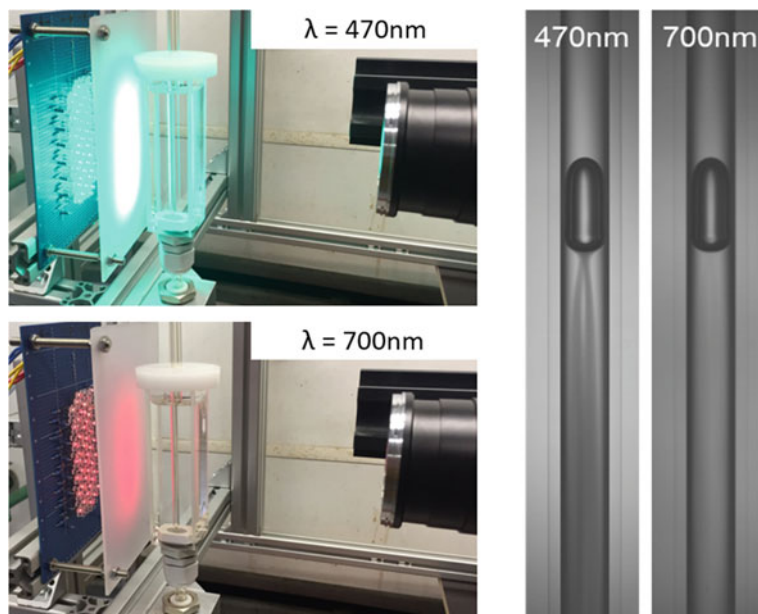
Fig. 5 Backlight illumination of Taylor bubbles with two different wavelengths

where N is the total number of pixels in the vertical direction, j the index denoting the pixel number in the vertical direction and r the disk radius. This post processing method is proven by analyzing images of a rigid sphere of $d = 5.0$ mm in diameter falling through a capillary with a diameter of $D_H = 6.0$ mm. The uncertainty estimated at 95% confidence in d_{eq} determined from the measurement of a rigid sphere are less than 1%.

For the backlight illumination, customized LED panels as a light source are used. The wavelengths of the LEDs are chosen to match the absorption peaks of the different products and side products allowing for a broad variability and easy adjustable system, with low time and cost effort (see Fig. 5).

2.2 Taylor Flow Experimental Setup

In a Taylor flow setup, multiple single Taylor bubbles are injected into the capillary in a row with a constant distance between the single bubbles and the liquid slugs (see Fig. 6).

For the investigation of a competitive consecutive reaction, the oxidation of leuco-indigo carmine can be used (Sect. 3.5). The image processing routine is extended to digital color images. The relevant image processing steps are similar to the ones used for the Taylor bubble:
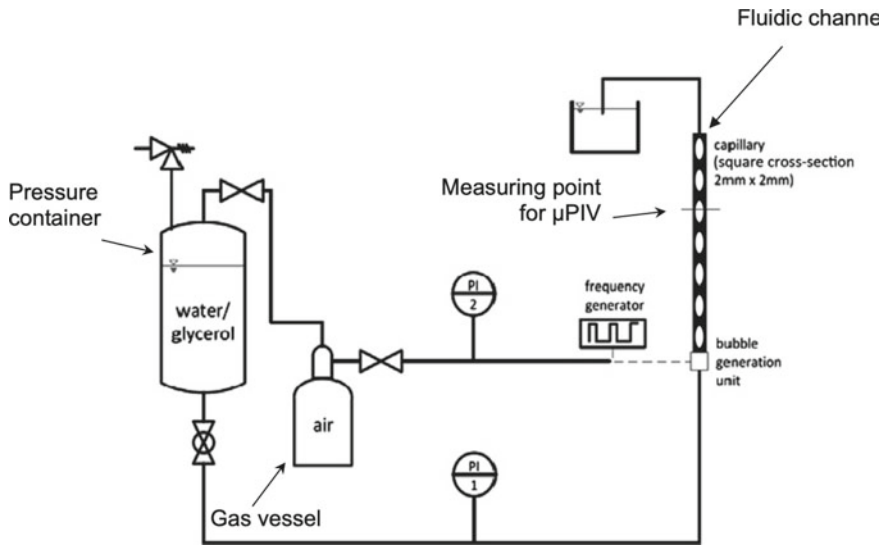
Fig. 6 Experimental setup for a gas–liquid Taylor flow [6]

- Subtraction of background image
- Masking of gas bubbles
- Extraction of color channels (CMY)
- Color compensation due to varying liquid phase thickness
- Conversion of color intensity to concentration.

As color intensity depends on the radial position due to the roundness of the capillary, a compensation step is applied in order to eliminate these differences in color intensity. By applying this step, it is possible to distinctly correlate concentration and color intensity. Calibration and validation are performed by means of UV spectroscopy, which is described in more detail in [7].

This measurement technique is developed for the purpose of (a) providing valuable information with high temporal and spatial resolution for the validation of numerical simulations (Sect. 4.2) and (b) investigating the interdependence of local fluid dynamics and selectivity in coiled capillaries (Sect. 3.5).

For the first objective (a) it is desirable to capture the entire lifetime of individual slugs and bubbles to ensure minimal changes in slug and bubble geometry over the capillary length. This challenge is addressed by constructing a slider setup that is capable of tracking individual slugs, while carrying the DSLR camera (*Nikon DS 5300*) required for image acquisition (Fig. 7, left). Flow generation occurs via a hypodermic needle that is positioned coaxially within a $d_i = 1.6$ mm inner diameter FEP tube. In order to capture the lifetime of the slugs and bubbles with high temporal resolution, videos are recorded and processed framewise according to the described routine. A more elaborate description of the slider setup and video processing is given in [8].
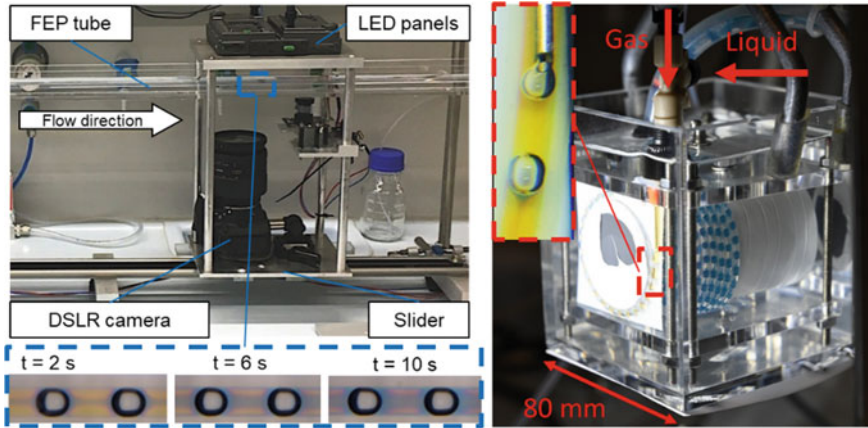
Fig. 7 Experimental setup for the gas-liquid slug flow tracking system (left) and for the gas-liquid slug flow investigation in a coiled capillary (right)

For the second objective (b) an experimental setup is developed that consists of a coiled FEP capillary on a cylindrical support structure, which is positioned within a PMMA box filled with deionized water (Fig. 7, right). As FEP and water have a similar refractive index [9] issues due to refraction are significantly reduced with this setup. Multiple designs with varying coil diameters are employed in order to change Re and Dn independently and analyze the respective effects on superimposed Taylor and Dean flow. Additionally, different inner tube diameters (1.0, 1.6, 2.0 mm) are investigated for the largest support structure (35 mm diameter). The corresponding dimensionless numbers are in the range of $Re = 10 - 400$ and $Dn = 2 - 110$ with

$$Dn = Re \cdot \sqrt{\frac{d_i}{d_c}} \tag{3}$$

and d_c as coil diameter (sum of outer tube diameter and support structure diameter). Investigated coil diameters are $d_c = 18.1, 28.1, 33.2, 36.6, 38.0$ and 38.2 mm.

3   Experimental Investigations on Chemical Reactions Induced by Taylor Bubbles and in Taylor Bubble Flows

In this section the chemical reaction systems will be presented that have been investigated in the Taylor bubble and Taylor flow setup for the priority program DFG SPP 1740. Table 1 summarizes the chemical reaction systems that have been used in the two setups and their particular features.

Table 1 Overview of the investigated systems

| Reaction system	Particular features	Measured with	Sections
Cu/Ammonia	Training system, inexpensive, easy to handle	Taylor bubble	Sect. 3.1
Bis(μ-oxido)dicopper complex	Consecutive reaction with color change	Taylor bubble	Sect. 3.2
Cu/DBED/+ Phenol	Competitive consecutive reaction detectable with UV/VIS	Taylor bubble	Sect. 3.3
Fe-NO MNIC-DNIC	Competitive consecutive reaction detectable with UV/VIS	Taylor bubble	Sect. 3.4
Oxidation of leuco-indigo carmine	Competitive consecutive reaction detectable by color change	Taylor flow	Sect. 3.5

When managing programmes with interdiscipline research groups the question must be raised, how to transfer the knowledge between the groups, especially speaking of realizing chemical reactions with hazardous substances under air exclusion in an engineering research environment. The transfer of chemistry laboratory knowledge to untrained staff in an engineer laboratory should not be underestimated! Thus, one essential task demands a user training on the spot for a few days, including handling toxic chemicals (e.g. NO, MeOH) safely and assisting with formal legislations like composing operating instructions adapted to the specific laboratory. The training should be focused on the safe usage and development of an e.g. NO-feeding gadget under oxygen exclusion (for more details see Chapter "Analysis of Turbulent Mixing and Mass Transport Processes in Bubble Swarms under the Influence of Bubble-Induced Turbulence") since lab workers are supposed to gain security and confidence in handling this gaseous chemical. This synthetic knowledge must be updated and revised during the whole programme, if necessary with repeated instructions on the spot.

In the following the chemical reaction systems will be described in detail.

3.1 Test Reaction for the Training of Engineers

Since most N-donor ligands are very expensive to produce and their peroxido complexes difficult to obtain in large scales, in the first SPP phase an inexpensive and simple reaction system was targeted which exhibits a fast color change upon oxygenation. Therefore, a copper(I)chloride was utilized which forms in aqueous ammonia-containing solution a copper-tetrammine complex. This changes its color from colorless in oxidation state $+$I (when prepared under exclusion of O_2) to deep blue in oxidation state $+$II upon oxygenation.

$$\left[Cu^{I}(NH_3)_4\right]^{+} (\text{colorless}) \xrightarrow{O_2} \left[Cu^{II}(NH_3)_4\right]^{2+} (\text{dark blue})$$
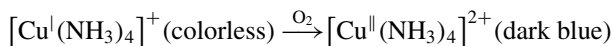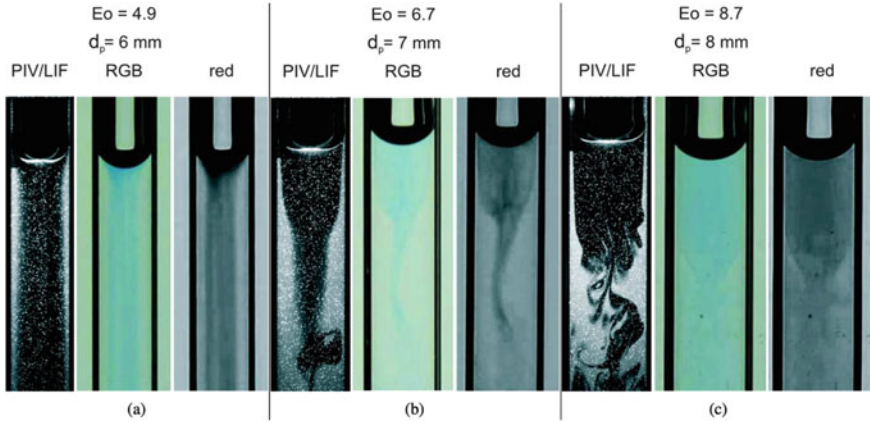
Fig. 8 Comparison of wake structures at rising Taylor bubbles in channels in stagnant liquid. **a** D_h = 6 mm: laminar wake, **b** D_h = 7 mm: toroidal ring vortex, **c** D_h = 8 mm: turbulent wake [10]

The starting chemicals are easily and low priced available. The Cu(I)Cl is sensitive to moisture and can be produced from $CuCl_2$ or by purification of commercially available CuCl. Dry CuCl is relatively stable at dry air. This chemical system can be easily synthesized in large scales and a detailed description for the production under simplistic laboratory conditions was developed (e.g. no Schlenk technique available). The rapid color change upon O_2 contact serves as a direct indicator for O_2 in the system as could be observed in a Taylor bubble [4].

The utilization of the ammonia containing solution showed to be a disadvantage since this solution possesses a fluorescence background traced back to production impurities. This prevents the application for LIF measurements. Moreover, a well running hood is always needed owing to the corrosive properties of ammonia.

However the Cu-ammonia test system is well suited to study the influence of the Taylor bubble geometry on the flow field and backmixing in a Taylor capillary. Figure 8 shows how different capillary diameters influence the flow field in the rear of a Taylor bubble. Whereas for small capillaries D_h = 6 mm a more or less laminar wake without backmixing can be expected, in a capillary of D_h = 7 mm a wake with a stable backmixing structure (toroidal wake) appears. For even larger capillary diameters D_h = 8 mm, an unsteady (turbulent) wake can be observed. The three pictures in each capillary have been taken from PIV images (compare Fig. 1), LIF images and backlight illumination filtered for two different wavelengths (RGB and Red). For more details please see [4] and Chapter "Experimental Investigation of Reactive Bubbly Flows—Influence of Boundary Layer Dynamics on Mass Transfer and Chemical Reactions".

3.2   Consecutive Reaction with Color Change

For studying the influence of the fluid dynamic on mass transfer and a consecutive chemical reaction without expensive analytical equipment, the oxidation of a copper complex in organic solvent can be used, that shows a first color change by reaction to a yellow intermediate and a second one by decay to greenish.

As described in Chapter "Control of the Formation and Reaction of Copper-Oxygen Adduct Complexes in Multiphase Streams", [Cu(btmgp)I] offers this consecutive reaction with O_2 and the subsequent decay of the intermediate orange-red bis(μ-oxido) dicopper(III) species (Figs. 9 and 10). The formation and decay of this species can be successfully monitored with the Taylor bubble setup [11].
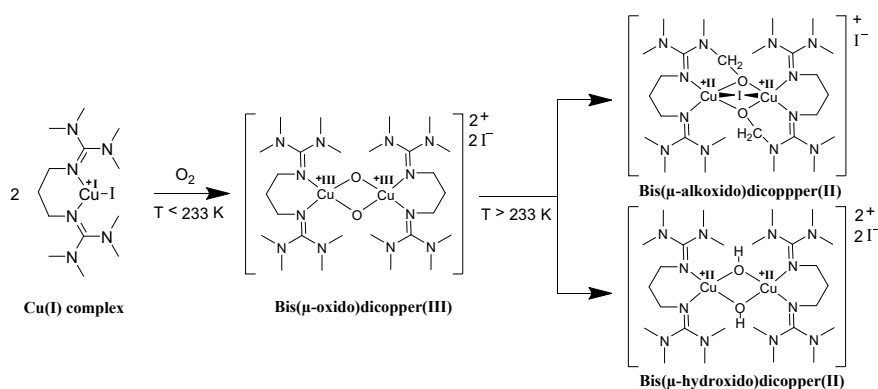

Fig. 9   Scheme of the consecutive reaction of [Cu(btmgp)I] to a bis(μ-oxido) species and subsequent decay
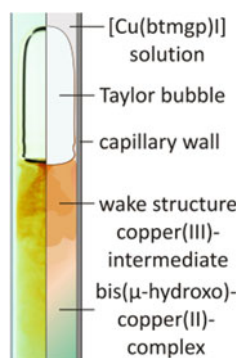

Fig. 10   Color change to yellow by oxidation of the [Cu(btmgp)I] to a bis(μ-oxido) species and subsequent decay to the greenish byproduct [11]

Figure 10 shows how an orange bis(μ-oxido) complex forms when the precursor complex is brought into contact with oxygen and is subsequently decomposing to a greenish bis(μ-hydroxido) complex. Through the mass transfer of oxygen from the Taylor bubble into the solution the orange copper(III)-intermediate is formed. In the shown case the discoloration occurs already within the boundary layer region. Through further bubble rise, the intermediate flows along the bubble according to the boundary layer theory and is merged at the lowest point where the flow detaches. Within the bubble wake mixing of the copper(III)-intermediate occurs through eddies, whereby simultaneously the intermediate decomposes into the green decay complexes. A comparison with the fluid dynamic timescales in Fig. 11 shows, that the first oxidation step appears immediately within the first second whereas the second decay process to the greenish product takes nearly a second. This is in good agreement with the kinetic studies that have been done in a SuperFocus Mixer by Schurr et al. [12] (see Chapter "Determination of Kinetics for Reactive Bubbly Flows Using SuperFocus Mixers") that provides a reaction rate of the first step being $r = 10 \text{ s}^{-1}$ and for the second step $r = 1.5 \text{ s}^{-1}$. This example shows that the Taylor bubble setup is an excellent tool for the determination of the interplay between fluid dynamics and chemical reaction.

This gets even more clear by comparing the influence of the wake structure on the formation of the intermediate and decay to the byproduct. In Fig. 11 the wake structure is well-defined and reproducibly influenced by the width of the capillary that can be characterized by the Eötvös number. At the lowest Eötvös number and

Fig. 11 Backlight image of the wake structures for the Cu(btmgp)I-oxygen system at a concentration of $c = 10 \text{ mmol L}^{-1}$ in argon saturated acetonitrile at Eo = 4.4, 6.8 and 9.8 [10]
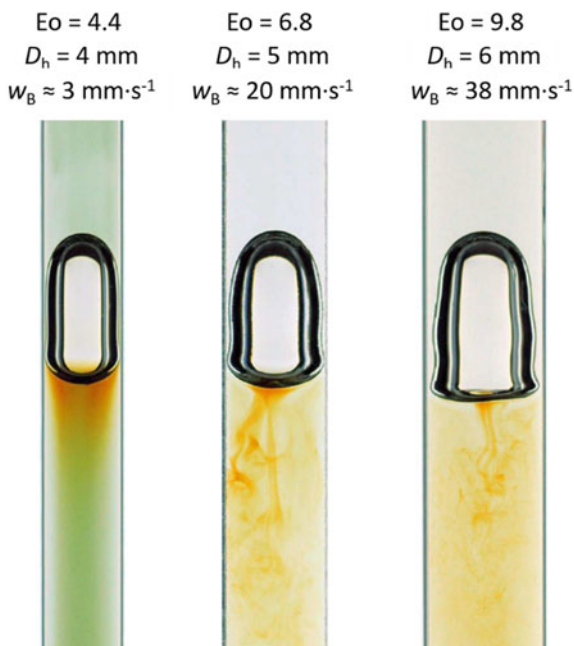
bubble velocity respectively, a more or less steady and laminar wake appears. This causes a residence time of the intermediate bis(μ-oxido) in the wake of the bubble longer than 1 s (about 4 s) which allows the decay to the greenish byproduct. The colorization indicating the second reaction step is clearly visible. With increasing Eötvös number, a more unsteady and well mixed wake structure appears by the higher rising velocity that causes a residence time much shorter than 1 s (about 0.6 s for Eo = 6.8 and 0.3 s for Eo = 9.8). Due to this, the decay takes place out of the field of view and only the yellow bis(μ-oxido) intermediate is visible.

But a second remarkable phenomenon gets visible, that is of great importance for mass transfer and chemical reactions. Related to the Eötvös number of Eo = 6.8, the wake of the bubble in Fig. 11, middle should be steady and closed whereas for an Eötvös number of Eo = 9.8, the wake should be unsteady, well mixed and turbulent (compare Fig. 8). Obviously the different wake structures from the Cu-Ammonia system are not transferable to the Cu-btmgp system. A detailed study shows that this different behavior is caused by interface phenomena. Whereas in the aqueous ammonia-containing solution the copper-tetrammine complex acts as a surface active agent, that hinders the free mobility of the interface and causes a stagnant cap at the rear of the bubble, in the organic solution of acetonitrile, no accumulation of Cu-complexes at the interface takes place and the interface keeps "slippy". This difference in interface mobility influences the separation of the fluid dynamic and concentration boundary layer and leads to the formation of a steady closed wake (aqueous) or the unsteady separation of an open wake (solvent). This might be of tremendous importance for the influence of surface active agents (any contamination) on mass transfer and chemical reaction including yield and selectivity and will be discussed further.

3.3 Influence of Fluid Dynamics on Yield and Selectivity of a Competitive-Consecutive Reaction Induced by a Taylor Bubble—Qualitative Verification with the Cu/DBED-System

For the qualitative verification of the influence of fluid dynamics on yield and selectivity, first a competitive-consecutive oxidation of [Cu(DBED)]OTf to a quinone (P1) and a coupling product (P2) is used (for details see Chapter "Investigation of Reactive Bubbly Flows in Technical Apparatuses"). The visualization of the concentration fields of the two products P1 and P2 in the wake of the single Taylor bubble is done by means of the imaging UV/VIS setup for oxygen free conditions (see Sect. 3 in Chapter "Experimental Investigation of Reactive Bubbly Flows—Influence of Boundary Layer Dynamics on Mass Transfer and Chemical Reactions"). The setup has been adjusted in such way that the characteristic absorption peaks of the two products are matched by the LED backlight illumination. In the observed case those characteristic wavelengths are $\lambda_1 = 420$ nm for product P1 and $\lambda_2 = 505$ nm for P2.

In contrast to the experiments conducted in a bubbly column by the group of Prof. Nieken at the University of Stuttgart (see Chapter "Investigation of Reactive Bubbly Flows in Technical Apparatuses"), the experimental conditions applied in the Taylor capillary have been adjusted to take place within seconds. Therefore, the concentration of the gaseous phase is increased by using pure oxygen bubbles and the concentration of the copper complex in the reaction solution is risen up to c_{Cu} = 3 mM. The experiments are conducted in two different capillaries with hydraulic diameters of D_h = 4 mm and D_h = 4.5 mm.

The analysis of the obtained greyscale images is similar to the method introduced and explained in Sect. 3.2 in Chapter "Experimental Investigation of Reactive Bubbly Flows—Influence of Boundary Layer Dynamics on Mass Transfer and Chemical Reactions". In order to convert the obtained grayscale images into concentration fields, the working principle of an UV/VIS spectrometer is used, which is utilizing Lambert-Beer's law

$$E_\lambda = \log\left(\frac{I_0}{I}\right) = \varepsilon_\lambda dc \tag{4}$$

E_λ represents the extinction, I_0 corresponds to the incident light intensity, I to the light intensity behind the sample, ε is the extinction coefficient, d is the layer thickness of the liquid and c is the concentration.

The layer thickness is assumed to be constant and is set equal to the respective capillary diameter of D_h = 4 and 4.5 mm. The initial light intensity I_0 is determined for both wavelengths individually prior each recording. For this purpose, the capillary filled with the reaction solution is recorded without a bubble and an average value is determined from 10 grayscale images. As the extinction coefficients of the two products are not known so far but should be with the same order of magnitude based on the UV/VIS spectra shown in Chapter "Chemical Reactions in Bubbly Flows", Fig. 7, it is assumed that the measured light absorption at the different wavelengths result solely from the corresponding product P1 or P2. Based on the made assumptions and the fact that the extinction coefficients are not known the Beer Lambert equation is therefore rearranged yielding

$$\log\left(\frac{I_0}{I}\right)d^{-1} = \varepsilon_\lambda c. \tag{5}$$

The images are then analyzed pixel wise within the region of interest. The resulting concentration fields are shown in Fig. 12, displaying the distribution of the two products P1 and P2 in the wake of the bubble. As the necessary information about the extinction coefficient is missing only qualitative statements about the concentration fields in the wake of the bubble can be made.

Nevertheless the results of the measurements in the two different capillaries show that the changing fluid dynamic conditions do again impact the formation of the desired product P1 and its side product P2. Within the D_h = 4 mm capillary in Fig. 12, the left (a) a steady state flow structure becomes visible, within the wake
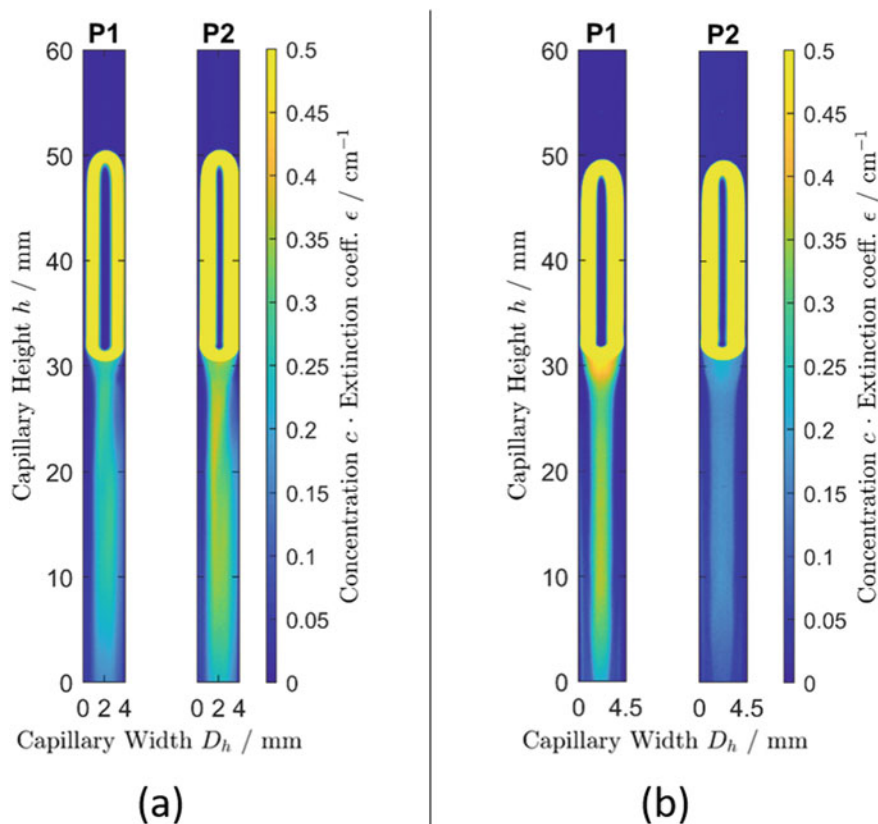
Fig. 12 Concentration gradients of the product P1 and P2 in the wake of a pure oxygen bubble within a $D_h = 4$ mm wide capillary (**a**) and $D_h = 4.5$ mm wide capillary (**b**)

of the bubble, resulting in a low degree of mixing. In contrast the wake in the $D_h = 4.5$ mm capillary in Fig. 12, right (**b**) tends to be rather non-stationary, forming small vortices, which are yielding an increased degree of mixing. By increasing the degree of mixing in the wake of the bubble, the product formation is shifted towards the product P1. The available gas-phase is brought into contact with the fresh solution much quicker due to the higher degree of mixing, allowing primarily the first reaction step to take place. Those results are in good agreement with the results obtained at the large scale bubble column (see Chapter "Investigation of Reactive Bubbly Flows in Technical Apparatuses") experiments and in addition with the MNIC-DNIC system, emphasizing the impact of the bubble size and the resulting mixing behavior especially on the selectivity of a fast gas liquid reaction.

3.4 Influence of Fluid Dynamics on Yield and Selectivity of a Competitive-Consecutive Reaction Induced by a Taylor Bubble—Quantitative Verification with the MNIC/DNIC-System

Investigation of the influence of fluid dynamics towards the yield of competing reaction products require a competitive-consecutive reaction pattern. Detection of the reaction process in the wake of a Taylor bubble should be application-friendly and relatively easy concerning the reaction process. The absorption of light in the visible region serves as a useful probe when distinguishing the educt from different products. This makes the recording of the wake structure during light exposure feasible.

A convenient system is the reaction sequence: $FeCl_2 \rightarrow$ mononitrosyl iron compound (MNIC) $\rightarrow$ dinitrosyl iron compound (DNIC) (see Sect. 3 in Chapter "In Situ Characterizable High-Spin Nitrosyl–Iron Complexes with Controllable Reactivity in Multiphase Reaction Media" for more details) realized with the transfer species NO as follows:

$$FeCl_2 + NO + HNEt_3Cl \rightleftarrows HNEt_3[FeCl_3(NO)]$$

$$HNEt_3[FeCl_3(NO)] + 2NO + MeOH + NEt_3$$
$$\rightarrow HNEt_3\big[FeCl_2(NO)_2\big] + MeONO + HNEt_3Cl$$
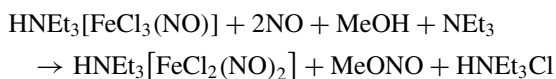
The reaction process can be monitored by observing the colour change from the colourless $FeCl_2$ towards the green MNIC ($\lambda_{max} = 472$ nm), ending up with the reddish DNIC ($\lambda_{max} = 505, 695$ nm). Adding the base NEt_3 and a chloride salt to a degassed methanolic solution of ferrous chloride produces in a first stage MNIC which transforms during reaction time to DNIC. Since kinetic measurements and practical experiments proofed the development of DNIC as too slow for detecting in a bubble wake, a faster system in terms of DNIC was developed, with the proposed equation:

$$FeCl_2 + 2\,NO + 3/2\,NEt_4I \rightarrow NEt_4\big[FeCl_2(NO)_2\big] + 1/2\,NEt_4I_3$$

The latter simple reaction requires no base, just an iodide salt soluble in methanol. Within the reaction process the development of MNIC is followed by a more accelerated formation of DNIC absorption bands ($\lambda_{max} = 505, 740$ nm).

As mentioned in the experimental setup section of this chapter, for the detection of the different products, imaging with backlight illumination by LEDs is used, covering the characteristic peaks of light absorbance. In the observed case those characteristic wavelengths are $\lambda_1 = 470$ nm and $\lambda_2 = 700$ nm. To convert the obtained grayscale images into concentration fields, the working principle of an UV/VIS spectrometer is used, which is utilizing Beer-Lamberts law (Eq. 5).

Table 2 Extinction coefficients of the two products MNIC and DNIC

Wavelength	MNIC	DNIC
$\lambda_1 = 470$ nm	0.4048	0.895
$\lambda_2 = 700$ nm	0.051	0.195

Since the products MNIC and DNIC have a certain absorption at both wavelengths, it is assumed that the total measured absorbance is a composition of the signals of both products. Therefore, two equations

$$E_{470} = \log\left(\frac{I_{0,\,470}}{I_{470}}\right) = d\big(c_{MNIC}\varepsilon_{MNIC,470} + c_{DNIC}\varepsilon_{DNIC,470}\big) \qquad (6)$$

$$E_{700} = \log\left(\frac{I_{0,\,700}}{I_{700}}\right) = d\big(c_{MNIC}\varepsilon_{MNIC,700} + c_{DNIC}\varepsilon_{DNIC,700}\big) \qquad (7)$$

describing the two wavelength are resulting [13]. The extinction coefficients of the two products required for evaluation are given in Table 2. The values are determined experimentally for the used wavelengths of $\lambda_1 = 470$ nm and $\lambda_2 = 700$ nm by measuring a concentration series of both products. The values are determined directly within the setup.

The layer thickness is assumed to be constant and is set equal to the respective capillary diameter of $D_h = 4$ and 5 mm. The initial light intensity I_0 is determined for both wavelengths. For this purpose, the capillary filled with the reaction solution is recorded without a bubble and an average value is determined from 10 grayscale images. With all the necessary information and values, Eqs. (6) and (7) are solved yielding the concentrations of the two products. The equations are then solved individually for each pixel within the region of interest. The resulting concentration fields are shown in Fig. 13, displaying the formation of the two products MNIC and DNIC in the wake of the bubble. Though the applied methodology it is possible to draw conclusions about the local yield and selectivity of the investigated model reaction.

The concentration fields shown in Fig. 13 indicate similar flow structures as the previous data in Fig. 12. With increasing capillary diameter the flow structure behind the bubble becomes more complex and turbulent as within the Cu(btmgp)I—oxygen system. As both systems are dissolved within an organic solvent, the similarity is therefore not unexpected. Likewise Fig. 13 shows clearly that the first product MNIC, following a rather fast kinetic of $k_{obs(MNIC)} = 5.0 \times 10^5$ s^{-1} ($T = 20$ °C), is formed directly at the bubble in both capillaries. In the further course of the flow the second product DNIC is formed in the $D_h = 4$ mm capillary (a). This means that there is still unreacted, dissolved nitrogen monoxide available in the flow, enabling the formation of the second reaction product DNIC, following a slower kinetic of $k_{obs(DNIC)} = 6.5 \times 10^{-4}$ s^{-1} ($T = 20$ °C). However, this second reaction step is not taking place within the $D_h = 5$ mm capillary. The nitrogen monoxide dissolved by the convective flow is strongly mixed immediately behind the bubble and reacts with the subsequent iron chloride almost completely. Though, only the first product

Fig. 13 Concentration gradients of the product MNIC and DNIC in the wake of a nitrogen monoxide bubble within a $D_h = 4$ mm wide capillary (**a**) and $D_h = 5$ mm wide capillary (**b**) [13]
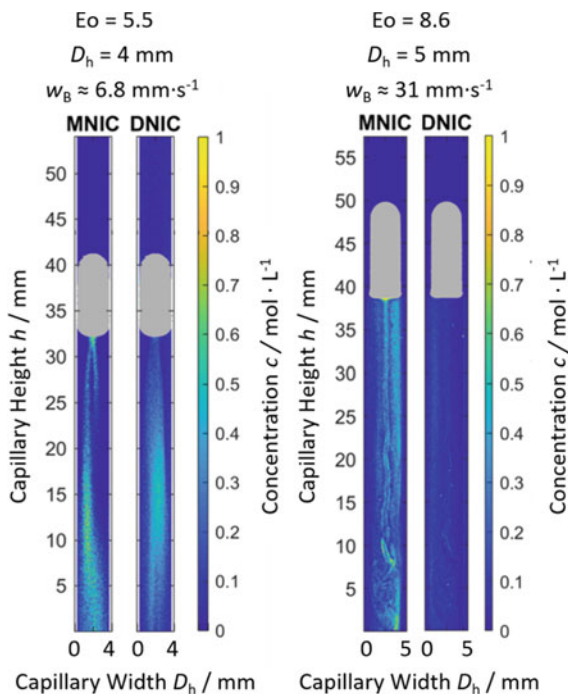
MNIC is formed and within the further course of the flow there is thus no free nitrogen monoxide available anymore, meaning that the second reaction step is almost absent. From this it can be concluded that the selectivity of this model reaction depends strongly on the mixing and its time scale in the bubble wake. If the time scale of mixing is faster than the time scale necessary for the second reaction step, as is the case with the $D_h = 5$ mm capillary, less further reaction takes place. Though, the nitrogen monoxide is mixed so quickly that it reacts almost exclusively with the fresh reaction solution. However, if the time scale of the mixing is longer than necessary for the second reaction, the second reaction step may occur as it happens within the smaller capillary. This results are in contradiction to earlier numerical investigations that found no influence of the bubble shape and wake structure on the selectivity of a competitive consecutive reaction [14].

3.5 Influence of Fluid Dynamics on Yield and Selectivity of a Competitive-Consecutive Reaction in Taylor Bubble Flow

To transfer the knowledge from a single Taylor bubble to a Taylor bubble flow, the oxidation of leuco-indigo carmine (Leuco-IC) over an intermediate form (Interm.)

Fig. 14 Redox reaction of leuco-indigo carmine to keto-indigo carmine in flask experiments. Adapted from [15]

to keto-indigo carmine (Keto-IC) is used. Two distinct color changes from yellow to red to blue occur during the oxidation (Fig. 14), which provides meaningful information regarding the selectivity of fast consecutive gas-liquid reactions. The reaction equations for the oxidation steps are as follows:

$$Leuco - IC + O_2 \rightarrow Interm. + O_2^- \tag{8}$$

$$Interm. + O_2 \rightarrow Keto - IC + O_2^- \tag{9}$$
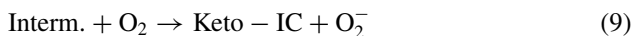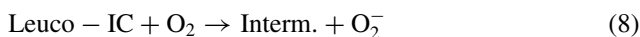
Additional information on the reaction system is provided in [7]. The local phenomena are studied in *straight* and *coiled* capillaries by acquiring and processing images and videos as described in Sect. 2.2. An exemplary frame showing the experimental concentration distribution of gas-liquid slug flow in a straight capillary is depicted in Fig. 15 for a reaction time of $t = 6$ s. The concentration distribution indicates the typical behavior of slug flow [16]. Well mixed areas, such as near the interfaces, in the channel center and near the tube wall, are quickly oxidized due to the Taylor vortices and Keto-IC is formed. Mass transfer towards the stagnant areas, between core and wall is dominated by diffusion and occurs significantly slower. In these areas the concentration of the reactant (Leuco-IC) remains higher. The intermediate species occurs in the transition region between stagnant areas and areas, where oxygen accumulates quickly due to advection. Enhancement of mass transfer at the interface due to the chemical reaction has been found negligible in a previous study [17].

These concentration distributions are acquired at a rate of $f = 50$ fps and evaluated to obtain the concentration development of the three species, which are required to calculate the conversion of Leuco-IC and the selectivity of intermediate towards
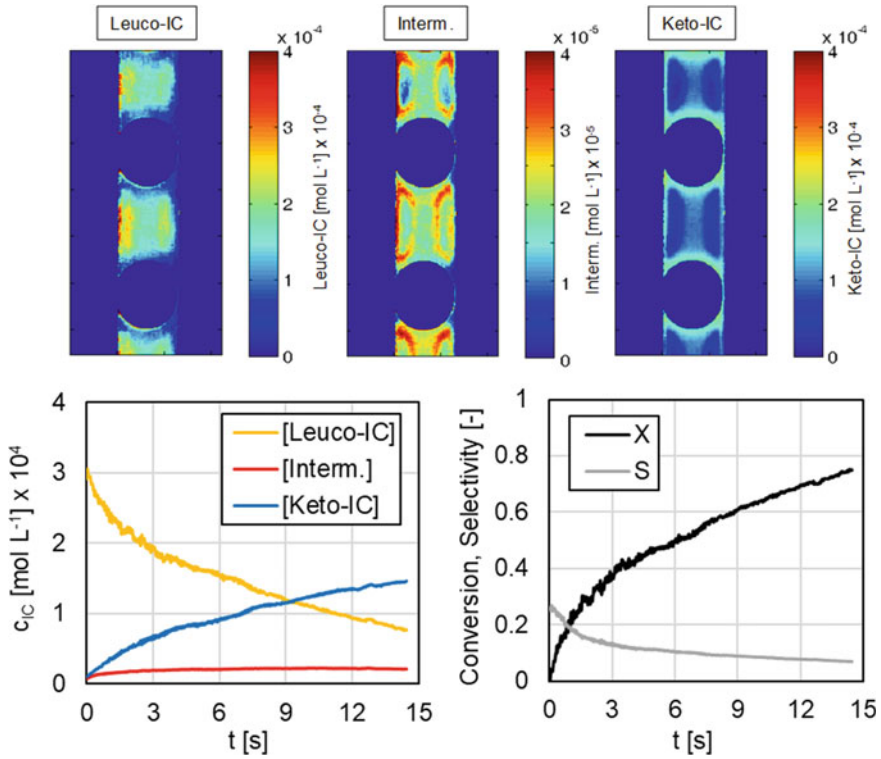
Fig. 15 Measured concentration profiles of the three indigo carmine species after $t = 6$ s reaction time (top); integrated concentration development and conversion, selectivity plot over time (bottom); total volumetric flow rate $\dot{V} = 4$ mL min^{-1} and gas/liquid ratio $= 0.5$, $Re = 48$

oxygen (Fig. 15). Concentrations are integrated over liquid slug volume and the well resolved temporal development is further used to determine the volumetric mass transfer coefficients for the investigated conditions.

The resulting mass transfer coefficients are in the range of $k_L = 0.160 - 0.554$ s^{-1}, which is comparable to data from literature [18] and underlines the quality of the data acquired by the developed measurement technique. A more detailed evaluation is described in [8] and further utilization of this data for the validation of numerical simulations is presented in Sect. 4.2 of this chapter.

Optical observations in the coiled capillary indicate that the flow patterns vary significantly depending on the investigated operating conditions. Five flow patterns are identified based on the shift of the core stream and the distribution of oxidized products (Fig. 16):

1. Stratified species distribution with product accumulation (Keto-IC) at the inner wall and reactant (Leuco-IC) at the outer wall; the core stream is deflected towards the inner tube wall
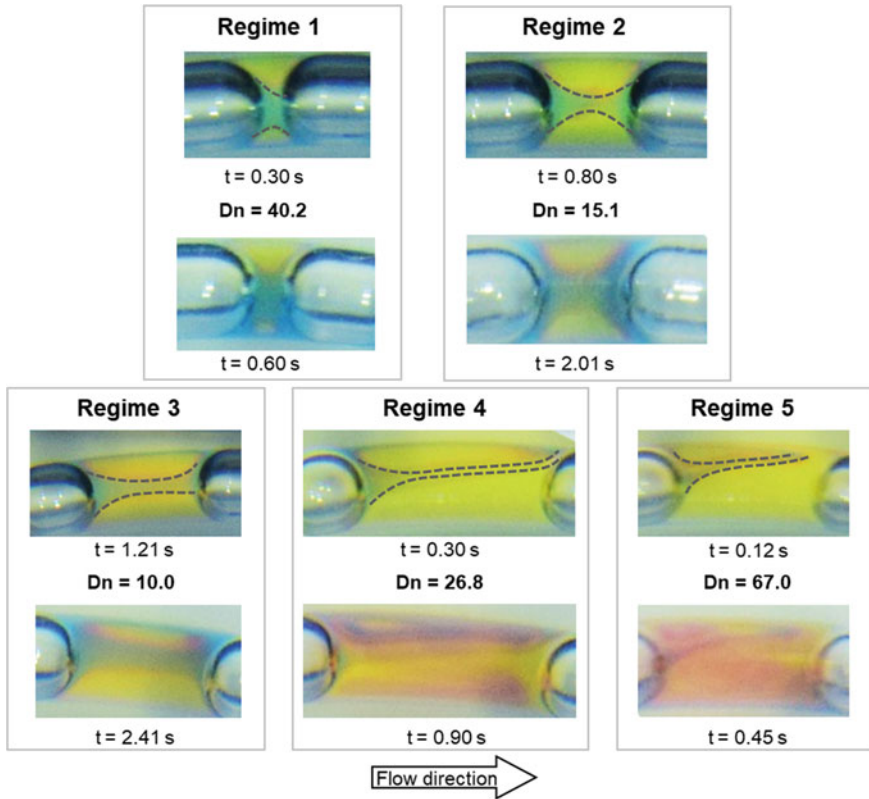
Fig. 16 Images of slug flow in a coiled capillary with inner tube diameter of $D_i = 1.6$ mm and coil diameter of $D_c = 38.2$ mm depicting the oxidation of leuco-indigo carmine by synthetic air. Five different flow regimes are shown at two different time steps

2. Transition regime between regime 1 and 3 with oxidized products in the core of the liquid phase
3. Opposite flow behavior to regime 1: stratified species distribution with product accumulation (Keto-IC) at the outer wall and reactant (Leuco-IC) at the inner wall; the core stream is deflected towards the outer wall
4. Transition regime between regime 3 and 5 with less product accumulation at the outer wall and intensified radial mixing; the core stream is deflected stronger towards the outer wall
5. Effective radial mixing with more homogeneous product distribution; the deflected core stream reaches the outer wall.

Note that regime 1 and 2 are only observed for small liquid slugs; hence, the liquid slug lengths in Fig. 16 deviate for the different flow regimes.

In order to predict the occurring flow regime and not rely on an optical evaluation, a modified Dean number Dn^* is proposed. It is derived from the mixing time scales
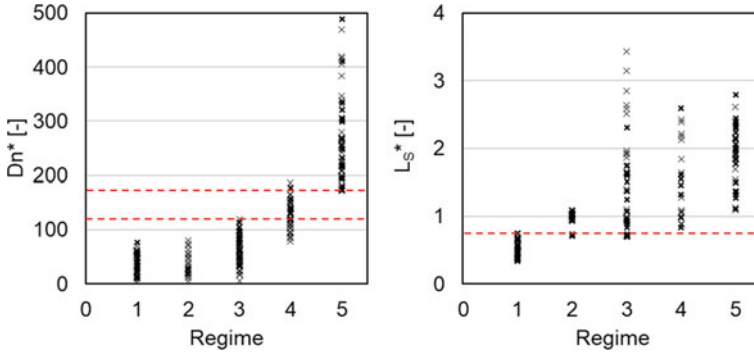
Fig. 17 Modified Dean number (left) and dimensionless slug length (right) for the five observed flow regimes of slug flow in a coiled capillary. Red lines indicate transitions between flow regimes

in axial (t_{ax}) and radial (t_{rad}) direction to describe the deflection of the core stream. Axial mixing is estimated from the length of the liquid slug L_S divided by the two-phase velocity u_{TP} and radial mixing is derived from the centrifugal acceleration over the inner tube radius r_i. Finally, the modified Dean number is expressed as product of Reynolds number and ratio of time scales of axial and radial mixing:

$$Dn^* = Re \cdot \frac{t_{ax}}{t_{rad}} = Dn \frac{\sqrt{8} \cdot L_S}{d_i} \tag{10}$$

A more thorough description of the superimposed Taylor-Dean flow and the modified Dean number is given in [17].

Plotting the modified Dean number for the different flow regimes (Fig. 17, left) reveals that the transitions between flow regimes 3, 4 and 5 are successfully captured. The transition between regime 3 and regime 4 occurs at $Dn^* = 120$ and the transition between regime 4 and 5 happens at $Dn^* = 175$, which is indicated by the red dotted lines. Regime 4 overlaps with regime 3 and 5 as it has been defined as a transition regime. Regimes 1, 2 and 3 on the other hand overlap for a wide range of operating conditions. Therefore, a different approach that is more focused on the slug length is chosen for the separation of these flow regimes. This attempt is based on the dimensionless slug length L_S^*, which is expressed as follows:

$$L_S^* = \frac{L_S}{d_i} \tag{11}$$

A plot of L_S^* for the different flow regimes is given in Fig. 17, right. The distinction of regime 1 from the other regimes is successful and indicated by the red dotted line for $L_S^* < 0.75$. Regime 2 as transition regime is observable for a narrow range of dimensionless slug lengths: $0.75 < L_S^* < 1.1$.

To summarize, it can be stated that regimes 1 and 2 are best described using the dimensionless slug length and regimes 3, 4 and 5 can be distinguished by the

proposed modified Dean number. Note that the modified Dean number increases with the length of the slug. Therefore, longer slugs tend towards regime 5, whereas shorter slugs require more effort (higher conventional Dean number Dn) to transition into regime 5 and benefit from the intensified mixing.

By means of these findings, the fluid dynamics and mixing behavior of gas-liquid slug flow can be controlled to some extent. A possible application with regard to the selectivity of a chemical reaction is discussed in the following chapter.

3.6 Influence of Fluid Dynamics on Yield and Selectivity of a Competitive Consecutive Reaction in Taylor Flow in Coiled Capillaries

The observed flow regimes in coiled capillaries (Sect. 3.5) are substantially different with regard to the distribution of oxygen and oxidized products within the liquid phase. This behavior may provide valuable information about the interplay between selectivity and hydrodynamics of gas-liquid flow. For the evaluation, selectivity of oxygen towards intermediate product is calculated according to the following equation with respect to the underlying stoichiometry (Eqs. 8 and 9):

$$S_{O_2,Int} = \frac{c_{Int}}{c_{Int} + 2 \cdot c_{KIC}} \qquad (12)$$

Concentrations of Interm. c_{Int} and Keto-IC c_{KIC} are obtained by integrating the local concentration distributions over the slug volume [7]. The selectivity S is plotted against the conversion X of reactant Leuco-IC to account for the influence of varying slug lengths and residence times when comparing the flow regimes (Fig. 18). For the selectivity over conversion plots, entire images of the first coil are processed and analyzed and the information from every liquid slug is evaluated to capture the reaction progress accurately. Note that regimes 1, 2 and 3 are grouped in Fig. 18 as their selectivity behavior is similar.

Generally, the selectivity of oxygen towards the intermediate product decreases as the conversion increases, which is expected from a consecutive reaction. Regimes 1-3 perform worse in terms of selectivity, which is related to the accumulation zones and a quick consecutive oxidation to the final product. Regime 4 as transition regime behaves very similar to regimes 1–3 and extends the trend for lower conversions. Regime 5, on the other hand, has the potential to achieve higher selectivity towards an intermediate product, also for higher conversion, but shows a more scattering trend. This is linked to the absence of an upper limit for this regime; the wide operating range could include various flow phenomena not yet considered.

Regardless, a decreasing selectivity at conversions of 10–20% is observed for all flow regimes, which is most noticeable for regime 5. This is an unusual phenomenon that highlights the interdependence of hydrodynamics and chemical reaction. In Fig. 18 two flow pictures are presented for high and low selectivity at a conversion
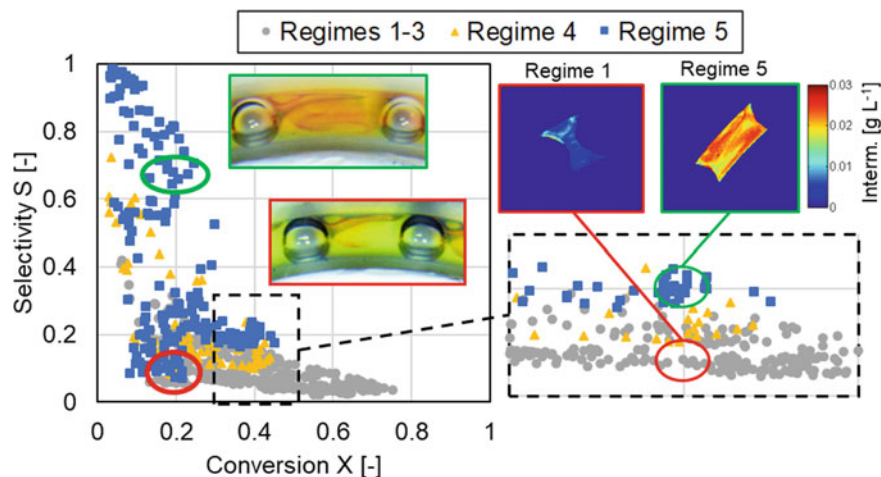
Fig. 18 Selectivity plotted against conversion for regimes 1–5 with varying total flow rates and gas/liquid ratios for gas-liquid slug flow in coiled capillaries

of 20% to explain this selectivity drop. The upper picture depicts a situation where the core stream reaches the outer wall early. Hence, radial distribution of dissolved oxygen is improved compared to the lower picture and more intermediate product is formed. In the lower picture, mainly the core stream and the recirculation zone (upper left corner) are oxidized and streamlines containing oxygen do not reach the inner half of the slug before those areas are heavily oxidized. Due to the funneling at the rear interface, streamlines forming the core stream are saturated quickly and cause this quick consecutive oxidation of Leuco-IC in the core region for all the observed flow regimes. The selectivity drop occurs at roughly 10–20% depending on the flow regime, which suggests that core and recirculation zone make up a similar volume fraction.

Focusing on the more stable area at 30–50% conversion (Fig. 18, right), the selectivity over conversion plot reveals that regime 5 leads to selectivities that are up to four times higher than for regimes 1–3, which is also indicated by the depicted concentration profiles of the intermediate product. These results demonstrate that the selectivity of gas-liquid slug flow in coiled capillaries depends drastically on the governing flow. Since the occurring flow regime can be controlled via the operating conditions (Sect. 3.5), these findings have huge potential as an additional means for process optimization in the design of microreactors.

4 Numerical Simulations of Chemical Reactions Induced by Taylor Bubbles and in Taylor Bubble Flows

4.1 Description of the Front Tracking FEM Framework

The here employed numerical framework used for the simulation of Taylor bubble flows is in details described in Chapter "Numerical Simulation Techniques for the Efficient and Accurate Treatment of Local Fluidic Transport Processes Together with Chemical Reactions" and has been already validated on the benchmark problem of the 3D rising bubble originally introduced by Adelsberger et al. [19] and also in the framework of Taylor bubble flow on the corresponding benchmark problem introduced by Marschall et al. [20]. Moreover, as a result of the respective validation studies both of these multiphase flow benchmark problems have been updated—up to the best knowledge of the authors—with the most accurate benchmark results [21]. For the sake of brevity, let us summarize only the main features of the developed numerical framework. The core component of the underlying simulation tool is a Finite Element Method (FEM) based flow solver FeatFlow [22] taking advantage of higher order isoparametric Q_2/P_1 basis functions. The employed non-stationary flow solver is following a Pressure Schur Complement technique in order to decouple the solution of the arising velocity and pressure systems. Due to the employed Arbitrary Lagrangian-Eulerian (ALE) front tracking technique the computational mesh needs to be always aligned with the gas/liquid interface which results in a mesh movement governed by an additional PDE for the displacement discretized by Q_1 FEM. The driving force for the mesh movement is subjected to the updated displacement of the gas/liquid interface nodal values, which therefore serve as boundary condition to the discretized mesh deformation equation. As a benefit of the adopted ALE technique (and alignment of the computational mesh with the interface), the interfacial tension force term can be introduced in the framework of the Laplace-Beltrami operator as a surface integral on the interface according to a semi-implicit realization originally proposed by Hysing [23]. This realization theoretically relaxes the capillary time-step restriction and allows for the use of relatively larger timestep values, however due to the employed ALE framework the here adopted temporal discretization is a related to a first order Backward Euler method thus still restricting the time step sizes. Nevertheless, the use of the isoparametric Q_2 basis functions at the interface aligned elements together with the Laplace-Beltrami transformation of the interfacial tension is the key feature being responsible for the overall high order accuracy of the developed numerical scheme [21]. The solution of the arising linear problems is accelerated (1) by the use of geometrical multigrid solvers and (2) by the use of domain-decomposition based parallelization method allowing a reasonable scaling of the computations up to a few hundreds of cores on the used LiDo computational cluster nodes.

The simulation of the additional system of PDEs related to the transport of species—discretized by Q_1 FEM—with chemical reaction exploits the large difference of time-scales related to the *fast* flow and *slow* transport of species. Accordingly,

the system of transport of species is decoupled from the flow solver and is computed after determining the steady state flow field (the existence of which is restricted to the underlying process parameters) which is used for the construction of the corresponding convection terms. The adopted flow/species transport decoupling technique allows for the use of different computational meshes for the two separated subsystems making it possible to use substantially finer computational meshes with additional boundary layers along the gas/liquid interfaces. Since, the resulting flux of the oxygen species from the bubble volume through the interface is negligible in the analyzed time intervals, the bubble volume was excluded from the specie-transport simulations and its presence was reflected only by the corresponding boundary concentrations by prescribing the equilibrium concentration of oxygen according to Henrys law. All other species were treated by a zero-flux boundary condition on the bubble surface. Interpolation of the velocity solution from the flow solution onto the specie-transport mesh was performed in the framework of an L_2 projection which due to the employed algebraic flux-correction method [24] guaranties conservation on the discrete level and offers the use of a high-resolution non-oscillatory numerical scheme. The reaction terms (representing the transport of species in the dimension of species) were treated in an operator splitting approach according to which a system of ODEs has been computed at each time step for each node of the computational mesh, independently from each other. For this purpose the numerical method and particular implementation of [25] has been used which takes place after the PDE based transportation of species in the physical space due to diffusion and convection.

4.2 Numerical Simulation of Large Taylor Bubbles with Chemical Reaction

According to the above given numerical description a validation study based on experimental results [10] has been performed. Since the here analyzed system refers to a rather complex multiphase flow problem which in addition is addressed by a large set of parameters, the precision of which might be subjected to different extent of prediction (i.e. measurement) errors, it was necessary to carry out sensitivity analysis of some critical parameters. From the geometrical point of view the setup is defined by a straight capillary of diameter d_c filled with acetonitrile as liquid phase entrapping a bubble of air of a specified volume V_g. The computationally considered capillary length L_c was chosen in a way to eliminate its influence on the resulting bubble shape and flow structures surrounding the bubble. The initial bubble centers were chosen to be in the vicinity of the geometrical center of the capillaries and due to the employed reference frame transformation—calibrated against the center of mass of the considered bubbles—remained at the chosen position. The above listed geometrical parameter values for the here considered two cases are summarized in Table 3.

Table 3 Summary of geometrical parameter defining the two Taylor bubble simulation cases

d_c (mm)	V_g (mm^3)	L_c (mm)	L_b (mm)	δ_f (µm)	$v_{b,exp}$ (mm s^{-1})	$v_{b,sim}$ (mm s^{-1})
4.0	88.0	18.0	1.966	34.5	~3.0	2.28
5.0	118.5	16.5	2.410	89.7	~20.0	18.7

d_c stands for the capillary diameter, V_g computationally determined bubble volume, L_c is the considered length of the capillary, L_b is the axial length of the bubble, δ_f is the minimum film thickness between the bubble interface and the capillary wall. $v_{b,\text{exp}}$ and $v_{b,sim}$ stand for the experimentally and computationally determined bubble rise velocities

The experimentally measured validation data comprises a point-segmentation of the bubble interface and a rise velocity $v_{b,\text{exp}}$ of the bubble, both measured under 'pseudo steady state' conditions. It has to noted, that the volume of the bubble in the experiment is monotonically decreasing due to the underlying chemical reaction which is consuming the oxygen species from the bubble. However, due to the different timescales of reaction and hydrodynamics a concept of a pseudo steady state could have been adopted for performing the numerical simulations. The experimentally recorded segmentation of the bubble surface is displayed in Fig. 19 and the bubble rise velocities are listed in Table 3. The set of adopted physical properties for the corresponding liquid and gas phase are listed in Table 4. The imposed boundary conditions of the numerical simulations are chosen as *no slip* boundary conditions on all surfaces, which in light of the adopted reference frame transformation affects only the axial velocity component, which is assigned during the non-stationary course of simulation to the negative bubble rise velocity $v_{b,sim}$.

The bubble interface during the fluid flow simulation undergoes dramatic changes, which is mainly depending on the initial bubble shape and reaches steady state (for the considered relatively small capillary diameters) where the buoyancy force finds equilibrium with the surface tension- and hydrodynamical forces. Temporal oscillations in the bubble shape (length, diameter) such as rise velocity are occurring and are more pronounced for the larger capillary diameter case. Typical evolution of the computationally recorded rise velocities for the considered cases are displayed in Fig. 19 (upper subfigures). The graphical representations of the rise velocities show the sensitivity of the results with respect to a $T = 21$ °C temperature difference change (from $T = 0$ °C to 21 °C) causing the resulting change of the viscosity of the liquid phase from $\mu_l = 0.48$ mPas to $\mu_l = 0.37$ mPas [26] which clearly approaches the experimentally measured bubble rise velocity for the experimentally recorded temperature of $T = 21$ °C. As it can be seen from the corresponding evolution of the bubble rise velocities the bubble reaches its nearly steady state (in the reference frame) in relatively very short time which is in both cases less than a second. From this point on the bubble shape also does not experience any movement any more what made it possible to extract the bubble surface and compare it with the experimentally captured and segmented data [10]. This comparison is visible in the lower subfigures of Fig. 19. As it can be seen from the figure, the agreement in this regards is even closer than for the rise velocities, only minimal differences are visible at the front side
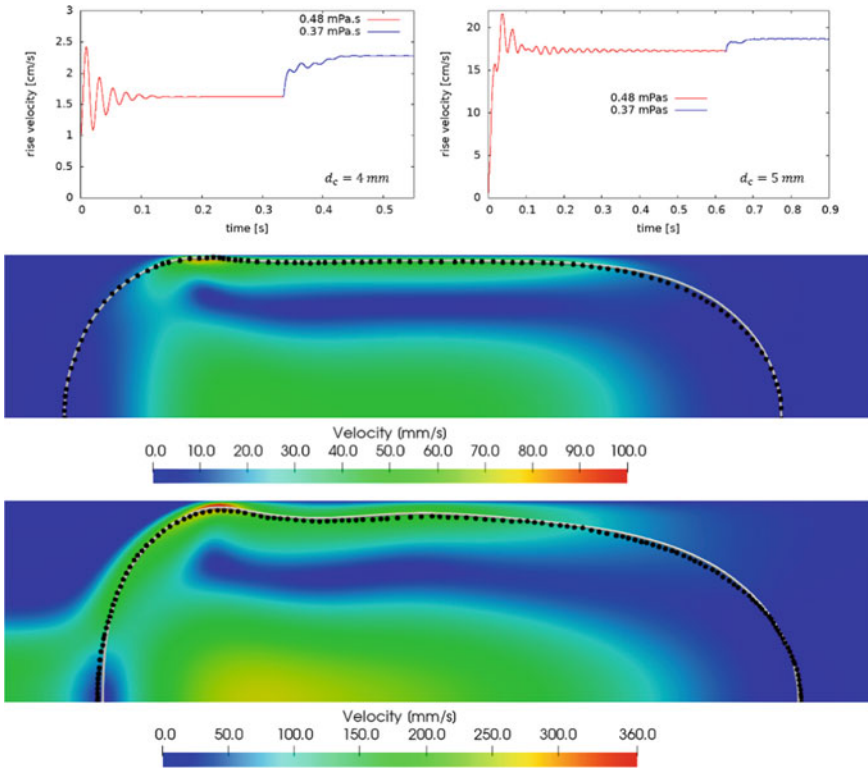
Fig. 19 Upper subfigures correspond to the time-evolution of bubble rise velocity for the 4.0 mm capillary (left) and for the 5.0 mm (right) capillary configuration, respectively. The lower two subfigures display the experimentally measured interface segmentation (black dots) for the 4.0 mm capillary (top) and for the 5.0 mm (bottom) capillary configuration, and the grey contour represents the computationally obtained interface reconstruction, respectively. The colorscale corresponds to the distribution of velocity magnitude

Table 4 Summary of physical parameter defining the two Taylor bubble simulation cases

μ_l (Pa s)	μ_g (Pa s)	ρ_l (kg m^{-3})	ρ_g (kg m^{-3})	$\sigma_{l/g}$ (N m^{-1})
0.48×10^{-3}	1.80×10^{-5}	780.0	1.3	0.0290

μ_l and μ_g represent the viscosity of liquid and gas phase, ρ_l and ρ_g stand for the density of the liquid and gas phase and $\sigma_{g/l}$ is the interfacial tension between the corresponding liquid/gas phases

of the bubble, but the wavy shape along the side of the bubble matches in an excellent manner for both capillary sizes. This implies also an accurate prediction of the thin film layer being squeezed between the bubble and the capillary, The corresponding minimal film thicknesses are on the order of $\delta = 0.0345$ mm and $\delta = 0.0897$ mm for the 4.0 mm and 5.0 mm capillary cases.
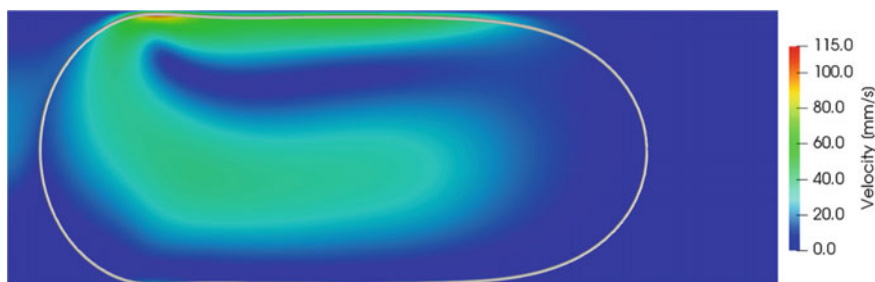
Fig. 20 Computationally obtained interface segmentation for the 1° inclination difference configuration. The colorscale corresponds to the distribution of velocity magnitude

Due to the related differences of the bubble rise velocities (especially for the 4.0 mm capillary case) investigation of other (aside of the already mentioned temperature adjustment) physically relevant sources have been performed. Since in the experimental setup and the resulting measurement data have been identified patterns questioning the presence of a perfectly axisymmetric realization, the consequences of such a geometrical realization have computationally also been analyzed. In this regards, geometrical setups with inclination differences of 1°, 2° and 4° (from the perfectly vertical realization) have been analyzed by the help of correspondingly rotated gravitational fields and the rise velocities of 1.7 mm/s, 2.1 mm/s and 3.0 mm/s have been estimated, which confirmed the experimentally found observation showing increasing rise velocities for increasing inclination angle differences [10]. Interestingly, the resulting change of the bubble shape shows only negligible deviation from the perfectly vertical realization (see Fig. 20 showing simulation results of a 1° inclination angle difference), only the bubble itself is located more eccentric, and therefore the thickness of the liquid film between the bubble and the capillary varies in a larger extent along the circumferential direction. This allows the bubble to travel faster in a realization attributed to a larger inclination angle difference. Even so, the internal recirculation inside of the bubble and along the bubble in the liquid is very similar already for small inclination angle differences (see Fig. 20). Since, experimental measurements were performed with a precision of $\pm 1°$ it might be indeed the reason for the additionally gained rising speed of the experimentally observed bubble with respect to its computational counterpart. This means, that already for small inclination angle differences the bubble might have travelled faster and might have exhibited sensibly large deviations of flow patterns from an axisymmetric flow.

The obtained results corresponding to the hydrodynamics have been further used in the framework of simulations of chemical reactions corresponding to the Cu^I/O_2 chemical reaction system according to Schurr [12] undergoing a consecutive reaction mechanism. Thanks to the optical activity of the intermediate product Cu^{III} species, the experimental observation of its distribution was enabled and therefore was recorded, as it is visible in Fig. 21 (left). By using the reaction orders and constants—characterizing these 2 chemical reactions—found experimentally [12]
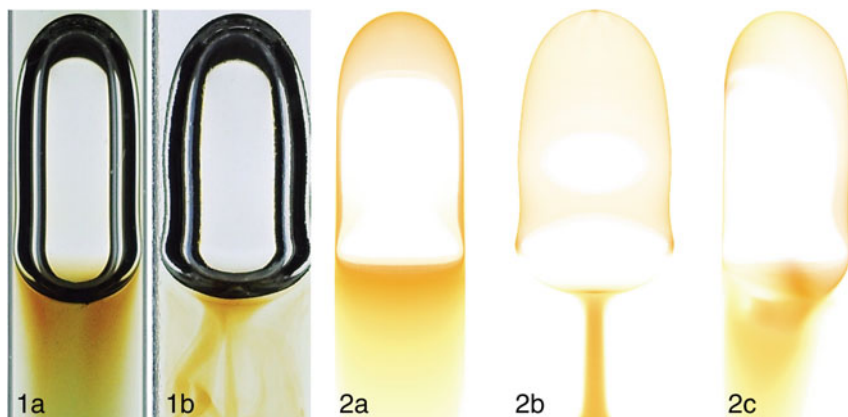
Fig. 21 Comparison of the experimentally measured concentration distributions of the intermediate Cu^{III} species (1a and 1b for the 4.0 mm and 5.0 mm capillary cases [10]) with respect to the computationally obtained steady state concentration distributions (2a and 2b for the 4.0 mm and 5.0 mm capillary cases). 2c displays the concentration distribution of Cu^{III} species for the 1° inclination difference configuration from the most un-symmetric view perspective for the 4.0 mm capillary diameter case

and computationally (Chapter "Numerical Simulation Techniques for the Efficient and Accurate Treatment of Local Fluidic Transport Processes together with Chemical Reactions")—the corresponding simulations of transport of species with chemical reactions have been performed and compared to the experimentally recorded images. The compilation of the obtained computational data is displayed in Fig. 21, which shows the pattern of the monitored species Cu^{III} in a very good agreement for both capillary size cases with the experiment. Unfortunately, the experimentally recorded distribution of the Cu^{III} species are due to the interface refractions not clearly visible in a close vicinity to the interface, therefore the comparisons can be done only in the bubble wake, which however shows very similar features of the computational predictions to the experimental images. In addition, the simulation result for the 1° inclination angle difference is also included showing the distribution of Cu^{III} species from the most un-symmetric view perspective for the 4.0 mm capillary size case. Inspecting this simulation result (for the 4.0 mm capillary) from a 90°-rotated perspective, however, shows an optically almost undistinguishably similar distribution as for the perfectly vertical configuration. Nevertheless, the simulation results obtained for the 4.0 mm diameter capillary clearly show the influence of an already slight inclination angle on the flow structures and therefore, also on the underlying chemical reaction. This influence might be the necessary component for breaking the perfectly axisymmetric flowstructures into the experimentally recorded non-axisymmetric performance for the 5.0 mm capillary case, which is therefore expected to break up the thin Cu^{III} stream into a wavy ribbon flow structure, as shown in the corresponding experimental subpicture 1b of Fig. 21. Therefore, the analysis concerning the inclination angle for the 5.0 mm capillary shall be subjected to future work.

Finally, it also has to be noted that the timescale corresponding to the achievement of the here presented nearly steady state concentration distributions were on the order of ≈ 5.0 s which is roughly an order larger than the timescale needed for the achievement of steady state of the hydrodynamics simulation. Therefore, the here adopted decoupling of hydrodynamics and transport of species has been justified.

4.3 Numerical Simulation of Taylor Flows with Chemical Reaction in Straight Capillaries

In this subchapter an insight into a study combining experimental and numerical techniques for a chemically reacting Taylor bubble flow is provided. The description of the experimental setup is described in Sect. 2.2 and the description of the corresponding numerical components used for the simulations are given in Sect. 2 in Chapter "Numerical Simulation Techniques for the Efficient and Accurate Treatment of Local Fluidic Transport Processes together with Chemical Reactions". From the numerical point of view, the here considered problem is very similar to the large Taylor bubble problem described in Sect. 4.1 with the difference of certain geometrical and physical parameters which are summarized in Table 5.

Moreover, the chemical reaction network corresponds to a competitive consecutive reaction system, which is represented by the following reaction scheme:

$$A + B \xrightarrow{k_1} C$$
$$A + C \xrightarrow{k_2} D$$
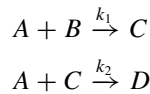
Table 5 Summary of geometrical and physical parameters defining the computational setup of the Taylor bubble flow

Geometrical parameters		Physical parameters	
Capillary diameter	1.6000 mm	Liquid viscosity	1.15×10^{-3} Pa s
Periodic length	3.6000 mm	Gas viscosity	1.8×10^{-5} Pa s
Bubble diameter	1.5576 mm	Liquid density	1015 kg m^{-3}
Bubble length	1.5617 mm	Gas density	1.200 kg m^{-3}
Bubble volume	0.49626 mm^3	Interfacial tension	68.9×10^{-3} N m^{-1}
Bubble surface area	1.9097 mm^2	Pressure gradient	11.94×10^{-3} bar m^{-1}
Film thickness	0.02119 mm	Bubble velocity	34.66×10^{-3} m s^{-1}

In the above equation (A) refers to the dissolved O_2 species in the liquid phase, (B, C, D) refer to the corresponding oxidation species of the leuco-indigo carmine reaction system (see Sect. 3.5) and k_1 and k_2 are the reaction constants determining the speed of the reaction rates r_1 and r_2 which are defined as follows:

$$r_1 = k_1 c_A c_B \quad \text{and} \quad r_2 = k_2 c_A c_c$$

The above defined reaction rates refer to a first order reaction mechanism with respect to both reactants in both chemical reactions. The values of the reaction constants have been experimentally determined in [17] as $k_1 = 6.35 \times 10 \, \text{L mol}^{-1} \text{s}^{-1}$ and $k_2 = 22.41 \times 10^5 \, \text{L mol}^{-1} \text{s}^{-1}$ and therefore were used for the primary numerical simulations and in the next step have been varied in order to find an agreement with the experimentally recorded concentration evolution of species. The particular realization of the numerical simulations from the point of view of the imposed boundary conditions is related to an assumption of periodicity along the capillary axis. The adopted assumption is fully justified concerning the flow field of a sample pair of bubble/slug—especially far downstream of the capillary—which is achieved by imposition of a simple periodic boundary condition for velocity but a periodic boundary condition with a jump for the pressure. The value of the jump corresponds to a $\frac{dp}{dx}$ pressure gradient, the value of which was iteratively found by enforcing the required flow rate through the capillary. It has to be noted that the adopted periodicity assumption (without concentration jump) imposed for the species concentration corresponds to slightly different realization of the problem than the real experimental setup. The difference between the two counterparts is that in the numerically reconstructed representation an infinite chain of bubble/slug units is considered to be travelling in time, where all these units have initially the same concentration distribution of species; and in the experiment each bubble/slug unit starts at the beginning of the capillary with the same initial concentration distribution and travel in space through the capillary. The similarity of these two representations are closest to each other under the condition that the exchange of species is as small as possible between the individual liquid slugs, which is roughly fulfilled due to the small liquid film thickness between the bubble and the wall of the capillary. An additional remark concerning the evaluation of the simulation results has to be stated and that is related to a conversion of the 3D simulation results to an equivalent representation captured by the corresponding experimental method. According to this equivalent representation, the 3D numerical results have been projected according to a "capillary-depth averaging" technique to a 2D representation which is fundamentally equivalent to the experimentally recorded optical exposition of species concentration through the capillary volume.

In Fig. 22 experimental and simulated concentration profiles of the three different indigo carmine species are compared for a volumetric flow rate of $\dot{V}_L = 4 \, \text{mL min}^{-1}$ and gas/liquid ratios of 0.5 and 0.33 for reaction times $t = 3$ s and 6 s. A complete comparison for the entire recorded time is presented in [8]. Note that the intermediate is shown on a scale one order of magnitude smaller.
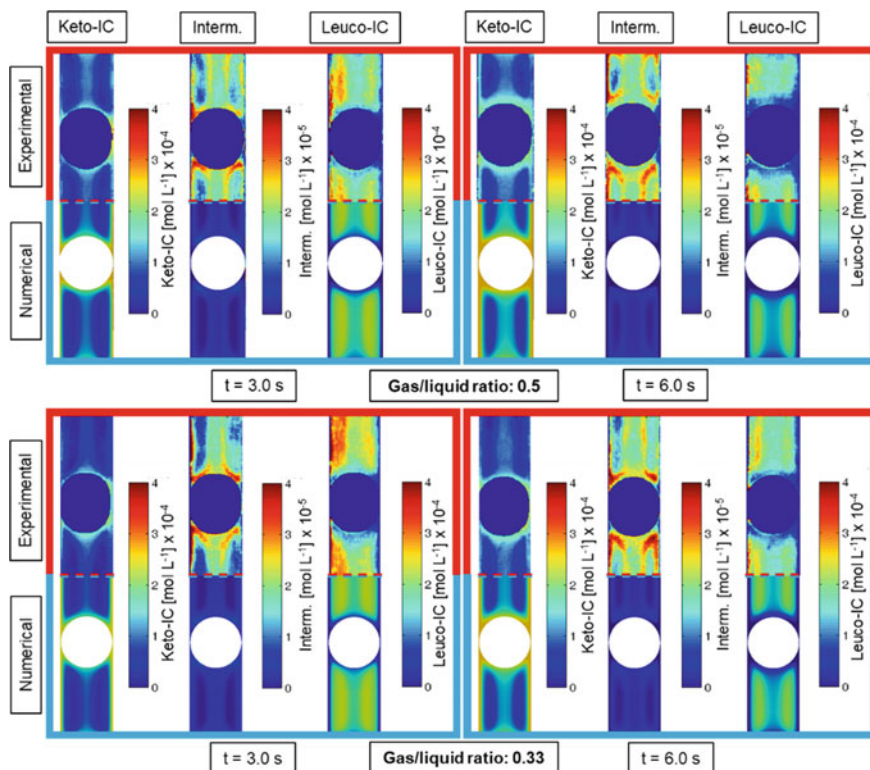
Fig. 22 Experimental and numerical concentration profiles of the three indigo carmine species at reaction times $t = 3.0$ s and $t = 6.0$ s. Total volumetric flow rate $\dot{V}_L = 4$ mL min^{-1}, gas/liquid ratios $= 0.5$ and 0.33, $Re = 48$ [8]

Both, the experimental and numerical results, describe the expected concentration profiles well, i.e. Keto-IC in the core stream, near the interface and the tube wall, and annular intermediate peaks in the transition zone between advection and diffusion dominated areas. The dynamics, which are seen in the experiments, are accurately captured by the simulations. In particular, the width of the core stream and the shape and thickness of the 'rings' containing the intermediate product are in good agreement between simulation and experiment. A quantitative comparison with integrated concentrations over liquid slug volume is given in Fig. 23 for the three indigo carmine species.

As the reaction progresses, Leuco-IC is consumed and the completely oxidized product Keto-IC is formed, while the intermediate remains at a low concentration level. The concentration profiles in the numerical simulations predict a slightly faster consumption of Leuco-IC and formation of Keto-IC. This deviation is related to the image processing routine that masks areas near the bubble interface, which mainly consist of oxidized products. Therefore, these areas cannot be included in the integrated concentration values leading to the described mismatch.
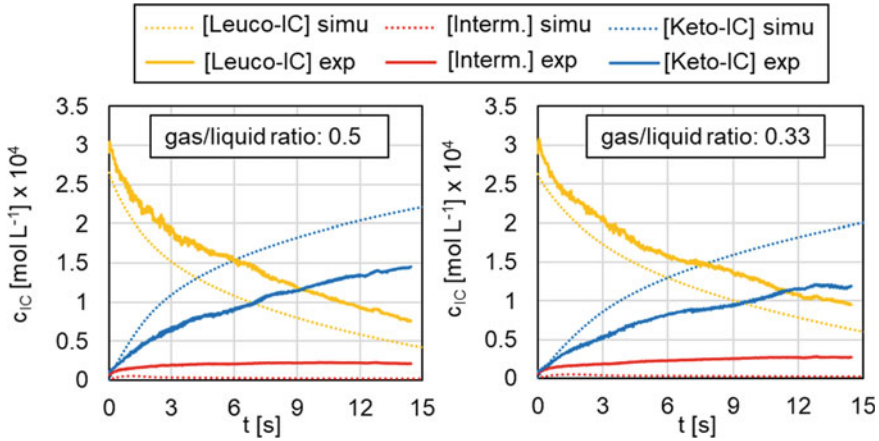
Fig. 23 Concentration development of the three indigo carmine species for a total volumetric flow rate of $\dot{V}_L = 4$ mL min^{-1} and gas/liquid ratios of 0.5 (left) and 0.33 (right). Solid lines indicate experimental and dotted lines simulated results [8]

However, the deviation for the intermediate concentration cannot be explained this way and is either related to numerical diffusion, non-ideal flow behavior in the experiments, inaccurate kinetic constants or a combination of these effects. Hence, another attempt with an adapted reaction constant for the second reaction is conducted that provides intermediate concentrations more similar to the experimental ones (Fig. 24), while barely affecting the other two species.

This proves that gas-liquid slug flow with a consecutive chemical reaction can be successfully simulated with the employed numerical methods. The dynamics of the flow are captured with high accuracy and the modelling of mass transfer with chemical reaction will be sharpened in future to resolve the intermediate concentration front even better. In a next step, the numerical methods will be transferred to more
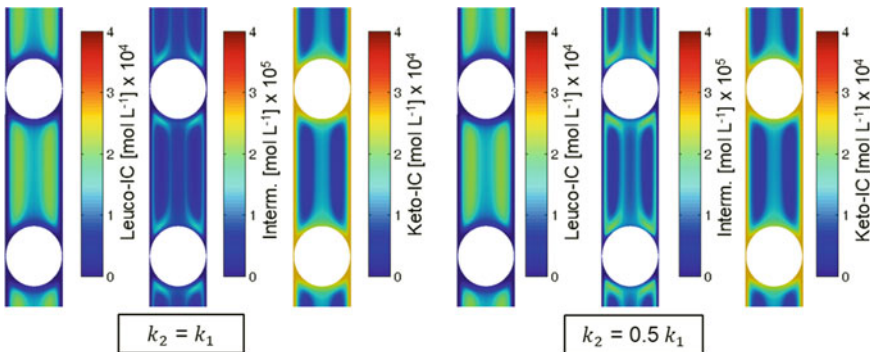

Fig. 24 Simulated concentration profiles of the three indigo carmine species after 6 s reaction time: (left) $k_2 = k_1$; (right) $k_2 = 0.5 \, k_1$ [8]

complex reactor geometries providing an important tool to find optimized process windows with improved mass transfer and chemical selectivity.

5　Conclusion

Within this chapter it has been shown, that Taylor bubbles are well suited, to study the influence of fluid dynamics on chemical reactions in detail, experimentally and numerically. The chemical reaction systems, that have been developed for this purpose are easy and cheap available and can be treated without deep expertise in chemistry. For the analytics, visual observations or UV/VIS imaging as well as common spectroscopic measurements can be utilized. The Taylor bubble benchmark experimental setup can be used for industrial relevant chemical reactions as well to proof their sensitivity concerning the influence of fluid dynamics on yield and selectivity. This has been shown with different competitive-consecutive reactions. For the numerical simulations the Arbitrary Lagrangian-Eulerian (ALE) front tracking technique has been used in a FEM framework to enable a high resolution of the interface and boundary layers and to track the concentration distribution in the vicinity of the Taylor bubbles. The interplay of mass transfer, hydrodynamics and chemical reaction could be successfully shown in agreement between experimental results and numerical simulations. Furthermore the experimental results for a competitive-consecutive reaction show, that the local fluid dynamics especially in the wake of a Taylor bubble or within the liquid slug in a Taylor flow can significantly affect the selectivity.

References

1. Kastens S, Hosoda S, Schlüter M, Tomiyama A (2015) Mass transfer from single Taylor Bubbles in minichannels. Chem Eng Technol 38:1925–1932. https://doi.org/10.1002/ceat.201500065
2. Kameke AV, Kastens S, Rüttinger S, Herres-Pawlis S, Schlüter M (2019) How coherent structures dominate the residence time in a bubble wake: an experimental example. Chem Eng Sci 207:317–326. https://doi.org/10.1016/j.ces.2019.06.033
3. Compart C (2017) Design of an experimental setup for the analysis of mass transfer on reactive Taylor-Bubbles, Masterthesis, Hamburg University of Technology
4. Kastens S, Timmermann J, Strassl F, Rampmaier RF, Hoffmann A, Herres-Pawlis S, Schlüter M (2017) Test system for the investigation of reactive Taylor Bubbles. Chem Eng Technol 40:1494–1501. https://doi.org/10.1002/ceat.201700047
5. Hayashi K, Hosoda S, Tryggvason, G, Tomiyama A (2014) Effect of shape oscillation on mass transfer from a Taylor bubble. Int J Multiph Flow 58:236–245

6. Meyer C, Hoffmann M, Schlüter M (2014) Micro-PIV analysis of gas–liquid Taylor flow in a vertical oriented square shaped fluidic channel. Int J Multiph Flow 67:140–148. https://doi.org/10.1016/j.ijmultiphaseflow.2014.07.004

7. Krieger W, Lamsfuß J, Zhang W, Kockmann N (2017) Local mass transfer phenomena and chemical selectivity of gas-liquid reactions in capillaries. Chem Eng Technol 40:2134–2143. https://doi.org/10.1002/ceat.201700420

8. Krieger W, Bayraktar E, Mierka O, Kaiser L, Dinter R, Hennekes J, Turek S, Kockmann N (2020) Arduino-based slider setup for gas–liquid mass transfer investigations: experiments and CFD simulations. AIChE J 66:e16953. https://doi.org/10.1002/aic.16953

9. Mizutani Y, Tomiyama A, Hosokawa S, Sou A, Kudo Y, Mishima K (2007) Two-phase flow patterns in a four by four rod bundle. J Nucl Sci Technol 44:894–901. https://doi.org/10.1080/18811248.2007.9711327

10. Timmermann J (2018) Experimental analysis of fast reactions in gas-liquid flows. Ph.D. thesis, TU Hamburg, Cuvillier Verlag Göttingen

11. Strassl F, Timmermann J, Schlüter M, Herres-Pawlis S (2016) Kinetik der Sauerstoffaktivierung. GIT Labor Fachz 9:39–41

12. Schurr D, Strassl F, Liebhäuser P, Rinke G, Dittmeyer R, Herres-Pawlis S (2016) Decay kinetics of sensitive bioinorganic species in a SuperFocus mixer at ambient conditions. React Chem Eng 1:485–493. https://doi.org/10.1039/C6RE00119J

13. Kexel F, von Kameke A, Oßberger M, Hoffmann M, Klüfers P, Schlüter M (2021) Bildgebende UV-VIS Spektroskopie zur Untersuchung des Einflusses der Fluiddynamik auf die Selektivität und Ausbeute von schnellen konkurrierenden konsekutiven gas-flüssig Reaktionen. Chem Ing Tech 93(1–2):1–10

14. Khinast JG, Koynov AA, Leib TM (2003) Reactive mass transfer at gas–liquid interfaces: impact of micro-scale fluid dynamics on yield and selectivity of liquid-phase cyclohexane oxidation. Chem Eng Sci 58:3961–3971. https://doi.org/10.1016/S0009-2509(03)00311-7

15. Sousa MM, Miguel C, Rodrigues I, Parola AJ, Pina F, Seixas de Melo JS, Melo MJ (2008) A photochemical study on the blue dye indigo: from solution to ancient Andean textiles. Photochem Photobiol Sci 7:1353. https://doi.org/10.1039/b809578g

16. Dittmar I, Ehrhard P (2013) Numerische Untersuchung einer Flüssig/flüssig-Pfropfenströmung in einem Mikrokapillarreaktor. Chem Ing Tech 85(10):1612–1618. https://doi.org/10.1002/cite.201200141

17. Krieger W, Hörbelt M, Schuster S, Hennekes J, Kockmann N (2019) Kinetic study of Leuco-Indigo carmine oxidation and investigation of Taylor and Dean flow superposition in a coiled flow inverter. Chem Eng Technol 42:2052–2060. https://doi.org/10.1002/ceat.201800753

18. Wang K, Luo G (2017) Microflow extraction: a review of recent development. Chem Eng Sci 169:18–33. https://doi.org/10.1016/j.ces.2016.10.025

19. Adelsberger J, Esser P, Griebel M, Groß S, Klitz M, Rüttgers A (2014) 3D incompressible two-phase flow benchmark computations for rising droplets, Proceedings of the 11th World Congress on Computational Mechanics (WCCM XI), Barcelona

20. Marschall H, Boden S, Lehrenfeld C, Falconi DCJ, Hampel U, Reusken A, Wörner M, Bothe D (2014) Validation of interface capturing and tracking techniques with different surface tension treatments against a Taylor bubble benchmark problem. Comput Fluids 102:336–352. https://doi.org/10.1016/j.compfluid.2014.06.030

21. Turek S, Mierka O, Bäumler K (2019) Numerical benchmarking for 3D multiphase flow: new results for a rising bubble. In: Numerical Mathematics and Advanced Applications ENUMATH 2017. Lecture notes in computational science and engineering, vol 126. Springer. https://doi.org/10.1007/978-3-319-96415-7_54

22. FeatFlow Homepage, www.featflow.de, version from July 2020

23. Hysing S (2007) Numerical simulation of immiscible fluids with FEM level set techniques. Ph.D. thesis, University of Dortmund, Dortmund

24. Kuzmin D, Turek S (2004) High-resolution FEM-TVD schemes based on a fully multi-dimensional flux limiter. J Comput Phys 198:131–158. https://doi.org/10.1016/j.jcp.2004.01.015

25. Shampine LF, Gordon MK (1975) Computer solution of ordinary differential equation. In: The initial value problem, Freeman, San Francisco
26. Dortmund Data Bank (2020) http://unifac.ddbst.de/en/EED/PCP/VIS_C3.php

Chemical Reactions at Freely Ascending Single Bubbles

Lutz Böhm, David Merker, Florian Strassl, Sonja Herres-Pawlis, Martin Oßberger, Peter Klüfers, Siegfried Schindler, Jajnabalkya Guhathakurta, Daniel Grottke, Sven Simon, Günter Rinke, Mark Hlawitschka, Alexandra von Kameke, Felix Kexel, Michael Schlüter, Sebastian Gast, Ute Tuttlies, Ulrich Nieken, Dennis Hillenbrand, Holger Marschall, Andre Weiner, Dieter Bothe, and Matthias Kraume

Abstract A joint approach of chemists, mathematicians and engineers in the field of chemical reaction enhanced gas-liquid mass transfer on single bubbles is presented. New chemical systems are developed for homogenous chemical reactions in the liquid. By applying different metal-complex based reaction systems with diverse ligands in different reaction media (water and organic solvents) a broad range of reaction kinetics is available. As one measure, the bubble size change over time

L. Böhm (✉) · D. Merker · M. Kraume
Technische Universität Berlin, Chair of Chemical and Process Engineering, ACK7,
Ackerstrasse 76, 13355 Berlin, Germany
e-mail: lutz.boehm@tu-berlin.de

F. Strassl · S. Herres-Pawlis
RWTH Aachen University, Institute of Inorganic Chemistry, Landoltweg 1, 52056 Aachen,
Germany

M. Oßberger · P. Klüfers
LMU München, Department Chemie, Butenandtstraße 5-13, 81377 Munich, Germany

S. Schindler
Justus-Liebig University Gießen, Institute of Inorganic and Analytical Chemistry,
Heinrich-Buff-Ring 17, 35392 Gießen, Germany

J. Guhathakurta · D. Grottke · S. Simon
Universität Stuttgart, Institute for Parallel and Distributed Systems, Universitätsstr. 38,
70569 Stuttgart, Germany

G. Rinke
Karlsruhe Institute of Technology, Institute for Micro Process Engineering,
Hermann-von-Helmholtz-Platz 1, 76344 Eggenstein-Leopoldshafen, Germany

M. Hlawitschka
Institute of Process Engineering, JKU Linz, 4040 Linz, Austria

A. von Kameke · F. Kexel · M. Schlüter
Hamburg University of Technology, Institute of Multiphase Flows, Eißendorfer Strasse 38,
21073 Hamburg, Germany

S. Gast · U. Tuttlies · U. Nieken
University of Stuttgart, Institute of Chemical Process Engineering, Böblinger Str. 78,
70199 Stuttgart, Germany

is investigated. The shrinking of the bubble allows the determination of overall mass transfer rates under diverse conditions. Numerous groups investigated the wake region of the bubble. The influence of the mixing behavior in this region on the mass transfer in general but also, e.g., on competitive consecutive chemical reactions is visualized. For a deeper understanding of the effect of surfactants on mass transfer, simulations are performed providing a high temporal and spatial resolution of the flow and concentration field near the bubbles surface. Furthermore, a compartment model for the description of the mass transfer near a single bubble is developed which allows the calculation of competitive consecutive chemical reactions with reasonable numerical effort.

1 Mass Transfer from Single Bubbles

The description of mass transfer in multiphase systems is a topic still dominated by either analytical approaches containing numerous simplifications (e.g., two film theory [1]) or correlations which are several decades old (for an overview, see, e.g., [2]). While the simplifications and the sheer age of the correlations for Sherwood numbers

$$Sh = \frac{k_L d}{D_{AB}} \tag{1}$$

(k_L: liquid mass transfer coefficient; d or d_B: equivalent bubble diameter; D_{AB}: diffusion coefficient of component A in B) do not necessarily compromise their applicability, developments in hardware and software following these published correlations should allow getting a deeper understanding of their limits and widen the limits for more complex cases. The following major gaps in the widely discussed literature on gas-liquid mass transfer under reactive conditions are addressed in this chapter:

1. effects of rising times of more than roughly one second

    (a) influence of desorption effects on the mass transfer results
    (b) rise behavior and/or mass transfer influenced by surface active components apparent in the system due to the chemical reaction, i.e., ligands

2. local mass transfer phenomena in the vicinity of the surface and influence of the wake mixing

    (a) experimental: accessibility of local information in the vicinity of the surface of the bubble
    (b) numerical: high Schmidt number problem

D. Hillenbrand · H. Marschall · A. Weiner · D. Bothe
Technical University of Darmstadt, Mathematical Modeling and Analysis, Alarich-Weiss-Str. 10, 64287 Darmstadt, Germany

$$Sc = \frac{\nu}{D_{AB}} \qquad (2)$$

(ν: kinematic viscosity of the liquid)

3. competitive consecutive chemical reactions in gas/liquid systems

    (a) influence of bubble and liquid dynamics on the chemical reaction

For the presented projects dealing with single bubbles within the priority program "DFG SPP1740-Reactive bubbly flows", a rather straightforward path was chosen to approach the topic. As proof of concept steps, the rise behavior of the bubble and physisorption cases will be discussed briefly. Furthermore, the influence of a chemical reaction on the mass transfer of the component transferred from gas to liquid which acts as an educt will be discussed. The highest level of complexity occurs in the case of a competitive consecutive chemical reaction.

This chapter documents how different groups of chemists, mathematicians and engineers have worked together to analyze the interaction between fluid dynamics and chemical reaction on a single, freely rising bubble. A brief visualization of the field of work of each partner co-authoring this chapter is given in Fig. 1. Detailed information for the work of each working group can be found in the project description chapters in the first part of the book. This joint chapter rather aims at pointing out a general idea what to consider while conducting the actual experiments, simulations and analysis and showing trends for selected cases rather than discussing all potential cases in detail.
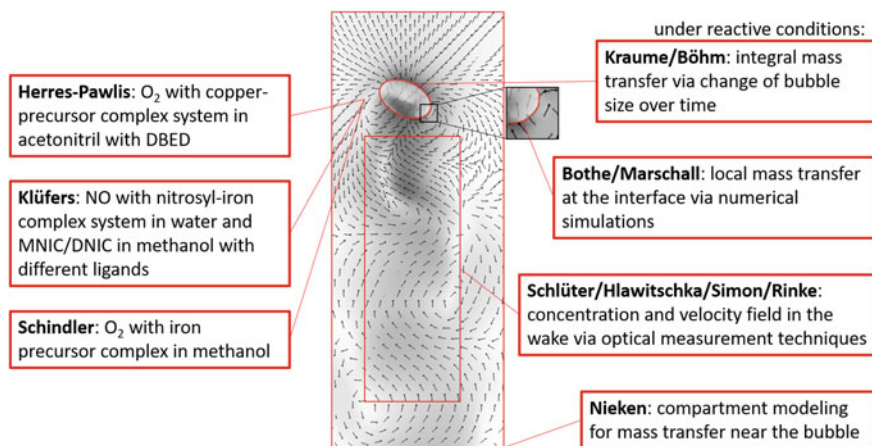

Fig. 1 Brief visualization of the related groups' work

2   Materials and Methods

Within this chapter, a brief description of the experimental setups and the applied chemical systems will be given. Table 1 gives a short overview of the following descriptions. Not every group worked with all chemical systems as the complexity of each system in combination with sophisticated measurement protocols demands a focusing on specific phenomena to push the limits of existing approaches and deepen the understanding of results identified within the priority program.

First, the gas-liquid systems will be discussed, starting with rather classical approaches using carbon dioxide in water or sodium hydroxide and oxygen in a sodium sulfite solution. Although not discussed in full extent here, this is followed by a rather detailed description of the chemical reaction systems developed within the frame of the priority program. Furthermore, the approach for the measurement of the integral mass transfer will be discussed, followed by the description of the local mass transfer measurements and the numerical approaches.

2.1   Chemical Reaction Systems

Some particular features of the chemical systems described afterwards are to be emphasized. All systems have reasonable reaction kinetics for the investigation under ambient conditions. Still, they show diverse reaction constants and, specifically valid for the newly investigated systems from the chemical groups, the kinetics are adjustable with diverse ligands. In parts, they have specifically designed fluorescent features. With respect to applications in the chemical industry, very particular for this program are chemical reactions in organic solvent systems and the investigation of competitive consecutive chemical reactions.

2.1.1 CO_2 in Water and in NaOH-Solution

To measure mass transfer in gas-liquid systems, there are many different requirements on test facilities and properties of the test systems. One of the simplest approaches due to its uncritical properties and easy handling is the mass transfer of carbon dioxide in aqueous solutions. The materials are inexpensive and commercially available.

The system CO_2-water can be modified by adding sodium hydroxide to the aqueous phase. The mass transfer is enhanced by the neutralization reaction. After the physical adsorption of the CO_2 in the water, the basic reactions in the liquid phase are:

$$CO_2(aq) + OH^- \rightleftharpoons HCO_3^-$$
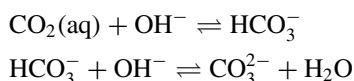$$HCO_3^- + OH^- \rightleftharpoons CO_3^{2-} + H_2O$$

Table 1 Overview of the gas-liquid systems used by each co-authoring group and the according investigation approaches

Working groups/methods/chapter	Bubble sizes (mm)	Materials	Analysis
Kraume/Böhm/image analysis, GC/ Chapter "Mass Transfer Around Gas Bubbles in Reacting Liquids"	2–8 (initial size)	CO_2 in water CO_2 in $NaOH_{aq}$ O_2/Ar/N_2/NO in methanol O_2 in DCM with copper-precursor complex CO_2/NO in water with nitrosyl-iron complex ligands: *edta, hedtra, nta, citrate, H_2O* O_2/N_2/NO in the MNIC/DNIC system	Bubble size, velocity, shape, gas composition and, therefore, mass transfer coefficient over time
Schlüter/pLIF, TRS-LIF/ Chapter "Experimental Investigation of Reactive Bubbly Flows—Influence of Boundary Layer Dynamics on Mass Transfer and Chemical Reactions"	ca. 3–7	O_2 in water	Influence of bubble bouncing on reactive mass transfer. Time resolved three-dimensional visualization of mass transfer at deforming bubbles
Bothe/Schlüter/CFD, PLIF/ Chapters "Experimental Investigation of Reactive Bubbly Flows—Influence of Boundary Layer Dynamics on Mass Transfer and Chemical Reactions" and "Modeling and Simulation of Convection-Dominated Species Transport in the Vicinity of Rising Bubbles"	0.7–0.8	O_2 in water	Experimentally validated numerical simulations of reactive single rising spherical bubbles influenced by surface active substances
Nieken/numerical/ Chapter "Determination of Intrinsic Gas-Liquid Reaction Kinetics in Homogeneous Liquid Phase and the Impact of the Bubble Wake on Effective Reaction Rates"	2	Toluene	Compartment model for process-oriented modeling of reactive flows around bubbles

Table 1 (continued)

| Working groups/methods/chapter	Bubble sizes (mm)	Materials	Analysis
Bothe/Marschall/CFD/ Chapters "Modeling and Simulation of Convection-Dominated Species Transport in the Vicinity of Rising Bubbles" and "Development and Application of Direct Numerical Simulations for Reactive Transport Processes at Single Bubbles"	1.45	O_2 in water	Influence of surfactant sorption and transport on rise velocity, bubble shape, wake structure

This has been extensively studied in the literature [3–5]. This system can be investigated with pure educts without having to consider major influences of surfactant. The enhancement factor
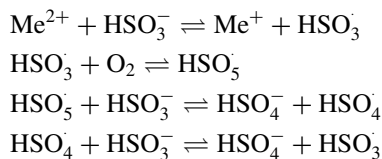
$$E = \frac{k_{L,reactive}}{k_{L,physical}} \tag{3}$$

of the mass transfer can be influenced by the concentration of sodium hydroxide [6].

2.1.2 O_2 in Water and Na_2SO_3 Solution

The absorption of oxygen in water is another classical approach. The effect of a chemical reaction consuming the dissolved oxygen released by the bubble can further be studied using a second order oxidation of sodium sulfite to sulfate in aqueous solution as reported in [7]. The typical reaction equation is

$$SO_3^{2-} + \frac{1}{2}O_2 \rightarrow SO_4^{2-}$$
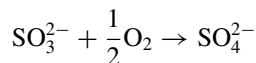
although this formal course of reaction is only the overall reaction equation [8]. It is presumed that the reaction is catalyzed by metal ions within the solution, in case of this experimental procedure by cobalt(II)sulfate according to

$$Me^{2+} + HSO_3^- \rightleftharpoons Me^+ + HSO_3^{\cdot}$$
$$HSO_3^{\cdot} + O_2 \rightleftharpoons HSO_5^{\cdot}$$
$$HSO_5^{\cdot} + HSO_3^- \rightleftharpoons HSO_4^- + HSO_4^{\cdot}$$
$$HSO_4^{\cdot} + HSO_3^- \rightleftharpoons HSO_4^- + HSO_3^{\cdot}$$

The advantage of this simplified mechanism is the possibility to formulate a second order kinetics, yielding

$$\frac{dc_{O_2}}{dt} = -k_1 c_{O_2} c_{HSO_3^-} \tag{4}$$

(k_1: reaction rate constant). To visualize and measure the transferred oxygen in the wake of a rising bubble, a solution of an oxygen sensitive dye, namely dichlorotris(1,10-phenanthroline)-ruthenium(II)hydrate, is added to deionized water. The fluorescence of the dye is quenched in dependency of the oxygen concentration, which allows to visualize the local oxygen concentration from camera recorded grey values. A prior calibration allows to quantify the local oxygen concentration in dependency of processes in the bubble wake such as mixing and reaction.

2.1.3   NO in a Nitrosyl-Iron Complex Solution

The in situ characterizable nitrosyl–iron complexes with aminecarboxylates have proven their utility since the 1980s in terms of a controllable reactivity in a multiphase reaction medium. In the turn of the millennium, the body of spectroscopic, kinetic and thermodynamic data was completed comprehensively by the van Eldik group [9–11].

The fundamental reaction of the adsorption of nitrogen monoxide (NO) by ferrous solutions follows the scheme:

$$Fe^{2+}(aq) + NO(g) \rightleftharpoons [Fe(NO)]^{2+}(aq)$$
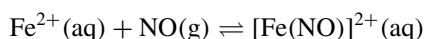
Using water as a ligand, NO substitutes one water molecule:

$$\left[Fe(H_2O)_6\right]^{2+} + NO \rightleftharpoons \left[Fe(H_2O)_5NO\right]^{2+} + H_2O$$
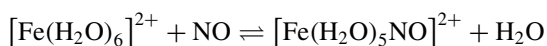
Adding aminecarboxylates as chelating ligands, their strong binding affinity to iron is reflected by the replacement of water molecules according to their denticity, respectively, binding sites towards a metal (see Fig. 2). Within the aminecarboxylate ligand group, a higher denticity results in higher stability constants of the Fe^{II}(ligand)/NO-complex. In the ligand sequence: *hedtra > edta > nta > (citric acid) citrate > ida > H_2O* stability constants K_{NO} for Fe^{II}(ligand)/NO complexes range from $(1.5 \pm 0.2) \times 107$ for *hedtra* to $(1.15 \pm 0.05) \times 103$ for the water complex showing the obvious stability effect. All complexes exhibit an intense colour, which makes this system very useful for optical detection (e.g. $\lambda = 435$ nm $= 820$ L mol^{-1} cm^{-1} for the *edta* complex).

The investigation of the influence of the hydrodynamic behavior towards the yield of competing reaction products requires a competitive consecutive reaction pattern. As nitrogen monoxide acts as a transfer species, this reaction pattern is realized in methanol in the reaction sequence: ferrous chloride $\rightarrow$ MNIC $\rightarrow$ DNIC (see

a) Iron/NO-Systems
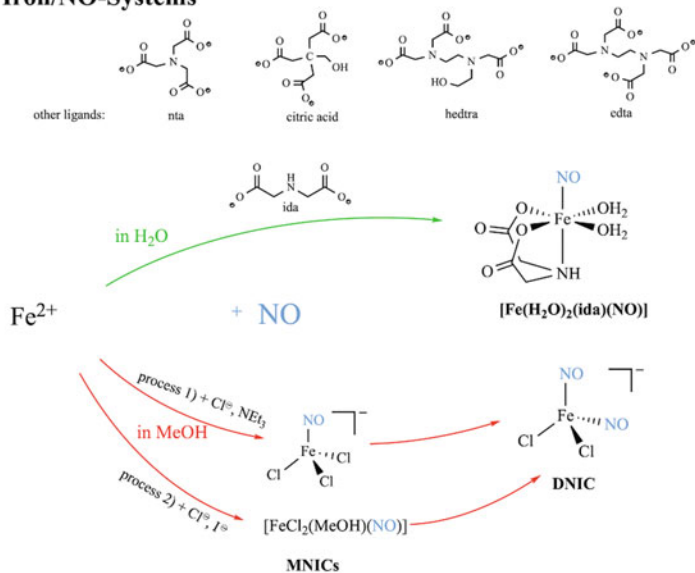
b) Iron/O₂-Systems
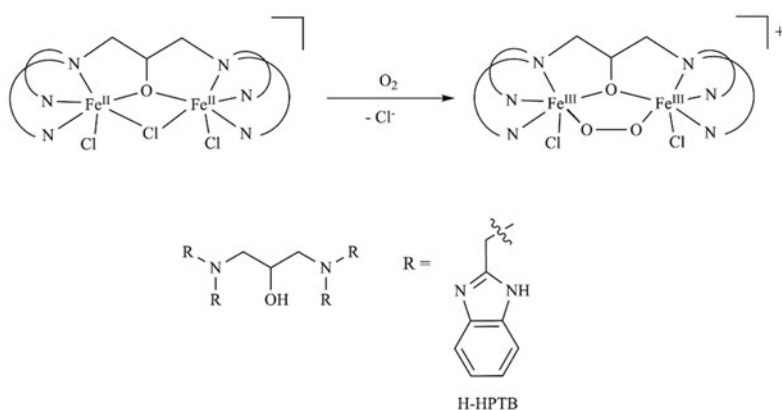
c) Copper/O₂-System

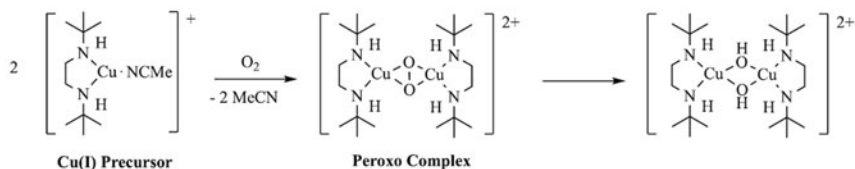**Fig. 2** Applied reactive systems: **a** upper part: reaction in aqueous media with used ligands, exemplified for the ligand ida; lower part: two processes for reaction in methanolic media with MNIC-DNIC sequence; **b** reaction of [Fe₂(H-HPTB)Cl₃] with dioxygen in methanol; **c** reaction of Cu(I) DBED complex in THF to the peroxido complex and subsequent decay to the bis(μ-hydroxido) complex

Fig. 2 and Chapter "In Situ Characterizable High-Spin Nitrosyl–Iron Complexes with Controllable Reactivity in Multiphase Reaction Media").

As shown in Chapter "In Situ Characterizable High-Spin Nitrosyl–Iron Complexes with Controllable Reactivity in Multiphase Reaction Media" in more detail, the question has to be raised, how to implement a safe environment for experiments with hazardous chemicals like gaseous nitrogen monoxide. This should not be seen as an underestimated challenge. The knowledge transfer from a chemistry to an engineer laboratory with training on the spot is supposed to be mandatory. Another problem emerges when working with a bubble column of several meters in height which cannot be enclosed in a fume hood. No direct connection with the NO-feeding gauge is advised. Instead, the NO production (see Chapter "Analysis of Turbulent Mixing and Mass Transport Processes in Bubble Swarms Under the Influence of Bubble-Induced Turbulence" for a detailed arrangement) can be realized within a fume hood, collecting the NO within a gas bag or a gastight syringe and connecting the reservoir in a trusted sealed way with the bubble column. Since experiments with single bubbles work with a very low reactive gas content, the flue gas does not need to be treated with a scrubbing solution. The single NO gas bubble reacts completely with the ferrous solution before reaching the upper liquid surface.

Changing from water to an organic solvent, the protective measures have to be enhanced. A local exhaust equipment connected with the outlet of the column is necessary to extract the potential explosive and toxic atmosphere caused by methanol and methylnitrite, the latter developing in the course of the reaction. Additional precautions must be taken when mixing the chemicals in containers with methanol and deoxygenating with inert gas.

2.1.4 O_2 in Iron-Peroxido Complex Solution

According to equation b) in Fig. 2, a labile iron(III) peroxido complex $[Fe_2(HPTB)(O_2)Cl_2]Cl$ is formed when the iron(II) complex, $[Fe_2(HPTB)Cl_3]$, reacts with dioxygen in methanol. The reaction has been studied in detail by stopped-flow techniques and kinetic data obtained were furthermore confirmed by continuous flow measurements using a SuperFocus mixer setup [12]. A huge advantage of this reaction system is the possibility to easily obtain the starting material in larger amounts and even more important, to "recycle/reactivate" it (details on this "recycling" are reported in Chapter "Formation, Reactivity Tuning and Kinetic Investigations of Iron "Dioxygen" Intermediate Complexes and Derivatives in Multiphase Flow Reactions" and [12]). While $[Fe_2(HPTB)Cl_3]$ is extremely sensitive towards dioxygen, the corresponding iron(III) complex $[Fe_2(HPTB)Cl_4]Cl$ is completely stable. Reducing this complex with ascorbic acid in a bubble column while an argon or nitrogen bubble swarm is used for mixing purposes, the solution regenerates back to the iron(II) complex that then once again can react with dioxygen (accompanied by characteristic color changes). Surprisingly, this procedure can be repeated several times (for other systems, usually, only one cycle is observed for oxidation reactions and often decomposition follows) and, therefore, this makes it a perfect system to be studied

under industrial conditions. Unfortunately, so far it was not possible to work with this system in water (decomposition of the peroxide complex is too fast under these conditions) [13]. Therefore, methanol was used as the continuous phase. Furthermore, while the iron peroxide formation was tested in bubble columns, the reaction rates (formation and decomposition of the peroxido complex) did not allow a detailed study on single bubbles. Work is in progress to optimize this reaction system accordingly.

2.1.5 O_2 in a Copper-Precursor Complex Solution

Another system that provides the opportunity to be used on a large scale is the Cu-O_2 system. The di-tert-butyl-ethylene-diamine (DBED) system offers numerous advantages: the ligand DBED is commercially available and cheap. Hence, the advantages of the Cu/O_2 chemistry known from small scale experiments [14] can be used in large scale experiments such as bubble columns (see Chapter "Investigation of Reactive Bubbly Flows in Technical Apparatuses"). As depicted in Fig. 2c, the ligand DBED stabilizes the copper(I) precursor complex [Cu(DBED)MeCN]OTf which easily reacts with air or pure oxygen to a side-on-peroxo species [Cu_2O_2(DBED)$_2$](OTf). This chemistry is normally performed at low temperatures below $T = -80$ °C to study tyrosinase model complexes [15]. At temperatures above $T = -80$ °C, the Cu(II) intermediate species decays to a bis(μ-hydroxido)dicopper(II) complex [16]. Details on the chemistry can be found in Chapter "Control of the Formation and Reaction of Copper-Oxygen Adduct Complexes in Multiphase Streams".

For the usage of the system in large scale at the location of measurement, simplified laboratory conditions have been developed: ligands and solvents were not dried but used directly from a freshly opened container. Dichloromethane (DCM) with a purity of 98% was stripped by inert gas to purge it from oxygen. The complex solutions were prepared in a standard glove box without any automated purification system and with a dioxygen content of approximately $c = 20$–50 ppm. Under ideal conditions, an average rate constant of peroxido formation of $k = 1.3$ s^{-1} was found at $T = 293$ K. An experiment under the simplified laboratory conditions resulted in a slightly increased rate constant of $k = 1.6$ s^{-1}. Interestingly, both experiments displayed a maximum extinction coefficient of $\varepsilon = 7800$ L mol^{-1} cm^{-1}, which accounts to a yield for the peroxido intermediate of 24% compared to a coefficient of 32,000 L mol^{-1} cm^{-1}, found at low temperatures.

Therefore, the DBED reaction system is suitable for experiments at locations with limited laboratory equipment.

2.2 Integral Mass Transfer Measurements and Bubble/Liquid Dynamics

For the investigation of integral mass transfer, a bubble rising test cell was developed (detailed description in [17] and Chapter "Mass Transfer Around Gas Bubbles in Reacting Liquids"). Integral mass transfer in this context means that for this part of the analysis, no local phenomena at different locations near the bubble surface were resolved. The idea here is to measure an overall change of the bubble volume and, therefore, change of the amount of substance in the bubble due to gas-liquid mass transfer. The analysis follows the equation

$$\frac{\Delta N_i}{\Delta t} = k_L A \Delta c_i \tag{5}$$

(N_i: amount of substance of component i; t: time; A: interfacial area; c_i: volumetric concentration of component i).

Once the transferred amount of substance over time and the current interfacial area of the bubble is measured and the driving concentration difference between the bubble surface and the bulk fluid is calculated, the mass transfer coefficient in the liquid can be determined. For such measurements, often small bubble rise test cells allowing only a rising duration of roughly one second have been used and, furthermore, the three-dimensional interfacial area was not precisely determined. The choice of rather small test cells was partly due to the fixed camera positions relative to the test cell which allows a reasonable two-dimensional spatial resolution for the recorded shadowgraphy image of the passing bubble. Such an approach does not allow the determination of bubble injection or long-time rising effects. If larger test cells for longer ascent durations were used, the change of the actual interfacial area over time cannot be resolved. Therefore, a bubble rise test cell has been developed with a height of $h = 2$ m and a bubble injection at the bottom through a needle. To realize a three-dimensional bubble shape analysis with a reasonable temporal and spatial resolution, on a vertical traverse system, two perpendicularly arranged cameras are moved with the bubble during its ascent. A servo motor is moving the carrier of two cameras controlled by a real-time image analysis. In contrast to single camera recordings, from the two images of the bubble recorded at the same time from two different perspectives, a pixel-wise 3D reconstruction of the bubble shape is possible allowing a determination of the volume and interfacial surface area at every point in time. Therefore, the mass transfer coefficient as a function of time ($k_L = f(t)$) can be calculated while the amount of substance and interfacial area were functions of time as well. The experiments showed that for such a long ascent, desorption effects lead to the fact that the driving concentration difference is a function of time as well. Therefore, for selected cases, not only the optical measurements are applied but, after certain ascent durations, the bubbles are collected in a funnel and a gas analysis is performed to determine the ratio between the masses of the components. This knowledge is necessary for accurate calculations of the mass transfer coefficient.

The bubble volume is used to calculate an equivalent diameter of the bubble and furthermore the bubble rise velocity is determined. In combination with all the determined material properties of the systems, this information is used to calculate the dimensionless numbers of interest for this system such as the Reynolds number

$$Re = \frac{v_z d}{\nu} \qquad (6)$$

(v_z also called v_B: vertical bubble rise velocity), the Peclet number

$$Pe = \frac{v_z d}{D_{AB}} \qquad (7)$$

and the Schmidt and Sherwood number.

2.3 Local Mass Transfer Measurements

For the detailed understanding of local mass transfer phenomena from a single rising bubble to the surrounding liquid, experimental visualisation techniques are necessary that are not affecting the mass transfer process itself. While smaller bubbles still might show a steady symmetrical behavior (no changes of the bubble shape and a straight rising path), the concentration field measurements become much more challenging for larger, freely ascending bubbles because these show a very dynamic behaviour with shape and velocity fluctuations. One opportunity for the measurement of a concentration field is to use instant 2D shadowgraphy with a liquid color change near the bubble due to the appearance of the reaction product. This can provide a concentration distribution that is integrated over the light path (light source through the measurement volume to camera). For non-symmetrical cases, this rather gives qualitative information. If the transferred species are showing fluorescence, the Laser Induced Fluorescence (LIF) can be used to detect even very fast processes. Unfortunately, the transferred species are often not fluorescent, not strong enough or in an unfavorable wavelength. To overcome this obstacle, a fluorescent dye can be added to the solution that is quenched by the transferred species (like oxygen). The common trade-off between integration time and size of the measurement volume of other measurement methods (IR, UV/VIS, Raman spectroscopy) make their application a difficult task in this case. Nonetheless, for certain cases, a higher resolution in 3D is possible with tomography approaches. Below, the different techniques will be described in detail with its advantages and disadvantages.

2.3.1 Visualization of Local Mass Transfer by a Color Change

One of the simplest methods to visualize and investigate mass transfer with chemical reactions at a freely ascending single bubble is to make use of the color change of the product. As material for such investigations in aqueous solution, the nitosyl-iron complex system with *edta* as ligand is suitable (see Sect. 2.1). This system shows a peak of light absorption at $\lambda = 472$ nm and, therefore, enables a qualitative reconstruction of the wake concentration field by a dual camera system equipped with respective bandpass filters. For a qualitative investigation within the bubble ascent setup, a single bubble investigation cell is mounted allowing optical access. The cell is made of stainless steel and glass and has a dimension of $90 \times 45 \times 115$ mm (width, depth, height). The cell is filled with nitosyl-iron complex solution. Single NO bubbles are generated by a triggered magnetic valve connected to a needle at the bottom of the cell. Two perpendicularly mounted high-speed cameras are applied. Both cameras are triggered to synchronize the capturing process. Behind the test cell in line with the cameras, LED light fields are installed to ensure a homogeneous background and a light emission peak at $\lambda = 472$ nm. This approach is also applicable for the MNIC/DNIC system, where both products of the consecutive reactions have emission peaks at differing wavelengths. Using two different types of LEDs with different wavelengths in one LED light field and applying according wavelength filters to the camera lenses, allows the separation of concentration fields for the two products (see Sect. 3.4 in Chapter "Visualization and Quantitative Analysis of Consecutive Reactions in Taylor Bubble Flows").

2.3.2 Visualization of Local Mass Transfer by 2D UV/VIS Tomography

The 2D UV/VIS tomography is similar to X-ray tomography, where an object is exposed to X-rays and the X-ray projection images are captured from various different angles around the object. These projection images are then used for the computer tomographic (CT) reconstruction algorithm to compute the 2D area or 3D volume data of the scanned object. As fast chemical reactions are causing strong concentration gradients at the moving boundaries of bubbles, the temporal resolution offered by X-ray tomography with spatial resolution in the double-digit micrometer range is not suitable to study local mass transfer. Instead, high-speed 2D fan-beam lasers were used to capture the projection of a 2D slice of the wake of the bubble. This computed tomography approach is beneficial as the time resolved 2D spatial concentration distribution of a wake behind rising bubbles provides a 3D concentration profile. This is useful as the profile is often inhomogeneous and irregular. Additionally, numerous wavelengths of laser pulses can be combined, each corresponding to the peak absorption spectrum in the best case of an educt, product or intermediate product such that the corresponding concentration fields can be determined simultaneously and selectively.

The setup uses the bubble column used in the integral mass transfer measurements (Fig. 3). It consists of a glass tube with $D = 75$ mm inner diameter which is surrounded
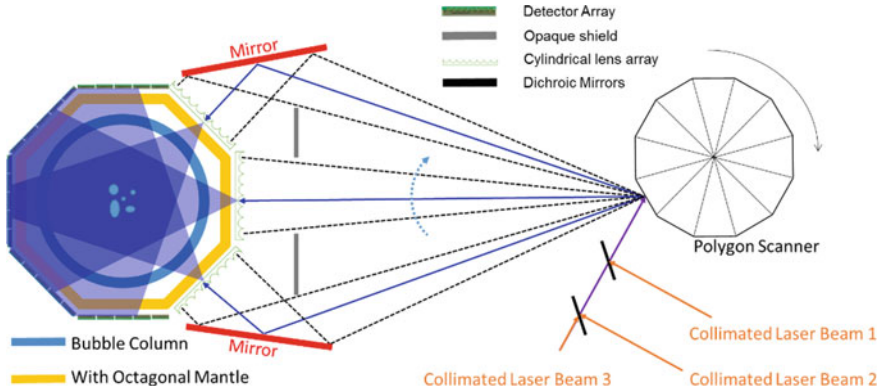
Fig. 3 Bubble column setup with laser sources and CMOS sensor arrays to obtain the 2D UV/VIS projections for the 2D computed tomography approach

by an octagonal PMMA tube. The volume in between serves to match the refractive indices of the curved glass tube (lens effect) and the medium outside. A laser beam is split into three beams which are guided to three sides of the plane surfaces of the octagonal tube. This laser beam can be composed of several laser beams of different wavelengths by a dichroic beam combiner. Close to each plane surface of the octagonal tube a $x = 40$ mm long optical element with 20 small cylindrical concave glass lenses is attached. Every lens produces a divergent laser beam of 60° width in the horizontal plane (perpendicular to the rising bubbles). A high-speed rotation polygon scanner consisting of 12 plane mirrors quickly shifts the position of the incoming laser beam on the lens array. On the opposite side of the cylindrical lens array, five adjacent $x = 40$ mm long plane surfaces of the octagonal tube are applied with a fast line sensor based on integrated silicon photodetectors CMOS chip. Each detector array consists of five CMOS photodetector array chips and each chip has 64 silicon photodiodes with 64 µm width and 127 µm length leading to an exceptionally large pixel area with a very fast readout speed of $f = 10$ MHz. These CMOS arrays with large pixel size generate analog signals with a sufficient signal-to-noise ratio for which an 18-bit analogue-to-digital converter (ADC) leads to a digital signal with high dynamic range. A field programmable gate array (FPGA) based data acquisition system was developed to capture data from all the 25 CMOS sensors at 5 Gb/s. The used setup which is based on the combination of the fast-rotating polygon mirror and the fast CMOS array readout which allows the real-time capture of the 2D projections. From these projections the chemical 2D concentration profile with high temporal resolution in the wake of a single bubble can be computed. The current hardware is designed to acquire a 2D image within $t = 1$ ms.

2.3.3 Visualization of Local Mass Transfer by LIF

To investigate local mass transfer and concentration fields in the wake of unconfined rising bubbles, Laser Induced Fluorescence (LIF)-measurements are highly suitable. While a planar approach with a single laser-light sheet is appropriate for bubbles that exhibit a rotational symmetric wake, a more complex scanning approach needs to be implemented for the wake of slightly larger, helically rising bubbles. Here, both approaches are considered. To study the interaction between fluid dynamics, mass transfer and a chemical reaction, the concentration field in the wake of a linearly ascending bubble has been quantified by time resolved planar-LIF experiments. For investigations of the interaction between fluid dynamics and mass transfer at free ascending bubbles that show wobbling and a helically rising paths, the 3D concentration wake has been quantified by Time Resolved Scanning LIF (TRS-LIF) [18]. Both setups share many aspects, such as the same measurement cell with a cross section of $A = 15 \times 15$ cm^2 and a height of $H = 30$ cm made of stainless steel and glass, allowing optical access from all directions (Fig. 14b (4)). A hypodermic needle of varying diameter can be placed rotatable within the center axis at the bottom allowing the adjustment of the trajectory. For illumination, a pulsed Nd:YLF laser with a wavelength of $\lambda = 527$ nm, pulse width < 210 ns and at a maximal repetition rate of 10 kHz is used (Fig. 14b (1)). For the TRS-LIF, the laser beam is reflected by a rotating mirror (Fig. 14b (3)) after passing a light sheet optic (Fig. 14b (2)), while a similar light sheet optic is directly passed for the planar LIF. The fluorescence illumination induced by the emitted laser light is then recorded with a high-speed camera (Fig. 14b (5)), positioned perpendicular to the light sheet, synchronized with the laser pulses. The camera chip is protected by a bandpass filter with a center wavelength of $\lambda = 590 \pm 2$ nm.

2.3.4 CFD Approach for Single Bubble Ascent and Local Mass Transfer

Since all experimental methods for local mass transfer enable only certain specific insights into single phenomena, for the whole picture of mass transfer and reaction processes, numerical simulations are a necessary and helpful complementary approach. It has been shown in the priority program SPP1740 that experiments without contaminations are nearly impossible, because most tracers, reactants and other chemicals act as surface active contaminants even at very low concentrations. Due to their strong impact on the flow dynamics, for a satisfying comparison, such effects must be modeled in the simulation approach. A numerical framework suitable to study the transport and adsorption of surfactant in bubbly flows is the Arbitrary Lagrangian Eulerian (ALE) interface tracking method, a solver of which is implemented in the OpenFOAM library [19, 20].

The interface tracking approach is based on the so-called sharp interface model; see Chapter "Reactive Bubbly Flows—An Interdisciplinary Approach" in [21] for a brief summary. The numerical setup consists of one volume mesh for each phase. One set of governing equations is solved for each phase, and the solutions of both domains

are coupled based on jump and transmission conditions arising from the balances of mass and momentum at the interface. The interface is approximated by parts of their mesh boundary. Both meshes can be moved such that they resemble the fluid phase motion. A typical interface tracking mesh for the simulation of a rising bubble consists of prismatic layers extending from the interface into both fluid phases as shown in Fig. 1 in Chapter "Development and Application of Direct Numerical Simulations for Reactive Transport Processes at Single Bubbles". For the mesh motion, a semi-Lagrangian approach is used in which points are only moved in an interfacial normal direction. The mesh motion is not straightforward because the quality of the cells has to be preserved. To keep the mesh motion at a minimum, the balance equations are solved in a reference frame moving with the bubble's center-of-mass velocity. An inlet velocity of the same magnitude as the instantaneous rise velocity vector, but pointing in the opposite direction, is prescribed at the outer domain boundary. Further details on the flow solution and mesh motion can be found in the articles [20, 22].

One advantage of the interface-aligned mesh is the possibility to solve the surfactant transport equation on the surface mesh. The interface tracking method has been enhanced and extended by a sorption library, which enables to account for the presence of surfactants [21, 22]. The library covers fast and slow sorption mechanisms together with various surface tension isotherms (functional relationships between the surface tension coefficient and the interface concentration). For the results presented in Sect. 3.2, a Langmuir fast sorption model has been employed.

The mesh setup allows for a high mesh density close to the interface, which is well suited to resolve the steep gradient occurring in velocity and concentration boundary layers. However, the molecular diffusivity of surfactant molecules is typically small (leading to high Schmidt numbers), and a direct solution of the surfactant transport in the bulk is currently out of reach due to high computational costs. If the normal derivative of the surfactant concentration at the interface cannot be approximated accurately, the interaction between flow dynamics and surfactant adsorption is deteriorated. To overcome this problem, a subgrid-scale model is employed to approximate the surfactant transport in the boundary layer. The model is based on the same principles as the one for mass transfer introduced in Chapter "Modeling and Simulation of Convection-Dominated Species Transport in the Vicinity of Rising Bubbles". Subgrid-scale modeling is used for both, the surfactant adsorption and the mass transfer. Details on the numerical combination of sorption and subgrid-scale modeling can be found in [21–23].

3 Results for Single Bubbles Under Reactive Conditions

3.1 Integral Mass Transfer Phenomena at a Single Ascending Bubble

The basis for the mass transfer measurement is the accurate determination of the bubble dynamics. While in Chapter "Mass Transfer Around Gas Bubbles in Reacting Liquids" more material systems and quantities related to the bubble dynamics are discussed, the focus in this chapter is on the rise velocity and according equivalent bubble diameter development over time in the chemical systems. Velocity and diameter are necessary for the calculation of the Reynolds or Peclet number, accordingly, which are usually used for the correlation with the mass transfer related Sherwood number. In the frame of mass transfer measurements in gas-liquid systems, the two main peculiar things about the tested systems are, first of all, that also non-aqueous, i.e., organic continuous phases are tested and, second of all, that due to the reactive system numerous components are in the liquid phase. This incorporates metal complexes and numerous ligands as described in Sect. 2.2.

In Chapter "Mass Transfer Around Gas Bubbles in Reacting Liquids", cases without mass transfer, with mass transfer and cases with mass transfer and chemical reaction are discussed for the reactive liquid systems. Figures 4, 5 and 6 show results of current bubble rise velocities in different liquid systems with mass transfer. Current
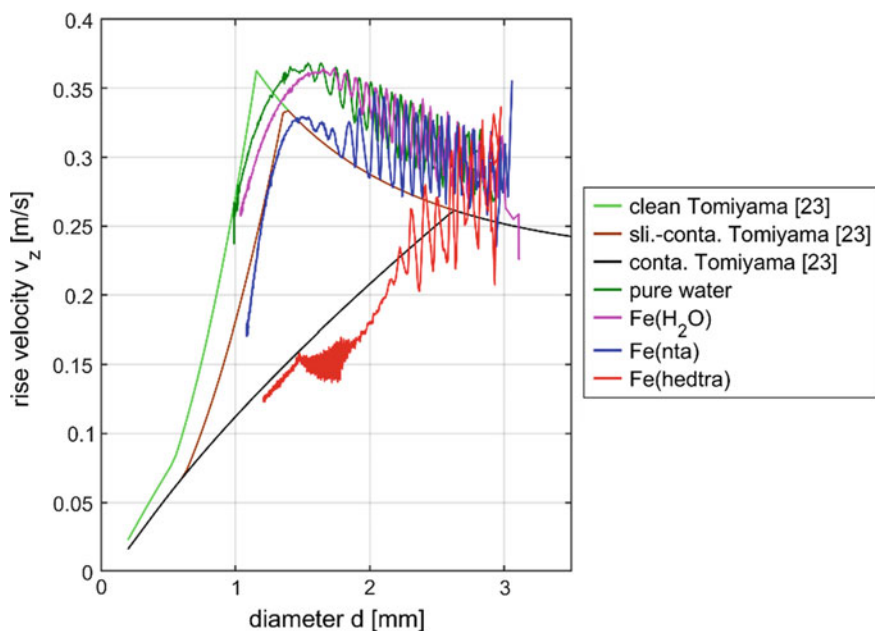

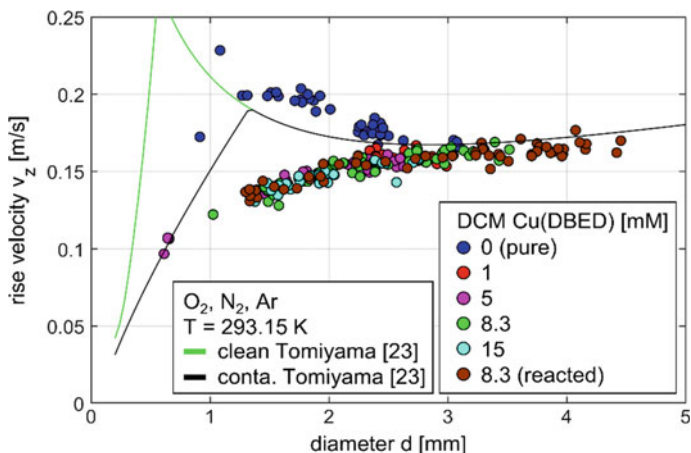**Fig. 4** Rise velocities of single CO_2 bubbles in different aqueous continuous phases

Fig. 5 Rise velocities of single O_2 bubbles in an organic continuous phase (DCM) with different concentrations of the copper-precursor complex
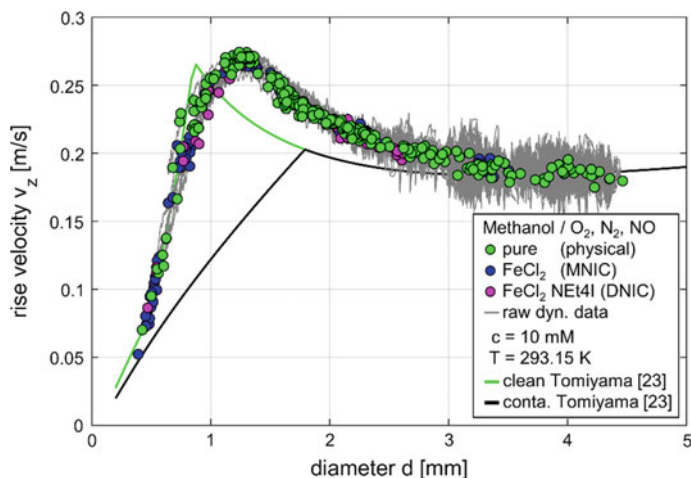

Fig. 6 Rise velocities of single O_2, N_2 and NO bubbles in an organic continuous phase (methanol) and with respect to the MNIC/DNIC system in methanol with $FeCl_2$ and methanol with $FeCl_2$ and NEt_4I

velocity means bubble velocity as a function of time starting from an initial bubble diameter with shrinking size due to mass transfer. Consequently, there are no terminal rise velocities. The initial bubble size can be seen from the highest value of the bubble diameter for one line.

In the aqueous nitrosyl-iron complex system (Fig. 4), the iron(II) sulphate heptahydrate does not influence the bubble dynamics but the applied ligands can (comparison with clean and contaminated cases [24]). E.g., with H_2O as ligand (only iron(II)

sulphate heptahydrate dissolved in water) the graph shows a typical curve for clear systems due to the change from deformed larger bubbles to smaller spherical bubbles. The maximum velocity is predicted for smaller bubble diameters and the measured ascent velocity for ellipsoidal bubbles is higher. In case of *hedtra* as ligand, the rise velocity curve clearly shows a contamination effect which incorporates differing bubble shapes and, therefore, differing flow behavior around the bubble which all affects the mass transfer. With different ligands, the curves lay between these extreme cases. To make this effect even more complex, it has to be mentioned that there are different kinetics to the contamination of the surface with the surface-active ligands. Therefore, ligands not only affect the kinetics of the chemical reaction but also the bubble dynamics which makes a concise description even harder.

Using organic solvents such as DCM (Fig. 5), one challenge is to actually measure a change in size of the bubble as the evaporation into the bubble is much more strongly enhanced in comparison to aqueous systems. This could partially be overcome by applying higher pressures to the system to reduce the influence of vapor pressure. Still, the integral mass transfer measurement based on the change of bubble size over time is not ideal for such systems. Nonetheless, results were found in the DCM system for numerous bubble diameters. While the results for the DCM system without copper-precursor complex indicate a typical curve for clear systems, the addition of the copper-precursor complex with different concentrations directly leads to a full contamination, independent of the tested concentration. It is worth mentioning that here, only DBED was used as the ligand. So, in contrast to the nitrosyl-iron complex which showed no contamination effect, but solely the applied ligands did, here, this differentiation cannot be made for the copper-precursor complex with the exisiting data as it was only tested in combination with the ligand.

For the O_2 in the iron-peroxido complex system and MNIC/DNIC trials (Fig. 6), methanol was used as an organic continuous phase. While the same evaporation problem as in DCM is apparent, affecting the mass transfer measurements, adding the MNIC/DNIC reactive components (iron chloride for the first reaction step, tetraethy-lammonium iodide (NEt_4I) for the consecutive reaction step) to the system does not influence the rise velocity of the bubble.

Such effects have to be considered once dimensionless numbers are used to describe the systems, as in the same system, just by adding one component, the same bubble size ends up in different Peclet numbers due to a reduction of the rise velocity.

Proof of concept mass transfer measurements were undertaken with absorption of CO_2 in water. Although it is not a completely surprising effect, the influence of desorption of dissolved gases in the liquid and of evaporating liquid from the contin-uous phase on the results of the mass transfer coefficient are not widely discussed (one example can be found in [25]). With a fairly high effort in the preparation of the liquid, e.g., by cooking the liquid before the experiments or stripping the liquid, ideally, with a weakly dissolving inert gas such as helium for quite some time, the continuous phase can be made nearly free of dissolved gases. Cooling down the liquid after cooking without gas contact and producing defined reproducible starting conditions for a measurement are challenging tasks. Controlling the concentration of

dissolved gases is difficult. Therefore, the solutions were gassed and saturated with
a known pure stripping gas (e.g., N_2) at ambient pressure for two hours to ensure
a controlled concentration and, therefore, constant boundary conditions for each
measurement. Still, especially for organic solvents as a continuous phase, the chal-
lenge of evaporation cannot be overcome by these measures. Increasing the overall
pressure in the system proved to help with this issue.

Due to the desorption of stripping gas and evaporation of the liquid, a correction
approach was followed. For selected cases, the results of a gas analysis of collected
bubbles with different ascent durations were used to incorporate the desorption effect
in the mass transfer coefficient determination (further discussed in Chapter "Mass
Transfer Around Gas Bubbles in Reacting Liquids").

Measurements of CO_2 absorption in water showed a good agreement with the
Sherwood correlation presented by Hughmark [26] (further discussed in Chapter
"Mass Transfer Around Gas Bubbles in Reacting Liquids"). For CO_2, Fig. 7a shows
an exemplary result with chemical reaction-based enhancement of the mass transfer
due to the addition of NaOH to water. In comparison to Hughmark's correlation for
non-reactive cases, a strong enhancement of the mass transfer was found. A detailed
discussion of the influence of NaOH on the mass transfer, including the peculiar
characteristic of an enhancement which also depends on the Peclet number for this
case can be found in Chapter "Mass Transfer Around Gas Bubbles in Reacting
Liquids". Here, this illustrates that such results of chemical enhanced mass transfer
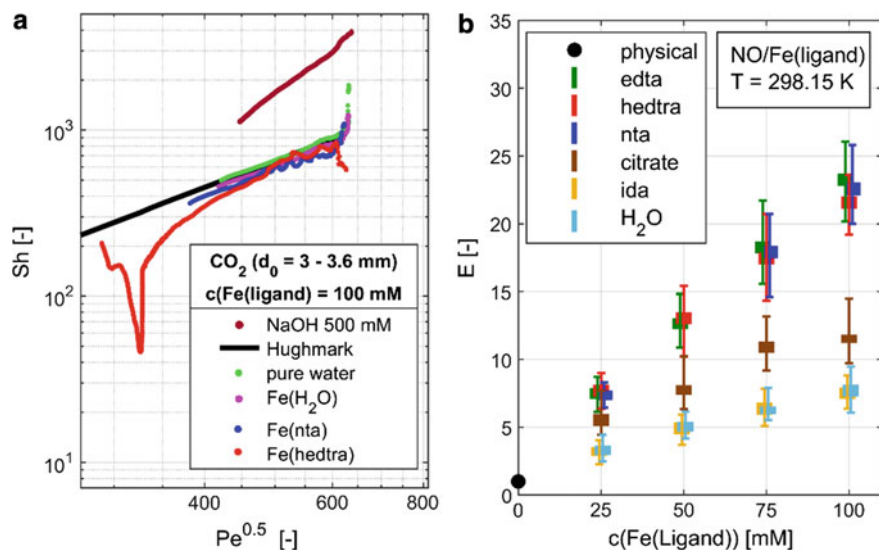can be investigated with the measuring setup.

Fig. 7 **a** Sherwood numbers for CO_2 in different systems and **b** Enhancement factors for different
ligands in the nitrosyl-iron complex system

To investigate the influence of ligands in the nitrosyl-iron complex system not only on the rise velocity but also on the mass transfer excluding the ligand's influence on the chemical reaction kinetics, the absorption of CO_2 in the nitrosyl-iron complex system with different ligands was tested (Fig. 7a). In case of water as ligand (no surfactant's influence), the mass transfer coefficient plotted as the Sherwood number still follows the correlation of Hughmark [26]. Investigating the same system, just with *hedtra* as ligand, the results show a very strong influence on the mass transfer which is not solely explainable with the influence on the rise velocity. With *hedtra*, lower Peclet numbers are reached due to the reduction of the rise velocity in comparison to equally sized bubbles in other systems. The surfactant might act as an additional mass transfer resistance and the strong influence of a differing bubble shape and, therefore, flow around the bubble (at the same equivalent diameter) can be seen. This effect cannot be fully elucidated by this kind of measurement.

Once NO is used as the gas phase, the chemical reaction is expected to enhance the mass transfer. With the same procedure of data analysis, enhancement factors for numerous reactive components and ligand concentrations (mostly, a ratio of 1:1.1 was set between nitrosyl-iron complex and ligand) can be evaluated. Figure 7b shows the results of the enhancement factor (ratio of chemical reaction enhanced Sherwood number over the Sherwood number calculated for non-reactive cases with the correlation of Hughmark). In Chapter "Mass Transfer Around Gas Bubbles in Reacting Liquids", for the nitrosyl-iron complex system, it was shown that the enhancement factors in Fig. 7b are on average mostly independent of the Peclet numbers for one reactive component concentration (although scattering is visible). The enhancement factor increases approximately linearly with increasing reactive component concentration independent of the type of ligand, just with different slopes. Such an increase is due to the concentration dependent reaction rates as usually found in reaction kinetics. Still, there is pretty much a distinction between three ligands or ligand groups, respectively. The ligands H_2O and *ida* show the lowest enhancement factors, *citrate* has intermediate values and *hedtra, nta* and *edta* were found to have the highest enhancement factors (roughly: *ida* < H_2O < *citrate* < *hedtra* < *nta* < *edta*). Regarding the stability constants (H_2O < *ida* < *citrate* < *nta* < *edta* < *hedtra*) and the reaction rate constants (H_2O < *ida* < *citrate* < *nta* < *hedtra* < *edta*) of the diverse ligands, this behavior can basically be explained with these chemical reaction-based quantities (see also Sect. 2.1). Still, the distinction between the three ligands or ligand groups, respectively, cannot be solely explained based on the chemical reaction behavior as there are orders of magnitudes between the according values. Analyzing the rise velocities at the same bubble diameter, for *hedtra* the lowest values and for *edta* an intermediate value were found and all other ligands are grouping at the highest rise velocity (rough order: *hedtra* < *edta* < *nta* < *citrate* < *ida* < H_2O; see Chapter "Mass Transfer Around Gas Bubbles in Reacting Liquids"). This is basically the inverse order in comparison to the enhancement factor regarding the ligands although the grouping effect is not the same.

The biggest challenge in the interpretation is here, that the same bubble size now ends up in different Peclet numbers due to the differing velocities. Furthermore, this is not only valid for different ligands but, especially the systems with stronger
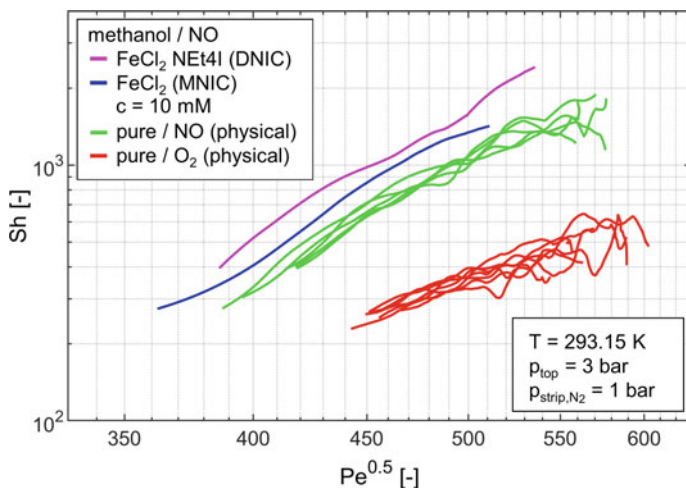
Fig. 8 Sherwood numbers for the absorption of NO in methanol without chemical reaction, with one chemical reaction and with two consecutive competitive chemical reactions

surfactant's influence show differing results (for velocity and Sherwood numbers) depending on the initial bubble size due to the contamination kinetics.

These complex interactions of ligand influenced rise velocities and reaction rates indicate that including, e.g., the Damköhler or Hatta number into a Sherwood correlation for reactive cases is reasonable but will not solve the issue of the influence of the surfactant behavior.

Figure 8 shows exemplary results for the iron-peroxido complex and the MNIC/DNIC system with methanol as organic continuous phase. With respect to the iron-peroxido complex system, the absorption of O_2, and for the MNIC/DNIC system, the absorption of NO was tested in non-reactive methanol and with NO in the system with one reaction step (by addition of $FeCl_2$) and the two consecutive competitive reaction steps (by addition of $FeCl_2$ and NEt_4I). Before discussing the graphs, it is worth mentioning that data about the solubility and diffusion coefficients of different components in methanol are not widely discussed in literature. Therefore, the results should be discussed with reservation. For O_2, the scattering results of numerous tests are shown. This illustrates the complexity of such measurement, especially in organic solvent systems. As expected, the Sherwood number decreases with decreasing Peclet number. The same qualitative behavior was found for the non-reactive absorption of NO. Still, the Sherwood number was higher by a factor of 2–5 for NO. This is most likely due to the values of the material properties used for the calculation and not necessarily a physical phenomenon.

For a qualitative discussion, the absorption of NO without reaction, with one reaction and with a consecutive competitive reaction is shown. As discussed before, the results do allow the conclusion that the first reaction step enhances the mass transfer and the second reaction step enhances the mass transfer even further. The enhancement for the given case is not as strongly emphasized as discussed before for

the nitrosyl-iron complex system in water. Besides the mentioned problem with the material properties, it still has to be emphasized, that these are not already results of large test series and that evaporation is still a factor even if applying a higher pressure (here: $p = 3$ bar).

The presented results illustrate that such an integral but, still, very precise approach allows the determination of Sherwood numbers for physisorption and chemisorption cases. Diverse conditions can be compared and deliver a concise picture. Especially with organic solvent systems where evaporation occurs the interpretation of the results gets even more complex. At ambient pressure, this can end up in an absorption and evaporation which almost compensate leading to only marginal change in size of the bubble although mass transfer happens. Applying higher pressures in the system helps to overcome this challenge up to a certain level but the combination with gas analysis tests of the collected bubbles should be considered as it was done here for certain material systems. Furthermore, the interpretation of cases with reactive components which act as surfactants is challenging, as well, as contamination kinetics, chemical reaction kinetics and bubble dynamics are interacting in a complex fashion. The more detailed the examination of the complex cases gets, the least a rather simple correlation is able to describe the found behavior. Investigating local mass transfer phenomena in the vicinity of the bubble and in the wake can bring features of the process to light that the integral approach is missing.

3.2 Local Mass Transfer Phenomena at a Single Ascending Bubble

Depending on the reaction system, different measurement techniques can be used to determine local mass transfer phenomena and chemical reactions at a single ascending bubble. For a color change by reaction, a simple backlight illumination can be used to achieve qualitative results. For UV/VIS sensitive educts and products, the 2D UV/VIS scanning method can be used and for fluorescing educts and products, the time resolved scanning laser induced fluorescence is applicable. All methods are showing advantages and disadvantages that will be discussed in detail in the following.

3.2.1 Fluid Dynamics in the Wake of the Bubble

Before discussing the measurements of local concentrations in the wake, a short discussion of the fluid dynamics is given. Bubble wake dynamics play a crucial role in reactive bubble columns. Gas bubbles are a source of reactant species. The transport phenomena and reaction in the liquid depends on the fluid flow around the bubble but also on the mixing in the liquid induced by the bubbles. A larger wake results in a greater mixing in this region. Hence, it is of primary importance to study

Fig. 9 Flow around a sphere at Re = 10 (left) and Re = 120 (right)
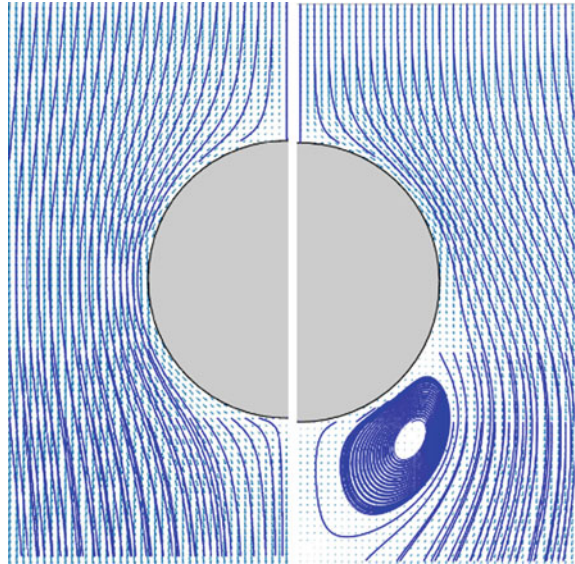
the reactive mass transfer/wake interaction. At low Reynolds numbers, the flow of the liquid will follow the bubble surface. However, at a critical Reynolds number, the flow starts to separate from the bubble and rejoins at some distance forming a closed region slightly above the critical Reynolds number. The critical Reynolds number depends, thereby, on the shape and surface nature of the bubble [27]. The closed region is also known as the wake. Both states are represented in Fig. 9.

The simplified assumptions of a steady dual-wake structure are valid for a perfect flow structure without flow instabilities. Based on the Reynolds number, five categories are described in literature [28]. The first one is the steady wake with negligible circulation region. The second wake structure is a steady wake with a well-developed recirculation region. This region is followed by a laminar streamwise tail. The third wake describes the unsteady wake with large-scale vortical structures. The fourth is an unsteady wake with a high degree of turbulence. The fifth structure describes a highly turbulent wake. Levy and Forsdyke [29] reported for example a helical vortex structure that rotates around its axis. Later, Lindt [30] explained the periodic change in bubble orientation is responsible for the helical vortex structure.

3.2.2 Results by Visualization of Local Mass Transfer with Color Change

The results of the measurement of a single bubble ascent using a single camera system is shown in Fig. 10. For these experiments, the NO in a nitrosyl-iron complex solution has been used. The bubble is generated at a needle with a diameter of 1 mm and the first image shows the bubble slightly above the needle. The rising NO bubble

Fig. 10 Color change in the wake of an NO bubble in the nitrosyl-iron complex solution (greyscale color bar with concentration values in mol/L)

has a diameter of $d_B = 2.7$ mm and is rising straight up to a velocity of $v_B = 26$ cm/s in the first period. In the second period, the bubble starts to oscillate leading to first disturbances in the wake and vortex-shedding. In the third period, the wake shows a helical structure, which leads to a slower bubble rise velocity of approximately $v_B = 20$ cm/s. The greyscale color bar shows the concentration profile in mol per liter. It can also be seen that a high concentration remains at the bottom of the images, closely above the needle, the bubble induced mixing is low and the diffusion process is dominant. Hence, the transition from steady laminar to helical wake structures can be observed with the well-known horseshoe-like vortex in the bubble wake [31].

A more detailed investigation of the bubble wake structure using the two-camera setup is given in Fig. 11. The figure shows the highly complex three-dimensional concentration wake structures which is dominated by the fluid dynamics in the wake. Also, the concentration shows locally varying values in the wake, which will finally influence competing reactions. While this single example shows an indication about the concentration wake, a multiple camera system of at least 10–20 cameras would be necessary to reconstruct the concentration wake with higher accuracy. For fluorescing systems, the TRS-LIF technique might be feasible (see Chapter "Experimental Investigation of Reactive Bubbly Flows—Influence of Boundary Layer Dynamics on Mass Transfer and Chemical Reactions").

Fig. 11 Reconstructed three-dimensional concentration wake below the NO bubble in the nitrosyl-iron complex solution

3.2.3   Visualization of Local Mass Transfer by 2D UV/VIS Tomography

Another opportunity to reach a higher spatial resolution than conventional integrated absorption spectroscopy is to use 2D UV/VIS spectroscopy for UV/VIS sensitive chemicals. The three-dimensional concentration measurements by 2D UV/VIS tomography are made by applying computer tomography reconstruction algorithms to the time resolved 2D UV/VIS projections discussed in Sect. 2.3.2. The reconstruction of the concentration profile is based on a combined classical filtered back projection with a convolutional neural network (CNN). The neural network is trained using a large number of CFD simulation data from the SPP1740 project 'Direct numerical simulation of multi-physics reactive mass transfer at single and multiple bubbles' directed by Professor Bothe at TU Darmstadt. These data are fed to the ray tracing model to calculate the projections which are then backprojected to get the reconstructed 2D concentration field. From the SPP1740, totally 2,184,000 reference cases obtained by CFD simulations are such pairs of reference CFD concentration field and the reconstructed ray tracing based backprojected concentration field is used to train the neural network to improving the reconstruction quality and optimize it. It should be mentioned that the CFD simulation data provided so far are 2D velocity data instead of 2D concentration data. However, this is not really a fundamental problem for the following reasons.

Firstly, the neural network works only with dimensionless quantities so that only the characteristics of the data are relevant but not the actual physical meaning of the data. Therefore, data of different physical quantities with similar characteristics regarding spatial distribution can be used for learning and for the application of the neural network. To what extent the spatial velocity field has a sufficiently similar characteristic for the spatial concentration still has to be investigated in principle. Intuitively, however, spatial structures like vortex structures should exist in a similar way in both physical field sizes.

Secondly, independent of these arguments based on the structure of the data, it can be easily verified that the neural network trained in the above mentioned way calculates physically meaningful concentration fields. In order to carry out this verification, the tomographic projection data of an arbitrarily assumed concentration field can be calculated with the physically accurate ray-tracing simulation model including the refractive index of all materials including the bubble column, the liquids and the octagonal PMMA tube. In the next step, the reconstructed tomographic concentration field of Fig. 12b, which would be applied in the same way to measured data, can be compared with the original, i.e. the exactly known concentration field of the first step in Fig. 12a. In this respect, the quality of the reconstruction of the concentration fields based on the neural network trained with the velocity data can be verified with highest accuracy. The results so far are very satisfactory as the shown concentration profile of Fig. 12a and b are very similar. A later change to concentration profiles for training when available would further improve the reconstruction accuracy which is already sufficient.

For applying the reference profiles to train the convolutional neural network for reconstruction, the UV/VIS projections according to the setup in Sect. 2.3.2 have to
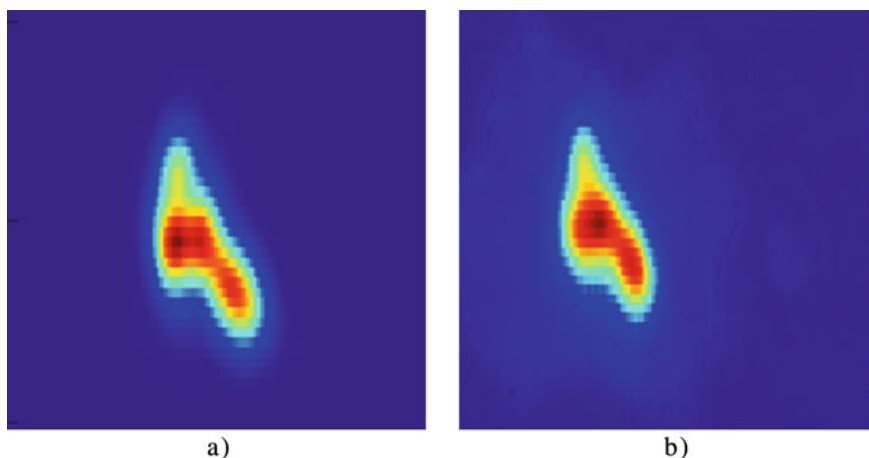
Fig. 12 a 2D cross-section of the 3D concentration field from which the laser based projections are computed in the wake behind a single bubble; **b** 2D cross-section of the CT-reconstructed 3D concentration field computed from the projections of **a** being the reference concentration

be obtained from 2D fields. A physical and geometrical accurate ray-tracing simulation model of the setup achieves this. The model consists of the full bubble column geometry including the refractive index and refractions at the media interfaces like the bubble column glass and liquid, each detector and lens as well as the PMMA octagon shell and other physical details such that the projections are computed by the simulation model with highest accuracy. Based on the projections and the reference profiles, a supervised learning of the CNN is realized. After training, the reconstructed 2D concentration profiles are generated by weighted backpropagation and normalization adapted to ray-tracing. Finally, the CNN with a novel regression layer optimizes the image quality and minimizes existing artefacts. The reconstruction results of an example are shown in Fig. 12b obtained from the 2D projections of a reference concentration given in Fig. 12a. Obviously, the reconstruction quality compared to the reference is sufficiently precise as the applied simulation model to compute the projections is accurate because the ray-tracing based simulation model includes the refractive index of all materials including the bubble column, the liquids and the octagonal PMMA tube. Based on a fast data capture of the projections and repetition of the 2D reconstruction, a 3D dimensional concentration profile of the wake can be determined experimentally if this UV/VIS tomography setup is integrated into a bubble column.

3.2.4 Visualization of Local Mass Transfer by LIF

Like 2D UV/VIS spectroscopy, laser induced fluorescence for fluorescing chemicals or additives reaches a high resolution. For oxygen bubbles with diameters below
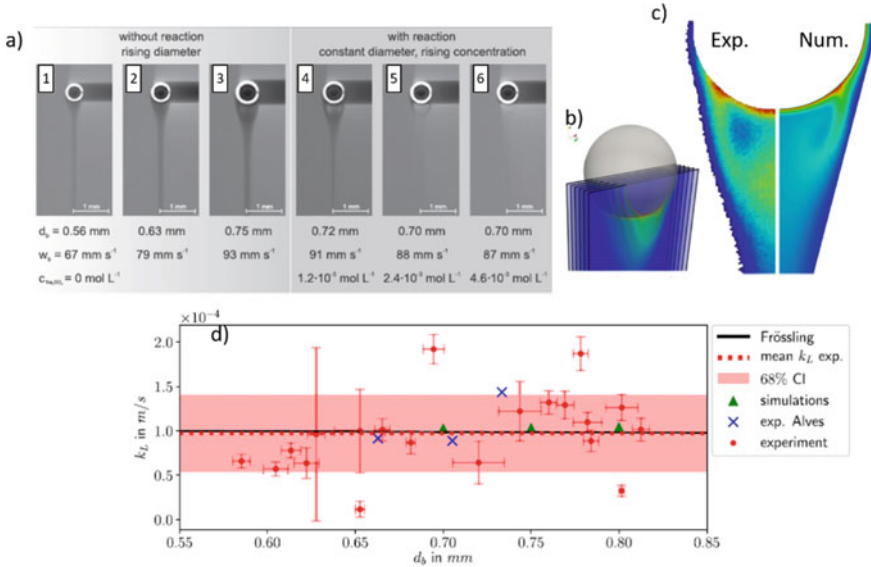
Fig. 13 a Experimental images of the oxygen concentration wakes of linearly rising bubbles of different size (1–3) and equal size but with additional chemical reaction (4–6). High oxygen levels appear black due to fluorescent quenching. **b** To obtain similar concentration wakes numerically as shown in **c** several adjacent slices have to be averaged. **d** The mean mass transfer coefficient from experiment matches the one predicted from simulations and analytical considerations

1 mm that are rising almost linearly, the p-LIF technique can be applied to visualize the mass transfer and concentration wake by using the oxygen sensitive ruthenium-complex dye. High image contrast is achieved by taking advantage of the linear bubble rise and automatic bubble center detection, which allows for a generous averaging of the background corrected high speed images ($f = 1000$ Hz) and thus a very low signal to noise ratio [18, 32]. Only sub-pixel shifts of the bubble center are not compensated, yielding a light blur (Fig. 13a) and thus the concentration in the immediate proximity to the bubble interface cannot be measured correctly.

The mass transfer from the bubble to the liquid is studied from the rotational symmetric bubble wake for two cases. Different bubble sizes and, thus, Reynolds numbers without any chemical reaction (Fig. 13a 1–3) and the effect of different sodium sulfite concentrations are presented (Fig. 13a 4–6). The experimentally observed concentration wakes have been compared to numerical results (Fig. 13c). Also, the rising velocities of both methods match well, as soon as the strong influence of the ruthenium dye as a surfactant in the aqueous solution is considered within the numerical simulation (discussed later for numerical results). However, to compare the experimental results, the light sheet thickness ($s \sim 5$ mm) and a possible parallel offset to the center plane of the bubble need to be considered to achieve agreement with the simulation. Therefore, the concentrations interpolated to several planes are averaged over the light sheet thickness to mimic the experimental settings (Fig. 13b).

A comparison of the mean mass transfer coefficient over all bubble sizes from the experiments shows a good agreement with the numerical and theoretically predicted one (Fig. 13d).

When larger bubbles are considered ($d_B = 2$–3 mm equivalent diameter), the trajectories of the bubbles become more complex and three-dimensional such that the p-LIF with its fixed position cannot capture their rise anymore. Therefore, the p-LIF setup is modified adding a rotating mirror with 36 facets (Fig. 14b (3)) and a cylindrical focus lens right behind the light sheet optics (Fig. 14b (2)).

The rotational speed of the polygon mirror is set to its maximum at $n = 10,000$ rpm, resulting in $f \approx 166.7$ Hz. The single light sheets were adjusted to an approximate minimal thickness of $s = 0.5$ mm. Using 40 light sheets and a laser pulse rate of $f = 6400$ Hz, the light sheets lay arbitrarily close together as monitored by a second high-speed camera looking at the light sheets from above (not shown). Both cameras
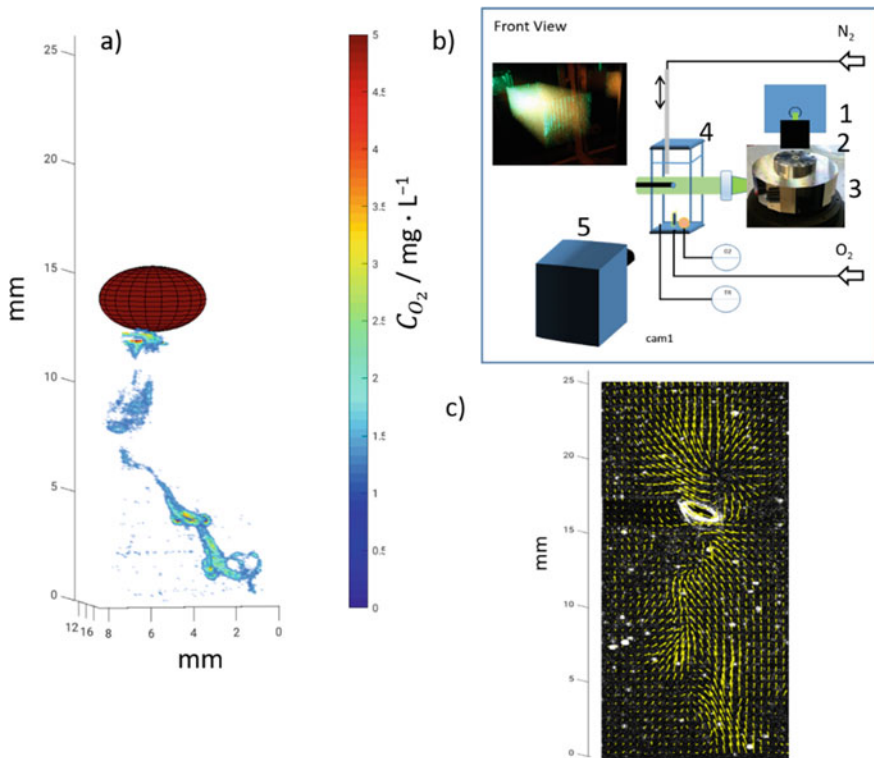

Fig. 14 a The oxygen concentration wake of an elliptical, helically rising bubble can be reconstructed from time resolved scanning LIF (TRS-LIF). A schematic of the setup is shown in **b**. Here, (1) denotes the high-speed laser, (2) a light sheet optic, (3) the rotating mirror with 36 facets, (4) the measuring cell and (5) the high-speed camera. The setup can be purged with nitrogen to ensure zero oxygen concentration previous to the bubble rise. **c** When fluorescent particles are added to the solution the scanning light sheets can also be used to measure the planar velocity fields developing from the bubble rise

were triggered with the same signal as the laser. The three-dimensional distribution of the oxygen concentration within the wake can be reconstructed from the volume scans by an elaborated pixel-wise analysis of each scan to a previously performed pixel-wise calibration to pre-adjusted oxygen levels (see Chapter "Experimental Investigation of Reactive Bubbly Flows—Influence of Boundary Layer Dynamics on Mass Transfer and Chemical Reactions" and [33] for more details). The resulting concentration wake is shown in Fig. 14a). Here the voxels have an approximate size of $V = 0.042 \times 0.042 \times 0.5$ mm^3. Two typical horseshoe-like structures are distinguishable in the oxygen concentration wake, similar to those described by Huang and Saito [31] that studies the concentration wake of several CO_2 bubbles of similar size rising in water using scanning that is not time resolved. Here, for the first time, a setup is developed that allows the quantitative reconstruction of the 3D concentration wake from single bubbles. Additionally, also time resolved scanning velocimetry can be performed in the same setup allowing a quantification of the velocity and vorticity in the scanning planes (Fig. 14c). Subsequently the velocity fields and the concentration fields measured from two different bubble rises can be compared since the bubble trajectory is reproducible due to the specific detachment from the hypodermic needle.

3.2.5 Numerical Simulation of Unconfined Ascending Bubbles

As stated in Sect. 3.2, incorporating the influence of surfactant is essential to find qualitative and quantitative agreement with experimental results. Deep insights may be gained from local interfacial data extracted from simulations that are not accessible by other measures. However, a thorough validation has to be performed to ensure that the numerical data is trustworthy. Typically, validation is based on integral experimental quantities like rise velocity, shape, or integral mass transfer rates. It must be stressed that the interface-tracking approach used to obtain the results presented hereafter has been extensively validated in these metrics against experiments from project partners. References [21, 22] contain a variety of test cases focusing on the surfactant modeling and the impact on the bubble dynamics. In [32], the experimentally and numerically obtained integral mass transfer coefficients at small oxygen bubbles rising in water have been compared, which is shown in Fig. 13d. In the following, the focus is put on local results at the interface. The main questions sought to answer in this chapter are:

1. How do the altered flow dynamics in the presence of contamination impact the mass transfer, and
2. how does this change affect the enhancement in case of reactive mass transfer?

It is known that the presence of surfactants can significantly reduce the rise velocity of a bubble. This observation is often attributed to an immobilization of the interface with the frequently stated comment that the bubble behaves very similar to a solid particle. This statement mainly holds for small bubbles rising on a straight path. However, when path instabilities occur, the surfactant influence on flow dynamics and mass transfer becomes much more complex.
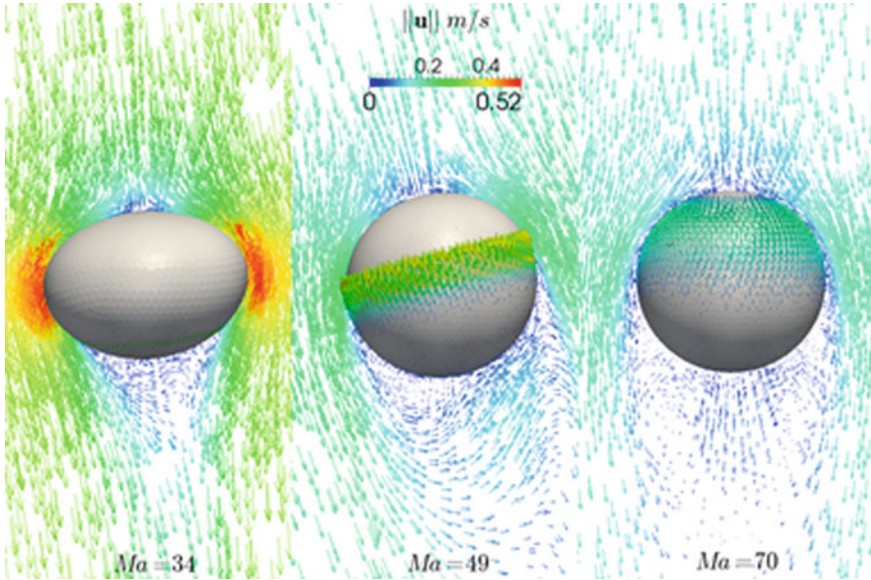
Fig. 15 Local velocity vectors (bulk) and Marangoni forces (interface) for three different degrees of contamination expressed by the Marangoni number *Ma*. Figure based on Fig. 25 in [22]; modified and reproduced with permission

Figure 15 depicts the flow field in the vicinity of the interface and the local Marangoni forces, which arise from different levels of contamination in different areas of the interface. Key observations are the decreasing deformation with increasing contamination along with the occurrence of a recirculation zone in the bubble wake and significantly reduced velocity close to the interface. With the newly developed experimental setup (compare Fig. 14) it will be possible to compare the 3D velocity fields of these complex bubble behaviors with experimental results in future work.

The mass transfer in the boundary layer around clean bubbles is dominated by advective transport in streamwise direction. Due to the Marangoni-induced surface retardation, the advective transport is strongly reduced and the species concentration boundary layer becomes thicker. This effect also causes a significant change in the local and global mass transfer. The thicker boundary layer gives a potential explanation for the behavior of the Sherwood number discussed for Fig. 7a, where the reduction of the overall bubble rise velocity due to contamination could not explain the decrease of the mass transfer. In the following, the impact on the local reactive mass transfer at a small bubble rising on a straight pass is analyzed in more detail.

Figure 16 depicts the normal derivative of the species concentration at the interface expressed by the local Sherwood number. All fields can be considered as axisymmetric around the rise direction. Therefore, the Sherwood number is plotted against the polar angle. A value of 0° corresponds to the bubble's front, whereas the rear
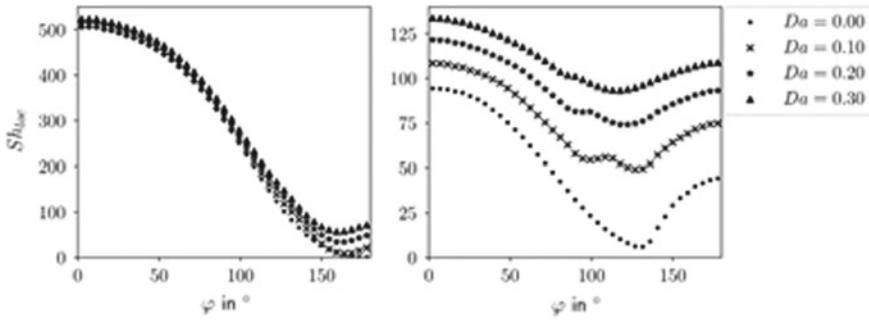
Fig. 16 Local reactive Sherwood number plotted against the polar angle for a clean (left, Re = 132) and contaminated (right, Re = 63) interface. Figure first published as Fig. 19 in [32]

pole is located at 180°. Comparing the curves for pure physisorption up to a polar angle of roughly 150° without (Fig. 16, left) and with contamination (Fig. 16, right) reveals a drastic drop in the local mass transfer. The reduction factor due to the presence of surfactant is about five. In the remaining rear part of the bubble, the surface contamination increases the mass transfer. This effect is a result of the recirculation zone in the bubble wake, which is not present in the absence of contamination. For a clean bubble, the transferred species is transported directly to the bubble's rear pole, where it accumulates at and around the stagnation point. Consequently, the species transfer in this region is comparatively low. In case of surface contamination, the local Marangoni forces cause a flow detachment somewhere between the bubble's rear pole and its equator. The species transfer around the detachment ring is close to zero, but since the species accumulates much slower in the bubble wake, the species transfer is increased in the remaining rear part. However, the integral mass transfer is dominated by the contribution of the bubble front. In total, the Sherwood number is approximately five times smaller in the contaminated case; see reference [32] for absolute values. To give a comparison, for the given example of the overall Sherwood number in Fig. 7a (in contrast to the local Sherwood number discussed here), a maximal reduction factor of roughly 7 was found.

To investigate the influence of surface contamination on the enhancement in case of reactive mass transfer, the comparison described before is repeated with an imposed first-order reaction taking place in the liquid phase. By comparing the clean and contaminated cases at equal Damköhler numbers, it is possible to isolate the impact of the different boundary layers on the species transfer. Note that this comparison would be hardly possible in an experimental setting. In contaminated systems, the rise velocity is reduced significantly which also has an impact on the Damköhler number. Therefore, the same reaction system has a larger Damköhler number for contaminated cases and the individual effect of contamination cannot be investigated separately. Comparing the clean and contaminated cases shows that the local enhancement is significantly stronger and less uniform in the latter case. The strongest local enhancement in both cases occurs in regions of low interfacial velocity. The non-uniform enhancement in the contaminated case poses a challenge for modeling

in closures, e.g., in Eulerian-Eulerian simulations. Basic one-dimensional enhancement factor correlations rely on an overall uniform enhancement over the entire bubble surface. Therefore, such models have a lower prediction accuracy in the presence of surface-active contamination; see [32] for more details. This confirms the statement conceived from the integral mass transfer measurements (Sect. 3.1).

The prediction in both clean and contaminated mass transfer scenarios becomes even more challenging when path and shape oscillations are relevant. Gathering high-fidelity data for both cases remains a challenge for numerical and experimental methods.

4 Opportunities of Experiments and Numerical Simulation on Freely Ascending Bubbles for Industrial Applications

Compartment modelling lays between high spatial and temporal resolution experiments and simulations, which need a high effort in conducting, and low-effort full apparatus black-box balancing, which is unable to reflect the strong influence of local phenomena. The general idea of the presented compartment model is to split up the ongoing processes in a reactive bubbly flow in two areas: the surface of the bubble on one side and the wake of the bubble on the other. Mass transfer and reaction at the gas-liquid interface are depicted by a surface model based on the penetration theory. The wake of the bubble can be seen as microreactor with a non-ideal mixing. This non-ideal reactor is described by the early-mixing model.

The surface model is based on the penetration theory according to Higbie [34]. In addition to the original model, a concentration profile within the first fluid element at the north pole of the bubble is imprinted (see Fig. 17, left). Further a velocity profile $u_s(\zeta)$ is imprinted on all fluid elements along the coordinate ζ. The velocity profile is determined according to flow over a plate and is constant over s. The surface model is applied from the north pole (0°) to the equator (90°) along the bubble, then the fluid element is assumed to detach from the bubble and to enter its wake.

The wake of the bubble is described with the early-mixing model as first suggested by Danckwerts and Zwietering [35, 36]. It describes the micromixing within a non-ideal mixed reactor based on a known residence time distribution (RTD). The RTD has been determined by inserting tracer molecules at the equator of the bubble from $\zeta = 0$ to $\zeta = \delta_L$. The early-mixing model can be visualized as an ideal plug flow tubular reactor with inlets on the side, which are located according to the determined RTD. Along the reactor, the time variable λ describes the residence time of each fluid element. For an inlet at the end of the reactor λ is zero, at its beginning it is $\lambda_{\max}$. A further description of the model is given in the dissertation of Gast [37], which is going to be published soon.

Figure 17 depicts the selectivity of the product C with respect to the gaseous educt B for the competitive-consecutive reaction
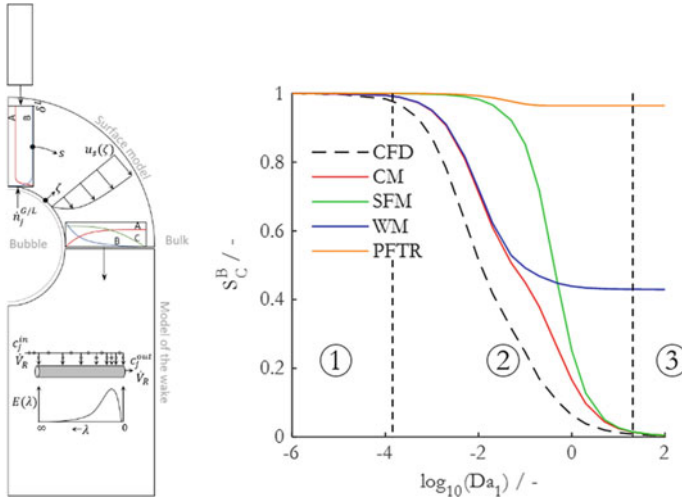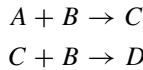
Fig. 17 Compartment model of reactive bubbly flow. Left: schematic drawing of the model. Right: Selectivity of product C with respect to educt B for the competitive consecutive reaction at Re = 30 calculated with detailed CFD, compartment model (CM), surface model (SFM), early-mixing model (WM), plug flow tubular reactor (PFTR)

$$A + B \rightarrow C$$
$$C + B \rightarrow D$$

Thereby, the selectivity is shown as a function of the first order Damköhler number (Da_1) which is varied by changing the reaction rates. The following models are compared:

- the detailed CFD calculation (CFD)
- the compartment model (CM) as described above
- the stand-alone surface model (SFM), which is combined with an ideal plug flow tubular reactor to reproduce the averaged residence time of the CFD-Model
- the stand-alone model of the wake (WM) with the input concentration c_B^{Abs} of B
- an ideal plug flow tubular reactor (PFTR) with the input concentration c_B^{Abs} of B

The amount of B transferred from the gas into the liquid phase has been calculated by averaging the output concentration of the CFD-Model for a non-reactive case.

The course of the selectivity as displayed in Fig. 17 can be classified into different reaction zones:

1. limited by reaction kinetics: the reaction is slow compared to the fluid dynamics, the mixture can be assumed as ideally mixed.
2. mixing masked area: the reaction is running on a similar time scale as the fluid dynamics, the non-ideal mixing within the wake of the bubble is influencing the path of the reaction and therefore the produced product spectrum.

3. limited by mass transfer: the reaction is fast compared to fluid dynamics, the ongoing reaction is limited by the mass transport.

To conclude, the compartment model is capable to picture the dependencies of the ongoing physical and chemical processes within the mixing masked reactive bubbly flow by using a reasonable computing time. All other compared models are only valid for very fast or very slow reactions. The quality of the compartment model depends on the information accessible for the different compartments. The information gained from integral and local fluid dynamic and mass transfer experiments as presented in Sect. 3 helps to feed and validate the model.

5 Conclusion

While single bubble ascents have been a widely investigated topic for decades, the uniqueness of the joint work presented here is its interdisciplinary approach in the field of gas-liquid mass transfer at single bubbles enhanced by chemical reactions. This topic, enormously important for the design of reactors in the chemical industry, was approached on different levels of detail. New chemical systems as model systems for scientific analyses were developed for homogenous chemical reactions in the liquid where the component transferred from the gas bubble served as an educt. By applying different metal-based reaction systems with diverse ligands in different reaction media (water and organic solvents), a broad range of reaction kinetics is now accessible at moderate conditions. In a rather classical approach, the bubble size change over time was investigated with an advanced three-dimensional reconstruction of the bubble. The analysis of the shrinking of the bubble allowed the determination of overall mass transfer coefficients and Sherwood numbers for diverse bubble sizes, physisorption and chemisorption cases all with diverse bubble rise dynamics including surfactant effects of ligands. With respect to different fluid dynamic effects, numerous groups investigated the wake region of the bubble. The wake region of non-spherical bubbles with different rising characteristics is of high importance due to the influence of its mixing effects on the mass transfer in general, but also, e.g., on consecutive competitive chemical reactions. For a deeper understanding of the effects of, for example, surfactants on the local mass transfer, detailed numerical simulations were performed with high temporal and spatial resolution of the flow and concentration fields in the vicinity of the bubble's surface. Such an approach allows the determination of local Sherwood numbers, giving deep insights into local influencing phenomena such as, e.g., Marangoni convection. The gained knowledge on different levels of detail was used to confirm, respectively improve existing Sherwood correlations, including cases with homogeneous chemical reactions, with the help of enhancement factors. Furthermore, a compartment model has been established for the rough estimation of the interplay between mass transfer near a single bubble and a chemical reaction. The Sherwood correlations and the compartment model provide a link to the bubble swarm cases and, therefore, industrial applications.

References

1. Whitman WG (1923) The two-film theory of gas absorption. Chem Met Eng 29:146–149
2. Deising D, Bothe D, Marschall H (2018) Direct numerical simulation of mass transfer in bubbly flows. Comp Fluids 172(30):524–537
3. Darmana D, Henket RLB, Deen NG, Kuipers JAM (2007) Detailed modelling of hydrodynamics, mass transfer and chemical reactions in a bubble column using a discrete bubble model: chemisorption of CO_2 into NaOH solution, numerical and experimental study. Chem Eng Sci 62:2556–2575
4. Krauß M, Rzehak R (2018) Reactive absorption of CO_2 in NaOH: An Euler-Euler simulation study. Chem Eng Sci 181:199–214
5. Yoo M, Han SJ, Wee J-H (2013) Carbon dioxide capture capacity of sodium hydroxide aqueous solution. J Environ Manage 114:512–519
6. Fleischer C, Becker S, Eigenberger G (1996) Detailed modeling of the chemisorption of CO_2 into NaOH in a bubble column. Chem Eng Sci 51:1715–1724
7. Kück UD, Kröger M, Bothe D, Räbiger N, Schlüter M, Warnecke H-J (2011) Skalenübergreifende Beschreibung der Transportprozesse bei Gas/Flüssig-Reaktionen. Chem Ing Tech 83(7):1084–1095
8. Bäckström HLJ (1934) Der Kettenmechanismus bei der Autoxydation von Aldehyden. Z Phys Chem 25B(1):99–121
9. Schneppensieper T, Wanat A, Stochel G, Goldstein S, Meyerstein D, van Eldik R (2001) Ligand effects on the kinetics of the reversible binding of NO to selected aminocarboxylato complexes of Iron(II) in aqueous solution. Eur J Inorg Chem 2001:2317–2325
10. Schneppensieper T, Finkler S, Czap A, van Eldik R, Heus M, Nieuwenhuizen P, Wreesmann C, Abma W (2001) Tuning the reversible binding of NO to Iron(II) aminocarboxylate and related complexes in aqueous solution. Eur J Inorg Chem 2001:491–501
11. Schneppensieper T, Wanat A, Stochel G, van Eldik R (2002) Mechanistic information on the reversible binding of NO to selected Iron(II) chelates from activation parameters. Inorg Chem 41(9):2565–2573
12. Miska A, Schurr D, Rinke G, Dittmeyer R, Schindler S (2018) From model compounds to applications: kinetic studies on the activation of dioxygen using an iron complex in a SuperFocus mixer. Chem Eng Sci 190:459–465
13. Miska A, Norbury J, Lerch M, Schindler S (2017) Dioxygen activation: potential future technical applications in reactive bubbly flows. Chem Eng Technol 40:1522–1526
14. Paul M, Strassl F, Hoffmann A, Hoffmann M, Schlüter M, Herres-Pawlis S (2018) Reaction systems for bubbly flows. Eur J Inorg Chem 2018(20–21):2101–2124
15. Mirica LM, Vance M, Rudd DJ, Hedman B, Hodgson KO, Solomon EI, Stack TDP (2005) Tyrosinase reactivity in a model complex: an alternative hydroxylation mechanism. Science 308(5703):1890–1982
16. Mirica LM, Stack TDP (2005) A Tris(μ-hydroxy)tricopper(II) complex as a model of the native intermediate in laccase and its relationship to a binuclear analogue. Inorg Chem 44(7):2131–2133

17. Merker D, Böhm L, Oßberger M, Klüfers P, Kraume M (2017) Mass transfer in reactive bubbly flows—a single-bubble study. Chem Eng Technol 40:1391–1399
18. Timmermann J (2018) Experimental analysis of fast reactions in gas-liquid flows. Ph.D. thesis, TU Hamburg-Hamburg
19. Muzaferija S, Peric M (1997) Computation of free-surface flows using the finite-volume method and moving grids. Numer Heat Transfer, Part B 32:369–384
20. Tukovic Z, Jasak H (2012) A moving mesh finite volume interface tracking method for surface tension dominated interfacial fluid flow. Comp Fluids 55:70–84
21. Pesci C (2019) Computational analysis of fluid interfaces influenced by soluble surfactant. Ph.D. thesis, Technical University of Darmstadt
22. Pesci C, Weiner A, Marschall H, Bothe D (2018) Computational analysis of a single rising bubble influenced by soluble surfactant. J Fluid Mech 856:709–763
23. Weiner A, Bothe D (2017) Advanced subgrid-scale modeling for convection-dominated species transport at fluid interfaces with application to mass transfer from rising bubbles. J Comput Phys 347(1):261–289
24. Tomiyama A, Katakoa I, Zun I, Sakaguchi T (1998) Drag coefficients of single bubbles under normal and micro gravity conditions. JSME Int J, Ser B 41(2):472–479
25. Hosoda S, Abe S, Hosokawa S, Tomiyama A (2014) Mass transfer from a bubble in a vertical pipe. Int J Heat Mass Transfer 69:215–222
26. Hughmark GA (1967) Holdup and mass transfer in bubble columns. Ind Eng Chem Process Des Dev 6(2):218–220
27. Fan LS, Tsuchiya K (1990) Bubble wake dynamics in liquids and liquid-solid suspensions. Butterworth-Heinemann, Stoneham
28. Yabe K, Kunii D (1978) Dispersion of molecules diffusing from a gas bubble into a liquid. Int Chem Eng 18:666–671
29. Levy H, Forsdyke AG (1928) The steady motion and stability of a helical vortex. Proc R Soc Lond A 120:670–690
30. Lindt JT (1972) On the periodic nature of the drag of a rising bubble. Chem Eng Sci 27:1775–1781
31. Huang J, Saito T (2017) Discussion about the differences in mass transfer, bubble motion and surrounding liquid motion between a contaminated system and a clean system based on consideration of three-dimensional wake structure obtained from LIF visualization. Chem Eng Sci 170:105–115
32. Weiner A, Timmermann J, Pesci C, Crewe J, Hoffmann M, Schlüter M, Bothe D (2019) Experimental and numerical investigations of reactive species transport around a small rising bubble. Chem Eng Sci X 1:
33. von Kameke A, Kexel F, Rüttinger S, Colombi R, Kastens S, Schlüter M (2019) 3D-reconstruction of O_2 bubble wake concentration. In: Proceedings of the 13th international symposium on particle image velocimetry, Munich
34. Higbie R (1935) Rate of absorption of a pure gas into still liquid during short periods of exposure. Trans Am Inst Chem Eng 31:365
35. Danckwerts PV (1958) The effect of incomplete mixing on homogeneous reactions. Chem Eng Sci 8(1–2):93–102
36. Zwietering TN (1959) The degree of mixing in continuous flow systems. Chem Eng Sci 11(1):1–15
37. Gast S (2021) Experimentelle und numerische Studie einer Gas-Flüssigreaktionskinetik in homogener flüssiger Phase und ihrer Mischungsmaskierung in reaktiven Blasenströmungen am Beispiel der Toluoloxidation, Ph.D. thesis, University of Stuttgart (to be published)

Chemical Reactions in Bubbly Flows

Uwe Hampel, Ragna Kipping, Katharina Zähringer, Péter Kováts,
Martin Sommerfeld, Manuel A. Taborda, Roland Rzehak,
Mark Hlawitschka, Peter Klüfers, and Martin Oßberger

Abstract Reactive bubbly flows are found in many chemical and biochemical
processes. They are characterized by complex hydrodynamics that govern global
mass transfer and reaction rates. Effects, which have to be taken into account when
modelling and simulating the reaction progress, are enhanced bubble–bubble inter-
action and bubble-induced turbulence as well as swarm-induced macro-convection.
This poses great challenges on both, experimental analysis and numerical simula-
tion. Bubble swarms at higher gas fractions are opaque, which limits the use of
optical flow measurement techniques. Moreover, simulations at industrial scale are
only feasible with point-bubble-based Euler-Euler or Euler–Lagrange approaches.
Such approaches require closure relations, which account for all relevant interfacial
forces as well as bubble-induced turbulence and coalescence including swarm effects.
This chapter describes the progress in the experimental analysis and CFD simulation
of reactive bubbly flows achieved during the time of the DFG Priority Programme
SPP 1740. Experimental studies in bubble columns reported in this chapter were
carried out at TU Dresden and OVGU Magdeburg. CFD model development and

U. Hampel (✉) · R. Kipping
Institut für Energietechnik, Technische Universität Dresden, 01062 Dresden, Germany
e-mail: uwe.hampel@tu-dresden.de

U. Hampel · R. Rzehak
Institut für Fluiddynamik, Helmholtz-Zentrum Dresden-Rossendorf, 01328 Dresden, Germany

K. Zähringer · P. Kováts
Lehrstuhl für Strömungsmechanik und Strömungstechnik, Otto-von-Guericke-Universität
Magdeburg, 39106 Magdeburg, Germany

M. Sommerfeld · M. A. Taborda
Institute for Process Engineering, Otto-von-Guericke University Magdeburg, Multiphase Flow
Systems, Hoher Weg 7b, 06120 Halle (Saale), Germany

M. Hlawitschka
Institute of Process Engineering, Johannes Kepler Universität Linz, Altenbergerstraße 69, 4040
Linz, Austria

P. Klüfers · M. Oßberger
Department Chemie, Lehrstuhl für Bioanorganische Chemie und Koordinationschemie,
Ludwig-Maximilians-Universität München, Butenandtstraße 5–13, 81377 München, Germany

simulation has been carried out at OVGU Magdeburg using the Euler-Euler and Euler–Lagrange method and at TU Kaiserslautern and Helmholtz-Zentrum Dresden-Rossendorf using the Euler-Euler approach. As reaction systems the chemisorption of CO_2 in NaOH solution and the reaction of $Fe^{II}(edta)$ with NO were studied.

1 Introduction to Bubbly Flows in Bubble Columns

Industrial bubble column design is today mainly based on simple reactor models and correlations obtained from extensive experimental work [1]. The most common engineering reactor model for bubble columns is the axial dispersion model, sometimes extended to the axial-radial dispersion model. For that, a number of correlations exist, relating bubble diameter, liquid and bubble rise velocity as well as their dispersion coefficients to dimensionless numbers, which encode the column geometry and fluid properties. Once hydrodynamics is known, the reaction progress can be modelled by a combination of suitable models for stationary [2] or unsteady [3] mass transfer and reaction kinetics.

Industrial bubble column reactors are mostly operated in the homogeneous bubbly flow regime, which is characterized by uniform bubble size distribution and uniform radial gas holdup profiles. For gas superficial velocities above 0.04 m/s the bubbly flow becomes heterogeneous. The transition starts with the development of a parabolic liquid velocity profile leading to liquid recirculation and increased bubble coalescence. Large bubbles with strong buoyancy appear in the center of the column and produce a pronounced liquid and gas velocity peak there. Beside the superficial gas velocity, the flow regime transition depends on the liquid properties, the gas distributor design and also the column diameter [4].

Bubbly flows are characterized by swarm effects as bubbles do no longer rise independently from each other but do interact. A major swarm effect in homogenous bubbly flow is the reduction of bubble rise velocity compared to single bubbles in quiescent liquid. In their pioneering work, Richardson and Zaki [5] proposed the correlation $V_{rel} = V_{\infty}(1 - \alpha_G)^n$ for bubble swarms with relative velocity V_{rel}, rise velocity V_{∞}, gas holdup α_G and the Richardson and Zaki exponent n, which accounts for bubble–bubble interactions. Subsequently, similar relations, which account for different bubble properties, have been derived by other groups, e.g. [6, 7]. Bubbles in a swarm arrange in clusters, which are energetically more optimal. This feeds back on turbulence generation and produces certain macroscopic flow patterns, which are again dependent on the large-scale geometry of the vessel. Fundamentally, it is assumed that small and spherical bubbles are less deformed and produce a small and less developed wake, which results in a low pressure drop. In this case, the impact of the lift force leads to a horizontal alignment. In contrast, large deformed bubbles tend to form an open wake, which results in a high pressure drop and consequently the neighboring bubbles are attracted to this region leading to a vertical bubble alignment [8, 9]. In bubbly flows, bubble-induced turbulence is higher and so is the

micro-mixing while mass transfer has been reported as less influenced by swarm effects [10].

With increasing computing power, computational fluid dynamics (CFD) nowadays enables to simulate the hydrodynamic transport processes in bubble columns more realistically and fully three-dimensional and hence to circumvent complicated multi-parametric models. However, large-scale simulations are still only feasible with the "point-bubble" Euler-Euler and Euler–Lagrange approaches, both of which rely on modelling phenomena occurring on the scale of individual bubbles or small groups thereof (see for example [11, 12]). Hence, there is still a need to improve such sub-models, e.g. regarding the forces acting on the bubbles or the mass transfer coefficient governing absorption or desorption. Since these models describe local physical effects, they depend only on the local flow conditions but are independent of the large-scale geometry and boundary conditions, the latter being resolved in the simulations. Therefore, a much larger range of applicability may be expected for such simulations compared with typical engineering design models. Nonetheless, these simulations need to be validated for a broad range of conditions representative of their intended applications.

In Euler-Euler simulations, both phases are treated as interpenetrating continua, each described by a set of conservation equations for mass and momentum. This implies that the bubbles are only represented by cell-averaged values and bubble-specific properties are lost. Momentum exchange between the phases is accounted for by coupling terms between both sets of conservation equations. Due to the direct coupling of the equations for both phases and the use of model closures, bubbly flows with high gas volume fraction may be effectively computed and therefore this approach is often preferred in bubble column engineering. The Euler-Euler approach is most frequently combined with a RANS (Reynolds-averaged Navier–Stokes) turbulence model, which is augmented by additional source terms describing the bubble-induced contribution to turbulence (see e.g. [13]). In the sub-models for momentum exchange and bubble-induced turbulence, the bubble size appears as a parameter. Setting this to a constant value gives the mono-disperse approximation, which has been adopted in the majority of studies up to date. Swarm-effects have not been considered in most previous studies. Within these approximations, a model that has been validated over an extended period of time for a rather large database of experimental test cases is described in [14].

A distribution of bubble sizes which changes in time may be accommodated by coupling the approach described so far to a population balance equation. In doing so, it is important to allow bubbles of different sizes to move in different directions when necessary. An example, where this is important, is furnished by the finding of e.g. Tomiyama et al. [15] that the lift force changes its direction at a certain bubble size. While different frameworks have been proposed to numerically solve the population balance equation, one that meets this requirement in a rather straight forward way is the so-called inhomogeneous MUSIG (multiple size group) model. Among physical phenomena that change the bubble size distribution, bubble coalescence and breakup have received most attention so far, but a consensus on the most appropriate models has not yet been reached [16].

In the hybrid Euler–Lagrange approach the bubble phase is represented by individual point-like particles, which are being tracked and from which averaged properties for the dispersed phase are obtained by ensemble averaging. Consequently, bubble-scale transport processes can be modelled at much more detail and in a more descriptive way. This concerns interfacial forces, bubble dynamics and oscillations, wake separation and turbulence production as well as coalescence. In addition, a bubble size distribution can be considered without additional numerical effort and with arbitrary resolution. Such a Lagrangian treatment allows for a very fundamental and detailed consideration of the relevant interfacial forces, including e. g. the Basset force (see for details [17]), which allows additional consideration of the bubble dynamics (e.g. shape and trajectory oscillations) as this is essential for correctly predicting bubble dispersion as shown in [18]. Recently, the Euler–Lagrange approach has mostly been used in connection with LES (large eddy simulations) as reviewed in [19]. Since the Euler–Lagrange method is a hybrid approach, the coupling between the phases is of huge significance, being based on the ensemble averaged coupling terms, which require a sufficiently large number of bubbles tracked through the evolving flow field. The possibilities for doing such a coupling in a reliable way are summarized in [20]. In bubbly flows the free distance between bubbles is continuously reduced (e.g. at a gas volume fraction of 20% the inter-bubble distance is only 1.37 diameters for a regular cubic packing). Therefore, it requires models for the hydrodynamic interaction between bubbles as well as efficient models for bubble collision detection and a possible coalescence. When the volume fraction of bubbles further increases and the free motion distance between subsequent collisions further decreases (see [11] for an estimate), a contact dominated bubble behavior will eventually be reached [20]. Then, the Lagrangian approach becomes numerically increasingly expensive (see e.g. [21]). Despite of that, this approach is a very powerful tool for analyzing basic transport processes and their role with respect to optimal operation of industrial-scale bubble column reactors at moderate volume fractions (see e.g. [22]). Moreover, the Euler–Lagrange approach allows for supporting closure developments to be used in the frame of a two-fluid (Euler-Euler) approach. Such Euler-Euler models are still preferred by industry due to the lower computational effort. However, it must be kept in mind that the latter goes at the cost of modelling depth. Nevertheless, both approaches the Euler-Euler and the Euler–Lagrange method are very much complementary and should both be further qualified in the future.

2   Setups for Experimental Studies

Experimental studies on reactive bubbly flows within the Priority Programme SPP 1740 were carried out for absorption of CO_2 into aqueous NaOH solution in different types of bubble columns and under different operating conditions. Outside this SPP, Darmana et al. performed experiments in a pseudo-2D rectangular bubble column of 0.2 m width and 0.03 m depth and a gas sparger consisting of 21 needles (volume flow rate per needle: $\dot{V} = 2.2$ ml/s) arranged with a square pitch of 5 mm

in the centre of the column bottom [23]. The column was initially filled up to 1 m with aqueous NaOH with pH 12.5. First, nitrogen gas was injected until steady flow conditions were reached. Then, gas supply was switched to pure CO_2. According to the authors, experimental conditions were: $j_G = 0.7$ cm/s superficial gas velocity, $d_B = 5.5$ mm bubble size at the inlet and a resulting total gas holdup of $\alpha_G = 1.2\%$. The time-dependent pH at a single point located 2 cm below the liquid surface and a time-averaged vertical bubble size profile, were measured, both in the centre of the column. Several groups within the consortium have used this data for numerical validation purposes, as it was available at an early stage.

At WG Hampel a lab-scale bubble column with an internal diameter of $D = 0.1$ m and a clear liquid height of $h = 1.4$ m was operated (Fig. 1, right). Gas was distributed via a capillary sparger, consisting of 84 individually addressable needles at the bottom of the column. Depending on the gas flow rate, between 13 and 84 needles were used. The gas operation was like in the Darmana case, i. e., operation with CO_2 just after a sufficient flushing with nitrogen. Experiments were conducted for different gas flow rates up to $j_G = 2.5$ cm s^{-1} and pH values between pH $= 11.0$ and 12.5. Measurement data was obtained at two axial locations, $z = 0.1$ m and $z = 0.7$ m above the sparger. Ultrafast electron beam X-ray computed tomography (UFXCT) was employed to obtain local gas holdup, bubble sizes and average axial gas phase velocities. Simultaneously, wire-mesh sensors were used for measurement of local species conversion during chemical absorption of CO_2.

In the group of Zähringer a bubble column of $D = 0.14$ m diameter and a filling height of $h = 0.73$ m was operated (Fig. 1, left). To allow for the use of optical
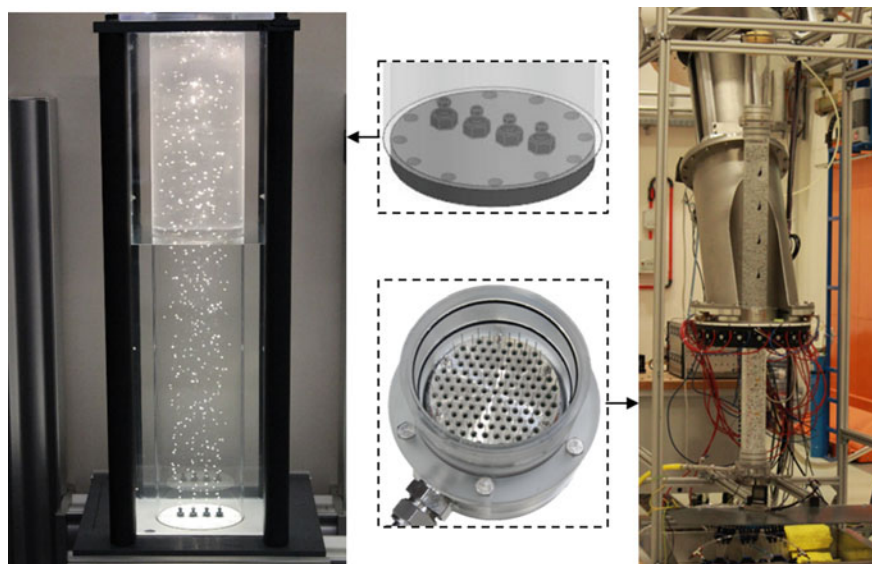

Fig. 1 Photographs of experimental facilities in the group of Zähringer (left) and Hampel (right) and detailed view of the gas spargers

measurement techniques, the bubble column is surrounded by a rectangular acrylic box for refractive index matching. This box has been filled with the working fluid, that is, deionized water or, for some cases, water-glycerol-surfactant mixtures (see chapter "Experimental Characterization of Gas–Liquid Mass Transfer in a Reaction Bubble Column Using a Neutralization Reaction"). The interchangeable bottom of the bubble column allowed for the production of bubble chains with one nozzle or a bubble curtain with four nozzles in a line. The nozzles produced CO_2 bubbles with a diameter of about $d_B = 2$–4 mm. The optical measurement techniques allowed for the two-dimensional determination of bubble size and velocity distributions, liquid velocity and pH change due to CO_2 absorption in the solution. In addition, the influence of viscosity and surface tension of the liquid on bubble parameters and mass transfer was studied in this column.

Essential parameters of the aforementioned three experimental setups are summarized in Tables 1 and 2. Further details can be found in the earlier chapters describing the individual results of the working groups.

Table 1 Overview of experimental setups

	Darmana et al.	Hampel	Zähringer
Column dimensions			
Column shape	Square	Circular	Circular
Dimension	0.2 m × 0.03 m	Ø 0.1 m	Ø 0.14 m
Clear liquid height	1.0 m	1.4 m	0.73 m
Sparger	21 needles	13–84 needles	1 or 4 needles
Operating conditions			
Bubble size	5.5 mm	4 – 5 mm	2 – 4 mm
Gas holdup	1.2%	<14%	<0.1%
pH value	12.5	11.0–12.5	9–5
Measurement techniques			
Hydrodynamics	High-speed camera	UFXCT	PIV, PTV, Shadowgraphy
Mass transfer	pH meter	Wire-mesh sensor	2 T-LIF

Table 2 Physical properties of the mixtures used in the bubble column experiments in the group of Zähringer

Case	Density (kg/m^3)	Viscosity (mPa·s)	Surface tension (mN/m)	Gas holdup (%)	Mean bubble size (mm)
Without Glycerol	996.89	0.9	72.24	0.03	2.75
50% Glycerol	1123.6	4.76	67.81	0.06	3.3

3 Applied Measurement Techniques

For the measurement of bubble size, aspect ratio and velocity, shadowgraphy combined with Particle Tracking Velocimetry (PTV) has been used in the group of Zähringer [24–28]. The method is based on the evaluation of shadow images of the bubbles, obtained by a camera and a homogeneous background illumination (see chapter "Experimental Characterization of Gas–Liquid Mass Transfer in a Reaction Bubble Column Using a Neutralization Reaction"). The influence of different parameters, such as liquid composition, filling height, surface tension and viscosity on bubble size, form, motion, and rising velocity, have been examined at different gas flow rates. Local liquid velocities in the column have been measured by Particle Image Velocimetry (PIV). This method allows for the determination of 2D velocity fields via the cross-correlation of particle images [29]. Depending on the parameters to be examined in the bubble column, different PIV setups have been used, starting with classical PIV at a frame rate of $f = 10$ Hz, over simultaneous 2 T-LIF and PIV at $f = 3.33$ Hz, to high-speed PIV (HS-PIV) at $f = 1000$ Hz. For this, different combinations of cameras, objectives and spatial arrangements have been used. Details can be found in chapter "Experimental Characterization of Gas–Liquid Mass Transfer in a Reaction Bubble Column Using a Neutralization Reaction" and [24–26].

Mass transfer in the group of Zähringer has been examined in the column through 2-Tracer Laser Induced Fluorescence (2T-LIF) of a tracer dye showing the pH in the liquid (see Fig. 2). Mass transfer from CO_2 bubbles rising in a stagnant, initially alkaline (pH $\approx$ 9) NaOH solution leads to a decrease of the pH value. This can be quantified and tracked optically by 2T-LIF, without being troubled by the shadows that are produced in a laser light sheet by the bubbles. Details of this method can
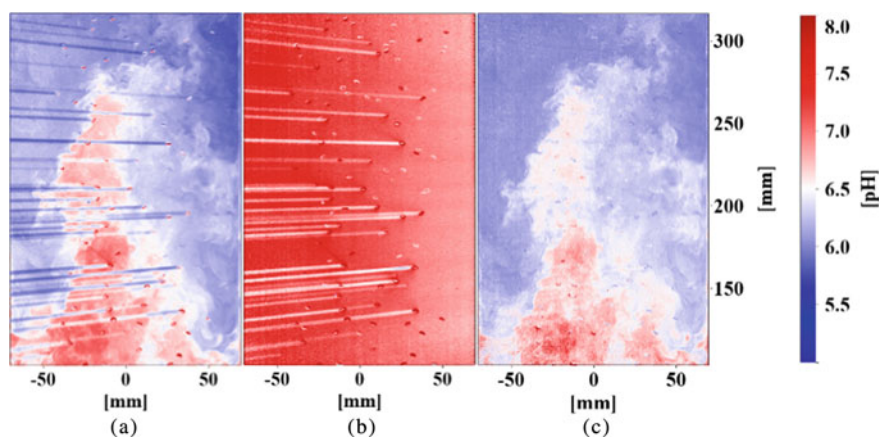

Fig. 2 Schematic of post processing of measurement data from 2 T-LIF: **a** raw image from 1st camera imaging the pH-tracer uranine; **b** raw image from 2nd camera imaging the inert tracer pyridine 2; *c* treated image after calibration showing the pH. Bottom part of the column (100–320 mm)
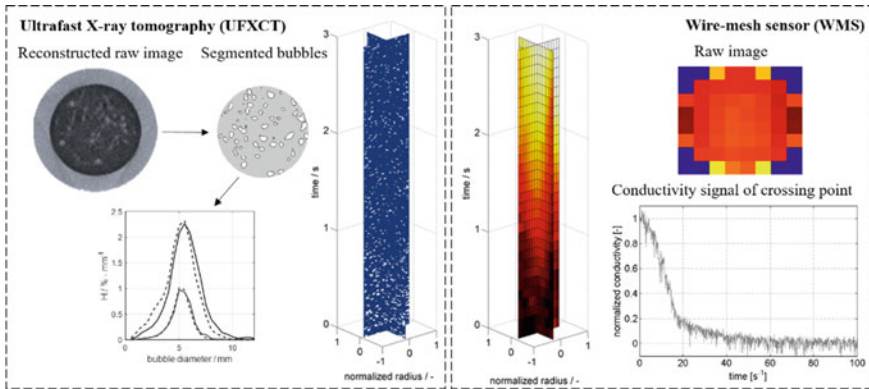
Fig. 3 Schematic of post processing steps of ultrafast X-ray tomography (left) and wire-mesh sensor data (right)

be found in chapter "Experimental Characterization of Gas–Liquid Mass Transfer in a Reaction Bubble Column Using a Neutralization Reaction" and [30, 31]. The liquid (de-ionised water and NaOH, pH ≈ 9) containing two fluorescent dyes, is filled into the column and the fluorescence of both dyes is imaged simultaneously but separately, by two cameras and appropriate optical filters. One of these dyes (uranine) is changing its fluorescence intensity with the pH, the other (pyridine 2) stays passive. The images from this dye serve as a live background, which significantly reduces artefacts from bubble shadows, reflections and laser sheet inhomogeneities on each image.

For experiments at the DN100 bubble column in the group of Hampel, ultra-fast electron beam X-ray computed tomography (UFXCT) has been used to determine local hydrodynamic parameters, such as local gas holdup, bubble sizes and interfacial area and wire-mesh sensor has been used for the measurement of cross-sectional resolved species conversion during chemical absorption of CO_2. The main post-processing steps are summarized in Fig. 3. Ultrafast electron beam X-ray computed tomography (UFXCT) is a fast cross-sectional imaging technique based on a scanned electron beam technology. Contrary to medical CT systems, a moving radiation source is generated by an electron beam which allows for fast imaging [32]. Here, measurements were carried out at a frame rate of 1000 frames per second in two planes and for 20 s scanning time. Image data were reconstructed using the method of filtered back-projection. Hereafter, several post-processing steps, such as normalization and binarization, are applied to obtain cross-sectional phase distribution, bubble sizes, Sauter diameter and average axial gas phase velocities [33]. In addition to UFXCT, two wire-mesh sensors (WMS) were simultaneously operated $z = 0.1$ and $z = 0.7$ m above the gas sparger to measure local species conversion during chemical absorption of CO_2. In a wire-mesh sensor, wire electrodes are spanned across the column's cross-section in a matrix-like arrangement. An electronics measures electrical conductivity in the volumes around the wire crossings. In this study, a

wire-mesh sensor with 2×8 equidistant wires, giving 52 spatial sampling points in the column cross-section, was used. From measured electrical conductivities one can get the concentration of the most active ions, here OH^- [34]. This in turn gives the local hydroxide conversion rate $\vartheta_{OH^-} = \frac{\Delta c_{OH^-}}{\Delta t_{OH^-}}$, where Δc_{OH^-} is the initial concentration of NaOH and Δt_{OH^-} is the time needed for consumption. In agreement with [23], this parameter is assumed to be proportional to the rate of CO_2 mass transfer, since dissolved CO_2 immediately reacts with OH^-.

4 Reaction Systems

One reaction system being considered within the Priority Programme SPP 1740 is the chemisorption of CO_2 in alkaline solutions. It starts with the physical absorption of gaseous CO_2 into the aqueous phase:

$$CO_{2(g)} \rightarrow CO_{2,(l)}. \tag{1}$$

According to [35] for pH > 10, the dissolved $CO_{2,(l)}$ reacts with hydroxide ions (OH^-) and forms hydrogen carbonate ions (HCO_3^-)

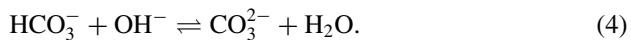$$CO_{2(l)} + OH^- \rightleftharpoons HCO_3^-. \tag{2}$$
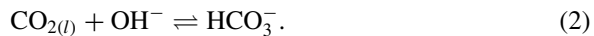
Forward and backward rate constants for this reaction are denoted as $k_1^\pm$ (Table 3).

Contrary, for pH < 8 the reaction pathway of dissolved $CO_{2,(l)}$ with water is

$$CO_{2(l)} + H_2O \rightleftharpoons HCO_3^- + H^+ \tag{3}$$
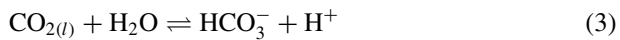
with rate constants $k_2^\pm$. As a second reaction step, the HCO_3^- ions react with OH^- ions to carbonate ions (CO_3^{2-}) at rates defined by $k_3^\pm$

$$HCO_3^- + OH^- \rightleftharpoons CO_3^{2-} + H_2O. \tag{4}$$

At high pH values the equilibrium concentration of HCO_3^- is negligible and thus for highly concentrated NaOH solution the reaction can be described by

$$CO_{2(l)} + 2OH^- \rightarrow CO_3^{2-} + H_2O. \tag{5}$$
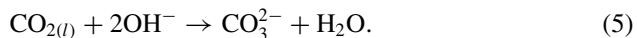
A second reaction system that has been developed and used within the Priority Programme for technical scale studies is the chemical reaction of NO with Fe^{II} complexes [36]. It is technically used, e.g. for extracting NO out of flue gas in combustion plants [37] or in the BioDeNOx process [38]. Since the complex in aqueous solution comes with an intense color ($\varepsilon_{435\,nm} = 820$ L mol^{-1} cm^{-1}), the system is useful for the visible detection of the $[Fe(edta)(NO)]^{2-}$ complex, e.g. in the

Table 3 Comparison of the different simulation setups (detailed descriptions of the models are given in the references at the top)
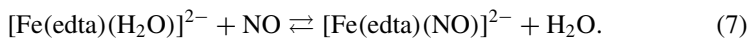
Identifier	DAR	SPP-EL	SPP-EE1	SPP-EE2	SPP-PM
Reference	Darmana et al. [23]	Taborda and Sommerfeld [48, 49]	Hlawitschka et al. [28, 51]	Krauß and Rzehak [46]	Krauß and Rzehak [47]
Approach	Euler–Lagrange	Euler–Lagrange	Euler-Euler	Euler-Euler	0-dim. model for species conc. at measurement point
Code basic	In house	OpenFOAM 4.1: own solver extended	OpenFOAM: v 2.3.0: own solver extended	ANSYS CFX 14.5	Matlab
Variation in bubble size	Yes	Yes, by mass transfer and pressure difference	Not for this case	Yes, by mass transfer and pressure difference	No
Variable enhancement factor	App. solution of penetration model for 2nd order reaction	App. solution of penetration model for 2nd order reaction	Yes, Fleischer et al. [50]	Full solution of penetration model for 2nd order reaction	Full solution of penetration model for 2nd order reaction
Bubble interaction	No	No	No	No	No
Bubble oscillation motion	No	No (NoOsc)/yes (FDM)	No	No	No
Reaction constant k_1^+ in Eq. (2)	Correlation including concentration and temperature	5436.9428 m^3/(kmol s) at 20 °C	Incl. temperature effects (9015 m^3/(kmol s @27 °C))	Correlation including concentration and temperature	Correlation including concentration and temperature
Reaction constant k_1^- in Eq. (2)	Correlation including concentration and temperature	9.29355E-5 m^3/(kmol s)	Incl. temperature effects (2.4E^{-4} m^3/(kmol s))	Correlation including concentration and temperature	Correlation including concentration and temperature
Reaction constant k_2^+ in Eq. (3)	Correlation including concentration and temperature	1E6 m^3/(kmol s)	1E6 m^3/(kmol s)	Correlation including concentration and temperature	Correlation including concentration and temperature
Reaction constant k_2^- in Eq. (3)	Correlation including concentration and temperature	168 m^3/(kmol s)	Incl. temperature effects 168 m^3/(kmol s)	Correlation including concentration and temperature	Correlation including concentration and temperature

(continued)

Table 3 (continued)

Identifier	DAR	SPP-EL	SPP-EE1	SPP-EE2	SPP-PM
Reaction constant k_3^+ in Eq. (4)	Reaction not included	0.0373946 m^3/(kmol s)	Reaction not included	Correlation including concentration and temperature	Correlation including concentration and temperature
Reaction constant k_3^- in Eq. (4)	Reaction not included	60,138.79 m^3/(kmol s)	Reaction not included	Correlation including concentration and temperature	Correlation including concentration and temperature
CO_2 Henry's constant	Correlation including concentration and temperature	0.84721	Correlation including temperature effects (0.81478)	Correlation including concentration and temperature	Correlation including concentration and temperature
CO_2 diffusion coefficient	Correlation including concentration and temperature	1.9182E−9	Correlation including temperature (2.0114E−9)	Correlation including concentration and temperature	Correlation including concentration and temperature

bubble wake. The preparation of the starting compound solution and the subsequent reaction with NO is given by the following equations:

$$\left[Fe(H_2O)_6\right]^{2+} + edta^{4-} \rightleftarrows [Fe(edta)(H_2O)]^{2-} + 5H_2O \tag{6}$$

$$[Fe(edta)(H_2O)]^{2-} + NO \rightleftarrows [Fe(edta)(NO)]^{2-} + H_2O. \tag{7}$$

Reaction rates for Eq. (6) are $r = 1.70 \times 10^8$ m^3/(kmol s) for the forward reaction and $r = 91$ m^3/(kmol s) for the backward reaction [37]. Due to the hazard potential of experiments with large NO amounts, some safety precautions are required. Useful information about the knowledge transfer from the chemistry to the engineering laboratory can be found in chapter "In Situ Characterizable High-Spin Nitrosyl–Iron Complexes with Controllable Reactivity in Multiphase Reaction Media".

5 Developed CFD Tools and Validation with the Darmana Case

Different solvers were developed and extended to describe the chemisorption in bubble columns. The group of Hlawitschka and the group of Rzehak applied Euler-Euler based solvers, enabling bubble column investigations with dense bubbly flows.
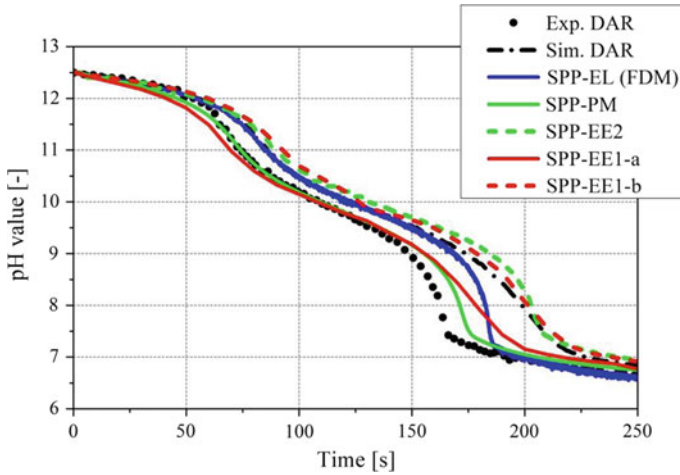
Fig. 4 pH value variation over time measured in the column centre at z/H $=$ 0.95 (i. e. close to the free surface of the column); Comparison of the different modelling approaches (label details see Table 3) with the experimental and numerical results of Darmana et al. [23]

The group of Sommerfeld improved the Euler–Lagrange simulations including individual bubble motion, extended beyond the standard point-bubble treatment. Therefore, the developed Euler–Lagrange framework serves as a bridge between the coarse-scale Euler-Euler approach and interface resolved simulations. The results of the three solvers are compared in Figs. 4 and 5 to the experimental and simulation results of Darmana et al. [23], described in Sect. 6.2.1 for the reaction of CO_2 in NaOH solution.

The OpenFOAM solver multiphaseEulerFoam (version 2.3.0) was extended by Hlawitschka [28, 39] to account for reactive mass transfer in industrial-scale bubble columns. Thereby, they followed the multi-scale approach for bubble column layout presented in chapter "Multi-scale Investigations of Reactive Bubbly Flows". The solver had to be extended by adequate drag, lift and bubble-induced turbulence models to account for the hydrodynamics in bubble columns. In addition to standard visualization techniques, such as that described in [40], newly developed feature-based as well as comparative visualization features were developed for bubble columns. These enabled an investigation of the hydrodynamics influence on reactive mass transfer, e.g. the influence of different sized bubbles and vortex structures [41]. For the reactive mass transfer, a reaction framework was developed and coupled to the solver, which could then be adopted directly for Euler–Lagrange simulations [42, 43]. Furthermore, population balance modelling was introduced to account for poly-disperse bubble size distributions [44, 45], enabling also predictions at higher gas flow rates.

Euler-Euler simulations were also performed by Rzehak using ANSYS CFX [46]. There, a previously established closure model for the fluid dynamics of bubbly flows was used [14]. This model comprises a set of forces acting on the bubbles, i. e.
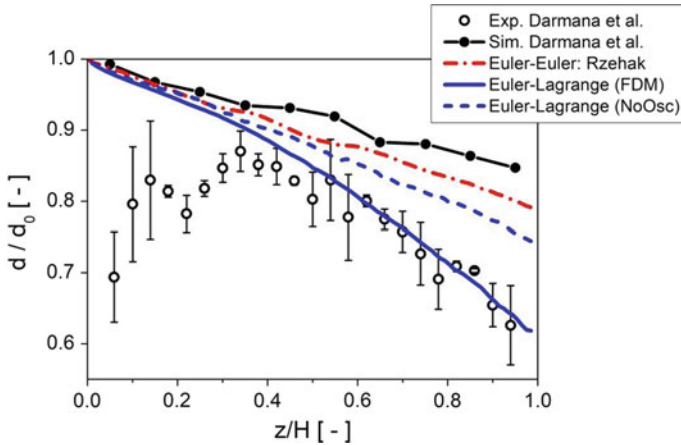
Fig. 5 Volume equivalent number-based bubble diameter ratio (normalized by the injection diameter of 5.5 mm) along the bubble column core region averaged over an interval of 20–95 s. Comparison of numerical simulations using different model assumptions (see Table 3 for details; Euler–Lagrange full dynamics model (FDM); Euler–Lagrange (NoOsc) no oscillations and point-bubble approximation (SPP-EL); Euler-Euler (Rzehak; SPP-EE2)) with experimental and simulation results of Darmana et al. [23]

drag, lift, wall, and turbulent dispersion, as well as source terms for the bubble-induced turbulence and shows good predictions for flows in bubble columns (see also "chapter Euler-Euler Modeling of Reactive Flows in Bubble Columns") as well as bubbly pipe flows.

Models for mass transfer and chemical reactions were first investigated in isolation. In [47] a simple zero-dimensional model was developed that describes the concentrations of all species at the measurement point in the experiment of [23]. For the bubble size, the measured value at this point $d_B = 3.5$ mm was imposed and for the gas fraction the measured average value over the entire column $\alpha_G = 1.2\%$ was used. This permitted the evaluation of different models for the enhancement factor and the reaction network. As described in more detail in chapter "Euler-Euler Modeling of Reactive Flows in Bubble Columns", it was found necessary to use an improved model for the enhancement factor and take into account the reaction between CO_2 and water in addition to that with hydroxide ions. In a second step, these models were then used in the full Euler-Euler simulation of the entire column attempting to predict also the evolution of bubble size and gas fraction [46]. In order to include the shrinkage of the bubbles, suitable source terms for the inhomogeneous MUSIG model were developed. For the material properties and the rate constants of all occurring reactions a detailed model including dependence on the ionic strength of the solution was assembled from the literature and applied in both approaches.

The applied Euler–Lagrange approach uses a fully coupled LES (large eddy simulation) method for the fluid flow by solving an additional transport equation for the SGS (sub-grid-scale) turbulence [48] and accounts thereby also for bubble-induced

turbulence as well as turbulence dissipation. The classical Lagrangian point-bubble approach has, especially for bubbly flows, strong limitations with respect to transport effects occurring on the scale of the bubbles. Therefore, this approach was thoroughly extended by a bubble dynamic oscillation model for eccentricity, trajectory as well as mass transfer through a dynamic Sherwood number. Consequently, the relevant forces acting on the bubbles (i. e. drag, lift, fluid inertia, added mass, Basset force and gravity buoyancy) could be, where possible and appropriate, extended in order to account for the instantaneous eccentricity [17]. In addition, bubble transport by SGS turbulence was modelled by generating randomly the instantaneous fluid velocity seen by the bubbles. Naturally, bubble size variations due to pressure change and mass transfer are accounted for. This involves also the solution of additional transport equations for the relevant species. For describing the reaction process, different reaction schemes may be considered. In this case, also an enhancement factor was accounted, which is in the considered case strongly dependent on pH (see also chapter "Modelling the Influence of Bubble Dynamics on Motion, Mass Transfer and Chemical Reaction in LES-Euler/Lagrange Computations"). The reaction constants used in the simulations are given in Table 3. The comprehensive model was implemented in the open source solver *OpenFOAM (v4.1)* as described in [48, 49].

In Table 3 all features of the numerical approaches and the applied reaction rate constants are summarised for convenience. In the first column the numerical method (i. e. Euler–Lagrange approach) used in [23] is included. In the present study, Euler–Lagrange as well as Euler-Euler computations were based on extensions of the *OpenFOAM* package, however using different versions. Moreover, Euler-Euler computations were conducted based on *ANSYS-CFX*. The last column summarizes the features of a zero-dimensional local model which was used to optimize the model closures. The specified references provide more details and with respect to the reaction mechanisms considered, it is referred to Eqs. (1)–(5) provided above. Bubble collisions and a possible coalescence are not accounted for in all computations. Moreover, it should be emphasized that the considered reaction is isothermal. As mentioned above, experimental data were considered in order to demonstrate the performance of the developed models. The reaction progress may be best visualized by the local and temporal variation of the pH value which reflects the consumption of hydroxide ions (see Fig. 4).

The results indicated by the two red curves were obtained in [39] as summarized in Table 3. The upper red dashed curve corresponds to the simulation with constant enhancement factor. The lower solid curve, fitting better to the experimental results of [23], was obtained with a pH dependent enhancement factor following Fleischer et al. [50].

The results obtained in [46, 47] correspond to the green curves in Fig. 4. The simplified approach (see Table 3, SPP-PM), which was used for deriving the reaction scheme (solid green line in Fig. 4) gives a good agreement with the measured values. This was achieved by the improved model for the enhancement factor and taking into account the reaction between CO_2 and water in addition to that with hydroxide ions. The Euler-Euler predictions, shown by the dashed green line in Fig. 4, however, were much less satisfying. The most likely cause for these deviations is the diffusive

nature of the MUSIG source terms describing the bubble shrinking, which causes an asymmetric broadening rather than a simple shift of the size distribution.

The result obtained with the advanced Euler–Lagrange approach with the full bubble dynamics model (shown as the blue line in Fig. 4) is much closer to the experiments than the standard Euler–Lagrange method applied in [23]. It should be noted that the dynamic model considerably enhances mass transfer due to variable bubble eccentricity and the dynamic Sherwood number. With the present Euler–Lagrange model, the initial part of the predicted pH variation (i. e. up to $t = 150$ s) runs almost parallel to the numerical result of [23]. This may be due to the different models considered in his work, that is, drag and lift coefficients and more important the Sherwood number. The improvement for the present numerical results with the dynamic model at a later stage of the reaction progress (i. e. from about $t = 175$ s) with respect to the experiments, is a consequence of the use of the second mechanism reaction (see Eq. (4)), neglected by Darmana et al. in the simulations and noticeable for pH < 9. Naturally, the result is also strongly influenced by the applied correlation for the enhancement factor. Only an increase of 5–10% would yield a shift of the pH curve to the left (faster reaction), similar to the results of [28].

The evolution of the bubble size along the column core region and averaged over a period of $t = 20$–95 s is influenced by hydrodynamic transport, mass transfer and chemical reaction (Fig. 5). In the experimental results, there exists an untrustworthy region (i. e. $z/H < 0.4$), since here bubbles are closely spaced and therefore may be identified as clusters and hence were rejected from further processing. Naturally, the bubble size gradually decreases in this region as predicted by all modelling approaches. For the region $z/H > 0.4$, the experimentally recorded bubble shrinkage becomes stronger and is only correctly captured by the advanced Euler–Lagrange approach, that is, the full bubble dynamics model (FDM). Here both, the effect of bubble dynamics on interfacial forces as well as the Sherwood number are responsible for such a good agreement. The original computations by Darmana et al. [23] also applying an Euler–Lagrange method give only a linear decrease of bubble size (black line in Fig. 5). Even the present Euler–Lagrange model considering also point-bubbles (NoOsc: no oscillations) gives already better results due to a number of models not considered in [23]. The Euler-Euler model developed in [46] using the MUSIG (multiple size group) model for describing bubble shrinkage shows already smaller mean sizes as the original computations of Darmana et al. [23].

It can be concluded, that all applied approaches for reactive bubbly flows give reasonable results in view of an application to industrial-scale processes. The correspondence with experiments may still be improved for both the Euler-Euler and the Euler–Lagrange approaches by further refining the closures and extending the modelling depth.

6 Validation of Numerical Simulation Tools with Different Cases of Reactive Bubbly Flows

Within the SPP 1740 experiments for reactive bubbly flows have been performed in the group of Hampel and in the group of Zähringer with the CO_2 chemisorption system. In the group of Hampel the focus of the studies was on high gas holdup, i.e. up to 14%, and high pH values up to 12.5. The applied imaging techniques UFXCT and wire-mesh sensor are cross-sectional techniques. That is, the depth of the column is resolved at any gas fraction. However, there is not much axial flow development information. Otherwise, in the group of Zähringer the focus was on 2D spatially and temporally resolved data, also of the axial flow development, but with a limited applicable gas holdup (<0.1%), due to the optical measurement techniques. The pH was lower (pH < 9) and viscosity and surface tension have been changed. Details of the setups were already given in Tables 1 and 2. In the following, we refer to experiments by the group of Hampel as Case 1 and to the ones of Zähringer as Case 2. Selected results are presented together with results of numerical simulations. For the reaction of Fe^{II}(edta) with NO so far no experimental data are available for comparison with numerical simulations. The group of Sommerfeld used the column parameters and operating conditions of the absorption measurements from the group of Hampel and carried out numerical simulations for the reaction of Fe^{II}(edta) with NO. In the following this study is referred as Case 3.

6.1 Case 1: Chemisorption of CO_2 in a DN100 Bubble Column

Experiments on the gas phase hydrodynamics and local species conversion in a DN 100 bubble column were carried out using ultrafast electron beam X-ray computed tomography (UFXCT) and wire-mesh sensors. In Fig. 6, the experimentally determined temporal evolution of the cross-sectional averaged gas volume fraction in the column of is depicted. The chemical absorption reaction is initiated by switching the gas from N_2 to CO_2. This is followed by a strong reduction of the gas holdup within the cross-section, due to gas–liquid mass transfer of CO_2 and thus decreased bubble size. Within the UFXCT measurement, the gas holdup decreases from the initial value of $\alpha_G = 0.02$–0.002. In Fig. 6 also the cross-sectional distribution of the phase fraction together with the 3D gas volume fraction data from UFXCT scans for a time interval of $\Delta t = 0.25$ s is depicted at the initial state of the reaction and after $t = 20$ s measurement time. The gas volume fraction data gives indications on the decreased bubble size and changing flow structure in the column. Euler–Lagrange simulations for these experiments were carried out by the group of Sommerfeld. Figure 6b shows the comparison of the experimental radial gas volume fraction profiles at the time levels indicated in Fig. 6a (i.e. at the beginning and at $t = 20$ s) with the Euler–Lagrange numerical simulations using the full bubble dynamics model (FDM) and the

Fig. 6 a Temporal evolution
of cross-sectional averaged
gas volume fraction during
chemical absorption of CO_2
and image stacks of the
X-ray scan at the beginning
of the reaction and after 20 s
measurement time;
b comparison of radial gas
volume fraction distribution
at the beginning of the
reaction and after 20 s
measurement time
determined from experiment
and numerical simulation.
Data are presented for $j_G =$
0.5 cm s^{-1} and pH = 12.5
and measurement position z
= 0.7 m
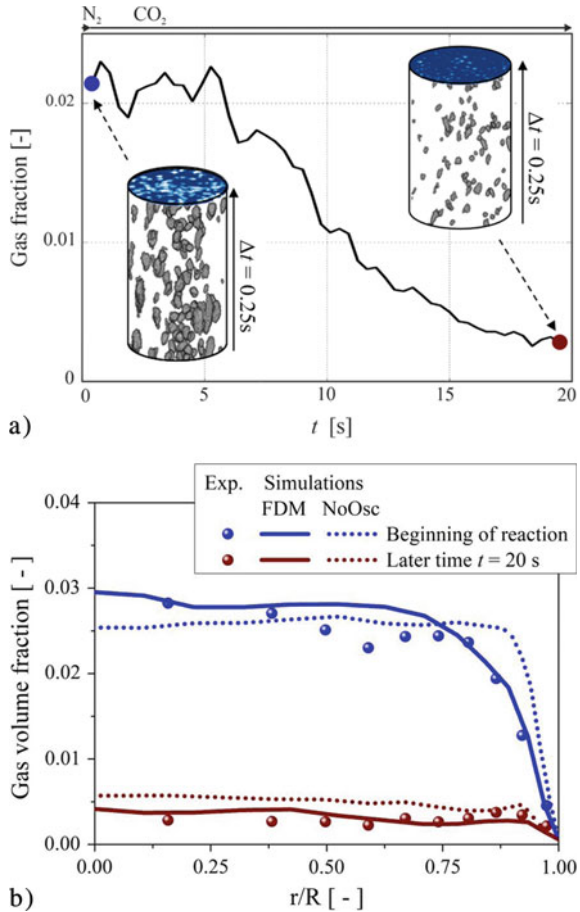
standard point-bubble approach (i. e. no bubble oscillations (NoOsc) are modelled).
Comparison between experiments and simulation results for both instants of time
show a very good agreement, but only if the bubble dynamics model is applied (i.
e. a stochastic variation of bubble eccentricity including a trajectory disturbance as
well as a dynamic Sherwood number for mass transfer, see chapter "Modelling the
Influence of Bubble Dynamics on Motion, Mass Transfer and Chemical Reaction in
LES-Euler/Lagrange Computations"). The classical point-bubble model yields lower
and flatter bubble volume fraction profiles, initially due to insufficient lateral bubble
dispersion and at the later stage too high gas holdup due to the under-prediction of
mass transfer when neglecting bubble dynamics in the Sherwood number [48].

Synchronously to UFXCT scans, data of the OH$^-$ concentrations from the wire-
mesh sensor have been acquired [34]. Based on this, the radial profile of the consump-
tion rate of OH$^-$ ions has been computed and is shown in Fig. 7 in comparison with
the numerical results for $j_G = 0.5$ cm s^{-1} and two different initial concentrations,

Fig. 7 Consumption rate of OH⁻ ions measured for different initial pH values (i. e. blue (the two lower lines): 11.5 and red (the two upper lines): 12.5); **a** measured at z = 0.1 m, **b** measured at z = 0.7 m
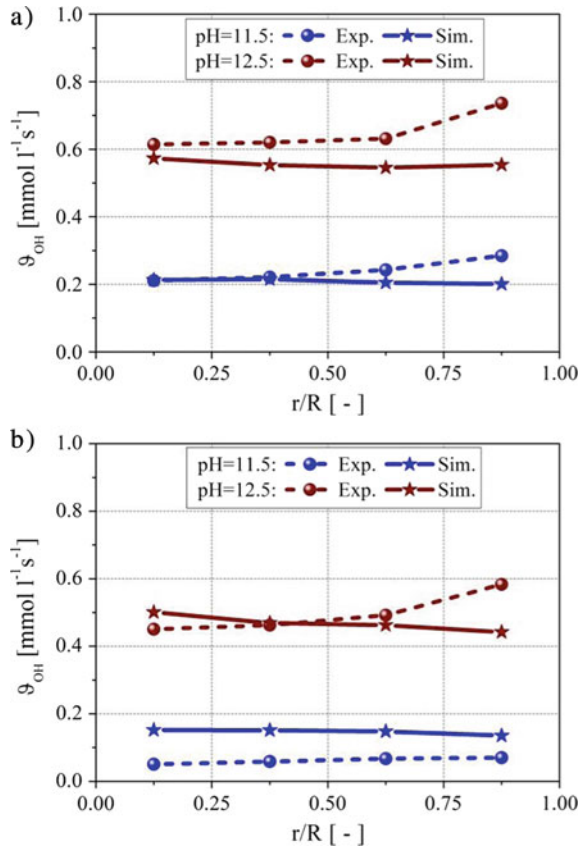
which are equivalent to an initial pH value of 11.5 and 12.5, respectively. Naturally, the consumption rates are larger for the higher initial pH value. For the lower cross-section at $z = 0.1$ m (Fig. 7a) the numerically obtained consumption rate agrees reasonably well with the measurements for both initial pH values (blue lines: pH $=$ 11.5 and red lines: pH $=$ 12.5) in the core region. While the numerical results yield almost constant consumption rates towards the wall, the experiments show a clear increase for both initial pH values. That is, the difference between experiment and computation increases for higher initial pH.

In Fig. 7b the consumption rates measured at $z = 0.7$ m are compared with the numerical simulation results, revealing similar trends as in Fig. 7a. At this higher position in the column, the consumption rate is of course smaller than at the lower cross-section, since the bubbles had to travel further up to this section, transfer the CO_2 into the liquid and start to react with the OH⁻ ions. For this profile, it also seems that the simulation results are shifted upwards compared to the measurements. Moreover, the numerical results show again almost constant consumption rate over the radius, whereas the experiments show a slight increase towards the wall. Thereby

the difference between experiment and simulation becomes quite large for the lower pH. It should be noted that the consumption rate is affected by all transport processes in the reactor, including hydrodynamics, which is responsible for species transport in the liquid phase and bubble distribution, i. e. profile of gas volume fraction, which also determines the local mass transfer rate. Even though the predicted gas volume fraction profiles are in very good agreement with the measurements (Fig. 6b), the liquid velocities need to be also analyzed and compared with measurements, for further understanding.

6.2 Case 2: Chemisorption of CO_2 in a DN140 Bubble Column

Experiments were executed at OVGU Magdeburg (see chapter "Experimental Characterization of Gas–Liquid Mass Transfer in a Reaction Bubble Column Using a Neutralization Reaction") to study the influence of various parameters as gas holdup, filling height, liquid viscosity and surface tension on bubble aspect, dispersion, hydrodynamics and mass transfer with chemical reaction [24]. This data has been used for the validation of the three following simulation tools.

6.2.1 Euler–Lagrange CFD Simulation

The developed bubble dynamics model by the group of Sommerfeld was adapted according to experimental information with respect to the PDFs (probability density function) of bubble eccentricity and trajectory deviation. Consequently, the conducted numerical computations may be regarded as a first step in generalizing the developed Lagrangian bubble dynamics model. The local bubble size is affected by all transport processes considered, namely hydrodynamics in the column, mass transfer and chemical reaction. Only a proper modelling of these transport processes is a good basis for correct computations of bubble sizes and their distributions. First of all, cross-sectional profiles of the computed bubble mean diameter are compared with two measured profiles, namely at 100 and 350 mm above the column bottom (Fig. 8). The volume equivalent bubble diameter is experimentally determined from the applied shadow imaging technique. From the simulations, the number mean diameter is determined by averaging over the entire computational cycle of 150 s, exactly as done in the experiment. For the case without glycerol (see Table 2), the mean bubble size matches quite well, although the measurements show a small size peak in the core (Fig. 8a). These profiles also demonstrate the lateral dispersion of the bubbles from 100 to 350 mm (i. e. the profiles become wider) as well as the associated mean size reduction due to mass transfer. This behavior is also obtained from the simulations of the higher viscosity case (Table 2 and Fig. 8b) and the bubble lateral dispersion (i. e. width of the profile) is similar to the experiments. Thus, as

Fig. 8 Profiles of number
mean bubble diameter at two
cross-sections within the
column (blue color: z =
100 mm and black color: z =
350 mm, symbols:
experiments, lines:
numerical simulations); **a** for
a NaOH solution without
glycerol; **b** for a NaOH
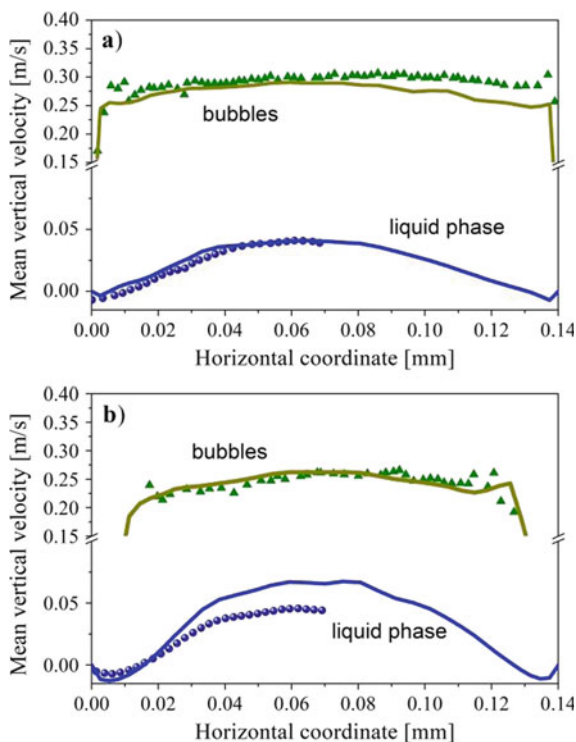solution with 50% glycerol
(averaging time 150s)
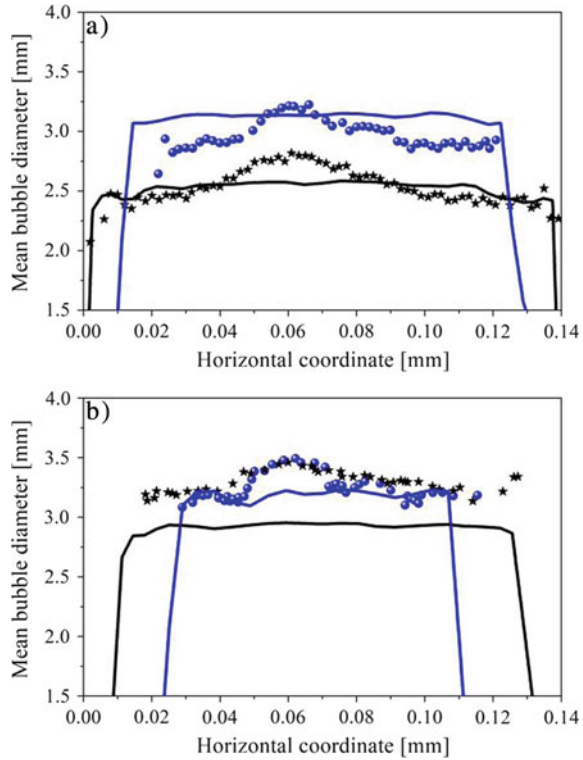
expected, the bubble lateral dispersion is lower compared to the low viscosity case.
The numerical results also show a visible reduction of the mean bubble size which is
for unknown reasons not observed in the experiments. Note that the computed size
change along the column is only about 0.2 mm, which is in the order of any possible
measurement error.

For investigating the effect of the novel bubble dynamics model on the hydrody-
namics, the mean vertical liquid and bubble velocity profiles are compared with the
experimental data in Fig. 9 for a cross-sectional plane in the center of the column,
i. e. at a height of $z = 350$ mm. In order to be comparable to the experiment, both
the liquid and bubble velocity fields were obtained as an average over the entire
simulation period of $\Delta t = 150$ s, although the process is completely transient.

It should be emphasized that a proper prediction of bubble mean and fluctuation
velocity is only possible if, for deformable bubbles as considered here, the bubble
dynamic behavior is modelled appropriately as demonstrated in [18]. A very similar
shape of the profiles is seen for experiment and computation (Fig. 9) and it is also
worth to point out the negative fluid velocities in the vicinity of the wall, supporting
a transport of species from the upper part to the bottom part of the column, which
is also properly captured by the simulations. Bubble velocity magnitudes for both
cases show a very good agreement with experimental observations, with a higher

Fig. 9 Profiles of measured (symbols) and computed (lines) mean vertical velocities (upper lines and symbols correspond to bubble velocity, lower lines and symbols correspond to liquid velocity, only the left half of the experimental liquid velocities is represented due to symmetry and accuracy concerns (see chapter "Experimental Characterization of Gas–Liquid Mass Transfer in a Reaction Bubble Column Using a Neutralization Reaction")); **a** measured for the case without glycerol (low viscosity); **b** measured for the 50% glycerol NaOH solution (averaging time 150 s)

mean bubble velocity for the case without glycerol (i. e. lower viscosity) and a stronger lateral dispersion of the bubbles over the column cross-section. For the case with 50% glycerol (i. e. about 5 times higher viscosity), bubbles are more concentrated in the core region of the cross-section, since the bubbles tend to rise in more straight paths (less bubble dynamics and oscillation) compared to the case without glycerol. Hence, as the bubbles are more concentrated in the core for the 50% glycerol case, the momentum transfer to the liquid and consequently the vertical liquid velocity are larger. For the low viscosity case without glycerol, the better lateral bubble dispersion results in lower upward liquid velocities. Nevertheless, with the somehow ad-hoc adaption of the bubble dynamics model, that is entirely based on experimental information, the effect of viscosity on bubble dispersion is captured sufficiently accurate.

Naturally, the different dynamic behavior of the bubbles in low and high viscosity liquids will also influence mass transfer and chemical reaction through the dynamic Sherwood number [48]. The resulting decay of pH values for the two simulated cases, i. e. without glycerol and with 50% glycerol (see Table 2), is shown in Fig. 10. It is striking that a faster descent in the pH value is found for the low viscosity case without glycerol, while in the case with 50% glycerol (5 times higher viscosity) mass transfer and chemical reaction are slower (bubble dynamics and hence Sherwood number are
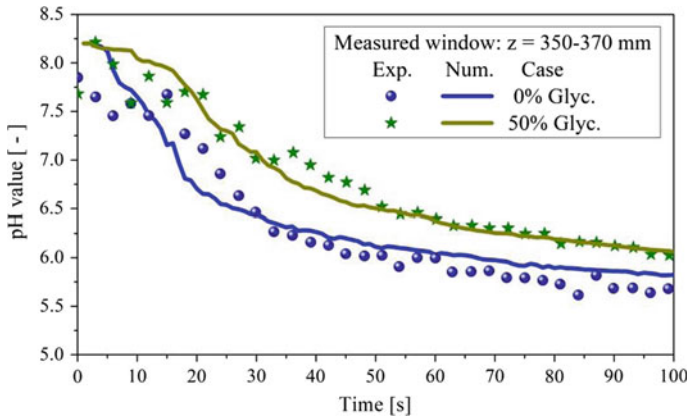
Fig. 10 Comparison of numerically computed and measured temporal decline of pH values (measurement window 350–370 mm above the column bottom) in a reactive bubble column with low and high (50% glycerol) viscosity NaOH solution

smaller), yielding a much more shallow decay in the pH value. This occurs because bubbles rise in a more viscous liquid, have straighter rising paths, tend to be more spherical and consequently experience less mass transfer leading to a slower reaction. In the low viscosity case without glycerol, mass transfer should be further enhanced due to the effective larger surface area of the stronger deformed bubbles. All these tendencies are correctly predicted by the developed dynamics model for bubble motion and Sherwood number and the agreement with the measurements is very good for reactive bubbly flows and liquids of different viscosity.

Consequently, a physically correct point-bubble numerical simulation of bubbly flows with deformable bubbles and chemical reactions can only be done properly if bubble dynamics are modelled with respect to shape and trajectory oscillations and the increased effective surface area as a result of deformation in combination with a dynamic Sherwood number. These first results on viscosity effects allow concluding that the developed bubble dynamics model may be also generalized with respect to different liquid properties.

6.2.2 Euler–Euler CFD Simulations

Simulations of bubbly flows within the Euler-Euler framework have been performed by the groups of Rzehak and Hlawitschka. Both groups used the experimental results from Zähringer for comparison and validation purposes. The group of Rzehak focused on fluid and turbulence in non-reactive cases, while the group of Hlawitschka considered a case with reaction. The applied experimental techniques are described in detail in chapter "Experimental Characterization of Gas–Liquid Mass Transfer in a Reaction Bubble Column Using a Neutralization Reaction", the numerical

models and methods in chapters "Euler-Euler Modeling of Reactive Flows in Bubble Columns" and "Multi-scale Investigations of Reactive Bubbly Flows", respectively.

An example of the non-reactive cases considered together with the groups of Zähringer and Rzehak is the CO_2/water system at a flow rate of $Q_G = 6.4$ l/h corresponding to a superficial gas velocity of $j_G = 0.011$ cm/s. Results for the gas fraction in this case [27] are shown in the top row of Fig. 11. The Figure shows the front view of the column. The two-dimensional distributions reveal that the overall pattern of the gas distribution is reproduced quite well by the simulations. Profiles extracted at three different height levels are shown in the bottom row of Fig. 11. It is seen that for this case the quantitative agreement between experiment and simulation is very good.

The vertical component of the mean liquid velocity v_L in the measurement plane is shown for this case in the top row of Fig. 12 for the whole column. In the central
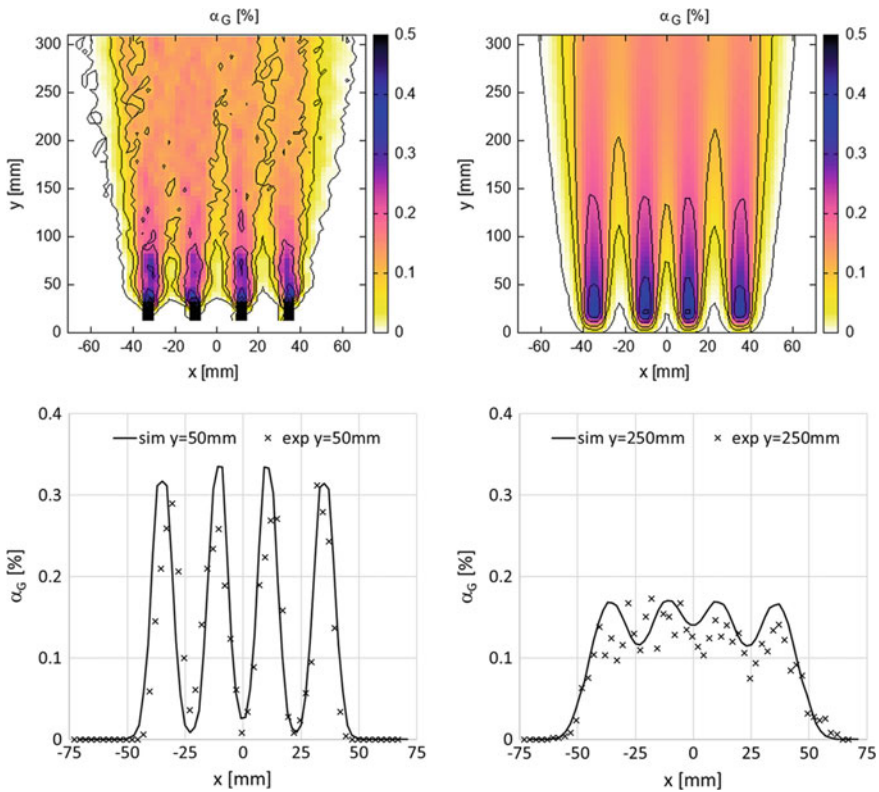
Fig. 11 Gas fraction α_G for CO_2 bubbles in water at $Q_G \approx 6.4$ l/h. Top row: Comparison of 2D distributions in the lower part of a vertical central plane through the column calculated from the shadowgraphy measurements (left) and from the simulation results (right). Bottom row: Extracted lateral profiles at two different heights $y = 50$ mm (left) and $y = 250$ mm (right) with measurements shown as symbols and simulations as lines
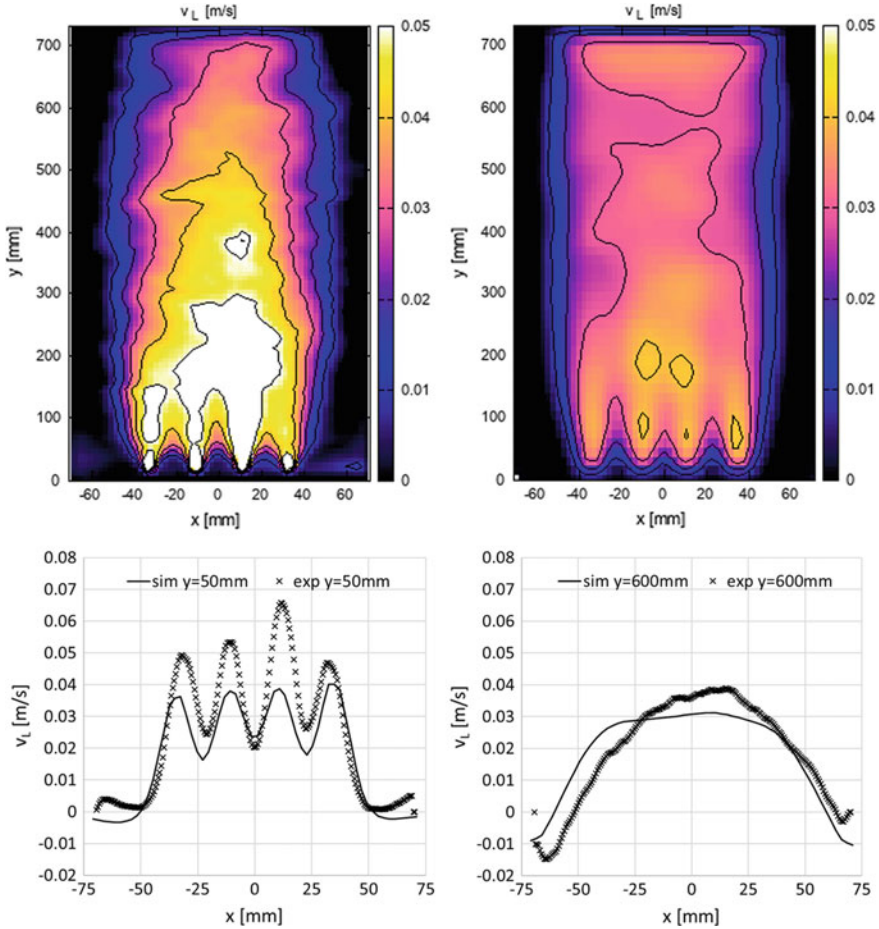
Fig. 12 Average vertical liquid velocity component v_L for CO_2 bubbles in water at $Q_G \approx 6.4$ l/h. Top row: Comparison of 2D distributions in a full vertical central plane through the column obtained from the PIV measurements (left) and from the simulation results (right). Bottom row: Extracted lateral profiles at two different heights $y = 50$ mm (left) and $y = 600$ mm (right) with measurements shown as symbols and simulations as lines

part of the column, the liquid moves upwards driven by the rising gas bubbles. Near the column walls, the liquid flows downwards. The mean horizontal motion of the liquid (not shown here) is nearly zero, apart from a narrow zone near the free surface at the top of the column.

A slight asymmetry is visible in both experimental and simulation results, which is due to the finite averaging time and, in the experimental case, also to slight manufacturing tolerances between the four nozzles. Good agreement is obtained in the extent of the up- and downflow regions as well as the horizontal motion near the

top surface, when comparing experiment and simulation with respect to the qualitative mean liquid flow pattern. However, the magnitude of the vertical velocity is under-predicted by the simulations.

A more quantitative analysis can be made by looking at the profiles of the vertical velocity component at $y = 50$ and 600 mm, near the lower and upper end of the range covered by the measurements in the bottom row of Fig. 12.

In the bottom region, it may be noted, that in the experiments the second to right nozzle apparently produced a faster liquid stream than the others. Since no difference is seen in the gas fraction for this nozzle, the reason for this remains unclear. But the effect may be seen as a representative for the many factors which are hard to control in laboratory experiments and which will inevitably be present in technical applications. A slight reminiscence of the resulting peak in the liquid velocity persists up to the higher level. Comparing experimental and simulation results, it is seen that at the lower cross-section, the simulations produce a too low liquid velocity in particular around the peaks in the profile. The difference to the experimental results is about the same as the variation between the outlier-nozzle and the others. At the higher section, the difference between simulation and experiment has become somewhat smaller and can partly be attributed to the remaining asymmetry in the latter.

The top row of Fig. 13 shows the two-dimensional fluctuations of the liquid velocity in vertical direction in the measurement plane. Once more, the expected symmetry with respect to the column center is not completely fulfilled in the experimental data due to the second injection nozzle. For the vertical velocity fluctuations, the simulations are in good qualitative agreement with the measured data. The horizontal fluctuations (not shown) are somewhat over-predicted in the simulations, but the pattern is similar. A quantitative comparison at height levels $y = 50$ and 600 mm by means of profiles of the fluctuations is shown in the bottom row of Fig. 13. Agreement between simulation and experiment is good for both heights. The horizontal fluctuations (also not shown here) are somewhat over-predicted in the simulations.

For comparison and validation of the numerical results obtained by the group of Hlawitschka using an Euler-Euler approach, the experimental data of the group of Zähringer were averaged corresponding to the numerical mesh [28]. Three positions were compared along the column height, i. e. at 33.5, 183.5 and 303.5 mm from the bottom.

The mean bubble sizes obtained for the investigated test case from experiments and used in the numerical calculations are shown in Fig. 14a. The bubbles at 33.5 mm are located close to the bubble nozzles on the bottom of the column. With increasing height, during their rise, the mean size does not change significantly in the experiment. The measured bubble sizes are on average $d_B = 2.65$, 2.71 and 2.80 mm at 33.5, 183.5 and 303.5 mm column height, respectively. Due to the low gas hold-up, there is no bubble coalescence and breakage. The very small change in bubble size, allowed the assumption of a constant bubble size of $d_B = 2.72$ mm for the simulations in the following.

The mean vertical bubble velocity components obtained this way are depicted in Fig. 14b. The measured mean bubble velocities are $v_B = 0.30$, 0.30 and 0.28 m s^{-1} at 33.5, 183.5 and 303.5 mm column height, respectively. The mean bubble velocity in
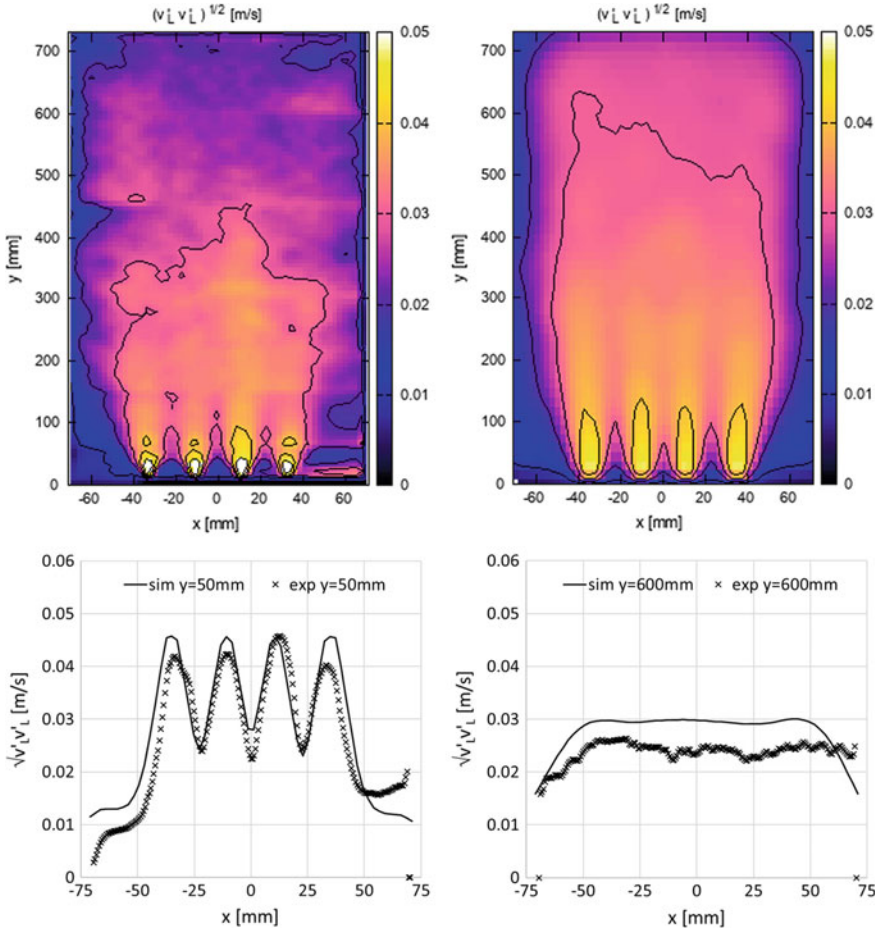
Fig. 13 Liquid velocity fluctuations $\sqrt{v'_L v'_L}$ for CO_2 bubbles in water at $Q_G \approx 6.4$ l/h. Top row: Comparison of 2D distributions in a full vertical central plane through the column obtained from the PIV measurements (left) and from the simulation results (right). Bottom row: Extracted lateral profiles at two different heights $y = 50$ mm (left) and $y = 600$ mm (right) with measurements shown as symbols and simulations as lines

the simulations reaches a value of about 0.30 m s^{-1} in the centre of the column. The velocity decrease in direction of the column walls at 183.5 and 303.5 mm column height is much stronger in the calculations than in the experiments, and results from a lower gas phase fraction in the simulations. In the lower part of the column (33.5 mm), bubbles only exist in the centre (25–115 mm) due to the position of the injection nozzles. Here, the velocity peaks at the injection positions are well reproduced. The phase fraction and residual velocities at this place are set to a minimum value for drag term calculation in the simulations, leading to a better stability.
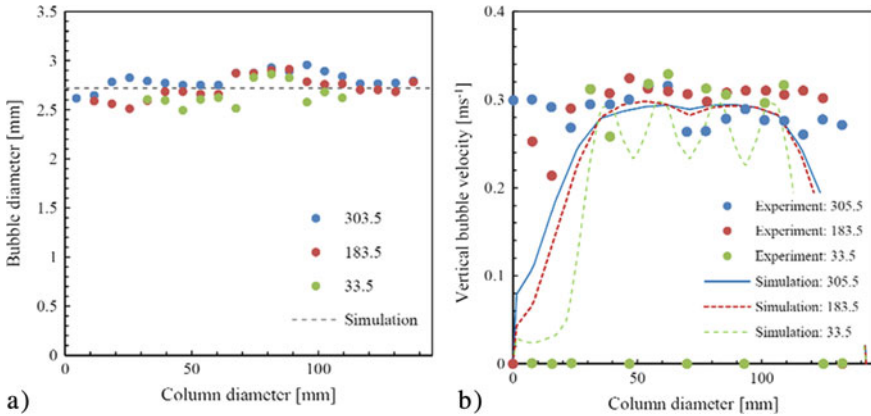
Fig. 14 **a** Mean bubble diameters at column heights of 33.5, 183.5 and 303.5 mm. **b** Mean vertical bubble velocity profiles at column heights of 33.5, 183.5 and 303.5 mm

The mean vertical liquid velocity component is depicted in green in Fig. 15, for a position of 33.5 mm. At this lowest position, the liquid velocity is influenced by the nozzle spacing. At 183.5 and 303.5 mm (Fig. 15, red and blue symbols/lines), the liquid velocity has a bell-shaped distribution, with a maximum of 0.063 m s^{-1} at 183.5 mm column height. A deviation between the experiments and the simulations is observed in the centre of the column, where the vertical liquid velocity is smaller in the simulation.

Fig. 15 Mean vertical liquid velocity profiles at column heights 33.5 mm (green), 183.5 mm (red) and 303.5 mm (blue)
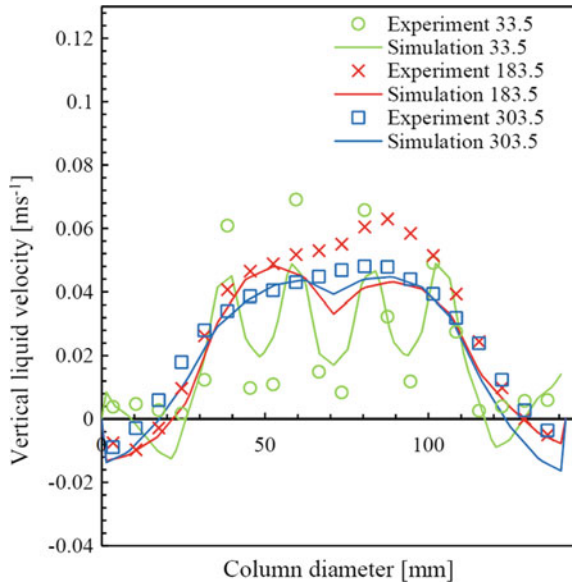
Fig. 16 Mean temporal pH value evolution averaged for a column section of 100–321 mm (green), 305–518 mm (red) and 503–716 mm (blue)
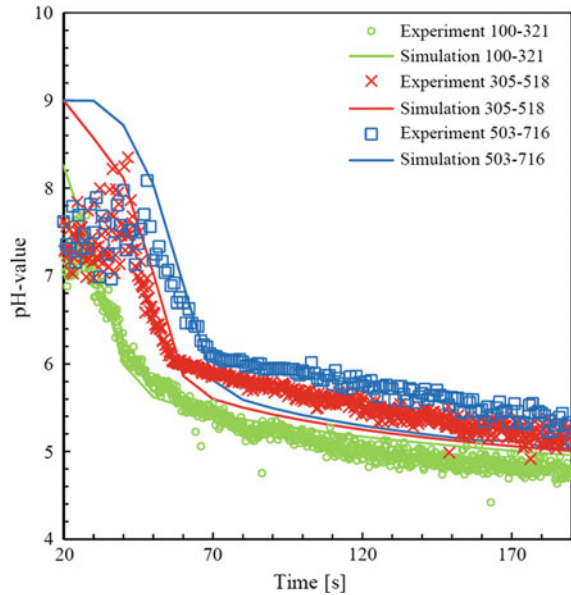
The temporal concentration developments determined for $t = 190$ s, are compared in Fig. 16. An initial pH value of 9 is used in both, experiment and simulation, but in the experiment only pH < 8 can be visualized reliably. All pH values larger than 8 appear at the same intensity. The measured concentrations were averaged for a vertical column height segment of 100–321, 305–518 and 503–716 mm. The simulation results were averaged over the same domain and intervals of $\Delta t = 10$ s simulation time. For the two lower sections (Fig. 16, green and red), the evolution of the pH value obtained from the simulation fits to the experimental values for a simulation time of $t = 40$ s until the end of the measurement. For the highest section (Fig. 16, blue), starting at $t = 60$ s, the pH value is slightly underestimated in the simulation. Here, an enhancement of the free surface treatment in the simulation could lead to improved results.

In conclusion, the Euler-Euler simulation approaches enabled, compared to the detailed experimental results, a satisfactory description of the local hydrodynamics and the local concentrations by accounting for the reaction network. As single input parameter, the average bubble size has to be known. In general, both frameworks were able to predict these profiles without further adaption.
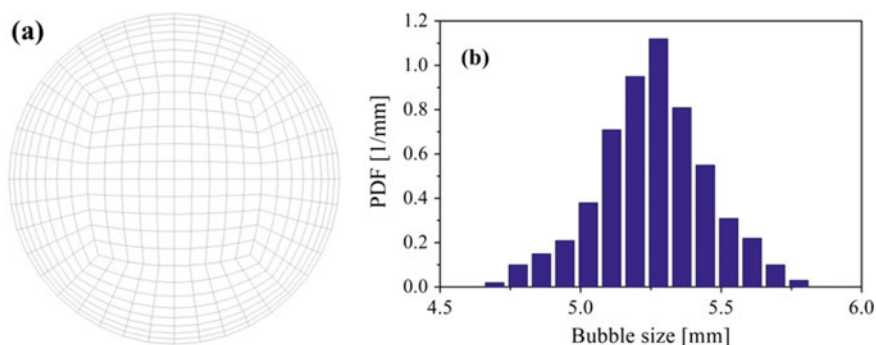
Fig. 17 a Cross-sectional numerical mesh for the considered circular bubble column with a diameter of 0.1 m and a height of 1.4 m; b Size distribution of injected bubbles (number weighted) with a mean diameter of 5.25 mm

6.3 Case 3: Reaction of Fe^{II}(Edta) with NO in DN100 Bubble Column

For the Fe^{II}(edta)/NO reaction system that was purposively developed for experimental studies within the priority research program (see Sect. 4) only numerical simulations are available on the full column scale. This has mainly to do with the hazards associated with handling large amounts of NO which made this endeavour a future task. However, numerical simulations are, in this case the LES-Euler–Lagrange approach, well suited to gain an understanding of the dynamics of this reaction in a bubble column. Simulations were made for the circular bubble column of the group of Hampel [34], for which a numerical grid with approximately 35,000 structured elements was generated. Figure 17a) presents the cross-sectional mesh used for the simulations. Aqueous $[Fe^{II}(edta)(H_2O)]^{2-}$ solution is modelled as the liquid phase and pure NO bubbles were virtually injected with a number-based PDF size distribution as measured in the CO_2 case of [34] (Fig. 17b). With the predefined superficial gas velocity of $j_G = 0.5$ cm/s, 504 bubbles are injected per second. Computations are done for two initial $[Fe^{II}(edta)(H_2O)]^{2-}$ concentrations over a time period of $t = 70$ s.

Indeed, the mass transfer rate for bubbles rising inside a bubble column is affected by the reaction process occurring in the vicinity of the bubbles, which is accounted for by an enhancement factor [48, 49]. Merker et al. found, that for different initial concentrations of $[Fe^{II}(edta)(H_2O)]^{2-}$ in the liquid phase, the mass transfer is increased at different levels, surprisingly reaching values of approximately 20 times higher in comparison to the case without adding $[Fe^{II}(edta)(H_2O)]^{2-}$ to the solution [53]. A continuous mathematical relation for the mass transfer enhancement factor in dependence of the $[Fe^{II}(edta)(H_2O)]^{2-}$ concentration in the range between $c = 0$ and 75 mmol L^{-1} was applied using a polynomial fitting curve as shown in Fig. 18.

Fig. 18 Enhancement factor
E as a function of the
concentration $c_{Fe^{II}(edta)}$ for
a range between c = 0 and c
= 75 mmol L^{-1}; Symbols
represent the experimental
values [53] and the line a
polynomial fitting

$$E = 1 + 0.22531 C_{Fe^{II}(edta)} + 0.0039 C^2_{Fe^{II}(edta)} - 4.18472 C^3_{Fe^{II}(edta)}$$
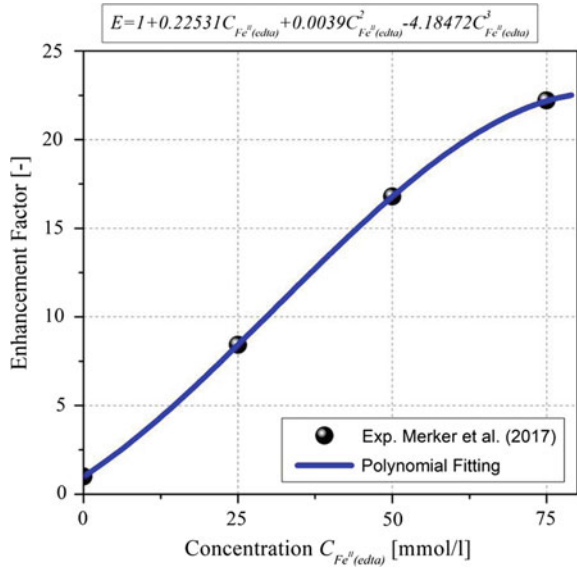
Two cases with different concentration of $[Fe^{II}(edta)(H_2O)]^{2-}$, namely $c = 25$ and 75 mmol L^{-1}, were simulated in order to understand their influence on the development of the flow field and the relevant species distribution. Figure 19 shows the evolution of the species concentration, numerically measured at the bottom of the column ($z = 0.1$), for the case with a concentration of $[Fe^{II}(edta)(H_2O)]^{2-}$ of 75 mmol L^{-1}, during the first stage of the simulations. The consumption of
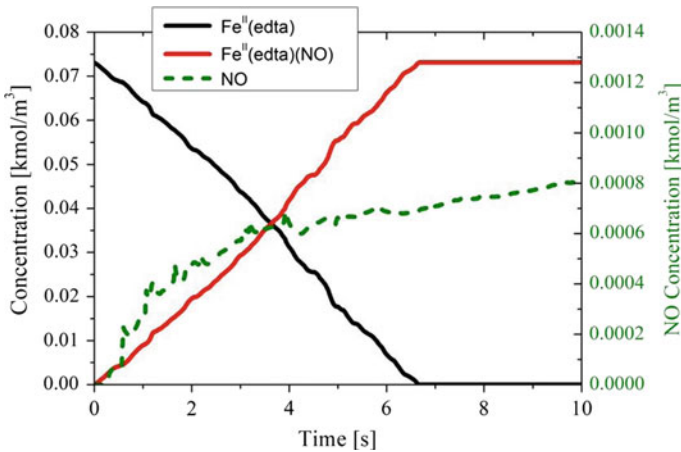
Fig. 19 Species concentration evolution during the first stage of the reaction process (i. e. up to t = 10 s) obtained from the simulations for the case with initial concentration c[Fe^{II}(edta)(H$_2$O)]$^{2-}$ = 75 mmol L^{-1}
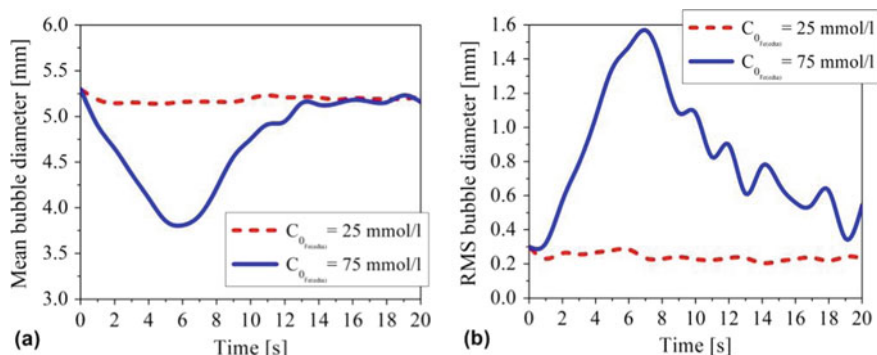
Fig. 20 Bubble diameter evolution during the first stage in the simulated reaction process. **a** Mean number-based bubble diameter, **b** rms value of bubble sizes (i. e. width of the diameter PDF)

the $[Fe^{II}(edta)(H_2O)]^{2-}$ is very fast, as a result of the reaction kinetics (see also chapter "In Situ Characterizable High-Spin Nitrosyl–Iron Complexes with Controllable Reactivity in Multiphase Reaction Media"). Conversely, the concentration of the anionic complex $[Fe^{II}(edta)(NO)]^{2-}$ increases at a rate similar to the decrease in $[Fe^{II}(edta)(H_2O)]^{2-}$ during the simulation run. As expected, the concentration of the aqueous NO is increasing during time and tends to accumulate in the liquid, however at a very low rate.

Figure 20 shows the time evolution of the mean bubble diameters and their corresponding rms (root mean square) values including all the bubbles inside the entire domain, tracked during the first stage of the simulation for the two cases with different initial concentration. The red line corresponds to $c([Fe^{II}(edta)(H_2O)]^{2-}) = 25$ mmol L^{-1} and the blue line to $c([Fe^{II}(edta)(H_2O)]^{2-}) = 75$ mmol L^{-1}. From Fig. 20a it is obvious that the two cases yield a completely different behaviour in the progression of the reaction, giving for the low $[Fe^{II}(edta)(H_2O)]^{2-}$ concentration almost no variation in bubble size, whereas a high $[Fe^{II}(edta)(H_2O)]^{2-}$ concentration results in drastic size reductions. Already during the first 6 s of the simulation, the mean bubble size is reduced by about 1.5 mm, reaching a mean size of approximately $d_B = 3.8$ mm. This can be explained by the high value of the enhancement factor (approximately 20 times) during the first second of simulations in which a high $[Fe^{II}(edta)(H_2O)]^{2-}$ concentration value yields a large increase in mass transfer rate (see also Fig. 19). When chemical reactions take place, the $[Fe^{II}(edta)(H_2O)]^{2-}$ molecules in the liquid are consumed, the enhancement factor decreases and the mean bubble size increases again to a similar value as in the case with the low initial concentration of $[Fe^{II}(edta)(H_2O)]^{2-}$ of 25 mmol L^{-1} (see Fig. 20a). On the other hand, for the case with only $c = 25$ mmol L^{-1} $[Fe^{II}(edta)(H_2O)]^{2-}$, a decrease in diameter is not noticeable, since, although the enhancement factor is still about *8* (Fig. 18), the solubility of NO in water based solutions is low compared to other gases, which affects directly the mass transfer. Finally, both cases show a roughly constant mean bubble size after $t = 18$ s, due to the complete consumption of the

Fig. 21 Images of instantaneous Fe^{II}(edta) concentration in the vertical mid-plane of the column for different simulations times for the case with the initial concentration of $[Fe^{II}(edta)(H_2O)]^{2-}$ of c = 75 mmol L^{-1}
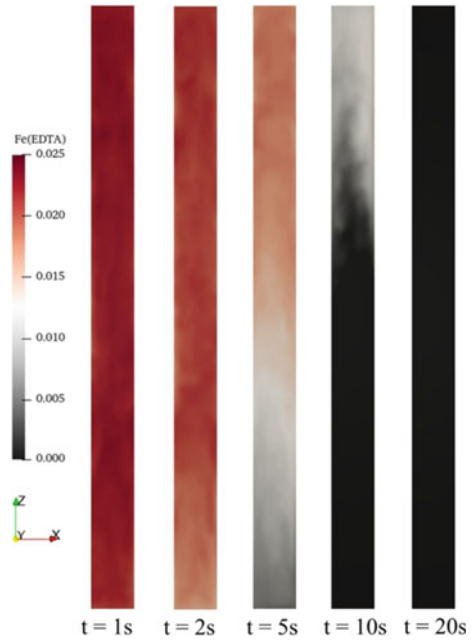
$[Fe^{II}(edta)(H_2O)]^{2-}$ after approximately $t = 10$ s (see also Fig. 19). The *rms* values of bubble size (Fig. 20b) show, that for the low concentration case almost mono-sized bubbles exist. For the high initial $[Fe^{II}(edta)(H_2O)]^{2-}$ concentration with the stronger mass transfer, the decrease of bubble mean size is also associated with a broadening of the size distribution. After the bubbles reached the smallest mean size and grow again, also the distribution becomes narrower again.

With the purpose of illustrating the temporal and spatial evolution of the reaction process, color fields of $[Fe^{II}(edta)(H_2O)]^{2-}$ concentration over time in a vertical middle plane through the column are shown in Fig. 21. At the beginning of the simulation, the concentration fields of $[Fe^{II}(edta)(H_2O)]^{2-}$ appears quite homogeneous, since the reaction has not yet taken place. As mass transfer proceeds, chemical reaction is initiated and until $t = 10$ s the $[Fe^{II}(edta)(H_2O)]^{2-}$ concentration has already drastically decreased with some spatial variation from the middle part to the top of the column. The decrease of the $[Fe^{II}(edta)(H_2O)]^{2-}$ concentration along the column is most pronounced for $t = 5$ s, where in the lower part of the column fresh bubbles enter, inducing high mass transfer and chemical reaction. After $t = 20$ s an almost complete consumption of $[Fe^{II}(edta)(H_2O)]^{2-}$ has occurred, however some inhomogeneity still exists in the upper part due to the transport processes involved.

7   Opportunities for Industrial Applications

Correct simulation of reactive bubbly flows is a key requirement for industrial reactor design and operation. CFD tools may there be used for simulating the full reactor in three dimensions, but also for analysis of certain compartments with pronounced 3D flows. For that, the SPP 1740 projects on reactive bubbly flow have made significant progress in both experimental technology and numerical simulations, including model and closure development. This success is greatly owed to a close and continuous collaboration between numerical and experimental oriented working groups.

The experimental setups introduced above are generally available for follow-up studies, e.g. for the $Fe^{II}(edta)$/NO system. Most notably a set of new measurement techniques has been qualified and used for studying reactive bubbly flow. Thus, ultrafast X-ray tomography was for the first time applied to reactive bubbly flows. It may be further used to study similar multiphase problems. The wire-mesh sensor was qualified for chemical species concentration measurement, which is very helpful in gaining complementary information to gas phase parameters and liquid velocity. Both measurement technologies together with the optical probe introduced in chapter "Experimental Studies on the Hydrodynamics, Mass Transfer and Reaction in Bubble Swarms with Ultrafast X-ray Tomography and Local Probes" can in principle be used in industrial devices, if appropriate safety provisions are made. Optical measurement techniques have been used to obtain spatially and temporally highly resolved data of bubble parameters, liquid velocity and mass transfer in the column. Especially the influences of viscosity and surface tension have been examined like this. The exhaustive data and its evaluations are available in a database (https://www.lss.ovgu.de/Info/Downloads.html), that can be accessed on demand. It has served as validation data for several numerical working groups inside SPP1740, that have been presented above.

An Euler–Lagrange solver has been qualified for reactive bubbly flow at the group of Sommerfeld. Most notably, the novel bubble dynamics model accounting for shape and trajectory fluctuations of wobbling bubbles as well as dynamics in mass transfer description improved the numerical prediction of bubbly flows without and with chemical reactions. This new modelling idea remarkably extends the classical point-bubble approach, that is typically used. It proved to predict the mass transfer and following global chemical species conversion in an excellent way for several experimental test cases. Further model extensions are required to account for bubble dynamics also in the enhancement factor and expand the applicability to liquids with different properties, e.g. higher viscosities. The code is now available for industrial use and has its particular strength in simulating large size compartment of reactors due to the high numerical efficiency.

Euler-Euler solvers have been qualified by the groups of Rzehak and Hlawitschka. They are particularly suited for large-scale simulations in industry. Developments in the group of Hlawitschka focused on the establishment of a framework for reactive mass transfer in bubble columns using *OpenFOAM*. The code was further extended

to account for the main forces as well as population balance modelling to account for the bubble interactions such as breakage and coalescence. Own experimental studies were performed as well as the developed solvers (Euler-Euler, Euler–Lagrange) were compared to experimental data from the group of Zähringer. New visualization approaches were specifically developed for the Euler-Euler approach that enhances visual inspection of the numerical results. From the Euler–Lagrange investigations, it can be concluded, that individual bubble motion plays an important role at low gas hold-ups. Thereby, the transition from straight to oscillative motion can be described in different viscous liquids.

Developments in the group of Rzehak focused entirely on the reactive mass transfer, building on a well-established model for the purely hydrodynamic aspects. Shrinkage/growth of the bubbles due to adsorption/desorption processes was included by source terms in the MUSIG model and a set of closures for the mass-transfer coefficient, enhancement factor and turbulent species diffusivity was tested. Availability of an accurate model for the reaction kinetics is found essential to reproduce experimental data. All additions are readily incorporated in commercial simulation software and hence directly applicable to solve industrial application problems. Further improvements should target more refined models for the mass-transfer coefficient such as those developed by the group of Sommerfeld.

As an outlook it may be stated that the fundamental developments presented here need further specific adaption and qualification for particular industrial problems. This concerns, for example, other types of reaction systems, which may be far more complex than the simple ones considered in the frame of this project. In addition, catalyzed reactions, three-phase flow and consideration of non-isothermal conditions are future topics of interest.

References

1. Deckwer WD, Field RW (1992) Bubble column reactors. Wiley. https://doi.org/10.1002/jctb.280580416
2. Lewis WK, Whitman WG (1924) Principles of gas absorption. Ind Eng Chem 16:1215–1220. https://doi.org/10.1021/ie50180a002
3. Higbie R (1935) The rate of absorption of a pure gas into still liquid during short periods of exposure. Inst Chem Eng 35:36–60
4. Ajbar A, Al-Masry W, Ali E (2009) Prediction of flow regimes transitions in bubble columns using passive acoustic measurements. Chem Eng Process Process Intensif 48:101–110. https://doi.org/10.1016/j.cep.2008.02.004
5. Richardson FF, Zaki WN (1954) Sedimentation and fluidisation. Trans Inst Chem Eng 32:35–53
6. Ishii M, Zuber N (1979) Drag coefficient and relative velocity in bubbly, droplet or particulate flows. AIChE J 25:843–855. https://doi.org/10.1002/aic.690250513

7. Krishna R, De Swart JWA, Hennephof DE, Ellenberger J, Hoefsloot HCJ (1994) Influence of increased gas density on hydrodynamics of bubble-column reactors. AIChE J 40:112–119. https://doi.org/10.1002/aic.690400113

8. Tagawa Y, Roghair I, Prakash VN, Van Sint Annaland M, Kuipers H, Sun C, Lohse D (2013) The clustering morphology of freely rising deformable bubbles. J Fluid Mech 721:R2–R2. https://doi.org/10.1017/jfm.2013.100

9. Simonnet M, Gentric C, Olmos E, Midoux N (2007) Experimental determination of the drag coefficient in a swarm of bubbles. Chem Eng Sci 62:858–866. https://doi.org/10.1016/j.ces.2006.10.012

10. Colombet D, Legendre D, Cockx A, Guiraud P, Risso F, Daniel C, Galinat S (2011) Experimental study of mass transfer in a dense bubble swarm. Chem Eng Sci 66:3432–3440. https://doi.org/10.1016/j.ces.2011.01.020

11. Sommerfeld M, van Wachem B, Oliemans R (2008) Best practice guidelines for computational fluid dynamics for dispersed multiphase flows. ERCOFTAC (European Research Community on Flow, Turbulence and Combustion). ISBN 978-91-633-3564-8

12. Yeoh GH, Tu JY (2006) Numerical modelling of bubbly flows with and without heat and mass transfer. Appl Math Model 30:1067–1095. https://doi.org/10.1016/j.apm.2005.06.012

13. Magolan B, Lubchenko N, Baglietto E (2019) A quantitative and generalized assessment of bubble-induced turbulence models for gas-liquid systems. Chem Eng Sci X 2. https://doi.org/10.1016/j.cesx.2019.100009

14. Rzehak R, Ziegenhein T, Kriebitzsch S, Krepper E, Lucas D (2017) Unified modeling of bubbly flows in pipes, bubble columns, and airlift columns. Chem Eng Sci 157:147–158. https://doi.org/10.1016/j.ces.2016.04.056

15. Tomiyama A, Tamai H, Zun I, Hosokawa S (2002) Transverse migration of single bubbles in simple shear flows. Chem Eng Sci 57:1849–1858. https://doi.org/10.1016/S0009-2509(02)00085-4

16. Liao Y, Rzehak R, Lucas D, Krepper E (2015) Baseline closure model for dispersed bubbly flow: bubble coalescence and breakup. Chem Eng Sci 122:336–349. https://doi.org/10.1016/j.ces.2014.09.042

17. Muniz M, Sommerfeld M (2020) On the force competition in bubble columns: a numerical study. Int J Multiph Flow 128. https://doi.org/10.1016/j.ijmultiphaseflow.2020.103256

18. Sommerfeld M, Muniz M, Reichardt T (2018) On the importance of modelling bubble dynamics for point-mass numerical calculations of bubble columns. J Chem Eng Jpn 301–317. https://doi.org/10.1252/jcej.17we277

19. Dhotre MT, Deen NG, Niceno B, Khan Z, Joshi JB (2013) Large eddy simulation for dispersed bubbly flows: a review. Int J Chem Eng. https://doi.org/10.1155/2013/343276

20. Sommerfeld M (2017) Numerical methods for dispersed multiphase flows. In: Particles in flows, springer series advances in mathematical fluid mechanics, pp 327–396. https://doi.org/10.1007/978-3-319-60282-0_6

21. Kamath S, Padding JT, Buist KA, Kuipers JAM (2018) Stochastic DSMC method for dense bubbly flows: Methodology. Chem Eng Sci 176:454–475. https://doi.org/10.1016/j.ces.2017.11.002

22. Darmana D, Deen NG, Kuipers JAM (2005) Detailed modeling of hydrodynamics, mass transfer and chemical reactions in a bubble column using a discrete bubble model. Chem Eng Sci 60:3383–3404. https://doi.org/10.1016/j.ces.2005.01.025

23. Darmana D, Henket RLB, Deen NG, Kuipers JAM (2007) Detailed modelling of hydrodynamics, mass transfer and chemical reactions in a bubble column using a discrete bubble model: chemisorption of CO_2 into NaOH solution, numerical and experimental study. Chem Eng Sci 62:2556–2575. https://doi.org/10.1016/j.ces.2007.01.065

24. Kováts P, Thévenin D, Zähringer K (2020) Influence of viscosity and surface tension on bubble dynamics and mass transfer in a model bubble column. Int J Multiph Flow 123. https://doi.org/10.1016/j.ijmultiphaseflow.2019.103174

25. Kováts P, Thévenin D, Zähringer K (2018) Characterizing fluid dynamics in a bubble column aimed for the determination of reactive mass transfer. Heat Mass Transf 54:453–461. https://doi.org/10.1007/s00231-017-2142-0

26. Kováts P, Thévenin D, Zähringer K (2017) Investigation of mass transfer and hydrodynamics in a model bubble column. Chem Eng Technol 40:1434–1444. https://doi.org/10.1002/ceat.201600679

27. Rzehak R, Krauß M, Kováts P, Zähringer K (2017) Fluid dynamics in a bubble column: new experiments and simulations. Int J Multiph Flow 89:299–312. https://doi.org/10.1016/j.ijmultiphaseflow.2016.09.024

28. Hlawitschka MW, Kováts P, Zähringer K, Bart HJ (2017) Simulation and experimental validation of reactive bubble column reactors. Chem Eng Sci 170:306–319. https://doi.org/10.1016/j.ces.2016.12.053

29. Raffel M, Willert CE, Scarano F, Kähler C, Wereley S, Kompenhans J (2018) Particle image velocimetry: a practical guide. Springer, Berlin. https://doi.org/10.1007/978-3-319-68852-7

30. Lehwald A, Thévenin D, Zähringer K (2010) Quantifying macro-mixing and micro-mixing in a static mixer using two-tracer laser-induced fluorescence. Exp Fluids 48:823–836. https://doi.org/10.1007/s00348-009-0769-4

31. Lehwald A, Janiga G, Thévenin D, Zähringer K (2012) Simultaneous investigation of macro- and micro-mixing in a static mixer. Chem Eng Sci 79:8–18. https://doi.org/10.1016/j.ces.2012.05.026

32. Fischer F, Hampel U (2010) Ultra fast electron beam X-ray computed tomography for two-phase flow measurement. Nucl Eng Des 240:2254–2259. https://doi.org/10.1016/j.nucengdes.2009.11.016

33. Kipping R, Kryk H, Hampel U (2020) Experimental analysis of gas phase dynamics in a lab scale bubble column operated with deionized water and NaOH solution under uniform bubbly flow conditions. Chem Eng Sci 229:116056. https://doi.org/10.1016/j.ces.2020.116056

34. Kipping R, Kryk H, Schleicher E, Gustke M, Hampel U (2017) Application of a wire-mesh sensor for the study of chemical species conversion in a bubble column. Chem Eng Technol 40:1425–1433. https://doi.org/10.1002/ceat.201700005

35. Kern DM (1960) The hydration of carbon dioxide. J Chem Educ 37:14–23. https://doi.org/10.1021/ed037p14

36. Ogura K, Watanabe M (1982) Nitrosylmetallochelates-II. composition of FeNO-aminocarboxylic acid complexes in solution, Electrochim. Acta 27:111–114. https://doi.org/10.1016/0013-4686(82)80068-6

37. Schneppensieper T, Finkler S, Czap A, van Eldik R, Heus M, Nieuwenhuizen P, Wreesmann C, Abma W (2001) Tuning the Reversible Binding of NO to Iron(II) Aminocarboxylate and Related Complexes in Aqueous Solution. Eur J Inorg Chem 2001:491. https://doi.org/10.1002/1099-0682(200102)2001:2%3c491::aid-ejic491%3e3.3.co;2-u

38. Zhao J, Xia Y, Li M, Li S, Li W, Zhang Z (2016) A Biophysicochemical Model for NO Removal by the Chemical Absorption-Biological Reduction Integrated Process. Environ Sci Technol 50:8705–8712. https://doi.org/10.1021/acs.est.6b01414

39. Hlawitschka M, Drefenstedt S, Bart H-J (2016) Local analysis of CO_2 chemisorption in a rectangular bubble column using a multiphase Euler-Euler CFD Code. J Chem Eng Process Technol 7:1–9. https://doi.org/10.4172/2157-7048.1000300

40. Jeong J, Hussain F (1995) On the identification of a vortex. J Fluid Mech 285:69–94. https://doi.org/10.1017/S0022112095000462

41. Hlawitschka M, Schäfer J, Jöckel L, Hummel M, Garth C, Bart H-J (2018) CFD simulation and visualization of reactive bubble columns. J Chem Eng Jpn 356–365. https://doi.org/10.1252/jcej.17we290

42. Weber (2018) Simulating bubble movement with the Euler-Lagrange approach, PhD Thesis, Technische Universität Kaiserslautern, Verlag Dr. Hut, München

43. Hlawitschka M, Kováts P, Dönmez B, Zähringer K, Bart H-J (2020) Bubble motion and reaction in different vicous liquids. Exp. Comput. Multiph. Flow. https://doi.org/10.1007/s42757-020-0072-4

44. Schäfer J, Hlawitschka MW, Attarakih MM, Bart H-J (2019) Experimental investigation of local bubble properties: comparison to the sectional quadrature method of moments. AIChE J 65. https://doi.org/10.1002/aic.16694

45. Hlawitschka M, Schäfer J, Hummel J, Garth C, Bart H-J (2016) Populationsbilanzmodellierung mit einem Mehrphasen-CFD-Code und vergleichende Visualisierung. Chem-Ing-Tech 88:1480–1491. https://doi.org/10.1002/cite.201600006

46. Krauß M, Rzehak R (2018) Reactive absorption of CO_2 in NaOH: an Euler-Euler simulation study. Chem Eng Sci 181:199–214. https://doi.org/10.1016/j.ces.2018.01.009

47. Krauβ M, Rzehak R (2017) Reactive absorption of CO_2 in NaOH: Detailed study of enhancement factor models. Chem Eng Sci 166:193–209. https://doi.org/10.1016/j.ces.2017.03.029

48. Taborda MA, Sommerfeld M, Muniz M (2021) LES-Euler/Lagrange modelling of bubble columns considering mass transfer, chemical reactions and effects of bubble dynamics. Chem Eng Sci 229. https://doi.org/10.1016/j.ces.2020.116121

49. Taborda MA, Sommerfeld M (2020) Reactive LES-Euler/Lagrange modelling of bubble columns considering effects of bubble dynamics. Chem Eng J 407:127222. https://doi.org/10.1016/j.cej.2020.127222

50. Fleischer C, Becker S, Eigenberger G (1996) Detailed modeling of the chemisorption of CO2 into NaOH in a bubble column. Chem Eng Sci 51:1715–1724. https://doi.org/10.1016/0009-2509(96)00030-9

51. Hlawitschka MW (2016) Local analysis of CO_2 chemisorption in a rectangular bubble column using a multiphase Euler-Euler CFD Code. J Chem Eng Process Technol 7. https://doi.org/10.4172/2157-7048.1000300

52. Krauß M, Rzehak R (2018) Reactive absorption of CO_2 in NaOH: an Euler-Euler simulation study. Chem Eng Sci 181:199–214. https://doi.org/10.1016/j.ces.2018.01.009

53. Merker D, Böhm L, Oßberger M, Klüfers P, Kraume M (2017) Mass transfer in reactive bubbly flows—a single-bubble study. Chem Eng Technol 40:1391–1399. https://doi.org/10.1002/ceat.201600715

Investigation of Reactive Bubbly Flows in Technical Apparatuses

Sebastian Gast, Ute Tuttlies, Larissa Laurini, Felix Kexel, David Merker, Lutz Böhm, Manuel A. Taborda, Martin Sommerfeld, Matthias Kraume, Michael Schlüter, Sonja Herres-Pawlis, and Ulrich Nieken

Abstract In the previous chapters it has been shown that the fluid dynamic conditions in bubbly flows might affect a competitive consecutive chemical reaction concerning yield and selectivity. The question arises if this results are transferable to technical apparatuses with industrial conditions. To clarify this question, the competitive consecutive DBED reaction system dissolved in tetrahydrofuran is transferred to an industrial apparatus that has been already used for a cyclohexane oxidation. First, it is shown with the Taylor bubble experiments that the DBED reaction system can be used as a model system for competitive consecutive reactions with adjustable kinetics. Afterwards, the DBED reaction system is applied to the technical apparatus. It shows that the yield and selectivity of the DBED reaction in the technical apparatus depends on the bubble size distribution and therefore potentially on the local wake structure. Even though numerical simulations with the Euler-Lagrange approach are already able to predict the formation of product and byproduct of a competitive consecutive reaction, the local flow structure within the bubble wake and its potential influence on yield and selectivity can not be covered so far.

S. Gast (✉) · U. Tuttlies · U. Nieken
Institute of Chemical Process Engineering, University of Stuttgart, Böblinger Str. 78, 70199 Stuttgart, Germany
e-mail: ulrich.nieken@icvt.uni-stuttgart.de

L. Laurini · S. Herres-Pawlis
Chair of Bioinorganic Chemistry, RWTH Aachen, Landoltweg 1a, 52056 Aachen, Germany

F. Kexel · M. Schlüter
Institute of Multiphase Flow, Hamburg University of Technology, Eissendorfer Str. 38, 21073 Hamburg, Germany

D. Merker · L. Böhm · M. Kraume
Chair of Chemical and Process Engineering, Technische Universität Berlin, Fraunhoferstr. 33-36, 10587 Berlin, Germany

M. A. Taborda · M. Sommerfeld
Institute for Process Engineering, Otto-von-Guericke University Magdeburg, Multiphase Flow Systems, Hoher Weg 7b, 06120 Halle (Saale), Germany

1 Introduction

As described in the previous chapters, there are many challenges at the scale up of gas-liquid multiphase reactors. One reason why the changes in the ongoing processes with the change of the reactor size is not yet understood and therefore not predictable are missing correlations for reaction systems of industrial interest [1, 2]. Rollbusch et al. [3] points out the gap between the industrial need for correlations with respect to an organics liquid phases as well as at elevated temperature and pressure and the academia reality, where the large majority of projects investigate aqueous systems, not being able to realize high temperatures or pressures. It is a known fact that bubble size and behavior vary with a change in the liquid viscosity, gas density and surface tension [4]. Both properties are strongly dependent on temperature. Yet, there are only a few studies of (reactive) bubbly flows at elevated pressure or temperature [3]. Furthermore, the majority of the publications focus on aqueous systems, such as water/air or water/CO_2, whereas in industry mainly organic systems are used. The limited number of studies dealing with organic liquids at elevated temperature and pressure, such as [4–6] focus on the fluid dynamics of the bubbly flow, not being able to perform a reaction at the investigated conditions, which is due to safety reasons. According to Rollbusch et al. [3] this existing gap between industrial needs and academic reality is due to three major challenges:

- Performing experiments at elevated temperature and pressure using organic solvents in technical apparatuses requires a certain laboratory infrastructure and safety precautions, which is not given in academia.
- Apparatuses as well as chemicals, which are needed in large amounts for experiments at industrial conditions, are pricey and require large financial resources.
- If the financial resources, apparatuses and laboratory infrastructure are available, the apparatuses are usually not accessible for analytic systems, for example to investigate the bubble size distribution which is most of the time done optically, since they are not built out of glass or acrylic glass.

So far, to the best of our knowledge there is no study taking into account the fluid dynamics, the mass transfer and the chemical reaction in technical apparatus at industrial conditions, using non-aqueous solutions at elevated temperature and pressure in order to study the interplay of these processes and their impacts on the yield and selectivity of an ongoing reaction. In order to better understand the interplay of the ongoing physico-chemical processes in organic liquid systems, in this chapter a reaction system dissolved in tetrahydrofuran (short: THF) is introduced and studied. The reaction system first is studied at single rising bubbles in a Taylor flow to gain more insight into the reaction kinetics. In a subsequent step, using an optically accessible high-pressure bubble column, experiments at different bubble sizes were performed. Thereby a dependence of the reaction conversion and selectivity to the bubble sizes could be found.

Further, the following chapter presents the interdisciplinary workflow using the aforementioned model system, from evolving and synthesizing of the reaction system, over running bubble column experiments on the technical scale and to the numerical description of the technical scale experiment by Euler-Lagrange calculations. This workflow, using state of the art methods, describes the up to date procedure of how to design and scale up an industrial bubble column.

2 Experimental Setup for the Investigation of Bubbly Flows in Technical Apparatuses

The experiments have been performed in an optically accessible bubble column designed by Schäfer [7]. It withstands temperatures up to $T = 200\,°C$ and pressures up to $p = 50$ bars. It has a volume of $V = 4\,L$ and a height of $H = 969$ mm (see Fig. 1, middle). Due to the construction in stainless steel and glass it can be operated with
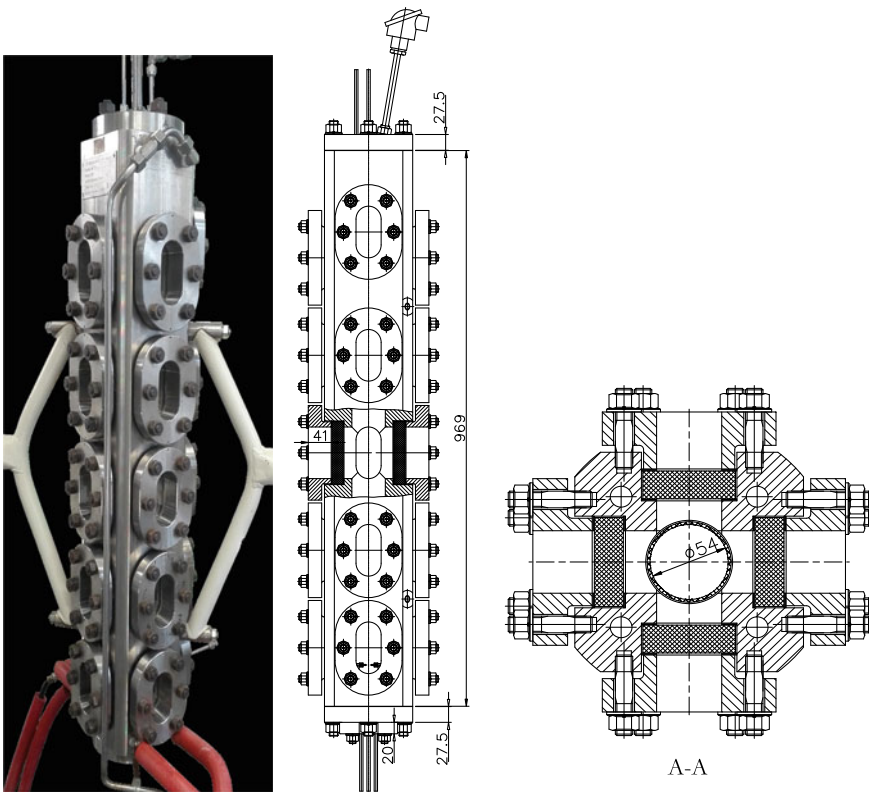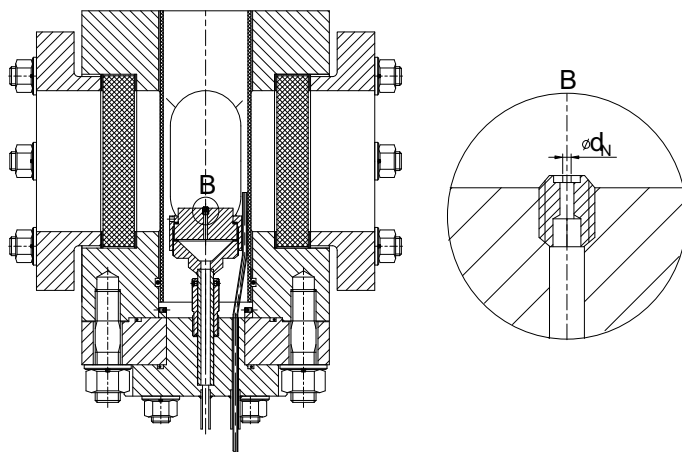

Fig. 1 Optical accessible bubble column

Fig. 2 Technical drawing of the bottom of the column

all kinds of organic solvents. Five oval viewing windows are installed on each lateral side which allow the observation of about 50% of the rising distance of a bubble from the sparging to the degassing region at the top of the column (see Fig. 1 left). With a width of $x = 44$ mm each pair of windows enables the observation of 91% of the cross-sectional area. The bubbles are injected into an inner glass cylinder which prevents the irregularities at the viewing sections to disturb the flow of the bubbles (see Fig. 1, right). The inside of the glass cylinder is the actual reaction chamber with a maximal volume of $V_R = 2.2$ L.

The reaction gas is introduced via a gas sparger at the bottom of the column (see Fig. 2). The sparger consists of a single, centered nozzle with a well-defined opening. In order to produce different sizes of bubbles the diameter of the nozzle opening can be varied from $d_N = 0.1$ mm to 0.4 mm.

The flow chart of the experimental setup of the reactor and its periphery is shown in Fig. 3. The center of the setup is the above described bubble column reactor (F). A gear pump (B) at the bottom of the column is used to fill the liquid phase to the reactor. By means of a three-way valve the reactor can be emptied via the same pipe. A separate capillary (see Fig. 2) which is controlled by a manual ball valve (C) can be used for insertion of additional liquids, e.g. DBED reaction solution. The reaction gas is supplied by two mass flow controllers (A). A check valve prevents the liquid from flowing back into the gas inlet. In the bottom of the column the supplied gas is distributed by the aforementioned gas sparger. The exhaust reaction gas is taken from the top of the column and added to the exhaust air system. For safety reasons, an optical liquid level sensor is installed (G). In case of an accumulation of liquid in the exhaust air, the experiment is automatically stopped to prevent the formation of an explosive mixture in the exhaust gas. The pressure control valve (I) controls the operating pressure in the reactor. Before the exhaust gas is discharged via the

Fig. 3 Flow chart of bubble column setup
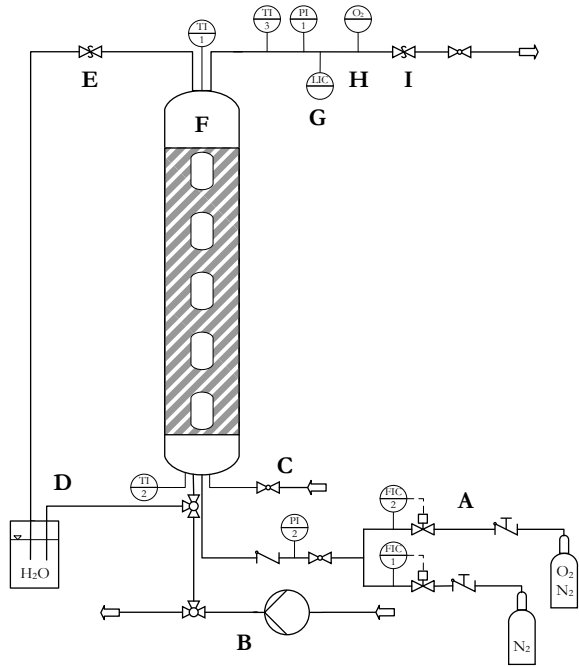
exhaust air system, the oxygen concentration is measured with the optical oxygen sensor *Firesting* by *PyroScience GmbH* (H).

The reactor can be emptied at any time into a barrel of $V = 120$ L (D) filled with water via a three-way valve at the bottom of the column. In case of a sudden pressure increase, for example due to failing temperature control, the content of the column is emptied via a safety valve (E) into the water-filled barrel (D). The temperature is monitored at the bottom and top of the bubble column as well as in the exhaust gas. The pressure is measured at the gas inlet and the exhaust gas.

The viewing windows installed on the reactor enable the detection of the generated bubble size distribution by means of an optical analysis at different rising heights. For the concentration measurements a UV/VIS or an ATR-FTIR Probe have been inserted into the inside of the glass cylinder by exchanging one glass window by a metal plate with a lead-through. This enables online concentration measurements on the chosen height of the viewing windows.

3 Experimental Analysis of Bubble Size Distribution and Gas Hold-up by Means of Optical Measurements

For the optical analysis a Dalsa Geni Nano-M1280 Camera with the telecentric lens TZM 1235/0,083-C by *Sill Optics* is used. To minimize the optical deformation due to
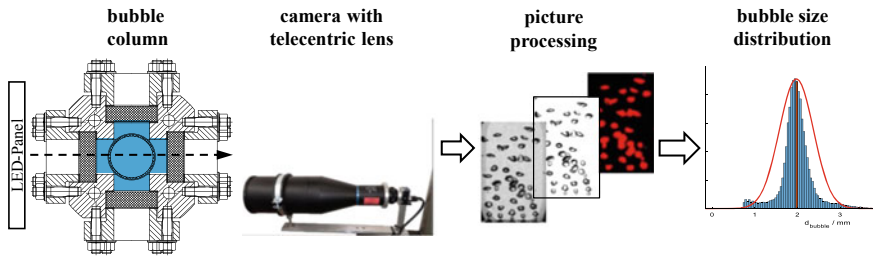
Fig. 4 Process of optical determination of the bubble size distribution

the round glass cylinder, the volume between the cylinder and the viewing windows is filled with the same fluid as the inside of the cylinder (see blue colored area in the cross-sectional drawing in Fig. 4). Operating the camera with backlight by a LED-Panel the whole cross section of the glass cylinder can be focused.

In the first step of the evaluation, a background image is calculated from a large number of images. By subtracting the calculated background image from the actual bubble image, contaminations or standing bubbles are removed in a second step. The individual bubbles are detected by means of a grey value analysis in the third step. To find the optimal threshold value for the greyscale analysis to differentiate between liquid phase and bubble, in the following referred to as the threshold, measurements were carried out at known volume flows. All bubbles were recorded across the cross-section. The gas holdup was so low that there was hardly any overlap between the detected bubbles. The two main axes of an ellipsoid can be determined via the projection area and the perimeter. Assuming the ellipsoids to be rotationally symmetric the volume of the single bubble can be calculated. Knowing the added volume flow and the rising velocities of the bubble, the actual gas hold-up was calculated and compared to the gas hold-up calculated from the image analysis. In this way an optimal threshold of 210 was determined for the used setup and settings. For image analysis the software package Vision from *National Instruments* was used.

For better comparability, the given ellipsoidal diameters are converted to the diameter of a sphere of equal volume. For the calculation of the bubble size distributions, $n_i = 1000$ images were evaluated, which corresponds to a total number of bubbles of $n_B = 5000$ to 35,000. The images were recorded at a frequency of $f = 3$ Hz to ensure that individual bubbles were not included in the evaluation multiple times.

In the following the bubble size distributions are given as a probability density $f(d)$ of the unit $\frac{1}{\text{mm}}$. For the determination of the bubble size distribution, the bubbles were divided into individual classes according to their size. The probability that a bubble of size d_b belongs to class k with a diameter from d_k to $d_k + \Delta d$ is given by

$$P(d_k < d_b \leq d_k + \Delta d) = \frac{N_k(d_k < d_b \leq d_k + \Delta d)}{N_B}$$

$$= \int\limits_{d_k}^{d_k + \Delta d} f(d_b)\delta d \tag{1}$$

Thereby N_k describes the number of bubbles in class k and N_B the number of all considered bubbles. Hence

$$f_k = \frac{N_k}{N_B \Delta d} \tag{2}$$

describes the discrete probability density.

4 Chemical Reaction System for the Investigation of Bubbly Flows in Technical Apparatuses

Bubbly flows are reaction systems with a massive volume in liter-scale. To minimize the expenses in terms of costs and time, chemicals used should either be purchasable or synthesizable in large amounts. For the [Cu(DBED)]OTf system, used in this study (see also Chapter "Control of the Formation and Reaction of Copper-Oxygen Adduct Complexes in Multiphase Streams" chemical details), five chemicals are necessary: N,N′-di-*tert*-butylethylenediamine (short: DBED), 4-methoxyphenol, triethylamine, tetrahydrofuran and tetrakisacetonitrile copper(I) triflate. Except for the latter one, all chemicals are inexpensive and purchasable by various manufactures (see Table 1). The copper(I) salt is quite expensive but can be synthesized cost-efficiently in gram level according to literature [8].

The core of the [Cu(DBED)]OTf system is the catalytically active Cu_2O_2 center (C). The so-called μ-η^2:η^2-peroxo complex (C) is synthesized in situ. At first equimolar amounts of DBED ligand (L) and copper(I) triflate (Cu) form the copper(I) complex [Cu(DBED)]OTf (A) in the reaction solution. The following competitive consecutive reaction consists of three reaction steps activated by the addition of dioxygen to the reaction mixture. In the first step two copper(I) species (A) activate the molecular oxygen to give the μ-η^2:η^2-peroxo complex (C). Secondly, complex C

Table 1 Used Chemicals

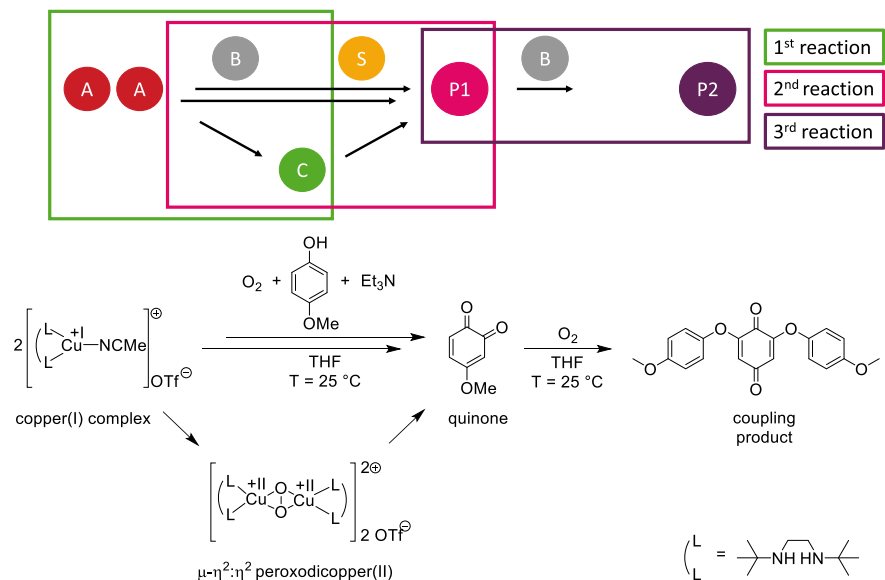| Name	CAS-Number	Purity (%)	Vendor
Tetrahydrofuran	109-99-9	$\geq$99.9	Merck
4-methoxyphenol	150-76-5	99	Sigma Aldrich
N,N′-di-tert-butylethylenediamine	4062-60-6	98	Sigma Aldrich
Triethylamine	121-44-8	$\geq$99	Sigma Aldrich

Fig. 5 Competitive consecutive reaction of [Cu(DBED)]OTf with dioxygen resulting to a quinone and a coupling product

oxidizes the substrate 4-methoxyphenol (S) supported by the auxiliary base trimethylamine in a competitive consecutive step to a quinone (4-methoxycyclohexa-3,5-diene-1,2-dione) (P1). Most ortho-quinones are highly reactive and undergo further coupling reactions [9, 10]. As a result, product (P1) reacts in a third reaction step with dioxygen to the coupling product (2,6-bis(4-methoxyphenoxy)cyclohexa-2,5-diene-1,4-dione) (P2) (see Fig. 5). For more information about the [Cu(DBED)]OTf-system see Chapter "Control of the Formation and Reaction of Copper-Oxygen Adduct Complexes in Multiphase Streams".

4.1 Oxygen-Free Handling of the Reaction System on the Technical Scale

The handling of the reaction system described above and specific safety information are summarized in the following section. The copper DBED system uses tetrahydrofuran as a solvent. Tetrahydrofuran forms highly reactive hydroperoxides in a radical reaction with molecular oxygen catalyzed by light. At higher concentrations peroxides are explosive [11, 12]. Thus, only peroxide-free tetrahydrofuran should be used. To avoid contact with dioxygen, the solvent needs to be stored under an inert gas atmosphere. For long-term storage, dark brown glass containers or stainless-steel barrels minimizing the contact with light are highly recommended. To reduce

the solvent consumption, tetrahydrofuran can be recycled from the reaction mixture afterwards. Tetrahydrofuran is distilled from the crude reaction mixture under inert gas conditions, preventing an oxidation to the peroxide. Traces of water are removed by adding molecular sieve to the distillation solution. To further increase the safety level, the reducing agent iron(II) chloride (1 g per 5 L of solvent) can be added to the reaction mixture as well. The iron salt does not affect the distillation process and remains in the crude solution.

To minimize the chemical costs, the oxygen-sensitive salt, tetrakis(acetonitrile) copper(I) triflate can be synthesized cost-effectively with high purity in a one-step synthesis [13].

The mixing of the reactants must be performed under inert gas conditions due to the oxygen-sensitivity of copper(I) triflate. In addition, the catalytically active peroxo species is water-sensitive and needs handling under inert gas conditions as well. The following method can be easily implemented in an already existing experimental setup. For an oxygen-free setup a moderate number of additional laboratory equipment is required: A pressure- and vacuum-resistant glass round flask with a glass stopcock (Schlenk flask), matching chemically resistant silicone rubbers and glass stoppers, PTFE tube, stainless steel canula and a diaphragm or rotary vane pump ($p < 1$ mbar).

At first the solid chemicals copper(I) triflate and 4-methoxyphenol (green, Fig. 6a) are weighted and added to the flask, which is flooded with inert gas (Fig. 6a). Directly after the addition of the copper salt the flask is closed with the glass stopper and evacuated for five minutes. Fast and clean working are of high importance because copper(I) triflate is oxidized to copper(II) triflate within several seconds in the presence of oxygen. Handling errors can be identified visually as the salt turns from colorless to blue during the oxidation process. After flushing the flask with inert gas (nitrogen or argon), the glass stopper is replaced by a silicone rubber stopper under an inert gas counterflow. With a PTFE tube fixed to the silicone rubber stopper, tetrahydrofuran (blue, Fig. 6b) could be pumped into the flask under inert gas atmosphere. To avoid overpressure and to control the flow of solvent, a stainless steel canula is used (Fig. 6b). When the required amount of solvent is transferred, removing the canula stops the solvent flow and enables the flushing of the PTFE tube with inert
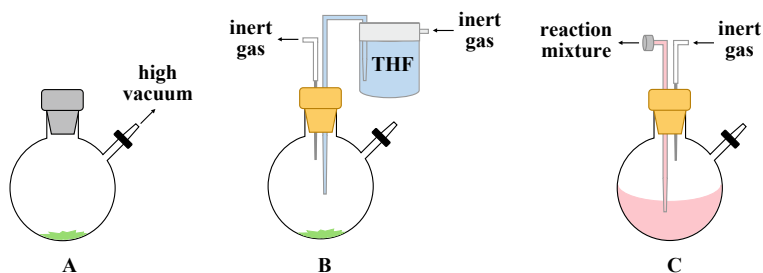

Fig. 6 Handling of oxygen-sensitive chemicals with simple techniques

gas. The auxiliary base triethylamine is added with a syringe. The flask is shaken until all chemicals are dissolved and a clear, purple solution occurs. The reaction mixture (pink, Fig. 6c) is transferred into the experimental setup by connecting the PTFE tube inserted into the reaction mixture with the bottom entrance of the bubble column. The flow velocity is controlled by a stainless-steel canula in the rubber stopper (Fig. 6c). The addition of the reaction solution at the bottom of the column prevents the contact to a gas phase at the top of the column which could still contain small amounts of oxygen.

4.2 Experimental Analysis of Concentrations by Means of ATR-FTIR and UV/VIS

Both products P1 (4-methoxycyclohexa-3,5-diene-1,2-dione) and P2 (2,6-bis(4-methoxyphenoxy)cyclohexa-2,5-diene-1,4-dione) can be detected and distinguished from other components in the spectra of the ATR-FTIR as well as the UV/VIS spectrometer, as can be seen in Fig. 7. Neither the solvent THF (black line in Fig. 7 left) nor the reaction mixture at the beginning of the reaction before oxygen was added (green line in Fig. 7 left and right) interfere with the characteristic peaks of the products P1 and P2. In the IR-Spectrum (Fig. 7 left) the product P1 builds up a peak at 1400 cm^{-1} while P2 produces peaks at 1500 cm^{-1} and 1200 cm^{-1}. For the experimental runs (purple curve after $t = 40$ min of oxygen-dosage in Fig. 7 left) a shift in the peaks of P2 of about 10 cm^{-1} occurs compared to the calibration measurements (red line in Fig. 7 left).

In the UV-spectrum P1 produces a maximum at $\lambda = 420$ nm while P2 has its maximum at $\lambda = 505$ nm.
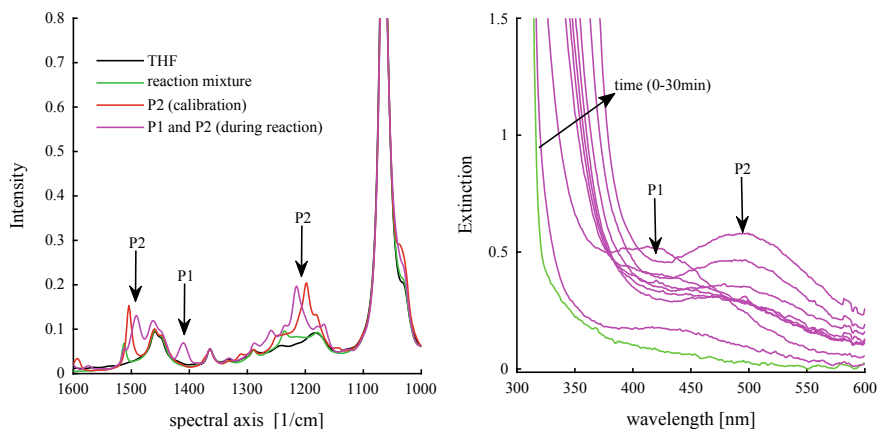

Fig. 7 Spectra of species measured with an ATR-FTIR (left) and an UV/VIS spectrometer (right)

Since product P1 is not stable enough for isolation, calibration is only possible for P2. Therefore, only the peak area (ATR-FTIR) or the extinction (UV/VIS) can be given for P1.

4.3 Characterisation of the [Cu(DBED)]OTf System by Means of Taylor Bubble Experiments

Before experiments in the technical bubble column are performed for the investigation of the influence of fluid dynamics on yield and selectivity, the reaction rates for the [Cu(DBED)]OTf system needs to be adjusted in the Taylor bubble setup (see Chapter "Experimental Investigation of Reactive Bubbly Flows—Influence of Boundary Layer Dynamics on Mass Transfer and Chemical Reactions"). Furthermore, the experiments aim to ensure the transferability of the results obtained by the experiments with the MNIC-DNIC system to the Cu-O_2 system used here.

In order to obtain visualized information about the concentration fields of the two products P1 and P2 in the wake of a single Taylor bubble, the imaging UV/VIS setup applicable for experiments conducted under oxygen free conditions and introduced in Sect. 3 in Chapter "Experimental Investigation of Reactive Bubbly Flows—Influence of Boundary Layer Dynamics on Mass Transfer and Chemical Reactions" is used. The setup is shown in Fig. 8 and has been adjusted in such way that the characteristic absorption peaks of the two products, shown in Fig. 7 in Chapter "Chemical Reactions in Bubbly Flows", are matched by the LED backlight illumination. In the observed case those characteristic wavelengths are $\lambda_1 = 420$ nm for product P1 and $\lambda_2 = 505$ nm for product P2.

As the experiments in the bubble column are within a timescale of several minutes, the experimental conditions applied in the Taylor bubble flow have been adjusted to take place within seconds. Therefore, the concentration of the gaseous phase oxygen is increased by using pure oxygen bubbles and the concentration of copper complex in the reaction solution is risen up to $c_{Cu} = 3$ mM. The experiments are conducted in two different capillaries with hydraulic diameters of $D_h = 4$ mm and $D_h = 4.5$ mm.

The analysis of the obtained greyscale images is similar to the method introduced and explained in Sect. 3.2 in Chapter "Experimental Investigation of Reactive Bubbly Flows—Influence of Boundary Layer Dynamics on Mass Transfer and Chemical Reactions". In order to convert the obtained greyscale images into concentration fields, the working principle of an UV/VIS spectrometer is used, which is utilizing Beer-Lambert law

$$E_\lambda = \log\left(\frac{I_0}{I}\right) = \varepsilon_\lambda dc. \tag{3}$$

E_λ represents the extinction, I_0 corresponds to the incident light intensity, I to the light intensity behind the sample, ε_λ is the wavelength-dependent extinction coefficient, d is the layer thickness of the liquid and c is the concentration.

Fig. 8 Taylor bubble setup for experiments under oxygen free conditions
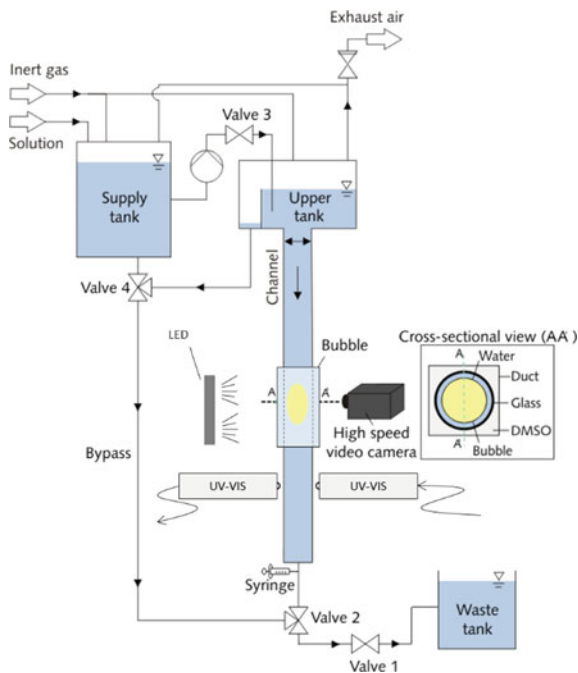
The layer thickness is assumed to be constant and is set equal to the respective capillary diameter of $D_h = 4$ and 4.5 mm. The initial light intensity I_0 is determined for both wavelengths individually prior each recording. For this purpose, the capillary filled with the reaction solution is recorded without a bubble and an average value is determined from 10 grayscale images. As the extinction coefficients of the two products are not known so far but should be with the same order of magnitude based on the UV/VIS spectra shown in Fig. 7 in Chapter "Chemical Reactions in Bubbly Flows", it is assumed that the measured light absorption at the different wavelengths result solely from the corresponding product P1 or P2. Based on the made assumptions and the fact that the extinction coefficients are not known, the Lambert-Beer equation is therefore rearranged yielding

$$\log\left(\frac{I_0}{I}\right)d^{-1} = \varepsilon_\lambda c. \tag{4}$$

The images are then analyzed pixel wise within the region of interest. The resulting concentration fields are shown in Fig. 9, displaying the distribution of the two products P1 and P2 in the wake of the bubble. As the necessary information about the extinction coefficient is missing, only qualitative statements about the concentration fields in the wake of the bubble can be made.

Nevertheless, the results of the measurements in the two different capillaries show that the changing fluid dynamic conditions do again impact the formation of
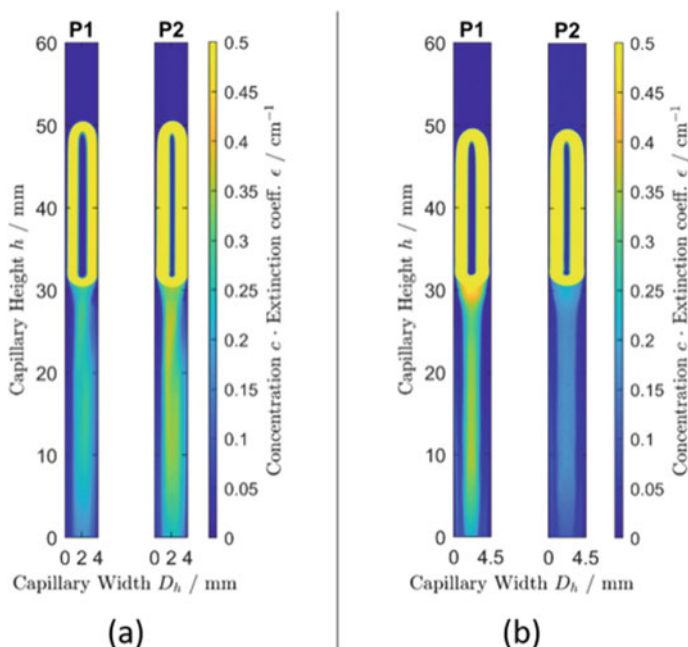
Fig. 9 Concentration distribution of the product P1 and P2 in the wake of a pure oxygen bubble within a $D_h = 4$ mm wide capillary (**a**) and $D_h = 4.5$ mm wide capillary (**b**)

the product P1 and its by-product P2. With an increasing degree of mixing in the wake of the bubble, the product formation is shifted towards the product P1.

This result is in good agreement with the results obtained with the MNIC-DNIC system, emphasizing the impact of the bubble size and the resulting mixing behavior on the selectivity of a fast competitive consecutive gas liquid reaction (compare Chapters "Experimental Investigation of Reactive Bubbly Flows—Influence of Boundary Layer Dynamics on Mass Transfer and Chemical Reactions" and "Visualization and Quantitative Analysis of Consecutive Reactions in Taylor Bubble Flows").

5 Experiments with Chemical Reactions in Bubbly Flows in Technical Apparatuses

5.1 Experimental Conditions and Procedure

To transfer the results from the Taylor bubble to a technical apparatus, the inside of the glass cylinder (see Fig. 3, F) is filled with $V = 1.5$ L of dried tetrahydrofuran which corresponds to a filling height of $H = 655$ mm and a maximal rising height of

$H = 585$ mm. The experiments are performed at ambient pressure and temperatures of $T = 25\,°C$. The tetrahydrofuran is of HPLC-grade with a purity of at least 99.9%. To create an oxygen-free atmosphere, the column is flushed with nitrogen for at least $t = 20$ min before filling. During the preparation of the reaction mixture as described above the column is continuously aerated with nitrogen. After the introduction of the liquid reaction mixture at the bottom of the column the reaction is started by changing the aeration gas from nitrogen to the oxygen/nitrogen mixture. The reaction gas is dispersed into the bubble with nozzle sizes varying from $d_N = 0.1$ mm to 0.4 mm and a flow rate of $\dot{V} = 50$ mLn min^{-1}. Within the resulting reaction mixture, the ratio of copper(I) triflate to 4-methoxyphenol is chosen to 25 mol equivalents or the ratio of catalyst to 4-methoxyphenol to 50 mol equivalents, respectively.

Two sets of experiments have been performed. For the first set the ATR-FTIR probe has been used for the online concentration analysis. The copper(I) triflate was set to a concentration of 5 mM resulting in a 125 mM concentration of the 4-methoxyphenol. As reaction gas a mixture of 8% oxygen with 92% nitrogen was used. For the second set the liquid concentrations have been detected by a UV/VIS probe. The copper(I) triflate was set to a concentration of 0.3 mM resulting in a 7.5 mM concentration of the 4-methoxyphenol. As reaction gas, a mixture of 20% oxygen with 80% nitrogen was used. All used gases had a purity of 99.9999% (grade 5.0).

In earlier experiments a good axial mixing within the column was found (see Sect. 4.3 in Chapter "Determination of Intrinsic Gas-Liquid Reaction Kinetics in Homogeneous Liquid Phase and the Impact of the Bubble Wake on Effective Reaction Rates"). This is why the concentration measurement has always been performed at the second viewing window, corresponding to a reactor height of $H = 282$ mm and a rising distance to the sparger of $H = 210$ mm.

In order to have bubbles of different sizes experiment with three different nozzle sizes ($d_{nozzle} = 0.1$ mm, 0.2 mm and 0.4 mm) in the gas sparger are performed.

5.2   Experimental Results

Figure 10 shows the bubble size distributions for the different nozzle sizes (from left to right) at different heights of the reactor. It is shown that for the three nozzles average bubble sizes of $d_B = 1.75$ mm (0.1 mm-nozzle), 2.75 mm (0.2 mm nozzle) and 3.8 mm (0.4 mm nozzle) are achieved and that there is no significant change in the bubble sizes over the height due to coalescence or break-up.

The liquid is mixed by the rising bubbles and therefor the reactor behaves like a semibatch-reactor with constant gas-inflow. The concentrations of P1 (4-methoxycyclohexa-3,5-diene-1,2-dione) and P2 (2,6-bis(4-methoxyphenoxy)cyclohexa-2,5-diene-1,4-dione) are measured with an ATR-FTIR probe which is inserted in the middle window. Since calibration of the evolving peaks in the ATR-spectra is possible only for P2 (P1 cannot be synthesized in a stable form) the results are shown as peak areas over time (Fig. 11). Since one cannot conclude
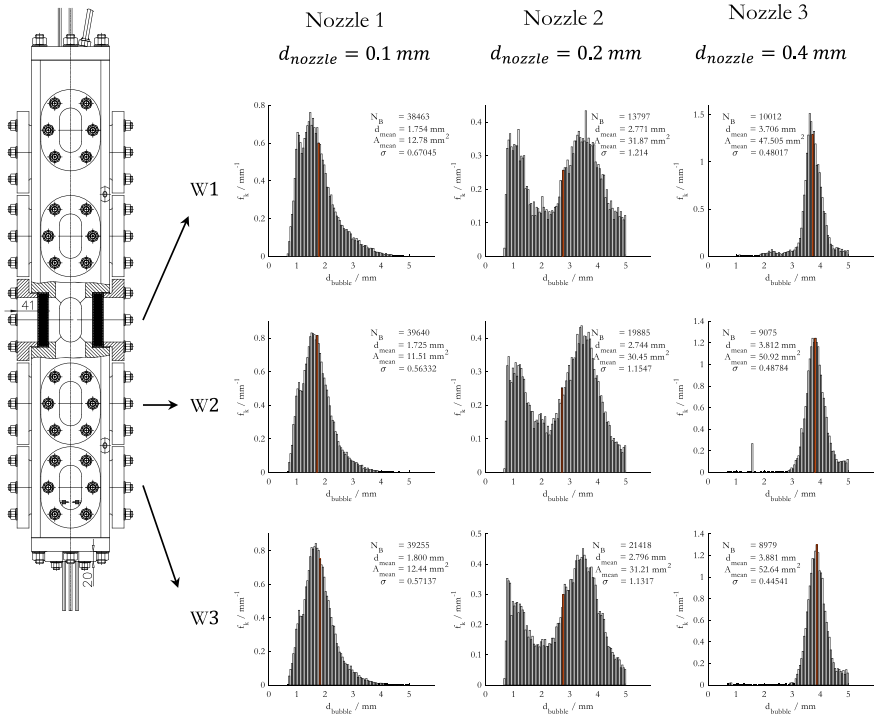
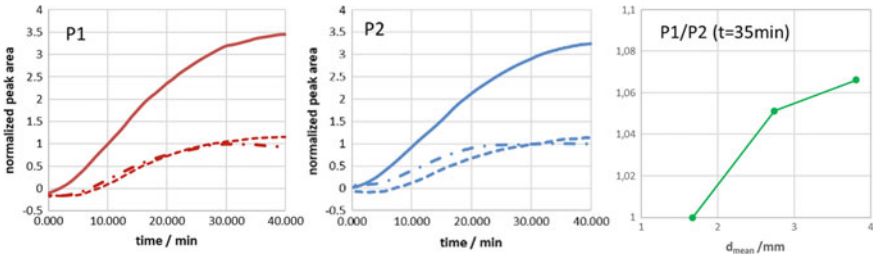**Fig. 10** Bubble sizes on different heights of the bubble column

Fig. 11 Left and middle: Evolution of the normalized peak area of products P1 and P2 from the start of the oxygen supply. Dot-dashed-line: $d_{nozzle} = 0.1$ mm; Dashed line: $d_{nozzle} = 0.2$ mm; Solid line: $d_{nozzle} = 0.4$ mm. Right: Ratio of P1 to P2 after t = 35 min

from the peak area to the concentrations of P1 and P2 the areas are normalized with the maximum of the areas for a 1 mm-nozzle. Figure 11, left and middle shows the peak areas of P1 and P2 over time for all three nozzle sizes. It is obvious that for a mean bubble size of $d_B = 3.81$ mm, more products are formed. This is unexpected, since the bigger bubbles provide less surface area for oxygen transfer and less gas holdup due to higher bubble velocities than smaller bubbles.

An explanation can be that the bubble wake of the bigger bubbles provides locations behind the bubbles with higher oxygen concentrations as shown in previous chapters experimentally and numerically (compare e.g. Chapters "Mass Transfer around Gas Bubbles in Reacting Liquids", Experimental Investigation of Reactive Bubbly Flows—Influence of Boundary Layer Dynamics on Mass Transfer and Chemical Reactions, Modeling and Simulation of Convection-Dominated Species Transport in the Vicinity of Rising Bubbles, Development and Application of Direct Numerical Simulations for Reactive Transport Processes at Single Bubbles, Multi-scale Investigations of Reactive Bubbly Flows, Visualization and Quantitative Analysis of Consecutive Reactions in Taylor Bubble Flows) and therefore with higher production rates of P1 and in succession of P2.

Plotting the ratio of the normalized peak areas of P1 to P2 (Fig. 11 right) shows that the bubble regime with bigger bubbles leads to an increased relative production of P1. This shows that the selectivity of a competitive consecutive reaction can be influenced by the utilization of a certain bubble wake structure. Additionally it means that with reaction systems which have reaction rates of the magnitude of the [Cu(DBED)]OTf-system, we cannot only investigate the influence of the bubble size on overall conversions in gas-liquid-systems but also the influence of the wake structure on the selectivity of consecutive reactions under nearly industrial conditions in bubbly flows. Consequently, in a next step the design of a gas sparger can be tailored according to the kinetic demands of the chemical reaction.

6 Numerical Simulation of Reactive Bubbly Flows in Technical Apparatuses

As already discussed in the previous chapters, the study of the coupled mass transfer, chemical reaction and fluid dynamics is relevant in the design and scale-up of transformation processes for different products in chemical industry. However, many previous numerical studies are based on aqueous solution systems, for which one obtains a great vision of the dynamics involved, but its use in real technical systems may be rather limited. On the other hand, the study of organic systems can expand the vision on the dynamic behavior of the participating species and its chemical transformation from one component to another. In the following section we present a preliminary numerical study applying the Euler/Lagrange approach (see also Chapter "Modelling the Influence of Bubble Dynamics on Motion, Mass Transfer and Chemical Reaction in LES-Euler/Lagrange Computations" and Taborda et al. [14]) for a reactive organic liquid system using tetrahydrofuran as a solvent in an experimental bubble column. The reaction model system used is presented in Eqs. 5–7:

$$O_{2_{(g)}} \rightleftharpoons O_{2_{(dissolved)}} \tag{5}$$

$$S + O_2 \rightarrow P1 + (\ldots) \tag{6}$$

$$P1 + 2S + O_2 \rightarrow P2 + (\ldots) \tag{7}$$

In which O_2, S, P1 and P2 stands for molecular oxygen, substrate 4-methoxyphenol, first product P1 (4-methoxycyclohexa-3,5-diene-1,2-dione) and second product P2 (2,6-bis(4-methoxyphenoxy)cyclohexa-2,5-diene-1,4-dione), respectively. The parentheses denote the eventual production of water as by-product which is captured by the auxiliary base triethylamine within the DBED system. As a first rough estimation the value of the reaction rate used for the first reaction (6) is $k_1 = 420$ m³/(kmol s) and for the second reaction (7) is $k_2 = k_1/500$ m³/(kmol s).

6.1 Case Description and Simulation Setup

Simulations have been performed in close collaboration of the Nieken and Sommerfeld group. The experimental setup is based on a circular bubble column reactor with a height of $H = 963$ mm, a diameter of $D = 54$ mm, filled up to a height of $H = 680$ mm with a stagnant solution of tetrahydrofuran having different initial DBED concentrations. Bubbles consisting of a gas mixture of 8% of O_2 and 92% of N_2 by volume, were generated by a single-needle gas distribution system located at $h = 65$ mm from the bottom of the reactor. The gas flow rate through the nozzle was adjusted to $\dot{V} = 50$ mlmin⁻¹ and the initial bubble size was specified with a number-based mean value of approximately $d_B = 3.88$ mm. The liquid temperature was controlled to a constant value of $T = 20$ °C. In the experiments, the bubble size was measured using an imaging technique. The concentration of P2 was measured at $h = 442$ mm from the bottom of the column during a period of approximately $t = 80$ min. The computational domain with a height of $H = 680$ mm and a diameter of $D = 54$ mm, which correspond to a solvent volume of $V = 1.5$ L, was discretized using 37,400 control volumes, in the cross-section designed as an O-grid with refinement towards the wall as shown in Fig. 12. Along the hight of the column 110 grid cells were used with constant height.

6.2 Results of the Numerical Simulation

Spatial and temporal color fields for P1 and P2 concentrations obtained from the simulations, for visualizing the reaction evolution in a vertical middle plane through the column, are shown in the Fig. 13. At $t = 500$ s after the simulation start, the concentration fields of P1 and P2 appear still very homogeneous. As the mass transfer proceeds, the oxygen transferred from the bubbles into the liquid reacts with the substrate S, producing P1. Afterwards, due to the reaction (7) production of P2 also occurs. Some traces of high local P2 at $t = 1000$ s and $t = 1500$ s are visible in the same plane which are originating from individual bubbles. Certainly, the concentration of
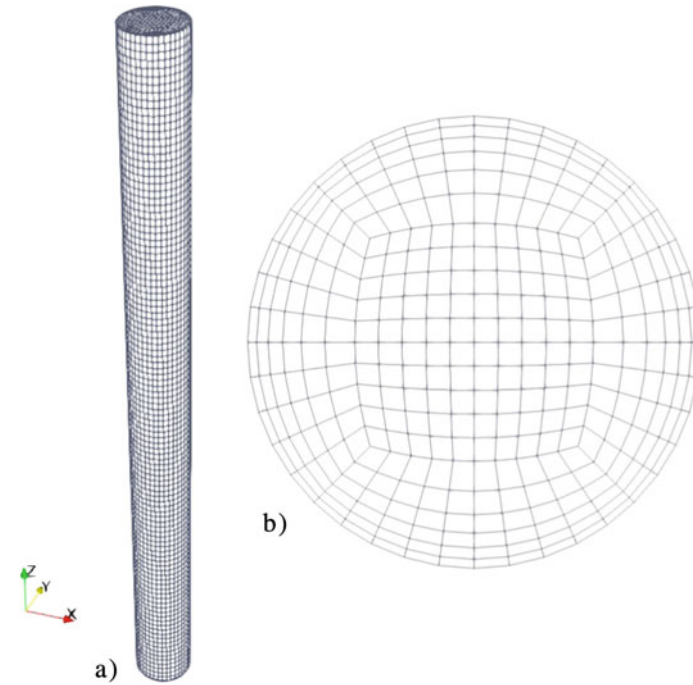
Fig. 12 Numerical grid for the considered bubble column with a height of $H = 680$ mm and a diameter of $D = 54$ mm, discretized by 37,400 control volumes in total, **a** three-dimensional view of the grid system including coordinate system, **b** cross-sectional grid

P1 and P2 increases during the reaction progress. However, the rate at which P1 is increasing between $t = 500$ s and 1000 s is different between $t = 1000$ s and 1500 s, in which some small local traces with high concentration of P1 value can be seen. A similar behavior is shown for the P2 concentration field. The rate at which P2 is increasing is different between $t = 500$ s and $t = 1000$ s, compared with $t = 1000$ s to 1500 s, in which the concentration is 2.5 times higher compared with $t = 500$ s. However some variations exist in the upper part due to the transport processes involved.

The mean vertical liquid and bubble velocity profiles for the same simulation case at a vertical cross-section of $z = 340$ mm (i.e. in the lower half of the column) are shown in Fig. 14. Also, the liquid and bubble velocity field was obtained as an average over the entire simulation period of $t = 1500$ s to get a statistically converged profile, although the process is certainly fully transient. As a result, both computational profiles become almost symmetric due to the averaging process. At this height the bubbles have already dispersed over the core region of the column (see solid line in Fig. 15) with a maximum velocity value of about $v = 0.27$ ms^{-1} in the center of the reactor. Naturally the bubbles transfer upward momentum to the liquid phase resulting in an upward liquid velocity (see dashed line) with a maximum of about

Fig. 13 Images of concentrations of P1 and P2 in the vertical mid-plane of the column for different simulations times
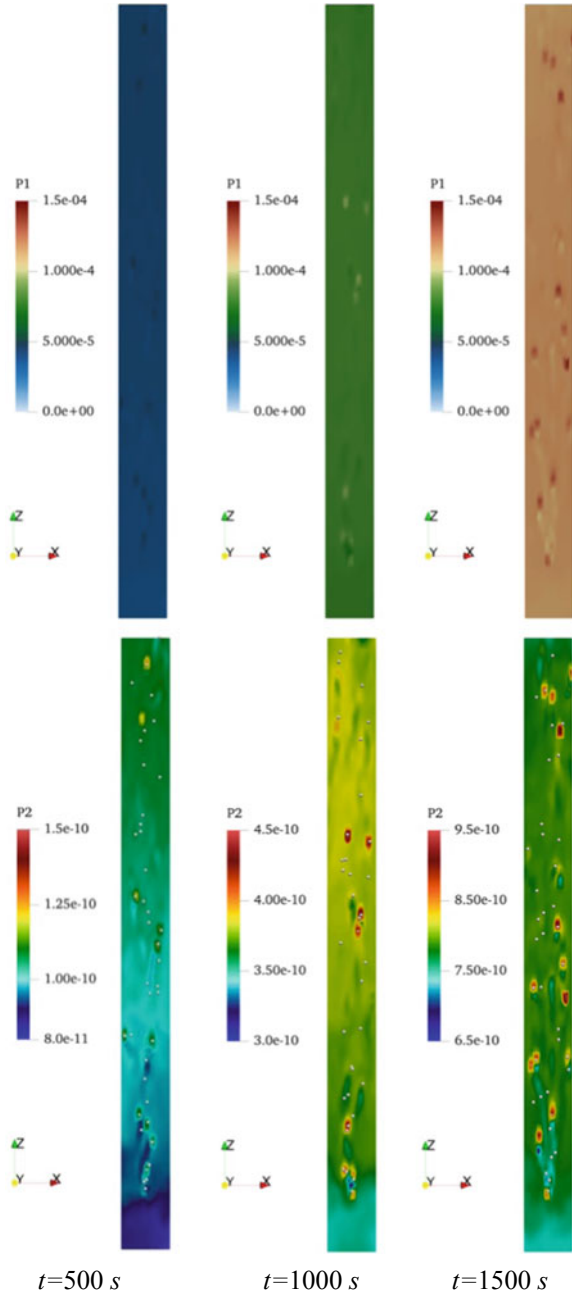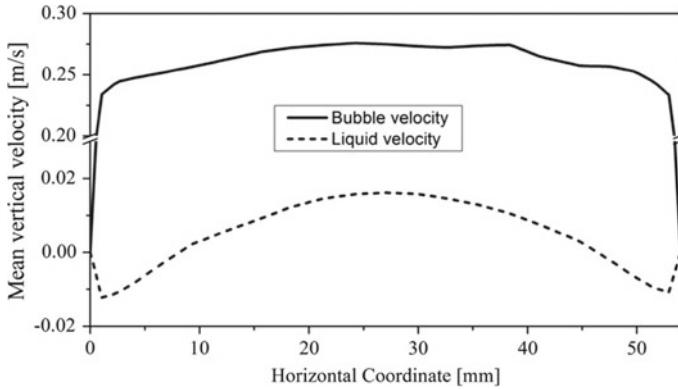
Fig. 14 Mean vertical liquid and bubble velocity profiles, the computations averaging is done over the entire simulation period of t = 1500 s; cross-sectional profiles at a height of t = 340 mm
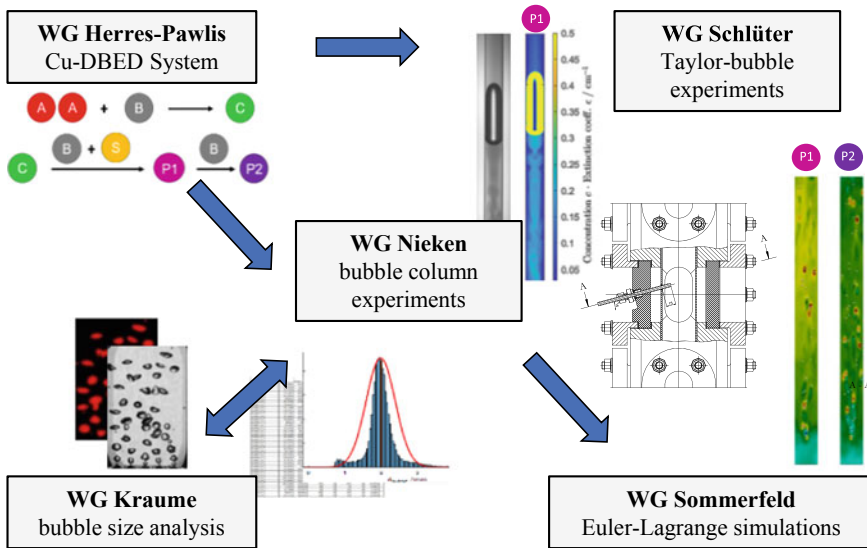

Fig. 15 Collaboration between the working groups

$v = 0.018 \, \text{ms}^{-1}$. This of course induces a liquid circulation and large scale backmixing in the column with negative liquid velocities in the vicinity of the wall. Thereby, the transport of species from the upper part to the bottom part of the reactor is realized.

7 Collaboration Between Working Groups and Conclusions

In order to realize the described experiments, working groups from all over Germany collaborated very closely (see Fig. 15).

The synthesis of the copper salt and the development of the consecutive competitive reaction system was done at the working group of Sonja Herres-Pawlis at the RWTH Aachen. The system was used to show the influence of fluid dynamics on selectivity in a Taylor bubble setup in the group of Michael Schlüter at Hamburg University of Technology. Additionally, the system was used for the bubble column experiments at the working group of Ulrich Nieken at the University of Stuttgart. The evaluation of the images and determination of the bubble size distribution was performed by the working group of Matthias Kraume at the Technical University Berlin. Combining all the measurements and results the working group of Martin Sommerfeld at the Otto-von-Guericke-Universität Magdeburg was able to perform large scale Euler-Lagrange simulations. The developed consecutive competitive chemical system is able to show the dependence of selectivities and conversions from the bubble sizes and the flow regime in gas-liquid systems. This dependence was shown in Taylor bubble experiments and consecutively the system had to prove that the dependence can also be seen in industrial processes. Therefore the experimental setup at the University of Stuttgart was used, which is able to provide oxygen-free conditions, solvent resistance and the possibility to measure bubble sizes over the rising height of the bubbles. These experiments showed that bigger bubbles lead to higher conversions, which is counterintuitive (since bigger bubbles have less surface for mass transfer) and can only be explained by the different flow regimes provided by different bubble sizes, e.g. the different wakes behind the bubbles, which could also be seen in Taylor bubble and Taylor flow experiments. For the experiments in the bubble column even a dependence of the selectivities could be seen which has to be confirmed by further experiments.

Concluding it can be remarked that with the collaboration between workgroups from chemistry and engineering a dependence of the performance of chemical reactions from the flow regime around bubbles and in bubbly flows could be proven. With this kind of collaborations it is possible to improve the understanding of chemical processes in gas-liquid-systems by combining experiments on the bubble scale (e.g. Taylor bubbles), experiments under technical conditions and simulation models.

References

1. Becker M, Tuinier M, Rollbusch P, Skillas G, Orabi M (2012) Mehrphasenreaktoren: Zusammenspiel von Prozessentwicklung und Hydrodynamik. Chem Ing Tech 84(8):1223. https://doi.org/10.1002/cite.201250497

2. Becker M, Franke R, Hamann I (2014) Mehr Einblicke in Blasensäulen," elements, vol 2/2014, pp 30–35

3. Rollbusch P et al (2015) Bubble columns operated under industrially relevant conditions—current understanding of design parameters. Chem Eng Sci 126:660–678. https://doi.org/10.1016/j.ces.2014.11.061

4. Schäfer R, Merten C, Eigenberger G (2002) Bubble size distributions in a bubble column reactor under industrial conditions. Exp Therm Fluid Sci 26(6):595–604. https://doi.org/10.1016/S0894-1777(02)00189-9

5. Clark KN (1990) The effect of high pressure and temperature on phase distributions in a bubble column. Chem Eng Sci 45(8):2301–2307. https://doi.org/10.1016/0009-2509(90)80109-R

6. Pohorecki R, Moniuk W, Zdrójkowski A, Bielski P (2001) Hydrodynamics of a pilot plant bubble column under elevated temperature and pressure. Chem Eng Sci 56(3):1167–1174. https://doi.org/10.1016/S0009-2509(00)00336-5

7. Schäfer R (2004) Bubble interactions, bubble size distributions and reaction kinetics for the autocatalytic oxidation of cyclohexane. University of Stuttgart

8. Kubas GJ, Monzyk B, Crumblis AL (1990) Tetrakis(Acetonitrile)Copper(1+) Hexafluorophosphate(1-). Inorganic Syntheses, pp 68–70, 01 Jan 1990. https://doi.org/10.1002/9780470132593.ch15

9. Land EJ, Ramsden CA, Riley PA (2003) Tyrosinase autoactivation and the chemistry of ortho-quinone amines. Acc Chem Res 36(5):300–308. https://doi.org/10.1021/ar020062p

10. Huang Z, Lumb J-P (2016) A catalyst-controlled aerobic coupling of ortho-quinones and phenols applied to the synthesis of aryl ethers. Angew Chem Int Ed 55(38):11543–11547. https://doi.org/10.1002/anie.201606359

11. Brückner R (2004) Reaktionsmechanismen. Organische Reaktionen, Stereochemie, Moderne Synthesemethoden, 3rd edn. Springer Spektrum Akademischer Verlag, Berlin

12. Schore KPC, Vollhardt NE (2011) Organische Chemie, 5th edn. Wiley-VCH, Weinheim

13. Kubas GJ, Monzyk B, Crumbliss AL (1979) Tetrakis(Acetonitrile)Copper(I) Hexafluorophosphate. Inorganic Syntheses, pp 90–92, 01 Jan 1979. https://doi.org/10.1002/9780470132500.ch18

14. Taborda MA, Sommerfeld M, Muniz M (2021) LES-Euler/Lagrange modelling of bubble columns considering mass transfer, chemical reactions and effects of bubble dynamics. Chem Eng Sci 229: https://doi.org/10.1016/j.ces.2020.116121

Further Demand in Fundamental Research

Michael Schlüter

Abstract After six years of research, new methods are available to get deeper insights into the interplay between chemical reactions and fluid dynamics. It has been shown that adjusting the local fluid dynamics in bubble wakes can offer promising opportunities for optimizing the yield and selectivity of competitive-consecutive reactions. Nevertheless, it became clear that more fundamental research is necessary in future. More sophisticated experimental and numerical methods with high spatial and temporal resolution are necessary, to discover the influences of fluid dynamics on yield and selectivity and bridge the scales to chemical engineering. However, the results from this priority program impressively demonstrate the great potential of close collaboration between process engineers and chemists. The new methods developed in this collaborative program may pave the way for a more sustainable chemical production in future.

This book reveals that an optimisation of chemical reactions in gas-liquid flows concerning yield and selectivity is possible by adjusting the fluid dynamics. On the other hand, however, it also makes clear that an enormous effort is required and progress can only be achieved if scientists from different disciplines work closely together. In particular, a bridge between chemistry and process engineering is needed to pave the way from the synthesis of certain molecules for analysis purposes to the production of sustainable bulk chemicals for our population.

How can the kinetics of a reaction network be adapted to the fluid dynamical time scales in technical apparatuses? How can the fluid dynamical time scales in a technical apparatus be adapted to the demand of a chemical reaction yield and selectivity? What are the critical reaction steps (gross kinetics) that have to be controlled and how is this possible by tailoring the mixing and residence time distribution under industrial conditions?

M. Schlüter (✉)
Institute of Multiphase Flows, Hamburg University of Technology, Eißendorfer Straße 38, 21073 Hamburg, Germany
e-mail: michael.schlueter@tuhh.de

We have seen, that new methods are now available to get deep insights into the interplay between chemical reactions and fluid dynamics but on the other hand it becomes clear that these insights are only possible through tiny windows under ideal and very specific conditions.

To widen these insights to cover more industrially relevant processes and to make this new knowledge and the recent methods applicable to the daily production, more sophisticated experimental methods are required for analytics (e.g. spectroscopy methods with higher temporal and spatial resolution as well as applicability to more substances, e.g. via multidimensional spectroscopy as combination of UV/VIS-spectroscopy with IR und fluorescence-spectroscopy) and numerical simulations (e.g. more powerful computations and machine learning algorithms to resolve large amounts of bubbles and its wake structures). This requires a second bridge between experiments and numerical simulations, since several processes are not accessible with experimental methods and many natural processes are not yet understood and computable with existing models.

For example, coalescence and break-up of bubbles is still not fully understood and has not been addressed in this book as well as dense bubbly flows and contamination effects, e.g. due to surfactants. Furthermore, non-Newtonian fluids are not covered as well as three phase flows.

From this point of view, substantially more fundamental research is necessary in the future and the research in the Priority Programme 1740 "Reactive Bubbly Flows" gives a strong impetus for intense and persistent further efforts in this field.

However, it has been shown that better control of yield and selectivity by adjusting fluid dynamics in gas-liquid reactions is a powerful lever for process optimization and can pave the way for a more sustainable chemical production in future.